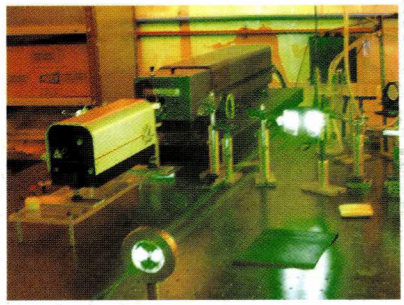
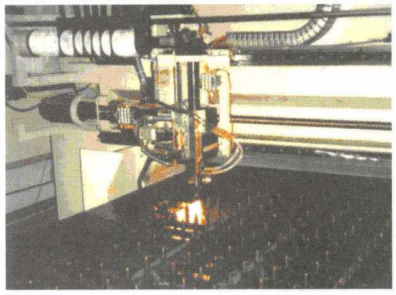
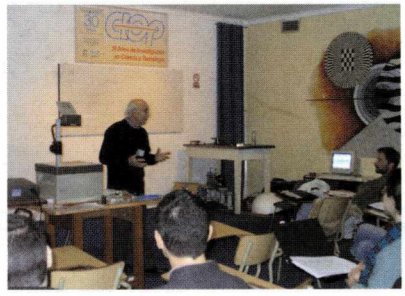










30 años

(1977 - 2007)

Centro de Investigaciones Ópticas

CONICET

Comisión de Investigaciones Científicas

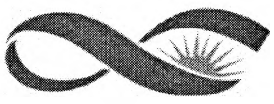
Gobierno de la Provincia de Buenos Aires

30 años

(1977 - 2007)



Centro de Investigaciones Ópticas



CONICET

Comisión de Investigaciones Científicas



Gobierno de la Provincia de Buenos Aires

CIOp 30 años / compilado por Marcelo Trivi; Daniel Schinca; Claudia González
- 1° Edición -

La Plata: Centro de Investigaciones Ópticas (CONICET - CIC); La Plata, 2007
560 p.; 21 x 29,7 cm.

ISBN 978-950-692-075-3
Edición bilingüe: español, inglés.

1. Investigación Científica Argentina. I. Trivi, Marcelo, comp. II Schinca, Daniel, comp.
III González, Claudia, comp.
CDD 001.429 82

Todos los derechos reservados / Hecho el depósito que marca la Ley N° 11.723

ISBN 13: 978-950-692-075-3

La edición de este libro fue financiada en parte por la Comisión de Investigaciones Científicas de la Provincia de Buenos Aires.

Autoridades CONICET

PRESIDENTE

Dr. Eduardo Hernán CHARREAU

VICEPRESIDENTE DE ASUNTOS CIENTÍFICOS

Dr. Ricardo Norberto FARIAS

VICEPRESIDENTE DE ASUNTOS TECNOLÓGICOS

Dr. Mario José LATTUADA

DIRECTORES

Lic. Carlos DEBANDI
Dr. Luis María FERNÁNDEZ
Dra. Noemí María GIRBAL BLACHA
Sr. Carlos Alberto MARTINEZ
Dr. Carlos W. RAPELA
Dr. Faustino SIÑERIZ

Autoridades CIC

PRESIDENTE

Dr. Néstor Julio AUZA

DIRECTORIO

Dr. Rodolfo Daniel BRAVO (Vicepresidente)
Lic. Jorge Luis CAJAL
Lic. Conrado Daniel Antonio GONZALEZ
Dr. Mario Alberto Juan MARISCOTTI

SECRETARIO ADMINISTRATIVO

Contador Fernando ROSSI

DIRECTOR DE ADMINISTRACION

Sra. Maria Rosa DI SOMMA

DIRECTOR DE SERVICIO DE PLANIFICACION Y COORDINACION CIENTIFICA Y TECNOLOGICA

Ing. Agr. José M. RODRIGUEZ SILVEIRA

Centro de Investigaciones Ópticas (CONICET – CIC)

Dirección Postal: Camino Parque Centenario e/ 505 y 508
Manuel B. Gonnet – La Plata
Dirección Postal: Casilla de Correo 124 – B1902WAB – La Plata – Argentina
Teléfonos: + 54 221 484 2957 / 484 0280
Fax: +54 221 471 2771
e-mail: info@ciop.unlp.edu.ar / www.ciop.unlp.edu.ar

Autoridades CIOp

DIRECTOR
Dr. Jorge Omar TOCHO

SUBDIRECTOR
Dr. Marcelo TRIVI

CONSEJO DIRECTIVO

Miembros titulares
Dr. Nestor A. BOLOGNINI
Dr. Ricardo DUCHOWICZ
Dr. Fausto O. BREDICE
Lic. Ricardo A. ARIZAGA
Ing. Pablo COSTANZO

Miembros suplentes
Dr. Héctor J. RABAL
Dra. Lucía B. SCAFFARDI
Ing. Anibal P. LAQUIDARA
Dr. Christian CUADRADO LABORDE

Índice

Prólogo

El CIOp, origen y trayectoria institucional 1

Breve reseña 3

Integrantes 5

Líneas de trabajo actuales 9

- Ablación, limpieza y restauración con láser 11
- Contaminantes atmosféricos 14
- Espectroscopia atómica 15
- Fenómenos dinámicos mediante técnicas de biospeckle 17
- Fotofísica de moléculas en solución y sistemas de interés biológico 19
- Materiales optoelectrónicos 21
- Metrología para las comunicaciones ópticas 23
- Procesamiento opto-digital de información: cristales fotorrefractivos, holografía dinámica, speckle 25
- Propagación de la luz y formación de imágenes a través de medios turbios y turbulentos 27
- Scattering óptico 29

Selección de trabajos 31

Espectroscopía atómica y aplicaciones 33

- Espectroscopia atómica 35
- Medición de gases contaminantes atmosféricos 117

Fibras Ópticas 135

Física del láser y aplicaciones 161

- Ablación, limpieza y restauración con láser 165
- Fotofísica de moléculas en solución y sistemas de interés biológico 181
- Láseres de colorante 203
- Láseres de estado sólido 217
- Láseres gaseosos 237
- Medición del tamaño de partículas 255
- Óptica integrada 281
- Pulsos cortos 297

Óptica física y aplicada 311

- Holografía 315
- Metrología empleando técnicas optoelectrónicas 325
- Óptica física y propagación de ondas 353
- Procesamiento óptico fotorrefractivo 417
- Procesamiento por medio de speckle digital 435
- Speckle dinámico 461
- Speckle modulado 481

Patentes, desarrollo de instrumentos y servicios 505

- Patentes
- Instrumentos
- Servicios

Publicaciones 525

Epílogo 557

Prólogo

Prólogo

No resulta tarea fácil presentar 30 años de vida institucional del Centro de Investigaciones Ópticas (CIOp), los cuales se cumplen el 12 de septiembre de 2007. Desde aquél lejano 1977, el Centro ha pasado por las mismas circunstancias que enmarcaron la historia de nuestro país, con períodos de sombras y luces que estuvieron presentes en toda su trayectoria. Sin embargo, el espíritu y la contracción al trabajo de todos los integrantes que pasaron por el Centro nunca decayeron y hoy podemos decir con orgullo que los 30 años de dedicación a la investigación científica y tecnológica en el área de la Fotónica, la Óptica y las Tecnologías de la Luz, llevaron al CIOp a ser uno de los Centros mas importantes del país y un referente en Latinoamérica en estas áreas del conocimiento. También ha alcanzado proyección mundial mediante una permanente presencia en distintos ámbitos a través de publicaciones en los medios más prestigiosos, la asistencia de sus integrantes a los principales Congresos y Reuniones, el dictado de cursos y seminarios en importantes instituciones del país y del extranjero y la visita al CIOp de Nicolaas Bloembergen, quien en 1981 obtuviera el Premio Nobel de Física, George Porter (Premio Nobel de Química 1967), y de los mas relevantes científicos de la especialidad, entre ellos Miguel Andrés, Pedro Andrés, Toshimitsu Asakura, Christopher Dainty, Maurice Françon, Joseph Goodman, Werner Juptner, Herwig Kogelnik, Emmet Leith, Indrek Martinsson, Giuseppe Molesini, Geoffry New, Jorge Ojeda Castañeda, Reiner Roehler, Willy Persson, Sune Svanberg, Hans Tiziani, Charles Vest, Jean Vienot, James Wyant y María Yzuel

Por todo ello, creemos que los objetivos iniciales que se propusieron cuando el Centro fue creado han sido cumplidos y los logros alcanzados han sentado las bases para encarar en el futuro nuevos desafíos que el desarrollo de la ciencia y la técnica nos imponen dentro de una de las ramas más dinámicas del conocimiento. Los integrantes del CIOp estamos convencidos que podemos realizar los esfuerzos para profundizar las líneas de trabajo existentes y abrir otras nuevas para mantener la competitividad internacional de nuestra institución, como así también transferir los resultados a nuestra sociedad y junto con otros colegas científicos y tecnólogos argentinos aportar nuestro pequeño grano de arena para el desarrollo del país.

Este libro que hoy presentamos es un esfuerzo muy grande de la comunidad que integra el CIOp para realizar un resumen de sus actividades y sus logros. Por supuesto que plasmar en unas cuantas páginas 30 años de trayectoria es una tarea casi imposible y necesariamente incompleta. Sin embargo, consideramos que es válido el intento y esperamos que las instituciones que nos patrocinan y los colegas que nos acompañan valoren esta presentación algo informal que cuenta el trabajo de nuestra gente desde 1977 hasta el presente. También es una manera de mirarnos a nosotros mismos, saber donde llegamos y ayudarnos a proyectar nuestro futuro.

Claudia Gonzalez, Daniel Schinca, Marcelo Trivi

Preface

It is not an easy task to present an outline of the institutional life of the Centro de Investigaciones Ópticas (CIOp), whose 30th anniversary is due on September 12, 2007.
Since 1977, our Center went through the same circumstances as the country did, with alternating periods of light and shadows. However, the high spirit and dedication to scientific and technological research work in the areas of Photonics, Optics and Light Technologies of its entire staff pushed the Center through these 30 years to a high rank level in the country and in Latinamerica. It is also well known worldwide through its hundreds of publications in peer-reviewed international journals, congress presentations, lectures and seminars in national scientific institutions and relevant international research visitors, including Nobel laureates George Porter and Nicolaas Bloembergen, and worldwide pioneering scientists like Miguel Andrés, Pedro Andrés, Toshimitsu Asakura, Christopher Dainty, Maurice Françon, Joseph Goodman, Werner Juptner, Herwig Kogelnik, Emmet Leith, Indrek Martinsson, Giuseppe Molesini, Geoffry New, Jorge Ojeda Castañeda, Reiner Roehler, Willy Persson, Sune Svanberg, Hans Tiziani, Charles Vest, Jean Vienot, James Wyant y María Yzuel, among others.

We believe that the initial goals proposed when the Center was created have been successfully met and the achievements of these 30 years set the basis for facing the new challenges that science and technology put forward in such a rapidly evolving area as Optics and Photonics. We are persuaded that we can put all the necessary effort to continue the current lines of research and open new ones to keep the Center at an international competitive level as well as to transfer the results of our research to society, joining with other colleagues to the development of our country.

The present book has been done thanks to the effort of the CIOp community in outlining 30 years of activities and achievements, a task forced to be incomplete. We hope that our sponsoring institutions and colleagues enjoy this somewhat informal presentation of our history since 1977. It is also a way of looking to ourselves; see where we are standing and where to head our steps in the future.

Claudia Gonzalez, Daniel Schinca, Marcelo Trivi

El CIOp, origen y trayectoria institucional

Breve reseña

Integrantes

Líneas de trabajo actuales

Breve Reseña Histórica

En 1905 fue constituida la Universidad Nacional de La Plata (UNLP) y - dentro del esquema académico de su fundador, el Dr. Joaquín V. González - se creó el Instituto de Física, luego Departamento de Física de la novel universidad platense de clara orientación científica. Sesenta años después dentro del Departamento de Física se estableció el Laboratorio de Espectroscopia, Optica y Láser (LEOL).

El LEOL contó desde su inicio con tres Secciones: la Sección de Espectroscopía Óptica - de fuerte inserción desde la misma creación del Instituto de Física, la Sección de Espectroscopía Láser - iniciada en 1966 respondiendo a un hecho histórico incontrastable: la aparición del láser en 1960- y la Sección de Interferometría y Holografía, iniciada en 1969.

Las actividades del LEOL fueron facilitadas por los valiosos aportes, mediante subsidios o cesión de instrumental o materiales, de la Universidad de Uppsala (Suecia), Consejo Nacional de Investigaciones Científicas y Técnicas (CONICET), Comisión de Investigaciones Científicas de la Provincia de Buenos Aires, Comisión de Investigación Científica de la Universidad Nacional de La Plata y Organización de los Estados Americanos. Los presupuestos propios del Departamento de Física de la Universidad Nacional de La Plata contribuyeron decididamente al establecimiento de las facilidades experimentales del Laboratorio como así también a satisfacer en gran medida los requerimientos bibliográficos y la imprescindible infraestructura técnica."

En 1974 se realizaron unos ensayos metrológicos fuera del LEOL para determinar ópticamente la calidad de las mesas de granito. Para ello se implemento en el Laboratorio de Ensayos de Materiales e Investigaciones Tecnológicas (LEMIT), dependiente del Ministerio de Obras Publicas de la Provincia de Buenos Aires, un experimento interferencial cuyos resultados se presentaron en la Conference on Laser Engineering and Applications, realizada en Washington, D.C. del 28 al 30 de mayo de 1975.

Ese antecedente motivó en 1976 al entonces Director del LEMIT, Ing. Luis A. Bonet, a sugerir que el personal del LEOL con parte su instrumental, trasladado temporalmente a uno de los pabellones del LEMIT en su sede de la localidad de Manuel B. Gonnet, pudieran emprender otras experiencias metrológicas, como la determinación de la calidad de los vidrios para la construcción, estudiar la factibilidad del empleo de láseres con emisiones visibles o infrarrojas en la determinación de la vertical o del plano horizontal del lugar, o introducir técnicas de *moire* para aplicaciones metrológicas. La Facultad de Ciencias Exactas prestó acuerdo al emprendimiento, permitiendo con ello una fructífera actividad de complementación, la que abrió posibilidades de realización de servicios de gran magnitud, como los realizados para la entonces empresa de Servicios Eléctricos del Gran Buenos Aires (SEGBA) para "determinar desplazamientos muy pequeños que sufren las vigas principales de las fundaciones de las turbinas", en 1975, o para los Astilleros y Fabricas Navales del Estado (AFNE) para "determinar la alineación y paralelismo de dos ejes en la maquina de timón de un buque en construcción en nuestro Astillero", en 1976.

Así las cosas, el LEMIT consideró la posibilidad de ofrecer al LEOL la constitución de un centro de investigaciones ópticas básicas y aplicadas, el que, además, debería ofrecer servicios, y debía contar con el sustento de la UNLP y del CONICET. Hacia fines de 1976 la entidad ya tenia designación -Centro de Investigaciones Ópticas (CIO)- y hasta se proyectaba un edificio para alojarlo en la sede del LEMIT en la localidad de Manuel B. Gonnet.

Las gestiones para este nuevo emprendimiento culminaron en setiembre de 1977 con la firma de un convenio entre el CONICET, la UNLP y el LEMIT, dependiente del Ministerio de Obras Publicas de la Provincia de Buenos Aires. Por entonces se mantuvo la denominación de Centro de Investigaciones Ópticas y se pensó en utilizar sigla CIO para su identificación. Esto cambió al intentar registrar dicha sigla en el CONICET. El día anterior a la presentación de la propuesta, el Centro de Investigaciones Oceánicas había registrado CIO como su sigla identificatoria en el CONICET. Por ello, al Centro de Investigaciones Ópticas se lo identifica desde entonces con su sigla CIOp. Y aquí comienza la historia que ahora ya lleva 30 años.

El CIOp, constituido el 12 de septiembre de 1977, nació por el impulso y la tenacidad del Dr, Mario Garavaglia, el Dr. Mario Gallardo y un pequeño grupo de jóvenes investigadores y becarios que se desempeñaban en el LEOL. En 1979, por Decreto N° 1476/79 del Poder Ejecutivo de la Provincia de Buenos Aires, el LEMIT es transferido a la Comisión de Investigaciones Científicas de la Provincia de Buenos Aires (CIC). La CIC tomó entonces el lugar del LEMIT entre las instituciones que patrocinan al CIOp. El 18 de noviembre de 1985, fue firmada por el CONICET, la UNLP y la CIC un acta de rescisión del Convenio de Constitución de Centros e Institutos, por la que el CIOp pasó a depender jurídica, orgánica y administrativamente de la CIC. El 2 de mayo de 1991, se firma entre el CONICET y la CIC un nuevo Convenio de Colaboración para el funcionamiento y desarrollo del instituto, pasando el CIOp, a depender nuevamente de las dos instituciones. Esta situación se mantiene en la actualidad. En estos 30 años de trayectoria sus directores fueron Mario Garavaglia (1977-1992), Mario Gallardo (1992-2004), Jorge Reyna Almandos (2004) y Jorge Tocho desde 2005.

El Centro de Investigaciones Ópticas (CIOp) es un Instituto que desde hace 30 años está dedicado a la investigación científica y tecnológica en el área de la Fotónica, la Óptica y las Tecnologías de la Luz. Desde su creación, los objetivos del CIOp son:

- Realizar investigación científica, tecnológica y desarrollos en el campo de la óptica, el láser, la fotónica, las tecnologías de la luz y temas afines.
- Asesorar a entes públicos y privados de producción de bienes y servicios, contribuyendo a la transferencia de conocimientos, técnicas y metodologías.
- Contribuir a la formación, perfeccionamiento y actualización de graduados universitarios, profesores y técnicos.
- Difundir los resultados de su trabajo (publicaciones, congresos, reuniones científicas, medios masivos de difusión, etc.)
- Establecer relaciones con instituciones del país y del exterior para organizar programas de intercambio científico y/o tecnológico.

Los principales logros del Centro en sus primeros 30 años de vida se resumen a continuación:

- Los integrantes del CIOp han realizado más de 600 publicaciones en revistas científicas con referato y más de 350 presentaciones a Congresos nacionales e internacionales.
- En nuestro Centro han obtenido su título de Dr. en Física o Ingeniería 37 graduados y más de 40 estudiantes han realizado su proyecto final profesional en Física e Ingeniería. Se ha atendido la formación de más de 75 becarios de universidades nacionales y extranjeras.
- El CIOp ha organizado de manera regular el dictado de 35 cursos de postgrado contribuyendo a consolidar la formación de más de 1.000 participantes. Nuestros investigadores han dictado más de 50 cursos y seminarios en Universidades de Argentina y el exterior.
- Se ha recibido la visita programada de más de 130 investigadores extranjeros y se ha participado en la organización de diversas Reuniones Científicas a nivel nacional e internacional.
- El CIOp ha brindado numerosos servicios tecnológicos de variada complejidad a empresas e instituciones públicas del país y del exterior.
- Más de 30 convenios de cooperación científica, tecnológica, intercambio de investigadores, etc. han sido firmados con Universidades, Centros y otras instituciones del país y del exterior.

Brief Historic Outline

The National University of La Plata (UNLP) was founded in 1905, and within the academic scope of his Founder, Dr. Joaquin V. Gonzalez, the Physics Institute was created. After an academically reorganization into Faculties, the Physics Institute resulted in the Physics Department, under a clear scientific orientation. Sixty years after this reorganization took place, the Laboratory of Spectroscopy, Optics and Lasers (LEOL) was started.

LEOL initially consisted in three Sections: Optical Spectroscopy - of strong insertion since the origins of the Physics Institute-, Laser Spectroscopy - originated in 1966 from a historical fact: the Laser invention in 1960 - and Interferometry and Holography since 1969.

LEOL's activities were prompted by "the valuable support, thanks to grants or instruments and material donations, from the following Institutions: Uppsala University (Sweden), Argentinean Research Council (CONICET), Commission for Scientific Research from the State of Buenos Aires, and the Organization of American States. The own budgets from the Physics Department definitely sustained the building of experimental facilities as well as to satisfy the Librarian and technical infrastructure".

During 1974, metrological essays were developed to optically determine the quality of granite tables. To this end, an interferential experiment was implemented in the Laboratory for Material Essays and Technological Research (LEMIT). The results were presented in the Conference on Laser Engineering and Applications, held at Washington, D.C. in May 1975.

This motivates the former LEMIT Director Ing. Luis Bonet, to suggest that the LEOL personnel, along with part of their instruments be temporally moved to the LEMIT offices at Manuel B. Gonnet. The aim was to accomplish further metrological experiences such as the building-glass quality assessment, the feasibility for determining in-place verticality or horizontality using visible or IR laser emissions, or introducing moiré techniques. The Faculty of Exact Sciences acknowledged this agreement, allowing a fruitful activity besides opening possibilities to bring services like the ones to the former Electrical Services (SEGBA) to size small displacements of turbine foundation levers in 1975 or to the State Naval Shipyards and Industries (AFNE) to certify the alignment and parallelism of two axis from the wheel machinery in a ship under construction in the shipyard in 1976.

In light of this situation, the LEMIT considered the chance to offer LEOL the formation of a basic and applied optics research center, which should also have the commitment to bring metrological assistance, and have the support from the UNLP and CONICET. By the end of 1976, this institute has a name Centro de Investigaciones Ópticas (CIO). The project included the use of a building in the LEMIT premises at Manuel B. Gonnet.

The approaches to this new settlement ended in September 1977 with a signed agreement among the CONICET, UNLP, and LEMIT. At that time, the denomination as Centro de Investigaciones Ópticas was kept, along using CIO for short. Although the situation changed when trying to register such abbreviation at CONICET. The day before the Oceanic Research Center registered CIO as identifying abbreviation. Due to this fact, the Centro de Investigaciones Ópticas is nowadays identified with CIOp. From here starts our present history, now reaching his 30 years.

The Centro de Investigaciones Ópticas (CIOp) is a 30 year old Institute devoted to scientific and technological research in the area of Photonics, Optics and Light Technologies.
It was created on September 12, 1977 by an official agreement between the Consejo Nacional de Investigaciones Científicas y Técnicas (CONICET), the Universidad Nacional de La Plata (UNLP) and the Laboratorio de Ensayo de Materiales e Investigaciones Tecnológicas (LEMIT). It was born due to the effort of Dr. Mario Garavaglia, Dr. Mario Gallardo and small group of yaung researchers and fellows belonging to the Laboratorio de Espectroscopía, Óptica y Láser (LEOL) del Departamento de Física de la Facultad de Ciencias Exactas de la UNLP, which was active since 1965. In 1979, LEMIT was transferred to the Comisión de Investigaciones Científicas de la Provincia de Buenos Aires (CIC). Since then, CIC is one of CIOp´s state-government sponsoring institution.
In November 18, 1985, CONICET, UNLP and CIC agreed a new way for Center´s management, by which CIOp depended organically of CIC. After that, on May 2, 1991, CIC and CONICET signed a new agreement by which CIOp depend on both granting institutions and which is the current administrative status.
During these 30 years, the responsibility of the direction of the Center fell on Dr. Mario Garavaglia (1977-1992), el Dr. Mario Gallardo (1992-2004), el Dr. Jorge Reyna Almandos (2004) y el Dr. Jorge Tocho, from 2005.

Since its creation, the objectives of CIOp are:

- *Conduct scientific and technological research in the area of Photonics, Optics, Lasers and Light Technologies.*
- *Advisory of public and private Offices and Bureaus, contributing to the transfer of knowledge, techniques and methods in the area of Optics and Lasers.*
- *Publish its results in international journals and congresses.*
- *Contribute to the formation teachers, university graduates and technicians in Optics.*
- *Establish cooperative relations with national and foreign institutions to enhance scientific and technological programs.*

The main achievements of CIOP in its first 30 years are:

- *More than 600 refereed publications in international journals together with more than 350 national and international congress presentations.*
- *37candidates have received their Ph.D. degree in Physics or Engineering at our Center, together with more than 40 students made their Final Project in the same disciplines.*
- *More than 75 fellowship-holders from national and foreign universities passed through our laboratories.*
- *CIOp has regularly organized and lectured 35 postgraduate courses contributing to the formation of more than 1000 participants.*
- *More than 135 foreign relevant scientific researchers visited the Center and have participated in the organization of several international and local scientific meetings.*
- *More than 30 scientific cooperation agreements were signed with universities and research centers worldwide.*

Integrantes / Staff

Investigadores / Researches

Dr. BILMES, Gabriel M.	Inv. Principal - CIC
Dr. BOLOGNINI, Néstor A.	Inv. Principal - CONICET
Dr. BRÉDICE, Fausto O.	Inv. Independiente - CIC
Dr. DUCHOWICZ, Ricardo	Inv. Independiente - CONICET
Dr. GALLARDO, Mario O.	Inv. Principal - CONICET
Dr. GARAVAGLIA, Mario J.	Inv. Superior - CONICET
Dr. ORZI, Daniel	Inv. Asistente - CIC
Dr. RABAL, Héctor J.	Inv. Principal - CONICET
Dra. RAINERI, María Mónica	Inv. Adjunto c/director - CIC
Dr. REYNA ALMANDOS, Jorge G.	Inv. Principal - CIC
Dra. RUSSO, Nélida A.	Inv. Adjunto c/director - CIC
Dra. SCAFFARDI, Lucía B.	Inv. Independiente - CONICET
Dr. SCHINCA, Daniel C.	Inv. Adjunto s/director - CIC
Dra. TEBALDI, Myrian C.	Inv. Adjunto - CONICET
Dr. TOCHO, Jorge O.	Inv. Principal - CONICET
Dr. TORCHIA, Gustavo	Inv. Asistente - CONICET
Dr. TORROBA, Roberto D.	Inv. Principal - CONICET
Dr. TRIVI, Marcelo R.	Inv. Principal- CIC
Dra ZERBINO, Lía María	Inv. Adjunto – CONICET
Dr. ZUNINO, Luciano J.	Inv. Beca Interna Doctoral - CONICET

Personal profesional / Professional Staff

Lic. ARIZAGA, Ricardo A.	Pofesional Principal - CONICET
Ing. BAVA, Alberto J.	Profesional Principal - CONICET
C.C. CAP, Nelly Lucía	Profesional Principal - CIC

Ing. CORTIZO, Eduardo C.	Profesional Principal - CIC
Ing. FRECCERO, Ruben E	Profesional Principal - CONICET
Bibl. GONZALEZ, Claudia M.	Profesional Asistente - CONICET
Ing. GRUMEL Eduardo E.	Profesional Principal - CIC
Ing. LAQUIDARA, Aníbal .	Profesional Principal - CONICET
Ing. NORIEGA, Sergio B.	Profesional Principal - CIC
Arq. RODRIGUEZ, Alexander	Profesional Principal - CONICET
Sr RODRIGUEZ, Edmundo J.	Profes. Asistente - CONICET
Lic. RUIZ, Beatriz N.	Profesional Principal - CONICET
Ing. VIDELA, Fabián A.	Profesional Asistente - CIC
Srta SEGOVIA, Vanessa	Soporte Informático

Becarios / Fellows

Lic. ALVIRA, Fernando	Beca - CIC
Ms. AMAYA ROBAYO, Dafne	Beca Doctoral Latinoamericana. - CONICET
Ing. COSTANZO, Pablo	Beca Doctoral Tipo II - CONICET
Dr. CUADRADO LABORDE, Christian	Beca Interna Postdoctoral - CONICET
Sr. DORBESI, Christian	Beca Entrenamiento - CIC
Sr. ENCINAS, Diego	Beca Entrenamiento - CIC
Srta. FACCIA, Paula	Beca Entrenamiento - CIC
Sr. LAMBERT, Claudio	Beca Entrenamiento - CIC
Srta. LARRAÑAGA, Carolina	Beca Entrenamiento - CIC
Dr. LENCINA, Alberto	Beca Interna Postdoctoral - CONICET
Ing. Fis. MOSSO, Edward Fabián	Beca Doctoral Latinoamericana. - CONICET
Ing. Elec. SENDRA, Hernán	Beca Doctoral Tipo II - CONICET
Ing. Agr. WEBER, Cristian	Beca Doctoral Tipo II- CONICET

Personal técnico y artesano / Technical Staff

Sra BRUNATTI, Raquel E.	Artesano Asociado - CONICET
Sr MELGAREJO, Ramón O.	Técnico Asociado - CONICET
Sr PIANCA, Daniel C.	Técnico Principal - CIC
Sr RAMPINI, Edgardo A.	Técnico Asistente - CONICET
Sra. ROBERTS, Adriana	Técnico Principal - CONICET

Personal administrativo / Administrative Staff

Sr. CANTEROS, Rolando D.	Categoría 04 - CIC
Lic. FORTE, Gustavo	Categoría 04 -
Sr. LOPEZ COSTA, Alexis	Categoría 04 - CIC
Sr. MANTESA, Augusto M.	Categoría 04 - CIC
Sr. MARIÑO, Raul H.	Categoría 17- CIC
Sr. CANEVARO, Reynaldo	Chofer - CIC



Líneas de trabajo actuales
Research lines



Ablación, limpieza y restauración con láser

Responsable: Dr. Gabriel M. Bilmes
Integrantes: Dr. Daniel J. Orzi
Lic. Fernando Alvira
Est. Leandro Jofré
Alberto Orsetti (Restaurador, Director del área de Restauración de la Secretaría de Cultura del Gobierno de la Ciudad de Bs.As.).

Temas de Investigación:

Investigación, desarrollo y servicios en el área de limpieza, restauración, análisis de superficies y caracterización de materiales, utilizando técnicas láser.
Limpieza por ablación láser de suciedad superficial de objetos de valor patrimonial (papeles antiguos, manuscritos, esculturas, piezas de vidrio, metal, tela o cuero).
Caracterización de composición elemental de materiales por medio de Espectroscopía de Plasmas generados por Ablación Láser (LIBS).
Desarrollo de métodos e instrumentos para aplicaciones industriales y control de calidad de procesos basados en técnicas ópticas y espectroscópicas, fotoacústicas y de luminiscencia.
Dictado de cursos de especialización en el tema Restauración y limpieza con láser, dirigido a restauradores, arquitectos, ingenieros, físicos, artistas, etc.

Trabajos más relevantes:

- Se inventó y patentó (AR 9906271. Argentina) un método para la Determinación de Suciedad en Superficies basado en ablación láser y detección acústica. Applied Physics B. 82, 643. (2006).
- Se inventó, patentó (P000101241- Argentina y Patente 6.546.784 de15-4-2003 al 15-4-2021en EEUU), construyó e instaló en la Empresa SIDERAR - Ensenada (Bs.AS- Argentina) el primer instrumento a nivel mundial que mide a tiempo real y en forma automática, la suciedad de chapas de acero producidas por laminación -ELMES 1: Equipo láser para medición de suciedad (Review of Progress in Quantitative Nondestructive Evaluation.Vol. 20,1944. American Institute of Physics, New York, . 2000. Surface Engineering Vol.18 N°1. 2002 y Latin American Applied Research. Vol.32 N3-263- 2002). Ver presentación Flash
- Se inventó y patentó (Reg. 18/99 CUBA) un método para la limpieza de vidrios con láser. (Laser cleaning of glassware by opposite incidence- III International Conference on Lasers in the Conservation of Artworks, Italia 1999).
- Se determinaron los umbrales de fluencia láser de daño y se realizaron trabajos de limpieza y eliminación de manchas en papeles antiguos, libros y manuscritos. (Seminario Iberoamericano sobre Procesamiento de Materiales con Láser, 1999).
- Se desarrolló un método que utiliza procesamiento de imágenes por computadora, para analizar el grado de limpieza de una superficie, cuando esta es tratada por diversos procedimientos, particularmente por técnicas láser (EFING 2000. La Habana-Cuba).
- Se determinó la composición elemental de piezas arqueológicas prehispánicas encontradas en Argentina y Chile mediante la técnica LIBS. Proceedings of the International Syposium on Optical Metrology 2005. International Society for Optical Engineering (SPIE). 2005
- Se desarrolló un método que permite conocer, en forma automática y en línea de producción, la composición cualitativa y cuantitativa de la suciedad superficial presente en chapas producidas industrialmente. Applied Spectroscopy 58, 7028 (2004)
- Se esta estudiando mediante la técnica LIBS, la presencia de trazas de Magnesio y Estroncio en dientes de homínidos, para su empleo como posible indicador alimentario y evolutivo.

Colaboración con otras Instituciones y grupos de Investigación:

- Laboratorio de Electrónica Cuántica- Depto. Física- FCEYN-UBA. Argentina.
- Laboratorio de Tecnología Láser- Universidad de la Habana-Cuba.
- Secretaría de Cultura del Gobierno de la Ciudad de Bs.As.
- Centro de Investigación Industrial -FUDETEC. Argentina.
- Empresa SIDERAR de Argentina

Equipamiento disponible:

- Láseres de Nd-YAG pulsados (1064 nm, 532 nm, 355 nm, 266nm).
- Microscopio.
- Espectrometros con cámaras CCD.
- Espectrofotómetros 200-900 nm.
- Osciloscopios digitales (300 y 150 MHz).
- Sistemas de procesamientos de datos y análisis óptico y acústico del proceso de limpieza.
- Archivo actualizado de antecedentes, trabajos, e imágenes relativas al uso de láser en limpieza y restauración y temas afines.

Ablation, clearing and restoration with lasers

Lines of research:

Research, development and services in clearing, restoration and análisis of surfaces and characterization of materials using laser techniques.
Laser ablation clearing of surface dirt in material of cultural value (antique manuscripts, scultures glassware, leather and fabric)
Elemental composition caracterization of materials using Laser Induced breakdown spectroscopy (LIBS).
Development of methods and instruments for industrial applications and quality control using optical, photoacoustics and luminiscence spectroscopies.
Lecturing on restoration and laser cleaning for architects, engineers, artists and physicists.

Most relevant works:

- *Invention and patenting (AR 9906271. Argentina) of a method for determining surface dirt base don laser ablation and acoustic detection Applied Physics B. 82, 643. (2006).*

- *Invention, patenting (P000101241- Argentina y Patente 6.546.784 de15-4-2003 al 15-4-2021en EEUU), construction and installation at SIDERAR site- Ensenada (Bs.AS-Argentina)- the first worldwide instrument capable of measuring steel-rolls surface dirt automatically and in real time. -ELMES 1: Equipo láser para medición de suciedad (Review of Progress in Quantitative Nondestructive Evaluation.Vol. 20,1944. American Institute of Physics, New York, . 2000. Surface Engineering Vol.18 N°1. 2002 y Latin American Applied Research. Vol.32 N3-263-2002).*

- *Invention and patenting (Reg. 18/99 CUBA) of a method for glassware laser clearing. (Laser cleaning of glassware by opposite incidence- III International Conference on Lasers in the Conservation of Artworks, Italia 1999).*

- *Determination of laser fluence damage threshold and cleaning of antique papers booksand manuscripts. (Seminario Iberoamericano sobre Procesamiento de Materiales con Láser, 1999).*

- *Development of a method based computer image processing for laser assisted surface-cleaning degree analysis (EFING 2000. La Habana-Cuba).*

- *Determination of elemental composition of prehispanic objects found in Argentina and Chile using LIBS. Proceedings of the International Syposium on Optical Metrology 2005. International Society for Optical Engineering (SPIE). 2005*

- *Development of an automatic, in-line method for qualitativeand quantitative determination of surface dirt in industrial rolls. Applied Spectroscopy 58, 7028 (2004)*

- *We are Currently studying the presence of Mg and Sr traces in hominid teeth using LIBS.*

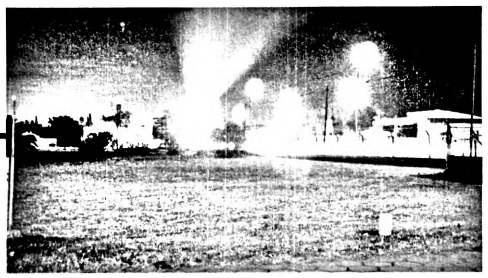
Colaboration with other institutions and Research Groups:

- *Quantum Electronics Lab- Depto. Física- FCEYN-UBA. Argentina.*
- *Laser Technology Lab- Universidad de la Habana-Cuba.*
- *Secretaría de Cultura del Gobierno de la Ciudad de Bs.As.*
- *Industrial research Center -FUDETEC. Argentina.*
- *SIDERAR, Argentina*

Equipment:

- *Pulsed Nd-YAG Lasers (1064 nm, 532 nm, 355 nm, 266nm).*
- *Microscope.*
- *Spectrometers with CCD cameras.*
- *Spectrophotometer 200-900 nm.*
- *Digital oscilloscopes (300 and 150 Mhz).*
- *Optical and acoustical detectors for laser clearing data processing*
- *Updated file of previous Works and images related with laser use for clearing and restoration.*

Contaminantes atmosféricos



Responsable: Dr. Jorge O. Tocho
Integrantes: Dr. Daniel Schinca
Ing. Fabián Videla

Temas de investigación:

Determinación de contaminantes atmosféricos gaseosos y particulados por métodos ópticos.

Trabajos más relevantes:

- Medición de SO2, NO2 en emisiones industriales con técnicas óptias no-dispersivas.
- Medición de ozono estratosférico con absorción diferencial no-dispersiva.
- Medición de SO2, NO2 y ozono con en columna abierta en ambiente urbano utilizando espectroscopía de absorción diferencial (DOAS).
- Medición de NO2 en columna troposférica con DOAS multiaxial.

Equipamiento disponible:

- Modelo de chimenea industrial con calentamiento y tomas de medición central de gases calibrados EPA.
- Interferómetro infrarrojo con transformada de Fourier, resolución máxima 0,125 cm-1.
- Espectrógrafos de 25 cm de focal.
- Espectrógrafo multicanal.
- Medidor no-dispersivo de gases.
- Equipo de absorción óptica diferencial (DOAS) para determinación de SO2, NO2 y ozono en ambientes urbanos.

Atmospheric gas pollutants

Research lines:

Determination of gaseous atmospheric pollutants and particulate matter using optical methods.

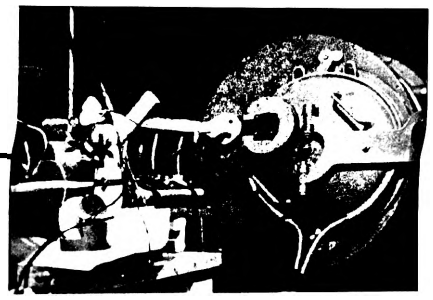
Most relevant works:

- *Determination of SO2, NO2 in industrial emissions with non-dispersive optical techniques.*
- *Measurementof stratospheric ozone concentration by non-dispersive optical techniques.*
- *Measurement of open column SO2, NO2 and ozone in urban environment using differential absorption spectroscopy (DOAS).*
- *Measurement of troposphric column NO2 with multiaxial DOAS.*

Equipment:

- *Industrial chimney lab cell with gas inlets and outlets and crossed optical paths.*
- *Fourier transform IR spectrophotometer, 0.125 cm-1 max resolution*
  25 cm focal length spectrograph.
- *Multichannel spectrograph.*
- *Non-dispersive optival gas detector.*
- *Differential optical absorption equipment (DOAS) for urban air SO2, NO2 and ozone determination.*

Espectroscopía Atómica



Responsable: Dr. Jorge Reyna Almandos
Integrantes: Dr. Mario Gallardo.
Dr. Fausto Bredice.
Dr. Monica Ranieri.

Temas de Investigación:

Espectroscopía atómica de gases nobles mediana y altamente ionizados en las regiones UV-VIS-IR.
Análisis de los espectros obtenidos en el marco de las regularidades propias de la estructura atómica tales como secuencias isoelectrónicas, isonucleares y homólogas.
Utilización de programas de cálculo tipo Hartree-Fock y de diagonalización de matrices de energía para la determinación de niveles de energía, probabilidades de transición, vidas medias y otros parámetros característicos.
Espectroscopia temporal de plasmas generados por pulsos láser (LIBS-OES). Determinación de temperaturas, densidades electrónicas, coeficientes de autoabsorción y caracterización del plasma mediante perturbaciones a campos eléctricos externos.
Aplicaciones tecnológicas de la espectroscopía óptica. Análisis de la radiación emitida por fuentes de iluminación.

Trabajos más relevantes:

Análisis de los espectros realizados (Referenciados por el NIST (National Institute for Standard and Technologies, EE. UU.)

- Xe II, III, IV, V, VI, VII, VIII
- Kr II, III, IV, V, VI, VII, VIII
- Ar III, IV, V, VI, VII,
- Ne II, III, IV

Colaboración con otras Instituciones y grupos de Investigación:

- Grupo de Espectroscopía, Universidad de Lund, Suecia
- Grupo de Fotofísica, CCADET, Universidad Nacional Autónoma de México.
- Applied Laser Spectroscopy Laboratory, Istituto per i Processi Chimico-Fisici (IPCF) CNR, Pisa, Italia
- Laboratorio de Plasma y Espectroscopía Atómica, Universidad Federal
- Fluminense, Niteroi, Brasil
- IFAS, UNCPBA, Tandil
- Facultad de Ciencias Exactas y Naturales, UNMdP
- Instituto de Física de Rosario (IFIR)

Equipamiento disponible:

- 2 espectrógrafos (UV-VIS-IR) montaje Ebert de 3,4 m de distancia focal con detección fotográfica y en tiempo real mediante arreglos de diodos.
- 1 espectrógrafo (V.U.V.) de incidencia normal de 3 m de distancia focal.
- 1 espectrógrafo (V.U.V) de incidencia rasante, de 3 m de distancia focal.
- Monocromador (UV-UV-IR) de 0,5 m de distancia focal equipado con cámara CCD.
- Equipos de alto vacío y fuentes de alta tensión.
- Microdensitómetro Jarrell Ash.

Atomic Spectroscopy

Research Lines:

Atomic spectroscopy of médium and highly ionized noble gases in the UV-VIS-IR region.
Isoelectronic, isonuclear and homolog atomic sequences spectra análisis.
Hartree-Fock and energy matrix diagonalization codes for energy level, transition probabilities and mean-life determination.

Time resolved spectroscopy of laser produced plasmas (LIBS-OES). Determination of electron temperatures, densities, self-absorption coefficients and plasma characterization through electric field perturbation.
Technological applications of optical spectroscopy. Illumination sources spectroscopic analysis.

Most relevant works:

Análisis de los espectros realizados (Referenced by NIST (National Institute for Standard and Technologies,USA.)

- *Xe II, III, IV, V, VI, VII, VIII*
- *Kr II, III, IV, V, VI, VII, VIII*
- *Ar III, IV, V, VI, VII,*
- *Ne II, III, IV*

Collaboration with other institutions and research groups:

- *Lund University Spectroscopy Group, Sweden.*
- *Photophysics Group, CCADET, Universidad Nacional Autónoma de México.*
- *Applied Laser Spectroscopy Laboratory, Istituto per i Processi Chimico-Fisici (IPCF) CNR, Pisa, Italia*
- *Atomic spectroscopy and plasma Lab Universidad Federal Fluminense, Niteroi, Brasil*
- *IFAS, UNCPBA, Tandil*
- *Facultad de Ciencias Exactas y Naturales, UNMdP*
- *Instituto de Física de Rosario (IFIR)*

Equipment:

- *2 UV-VIS-IR Ebert mount 3,4 m focal length spectrographs with photographic and diode array detection.*
- *1 V.U.V. normal incidence 3 m focal length spectrograph.*
- *1 V.U.V. grazing incidence 3 m focal length spectrograph.*
- *1 UV-VIS-IR 0,5 m focal length monochromator with CCD.*
- *High vacuum pumps and lines. High voltage sources.*
- *Microdensitometer Jarrell Ash.*



Fenómenos dinámicos mediante técnicas de biospeckle

Responsables: Dr. Héctor Rabal
Dr. Marcelo Trivi
Integrantes: Lic. Ricardo Arizaga
Lic Beatriz Ruiz
Lic. Nelly Cap
Ing. Eduardo Grumel
Ing. Hernan Sendra
Lic. Paula Faccia

Temas de investigación:

Desarrollo de modelos numéricos para caracterización de speckle dinámico
Desarrollo de métodos de medida de actividad óptica utilizando speckle
Estudio de procesos biológicos e industriales mediante técnicas de speckle

Colaboración con otras Instituciones y grupos de Investigación:

- Facultad Ingeniería U.N. Mar del Plata
- Facultad Ciencias Exactas y Veterinaria U.N. Centro (Tandil)
- Grupo Laser U. Salta.
- IFIR, U.N. Rosario.
- INTA.
- INTI.
- Universidad Federal de Lavras (Brasil).
- U. San Pablo (Brasil).
- UdeAntioquia (Colombia).
- Pontificia Universidad Católica de Perú (Perú).
- Istituto Nazionale di Ottica Applicata (Italia).
- Instituto Politécnico ISPJAE (Cuba).

Equipamiento disponible:

- Mesa antivibratoria "Newport RC"
- 2 Láseres de He-Ne de 10 mW c/u "Melles Griot"
- Componentes ópticos varios de precisión (divisores, polarizadores, espejos, lentes, etc.)
- Procesador de imágenes "Imaging Technology" serie 151.
- Procesador de imágenes "Matrox" Pulsar.
- Posicionador piezoeléctrico de alta precisión con consola de comando "New
- Focus" Modelo Optic Claw.
- Video Printer "Sony".
- 2 Cámaras CCD de video "Pulnix 765".

Study of dynamic processes by biospeckle techniques

Research Lines:

Numerical model development for dynamic speckle characterization.
Development of optical activity measurement methods using speckle.
Study of biological and industrial processes using speckle techniques.

Collaboration with other institutions and research groups:

- *Facultad Ingeniería U.N. Mar del Plata*
- *Facultad Ciencias Exactas y Veterinaria U.N. Centro (Tandil)*
- *Grupo Laser ,Universidad de Salta, Argentina*
- *IFIR, Universidad Nacional de Rosario, Argentina.*

- *INTA.*
- *INTI.*
- *Universidad Federal de Lavras (Brasil).*
- *University of San Pablo (Brasil).*
- *Antioquia University (Colombia).*
- *Pontificia Universidad Católica de Perú (Perú).*
- *Istituto Nazionale di Ottica Applicata (Italia).*
- *ISPJAE (Cuba)*

Equipment:

- *Antivibration table "Newport RC"*
- *2 He-Ne lasers , 10 mW "Melles Griot"*
- *Precision optical components (polarizers, beam splitters, mirrors, lenses, etc.)*
- *Image processor "Imaging Technology" serie 151.*
- *Image processor "Matrox" Pulsar.*
- *High precision piezo positioner "New Focus" Model Optic Claw.*
- *Video Printer "Sony".*
- *2 video CCD cameras "Pulnix 765".*

Fotofísica de moléculas en solución y sistemas de interés biológico

Responsable: Dr. Gabriel M. Bilmes
Integrantes: Lic. Mariana Mesaros
Ing. Anibal Laquidara

Temas de investigación:

Estudio de procesos fotofísicos y fotoquímicos de moléculas en solución, utilizando láseres como fuentes de excitación y técnicas fotoacústicas, espectroscópicas y de luminiscencia para su caracterización y análisis.
Identificación de mecanismos de conversión de energía a estados transientes (tripletes, fotoisómeros, etc.); caracterización de procesos de absorción y emisión de radiación, emisión estimulada, absorción de estados excitados y procesos multifotónicos.
Desarrollo e implementación de técnicas láser de alta resolución y sensibilidad (fotoacústica inducida por láser, fotoacústica resuelta en tiempo, fluorescencia y absorción inducida por láser) para la realización de los estudios propuestos.
Estudio de procesos de cavitación en plantas mediante detección acústica.

Colaboración con otras Instituciones y grupos de Investigación:

- Max-Planck I. fur Strahlenchemie, Mulheim a.d. Ruhr, Alemania (Prof. S.E. Braslavsky).
- Universidad de Parma, Italia, Depto. de Física (Prof. C. Viappiani).
- Universidad de Santander, Bucaramanga , Colombia (Prof. Orlando Haya).
- CIHIDECAR-CONICET, Q. Orgánica, FCEyN-UBA Argentina (Prof. R.Erra-Balsells).
- INIFTA- UNLP-La Plata, Argentina (Dr. Daniel Martire).
- INQIMAE- FCEyN-UBA (Dr. Pedro Aramendia).
- Facultad de Agronomía y Agroindustrias, UNSE, Argentina (Dr. Claudio Borsarelli).
- IFEVA Facultad de Agronomía- UBA.

Equipamiento disponible:

- Láseres de Nd-YAG pulsados (1064 nm, 532 nm, 355 nm, 266 nm) y OPO.
- Láser CW Argón, láser de colorantes continuo.
- Sistemas para mediciones fotoacústicas (celdas, montajes, detectores, procesamiento).
- Sistema de detección de oxígeno singlete.

Photophysics of molecules in solution and biological systems.

Research Lines:

Photophysical and photchemistry processes of molecules in solution using laser based spectroscopic techniques.
Identification of the mechanisms for transient status energy conversion (triplets, photoisomers, etc.); characterization of absorption and emisión processes , excited stateabsorption and multiphotonic processes.
Development of high resolution high sensitivity laser techniques (laser induced photoacoustics, time resolved photoacoustics, laser induced fluorescente and absorption)
Study of cavitation processes in plants through acoustic detection.

Collaboration with other institutions and research groups:

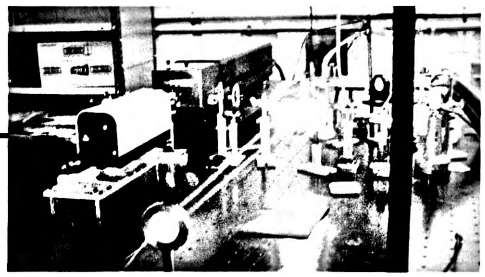
- *Max-Planck I. fur Strahlenchemie, Mulheim a.d. Ruhr, Alemania (Prof. S.E. Braslavsky).*

- *Universidad de Parma, Italia, Depto. de Física (Prof. C. Viappiani).*
- *Universidad de Santander, Bucaramanga , Colombia (Prof. Orlando Haya).*
- *CIHIDECAR-CONICET, Q. Orgánica, FCEyN-UBA Argentina (Prof. R.Erra-Balsells).*
- *INIFTA- UNLP-La Plata, Argentina (Dr. Daniel Martire).*
- *INQIMAE- FCEyN-UBA (Dr. Pedro Aramendia).*
- *Facultad de Agronomía y Agroindustrias, UNSE, Argentina (Dr. Claudio Borsarelli).*
- *IFEVA Facultad de Agronomía- UBA.*

Equipment:

- *Pulsed Nd-YAG lasers (1064 nm, 532 nm, 355 nm, 266 nm) and OPO.*
- *CW Argon laser, CW dye laser.*
- *Systems for photoacoustic measurements .*
- *Detection systems for singlet oxygen.*

Materiales optoelectrónicos



Responsable: Dr. Jorge O. Tocho

Integrantes: Dra. Lucía Scaffardi
Dr. Daniel Schinca
Dr. Gustavo Torchia

Temas de investigación:

Absorción de estado excitado en KCl: Eu
Estudios de transiciones de fase en sólidos amorfos y en polímeros.
Resolución de sitios cristalinos en niobato de litio dopado con cromo y zinc.
Determinación del rendimiento cuántico de fluorescencia en cristales dopados con cromo
Caracterización de microguías de luz en niobato de litio fabricadas con láseres de fs.
Estudio del guiado de luz por arreglo 2D de microguías fabricadas con láseres de fs.

Colaboración con otras Instituciones y grupos de Investigación:

- Servicio Láser, Dto de Física, Facultad de Ciencias Exactas, Universidad de Salamanca, España.
- Grupo Física de Materiales, Dto de Física, Universidad Autónoma de Madrid, España.
- Laboratorio de Materiales Cerámicos, FCEIyA, IFIR, Universidad Nacional de Rosario, Argentina

Equipamiento disponible:

- Láser de neodimio Q-switch, 10 ns, 750 mJ, con generadores de 2da., 3ra. y 4ta. Armónica.
- Generador paramétrico OPO, 400 2500 nm.
- Láser de Argón, 5 W.
- Láser de colorante contínuo.
- Espectrógrafo de 25 cm de focal.
- Espectrógrafo multicanal.
- Espectrofotómetro 200-1100 nm.
- Espectrógrafo infrarrojo por Transformada de Fourier 1 15 µm
- Fotodiodos - Fotomultiplicadores.
- Contador de fotones.
- Amplificador Boxcar.
- Amplificador Lock-in.
- Osciloscopio digital 300 Mhz.
- Cámara CCD intensificada con gate temporal.
- Crióstato para nitrógeno líquido.

Optoelectronic materials

Research Lines:

Laser, optical and photoacoustic spectroscopy of optoelectronic crystals.
Photophysics of rare-earth doped alkali-halide crystals.
Photophysics of microstructured light waveguides generated by ultrashort laser pulses. Application to Integrated Optics.
Study of solid state sensors based on multilayered structures

Most relevant works:

- *KCl: Eu excited state absorption*
- *Phase transitions in amorphous solids and polymers.*
- *Site resolution in lithium niobate doped with Cr and Zn.*
- *Determination of fluorescente quantum yield in Cr doped crystals.*

- *KCl: Eu excited state absorption*
  Phase transitions in amorphous solids and polymers.
- *Site resolution in lithium niobate doped with Cr and Zn.*
  Determination of fluorescente quantum yield in Cr doped crystals.

Collaboration with other institutions and research groups:

- *Servicio Láser, Dto de Física, Facultad de Ciencias Exactas, Universidad de Salamanca, España.*
- *Grupo Física de Materiales, Dto de Física, Universidad Autónoma de Madrid, España.*
- *Laboratorio de Materiales Cerámicos, FCEIyA, IFIR, Universidad Nacional de Rosario, Argentina*

Equipment:

- *Nd-YAG laser, Q-switch, 10 ns, 750 mJ, with 2nd., 3rd. and 4th. harmonic.*
- *Optical parametric generator OPO, 400 2500 nm.*
- *Argon laser, 5 W.*
- *CW tunable dye laser.*
- *25 cm focal length spectrograph.*
- *Multichannel spectrograph.*
- *UV-Vis-NIR spectrophotometer 200-1100 nm.*
- *Fourier Transform IR spectrophotometer, 1 15 µm*
- *Photodiodes, photomultipliers.*
- *Photon-counter.*
- *Boxcar.*



Metrología para las comunicaciones ópticas

Responsable: **Dr. Ricardo Duchowicz**
Integrantes: **Dra. Nélida Russo**
Dr. Christian Cuadrado Laborde
Ing. Sergio Noriega
Ing. Pablo Costanzo Caso
Sr. Augusto Mantesa (colaborador)
Sr. Claudio Lambert
Sr. Emanuel Paulucci

Temas de investigación:

Estudios de procesos fotofísicos en fibras dopadas.
Análisis y desarrollo de amplificadores ópticos de fibras.
Estudio, modelado teórico y desarrollo de láseres de fibra óptica.
Análisis de la propagación de pulsos luminosos en medios guiados. Estudios de procesos lineales y no lineales.
Desarrollo de dispositivos sensores por fibras ópticas.
Diseño y aplicación de redes de Bragg en fibra óptica.
Diseño e implementación de técnicas e instrumental para análisis de componentes ópticos utilizados en sistemas de fibras.

Colaboración con otras Instituciones y grupos de Investigación:

- Dep. de Física Aplicada, Universidad de Valencia, España; Dr. Miguel Andrés.
- Laboratorio de Láser, Facultad de Ingeniería, Universidad Nacional de Mar del Plata; Ing. Gustavo Arenas.
- Facultad de Ingeniería y Ciencias Exactas, Universidad Argentina de la Empresa (UADE), Buenos Aires; Dr. Enrique Sicre.

Equipamiento principal:

- Analizador de Fibra Optica (OTDR), marca Ando.
- Monocromador marca CVI Digikrom, de 0,48 m de distancia focal y 0.03 nm de resolución.
- Osciloscopio Digital Marca Hewlett & Packard, de 500 MHz, 2 Gsample/sec.
- Medidor de potencia óptica Wander & Goltermann, OMS-200, de 800 a 1600 nm, rango dinámico: +13 a 110 dBm y precisión de +-2%, trazable al PTB.
- Medidor de potencia óptica piroeléctrico, marca Laser Probe, rango espectral de 250 a 2000nm y precisión de +- 1%, trazable al NIST.
- Empalmadora de fibras ópticas, marca Ericsson.
- Láser sintonizable, marca Photonetics. Rango espectral: 1480 1550nm.
- Fuentes láser estabilizadas en potencia, con emisión en 1550 nm y 1310 nm, marca Ando.
- Láseres de He-Ne.
- Fotodetectores para diferentes regiones espectrales.
- Mesa antivibratoria marca Melles Griot.
- Módulos láser de semiconductor de emisión continua en 980 nm.

Optic Communication Metrology

Research Lines:

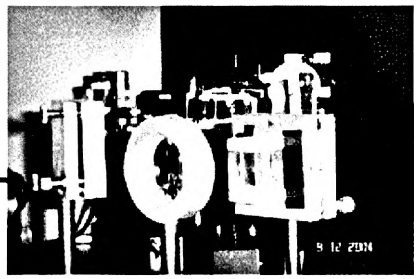
Study of photophysial processes in doped fibers.
Análisis and development of optical fiber amplifiers.
Theoretical modeling and development of optical fiber lasers.
Propagation of optical pulses in guided media. Study of linear and non-linear processes..
Development of optical fiber sensors. .
Design and application of Bragg gratings in optical fibers.
Development of techniques and instruments for optical component analysis in optical fiber systems.

Collaboration with other institutions and research groups:

- *Dep. de Física Aplicada, Universidad de Valencia, España; Dr. Miguel Andrés.*
- *Laboratorio de Láser, Facultad de Ingeniería, Universidad Nacional de Mar del Plata; Ing. Gustavo Arenas.*
- *Facultad de Ingeniería y Ciencias Exactas, Universidad Argentina de la Empresa (UADE), Buenos Aires; Dr. Enrique Sicre.*

Equipment:

- *Optical fiber analyzer (OTDR), Ando.*
- *CVI Digikrom Monocromator , 0.48 m focal length and 0.03 nm resolution.*
- *Digital Osciloscope Hewlett & Packard, 500 MHz, 2 Gsample/sec.*
- *Power meter Wander & Goltermann, OMS-200, 800 to 1600 nm, dynamic range: +13 to 110 dBm and +-2%, precision, traceable to PTB.*
- *Pyroelectric power meter, Laser Probe, 250 to 2000nm, +- 1%, precision NIST traceable.*
- *Optical fiber splicer, Ericsson.*
- *Tuneable laser, Photonetics, 1480 to 1550nm.*
- *Power-stabilized laser sources, for lasers at 1550 nm and 1310 nm, Ando.*
- *He-Ne lasers.*
- *Photodetectors forseveral spectral regions .*
- *Antivibration table, Melles Griot.*
- *Semiconductor laser modules CW@ 980 nm.*



Procesamiento opto-digital de la información: cristales fotorrefractivos, holografía dinámica, speckle

Responsable: Dr. Néstor Bolognini
Integrantes: Dr. Roberto Torroba
Dra. Myrian Tebaldi
Dr. Alberto Lencina
Lic. Beatriz N. Ruiz
Lic. Gustavo Forte (colaborador)
Ms. Dafne Amaya Roboayo
Ing. Fis. Edward Fabián Mosso

Temas de investigación:

Desarrollo de técnicas de holografía dinámica.
Implementación de correladores ópticos para el reconocimiento de imágenes mediante el registro holográfico de volumen en un medio fotorrefractivo.
Implementación de correladores conjuntos completamente digitales.
Desarrollo de métodos para validación, encriptación y codificación de información mediante técnicas de procesamiento digital de imágenes.
Arreglos ópticos de encriptación múltiple utilizando cristales fotorrefractivos.
Diseño de nuevas máscaras de fase aleatorias para utilizarlas en el campo de la encriptación y/o validación de la información para generar jerarquías de acceso.
Estudio del registro de distribuciones de speckle en medios de registro volumétricos (cristales fotorrefractivos).
Estudio de filtros holográficos fijados en cristales ferroeléctricos.
Caracterización de materiales mediante técnicas de speckle con luz blanca.
Desarrollo de VOIS (Virtual Optics Imaging Systems).
Estudio y aplicaciones de procesadores acromáticos.
Estudio de distribuciones de cluster de speckle.
Momento angular de la luz.

Colaboración con otras Instituciones y grupos de Investigación:

- Universidad EAFIT, Medellín (Colombia)
- Universidad de Antioquia, Medellín (Colombia)
- Fundação Visconde de Cairu (Brasil)
- Universidad Autónoma de Madrid, Madrid (España)
- Universidad Jaime I, Castellón (España)

Equipamiento disponible:

- Mesas antivibratorias.
- Láser Nd YAG CW 532 nm, 150 mW; He-Ne, 30 mW.
- Láseres de He-Ne.
- Cristales fotorrefractivos tipo selenitas (BSO, BGO, BTO) y ferroeléctricos (LiNbO3).
- Moduladores espaciales de luz.

Opto-digital information processing: photorefractive crystals, dynamic holography and speckle

Research Lines:

Development of dynamic holography techniques.
Optical correlators for image recognition through volume holography in photorefractive media.
All-digital joint transform correlators.

Development of methods for validation, encryption and information coding using digital image processing techniques
Multiplexed encryption optical arrays using photorefractive crystals.
New random phase masks for encryption/validation of information for access hierarchy generation.
Speckle distributions recordings in volume media (photorefractive crystals). Holographic filters in ferroelectric crystals.
Material characterization through white light speckle.
Development of VOIS (Virtual Optics Imaging Systems).
Acromatic optical processors .
Speckel cluster distributions studies.
Optical angular moment.

Collaboration with other institutions and research groups:

- *Universidad EAFIT, Medellín (Colombia)*
- *Universidad de Antioquia, Medellín (Colombia)*
- *Fundação Visconde de Cairu (Brasil)*
- *Universidad Autónoma de Madrid, Madrid (España)*
- *Universidad Jaime I, Castellón (España)*

Equipment:

- *Antivibration tables.*
- *Nd YAG CW laser @ 532 nm, 150 mW; He-Ne, 30 mW.*
- *He-Ne Lasers.*
- *Selenite - type photorefractive crystals (BSO, BGO, BTO) y ferroelectric (LiNbO3).*
- *Light spacial modulators.*



Propagación de la luz y formación de imágenes a través de medios turbios y turbulentos

Responsable: Dr. Mario Garavaglia
Integrantes: Dra. Lía M. Zerbino (Co-Director)
Dr. Luciano J. Zunino
Ing. Anibal P. Laquidara
Ing. Eduardo C. Cortizo
Ing. José A. Bava
Ing. Rubén Freccero
Arq. Alexander Rodríguez
Sr. Pablo F. Meilán
Colaboradores: Prof. Diego Palazzesi
Srta. Paula Bergero
Sr. Héctor Rioja Roldán

Temas de investigación:

Propagación y formación de imágenes a través de medios con índices de refracción estructurados, como son los medios anisótropos, los medios GRIN (Graded Index of refraction), las fibras ópticas, etc.
Perturbaciones sobre la estructura modal de un haz láser debidas a la propagación en una atmósfera turbulenta a nivel de laboratorio.
Desviaciones estadísticas de la propagación de un haz láser provocadas por las perturbaciones atmosféricas en experimentos a nivel de laboratorio y a nivel de campo.
Desviaciones estadísticas de la formación de una autoimagen de una grilla provocadas por las perturbaciones atmosféricas a nivel de laboratorio.
Transmisión de un haz láser a través de medios turbios.
Formación de imágenes a través de medios turbios y turbulentos por microscopía de barrido láser confocal.

Colaboración con otras Instituciones y grupos de Investigación:

- Se encontró que el índice de refracción del aire tiene un comportamiento Browniano fraccionario.
- Se explicó la formación de autoimágenes mediante el formalismo Feynman.
- Se encontró un método para medir la lacunaridad de una estructura fractal por difracción.
- Mediante la introducción de una técnica interferencial microscópica se determinaron variaciones morfológicas de células vivas.
- Se lograron determinar las variaciones topográficas del pie humano durante la pisada por iluminación estructurada.
- Se establecieron las bases para la formación de moiré mediante grillas ocultas o implícitas y se realizó una ampliación a la medición de distancias.

Equipamiento disponible:

- Láseres visible e infrarrojo.
- Banco óptico y mesa óptica completos.
- Detectores, cámaras fotográficas, videocámaras, cámaras CCD.
- Computadoras de cálculo y de simulación

Light propagation and imaging through turbid media

Research Lines:

Propagation and imaging through structured refractive index media (Graded Index of refraction, optical fibers, etc.)
Perturbations of the modal structure of a laser beam due to propagation through turbulent atmosphere.
Statistical deviations in the propagation of a laser beam due to atmospheric perturbations in the lab

Statistical deviations in self imaging of a grid due to atmospheric perturbations at the lab.
Transmission of a laser beam through turbid media.
Image formation through turbulent media by confocal laser scanning microscopy.

Most relevant works:

- *It was found that air refractive index has a fractinary Brownian behaviour.*
- *The formation of selfimages was explained through the Feynman formalism.*
- *A method was found to measure the lacunarity of a diffraction fractal structure.*
- *Living cells morflogical variations were determined using a microscopic interferential technique.*
- *Topographic variations of a human foot were determined using structured illumination.*
- *Moiré formation through hidden gratings.*

Equipment:

- *Visible and IR lasers.*
- *Optical bench and antivibration table.*
- *Detectors, cameras, videocameras, CCD.*
- *PC for simulations .*

Scattering óptico

Responsables: Dra. Lucía B. Scaffardi
Dr. Jorge O. Tocho

Integrantes: Dr. Daniel Schinca
Ing. Fabián Videla

Temas de investigación:

Medición de radios medios y distribución de tamaños de material nanoparticulado en solución mediante scattering óptico angular.

Desarrollo y aplicación de espectroscopías de backscattering y de scattering a bajo ángulo para caracterización de nanopartículas dieléctricas.

Estudio de propiedades ópticas de nanopartículas metálicas por espectroscopia de extinción

Trabajos más relevantes:

- Medición de la distribución de tamaños de partículas dieléctricas en solución por espectroscopía de backscattering en el visible y cercano infrarrojo.
- Estudio de la influencia de los electrones libres en el espectro de extinción de partículas metálicas nanométricas.
- Estudio de la dependencia de la función dieléctrica con los electrones ligados para partículas metálicas subnanométricas.
- Medición de distribuciones de tamaño y composición de aerosoles atmosféricos (en curso).
- Medición de radio medio de partículas nanométricas semiconductoras (en curso).

Colaboración con otras Instituciones y grupos de Investigación:

- Servicio Láser, Dto de Física, Facultad de Ciencias Exactas, Universidad de Salamanca, España.
- Grupo Física de Materiales, Dto de Física, Universidad Autónoma de Madrid, España.
- Grupo del Laboratorio de Materiales Cerámicos, FCElyA, IFIR, Universidad Nacional de Rosario, Argentina

Equipamiento disponible:

- Equipo de scattering angular.
- Opacímetro.
- Contador de partículas micrométricas.
- Partículas patrón calibradas EPA.
- Nanopartículas metálicas Standard de oro.
- Espectrofotómetro UV-Visible de doble haz con barrido de alta velocidad, computarizado, marca Shimadzu, modelo UV-1650PC

Optical Scattering

Research Lines:

Mean radius measurement and size distribution of nanoparticles in solution using angular scattering.

Development and application of backscattering spectroscopy and low-angle scattering for sizing dielectric nanoparticles.

Optical properties of metal nanoparticles using extinction spectroscopy.

Most relevant works:

- *Measurement of size distribution of dielectric microparticles in solution using Vis-NIR backscattering spectroscopy.*
- *Study of the influence of free electrons in the extinction spectrum of metal nanoparticles.*
- *Study of the dependence of the dielectric function on bound electrons for subnanometric metal particles.*
- *Size distribution and composition of atmospheric aerosols (in due course).*
- *Mean radius measurementof semiconductor nanométrica particles (in due course).*

Collaboration with other institutions and research groups:

- *Servicio Láser, Dto de Física, Facultad de Ciencias Exactas, Universidad de Salamanca, España.*
- *Grupo Física de Materiales, Dto de Física, Universidad Autónoma de Madrid, España.*
- *Grupo del Laboratorio de Materiales Cerámicos, FCEIyA, IFIR, Universidad Nacional de Rosario, Argentina*

Equipment:

- *Angular scattering system*
- *Opacimeter*
- *Particle counter.*
- *EPA calibrated particles*
- *Standard gold manoparticles.*
- *UV-Visible-NIR spectrophotometer, Shimadzu, UV-1650PC*

Selección de trabajos

Espectroscopía atómica y aplicaciones

Fibras Ópticas

Física del láser y aplicaciones

Óptica física y aplicada

Desde de la creación del CIOP en 1977 las primeras investigaciones en espectroscopia láser y espontánea se centraron en el estudio del nitrógeno molecular y en gases nobles. El láser de N2 fue utilizado como una intensa fuente de radiación ultravioleta (337.1 nm) y permitía el estudio temporal y en frecuencia de sus bandas en el cercano infrarrojo. La investigación más importante se llevó a cabo empleando un láser de nitrógeno molecular pulsado y refrigerado a temperatura de aire líquido conjuntamente con espectrógrafos de alta resolución los cuales podian transformarse en monocromadores a través de la detección por fotomultiplicadores.

Por otra parte, utilizando Xe como medio activo, el láser fue empleado como generador de emisión estimulada en la zona del azul-verde, y el mismo láser pero sin los espejos, como fuente espectral por emitir espectros de iones del Xe muy ricos en líneas espectrales. La investigación en Xe muestra como un uso apropiado de las técnicas espectroscópicas puede resolver problemas y contribuir a generar nuevos trabajos en el mismo tema.. Como en la metodología de trabajo el análisis de la radiación espontánea es sistemático, el estudio de los espectros dio como resultado la detección de alrededor de 2000 líneas espectrales que no se correlacionaban con ninguna de las tabuladas en las bibliografías existentes, y en algunos casos, las líneas láser tenían asignación iónica desconocida.

Trabajos posteriores consistieron en el análisis de datos obtenidos de una fuente spectral donde un banco de capacitores se descarga mediante una "llave rápida" a través del tubo que contiene éste gas noble, como también Ne, Ar y Kr a baja presión. La radiación generada de este modo es registrada por un espectrógrafo de alta resolución. Los espectros así obtenidos son medidos en el comparador fotoeléctrico de la Facultad de Ciencias Astronómicas y Geofísicas de la Universidad Nacional de La Plata (UNLP).

Además de estos trabajos se deben también mencionar aquellos orientados al estudio de los parámetros de las descargas, a la obtención de espectros de distintis gases nobles mediana y altamente ionizados mediante la variación de la energía de excitación, la asignación iónica de las transiciones, la construcción de tablas espectrales. El análisis espectral se encuentra sustentado mediante cálculos teóricos de diagonalización de matrices de energía para la determinación de los parámetros atómicos, que permiten una mejor interpretación de los resultados experimentales.

Desde 1984 el CIOp cuenta con un espectrógrafo para trabajar en la zona del ultravioleta de vacío del espectro electromagnético, el cual fue donado por la Universidad de Lund, Suecia, con la cual se mantiene una fuerte relación científica en espectroscopia atómica desde hace varios años. Este instrumento permitió que el CIOp comenzara el estudio de gases nobles ionizados en la región del VUV, de especial interés en astrofísica y física de láser. Además de este instrumento, el CIOp posee dos espectrógrafos que cubren el UV, visible, IR e IR cercano del espectro electromagnético. Uno de ellos, Shimazdu, pertenece a la Universidad Nacional de La Plata y el otro, Hilger Watts a la Universidad Nacional de Córdoba, Argentina. Otro espectrógrafo Hilger Watts perteneciente a la Universidad Nacional de Tucumán, Argentina, fue transferido al CIOp mediante un acuerdo. Todo este equipamiento permite por medio de registros fotográficos, el estudio de una amplia zona del espectro electromagnético desde los 30 hasta los 1200 nm aproximadamente. Mediante detección electrónica, la zona puede ser ampliada hasta longitudes de onde de varios microns. Actualmente se utilizan arreglos lineales de diodos y cámaras CCD.

Recientemente otro tipo de técnica denominada LIBS (Laser Induced Breakdown Spectroscopy) fue incorporada a nuestro grupo. Este método involucra láseres de alta potencia que son focalizados sobre un blanco sólido o gaseoso produciendo un plasma ionizado. Estos espectros son registrados por un monocromador con una cámara ICCD la cual permite registrar la evolución temporal de las líneas espectrales.

Cabe mencionar que todos estos trabajos brevemente descriptos dieron lugar a una docena de tésis doctorales y un número importante de tésis de licenciatura. Por otra parte mantenemos estrechas relaciones institucionales con otros grupos que trabajan en temas similares en nuestro país y en el exterior, especialmente con los grupos de plasma y espectroscopia óptica de las Universidades de Tandil, Rosario y Mar del Plata, Argentina, y las Universidades de Lund, Suecia, Universidad de Campinas y Universidad Federal Fluminense, Brasil. Esto incluye el intercambio de material científico, viajes y estadías de estudiantes e investigadores para la realización de trabajos, cursos y la difusón de los resultados obtenidos.

Finalmente, los datos producidos en nuestro grupo sobre argón fueron reportados por el NIST, USA y tres compilaciones sobre gases nobles, Kr y Xe, fueron también publicados por el NIST J. Phys. Chem Ref. Data 20, 859-915, 1991; J. Phys. Chem Ref. Data 24, 1577-1608, 1995); J. Phys. Chem Ref. Data 33, 765-921, 2004) y http://physics.nist.gov/PhysRefData/ASD/index.html)

When CIOp was created in 1977, investigations of spontaneous spectroscopy and laser were centered on studies of molecular nitrogen and noble gases. The N2 laser was used as an intense source of ultraviolet emission (337,1 nm) and had possibilities for the study in time and frequency of its radiation in the bands of the near infrared. The main research was carried out with a pulsed molecular nitrogen laser refrigerated at liquid air temperature, employing already known technologies but with the support of a high resolution spectrograph having the possibility of being converted into a monochromator with detection by means of lead sulfide detectors, photomultipliers, oscilloscopes, etc.

Besides using Xe as a basis, the laser was employed as generator of stimulated emission in the blue-green zone and the tube as light source, generating rich-in-lines spectra of the first ions of the gas. Our research on Xe laser shows how a proper employment of spectroscopic techniques can solve problems and contribute to generate new research works in the same subject. As in our methodology the analysis of spontaneous radiation was systematic, the study of the measurements gave as a result the detection of about 2000 spectral lines that did not correlate with the existent bibliography and in some cases, showed the correspondence with laser lines having unknown assignments.

Later work consisted of the analysis of data obtained from an spectral source, where a capacitor bank discharged by "quick switches" through a tube containing this noble gas or others like Ne, Ar, Kr at low pressure. The radiation generates in this way is received at the plate holder of a great-dispersion spectrograph. The obtained records are measured by comparison with that of thorium 232, in the photoelectric comparator at the Facultad de Ciencias Astronómicas y Geofísicas de la Universidad Nacional de La Plata (UNLP)., and final data are managed by proper methods to reach the determination of the atomic structure of studied spectra.

Among this general sequence of works, we must also mention those oriented to the study of the discharge parameters, the attainment of spectra by varying the excitation energy of the discharge to be able to assign the ionization state of each transition and to prepare spectroscopy tables. The employment of theoretical calculations programs for the diagonalization of energy matrices and for the attainment of other type of atomic parameters, which allows a better interpretation of experimental results, were also used.

Since 1984, the CIOp has had a spectrograph for working in the vacuum ultraviolet zone of the electromagnetic spectrum, donated by Lund Universitet, Sweden, with which we have maintained a strong scientific relationship on atomic spectroscopy subjects since several years. This instrument has allowed the CIOp to begin the study on ionized noble gases in the V.U.V. zone, which is of interest in astrophysics subjects and in V.U.V. and X-ray lasers.

Appart from this instrument, the CIOp has two spectrographs to cover the U.V. visible and near IR zones of the electromagnetic spectrum. One of them, a Shimadzu, belongs to the Universidad Nacional de La Plata, and another one, Hilger Watts, that belongs to the Universidad Nacional de Córdoba, Argentina. Another Hilger Watts instrument belonging to the Universidad Nacional de Tucumán, Argentina, was transferred to CIOp, through an agreement like the previous ones,.

All this equipment allows studies on a wide zone of the electromagnetic spectrum by photographic means, from 30 to 1200 nm approximately. Employing electronic detection, the zone can be widened up to wavelengths of several microns. Lately, new detection techniques including linear diode arrays, modern monocromators and CCD cameras, have been used.

Recently, another kind of techniques was performed in our group, the Laser Induced Breakdown Spectroscopy (LIBS). This process involves high-power laser beam focused onto a sample surface or gas producing a ionized plasma and excited elemental components. These spectra are recording in a monochromator with an ICCD camera wich allows to record the temporal evolution of the spectra lines.

It is worth mentioning that all these works briefly described here have resulted in dozen of doctoral theses, some in course at present, and an important number of pregraduate theses. Furthermore we maintain close interinstitutional relations with other groups working on similar subjects, in our country and abroad, especially with the groups of plasma and optical spectroscopy in the universities of Tandil, Rosario, and Mar del Plata, Argentina; and the University of Lund, Sweden, the University of Campinas, and the Universidad Federal Fluminense, Río de Janeiro, Brazil. These include the interchange of scientific material, trips and visits of scientists and students for courses and/or joint works, and the publication of the results in specialized journals.

Finally, data produced in our group about Argon were reported by the NIST, USA, and three compilations about noble gases were also published by the NIST, including the Krypton material J. Phys. Chem Ref. Data 20, 859-915, 1991; J. Phys. Chem Ref. Data 24, 1577-1608, 1995 recently the Xenon data in J. Phys. Chem Ref. Data 33, 765-921, 2004 and also in http://physics.nist.gov/PhysRefData/ASD/index.html)

Physica Scripta. Vol. 34, 164–166, 1986.

Transitions Within the $n = 4$ Complex of Kr VII Obtained from a Theta-Pinch Light Source

A. Trigueiros*, S.-G. Pettersson and J. G. Reyna Almandos†

Department of Physics, Lund Insitute of Technology, Box 118, S-221 00 Lund, Sweden

Received January 10, 1986; accepted February 22, 1986

Abstract

The spectrum of six times ionized krypton (Kr VII) has been observed in the 430–1000 Å wavelength range and 23 lines have been identified as transitions between levels of the $4s^2$, $4s4d$, $4p^2$ and $4s4p$ configurations. For 13 of the lines the classification is new. Revised values are proposed for three levels while for the rest the uncertainty in the existing level values has been considerably decreased.

The results are supported by isoelectronic comparisons along the Zn I isoelectronic sequence. The configurations are interpreted by fitting the theoretical energy expressions to the observed energy levels using least-squares techniques. The parameter values are compared with results from Hartree-Fock calculations.

1. Introduction

The Kr^{6+} ion belongs to the Zn I isoelectronic sequence. The knowledge of the spectra in this sequence with the exception of the Zn I spectrum was for a long time limited [1]. A small number of levels were reported for Ga II–Br VI [1], but for Kr VII and more highly ionized ions, no information was available. For Zn I the analysis presented in Atomic Energy Levels [1] has been extended [2–4], and a few levels of Ga II [5] were added by Denne et al. Recently Isberg and Litzén revised and extended the analysis of Ga II [6]. The analyses of Se V and Br VI have also been extended [7, 8]. For more highly ionized ions the $4s$–$4p$ resonance transition of Rb VIII–Mo XIII and Ru XV–Dy XXXVII was observed by Reader and Acquista [9, 10]. Litzén and Ando reported the $4s$–$4p$ transitions including intercombination lines in Zr XI, Nb XII and Mo XIII [11]. Observations of the Kr VII spectrum were reported by Fawcett et al. using a zeta-pinch [12]. Several reports on observations of Kr VII spectra using the beam-foil technique [13–16] have appeared. The Zn I isoelectronic sequence has been studied theoretically in a number of papers [17–20].

The present work concerns the study of the $4s^2$, $4s4d$, $4p^2$ and $4s4p$ configurations in Kr VII.

The revival of the interest in data on the Zn I isoelectronic sequence is due to observations of impurity-lines from highly ionized heavy ions with few valence electrons in high temperature plasmas [21, 22]. Such lines have been used for diagnostic purposes. The resonance transition $4s^2\ {}^1S_0$–$4s4p\ {}^1P_1$ has been observed for a large range of Z values in the Zn I isoelectronic sequence [9, 23].

2. Experimental arrangements

The light source used in the present work is a theta-pinch discharge built at Lund Institute of Technology [24].

The spectra were recorded using a 3 m normal-incidence spectrograph equipped with a 1200 lines/mm grating blazed for 1380 Å. The plate factor in the first diffraction order is 2.77 Å mm^{-1}.

To distinguish between different stages of ionization, a number of experimental parameters, i.e., gas pressure, discharge voltage and number of discharges, were varied. A well developed Kr VII spectrum was obtained with the following parameters: 4 mTorr, 13 kV and 800 discharges.

The spectra were exposed on Kodak SWR plates and lines from C III, N III, O III, Kr II and Kr III were used as internal standards. The plates were measured with a semi-automatic comparator with a photoelectric setting device [25]. For sharp lines the settings are reproducible to within $\pm 0.5\ \mu$m. Third order interpolation formulas, together with correction curves, were employed to reduce the comparator settings to wavelength values. The accuracy of the wavelength values is estimated to be ± 0.01 Å.

3. Analysis

The Kr VII lines observed in the present work are given in Table I, 13 of them being without previous classification. The intensity figures given in the table are based on visual estimates.

The energy levels derived from the observed lines are given in Table II, and the general structure of the term system is shown in Fig. 1. When establishing the energy levels, we were guided by isoelectronic comparisons taking into account Zn I [1], Ga II [6], Ge III [1], As IV [1], Se V [7] and Br VI [7, 8].

When performing the analysis we also used theoretical predictions of the structures of the configurations. The predictions were obtained by diagonalizing the energy matrices with appropriately scaled Hartree–Fock (HF) values for the energy parameters. For this purpose the computer code developed by Cowan [26] was used. A comparison with the level system given by Pinnington et al. [16] shows that eight of their levels values have been confirmed, although the accuracy has been considerably improved. However, for three levels we propose new identifications as discussed below.

For the level $4s4p\ {}^3P_0$ we propose the new value 117 389 cm^{-1}. The level is established from a line at 617.18 Å, classified as the $4s4p\ {}^3P_0$–$4p^2\ {}^3P_1$ transition. This position is in reasonable agreement with the value predicted by Curtis [20].

For the level $4s4d\ {}^3D_1$ we propose a new value at 349 973 cm^{-1}. The level is determined by a line at 558.22 Å

* Permanent address: UNICAMP, Instituto de Física DEQ – Plasma, 13 100 Campinas SP, Brasil.

† Permanent address: Centro de Investigaciones Opticas (CIOp), La Plata, Argentina.

Table I. *Identified lines of Kr VII*

Intensity	λ(Å)	σ(cm⁻¹) Obs.	Calc.	Combination
15	434.140[a]	230 340.4	22.0	$4s4p\ ^3P_1$–$4s4d\ ^3D_2$
8	435.018	229 875.5	8.3	$^3P_1$– $^3D_1$
20	445.309	224 563.2	.2	$^3P_2$– $^3D_3$
8	446.700	223 863.9	.8	$^3P_2$– $^3D_2$
3	447.606	223 410.8	20.1	$^3P_2$– $^3D_1$
25	479.264	208 653.3	.3	$^1P_1$– $^1D_2$
4	556.855	179 580.0	1.8	$^1P_1$– $^3D_2$
4	558.221	179 140.5	38.1	$^1P_1$– $^3D_1$
15	585.361	170 834.8	5.0	$4s^2\ ^1S_0$–$4s4p\ ^1P_1$
30	594.899	168 095.8	.4	$4s4p\ ^3P_1$– $4p^2\ ^3P_2$
30	617.189	162 024.9	.9	$^3P_0$– $^3P_1$
40	618.664	161 638.6	7.2	$^3P_2$– $^3P_2$
4	626.486	159 620.5	.0	$^3P_1$– $^1D_2$
30	627.668	159 319.9	.7	$^3P_1$– $^3P_1$
30	645.847	154 835.4	6.9	$^3P_1$– $^3P_0$
5	652.905	153 161.6	.8	$^3P_2$– $^1D_2$
50	654.189	152 861.0	.5	$^3P_2$– $^3P_1$
9	832.682	120 093.9	4.8	$4s^2\ ^1S_0$–$4s4p\ ^3P_1$
5	852.120	117 354.4	5.2	$4s4p\ ^1P_1$– $4p^2\ ^3P_2$
60	918.446	108 879.6	.8	$^1P_1$– $^1D_2$
5	920.983	108 579.6	.5	$^1P_1$– $^3P_1$
5	960.638	104 097.5	6.7	$^1P_1$– $^3P_0$

[a] Asymmetric line.

classified as the $4s4p\ ^1P_1$–$4s4d\ ^3D_1$ transition. This identification is confirmed by the lines at 435.01 Å and 447.60 Å corresponding to the $4s4p\ ^3P_1$–$4s4d\ ^3D_1$ and $4s4p\ ^3P_2$–$4s4d\ ^3D_1$ transitions. This new level value is in agreement with the theoretically predicted value by Ivanova et al. [19].

For the level $4p^2\ ^1D_2$ we propose the value 279 714 cm⁻¹, determined by a line at 918.45 Å and classified as the $4s4p\ ^1P_1$–$4p^2\ ^1D_2$ transition. The identification is confirmed by a line at 626.48 Å classified as $4s4p\ ^3P_1$–$4p^2\ ^1D_2$ and a line at 652.90 Å classified as $4s4p\ ^3P_2$–$4p^2\ ^1D_2$. This new level value fits well with the graphic prediction that can be made from the work by Litzén and Ando [11]. The calculated eigenvector composition shows that this level is strongly mixed with the level $4p^2\ ^3P_2$. In the work by Ivanova et al. [19] the two designations are interchanged but we prefer to maintain the old designation.

Table II. *Energy levels of Kr VII*

Designation	Energy (cm⁻¹)	Obs.–Calc. (cm⁻¹)	Percentage[a] composition
$4s^2\ ^1S_0$	0.0		98
$4s4p\ ^3P_0$	117 389.6	9	100
$^3P_1$	120 094.8	13	100
$^3P_2$	126 553.0	3	100
$^1P_1$	170 835.0	0	100
$4p^2\ ^3P_0$	274 931.7	0	98
$^3P_1$	279 414.5	0	100
$^3P_2$	288 190.2	1	$72p^2\ ^3P + 22p^2\ ^1D + 4sd\ ^1D$
$^1D_2$	279 714.8	1	$62p^2\ ^1D + 27p^2\ ^3P + 11sd\ ^1D$
$4s4d\ ^3D_1$	349 973.1	2	100
$^3D_2$	350 416.8	4	100
$^3D_3$	351 116.2	1	100
$^1D_2$	379 488.3[b]	0	$85sd\ ^1D + 15p^2\ ^1D$

[a] Percentages lower than 4% are omitted. The average *LS* purities of the $4s^2$, $4s4d$ and $4p^2$ configurations are 91% and for $4s4p$ 90%.

[b] This level was determined by one line only.

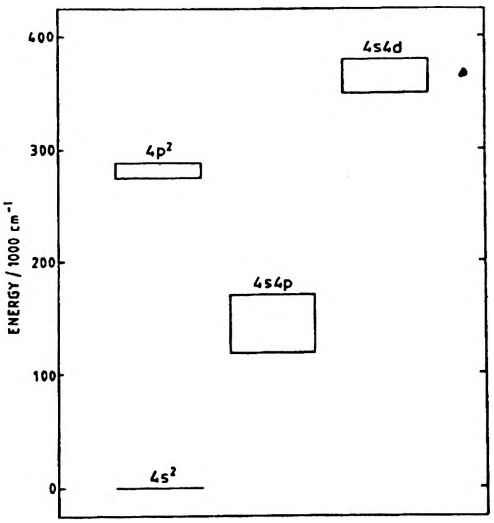


Fig. 1. The gross structure of the lower part of the Kr VIII energy level system.

Table III. *Energy parameters for the 4s4p configuration of Kr VII*

Parameter	HF value (cm⁻¹)	Fitted value[a] (cm⁻¹)	Fit/HF
E_{av}	117 277	135 244	1.153
$G^1(4s, 4p)$	93 240	70 442	0.755
ξ_{4p}	5 256	6 105	1.161

[a] The rms deviation of the fit is 17 cm⁻¹ for 4 observed levels.

Table IV. *Energy parameters for the $4s^2$, $4s4d$, $4p^2$, $4s5s$ and $4d^2$ configurations of Kr VII*

Configuration	Parameter	HF value (cm⁻¹)	Fitted value[a] (cm⁻¹)	Fit/HF
$4s^2$	E_{av}	0	9 269	
$4s4d$	E_{av}	330 775	354 121	1.071
	$G^2(4s, 4d)$	54 420	34 635	0.636
	ξ_{4d}	406	458	1.128
$4p^2$	E_{av}	260 760	292 271	1.121
	$F^2(4p, 4p)$	70 181	68 692	0.979
	ξ_{4p}	5 241	6 138	1.171
$4s5s$	E_{av}	419 161	419 161(fix)	1.000
	$G^0(4s, 5s)$	3 203	3 203(fix)	1.000
$4d^2$	E_{av}	677 283	677 283(fix)	1.000
	$F^2(4d, 4d)$	57 766	57 766(fix)	1.000
	$F^4(4d, 4d)$	38 999	38 999(fix)	1.000
	ξ_{4d}	425	425(fix)	1.000
Configuration interaction integrals				
$4s^2$–$4p^2$	$R^1(4s4s, 4p4p)$	93 147	93 147(fix)	1.000
$4s^2$–$4d^2$	$R^2(4s4s, 4d4d)$	56 228	56 228(fix)	1.000
$4s4d$–$4p^2$	$R^1(4s4d, 4p4p)$	81 966	73 052	0.891
$4s4d$–$4d^2$	$R^2(4s4d, 4d4d)$	54 838	54 838(fix)	1.000
$4p^2$–$4s5s$	$R^1(4p4p, 4s5s)$	−5 944	−5 944(fix)	1.000
$4p^2$–$4d^2$	$R^1(4p4p, 4d4d)$	76 105	76 105(fix)	1.000
	$R^3(4p4p, 4d4d)$	47 659	47 659(fix)	1.000
$4s5s$–$4d^2$	$R^2(4s5s, 4d4d)$	−12 341	−12 341(fix)	1.000

[a] The rms deviation of the fit is 5 cm⁻¹ for 9 observed levels.

This is in accordance with our theoretical prediction and with the graphic extrapolation along the isoelectronic sequence shown in the work of Litzén and Ando [11].

4. Theoretical interpretation

The level structure was theoretically interpreted by a least-squares fit of the energy parameters to the experimental level values. The computer code by Cowan [26] was used (Tables III and IV). In the calculation for the even parity configurations, i.e., $4s^2$, $4s4d$ and $4p^2$, configuration interaction was included. The experimentally unknown $4s5s$ and $4d^2$ were also included in the theoretical calculation. The configuration interaction parameters were kept fixed at their Hartree–Fock (HF) values. However, due to the strong interaction between the terms $4p^2\ ^1D$ and $4s4d\ ^1D$ [17] the configuration interaction parameter $R^1(4s4d, 4p4p)$ was free to vary. This reduced the mean error of the least-squares fit from 56 cm^{-1} to 5 cm^{-1}.

The odd parity $4s4p$ configuration was interpreted without inclusion of configuration interactions, the reason being that the only experimentally known levels belong to this configuration.

Acknowledgements

We are grateful to Dr van Kleef for providing us with unpublished results on Se and Br and to Dr W. Persson and C. G. Wahlström for enlightening discussions. The financial support of the Swedish Natural Science Research Council (NFR) is gratefully acknowledged. A. Trigueiros has been supported by the Conselho Nacional de Desenvolvimento Científico e Technológico (CNPq), Brazil and J. G. Reyna Almandos by the Consejo Nacional de Investigaciones Científicas y Técnicas (CONICET), Argentina.

References

1. Moore, C. E., Atomic Energy Levels, Vol. II, National Bureau of Standards, U.S.A. (1971).
2. Johansson, I. and Contreras, R., Arkiv för Fysik **37**, 513 (1968).
3. Brown, C. M., Tilford, S. G. and Ginter, M. L., J. Opt. Soc. Am. **65**, 1404 (1975).
4. Martin, W. C. and Kaufman, V., J. Opt. Soc. Am. **60**, 1096 (1979).
5. Denne, B., Litzén, U. and Curtis, L. J., Phys. Lett. **71A**, 35 (1979).
6. Isberg, B. and Litzén, U., Physica Scripta **31**, 533 (1985).
7. van Kleef, T. A. M. (private communication).
8. Curtis, L. J., Martinson, I., Leavitt, J. A., Dietrich, D. D., Bashkin, S. and Denne, B., Phys. Lett. **105A**, 212 (1984).
9. Reader, J. and Acquista, N., Phys. Rev. Lett. **39**, 184 (1977).
10. Acquista, N. and Reader, J., J. Opt. Soc. Am. **B1**, 649 (1984).
11. Litzén, U. and Ando, K., Phys. Lett. **10A**, 411 (1984).
12. Fawcett, B. C., Jones, B. B. and Wilson, R., Proc. Phys. Soc. London **78**, 1223 (1961).
13. Druetta, M. and Buchet, J. P., J. Opt. Soc. Am. **66**, 433 (1976).
14. Irwin, D. J. G., Kernahan, J. A., Pinnington, E. H. and Livingston, A. E., J. Opt. Soc. Am. **66**, 1396 (1976).
15. Livingston, A. E., J. Phys. **B9**, L215 (1976).
16. Pinnington, E. H., Ansbacher, W. and Kernahan, J. A., J. Opt. Soc. Am. **B1**, 30 (1984).
17. Froese Fischer, C. and Hansen, J. E., Phys. Rev. **A19**, 1819 (1979).
18. Victor, G. A. and Taylor, W. R., Atomic Data and Nuclear Data Tables **28**, 107 (1983).
19. Ivanova, E. P., Ivanov, L. N., Gurchumelya, A. D., Tsirekidze, M. A. and Tsirekidze, T. A., J. Phys. **B18**, 1467 (1985).
20. Curtis, L. J., J. Opt. Soc. Am. **B2**, 407 (1985).
21. Hinnov, E., Phys. Rev. **A14**, 1533 (1976).
22. Finkenthal, M. et al., Phys. Lett. **82A**, 123 (1981).
23. Reader, J. and Luther, G., Phys. Rev. Lett. **45**, 609 (1980).
24. Pettersson, S.-G., Physica Scripta **26**, 296 (1982).
25. Gunnvald, P., Arkiv för Fysik **22**, 333 (1962).
26. Cowan, R. D., The Theory of Atomic Structure and Spectra, Univ. of California Press, Berkeley, U.S.A. (1981).

Physica Scripta. Vol. 38, 347–369, 1988.

Spectrum of Doubly Ionized Xenon (Xe III)

W. Persson and C.-G. Wahlström

Department of Physics, Lund Institute of Technology, Box 118, S-221 00 Lund, Sweden

G. Bertuccelli and H. O. Di Rocco

Departamento de Fisica, Facultad de Ciencias Exactas, Pinto 399, 7000 Tandil, Argentina

and

J. G. Reyna Almandos and M. Gallardo

Centro de Investigaciones Opticas, Casilla de Correo 124, 1900 La Plata, Argentina

Received September 15, 1987; accepted November 12, 1987

Abstract

The spectrum of doubly ionized xenon has been investigated. The study is based on photographic recordings of xenon spectra in the 490–8900 Å range. The number of classified lines has been increased from about 300 to about 1400. The lines have been classified as transitions between 73 even levels belonging to the $5s^25p^4$, $5s^25p^36p$, $4f$, $5f$ and $5s^05p^6$ configurations, and 83 odd levels belonging to the $5s5p^5$, $5s^25p^36s$, $7s$, $5d$ and $6d$ configurations. In particular, the classifications include most of the Xe III laser lines. The experimentally observed level structures are compared with the results of Hartree–Fock calculations and least-squares fits. A comparison is also made between the results of the present analysis and the published data on the Xe $N_{4,5}OO$ Auger spectrum.

1. Introduction

The doubly ionized xenon atom, Xe^{2+} ($Z = 54$), is isoelectronic with neutral tellurium. The ground configuration in this sequence is $5s^25p^4$. Although there has been a great demand, e.g., from laser and collision physics, for improved data on the Xe III spectrum and energy level system for many years, very little work has been reported since the 1930's when Boyce [1], Humphreys [2] and Humphreys *et al.* [3] undertook extensive studies of the spectrum. A few reports have appeared treating the lower levels of the spectrum [4–6] and the $5s^05p^6\ ^1S_0$ level [7, 8].

A large number of strong xenon laser lines were reported some 20 years ago [9]. Primarily due to the work of the group in La Plata, the laser lines were classified as originating in doubly and trebly ionized xenon, but no further classifications were possible due to the lack of relevant spectroscopic data.

In the present investigation we have recorded xenon spectra photographically in the 490–6900 Å range. When analysing the vast amount of experimental data we have made extensive use of Hartree–Fock calculations and parametric fits. Configuration-interaction (CI) effects, including Rydberg series CI, have been included in the calculations. The configurations studied are $5s^25p^4$, $5s5p^5$, $5s^05p^6$, $5s^25p^36p$, $6s$, $7s$, $5d$, $6d$ and $4f$. The lowest term of the $5f$ configuration has also been located. The number of classified lines has been increased from about 300 to, in all, 1400. These lines originate from transitions between 73 even- and 83 odd-parity levels. As a consequence of the present analysis it has been possible to classify the majority of the laser lines ascribed to Xe III.

The extended analysis of the Xe III spectrum also has some consequences for the interpretation of the Auger spectrum following ionization in the $4d$ subshell of neutral xenon.

2. Experimental

The vacuum-ultraviolet part of the spectrum was recorded in Lund. Two different light sources were used: a direct-current hollow-cathode discharge [10] and a theta-pinch discharge [11]. The hollow-cathode source gives a Xe III spectrum of better quality as regards resolution and obtainable wavelength accuracy, while the theta-pinch exposures were of great value in the determination of the ionization stages of the observed lines. The spectrum was photographed on a 3 m normal-incidence spectrograph with a plate factor of 2.77 Å/mm in the first diffraction order [12]. The wavelength range above 2000 Å was recorded on a 3.4 m Ebert plane-grating spectrograph in La Plata. This instrument has a plate factor of 5 Å/mm in the first diffraction order. The results of the wavelength measurements in air have been discussed previously [13]. The spectrum was excited in a laser-tube-like source (without end-mirrors) about 1 m in length and with an inner diameter of 3 mm. The tube has inner electrodes and was viewed end-on [14].

The wavelengths and intensities of all classified Xe III lines are given in Table I. In the long-wavelength end of the spectrum, outside the range covered by the present recording, a few lines have been included from an unpublished xenon line-list by Humphreys [15]. The quality of the recorded spectra does not permit very accurate wavelength determination. Most lines are fairly wide. The overall wavelength accuracy is estimated to be 0.05 Å in the air region and 0.02 Å in the vacuum-ultraviolet wavelength region.

The intensity figures are visual estimates of photographic density, and are on a uniform scale only within limited wavelength ranges. For the lines quoted from Humphreys' list the intensities are on a completely different scale.

All the experimentally established Xe III levels are given in Tables II and III. The level values were determined by a least-squares procedure in which the appropriately weighted wave numbers of the identified lines were used as input. All level designations are in LS notation. In most cases the names given to the levels were taken from least-squares fits of the theoretical energy expressions to the experimentally observed level values. In general, the calculated purities of the states

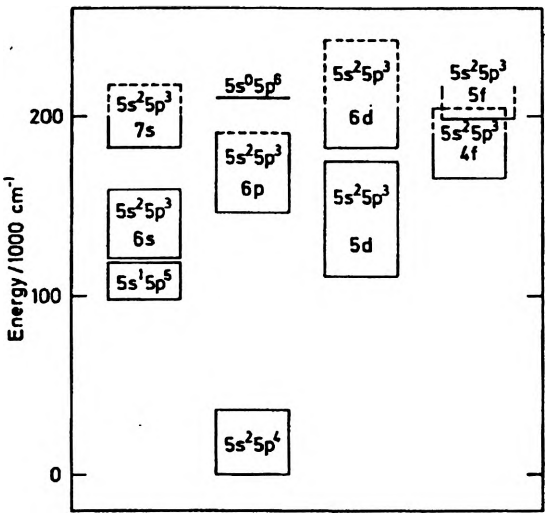


Fig. 1. Gross structure of the observed Xe III configurations. Broken lines indicate that not all levels of the configuration have been located.

(Tables II and III) are low, showing that the coupling conditions in the configurations investigated are intermediate.

3. Analysis

When performing the analysis of the experimental data we were guided by theoretical predictions of the level structures. Such predictions were obtained by diagonalization of the appropriate energy matrices, including CI matrix elements. The radial parts of the matrix elements were determined in Hartree–Fock calculations. Approximate scaling factors were determined from comparisons with calculations for similar structures. Figure 1 shows the relative positions and extensions of the configurations studied. The levels in $5s^25p^4$, $5s5p^5$ and $5s^05p^6$ were known from earlier investigations, though the designation of one level, $5s5p^5\ ^1P_1$ has been revised. The $5s^25p^3nl$ configurations can be considered as being built on the ground configuration of Xe IV, $5s^25p^3$, with the addition of an outer electron. The parent configuration gives three terms, namely ^4S, ^2D and ^2P. Almost all levels of the $5s^25p^36p$, $6s$ and $5d$ configurations have been experimentally established or verified in this work. In the $4f$ configuration, five of the levels based on the ^2P parent term are missing and in the $5s^25p^37s$ and $6d$ configurations only levels based on the ^4S and ^2D parent terms have been located. In the $5f$ configuration, only the levels belonging to the lowest term, $(^4S)^5F$, have been located with certainty.

Figure 1 shows that there is severe overlapping of configurations of the same parity. This leads to heavy mixing of states belonging to different configurations, even if the matrix elements connecting the states are small. Such mixing occurs between $6s$ and $5d$, $7s$ and $6d$ and between $6p$ and $4f$ states.

3.1. *Even configurations*

When interpreting the observed energy-level structure of the even-parity configurations, the total energy matrix for the $5s^25p^4 + 5s^25p^3(6p + 4f + 5f) + 5s5p^45d + 5s^05p^6$ configurations was diagonalized. The calculated energy-level values were fitted to the observed ones by least-squares fits in which some of the energy parameters were treated as free parameters (Tables IV and V).

As is evident from Fig. 1, there are large energy separations between the levels of the ground configuration and the excited configurations. In cases like this, it is customary to diagonalize the energy matrix and to perform a least-squares fit for the ground configuration separately. However, it was found that a least-squares fit to the levels of the ground configuration, omitting the effective configuration-interaction parameter α, gives a large discrepancy between the observed and the calculated positions of the $5s^25p^4\ ^1D_2$ level. The radial integral in the CI matrix element between the s^2p^4 and s^0p^6 configurations is very large ($\sim 67000\,\mathrm{cm}^{-1}$). A simple perturbation calculation indicates that this interaction gives rise to a large shift ($\sim 8000\,\mathrm{cm}^{-1}$) of the $^1S_0$ level of the ground configuration. In a similar way, it was found that the interaction between the ground configuration and a "pure" $5s5p^45d$ configuration gives rise to large shifts ($\sim 4000\,\mathrm{cm}^{-1}$) of the ^3P and ^1D levels, but not to the $^1S_0$ level. Evidently, large specific level shifts may occur from these interactions between distant configurations. It was also found that the $5s^05p^6\ ^1S_0$ state interacts strongly with the $^1S_0$ state of the $5s5p^45d$ configuration and a substantial mixing of these two states occurs.

In the light of the above discussion we decided to include the ground configuration and the high-lying $5s5p^45d$ configuration in the energy matrix of the even configurations. CI effects between all the configurations were taken into account. In particular, it was found that the large specific deviation of the $p^4\ ^1D_2$ level was removed in this way, even with the configuration interaction parameters fixed at their HF values. As none of the levels belonging to the $5s5p^45d$ configuration has been established experimentally, the energy parameters of this configuration were held fixed at their HF values during the fitting process (except the $F^2(5p, 5p)$ integral which was scaled to 0.8 times the HF value.)

The level structure of the $5s^25p^36p$ and $4f$ configurations is given in Fig. 2. The positions of the observed levels of the lowest term of the $5f$ configuration are also indicated. It turns out that $4f$ is almost as low a configuration as $6p$. This reflects the fact that Xe III is close to the lanthanides and $4f$ is no longer hydrogenic. All levels are given in LS notation. Generally the designations given represent the largest contribution to the eigenvector. However, for many levels the purities are very low, the largest component amounting to only about 30% in some cases. In one case we have used the second largest eigenvector component to name the level. Thus the LS designations often have very little physical significance.

3.2. *Odd configurations*

The odd-parity configurations were also interpreted by means of energy matrix diagonalizations and parametric least-squares fits to the energy levels. The energy matrix included the $5s5p^5 + 5s^25p^3(6s + 7s + 5d + 6d)$ configurations (Tables VI and VII).

The detailed structure of the $5s5p^5$ and the $5s^25p^3(5d + 6s)$ configurations is shown in Fig. 3. The experimentally established part of the $5s^25p^3(6d + 7s)$ configurations is shown in Fig. 4. As can be seen from the figures, there are a number of fortuitous coincidences between $6s$ and $5d$ levels, and between $7s$ and $6d$ levels causing severe mixing of the corresponding states.

All levels are given in LS notation, but, as for the even-parity levels, the designations often have very little physical significance because of the severe mixing of states with

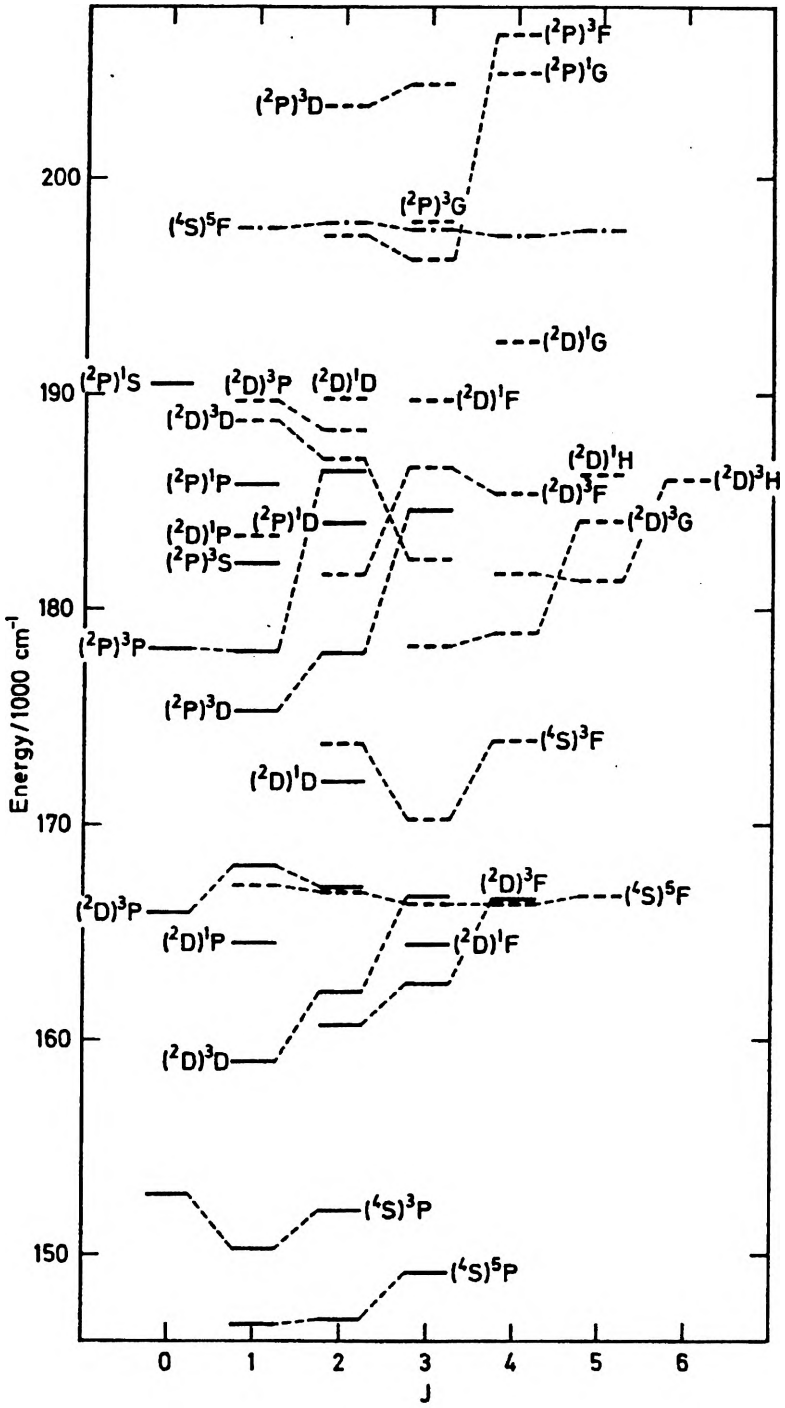


Fig. 2. Structure of the $5s^2 5p^3(6p + 4f)$ configurations of Xe III. The position of the lowest $5f$ term is also indicated. $6p$ levels are indicated by fully drawn lines, $4f$ levels by dashed and $5f$ levels by broken lines with dots in the centre. All levels are given in the LS coupling scheme.

different L and S values. To avoid duplication of labels it has sometimes been necessary to use the second largest or even the third largest eigenvector component to name the level.

There is also strong mixing between $5s5p^5$ and $5s^2 5p^3 5d$ states. Primarily this mixing is not caused by close level coincidences, but rather by large matrix elements connecting the states. The mixing is most pronounced for the singlets. In fact, there is no level having $5s5p^5\ ^1P$ as its largest eigenvector component. On the other hand, there are five levels having a substantial $5s5p^5\ ^1P$ contribution to their eigenvectors. As will be discussed below, this mixing has some consequences for the Auger spectrum following ionization of an inner $4d$ electron.

A general observation regarding $p^3 d$ configurations seems to be that the ^3S term of the lowest d configuration is predicted far below its observed position. In the $4p^3 4d$ configuration of Kr III [16], Rb IV [17], Sr V [18], and Y VI [19] the discrepancy is of the order of 3000 cm^{-1}. The discrepancy is also present in lighter elements, for instance in the $2p^3 3d$ configuration of Ne III [20]. It was shown in Refs [17] and [18] that, to a large extent, the discrepancy in the $4p^3 4d$ configurations of Sr V and Rb IV could be accounted for by the introduction of Rydberg-series configuration interactions, in

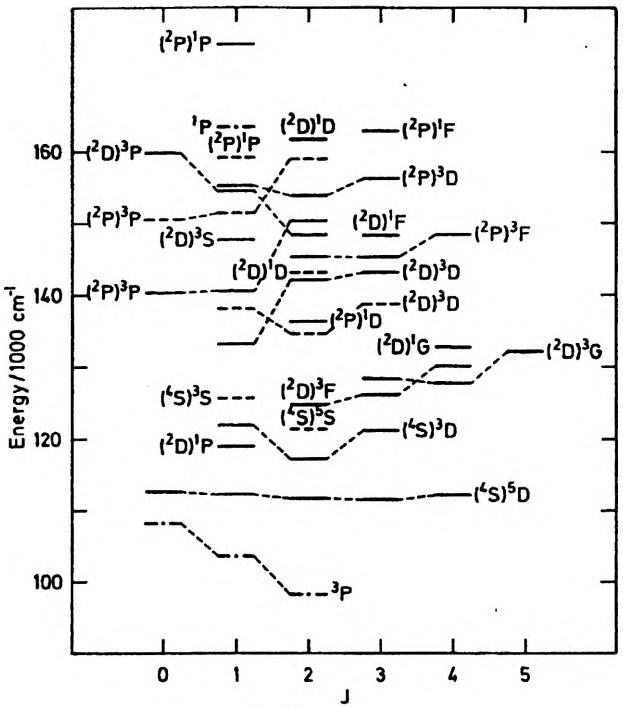


Fig. 3. Structure of the $5s5p^5 + 5s^25p^1(5d + 6s)$ configurations of Xe III. $5p^5$ levels are indicated by broken lines with dots in the centre, $6s$ levels by dashed and $5d$ by fully drawn lines. All levels are given in the *LS* coupling scheme.

particular the $4d \leftrightarrow 5d$ interaction, in the theoretical predictions of the level structure.

In Xe III the deviation between the observed and the calculated positions of the $5p^35d\ ^3S_1$ level is 700 cm^{-1}, even when using fitted values of the energy parameters. When introducing the Rydbergseries configuration interaction the deviation decreases to 170 cm^{-1}. At the same time the overall mean error of the fit decreases by approximately 20%. The $5d \leftrightarrow 6d$ R^3 CI integral could not be treated as an adjustable parameter at the same time as the R^1 and R^2 CI integrals. The R^3 integral was therefore optimized in a series of separate calculations and kept fixed in the final calculation.

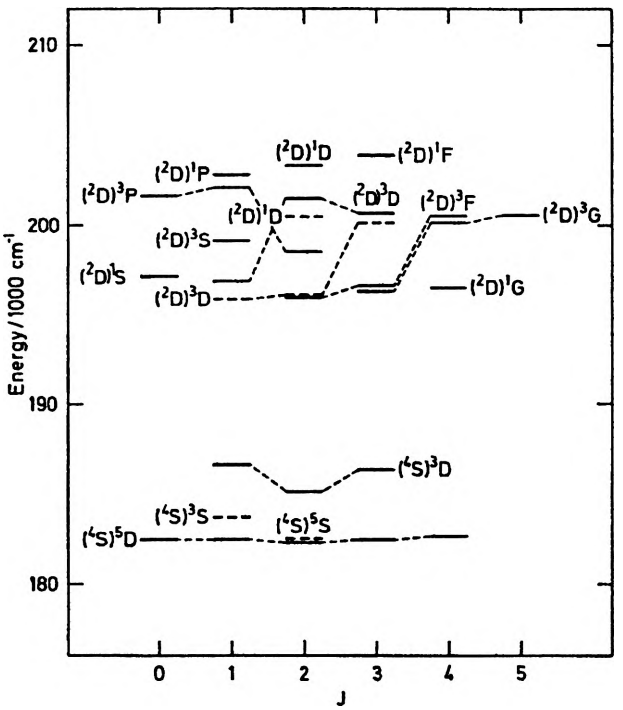


Fig. 4. Structure of the $5s^25p^3(6d + 7s)$ configurations of Xe III. Only levels based on the ^4S and ^2D parent terms are experimentally established and indicated in the figure. $6d$ levels are indicated by fully drawn lines and $7s$ levels by dashed lines. All levels are given in the *LS* coupling scheme.

In general there is good agreement between the g_J factors determined in the least-square fit and those obtained experimentally by Humphreys *et al.* [3] (Table VI). We have no reasonable explanation for the small observed g_J factors of the two $J = 1$ levels at 133 234 and 138 145 cm^{-1}.

4. Discussion

Recently, much effort has been devoted to the construction of VUV lasers. One recently observed [21] VUV laser transition is the transition at 1089 Å in Xe^{2+} connecting the odd level at 119 026 cm^{-1} above the ground state, and the even-parity $5s^05p^6\ ^1S_0$ state at 210 857 cm^{-1}. The lower state, previously designated as $5s5p^5\ ^1P_1$, is considered to decay rapidly to the ground state while the upper state can be populated by Auger processes.

As already pointed out, there is considerable mixing between the $5s5p^5$ and the $5s^25p^35d$ states, and in the present analysis the lower level has been designated $5s^25p^3(^2D)5d\ ^1P_1$. The purity of the state is only 44% and the $5s5p^5\ ^1P_1$ contribution is 28%. The $5s5p^5\ ^1P_1$ state is mixed into a number of different $5d$ states and this opens many different decay modes for the upper $5s^05p^6\ ^1S_0$ state. This fact probably has to be taken into account when discussing the possible efficiency of the laser action of this particular transition.

The present analysis, in particular as regards the mixing between the $5s5p^5$ and the $5s^25p^35d$ states, also has consequences for the intrepretation of the Auger spectrum of xenon following the ionization of a $4d$ electron, the $N_{4,5}OO$ spectrum (Fig. 5). The spectrum shown was recorded by Werme *et al.* [22], but has also been extensively studied by Southworth *et al.* [23], and Aksela *et al.* [24].

The spectrum consists of lines corresponding to the Xe^{2+} ion being left in different final states. There are two lines possible for each final state, corresponding to the fine structure of the initial hole in the $4d$ shell. One group of strong lines corresponds to the ion being left in the $5s^25p^4$ configuration, another group to the $5s5p^5$ final states and a third group corresponds to the ion being left with an empty $5s$ shell, i.e., the configuration $5s^05p^6$. The additional strong lines are satellites and are mainly caused by final-state configuration interaction, i.e., in the terminology of the present study, by the mixing between the $5s5p^5$ and the $5s^25p^35d$ (and possibly $6s$) states.

A detailed comparison between the Auger data and the present optical data is given in Table VIII. The energy of the $5s^25p^4\ ^3P_2$ ground level is set to zero. The agreement in relative energies is very good; the deviation never exceeding the estimated uncertainties in the Auger values (≈ 0.05 eV). The largest discrepancy is found for the $(^2P)6s\ ^1P_1$ level. However, the identification of this state in the Auger spectrum is tentative as it is based on a single line. Moreover, this line is doubly classified. It can also be seen that those $5d$ levels which have a significant $5s5p^5$ contribution to the eigenvector give rise to strong satellite lines in the Auger spectrum.

The new classifications for the Xe^{2+} laser lines are sum-

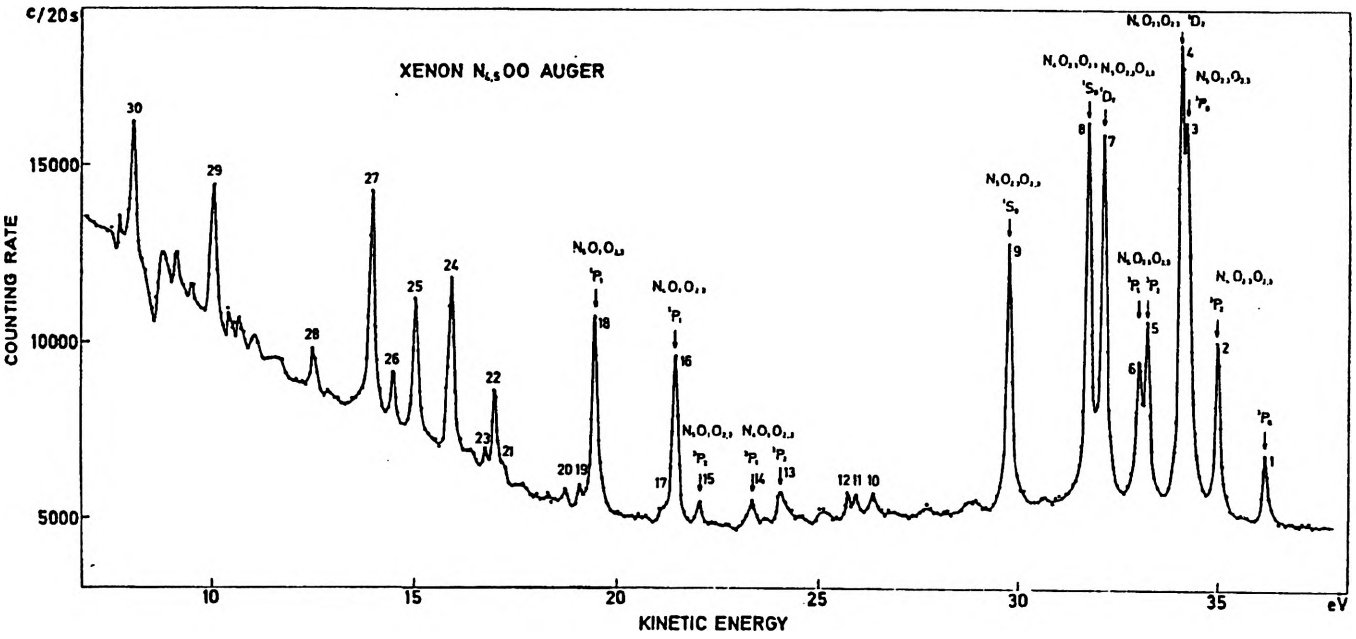


Fig. 5. Xenon $N_{4,5}OO$ Auger spectrum, from Ref. [22] (with permission from the authors).

marized in Table IX. The laser data are taken from the compilation by Beck et al. [9]. Table IX includes all laser lines ascribed with certainty or with some doubt to Xe^{2+}. Only very few lines remain unclassified. We have also included a laser line at 3349 Å, which, with a question mark, has been ascribed to Xe^{3+}, but in the present analysis has been classified as a Xe^{2+} line.

Based on a revised analysis and isoelectronic comparisons, Gallardo *et al.* [5] determined the value of 250400 ± 300 cm^{-1} (31.05 ± 0.04 eV) for the ionization energy of Xe^{2+}. Their value, which was about 9000 cm^{-1} lower than the previously accepted value [25], is in fairly good agreement with the later value by Dutil and Marmet [26]. Using electron-impact ionization of xenon they arrived at the value of 31.24 ± 0.10 eV. The present analysis does not indicate any need for revising the value of the ionization energy.

Acknowledgements

We are grateful for the financial support of the Consejo Nacional de Investigaciones Cientificas y Técnicas, Argentina and the Swedish Natural Science Research Council.

References

1. Boyce, J. C., Phys. Rev. **49**, 730 (1936).
2. Humphreys, C. J., J. Res. Natl. Bur. Stand. **16**, 639 (1936).
3. Humphreys, C. J., Meggers, W. F. and deBruin, T. L., J. Res. Natl. Bur. Stand. **23**, 683 (1939).
4. Edlén, B., Phys. Rev. **65**, 248 (1944).
5. Gallardo, M., Massone, C. A., Tagliaferri, A. A., Garavaglia, M. and Persson, W., Physica Scripta **19**, 538 (1979).
6. Hansen, J. E. and Persson, W., Physica Scripta **25**, 487 (1982).
7. Hertz, H., Z. Phys. **A274**, 289 (1975).
8. Hansen, J. E., Meijer, F. G., Outred, M., Persson, W. and Di Rocco, H. O., Physica Scripta **27**, 254 (1983).
9. Beck, R., Englisch, W. and Gürs, K., Table of Laser Lines in Gases and Vapors, p. 7, Springer-Verlag Berlin, Heidelberg, New York (1978).
10. Persson, W. and Minnhagen, L., Ark. Fys. **37**, 273 (1968).
11. Pettersson, S. -G., Physica Scripta **26**, 296 (1982).
12. Minnhagen, L., Physica Scripta **11**, 38 (1975).
13. Gallardo, M. and Reyna Almandos, J. G., Xenon Lines in the Range from 2000 Å to 7000 Å, Serie "Monografias Cientificas" No. 1, Centro de Investigaciones Opticas, La Plata (1981).
14. Reyna Almandos, J. G., Gallardo, M. and Garavaglia, M., Opt. Pura Appl. **15**, 1 (1982).
15. Humphreys, C. J., Unpublished.
16. Persson, W., Unpublished.
17. Persson, W. and Wahlström, C. -G., Physica Scripta **31**, 487 (1985).
18. Persson, W. and Wahlström, C. -G., Physica Scripta **30**, 169 (1984).
19. Persson, W. and Reader, J., J. Opt. Soc. Am. **B3**, 959 (1986).
20. Persson, W. and Di Rocco, H. O., Work in progress; Hansen, J. E., Judd, B. R., Lister, G. M. S. and Persson, W., J. Phys. B: At. Mol. Phys. **18**, L275 (1985).
21. Kapteyn, H. C., Lee, R. W. and Falcone, R. W., Phys. Rev. Lett. **57**, 2939 (1986).
22. Werme, L. O., Bergmark, T. and Siegbahn, K., Physica Scripta **6**, 141 (1972).
23. Southworth, S., Becker, U., Truesdale, C. M., Kobrin, P. H., Lindle, D. W., Owaki, S. and Shirley, D. A., Phys. Rev. **A28**, 261 (1983).
24. Aksela, H., Aksela, S. and Pulkkinen, H., Phys. Rev. **A30**, 865 (1984).
25. Moore, C. E., Ionization Potentials and Ionization Limits Derived from the Analyses of Optical Spectra, Nat. Stand. Ref. Data Ser., Nat. Bur. Stand. NSRDS-NBS 34, Washington (1970).
26. Dutil, R. and Marmet, P., Int. J. Mass. Spectrom. & Ion Phys. **35**, 371 (1980).
27. Reyna Almandos, J. G., Bredice, F., Di Rocco, H. and Gallardo, M., Opt. Pura Appl. **18**, 87 (1985).

Table I. *Observed spectral lines of Xe III. Wavelengths in air are given for lines with λ > 2000 Å. The intensity figures are visual estimates from the photographic density of the lines. An intensity figure in parenthesis indicates that the experimental data for the line stem from the unpublished wavelength list of Dr Humphreys. The calculated wavenumbers have been obtained from the level values given in Tables II and III by means of the Ritz combination principle. Only that part of the calculated wavenumber which differs from the observed is given. Level designations are given in LS notation*

Intensity[1]		λ (Å)	σ (cm⁻¹) obs	σ (cm⁻¹) calc	Classification
(2)	H	8869.40	11 271.62	.23	$(^4S)6d\ ^3D_1 - (^4S)5f\ ^5F_2$
(2)		8369.9	11 944.3	3.63	$(^2P)6p\ ^3D_3 - (^2D)6d\ ^1G_4$
(1)	h	8241.1	12 131.0	.83	$(^2P)6p\ ^1D_2 - (^2D)7s\ ^3D_2$
(2)	h	8239.3	12 133.6	.35	$(^4S)6d\ ^3D_2 - (^2P)4f\ ^3F_2$
(20)	h	8047.28	12 423.14	.55	$(^2D)4f\ ^3G_5 - (^2D)6d\ ^1G_4$
(100)	h, b	8038.26	12 437.08	.51	$(^4S)4f\ ^3F_4 - (^4S)6d\ ^3D_3$
(5)	b	8020.07	12 465.29	4.92	$(^4S)6d\ ^3D_2 - (^4S)5f\ ^5F_3$
(4)		7902.9	12 650.1	49.92	$(^4S)4f\ ^3F_2 - (^4S)6d\ ^3D_3$
(1)		7790.5	12 832.6	.39	$(^4S)6d\ ^3D_2 - (^2P)4f\ ^3G_3$
(10)		7777.1	12 854.7	5.03	$(^4S)4f\ ^3F_2 - (^4S)6d\ ^3D_1$
(10)	h	7589.40	13 172.65	3.12	$(^2P)5d\ ^3D_2 - (^2D)6p\ ^3P_2$
(1)	H	7483.2	13 359.6	60.20	$(^2P)5d\ ^1P_1 - (^2D)4f\ ^3P_2$
(5)	Hw	7353.0	13 596.1	7.10	$(^2D)4f\ ^1F_3 - (^2D)6d\ ^1D_2$
(10)	h	7311.15	13 673.97	.47	$(^4S)7s\ ^5S_2 - (^2P)4f\ ^3F_3$
(10)	Hw	7127.3	14 026.7	7.68	$(^2D)4f\ ^1H_5 - (^2D)6d\ ^3G_4$
(100)	H	6949.93	14 384.67	5.31	$(^2D)4f\ ^3H_6 - (^2D)6d\ ^3G_5$
0		6918.74	14 449.53	8.91	$(^2D)4f\ ^1H_5 - (^2D)6d\ ^3G_5$
0		6895.69	14 497.83	.38	$(^2D)5d\ ^3P_0 - (^2P)6p\ ^3D_1$
0		6858.44	14 576.55	.56	$(^2D)4f\ ^3H_4 - (^2D)6d\ ^3G_3$
1		6850.12	14 594.27	.24	$(^4S)6d\ ^5D_4 - (^4S)5f\ ^5F_4$
4		6847.83	14 599.14	.32	$(^2D)6p\ ^1D_2 - (^4S)6d\ ^3D_1$
0		6826.81	14 644.09	3.86	$(^2D)4f\ ^3F_4 - (^2D)6d\ ^3G_4$
0	h	6815.76	14 667.85	.80	$(^2D)4f\ ^3F_2 - (^2D)6d\ ^3G_3$
4		6799.47	14702.97	.93	$(^4S)6d\ ^5D_1 - (^2P)4f\ ^3F_2$
22	a	6780.40	14 744.34	.34	$(^4S)6d\ ^5D_4 - (^4S)5f\ ^5F_5$
4		6767.94	14 771.47	.71	$(^2P)5d\ ^1P_1 - (^2D)4f\ ^1D_2$
4		6767.94	14 771.47	.51	$(^4S)7s\ ^5S_2 - (^2P)4f\ ^3F_2$
2	h	6759.44	14 790.04	89.77	$(^4S)6d\ ^5D_3 - (^2P)4f\ ^3F_2$
15		6733.87	14 846.22	.09	$(^4S)6d\ ^5D_3 - (^4S)5f\ ^5F_4$
6		6722.74	14 870.78	.75	$(^4S)4f\ ^3F_3 - (^4S)6d\ ^3D_2$
0		6710.60	14 897.68	.94	$(^2D)4f\ ^3F_3 - (^2D)6d\ ^3D_2$
2		6698.81	14 923.92	.97	$(^2D)4f\ ^3H_4 - (^2D)6d\ ^3F_3$
2		6665.55	14 998.39	.44	$(^2P)5d\ ^1F_3 - (^2P)6p\ ^3D_2$
2		6657.74	15 015.96	.21	$(^2D)4f\ ^3F_2 - (^2D)6d\ ^3F_3$
15		6656.17	15 019.50	.03	$(^2D)4f\ ^1P_1 - (^2D)6d\ ^3P_2$
15		6656.17	15 019.50	8.94	$(^2D)4f\ ^3F_4 - (^2D)6d\ ^3F_4$
3	a	6638.35	15 059.84	.68	$(^4S)6d\ ^5D_1 - (^4S)5f\ ^5F_1$
8		6625.46	15089.14	.06	$(^4S)6d\ ^5D_0 - (^4S)5f\ ^5F_1$
2		6622.88	15 095.00	.02	$(^2P)6p\ ^1D_2 - (^2D)6d\ ^3S_1$
15		6619.33	15 103.11	.08	$(^4S)7s\ ^5S_2 - (^4S)5f\ ^5F_3$
7		6611.28	15 121.49	.34	$(^4S)6d\ ^5D_3 - (^4S)5f\ ^5F_3$
2		6608.30	15 128.32	.26	$(^4S)7s\ ^5S_2 - (^4S)5f\ ^5F_1$
3		6585.26	15 181.25	.28	$(^2D)4f\ ^3H_5 - (^2D)6d\ ^1G_4$
(6)	Hw	6558.5	15 243.2	.49	$(^2D)4f\ ^3F_4 - (^2D)6d\ ^3D_3$
3	a	6556.35	15 248.17	7.94	$(^4S)6d\ ^5D_2 - (^4S)5f\ ^5F_3$
2		6541.47	15 282.86	.93	$(^2D)4f\ ^3F_2 - (^2D)6d\ ^3D_1$
7		6530.17	15 309.32	.06	$(^4S)6d\ ^5D_1 - (^4S)5f\ ^5F_2$
7		6530.17	15 309.32	.20	$(^4S)4f\ ^5F_1 - (^4S)7s\ ^5S_2$
2		6513.62	15 348.20	.59	$(^2P)5d\ ^1F_3 - (^2D)4f\ ^3G_3$
2		6513.62	15 348.20	.41	$(^4S)4f\ ^5F_1 - (^4S)6d\ ^5D_0$
7		6501.08	15 377.81	.64	$(^4S)7s\ ^5S_2 - (^4S)5f\ ^5F_2$
7		6501.08	15 377.81	.78	$(^4S)4f\ ^5F_1 - (^4S)6d\ ^5D_1$
1		6493.33	15 396.16	5.90	$(^4S)6d\ ^5D_3 - (^4S)5f\ ^5F_2$
3		6484.78	15 416.46	.42	$(^2D)6p\ ^3P_2 - (^4S)7s\ ^5S_2$
1		6462.19	15 470.37	.55	$(^4S)7s\ ^5S_2 - (^2P)4f\ ^3G_3$
3		6456.10	15 484.96	5.00	$(^2D)6p\ ^3P_2 - (^4S)6d\ ^5D_1$
2		6454.53	15 488.71	.81	$(^4S)6d\ ^5D_3 - (^2P)4f\ ^3G_3$

Table I. *Continued*

Intensity[1]		λ (Å)	σ (cm⁻¹) obs	σ (cm⁻¹) calc	Classification
1		6409.67	15 597.11	.15	$(^2P)5d\ ^3D_3 - (^2D)6p\ ^1D_2$
1		6407.53	15 602.34	.65	$(^4S)4f\ ^5F_2 - (^4S)7s\ ^5S_2$
1		6396.07	15 630.28	1.17	$(^2D)4f\ ^1P_1 - (^2D)6d\ ^3S_1$
3		6367.63	15 700.09	.25	$(^2D)6p\ ^3P_1 - (^4S)7s\ ^3S_1$
5		6359.46	15 720.26	.68	$(^4S)4f\ ^5F_5 - (^4S)6d\ ^5D_3$
3		6341.26	15 765.37	.37	$(^2D)6p\ ^3D_3 - (^4S)6d\ ^5D_3$
6		6333.90	15 783.69	.63	$(^2D)6p\ ^3D_3 - (^4S)7s\ ^5S_2$
2		6283.74	15 909.68	.66	$(^2D)6p\ ^3F_4 - (^4S)6d\ ^5D_3$
1	a	6275.94	15 929.46	.68	$(^2P)5d\ ^1F_3 - (^2D)4f\ ^3G_4$
2		6273.33	15 936.09	.07	$(^2D)4f\ ^3G_5 - (^2D)6d\ ^3G_4$
1		6268.33	15 948.82	.78	$(^2D)6s\ ^1D_2 - (^2D)6p\ ^3D_1$
7		6260.10	15 969.79	.82	$(^2P)5d\ ^3P_2 - (^4S)4f\ ^5F_3$
14		6259.05	15 972.47	.53	$(^4S)4f\ ^5F_5 - (^4S)6d\ ^5D_4$
13		6238.19	16 025.88	.81	$(^2D)5d\ ^1F_3 - (^2D)6p\ ^1F_3$
5		6221.64	16 068.51	.52	$(^2D)5d\ ^3P_2 - (^2D)6p\ ^1F_3$
10		6205.96	16 109.10	8.68	$(^4S)4f\ ^5F_3 - (^4S)7s\ ^5S_2$
10		6205.96	16 109.10	.21	$(^4S)4f\ ^5F_4 - (^4S)6d\ ^5D_3$
1		6203.81	16 114.66	.97	$(^2D)4f\ ^3D_3 - (^2D)6d\ ^3P_2$
1		6196.42	16 133.88	.88	$(^4S)4f\ ^3F_3 - (^4S)6d\ ^3D_3$
1		6129.10	16 311.11	.15	$(^2D)4f\ ^3G_5 - (^2D)6d\ ^3F_4$
0	a	6111.90	16 356.99	.95	$(^2P)5d\ ^3D_2 - (^4S)4f\ ^3F_3$
0	a	6111.78	16 357.34	.30	$(^2D)4f\ ^3G_5 - (^2D)6d\ ^3G_5$
3		6110.35	16 361.14	.06	$(^4S)4f\ ^5F_4 - (^4S)6d\ ^5D_4$
(1)		6060.35	16 496.13	.10	$(^2D)5d\ ^1D_2 - (^2D)4f\ ^3G_3$
1	a	6026.51	16 588.78	.92	$(^2P)5d\ ^3D_1 - (^2D)6p\ ^1D_2$
(1)		5970.0	16 745.8	.92	$(^4S)6p\ ^5P_1 - 5s5p^5\ ^1P_1$
(10)	H	5961.15	16 770.64	.76	$(^4S)6d\ ^3D_1 - (^2P)4f\ ^3D_2$
(1)		5913.6	16 905.5	6.16	$(^4S)4f\ ^5F_2 - (^4S)7s\ ^3S_1$
3		5857.55	17 067.27	6.76	$(^2D)4f\ ^1P_1 - (^2D)7s\ ^1D_2$
3		5857.55	17 067.27	.08	$(^2D)5d\ ^3D_1 - (^4S)6p\ ^3P_1$
2		5780.51	17 294.73	.68	$(^2P)5d\ ^3F_2 - (^2D)6p\ ^3F_3$
1		5761.94	17 350.45	.45	$(^2D)5d\ ^3P_1 - (^2D)6p\ ^1D_2$
4		5754.03	17 374.33	.33	$(^2D)4f\ ^3G_4 - (^2D)6d\ ^3G_3$
6		5748.67	17 390.50	.31	$(^2D)6s\ ^3D_2 - (^4S)6p\ ^3P_2$
3		5701.24	17 535.20	.06	$(^2D)5d\ ^3D_3 - (^2D)6p\ ^3F_2$
1		5663.85	17 650.96	.90	$(^2D)4f\ ^3G_4 - (^2D)6d\ ^1G_4$
1		5657.24	17 671.58	.59	$(^2D)4f\ ^3G_3 - (^2D)6d\ ^3F_2$
1		5653.87	17 682.09	1.76	$(^2P)5d\ ^3P_2 - (^2D)6p\ ^3P_1$
1		5641.26	17 721.64	.74	$(^2D)4f\ ^3G_4 - (^2D)6d\ ^3F_3$
2		5610.18	17 819.79	.75	$(^2P)5d\ ^3F_4 - (^4S)4f\ ^5F_4$
4		5604.33	17 838.39	.54	$(^2P)5d\ ^3F_4 - (^4S)4f\ ^5F_5$
1	a	5565.83	17 961.78	.22	$(^2D)5d\ ^1F_3 - (^4S)4f\ ^5F_3$
5		5552.78	18 004.02	3.93	$(^2D)5d\ ^3P_2 - (^4S)4f\ ^5F_3$
2		5548.05	18 019.37	.30	$(^2P)5d\ ^3F_4 - (^2D)6p\ ^3F_4$
8		5524.33	18 096.73	.62	$(^2P)5d\ ^3D_2 - (^2D)6p\ ^1D_2$
2		5510.53	18 142.06	1.99	$(^2D)5d\ ^1F_3 - (^2D)6p\ ^3F_4$
3		5509.65	18 144.95	.28	$(^2D)5d\ ^3S_1 - (^2D)6p\ ^3P_0$
2		5503.98	18 163.65	.59	$(^2P)5d\ ^3F_4 - (^2D)6p\ ^3D_3$
1		5481.19	18 239.14	.01	$(^4S)6d\ ^3D_2 - (^2P)4f\ ^3D_2$
2		5470.94	18 273.34	.22	$(^2D)4f\ ^3D_3 - (^2D)6d\ ^3D_3$
1		5462.12	18 302.82	.83	$(^2D)4f\ ^3G_3 - (^2D)6d\ ^3F_3$
5		5453.06	18 333.25	.21	$(^2P)5d\ ^3D_1 - (^4S)4f\ ^3F_2$
10		5413.49	18 467.23	.25	$(^2D)5d\ ^1F_3 - (^4S)4f\ ^5F_2$
17		5401.01	18 509.93	.96	$(^2D)5d\ ^3P_2 - (^4S)4f\ ^5F_2$
6		5386.64	18 559.31	.20	$(^2P)5d\ ^3P_0 - (^2D)6p\ ^3D_1$
1		5384.15	18 567.89	.76	$(^2P)6s\ ^1P_1 - (^2P)6p\ ^3D_2$
3	a	5372.83	18 607.01	6.74	$5s5p^5\ ^1P_1 - (^2P)6p\ ^3S_1$
2		5371.01	18 613.32	.26	$(^2D)5d\ ^3G_3 - (^4S)6p\ ^5P_2$
14		5367.03	18 627.09	.03	$(^2D)5d\ ^3D_2 - (^2D)6p\ ^3F_2$
1		5364.39	18 636.29	.20	$(^2P)5d\ ^1F_3 - (^2D)4f\ ^3F_2$
6		5347.87	18 693.83	.80	$(^2D)4f\ ^3H_5 - (^2D)6d\ ^3G_4$
5		5347.17	18 696.27	.19	$(^2D)5d\ ^3P_2 - (^2D)6p\ ^3P_2$
1		5322.80	18 781.90	.60	$(^2P)6p\ ^3D_3 - (^2D)6d\ ^1D_2$
7		5310.97	18 823.73	.71	$(^2D)5d\ ^3D_1 - (^4S)6p\ ^3P_2$
4		5292.92	18 887.93	.83	$(^2D)5d\ ^3F_4 - (^4S)6p\ ^5P_3$
1		5242.67	19 068.96	.89	$(^2D)4f\ ^3H_5 - (^2D)6d\ ^3F_4$
16		5238.92	19 082.58	.67	$(^2D)5d\ ^3S_1 - (^4S)4f\ ^5F_2$
1		5233.96	19 100.70	1.23	$(^2P)6s\ ^3P_2 - (^2P)6p\ ^3P_1$

Table I. *Continued*

Intensity[a]		λ (Å)	σ (cm⁻¹) obs	calc	Classification
3		5233.10	19 103.81	.73	$(^2D)5d\ ^3D_3-(^2D)6p\ ^3D_2$
1		5229.99	19 115.17	.03	$(^2D)4f\ ^3H_5-(^2D)6d\ ^3G_5$
11		5223.62	19 138.51	.51	$(^2P)5d\ ^3F_2-(^2D)6p\ ^1F_3$
1		5203.67	19 211.88	.77	$(^2D)6s\ ^1D_2-(^2D)6p\ ^3D_2$
1		5148.03	19 419.49	.51	$(^2P)5d\ ^1F_3-(^2D)4f\ ^3D_3$
6		5142.98	19 438.59	.57	$(^2D)5d\ ^3D_3-(^2D)6p\ ^3F_3$
1		5114.53	19 546.72	.61	$(^2D)6s\ ^1D_2-(^2D)6p\ ^3F_3$
14		5107.33	19 574.24	.15	$(^2D)5d\ ^3D_1-(^4S)6p\ ^3P_0$
9		5041.40	19 830.25	.25	$(^2P)5d\ ^3D_1-(^2P)6p\ ^3D_1$
1	b	5040.06	19 835.52	6.26	$(^2P)6p\ ^1D_2-(^2D)6d\ ^1F_3$
2		5038.62	19 841.20	0.92	$(^2P)5d\ ^3D_2-(^4S)4f\ ^3F_2$
3		5023.01	19 902.85	3.09	$(^2D)4f\ ^1P_1-(^2D)6d\ ^1D_2$
23		5008.53	19 960.40	.37	$(^2P)5d\ ^3P_1-(^2D)6p\ ^3F_2$
0		4996.10	20 010.02	9.98	$(^4S)4f\ ^5F_3-(^4S)6d\ ^3D_3$
1		4952.53	20 186.06	5.89	$(^2D)4f\ ^3G_3-(^2D)6d\ ^3P_2$
5		4927.51	20 288.55	.58	$(^2D)5d\ ^3S_1-(^2D)6p\ ^3P_1$
1	a	4926.72	20 291.83	.35	$(^2D)6p\ ^3D_2-(^4S)6d\ ^5D_1$
1		4918.87	20 324.22	.16	$(^2D)5d\ ^1D_2-(^2P)6p\ ^3S_1$
2		4881.05	20 481.70	.70	$5s5p^5\ ^1P_1-(^2P)6p\ ^1D_2$
21		4869.40	20 530.66	.55	$(^2D)5d\ ^3D_2-(^2D)6p\ ^3F_3$
8	a	4796.51	20 842.69	.65	$(^2D)5d\ ^3F_3-(^4S)6p\ ^5P_2$
25		4794.49	20 851.44	.49	$(^2D)6s\ ^3D_1-(^2D)6p\ ^3D_1$
3	h	4781.08	20 909.92	.78	$(^2P)6p\ ^3D_1-(^2D)7s\ ^3D_2$
10		4757.32	21 014.39	.36	$(^2P)5d\ ^3F_3-(^4S)4f\ ^5F_4$
18		4748.94	21 051.47	.60	$(^2P)5d\ ^1F_3-(^2P)6p\ ^1D_2$
10		4743.90	21 073.83	.93	$(^2P)5d\ ^3F_2-(^4S)4f\ ^5F_3$
16		4723.60	21 164.40	.42	$(^4S)6s\ ^3S_1-(^4S)6p\ ^5P_1$
20	b	4712.58	21 213.89	.92	$(^2P)5d\ ^3F_3-(^2D)6p\ ^3F_4$
6		4697.42	21 282.35	.41	$(^2D)5d\ ^3D_3-(^2D)6p\ ^1F_3$
2	a	4685.19	21 337.87	.96	$(^2P)5d\ ^3D_2-(^2P)6p\ ^3D_1$
20		4683.55	21 345.38	.36	$(^4S)6s\ ^3S_1-(^4S)6p\ ^5P_2$
1	h	4680.73	21 358.24	.21	$(^2P)5d\ ^3F_3-(^2D)6p\ ^3D_3$
18	a	4673.67	21 390.46	.44	$(^2D)6s\ ^1D_2-(^2D)6p\ ^1F_3$
3		4671.81	21 399.01	8.98	$(^2P)5d\ ^3F_2-(^2D)6p\ ^3D_3$
8		4671.60	21 399.98	400.37	$(^2D)5d\ ^3P_0-(^2P)6p\ ^3S_1$
17	a	4657.78	21 463.47	.45	$(^2D)6s\ ^1D_2-(^2D)6p\ ^1P_1$
1	h	4656.73	21 468.32	.35	$(^2D)4f\ ^3D_3-(^2D)6d\ ^1F_3$
5		4644.17	21 526.33	.27	$(^2D)6p\ ^3D_2-(^4S)7s\ ^3S_1$
1		4643.60	21 529.01	.04	$(^2P)5d\ ^3P_1-(^2D)6p\ ^3D_2$
15		4641.40	21 539.18	.18	$(^2P)5d\ ^3F_3-(^4S)4f\ ^5F_2$
8		4632.64	21 579.95	.96	$(^2P)5d\ ^3F_2-(^4S)4f\ ^5F_2$
2	a	4631.65	21 584.56	.65	$(^2D)4f\ ^3G_4-(^2D)6d\ ^3G_5$
6		4620.42	21 636.98	.95	$(^2P)5d\ ^1F_3-(^2P)6p\ ^3D_3$
2		4614.83	21 663.19	2.97	$(^2D)5d\ ^1D_2-(^2D)4f\ ^1P_1$
2		4601.60	21 725.47	.41	$(^2P)5d\ ^3F_3-(^2D)6p\ ^3P_2$
2	h	4592.98	21 766.29	.19	$(^2P)5d\ ^3F_2-(^2D)6p\ ^3P_2$
2		4578.03	21 837.33	.32	$(^2D)5d\ ^1F_3-(^4S)4f\ ^3F_3$
7		4569.12	21 879.95	80.02	$(^2D)5d\ ^3P_2-(^4S)4f\ ^3F_3$
1	a	4555.51	21 945.28	.39	$(^2D)6p\ ^1F_3-(^4S)6d\ ^3D_3$
9	a	4537.38	22 032.99	3.10	$(^2D)6s\ ^3D_3-(^2D)6p\ ^3F_2$
2	h	4528.24	22 077.47	.52	$(^2P)6p\ ^3D_2-(^2D)7s\ ^3D_3$
2	h	4528.24	22 077.47	.49	$(^2D)6p\ ^1P_1-(^4S)6d\ ^3D_1$
1		4525.63	22 090.20	.16	$(^2D)5d\ ^3F_2-(^4S)6p\ ^5P_1$
14	a	4503.41	22 199.20	.12	$(^2D)5d\ ^1D_2-(^2P)6p\ ^1D_2$
5	a	4492.80	22 251.62	.69	$(^2P)6s\ ^3P_1-(^4S)4f\ ^3F_2$
5	a	4492.80	22 251.62	.66	$(^2D)4f\ ^3F_2-(^2D)6d\ ^1F_3$
4	a	4488.90	22 270.95	1.09	$(^2D)5d\ ^3F_2-(^4S)6p\ ^5P_2$
2		4480.05	22 314.95	.98	$(^4S)4f\ ^3F_4-(^2D)6d\ ^3G_5$
8	b	4470.90	22 360.61	.63	$5s5p^5\ ^1P_1-(^2P)6p\ ^1P_1$
5		4468.16	22 374.33	.38	$(^2D)5d\ ^3D_2-(^2D)6p\ ^1F_3$
7		4453.60	22 447.47	.39	$(^2D)5d\ ^3D_2-(^2D)6p\ ^1P_1$
1		4453.29	22 449.03	.24	$(^2P)5d\ ^1F_3-(^2D)4f\ ^3F_4$
15		4434.17	22 545.83	.81	$(^2D)6s\ ^3D_1-(^2D)6p\ ^3F_2$
3		4417.97	22 628.50	.43	$(^2P)5d\ ^3D_1-(^2P)6p\ ^3P_1$
2		4417.78	22 629.48	.50	$(^2P)5d\ ^1D_2-(^2D)6p\ ^3D_1$
8		4413.06	22 653.67	.63	$(^2P)5d\ ^3D_1-(^2P)6p\ ^3P_0$
13		4395.17	22 745.84	.97	$(^2P)6s\ ^1P_1-(^2P)6p\ ^3S_1$
4		4387.72	22 784.50	.46	$(^2D)5d\ ^1D_2-(^2P)6p\ ^3D_3$

Table I. *Continued*

Intensity[a]		λ (Å)	σ (cm⁻¹) obs	calc	Classification
4		4387.47	22 785.80	.87	$(^2P)5d\ ^3F_2-(^2D)6p\ ^3P_1$
4		4386.01	22 793.35	.48	$5s5p^5\ ^1P_1-(^2P)6p\ ^3P_2$
3		4373.06	22 860.88	.93	$(^2D)6p\ ^3D_2-(^4S)6d\ ^3D_2$
3		4357.63	22 941.83	.80	$(^2D)5d\ ^3F_3-(^4S)6p\ ^3P_2$
2		4319.85	23 142.47	.51	$(^4S)4f\ ^3F_2-(^2D)6d\ ^3D_1$
7		4309.32	23 199.03	.03	$(^2D)5d\ ^3D_3-(^4S)4f\ ^5F_4$
6		4308.01	23 206.07	.12	$(^2D)4f\ ^3G_3-(^2D)6d\ ^3D_2$
6		4308.01	23 206.07	.04	$(^2P)6s\ ^3P_2-(^2P)6p\ ^3S_1$
1	a	4305.83	23 217.82	.82	$(^2D)5d\ ^3D_3-(^4S)4f\ ^5F_3$
1	a	4297.96	23 260.34	.82	$(^2P)6p\ ^3D_1-(^2D)6d\ ^3P_2$
4		4289.33	23 307.13	.07	$(^2D)6s\ ^1D_2-(^4S)4f\ ^5F_4$
5	a	4287.58	23 316.65	.56	$(^2D)5d\ ^3P_1-(^2P)6p\ ^3D_2$
20		4285.89	23 325.85	.86	$(^2D)6s\ ^1D_2-(^4S)4f\ ^5F_3$
4		4278.91	23 363.90	.39	$(^2P)5d\ ^1F_3-(^2P)6p\ ^3P_2$
4		4274.14	23 389.97	.96	$(^2D)5d\ ^3P_1-(^2P)6p\ ^3P_1$
17		4272.58	23 398.50	.59	$(^2D)5d\ ^3D_3-(^2D)6p\ ^3F_4$
12		4263.40	23 448.88	.91	$(^2P)6s\ ^3P_2-(^2D)4f\ ^3D_3$
2		4246.38	23 542.86	.88	$(^2D)5d\ ^3D_3-(^2D)6p\ ^3D_3$
16		4240.24	23 576.96	.99	$(^2D)5d\ ^1F_3-(^2D)6p\ ^1D_2$
2	a	4235.76	23 601.90	.77	$(^2D)6s\ ^3D_3-(^2D)6p\ ^3D_2$
13		4226.97	23 650.97	.91	$(^2D)6s\ ^1D_2-(^2D)6p\ ^3D_3$
0		4225.96	23 656.63	.76	$(^2P)5d\ ^1F_3-(^2D)4f\ ^3F_3$
10		4216.71	23 708.53	.57	$(^2D)5d\ ^3G_3-(^4S)6p\ ^3P_2$
24		4213.99	23 723.82	.85	$(^2D)5d\ ^3D_3-(^4S)4f\ ^5F_2$
14		4209.58	23 748.63	.73	$(^2P)6s\ ^3P_1-(^2P)6p\ ^3D_1$
13		4203.89	23 780.83	.72	$(^2P)5d\ ^3P_1-(^2D)6p\ ^1P_1$
2	a	4202.39	23 789.32	.22	$(^2D)6p\ ^3F_3-(^4S)6d\ ^3D_3$
9		4194.87	23 831.96	.89	$(^2D)6s\ ^1D_2-(^4S)4f\ ^5F_2$
4		4181.15	23 910.15	.08	$(^2D)5d\ ^3D_3-(^2D)6p\ ^3P_2$
16		4176.53	23 936.61	.61	$(^2D)6s\ ^3D_3-(^2D)6p\ ^3F_3$
2		4167.60	23 987.89	.85	$(^2D)6p\ ^1D_2-(^2D)6d\ ^3F_2$
2		4162.37	24 018.04	.12	$(^2D)6s\ ^1D_2-(^2D)6p\ ^3P_2$
5	b	4154.66	24 062.61	.73	$(^2P)5d\ ^3D_2-(^2P)6p\ ^3D_2$
4	b	4152.74	24 073.73	.87	$(^2P)5d\ ^3P_0-(^2D)6p\ ^1P_1$
8	a	4152.04	24 077.78	8.05	$(^2D)5d\ ^1D_2-(^2P)6p\ ^1P_1$
3	b	4150.78	24 085.10	4.77	$(^2P)6s\ ^1P_1-(^2D)4f\ ^1P_1$
22	a	4145.74	24 114.33	.48	$(^2D)6s\ ^3D_1-(^2D)6p\ ^3D_2$
5		4143.92	24 124.92	5.34	$(^2D)6s\ ^1D_2-(^4S)4f\ ^5F_1$
13	b	4141.99	24 136.16	.13	$(^2P)5d\ ^3D_2-(^2P)6p\ ^3P_1$
12		4132.40	24 192.21	.41	$(^2D)5d\ ^3S_1-(^2D)6p\ ^1D_2$
12		4110.05	24 323.78	.82	$(^2P)5d\ ^1D_2-(^2D)6p\ ^3F_2$
20		4109.08	24 329.51	.56	$(^2D)6s\ ^3D_2-(^2D)6p\ ^3D_1$
5	b	4095.03	24 412.98	.88	$(^2P)5d\ ^3D_2-(^2D)4f\ ^3G_3$
21		4078.70	24 510.72	.90	$(^2D)5d\ ^1D_2-(^2P)6p\ ^3P_2$
7		4072.97	24 545.20	4.85	$(^2P)6s\ ^3P_2-(^2D)4f\ ^1P_1$
25		4060.45	24 620.88	.92	$(^2P)6s\ ^1P_1-(^2P)6p\ ^1D_2$
5		4058.15	24 634.84	.85	$(^2D)5d\ ^3D_2-(^2D)6p\ ^3D_3$
22		4050.07	24 683.98	4.04	$(^4S)6s\ ^3S_1-(^4S)6p\ ^3P_1$
14		4043.23	24 725.74	.85	$(^2P)6s\ ^3P_0-(^2P)6p\ ^3D_1$
4	a	4032.91	24 789.01	.26	$(^2D)6p\ ^3D_1-(^4S)7s\ ^3S_1$
1		4030.46	24 804.08	.28	$(^2D)5d\ ^1D_2-(^2D)4f\ ^3F_3$
15		4028.56	24 815.78	.82	$(^2D)5d\ ^3D_2-(^4S)4f\ ^5F_2$
2		4026.82	24 826.50	.92	$(^2P)5d\ ^3P_2-(^2P)6p\ ^3D_1$
7		4021.60	24 858.72	.73	$(^4S)5d\ ^3D_1-(^4S)6p\ ^5P_1$
4		3998.55	25 002.02	.06	$(^2D)5d\ ^3D_2-(^2D)6p\ ^3P_2$
21		3992.85	25 037.71	.80	$(^2D)6s\ ^1D_2-(^2D)6p\ ^3P_1$
3		3992.54	25 039.65	.66	$(^4S)5d\ ^3D_1-(^4S)6p\ ^5P_2$
12		3985.96	25 080.99	1.00	$(^2P)6s\ ^3P_2-(^2P)6p\ ^1D_2$
8		3969.91	25 182.39	.45	$(^2D)5d\ ^1D_2-(^2D)4f\ ^3D_2$
8		3965.45	25 210.71	.76	$(^2P)5d\ ^3P_1-(^2D)6p\ ^3P_0$
25		3950.59	25 305.54	.54	$(^4S)6s\ ^5S_2-(^4S)6p\ ^5P_1$
3		3950.12	25 308.55	.56	$(^2P)6p\ ^3D_1-(^2D)7s\ ^1D_2$
3		3941.50	25 363.90	.99	$(^2D)5d\ ^3P_2-(^4S)4f\ ^3F_2$
2		3932.81	25 419.94	20.11	$(^2P)6p\ ^3D_2-(^2D)6d\ ^1D_2$
25		3922.55	25 486.43	.47	$(^4S)6s\ ^5S_2-(^4S)6p\ ^5P_2$
8		3915.31	25 533.55	.69	$(^2D)5d\ ^1F_3-(^4S)4f\ ^3F_4$
8		3903.67	25 609.69	.77	$(^2D)5d\ ^3F_2-(^4S)6p\ ^3P_1$
19		3895.05	25 666.36	.34	$(^2P)6s\ ^3P_2-(^2P)6p\ ^3D_3$

Table I. *Continued*

Intensity[a]		λ (Å)	σ (cm⁻¹) obs	σ (cm⁻¹) calc	Classification
2		3890.98	25 693.21	2.74	$(^2D)6p\ ^3F_2 - (^4S)6d\ ^3D_3$
13		3884.99	25 732.82	.84	$(^4S)5d\ ^3D_3 - (^4S)6p\ ^5P_2$
18		3880.46	25 762.86	.97	$(^2D)5d\ ^3D_1 - (^2D)6p\ ^3D_1$
20		3877.82	25 780.40	.44	$(^2D)6s\ ^3D_3 - (^2D)6p\ ^1F_3$
7		3861.51	25 889.29	.42	$(^2P)6p\ ^3D_2 - (^2D)6d\ ^1F_3$
19		3861.04	25 892.44	.49	$(^2P)5d\ ^1D_2 - (^2D)6p\ ^3D_2$
2		3860.19	25 898.14	7.85	$(^2D)6p\ ^3F_2 - (^4S)6d\ ^3D_1$
14		3854.28	25 937.85	.95	$(^2D)5d\ ^3F_3 - (^4S)6p\ ^3P_2$
8		3847.40	25 984.23	.33	$(^2P)5d\ ^3D_3 - (^2D)4f\ ^3D_3$
18		3841.87	26 021.63	.73	$(^2D)5d\ ^3D_2 - (^2D)6p\ ^3P_1$
20		3841.53	26 023.94	.88	$(^2D)6s\ ^3D_2 - (^2D)6p\ ^3F_2$
8		3829.71	26 104.26	.07	$(^4S)4f\ ^3F_4 - (^2D)6d\ ^3G_4$
3		3823.15	26 149.05	.15	$(^2P)5d\ ^3P_1 - (^4S)4f\ ^5F_2$
2		3819.49	26 174.10	.06	$5s5p^5\ ^1P_1 - (^2D)4f\ ^3P_1$
7		3816.78	26 192.69	.79	$(^2P)5d\ ^3D_1 - (^2D)4f\ ^3F_2$
3		3811.74	26 227.32	.34	$(^2P)5d\ ^1D_2 - (^2D)6p\ ^3F_3$
4	w	3802.98	26 287.73	.92	$(^4S)4f\ ^3F_3 - (^2D)6d\ ^1G_4$
8		3801.71	26 296.51	.66	$5s5p^5\ ^1P_1 - (^2D)4f\ ^1D_2$
2		3792.74	26 358.70	.76	$(^4S)4f\ ^3F_3 - (^2D)6d\ ^3F_3$
15		3791.67	26 366.14	.16	$(^2D)6s\ ^3D_1 - (^2D)6p\ ^1P_1$
28		3781.00	26 440.54	.66	$(^4S)6s\ ^3S_1 - (^4S)6p\ ^3P_2$
24		3776.32	26 473.31	.50	$(^2P)6s\ ^3P_1 - (^2P)6p\ ^3D_2$
2	b	3775.49	26 479.13	.16	$(^4S)4f\ ^3F_4 - (^2D)6d\ ^3F_4$
15		3772.53	26 499.91	.86	$(^2P)6s\ ^1P_1 - (^2P)6p\ ^1P_1$
1		3772.25	26 501.87	2.15	$(^2D)6p\ ^1D_2 - (^2D)6d\ ^3P_2$
12		3768.93	26 525.22	.30	$(^4S)4f\ ^3F_4 - (^2D)6d\ ^3G_5$
14		3765.85	26 546.91	.90	$(^2P)6s\ ^3P_1 - (^2P)6p\ ^3P_1$
19		3762.28	26 572.10	.10	$(^2P)6s\ ^3P_1 - (^2P)6p\ ^3P_0$
5		3757.98	26 602.51	.58	$(^2D)5d\ ^1D_2 - (^2D)4f\ ^3P_2$
3		3751.44	26 648.88	.91	$(^2P)5d\ ^3F_3 - (^2D)6p\ ^1D_2$
18		3745.71	26 689.65	.69	$(^2P)5d\ ^3F_2 - (^2D)6p\ ^1D_2$
2		3743.74	26 703.69	.70	$(^4S)4f\ ^3F_4 - (^2D)6d\ ^3D_3$
2		3739.60	26 733.25	.24	$(^2P)5d\ ^3D_1 - (^2P)6p\ ^3S_1$
5	b	3728.91	26 809.89	10.19	$(^2P)6p\ ^1D_2 - (^2P)6d\ ^3D_1$
1		3721.82	26 860.96	1.03	$(^2D)5d\ ^3P_2 - (^2P)6p\ ^3D_1$
1		3721.03	26 866.66	.57	$(^2P)5d\ ^1F_3 - (^2D)4f\ ^1D_2$
10		3711.91	26 932.67	.71	$(^2P)6s\ ^1P_1 - (^2P)6p\ ^3P_2$
8		3708.94	26 954.24	.33	$(^2D)5d\ ^3P_1 - (^2D)4f\ ^3F_2$
10		3708.15	26 959.98	.93	$(^2P)6s\ ^3P_2 - (^2P)6p\ ^1P_1$
1		3707.63	26 963.76	.76	$5s5p^5\ ^1P_1 - (^2P)6p\ ^1S_0$
6		3689.83	27 093.83	.91	$(^2D)5d\ ^3D_3 - (^4S)4f\ ^3F_3$
3		3687.04	27 114.33	.30	$(^2D)6p\ ^1D_2 - (^2D)6d\ ^3S_1$
23		3676.63	27 191.10	.11	$(^4S)6s\ ^3S_1 - (^4S)6p\ ^3P_0$
2		3675.17	27 201.90	.95	$(^2D)6s\ ^1D_2 - (^4S)4f\ ^3F_3$
16		3654.61	27 354.93	5.06	$(^2P)5d\ ^3P_1 - (^2D)6p\ ^3P_1$
8		3653.09	27 366.31	.40	$(^2D)5d\ ^3F_2 - (^4S)6p\ ^3P_2$
13		3649.57	27 392.71	.78	$(^2P)6s\ ^3P_2 - (^2P)6p\ ^3P_2$
10		3644.14	27 433.52	.74	$(^2D)5d\ ^3S_1 - (^2P)6p\ ^3D_1$
15		3640.99	27 457.26	.29	$(^2D)5d\ ^3D_1 - (^2D)6p\ ^3F_2$
11		3636.02	27 494.79	.78	$(^2D)5d\ ^3P_1 - (^2P)6p\ ^3S_1$
15		3632.14	27 524.16	.02	$(^2P)6s\ ^3P_0 - (^2P)6p\ ^3P_1$
8		3628.52	27 551.62	.69	$(^2P)5d\ ^3P_2 - (^2P)6p\ ^3D_2$
25		3624.06	27 585.52	.62	$(^4S)6s\ ^5S_2 - (^4S)6p\ ^5P_3$
21	a	3623.13	27 592.60	.55	$(^2D)6s\ ^3D_2 - (^2D)6p\ ^3D_2$
4		3621.59	27 604.34	.25	$(^2P)6s\ ^1P_1 - (^2D)4f\ ^3D_2$
11		3620.00	27 616.46	.42	$(^2P)5d\ ^3D_3 - (^2P)6p\ ^1D_2$
8		3618.86	27 625.16	.09	$(^2P)5d\ ^3P_2 - (^2P)6p\ ^3P_1$
10		3615.86	27 648.08	.21	$(^2P)5d\ ^3P_0 - (^2D)6p\ ^3P_1$
0		3610.97	27 685.52	6.16	$(^2P)6s\ ^3P_2 - (^2D)4f\ ^3F_3$
22	a	3609.46	27 697.10	.07	$(^2D)6s\ ^3D_3 - (^4S)4f\ ^5F_4$
8	h	3609.07	27 700.09	.50	$(^2P)5d\ ^3D_2 - (^2D)4f\ ^3F_2$
22	a	3607.02	27 715.84	.86	$(^2D)6s\ ^3D_3 - (^4S)4f\ ^5F_3$
12		3601.87	27 755.46	.46	$(^2D)5d\ ^1P_1 - (^4S)6p\ ^5P_1$
17		3596.59	27 796.21	.20	$(^2D)6s\ ^3D_1 - (^2D)6p\ ^3P_0$
5		3593.38	27 821.04	.05	$(^2D)6p\ ^3P_1 - (^2D)7s\ ^3D_1$
8		3591.98	27 831.88	.99	$(^4S)5d\ ^3D_3 - (^4S)6p\ ^5P_3$
5		3584.27	27 891.75	.48	$(^2D)5d\ ^1D_2 - (^2D)4f\ ^3P_1$
5		3584.27	27 891.75	.67	$(^2D)6p\ ^3P_1 - (^2D)6d\ ^3F_2$

Table I. *Continued*

Intensity[a]		λ (Å)	σ (cm⁻¹) obs	σ (cm⁻¹) calc	Classification
25		3583.65	27 896.57	.63	$(^2D)6s\ ^3D_3 - (^2D)6p\ ^3F_4$
25		3579.70	27 927.36	.40	$(^2D)6s\ ^3D_2 - (^2D)6p\ ^3F_3$
6	b	3578.54	27 936.41	.39	$(^2D)5d\ ^1P_1 - (^4S)6p\ ^3P_2$
5		3574.40	27 968.76	.96	$(^2D)5d\ ^1D_2 - (^2D)4f\ ^1F_3$
2		3568.63	28 013.98	4.08	$(^2D)5d\ ^1D_2 - (^2D)4f\ ^1D_2$
17		3565.19	28 041.01	0.91	$(^2D)6s\ ^3D_3 - (^2D)6p\ ^3D_3$
4		3564.86	28 043.61	.63	$(^2D)6p\ ^1D_2 - (^2D)7s\ ^3D_3$
10		3562.99	28 058.33	.74	$(^2D)5d\ ^3P_0 - (^2D)4f\ ^3D_1$
14		3562.22	28 064.39	.33	$(^2P)6s\ ^3P_2 - (^2D)4f\ ^3D_2$
14		3561.37	28 071.09	.17	$(^2P)5d\ ^1D_2 - (^2D)6p\ ^1F_3$
10		3561.23	28 072.19	.04	$(^2P)5d\ ^3D_1 - (^2D)4f\ ^1P_1$
18		3552.12	28 144.19	.18	$(^2P)5d\ ^1D_2 - (^2D)6p\ ^1P_1$
5		3546.88	28 185.77	.89	$(^2D)5d\ ^3D_2 - (^4S)4f\ ^3F_3$
10		3544.86	28 201.83	.77	$(^2P)5d\ ^3D_3 - (^2P)6p\ ^3D_3$
20		3542.35	28 221.81	.89	$(^2D)6s\ ^3D_3 - (^4S)4f\ ^5F_2$
12		3539.94	28 241.02	0.94	$(^2P)5d\ ^3D_2 - (^2P)6p\ ^3S_1$
12		3539.94	28 241.02	.82	$(^4S)4f\ ^3F_3 - (^2D)6d\ ^3P_2$
7		3531.82	28 305.95	6.17	$(^4S)6d\ ^5D_1 - 5s^25p^6\ ^1S_0$
3		3531.62	28 307.55	.55	$(^2P)5d\ ^1P_1 - (^2P)4f\ ^3D_2$
16		3522.80	28 378.42	.34	$(^4S)5d\ ^3D_1 - (^4S)6p\ ^3P_1$
11		3519.11	28 408.18	.12	$(^2D)6s\ ^3D_3 - (^2D)6p\ ^3P_2$
13	b	3509.77	28483.78	.81	$(^2P)5d\ ^3D_2 - (^2D)4f\ ^3D_3$
11		3501.65	28 549.82	.89	$(^2D)6p\ ^1D_2 - (^2D)7s\ ^1D_2$
4		3494.82	28 605.62	.62	$(^2P)5d\ ^3F_3 - (^4S)4f\ ^3F_4$
8		3494.51	28 608.16	.20	$(^2P)5d\ ^3D_1 - (^2P)6p\ ^1D_2$
6		3488.13	28 660.48	.40	$(^2D)6p\ ^1D_2 - (^2D)6d\ ^3D_3$
4		3479.14	28 734.54	.59	$(^2D)6s\ ^3D_1 - (^4S)4f\ ^5F_2$
10		3472.35	28 790.72	.63	$(^2D)6p\ ^3P_1 - (^2D)6d\ ^3D_1$
14		3468.22	28 825.01	.15	$(^4S)6s\ ^5S_2 - (^4S)6p\ ^3P_1$
15		3467.22	28 833.32	.58	$(^2D)5d\ ^3D_3 - (^2D)6p\ ^1D_2$
15		3467.22	28 833.32	.58	$(^2D)5d\ ^3P_1 - (^2D)4f\ ^1P_1$
16		3454.27	28 941.41	.62	$(^2D)6s\ ^1D_2 - (^2D)6p\ ^1D_2$
11		3451.23	28 966.90	7.69	$(^2D)5d\ ^3P_0 - (^2D)4f\ ^3P_1$
15	a	3444.39	29 024.43	.38	$(^2P)6s\ ^1P_1 - (^2D)4f\ ^3P_2$
20	a	3444.24	29 025.69	.95	$(^2D)5d\ ^3D_1 - (^2D)6p\ ^3D_2$
8		3435.74	29 097.50	.58	$(^4S)4f\ ^5F_2 - (^2D)6d\ ^3F_2$
2		3414.54	29 278.15	.56	$(^2D)6p\ ^3D_3 - (^2D)6d\ ^3F_2$
8		3403.91	29 369.58	.73	$(^2D)5d\ ^3P_1 - (^2P)6p\ ^1D_2$
7		3399.87	29 404.48	.34	$(^2P)6s\ ^1P_1 - (^2D)4f\ ^3D_1$
2	b	3395.53	29 442.06	1.82	$(^2D)6p\ ^3D_3 - (^2D)7s\ ^3D_2$
3		3392.58	29 467.66	.71	$(^2P)5d\ ^1F_3 - (^2D)4f\ ^1G_4$
10		3390.64	29 484.52	.46	$(^2P)6s\ ^3P_2 - (^2D)4f\ ^3P_2$
4		3386.23	29 522.92	.38	$(^2D)6p\ ^1D_2 - (^2D)6d\ ^3D_2$
12	b	3384.10	29 541.50	.40	$(^4S)5d\ ^3D_2 - (^4S)6p\ ^5P_1$
10		3383.92	29 543.07	2.59	$(^2D)6p\ ^3P_2 - (^2D)6d\ ^3F_3$
10		3383.92	29 543.07	.10	$(^2D)5d\ ^1F_3 - (^2P)6p\ ^3D_2$
4		3381.64	29 562.99	.39	$(^2D)6p\ ^3D_3 - (^2D)6d\ ^3G_3$
9		3379.03	29 585.82	.80	$(^2D)5d\ ^3P_2 - (^2P)6p\ ^3D_2$
3		3376.98	29 603.78	.61	$(^4S)4f\ ^5F_3 - (^2D)6d\ ^3F_2$
9		3370.65	29 659.38	.20	$(^2D)5d\ ^3P_2 - (^2P)6p\ ^3P_1$
3		3365.70	29703.00	.09	$(^4S)4f\ ^5F_1 - (^2D)6d\ ^3D_1$
3		3365.32	29 706.35	.68	$(^2D)6p\ ^3F_4 - (^2D)6d\ ^3G_3$
2		3363.50	29 722.42	.33	$(^4S)5d\ ^3D_2 - (^4S)6p\ ^5P_2$
8		3362.77	29 728.87	.83	$(^4S)4f\ ^5F_2 - (^2D)6d\ ^3F_3$
3		3358.50	29 766.67	.87	$(^4S)4f\ ^5F_3 - (^2D)7s\ ^3D_2$
15		3357.99	29 771.19	.23	$(^2D)6s\ ^3D_2 - (^2D)6p\ ^1F_3$
4		3353.54	29 810.70	.30	$(^2D)6p\ ^3P_2 - (^2D)6d\ ^3D_1$
6		3350.35	29 839.08	8.96	$(^2D)6p\ ^3D_3 - (^2D)6d\ ^1G_4$
12		3349.76	29 844.33	.24	$(^2D)6s\ ^3D_2 - (^2D)6p\ ^1P_1$
2		3345.49	29 882.42	3.03	$(^2D)5d\ ^1G_4 - (^2D)6p\ ^3F_3$
7		3344.93	29 887.43	.44	$(^4S)4f\ ^5F_3 - (^2D)6d\ ^3G_3$
4		3344.27	29 893.32	.25	$(^2D)5d\ ^1F_3 - (^2D)4f\ ^3G_3$
16	a	3340.67	29 925.54	.56	$(^2D)5d\ ^3D_2 - (^2D)6p\ ^1D_2$
14	a	3340.37	29 928.23	.21	$(^2P)5d\ ^3D_3 - (^2P)6p\ ^3P_2$
13		3340.06	29 931.00	.03	$(^2P)5d\ ^3F_2 - (^2P)6p\ ^3D_1$
12	b	3339.50	29 936.02	5.95	$(^2D)5d\ ^3P_2 - (^2D)4f\ ^3G_3$
15	a	3338.99	29 940.59	.50	$(^2D)6s\ ^3D_1 - (^2D)6p\ ^3P_1$
7		3336.24	29 965.27	.35	$(^2D)6p\ ^3P_0 - (^2D)7s\ ^3D_1$

Table I. *Continued*

Intensity[a]		λ (Å)	σ (cm⁻¹) obs	σ (cm⁻¹) calc	Classification
8		3334.23	29983.34	.25	$(^2D)6p\ ^3F_4 - (^2D)6d\ ^1G_4$
15	a	3331.65	30006.56	.58	$(^2P)5d\ ^1D_2 - (^4S)4f\ ^5F_3$
5		3326.39	30054.00	.09	$(^2D)6p\ ^3F_4 - (^2D)6d\ ^3F_3$
8		3320.07	30111.21	.24	$(^4S)4f\ ^3F_2 - (^2D)6d\ ^1F_3$
8		3320.07	30111.21	.27	$(^2P)6s\ ^3P_1 - (^2D)4f\ ^3F_2$
7		3319.55	30115.93	.90	$(^2P)5d\ ^3D_2 - (^2P)6p\ ^1D_2$
6		3317.45	30134.99	.97	$(^4S)5d\ ^3D_1 - (^4S)6p\ ^3P_2$
12		3314.87	30158.45	.52	$(^2D)5d\ ^3S_1 - (^2P)6p\ ^3D_2$
6		3314.26	30163.99	4.01	$(^4S)4f\ ^5F_3 - (^2D)6d\ ^1G_4$
11	a	3306.80	30232.04	1.92	$(^2D)5d\ ^3S_1 - (^2P)6p\ ^3P_1$
11	a	3306.46	30235.15	4.85	$(^4S)4f\ ^5F_3 - (^2D)6d\ ^3F_3$
8		3304.05	30257.20	.12	$(^2D)5d\ ^3S_1 - (^2P)6p\ ^3P_0$
14		3301.54	30280.20	.16	$(^4S)6p\ ^3P_2 - (^4S)6d\ ^5D_2$
14		3295.94	30331.65	.64	$(^2P)5d\ ^1D_2 - (^2D)6p\ ^3D_3$
5		3288.54	30399.90	400.07	$(^4S)4f\ ^3F_3 - (^2D)6d\ ^3D_3$
16		3287.91	30405.73	.98	$(^2D)6p\ ^3P_1 - (^2D)6d\ ^3P_2$
13		3287.80	30406.75	.76	$(^4S)6p\ ^3P_2 - (^4S)6d\ ^5D_3$
14		3285.82	30425.07	.02	$(^4S)6p\ ^3P_2 - (^4S)7s\ ^5S_2$
8		3284.64	30436.00	5.89	$(^2P)6s\ ^1P_1 - (^2D)4f\ ^1D_2$
14		3280.50	30474.41	.34	$(^2D)5d\ ^1F_3 - (^2D)4f\ ^3G_4$
3		3279.13	30487.14	.13	$(^2P)5d\ ^3D_1 - (^2P)6p\ ^1P_1$
12		3278.44	30493.55	.60	$(^4S)6p\ ^3P_2 - (^4S)6d\ ^5D_1$
13		3276.39	30512.63	.61	$(^2P)5d\ ^1D_2 - (^4S)4f\ ^5F_2$
3		3269.40	30577.87	.88	$(^2D)5d\ ^3D_3 - (^4S)4f\ ^3F_2$
22		3268.98	30581.79	.78	$(^4S)6s\ ^5S_2 - (^4S)6p\ ^3P_2$
20		3267.05	30599.86	.75	$(^2P)5d\ ^3D_3 - (^2D)4f\ ^3D_2$
1		3261.46	30652.21	1.72	$(^2P)6s\ ^3P_1 - (^2P)6p\ ^3S_1$
5		3257.85	30686.27	5.92	$(^2D)6s\ ^1D_2 - (^4S)4f\ ^3F_2$
2		3256.52	30698.80	.84	$(^2P)5d\ ^1D_2 - (^2D)6p\ ^3P_2$
12		3256.25	30701.35	.25	$(^2P)5d\ ^3D_2 - (^2P)6p\ ^3D_3$
7		3248.62	30773.45	.36	$(^2P)6s\ ^3P_2 - (^2D)4f\ ^3P_1$
22		3246.85	30790.23	.29	$(^2D)5d\ ^3D_3 - (^4S)4f\ ^3F_4$
12		3244.13	30816.04	.08	$(^2D)6p\ ^1D_2 - (^2D)6d\ ^1P_1$
25		3242.86	30828.11	.14	$(^4S)5d\ ^3D_3 - (^4S)6p\ ^3P_2$
10		3240.47	30850.85	.84	$(^2P)6s\ ^3P_2 - (^2D)4f\ ^1F_3$
25		3236.84	30855.45	.41	$(^4S)5d\ ^3D_1 - (^4S)6p\ ^3P_0$
13		3235.73	30896.04	5.96	$(^2P)6s\ ^3P_2 - (^2D)4f\ ^1D_2$
12		3227.16	30978.08	.08	$(^4S)6p\ ^3P_0 - (^4S)7s\ ^3S_1$
12		3222.99	31018.16	.12	$(^2D)6p\ ^3P_1 - (^2D)6d\ ^3S_1$
2		3214.12	31103.76	2.98	$(^2P)6s\ ^1P_1 - (^2P)6p\ ^1S_0$
7		3199.22	31248.62	.66	$(^2D)5d\ ^3P_1 - (^2P)6p\ ^1P_1$
14		3196.51	31275.11	.07	$(^2D)5d\ ^1P_1 - (^4S)6p\ ^3P_1$
15		3196.25	31277.65	.64	$(^2D)5d\ ^3D_1 - (^2D)6p\ ^1P_1$
16		3185.21	31386.06	.22	$(^2D)6p\ ^1D_2 - (^2D)6d\ ^1D_2$
11		3184.27	31395.32	.39	$(^2D)6p\ ^1P_1 - (^2D)7s\ ^3D_1$
7		3177.11	31466.07	.02	$(^2D)6p\ ^1P_1 - (^2D)6d\ ^3F_2$
7		3169.75	31539.13	.03	$(^2D)6p\ ^1F_3 - (^2D)6d\ ^3F_2$
9		3164.47	31591.75	.95	$(^2D)6s\ ^3D_3 - (^4S)4f\ ^3F_3$
8		3160.66	31629.84	.28	$(^2D)6p\ ^1P_1 - (^2D)7s\ ^3D_2$
8		3160.66	31629.84	8.83	$(^2P)6s\ ^3P_0 - (^2P)6p\ ^3S_1$
7		3156.67	31669.81	.85	$(^2D)5d\ ^3D_2 - (^4S)4f\ ^3F_2$
10		3155.51	31681.46	.51	$(^2D)5d\ ^3P_1 - (^2P)6p\ ^3P_2$
11		3153.44	31702.25	.29	$(^2D)6p\ ^1F_3 - (^2D)7s\ ^3D_2$
13		3153.00	31706.67	.64	$(^2D)6s\ ^3D_2 - (^4S)4f\ ^5F_3$
15		3151.83	31718.45	.52	$(^2P)5d\ ^1D_2 - (^2D)6p\ ^3P_1$
18		3150.97	31727.10	6.87	$(^2D)5d\ ^1G_4 - (^2D)6p\ ^1F_3$
14		3150.83	31728.51	.52	$(^4S)6p\ ^3P_2 - (^4S)7s\ ^3S_1$
15		3150.69	31729.92	.90	$(^2P)5d\ ^3P_2 - (^2P)6p\ ^3S_1$
11		3141.63	31821.42	.48	$(^4S)5d\ ^3D_2 - (^4S)6p\ ^5P_3$
20		3138.28	31855.39	.53	$(^2D)6p\ ^1D_2 - (^2D)6d\ ^1F_3$
3		3126.77	31972.65	.77	$(^2P)5d\ ^3P_2 - (^2D)4f\ ^3D_3$
9		3124.95	31991.27	0.52	$(^2P)6s\ ^3P_1 - (^2D)4f\ ^1P_1$
3		3124.60	31994.85	.83	$(^2P)5d\ ^3D_2 - (^2P)6p\ ^1P_1$
9		3122.15	32019.96	.88	$(^2P)5d\ ^3D_3 - (^2D)4f\ ^3P_2$
5		3121.01	32031.65	.70	$(^2D)6s\ ^3D_2 - (^2D)6p\ ^3D_3$
10		3120.52	32036.68	.78	$(^4S)6p\ ^3P_1 - (^4S)6d\ ^5D_2$
12		3114.41	32099.53	.43	$(^2D)6p\ ^1F_3 - (^2D)6d\ ^1G_4$
6		3107.56	32170.28	.27	$(^2D)6p\ ^1F_3 - (^2D)6d\ ^3F_3$

Table I. *Continued*

Intensity[a]		λ (Å)	σ (cm⁻¹) obs	σ (cm⁻¹) calc	Classification
9		3106.47	32181.57	.64	$(^4S)6p\ ^3P_1 - (^4S)7s\ ^5S_2$
13		3106.34	32182.92	.95	$(^2D)6s\ ^1D_2 - (^2P)6p\ ^3D_1$
13		3103.47	32212.68	.67	$(^2D)6s\ ^3D_2 - (^4S)4f\ ^5F_2$
10		3102.69	32220.78	.85	$(^4S)6p\ ^3P_1 - (^4S)6d\ ^5D_0$
9		3102.36	32224.21	.03	$(^4S)4f\ ^5F_2 - (^2D)6d\ ^3S_1$
11		3099.87	32250.09	.23	$(^4S)6p\ ^3P_1 - (^4S)6d\ ^5D_1$
18		3091.05	32342.11	.15	$(^2D)5d\ ^3G_3 - (^2D)6p\ ^3F_2$
11		3090.00	32353.10	.06	$(^2D)5d\ ^3P_1 - (^2D)4f\ ^3D_2$
3		3088.87	32364.93	.97	$(^2D)6p\ ^1P_1 - (^2D)6d\ ^3D_1$
18		3083.53	32420.98	1.08	$(^2D)5d\ ^3F_4 - (^2D)6p\ ^3F_3$
4	b	3082.89	32427.71	.68	$(^2P)5d\ ^3D_2 - (^2P)6p\ ^3P_2$
11		3080.42	32453.71	.72	$(^2D)6p\ ^3P_1 - (^2D)7s\ ^1D_2$
6		3073.51	32526.67	.67	$(^2P)6s\ ^3P_1 - (^2P)6p\ ^1D_2$
2		3068.57	32579.03	.21	$(^2D)6p\ ^1P_1 - (^2D)6d\ ^1S_0$
18		3065.19	32614.96	5.02	$(^2P)5d\ ^3F_3 - (^2P)6p\ ^3D_2$
1		3055.26	32720.95	1.06	$(^2P)5d\ ^3D_2 - (^2D)4f\ ^3F_3$
14		3054.48	32729.31	.20	$(^2P)5d\ ^3F_2 - (^2P)6p\ ^3P_1$
6		3051.21	32764.39	.76	$(^2P)6p\ ^3P_0 - (^2P)6d\ ^3D_1$
7		3048.86	32789.64	.96	$(^2P)6p\ ^3P_1 - (^2P)6d\ ^3D_1$
12		3042.04	32863.15	.36	$(^2P)6p\ ^3D_2 - (^2P)6d\ ^3D_1$
12		3026.52	33031.66	.70	$(^2D)5d\ ^1P_1 - (^4S)6p\ ^3P_2$
25		3023.83	33061.04	.01	$(^4S)5d\ ^3D_2 - (^4S)6p\ ^3P_1$
18		3023.65	33063.01	.18	$(^4S)6p\ ^3P_2 - (^4S)6d\ ^3D_2$
6		3020.33	33099.35	.23	$(^2P)5d\ ^3D_2 - (^2D)4f\ ^3D_2$
2		3015.77	33149.40	.42	$(^2P)5d\ ^3F_4 - (^2D)4f\ ^3H_4$
11		3015.41	33153.36	.36	$(^4S)4f\ ^5F_2 - (^2D)7s\ ^3D_3$
11		3014.59	33162.38	.43	$(^2D)6p\ ^3P_0 - (^2D)6d\ ^3S_1$
15	a	3014.13	33167.44	6.89	$(^2D)5d\ ^3D_2 - (^2P)6p\ ^3D_1$
1	b	3009.03	33223.65	.57	$(^2D)5d\ ^3P_2 - (^2D)4f\ ^3F_2$
5		3004.65	33272.08	.11	$(^2D)5d\ ^1F_3 - (^2D)4f\ ^3H_4$
18	a	3004.26	33276.40	.31	$(^4S)6p\ ^5P_3 - (^4S)6d\ ^5D_2$
11		3001.52	33306.77	.79	$(^4S)4f\ ^5F_5 - (^2D)6d\ ^3G_4$
9		2999.29	33331.54	.62	$(^2D)6s\ ^3D_3 - (^2D)6p\ ^1D_2$
11	a	2999.03	33334.43	.33	$(^2D)6p\ ^3D_3 - (^2D)7s\ ^3D_3$
9		2997.50	33351.44	.48	$(^2D)6p\ ^3D_3 - (^2D)6d\ ^3G_4$
8		2994.95	33379.84	.92	$(^4S)6s\ ^3S_1 - (^2D)6p\ ^3D_1$
14		2994.67	33382.96	.86	$(^2D)6p\ ^3F_3 - (^2D)6d\ ^3F_2$
4		2994.37	33386.30	.27	$(^2P)5d\ ^3D_3 - (^2D)4f\ ^1F_3$
15		2992.89	33402.81	.91	$(^4S)6p\ ^5P_3 - (^4S)6d\ ^5D_3$
11		2991.49	33418.44	.58	$(^2D)6s\ ^3D_2 - (^2D)6p\ ^3P_1$
14		2991.25	33421.12	.17	$(^4S)6p\ ^5P_3 - (^4S)7s\ ^5S_2$
3		2990.82	33425.93	6.20	$(^2D)6p\ ^3P_1 - (^2D)6d\ ^3D_2$
7		2990.33	33431.40	.39	$(^2P)5d\ ^3D_3 - (^2D)4f\ ^1D_2$
11		2986.11	33478.65	.62	$(^2D)6p\ ^3F_4 - (^2D)7s\ ^3D_3$
14		2985.53	33485.15	.15	$(^4S)6p\ ^3P_1 - (^4S)7s\ ^3S_1$
16		2984.58	33495.81	.77	$(^2D)6p\ ^3F_4 - (^2D)6d\ ^3G_4$
8		2981.32	33532.44	.48	$(^2D)6p\ ^3P_1 - (^2D)6d\ ^3P_0$
3		2980.09	33546.27	.12	$(^2D)6p\ ^3F_3 - (^2D)7s\ ^3D_2$
3		2980.09	33546.27	.27	$(^2P)5d\ ^3F_3 - (^2D)4f\ ^3G_4$
10		2976.75	33583.91	.90	$(^2D)6p\ ^3P_2 - (^2D)6d\ ^3D_3$
6	b	2974.90	33604.80	.86	$(^2P)5d\ ^3P_2 - (^2P)6p\ ^1D_2$
9		2971.26	33645.96	6.07	$(^2D)5d\ ^3D_1 - (^4S)4f\ ^5F_2$
11		2971.17	33646.98	7.07	$(^2D)6p\ ^3D_2 - (^2D)7s\ ^3D_1$
19		2970.49	33654.69	.77	$(^4S)6p\ ^5P_3 - (^4S)6d\ ^5D_4$
10		2970.08	33659.33	.39	$(^4S)4f\ ^5F_3 - (^2D)7s\ ^3D_3$
10		2970.08	33659.33	.62	$(^4S)4f\ ^5F_2 - (^2D)7s\ ^1D_2$
23		2969.77	33662.84	.28	$(^2D)5d\ ^1G_4 - (^4S)4f\ ^5F_3$
9		2969.43	33666.70	.69	$(^2D)6p\ ^3F_3 - (^2D)6d\ ^3G_3$
12		2968.57	33676.45	.54	$(^4S)4f\ ^5F_3 - (^2D)6d\ ^3G_4$
10		2968.43	33678.04	.18	$(^4S)4f\ ^5F_4 - (^2D)7s\ ^3D_3$
10	a	2966.92	33695.18	.33	$(^4S)4f\ ^5F_4 - (^2D)6d\ ^3G_4$
11		2964.93	33717.79	.70	$(^2D)6p\ ^3D_2 - (^2D)6d\ ^3F_2$
13		2964.17	33726.44	.57	$(^2D)6p\ ^3D_3 - (^2D)6d\ ^3F_4$
4		2960.87	33764.03	.02	$(^2D)5d\ ^3P_2 - (^2P)6p\ ^3S_1$
13		2960.34	33770.07	.14	$(^4S)4f\ ^5F_2 - (^2D)6d\ ^1D_2$
6		2960.07	33773.15	.19	$(^2D)5d\ ^3P_1 - (^2D)4f\ ^3P_2$
15	a	2959.36	33781.25	0.98	$(^4S)6p\ ^3P_0 - (^4S)6d\ ^1D_1$
9	a	2959.28	33782.17	.14	$(^2D)5d\ ^1P_1 - (^4S)6p\ ^3P_0$

Table I. *Continued*

Intensity[1]		λ (Å)	σ (cm⁻¹) obs	σ (cm⁻¹) calc	Classification
17		2954.93	33 831.90	2.31	$(^2D)5d\ ^3D_1-(^2D)6p\ ^3P_2$
10	a	2954.17	33 840.60	.60	$(^2D)6p\ ^3D_3-(^2D)7s\ ^1D_2$
10	a	2954.10	33 841.40	.49	$(^2P)5d\ ^3F_4-(^2D)4f\ ^3D_3$
7		2953.94	33 843.23	.05	$(^2D)5d\ ^1G_4-(^2D)6p\ ^3F_4$
6		2953.86	33 844.15	.33	$(^2D)6s\ ^3D_1-(^2D)6p\ ^1D_2$
3		2951.53	33 870.87	.86	$(^2D)6p\ ^3F_4-(^2D)6d\ ^3F_4$
19		2948.07	33 910.62	.81	$(^2D)5d\ ^3G_3-(^2D)6p\ ^3D_2$
17		2947.51	33 917.06	.00	$(^2D)6p\ ^3F_4-(^2D)6d\ ^3G_5$
18		2945.23	33 943.32	.26	$(^2D)6p\ ^3F_3-(^2D)6d\ ^1G_4$
10		2944.68	33949.66	.69	$(^2D)6p\ ^3P_1-(^2D)6d\ ^3P_1$
7		2944.56	33 951.04	.11	$(^2D)6p\ ^3D_3-(^2D)6d\ ^3D_3$
7		2943.43	33 964.07	.17	$(^2D)5d\ ^1F_3-(^2D)4f\ ^3D_3$
11	b	2942.06	33 979.89	80.32	$(^2D)6p\ ^1P_1-(^2D)6d\ ^3P_2$
12		2941.39	33 987.63	.34	$(^2D)5d\ ^1G_4-(^2D)6p\ ^3D_3$
17		2940.21	34 001.27	.53	$(^2D)6p\ ^3D_2-(^2D)6d\ ^3G_3$
10		2939.73	34 006.82	.88	$(^2D)5d\ ^3P_2-(^2D)4f\ ^3D_3$
12		2939.11	34 013.99	4.10	$(^2D)6p\ ^3F_3-(^2D)6d\ ^3F_3$
15	b	2935.86	34 051.64	.62	$(^4S)4f\ ^5F_3-(^2D)6d\ ^3F_4$
10		2935.72	34 053.27	.33	$(^2D)6p\ ^1F_3-(^2D)6d\ ^3P_2$
18		2932.76	34 087.63	.53	$(^4S)5d\ ^5D_0-(^4S)6p\ ^5P_1$
10	b	2932.09	34 095.42	.40	$(^2D)6p\ ^3F_4-(^2D)6d\ ^3D_3$
18		2930.27	34 116.60	.56	$(^4S)4f\ ^5F_4-(^2D)6d\ ^3G_5$
4		2927.13	34 153.20	.15	$(^2D)5d\ ^3P_1-(^2D)4f\ ^3D_1$
11		2926.07	34 165.57	.65	$(^4S)4f\ ^5F_3-(^2D)7s\ ^1D_2$
11		2923.96	34 190.22	.21	$(^2P)5d\ ^3P_2-(^2P)6p\ ^3D_3$
16		2923.53	34 195.25	.33	$(^2D)5d\ ^3G_5-(^4S)4f\ ^5F_4$
15		2917.60	34 264.75	.91	$(^2D)5d\ ^3F_4-(^2D)6p\ ^1F_3$
8		2916.63	34 276.14	.17	$(^4S)4f\ ^5F_3-(^2D)6d\ ^3D_3$
7		2915.04	34 294.84	.96	$(^4S)4f\ ^5F_4-(^2D)6d\ ^3D_3$
18		2914.14	34 305.43	.66	$(^2D)5d\ ^3F_2-(^2D)6p\ ^3D_1$
20		2912.38	34 326.16	.31	$(^4S)6p\ ^3P_2-(^4S)6d\ ^3D_3$
19		2911.91	34 331.70	.58	$(^4S)5d\ ^5D_1-(^4S)6p\ ^5P_1$
6		2911.48	34 336.77	.73	$(^2D)5d\ ^3S_1-(^2P)6p\ ^3S_1$
12		2910.37	34 349.86	8.94	$(^2D)6p\ ^3D_2-(^2D)6d\ ^3F_3$
3		2910.09	34 353.17	.07	$(^2P)5d\ ^1F_3-(^4S)5f\ ^5F_4$
15		2906.56	34 394.89	.88	$(^2D)5d\ ^3G_5-(^2D)6p\ ^1F_4$
7		2904.17	34 423.19	.16	$(^2P)5d\ ^3D_1-(^2D)4f\ ^1D_2$
5		2902.29	34 445.49	.88	$(^2D)6p\ ^3P_2-(^2D)6d\ ^3D_2$
4		2897.70	34 500.05	.22	$(^2P)5d\ ^3P_1-(^2P)6p\ ^3D_1$
14		2896.65	34 512.56	.52	$(^4S)5d\ ^5D_1-(^4S)6p\ ^5P_2$
2		2896.07	34 519.47	.36	$(^2P)5d\ ^3D_2-(^2D)4f\ ^3P_2$
6		2895.04	34531.75	.42	$(^4S)6p\ ^3P_2-(^4S)6d\ ^3D_1$
18		2891.72	34 571.39	.53	$(^2D)5d\ ^3F_3-(^2D)6p\ ^3F_2$
8		2889.97	34 592.33	.47	$(^2D)6p\ ^1P_1-(^2D)6d\ ^3S_1$
2		2886.93	34 628.75	.32	$(^2P)5d\ ^1F_3-(^4S)5f\ ^5F_3$
12		2886.68	34 631.75	2.11	$(^4S)4f\ ^5F_2-(^2D)6d\ ^3D_2$
5		2879.36	34 719.79	.91	$(^2D)6p\ ^3P_1-(^2D)6d\ ^1P_1$
4		2873.29	34 793.13	.37	$(^2P)5d\ ^3P_0-(^2P)6p\ ^3D_1$
4		2872.75	34 799.67	.69	$(^2D)5d\ ^3D_3-(^2P)6p\ ^3D_2$
25		2871.69	34 812.52	.68	$(^2D)5d\ ^3G_4-(^2D)6p\ ^3F_3$
25		2871.69	34 812.52	3.08	$(^2D)6p\ ^3D_3-(^2D)6d\ ^3D_2$
17		2871.27	34 817.61	.64	$(^4S)5d\ ^3D_2-(^4S)6p\ ^3P_2$
17		2871.10	34 819.67	.80	$(^4S)6p\ ^3P_1-(^4S)6d\ ^3D_2$
3		2869.52	34 838.84	.45	$(^2P)6s\ ^3P_1-(^2P)6p\ ^3P_2$
3		2868.45	34 851.84	.98	$(^2D)5d\ ^3D_1-(^2D)6p\ ^3P_1$
8		2864.62	34 898.43	9.32	$(^2P)5d\ ^3D_3-(^2D)4f\ ^3D_1$
2		2863.86	34 907.69	.73	$(^2D)6s\ ^1D_2-(^2P)6p\ ^3D_2$
25		2862.42	34 925.25	.10	$(^4S)5d\ ^5D_2-(^4S)6p\ ^5P_1$
3		2856.67	34 995.55	.79	$(^2P)5d\ ^1F_3-(^2P)4f\ ^3G_3$
4		2850.27	35 074.12	.24	$(^4S)6s\ ^3S_1-(^2D)6p\ ^3F_2$
10		2847.92	35 103.06	2.82	$(^2D)5d\ ^3P_2-(^2D)4f\ ^1P_1$
14		2847.67	35 106.15	.04	$(^4S)5d\ ^5D_2-(^4S)6p\ ^5P_2$
7		2845.06	35 138.35	.14	$(^4S)4f\ ^5F_3-(^2D)6d\ ^3D_2$
4		2844.12	35 149.96	.84	$(^2D)5d\ ^3D_3-(^2D)4f\ ^3G_3$
5		2838.81	35 215.71	.74	$(^2D)6p\ ^3F_2-(^2D)7s\ ^3D_1$
8		2833.12	35 286.43	.37	$(^2D)6p\ ^3F_2-(^2D)6d\ ^3F_2$
6		2832.97	35 288.30	.33	$(^2D)6s\ ^3D_3-(^4S)4f\ ^3F_4$
2		2832.83	35 290.04	.05	$(^2D)6p\ ^3P_1-(^2D)6d\ ^1D_2$

Table I. *Continued*

Intensity[1]		λ (Å)	σ (cm⁻¹) obs	σ (cm⁻¹) calc	Classification
17		2827.46	35 357.06	.01	$(^4S)5d\ ^5D_3-(^4S)6p\ ^5P_2$
14		2825.99	35 375.45	.46	$(^4S)6p\ ^5P_2-(^4S)6d\ ^5D_2$
8	b	2817.36	35 483.81	.79	$(^2P)5d\ ^3P_2-(^2P)6p\ ^1P_1$
16		2815.92	35 501.95	2.06	$(^4S)6p\ ^5P_2-(^4S)6d\ ^5D_3$
1		2815.27	35 510.15	.00	$(^2P)6s\ ^3P_1-(^2D)4f\ ^3D_2$
13	a	2814.46	35 520.37	.32	$(^4S)6p\ ^5P_2-(^4S)7s\ ^5S_2$
8		2811.61	35 556.37	.40	$(^4S)6p\ ^5P_1-(^4S)6d\ ^5D_2$
7	b	2810.46	35 570.92	.20	$(^2D)6p\ ^3F_2-(^2D)6d\ ^3G_3$
3		2809.53	35 582.69	.74	$(^2D)6s\ ^3D_2-(^4S)4f\ ^3F_3$
10	a	2809.06	35 588.65	.62	$(^2D)6s\ ^3D_1-(^4S)4f\ ^3F_2$
10	a	2809.06	35 588.65	.90	$(^4S)6p\ ^5P_2-(^4S)6d\ ^5D_1$
7		2808.57	35 594.86	.80	$(^2D)6p\ ^1F_3-(^2D)7s\ ^3D_3$
7		2808.46	35 596.25	.26	$(^2D)5d\ ^1F_3-(^2P)6p\ ^1D_2$
12		2807.22	35 611.97	.95	$(^2D)6p\ ^1F_3-(^2D)6d\ ^3G_4$
6		2806.40	35 622.38	.35	$(^2P)5d\ ^1D_2-(^2D)6p\ ^1D_2$
4		2805.09	35 639.01	8.97	$(^2D)5d\ ^3P_2-(^2P)6p\ ^1D_2$
3		2802.19	35 675.90	.54	$(^2D)5d\ ^3S_1-(^2D)4f\ ^1P_1$
17		2800.20	35 701.25	.26	$(^4S)6p\ ^5P_1-(^4S)7s\ ^5S_2$
9		2797.87	35 730.98	.94	$(^2D)5d\ ^3D_3-(^2D)4f\ ^3G_4$
12		2797.12	35 740.56	.46	$(^4S)6p\ ^5P_1-(^4S)6d\ ^5D_0$
14		2794.84	35 769.71	.84	$(^4S)6p\ ^5P_1-(^4S)6d\ ^5D_1$
3		2792.47	35 800.07	1.02	$(^2D)5d\ ^1D_2-(^4S)5f\ ^5F_1$
7		2785.80	35 885.78	.74	$(^2P)5d\ ^3D_2-(^2D)4f\ ^1F_3$
6		2785.33	35 891.83	.67	$(^2D)5d\ ^3D_2-(^2P)6p\ ^3D_2$
7		2784.93	35 896.99	7.16	$(^2D)6p\ ^3F_3-(^2D)6d\ ^3P_2$
17		2783.33	35 917.62	.61	$(^2D)6p\ ^3F_2-(^2D)6d\ ^3F_3$
10		2782.69	35 925.89	.81	$(^4S)4f\ ^5F_2-(^2D)6d\ ^1P_1$
4		2782.30	35 930.92	.87	$(^2P)5d\ ^3D_2-(^2D)4f\ ^1D_2$
11		2779.64	35 965.30	.07	$(^2D)5d\ ^3D_2-(^2P)6p\ ^3P_1$
13		2777.94	35 987.31	.04	$(^2D)6p\ ^1F_3-(^2D)6d\ ^3F_4$
16		2776.96	36 000.01	5999.97	$(^2D)5d\ ^3F_2-(^2D)6p\ ^3F_2$
6	a	2774.79	36 028.16	.06	$(^2D)6p\ ^1P_1-(^2D)7s\ ^1D_2$
0		2774.44	36 032.71	.53	$(^2P)5d\ ^3D_3-(^2D)4f\ ^1G_4$
16		2772.40	36059.22	8.92	$(^2P)5d\ ^3F_4-(^2P)6p\ ^3D_3$
16		2772.40	36 059.22	.33	$(^4S)6p\ ^5P_3-(^4S)6d\ ^3D_2$
10		2769.17	36 101.28	.07	$(^2D)6p\ ^1F_3-(^2D)7s\ ^1D_2$
15		2766.18	36 140.30	.20	$(^2D)5d\ ^3F_3-(^2D)6p\ ^3D_2$
5		2765.95	36 143.30	.31	$(^2D)5d\ ^1D_2-(^2P)4f\ ^3G_3$
6		2763.01	36 181.76	.53	$(^2D)5d\ ^3F_4-(^4S)4f\ ^5F_4$
6		2763.01	36 181.76	.61	$(^2D)5d\ ^1F_3-(^2P)6p\ ^3D_3$
9	b	2762.73	36 185.43	.33	$(^2D)6p\ ^3F_2-(^2D)6d\ ^3D_1$
15		2761.58	36 200.49	.32	$(^2D)5d\ ^3F_4-(^4S)4f\ ^5F_3$
13		2760.72	36 211.77	.58	$(^2D)6p\ ^1F_3-(^2D)6d\ ^3D_3$
13		2760.72	36211.77	.69	$(^2D)5d\ ^3S_1-(^2P)6p\ ^1D_2$
11		2759.19	36 231.85	2.01	$(^2D)6p\ ^3D_2-(^2D)6d\ ^3P_2$
3		2757.56	36 253.26	2.79	$(^2P)5d\ ^3F_3-(^2D)4f\ ^3F_2$
13		2754.88	36 288.53	.05	$(^4S)6p\ ^3P_1-(^4S)6d\ ^3D_1$
14		2747.86	36 381.23	.09	$(^2D)5d\ ^3F_4-(^2D)6p\ ^3F_4$
16		2740.78	36 475.21	.04	$(^2D)5d\ ^3F_3-(^2D)6p\ ^3F_3$
4		2739.19	36 496.38	5.95	$(^4S)4f\ ^5F_2-(^2D)6d\ ^1D_2$
14		2736.99	36 525.71	.38	$(^2D)5d\ ^3F_4-(^2D)6p\ ^3D_3$
9		2728.20	36 643.39	2.91	$(^4S)6s\ ^3S_1-(^2D)6p\ ^3D_2$
11	a	2727.20	36 656.83	.51	$(^2D)5d\ ^3G_4-(^2D)6p\ ^1F_3$
1	w, b	2725.69	36 677.13	6.93	$(^2D)6p\ ^3D_3-(^2D)6d\ ^1D_2$
2		2718.10	36 779.54	.03	$(^2D)6p\ ^3P_2-(^2D)6d\ ^1F_3$
2		2714.05	36 834.42	.01	$(^2P)5d\ ^3F_2-(^2P)6p\ ^3S_1$
10	a	2713.39	36 843.38	4.15	$(^2D)6p\ ^3D_2-(^2D)6d\ ^3S_1$
0		2711.34	36 871.24	.22	$(^2P)5d\ ^3F_4-(^2D)4f\ ^3F_4$
6		2710.94	36 876.68	7.23	$(^2D)5d\ ^3P_0-(^4S)5f\ ^5F_1$
12		2708.45	36 910.58	.06	$(^2D)6p\ ^3D_1-(^2D)7s\ ^3D_1$
3		2704.41	36 965.71	.27	$(^4S)4f\ ^5F_2-(^2D)6d\ ^1F_3$
2		2702.31	36 994.44	3.90	$(^2D)5d\ ^1F_3-(^2D)4f\ ^3F_4$
0		2701.71	37002.66	1.98	$(^4S)4f\ ^5F_3-(^2D)6d\ ^1D_2$
5		2701.50	37005.53	4.76	$(^4S)6p\ ^5P_1-(^4S)7s\ ^3S_1$
15	b	2696.51	37074.01	.23	$(^4S)5d\ ^3D_1-(^2D)6p\ ^3D_1$
15	b	2696.51	37074.01	3.55	$(^2D)6p\ ^1F_3-(^2D)6d\ ^3D_2$
3		2695.65	37085.83	.18	$(^4S)4f\ ^3F_2-(^2P)6d\ ^3D_1$
3		2695.65	37085.83	.66	$(^2D)6s\ ^3D_1-(^2P)6p\ ^3D_1$

Table I. *Continued*

Intensity[1]		λ (Å)	σ (cm⁻¹) obs	σ (cm⁻¹) calc	Classification
5		2694.12	37 106.89	.82	$(^2D)6p\ ^1P_1 - (^2D)6d\ ^3P_0$
12	a	2691.44	37143.84	.95	$(^2D)6p\ ^3D_1 - (^2D)7s\ ^3D_2$
4		2691.22	37 146.88	.24	$(^2D)6p\ ^3D_3 - (^2D)6d\ ^1F_3$
5		2685.51	37225.86	.00	$(^2P)5d\ ^3P_1 - (^2P)6p\ ^3D_2$
6		2678.55	37 322.58	.41	$(^2D)6s\ ^3D_2 - (^2D)6p\ ^1D_2$
6		2678.55	37 322.58	.47	$(^4S)6p\ ^5P_3 - (^4S)6d\ ^3D_3$
6		2670.25	37438.58	.64	$(^2D)6p\ ^3F_3 - (^2D)7s\ ^3D_3$
20		2669.01	37455.98	.79	$(^2D)6p\ ^3F_3 - (^2D)6d\ ^3G_4$
20		2669.01	37455.98	6.16	$(^4S)5d\ ^5D_3 - (^4S)6p\ ^5P_3$
10	a	2667.94	37471.00	.30	$(^4S)4f\ ^5F_3 - (^2D)6d\ ^1F_3$
7		2661.00	37 568.72	.64	$(^2D)5d\ ^3F_2 - (^2D)6p\ ^3D_2$
5		2659.36	37 591.88	.55	$(^2P)5d\ ^3P_0 - (^2P)6p\ ^3P_1$
9		2658.27	37607.30	.15	$(^4S)5d\ ^5D_0 - (^4S)6p\ ^3P_1$
2		2641.13	37851.34	.20	$(^4S)5d\ ^5D_1 - (^4S)6p\ ^3P_1$
9		2639.15	37879.74	.64	$(^2D)6p\ ^3D_1 - (^2D)6d\ ^3D_1$
13		2634.21	37950.77	.75	$(^2D)5d\ ^3P_2 - (^2P)6p\ ^3P_2$
7		2626.98	38055.21	.41	$(^2D)6p\ ^3F_3 - (^2D)6d\ ^3D_3$
4		2624.52	38090.88	.62	$(^2D)5d\ ^3S_1 - (^2P)6p\ ^1P_1$
8	w	2619.85	38158.77	.48	$(^4S)6p\ ^5P_2 - (^4S)6d\ ^3D_2$
0		2616.90	38201.79	.42	$(^2D)5d\ ^1F_3 - (^2D)4f\ ^3F_3$
1		2616.63	38205.73	.67	$(^2D)5d\ ^3G_3 - (^2D)6p\ ^3F_4$
1		2613.99	38244.31	.13	$(^2D)5d\ ^3P_2 - (^2D)4f\ ^3F_3$
1		2611.03	38287.67	.21	$(^2P)6s\ ^3P_0 - (^2D)4f\ ^3D_1$
5		2610.57	38294.41	.25	$(^2D)6p\ ^1P_1 - (^2D)6d\ ^1P_1$
7	b	2607.50	38339.50	.42	$(^4S)6p\ ^5P_1 - (^4S)6d\ ^3D_2$
15	a	2600.12	38448.31	7.72	$5s5p^5\ ^3P_0 - (^4S)6p\ ^5P_1$
7	a	2595.03	38523.72	.47	$(^2D)5d\ ^3S_1 - (^2P)6p\ ^3P_2$
7		2594.53	38531.14	0.93	$(^2D)5d\ ^3G_3 - (^4S)4f\ ^5F_2$
10		2591.69	38573.36	.13	$(^2D)5d\ ^3G_4 - (^4S)4f\ ^5F_4$
8		2591.24	38580.06	79.59	$(^2D)5d\ ^1F_3 - (^2D)4f\ ^3D_2$
12		2590.42	38592.27	1.92	$(^2D)5d\ ^3G_4 - (^4S)4f\ ^5F_3$
9		2578.62	38768.86	.55	$(^4S)5d\ ^3D_1 - (^2D)6p\ ^3F_2$
13		2578.37	38772.62	.69	$(^2D)5d\ ^3G_4 - (^2D)6p\ ^3F_4$
2		2574.61	38829.24	.47	$(^2D)6p\ ^1D_2 - (^2P)6d\ ^3D_1$
7		2572.33	38863.66	.68	$(^2P)5d\ ^1D_2 - (^2P)6p\ ^3D_1$
7		2572.33	38863.66	4.39	$(^2D)6p\ ^1P_1 - (^2D)6d\ ^1D_2$
5		2570.26	38894.96	.59	$(^4S)6s\ ^3S_1 - (^2D)6p\ ^1P_1$
9		2568.81	38916.91	.98	$(^2D)5d\ ^3G_4 - (^2D)6p\ ^3D_3$
9		2568.81	38916.91	7.39	$(^2D)6p\ ^3F_3 - (^2D)6d\ ^3D_2$
3		2550.55	39195.51	.02	$(^2D)5d\ ^3S_1 - (^2D)4f\ ^3D_2$
2		2544.10	39294.87	.32	$(^2P)5d\ ^3F_2 - (^2P)6p\ ^3D_3$
3		2541.88	39329.19	8.81	$(^2D)6s\ ^1D_2 - (^2D)4f\ ^3D_3$
1		2541.028	39342.34	.15	$(^2D)6p\ ^3F_2 - (^2D)7s\ ^3D_3$
1		2538.918	39375.03	4.70	$(^2P)5d\ ^3P_2 - (^2D)4f\ ^1F_3$
7		2536.868	39406.85	.71	$(^2D)6p\ ^1F_3 - (^2D)6d\ ^1F_3$
7		2533.318	39462.07	1.72	$(^4S)5d\ ^3D_3 - (^2D)6p\ ^3F_2$
7		2523.967	39608.25	7.83	$(^4S)5d\ ^5D_1 - (^4S)6p\ ^3P_2$
5		2521.428	39648.14	7.88	$(^2D)6s\ ^3D_3 - (^2D)4f\ ^3G_3$
6		2515.117	39747.61	.32	$(^2D)5d\ ^3F_2 - (^2D)6p\ ^1F_3$
0	h	2514.09	39763.89	.53	$(^2P)5d\ ^3D_3 - (^2P)4f\ ^3F_3$
1		2513.337	39775.76	.71	$(^2D)6p\ ^3D_2 - (^2D)6d\ ^3P_1$
1		2511.288	39808.22	7.66	$(^4S)6p\ ^5P_1 - (^4S)6d\ ^3D_1$
4		2509.74	39832.81	.51	$5s5p^5\ ^1P_1 - (^2P)4f\ ^3D_2$
11		2504.907	39909.61	.04	$(^2D)6s\ ^3D_1 - (^2P)6p\ ^3P_0$
12		2501.037	39971.36	0.95	$(^2D)5d\ ^1P_1 - (^2D)6p\ ^3D_1$
9		2486.727	40201.37	.34	$(^4S)5d\ ^5D_2 - (^4S)6p\ ^3P_2$
7		2485.006	40229.20	8.98	$(^2D)6s\ ^3D_3 - (^2D)4f\ ^3G_4$
6		2483.464	40254.18	.29	$(^2D)5d\ ^3F_3 - (^4S)4f\ ^5F_3$
8		2479.876	40312.42	.74	$(^2D)5d\ ^3D_2 - (^2D)4f\ ^3D_3$
7		2479.130	40324.56	.63	$(^4S)6s\ ^3S_1 - (^2D)6p\ ^3P_0$
0		2477.062	40358.21	.27	$(^4S)5d\ ^5D_1 - (^4S)6p\ ^3P_0$
7		2472.377	40434.68	5.05	$(^2D)5d\ ^3F_3 - (^2D)6p\ ^3F_4$
10		2471.319	40452.00	.31	$(^4S)5d\ ^5D_3 - (^4S)6p\ ^3P_2$
7	b	2468.393	40499.94	500.10	$(^2D)5d\ ^3D_1 - (^4S)4f\ ^3F_2$
2		2464.555	40563.01	.73	$(^2D)6s\ ^3D_2 - (^2P)6p\ ^3D_1$
10		2463.557	40579.44	.34	$(^2D)5d\ ^3F_3 - (^2D)6p\ ^3D_3$
10		2463.061	40587.61	.90	$(^2P)5d\ ^3F_2 - (^2P)6p\ ^1P_1$
11		2452.644	40759.98	60.32	$(^2D)5d\ ^3F_3 - (^4S)4f\ ^5F_2$

Table I. *Continued*

Intensity[1]		λ (Å)	σ (cm⁻¹) obs	σ (cm⁻¹) calc	Classification
10		2447.083	40852.60	.86	$(^2D)5d\ ^3D_3 - (^2P)6p\ ^1D_2$
8		2446.503	40862.29	.77	$(^2P)5d\ ^3P_1 - (^2D)4f\ ^3F_2$
11		2441.523	40945.63	6.55	$(^2D)5d\ ^3F_3 - (^2D)6p\ ^3P_2$
6	w	2439.516	40979.32	.97	$(^2P)5d\ ^3F_3 - (^2P)6p\ ^3P_2$
12		2436.491	41030.18	.39	$(^4S)5d\ ^3D_3 - (^2D)6p\ ^3D_2$
3		2423.918	41243.00	.42	$(^2P)5d\ ^3F_4 - (^2D)4f\ ^1F_3$
9		2422.767	41262.59	3.03	$(^4S)6s\ ^3S_1 - (^4S)4f\ ^5F_2$
14	b	2422.139	41273.29	.35	$(^2P)5d\ ^3F_3 - (^2D)4f\ ^3F_3$
7		2419.740	41314.20	.13	$(^2P)5d\ ^3F_2 - (^2D)4f\ ^3F_3$
8		2418.744	41331.22	.33	$(^2D)5d\ ^3P_2 - (^2D)4f\ ^3P_1$
12		2416.744	41365.41	.23	$(^4S)5d\ ^3D_3 - (^2D)6p\ ^3F_3$
9		2414.544	41403.10	.21	$(^2P)5d\ ^3P_1 - (^2P)6p\ ^3S_1$
4		2414.230	41408.49	.68	$(^2D)5d\ ^3D_2 - (^2D)4f\ ^1P_1$
4		2414.230	41408.49	.82	$(^2D)5d\ ^3P_2 - (^2D)4f\ ^1F_3$
2		2414.104	41410.64	1.23	$(^2D)5d\ ^1F_3 - (^2D)4f\ ^1D_2$
6		2412.505	41438.10	.21	$(^2D)5d\ ^3D_3 - (^2P)6p\ ^3D_3$
1		2406.229	41546.16	.25	$(^2D)6s\ ^1D_2 - (^2P)6p\ ^3D_3$
9		2403.792	41588.28	.45	$(^2P5d\ ^1D_2 - (^2P)6p\ ^3D_2$
8		2397.566	41696.27	.36	$(^2P)5d\ ^3P_0 - (^2P)6p\ ^3S_1$
10		2394.083	41756.92	.90	$(^4S)5d\ ^3D_2 - (^2D)6p\ ^3D_1$
4	b	2392.376	41786.71	.59	$(^2D)5d\ ^3G_5 - (^4S)4f\ ^5F_4$
11		2388.573	41853.25	.35	$(^2P)5d\ ^3D_1 - (^2P)4f\ ^3F_2$
8	b	2385.902	41900.09	1.00	$(^2D)5d\ ^3G_3 - (^4S)4f\ ^3F_3$
11		2385.673	41904.11	.05	$(^2D)5d\ ^3S_1 - (^2D)4f\ ^3P_1$
13		2383.947	41946.77	.90	$(^2P)5d\ ^1F_3 - (^2P)4f\ ^1G_4$
11		2382.087	41967.19	.34	$5s5p^5\ ^3P_0 - (^4S)6p\ ^3P_1$
3		2379.783	42007.82	.79	$(^2D)5d\ ^3F_2 - (^2D)6p\ ^3D_3$
0		2378.714	42026.69	.65	$(^2D)5d\ ^3S_1 - (^2D)4f\ ^1D_2$
18	b	2369.595	42188.42	.76	$(^2D)5d\ ^3F_2 - (^4S)4f\ ^5F_2$
12		2366.115	42250.46	.50	$(^2D)5d\ ^3D_3 - (^2D)4f\ ^3F_4$
14		2365.416	42262.94	3.01	$(^2P)5d\ ^3D_2 - (^2P)4f\ ^3F_3$
0		2359.159	42375.02	.00	$(^2D)5d\ ^3F_2 - (^2D)6p\ ^3P_2$
11		2354.456	42459.67	.48	$(^2P)5d\ ^3D_1 - (^4S)5f\ ^5F_2$
8	b	2353.936	42469.04	8.93	$(^4S)6s\ ^3S_1 - (^2D)6p\ ^3P_1$
8		2350.563	42529.98	30.18	$(^2D)5d\ ^3D_2 - (^2P)6p\ ^3D_3$
1		2339.398	42732.94	3.30	$(^2D)6p\ ^3P_1 - (^2P)6d\ ^3D_1$
9		2338.884	42742.34	.02	$(^2P)5d\ ^3P_1 - (^2D)4f\ ^1P_1$
7		2333.555	42839.94	.83	$(^2D)6s\ ^1D_2 - (^2P)6p\ ^1P_1$
0		2326.369	42972.26	1.63	$(^2D)5d\ ^3P_1 - (^4S)5f\ ^5F_1$
3		2323.455	43026.14	.74	$(^2D)6s\ ^3D_3 - (^2D)4f\ ^3H_4$
5		2320.992	43071.79	.65	$(^2P)5d\ ^3F_3 - (^2D)4f\ ^3P_2$
10		2316.583	43153.76	4.06	$(^2D)6p\ ^3F_2 - (^2D)6d\ ^1F_3$
12		2313392	43213.29	.28	$5s5p^5\ ^3P_1 - (^4S)6p\ ^5P_1$
11		2312.276	43234.14	3.94	$(^2D)5d\ ^1P_1 - (^2D)6p\ ^3D_2$
7		2309.922	43278.20	.17	$(^2P)5d\ ^3P_1 - (^2P)6p\ ^1D_2$
5		2305.502	43361.15	.05	$(^2P)5d\ ^3D_2 - (^2P)4f\ ^3F_2$
5		2305.502	43361.15	.92	$(^2D)6s\ ^3D_2 - (^2P)6p\ ^3P_1$
9		2303.735	43394.42	.21	$5s5p^5\ ^3P_1 - (^4S)6p\ ^5P_2$
9		2303.735	43394.42	.67	$(^2D)5d\ ^3F_2 - (^2D)6p\ ^3P_1$
9		2300.876	43448.33	.21	$(^2D)6s\ ^3D_1 - (^2D)4f\ ^3F_2$
9		2300.716	43451.35	.22	$(^4S)5d\ ^3D_2 - (^2D)6p\ ^3F_2$
9		2300.353	43458.22	.02	$(^2D)5d\ ^3D_3 - (^2D)4f\ ^3F_3$
1		2298.540	43492.48	.39	$(^2P)5d\ ^3F_2 - (^2D)4f\ ^3D_1$
12	b	2290.834	43638.77	.67	$(^2D)6s\ ^3D_2 - (^2D)4f\ ^3G_3$
2		2288.009	43692.65	.62	$(^2P)5d\ ^3D_2 - (^4S)5f\ ^5F_3$
7		2286.634	43718.91	.81	$(^2D)6s\ ^3D_3 - (^2D)4f\ ^3D_3$
5		2283.828	43772.63	.79	$(^2D)5d\ ^3F_4 - (^4S)4f\ ^3F_4$
1		2273.709	43967.41	.18	$(^2P)5d\ ^3D_2 - (^4S)5f\ ^5F_2$
3		2273.488	43971.70	.73	$(^2P)6s\ ^1P_1 - (^2P)4f\ ^3D_2$
2		2272.609	43988.70	.65	$(^2D)6s\ ^3D_1 - (^2P)6p\ ^3S_1$
11	w	2271.382	44012.46	.37	$(^2D)5d\ ^1F_3 - (^2D)4f\ ^1G_4$
8		2271.055	44018.80	.94	$(^4S)5d\ ^3D_1 - (^2D)6p\ ^3P_0$
4		2268.923	44060.15	.09	$(^2P)5d\ ^3D_2 - (^2P)4f\ ^3G_3$
5		2258.847	44256.68	.62	$(^2D)5d\ ^3D_2 - (^2P)6p\ ^3P_2$
0		2249.630	44437.97	8.04	$(^2P)5d\ ^3F_3 - (^2D)4f\ ^1F_3$
6		2247.556	44478.99	.82	$(^2P)5d\ ^3F_2 - (^2D)4f\ ^1F_3$
5		2247.335	44483.36	.16	$(^2P)5d\ ^3F_3 - (^2D)4f\ ^1D_2$
8		2245.280	44524.07	3.94	$(^2P)5d\ ^3F_2 - (^2D)4f\ ^1D_2$

Table I. *Continued*

Intensity[1]		λ (Å)	σ (cm⁻¹) obs	calc	Classification
11		2243.970	44 550.06	49.99	$(^2P)5d\ ^3D_2-(^2D)4f\ ^3F_3$
2		2235.349	44 721.86	.92	$(^2P)5d\ ^3D_1-(^2P)6p\ ^3D_2$
7		2231.673	44 795.52	.32	$(^2P)5d\ ^3D_1-(^2P)6p\ ^3P_1$
6		2230.419	44 820.69	.52	$(^2P)5d\ ^3D_1-(^2P)6p\ ^3P_0$
3		2227.588	44 877.64	.60	$(^2D)6p\ ^3P_0-(^2P)6d\ ^3D_1$
9		2225.071	44 928.41	.16	$(^2D)5d\ ^3D_2-(^2D)4f\ ^3D_2$
5		2223.640	44 957.33	.34	$(^4S)5d\ ^3D_1-(^4S)4f\ ^5F_2$
2		2220.544	45 019.99	.89	$(^4S)5d\ ^3D_2-(^2D)6p\ ^3D_2$
9		2214.382	45 145.26	4.48	$(^4S)5d\ ^3D_3-(^4S)4f\ ^5F_3$
0		2213 799	45 157.14	.10	$(^2P)5d\ ^3P_1-(^2P)6p\ ^1P_1$
9		2210.420	45 226.17	.22	$(^2P)5d\ ^1D_2-(^2D)4f\ ^3F_2$
3		2205.587	45 325.27	.24	$(^4S)5d\ ^3D_3-(^2D)6p\ ^3F_4$
5		2204.333	45 351.04	0.90	$(^2D)6s\ ^3D_3-(^2P)6p\ ^1D_2$
0		2203.682	45 364.44	.36	$(^2D)6s\ ^1D_2-(^2D)4f\ ^3P_2$
7		2202.695	45 384.76	.96	$(^2D)5d\ ^3G_3-(^4S)4f\ ^3F_2$
6		2199.514	45 450.39	.25	$(^2P)5d\ ^3P_0-(^2P)6p\ ^1P_1$
6		2199.287	45 455.09	4.77	$(^2P)6s\ ^3P_2-(^2P)4f\ ^3D_3$
1		2198.583	45 469.64	.53	$(^4S)5d\ ^3D_3-(^2D)6p\ ^3D_3$
10		2197.801	45 485.82	.63	$(^2D)5d\ ^1P_1-(^2D)6p\ ^1P_1$
1		2194.292	45 558.56	.83	$(^2D)5d\ ^3F_2-(^4S)4f\ ^3F_3$
1		2192.428	45 597.28	.37	$(^2D)5d\ ^3G_3-(^4S)4f\ ^3F_4$
12	w	2189.828	45 651.42	0.51	$(^4S)5d\ ^3D_3-(^4S)4f\ ^5F_2$
3		2185.701	45 751.90	.97	$(^2P)5d\ ^3P_2-(^2P)4f\ ^3F_3$
7		2179.684	45 863.84	.61	$(^2D)6s\ ^3D_1-(^2P)6p\ ^1D_2$
9		2172.779	46 009.58	.53	$(^2P)5d\ ^1D_2-(^2D)4f\ ^3D_3$
3		2165.526	46 163.67	.24	$(^4S)5d\ ^3D_1-(^2D)6p\ ^3P_1$
3		2165.526	46 163.67	4.39	$(^2D)5d\ ^3G_4-(^4S)4f\ ^3F_4$
7		2160.935	46 261.74	.50	$(^2P)5d\ ^3P_1-(^2D)4f\ ^3D_2$
8		2156.896	46 348.36	.29	$(^2D)5d\ ^3D_2-(^2D)4f\ ^3P_2$
7		2147.683	46 547.15	.08	$(^4S)5d\ ^5D_1-(^2D)6p\ ^3D_1$
0		2144.189	46 623.00	2.71	$(^2D)5d\ ^3D_3-(^2D)4f\ ^1F_3$
2		2142.129	46 667.82	.83	$(^2D)5d\ ^3D_3-(^2D)4f\ ^1D_2$
7		2139.375	46 727.90	.23	$(^2D)5d\ ^3G_5-(^2D)4f\ ^3G_4$
7		2139.375	46 727.90	8.25	$(^2D)5d\ ^3D_2-(^2D)4f\ ^3D_1$
6		2139.236	46 730.93	.74	$(^2D)6s\ ^1D_2-(^2D)4f\ ^1F_3$
9		2138.432	46 748.50	.54	$(^2D)6s\ ^3D_3-(^2D)4f\ ^3F_4$
3		2130.809	46 915.73	.66	$(^2D)5d\ ^1P_1-(^2D)6p\ ^3P_0$
1		2128.473	46 967.20	.23	$(^2P)5d\ ^3D_3-(^2P)4f\ ^3D_2$
4		2123.163	47 084.65	.30	$(^2P)5d\ ^3F_3-(^2D)4f\ ^1G_4$
2		2122.205	47 105.90	.47	$(^2P)5d\ ^1D_2-(^2D)4f\ ^1P_1$
9		2118.036	47 198.62	.56	$(^4S)5d\ ^3D_2-(^2D)6p\ ^1F_3$
7		2114.762	47 271.68	.57	$(^4S)5d\ ^3D_2-(^2D)6p\ ^1P_1$
1		2106.354	47 456.31	.14	$(^2P)5d\ ^3P_2-(^4S)5f\ ^5F_2$
0		2099.545	47 614.26	.34	$(^2D)5d\ ^3F_3-(^4S)4f\ ^3F_2$
9		2096.570	47 681.81	.63	$(^2P)5d\ ^3P_1-(^2D)4f\ ^3P_2$
3		2095.350	47 709.56	.59	$(^2D)6s\ ^3D_2-(^2D)4f\ ^3D_3$
6		2095.126	47 714.67	.68	$(^2D)5d\ ^3D_2-(^2D)4f\ ^1F_3$
5		2093.862	47 743.47	.37	$(^2D)5d\ ^1F_3-(^2P)4f\ ^3F_3$
9		2091.996	47 786.06	.08	$(^2D)5d\ ^3P_2-(^2P)4f\ ^3F_3$
7		2090.225	47 826.52	.76	$(^2D)5d\ ^3F_3-(^4S)4f\ ^3F_4$
9		2084.598	47 955.61	6.06	$(^2D)6s\ ^3D_3-(^2D)4f\ ^3F_3$
2		2084.461	47 958.77	9.01	$(^2P)5d\ ^3D_1-(^2P)4f\ ^3D_2$
6		2083.088	47 990.37	.19	$(^2P)5d\ ^3D_3-(^2P)4f\ ^3D_3$
5		2079.995	48 061.73	.58	$(^2P)5d\ ^3P_1-(^2D)4f\ ^3D_1$
0		2077.610	48 116.88	7.06	$(^4S)6s\ ^3S_1-(^4S)4f\ ^3F_2$
7		2075.090	48 175.32	.39	$(^2D)6s\ ^3D_1-(^2P)6p\ ^3P_2$
7		2072.866	48 226.99	.97	$(^2P)5d\ ^1D_2-(^2P)6p\ ^3D_3$
0		2072.247	48 241.41	.40	$(^4S)5d\ ^5D_1-(^2D)6p\ ^3F_2$
7		2067.384	48 354.87	.73	$(^2P)5d\ ^3P_0-(^2D)4f\ ^3D_1$
9		2067.175	48 359.74	.68	$(^2D)5d\ ^3D_1-(^2D)4f\ ^3F_2$
3		2060.702	48 511.63	.72	$(^2P)5d\ ^3D_3-(^2P)4f\ ^1G_4$
0		2060.385	48 519.10	.01	$5s5p^5\ ^3P_2-(^4S)6p\ ^5P_1$
6		2055.034	48 645.42	.02	$(^2D)5d\ ^1G_4-(^2D)4f\ ^1H_5$
8		2052.729	48 700.03	699.95	$5s5p^5\ ^3P_2-(^4S)6p\ ^5P_2$
5		2052.166	48713.39	.44	$(^2D)5d\ ^3F_4-(^2D)4f\ ^3G_4$
7		2051.875	48 720.31	.54	$(^2D)5d\ ^3P_1-(^2P)4f\ ^3D_2$
8		2046.555	48 846.93	.94	$(^2D)6s\ ^3D_1-(^2D)4f\ ^3D_2$
1		2044.430	48 897.70	.73	$(^2D)5d\ ^1F_3-(^4S)5f\ ^5F_4$

Table I. *Continued*

Intensity[1]		λ (Å)	σ (cm⁻¹) obs	calc	Classification
2		2043.286	48 925.07	.15	$(^2P)5d\ ^3F_4-(^4S)5f\ ^5F_5$
1		2041.276	48 973.24	.17	$(^2D)5d\ ^1G_4-(^2D)4f\ ^3H_4$
7		2039.314	49 020.36	.57	$(^4S)5d\ ^3D_3-(^4S)4f\ ^3F_3$
6		2038.394	49 042.48	.79	$(^2D)5d\ ^3F_2-(^4S)4f\ ^3F_2$
7		2037.670	49 059.89	.97	$(^2D)5d\ ^1P_1-(^2D)6p\ ^3P_1$
8		2031.996	49 196.86	.86	$(^2D)5d\ ^3G_5-(^2D)4f\ ^3H_5$
9		2029.216	49 264.25	3.67	$(^2P)5d\ ^3P_0-(^2D)4f\ ^3P_1$
8		2029.023	49 268.94	.97	$(^2D)5d\ ^3D_3-(^2D)4f\ ^1G_4$
10		2026.062	49 340.94	1.68	$(^2D)6s\ ^3D_2-(^2P)6p\ ^1D_2$
2		2021.304	49 457.06	6.84	$(^2D)5d\ ^3S_1-(^2P)4f\ ^3F_2$
6		2020.914	49 466.60	.71	$(^2P)5d\ ^3D_2-(^2P)4f\ ^3D_2$
5		2018.714	49 520.52	.55	$(^2P)5d\ ^1D_2-(^2P)6p\ ^1P_1$
2		2017.911	49 540.22	.45	$(^2D)5d\ ^1F_3-(^2P)4f\ ^3G_3$
2		2016.174	49 582.89	3.16	$(^2D)5d\ ^3P_2-(^2P)4f\ ^3G_3$
8		2013.859	49 639.88	40.00	$(^4S)5d\ ^3D_2-(^4S)4f\ ^5F_2$
4		2006.317	49 826.46	.24	$(^4S)5d\ ^3D_2-(^2D)6p\ ^3P_2$
1		2001.085	49 956.71	.93	$(^2D)5d\ ^3G_3-(^2D)4f\ ^3G_3$
0		1997.497	50 062.65	.97	$(^2D)5d\ ^3S_1-(^4S)5f\ ^5F_2$
6		1997.330	50 066.83	7.07	$(^4S)5d\ ^3D_1-(^2D)6p\ ^1D_2$
7		1990.182	50 246.66	.78	$(^2P)5d\ ^1D_2-(^2D)4f\ ^3F_3$
1		1989.377	50 267.00	.07	$(^2D)6s\ ^3D_1-(^2D)4f\ ^3P_2$
10		1985.405	50 367.56	.32	$(^2P)5d\ ^3D_3-(^2P)4f\ ^3F_4$
5		1983.985	50 403.61	.59	$(^4S)5d\ ^5D_2-(^2D)6p\ ^3D_2$
2		1980.606	50 489.61	.67	$(^2P)5d\ ^3D_2-(^2P)4f\ ^3D_3$
2		1979.266	50 523.78	.95	$(^2D)5d\ ^3G_4-(^2D)4f\ ^3G_3$
8		1978.705	50 538.10	.02	$(^2D)5d\ ^3G_3-(^2D)4f\ ^3G_4$
1		1974.445	50 647.15	.02	$(^2D)6s\ ^3D_1-(^2D)4f\ ^3D_1$
4		1973.829	50 662.96	3.22	$5s5p^5\ ^3P_0-(^2D)6p\ ^3D_1$
1		1970.899	50 738.26	.43	$(^4S)5d\ ^5D_2-(^2D)6p\ ^3F_3$
7		1970.059	50 759.90	60.24	$(^4S)5d\ ^3D_3-(^2D)6p\ ^1D_2$
4		1969.474	50 774.98	5.09	$(^2D)5d\ ^3D_1-(^2P)6p\ ^1D_2$
6		1967.905	50 815.46	.30	$(^2P)5d\ ^3F_3-(^2P)4f\ ^3F_3$
1		1966.733	50 845.75	.91	$(^4S)5d\ ^3D_2-(^2D)6p\ ^3P_1$
7		1966.345	50 855.78	6.08	$(^2P)5d\ ^3F_2-(^2P)4f\ ^3F_3$
7		1956.759	51 104.92	5.04	$(^2D)5d\ ^3G_4-(^2D)4f\ ^3G_4$
2		1956.154	51 120.73	.75	$(^2D)6s\ ^3D_3-(^2D)4f\ ^1F_3$
1		1945.419	51 402.81	.75	$(^2D)5d\ ^1G_4-(^2D)4f\ ^3G_5$
12		1942.913	51 469.11	.31	$(^2P)6s\ ^1P_1-5s^25p^6\ ^1S_0$
4		1941.329	51 511.11	.21	$(^2D)5d\ ^3F_4-(^2D)4f\ ^3H_4$
6		1935.038	51 678.58	.57	$(^2D)6s\ ^3D_1-(^2D)4f\ ^1D_2$
11		1930.083	51 811.25	.36	$(^4S)5d\ ^3D_1-(^4S)4f\ ^3F_2$
6		1929.158	51 836.09	.16	$(^2D)5d\ ^3F_3-(^2P)6p\ ^3D_2$
5		1927.622	51 877.40	.48	$(^2P)6s\ ^3P_1-(^2P)4f\ ^3D_2$
2		1926.291	51 913.24	.34	$(^2P)5d\ ^3F_3-(^2P)4f\ ^3F_2$
4		1924.757	51 954.60	.12	$(^2P)5d\ ^3F_2-(^2P)4f\ ^3F_2$
4		1924.757	51 954.60	.59	$(^2D)5d\ ^3G_5-(^2D)4f\ ^3G_5$
8		1924.197	51 969.74	.66	$(^2P)5d\ ^3F_3-(^4S)5f\ ^5F_4$
5		1921.644	52 038.77	.63	$5s5p^5\ ^3P_2-(^4S)6p\ ^3P_1$
5		1916.211	52 186.31	.31	$(^2D)5d\ ^3F_3-(^2D)4f\ ^3G_3$
2		1915.595	52 203.09	.27	$(^2D)5d\ ^3F_4-(^2D)4f\ ^3D_3$
2		1912.564	52 285.82	.69	$(^2P)5d\ ^3F_2-(^4S)5f\ ^5F_3$
0		1911.131	52 325.03	.01	$(^2D)6s\ ^3D_2-(^2D)4f\ ^3D_2$
1		1910.626	52 338.88	.87	$(^4S)6s\ ^3S_1-(^2P)6p\ ^3D_2$
0		1907.038	52 437.33	.47	$(^4S)6s\ ^3S_1-(^2P)6p\ ^3P_0$
6		1904.599	52 504.50	.54	$(^4S)5d\ ^3D_3-(^4S)4f\ ^3F_2$
0		1901.779	52 582.35	.26	$(^4S)5d\ ^5D_2-(^2D)6p\ ^1F_3$
4		1900.693	52 612.39	.38	$(^2P)5d\ ^3F_3-(^2P)4f\ ^3G_3$
9		1899.216	52 653.31	4.02	$(^2D)5d\ ^3D_1-(^2P)6p\ ^1P_1$
9		1899.216	52 653.31	.16	$(^2P)5d\ ^3F_2-(^2P)4f\ ^3G_3$
7		1899.156	52 654.98	5.27	$(^4S)5d\ ^5D_2-(^2D)6p\ ^1P_1$
10		1896.921	52 717.02	6.95	$(^4S)5d\ ^3D_3-(^4S)4f\ ^3F_4$
11		1895.099	52 767.68	.40	$(^2D)5d\ ^3F_3-(^2D)4f\ ^3G_4$
0		1892.723	52 833.94	.23	$(^4S)5d\ ^5D_3-(^2D)6p\ ^1F_3$
7		1888.374	52 955.62	.67	$(^2P)5d\ ^3P_2-(^2P)4f\ ^3D_2$
8		1888.083	52 963.76	.80	$(^2D)5d\ ^1P_1-(^2D)6p\ ^1D_2$
11		1886.426	53 010.29	.07	$(^4S)5d\ ^3D_2-(^4S)4f\ ^3F_3$
3		1883.687	53 087.38	6.87	$(^2D)5d\ ^3D_1-(^2P)6p\ ^3P_2$
1		1882.957	53 107.97	8.01	$(^2D)6s\ ^1D_2-(^2P)4f\ ^3F_3$

Table I. *Continued*

Intensity[a]	λ (Å)	σ (cm⁻¹) obs	σ (cm⁻¹) calc	Classification
1	1878.049	53246.74	.80	$(^2D)5d\ ^3G_5-(^2D)4f\ ^3F_4$
8	1875.878	53308.36	.40	$(^4S)5d\ ^3D_1-(^2P)6p\ ^3D_1$
10	1875.772	53311.38	.14	$(^2D)5d\ ^1G_4-(^2D)4f\ ^1H_5$
10	1874.915	53335.76	.79	$(^2D)5d\ ^3G_3-(^2D)4f\ ^3H_4$
9	1872.254	53411.57	.47	$(^2P)5d\ ^1D_2-(^2D)4f\ ^1F_3$
9	1870.665	53456.94	.59	$(^2P)5d\ ^1D_2-(^2D)4f\ ^1D_2$
0	1869.447	53491.76	.79	$(^4S)5d\ ^5D_1-(^2D)6p\ ^3P_0$
10	1866.547	53574.85	.66	$(^2D)5d\ ^3G_4-(^2D)4f\ ^3H_5$
10	1865.157	53614.80	.76	$(^2D)5d\ ^3F_2-(^2D)4f\ ^3G_3$
4	1860.631	53745.21	.14	$(^2D)6s\ ^3D_2-(^2D)4f\ ^3P_2$
8	1860.181	53758.21	.42	$(^2D)5d\ ^3D_1-(^2D)4f\ ^3D_2$
9	1859.877	53766.99	7.01	$(^2D)6s\ ^3D_3-(^2D)4f\ ^1G_4$
2	1856.569	53862.81	.98	$(^2D)5d\ ^3G_5-(^2D)4f\ ^1H_5$
9	1855.196	53902.66	.81	$(^2D)5d\ ^3G_4-(^2D)4f\ ^3H_4$
11	1854.375	53926.53	.58	$(^2D)5d\ ^3G_5-(^2D)4f\ ^3H_6$
10	1853.884	53940.82	.79	$(^2D)5d\ ^3F_4-(^2D)4f\ ^3G_5$
9	1852.583	53978.68	.63	$(^2P)5d\ ^3P_2-(^2P)4f\ ^3D_3$
6	1850.903	54027.68	.85	$(^2D)5d\ ^3G_3-(^2D)4f\ ^3D_3$
8	1848.989	54083.60	.49	$(^4S)5d\ ^5D_4-(^4S)4f\ ^5F_4$
9	1848.695	54092.20	1.94	$(^2D)5d\ ^3D_2-(^2P)4f\ ^3F_3$
5	1837.300	54427.68	.34	$(^4S)5d\ ^5D_4-(^2D)6p\ ^3D_3$
4	1837.223	54429.98	30.19	$(^4S)5d\ ^5D_1-(^4S)4f\ ^5F_2$
15	1835.811	54471.84	2.03	$(^4S)5d\ ^5D_4-(^4S)4f\ ^5F_5$
9	1835.532	54480.13	79.59	$(^4S)5d\ ^5D_0-(^4S)4f\ ^5F_1$
9	1834.255	54518.04	7.68	$(^4S)5d\ ^5D_2-(^4S)4f\ ^5F_3$
1	1833.588	54537.87	.62	$(^2D)6s\ ^1D_2-(^4S)5f\ ^5F_3$
1	1831.680	54594.69	.87	$(^2D)5d\ ^3G_4-(^2D)4f\ ^3D_3$
9	1830.939	54616.78	.43	$(^4S)5d\ ^5D_1-(^2D)6p\ ^3P_2$
9	1827.883	54708.10	.09	$(^2D)5d\ ^1P_1-(^4S)4f\ ^3F_2$
9	1827.367	54723.55	.64	$(^4S)5d\ ^5D_1-(^4S)4f\ ^5F_1$
12	1826.490	54749.82	.86	$(^4S)5d\ ^5D_3-(^4S)4f\ ^5F_4$
12	1826.490	54749.82	.74	$(^4S)5d\ ^3D_2-(^2D)6p\ ^1D_2$
9	1825.867	54768.49	.65	$(^4S)5d\ ^5D_3-(^4S)4f\ ^5F_3$
11	1823.391	54842.88	.73	$(^4S)5d\ ^5D_2-(^2D)6p\ ^3D_3$
10	1821.334	54904.82	5.09	$(^2D)6s\ ^1D_2-(^2P)4f\ ^3G_3$
11	1819.857	54949.37	.41	$(^4S)5d\ ^5D_3-(^2D)6p\ ^3F_4$
9	1817.397	55023.74	.71	$(^4S)5d\ ^5D_2-(^4S)4f\ ^5F_2$
11	1815.085	55093.85	.70	$(^4S)5d\ ^5D_3-(^2D)6p\ ^3D_3$
10	1814.503	55111.51	.53	$(^2D)6s\ ^3D_2-(^2D)4f\ ^1F_3$
3	1812.301	55178.48	.55	$(^2D)5d\ ^3D_1-(^2D)4f\ ^3P_2$
11	1811.263	55210.08	09.94	$(^4S)5d\ ^5D_2-(^2D)6p\ ^3P_2$
11	1810.520	55232.75	3.01	$(^2D)5d\ ^3F_4-(^2D)4f\ ^3F_4$
7	1807.746	55317.51	.16	$(^4S)5d\ ^5D_2-(^4S)4f\ ^5F_1$
4	1805.316	55391.96	2.05	$(^4S)5d\ ^5D_0-(^2D)6p\ ^3P_1$
10	1804.117	55428.78	.78	$5s5p^5\ ^3P_1-(^2D)6p\ ^3D_1$
8	1803.073	55460.87	.91	$(^4S)5d\ ^5D_3-(^2D)6p\ ^3P_2$
9	1799.900	55558.64	.50	$(^2D)5d\ ^3D_1-(^2D)4f\ ^3D_1$
7	1799.769	55562.68	.50	$(^2D)5d\ ^3S_1-(^2P)4f\ ^3D_2$
10	1799.691	55565.08	.17	$(^2D)5d\ ^3F_3-(^2D)4f\ ^3H_4$
6	1790.544	55848.96	9.19	$(^2D)5d\ ^3F_4-(^2D)4f\ ^1H_5$
7	1789.258	55889.09	.02	$(^2D)5d\ ^3D_2-(^2P)4f\ ^3G_3$
8	1786.678	55969.79	70.03	$(^2D)5d\ ^1F_3-(^2P)4f\ ^3D_3$
2	1785.311	56012.64	.74	$(^2D)5d\ ^3P_2-(^2P)4f\ ^3D_3$
8	1784.661	56033.05	.18	$(^4S)5d\ ^3D_1-(^2P)6p\ ^3D_2$
3	1780.067	56177.66	.89	$5s5p^5\ ^3P_0-(^2D)6p\ ^1P_1$
9	1778.783	56218.22	.12	$(^2D)5d\ ^3P_1-5s^25p^6\ ^1S_0$
2	1788.425	56229.54	.62	$(^4S)5d\ ^5D_2-(^2D)6p\ ^3P_1$
11	1777.910	56245.82	.29	$(^2D)5d\ ^3G_3-(^2P)6p\ ^3D_3$
6	1777.551	56257.19	.24	$(^2D)5d\ ^3F_3-(^2D)4f\ ^3D_3$
9	1775.174	56332.50	.39	$(^2D)5d\ ^3G_4-(^2D)4f\ ^3G_5$
9	1774.033	56368.75	.88	$(^2P)5d\ ^3F_4-(^2P)4f\ ^1G_4$
5	1771.778	56440.47	.53	$(^2D)5d\ ^3F_4-(^2D)4f\ ^3F_3$
0	1770.919	56467.87	.45	$(^2D)5d\ ^3D_1-(^2D)4f\ ^3P_1$
10	1770.174	56491.62	.56	$(^2D)5d\ ^1F_3-(^2P)4f\ ^1G_4$
10	1770.099	56494.01	.03	$(^4S)5d\ ^3D_2-(^4S)4f\ ^3F_2$
10	1767.089	56590.26	.05	$(^2D)5d\ ^3D_1-(^2D)4f\ ^1D_2$
6	1760.178	56812.45	.31	$(^2D)5d\ ^3G_4-(^2P)6p\ ^3D_3$
0	1759.622	56830.40	.14	$(^4S)6s\ ^5S_2-(^2D)4f\ ^3G_3$

Table I. *Continued*

Intensity[a]	λ (Å)	σ (cm⁻¹) obs	σ (cm⁻¹) calc	Classification
10	1757.396	56902.37	.37	$(^2D)5d\ ^3F_2-(^2D)4f\ ^3F_2$
11	1752.626	57057.24	.59	$(^2D)5d\ ^3G_3-(^2D)4f\ ^3F_4$
4	1752.318	57067.27	.17	$(^2D)5d\ ^1G_4-(^2D)4f\ ^1F_3$
4	1752.022	57076.90	.50	$(^4S)5d\ ^3D_3-(^2D)4f\ ^3G_3$
5	1750.609	57122.99	3.09	$5s5p^5\ ^3P_1-(^2D)6p\ ^3F_2$
9	1735.371	57642.56	.60	$(^2D)5d\ ^3G_4-(^2D)4f\ ^3F_4$
7	1734.368	57657.90	.59	$(^4S)5d\ ^3D_3-(^2D)4f\ ^3G_4$
3	1733.536	57685.55	.68	$(^2D)5d\ ^3F_2-(^2D)4f\ ^3D_3$
5	1728.420	57856.31	5.89	$(^4S)6s\ ^3S_1-(^2D)4f\ ^1P_1$
9	1727.429	57889.49	.33	$(^2D)5d\ ^3F_3-(^2P)6p\ ^1D_2$
7	1724.983	57971.60	.73	$(^2D)5d\ ^3G_3-(^2P)6p\ ^3P_2$
2	1724.776	57978.54	.38	$(^4S)5d\ ^5D_4-(^4S)4f\ ^3F_3$
8	1722.358	58059.92	.78	$(^2P)5d\ ^3F_2-(^2P)4f\ ^3D_2$
12	1717.515	58223.66	4.48	$(^2P)5d\ ^3F_4-(^2P)4f\ ^3F_4$
5	1717.005	58240.95	.78	$(^2D)5d\ ^3G_4-(^2D)4f\ ^1H_5$
5	1716.290	58265.21	.11	$(^2D)5d\ ^3G_3-(^2D)4f\ ^3F_3$
3	1713.867	58347.59	.16	$(^2D)5d\ ^1F_3-(^2P)4f\ ^3F_4$
10	1712.522	58393.42	.77	$(^4S)5d\ ^5D_2-(^4S)4f\ ^3F_3$
12	1705.178	58644.89	.74	$(^4S)5d\ ^5D_3-(^4S)4f\ ^3F_3$
1	1704.946	58652.88	.37	$(^2D)6s\ ^3D_3-(^4S)5f\ ^5F_4$
8	1703.820	58691.66	.76	$5s5p^5\ ^3P_1-(^2D)6p\ ^3D_2$
9	1699.754	58832.03	.12	$(^2D)5d\ ^3G_4-(^2D)4f\ ^3F_3$
10	1699.515	58840.31	39.78	$5s5p^5\ ^3P_0-(^4S)4f\ ^5F_1$
4	1696.936	58929.74	.91	$(^2D)5d\ ^1P_1-(^2P)6p\ ^1D_2$
7	1694.820	59003.30	.31	$(^2D)5d\ ^1P_1-(^2P)6p\ ^3P_1$
7	1694.134	59027.21	8.51	$(^2D)5d\ ^1P_1-(^2P)6p\ ^3P_0$
9	1693.703	59042.24	1.96	$(^2P)5d\ ^3F_3-(^2P)4f\ ^3D_3$
5	1691.798	59108.71	.76	$(^2D)6s\ ^3D_1-(^2P)4f\ ^3F_2$
9	1685.823	59318.20	7.77	$(^2D)5d\ ^3F_2-(^2P)6p\ ^1D_2$
2	1684.194	59375.59	.06	$(^2P)6s\ ^3P_1-5s^25p^6\ ^1S_0$
6	1678.873	59563.78	.49	$(^2P)5d\ ^3F_3-(^2P)4f\ ^1G_4$
11	1675.824	59672.13	0.95	$(^4S)5d\ ^3D_1-(^2D)4f\ ^3F_2$
11	1674.633	59714.57	.89	$(^2D)6s\ ^3D_1-(^4S)5f\ ^5F_2$
9	1673.566	59752.66	.24	$5s5p^5\ ^3P_0-(^2D)6p\ ^3P_1$
9	1672.557	59788.71	.73	$(^2P)5d\ ^1D_2-(^2P)4f\ ^3F_3$
7	1669.355	59903.37	.12	$(^2D)5d\ ^3F_2-(^2P)6p\ ^3D_3$
9	1663.390	60118.18	7.76	$(^4S)6s\ ^5S_2-(^2D)4f\ ^3F_2$
6	1661.093	60201.31	.11	$(^2D)5d\ ^3F_3-(^2P)6p\ ^3P_2$
1	1661.029	60203.63	.67	$(^2D)5d\ ^3D_3-(^2P)4f\ ^3D_2$
4	1660.808	60211.67	.39	$(^4S)5d\ ^3D_1-(^2P)6p\ ^3S_1$
10	1656.612	60364.15	.12	$(^4S)5d\ ^3D_3-(^2D)4f\ ^3F_2$
3	1656.069	60383.96	4.41	$(^4S)5d\ ^5D_3-(^2D)6p\ ^1D_2$
10	1653.039	60494.65	.49	$(^2D)5d\ ^3F_3-(^2D)4f\ ^3F_3$
10	1647.338	60704.01	3.82	$(^4S)6s\ ^3S_1-(^2P)6p\ ^3P_2$
8	1647.010	60716.09	5.85	$(^4S)5d\ ^3D_2-(^2P)6p\ ^3D_2$
2	1646.504	60734.75	.51	$5s5p^5\ ^3P_2-(^2D)6p\ ^3D_1$
10	1642.767	60872.91	.66	$(^2D)5d\ ^3F_3-(^2D)4f\ ^3D_2$
3	1642.395	60886.68	.77	$(^2P)5d\ ^1D_2-(^2P)4f\ ^3F_2$
3	1637.572	61066.01	.00	$(^4S)5d\ ^3D_2-(^2D)4f\ ^3G_3$
11	1635.382	61147.81	.43	$(^4S)5d\ ^3D_3-(^2D)4f\ ^3D_3$
3	1634.072	61196.81	.71	$(^2D)5d\ ^3F_2-(^2P)6p\ ^1P_1$
7	1633.489	61218.65	.34	$(^2P)5d\ ^1D_2-(^4S)5f\ ^5F_3$
10	1633.255	61227.42	6.63	$(^2D)5d\ ^3D_3-(^2P)4f\ ^3D_3$
10	1631.429	61295.96	.64	$(^2D)5d\ ^3D_2-(^2P)4f\ ^3D_2$
6	1629.312	61375.60	.37	$(^4S)6s\ ^3S_1-(^2D)4f\ ^3D_2$
1	1628.148	61419.48	.09	$(^2P)5d\ ^3F_3-(^2P)4f\ ^3F_4$
1	1626.309	61488.93	.79	$(^2D)6s\ ^3D_2-(^2P)4f\ ^3F_3$
3	1626.183	61493.68	2.90	$(^2P)5d\ ^1D_2-(^4S)5f\ ^5F_2$
5	1624.678	61550.66	.20	$(^4S)5d\ ^3D_1-(^2D)4f\ ^1P_1$
6	1623.748	61585.90	.81	$(^2P)5d\ ^1D_2-(^2P)4f\ ^3G_3$
8	1622.595	61629.67	.56	$(^2D)5d\ ^3F_2-(^2P)6p\ ^3P_2$
7	1621.407	61674.84	.75	$(^4S)5d\ ^5D_4-(^4S)4f\ ^3F_4$
8	1619.484	61748.05	.16	$(^2D)5d\ ^3D_3-(^2P)4f\ ^1G_4$
3	1616.083	61878.00	7.74	$(^4S)5d\ ^5D_2-(^4S)4f\ ^3F_2$
6	1612.970	61997.45	6.81	$(^2D)5d\ ^3G_4-(^2D)4f\ ^1F_3$
6	1612.970	61997.45	.01	$(^4S)6s\ ^5S_2-(^2D)4f\ ^1P_1$
5	1610.658	62086.42	.35	$(^4S)5d\ ^3D_1-(^2P)6p\ ^1D_2$
2	1606.393	62251.26	.48	$(^2D)5d\ ^3F_4-(^2D)4f\ ^1G_4$

Table I. *Continued*

Intensity[1]		λ (Å)	σ (cm⁻¹) obs	calc	Classification
9		1605.322	62 292.78	.79	$(^2D)5d\ ^3F_3 - (^2D)4f\ ^3P_2$
10		1605.106	62 301.19	.10	$(^2D)5d\ ^3F_2 - (^2D)4f\ ^3D_2$
8		1604.074	62 341.26	.12	$(^4S)5d\ ^5D_3 - (^4S)4f\ ^3F_4$
10		1603.241	62 373.67	.48	$5s5p^5\ ^3P_1 - (^2D)6p\ ^3P_0$
9		1601.817	62 429.09	8.83	$5s5p^5\ ^3P_2 - (^2D)6p\ ^3F_2$
11		1598.260	62 568.05	7.67	$(^2D)5d\ ^1P_1 - (^2D)4f\ ^3F_2$
11	w	1596.687	62 629.68	8.98	$(^2P)5d\ ^3P_1 - (^2P)4f\ ^3D_2$
10		1592.466	62 795.69	.50	$(^4S)6s\ ^3S_1 - (^2D)4f\ ^3P_2$
4		1589.351	62 918.75	.40	$(^2D)6s\ ^3D_2 - (^4S)5f\ ^5F_3$
12		1585.770	63 060.83	.07	$(^2D)5d\ ^3S_1 - 5s^05p^6\ ^1S_0$
9		1584.577	63 108.33	.12	$(^2D)5d\ ^1P_1 - (^2P)6p\ ^3S_1$
10		1579.476	63 312.15	1.88	$5s5p^5\ ^3P_1 - (^4S)4f\ ^5F_2$
9		1578.154	63 365.16	4.87	$(^4S)5d\ ^3D_3 - (^2P)6p\ ^3D_3$
9		1574.847	63 498.22	.12	$5s5p^5\ ^3P_1 - (^2D)6p\ ^3P_2$
9		1572.188	63 605.62	.33	$5s5p^5\ ^3P_1 - (^4S)4f\ ^5F_1$
6		1570.865	63 659.19	.17	$(^2D)5d\ ^3F_3 - (^2D)4f\ ^1F_3$
9		1569.753	63 704.28	.29	$(^2D)5d\ ^3F_3 - (^2D)4f\ ^1D_2$
10		1569.338	63 721.14	.24	$(^2D)5d\ ^3F_2 - (^2D)4f\ ^3P_2$
12		1562.547	63 998.06	7.50	$5s5p^5\ ^3P_2 - (^2D)6p\ ^3D_2$
9		1562.006	64 020.25	.24	$(^2D)5d\ ^3D_1 - (^2P)4f\ ^3F_2$
10		1560.437	64 084.60	.40	$(^4S)6s\ ^3S_1 - (^2D)4f\ ^3P_1$
11		1560.011	64 102.10	1.19	$(^2D)5d\ ^3F_2 - (^2D)4f\ ^3D_1$
7		1558.178	64 177.53	.16	$(^4S)5d\ ^3D_3 - (^2D)4f\ ^3F_4$
5		1557.460	64 207.12	.00	$(^4S)6s\ ^3S_1 - (^2D)4f\ ^1D_2$
8		1554.426	64 332.43	.34	$5s5p^5\ ^3P_2 - (^2D)6p\ ^3F_3$
10		1553.907	64 353.91	.62	$(^4S)5d\ ^3D_2 - (^2D)4f\ ^3F_2$
10		1551.651	64 447.50	6.92	$(^2D)5d\ ^1P_1 - (^2D)4f\ ^1P_1$
9		1549.961	64 517.77	.79	$5s5p^5\ ^3P_1 - (^2D)6p\ ^3P_1$
9		1548.008	64 599.14	8.79	$(^2D)5d\ ^1G_4 - (^4S)5f\ ^5F_4$
7		1547.346	64 626.80	.37	$(^2D)5d\ ^3D_1 - (^4S)5f\ ^5F_2$
9		1546.952	64 643.24	.07	$(^2D)5d\ ^3G_4 - (^2D)4f\ ^1G_4$
2		1540.970	64 894.18	.06	$(^4S)5d\ ^3D_2 - (^2P)6p\ ^3S_1$
8		1538.863	64 983.05	.07	$(^2D)5d\ ^1P_1 - (^2P)6p\ ^1D_2$
7		1538.220	65 010.22	.13	$(^2D)5d\ ^3F_2 - (^2D)4f\ ^3P_1$
2		1536.812	65 069.76	.68	$(^4S)5d\ ^3D_1 - (^2D)4f\ ^3D_2$
9		1536.386	65 087.81	.62	$(^2D)5d\ ^3F_2 - (^2D)4f\ ^1F_3$
7		1535.328	65 132.65	.74	$(^2D)5d\ ^3F_2 - (^2D)4f\ ^1D_2$
3		1535.224	65 137.09	6.93	$(^4S)5d\ ^3D_2 - (^2D)4f\ ^3D_3$
6		1533.416	65 213.86	4.42	$(^2D)6s\ ^3D_1 - (^2P)4f\ ^3D_2$
2		1532.765	65 241.58	.51	$(^2D)5d\ ^1G_4 - (^2P)4f\ ^3G_3$
0		1530.558	65 335.64	.39	$(^4S)5d\ ^5D_0 - (^2P)6p\ ^3P_1$
7		1526.586	65 505.65	6.04	$(^4S)5d\ ^5D_1 - (^2P)6p\ ^3D_2$
4		1524.280	65 604.76	.64	$(^4S)5d\ ^3D_1 - (^2P)6p\ ^3P_0$
5		1521.501	65 724.58	.67	$(^2D)6s\ ^3D_3 - (^2P)4f\ ^3D_3$
5		1520.619	65 762.71	.85	$(^4S)5d\ ^3D_3 - (^2D)4f\ ^3D_2$
0		1515.558	65 982.31	.48	$(^2D)5d\ ^3F_4 - (^2P)4f\ ^3F_3$
6		1511.119	66 176.14	.17	$5s5p^5\ ^3P_2 - (^2D)6p\ ^1F_3$
5		1509.841	66 232.15	.87	$(^4S)5d\ ^3D_2 - (^2D)4f\ ^1P_1$
3		1509.530	66 245.78	6.20	$(^2D)6s\ ^3D_3 - (^2P)4f\ ^1G_4$
7		1509.458	66 248.96	9.18	$5s5p^5\ ^3P_2 - (^2D)6p\ ^1P_1$
5		1508.178	66 305.15	.44	$(^2D)5d\ ^3F_3 - (^2D)4f\ ^1G_4$
3		1504.900	66 449.59	.70	$(^4S)5d\ ^5D_2 - (^2D)4f\ ^3G_3$
0		1503.997	66 489.51	.81	$(^4S)5d\ ^3D_1 - (^2D)4f\ ^3P_2$
1		1501.157	66 615.30	.40	$(^4S)5d\ ^5D_4 - (^2D)4f\ ^3G_4$
4		1497.708	66 768.67	9.02	$(^4S)5d\ ^3D_2 - (^2P)6p\ ^1D_2$
8		1495.446	66 869.67	.76	$(^4S)5d\ ^3D_1 - (^2D)4f\ ^3D_1$
4		1488.474	67 182.92	.98	$(^4S)5d\ ^3D_3 - (^2D)4f\ ^3P_2$
7		1486.291	67 281.56	.76	$(^4S)5d\ ^5D_3 - (^2D)4f\ ^3G_4$
6		1484.688	67 354.20	.36	$(^4S)5d\ ^3D_2 - (^2P)6p\ ^3D_3$
9	w	1482.243	67 465.34	.26	$5s^25p^4\ ^1S_0 - 5s5p^5\ ^3P_1$
2		1474.781	67 806.69	7.06	$(^2D)5d\ ^3G_3 - (^2P)4f\ ^3F_3$
7		1472.727	67 901.25	.31	$(^4S)5d\ ^3D_1 - (^2D)4f\ ^1D_2$
9		1471.312	67 966.57	.40	$(^2D)5d\ ^1P_1 - (^2D)4f\ ^3D_2$
1		1468.378	68 102.35	1.80	$(^2D)6s\ ^3D_3 - (^2P)4f\ ^3F_4$
6		1468.178	68 111.62	.59	$5s5p^5\ ^3P_2 - (^4S)4f\ ^5F_3$
2		1462.549	68 373.79	4.07	$(^2D)5d\ ^3G_4 - (^2P)4f\ ^3F_3$
5		1461.206	68 436.61	.64	$5s5p^5\ ^3P_2 - (^2D)6p\ ^3D_3$
4		1458.806	68 549.23	.36	$(^4S)5d\ ^3D_3 - (^2D)4f\ ^1F_3$

Table I. *Continued*

Intensity[1]		λ (Å)	σ (cm⁻¹) obs	calc	Classification
6		1457.845	68 594.40	.48	$(^4S)5d\ ^3D_3 - (^2D)4f\ ^1D_2$
8		1457.351	68 617.66	.62	$5s5p^5\ ^3P_2 - (^4S)4f\ ^5F_2$
1		1455.769	68 692.20	.49	$(^2D)6s\ ^3D_2 - (^2P)4f\ ^3D_2$
7		1453.408	68 803.79	.85	$5s5p^5\ ^3P_2 - (^2D)6p\ ^3P_2$
3		1451.141	68 911.30	.07	$5s5p^5\ ^3P_2 - (^4S)4f\ ^5F_1$
7		1450.093	68 961.10	.42	$(^2D)5d\ ^3G_3 - (^4S)5f\ ^5F_4$
8		1447.580	69 080.82	.80	$(^4S)5d\ ^3D_2 - (^2P)6p\ ^3P_2$
5		1447.487	69 085.26	.02	$(^4S)5d\ ^5D_4 - (^2D)4f\ ^3H_5$
8		1446.268	69 143.49	.80	$(^4S)5d\ ^5D_1 - (^2D)4f\ ^3F_2$
2		1441.199	69 386.67	.53	$(^2D)5d\ ^1P_1 - (^2D)4f\ ^3P_2$
2		1440.650	69 413.11	.17	$(^4S)5d\ ^5D_4 - (^2D)4f\ ^3H_4$
7		1440.089	69 440.17	.20	$(^4S)5d\ ^5D_0 - (^2P)6p\ ^3S_1$
1		1438.259	69 528.49	.43	$(^2D)5d\ ^3G_4 - (^4S)5f\ ^5F_4$
6		1436.707	69 603.61	4.14	$(^2D)5d\ ^3G_3 - (^2P)4f\ ^3G_3$
7		1435.045	69 684.23	.25	$(^4S)5d\ ^5D_1 - (^2P)6p\ ^3S_1$
2		1434.820	69 695.13	.57	$5s5p^5\ ^3P_0 - (^2P)6p\ ^3P_1$
3		1433.956	69 737.16	.32	$(^4S)5d\ ^5D_2 - (^2D)4f\ ^3F_2$
9		1432.185	69 823.37	.53	$5s5p^5\ ^3P_2 - (^2D)6p\ ^3P_1$
8		1428.810	69 988.31	.29	$(^4S)5d\ ^5D_3 - (^2D)4f\ ^3F_2$
7		1427.844	70 035.68	6.44	$(^2D)5d\ ^3F_3 - (^2P)4f\ ^3F_3$
10		1425.999	70 126.29	.56	$(^2P)5d\ ^3P_1 - 5s^05p^6\ ^1S_0$
6		1425.200	70 165.59	.91	$5s5p^5\ ^3P_1 - (^4S)4f\ ^3F_2$
8		1418.027	70 520.51	.63	$(^4S)5d\ ^5D_2 - (^2D)4f\ ^3D_3$
10		1414.921	70 675.30	.43	$(^2D)5d\ ^1P_1 - (^2D)4f\ ^3P_1$
0.5		1413.006	70 771.09	.60	$(^4S)5d\ ^5D_3 - (^2D)4f\ ^3D_3$
0.5		1412.846	70 779.11	.00	$(^4S)5d\ ^5D_0 - (^2D)4f\ ^1P_1$
15		1412.466	70 798.14	.04	$(^2D)5d\ ^1P_1 - (^2D)4f\ ^1D_2$
4		1407.990	71 023.22	.05	$(^4S)5d\ ^5D_1 - (^2D)4f\ ^1P_1$
8		1405.042	71 172.27	.48	$(^4S)5d\ ^3D_2 - (^2D)4f\ ^3P_2$
2		1404.681	71 190.55	.80	$(^2D)5d\ ^3F_3 - (^4S)5f\ ^5F_4$
3		1404.586	71 195.37	.63	$(^4S)5d\ ^3D_3 - (^2D)4f\ ^1G_4$
8		1402.224	71 315.26	.15	$(^4S)5d\ ^5D_0 - (^2P)6p\ ^1D_2$
4		1399.271	71 465.79	4.88	$(^2D)5d\ ^3F_2 - (^2P)4f\ ^3F_3$
4		1399.271	71 465.79	.13	$(^2D)5d\ ^1P_1 - (^2P)6p\ ^1S_0$
4		1399.271	71 465.79	6.05	$(^2D)5d\ ^3F_3 - (^4S)5f\ ^5F_3$
2	u	1397.573	71 552.63	.43	$(^4S)5d\ ^3D_2 - (^2D)4f\ ^3D_1$
1		1392.122	71 832.78	3.52	$(^2D)5d\ ^3F_3 - (^2P)4f\ ^3G_3$
5		1391.936	71 842.37	.75	$(^4S)5d\ ^5D_4 - (^2D)4f\ ^3G_5$
11		1389.129	71 987.53	.68	$5s5p^5\ ^3P_2 - (^4S)4f\ ^3F_3$
9		1380.055	72 460.90	1.38	$(^4S)5d\ ^3D_3 - (^2D)4f\ ^3P_1$
3		1378.128	72 562.23	.92	$(^2D)5d\ ^3F_2 - (^2P)4f\ ^3F_2$
10		1377.722	72 583.58	.98	$(^4S)5d\ ^3D_3 - (^2D)4f\ ^1D_2$
8		1375.295	72 711.67	2.00	$(^2D)6s\ ^3D_1 - 5s^05p^6\ ^1S_0$
3		1374.809	72 737.36	8.07	$(^4S)5d\ ^5D_2 - (^2P)6p\ ^3D_3$
0.5	h	1370.076	72 988.64	9.04	$(^4S)5d\ ^5D_3 - (^2P)6p\ ^3D_3$
8		1366.709	73 168.47	9.05	$(^2D)5d\ ^3F_2 - (^4S)5f\ ^5F_2$
3		1364.977	73 261.32	.96	$(^2D)5d\ ^3F_2 - (^2P)4f\ ^3G_3$
11		1356.358	73 726.86	7.35	$5s5p^5\ ^3P_2 - (^2D)6p\ ^1D_2$
10		1355.012	73 800.10	.38	$5s5p^5\ ^3P_0 - (^2P)6p\ ^3S_1$
6		1347.545	74 209.01	.14	$(^2D)5d\ ^3F_4 - (^2P)4f\ ^3D_3$
5		1344.320	74 387.03	.73	$5s5p^5\ ^3P_1 - (^2P)6p\ ^3D_2$
6		1342.928	74 464.17	.50	$(^4S)5d\ ^5D_2 - (^2P)6p\ ^3P_2$
11		1342.534	74 486.02	.33	$5s5p^5\ ^3P_1 - (^2P)6p\ ^3P_0$
9		1341.518	74 542.43	.53	$(^4S)5d\ ^5D_1 - (^2D)4f\ ^3D_2$
5		1338.153	74 729.85	30.67	$(^2D)5d\ ^3F_4 - (^2P)4f\ ^1G_4$
4		1337.652	74 757.88	.88	$(^4S)5d\ ^5D_2 - (^2D)4f\ ^3F_3$
11		1333.145	75 010.60	.76	$(^2D)5d\ ^3G_3 - (^2P)4f\ ^3D_2$
3		1330.927	75 135.60	6.05	$(^4S)5d\ ^5D_2 - (^2D)4f\ ^3D_2$
1		1327.475	75 331.01	.50	$(^4S)5d\ ^3D_1 - (^2P)4f\ ^3F_2$
2		1325.014	75 470.91	1.65	$5s5p^5\ ^3P_2 - (^4S)4f\ ^3F_2$
6		1320.689	75 718.03	.61	$(^4S)5d\ ^5D_0 - (^2D)4f\ ^3P_2$
2		1316.873	75 937.45	.63	$(^4S)5d\ ^3D_1 - (^4S)5f\ ^5F_2$
8		1316.442	75 962.30	.66	$(^4S)5d\ ^5D_1 - (^2D)4f\ ^3P_2$
1		1314.390	76 080.92	.99	$(^4S)5d\ ^3D_3 - (^4S)5f\ ^5F_4$
10		1314.088	76 098.41	.57	$(^4S)5d\ ^5D_0 - (^2D)4f\ ^3D_1$
4	u	1309.881	76 342.84	.62	$(^4S)5d\ ^5D_1 - (^2D)4f\ ^3D_1$
10		1309.818	76 346.46	.95	$5s^25p^4\ ^1S_0 - (^4S)5d\ ^5D_1$
2		1309.656	76 355.92	6.24	$(^4S)5d\ ^3D_3 - (^4S)5f\ ^5F_3$

Table I. *Continued*

Intensity[1]		λ (Å)	σ (cm⁻¹) obs	σ (cm⁻¹) calc	Classification
9		1306.260	76 554.46	5.25	$(^2D)5d\ ^3G_3 - (^2P)4f\ ^1G_4$
4		1305.721	76 586.02	.27	$(^2D)5d\ ^3F_4 - (^2P)4f\ ^3F_4$
0		1305.475	76 600.49	.73	$(^2D)5d\ ^3G_4 - (^2P)4f\ ^3D_3$
2		1303.385	76 723.29	.71	$(^4S)5d\ ^3D_3 - (^2P)4f\ ^3G_3$
2		1299.234	76 968.45	.69	$5s5p^5\ ^3P_2 - (^2P)6p\ ^3D_1$
7		1294.672	77 239.62	40.14	$(^2D)5d\ ^3F_3 - (^2P)4f\ ^3D_2$
6		1294.477	77 251.26	.56	$(^4S)5d\ ^5D_1 - (^2D)4f\ ^3P_1$
4		1292.427	77 373.82	4.17	$(^4S)5d\ ^5D_1 - (^2D)4f\ ^1D_2$
11		1281.633	78 025.43	.49	$5s5p^5\ ^3P_1 - (^2D)4f\ ^3F_2$
2		1278.311	78 228.25	.22	$(^2D)5d\ ^1P_1 - (^2P)4f\ ^3F_2$
3		1277.742	78 263.07	.10	$(^2D)5d\ ^3F_3 - (^2P)4f\ ^3D_3$
10		1272.819	78 565.77	.94	$5s5p^5\ ^3P_1 - (^2P)6p\ ^3S_1$
2		1269.293	78 784.02	.63	$(^2D)5d\ ^3F_3 - (^2P)4f\ ^1G_4$
7		1267.171	78 915.95	6.13	$(^4S)5d\ ^3D_2 - (^2P)4f\ ^3F_3$
10		1253.650	79 767.06	6.86	$5s5p^5\ ^3P_2 - (^2P)6p\ ^3P_1$
0		1251.484	79 905.14	4.74	$5s5p^5\ ^3P_1 - (^2D)4f\ ^1P_1$
7		1249.319	80 043.61	.61	$5s5p^5\ ^3P_2 - (^2D)4f\ ^3G_3$
3		1247.610	80 153.27	.43	$(^4S)5d\ ^5D_4 - (^2D)4f\ ^1G_4$
2		1244.235	80 370.66	.92	$(^4S)5d\ ^3D_2 - (^4S)5f\ ^5F_1$
10		1242.875	80 458.63	.76	$5s5p^5\ ^3P_0 - (^2D)4f\ ^3D_1$
1		1238.955	80 713.18	.21	$(^4S)5d\ ^3D_2 - (^2P)4f\ ^3G_3$
2	u	1237.316	80 820.08	19.80	$(^4S)5d\ ^5D_3 - (^2D)4f\ ^1G_4$
12	u	1232.070	81 164.24	3.74	$5s^25p^4\ ^1D_2 - 5s5p^5\ ^3P_2$
0.5		1228.991	81 367.53	.70	$5s5p^5\ ^3P_0 - (^2D)4f\ ^3P_1$
2		1227.943	81 437.00	.16	$(^4S)5d\ ^3D_1 - (^2P)4f\ ^3D_2$
12		1205.929	82 923.60	.08	$5s^25p^4\ ^1S_0 - (^2D)5d\ ^1P_1$
2		1202.593	83 153.65	.29	$(^4S)5d\ ^3D_3 - (^2P)4f\ ^3D_3$
4		1200.033	83 331.02	.23	$5s5p^5\ ^3P_2 - (^2D)4f\ ^3F_2$
11		1198.683	83 424.86	.22	$5s5p^5\ ^3P_1 - (^2D)4f\ ^3D_2$
2		1195.107	83 674.55	.82	$(^4S)5d\ ^3D_3 - (^2P)4f\ ^1G_4$
11		1188.853	84 114.69	.54	$5s5p^5\ ^3P_2 - (^2D)4f\ ^3D_3$
1		1186.249	84 299.35	.83	$(^4S)5d\ ^5D_2 - (^2P)4f\ ^3F_3$
2		1185.767	84 333.60	.88	$(^2D)5d\ ^1P_1 - (^2P)4f\ ^3D_2$
1		1182.729	84 550.21	.80	$(^4S)5d\ ^5D_3 - (^2P)4f\ ^3F_3$
4		1179.186	84 804.29	.35	$(^4S)5d\ ^5D_1 - (^2P)4f\ ^3F_2$
8		1178.630	84 844.30	.36	$5s5p^5\ ^3P_1 - (^2D)4f\ ^3P_2$
1		1177.617	84 917.28	.05	$(^4S)5d\ ^5D_0 - (^4S)5f\ ^5F_1$
2		1174.243	85 161.27	.10	$(^4S)5d\ ^5D_1 - (^4S)5f\ ^5F_1$
7		1173.857	85 189.24	8.89	$(^4S)5d\ ^5D_4 - (^4S)5f\ ^5F_5$
0.5		1173.370	85 224.64	.31	$5s5p^5\ ^3P_1 - (^2D)4f\ ^3D_1$
9		1173.146	85 240.89	.43	$(^4S)6s\ ^3S_1 - 5s^05p^6\ ^1S_0$
2		1170.988	85 397.97	.87	$(^4S)5d\ ^5D_2 - (^2P)4f\ ^3F_2$
2		1170.812	85 410.79	.48	$(^4S)5d\ ^5D_1 - (^4S)5f\ ^5F_2$
9		1166.789	85 705.29	.16	$(^4S)5d\ ^5D_3 - (^4S)5f\ ^5F_4$
8		1166.467	85 728.92	9.44	$(^4S)5d\ ^5D_2 - (^4S)5f\ ^5F_3$
0.5		1166.228	85 746.53	.63	$5s5p^5\ ^3P_2 - (^2P)6p\ ^1D_2$
1		1163.061	85 980.05	.41	$(^4S)5d\ ^5D_3 - (^4S)5f\ ^5F_3$
2		1160.992	86 133.25	.26	$5s5p^5\ ^3P_1 - (^2D)4f\ ^3P_1$
10		1158.329	86 331.26	.98	$5s5p^5\ ^3P_2 - (^2P)6p\ ^3D_3$
11		1156.475	86 469.69	.47	$5s^25p^4\ ^1D_2 - 5s5p^5\ ^3P_1$
7		1135.613	88 058.15	.41	$5s5p^5\ ^3P_2 - (^2P)6p\ ^3P_2$
0		1131.838	88 351.89	.79	$5s5p^5\ ^3P_2 - (^2D)4f\ ^3F_3$
12		1130.348	88 468.32	.11	$5s^25p^4\ ^3P_1 - 5s5p^5\ ^3P_2$
2		1127.018	88 729.74	.96	$5s5p^5\ ^3P_2 - (^2D)4f\ ^3D_2$
7		1124.428	88 934.09	.74	$(^4S)5d\ ^3D_1 - 5s^05p^6\ ^1S_0$
10		1109.257	90 150.46	.09	$5s5p^5\ ^3P_2 - (^2D)4f\ ^3P_2$
10		1092.168	91 561.03	.60	$5s5p^5\ ^3P_2 - (^2D)4f\ ^1D_2$
20		1088.954	91 831.25	.46	$(^2D)5d\ ^1P_1 - 5s^05p^6\ ^1S_0$
1		1077.844	92 777.81	.46	$(^4S)5d\ ^5D_3 - (^2P)4f\ ^3D_3$
18		1066.393	93 774.02	3.85	$5s^25p^4\ ^3P_1 - 5s5p^5\ ^3P_1$
1		1060.529	94 292.61	.18	$5s5p^5\ ^3P_1 - (^4S)5f\ ^5F_2$
9		1058.136	94 505.83	6.68	$5s^25p^4\ ^1D_2 - (^4S)5d\ ^5D_3$
11		1055.326	94 757.44	.65	$5s^25p^4\ ^1D_2 - (^4S)5d\ ^5D_2$
11		1048.755	95 351.18	.16	$5s^25p^4\ ^1D_2 - (^4S)5d\ ^5D_1$
15		1047.799	95 438.18	.12	$5s^25p^4\ ^3P_0 - 5s5p^5\ ^3P_1$
13		1017.682	98 262.53	.47	$5s^25p^4\ ^3P_2 - 5s5p^5\ ^3P_2$
2		1016.188	98 406.97	7.59	$(^4S)5d\ ^5D_1 - 5s^05p^6\ ^1S_0$
12		1014.825	98 539.15	.40	$5s^25p^4\ ^3P_1 - 5s5p^5\ ^3P_0$

Table I. *Continued*

Intensity[1]	λ (Å)	σ (cm⁻¹) obs	σ (cm⁻¹) calc	Classification
6	1002.087	99 791.73	.71	$5s5p^5\ ^3P_1 - (^2P)4f\ ^3D_2$
12	981.097	101 926.8	7.29	$5s^25p^4\ ^1D_2 - (^2D)5d\ ^1P_1$
(1)	979.980	102 043.	2.55	$5s^25p^4\ ^1S_0 - (^2D)6s\ ^3D_1$
12	974.133	102 655.4	.54	$5s^25p^4\ ^3P_1 - (^4S)5d\ ^5D_1$
15	971.818	102 899.9	.59	$5s^25p^4\ ^3P_1 - (^4S)5d\ ^5D_0$
10	965.548	103 568.2	.20	$5s^25p^4\ ^3P_2 - 5s5p^5\ ^3P_1$
(1)	960.325	104 131.	0.85	$5s^25p^4\ ^1D_2 - (^4S)5d\ ^3D_3$
10	958.591	104 319.8	.82	$5s^25p^4\ ^3P_0 - (^4S)5d\ ^5D_1$
11	953.983	104 823.7	4.02	$5s^25p^4\ ^1D_2 - (^4S)5d\ ^3D_1$
2	930.702	107 445.7	.72	$5s^25p^4\ ^3P_1 - (^4S)5d\ ^3D_2$
1	917.258	109 020.6	1.04	$5s^25p^4\ ^1D_2 - (^2D)5d\ ^3F_3$
10	915.487	109 231.5	.67	$5s^25p^4\ ^3P_1 - (^2D)5d\ ^1P_1$
13	901.745	110 896.1	5.95	$5s^25p^4\ ^3P_0 - (^2D)5d\ ^1P_1$
7	898.870	111 250.8	.42	$5s^25p^4\ ^1D_2 - (^2D)5d\ ^3G_3$
13	896.014	111 605.4	.41	$5s^25p^4\ ^3P_2 - (^4S)5d\ ^5D_3$
6	895.401	111 681.8	.58	$5s^25p^4\ ^3P_1 - (^4S)6s\ ^5S_2$
13	894.003	111 856.5	.38	$5s^25p^4\ ^3P_2 - (^4S)5d\ ^5D_2$
11	891.835	112 128.4	.39	$5s^25p^4\ ^3P_1 - (^4S)5d\ ^3D_1$
13	889.284	112 450.0	49.90	$5s^25p^4\ ^3P_2 - (^4S)5d\ ^5D_1$
10	878.789	113 793.0	2.67	$5s^25p^4\ ^3P_0 - (^4S)5d\ ^3D_1$
2	870.342	114 897.4	6.97	$5s^25p^4\ ^3P_1 - (^2D)5d\ ^3F_2$
1	863.385	115 823.2	2.70	$5s^25p^4\ ^3P_1 - (^4S)6s\ ^3S_1$
6	861.064	116 135.4	.28	$5s^25p^4\ ^1D_2 - (^2D)5d\ ^3D_1$
13	852.947	117 240.6	.08	$5s^25p^4\ ^3P_2 - (^4S)5d\ ^3D_2$
2	851.152	117 487.8	6.98	$5s^25p^4\ ^3P_0 - (^4S)6s\ ^3S_1$
3	850.563	117 569.2	8.68	$5s^25p^4\ ^1D_2 - (^2D)6s\ ^3D_2$
11	840.151	119 026.2	.03	$5s^25p^4\ ^3P_2 - (^2D)5d\ ^1P_1$
0	838.441	119 269.0	8.74	$5s^25p^4\ ^1D_2 - (^2P)5d\ ^1D_2$
(1)	838.244	119 297.	.96	$5s^25p^4\ ^1S_0 - (^2P)5d\ ^3D_1$
(3)	826.132	121 046.	.76	$5s^25p^4\ ^1D_2 - (^2D)6s\ ^3D_1$
12	824.878	121 230.1	29.58	$5s^25p^4\ ^3P_2 - (^4S)5d\ ^3D_3$
15	823.202	121 476.9	5.94	$5s^25p^4\ ^3P_2 - (^4S)6s\ ^5S_2$
8	822.640	121 559.8	.47	$5s^25p^4\ ^1D_2 - (^2D)6s\ ^3D_3$
(4)	820.166	121 926.	2.75	$5s^25p^4\ ^3P_2 - (^4S)5d\ ^3D_1$
(2)	811.138	123 284.	5.23	$5s^25p^4\ ^1S_0 - (^2P)6s\ ^1P_1$
10	810.110	123 440.0	39.66	$5s^25p^4\ ^3P_1 - (^2D)5d\ ^3D_1$
(2)	808.860	123 631.	2.20	$5s^25p^4\ ^1D_2 - (^2P)5d\ ^3P_1$
11	801.978	124 691.6	.33	$5s^25p^4\ ^3P_2 - (^2D)5d\ ^3F_2$
2	800.835	124 869.6	73.06	$5s^25p^4\ ^3P_1 - (^2D)6s\ ^3D_2$
(0)	800.228	124 964.	5.53	$5s^25p^4\ ^1D_2 - (^2D)5d\ ^3D_2$
11	799.333	125 104.2	3.93	$5s^25p^4\ ^3P_0 - (^2D)5d\ ^3D_1$
11	796.067	125 617.5	.06	$5s^25p^4\ ^3P_2 - (^4S)6s\ ^3S_1$
9	793.968	125 949.6	.47	$5s^25p^4\ ^1D_2 - (^2D)6s\ ^1D_2$
0	793.282	126 058.5	7.51	$5s^25p^4\ ^1D_2 - (^2D)5d\ ^3D_3$
12	792.896	126 120.0	19.77	$5s^25p^4\ ^3P_2 - (^2D)5d\ ^3F_3$
4	790.056	126 573.2	.12	$5s^25p^4\ ^3P_1 - (^2P)5d\ ^1D_2$
(1)	784.785	127 423.	4.46	$5s^25p^4\ ^1S_0 - 5s5p^5\ ^1P_1$
8	780.027	128 200.6	1.40	$5s^25p^4\ ^1D_2 - (^2P)5d\ ^3F_2$
(4)	779.782	128 241.	2.18	$5s^25p^4\ ^1D_2 - (^2P)5d\ ^3F_3$
13	779.124	128 349.3	.15	$5s^25p^4\ ^3P_2 - (^2D)5d\ ^3G_3$
13	779.124	128 349.3	51.13	$5s^25p^4\ ^3P_1 - (^2D)6s\ ^3D_1$
8	769.140	130 015.3	.41	$5s^25p^4\ ^3P_0 - (^2D)6s\ ^3D_1$
2	765.442	130 643.5	.43	$5s^25p^4\ ^3P_1 - (^2P)5d\ ^3P_0$
(7)	765.120	130 698.	.68	$5s^25p^4\ ^1D_2 - (^2D)5d\ ^3S_1$
9	763.729	130 936.5	.57	$5s^25p^4\ ^3P_1 - (^2P)5d\ ^3P_1$
(5)	761.790	131 270.	1.40	$5s^25p^4\ ^1D_2 - (^2D)5d\ ^3P_2$
1	761.532	131 314.2	.10	$5s^25p^4\ ^1D_2 - (^2D)5d\ ^1F_3$
6	756.031	132 269.7	.91	$5s^25p^4\ ^3P_1 - (^2D)5d\ ^3D_2$
(6)	754.144	132 601.	0.85	$5s^25p^4\ ^3P_0 - (^2P)5d\ ^3P_1$
5	750.451	133 253.2	.84	$5s^25p^4\ ^3P_1 - (^2D)6s\ ^1D_2$
4	750.160	133 305.0	.51	$5s^25p^4\ ^1D_2 - (^2P)5d\ ^3P_2$
2	744.142	134 382.9	3.70	$5s^25p^4\ ^1D_2 - (^2P)6s\ ^3P_1$
13	742.570	134 667.5	.42	$5s^25p^4\ ^3P_2 - (^2D)6s\ ^3D_2$
7	737.977	135 505.6	.77	$5s^25p^4\ ^3P_1 - (^2P)5d\ ^3F_2$
12	733.314	136 367.3	.48	$5s^25p^4\ ^3P_2 - (^2P)5d\ ^1D_2$
5	731.023	136 794.6	.47	$5s^25p^4\ ^1D_2 - (^2P)5d\ ^3D_2$
12	727.042	137 543.6	0.64	$5s^25p^4\ ^1D_2 - (^2D)5d\ ^3P_1$
(1)	724.623	138 003.	.06	$5s^25p^4\ ^3P_1 - (^2D)5d\ ^3S_1$

Table I. *Continued*

Intensity[1]	λ (Å)	σ (cm⁻¹) obs	σ (cm⁻¹) calc	Classification
(5)	723.873	138 146.	5.49	$5s^25p^4\ ^3P_2-(^2D)6s\ ^3D_1$
(−1)	723.055	138 302.	.17	$5s^25p^4\ ^1D_2-(^2P)5d\ ^3D_1$
(2d)	721.630	138 575.	.77	$5s^25p^4\ ^3P_1-(^2D)5d\ ^3P_2$
13	721.199	138 658.1	.20	$5s^25p^4\ ^3P_2-(^2D)6s\ ^3D_3$
12	719.694	138 947.9	9.42	$5s^25p^4\ ^1S_0-(^2P)5d\ ^1P_1$
2	717.911	139 293.0	.94	$5s^25p^4\ ^1D_2-(^2P)5d\ ^3D_3$
(2)	715.986	139 668.	7.33	$5s^25p^4\ ^3P_0-(^2D)5d\ ^3S_1$
(4)	711.190	140 609.	.88	$5s^25p^4\ ^3P_1-(^2P)5d\ ^3P_2$
4	710.680	140 710.3	.95	$5s^25p^4\ ^3P_1-(^2P)6s\ ^3P_0$
4	710.575	140 731.1	0.93	$5s^25p^4\ ^3P_2-(^2P)5d\ ^3P_1$
2	705.777	141 687.8	8.07	$5s^25p^4\ ^3P_1-(^2P)6s\ ^3P_1$
12	705.095	141 824.9	9.37	$5s^25p^4\ ^1D_2-(^2P)6s\ ^3P_2$
3	703.906	142 064.5	.27	$5s^25p^4\ ^3P_2-(^2D)5d\ ^3D_2$
10	702.795	142 289.0	.44	$5s^25p^4\ ^1D_2-(^2P)6s\ ^1P_1$
5	699.069	143 047.5	8.20	$5s^25p^4\ ^3P_2-(^2D)6s\ ^1D_2$
12	698.550	143 153.7	6.24	$5s^25p^4\ ^3P_2-(^2D)5d\ ^3D_3$
7	697.584	143 352.0	.35	$5s^25p^4\ ^3P_0-(^2P)6s\ ^3P_1$
10	693.971	144 098.3	.84	$5s^25p^4\ ^3P_1-(^2P)5d\ ^3D_2$
8	691.036	144 710.3	1.25	$5s^25p^4\ ^1D_2-(^2D)5d\ ^1D_2$
12	690.400	144 843.7	5.01	$5s^25p^4\ ^3P_1-(^2D)5d\ ^3P_1$
1	688.239	145.298.3	300.13	$5s^25p^4\ ^3P_2-(^2P)5d\ ^3F_2$
10	688.044	145 339.6	40.91	$5s^25p^4\ ^3P_2-(^2P)5d\ ^3F_3$
(5)	686.792	145 604.	6.55	$5s^25p^4\ ^3P_1-(^2P)5d\ ^3D_1$
10	685.599	145 857.9	8.76	$5s^25p^4\ ^1D_2-(^2P)5d\ ^1F_3$
13	682.926	146 428.7	.67	$5s^25p^4\ ^1D_2-5s5p^5\ ^1P_1$
12	682.563	146 506.6	9.29	$5s^25p^4\ ^3P_0-(^2D)5d\ ^3P_1$
6	679.022	147 270.7	.82	$5s^25p^4\ ^3P_0-(^2P)5d\ ^3D_1$
9	676.602	147 797.4	.41	$5s^25p^4\ ^3P_2-(^2D)5d\ ^3S_1$
9	673.991	148 369.9	70.13	$5s^25p^4\ ^3P_2-(^2D)5d\ ^3P_2$
7	673.798	148 412.5	.84	$5s^25p^4\ ^3P_2-(^2D)5d\ ^1F_3$
(1)	670.550	149 132.	3.74	$5s^25p^4\ ^3P_1-(^2P)6s\ ^3P_2$
1	668.476	149 593.9	.82	$5s^25p^4\ ^3P_1-(^2P)6s\ ^1P_1$
8	664.878	150 403.5	4.24	$5s^25p^4\ ^3P_2-(^2P)5d\ ^3P_2$
2	662.516	150 939.8	.41	$5s^25p^4\ ^3P_1-(^2D)5d\ ^3P_0$
1	661.125	151 257.4	8.09	$5s^25p^4\ ^3P_0-(^2P)6s\ ^1P_1$
1	660.133	151 484.6	2.43	$5s^25p^4\ ^3P_2-(^2P)6s\ ^3P_1$
0	657.831	152 014.8	5.62	$5s^25p^4\ ^3P_1-(^2D)5d\ ^1D_2$
12	650.479	153 732.9	3.04	$5s^25p^4\ ^3P_1-5s5p^5\ ^1P_1$
10	646.667	154 639.2	.37	$5s^25p^4\ ^3P_2-(^2D)5d\ ^3P_1$
8	639.419	156 392.0	.68	$5s^25p^4\ ^3P_2-(^2P)5d\ ^3D_3$
(1)	633.089	157 956.	3.63	$5s^25p^4\ ^1D_2-(^2P)5d\ ^1P_1$
7	629.216	158 927.9	8.10	$5s^25p^4\ ^3P_2-(^2P)6s\ ^3P_2$
1	627.403	159 387.1	8.18	$5s^25p^4\ ^3P_2-(^2P)6s\ ^1P_1$
(0)	611.511	163 529.	7.40	$5s^25p^4\ ^3P_2-5s5p^5\ ^1P_1$
(1)	590.707	169 289.	5.30	$5s^25p^4\ ^1D_2-(^4S)6d\ ^3D_3$

Table I. *Continued*

Intensity[1]	λ (Å)	σ (cm⁻¹) obs	σ (cm⁻¹) calc	Classification
(3)	574.738	173 992.	1.88	$5s^25p^4\ ^3P_1-(^4S)7s\ ^3S_1$
(5)	570.365	175 326.	.54	$5s^25p^4\ ^3P_1-(^4S)6d\ ^3D_2$
(1)	569.292	175 657.	6.16	$5s^25p^4\ ^3P_0-(^4S)7s\ ^3S_1$
(3)	565.620	176 797.	4.79	$5s^25p^4\ ^3P_1-(^4S)6d\ ^3D_1$
(5)	560.355	178.458.	9.06	$5s^25p^4\ ^3P_0-(^4S)6d\ ^3D_1$
(0)	559.256	178 809.	8.31	$5s^25p^4\ ^1D_2-(^2D)7s\ ^3D_1$
(0)	559.030	178 881.	78.94	$5s^25p^4\ ^1D_2-(^2D)6d\ ^3F_2$
(−1)	549.447	182 001.	5.39	$5s^25p^4\ ^1D_2-(^2D)6d\ ^3S_1$
(4)	548.444	182 334.	7.88	$5s^25p^4\ ^3P_2-(^4S)6d\ ^5D_2$
(−1)	548.021	182 475.	82.74	$5s^25p^4\ ^3P_2-(^4S)7s\ ^5S_2$
(−1)	548.021	182 475.	64.48	$5s^25p^4\ ^3P_2-(^4S)6d\ ^5D_3$
(0)	547.790	182 552.	1.32	$5s^25p^4\ ^3P_2-(^4S)6d\ ^5D_1$
(5)	544.108	183 787.	6.24	$5s^25p^4\ ^3P_2-(^4S)7s\ ^3S_1$
(4)	540.190	185 120.	.90	$5s^25p^4\ ^3P_2-(^4S)6d\ ^3D_2$
(1)	538.490	185 704.	7.17	$5s^25p^4\ ^1D_2-(^2D)6d\ ^1P_1$
(0)	537.287	186 120.	12.68	$5s^25p^4\ ^3P_1-(^2D)7s\ ^3D_1$
(−1)	537.106	186 183.	.31	$5s^25p^4\ ^3P_1-(^2D)6d\ ^3F_2$
(3)	536.844	186 274.	7.31	$5s^25p^4\ ^1D_2-(^2D)6d\ ^1D_2$
(5)	536.524	186 385.	4.04	$5s^25p^4\ ^3P_2-(^4S)6d\ ^3D_3$
(4)	535.476	186 750.	46.62	$5s^25p^4\ ^1D_2-(^2D)6d\ ^1F_3$
(−2)	534.537	187 078.	82.27	$5s^25p^4\ ^3P_1-(^2D)6d\ ^3D_1$
(−1) a	533.910	187 297.	6.50	$5s^25p^4\ ^3P_1-(^2D)6d\ ^1S_0$
(2)	529.955	188 695.	7.62	$5s^25p^4\ ^3P_1-(^2D)6d\ ^3P_2$
(−1)	529.826	188 741.	6.54	$5s^25p^4\ ^3P_0-(^2D)6d\ ^3D_1$
(1)	528.235	189 310.	09.76	$5s^25p^4\ ^3P_1-(^2D)6d\ ^3S_1$
(2)	524.258	190 746.	5.35	$5s^25p^4\ ^3P_1-(^2D)7s\ ^1D_2$
(−1)	523.644	190 969.	74.04	$5s^25p^4\ ^3P_0-(^2D)6d\ ^3S_1$
(0)	521.315	191 823.	4.12	$5s^25p^4\ ^3P_1-(^2D)6d\ ^3P_0$
(1)	520.194	192 236.	41.32	$5s^25p^4\ ^3P_1-(^2D)6d\ ^3P_1$
(−2)	516.578	193 582.	1.68	$5s^25p^4\ ^3P_1-(^2D)6d\ ^1D_2$
(1)	510.252	195 982.	77.67	$5s^25p^4\ ^3P_2-(^2D)6d\ ^3F_2$
(1)	509.519	196 264.	1.50	$5s^25p^4\ ^3P_2-(^2D)6d\ ^3G_3$
(2)	508.625	196 608.	.91	$5s^25p^4\ ^3P_2-(^2D)6d\ ^3F_3$
(−2)	507.960	196 866.	76.63	$5s^25p^4\ ^3P_2-(^2D)6d\ ^3D_1$
(−1)	503.802	198 491.	.98	$5s^25p^4\ ^3P_2-(^2D)6d\ ^3P_2$
(0)	499.923	200 031.	3.45	$5s^25p^4\ ^3P_2-(^2D)7s\ ^3D_3$
(2)	498.378	200 651.	0.23	$5s^25p^4\ ^3P_2-(^2D)6d\ ^3D_3$
(−2)	497.457	201 022.	4.94	$5s^25p^4\ ^3P_1-(^2P)6d\ ^3D_1$
(2)	496.260	201 507.	12.20	$5s^25p^4\ ^3P_2-(^2D)6d\ ^3D_2$
(0)	493.092	202 802.	5.90	$5s^25p^4\ ^3P_2-(^2D)6d\ ^1P_1$
(−2)	490.579	203 841.	5.36	$5s^25p^4\ ^3P_2-(^2D)6d\ ^1F_3$

[1] Meaning of the letters in the column "Intensity": a = affected, b = blend, h = hazy (diffuse), H = very hazy, u = unsymmetric and w = wide.

Table II. *Even levels of Xe III. All levels are given in LS notation. The numbers in parentheses indicate the purities (in %) of the states*

Designation		E (cm^{-1})
$5s^25p^4$	$^3P_2$	0.00 (86)
	$^3P_1$	9 794.36 (98)
	$^3P_0$	8 130.08 (79)
	$^1D_2$	17 098.73 (86)
	$^1S_0$	36 102.94 (78)
$5s^25p^3(^4S)6p$	$^5P_3$	149 061.57 (84)
	$^5P_2$	146 962.42 (66)
	$^5P_1$	146 781.48 (73)
	$^3P_2$	152 057.72 (64)
	$^3P_1$	150 301.10 (57)
	$^3P_0$	152 808.17 (89)
$(^2D)6p$	$^3F_4$	166 554.82 (82)
	$^3F_3$	162 594.81 (56)
	$^3F_2$	160 691.30 (54)
	$^3D_3$	166 699.11 (66)
	$^3D_2$	162 259.97 (47)
	$^3D_1$	158 996.98 (38)
	$^3P_2$	167 066.32 (55)
	$^3P_1$	168 086.00 (62)
	$^3P_0$	165 941.69 (84)
	$^1F_3$	164 438.64 (49)
	$^1D_2$	171 989.82 (70)
	$^1P_1$	164 511.65 (41)
$(^2P)6p$	$^3D_3$	184 594.45 (57)
	$^3D_2$	177 955.93 (59)
	$^3D_1$	175 231.15 (66)
	$^3P_2$	186 320.88 (27)
	$^3P_1$	178 029.33 (59)
	$^3P_0$	178 054.53 (83)
	$^3S_1$	182 134.14 (58)
	$^1D_2$	184 009.10 (44)
	$^1P_1$	185 888.03 (37)
	$^1S_0$	190 491.16 (67)
$5s^25p^3(^4S)4f$	$^5F_5$	166 743.80 (84)
	$^5F_4$	166 355.27 (64)
	$^5F_3$	166 374.06 (74)
	$^5F_2$	166 880.09 (81)
	$^5F_1$	167 173.54 (87)
	$^3F_4$	173 946.53 (65)
	$^3F_3$	170 250.15 (42)
	$^3F_2$	173 734.12 (77)
$(^2D)4f$	$^3H_6$	186 086.52 (100)
	$^3H_5$	181 356.80 (36)
	$^3H_4$	181 684.94 (56)
	$^3G_5$	184 114.53 (81)
	$^3G_4$	178 887.17 (58)
	$^3G_3$	178 306.08 (51)
	$^3F_4$	185 406.74 (42)
	$^3F_3$	186 614.26 (67)
	$^3F_2$	181 593.70 (41)
	$^3D_3$	182 377.01 (42)
	$^3D_2$	186 992.43 (25)
	$^3D_1$	188 792.52 (92)
	$^3P_2$	188 412.56 (38)
	$^3P_1$	189 701.46 (79)
	$^3P_0$	
	$^1H_5$	186 022.92 (62)
	$^1G_4$	192 425.21 (76)
	$^1F_3$	189 778.94 (55)
	$^1D_2$	189 824.07 (50)
	$^1P_1$	183 472.95 (70)
$(^2P)4f$	$^3G_3$	197 953.29 (29)
	$^3F_4$	206 760.00 (30)
	$^3F_3$	196 156.21 (51)
	$^3F_2$	197 254.25 (43)
	$^3D_3$	204 382.87 (43)
	$^3D_2$	203 359.91 (51)
	$^3D_1$	
	$^1G_4$	204 904.40 (34)
$5s^25p^3(^4S)5f$	$^5F_5$	197 460.67 (89)
	$^5F_4$	197 310.57 (74)
	$^5F_3$	197 585.82 (56)
	$^5F_2$	197 860.38 (68)
	$^5F_1$	197 611.00 (90)
$5s^05p^6$	$^1S_0$	210 857.49 (56)

Table III. *Odd levels of Xe III. All levels are given in LS notation. The numbers in parentheses indicate the purities (in %) of the states*

Designation		E (cm^{-1})	
$5s5p^5$	$^3P_2$	98 262.47 (75)	
	$^3P_1$	103 568.20 (62)	
	$^3P_0$	108 333.76 (55)	
	$^1P_1$	163 527.40 (27)	
		n = 6	n = 7
$5s^25p^3(^4S)ns$	$^5S_2$	121 475.94 (87)	182 482.74 (45)
	$^3S_1$	125 617.06 (78)	183 786.24 (84)
$(^2D)ns$	$^3D_3$	138 658.20 (83)	200 033.45 (99)
	$^2D_2$	134 667.42 (33)	196 140.93 (38)
	$^3D_1$	138 145.49 (49)	195 907.04 (57)
	$^1D_2$	143 048.20 (54)	200 539.71 (64)
$(^2P)ns$	$^3P_2$	158 928.10 (53)	
	$^3P_1$	151 482.43 (46)	
	$^3P_0$	150 505.31 (87)	
	$^1P_1$	159 388.18 (32)	
		n = 5	n = 6
$5s^25p^3(^4S)nd$	$^5D_4$	112 271.78 (88)	182 716.33 (85)
	$^5D_3$	111 605.41 (80)	182 464.48 (79)
	$^5D_2$	111 856.38 (78)	182 337.88 (42)
	$^5D_1$	112 449.90 (87)	182 551.32 (85)
	$^5D_0$	112 693.95 (69)	182 521.94 (86)
	$^3D_3$	121 229.58 (37)	186 384.04 (71)
	$^3D_2$	117 240.08 (27)	185 120.90 (62)
	$^3D_1$	121 922.75 (51)	186 589.15 (76)
$(^2D)nd$	$^3G_5$	132 159.94 (100)	200 471.83 (100)
	$^3G_4$	127 782.14 (40)	200 050.60 (43)
	$^3G_3$	128 349.15 (66)	196 261.50 (58)

Table III. *Continued*

Designation		E (cm^{-1})	
	$^1G_4$	132 711.78 (73)	196 538.07 (31)
	$^3F_4$	130 173.73 (71)	200 425.68 (82)
	$^3F_3$	126 119.77 (58)	196 608.91 (43)
	$^3F_2$	124 691.33 (52)	195 977.67 (47)
	$^1F_3$	148 412.84 (42)	203 845.36 (71)
	$^3D_3$	143 156.24 (38)	200 650.23 (64)
	$^3D_2$	142 064.27 (24)	201 512.20 (44)
	$^3D_1$	133 234.01 (36)	196 876.63 (45)
	$^1D_2$	161 809.98 (39)	203 376.04 (54)
	$^3P_2$	148 370.13 (39)	198 491.98 (22)
	$^3P_1$	154 639.37 (20)	202 035.68 (46)
	$^3P_0$	160 733.77 (43)	201 618.48 (62)
	$^1P_1$	119 026.03 (44)	202 805.90 (37)
	$^3S_1$	147 797.41 (49)	199 104.12 (45)
	$^1S_0$		197 090.86 (58)
$(^2P)nd$	$^3F_4$	148 535.52 (70)	
	$^3F_3$	145 340.91 (56)	
	$^3F_2$	145 300.13 (50)	
	$^1F_3$	162 957.50 (40)	
	$^3D_3$	156 392.68 (33)	
	$^3D_2$	153 893.20 (28)	
	$^3D_1$	155 400.90 (45)	
	$^1D_2$	136 367.48 (15)	
	$^3P_2$	150 404.24 (54)	
	$^3P_1$	140 730.93 (44)	
	$^3P_0$	140 437.79 (42)	
	$^1P_1$	175 052.36 (64)	

Table IV. *Comparison between observed and calculated energy-level values (in cm^{-1}) and calculated percentage compositions for the $5s^25p^4 + 5s^25p^3(6p + 4f + 5f) + 5s^05p^6 + (5s5p^45d)$[a] configurations of Xe III. Eigenvector components larger than 5% are given. Observed [3] and calculated g_J factors are listed*

J	E(obs)	E(calc)	obs − calc	g_J(obs)	g_J(calc)	Percentage composition
6	186 087	185 871	215		1.167	100 $(^2D)4f^3H$
5	166 744	166 592	152		1.37	84 $(^4S)4f^5F$ + 11 $(^2P)4f^3G$
	181 357	181 345	12		1.11	36 $(^2D)4f^3H$ + 22 $(^2D)4f^1H$ + 17 $(^2P)4f^3G$ + 15 $(^2D)4f^3G$ + 9 $(^4S)4f^5F$
	184 115	184 477	−363		1.18	81 $(^2D)4f^3G$ + 13 $(^2D)4f^3H$
	186 023	186 324	−301		1.01	62 $(^2D)4f^1H$ + 38 $(^2D)4f^3H$
	197 461	197 583	−123		1.38	89 $(^4S)5f^5F$ + 7 $(^2P)5f^3G$
4	166 355	166 084	271		1.30	64 $(^4S)4f^5F$ + 17 $(^2D)6p^3F$ + 7 $(^2P)4f^3F$ + 5 $(^2P)4f^3G$
	166 555	166 999	−444		1.26	82 $(^2D)6p^3F$ + 13 $(^4S)4f^5F$
	173 947	174 182	−235		1.21	65 $(^4S)4f^3F$ + 9 $(^2D)4f^3F$ + 8 $(^4S)4f^5F$ + 6 $(^2D)4f^3H$ + 6 $(^2P)4f^1G$
	178 887	179 265	−378		1.11	58 $(^2D)4f^3G$ + 9 $(^4S)4f^5F$ + 6 $(^2P)4f^3G$ + 6 $(^2P)4f^1G$ + 6 $(^4S)4f^3F$ + 6 $(^2P)4f^3F$ + 5 $(^2D)4f^3F$
	181 685	181 834	−149		0.96	56 $(^2D)4f^3H$ + 23 $(^2D)4f^3F$ + 8 $(^2P)4f^3G$
	185 407	185 544	−137		1.14	42 $(^2D)4f^3F$ + 20 $(^2D)4f^3H$ + 16 $(^2D)4f^3G$ + 12 $(^4S)4f^3F$
	192 425	192 122	303		1.03	76 $(^2D)4f^1G$ + 6 $(^2D)4f^3G$ + 5 $(^2D)4f^3F$
	197 311	197 619	−309		1.31	74 $(^4S)5f^5F$ + 8 $(^2P)4f^3G$
	204 904	205 178	−273		1.06	34 $(^2P)4f^1G$ + 17 $(^2P)4f^3G$ + 10 $(^2D)4f^3H$ + 9 $(^2P)4f^3F$ + 7 $(^4S)5f^3F$ + 7 $(^4S)4f^1F$
	206 760	206 576	184		1.07	30 $(^2P)4f^1F$ + 30 $(^2P)4f^1G$ + 10 $(^2D)4f^1G$ + 9 $(^2D)4f^3G$ + 7 $(^2P)4f^3G$ + 5 $(^2D)4f^3F$
3	149 062	148 836	225	1.57	1.61	84 $(^4S)6p^5P$ + 12 $(^2P)6p^3D$
	162 595	162 680	−85		1.16	56 $(^2D)6p^3F$ + 17 $(^2D)6p^1F$ + 14 $(^2P)6p^3D$ + 10 $(^4S)6p^5P$
	164 439	164 862	−424		1.13	49 $(^2D)6p^1F$ + 32 $(^2D)6p^3D$ + 16 $(^2D)6p^3F$
	166 374	166 433	−59		1.20	74 $(^4S)4f^5F$ + 7 $(^2P)4f^3F$
	166 699	166 812	−113		1.23	66 $(^2D)6p^3D$ + 21 $(^2D)6p^1F$ + 12 $(^2D)6p^3F$
	170 250	170 166	85		1.05	42 $(^4S)4f^3F$ + 12 $(^2D)4f^3F$ + 11 $(^2P)4f^1F$ + 10 $(^2D)4f^3G$ + 8 $(^4S)4f^5F$ + 5 $(^2P)4f^3D$ + 5 $(^2P)4f^3G$
	178 306	178 780	−474		0.89	51 $(^2D)4f^3G$ + 13 $(^4S)4f^3F$ + 12 $(^2P)4f^3G$ + 6 $(^4S)4f^5F$
	182 377	181 721	656		1 25	42 $(^2D)4f^3D$ + 12 $(^2P)4f^3D$ + 12 $(^4S)4f^3F$
	184 594	184 505	90		1.27	57 $(^2P)6p^3D$ + 9 $(^2D)6p^3F$ + 8 $(^2D)4f^3D$ + 7 $(^2D)6p^1F$
	186 614	186 511	103		1.10	67 $(^2D)4f^3F$ + 15 $(^4S)4f^3F$ + 7 $(^2P)4f^3F$ + 5 $(^2D)4f^3D$
	189 779	189 591	188		1.03	55 $(^2D)4f^1F$ + 18 $(^2P)4f^1F$ + 9 $(^2D)4f^3D$
	196 156	196 050	106		1.11	51 $(^2P)4f^3F$ + 17 $(^2P)4f^3D$ + 12 $(^2P)4f^1F$ + 6 $(^4S)5f^5F$
	197 586	197 457	129		0.96	56 $(^4S)5f^5F$ + 21 $(^2P)4f^3G$
	197 953	197 931	23		1.11	29 $(^2P)4f^3G$ + 25 $(^4S)5f^5F$ + 16 $(^2P)4f^1F$ + 12 $(^2D)4f^1F$ + 8 $(^2D)4f^3G$
	204 383	204 551	−168		1.22	43 $(^2P)4f^3D$ + 24 $(^2D)4f^3D$ + 14 $(^2P)4f^1F$ + 6 $(^2P)4f^3F$
2	0	−146	146		1.44	86 $p^4\ ^3P$ + 11 $p^4\ ^1D$
	17 099	17 246	−148		1.06	86 $p^4\ ^1D$ + 11 $p^4\ ^3P$
	146 962	146 789	173	1.70	1.67	66 $(^4S)6p^5P$ + 14 $(^4S)6p^3P$ + 7 $(^2P)6p^3P$ + 6 $(^2P)6p^3D$
	152 058	151 885	173	1.50	1.48	64 $(^4S)6p^3P$ + 19 $(^4S)6p^5P$ + 8 $(^2P)6p^1D$
	160 691	160 864	−173		0.95	54 $(^2D)6p^3F$ + 15 $(^2D)6p^3D$ + 10 $(^4S)6p^3P$ + 9 $(^2P)6p^3D$
	162 260	162 342	−82		1.18	47 $(^2D)6p^3D$ + 16 $(^2D)6p^3D$ + 10 $(^2P)6p^3P$ + 10 $(^2D)6p^3P$ + 6 $(^2P)6p^1D$ + 6 $(^4S)6p^5P$
	166 880	166 832	48		1.02	81 $(^4S)4f^5F$ + 7 $(^2P)4f^3D$
	167 066	167 057	9		1.36	55 $(^2D)6p^3P$ + 20 $(^2D)6p^3D$ + 10 $(^2D)6p^1D$ + 5 $(^2P)6p^3P$
	171 990	172 231	−242		1.10	70 $(^2D)6p^1D$ + 20 $(^2D)6p^3P$
	173 734	173 626	108		0.72	77 $(^4S)4f^3F$ + 6 $(^2P)4f^3F$ + 5 $(^2P)4f^1D$
	177 956	177 530	426		1.18	59 $(^2P)6p^3D$ + 19 $(^2P)6p^1D$ + 14 $(^2P)6p^3P$
	181 594	181 005	588		0.86	41 $(^2D)4f^3F$ + 15 $(^2D)4f^1D$ + 14 $(^2D)4f^3D$ + 7 $(^2P)4f^1D$ + 7 $(^2P)4f^3D$ + 6 $(^4S)4f^5F$
	184 009	183 888	121		1.00	44 $(^2P)6p^1D$ + 17 $(^2P)6p^3D$ + 14 $(^2D)6p^3F$ + 8 $(^2D)4f^3F$
	186 321	186 108	213		1.34	27 $(^2P)6p^3P$ + 27 $(^2D)4f^3P$ + 11 $(^2P)6p^1D$ + 7 $(^2D)6p^3D$
	186 992	187 118	−125		1.03	31 $(^2D)4f^3F$ + 25 $(^2D)4f^3D$ + 12 $(^2P)6p^3P$ + 10 $(^2D)4f^1D$ + 6 $(^2P)4f^3D$
	188 413	188 681	−268		1.28	38 $(^2D)4f^3P$ + 25 $(^2D)4f^3D$ + 12 $(^2P)6p^3P$ + 8 $(^2P)4f^3D$
	189 824	190 397	−573		1.10	50 $(^2D)4f^1D$ + 21 $(^2D)4f^3D$ + 7 $(^2D)4f^3P$
	197 254	197 145	109		0.81	43 $(^2P)4f^3F$ + 22 $(^4S)5f^5F$ + 17 $(^4S)5f^3F$ + 6 $(^2P)4f^3D$
	197 860	197 695	165		0.94	68 $(^4S)5f^5F$ + 11 $(^2P)4f^3F$ + 7 $(^4S)5f^3F$
	203 360	202 682	678		1.10	51 $(^2P)4f^3D$ + 16 $(^2D)4f^3P$ + 13 $(^4S)5f^3F$ + 7 $(^2D)4f^1D$
1	9 794	9 739	55		1.50	98 $p^4\ ^3P$
	146 781	146 609	173	2.28	2.19	73 $(^4S)6p^5P$ + 9 $(^4S)6p^3P$ + 6 $(^2P)6p^3P$
	150 301	150 097	204	1.59	1.55	57 $(^4S)6p^3P$ + 14 $(^4S)6p^5P$ + 10 $(^2P)6p^1P$ + 6 $(^2D)6p^3P$
	158 997	159 349	−352		1.01	38 $(^2D)6p^3D$ + 26 $(^2D)6p^1P$ + 12 $(^4S)6p^3P$ + 5 $(^4S)6p^5P$
	164 512	164 853	−341		0.97	41 $(^2D)6p^1P$ + 32 $(^2D)6p^3D$ + 8 $(^2P)6p^1S$ + 6 $(^2P)6p^3D$ + 6 $(^2D)6p^3P$ + 5 $(^4S)6p^3P$
	167 174	166 984	190		0.06	87 $(^4S)4f^5F$ + 10 $(^2P)4f^3D$
	168 086	168 301	−215		1.42	62 $(^2D)6p^3P$ + 12 $(^2D)6p^1P$ + 11 $(^4S)6p^3P$ + 5 $(^2P)6p^1S$
	175 231	175 094	137		0.66	66 $(^2P)6p^3D$ + 20 $(^2P)6p^1P$ + 6 $(^2D)6p^1P$
	178 029	177 703	327		1.40	59 $(^2P)6p^3P$ + 18 $(^2P)6p^1P$ + 12 $(^2P)6p^3S$ + 7 $(^2P)6p^3D$
	182 134	181 990	144		1.80	58 $(^2P)6p^3S$ + 17 $(^2D)6p^3P$ + 11 $(^2P)6p^3P$ + 7 $(^2D)6p^1P$

Table IV. *Continued*

J	E(obs)	E(calc)	obs − calc	g_J(obs)	g_J(calc)	Percentage composition
	183 473	183 352	121		0.91	70 $(^2D)4f\,^1P$ + 12 $(^2P)4f\,^3D$
	185 888	186 233	−345		0.99	37 $(^2P)6p\,^1P$ + 15 $(^2P)6p\,^3P$ + 14 $(^2D)6p\,^3D$ + 8 $(^2P)6p\,^3D$
	188 793	188 447	345		0.54	92 $(^2D)4f\,^3D$
	189 701	190 482	−780		1.37	79 $(^2D)4f\,^3P$ + 10 $(^2D)4f\,^1P$ + 5 $(^2P)4f\,^3D$
	197 611	197 587	24		0.05	90 $(^4S)5f\,^5F$ + 7 $(^2P)5f\,^3D$
0	8 130	8 271	−141			79 $p^4\,^3P$ + 19 $p^4\,^1S$
	36 103	36 012	91			78 $p^4\,^1S$ + 19 $p^4\,^3P$
	152 808	152 577	231			89 $(^4S)6p\,^3P$ + 6 $(^2P)6p\,^3P$
	165 942	166 239	−297			84 $(^2D)6p\,^3P$ + 13 $(^2P)6p\,^1S$
	178 055	177 654	400			83 $(^2P)6p\,^3P$ + 13 $(^2P)6p\,^1S$
	190 491	190 484	7			67 $(^2P)6p\,^1S$ + 15 $(^2D)6p\,^3P$ + 7 $(^4S)6p\,^3P$ + 6 $(^2P)6p\,^3P$ + 5 $(^2D)4f\,^3P$
		191 529				91 $(^2D)4f\,^3P$
	210 857	210 861	−3			56 $p^4\,^1S$ + 39 $(^1D)5d\,^1S$

[a] No levels of $5s5p^4 5d$ have been established experimentally but the configuration is included in the theoretical treatment of the even configurations (see Section 3.1).

Table V. *Energy parameters (in cm^{-1}) for the $5s^25p^4 + 5s^25p^3(6p + 4f + 5f) + 5s^05p^6 + 5s5p^45d$ configurations of Xe III. Mean error of the least-squares fit $\sigma = [\Sigma(E_{obs} - E_{calc})^2/(N - P)]^{1/2} = 331\,cm^{-1}$ with $N = 73$ known levels and $P = 22$ adjustable parameters*

Parameter	HF(E_{av})	Fitted	Fitted/HF
$5s^25p^4$			
E_{av}		16905 ± 160	
$F^2(5p, 5p)$	50596	43681 ± 1300	0.863 ± 0.026
ζ_{5p}	6626	7995 ± 300	1.207 ± 0.045
$5s^25p^36p$			
E_{av}		167407 ± 70	
$F^2(5p, 5p)$	52840	39889 ± 630	0.755 ± 0.012
$F^2(5p, 6p)$	12549	11964 ± 760	0.953 ± 0.061
$G^0(5p, 6p)$	2072	2007 ± 80	0.969 ± 0.039
$G^2(5p, 6p)$	2982	2443 ± 600	0.819 ± 0.200
ζ_{5p}	7301	8688 ± 150	1.190 ± 0.021
ζ_{6p}	939	1526 ± 120	1.625 ± 0.130
$5s^25p^34f$			
E_{av}		187817 ± 110	
$F^2(5p, 5p)$	51553	38033 ± 720	0.738 ± 0.014
$F^2(5p, 4f)$	29252	24040 ± 900	0.822 ± 0.031
$G^2(5p, 4f)$	22845	18859 ± 720	0.825 ± 0.032
$G^4(5p, 4f)$	15446	9950 ± 920	0.644 ± 0.060
ζ_{5p}	6920	8421 ± 190	1.217 ± 0.027
ζ_{4f}	48	0 ± 60	0.000 ± 1.250
$5s^25p^35f$			
E_{av}		216345 ± 180	
$F^2(5p, 5p)$	52207	41766 (fix)	0.800
$F^2(5p, 5f)$	12582	12582 (fix)	1.0
$G^2(5p, 5f)$	8811	8811 (fix)	1.0
$G^4(5p, 5f)$	6274	6274 (fix)	1.0
ζ_{5p}	7102	7102 (fix)	1.0
ζ_{5f}	33	33 (fix)	1.0
p^6			
E_{av}		251540 ± 590	
$5s5p^45d$			
E_{av}		263000 (fix)	
$F^2(5p, 5p)$	51463	41170 (fix)	0.800
$F^2(5p, 5d)$	36501	36501 (fix)	1.0
$G^1(5s, 5p)$	68320	68320 (fix)	1.0
$G^1(5s, 5d)$	26862	26862 (fix)	1.0
$G^1(5p, 5d)$	41701	41701 (fix)	1.0
$G^3(5p, 5d)$	25951	25951 (fix)	1.0
ζ_{5p}	6893	6893 (fix)	1.0
ζ_{5d}	381	381 (fix)	1.0
Configuration interaction integrals			
p^4–$6p$			
$R^2(5p5p, 5p6p)$	5419(.349)[a]	5419 (fix)	1.0
p^4 – $4f$			
$R^2(5p5p, 5p4f)$	−32918(−.940)	−32918 (fix)	1.0
p^4–$5f$			
$R^2(5p5p, 5p5f)$	−20304(−.911)	−20304 (fix)	1.0
p^4–$5d$			
$R^1(5s5p, 5p5d)$	51463(.998)	51463 (fix)	1.0
$R^2(5s5p, 5d5p)$	37121(.996)	37121 (fix)	1.0
p^4–p^6			
$R^1(5s5s, 5p5p)$	67375(1.000)	67375 (fix)	1.0
$6p$–$4f$			
$R^2(5p6p, 5p4f)$	3107(.197)	3107 (fix)	1.0
$R^2(5p6p, 4f5p)$	−2428(−.220)	−2428 (fix)	1.0
$6p$–$5f$			
$R^2(5p6p, 5p5f)$	−4503(−.530)	−4503 (fix)	1.0
$R^2(5p6p, 5f5p)$	2450(−.360)	2450 (fix)	1.0
$6p$–$5d$			
$R^1(5s6p, 5p5d)$	7831(.331)	7831 (fix)	1.0
$R^2(5s6p, 5d5p)$	−2443(−.199)	−2443 (fix)	1.0
$4f$–$5f$			
$R^2(5p4f, 5p5f)$	15068(.859)	8670 ± 5160	0.575 ± 0.340
$R^2(5p4f, 5f5p)$	13820(.896)	13159 ± 1584	0.952 ± 0.120
$R^4(5p4f, 5f5p)$	9594(.960)	9594 (fix)	1.0
$4f$–$5d$			
$R^1(5s4f, 5p5d)$	−37462(−.894)	−17636 (fix)	0.471
$R^2(5s4f, 5d5p)$	−24234(−.941)	−24234 (fix)	1.0
$5f$–$5d$			
$R^1(5s5f, 5p5d)$	−16823(−.720)	−7920 (fix)	0.471
$R^2(5s5f, 5d5p)$	−14589(−.910)	−14589 (fix)	1.0
$5d$–p^6			
$R^1(5s5d, 5p5p)$	50988(.998)	50988 (fix)	1.0

[a] The values in parentheses are a measure of the amount of cancellation which occurred in forming the integral. These numbers are the ratio of the true R^k value to an R^k value calculated using the absolute value of each wavefunction.

Table VI. *Comparison between observed and calculated energy-level values (in cm^{-1}) and calculated percentage compositions for the $5s5p^5 + 5s^25p^3(6s + 7s + 5d + 6d)$ configurations of Xe III. Eigenvector components larger than 5% are given. Observed [3] and calculated g_J factors are listed*

J	E(obs)	E(calc)	obs − calc	g_J(obs)	g_J(calc)	Percentage composition
5	132160	132443	−283		1.20	100 $(^2D)5d^3G$
	200472	200436	35		1.20	100 $(^2D)6d^3G$
4	112272	112250	21		1.47	88 $(^4S)5d^5D$ + 10 $(^2P)5d^3F$
	127782	127735	47		1.16	40 $(^2D)5d^3G$ + 27 $(^2D)5d^3F$ + 16 $(^2P)5d^3F$ + 9 $(^2D)5d^1G$ + 7 $(^4S)5d^5D$
	130174	130702	−528		1.20	71 $(^2D)5d^3F$ + 22 $(^2D)5d^3G$
	132712	132800	−88		1.02	73 $(^2D)5d^1G$ + 25 $(^2D)5d^3G$
	148536	148459	76		1.21	70 $(^2P)5d^3F$ + 13 $(^2D)5d^1G$ + 12 $(^2D)5d^3G$
	182716	182754	−37		1.46	85 $(^4S)6d^5D$ + 12 $(^2P)6d^3F$
	196538	196411	127		1.13	42 $(^2D)6d^3G$ + 31 $(^2D)6d^1G$ + 15 $(^2P)6d^3F$ + 10 $(^4S)6d^5D$
	200051	200074	−24		1.06	43 $(^2D)6d^3G$ + 42 $(^2D)6d^1G$ + 15 $(^2D)6d^3F$
	200426	200451	−25		1.21	82 $(^2D)6d^3F$ + 16 $(^2D)6d^1G$
3	111605	111401	204		1.44	80 $(^4S)5d^5D$ + 6 $(^2P)5d^3F$ + 6 $(^2P)5d^3D$
	121230	121363	−133		1.29	37 $(^4S)5d^3D$ + 25 $(^2D)5d^3D$ + 15 $(^4S)5d^5D$ + 6 $(^2D)5d^3G$ + 6 $(^2P)5d^3F$ + 5 $(^2D)5d^3F$
	126120	126121	−1		1.12	58 $(^2D)5d^3F$ + 11 $(^4S)5d^3D$ + 11 $(^2D)5d^3D$ + 10 $(^2P)5d^3F$ + 8 $(^2D)5d^3G$

Table VI. *Continued*

J	*E*(obs)	*E*(calc)	obs − calc	g_J(obs)	g_J(calc)	Percentage composition
	128 349	128 385	−35		0.87	66 $(^2D)5d^3G$ + 18 $(^2D)5d^3F$ + 7 $(^4S)5d^5D$
	138 658	139 048	−389	1.33	1.33	83 $(^2D)6s^3D$ + 8 $(^2D)5d^3D$
	143 156	143 110	46	1.22	1.22	38 $(^2D)5d^3D$ + 21 $(^4S)5d^3D$ + 12 $(^2P)5d^3F$ + 10 $(^2D)5d^3G$ + 7 $(^2P)5d^1F$ + 6 $(^2D)6s^3D$ +
	145 341	145 259	83		1.14	56 $(^2P)5d^3F$ + 11 $(^2P)5d^3D$ + 7 $(^2D)6s^3D$ + 6 $(^2D)5d^3F$ + 6 $(^2D)5d^3D$ + 5 $(^4S)5d^3D$
	148 413	148 691	−278		1.16	42 $(^2D)5d^1F$ + 31 $(^2P)5d^3D$ + 10 $(^4S)5d^3D$
	156 393	156 261	132		1.15	33 $(^2P)5d^3D$ + 32 $(^2P)5d^1F$ + 15 $(^2D)5d^1F$ + 6 $(^2D)5d^3F$ + 5 $(^2D)5d^3D$
	162 958	163 174	−216		1.04	40 $(^2P)5d^1F$ + 35 $(^2D)5d^1F$ + 7 $(^2P)5d^3D$ + 5 $(^4S)5d^3D$ + 5 $(^2D)6d^1F$
	182 464	182 430	34		1.44	79 $(^4S)6d^5D$ + 6 $(^2P)6d^3D$ + 6 $(^2P)6d^3F$
	186 384	186 311	74		1.28	71 $(^4S)6d^3D$ + 9 $(^2P)6d^1F$ + 6 $(^4S)6d^5D$
	196 262	196 304	−42		0.93	58 $(^2D)6d^3G$ + 11 $(^4S)6d^3D$ + 11 $(^2D)6d^3F$ + 8 $(^2P)6d^1F$ + 7 $(^2D)6d^3D$
	196 609	196 640	−31		1.13	43 $(^2D)6d^3F$ + 13 $(^2D)6d^3G$ + 11 $(^2D)6d^3D$ + 9 $(^2P)6d^3D$ + 9 $(^4S)6d^3D$ + 6 $(^2D)6d^1F$ + 6 $(^2P)6d^3F$
	200 033	200 054	−21		1.33	99 $(^2D)7s^3D$
	200 650	200 815	−165		1.25	64 $(^2D)6d^3D$ + 30 $(^2D)6d^3F$
	203 845	203 921	−76		1.04	71 $(^2D)6d^1F$ + 11 $(^2D)6d^3D$ + 5 $(^2D)6d^3G$
2	98 262	98 217	45		1.50	75 $p^5\,{}^3P$ + 16 $(^2D)5d^3P$ + 8 $(^2P)5d^3P$
	111 856	111 593	264		1.40	78 $(^4S)5d^5D$ + 6 $(^2P)5d^3D$
	117 240	117 130	110		1.09	27 $(^4S)5d^3D$ + 17 $(^2D)5d^3D$ + 16 $(^2D)5d^3F$ + 15 $(^4S)5d^5D$ + 12 $(^2P)5d^3D$ + 6 $(^2P)5d^3F$
	121 476	121 343	133	1.95	1.93	87 $(^4S)6s^5S$ + 10 $(^2P)6s^3P$
	124 691	124 721	−30		0.86	52 $(^2D)5d^3F$ + 18 $(^2D)5d^3D$ + 16 $(^4S)5d^3D$ + 11 $(^2P)5d^3F$
	134 667	134 767	−99	1.18	1.20	33 $(^2D)6s^3D$ + 20 $(^2D)6s^1D$ + 12 $(^2P)5d^1D$ + 11 $(^2P)6s^3P$ + 6 $(^4S)6s^3S$ + 6 $(^2D)5d^1D$
	136 367	136 137	231	0.90	1.08	22 $(^2D)6s^3D$ + 16 $(^2D)5d^3D$ + 15 $(^2P)5d^1D$ + 15 $(^2D)5d^1D$ + 10 $(^2P)5d^3F$ + 8 $(^2P)5d^3D$
	142 064	141 824	241	1.12	1.17	24 $(^2D)5d^3D$ + 22 $(^4S)5d^3D$ + 18 $(^2P)5d^3D$ + 11 $(^2D)6s^3D$ + 10 $(^2P)5d^1D$ + 6 $(^2P)6s^3P$
	143 048	143 109	−61	0.96	1.02	54 $(^2D)6s^1D$ + 19 $(^2D)6s^3D$ + 12 $(^2P)5d^3F$ + 5 $(^2P)5d^1D$
	145 300	145 112	188	0.81	0.85	50 $(^2P)5d^3F$ + 18 $(^2D)5d^3F$ + 13 $(^2P)5d^3P$ + 8 $(^2D)5d^1D$
	148 370	148 590	−220		1.37	39 $(^2D)5d^3P$ + 14 $p^5\,{}^3P$ + 10 $(^2P)5d^3P$ + 9 $(^2D)5d^3D$ + 6 $(^2P)5d^1D$ + 6 $(^2P)5d^3D$
	150 404	150 246	159		1.37	54 $(^2P)5d^3P$ + 12 $(^2D)5d^3P$ + 6 $(^2D)5d^1D$ + 5 $(^2P)6s^3P$
	153 893	153 614	279		1.22	28 $(^2P)5d^3D$ + 12 $(^2D)5d^1D$ + 11 $(^2D)5d^3P$ + 11 $(^2P)6s^3P$ + 10 $(^4S)5d^3D$ + 6 $(^2P)5d^1D$ + 6 $(^2D)5d^3D$
	158 928	159 117	−189		1.41	53 $(^2P)6s^3P$ + 18 $(^2D)5d^3P$ + 8 $(^2D)6s^3D$ + 8 $(^2D)6s^1D$
	161 810	162 283	−473		1.04	39 $(^2D)5d^1D$ + 20 $(^2P)5d^1D$ + 19 $(^2P)5d^3D$ + 7 $(^4S)5d^3D$
	182 338	182 357	−19		1.66	42 $(^4S)6d^5D$ + 41 $(^4S)7s^5S$ + 5 $(^2P)7s^3P$
	182 483	182 450	33		1.69	45 $(^4S)7s^5S$ + 38 $(^4S)6d^5D$ + 6 $(^2P)7s^3P$
	185 121	185 220	−99		1.16	62 $(^4S)6d^3D$ + 10 $(^2P)6d^1D$ + 6 $(^2D)6d^3D$ + 6 $(^4S)6d^3D$
	195 978	195 970	7		0.95	47 $(^2D)6d^3F$ + 11 $(^2D)7s^3D$ + 7 $(^4S)6d^3D$ + 7 $(^2D)6d^1D$
	196 141	196 103	38		1.16	38 $(^2D)7s^3D$ + 20 $(^2D)7s^1D$ + 13 $(^2D)6d^3F$ + 13 $(^2P)7s^3P$ + 7 $(^4S)7s^5S$
	198 492	198 506	−14		1.26	37 $(^2D)6d^3D$ + 22 $(^2D)6d^3P$ + 10 $(^4S)6d^3D$ + 9 $(^2P)6d^3P$
	200 540	200 520	20		1.06	64 $(^2D)7s^1D$ + 34 $(^2D)7s^3D$
	201 512	201 507	5		1.22	44 $(^2D)6d^3D$ + 30 $(^2D)6d^3P$ + 13 $(^2D)6d^1D$ + 6 $(^2D)6d^3F$
	203 376	203 194	183		1.13	54 $(^2D)6d^1D$ + 30 $(^2D)6d^3P$ + 7 $(^2D)6d^3F$
1	103 568	103 639	−71		1.45	62 $p^5\,{}^3P$ + 14$(^2D)5d^3P$ + 8 $(^2P)5d^3P$
	112 450	112 328	122		1.48	87 $(^4S)5d^5D$ + 6 $p^5\,{}^3P$
	119 026	118 935	91		1.01	44 $(^2D)5d^1P$ + 28 $p^5\,{}^1P$ + 7 $(^2P)5d^1P$ + 7 $p^5\,{}^3P$ + 6 $(^4S)5d^3D$
	121 923	122 282	−359		0.60	51 $(^4S)5d^3D$ + 31 $(^2D)5d^3D$ + 5 $(^2P)5d^3D$
	125 617	125 594	23	1.77	1.80	78 $(^4S)6s^3S$ + 7 $(^2P)6s^1P$
	133 234	133 412	−178	0.38	0.65	36 $(^2D)5d^3D$ + 25 $(^2D)6s^3D$ + 22 $(^2P)5d^3D$ + 6 $(^4S)6s^3S$
	138 145	138 128	17	0.50	0.70	49 $(^2D)6s^3D$ + 17 $(^2D)5d^3D$ + 9 $(^2P)5d^3D$ + 6 $(^2P)6s^1P$ + 6 $(^4S)6s^3S$ + 5 $(^4S)5d^3D$
	140 731	140 464	267		1.53	44 $(^2P)5d^3P$ + 19 $(^2D)5d^3S$ + 18 $(^2D)5d^3P$
	147 797	147 630	168		1.70	49 $(^2D)5d^3S$ + 20 $(^2P)6s^3P$ + 18 $(^2D)5d^3P$
	151 482	151 584	−102	1.47	1.46	46 $(^2P)6s^3P$ + 22 $(^2P)6s^1P$ + 15 $(^2D)5d^3S$ + 12 $(^2P)5d^3P$
	154 639	154 546	93		1.30	20 $(^2D)5d^3P$ + 18 $p^5\,{}^1P$ + 15 $(^2P)5d^3P$ + 13 $(^2P)6s^1P$ + 9 $(^2D)\ 5d^3S$ + 7 $p^5\,{}^3P$ + 7 $(^2D)5d^1P$
	155 401	155 333	68		0.64	45 $(^2P)5d^3D$ + 16 $(^4S)5d^3D$ + 12 $(^4P)5d^1P$ + 8 $(^2D)5d^3D$ + 6 $(^4S)6d^3D$
	159 388	159 126	262		1.20	32 $(^2P)6s^1P$ + 20 $(^2P)6s^3P$ + 14 $(^2D)5d^3P$ + 13 $(^2D)6s^3D$ + 6$p^5\,{}^3P$ + 6 $(^2P)5d^3P$
	163 527	163 844	−316		0.99	33 $(^2D)5d^1P$ + 27 $p^5\,{}^1P$ + 10 $(^2P)6s^1P$ + 7 $(^2P)5d^3D$ + 7 $(^2P)5d^3P$
	175 052	174 482	570		0.99	64 $(^2P)5d^1P$ + 8 $p^5\,{}^1P$ + 6 $(^2P)6d^1P$ + 5 $(^4S)5d^3D$
	182 551	182 496	55		1.45	85 $(^4S)6d^5D$ + 8 $(^2P)6d^3P$
	183 786	183 795	−9		1.84	84 $(^4S)7s^3S$ + 8 $(^2P)7s^1P$
	186 589	186 645	−56		0.60	76 $(^4S)6d^3D$ + 5 $(^2P)6d^3D$ + 5 $(^2P)6d^1P$
	195 907	195 948	−41		0.77	57 $(^2D)7s^3D$ + 11 $(^2D)6d^3D$ + 8 $(^4S)7s^3S$ + 7 $(^2P)7s^1P$
	196 877	196 881	−5		0.74	45 $(^2D)6d^3D$ + 18 $(^2D)7s^3D$ + 12 $(^2D)6d^1P$
	199 104	199 122	−18		1.58	45 $(^2D)6d^3S$ + 21 $(^2D)6d^3P$ + 10 $(^2P)6d^3P$ + 7 $(^2D)6d^1P$
	202 036	202 066	−31		1.16	46 $(^2D)6d^3P$ + 22 $(^2D)6d^1P$ + 22 $(^2D)6d^3D$
	202 806	202 589	217		1.45	38 $(^2D)6d^3S$ + 37 $(^2D)6d^1P$ + 16 $(^2D)6d^3P$
0	108 334	108 380	−46			55 $p^5\,{}^3P$ + 22 $(^4S)5d^5D$ + 12 $(^2D)5d^3P$ + 10 $(^2P)5d^3P$
	112 694	112 591	103			69 $(^4S)5d^5D$ + 20 $p^5\,{}^3P$ + 9 $(^2D)5d^3P$
		126 871				85 $(^2D)\ 5d^1S$ + 8 $(^2P)5d^3P$
	140 438	140 556	−118			42 $(^2P)5d^3P$ + 31 $(^2D)5d^3P$ + 12 $(^2D)5d^1S$ + 8 $(^2P)6s^3P$
	150 505	150 324	181			87 $(^2P)6s^3P$ + 10 $(^2P)5d^3P$
	160 734	160 743	−9			43 $(^2D)5d^3P$ + 28 $(^2P)5d^3P$ + 20 $p^5\,{}^3P$
	182 522	182 482	40			86 $(^4S)6d^5D$ + 11 $(^2P)6d^3P$
	197 091	197 024	67			58 $(^2D)6d^1S$ + 19 $(^2D)6d^3P$ + 15 $(^2P)6d^3P$ + 8 $(^4S)6d^5D$
	201 618	201 847	−228			62 $(^2D)6d^1P$ + 32 $(^2D)6d^1S$

Table VII. *Energy parameters (in cm^{-1}) for the $5s5p^5 + 5s^25p^3(5d + 6d + 6s + 7s)$ configurations of Xe III. Mean error of the least-squares fit $\sigma = [\Sigma (E_{obs} - E_{calc})^2/(N - P)]^{1/2} = 217\,cm^{-1}$ with $N = 83$ known levels and $P = 30$ adjustable parameters*

Parameter	HF(E_{av})	Fitted	Fitted/HF
p^5			
E_{av}		123 209 ± 430	
$G^1(5s, 5p)$	67 295	47 314 ± 950	0.703 ± 0.014
ζ_{5p}	6 605	7 760 ± 310	1.175 ± 0.047
$6s$			
E_{av}		140 786 ± 90	
$F^2(5p, 5p)$	52 231	41 089 ± 630	0.787 ± 0.012
$G^1(5p, 6s)$	4 544	3 795 ± 250	0.835 ± 0.055
ζ_{5p}	7 169	8 078 ± 190	1.127 ± 0.027
$7s$			
E_{av}		200 200 ± 160	
$F^2(5p, 5p)$	52 644	40 033 ± 1320	0.760 ± 0.025
$G^1(5p, 7s)$	1 376	1 072 ± 300	0.779 ± 0.220
ζ_{5p}	7 261	8 072 ± 490	1.112 ± 0.360
$5d$			
E_{av}		136 928 ± 130	
$F^2(5p, 5p)$	51 522	39 438 ± 440	0.765 ± 0.009
$F^2(5p, 5d)$	35 641	29 232 ± 440	0.820 ± 0.012
$G^1(5p, 5d)$	40 265	28 868 ± 570	0.717 ± 0.014
$G^3(5p, 5d)$	25 050	16 810 ± 560	0.671 ± 0.022
ζ_{5p}	6 933	8 308 ± 100	1.198 ± 0.014
ζ_{5d}	358	467 ± 60	1.304 ± 0.170
$6d$			
E_{av}		200 589 ± 140	
$F^2(5p, 5p)$	52 621	40 006 ± 630	0.760 ± 0.012
$F^2(5p, 6d)$	8 853	6 757 ± 820	0.763 ± 0.093
$G^1(5p, 6d)$	6 482	2 384 ± 580	0.368 ± 0.089
$G^3(5p, 6d)$	4 400	1 089 ± 710	0.248 ± 0.160
ζ_{5p}	7 239	8 456 ± 240	1.168 ± 0.033
ζ_{6d}	98	161 ± 52	1.643 ± 0.530
Configuration interaction integrals			
p^5–$6s$			
$R^1(5p5p, 5s6s)$	375(.014)[a]	375 (fix)	1.0
p^5–$7s$			
$R^1(5p5p, 5s7s)$	−318(−.021)	−318 (fix)	1.0
p^5–$5d$			
$R^1(5p5p, 5s5d)$	50 086(.998)	33 048 ± 300	0.660 ± 0.006
p^5–$6d$			
$R^1(5p5p, 5s6d)$	20 212(.919)	16 016 ± 1760	0.792 ± 0.087
$6s$–$7s$			
$R^1(5p6s, 7s5p)$	2 426(.370)	2 426 (fix)	1.0
$6s$–$5d$			
$R^2(5p6s, 5p5d)$	−9 991(−.507)	−9 991 (fix)	1.0
$R^1(5p6s, 5d5p)$	−2 966(−.141)	−2 966 (fix)	1.0
$6s$–$6d$			
$R^2(5p6s, 5p6d)$	3 214(.379)	3 214 (fix)	1.0
$R^1(5p6s, 6d5p)$	271(.031)	271 (fix)	1.0
$7s$–$5d$			
$R^2(5p7s, 5p5d)$	−4 994(−.453)	−4 994 (fix)	1.0
$R^1(5p7s, 5d5p)$	−2 042(−.167)	−2 042 (fix)	1.0
$7s$–$6d$			
$R^2(5p7s, 5p6d)$	−2 138(−.384)	−2 138 (fix)	1.0
$R^1(5p7s, 6d5p)$	−148(−.029)	−148 (fix)	1.0
$5d$–$6d$			
$R^2(5p5d, 5p6d)$	11 112(.756)	11 638 ± 1720	1.047 ± 0.160
$R^1(5p5d, 6d5p)$	15 402(.901)	14 647 ± 1150	0.951 ± 0.075
$R^3(5p5d, 6d5p)$	9 957(.943)	5 000 (fix)	0.502

[a] The values in parentheses are a measure of the amount of cancellation which occurred in forming the integral. These numbers are the ratio of the true R^k value to an R^k value calculated using the absolute value of each wavefunction.

Table VIII. *Comparison between xenon $N_{4,5}OO$ Auger spectrum and optical spectrum of Xe^{2+}. Optical data: Present work. Auger data: L. O. Werme, T. Bergmark and K. Siegbahn [22]*

Auger data			Optical data			Energy difference
				% $5s5p^5$		Optical-Auger
Line No.	Intensity	Energy eV	Classification	^1P	^3P	eV[a]
1, 3	15, 86	0	$5s^25p^4\ ^3P_2$			0.00
2, 6	43, 39	1.21	$^3P_1$			0.00
−, 5	−, 48	1.00	$^3P_0$			+0.01
4, 7	104, 97	2.12	$^1D_2$			0.00
8, 9	100, 73	4.49	$^1S_0$			0.00
13, 15	11, 7	12.17	$5s5p^5\ ^3P_2$	−	75	+0.01
14, −	10, −	12.85	$^3P_1$	5	62	−0.01
16, 18	62, 80	14.76	$(^2D)5d\ ^1P_1$	28	7	0.00
17, 19	3, 8	15.13	$(^4S)5d\ ^3D_1$	2	1	−0.01
20, 23	7, 11	17.44	$(^2P)5d\ ^3P_1$	2	−	+0.01
22, 25	41, 74	19.17	$(^2D)5d\ ^3P_1$	18	7	0.00
−, 26[b]	−, 31	19.73	$(^2P)6s\ ^1P_1$	1	6	+0.03
24, 27	90, 134	20.27	$5s5p^5\ ^1P_1$	27	2	0.00
26, 28	31, 25	21.70	$(^2P)5d\ ^1P_1$	8	1	0.00
29, 30	107, 133	26.13	$5s^05p^6\ ^1S_0$			+0.01

[a] 1 eV = 8065.545 cm^{-1}.
[b] Doubly classified.

Table IX. *Classification of Xe^{2+} laser lines. Data on laser lines are from Beck et al. [9]*

Laser data		Spontaneous data	
Wavelength	Comment[a]	Intensity	Classification
2477.18	Xe^{2+}?	0	$(^4S)5d\ ^5D_1$–$(^4S)6p\ ^3P_0$
2691.939			Xe IV[b]
3079.738			
3305.99	Xe^{2+}?		Xe IV[c]
3349.74	Xe^{3+}?	12	$(^2D)6s\ ^3D_2$–$(^2D)6p\ ^1P_1$
3454.248		16	$(^2D)6s\ ^1D_2$–$(^2D)6p\ ^1D_2$
3596.61		17	$(^2D)6s\ ^3D_1$–$(^2D)6p\ ^3P_0$
3669.21			Xe IV[b]
3745.71		18	$(^2P)5d\ ^3F_2$–$(^2D)6p\ ^1D_2$
3780.990		28	$(^4S)6s\ ^3S_1$–$(^4S)6p\ ^3P_2$
4050.05		22	$(^4S)6s\ ^3S_1$–$(^4S)6p\ ^3P_1$
4060.48		25	$(^2P)6s\ ^1P_1$–$(^2P)6p\ ^1D_2$
4214.01		24	$(^2D)5d\ ^3D_3$–$(^4S)4f\ ^5F_2$
4240.24		16	$(^2D)5d\ ^1F_3$–$(^2D)6p\ ^1D_2$
4272.59		17	$(^2D)5d\ ^3D_3$–$(^2D)6p\ ^3F_4$
4285.88		20	$(^2D)6s\ ^1D_2$–$(^4S)4f\ ^5F_3$
4413.14		8	$(^2P)5d\ ^3D_1$–$(^2P)6p\ ^3P_0$
4434.15		15	$(^2D)6s\ ^3D_1$–$(^2D)6p\ ^3F_2$
4673.68		18a	$(^2D)6s\ ^1D_2$–$(^2D)6p\ ^1F_3$
4683.54		20	$(^4S)6s\ ^3S_1$–$(^4S)6p\ ^3P_2$
4723.57		16	$(^4S)6s\ ^3S_1$–$(^4S)6p\ ^3P_1$
4748.95		18	$(^2P)5d\ ^1F_3$–$(^2P)6p\ ^1D_2$
4869.46		21	$(^2D)5d\ ^3D_2$–$(^2D)6p\ ^3F_3$
5238.93		16	$(^2D)5d\ ^3S_1$–$(^4S)4f\ ^5F_2$
5401.04		17	$(^2D)5d\ ^3P_2$–$(^4S)4f\ ^5F_2$
5524.42	Xe^{2+}?	8	$(^2P)5d\ ^3D_2$–$(^2D)6p\ ^1D_2$
6176.6			
6238.24		13	$(^2D)5d\ ^1F_3$–$(^2D)6p\ ^1F_3$
6343.5			
7148.94			
8571.6			

[a] ? Ionisation stage of laser line uncertain.
[b] Ref. [27].
[c] Ref. [13].

PHYSICAL REVIEW A VOLUME 43, NUMBER 11 1 JUNE 1991

$5s^25p^2(5d+6s)$ configurations in triply ionized xenon (Xe IV)

J. G. Reyna Almandos, F. Bredice, M. Gallardo, and C. J. B. Pagan*
Centro de Investigaciones Opticas, Casilla de Correo 124, 1900 La Plata, Argentina

H. O. Di Rocco
Departamento de Física, Facultad de Ciencias Exactas, Universidad Nacional del Centro de la Provincia de Buenos Aires, Pinto 399, 7000 Tandil, Argentina

A. G. Trigueiros*
Department of Physics, University of Lund, S-223 62 Lund, Sweden
(Received 4 September 1990)

The spectrum of triply ionized xenon (Xe IV) has been observed in the region 570–6900 Å. The configurations $5s^25p^25d$ and $5s^25p^26s$ have been studied and the energy levels reported for these configurations by Moore [*Atomic Energy Levels*, Natl. Bur. Stand. Ref. Data Ser., Natl. Bur. Stand. (U.S.) Circ. No. 467 (U.S. GPO, Washington, D.C., 1971)] were revised and extended to include seven new levels. The configuration $5s5p^4$ was included in the analysis to take into account the strong interaction between this configuration and $5s^25p^25d$. Configuration-interaction Rydberg series have been also included in the calculations. This investigation was supported by Hartree-Fock calculations.

INTRODUCTION

The triply ionized xenon atom is isoelectronic with neutral antimony. The ground-state configuration is $5s^25p^3$ and the lowest excited configuration is $5s5p^4$. The spectrum of Xe IV was studied by Boyce and Hymphreys and the results were published in *Atomic Energy Levels*[1] (AEL). Subsequently, Di Rocco *et al.*[2] published the results of the analysis of the ground-state configuration and the first excited-state configuration.

There is great interest in spectroscopy data from xenon due to applications in collision physics and laser physics. In the present investigation we have photographically recorded xenon spectra in the 240–6900-Å range. When analyzing the experimental data we have made use of Hartree-Fock calculations and parametric fits. Configuration-interaction (CI) effects, including Rydberg-series CI, have been included in the calculations. The present work concerns the study of the configurations $5s^25p^25d$ and $5s^25p^26s$.

EXPERIMENTAL METHODS

In the vacuum ultraviolet region we have used three different light sources: a direct-current hollow cathode discharge,[3] a θ-pinch discharge,[4] and a capillary pulsed discharge.[5] The first two light sources, built at the Lund Institute of Technology, Sweden, and a 3-m normal incidence spectrograph, built at Lund, were used to record the spectra. This spectrograph is equipped with a ruled grating having 1200 lines/mm. The plate factor in the first diffraction order is 2.77 Å/mm. The spectra were exposed on Kodak standing-wave radio plates, and lines from C, N, and O were used as internal standards.

The capillary pulsed discharge source was built at the Centro de Investigaciones Opticas, Argentina, and a 3-m normal incidence spectrograph (Hilger & Watts) was used to record the spectra. This spectrograph is equipped with a ruled grating having 1200 lines/mm. The plate factor in the first diffraction order is 2.77 Å/mm. Ilford Q-2 plates were used to record the spectra. Known lines of C, N, and O were used as internal standards.

In the 2500–6900-Å range the spectrum was obtained using two different laser-tube-like sources. One of them is 1 m in length and has a 3-mm inner diameter,[6] and the other is 20 cm long and has a 3-mm inner diameter.[7] Both tubes were viewed end on. To record the spectra, the 3.4 m Ebert plane-grating spectrograph at Centro de Investigaciones Opticas was used. The grating has 600 lines/mm, corresponding to a plate factor of 5 Å/mm in the first diffraction order. Kodak 103 a-O and Kodak 103 *a*-F plates were used to record the spectra in the first, second, the third diffraction orders.

The $5s^25p^3$-$5s^25p^25d$ and $5s^25p^3$-$5s^25p^26s$ combinations observed in the present work are listed in Table I. The wavelength values are estimated to be correct to ±0.01 Å and the intensities of the lines are based on visual estimates.

ANALYSIS

We present in Table II the values of the energy levels experimentally established in the present work. Seven of them are new and the rest correspond to undesignated levels from Boyce and Humphreys.[1] The levels were determined from combinations with levels of the ground-state configuration and also from combinations with higher-lying odd levels tentatively assigned to the

 ©1991 The American Physical Society

TABLE I. Classified $5s^25p^3$-$5s^25p^25d$, 6s lines in the Xe IV spectrum.

Intensity	λ_{vac} (Å)	σ (cm^{-1}) Obs.	Calc.[b]	Classification
0.5	558.65	179003.0	2.1	$^4S_{3/2}$-(^1D)5d $^2D_{5/2}$
−1[a]	577.295[a]	173221.7	2.0	$^4S_{3/2}$-(^3P)6s $^2P_{3/2}$
10	578.40	172890.7	2.4	$^4S_{3/2}$-(^1D)5d $^2P_{1/2}$
2	578.76	172783.2	2.3	$^2D_{3/2}$-(^1D)5d $^2D_{3/2}$
2	586.54	170491.4	0.0	$^4S_{3/2}$-(^1D)5d $^2P_{3/2}$
6	587.77	170134.6	2.6	$^4S_{3/2}$-(^3P)6s $^4P_{5/2}$
4	591.70	169004.6	1.8	$^4S_{3/2}$-(^3P)5d $^2D_{5/2}$
3	593.34	168537.4	8.2	$^2D_{5/2}$-(^1D)5d $^2D_{3/2}$
1	598.06	167207.3	6.9	$^4S_{3/2}$-(^3P)6s $^2P_{1/2}$
8	603.38	165733.0	4.1	$^2D_{3/2}$-(^1D)5d $^2D_{5/2}$
11	605.03	165281.1	0.5	$^4S_{3/2}$-(^3P)6s $^4P_{3/2}$
2	611.27	163593.8	6.2	$^4S_{3/2}$-(^3P)5d $^2D_{3/2}$
6[a]	619.238[a]	161488.8	90.0	$^2D_{5/2}$-(^1D)5d $^2D_{5/2}$
8	619.45	161433.5	4.1	$^4S_{3/2}$-(^3P)5d $^4P_{3/2}$
4	625.17	159956.5	4.0	$^2D_{3/2}$-(^3P)6s $^2P_{3/2}$
10	626.40	159642.4	3.1	$^4S_{3/2}$-(^3P)5d $^4P_{5/2}$
7	626.47	159624.6	4.4	$^2D_{3/2}$-(^1D)5d $^2P_{1/2}$
7	636.05	157220.3	2.0	$^2D_{3/2}$-(^1D)5d $^2P_{3/2}$
6	637.50	156862.7	4.6	$^2D_{3/2}$-(^3P)6s $^4P_{5/2}$
11	642.12	155734.1	3.8	$^2D_{3/2}$-(^3P)5d $^2D_{5/2}$
11	642.22	155709.9	9.9	$^2D_{5/2}$-(^3P)6s $^2P_{3/2}$
5	647.11	154533.2	2.0	$^4S_{3/2}$-(^3P)6s $^4P_{1/2}$
6	649.61	153938.5	8.9	$^2D_{3/2}$-(^3P)6s $^2P_{1/2}$
6	653.69	152977.7	7.9	$^2D_{5/2}$-(^1D)5d $^2P_{3/2}$
6	655.22	152620.5	0.5	$^2D_{5/2}$-(^3P)6s $^4P_{5/2}$
0.5	657.83	152015.0	2.5	$^2D_{3/2}$-(^3P)6s $^4P_{3/2}$
4	660.12	151487.6	9.7	$^2D_{5/2}$-(^3P)5d $^2D_{5/2}$
8	665.21	150328.5	8.2	$^2D_{3/2}$-(^3P)5d $^2D_{3/2}$
11	672.56	148685.6	5.2	$^4S_{3/2}$-(^3P)5d $^4D_{3/2}$
2[a]	674.919[a]	148165.9	6.1	$^2D_{3/2}$-(^3P)5d $^4P_{3/2}$
4	676.74	147767.2	8.4	$^2D_{5/2}$-(^3P)6s $^4P_{3/2}$
4	683.17	146376.5	5.1	$^2D_{3/2}$-(^3P)5d $^4P_{5/2}$
9	683.97	146205.2	6.4	$^4S_{3/2}$-(^3P)5d $^4D_{3/2}$
7	684.54	146083.5	4.1	$^4D_{5/2}$-(^3P)5d $^2D_{3/2}$
0.5	688.78	145184.2	6.0	$^2P_{1/2}$-(^3P)6s $^2P_{3/2}$
0[a]	689.147[a]	145106.9	5.7	$^4S_{3/2}$-(^3P)5d $^4D_{1/2}$
4	690.33	144858.3	6.4	$^2P_{1/2}$-(^1D)5d $^2P_{1/2}$
7	697.58	143352.7	1.7	$^2P_{3/2}$-(^1D)5d $^2D_{5/2}$
5	703.57	142132.3	1.0	$^2D_{5/2}$-(^3P)5d $^4P_{5/2}$
12	705.09	141825.9	4.4	$^4S_{3/2}$-(^1D)5d $^2F_{5/2}$
8	707.90	141262.9	4.0	$^2D_{3/2}$-(^3P)6s $^4P_{1/2}$
8	718.54	139171.1	0.9	$^2P_{1/2}$-(^3P)6s $^2P_{1/2}$
11	722.80	138350.9	1.8	$^2D_{5/2}$-(^3P)5d $^2F_{7/2}$
4[a]	728.634[a]	137243.1	4.5	$^2P_{1/2}$-(^3P)6s $^4P_{3/2}$
12	732.63	136494.5	5.7	$^4S_{3/2}$-(^3P)5d $^4F_{5/2}$
4	737.67	135562.0	0.2	$^2P_{1/2}$-(^3P)5d $^2D_{3/2}$
1	738.46	135416.9	7.2	$^2D_{3/2}$-(^3P)5d $^4D_{5/2}$
11	740.85	134980.1	0.6	$^4S_{3/2}$-(^3P)5d $^4F_{3/2}$

TABLE I. (*Continued*).

Intensity	λ_{vac} (Å)	σ (cm^{-1}) Obs.	Calc.[b]	Classification
0[a]	741.621[a]	134 839.8	39.6	$^2P_{3/2}$–$(^1D)5d\ ^2P_{3/2}$
4	749.64	133 397.4	8.1	$^2P_{1/2}$–$(^3P)5d\ ^4P_{3/2}$
5	751.73	133 026.5	7.1	$^4S_{3/2}$–$(^3P)5d\ ^2P_{3/2}$
3	752.23	132 938.1	8.4	$^2D_{3/2}$–$(^3P)5d\ ^4D_{3/2}$
8	758.51	131 837.4	7.7	$^2D_{3/2}$–$(^3P)5d\ ^4D_{1/2}$
2	762.35	131 173.3	3.1	$^2D_{5/2}$–$(^3P)5d\ ^4D_{5/2}$
3	777.04	128 693.5	4.3	$^2D_{5/2}$–$(^3P)5d\ ^4D_{3/2}$
6	777.88	128 554.5	6.4	$^2D_{3/2}$–$(^1D)5d\ ^2F_{5/2}$
6	781.58	127 946.0	5.8	$^2P_{3/2}$–$(^3P)5d\ ^2D_{3/2}$
11	784.32	127 499.0	9.2	$^2D_{5/2}$–$(^3P)5d\ ^4D_{7/2}$
11	805.71	124 114.1	3.0	$^2D_{5/2}$–$(^3P)5d\ ^4F_{7/2}$
2	811.50	123 228.6	7.7	$^2D_{3/2}$–$(^3P)5d\ ^4F_{5/2}$
2	821.60	121 713.7	2.6	$^2D_{3/2}$–$(^3P)5d\ ^4F_{3/2}$
7	835.01	119 759.0	9.1	$^2D_{3/2}$–$(^3P)5d\ ^2P_{3/2}$
6	840.44	118 985.3	3.6	$^2D_{5/2}$–$(^3P)5d\ ^4F_{5/2}$
0.5	846.23	118 171.2	0.4	$^2P_{1/2}$–$(^3P)5d\ ^4D_{3/2}$
10	851.29	117 468.8	8.5	$^2D_{5/2}$–$(^3P)5d\ ^4F_{3/2}$
6	854.19	117 070.0	69.7	$^2P_{1/2}$–$(^3P)5d\ ^4D_{1/2}$
6	865.68	115 516.1	5.0	$^2D_{5/2}$–$(^3P)5d\ ^2P_{3/2}$
8	904.51	110 557.1	6.0	$^2P_{3/2}$–$(^3P)5d\ ^4D_{3/2}$
4	952.47	104 990.2	1.1	$^2P_{1/2}$–$(^3P)5d\ ^2P_{3/2}$
11	1006.75	99 329.5	30.2	$^2P_{3/2}$–$(^3P)5d\ ^4F_{3/2}$
1[a]	1026.935[a]	97 377.1	6.7	$^2P_{3/2}$–$(^3P)5d\ ^2P_{3/2}$

[a]From an unpublished Xenon line list by Boyce, kindly put at our disposal by Humphreys (Ref. 11).
[b]From the level values given in Table II by means of the Ritz combination principle. Only that part which differs from the observed is given.

TABLE II. Energy levels of Xe IV.

Designation	Energy (cm^{-1})	Percentage composition[a]
$5s^25p^3\,^4S_{3/2}$	0.0	$86(5s^25p^3\,^4S)+11(5s^25p^3\,^2P)$
$5s^25p^3\,^2D_{3/2}$	13 268.0	$76(5s^25p^3\,^2D)+15(5s^25p^3\,^2P)+9(5s^25p^3\,^4S)$
$5s^25p^3\,^2D_{5/2}$	17 512.1	100
$5s^25p^3\,^2P_{1/2}$	28 036.0	100
$5s^25p^3\,^2P_{3/2}$	35 650.4	$74(5s^25p^3\,^2P)+21(5s^25p^3\,^2D)+5(5s^25p^3\,^4S)$
$5s5p^4\,^4P_{5/2}$	99 663.8	$85(5s5p^4\,^4P)+10[5s^25p^2(^3P)5d\ ^4P]$
$5s5p^4\,^4P_{3/2}$	106 923.3	$85(5s5p^4\,^4P)+11[5s^25p^2(^3P)5d\ ^4P]$
$5s5p^4\,^4P_{1/2}$	109 254.4	$83(5s5p^4\,^4P)+11[5s^25p^2(^3P)5d\ ^4P]+5(5s5p^4\,^2S)$
$5s5p^4\,^2D_{3/2}$	121 928.8	$61(5s5p^4\,^2D)+18[5s^25p^2(^1D)5d\ ^2D]+6[5s^25p^2(^3P)5d\ ^2P]$
$5s5p^4\,^2D_{5/2}$	125 474.9	$70(5s5p^4\,^2D)+21[5s^25p^2(^1D)5d\ ^2D]$
$5s^25p^2(^3P)5d\ ^2P_{3/2}$	133 027.1	$33[5s^25p^2(^3P)5d\ ^2P]+21[5s^25p^2(^3P)5d\ ^4F]$ $+12(5s5p^4\,^2P)+12(5s5p^4\,^2D)+11[5s^25p^2(^3P)5d\ ^4D]$
$5s^25p^2(^3P)5d\ ^4F_{3/2}$	134 980.6	$62[5s^25p^2(^3P)5d\ ^4F]+20[5s^25p^2(^3P)5d\ ^2P]+12(5s5p^4\,^2P)$
$5s^25p^2(^3P)5d\ ^4F_{5/2}$	136 495.7	$71[5s^25p^2(^3P)5d\ ^4F]+20[5s^25p^2(^3P)5d\ ^4D]$
$5s5p^4\,^2P_{1/2}$	136 795.8	$22(5s5p^4\,^2P)+36[5s^25p^2(^3P)5d\ ^2P]$ $+23(5s5p^4\,^2S)+8[5s^25p^2(^3P)5d\ ^4D]+8[5s^25p^2(^1D)5d\ ^2S]$

TABLE II. (*Continued*).

Designation	Energy (cm^{-1})	Percentage composition[a]
$5s^25p^2(^3P)5d\ ^4F_{7/2}$	141 625.1[b]	82[$5s^25p^2(^3P)5d\ ^4F$]+16[$5s^25p^2(^3P)5d\ ^4D$]
$5s^25p^2(^1D)5d\ ^2F_{5/2}$	141 824.4[b]	37[$5s^25p^2(^1D)5d\ ^2F$]+30[$5s^25p^2(^3P)5d\ ^2F$] +16[$5s^25p^2(^3P)5d\ ^4F$]+15[$5s^25p^2(^3P)5d\ ^4D$]
$5s^25p^2(^3P)5d\ ^4D_{7/2}$	145 011.3[b]	41[$5s^25p^2(^3P)5d\ ^4D$]+30[$5s^25p^2(^1D)5d\ ^2F$] +16[$5s^25p^2(^3P)5d\ ^2F$]+8[$5s^25p^2(^3P)5d\ ^4F$]
$5s^25p^2(^3P)5d\ ^4D_{1/2}$	145 105.7	62[$5s^25p^2(^3P)5d\ ^4D$]+24($5s5p^4\ ^2S$)+8[$5s^25p^2(^1D)5d\ ^2S$]
$5s^25p^2(^3P)5d\ ^4F_{9/2}$	145 991.6[b]	86[$5s^25p^2(^3P)5d\ ^4F$]+14[$5s^25p^2(^1D)5d\ ^2G$]
$5s^25p^2(^3P)5d\ ^4D_{3/2}$	146 206.4	83[$5s^25p^2(^3P)5d\ ^4D$]+8[$5s^25p^2(^3P)5d\ ^4F$]
$5s^25p^2(^3P)5d\ ^4D_{5/2}$	148 685.2	55[$5s^25p^2(^3P)5d\ ^4D$]+16[$5s^25p^2(^3P)5d\ ^2F$] +14[$5s^25p^2(^1D)5d\ ^2F$]+10[$5s^25p^2(^3P)5d\ ^4F$]
$5s5p^4\ ^2S_{1/2}$	150 737.4	24($5s5p^4\ ^2S$)+28[$5s^25p^2(^3P)5d\ ^4D$] +27[$5s^25p^2(^3P)5d\ ^2P$]+11($5s5p^4\ ^2P$)+7[$5s^25p^2(^1D)5d\ ^2S$]
$5s^25p^2(^3P)6s\ ^4P_{1/2}$	154 532.0	75[$5s^25p^2(^3P)6s\ ^4P$]+13[$5s^25p^2(^3P)6s\ ^2P$]+9[$5s^25p^2(^1S)6s\ ^2S$]
$5s^25p^2(^3P)5d\ ^2F_{7/2}$	155 863.9[b]	22[$5s^25p^2(^3P)5d\ ^2F$]+39[$5s^25p^2(^3P)5d\ ^4D$]+16[$5s^25p^2(^1D)5d\ ^2G$] +14[$5s^25p^2(^1D)5d\ ^2F$]+9[$5s^25p^2(^3P)5d\ ^4F$]
$5s^25p^2(^3P)5d\ ^4P_{5/2}$	159 643.1	78[$5s^25p^2(^3P)5d\ ^4P$]+5[$5s^25p^2(^3P)5d\ ^4D$]
$5s^25p^2(^3P)5d\ ^4P_{3/2}$	161 434.1	40[$5s^25p^2(^3P)5d\ ^4P$]+18[$5s^25p^2(^3P)5d\ ^2D$]+15[$5s^25p^2(^1D)5d\ ^2P$] +11[$5s^25p^2(^1S)5d\ ^2D$]+5($5s5p^4\ ^4P$)
$5s^25p^2(^3P)5d\ ^2D_{3/2}$	163 596.2	33[$5s^25p^2(^3P)5d\ ^2D$]+23[$5s^25p^2(^3P)5d\ ^4P$] +17[$5s^25p^2(^1S)5d\ ^2D$]+10($5s5p^4\ ^2P$)
$5s^25p^2(^3P)6s\ ^4P_{3/2}$	165 280.5	82[$5s^25p^2(^3P)6s\ ^4P$]+7[$5s^25^2(^1D)5d\ ^2P$]+7[$5s^25p^2(^3P)6s\ ^2P$]
$5s^25p^2(^3P)6s\ ^2P_{1/2}$	167 206.9	58[$5s^25p^2(^3P)6s\ ^2P$]+18[$5s^25p^2(^3P)6s\ ^4P$] +11[$5s^25p^2(^3P)5d\ ^4P$]+7[$5s^25p^2(^1D)5d\ ^2P$]
$5s^25p^2(^3P)5d\ ^2D_{5/2}$	169 001.8[b]	49[$5s^25p^2(^3P)5d\ ^2D$]+20[$5s^25p^2(^3P)6s\ ^4P$] +11[$5s^25p^2(^1D)6s\ ^2D$]+8[$5s^25p^2(^3P)5d\ ^2F$]
$5s^25p^2(^3P)6s\ ^4P_{5/2}$	170 132.6	49[$5s^25p^2(^3P)6s\ ^4P$]+17[$5s^25p^2(^3P)5d\ ^2D$] +15[$5s^25p^2(^1D)6s\ ^2D$]+7[$5s^25p^2(^1D)5d\ ^2D$]
$5s^25p^2(^1D)5d\ ^2P_{3/2}$	170 490.0	23[$5s^25p^2(^1D)5d\ ^2P$]+35($5s5p^4\ ^2P$)+12[$5s^25p^2(^3P)5d\ ^4P$] +9[$5s^25p^2(^1D)5d\ ^2D$]+9[$5s^25p^2(^3P)5d\ ^2P$]
$5s^25p^2(^1D)5d\ ^2P_{1/2}$	172 892.4[b]	59[$5s^25p^2(^1D)5d\ ^2P$]+14($5s5p^4\ ^2P$) +12[$5s^25p^2(^3P)5d\ ^4P$]+10[$5s^25p^2(^3P)6s\ ^2P$]
$5s^25p^2(^3P)6s\ ^2P_{3/2}$	173 222.0	58[$5s^25p^2(^3P)6s\ ^2P$]+29[$5s^25p^2(^1D)6s\ ^2D$]
$5s^25p^2(^1D)5d\ ^2D_{5/2}$	179 002.1	50[$5s^25p^2(^1D)5d\ ^2D$]+12($5s5p^4\ ^2D$)+9[$5s^25p^2(^3P)5d\ ^2F$] +8[$5s^25p^2(^1D)5d\ ^2F$]+7[$5s^25p^2(^3P)6s\ ^4P$]
$5s^25p^2(^1D)5d\ ^2D_{3/2}$	186 050.3	20[$5s^25p^2(^1D)5d\ ^2D$]+23[$5s^25p^2(^1D)6s\ ^2D$]+16[$5s^25p^2(^3P)5d\ ^2P$] +16[$5s^25p^2(^1D)5d\ ^2P$]+13($5s^25p^4\ ^2P$)+7($5s5p^4\ ^2D$)

[a]Percentages lower than 5% are omitted. The average *LS* purity of the $5s5p^4$, $5s^25p^2(5d+6s)$ is 58%.
[b]New level.

$5s^25p^26p$ configuration, except for the levels at 154 532, 170 132, 179 001, and 186 052 cm^{-1}, which were previously observed by Boyce and Humphreys,[1] where we mainly observed transitions with the ground-state configuration. The levels corresponding to the $5s^25p^26p$ configuration will be discussed elsewhere.

The energy-level values shown in Table II were determined in an iterative procedure that takes into account the wave numbers of the observed lines, weighted according to their estimated uncertainties. All level designations are in *LS* notation, and in the same table we present the percentage composition of the levels in *LS* coupling.

We confirm the energy levels of the $5s5p^4$ configuration previously classified by Di Rocco *et al.*,[2] except for the level at 134 980.1 cm^{-1}, which is now designated as $5s^25p^25d(^3P)^4F_{3/2}$ in accordance with the percentage composition of the level for *LS* coupling.

All levels presented in Table II are now classified through a least-squares fit of the observed levels. So we have classified 23 energy levels belonging to the $5s^25p^25d$ and $5s^25p^26s$ configurations.

THEORETICAL INTERPRETATION

Theoretical calculations were made at the Department of Physics, University of Lund, using a vax computer, model Vax/VMS version V5.2 from Digital Equipment Corporation.

Theoretical predictions of the energy levels of the configurations have been used in the analysis of the spectra. The predictions were obtained by diagonalizing the energy matrices with appropriate Hartree-Fock[8] (HF) values for the energy parameters. For this purpose the computer code developed by Cowan[9] was used.

In the initial phase of the analysis we did not take into account the interactions between the $5s5p^4$, $5s^25p^25s$, and $5s^25p^26s$ configurations. The results showed the necessity of considering configuration-interaction integrals. The $5s5p^4$-$5s^25p^26s$ configuration interaction can be neglected because its HF value is 543.0 cm^{-1}, but the $5s5p^4$-$5s^25p^25d$ interaction is very strong since its Hartree-Fock value for the interaction integral is 53 723.5 cm^{-1}. In spite of considering the interactions, the interpretation of the configuration-level structures using a least-squares fit was not good.

In order to obtain a better interpretation of the levels it was necessary to introduce the $5s^25p^26d$ configuration that forms a Rydberg series with the $5s^25p^25d$ configuration. The $5s5p^4$-$5s^25p^26d$ configuration interaction has a value of 21 420.0 cm^{-1}. On the other side, the $5s^25p^25d$-$5s^25p^26d$ Rydberg-series configuration interaction has, for one of the integrals, the Hartree-Fock value 16 500.0 cm^{-1}. Calculations considering the introduction of Rydberg-series configuration interactions in Xe III were made by Persson *et al.*[10] The results of the parametric calculations are present in Table III. In our case, all the experimental level values of the $5s^25p^26d$ configuration are unknown, and due to this, all parameters of this configuration were held fixed in the least-squares-fit calculations. All the configuration-interaction integrals were held fixed in the calculation at scaled Hartree-Fock values. The scaled Hartree-Fock factor is

TABLE III. Energy parameters (cm^{-1}) for the $5s5p^4$, $5s^25p^2(5d+6s+6d)$ configurations of Xe IV. V represents the value in column four divided by the value in column three.

Configuration	Parameter	HF value	Fitted value[a]	V
$5s5p^4$	E_{av}	116 163	137 902±274	1.187±0.002
	$F^2(5p,5p)$	53 058	44 580±2019	0.840±0.038
	ζ_{5p}	9 470	8 836±465	0.933±0.049
	$G^1(5s,5p)$	69 722	56 145±979	0.805±0.014
$5s^25p^25d$	E_{av}	141 182	158 033±136	1.119±0.001
	$F^2(5p,5p)$	53 339	34 832±1473	0.653±0.028
	ζ_{5p}	9 639	8 857±249	0.919±0.026
	ζ_{5d}	684	762±164	1.114±0.240
	$F^2(5p,5d)$	39 919	36 251±1039	0.908±0.026
	$G^1(5p,5d)$	45 262	31 365±414	0.693±0.009
	$G^3(5p,5d)$	28 429	25 941±1196	0.912±0.042
$5s^25p^26s$	E_{av}	158 554	175 432±335	1.106±0.002
	$F^2(5p,5p)$	53 878	44 941±3839	0.834±0.071
	ζ_{5p}	9 925	9 935±269	1.001±0.027
	$G^1(5p,6s)$	6 361	5 777±602	0.908±0.095
$5s^25p^26d$	E_{av}	235 367	276 902 (fix)	1.176
	$F^2(5p,5p)$	54 529	46 350 (fix)	0.850
	ζ_{5p}	10 137	9 630 (fix)	0.950
	ζ_{6d}	201	191 (fix)	0.950
	$F^2(5p,6d)$	11 566	9 831 (fix)	0.850
	$G^1(5p,6d)$	7 111	6 044 (fix)	0.850
	$G^3(5p,6d)$	5 058	4 299 (fix)	0.850
CI integrals				
$5s5p^4$-$5s^25p^25d$	$R^1(5p5p,5s5d)$	53 724	43341 (fix)	0.807
$5s5p^4$-$5s^25p^26s$	$R^1(5p5p,5s6s)$	543	462 (fix)	0.850
$5s5p^4$-$5s^25p^26d$	$R^1(5p5p,5s6d)$	21 420	18207 (fix)	0.850
$5s^25p^25d$-$5s^25p^26s$	$R^2(5p5d,5p6s)$	−12 211	−10 379 (fix)	0.850
$5s^25p^25d$-$5s^25p^26s$	$R^1(5p5d,5p6s)$	−4 221	−3 588 (fix)	0.850
$5s^25p^25d$-$5s^25p^26d$	$R^0(5p5d,5p6d)$	0	0 (fix)	
$5s^25p^25d$-$5s^25p^26d$	$R^2(5p5d,5p6d)$	11 451	9 733 (fix)	0.850
$5s^25p^25d$-$5s^25p^26d$	$R^1(5p5d,5p6d)$	16 500	14 025 (fix)	0.850
$5s^25p^25d$-$5s^25p^26d$	$R^3(5p5d,5p6d)$	10 846	9 219 (fix)	0.850
$5s^25p^26s$-$5s^25p^26d$	$R^2(5p6s,5p6d)$	5 688	4 835 (fix)	0.850
$5s^25p^26s$-$5s^25p^26d$	$R^1(5p6s,5p6d)$	780	663 (fix)	0.850

[a]The rms deviation of the fit is 325 cm^{-1} for 31 observed levels.

0.85 in all the integrals, except for $5s5p^4$-$5s^25p^25d$ where the value is 0.81. For the configurations $5s5p^4$ and $5s^25p^26s$ all parameters were let free. The standard deviation for the 31 observed levels is 325 cm^{-1}.

ACKNOWLEDGMENTS

We are grateful to Dr. W. Persson for the use of experimental facilities and discussions concerning the experiment. Support from Swedish Natural Science Research Council; Conselho Nacional de Desenvolvimento Científico e Tecnológico, Brazil; Fundação de Amparo a Pesquisa do Estado de São Paulo, Brazil; Comisión de Investigaciones Científicas de la Provincia de Buenos Aires, Argentina, where J.G.R.Al. and F.B. belong as Researchers; and Consejo Nacional de Investigaciones Científicas y Técnicas, Argentina, is gratefully acknowledged.

---

*Permanent address: Instituto de Física, DEQ-Plasma, Universidade Estadual de Campinas, Caixa Postal 6165, 13081 Campinas, São Paulo, Brazil.

[1]C. E. Moore, *Atomic Energy Levels*, Natl. Bur. Stand. Ref. Data Ser., Natl. Bur. Stand. (U.S.) Circ. No. 467 (U.S. GPO, Washington, D.C., 1971).

[2]H. O. Di Rocco, J. G. Reyna Almandos, M. Gallardo, and W. Persson, Phys. Rev. A 33, 2114 (1986).

[3]W. Persson and L. Minnhagen, Ark. Fys. **37**, 273 (1968).

[4]S. G. Pettersson, Phys. Scr. **26**, 296 (1982).

[5]M. Gallardo, F. Bredice, M. Raineri, and J. Reyna Almandos, Appl. Opt. **28**, 4513 (1989).

[6]J. G. Reyna Almandos, M. Gallardo, and M. Garavaglia, Opt. Pura Apl. **15**, 1 (1982).

[7]J. G. Reyna Almandos, F. Bredice, H. Di Rocco, and M. Gallardo, Opt. Pura Apl. **18**, 87 (1985).

[8]C. Froese Fischer, Can. J. Phys. **41**, 1895 (1963).

[9]R. D. Cowan, *The Theory of Atomic Structure and Spectra* (University of California Press, Berkeley, 1981).

[10]W. Persson, C.-G. Wahlström, G. Bertuccelli, H. O. Di Rocco, J. G. Reyna Almandos, and M. Gallardo, Phys. Scr. **38**, 347 (1988).

[11]C. J. Humphreys (private communication).

Physica Scripta. Vol. 45, 584–589, 1992.

Revised and Extended Analysis of Five Times Ionized Argon (Ar VI)

M. Raineri, F. Bredice, M. Gallardo and J. G. Reyna Almandos

Centro de Investigaciones Opticas, (CIOp), Casilla de Correo 124, 1900 La Plata, Argentina

C. J. B. Pagan

Instituto de Física "Gleb Wataghin", Universidade Estadual de Campinas (UNICAMP), C.P. 6165, 13081 Campinas, São Paulo, Brasil

and

A. G. Trigueiros*

Department of Physics, University of Lund, S-223 62 Lund, Sweden

Received September 20, 1991; accepted November 22, 1991

Abstract

The spectrum of five times ionized argon, (Ar VI), has been observed in the 280–2100 Å wavelength range. Eighty-seven lines have been identified as transitions between levels of the $3s^23p$, $3s3p^2$, $3s^23d$, $3p^3$, $3s3p3d$, $3s^24s$, $3s^24d$ and $3s3p4s$ configurations. For 33 of the lines the classification is new. Forty-one energy level values belonging to these configurations were analyzed and we propose 9 new energy level values for levels corresponding to odd parity configurations. The configurations are interpreted by fitting the theoretical energy expressions to the observed energy levels using least-squares techniques. The parameter values are compared with results from Hartree–Fock calculations.

1. Introduction

The ground-state configuration of five times ionized argon, (Ar^{5+}), is $3s^23p$ with the term ^2P. Ar VI belongs to the Al I isoelectronic sequence. Excited states either belong to simple one-electron configuration of the type $3s^2nl$ or to three-electron configurations such as $3s3p^2$, $3p^3$ and $3s3p(^{1,3}P)nl$ etc., giving both doublets and quartets.

The spectra of the first, second and third elements in this sequence are presented in Atomic Energy Levels (AEL), Ref. [1]. Subsequent to this tabulation, the Al I spectrum was investigated by Eriksson and Isberg [2]. Results about Si II were published by Shenstone [3] and the P III spectrum was studied by Magnusson and Zetterberg [4]. Early results on the spectra of S IV and Cl V have been published in AEL but later results of S IV were compiled by Martin *et al.*, see Ref. [5] and references therein. The first results about the spectrum of Ar VI in the vacuum ultraviolet were published by Phillips and Parker [6]. Fawcett *et al.* [7] studied the spectra of multiple ionized inert gases, including Ar, and Schönheit [8] made a similar study finding a large quantity of new lines. Lines corresponding to the spin-forbidden resonance multiplet $3s^23p^2P$–$3s3p^2{}^4P$ were reported by Ekberg and Svensson [9]. Using a Theta-Pinch light source Fawcet *et al.* [10] classified some lines of Ar VI. Using the beam-foil technique Livingston *et al.* [11] have studied the argon spectra from Ar V to Ar VIII and using the same technique Buchet–Poulizac *et al.* [12] have studied the argon spectra from Ar VI to Ar VIII. A few lines of Ar VI were classified in the work of De-Ye *et al.* [13].

Theoretical calculations for the Al I isoelectronic sequence were made by Fawcett [14]. Computed *ab-initio* transition probabilities and energy levels for Al I-like ions were made by Huang [15] and data about highly ionized copper and zinc, belonging to this sequence, were published by Sugar and Kaufman [16–17].

Recently, Träbert *et al.* [18–19] have studied the spectrum of argon and other ions in the vacuum ultraviolet. They searched for lines of Mg-, Al- and Si-like ions. Recoil ion spectroscopy was used by Lesteven–Vaïsse *et al.* [20] who have studied all argon spectra from Ar I to Ar IX. Some anomalies in resonance transitions in the Al I isoelectronic sequence were observed by Engström *et al.* [21] and a new work about energy levels and lifetimes of Ar VI was recently published by Pinnington *et al.* [22]. An extended analysis of spectra and term systems in Al-like Ca VIII to Ni XVI was published by Redfors and Litzén [23] and lifetimes of the $3s^24s\,^2S$ states for Al-like ions from S IV to Fe XIV were published by Thornbury *et al.* [24]. Transitions in spectra of highly ionized Kr and Mo belonging to the Al I isoelectronic sequence were recently reported by Jupén *et al.* [25]. In the present work we report a revised and extended analysis of Ar VI that includes 33 newly classified lines and 9 new energy level values.

Experiment

The light source used in the present work is a discharge tube built at the Centro de Invesitgaciones Opticas, (CIOp), to study highly ionized gases [26]. It is a 30 cm long Pyrex tube with an inner diameter of 3 mm. Gas excitation was produced by discharging a bank of low inductance capacitors varying between 2.5 and 100 nF and charged up to 19 kV through the tube. Light radiation emitted axially was analyzed using a 3 m normal incidence vacuum spectro-

* *Permanent address:* Instituto de Fisica "Gleb Wataghin", Universidade Estadual de Campinas (UNICAMP), C.P. 6165, 13081 Campinas, São Paulo, Brasil.

graph with a concave diffraction grating of 1200 lines/mm, blazed for 1200 Å. The plate factor in the first order is 2.77 Å/mm. Ilford Q-2 plates were used to record the spectra between 280–2100 Å. C III and N II [27], O III [28] and lines of Ar III–Ar V [27] were recorded as internal wavelength standards. Exposing the plates with 10^4 shots we were able to obtain good spectra of argon below 300 Å. The lines were observed in the first, second, and in some cases, third order of diffraction.

The gas pressure, the discharge voltage, and the capacitance were varied to distinguish between different stages of ionization. A well developed Ar VI spectrum was obtained with the following parameters: 120 mTorr, 18 kV and 20 nF. The positions of spectral lines on the plates were determined with a rotating prism photoelectric automatic Grant comparator whose precision is 1 μm. The uncertainty in determining the wavelength of unperturbed lines by this procedure is estimated to be ± 0.01 Å in the first diffraction order.

Analysis

The Ar VI lines observed in the present work are given in Table I, 33 of them being without previous classification. The intensities of the lines given in the table are based on visual estimates and the values given in the calculated column are deduced from the optimized level values. The optimized energy values derived from the observed lines are given in Table II and the general structure of the term system is shown in Fig. 1. The level values were determined in an iterative procedure where the wavenumbers of the observed lines are weighted according to their estimated uncertainties. Theoretical predictions of the structure of the configurations made at the Department of Physics, University of Lund, were also used in the analysis. The predictions were obtained by diagonalizing the energy matrices with appropriately scaled Hartree–Fock (HF) values for the energy parameters. The computer code developed by Cowan [29] was used. All levels designations in Table II are in *LS* notation, and in the same table we present the percentage composition of the levels.

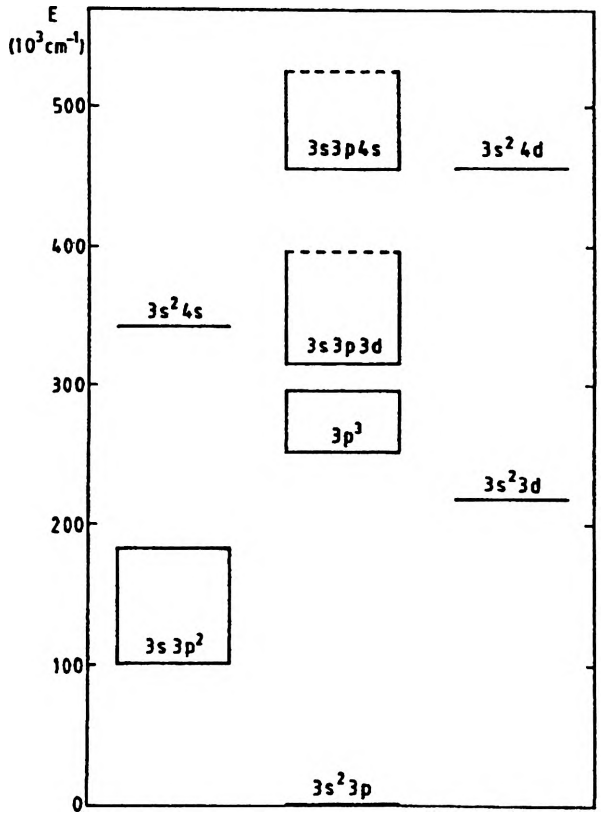


Fig. 1. Gross structure of the observed Ar VI configurations

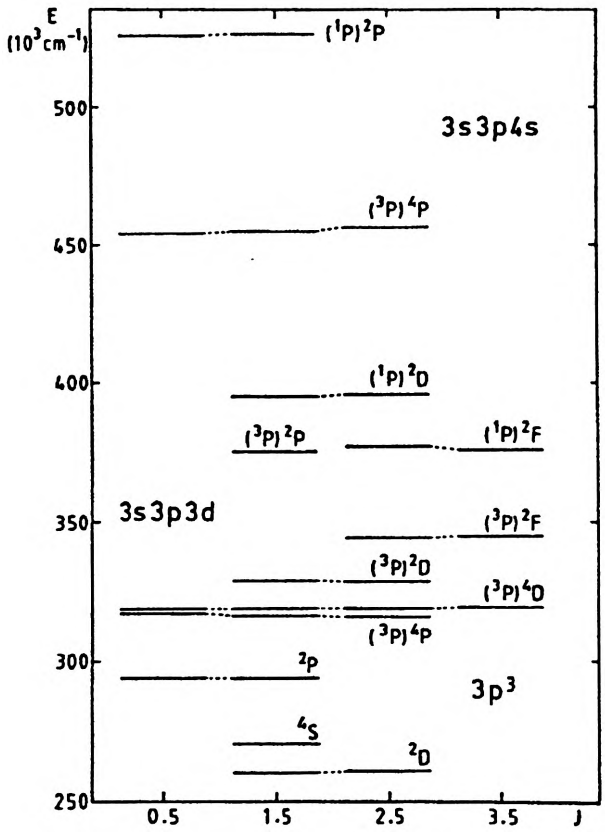


Fig. 2. Level structure of the observed $3p^3$, $3s3p3d$ and $3s3p4s$ configurations in Ar VI

A comparison with the level system given by Pinnington *et al.* [22] shows that six of their level values have been confirmed, although the accuracy has been considerably improved. However, for seven levels we propose new identifications as discussed below.

The observed structure of the configurations $3p^3$, $3s3p3d$ and $3s3p4s$ is shown in Fig. 2. For the level $3s3p(^3P)3d\,^2F_{5/2}$ we propose the new value 344 307.9 cm^{-1}. The level is established by five new lines that are given in Table I.

For the level $3s3p(^3P)3d\,^2F_{7/2}$ we propose the new value 346 073.4 cm^{-1} determined by two new lines, see Table I. Both level values fit well with the extrapolation that can be done from the isoelectronic data published in Ref. [23].

For the level $3s3p(^3P)3d\,^2P_{3/2}$ we propose the new value 375 657.6 cm^{-1}. This level is determined by four new lines, see Table I. The level value fits very well with the isoelectronic trend from Ref. [23]. The isoelectronic graph gives for the $3s3p(^3P)3d\,^2P_{1/2}$ level a probable value near 376 300 cm^{-1}. We were not able to find the transitions establishing this level, but according to the extrapolated values mentioned above and our theoretical predictions we reject the experimental value published in the work of Pinnington *et al.* [22] for this level.

Table I. *Classified lines in the Ar VI spectrum*

Int.	λ (Å)	σ (cm⁻¹) Observed	Calculated	Transition
4	219.91[c,d]	454 736.6	45.6	$3s^23p\,^2P_{1/2} - 3s^24d\,^2D_{3/2}$
6bl	220.93[c,d]	452 622.7	591.7	$3s^23p\,^2P_{3/2} - 3s^24d\,^2D_{5/2}$
1	281.43[c,d]	355 321.2	16.8	$3s3p^2\,^4P_{3/2} - 3s3p(^3P)4s\,^4P_{5/2}$
1	281.91[c,d]	354 723.8	14.3	$3s3p^2\,^4P_{1/2} - 3s3p(^3P)4s\,^4P_{3/2}$
2	282.42[c,d]	354 077.9	82.2	$3s3p^2\,^4P_{5/2} - 3s3p(^3P)4s\,^4P_{5/2}$
1	282.55[c,d]	353 917.7	7.7	$3s3p^2\,^4P_{3/2} - 3s3p(^3P)4s\,^4P_{3/2}$
1	283.16[c,d]	353 155.0	5.0	$3s3p^2\,^4P_{3/2} - 3s3p(^3P)4s\,^4P_{1/2}$
1	283.55[b]	352 676.0	83.1	$3s3p^2\,^4P_{5/2} - 3s3p(^3P)4s\,^4P_{3/2}$
2	294.03[c,d]	340 095.7	5.7	$3s^23p\,^2P_{3/2} - 3s^24s\,^2S_{1/2}$
2bl	326.15[c,e]	306 609.2	598.3	$3s^23d\,^2D_{3/2} - 3s3p(^1P)4s\,^2P_{3/2}$
4	326.22[c,e]	306 537.4	8.5	$3s^23d\,^2D_{5/2} - 3s3p(^1P)4s\,^2P_{3/2}$
4	326.32[c,e]	306 448.7	50.6	$3s^23d\,^2D_{3/2} - 3s3p(^1P)4s\,^2P_{1/2}$
6	409.10[a]	244 440.4	0.1	$3s3p^2\,^2D_{3/2} - 3s3p(^1P)3d\,^2F_{5/2}$
2	409.28[c,e]	244 328.9	7.4	$3s3p^2\,^2D_{3/2} - 3s3p(^1P)3d\,^2F_{5/2}$
6bl	410.10[c,e]	243 842.4	3.1	$3s3p^2\,^2D_{5/2} - 3s3p(^1P)3d\,^2F_{7/2}$
6A	455.83[c,d]	219 379.6	8.3	$3s3p^2\,^4P_{1/2} - 3s3p(^3P)3d\,^4D_{3/2}$
6	456.38[c,d]	219 113.5	3.8	$3s3p^2\,^4P_{1/2} - 3s3p(^3P)3d\,^4D_{1/2}$
8	457.01[c,d]	218 812.2	2.2	$3s3p^2\,^4P_{3/2} - 3s3p(^3P)3d\,^4D_{5/2}$
8bl	457.46[c,d]	218 598.3	3.0	$3s^23p\,^2P_{1/2} - 3s^23d\,^2D_{3/2}$
4bl	457.51[c,e]	218 574.5	81.7	$3s3p^2\,^4P_{3/2} - 3s3p(^3P)3d\,^4D_{3/2}$
8bl	458.05[c,d]	218 318.6	7.2	$3s3p^2\,^4P_{3/2} - 3s3p(^3P)3d\,^4D_{1/2}$
8w	459.32[c,d]	217 714.5	4.5	$3s3p^2\,^4P_{5/2} - 3s3p(^3P)3d\,^4D_{7/2}$
6	460.09[c,d]	217 346.0	7.1	$3s3p^2\,^4P_{5/2} - 3s3p(^3P)3d\,^4D_{3/2}$
6	460.19[c,d]	217 300.7	0.6	$3s3p^2\,^4P_{1/2} - 3s3p(^3P)3d\,^4P_{1/2}$
8w	461.23[c,d]	216 811.3	2.3	$3s3p^2\,^4P_{1/2} - 3s3p(^3P)3d\,^4P_{3/2}$
4	461.89[d]	216 501.8	504.0	$3s3p^2\,^4P_{3/2} - 3s3p(^3P)3d\,^4P_{1/2}$
6	462.01[d]	216 445.3	5.7	$3s^23p\,^2P_{3/2} - 3s^23d\,^2D_{5/2}$
6	462.13[d]	216 386.7	5.9	$3s^23p\,^2P_{3/2} - 3s^23d\,^2D_{3/2}$
2	462.93[e]	216 013.8	5.7	$3s3p^2\,^4P_{3/2} - 3s3p(^3P)3d\,^4P_{3/2}$
8	464.26[c,d]	215 397.0	6.8	$3s3p^2\,^4P_{5/2} - 3s3p(^3P)3d\,^4P_{5/2}$
6	465.58[c,d]	214 783.2	1.1	$3s3p^2\,^4P_{5/2} - 3s3p(^3P)3d\,^4P_{3/2}$
8	466.94[c,d]	214 161.5	2.2	$3s3p^2\,^4P_{5/2} - 3s3p(^3P)3d\,^4P_{5/2}$
4	468.39[a]	213 498.6	9.3	$3s3p^2\,^2D_{5/2} - 3s3p(^3P)3d\,^2F_{7/2}$
6	468.80[c,e]	213 310.3	0.9	$3s3p^2\,^2P_{1/2} - 3s3p(^1P)3d\,^2D_{3/2}$
8	471.19[c,e]	212 227.8	7.9	$3s3p^2\,^2P_{3/2} - 3s3p(^1P)3d\,^2D_{5/2}$
4A	471.87[a]	211 922.6	15.9	$3s3p^2\,^2P_{3/2} - 3s3p(^1P)3d\,^2D_{3/2}$
6	472.04[a,e]	211 844.4	6.5	$3s3p^2\,^2D_{3/2} - 3s3p(^1P)3d\,^2F_{5/2}$
4	472.29[c,e]	211 735.2	3.8	$3s3p^2\,^2D_{5/2} - 3s3p(^3P)3d\,^2F_{5/2}$
6	485.78[c,e]	205 853.5	3.9	$3s3p^2\,^2S_{1/2} - 3s3p(^3P)3d\,^2P_{3/2}$
8	508.83[c,e]	196 528.6	8.5	$3s3p^2\,^2D_{3/2} - 3s3p(^3P)3d\,^2D_{3/2}$
8	508.91[a,e]	196 496.9	7.4	$3s3p^2\,^2D_{3/2} - 3s3p(^3P)3d\,^2D_{5/2}$
4bl	509.12[a]	196 417.0	5.8	$3s3p^2\,^2D_{5/2} - 3s3p(^3P)3d\,^2D_{3/2}$
8	509.20[c,e]	196 385.3	4.7	$3s3p^2\,^2D_{5/2} - 3s3p(^3P)3d\,^2D_{5/2}$
4	516.86[a,e]	193 476.2	6.5	$3s3p^2\,^2P_{1/2} - 3s3p(^3P)3d\,^2P_{3/2}$
4	520.61[a,e]	192 082.7	1.5	$3s3p^2\,^2P_{3/2} - 3s3p(^3P)3d\,^2P_{3/2}$
10	544.73[c,d]	183 576.3	6.1	$3s^23p\,^2P_{1/2} - 3s3p^2\,^2P_{3/2}$
10	548.91[c,d]	182 179.2	81.1	$3s^23p\,^2P_{1/2} - 3s3p^2\,^2P_{1/2}$
6bl	551.35[d]	181 373.6	69.0	$3s^23p\,^2P_{3/2} - 3s3p^2\,^2P_{3/2}$
8	555.63[c,d]	179 975.5	4.0	$3s^23p\,^2P_{3/2} - 3s3p^2\,^2P_{1/2}$
4	564.30[a]	177 209.9	11.1	$3s^23d\,^2D_{3/2} - 3s3p(^1P)3d\,^2D_{3/2}$
6	564.49[a,e]	177 151.9	0.3	$3s^23d\,^2D_{3/2} - 3s3p(^1P)3d\,^2D_{5/2}$
6bl	565.29[a]	176 901.4	899.0	$3s^23d\,^2D_{3/2} - 3s3p(^1P)3d\,^2D_{3/2}$
4	565.49[a,e]	176 838.4	9.2	$3s^23d\,^2D_{5/2} - 3s3p(^1P)3d\,^2D_{3/2}$
8	587.02[c,d]	170 351.5	2.2	$3s3p^2\,^4P_{1/2} - 3p^3\,^4S_{3/2}$
8w	588.91[c,d]	169 803.9	3.7	$3s^23p\,^2P_{1/2} - 3s3p^2\,^2S_{1/2}$
8	589.78[c,d]	169 555.4	5.6	$3s3p^2\,^4P_{3/2} - 3p^3\,^4S_{3/2}$
8	594.10[c,d]	168 322.2	1.0	$3s3p^2\,^4P_{5/2} - 3p^3\,^4S_{3/2}$
6w	596.67[d]	167 596.8	6.6	$3s^23p\,^2P_{3/2} - 3s3p^2\,^2S_{1/2}$
8bl	618.67[c,f]	161 637.5	8.1	$3s3p^2\,^2D_{3/2} - 3p^3\,^2P_{1/2}$
6bl	618.72[a,e]	161 624.0	3.4	$3s3p^2\,^2D_{3/2} - 3p^3\,^2P_{3/2}$
8	619.16[c,f]	161 508.7	10.7	$3s3p^2\,^2D_{5/2} - 3p^3\,^2P_{3/2}$
6	622.15[a,e]	160 732.1	1.8	$3s3p^2\,^2P_{3/2} - 3s3p(^3P)3d\,^2F_{5/2}$
6	631.68[a]	158 307.9	8.5	$3s^23d\,^2D_{3/2} - 3s3p(^1P)3d\,^2F_{5/2}$
4	631.91[a,e]	158 248.9	8.7	$3s^23d\,^2D_{5/2} - 3s3p(^1P)3d\,^2D_{3/2}$
6A	633.85[a]	157 765.0	4.4	$3s^23d\,^2D_{5/2} - 3s3p(^1P)3d\,^2F_{7/2}$
4	636.94[a,e]	157 001.5	4.8	$3s^23d\,^2D_{5/2} - 3s3p(^3P)3d\,^2P_{3/2}$
6	687.84[f]	145 382.8	2.7	$3s3p^2\,^2P_{3/2} - 3s3p(^3P)3d\,^2D_{5/2}$
10w	754.93[c,d]	132 462.1	1.4	$3s^23p\,^2P_{1/2} - 3s3p^2\,^2D_{3/2}$
6A	767.07[c,d]	130 366.3	7.0	$3s^23p\,^2P_{3/2} - 3s3p^2\,^2D_{3/2}$
10	767.73[c,d]	130 253.2	4.3	$3s^23p\,^2P_{3/2} - 3s3p^2\,^2D_{3/2}$
6	782.41[f]	127 810.7	0.0	$3s3p^2\,^2D_{3/2} - 3p^3\,^2D_{5/2}$
8A	783.07[f]	127 702.5	697.3	$3s3p^2\,^2D_{5/2} - 3p^3\,^2D_{5/2}$
8A	783.66[f]	127 606.2	5.5	$3s3p^2\,^2D_{3/2} - 3p^3\,^2D_{3/2}$
6	784.35[f]	127 494.0	2.8	$3s3p^2\,^2D_{5/2} - 3p^3\,^2D_{3/2}$
6	784.80[a]	127 420.9	0.6	$3s^23d\,^2D_{5/2} - 3s3p(^3P)3d\,^2F_{7/2}$
6A	795.44[a]	125 716.8	4.9	$3s^23d\,^2D_{3/2} - 3s3p(^3P)3d\,^2F_{5/2}$
6bl	795.85[a]	125 651.8	5.1	$3s^23d\,^2D_{5/2} - 3s3p(^3P)3d\,^2F_{5/2}$
8	804.62[f]	124 282.3	1.1	$3s3p^2\,^2S_{1/2} - 3p^3\,^2P_{3/2}$
8	893.50[f]	111 919.3	8.4	$3s3p^2\,^2P_{1/2} - 3p^3\,^2P_{1/2}$
6bl	893.63[f]	111 903.3	3.7	$3s3p^2\,^2P_{1/2} - 3p^3\,^2P_{3/2}$
6	904.90[f]	110 509.0	8.7	$3s3p^2\,^2P_{3/2} - 3p^3\,^2P_{3/2}$
8	998.43[d]	100 157.6	8.2	$3s3p^2\,^2P_{1/2} - 3p^3\,^4P_{1/2}$
1	1000.16[c,d]	99 983.8	2.3	$3s3p^2\,^2P_{3/2} - 3p^3\,^4P_{3/2}$
6	1012.66[d]	98 749.4	7.7	$3s3p^2\,^2P_{3/2} - 3p^3\,^4P_{3/2}$
10w	1303.87[f]	76 694.6	5.3	$3s3p^2\,^2P_{3/2} - 3p^3\,^2D_{5/2}$
4	1420.60[a]	70 392.5	2.5	$3s^24d\,^2D_{5/2} - 3s3p(^1P)4s\,^2P_{3/2}$
4	1422.51[a]	70 298.0	8.0	$3s^24d\,^2D_{3/2} - 3s3p(^1P)4s\,^2P_{1/2}$

[a] New line
[b] Previously identified by Lesteven–Vaïsse (Ref. [20])
[c] Measured in second order
[d] Previously identified according to Ref. [27]
[e] Previously identified by De-Ye *et al.* (Ref. [13])
[f] Previously identified by Pinnington *et al.* (Ref. [22])
A = Asimetric line
w = Wide line
bl = Blended line

For the levels $3s3p(^1P)3d\,^2D_{3/2}$ and $3s3p(^1P)3d\,^2D_{5/2}$ we propose the new values 395 492.0 cm^{-1} and 395 804.1 cm^{-1} respectively. These level values are in accordance with the values obtained along the isoelectronic sequence using data of Ref. [23] and with our theoretical predictions. The $3s3p(^1P)3d\,^2D_{3/2}$ level is determined by four new lines, see Table I. For the other level of the same multiplet we classified three lines that are given in the same table.

For the $3s3p(^1P)3d\,^2F_{7/2}$ level we propose the new value 376 417.2 cm^{-1}. This level is determined by a new line at 410.10 Å, classified as $3s3p^2\,^2D_{5/2}$–$3s3p(^1P)3d\,^2F_{7/2}$ and another new line at 633.85 Å, classified as $3s^23d\,^2D_{5/2}$–$3s3p(^1P)3d\,^2F_{7/2}$. For the $3s3p(^1P)3d\,^2F_{5/2}$ level we propose the new value 376 901.5 cm^{-1}. The level is determined by four new lines that are classified in Table I. Both level values of this multiplet are in good agreement with our theoretical predictions and with the graphic extrapolation along the isoelectronic sequence based on the work of Ref. [23].

For the level $3s3p(^1P)4s\,^2P_{1/2}$ we propose the new value 525 043.6 cm^{-1}. The level is determined by a new line at 326.32 Å, classified as $3s^23d\,^2D_{3/2}$–$3s3p(^1P)4s\,^2P_{1/2}$, and

Table II. *Energy levels of Ar VI*

Designation	Energy (cm^{-1})		Percentage composition[a]
$3s^23p\ ^2P_{1/2}$	0.0	97	
$3s^23p\ ^2P_{3/2}$	2 207.1	97	
$3s3p^2\ ^4P_{1/2}$	100 158.2	99	
$3s3p^2\ ^4P_{3/2}$	100 954.8	99	
$3s3p^2\ ^4P_{5/2}$	102 189.2	99	
$3s3p^2\ ^2D_{3/2}$	132 461.4	87	$3s3p^2\ ^2D$ + 12 $3s^23d\ ^2D$
$3s3p^2\ ^2D_{5/2}$	132 574.1	87	$3s3p^2\ ^2D$ + 12 $3s^23d\ ^2D$
$3s3p^2\ ^2S_{1/2}$	169 803.7	99	
$3s3p^2\ ^2P_{1/2}$	182 181.1	99	
$3s3p^2\ ^2P_{3/2}$	183 576.1	99	
$3s^23d\ ^2D_{3/2}$	218 593.0	87	$3s^23d\ ^2D$ + 12 $3s3p^2\ ^2D$
$3s^23d\ ^2D_{5/2}$	218 652.8	87	$3s^23d\ ^2D$ + 12 $3s3p^2\ ^2D$
$3p^3\ ^2D_{3/2}$	260 066.9	64	$3p^3\ ^2D$ + 35 $3s3p(^3P)3d\ ^2D$
$3p^3\ ^2D_{5/2}$	260 271.4	64	$3p^3\ ^2D$ + 35 $3s3p(^3P)3d\ ^2D$
$3p^3\ ^4S_{3/2}$	270 510.4	99	
$3p^3\ ^2P_{3/2}$	294 084.8	73	$3p^3\ ^2P$ + 19 $3s3p(^3P)3d\ ^2P$ + 6 $3s3p(^1P)3d\ ^2P$
$3p^3\ ^2P_{1/2}$	294 099.5	74	$3p^3\ ^2P$ + 19 $3s3p(^3P)3d\ ^2P$ + 6 $3s3p(^1P)3d\ ^2P$
$3s3p(^3P)3d\ ^4P_{5/2}$	316 351.6	98	
$3s3p(^3P)3d\ ^4P_{3/2}$	316 970.5	97	
$3s3p(^3P)3d\ ^4P_{1/2}$	317 458.8	98	
$3s3p(^3P)3d\ ^4D_{1/2}$	319 272.0	98	
$3s3p(^3P)3d\ ^4D_{3/2}$	319 536.5	97	
$3s3p(^3P)3d\ ^4D_{5/2}$	319 767.0	98	
$3s3p(^3P)3d\ ^4D_{7/2}$	319 903.9	99	
$3s3p(^3P)3d\ ^2D_{5/2}$	328 958.8	47	$3s3p3d(^3P)\ ^2D$ + 32 $3s3p(^1P)3d\ ^2D$ + 20 $3p^3\ ^2D$
$3s3p(^3P)3d\ ^2D_{3/2}$	328 989.9	47	$3s3p3d(^3P)\ ^2D$ + 32 $3s3p(^1P)3d\ ^2D$ + 20 $3p^3\ ^2D$
$3s^24s\ ^2S_{1/2}$	342 302.8	99	
$3s3p(^3P)3d\ ^2F_{5/2}$	344 307.9[n]	71	$3s3p3d(^3P)\ ^2F$ + 28 $3s3p(^1P)3d\ ^2F$
$3s3p(^3P)3d\ ^2F_{7/2}$	346 073.4[n]	71	$3s3p3d(^3P)\ ^2F$ + 28 $3s3p(^1P)3d\ ^2F$
$3s3p(^3P)3d\ ^2P_{3/2}$	375 657.6[n]	78	$3s3p3d(^3P)\ ^2P$ + 16 $3p^3\ ^2P$
$3s3p(^1P)3d\ ^2F_{7/2}$	376 417.2[n]	71	$3s3p3d(^1P)\ ^2F$ + 28 $3s3p(^3P)3d\ ^2F$
$3s3p(^1P)3d\ ^2F_{5/2}$	376 901.5[n]	71	$3s3p3d(^1P)\ ^2F$ + 28 $3s3p(^3P)3d\ ^2F$
$3s3p(^1P)3d\ ^2D_{3/2}$	395 492.0[n]	66	$3s3p3d(^1P)\ ^2D$ + 17 $3s3p(^3P)3d\ ^2D$ + 15 $3p^3\ ^2D$
$3s3p(^1P)3d\ ^2D_{5/2}$	395 804.1[n]	67	$3s3p3d(^1P)\ ^2D$ + 17 $3s3p(^3P)3d\ ^2D$ + 15 $3p^3\ ^2D$
$3s3p(^3P)4s\ ^4P_{1/2}$	454 109.8	99	
$3s^24d\ ^2D_{3/2}$	454 745.6	99	
$3s^24d\ ^2D_{5/2}$	454 798.8	99	
$3s3p(^3P)4s\ ^4P_{3/2}$	454 872.5	99	
$3s3p(^3P)4s\ ^4P_{5/2}$	456 271.6	99	
$3s3p(^1P)4s\ ^2P_{1/2}$	525 043.6[n]	99	
$3s3p(^1P)4s\ ^2P_{3/2}$	525 191.3[n]	98	

[a] Percentages lower than 5% are omitted
[n] New level

another new line at 1422.51 Å, classified as $3s^24d\ ^2D_{3/2}$–$3s3p(^1P)4s\ ^2P_{1/2}$.

For the level $3s3p(^1P)4s\ ^2P_{3/2}$ we propose the new value 525 191.3 cm^{-1}. This level is supported by three new lines that are classified in Table I.

We report a new line at 618.72 Å, classified as $3s3p^2\ ^2D_{3/2}$–$3p^3\ ^2P_{3/2}$ transition. For us, the line at 804.62 Å, corresponds to the $3s3p^2\ ^2S_{1/2}$–$3p^3\ ^2P_{3/2}$ transition. This line has a double classification in the previous work of Ref. [22]. In the same work, some other lines also appear with double classification, but for us, the lines at 893.50 Å, 893.63 Å and 904.90 Å correspond to the $3s3p^2\ ^2P$–$3p^3\ ^2P$ multiplet. These transitions confirm (fairly well) the previously observed values of the $3p^3\ ^2P_{1/2}$ and $^2P_{3/2}$ levels, see Ref. [22].

We report two new lines at 508.91 Å and 509.12 Å, classified as $3s3p^2\ ^2D_{3/2}$–$3s3p(^3P)3d\ ^2D_{5/2}$ and $3s3p^2\ ^2D_{5/2}$–$3s3p(^3P)3d\ ^2D_{3/2}$ transitions. These lines confirm the previously observed values of the $3s3p(^3P)3d\ ^2D$ doublet, see Ref. [22].

Theoretical Interpretation

The level structure was theoretically interpreted by a least-squares fit of the energy parameters to the experimental level values. For this purpose the computer code developed by Cowan [29] was used.

The scaled Hartree–Fock factor was 0.85 for all parameters, except for ζ_{nl} where the scaled factor was 0.95 and for E_{av} where the scaled factor was 1.00. These scaled factors were taken in this form because the computed energy-level intervals agree better with the experimental ones.

In order to obtain a better interpretation of the levels it was necessary to introduce the $3s^24p$ configuration. The results of the parametric calculations are presented in Table III.

The α parameter was kept free because all the levels of the $3p^3$ configuration are known. The first three configuration interaction integrals were held fixed in the calculation scaled at 0.75, 0.95 and 0.95 of their Hartree–Fock values. The rest of the configuration interaction integrals were held fixed at

Table III. *Energy parameters (cm^{-1}) for the $3s^23p$, $3s^24p$, $3p^3$, $3s3p3d$, $3s3p4s$ configurations of Ar VI*

Configuration	Parameter	Scaled Hf Value	Fitted Value[a]	Ratio Fitted Value SHF Value
$3s^23p$	E_{av}	0	13738	
$3s^23p$	ζ_{3p}	1307	1512	1.157
$3s^24p$	E_{av}	391438	393887	1.006
$3s^24p$	ζ_{4p}	394	394 (FIX)	
$3p^3$	E_{av}	287614	294987	1.026
$3p^3$	$F^2(3p,3p)$	66962	68868	1.028
$3p^3$	$\alpha(3p,3p)$		−112	
$3p^3$	ζ_{3p}	1306	1610	1.233
$3s3p3d$	E_{av}	323495	332094	1.027
$3s3p3d$	$F^2(3p,3d)$	63506	63334	0.997
$3s3p3d$	$G^1(3s,3p)$	90341	70384	0.779
$3s3p3d$	$G^2(3s,3d)$	61497	66186	1.076
$3s3p3d$	$G^1(3p,3d)$	78310	76869	0.982
$3s3p3d$	$G^3(3p,3d)$	48916	44557	0.911
$3s3p3d$	ζ_{3p}	1319	1797	1.362
$3s3p3d$	ζ_{3d}	60	60 (FIX)	
$3s3p4s$	E_{av}	463784	475779	1.026
$3s3p4s$	$G^1(3s,3p)$	82900	95501	1.152
$3s3p4s$	$G^0(3s,4s)$	5896	6137	1.041
$3s3p4s$	$G^1(3p,4s)$	7775	7775 (FIX)	
$3s3p4s$	ζ_{3p}	1405	1420	1.011
Configuration Interaction Integrals				
$3s^23p - 3p^3$	$R^1(3s3s,3p3p)$	79351	79351 (FIX)	
$3s^23p - 3s3p3d$	$R^1(3s3p,3p3d)$	92765	92765 (FIX)	
$3s^23p - 3s3p3d$	$R^2(3s3p,3d3p)$	70775	70775 (FIX)	
$3s^23p - 3s3p4s$	$R^0(3s3s,3s4s)$	4725	4725 (FIX)	
$3s^23p - 3s3p4s$	$R^1(3s3p,3p4s)$	7557	7557 (FIX)	
$3s^23p - 3s3p4s$	$R^0(3s3p,4s3p)$	1368	1368 (FIX)	
$3s^24p - 3s3p3d$	$R^1(3s4p,3p3d)$	8998	8998 (FIX)	
$3s^24p - 3s3p3d$	$R^2(3s4p,3d3p)$	10777	10777 (FIX)	
$3s^24p - 3s3p4s$	$R^1(3s4p,3p4s)$	38098	38098 (FIX)	
$3s^24p - 3s3p4s$	$R^0(3s4p,4s3p)$	6074	6074 (FIX)	
$3p^3 - 3s3p3d$	$R^1(3p3p,3s3d)$	82900	82900 (FIX)	
$3p^3 - 3s3p4s$	$R^1(3p3p,3s4s)$	7384	7384 (FIX)	
$3s3p3d - 3s3p4s$	$R^2(3p3d,3p4s)$	2974	2974 (FIX)	
$3s3p3d - 3s3p4s$	$R^1(3p3d,4s3p)$	5010	5010 (FIX)	

[a] The RMS deviation of the fit is 210 cm^{-1} for 28 observed levels

the standard 85% of the Hartree–Fock values. The standard-deviation for the 28 observed levels was 210 cm^{-1}.

Acknowledgements

Support from Conselho Nacional de Desenvolvimento Científico e Tecnológico (CNPq), Brasil, Fundação de Amparo à Pesquisa do Estado de São Paulo (FAPESP), Brasil, Comisión de Investigaciones Científicas de la Provincia de Buenos Aires (CIC), Argentina, where J. G. Reyna Almandos and F. Bredice belong as researchers and M. Raineri as fellow, and Consejo Nacional de Investigaciones Científicas e Técnicas (CONICET), Argentina is gratefully acknowledged.

References

1. Moore, C. E., Atomic Energy Levels, Vol. I. Nat. Bur. Stand., Ref. Data Ser. Circ. N: 467 (U.S. GPO, Washington D.C. 1971).
2. Eriksson, K. B. S. and Isberg, H. B. S., Ark. Fys. 23, 527 (1963).
3. Shenstone, A. G., Proc. Roy. Soc. A261, 153 (1961).
4. Magnusson, C. E. and Zetterberg, P. O., Phys. Scr. 15, 237 (1977).
5. Martin, W. C., Zalubas, R. and Musgrove, A. J., J. Phys. Chem. Ref. Data 19, 821 (1990).
6. Phillips, L. W. and Parker, W. L., Phys. Rev. 60, 301 (1941).
7. Fawcett, B. C., Jones, B. B. and Wilson, R., Proc. Phys. Soc. 78, 1223 (1961).
8. Schönheit, E., Optik 23, 409 (1966).
9. Ekberg, J. O. and Svensson, L. A., Phys. Scr. 2, 283 (1970).
10. Fawcett, B. C., Ridgeley, A. and Bromage, G. E., Phys. Scr. 18, 315 (1978).
11. Livingston, A. E., Pinnington, E. H., Irwin, J. G., Kernahan, J. A. and Brooks, R. L., J. Opt. Soc. Am. 71, 442 (1981).
12. Buchet-Poulizac, M. C., Buchet, J. P. and Ceyzeriat, P., Nucl. Instr. and Meth. 202, 13 (1982).
13. De-Ye, J., Li-Kang, S., Li-Zeng, Z. and Wen-Shu, W., Chin. J. Phys. 33, 508 (1984).
14. Fawcett, B. C., At. Data and Nucl. Data Tables 28, 557 (1983).
15. Huang, K.-N., At. Data and Nucl. Data Tables 34, 1 (1986).
16. Sugar, J. and Kaufman, V., J. Opt. Soc. Am. B3, 704 (1986).
17. Sugar, J. and Kaufman, V., Phys. Scr. 34, 797 (1986).
18. Träbert, E., Hutton, R., Engström, L., Bliman, S. L., Berry, H. G. and Kurtz, C., Phys. Lett. A129, 381 (1988).
19. Träbert, E., Heckmann, P. M., Hutton, R. and Martinson, I., J. Opt. Soc. Am. B5, 2173 (1988).
20. Lesteven-Vaïsse, I., Folkmann, F., Ben Sitel, A., Chantepie, M. and Lecler, D., Phys. Scr. 38, 45 (1988).

21. Engström, L., Reistad, N., Jupén, C. and Westerlind, M., Phys. Scr. **39**, 66 (1989).
22. Pinnington, E. H., Ge, Z.-Q., Ansbacher, W., Kernahan, J. A. and Goselin, R. N., Phys. Scr. **39**, 321 (1989).
23. Redfors, A. and Litzén, U., J. Opt. Soc. Am. **B6**, 1447 (1989).
24. Thornbury, J. F., Hibbert, A. and Träbert, E., Phys. Scr. **40**, 472 (1989).
25. Jupén, C., Denne, B. and Martinson, I., Phys. Scr. **41**, 669 (1990).
26. Gallardo, M., Bredice, F., Raineri, M. and Reyna Almandos, J. G., Appl. Opt. **28**, 4513 (1989).
27. Kelly, R. L., J. Phys. Chem. Ref. Data **16**, Suppl. 1 (1987).
28. Pettersson, S.-G., Phys. Scr. **26**, 296 (1982).
29. Cowan, R. D., "The Theory of Atomic Structure and Spectra" (University of California Press, Berkeley, U.S.A. 1981).

Pergamon

PII: S0022-4073(97)00237-9

J. Quant. Spectrosc. Radiat. Transfer Vol. 61, No. 3, pp. 319–327, 1999
© 1998 Elsevier Science Ltd. All rights reserved
Printed in Great Britain
0022-4073/98 $19.00 + 0.00

REVISED AND EXTENDED ANALYSIS IN FOUR TIMES IONIZED XENON XE V

M. GALLARDO,† M. RAINERI, J. G. REYNA ALMANDOS, H. SOBRAL and F. CALLEGARI

Centro de Investigaciones Opticas (CIOp), C.C 124, 1900 La Plata, Argentina

(Received 17 May 1997)

Abstract—The atomic-emission spectrum of four times ionized xenon (Xe V) has been observed in the region 500–6700 Å; 233 lines were classified as transition between $5s5p^3$, $5s^25p5d$, $5s^25p6s$ with $5s^25p^2$, $5s^25p6p$ and $5s^25p4f$ configurations. Ninty-seven of these lines are reported for the first time. Two new energy level values corresponding to the $5s^25p4f$ configuration have been determined, and we proposed two new values for the previously reported $^3D_1$ and $^3G_5$ energy levels of this configuration. The value of the $5s^25p6p$ $^1S_0$ energy level has also been determined, and we propose a new value for the previously reported $5s^25p5d$ $^3F_4$ energy level. New adjusted values for the previously known levels of the studied configurations are included. Least-squares fitted parametric calculations involving configuration interactions have been carried out to interpret the observed spectrum. © 1998 Elsevier Scince Ltd. All rights reserved.

1. INTRODUCTION

There is great interest in spectroscopy data from xenon due to applications in collision physics, high-temperature plasmas and laser physics. In this last point, the understanding of the population mechanisms that affect the laser action for this element, require a knowledge of the spectral analysis corresponding to the different ions involved.

The spectrum of four times ionized xenon (Xe V) has the ground configuration $5s^25p^2$, the same as Sn I. Spectra of Sb II,[1] I IV,[2] Cs VI[3] and Ba VII[4] in this sequence were previously analysed by other authors. Several ionic UV-visible Xe lines were charge-state assigned to Xe V by Duchowicz et al[5] but not classifications. Gallardo et al[6] obtained nine new levels of the $5s^25p6p$ configuration, the first established energy levels of an even excited configuration. Pinnington et al[7] have presented a study of the beam-foil spectrum of Xe V. Recently, Tauheed et al[8] made the analysis of several configurations of this ion using a gas-triggered spark as a light source. Very recently, a work concerning $5s^25p5d$–$5s^25p4f$ and $5s5p^3$–$5s^25p4f$ transitions, establishing 10 new levels of the $5s^25p4f$ configuration, the remaining $^3F_4$ level of $5s^25p5d$ and the classification of several known Xe V laser lines, was reported by Larsson et al,[9] using collision-based spectroscopy.

With the final goal of completing the classification of the most prominent UV-visible Xe laser lines, we have continued an investigation of the Xe V spectrum that concerns the study of the energy levels in the configuration $5s^25p4f$, and the transitions $5s5p^3$–$5s^25p4f$, $5s^25p5d$–$5s^25p4f$, $5s^25p6s$–$5s^25p4f$, and the classification of lines belonging to transitions between the $5s^25p6p$ configuration with odd parity configurations.

2. EXPERIMENT

The experimental set-up is similar to that described in the work of Gallardo et al[6] SWR plates were used to record the new spectra in the vacuum ultraviolet region, where known lines of C, N, O, Xe II and Xe III were used as internal standards. In the UV-visible region new spectra were recorded using a water-cooled Pyrex tube 1.3 m long and 3 mm internal bore. The indium-coated tungsten

† To whom all the correspondence should be addressed.

electrodes were placed in side arms 1 m apart. Using a 140 nF capacitor, peak current pulses of 3.5 kA and 1 μs (FWHM) were obtained. In certain cases, larger capacitances up to 280 nF were used. Thorium lines from an electrodless discharge were superimposed on the spectrograms and served as reference lines.[10]

The spectrograms were measured with a photoelectric automatic Grant comparator, and the accuracy of the wavelength values is estimated to be ± 0.01 Å in the first diffraction order. The intensities of the lines were based on visual estimates. To distinguish among different states of ionization, we studied the behaviour of the spectral lines intensities as a function of pressure.

3. RESULT AND DISCUSSION

The lines observed in the present work, are listed in Table 1. The total number of observed lines is 233, of which 97 correspond to new classified lines. Table 1 also contains almost all the lines previously reported in the work of Duchowicz et al[5] as laser lines. It is interesting to note that most of these laser lines correspond, in spontaneous emission, to high intensity transitions between the

Table 1. Classified lines in the Xe V spectrum

Intensity	λ [Å] (vac.)	σ [cm^{-1}]		Ref.	Classification		
		Obs	Calc				
10	543.05	184145.1	7.6	6	$5s^25p^2$	$^3P_0$–$5s^25p5d$	$^3P_1$
11	566.57	176500.7	3.2	6	$5s^25p^2$	$^3P_1$–$5s^25p5d$	$^1D_2$
8	571.90	174855.7	5.8	7,8	$5s^25p^2$	$^3P_1$–$5s^25p5d$	$^3P_1$
7	575.59	173734.7	3.4	8	$5s^25p^2$	$^3P_1$–$5s^25p5d$	$^3P_0$
6	577.79	173073.3	1.7	8	$5s^25p^2$	$^3P_0$–$5s^25p5d$	$^3D_1$
7	582.52	171667.9	8.3	8	$5s^25p^2$	$^3P_2$–$5s^25p5d$	$^1D_2$
6	582.93	171547.2	7.8	8	$5s^25p^2$	$^1D_2$–$5s^25p5d$	$^1P_1$
5	588.16	170021.8	0.9	8	$5s^25p^2$	$^3P_2$–$5s^25p5d$	$^3P_1$
4	593.22	168571.5	69.8	7,8	$5s^25p^2$	$^1S_0$–$5s^25p6s$	$^1P_1$
8	595.09	168040.9	0.5	7,8	$5s^25p^2$	$^3P_2$–$5s^25p5d$	$^3D_3$
1	599.24	166878.0	7.6	8	$5s^25p^2$	$^3P_2$–$5s^25p5d$	$^3D_2$
7	603.40	165727.5	6.8	7,8	$5s^25p^2$	$^1D_2$–$5s^25p5d$	$^1F_3$
6	610.57	163781.4	79.9	8	$5s^25p^2$	$^3P_1$–$5s^25p5d$	$^3D_1$
9	635.39	157383.7	3.8	7,8	$5s^25p^2$	$^1D_2$–$5s^25p5d$	$^1D_2$
8	637.51	156860.2	0.9	7,8	$5s^25p^2$	$^3P_2$–$5s^25p5d$	$^3D_2$
6	662.10	151034.5	3.7	6	$5s^25p^3$	$^5S_2$–$5s^25p6p$	$^1P_1$
7	679.28	147214.7	5.0	7,8	$5s^25p^2$	$^3P_1$–$5s^25p5d$	$^3F_2$
7	691.27	144661.3	0.5	8	$5s^25p^2$	$^1D_2$–$5s^25p5d$	$^3D_1$
6	701.38	142576.1	6.4	8	$5s^25p^2$	$^1D_2$–$5s^25p5d$	$^3P_2$
12	702.34	142381.2	0.1	8	$5s^25p^2$	$^3P_2$–$5s^25p5d$	$^3F_2$
12A	702.87	142273.8	2.8	6	$5s5p^3$	$^5S_2$–$5s^25p6p$	$^3P_1$
10	707.26	141390.7	1.4	7,8	$5s^25p^2$	$^3P_2$–$5s5p^3$	$^3S_1$
6	707.90	141263.0	1.4	8	$5s^25p^2$	$^1D_2$–$5s5p^3$	$^1P_1$
3	735.94	135880.6	2.1	6	$5s5p^3$	$^5S_2$–$5s^25p6p$	$^3D_1$
2	765.47	130638.7	8.2		$5s5p^3$	$^3D_3$–$5s^25p6p$	$^1D_2$
3	768.58	130110.1	1.0		$5s5p^3$	$^3D_2$–$5s^25p6p$	$^3D_3$
7	772.00	129533.7	5.0	6	$5s5p^3$	$^3D_1$–$5s^25p6p$	$^3P_2$
6 bl	776.87	128721.7	4.3	6	$5s5p^3$	$^3D_2$–$5s^25p6p$	$^3P_2$
6	777.61	128599.2	601.3	8	$5s^25p^2$	$^1S_0$–$5s^25p5d$	$^3D_1$
7	780.67	128095.1	5.6	7,8	$5s^25p^2$	$^1D_2$–$5s^25p5d$	$^3F_2$
3	786.66	127119.7	9.5		$5s5p^3$	$^3D_2$–$5s^25p6p$	$^1P_1$
8	791.84	126288.1	9.0	6	$5s5p^3$	$^3D_3$–$5s^25p6p$	$^3D_3$
5	797.38	125410.7	0.9	8	$5s^25p^2$	$^3P_1$–$5s5p^3$	$^3P_2$
7	798.19	125283.5	3.4	8	$5s^25p^2$	$^3P_1$–$5s5p^3$	$^3P_1$
5	798.71	125201.9	2.2	8	$5s^25p^2$	$^1S_0$–$5s5p^3$	$^1P_1$

continued

Table 1—*continued*

Intensity	λ [Å] (vac.)	σ [cm^{-1}]		Ref.	Classification		
		Obs	Calc				
7	805.70	124115.7	6.3	8	$5s^25p^2$	$^3P_1$–$5s5p^3$	$^3P_0$
9	829.35	120576.4	6.0	7,8	$5s^25p^2$	$^3P_2$–$5s5p^3$	$^3P_2$
6	830.23	120448.6	8.5	8	$5s^25p^2$	$^3P_2$–$5s5p^3$	$^3P_1$
1	834.08	119892.6	2.6	6	$5s5p^3$	$^3D_1$–$5s^25p6p$	$^3D_2$
2	839.15	119168.2	9.3		$5s5p^3$	$^3D_1$–$5s^25p6p$	$^3P_1$
6	844.89	118358.6	8.6	6	$5s5p^3$	$^3D_2$–$5s^25p6p$	$^3P_1$
7	851.82	117395.7	5.8	7,8	$5s^25p^2$	$^1D_2$–$5s5p^3$	$^1D_2$
6	862.20	115982.4	2.0	6	$5s5p^3$	$^3P_1$–$5s^25p6p$	$^1D_2$
3	863.15	115854.7	4.5		$5s5p^3$	$^3P_2$–$5s^25p6p$	$^1D_2$
8	867.40	115287.1	6.3	7,8	$5s^25p^2$	$^3P_0$–$5s5p^3$	$^3D_1$
9A	886.68	112780.3	78.6	6	$5s5p^3$	$^5S_2$–$5s^25p6p$	$^3D_1$
1	893.12	111967.0	7.9	6	$5s5p^3$	$^3D_2$–$5s^25p6p$	$^3D_1$
10	896.82	111505.1	5.3	6	$5s5p^3$	$^3P_2$–$5s^25p6p$	$^3D_3$
6	900.51	111048.2	7.7	8	$5s^25p^2$	$^1S_0$–$5s5p^3$	$^3S_1$
9	907.06	110246.3	6.1	6	$5s5p^3$	$^3P_1$–$5s^25p6p$	$^3P_2$
6	908.11	110118.8	8.6	6	$5s5p^3$	$^3P_2$–$5s^25p6p$	$^3P_2$
7	921.54	108514.0	3.8	6	$5s5p^3$	$^3P_2$–$5s^25p6p$	$^1P_1$
13	936.29	106804.5	5.2	7,8	$5s^25p^2$	$^3P_1$–$5s5p^3$	$^3D_2$
8	940.81	106291.4	1.5	7,8	$5s^25p^2$	$^1D_2$–$5s5p^3$	$^3P_2$
5	941.95	106162.7	4.0	6	$5s^25p^2$	$^1D_2$–$5s5p^3$	$^3P_1$
7	943.44	105995.1	4.5	8	$5s^25p^2$	$^3P_1$–$5s5p^3$	$^3D_1$
7	954.66	104749.3	50.2	6	$5s5p^3$	$^1D_2$–$5s^25p6p$	$^1D_2$
12	980.68	101970.1	0.3	6	$5s^25p^2$	$^3P_2$–$5s5p^3$	$^3D_2$
10	988.55	101158.3	9.6	7,8	$5s^25p^2$	$^3P_2$–$5s5p^3$	$^3D_1$
3	989.63	101047.9	7.5		$5s5p^3$	$^3P_0$–$5s^25p6p$	$^3P_1$
5	995.26	100476.3	6.2		$5s5p^3$	$^3P_2$–$5s^25p6p$	$^3D_2$
10	1002.48	99752.6	2.9		$5s5p^3$	$^3P_2$–$5s^25p6p$	$^3P_1$
9	1026.60	97408.9	9.5	6	$5s5p^3$	$^1D_2$–$5s^25p6p$	$^1P_1$
3	1056.47	94654.8	6.8	6	$5s5p^3$	$^3P_0$–$5s^25p6p$	$^3D_1$
6	1059.34	94398.4	8.7		$5s5p^3$	$^3D_3$–$5s^25p4f$	$^1G_4$
4	1063.26	94050.4	0.4	6	$5s^25p5d$	$^3F_2$–$5s^25p6p$	$^1D_2$
7	1063.55	94024.7	4.4		$5s5p^3$	$^3D_1$–$5s^25p4f$	$^3D_1$
8	1071.10	93362.0	2.2		$5s5p^3$	$^3P_2$–$5s^25p6p$	$^3D_1$
6	1072.81	93213.2	3.7		$5s5p^3$	$^3D_2$–$5s^25p4f$	$^3D_1$
3	1083.53	92290.9	2.3	6	$5s5p^3$	$^3S_1$–$5s^25p6p$	$^3S_1$
4	1086.01	92080.1	0.4		$5s5p^3$	$^3D_1$–$5s^25p4f$	$^3D_2$
6	1092.79	91508.9	7.8	7,8	$5s5p^2$	$^1D_2$–$5s5p^3$	$^3D_3$
8	1095.65	91270.0	69.7		$5s5p^3$	$^3D_2$–$5s^25p4f$	$^3D_2$
6	1109.81	90105.5	4.8	8	$5s^25p^2$	$^1S_0$–$5s5p^3$	$^3P_1$
5	1111.49	89969.3	9.7		$5s5p^3$	$^1P_1$–$5s^25p6p$	$^1S_0$
3	1114.82	89700.6	1.2	6	$5s^25p5d$	$^3F_2$–$5s^25p6p$	$^3D_3$
1	1115.28	89663.6	1.8		$5s5p^3$	$^3D_2$–$5s^25p4f$	$^3D_3$
6	1118.92	89371.9	1.9	6	$5s5p^3$	$^1D_2$–$5s^25p6p$	$^3D_2$
4	1119.77	89304.1	3.2	6	$5s5p^3$	$^3S_1$–$5s^25p6p$	$^3P_2$
3	1128.06	88647.8	8.6	6	$5s5p^3$	$^1D_2$–$5s^25p6p$	$^3P_1$
5	1132.32	88314.3	4.5	6	$5s^25p5d$	$^3F_2$–$5s^25p6p$	$^3P_2$
6	1140.28	87697.8	8.4	6	$5s5p^3$	$^3S_1$–$5s^25p6p$	$^1P_1$
8	1143.53	87448.5	7.7		$5s5p^3$	$^3D_3$–$5s^25p4f$	$^3D_2$
6	1153.27	86710.0	9.7	6	$5s^25p5d$	$^3F_2$–$5s^25p6p$	$^1P_1$
4	1155.13	86570.3	0.6		$5s^25p5d$	$^3F_2$–$5s^25p6p$	$^1S_0$
11	1164.96	85839.9	9.8	9	$5s5p^3$	$^3D_3$–$5s^25p4f$	$^3D_3$
9	1168.52	85578.3	7.6		$5s^25p5d$	$^3F_3$–$5s^25p6p$	$^3D_3$
10	1191.69	83914.4	3.2	9	$5s5p^3$	$^3D_2$–$5s^25p4f$	$^1F_3$
7	1218.88	82042.5	2.9		$5s5p^3$	$^3P_2$–$5s^25p4f$	$^1D_2$
12	1225.10	81626.0	6.2	9	$5s5p^3$	$^3D_3$–$5s^25p4f$	$^3F_4$
4	1236.34	80883.9	4.6	6	$5s5p^3$	$^1P_1$–$5s^25p6p$	$^1D_2$
7	1248.58	80091.0	1.2		$5s5p^3$	$^3D_3$–$5s^25p4f$	$^1F_3$
5	1255.32	79661.0	0.8	6	$5s5p^3$	$^3S_1$–$5s^25p6p$	$^3D_2$

continued

Table 1—*continued*

Intensity	λ [Å] (vac.)	σ [cm^{-1}]		Ref.	Classification		
		Obs	Calc				
6	1256.75	79570.3	69.6	6	$5s^25p5d$	$^3P_2$–$5s^25p6p$	$^1D_2$
6	1271.10	78672.0	2.1	6	$5s^25p5d$	$^3F_2$–$5s^25p6p$	$^3D_2$
12	1281.13	78056.1	6.1	7,8	$5s^25p^2$	$^3P_2$–$5s5p^3$	$^5S_2$
12	1282.89	77949.0	8.8	6	$5s^25p5d$	$^3F_2$–$5s^25p6p$	$^3P_1$
3	1290.57	77485.1	5.5	6	$5s^25p5d$	$^3D_1$–$5s^25p6p$	$^1D_2$
4	1301.69	76823.2	2.8	6	$5s^25p5d$	$^3P_2$–$5s^25p6p$	$^3S_1$
12	1317.46	75903.6	26		$5s5p^3$	$^3P_0$–$5s^25p4f$	$^3D_1$
9	1324.38	75507.0	6.5	9	$5s5p^3$	$^3D_2$–$5s^25p4f$	$^3F_2$
4	1324.58	75495.6	4.7		$5s^25p5d$	$^3P_1$–$5s^25p6p$	$^1S_0$
4	1329.44	75219.6	20.4	6	$5s^25p5d$	$^3P_2$–$5s^25p6p$	$^3D_3$
3	1330.70	75148.4	8.7	6	$5s5p^3$	$^1P_1$–$5s^25p6p$	$^3P_2$
10	1338.05	74735.6	5.5		$5s5p^3$	$^3P_1$–$5s^25p4f$	$^3D_1$
5	1340.34	74607.9	8.0		$5s5p^3$	$^3P_2$–$5s^25p4f$	$^3D_1$
12	1341.42	74547.9	8.5	6	$5s^25p5d$	$^3F_3$–$5s^25p6p$	$^3D_2$
7	1354.40	73833.4	3.7	6	$5s^25p5d$	$^3P_2$–$5s^25p6p$	$^3P_2$
13	1359.31	73566.7	6.8	9	$5s5p^3$	$^3D_2$–$5s^25p4f$	$^3F_3$
4	1359.74	73543.5	3.9	6	$5s5p^3$	$^1P_1$–$5s^25p6p$	$^1P_1$
11	1373.79	72791.3	1.5		$5s5p^3$	$^3P_1$–$5s^25p4f$	$^3D_2$
10	1376.20	72663.9	4.0		$5s5p^3$	$^3P_2$–$5s^25p4f$	$^3D_2$
6	1393.73	71749.9	9.6	6	$5s^25p5d$	$^3D_1$–$5s^25p6p$	$^3P_2$
9A	1397.45	71558.9	8.1	6	$5s^25p5d$	$^3F_2$–$5s^25p6p$	$^3D_1$
9	1407.34	71056.0	6.1	9	$5s5p^3$	$^3P_2$–$5s^25p4f$	$^3D_3$
7	1409.67	70938.6	8.6		$5s5p^3$	$^1D_2$–$5s^25p4f$	$^1D_2$
10	1412.12	70815.5	5.9	6	$5s^25p^2$	$^1S_0$–$5s5p^3$	$^3D_1$
12	1413.91	70725.9	5.6	9	$5s5p^3$	$^3D_3$–$5s^25p4f$	$^3G_4$
3	1425.61	70145.4	4.8	6	$5s^25p5d$	$^3D_1$–$5s^25p6p$	$^1P_1$
1	1433.80	69744.7	4.8		$5s5p^3$	$^3D_3$–$5s^25p4f$	$^3F_3$
1	1437.75	69553.1	2.9	6	$5s^25p5d$	$^3D_2$–$5s^25p6p$	$^1D_2$
8	1496.38	66827.9	7.7	9	$5s5p^3$	$^3D_3$–$5s^25p4f$	$^3G_3$
9	1505.80	66409.9	9.6	6	$5s^25p5d$	$^3P_1$–$5s^25p6p$	$^1D_2$
12	1531.22	65307.4	7.5	9	$5s5p^3$	$^3P_2$–$5s^25p4f$	$^1F_3$
4	1533.66	65203.5	3.7	6	$5s^25p5d$	$^3D_2$–$5s^25p6p$	$^3D_3$
6	1543.61	64783.2	3.0	6	$5s5p^3$	$^1P_1$–$5s^25p6p$	$^3P_1$
9	1544.11	64762.2	2.2	6	$5s^25p5d$	$^1D_2$–$5s^25p6p$	$^1D_2$
6	1557.84	64191.4	1.3	6	$5s^25p5d$	$^3P_2$–$5s^25p6p$	$^3D_2$
14	1561.47	64042.2	0.8		$5s^25p5d$	$^3D_3$–$5s^25p6p$	$^3D_3$
7	1566.96	63817.8	7.0	6	$5s^25p5d$	$^3D_2$–$5s^25p6p$	$^3P_2$
5	1568.10	63771.4	1.6	6,7	$5s^25p^2$	$^1D_2$–$5s5p^3$	$^5S_2$
7	1574.73	63502.9	3.7		$5s5p^3$	$^1D_2$–$5s^25p4f$	$^3D_1$
8	1575.59	64468.3	8.0	6	$5s^25p5d$	$^3P_2$–$5s^25p6p$	$^3P_1$
7	1607.41	62211.9	2.2	6	$5s^25p5d$	$^3D_2$–$5s^25p6p$	$^1P_1$
3	1610.11	62107.6	7.2	6	$5s^25p5d$	$^3D_1$–$5s^25p6p$	$^3D_2$
8	1624.41	61560.8	59.7		$5s5p^3$	$^1D_2$–$5s^25p4f$	$^3D_2$
2	1629.08	61384.3	3.9	6	$5s^25p5d$	$^3D_1$–$5s^25p6p$	$^3P_1$
6	1648.14	60674.5	3.7	6	$5s^25p5d$	$^3P_1$–$5s^25p6p$	$^3P_2$
8	1655.26	60413.5	3.0		$5s^25p5d$	$^1D_2$–$5s^25p6p$	$^3D_3$
12	1668.00	59952.0	1.8	9	$5s5p^3$	$^1D_2$–$5s^25p4f$	$^3D_3$
10	1675.51	59683.3	3.3		$5s^25p5d$	$^1P_1$–$5s^25p6p$	$^1S_0$
7	1692.91	59069.9	8.9		$5s^25p5d$	$^3P_1$–$5s^25p6p$	$^1P_1$
10	1712.52	58393.5	2.3		$5s5p^3$	$^1P_1$–$5s^25p6p$	$^3D_1$
3	1741.50	57421.8	1.5		$5s^25p5d$	$^1D_2$–$5s^25p6p$	$^1P_1$
6	1753.52	57028.1	8.3		$5s5p^3$	$^3P_1$–$5s^25p4f$	$^3F_2$
6	1775.44	56324.1	4.5		$5s^25p6s$	$^3P_1$–$5s^25p6p$	$^1D_2$
8	1782.05	56115.1	5.2		$5s^25p5d$	$^3F_3$–$5s^25p4f$	$^1D_2$
5	1818.40	54993.4	3.2		$5s^25p5d$	$^3D_1$–$5s^25p6p$	$^3D_1$
9	1844.91	54203.2	3.2	9	$5s5p^3$	$^1D_2$–$5s^25p4f$	$^1F_3$
5	1845.87	54175.0	4.6		$5s^25p5d$	$^3D_2$–$5s^25p6p$	$^3D_2$
6	1862.62	53687.8	7.3	9	$5s^25p5d$	$^3F_3$–$5s^25p4f$	$^1G_4$

continued

Table 1—*continued*

Intensity	λ [Å] (vac.)	σ [cm^{-1}]		Ref.	Classification		
		Obs	Calc				
4	1870.87	53451.1	1.3		$5s^25p5d$	$^3D_2$–$5s^25p6p$	$^3P_1$
3	1893.79	52804.2	3.9		$5s^25p5d$	$^3F_2$–$5s^25p4f$	$^3D_1$
2	1920.49	52070.0	0.0		$5s^25p5d$	$^1F_3$–$5s^25p6p$	$^3D_3$
10	1921.44	52044.3	4.0	9	$5s5p^3$	$^3P_2$–$5s^25p4f$	$^3G_3$
3	1928.68	51848.9	8.6		$5s5p^3$	$^3S_1$–$5s^25p4f$	$^3D_2$
2	1944.34	51431.3	0.4		$5s^25p5d$	$^3P_0$–$5s^25p6p$	$^3P_1$
4	1959.60	51030.8	1.3		$5s^25p5d$	$^3P_1$–$5s^25p6p$	$^3D_2$
6	1976.36	50598.1	8.2		$5s^25p5d$	$^1P_1$–$5s^25p6p$	$^1D_2$
5	1987.79	50307.1	8.0		$5s^25p5d$	$^3P_1$–$5s^25p6p$	$^3P_1$
	λ (Å) (air)						
2	2024.35	49382.7	3.9		$5s^25p5d$	$^1D_2$–$5s^25p6p$	$^3D_2$
8	2029.75	49251.3	2.0		$5s^25p5d$	$^3F_2$–$5s^25p4f$	$^3D_3$
6	2032.56	49183.2	3.4		$5s^25p6s$	$^3P_0$–$5s^25p6p$	$^1P_1$
5	2040.86	48983.2	3.6		$5s^25p6s$	$^3P_1$–$5s^25p6p$	$^3S_1$
1	2089.12	47851.8	1.4		$5s^25p5d$	$^1P_1$–$5s^25p6p$	$^3S_1$
8	2123.69	47073.0	3.0		$5s5p^3$	$^1P_1$–$5s^25p4f$	$^1D_2$
4	2124.25	47060.6	0.6		$5s^25p5d$	$^3D_2$–$5s^25p6p$	$^3D_1$
5	2138.99	46736.3	6.3		$5s^25p5d$	$^3F_3$–$5s^25p4f$	$^3D_2$
9	2145.16	46601.9	2.1		$5s^25p6s$	$^1P_1$–$5s^25p6p$	$^1S_0$
8	2184.69	45758.8	8.0		$5s^25p5d$	$^3P_2$–$5s^25p4f$	$^1D_2$
3	2228.33	44862.7	2.3	6	$5s^25p5d$	$^1P_1$–$5s^25p6p$	$^3P_2$
4	2311.04	43257.3	7.5	6	$5s^25p5d$	$^1P_1$–$5s^25p6p$	$^1P_1$
11	2409.59	41488.3	8.3	6	$5s^25p6s$	$^3P_2$–$5s^25p6p$	$^1D_2$
2	2435.82	41041.5	0.9		$5s^25p5d$	$^1F_3$–$5s^25p6p$	$^3D_2$
14bl	2441.49	40946.2	6.0		$5s^25p6s$	$^3P_1$–$5s^25p6p$	$^3D_2$
15	2441.86	40940.0	39.7		$5s5p^3$	$^1D_2$–$5s^25p4f$	$^3G_3$
10	2443.37	40914.7	4.8	9	$5s^25p5d$	$^3F_3$–$5s^25p4f$	$^3F_4$
12	2473.11	40422.7	2.5	6	$5s^25p6s$	$^3P_0$–$5s^25p6p$	$^3P_1$
9	2485.41	40222.7	2.7	6	$5s^25p6s$	$^3P_1$–$5s^25p6p$	$^3P_1$
5	2513.88	39767.1	6.4	6	$5s^25p6s$	$^3P_1$–$5s^25p6p$	$^3P_0$
1	2522.04	39638.6	8.1		$5s5p^3$	$^1P_1$–$5s^25p4f$	$^3D_1$
11	2538.60	39380.0	79.8	9	$5s^25p5d$	$^3F_3$–$5s^25p4f$	$^1F_3$
6	2664.68	37516.8	7.0	6	$5s^25p6s$	$^1P_1$–$5s^25p6p$	$^1D_2$
15w	2691.74	37139.7	9.1	5,6	$5s^25p6s$	$^3P_2$–$5s^25p6p$	$^3D_3$
3	2780.10	35959.4	9.4		$5s^25p5d$	$^3F_4$–$5s^25p4f$	$^3D_3$
6	2796.17	35752.7	2.4	6	$5s^25p6s$	$^3P_2$–$5s^25p6p$	$^3P_2$
9	2848.43	35096.8	6.7	9	$5s^25p5d$	$^3F_2$–$5s^25p4f$	$^3F_2$
11	2875.15	34770.6	1.2 0.2	 6	$5s^25p5d$ $5s^25p6s$	$^1P_2$–$5s^25p4f$ $^1P_1$–$5s^25p6p$	$^3D_3$ $^3S_1$
10	2927.64	34147.3	7.6	6	$5s^25p6s$	$^3P_2$–$5s^25p6p$	$^1P_1$
3	2936.86	34040.1	0.3	6	$5s^25p5d$	$^1P_1$–$5s^25p6p$	$^3P_0$
12	2937.57	34031.8	1.8	6	$5s^25p6s$	$^3P_0$–$5s^25p6p$	$^3D_1$
10	2954.93	33831.9	2.0	6	$5s^25p6s$	$^3P_1$–$5s^25p6p$	$^3D_1$
13	3015.09	33156.9	7.0	9	$5s^25p5d$	$^3F_2$–$5s^25p4f$	$^3F_3$
16	3077.71	32485.5	2.4		$5s^25p5d$	$^3F_4$–$5s^25p4f$	$^3G_5$
9	3109.49	32150.3	0.5	9	$5s^25p5d$	$^3D_3$–$5s^25p4f$	$^1G_4$
10	3145.57	31781.6	1.1	6	$5s^25p6s$	$^1P_1$–$5s^25p6p$	$^3P_2$
13	3149.11	31745.8	5.8		$5s^25p5d$	$^3F_4$–$5s^25p4f$	$^3F_4$
5	3227.69	30973.0	3.1		$5s^25p5d$	$^3F_3$–$5s^25p4f$	$^3F_2$
6	3230.04	30950.5	0.6		$5s^25p5d$	$^1D_2$–$5s^25p4f$	$^1D_2$
16	3305.96	30242.5	9.9	5	$5s^25p5d$	$^3F_2$–$5s^25p4f$	$^3G_3$
2	3309.11	30210.9	0.8		$5s^25p5d$	$^3F_4$–$5s^25p4f$	$^1F_3$
9	3312.92	30176.2	6.3	6	$5s^25p6s$	$^1P_1$–$5s^25p6p$	$^1P_1$
16	3330.84	30013.9	4.2	5	$5s^25p5d$	$^3F_3$–$5s^25p4f$	$^3F_4$
9	3443.32	29033.4	3.4		$5s^25p5d$	$^3F_3$–$5s^25p4f$	$^3F_3$
8	3444.70	29021.8	2.6		$5s^25p5d$	$^3P_2$–$5s^25p4f$	$^1F_3$

continued

Table 1—*continued*

Intensity	λ [Å] (vac.)	σ [cm^{-1}]		Ref.	Classification	
		Obs	Calc			
3	3556.98	28105.7	5.9		$5s^25p5d$	$^1P_1$–$5s^25p6p$ $^3D_1$
11	3792.31	26361.7	2.4		$5s^25p5d$	$^3D_2$–$5s^25p4f$ $^3D_2$
12	3803.26	26285.8	5.7	5	$5s^25p5d$	$^3P_0$–$5s^25p4f$ $^3D_1$
14	3827.98	26116.1	6.3		$5s^25p5d$	$^3F_3$–$5s^25p6p$ $^3G_3$
6	3828.89	26109.8	10.0	6	$5s^25p6s$	$^3P_2$–$5s^25p6p$ $^3D_2$
3	3938.04	25386.2	6.7	6	$5s^25p6s$	$^3P_2$–$5s^25p6p$ $^3P_1$
6	3967.25	25199.3	9.5		$5s^25p5d$	$^3D_3$–$5s^25p4f$ $^3D_2$
8	3973.01	25162.7	3.1	5	$5s^25p5d$	$^3P_1$–$5s^25p4f$ $^3D_1$
4	4038.46	24754.9	4.5		$5s^25p5d$	$^3D_2$–$5s^25p4f$ $^3D_3$
10	4237.66	23591.3	1.6		$5s^25p5d$	$^3D_3$–$5s^25p4f$ $^3D_3$
15	4305.69	23218.5	9.1	5	$5s^25p5d$	$^3P_1$–$5s^25p4f$ $^3D_2$
12	4422.08	22607.5	7.6		$5s^25p5d$	$^1F_3$–$5s^25p4f$ $^1D_2$
1	4515.67	22138.9	8.7	6	$5s^25p6s$	$^1P_1$–$5s^25p6p$ $^3D_2$
15	4558.49	21931.0	0.9	12	$5s5p^3$	$^1P_1$–$5s^25p4f$ $^3F_2$
12	4634.49	21571.3	1.7		$5s^25p5d$	$^1D_2$–$5s^25p4f$ $^3D_2$
7	4769.94	20958.8	9.1	6	$5s^25p6s$	$^1P_1$–$5s^25p6p$ $^3P_0$
9	4849.30	20615.8	5.9		$5s^25p5d$	$^3P_2$–$5s^25p4f$ $^3F_3$
15	4954.13	20179.6	9.7	5,9	$5s^25p5d$	$^1F_3$–$5s^25p4f$ $^1G_4$
12	5007.80	19963.3	3.8	5	$5s^25p5d$	$^1D_2$–$5s^25p4f$ $^3D_3$
1	5151.90	19405.0	5.1		$5s^25p6s$	$^3P_2$–$5s^25p4f$ $^3F_3$
15	5159.08	19377.9	8.0	5	$5s^25p5d$	$^3D_3$–$5s^25p4f$ $^3F_4$
15	5260.19	19005.4	5.9	5	$5s^25p5d$	$^3D_2$–$5s^25p4f$ $^1F_3$
16	5352.92	18676.2	6.2	5	$5s^25p5d$	$^3P_2$–$5s^25p4f$ $^3F_3$
15	5394.62	18531.9	1.8	5	$5s^25p5d$	$^3D_1$–$5s^25p4f$ $^3F_2$
9	5602.83	17843.2	3.0		$5s^25p5d$	$^3D_3$–$5s^25p4f$ $^1F_3$
2	5899.11	16947.0	7.3		$5s^25p5d$	$^3F_4$–$5s^25p4f$ $^3G_3$
12	5955.67	16786.1	6.6	5	$5s^25p5d$	$^1P_1$–$5s^25p4f$ $^1D_2$
1	6653.85	15024.7	4.7		$5s^25p6s$	$^1P_1$–$5s^25p6p$ $^3D_1$

Notes: Int. Observed line intensity from visual estimation.
λ (Å): Observed wavelength in Å.
vac. Values of the observed wavelength in vacuum.
air Values of the observed wavelength in air.
σ (cm^{-1}): Wave number in cm^{-1}.
Obs. Observed wave number.
Calc. Calculated wave number from the level values given in Table 2 and the work of Tauheed *et al.*[8] by the Ritz combination principle.
Ref: References of previously published lines.
Classification: Level designations for the transition including configuration, term and total angular momentum.

levels involved. We present in total, 14 classified laser lines, 11 more than were observed in the work of Larsson et al[9] using collision-based spectroscopy.

We present in Table 2 the adjusted energy level values corresponding to the analysed configurations. We have revised the energy values corresponding to the $5s^25p4f$ $^3D_1$ and $^3G_5$ levels reported in the work of Larsson et al,[9] and changed them to 209310.0 and 202281.5 cm^{-1}, respectively. We also present in Table 2 two new energy levels values in 207366.7 and 216745.6 cm^{-1} that correspond to the levels $5s^25p4f$ $^3D_2$ and $^1D_2$, respectively, in order to complete all the energy level of this configuration. Our fitted values for these levels are also in agreement with the predicted values showed in the work of Larsson et al[9] In the same table is presented also the new value in 169799.4 cm^{-1} for the $5s^25p5d$ $^3F_4$ energy level reported in the same reference. This new value is supported by four new classified lines and by the line in 3077.71 Å corresponding to the $5s^25p5d$ $^3F_4$–$5s^25p4f$ $^3G_5$ transition.

Table 2. Energy level values of Xe V

Designation		E_{Obs} (cm^{-1})	E_{Calc} (cm^{-1})	Percentage composition
$5s^25p^2$	$(^3P)^3P_0$	0.0	15.3	89 + 10 $(^1S)^1S$
	$(^3P)^3P_1$	9291.8	9300.8	99
	$(^3P)^3P_2$	14126.7	14150.2	67 + 32 $(^1D)^1D$
	$(^1D)\ ^1D_2$	28411.2	28387.8	66 + 32 $(^3P)^3P$
	$(^1S)^1S_0$	44470.4	44476.1	87 + 10 $(^3P)\ ^3P$
$5s^25p6p$	$(^2P)^3D_1$	228064.9	228484.3	67 + 30 $(^2P)^1P$
	$(^2P)^3D_2$	235178.9	234968.0	74 + 13 $(^2P)^3P$ + 12 $(^2P)^1D$
	$(^2P)^3D_3$	246208.0	246101.9	100
	$(^2P)^3P_0$	233999.3	233755.0	89 + 11 $(^2P)\ ^1S$
	$(^2P)^3P_1$	234459.6	234452.7	45 + 20 $(^2P)^1P$ + 19 $(^2P)^3S$ + 16 $(^2P)^3D$
	$(^2P)^3P_2$	244821.3	244805.1	62 + 24 $(^2P)^3D$ + 14 $(^2P)^1D$
	$(^2P)^3S_1$	247810.4	247814.9	77 + 15 $(^2P)^5P$ + 6 $(^2P)^3P$
	$(^2P)^1D_2$	250557.2	251227.1	73 + 24 $(^3P)^3P$
	$(^2P)^1P_1$	243216.5	242881.6	49 + 34 $(^2P)^1P$ + 16 $(^2P)^3D$
	$(^2P)^1S_0$	259642.3	259465.7	89 + 11 $(^2P)^3P$
$5s^25p4f$	$(^2P)^3G_3$	186746.7	186752.3	57 + 38 $(^2P)^1F$
	$(^2P)^3F_4$	190644.7	190712.6	53 + 39 $(^2P)^3F$ + 8 $(^2P)^1G$
	$(^2P)^3G_5$	202281.8	202517.7	100
	$(^2P)^3F_2$	191603.5	191268.2	81 + 11$(^2P)^3D$ + 7$(^2P)^1D$
	$(^2P)^3F_3$	189663.8	189876.0	47 + 22 $(^2P)^3D$ + 22 $(^2P)^1F$ + 9 $(^2P)^3G$
	$(^2P)^3G_4$	201545.2	201559.1	58 + 42 $(^2P)^3G$
	$(^2P)^3D_1$	209310.7	209139.1	100
	$(^2P)^3D_2$	207366.7	207204.4	80 + 16 $(^2P)^3F$
	$(^2P)^3D_3$	205758.8	205913.2	74 + 18 $(^2P)^3F$ + 7 $(^2P)^5F$
	$(^2P)^1G_4$	214317.7	214683.1	92
	$(^2P)^1F_3$	200010.2	199883.4	33 + 33 $(^2P)^3G$ + 32 $(^2P)^3F$
	$(^2P)^1D_2$	216745.6	216483.3	86 + 9 $(^2P)^3D$
$5s5p^3$	$(^4S)^5S_2$	92182.8	92202.7	93 + 6 $(^2P)^3P$
	$(^2D)^3D_1$	115286.3	115276.0	75 + 11 $(^2P)^3P$ + 8 $5s^25p5d$ $(^2P)^3D$
	$(^2D)^3D_2$	116097.0	116021.0	73 + 14 $(^2P)^3P$ + 8 $5s^25p5d$ $(^2P)^3D$
	$(^2D)^3D_3$	119919.0	119931.7	91 + 9 $5s^25p5d$ $(^2P)^3D$
	$(^2P)^3P_0$	133408.1	133406.5	92 + 8 $5s^25p5d$ $(^2P)^3P$
	$(^2P)^3P_1$	134575.2	134536.5	77 + 7 $5s^25p5d$ $(^2P)^3P$
	$(^2P)^3P_2$	134702.7	134737.0	43 + 21 $(^2D)^1D$ + 11 $5s^25p5d$ $(^2P)^1D$ + 6 $5s^25p5d$ $(^2P)^3P$
	$(^4S)^3S_1$	155518.1	155545.3	62 + 30 $(^2P)^1P$
	$(^2P)^1P_1$	169672.6	169435.1	28 + 23 $5s^25p5d$ $(^2P)^5P$ + 13 $5s^25p5d$ $(^2P)^3P$ + 9 $5s^25p5d$ $(^2P)^3D$ + 5 $5s^25p5d$ $(^2D)^3D$
	$(^2P)^1D_2$	145807.0	145976.2	29 + 27 $(^2P)^3P$ + 32 $5s^25p5d$ $(^2P)^1D$ + 6 $5s^25p5d$ $(^2P)^3F$
$5s^25p5d$	$(^2P)^3F_2$	156506.8	156462.7	89 + 8 $5s5p^3$ $(^2D)^1D$
	$(^2P)^3F_3$	160630.4	160663.5	93
	$(^2P)^3F_4$	169799.4	169759.2	100
	$(^2P)^3D_1$	173071.7	173220.1	57 + 9 $(^2P)^3P$ + 19 $5s5p^3$ $(^2P)^1P$ + 11 $5s5p^3$ $(^4S)^3S$
	$(^2P)^3D_2$	181004.3	181050.6	41 + 31 $(^2P)^1D$ + 19 $5s5p^3$ $(^2D)^1D$
	$(^2P)^3D_3$	182167.2	181959.0	80 + 6 $(^2P)^3F$ + 6 $(^2P)^1F$ + 8 $5s5p^3$ $(^2D)^3D$
	$(^2P)^3P_0$	183025.2	183059.3	92 + 8 $5s5p^3$ $(^2P)^3P$
	$(^2P)^3P_1$	184147.6	184139.3	68 + 18 $(^2P)^3D$ + 7 $5s5p^3$ $(^2P)^3P$

continued

Table 2—*continued*

Designation		E_{Obs} (cm^{-1})	E_{Calc} (cm^{-1})	Percentage composition
	$(^2P)^3P_2$	170987.6	171018.9	48 + 25 $(^2P)^3D$ + 10 $(^2P)^1D$ + 12 $5s5p^3$ $(^2D)^1D$
	$(^2P)^1F_3$	194138.0	194190.1	90 + 8 $(^2P)^3D$
	$(^2P)^1D_2$	185795.0	185803.9	15 + 43 $(^2P)^3P$ + 22 $(^2P)^3D$ + 10 $5s5p^3$ $(^2D)^1D$ + 7 $5s5p^3$ $(^2P)^3P$
	$(^2P)^1P_1$	199959.0	200018.4	55 + 13 p^3 $(^2P)^1P$ + 24 $5s^25p6s$ $(^2P)^3P$
$5s^25p6s$	$(^2P)^3P_0$	194033.1	194065.0	99
	$(^2P)^3P_1$	194232.9	194182.5	57 + 26 $(^2P)^1P$ + 10 $5s^25p5d$ $(^2P)^1P$
	$(^2P)^3P_2$	209068.9	209045.5	100
	$(^2P)^1P_1$	213040.2	213058.2	73 + 18 $(^2P)^3P$ + 8 $5s^25p5d$ $(^2P)^1P$

Notes:

Designation: Level designation, including configuration, parentage, term and total angular momentum.

E_{Obs}: Experimental energies in cm^{-1}. The energy values for the even parity are based on odd parity levels given in the work of Tauheed *et al.*[8] and wave numbers of Table 1 weighted according to their estimated uncertainties.

E Calc: Values obtained from the least-squares fitting.

Percentage Composition: Percentage composition of the experimental energy level. Percentages lower than 5% are omitted.

In accordance with our wavelength values, we classified the laser line in 3305.96 Å as a $5s^25p5d\ ^3F_2$–$5s^25p4f\ ^3G_3$ transition, rejecting the previous classification reported by Larsson et al[9] We also report in this work a new value in 259642.3 cm^{-1} for the $5s^25p6p\ ^1S_0$ energy level.

The level values were determined in an iterative procedure where the wavenumbers of the observed lines were weighted according to their estimated uncertainties.

Theoretical predictions of the energy levels have been used in our analysis of the spectra. Relativistic Hartree–Fock calculations were used to obtain the energy parameters with the computer code developed by Cowan.[12] Predictions of the energy levels are then made by diagonalizing the energy matrices. A least-squares fit of the parameters to the observed levels was carried out involving configuration interactions.

In Table 3 we present the parameters obtained in the LSF calculations for the $5s^25p^2$, $5s^25p6p$ and $5s^25p4f$ configurations with their corresponding Hartree–Fock values and scaling factors. We have included the $5p^4$ configuration in this calculation because the $5s^25p^2$ configuration structure is affected through the s^2–p^2 interaction and the standard deviation was reduced from 368 to 328 cm^{-1}. The inclusion of the $5s^25p6p\ ^1S_0$ level made possible to let free the G^2 (5p6p) parameter, which was fixed in the table of energy parameters reported by Gallardo et al[6]

All the configuration interaction integrals were fixed at their Hartree–Fock values in the calculation except the $5s^25p^2$–$5p^4$ integral that it was fixed at 85% of its Hartree–Fock value. Hereby we achieved better results in the least-squares fit and the standard deviation was slightly reduced. These configurations structures are also affected by the interaction with the experimental unknown $5s5p^25d$ configuration, but its inclusion in this calculation significantly increases the standard deviation.

The fitted values for the odd configurations were calculated including configuration Rydberg series interaction and the new experimental value for the $5s5p^25d\ ^3F_4$ energy level. The results were in general accordance with the previously published values,[8] except that our calculation shows a small reduction of the standard deviation value, considering that we were using different scaled values for the interaction integrals.

Table 3. Energy parameters for the $5s^25p^2$, $5s^25p6p$, $5s^25p4f$ and $5p^4$ configurations of Xe V

Configuration	Parameter	HFR value (cm^{-1})	Fitted value (cm^{-1})	Fit/HF
$5s^25p^2$	E_{av}		21403	
	$F^2(5p,5p)$	55554	50278 ± 1007	0.905 ± 0.018
	$\alpha(5p,5p)$		− 143 (FIX)[a]	
	ζ_{5p}	9095	9593 ± 202	1.055 ± 0.022
$5s^25p6p$	E_{av}	225119	242484 ± 113	1.077 ± 0.001
	ζ_{5p}	9793	8739 ± 167	0.892 ± 0.017
	ζ_{6p}	2586	2594 ± 213	1.003 ± 0.082
	$F^2(5p,6p)$	19780	17839 ± 902	0.902 ± 0.046
	$G^0(5p,6p)$	4267	3503 ± 149	0.821 ± 0.035
	$G^2(5p,6p)$	5648	5846 ± 809	1.035 ± 0.143
$5s^25p4f$	E_{av}	187936	200751 ± 96	1.068 ± 0.001
	ζ_{5p}	8858	9330 ± 191	1.053 ± 0.021
	ζ_{4f}	168	168 (FIX)	1.000
	$F^2(5p,4f)$	48022	39199 ± 1173	0.816 ± 0.024
	$G^2(5p,4f)$	37402	29201 ± 825	0.781 ± 0.022
	$G^4(5p,4f)$	26627	18663 ± 1123	0.700 ± 0.042
$5p^4$	E_{av}	249988	249988 (FIX)	1.000
	$F^2(5p,5p)$	55559	55559 (FIX)	1.000
	$\alpha(5p,5p)$		0 (FIX)	
	ζ_{5p}	8994	8994 (FIX)	1.000
Configuration interaction integrals				
$5s^25p^2$–$5s^25p6p$	$R^0(5p5p, 5p6p)$	1851	1851 (FIX)	1.000
$5s^25p^2$–$5s^25p6p$	$R^2(5p5p, 5p6p)$	8658	8658 (FIX)	1.000
$5s^25p^2$–$5s^25p4f$	$R^2(5p5p, 5p4f)$	− 43668	− 43668 (FIX)	1.000
$5s^25p^2$–$5p^4$	$R^1(5s5s, 5p5p)$	72662	55680 (FIX)	0.766
$5s^25p6p$–$5s^25p4f$	$R^2(5p6p, 5p4f)$	− 5314	− 5314 (FIX)	1.000
$5s^25p6p$–$5s^25p4f$	$R^2(5p6p, 4f5p)$	− 6025	− 6025 (FIX)	1.000
	σ[b]		328	

Notes:

Configuration: Configurations involved in the calculation.

Parameter: Energy parameters.

HFR: Hartree–Fock values in cm^{-1} of the energy parameters.

Fitted value: Fitted value of the energy parameters: a, The α value is taken from the work of Tauheed *et al.*[8].

Fit/HF: Rate between fitted and Hartree–Fock energy parameter values.

Configuration interaction integrals: Values of the Configuration interaction integrals for the involved configurations.

b, The rms. deviation of the fit.

Acknowledgements—Support from the Consejo Nacional de Investigaciones Cientificas y Técnicas (CONICET), Argentina, where M. Gallardo belong as researcher, Comisión de Investigaciones Científicas de la Provincia de Buenos Aires (CIC), where M. Raineri and J.G. Reyna Almandos belong as researchers, F. Callegari and H. Sobral belong as fellows, and the Universidad Nacional de Cordoba, Argentina, for the use of the Ebert Mount Spectrograph, is gratefully acknowledged.

REFERENCES

1. Arcimowicz, B., Yoshi, Y. N. and Kaufman, V., *Can. J. Phys.*, 1989, **67**, 572.
2. Tauheed, A., Yoshi, Y. N. and Kaufman, V., *J. Phys. B*, 1991, **24**, 3701.
3. Tauheed, A., Yoshi, Y. N. and Kaufman, V., *Phys. Scr.*, 1991, **44**, 579.
4. Tauheed, A. and Yoshi, Y. N., *Phys. Scr.*, 1992, **46**, 403.
5. Duchowicz, R., Schinca, D. and Gallardo, M., *IEEE J. Quantum Electron.*, 1994, **30**, 155.
6. Gallardo, M., Raineri, M. and Reyna Almandos, J.G., *Z. Phys. D*, 1994, **30**, 261
7. Pinnington, E. H., Gosselin, R.N., Ji, Q., Kernahan, J. A. and Guo, B., *Phys. Scr.*, 1992, **46**, 40.
8. Tauheed, A., Yoshi, Y. N., Kaufman, V., Sugar, J. and Pinnington, E. H., *J. Opt. Soc. Am. B*, 1993, **10**, 561.
9. Larsson, M. O., Gonzales, A. M., Hallin, R., Heijkenskjöld, F., Nyström,B., O'Sullivan, G., Weber, C. and Wännström, A., *Phys. Scr.*, 1996, **53**, 317.
10. Valero, F. P. J., *J. Opt. Soc. Am.*, 1968, **58**, 1048.
11. Hoffmann, V. and Toschek, P., *IEEE J of Quantum Electron.*, 1970, **6**, 757.
12. Cowan, R.D., *The Theory of Atomic Structure and Spectra.* University of California Press, Berkeley, 1981.

INSTITUTE OF PHYSICS PUBLISHING JOURNAL OF PHYSICS B: ATOMIC, MOLECULAR AND OPTICAL PHYSICS

J. Phys. B: At. Mol. Opt. Phys. 35 (2002) 3411–3419 PII: S0953-4075(02)34825-9

New energy levels of the $4s^24p5s$, $4s^24p4d$ and $4s^24p5p$ configurations of the Kr V spectrum

M Raineri[1], F Bredice[1], M Gallardo[1], A G Trigueiros[2] and J Reyna Almandos[1]

[1] Centro de Investigaciones Opticas, CC 124, 1900 La Plata, Argentina
[2] Instituto de Química, Universidade do Estado do Rio de Janeiro, UERJ 20550-013, Maracana, Rio de Janeiro, Brazil

E-mail: monicar@ciop.unlp.edu.ar (M Raineri) and jreyna@ciop.unlp.edu.ar

Received 8 March 2002, in final form 3 July 2002
Published 7 August 2002
Online at stacks.iop.org/JPhysB/35/3411

Abstract

The spectrum of four-times-ionized krypton (Kr V) has been observed in the 240–2500 Å wavelength range. Three of the four possible levels of the $4s^24p5s$ configuration and two of the three remaining energy level values for the $4s^24p4d$ configurations were determined. Nine of the ten possible levels for the $4s^24p5p$ configuration are also reported. The observed configurations were interpreted theoretically by means of Hartree–Fock relativistic calculations and a least-squares fit of the energy parameters to the observed levels. 111 new classified lines are reported among the $4s^24p^2$, $4s^24p5p$, $4s4p^3$, $4s^24p5s$, and $4s^24p4d$ configurations.

1. Introduction

Energy levels of Kr I to Kr XXXVI were reviewed and compiled by Sugar and Musgrove (1991) and tables of the classified lines of Kr V to Kr XXXVI were compiled by Shirai *et al* (1995).

Four-times-ionized krypton, Kr V, belongs to the Ge I isoelectronic sequence and has the ground configuration $4s^24p^2$. The spectra of the first, second, third and fourth elements of this sequence were presented in the book *Atomic Energy Levels* (Moore 1971). The As II spectrum was reinvestigated by Li and Andrew (1971) and the Br IV spectrum was revised by Joshi and Budhiraja (1971).

The krypton isonuclear sequence has also been studied in different works by members of the Centro de Investigaciones Opticas Group, La Plata, Argentina and the Campinas Group, São Paulo, Brazil. Reyna Almandos *et al* (1996, 1998) published new energy levels for Kr III and Kr IV. Pagan *et al* (1995) reported the study of the 4s4p4d and 4s4p5s configurations of Kr VI and Raineri *et al* (2000) presented the spectroscopic analysis of the 4p4d configuration of Kr VII. All these experiments were carried out using a discharge tube and a theta-pinch discharge.

0953-4075/02/163411+09$30.00 © 2002 IOP Publishing Ltd Printed in the UK

Trigueiros *et al* (1989, 1993), and references therein, studied the Kr v spectrum using different spectral sources. These authors presented new energy levels of the $4s^24p^2$, $4s4p^3$, $4s^24p4d$ and $4p^4$ configurations.

In this work we report an extended analysis of the four-times-ionized krypton (Kr v). We have established three new energy levels for the $4s^24p5s$, two for the $4s^24p4d$ and nine for the $4s^24p5p$ configurations. 111 new lines were classified as combinations between levels of $4s^24p^2$, $4s^24p5p$, $4s4p^3$, $4s^24p5s$, and $4s^24p4d$ configurations. Analysis of the experimental data used Hartree–Fock calculation and parametric fit.

Configurations of the type $ns^2np n'p$ have been studied by Kramida *et al* (1999) ($n = 2$, $n' = 3$) and Gallardo *et al* (1999) ($n = 5$, $n' = 6$) for elements of the same homologous sequence.

The interest in spectroscopic data for rare gases is due to applications in collision physics, laser physics, photo-electron spectroscopy and fusion diagnostics.

2. Experiment

The work is based on photographic recordings of the spectra of krypton between 240 and 2500 Å. We have used two different light sources in our experiment, a discharge tube and a theta-pinch discharge. In both cases the energy is fed into the plasma using a capacitor bank, charged from a high-voltage power supply. The discharge tube was built at the Centro de Investigaciones Opticas (CIOp), La Plata, Argentina, to study highly ionized gases (Gallardo *et al* 1989). It is made with a Pyrex tube ending in a quartz window. The electrodes, 20 cm apart, were made of tungsten and covered with indium. The gas pressure was measured by a thermocouple vacuum gauge before and after exposures. The pressure range was varied between 20 and 300 mTorr. Gas excitation was produced by discharging through the tube a bank of low-inductance capacitors varying between 2.5 and 100 nF and charged up to 19 kV. A normal-incidence vacuum spectrograph with a concave diffraction grating of 1200 lines mm^{-1} was used. The plate factor in the first order is 2.77 Å mm^{-1}. Kodak SWR plates were used to record the spectra. C III, N II and N III (Kelly 1987), O III (Pettersson 1982) and known lines of krypton (Kelly 1987, Shirai *et al* 1995, Raineri *et al* 1998) were recorded as internal standard lines.

The other experimental data were obtained several years ago by two of the authors (JRA and AGT) at the Lund Institute of Technology, Sweden, using the theta pinch discharge. This consisted primarily of a cylindrical discharge tube, excited by an induction coil. The spark gap was pressurized with air. It was ignited by lowering the pressure in the spark chamber by means of a magnetic valve and triggered when the capacitor voltage reached a preset value. The theta pinch device had the following specifications: total capacitance 7.7 μF, total inductance 76 nH, period of damped oscillation 4.8 μs. Maximum current at 10 kV discharge voltage is about 100 kA. The repetition rate of the discharge was about 15 min^{-1} at a capacitor bank voltage of 10 kV. A 3 m normal-incidence vacuum spectrograph with a concave diffraction grating of 1200 lines mm^{-1} was used. The plate factor in the first order was 2.77 Å mm^{-1}. The spectra were exposed on Kodak SWR plates and the lines from C III, N II and N III (Kelly 1987), O III (Pettersson 1982) and known lines of krypton (Kelly 1987) were used as internal standards.

To distinguish between different states of ionization in both spectral sources, a number of experimental parameters, e.g., gas pressure, discharge voltage, capacitance and the number of discharges were varied (Gallardo *et al* 1989, Trigueiros *et al* 1989). The approximate total number of Kr lines for all stages observed over the pertinent wavelength range was 7500. The accuracy of the wavelength values is estimated to be ± 0.01 and ± 0.02 Å in the measurements of Lund and La Plata respectively.

3. Analysis

The line identifications were guided by theoretical predictions of the energy level structure and line strengths obtained from the Cowan (1981) computer code, using Hartree–Fock relativistic (HFR) wavefunctions.

The new Kr v classified lines observed in the present work are given in table 1. The intensities of the lines are based on visual estimates and the wavenumber values in the calculated column are derived from the experimental energy level values, which, in turn, were derived from the observed lines. The predicted wavelength and log gf values, shown in columns 3 and 4 of this table, were obtained considering the fitted values for the energy parameters, in the HF calculation. This kind of calculation was also used to obtain the values of weighted oscillator strengths for Kr III and Kr IV spectra (Raineri *et al* 1998, Bredice *et al* 2000).

The new energy level values derived from the observed lines belonging to the $4s^24p5p$, $4s^24p4d$ and $4s^24p5s$ configurations are given in table 2. The energy level values were determined from the observed wavelengths. In our case the uncertainties of the adjusted experimental energy level values are generally less than 2 cm^{-1}. All level designations in table 2 are in LS notation, and in the same table we present the percentage composition of the levels that were taken from the least-squares fit.

The configuration set used in the calculation was $4s^24p^2$, $4s^24p5p$, $4s4p^24d$, $4p^4$ and $4s^24p4f$ for the even parity and $4s4p^3$, $4s^24p4d$ and $4s^24p5s$ for the odd parity.

(i) $4s^24p4d$. The $4s^24p4d$ configuration was studied by Trigueiros *et al* (1989). In this work we have extended the analysis reporting the new values 190279 and 192949 cm^{-1} for the $^3F_2$ and $^3F_3$ energy levels respectively. These levels were found by transitions with the new $4s^24p5p$ and ground configurations. The theoretical value for the remaining $^3F_4$ energy level of the $4s^24p4d$ configuration obtained from the least-squares fit is 196425 cm^{-1}.

(ii) $4s^24p5s$. We propose three new energy level values of this configuration. For the $^3P_1$, $^3P_2$ and $^1P_1$ levels, the experimental values are 240926, 246798 and 250993 cm^{-1} respectively. These levels were also found by transitions with the new $4s^24p5p$ and ground configurations. The calculated value for the $^3P_0$ energy level, obtained from the least-squares fit, is 238871 cm^{-1}.

(iii) $4s^24p5p$. Of the ten possible levels of this configuration, we found nine of them by transitions with the $4s4p^3$ and $4s^24p4d$ configurations. Only the level $4s^24p5p$ $^3P_0$ was not determined. The theoretical value for this level obtained from the least-squares fit is 284942 cm^{-1}. From the percentage composition of table 1, we can observe that the $^3D_1$ and $^1P_1$ levels are very mixed. In this case the LS designation has very little physical significance.

4. Theoretical interpretation

The configurations were interpreted by fitting the theoretical energy expression to the observed energy levels using least-squares techniques. The adjusted parameter values for the odd and even configurations are compared with results from HFR calculations in tables 3 and 4 respectively.

For the odd parity the matrix included the $4s4p^3 + 4s^24p4d + 4s^24p5s$ configurations. The fitted energy parameters were in accordance with scaled Hartree–Fock values. The effective electrostatic parameter α(4p, 4p) and the configuration interaction integral R^1(4p4p, 4s4d) between $4s4p^3$ and $4s^24p4d$ configurations were optimized and fixed in order to obtain better

Table 1. Classified lines of Kr v. Int: line intensities from visual estimation. Key to symbols: w, this line appeared wider than the others in our experiment; d, the line contour is not clear in our plate, increasing the error in the measurement; us, shaded to shorter wavelengths; ul, shaded to longer wavelengths. (,): these lines appeared blended.

Int. and shape[a]	λ_{obs} (Å)	λ_{pred} (Å)	Log gf	σ_{obs} (cm^{-1})	σ_{cal} (cm^{-1})[b]	Transition
12	2490.95	2495.11	−1.043	40 145	40 145	$4s^24p5p\ ^3P_2$–$4s^24p5s\ ^1P_1$
9	2426.80	2429.37	−0.267	41 206	41 207	$4s^24p5p\ ^3D_1$–$4s^24p4d\ ^1P_1$
20w	2387.50	2386.44	−0.596	41 885	41 885	$4s^24p5p\ ^3P_1$–$4s^24p5s\ ^3P_2$
10w	2341.13	2341.95	−0.911	42 714	42 712	$4s^24p5p\ ^3S_1$–$4s^24p5s\ ^1P_1$
50w	2339.19	2335.17	0.141	42 750	42 751	$4s^24p5p\ ^3D_2$–$4s^24p5s\ ^3P_1$
100w	2314.79	2316.24	0.475	43 200	43 200	$4s^24p5p\ ^3D_3$–$4s^24p5s\ ^3P_2$
100w	2255.34	2259.41	0.280	44 339	44 340	$4s^24p5p\ ^3P_2$–$4s^24p5s\ ^3P_2$
100w	2192.60	2190.33	0.290	45 608	45 607	$4s^24p5p\ ^1D_2$–$4s^24p5s\ ^1P_1$
20w	2181.60	2186.99	−0.659	45 838	45 838	$4s^24p5p\ ^1P_1$–$4s^24p4d\ ^1P_1$
50w	2176.02	2174.76	−0.194	45 955	45 956	$4s^24p5p\ ^3D_2$–$4s^24p4d\ ^1P_1$
20w	2131.83	2133.08	0.054	46 908	46 907	$4s^24p5p\ ^3S_1$–$4s^24p5s\ ^3P_2$
10	2007.96	2006.57	−0.869	49 802	49 802	$4s^24p5p\ ^1D_2$–$4s^24p5s\ ^3P_2$
9	1991.63	1993.77	−1.269[a]	50 210	50 212	$4s^24p5p\ ^3P_2$–$4s^24p5s\ ^3P_1$
11	1894.70	1894.75	−0.700	52 779	52 779	$4s^24p5p\ ^3S_1$–$4s^24p5s\ ^3P_1$
8	1796.21	1794.26	−1.629[a]	55 673	55 674	$4s^24p5p\ ^1D_2$–$4s^24p5s\ ^3P_1$
7	1789.65	1790.12	−2.806	55 877	55 877	$4s^24p5p\ ^3D_3$–$4s^24p4d\ ^1F_3$
6	1764.47	1765.43	−0.370	56 674	56 674	$4s^24p5p\ ^1S_0$–$4s^24p5s\ ^1P_1$
3	1698.42	1698.03	−0.778	58 878	58 879	$4s^24p5p\ ^1D_2$–$4s^24p4d\ ^1P_1$
10	1661.72	1657.07	−2.726[b]	60 179	60 181	$4s^24p5p\ ^3D_1$–$4s^24p4d\ ^3D_1$
10	1611.49	1616.72	−1.050	62 054	62 053	$4s^24p5p\ ^3D_1$–$4s^24p4d\ ^1D_2$
8	1599.82	1603.29	−2.786[b]	62 507	62 508	$4s^24p5p\ ^3D_1$–$4s^24p4d\ ^3P_0$
10	1568.91	1568.57	−1.279	63 738	63 736	$4s^24p5p\ ^1P_1$–$4s^24p4d\ ^3D_2$
9	1566.03	1562.27	−1.653	63 856	63 854	$4s^24p5p\ ^3D_2$–$4s^24p4d\ ^3D_2$
12w	1555.39	1555.69	−0.883	64 293	64 295	$4s^24p5p\ ^3D_2$–$4s^24p4d\ ^3D_3$
3d	1542.91	1540.61	−2.862[b]	64 813	64 812	$4s^24p5p\ ^1P_1$–$4s^24p4d\ ^3D_1$
15w	1540.07	1534.53	−3.522[b]	64 932	64 930	$4s^24p5p\ ^3D_2$–$4s^24p4d\ ^3D_1$
9	1538.55	1539.95	−1.294	64 996	64 995	$4s^24p5p\ ^3D_1$–$4s^24p4d\ ^3P_1$
5	1499.64	1505.67	−2.587[b]	66 683	66 684	$4s^24p5p\ ^1P_1$–$4s^24p4d\ ^1D_2$
2d	1498.28	1498.77	−1.876[b]	66 743	66 741	$4s^24p5p\ ^1S_0$–$4s^24p5s\ ^3P_1$
10ul	1452.26	1449.56	−1.564	68 858	68 860	$4s^24p5p\ ^3P_1$–$4s^24p4d\ ^3D_2$
10	1436.20	1438.86	−2.530[b]	69 628	69 626	$4s^24p5p\ ^1P_1$–$4s^24p4d\ ^3P_1$
10)	1433.78	1433.56	−1.551	69 746	69 744	$4s^24p5p\ ^3D_2$–$4s^24p4d\ ^3P_1$
15wul	1429.84	1425.65	−0.811	69 938	69 936	$4s^24p5p\ ^3P_1$–$4s^24p4d\ ^3D_1$
15wul	1429.84	1431.02	−4.565[b]	69 938	69 946	$4s^24p5p\ ^1S_0$–$4s^24p4d\ ^1P_1$
12w	1424.97	1423.36	−1.668	70 177	70 175	$4s^24p5p\ ^3D_3$–$4s^24p4d\ ^3D_2$
15w	1416.14	1417.90	−0.516	70 614	70 616	$4s^24p5p\ ^3D_3$–$4s^24p4d\ ^3D_3$
15	1402.20	1401.70	−0.360	71 316	71 315	$4s^24p5p\ ^3P_2$–$4s^24p4d\ ^3D_2$
14)	1393.61	1396.40	−0.197	71 756	71 756	$4s^24p5p\ ^3P_2$–$4s^24p4d\ ^3D_3$
15	1392.63	1395.68	−0.447	71 807	71 808	$4s^24p5p\ ^3P_1$–$4s^24p4d\ ^1D_2$
20	1384.59	1386.03	−0.379	72 223	72 222	$4s^24p5p\ ^1P_1$–$4s^24p4d\ ^3P_2$
9	1383.86	1385.66	−1.350	72 262	72 263	$4s^24p5p\ ^3P_1$–$4s^24p4d\ ^3P_0$
11	1382.35	1381.11	−1.170	72 341	72 340	$4s^24p5p\ ^3D_2$–$4s^24p4d\ ^3P_2$
8	1367.56	1371.37	−2.130	73 123	73 123	$4s^24p5p\ ^3D_3$–$4s^24p4d\ ^1D_2$
10	1337.77	1338.09	−1.932[b]	74 751	74 750	$4s^24p5p\ ^3P_1$–$4s^24p4d\ ^3P_1$
9)	1334.08	1331.19	−0.729	74 958	74 958	$4s^24p5p\ ^3S_1$–$4s^24p4d\ ^3D_1$
11	1302.43	1300.06	−1.258	76 780	76 777	$4s^24p5p\ ^1D_2$–$4s^24p4d\ ^3D_2$
10	1301.58	1305.03	−1.339	76 830	76 830	$4s^24p5p\ ^3S_1$–$4s^24p4d\ ^1D_2$

Table 1. (Continued.)

Int. and shape[a]	λ_{obs} (Å)	λ_{pred} (Å)	Log gf	σ_{obs} (cm^{-1})	σ_{cal} (cm^{-1})[c]	Transition
10	1295.08	1295.51	−1.291	77215	77218	$4s^24p5p\ ^1D_2$–$4s^24p4d\ ^3D_3$
(10	1292.87	1292.29	−0.992	77347	77346	$4s^24p5p\ ^3P_1$–$4s^24p4d\ ^3P_2$
7	1284.47	1280.80	−2.370	77853	77853	$4s^24p5p\ ^1D_2$–$4s^24p4d\ ^3D_1$
6d	1271.28	1271.42	−2.300[b]	78661	78661	$4s^24p5p\ ^3D_3$–$4s^24p4d\ ^3P_2$
12w	1254.32	1256.55	−1.000	79724	79725	$4s^24p5p\ ^1D_2$–$4s^24p4d\ ^1D_2$
12	1253.54	1254.54	−0.881	79774	79772	$4s^24p5p\ ^3S_1$–$4s^24p4d\ ^3P_1$
10)	1253.12	1254.10	−1.022	79801	79801	$4s^24p5p\ ^3P_2$–$4s^24p4d\ ^3P_2$
10	1214.07	1214.19	−1.119	82368	82368	$4s^24p5p\ ^3S_1$–$4s^24p4d\ ^3P_2$
10	1209.63	1209.68	−1.886	82670	82667	$4s^24p5p\ ^1D_2$–$4s^24p4d\ ^3P_1$
7	1128.04	1129.30	−0.268	88649	88649	$4s^24p5p\ ^3D_1$–$4s^24p4d\ ^3F_2$
3d	1117.09	1117.40	−1.813	89518	89518	$4s^24p5p\ ^1P_1$–$4s4p^3\ ^1P_1$
12w	1102.19	1099.36	0.108	90728	90728	$4s^24p5p\ ^3D_2$–$4s^24p4d\ ^3F_3$
(12	1072.04	1073.97	−0.498	93280	93280	$4s^24p5p\ ^1P_1$–$4s^24p4d\ ^3F_2$
15w	1070.69	1071.01	−0.867	93397	93398	$4s^24p5p\ ^3D_2$–$4s^24p4d\ ^3F_2$
12	1030.40	1028.71	−0.841	97050	97049	$4s^24p5p\ ^3D_3$–$4s^24p4d\ ^3F_3$
11	1018.44	1017.35	−0.904	98189	98189	$4s^24p5p\ ^3P_2$–$4s^24p4d\ ^3F_3$
11	1016.22	1016.81	−1.041	98404	98404	$4s^24p5p\ ^3P_1$–$4s^24p4d\ ^3F_2$
5	1003.37	1002.96	−5.744[b]	99664	99664	$4s^24p5p\ ^3S_1$–$4s4p^3\ ^1P_1$
20wus	1002.74	1003.85	−2.444	99727	99719	$4s^24p5p\ ^3D_3$–$4s^24p4d\ ^3F_2$
20wus	965.09	964.78	−1.784	103617	103619	$4s^24p5p\ ^3P_1$–$4s4p^3\ ^3S_1$
7	964.77	962.73	−1.770	103652	103651	$4s^24p5p\ ^1D_2$–$4s^24p4d\ ^3F_3$
2	940.55	940.92	−2.342	106321	106321	$4s^24p5p\ ^1D_2$–$4s^24p4d\ ^3F_2$
9	880.08	879.90	−0.807	113626	113626	$4s^24p5p\ ^1S_0$–$4s4p^3\ ^1P_1$
2	815.62	815.85	−0.572	122606	122603	$4s^24p5p\ ^1S_0$–$4s4p^3\ ^3S_1$
4d	767.69	768.03	−1.736	130261	130260	$4s^24p5p\ ^3D_1$–$4s4p^3\ ^3P_2$
8	767.35	767.75	−1.467	130319	130318	$4s^24p5p\ ^3S_1$–$4s4p^3\ ^1D_2$
50w	763.35	763.03	−3.652[b]	131001	131003	$4s^24p5p\ ^3D_1$–$4s4p^3\ ^3P_0$
11	750.67	750.72	−0.583	133214	133213	$4s^24p5p\ ^1D_2$–$4s4p^3\ ^1D_2$
3d	707.56	707.87	−2.046	141330	141330	$4s^24p5p\ ^3D_3$–$4s4p^3\ ^3P_2$
9	701.9	702.47	−1.216	142470	142470	$4s^24p5p\ ^3P_2$–$4s4p^3\ ^3P_2$
10	689.47	689.77	−1.234	145039	145037	$4s^24p5p\ ^3S_1$–$4s4p^3\ ^3P_2$
9	687.66	687.71	−1.226	145421	145418	$4s^24p5p\ ^3S_1$–$4s4p^3\ ^3P_1$
4d	685.98	685.73	−1.683	145777	145780	$4s^24p5p\ ^3S_1$–$4s4p^3\ ^3P_0$
3d	676.00	675.99	−2.798[b]	145929	147932	$4s^24p5p\ ^1D_2$–$4s4p^3\ ^3P_2$
6)	674.24	674.01	−3.251[b]	148315	148313	$4s^24p5p\ ^1D_2$–$4s4p^3\ ^3P_1$
7	655.05	655.24	−1.177	152660	152661	$4s^24p5p\ ^3D_2$–$4s4p^3\ ^3D_3$
10	650.27	650.26	−1.046	153782	153780	$4s^24p5p\ ^1P_1$–$4s4p^3\ ^3D_2$
6	649.78	650.17	−2.361[b]	153898	153900	$4s^24p5p\ ^1P_1$–$4s4p^3\ ^3D_1$
6	649.78	649.17	−2.135	153898	153898	$4s^24p5p\ ^3D_2$–$4s4p^3\ ^3D_2$
9	629.00	629.47	−1.414	158982	158982	$4s^24p5p\ ^3D_3$–$4s4p^3\ ^3D_3$
9	628.83	628.86	−1.018	159025	159025	$4s^24p5p\ ^3P_1$–$4s4p^3\ ^3D_1$
8	627.40	627.53	−2.219	159388	159380	$4s^24p5p\ ^1S_0$–$4s4p^3\ ^3P_1$
40wul	624.53	625.20	−0.664	160120	160122	$4s^24p5p\ ^3P_2$–$4s4p^3\ ^3D_3$
3	624.13	623.88	−2.660[b]	160223	160219	$4s^24p5p\ ^3D_3$–$4s4p^3\ ^3D_2$
8	619.73	619.68	−1.339	161361	161359	$4s^24p5p\ ^3P_2$–$4s4p^3\ ^3D_2$
5	619.31	619.60	−2.426	161470	161480	$4s^24p5p\ ^3P_2$–$4s4p^3\ ^3D_1$
(4	603.91	604.14	−1.368	165588	165584	$4s^24p5p\ ^1D_2$–$4s4p^3\ ^3D_3$

Table 1. (Continued.)

Int. and shape[a]	λ_{obs} (Å)	λ_{pred} (Å)	Log gf	σ_{obs} (cm^{-1})	σ_{cal} (cm^{-1})[c]	Transition
12ul	586.31	585.90	−1.519	170 555	170 556	$4s^24p^2\ ^1D_2$–$4s^24p4d\ ^3F_2$
10	577.28	577.75	−2.109	173 226	173 226	$4s^24p^2\ ^1D_2$–$4s^24p4d\ ^3F_3$
9	547.38	547.08	−1.822	182 688	182 684	$4s^24p^2\ ^3P_2$–$4s^24p4d\ ^3F_2$
11w	539.50	539.97	−1.210	185 357	185 354	$4s^24p^2\ ^3P_2$–$4s^24p4d\ ^3F_3$
11ul	536.08	535.91	−1.854	186 539	186 536	$4s^24p^2\ ^3P_1$–$4s^24p4d\ ^3F_2$
7	495.72	495.82	0.019	201 727	201 722	$4s^24p^2\ ^1S_0$–$4s^24p5s\ ^3P_1$
7	472.19	472.22	0.037	211 779	211 789	$4s^24p^2\ ^1S_0$–$4s^24p5s\ ^1P_1$
5	452.08	452.03	−2.672[b]	221 200	221 203	$4s^24p^2\ ^1D_2$–$4s^24p5s\ ^3P_1$
6	440.37	440.29	−1.168	227 082	227 075	$4s^24p^2\ ^1D_2$–$4s^24p5s\ ^3P_2$
15	432.41	432.33	0.034	231 262	231 270	$4s^24p^2\ ^1D_2$–$4s^24p5s\ ^1P_1$
12d	428.56	428.57	−0.679	233 340	233 331	$4s^24p^2\ ^3P_2$–$4s^24p5s\ ^3P_1$
10	421.63	421.68	−0.855	237 175	237 183	$4s^24p^2\ ^3P_1$–$4s^24p5s\ ^3P_1$
15w	418.08	418.01	−0.109	239 234	239 203	$4s^24p^2\ ^3P_2$–$4s^24p5s\ ^3P_2$
10	415.08	415.13	−0.692	240 917	240 926	$4s^24p^2\ ^3P_0$–$4s^24p5s\ ^3P_1$
10	411.45	411.45	−0.519	243 043	243 055	$4s^24p^2\ ^3P_1$–$4s^24p5s\ ^3P_2$
6	410.87	410.83	−1.658[b]	243 386	243 398	$4s^24p^2\ ^3P_2$–$4s^24p5s\ ^1P_1$
6	404.45	404.49	−1.761	247 249	247 250	$4s^24p^2\ ^3P_1$–$4s^24p5s\ ^1P_1$

[a] Lines with cancellation factor (Cowan 1981) <0.05.
[b] Calculated wavenumber.

Table 2. New energy levels of the $4s^24p4d$, $4s^24p5s$ and $4s^24p5p$ configurations of Kr v.

Designation		E_{exp} (cm^{-1})	E_{calc} (cm^{-1})[a]	Percentage composition[b]
$4s^24p4d$	$^3F_2$	190 279	190 362	99
	$^3F_3$	192 949	192 770	99
	$^3F_4$	—	196 425	100
$4s^24p5s$	$^3P_0$		238 871	99
	$^3P_1$	240 926	240 908	67 + 24 $4s^24p4d\ ^1P$ + 5 $4s4p^3\ ^1P$
	$^3P_2$	246 798	246 806	100
	$^1P_1$	250 993	250 987	79 + 12 $4s^24p5s\ ^3P$ + 7 $4s^24p4d\ ^1P$
$4s^24p5p$	$^3D_1$	278 928	278 926	56 + 42 $4s^24p5p\ ^1P$
	$^3D_2$	283 677	283 745	85 + 8 $4s^24p5p\ ^3P$ + 6 $4s^24p5p\ ^1D$
	$^3D_3$	289 998	289 992	99
	$^3P_0$	—	284 942	92 + 6 $4s^24p5p\ ^1S$
	$^3P_1$	288 683	288 722	64 + 22 $4s^24p5p\ ^1P$ + 12 $4s^24p5p\ ^3D$
	$^3P_2$	291 138	291 079	78 + 13 $4s^24p5p\ ^3D$ + 8 $4s^24p5p\ ^1D$
	$^3S_1$	293 705	293 699	86 + 9 $4s^24p5p\ ^3P$
	$^1D_2$	296 600	296 656	85 + 13 $4s^24p5p\ ^3P$
	$^1P_1$	283 559	283 488	32 + 32 $4s^24p5p\ ^3D$ + 26 $4s^24p5p\ ^3P$ + 9 $4s^24p5p\ ^3S$
	$^1S_0$	307 667	307 640	68 + 21 $4p^4\ ^1S$

[a] Calculated energy level values obtained using the fitted energy parameters.
[b] Percentages below 5% have been omitted.

results in the least-squares fit. The standard deviation was 124 cm^{-1}. If we compare this work with the report of Trigueiros *et al* (1989), we find that our electrostatic energy parameters are lower than those reported in that paper, except for the $G^3(4p4d)$ parameter of the $4s^24p4d$

Table 3. Energy parameters (cm^{-1}) for the odd-parity configurations of Kr v studied.

Configuration	Parameter	HF value	Fitted value	F/HF
$4s4p^3$	E_{av}	148 381	151 658 ± 63	1.022 ± 0.001
	$F^2(4p, 4p)$	65 943	48 764 ± 493	0.739 ± 0.007
	$\alpha(4p, 4p)$		−659 (FIX)	
	ζ_{4p}	4619	5949 ± 106	1.287 ± 0.023
	$G^1(4s,4p)$	88 242	64 666 ± 181	0.733 ± 0.002
$4s^24p4d$	E_{av}	208 466	206 922 ± 52	0.993 ± 0.001
	ζ_{4p}	4784	4528 ± 109	0.946 ± 0.023
	ζ_{4d}	273	273 (FIX)	1.000
	$F^2(4p,4d)$	52 205	41 807 ± 426	0.801 ± 0.008
	$G^1(4p, 4d)$	62 999	48 954 ± 204	0.777 ± 0.003
	$G^3(4p, 4d)$	39 020	29 318 ± 485	0.751 ± 0.012
$4s^24p5s$	E_{av}	245 727	245 132 ± 97	0.998 ± 0.001
	ζ_{4p}	4953	5309 ± 182	1.172 ± 0.036
	$G^1(4p, 5s)$	7504	6283 ± 306	0.837 ± 0.041
Configuration interaction integrals				
$4s4p^3$–$4s^24p4d$	$R^1(4p4p, 4s4d)$	72 645	57 252 (FIX)	0.788
$4s4p^3$–$4s^24p5s$	$R^1(4p4p, 4s5s)$	1472	1252 (FIX)	0.850
$4s^24p4d$–$4s^24p5s$	$R^2(4p4d, 4p5s)$	−10 756	−9143 (FIX)	0.850
	R^1 (4p4d, 5s4p)	−3103	−2638 (FIX)	0.850

configuration. The inclusion of the $^3F_2$ and $^3F_3$ levels of the $4s^24p4d$ configuration and the three new energy levels of the $4s^24p5s$ configuration affect this calculation, although the interaction integrals with the latter are not very significant.

For the even parity the matrix included the $4s^24p^2 + 4s^24p5p + 4s4p^24d + 4p^4 + 4s^24p4f$ configurations. The configuration interaction integrals among these configurations are very strong except for those involving the $4s^24p5p$ because this has little influence on the calculation. The fitted average energy value of the $4s^24p^2$ configuration is affected when we include the $4p^4$ and $4s4p^24d$ configurations in the calculation. The fitted value is increased by 8022.74 cm^{-1} with respect to the experimental energy value. If we consider in the calculation only the $4s^24p^2 + 4s^24p5p$ configurations, the average energy value maintains its real value but the standard deviation increases substantially.

The levels belonging to the $4s4p^24d$ configuration are intermixed with the levels of the $4p^4$ configuration. For this reason we did not fix E_{av} for both configurations in the least-squares fit calculation. The energy parameters ζ_{nl}, $F^k(nl, nl)$ and $G^k(nl, nl)$ for the $4s4p^24d$ configuration were fixed at 1.00, 0.85 and 0.85 of their Hartree–Fock values respectively.

From the $4s^24p^2$ and $4p^4$ we obtained two adjusted parameters (in addition to E_{av}), by linking together all Coulomb parameters $F_2(4p4p)$ in one group and the spin–orbit parameter ζ_{4p} in a second group. A similar procedure was adopted in the work of Cavalcanti *et al* (1996) for Ar v. These authors also include ns^2nd^2 ($n = 3$) type configurations in the calculation, but in our case ($n = 4$) this was not necessary because the E_{av} is so far from the other configurations. However, we included the same ns^2np4f ($n = 4$) type configurations as Gallardo *et al* (1999) for Xe v ($n = 5$), as this reduces the standard deviation in our calculation. The energy parameters E_{av}, ζ_{nl}, $F^k(nl, nl)$ and $G^k(nl, nl)$ for the ns^2np4f configuration were fixed at 1.00, 1.00, 0.85 and 0.85 of their Hartree–Fock values respectively.

All the configuration interaction integrals were held fixed in the calculation at 0.85 of their Hartree–Fock values, except for the direct radial integrals of the $4s^24p^2$–$4p^4$, $4s4p^24d$–$4p^4$ and $4s4p^24d$–$4s^24p4f$ that were fixed in the calculation to 0.75, 0.70 and 0.75 of their Hartree–Fock

Table 4. Energy parameters (cm^{-1}) for the even-parity configurations of Kr v studied. (Note: the values for the E_{av} listed in the column 'HF value' were obtained by adding the experimental average energy of the ground configuration to the Hartree–Fock values.)

Configuration	Parameter	HF value	Fitted value	F/HF
$4s^24p^2$	E_{av}	12468	20491 ± 43	1.643 ± 0.003
	$F^2(4p, 4p)$	65984[a]	52183 ± 216	0.791 ± 0.003
	$\alpha(4p, 4p)$		90 (FIX)	
	ζ_{4p}	4627[a]	5008 ± 64	1.082 ± 0.014
$4s^24p5p$	E_{av}	289834	289398 ± 31	0.998 ± 0.001
	ζ_{4p}	5014	5379 ± 72	1.073 ± 0.014
	ζ_{5p}	1255	1420 ± 69	1.131 ± 0.055
	$F^2(4p, 5p)$	21614	19865 ± 303	0.919 ± 0.014
	$G^0(4p, 5p)$	5302	4036 ± 57	0.761 ± 0.011
	$G^2(4p, 5p)$	6671	4961 ± 332	0.744 ± 0.050
$4p^4$	E_{av}	309959	291684 ± 997	0.941 ± 0.003
	$F^2(4p, 4p)$	65920[a]	443212 ± 184	0.672 ± 0.003
	$\alpha(4p, 4p)$		0 (FIX)	
	ζ_{4p}	4616[a]	4995 ± 63	1.082 ± 0.013
$4s4p^24d$	E_{av}	335994	333337 ± 398	0.992 ± 0.001
	$F^2(4p, 4p)$	66699	56694 (FIX)	0.85
	$\alpha(4p, 4p)$		0 (FIX)	
	ζ_{4p}	4769	4769 (FIX)	1.000
	ζ_{4d}	282	282	1.000
	$F^2(4p, 4d)$	52804	44884 (FIX)	0.850
	$G^1(4s, 4p)$	89160	75786 (FIX)	0.850
	$G^2(4s, 4d)$	44464	37795 (FIX)	0.850
	$G^1(4p, 4d)$	64061	54452 (FIX)	0.850
	$G^3(4p, 4d)$	39678	33726 (FIX)	0.850
$4s^24p4f$	E_{av}	341257	341257 (FIX)	1.000
	ζ_{4p}	4986	4986 (FIX)	1.000
	ζ_{4f}	3	3 (FIX)	1.000
	$F^2(4p, 4f)$	27406	23295(FIX)	0.850
	$G^2(4p, 4f)$	18274	15533 (FIX)	0.850
	$G^4(4p, 4f)$	12165	10339 (FIX)	0.850
Configuration interaction integrals				
$4s^24p^2$–$4s^24p5p$	$R^0(4p4p, 4p5p)$	2325	1976 (FIX)	0.850
	$R^2(4p4p, 4p5p)$	10824	9200 (FIX)	0.850
$4s^24p^2$–$4p^4$	$R^1(4s4s, 4p4p)$	88211	66159 (FIX)	0.750
$4s^24p^2$–$4s4p^24d$	$R^1(4s4p, 4p4d)$	73683	62631 (FIX)	0.850
	$R^2(4s4p, 4d4p)$	54405	46245 (FIX)	0.850
$4s^24p^2$–$4s^24p4f$	$R^2(4p4p, 4p4f)$	32895	27961 (FIX)	0.850
$4s^24p5p$–$4s4p^24d$	$R^1(4s5p, 4p4d)$	−2359	−2005 (FIX)	0.850
	$R^2(4s5p, 4d4p)$	7837	6662 (FIX)	0.850
$4s^24p5p$–$4s^24p4f$	$R^2(4p5p, 4p4f)$	−9187	−7809 (FIX)	0.850
	$R^2(4p5p, 4p4f)$	2381	2025 (FIX)	0.850
$4p^4$–$4s4p^24d$	$R^1(4p4p, 4s4d)$	73265	51285 (FIX)	0.700
$4s4p^24d$–$4s^24p4f$	$R^1(4p4d, 4s4f)$	46595	34946 (FIX)	0.750
	$R^2(4p4d, 4f4s)$	27418	23306 (FIX)	0.850

[a] Linked parameters. These parameters were linked (i.e. the mutual ratios of their values remained constant during the iteration) during the least-squares calculation (Cowan 1981).

values respectively. In this way we achieved better results in the least-squares fit. The standard deviation was 82 cm^{-1}.

Acknowledgments

We are grateful to Dr W Persson and Dr S-G Pettersson for the use of experimental facilities, and support from the Swedish Natural Science Research Council (NFR), the Conselho Nacional de Desemvolvimiento Científico e Tecnológico, Brazil, the Fundação de Amparo à Pesquisa do Estado de São Paulo (Fapesp), Brazil and the Consejo Nacional de Investigaciones Científicas y Técnicas (CONICET). The Comisión de Investigaciones Científicas (CIC) de la Provincia de Buenos Aires, Argentina, where MR, FB and JRA are researchers, is gratefully acknowledged.

References

Bredice F, Raineri M, Reyna Almandos J, Gallardo M and Trigueiros A G 2000 *J. Quant. Spectrosc. Radiat. Transfer* **65** 805–19

Cavalcanti G H, Gallardo M, Reyna Almandos J G, Gomide J V B and Trigueiros A G 1996 *J. Phys. B: At. Mol. Opt. Phys.* **29** 6049–53

Cowan R D 1981 *The Theory of Atomic Structure and Spectra* (Berkeley, CA: University of California Press)

Gallardo M, Bredice F, Raineri M and Reyna Almandos J G 1989 *Appl. Opt.* **28** 4513–15

Gallardo M, Raineri M, Reyna Almandos J G, Sobral H and Callegari F 1999 *J. Quant. Spectrosc. Radiat. Transfer* **61** 319–27

Joshi Y N and Budhiraja C L 1971 *Can. J. Phys.* **49** 670–7

Kelly R L 1987 *J. Phys. Chem. Ref. Data Suppl.* **16** 1

Kramida A E, Bastin T, Biemont E, Dumont P-D and Garnir H-P 1999 *Eur. Phys. J.* D **7** 547–65

Li H and Andrew K L 1971 *J. Opt. Soc. Am.* **61** 96–109

Moore C E 1971 *Atomic Energy Levels* NBS Circular no 467 (Washington, DC: US Government Printing Office)

Pagan C J B, Reyna Almandos J G, Gallardo M, Pettersson S-G, Cavalcanti G H and Trigueiros A G 1995 *J. Opt. Soc. Am.* B **12** 203–11

Pettersson S-G 1982 *Phys. Scr.* **26** 296–318

Raineri M, Reyna Almandos J, Bredice F, Gallardo M, Trigueiros A G and Pettersson S-G 1998 *J. Quant. Spectrosc. Radiat. Transfer* **60** 25–42

Raineri M, Trigueiros A G, Gallardo M and Reyna Almandos J G 2000 *Phys. Scr.* **62** 474–8

Reyna Almandos J G, Bredice F, Raineri M, Gallardo M and Trigueiros A G 1996 *J. Phys. B: At. Mol. Opt. Phys.* **29** 5643–50

Reyna Almandos J G, Bredice F, Raineri M, Gallardo M and Trigueiros A G 1998 *J. Phys. B: At. Mol. Opt. Phys.* **31** 3129–36

Shirai T, Okazaki K and Sugar J 1995 *J. Phys. Chem. Ref. Data* **24** 1577–608

Sugar J and Musgrove A 1991 *J. Phys. Chem. Ref. Data* **20** 8599–915

Trigueiros A G, Pagan C J B, Petersson S-G and Reyna Almandos J G 1989 *Phys. Rev.* A **40** 3911–14

Trigueiros A G, Mania A J, Pettersson S-G and Reyna Almandos J G 1993 *Phys. Rev.* A **48** 3595–7

ELSEVIER

Journal of Quantitative Spectroscopy & Radiative Transfer 102 (2006) 391–395

Journal of Quantitative Spectroscopy & Radiative Transfer

www.elsevier.com/locate/jqsrt

Spectral analysis of the $4d^96s$ configuration in eight times ionized xenon, Xe IX

M. Raineri*, M. Gallardo, J.G. Reyna Almandos

Centro de Investigaciones Opticas (CIOp), Casilla de Correo 124, 1900 La Plata, Argentina

Received 24 August 2005; accepted 6 February 2006

Abstract

A capillary light source was used to observe the spectrum of eight times ionized xenon, Xe IX, in the vacuum ultraviolet range, 270–2000 Å. Sixteen transitions have been identified as combinations between energy levels of the $4d^96s$ with $4d^95p$ configuration, and all $4d^96s$ levels have been determined. The present analysis is based on an accurate extrapolation of energy parameters and experimental energy level values in the Pd I isoelectronic sequence. The energy parameters were obtained with Hartree–Fock relativistic calculations. Least-squares parametric calculation has been carried out to study the fit between experimental and theoretical values.
© 2006 Elsevier Ltd. All rights reserved.

PACS: 32.30 Jc; 52.80 Yr

Keywords: Atomic spectroscopy; Energy levels; Nobles gases; Isoelectronic sequences; Transition probabilities

1. Introduction

Palladium-like xenon, Xe IX, has a closed $4d^{10}$ shell in its ground state. Data for higher members of the Pd I sequence are important for achieving the laser action at shorter wavelengths, and laser effect was demonstrated for Xe IX at the wavelength of 418, 1 Å [1]. Resonant transitions against the $4d^9(np+n'f)$ configurations were studied in the Pd I isoelectronic sequence from Cd III to Cs X by Churilov et al. [2], and also in [3].

The spectra of Cd III, In IV, and Sn V, were studied by Joshi and van Kleef [4,5], and the previous studies on Sb VI and Te VII [6] were revised and extended, including I VIII, by Churilov et al. [7], and Xe IX [8,9]. Recent analysis of the Cs X–Ce XIII, and Pr XIV–Nd XV [10,11] has been published.

Spectroscopic data from rare gases can be used in studies related with collision physics, photoelectron spectroscopy, fusion diagnostic, and as mentioned, in laser physics. For a better understanding of the eight times ionized xenon atomic structure, the present investigation was undertaken to study the $4d^96s$ configuration of the Xe IX ion, and all energy levels belonging to this configuration were determined by $4d^95p$–$4d^96s$ transitions.

*Corresponding author. Tel.: +54 221 4840280; fax: +54 221 4712771.
E-mail addresses: monicar@ciop.unlp.edu.ar (M. Raineri), jreyna@ciop.unlp.edu.ar (J.G. Reyna Almandos).

0022-4073/$ - see front matter © 2006 Elsevier Ltd. All rights reserved.
doi:10.1016/j.jqsrt.2006.02.020

The spectral analysis was supported by theoretical calculation using the Cowan codes [12] and by means of least squares fits along the Pd I sequence for the $4d^9 6s$ configuration [7]. For this configuration we also extrapolated accurate energy level values along the isoelectronic sequence, using the multiconfiguration Dirac Fock (MCDF) method [13], and Hartree–Fock relativistic calculations [12].

2. Experimental

To excite the xenon spectra we used a capillary pulsed discharge that is a Pyrex tube, 100 cm long, and with an inner diameter of 0.3 cm. The electrodes, placed 80 cm apart, were made of tungsten covered with indium, this one, used to avoid the impurities coming from the electrodes. At one side of the tube there is an inlet connected via a pressure reduction system to the bottle of xenon. In this way a continuous flow of gas was achieved during the exposures.

Gas excitation is produced by discharging a bank of low-inductance capacitors of 240 nF and charged up to 19 kV through the tube. The gas pressure was measured by a thermocouple vacuum gauge before and after the exposures. The pressure range was varied between 5 and 150 mTorr. Light emitted axially was analysed using a 3 m normal incidence vacuum spectrograph with a concave diffraction grating with 1200 lines/mm, blazed for 1200 Å, with plate factor 2.77 Å/mm in the first diffraction order. Ilford Q-2 and Kodak SWR plates were used to record the spectra. Known lines of Xe and C, N, O, were used as internal wavelength standards.

The wavelength values of the measured lines are estimated to be correct to ± 0.02 Å. The intensities figures are visual estimates of photographic density, and are on a uniform scale only within limited wavelength ranges. To distinguish among different states of ionization, we studied the behaviour of the spectral lines intensity as a function of pressure.

3. Results and discussion

Theoretical predictions were used in the analysis of the spectra. To obtain these predicted energy level values and the transition probabilities from de Cowan computer codes [12], we included into calculation the even $4d^{10}$, $4d^9$ ns (n = 5, 6), $4d^9$ nd (n = 5, 6), $4d^8\ 5s^2$, $4d^8\ 5s5d$, $4d^8\ 5d^2$, $4p^5\ 5d^{10}\ 5p$ and $4p^5\ 5d^{10}$ nf (n = 4, 5) configurations and the odd $4d^9$ np (n = 5, 6), $4d^9$ nf (n = 4 − 6), $4d^8\ 5s5p$, $4d^8\ 5p5d$, $4d^8\ 5s$ nf (n = 4, 5), $4p^5\ 4d^{10}\ 5s$ and $4p^5\ 4d^{10}\ 5d$ configurations. The radial parameters were scaled to 0.85 of their ab initio Hartree–Fock values.

The transitions observed in the present investigation are listed in Table 1. They are shown as combinations between energy levels of the $4d^9 6s$ configuration, against levels of the $4d^9 5p$ configuration, taken from the work of Churilov et al. [9]. The intensities of the observed lines, marked by Int. in the table, are based on visual estimates and the wavenumber values given in the calculated column are deduced from the optimized level values. The level values were determined in a procedure where the wavenumbers of the observed lines are weighted according to their estimated uncertainties. We also presented in this table the calculated transition probabilities (gA, where g is the statistical weight of the upper level and A, the Einstein coefficient for spontaneous emission).

Theoretical calculations along the isoelectronic sequence were also made using the MCDF code of Grant [13]. We also use the predicted MCDF and HFR [12,13] energy levels together the reported experimental $4d^9 6s$ energy levels in the sequence, to help us in the search of the energy levels. Studying the behaviour of the difference between the observed and calculated energies along the isoelectronic sequence and using the energy of $^3D_3$ as reference value, we established all the extrapolated energy level values of the configuration. Fig. 1 shows the $^3D_1$–$^3D_3$ and $^3D_2$–$^3D_3$ energy level differences using E_{obs}–E_{cal} (HFR) values, along the isoelectronic sequence.

Table 2 shows the experimental energy level values of the $4d^9$ 6s configuration and the percentage composition of the $4d^9 6s$ energy levels in L–S coupling. The designation of the levels $^1D_2$ and $^3D_2$ is a little ambiguous. The contribution to the $^3D_2$ level is 54% ^3D and 46% ^1D. The same fact can be seen with these levels in other ions belonging to the isoelectronic sequence.

To give the best possible fit between the calculated eigenvalues and the observed energy levels, the radial integrals E_{av}, F^k, G^k, ζ and R^k were considered as adjustable parameters, whose values were determined considering their behaviour through the isoelectronic sequence. The accuracy of the fit is measured by means of the standard deviation in a least-squares calculation [12].

Table 1
Classified lines in the $4d^9 5p–4d^9 6s$ transitions in Xe IX

gA[a]	Int.	Wavelengths λ (Å)	Wavenumber		Classification
			σ_{obs} (cm^{-1})	σ_{cal} (cm^{-1})	
57	2	306.52	326 243	326 248	$5p\ ^3P_2–6s\ ^3D_3$
33	1	307.50	325 203	325 192	$5p\ ^3F_2–6s\ ^3D_1$
18	1	308.02	324 650	323 654	$5p\ ^3P_1–6s\ ^3D_2$
0.1	1	308.80[b]	323 834	324 824	$5p\ ^3P_1–6s\ ^3D_1$
0.3	1	308.80[b]	323 834	323 824	$5p\ ^3F_3–6s\ ^1D_2$
27	1	309.88	322 706	322 700	$5p\ ^3F_3–6s\ ^3D_3$
15	1	318.15	314 317	314 299	$5p\ ^1P_1–6s\ ^3D_2$
10	1	322.10	310 463	310 440	$5p\ ^3P_0–6s\ ^3D_1$
14	1	324.38	308 282	308 288	$5p\ ^3P_1–6s\ ^1D_2$
92	3	328.04	304 841	304 832	$5p\ ^3F_4–6s\ ^3D_3$
68	3	330.03	303 003	303 019	$5p\ ^1F_3–6s\ ^3D_2$
41	2	333.05	300 255	300 269	$5p\ ^1D_2–6s\ ^1D_2$
24	1	333.27	300 057	300 077	$5p\ ^3D_1–6s\ ^3D_1$
30	1	335.53	298 032	298 029	$5p\ ^3D_2–6s\ ^3D_2$
21	1	336.24	297 411	297 400	$5p\ ^3D_3–6s\ ^1D_2$
17	1	336.51	297 168	297 199	$5p\ ^3D_2–6s\ ^3D_1$
42	1	337.53	296 270	296 276	$5p\ ^3D_3–6s\ ^3D_3$

[a]Calculated gA values (given in the $10^9\ s^{-1}$ units) where g stands for statistical weight of the transition upper level and A, for Einstein's coefficient for spontaneous emission.
[b]Double classification.

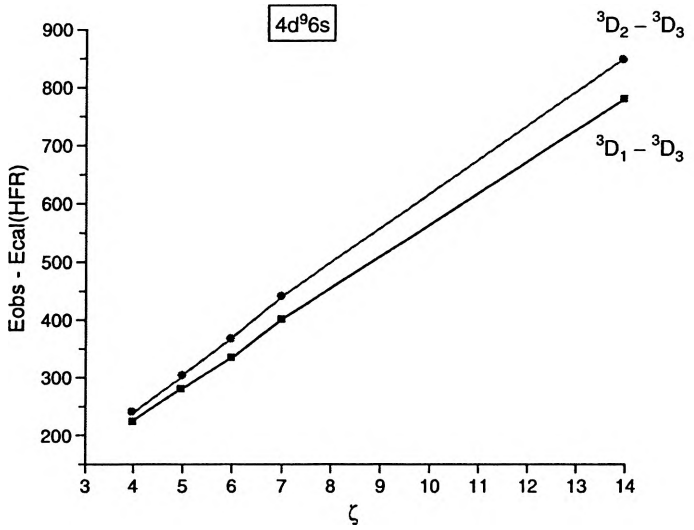


Fig. 1. $^3D_1–^3D_3$ and $^3D_2–^3D_3$ energy level differences using $E_{obs}–E_{cal}$ (HFR) values, along the isoelectronic sequence.

Table 3 shows the energy parameters for the $4d^{10}$, $4d^9$ 5s, 6s and $4d^9$ 5d configurations of Xe IX. All the parameters are free except the configuration interaction integrals which were fixed at 0.85 of their Hartree–Fock value. The average parameter deviations of the fits are also given in this table. The Fit/HF parameter ratios for the ζ_{4d} and $G^2(4d,6s)$ of the $4d^9$ 6s configuration are in accordance with the scaled factor of the isoelectronic sequence [7]. The configuration interaction integral for the $4d^9$ 6s configuration are not significant with respect to the other interactions involved in the calculation. The standard deviation of the least squares fit of the observed levels is $85\ cm^{-1}$.

Table 2
New energy level values of the $4d^9 6s$ configuration of Xe IX

Designation	E_{exp} (cm^{-1})	E_{calc} (cm^{-1})[a]	Percentage composition
$^3D_1$	918 346	918 340	100 ^3D
$^3D_2$	919 176	919 178	54 $^3D_2$ + 46 $^1D_2$
$^3D_3$	901 686	901 685	100 ^3D
$^1D_2$	902 810	902 801	54 $^1D_2$ + 46 $^3D_2$

[a]Calculated energy level values obtained using the fitted energy parameters.

Table 3
Energy parameters for the $4d^{10}$, $4d^9 5s$, $4d^9 6s$ and $4d^9 5d$ configurations of Xe IX

Configuration	Parameter	H–F value	Fitted value	Fitt/H–F
$4d^{10}$	E_{av}	0	1482	
$4d^9 5s$	E_{av}	465 886	461 992 ± 44	0.99
	ζ_{4d}	6397	6614 ± 36	1.03
	G^2 (4d, 5s)	18 847	16 922 ± 416	0.90
$4d^9 6s$	Eav	908 208	908 853 ± 43	1.00
	ζ_{4d}	6447	6663 ± 34	1.03
	G^2 (4d, 6s)	5128	4797 ± 425	0.93
$4d^9 5d$	E_{av}	799 545	799 392 ± 24	1.00
	ζ_{4d}	6439	6635 ± 19	1.03
	ζ_{5d}	1181	1389 ± 27	1.17
	F^2 (4d, 5d)	32 600	28 716 ± 356	0.88
	F^4 (4d, 5d)	15 408	14 918 ± 565	0.97
	G^0 (4d, 5d)	7692	6103 ± 28	0.79
	G^2 (4d, 5d)	9742	8930 ± 242	0.92
	G^4 (4d, 5d)	8195	7438 ± 544	0.91
Configuration interaction integrals				
$4d^{10}$–$4d^9 5s$	R^2 (4d4d, 4d5s)	−7893	−6709 (FIX)	0.85
$4d^{10}$–$4d^9 6s$	R^2 (4d4d, 4d6s)	−5348	4546 (FIX)	0.85
$4d^{10}$–$4d^9 5d$	R^0 (4d4d, 4d5d)	2284	1942 (FIX)	0.85
$4d^{10}$–$4d^9 5d$	R^2 (4d4d, 4d5d)	17 038	14 483 (FIX)	0.85
$4d^{10}$–$4d^9 5d$	R^4 (4d4d, 4d5d)	13 162	11 188 (FIX)	0.85
$4d^9 5s$–$4d^9 6s$	R^2 (4d5s, 6s4d)	9287	7894 (FIX)	0.85
$4d^9 5s$–$4d^9 5d$	R^2 (4d5s, 4d5d)	35 703	30 348 (FIX)	0.85
$4d^9 5s$–$4d^9 5d$	R^2 (4d5s, 5d4d)	10 134	8614 (FIX)	0.85
$4d^9 6s$–$4d^9 5d$	R^2 (4d6s, 4d5d)	5680	4828	0.85
$4d^9 6s$–$4d^9 5d$	R^2 (4d6s, 5d4d)	4335	3685	0.85

The standard deviation of the fit is 85 cm^{-1} for 26 observed levels.

Acknowledgments

It is gratefully acknowledged the Comisión de Investigaciones Científicas de la Provincia de Buenos Aires (CIC), Argentina, where J.G. Reyna Almandos and M. Raineri are researchers; and the Consejo Nacional de Investigaciones Científicas y Técnicas (CONICET), Argentina, where M. Gallardo is researcher. We are also grateful to Dr. F.A. Callegari for fruitful discussions.

References

[1] Lemoff BE, Yin GY, Gordon III CL, Barty CPJ, Harris SE. J Opt Soc Am B 1996;13:180–4.
[2] Churilov SS, Joshi YN, Ryabtsev AN. J Phys B 1994;27:5485–95.
[3] Churilov SS, Joshi YN. Phys Scr 2002;65:40–5.

[4] van Kleef ThAM, Joshi YN, Uijlings P. Phys Scr 1980;22:353–62.
[5] van Kleef ThAM, Joshi YN. Phys Scr 1981;24:557–65.
[6] Joshi YN, van Kleef ThAM. Can J Phys 1979;57:1982–9.
[7] Churilov SS, Azarov VI, Ryabtsev AN, Tchang-Brillet W-ÜL, Wyart J-F. Phys Scr 2000;61:420–30.
[8] Ryabtsev AN, Antsiferov PS, Nazarenko AV, Churilov SS, Tchang-Brillet Ü-L, Wyart J-F. J Phys IV 2001;Pr2:317–9.
[9] Churilov SS, Ryabtsev AN, Tchang-Brillet W-ÜL, Wyart JF. Phys Scr 2002;66:293–307.
[10] Churilov SS, Ryabtsev AN, Tchang-Brillet W-ÜL, Wyart J-F. Phys Scr 2002;T100:98–103.
[11] Churilov SS, Ryabtsev AN, Wyart J-F, Tchang-Brillet W-ÜL, Joshi YN. Phys Scr 2005;71:589–98.
[12] Cowan RD. The theory of atomic structure and spectra. Berkeley, CA: University of California Press; 1981.
[13] Grant IP, Mc Kenzie BJ, Norrington PH, Mayers DF, Pyper NC. Comput Phys Commun 1980;21:207–31; McKenzie BJ, Grant IP, Norrington PH. Comput Phys Commun 1980;21:233–46.

ELSEVIER

Spectrochimica Acta Part B 61 (2006) 1294 - 1303

SPECTROCHIMICA ACTA PART B

www.elsevier.com/locate/sab

Evaluation of self-absorption of manganese emission lines in Laser Induced Breakdown Spectroscopy measurements

F. Bredice [a], F.O. Borges [b], H. Sobral [c], M. Villagran-Muniz [c], H.O. Di Rocco [d], G. Cristoforetti [e,*], S. Legnaioli [e], V. Palleschi [e], L. Pardini [e], A. Salvetti [e], E. Tognoni [e]

[a] *Centro de Investigaciones Opticas, P.O. Box 124, (1900) La Plata, Argentina*
[b] *Instituto de Física, Universidade Federal Fluminense, UFF, Campus da Praia Vermelha-Gragoatá, 24210-340 Niterói, Rio de Janeiro, Brazil*
[c] *Laboratorio de Fotofísica, Centro de Ciencias Aplicadas y Desarrollo Tecnológico, Universidad Nacional Autónoma de México, Apartado Postal 70-186 México Distrito Federal, P. O. Box 04510, Mexico*
[d] *Instituto de Física "Arroyo Seco", Facultad de Ciencias Exactas, U.N.C.P.B.A., Pinto 399, 7000 Tandil, Argentina*
[e] *Applied Laser Spectroscopy Laboratory, IPCF-CNR, Area della Ricerca di Pisa, Via G. Moruzzi 1, 56124 Pisa, Italy*

Received 26 January 2006; accepted 29 October 2006

Abstract

This paper is part of a more general study aimed to the determination of the best experimental procedures for reliable quantitative measurements of Fe–Mn alloys by LIBS. In this work, attention is pointed on the self-absorption processes, whose effect deeply influences the LIBS measurements, reflecting in non-linear calibration curves. The effect of self-absorption on the line intensity can be quantified by defining a self-absorption coefficient, that measures the deviation of the line intensity from the linear extrapolation of the curve of growth in the optically thin regime. The authors demonstrated in a previous paper that self-absorption coefficients could be calculated once the electron density of the plasma is known and the Stark coefficients of the lines are available. However, when the Stark coefficients of the lines of interest are not known, a different approach is needed. In this work a new method for evaluation of self-absorption coefficients in LIBS measurements is presented, which does not require the knowledge of Stark coefficients. In order to understand the basic principles and setting out the theoretical tools that will be used for the analysis of the alloys, a preliminary study was done on pure Mn; LIBS spectra were acquired in different experimental conditions, at different laser energies and different delays after the laser irradiation of the sample. Moreover, collinear double pulse measurements were also performed. Analytical relations were derived and experimental procedures devised for evaluation of the self-absorption coefficients of several Mn lines, which are important for characterization and control of the experimental conditions in which the analysis is performed.
© 2006 Elsevier B.V. All rights reserved.

Keywords: Laser-Induced Breakdown Spectroscopy; Fe–Mn alloys; Self-absorption

1. Introduction

In recent years, the Laser-Induced Breakdown Spectroscopy (LIBS) technique affirmed as a powerful analytic tool for the determination of the elemental composition of materials [1–4]. Due to its intrinsic fastness of analysis, limited dimensions of the experimental setup and no need for sample pre-treatment, LIBS has been proposed and used for in-situ and on-line analysis of materials even in hostile environments characterized by high temperatures [5,6] or radiation hazards [7,8], in the presence of toxic wastes [9,10] or in potentially harmful situations [11]. The analysis of industrial materials, as ferrous and non-ferrous alloys has also attracted the attention of many researchers, for the potential use of LIBS in closed-loop diagnostic systems and as a non-invasive, minimally destructive method capable to operate as a fast screening technique [6,12–16]. In this framework, it seems particularly interesting to see the use of LIBS for the analysis of Fe–Mn alloys, which are extremely important, for example, in shape-memory alloys applications [17–21].

However, a precise compositional analysis of these alloys by LIBS requires a clear understanding of the main effects

Abbreviations: LIBS; Fe–Mn alloys; Self-absorption.

* Corresponding author. Tel.: +39 050 3152222; fax: +39 050 3152230.
E-mail address: gabriele@ipcf.cnr.it (G. Cristoforetti).

0584-8547/$ - see front matter © 2006 Elsevier B.V. All rights reserved.
doi:10.1016/j.sab.2006.10.015

influencing the LIBS spectrum, and in particular self-absorption effects [22–28] and matrix effects [29–31]. In this work, the self-absorption effects on pure manganese will be studied, and the theoretical basis of the spectral analysis will be laid.

In a previous paper [28] it was demonstrated that the self-absorption effect on spectral line intensity can be calculated once the electron density of the plasma is known and the Stark coefficients of the lines are available. Unfortunately, in literature the measured Stark coefficients are available only for a few ionic Mn lines [32]; moreover the measured values differ substantially from the calculated analogues [33]. Therefore, a different approach is needed. The method here proposed is based on the measurement of the intensity ratio of two lines of the same ionization stage and on the comparison of the experimental to the theoretically predicted value; this approach is well known in the literature as a direct check of the absence of important self-absorption effects in spectroscopic measurements [34]. In a recent paper [35], Amamou et al. used the ratio of emission lines coming from the same multiplet for correcting the self-absorption effects in the measurements of transition probabilities of silicon lines, in the limit of moderate self-absorption. The analysis of emission lines belonging to several multiplets is also the basis of the semi-empirical method developed by Friedjung and Muratorio [36,37].

In this paper, starting from the theoretical treatment of these effects, we propose a method for quantifying the influence of self-absorption on the measured intensity of the lines considered, at the same time providing a quick way of determining, among the different emission lines of a given element, the ones more appropriate for the calculation of plasma parameters (temperature and electron density) as well as for LIBS analytical measurements.

2. Theoretical analysis: emission from a homogeneous plasma rod

According to the two-levels treatment of atomic emission [38], the light intensity, i.e. the energy emitted per unit time, unit surface and unit wavelength (erg s^{-1} cm^{-3}) by a homogeneous plasma rod of length l can be calculated writing the so-called transport equation, which describes the change in radiation intensity after travelling a distance dx into the rod, in the form

$$dI(\lambda,x) = \varepsilon(\lambda)dx - \kappa(\lambda)I(\lambda,x)dx \tag{1}$$

where $\varepsilon(\lambda)$ represents the plasma spontaneous emissivity, i.e. the energy emitted per unit time, unit volume and unit wavelength (erg s^{-1} cm^{-4}):

$$\varepsilon(\lambda) = \frac{hc}{4\pi\lambda_0} A_{ki} n_k L(\lambda) \tag{2}$$

h is the Planck constant (erg s), c is the speed of light (cm s^{-1}), λ_0 is the central wavelength of the transition (cm), A_{ki} represents the transition probability between the upper level k and the lower level i (s^{-1}), n_k is the population (cm^{-3}) of the upper level and $L(\lambda)$ is the spectral emission profile (cm^{-1}).

The $\kappa(\lambda)$ coefficient is the absorption coefficient (cm^{-1}), which takes into account both the absorption by lower level atoms and the stimulated emission of the upper level atoms under the effect of the radiation $I(\lambda,x)$:

$$\kappa(\lambda) = \frac{\lambda_0^4}{8\pi c} A_{ki} g_k \frac{n_i}{g_i}\left(1 - \frac{n_k g_i}{g_k n_i}\right) L(\lambda) \tag{3}$$

where g_k and g_i are the degeneracies of the upper and lower level (dimensionless), respectively, and n_i is the population (cm^{-3}) of the lower level.

Since in typical LIBS experiments the detectors used do not give the intensity of the emission, but a measure of the number of photons emitted (per second) at a given wavelength, Eq. (1) should be divided by the energy of the photon hc/λ_0 for obtaining the transport equation for the photon number n_p, yielding:

$$\begin{aligned} dn_p(\lambda,x) &= \frac{\varepsilon(\lambda)}{hc}\lambda_0 dx - \kappa(\lambda) n_p(\lambda,x)dx \\ &= \varepsilon'(\lambda)dx - \kappa(\lambda) n_p(\lambda,x)dx \end{aligned} \tag{4}$$

where $\varepsilon'(\lambda)$ is defined as $\varepsilon'(\lambda) \equiv \frac{1}{4\pi} A_{ki} n_k L(\lambda)$.

The solution of Eq. (4) gives the number of photons emitted by a homogeneous plasma rod of length l, in the form

$$n_p(\lambda, l) = \frac{\varepsilon'(\lambda)}{\kappa(\lambda)}\left(1 - e^{-\kappa(\lambda)l}\right). \tag{5}$$

Assuming the Local Thermal Equilibrium in the plasma rod, the population of the energy level k,i can be expressed through the Boltzmann distribution of equilibrium:

$$n_{k,i} = g_{k,i} n \frac{e^{-\frac{E_{k,i}}{k_B T}}}{U(T)} \tag{6}$$

where n is the total number of atoms of the species per unit volume (cm^{-3}), $E_{k,i}$ is the energy of the level (erg), k_B is the Boltzmann constant (erg K^{-1}), T is the plasma temperature (K) and $U(T)$ is the partition function for the species (dimensionless).

Therefore, in this approximation

$$\varepsilon'(\lambda) = \frac{1}{4\pi} A_{ki} g_k n \frac{e^{-\frac{E_k}{k_B T}}}{U(T)} L(\lambda) \tag{7}$$

and

$$\kappa(\lambda) = \frac{\lambda_0^4}{8\pi c} A_{ki} g_k n \frac{e^{\frac{E_i}{k_B T}}}{U(T)} L(\lambda) \tag{8}$$

where the further approximation $\frac{n_k g_i}{g_k n_i} \ll 1$ was introduced, corresponding to neglecting the stimulated emission effect with respect to plasma absorption.

2.1. Self-absorption

In order to quantify the effect of self-absorption on the emission lines intensity, let us introduce the self-absorption coefficient SA, defined as the ratio of the actual intensity of the emission line at its maximum ($n_p(\lambda_0)$, in counts per seconds) over the value ($n_{p_0}(\lambda_0)$) obtained by extrapolating the curve of

growth valid in the optically thin regime to the same emitters number density of the actual measurement [27]:

$$SA = \frac{n_p(\lambda_0)}{n_{p_0}(\lambda_0)} = \frac{(1-e^{-\kappa(\lambda_0)l})}{\kappa(\lambda_0)l}. \quad (9)$$

The number density of the emitters is in general not known and therefore the actual value of SA cannot be directly calculated; notwithstanding, the definition given in expression (9) is useful for deriving the expected behaviour of the line intensity in correspondence of change in the global plasma parameters (size, total density, electron density and temperature).

In a previous paper [28], it was demonstrated that the ratio of the integral intensity of the self-absorbed emission line N_p over the non self-absorbed one N_{p_0} (defined by extrapolation as in expression 9) scales as

$$\frac{N_p}{N_{p_0}} = \frac{\int n_p(\lambda)d\lambda}{\int n_{p_0}(\lambda)d\lambda} = (SA)^{\beta} \quad (10)$$

with β=0.44.

Bearing in mind that in typical laser-induced plasmas the Stark effect is the dominant line broadening mechanism, while the Doppler effect can be safely neglected, we can assume that the emission lineshape $L(\lambda)$ has a normalized Lorentzian shape

$$L(\lambda) = \frac{\Delta\lambda_0}{4(\lambda-\lambda_0)^2 + \Delta\lambda_0^2} \quad (11)$$

In this case, it has been demonstrated [28] that the FWHM of the measured emission lines becomes

$$\Delta\lambda = \Delta\lambda_0(SA)^{\alpha} \quad (12)$$

with α=−0.56.

The equations here reported are the basic tools that we will use in the following for the interpretation of the experimental data.

2.2. Intensity ratio of two lines

According to Eq. (10), and taking into account the definition of SA coefficient (Eq. (9)), the intensity ratio of two lines of the same species can be written as:

$$\frac{(N_p)_2}{(N_p)_1} = \frac{(N_{p_0})_2}{(N_{p_0})_1}\frac{(SA)_2^{\beta}}{(SA)_1^{\beta}} = \frac{\left(A_{ki}g_k e^{-\frac{E_k}{k_B T}}\right)_2}{\left(A_{ki}g_k e^{-\frac{E_k}{k_B T}}\right)_1}\frac{(SA)_2^{\beta}}{(SA)_1^{\beta}} \quad (13)$$

where the subscripts 1 and 2 correspond to the lines considered. In turn, the self-absorption coefficient ratio is by definition (Eq. (9))

$$\frac{(SA)_2}{(SA)_1} = \frac{\kappa(\lambda_0)_1}{\kappa(\lambda_0)_2}\frac{(1-e^{-\kappa(\lambda_0)_2 l})}{(1-e^{-\kappa(\lambda_0)_1 l})}. \quad (14)$$

Moreover, from Eqs. (8) and (11) we can write

$$\frac{\kappa(\lambda_0)_2}{\kappa(\lambda_0)_1} = \left(\frac{\lambda_0^4 A_{ki}g_k e^{-\frac{E_i}{k_B T}}}{\Delta\lambda_0}\right)_2 \Bigg/ \left(\frac{\lambda_0^4 A_{ki}g_k e^{-\frac{E_i}{k_B}}}{\Delta\lambda_0}\right)_1. \quad (15)$$

From Eqs. (13), (14) and (15) we can immediately see that the dependence of the line intensity ratio on the plasma parameters is quite complex, since both the absolute values of the $\kappa(\lambda_0)$ coefficients and their ratio depend on plasma temperature; moreover, both the absolute values of the self-absorption coefficients and their ratio depend on the plasma dimensions l and, through the parameter n (the total number of atoms of the species considered), on the plasma electron density n_e.

In fact, the number density of the species considered obeys, under the approximation of LTE, the Saha–Boltzmann equation (which also depends on the plasma temperature) [39]

$$n_e\frac{n^{II}}{n^{I}} = \frac{(2\pi m_e k_B T)^{3/2}}{h^3}\frac{2U^{II}(T)}{U^{I}(T)}e^{-\frac{E_{ion}}{k_B T}} \quad (16)$$

where m_e is the electron mass (g) and E_{ion} is the ionization energy (erg) of the element.

The superscripts I and II refer, respectively, to the neutral and singly ionized species of the element under study, which in typical LIBS experiments are the only dominant species, i.e. $n^{Tot} \approx n^{I} + n^{II}$ where n^{Tot} is total number density of the element.

A further dependence on the electron temperature and density is brought into the equations by the line width $\Delta\lambda_0$, which, in first approximation (i.e. neglecting the atom and ion impact contribution to the broadening), is proportional to the electron density through the temperature-dependent Stark coefficient w_s (T) [40]

$$\Delta\lambda_0 \approx 2w_s(T)n_e. \quad (17)$$

2.2.1. Limit case: weakly self-absorbed lines

In the limit case of low self-absorption ($\kappa(\lambda_0)$ l<<1) the SA coefficient defined in Eq. (9) equals unity, therefore the ratio of the integrated intensities of two lines of the same species in this limit becomes:

$$\frac{(N_p)_2}{(N_p)_1} \approx \frac{\left(A_{ki}g_k e^{-\frac{E_k}{k_B T}}\right)_2}{\left(A_{ki}g_k e^{-\frac{E_k}{k_B T}}\right)_1} \qquad \kappa_{1,2}(\lambda_0)l<<1. \quad (18)$$

2.2.2. Limit case: strongly self-absorbed lines

Despite the intrinsic complexity of Eqs. (13)–(15), we can easily derive the SA coefficients in the limit $\kappa(\lambda_0)$ l>>1, which corresponds to the condition of very high self-absorption. In this case

$$SA \approx \frac{1}{\kappa(\lambda_0)l}. \quad (19)$$

The ratio of the integrated intensities of two lines of the same species, both subjected to strong self-absorption, can be obtained by putting Eq. (19) together with the equation system (13)–(15), as

$$\frac{(N_p)_2}{(N_p)_1} \approx \frac{\left(A_{ki}g_k e^{-\frac{E_k}{k_B T}}\right)_2}{\left(A_{ki}g_k e^{-\frac{E_k}{k_B T}}\right)_1}\left[\frac{\left(\frac{\lambda_0^4 A_{ki}g_k e^{-\frac{E_i}{k_B T}}}{\Delta\lambda_0}\right)_1}{\left(\frac{\lambda_0^4 A_{ki}g_k e^{-\frac{E_i}{k_B T}}}{\Delta\lambda_0}\right)_2}\right]^{\beta} \qquad \kappa_{1,2}(\lambda_0)l>>1. \quad (20)$$

2.2.3. Limit case: lines belonging to the same multiplet

We expect that the intensity ratio of lines connecting levels with similar E_k and E_i, i.e. lines belonging to the same multiplet, would not change with the plasma temperature. From the point of view of the real measurements, if the plasma temperature was the only time-varying parameter during the plasma evolution, in this limit case the intensity ratio should be independent on the delay of acquisition of the LIBS spectra. By resorting to the previous expressions (18) and (20), the intensity ratio in this limit case should then be comprised between the two extremes

$$\frac{(N_p)_2}{(N_p)_1} = \frac{(A_{ki}g_k)_2}{(A_{ki}g_k)_1} \qquad \kappa_{1,2}(\lambda_0)l \ll 1 \tag{21}$$

and

$$\frac{(N_p)_2}{(N_p)_1} = \left[\frac{(A_{ki}g_k)_2}{(A_{ki}g_k)_1}\right]^{(1-\beta)} \left[\frac{(\lambda_0^4)_1}{(\lambda_0^4)_2}\right]^{\beta} \qquad \kappa_{1,2}(\lambda_0)l \gg 1 \tag{22}$$

in the limit of low and high self-absorption, respectively, since the Lorentzian width of the lines, mainly dominated by the Stark broadening effect, is the same for lines belonging to the same multiplet. Considering that, in general, $\left[\frac{(\lambda_0^4)_1}{(\lambda_0^4)_2}\right]^{\beta} \approx 1$ for lines belonging to the same multiplet, we observe that the most intense line of the multiplet is always more self-absorbed than the less intense. Therefore, if the intensity ratio of two lines belonging to the same multiplet is greater than one in low self-absorption conditions, at the increase of self-absorption the ratio will decrease, and vice-versa.

2.2.4. General case

In the general case, according to Eq. (15), the ratio $\frac{(\Delta\lambda_0)_2}{(\Delta\lambda_0)_1}$ must be known for obtaining the predicted intensity ratio of two lines. If the Stark coefficients of the two lines are known, according to Eq. (17) the above mentioned ratio can be immediately calculated as

$$\frac{(\Delta\lambda_0)_2}{(\Delta\lambda_0)_1} \approx \frac{(w_s)_2}{(w_s)_1}. \tag{23}$$

If the Stark coefficients of the lines are not known, on the other hand, the ratio of the Lorentzian widths of the emission lines can be derived from the experimental data combining Eqs. (12) and (13), in the form

$$\frac{(\Delta\lambda_0)_2}{(\Delta\lambda_0)_1} = \frac{(\Delta\lambda)_2}{(\Delta\lambda)_1}\left(\frac{(N_p)_2}{(N_p)_1}\right)^{-\frac{\alpha}{\beta}}\left(\frac{\left(A_{ki}g_k e^{-\frac{E_k}{k_B T}}\right)_2}{\left(A_{ki}g_k e^{-\frac{E_k}{k_B T}}\right)_1}\right)^{\frac{\alpha}{\beta}}. \tag{24}$$

The knowledge of the $\frac{(\Delta\lambda_0)_2}{(\Delta\lambda_0)_1}$ ratios for the lines here considered can now be exploited for obtaining, from Eq. (15), the ratio of the $\kappa(\lambda_0)_1$ and $\kappa(\lambda_0)_2$ coefficients.

This ratio can be substituted in Eq. (13), yielding:

$$\frac{(N_p)_2}{(N_p)_1} = \frac{\left(A_{ki}g_k e^{-\frac{E_k}{k_B T}}\right)_2}{\left(A_{ki}g_k e^{-\frac{E_k}{k_B T}}\right)_1}\left(\frac{\kappa(\lambda_0)_1}{\kappa(\lambda_0)_2}\frac{(1-e^{-\kappa(\lambda_0)_2 l})}{(1-e^{-\kappa(\lambda_0)_1 l})}\right)^{\beta} = a\left[\frac{b(1-e^{-\kappa(\lambda_0)_2 l})}{(1-e^{b\kappa(\lambda_0)_2 l})}\right]^{\beta} \tag{25}$$

where

$$a = \frac{\left(A_{ki}g_k e^{-\frac{E_k}{k_B T}}\right)_2}{\left(A_{ki}g_k e^{-\frac{E_k}{k_B T}}\right)_1} \tag{26}$$

is the low self-absorption limit of the intensity ratio (Eq. (18)) and

$$b = \frac{\left(\lambda_0^4 A_{ki}g_k e^{-\frac{E_i}{k_B T}}\right)_1}{\left(\lambda_0^4 A_{ki}g_k e^{-\frac{E_i}{k_B T}}\right)_2}\left(\frac{(\Delta\lambda_0)_2}{(\Delta\lambda_0)_1}\right). \tag{27}$$

Eq. (25) can be numerically solved for the opacity $\kappa(\lambda_0)_2 l$ since the intensity ratio $\frac{(N_p)_2}{(N_p)_1}$ of the two lines, the $\frac{(\Delta\lambda_0)_2}{(\Delta\lambda_0)_1}$ parameter and the plasma temperature T are known from the experimental data. Once the $\kappa(\lambda_0)l$ parameter is known, for a given line, at given experimental conditions, the self-absorption coefficient SA can be easily calculated from Eq. (9).

3. Experimental results

The Fe–Mn alloys will be analysed, using the LIBS technique, in the different laboratories participating to the SAILORMAN (Southern American–Italian LIBS-Oriented Research for Material Analysis Network), a cooperative research network connecting LIBS laboratories in Argentina (CIOP, La Plata and University of Tandil), Mexico (Universidad Nacional Autónoma de México), Brazil (Universidade Federal Fluminense) and Italy (ALS Lab.-CNR in Pisa), using the experimental facilities and the specific know-how in spectroscopy there available. For this preliminary work on pure manganese, the samples were analysed at CIOP (La Plata, Argentina) and at ALS Lab (Pisa, Italy). The CIOP LIBS setup used a Nd-YAG Laser emitting pulses at 1064 nm with 200 mJ energy and 7 ns FWHM, coupled to a Czerny-Turner spectrometer (50 cm focal length, 1200 grooves/mm grating) equipped with an Andor iCCD for time-resolved spectral analysis. At ALS Laboratories the measurements on the same pure Mn sample were performed using Modì (Mobile Dual-Pulse Instrument) [41], a double pulse mobile LIBS system using a Double-Pulse Nd-YAG Laser emitting pulses at 1064 nm with 60 mJ energy per pulse and 12 ns FWHM, coupled with an Echelle spectrometer equipped with an iCCD. The measurements in Pisa were performed both in single pulse, at two energies (60 and 120 mJ) and double pulse regime (60+60 mJ with an interpulse delay of 2 μs). In particular, the evolution of the plasma in time has been studied by varying the acquisition delay for every given irradiation regime. Fifty LIBS spectra were averaged for each of the different acquisition delay times considered, calculated after the (second) laser pulse, with a 50 ns gate in La Plata

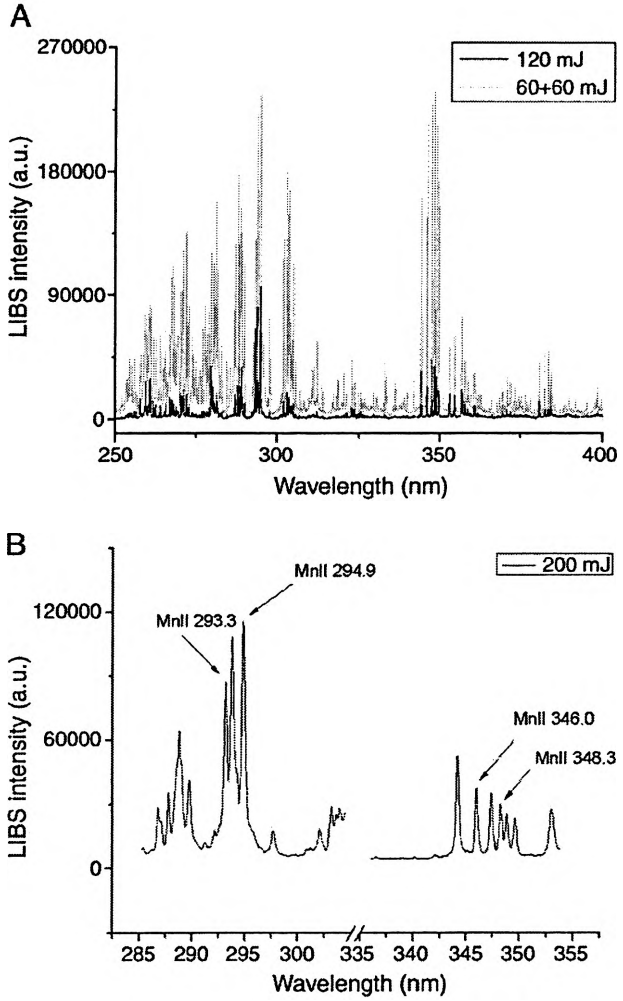


Fig. 1. Typical LIBS spectra on pure manganese obtained A) at ALS Lab. in Pisa (only a portion of the spectrum is shown, where the most intense Mn lines are present). Black: single pulse at 120 mJ; Gray: Double pulse at 60+60 mJ with 2 μs interpulse delay. B) At CIOP, La Plata (single pulse at 200 mJ). The spectra shown were acquired 1 μs after the laser spark. Some of spectral lines considered in this paper are marked.

measurements and 500 ns gate in Pisa measurements. While the measurements in Pisa were performed with a broadband spectrometer, which allowed for acquisition of the whole LIBS spectrum from 230 to 900 nm in a single run, the La Plata spectrometer was operated in two spectral windows between 285–304 nm and 336–354 nm, where several intense Mn II lines are well visible. A comparison between the LIBS spectra taken in Pisa and La Plata is shown in Fig. 1A and B.

In order to calculate the self-absorption coefficients of the Mn lines under study, the main parameters characterizing the laser-induced plasma (temperature and electron density) were measured. In particular, electron density was determined from the spectra acquired in Pisa, in both single and double pulse configuration, measuring the Stark broadening of the Hydrogen Balmer alpha at 656.3 nm [28,42]. The use of the hydrogen lines for electron density measurements has been demonstrated to yield a precise

Table 1
Spectral parameters of the Mn lines considered in this paper

Species	Wavelength (nm)	g_i	g_k	E_i (cm^{-1})	E_k (cm^{-1})	A_{ki} (s^{-1})
Mn I	382.4	6	6	1.75×10^4	4.36×10^4	2.3×10^7
Mn I	383.4	6	8	1.75×10^4	4.35×10^4	4.3×10^7
*Mn I	471.0	8	8	2.33×10^4	4.45×10^4	1.7×10^7
*Mn I	472.7	6	6	2.35×10^4	4.47×10^4	1.7×10^7
*Mn I	473.9	4	4	2.37×10^4	4.48×10^4	2.4×10^7
Mn I	478.5	8	8	1.85×10^4	3.94×10^4	4.0×10^7
Mn I	482.4	10	8	1.87×10^4	3.94×10^4	5.0×10^7
Mn II	261.8	11	13	2.76×10^4	6.58×10^4	2.9×10^8
Mn II	293.3	5	3	9.47×10^3	4.36×10^4	2.0×10^8
Mn II	293.9	5	5	9.47×10^3	4.35×10^4	1.9×10^8
Mn II	294.9	5	7	9.47×10^3	4.37×10^4	1.9×10^8
*Mn II	344.2	9	7	1.43×10^4	4.34×10^4	4.3×10^7
*Mn II	346.0	7	5	1.46×10^4	4.35×10^4	3.2×10^7
*Mn II	347.4	5	3	1.48×10^4	4.36×10^4	1.5×10^7
*Mn II	348.3	5	5	1.47×10^4	4.35×10^4	2.0×10^7
*Mn II	348.9	3	3	1.49×10^4	4.36×10^4	2.5×10^7

The spectral lines used for plasma temperature measurements are marked with an asterisk.

determination of the plasma electron density, which is not affected by self-absorption and does not depend on any specific hypothesis of Local Thermal Equilibrium [28]. The error estimated on the electron density measurements is of the order of 10%. The plasma temperature was measured using the Saha–Boltzmann plot method, described in Ref. [43]. The lines used for the determination of the temperature are shown in Table 1; all of them are relatively isolated, non-resonant emission lines. As shown in the following discussion, these lines are weakly to moderately self-absorbed, and thus they can be considered appropriate for temperature measurements using the Saha–Boltzmann method. In this case, since a single plasma temperature can be defined only in the presence of thermal equilibrium, the hypothesis of LTE has to be introduced. As demonstrated in a previous paper [28], this procedure guarantees an accuracy in plasma temperature determination around ±5%, which is more than satisfactory considering the

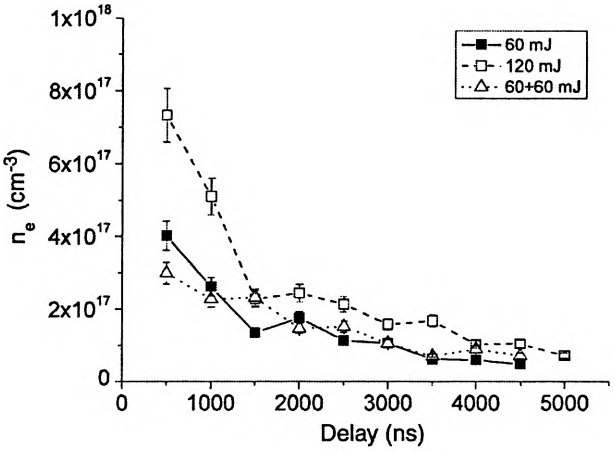


Fig. 2. Time dependence of the electron density, at 60 mJ laser energy (full squares), 120 mJ laser energy (open squares), 60+60 mJ with 2 μs interpulse delay (open triangles). The relative errors are of the order of 10%.

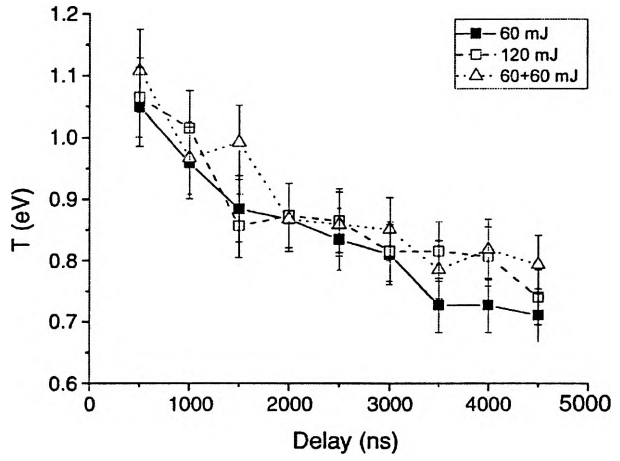


Fig. 3. Time dependence of the plasma temperature, at 60 mJ laser energy (full squares), 120 mJ laser energy (open squares), 60+60 mJ with 2 μs interpulse delay (open triangles). The relative errors are of the order of 5%.

above discussion about LTE and the uncertainties related to the use of the approximation of homogeneous plasma (see below).

The evolution of plasma electron density and temperature is plotted in Figs. 2 and 3, as a function of the acquisition delay. In the time window investigated, the electron density varies from about 8×10^{17} cm^{-3} to 4×10^{16} cm^{-3}. At a given delay time, the electron density corresponding to laser energy of 120 mJ is roughly double of the one corresponding to 60 mJ. The electron density measured in double pulse mode (60+60 mJ with a 2 μs interpulse delay) is essentially the same, within the experimental errors, of the one corresponding to a single pulse of 60 mJ. As for the plasma temperature, in the explored time window it decays from values of about 1.1 eV to 0.7 eV.

Within the experimental errors, the plasma temperature is about the same in all the configurations studied (single pulse 60 mJ, single pulse 120 mJ, double pulse 60+60 mJ). These results are coherent with the behaviours reported in the literature in similar conditions [44].

It is important to note, at this point, that both the evaluation of electron density through the Stark broadening of H_α line and the evaluation of the plasma temperature through the Saha–Boltzmann plot method rely on the hypothesis of homogeneous plasma. However, in recent years several experimental works [23,26] have shown that laser-induced plasmas in LIBS experiments are characterized by spatial variation of their main parameters (temperature and electron density) which obviously cannot be reproduced in the framework of the homogeneous plasma approximation. On the other hand, at least in the limit of small to medium self-absorption, it has been demonstrated that a realistic evaluation – and, possibly, correction – of the self-absorption effects can be obtained using the homogeneous plasma approximation (see, for example, Gornushkin et al. [22], Bulajic et al. [27], El Sherbini et al. [28], Amamou et al. [35]). Obviously, the extension of the self-absorption theoretical treatment to the more realistic case of inhomogeneous plasma would be highly desirable; however, at the moment, it seems that only the limit situation of strong plasma inhomogeneity (leading to self-reversal effect) can be treated in a relatively easy way using space-integrated LIBS spectra (see Amamou et al. [24] and Gornuskin et al. [25], for example). A more detailed calculation of the self-absorption coefficients, taking into account the plasma inhomogeneity, calls for different and more complex experimental strategies, involving tomographic reconstruction of the plasma parameters (see for example Aguilera et al. [26], Corsi et al. [44], and Cristoforetti et al. [45]).

3.1. Measurements on ionized Mn lines

Using the theoretical treatment described in previous section, we have evaluated the self-absorption coefficients of 9 intense ionized Mn lines (Mn II at 261.8; 293.3; 293.9; 294.9; 344.2; 346.0; 347.4; 348.3; 348.9 nm). These lines have been chosen since they are well insulated and free from interferences of other Mn lines, therefore they are good candidates for analytical LIBS measurements. The spectroscopic parameters of these lines are shown in Table 1. As an example of the application of the theoretical treatment described in previous sections, in Fig. 4 are shown the intensity ratios of the lines Mn II at 293.3/Mn II at 294.9 nm (lines belonging to the same multiplet) and Mn II at 293.3/Mn II at 348.3 nm (lines belonging to different multiplets). The intensity ratios are plotted as a function of the acquisition delay after the laser pulse. In case of double pulse measurements, the delay is calculated after the arrival on the sample of the second laser pulse. Since the first couple of lines in Fig. 4 (Mn II at 293.3 and Mn II at 294.9 nm) belongs to the same multiplet, the theoretical treatment of Section 2.2.3 is applicable. According to the theory, if a limit case (low or high self-absorption limit) is applicable, the intensity ratio of these two lines is essentially independent on the variation in plasma

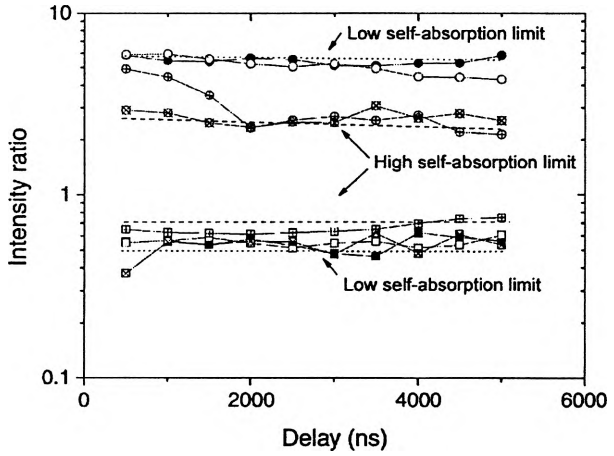


Fig. 4. Time dependence of the intensity ratios of Mn II at 293.3/Mn II at 294.9 nm lines (full squares, 60 mJ laser energy, open squares, 120 mJ laser energy, crossed squares, 200 mJ laser energy (La Plata measurements), diagonally crossed squares, 60+60 mJ double pulse measurements) and Mn II at 293.3/Mn II at 348.3 nm lines (full circles, 60 mJ laser energy, open circles, 120 mJ laser energy, crossed circles, 200 mJ laser energy (La Plata measurements), diagonally crossed circles, 60+60 mJ double pulse measurements). The dotted and dashed lines represent the low self-absorption and high self-absorption limits, respectively, for the two line pairs. Note the logarithmic scale on the y axis.

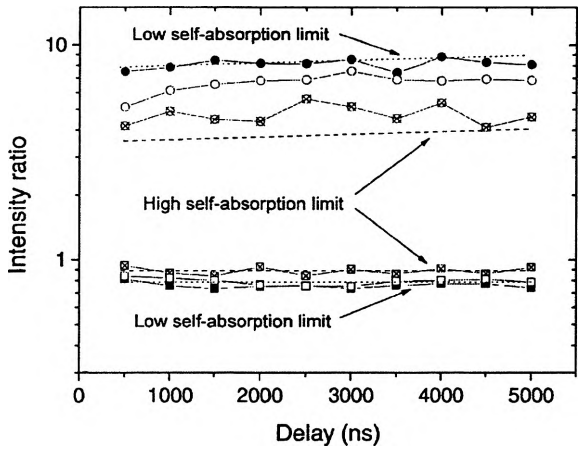


Fig. 5. Time dependence of the intensity ratios of Mn I at 478.5/Mn I at 482.4 nm lines (full squares, 60 mJ laser energy; open squares, 120 mJ laser energy; diagonally crossed squares, 60+60 mJ double pulse measurements) and Mn I at 482.4/Mn I at 472.7 nm lines (full circles, 60 mJ laser energy; open circles, 120 mJ laser energy; diagonally crossed circles, 60+60 mJ double pulse measurements). The dotted and dashed lines represent the low self-absorption and high self-absorption limits, respectively, for the two line pairs. Note the logarithmic scale on the y axis.

temperature and, consequently, on the increasing acquisition delay. The theoretically predicted values of the ratio are about 0.5 for the low self-absorption limit and about 0.7 for the high self-absorption limit.

Even though the two limit values are quite close, it can be noticed that single pulse irradiation leads to optically thin lines, while the double pulse irradiation shifts the plasma conditions toward the high self-absorption limit.

In the same figure, the intensity ratio Mn II at 293.3/Mn II at 348.3 nm is also shown. In this case, since these lines do not belong to the same multiplet, the general theoretical treatment of Section 2.2.4 should be applied. As predicted by the theory, the intensity ratio Mn II at 293.3/Mn II at 348.3 nm indeed depends on the acquisition delay (especially in single pulse high energy measurements). Moreover, for the intensity ratio of lines belonging to different multiplets, a strong dependence on the experimental configuration used is evident. This behaviour is made clear considering the two limits of weak and strong self-absorption (Eqs. (18) and (20)), represented in figure with dotted and dashed lines, respectively. The experimental results are coherent with a strong increase of the self-absorption of the lines changing the experimental conditions from the lowest laser energy (60 mJ single pulse) to the highest laser energy

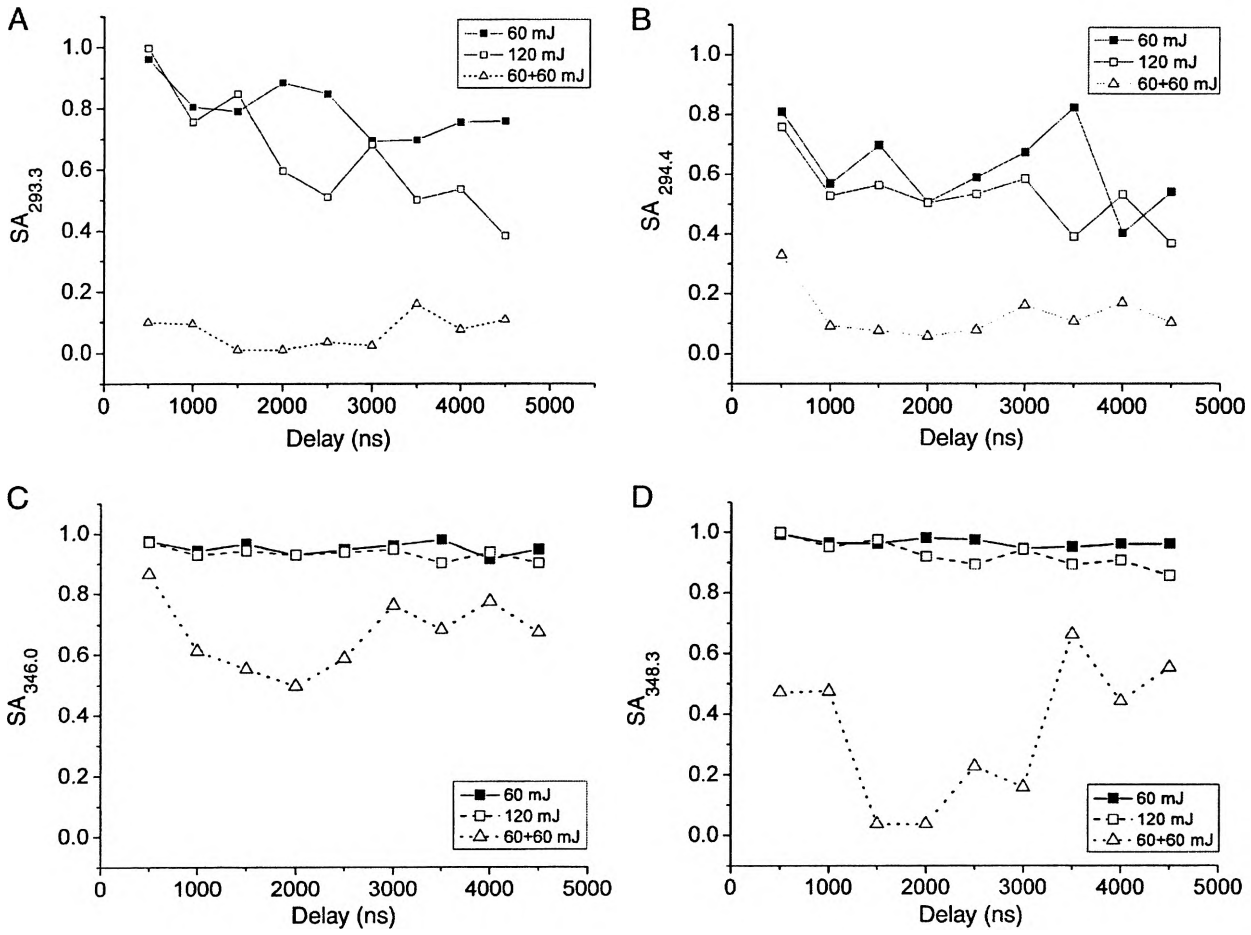


Fig. 6. Time dependence of the self-absorption coefficients SA for some of the Mn II lines considered in this paper (full squares, 60 mJ laser energy; open squares, 120 mJ laser energy; open triangles, 60+60 mJ double pulse measurements). A) Mn II at 293.3 nm, B) Mn II at 294.9 nm, C) Mn II at 346.0 nm, D) Mn II at 348.3 nm.

(200 mJ single pulse) and finally to double pulse configuration (60+60 mJ). In this case the dependence of the intensity ratio on time delay practically coincides with the temperature dependence of the strong self-absorption limit at each time delay considered. The same considerations apply for the other line intensity ratios of the lines reported in Table 1 (not shown here). The opacities and therefore the SA coefficients of the Mn II lines here considered can be calculated using Eq. (25). Some results are reported in Fig. 6.

3.2. Measurements on neutral Mn lines

Seven Mn I lines have been considered for this study (Mn I at 382.4; 383.4; 471.0; 472.7; 473.9; 478.5; 482.4 nm). Also in this case, the lines are well insulated and free from interferences of other Mn lines. The spectroscopic parameters of the lines considered are reported in Table 1. In Fig. 5, the intensity ratio of three neutral Mn lines (Mn I at 478.5/Mn I at 482.4 nm and Mn I at 482.4/Mn I at 472.7 nm) is reported, in single pulse configuration (60 mJ and 120 mJ) and double pulse configuration (60+60 mJ). Since the spectral windows used in the La Plata experiment did not include these Mn I lines, only the Pisa results will be shown here. The first couple of lines in Fig. 5 (Mn I at 478.5 and Mn I at 482.4 nm) belongs to the same multiplet, so that the theoretical treatment of Section 2.2.3 is applicable. It is evident that the intensity ratio of these two lines is essentially independent on the acquisition delay. On the other hand, the low self-absorption limit predicted for these two lines (0.8) is very close to the high self-absorption limit (0.9), so that no appreciable difference can be observed, within the experimental error, between the measurements corresponding to different experimental configurations.

In the same figure, the intensity ratio of Mn I line at 482.4 nm with Mn I line at 472.7 nm is also shown. In this case, since these lines do not belong to the same multiplet, the general theoretical treatment of Section 2.2.4 should be applied. In fact, the intensity ratio Mn I at 482.4/Mn I at 472.7 nm depends, although weakly, on the acquisition delay, as expected from Eq. (25), due to the variation in plasma temperature with time.

As in the case of ionized Mn lines, the ratio of lines belonging to different multiplets shows a dependence on the experimental configuration, which is coherent with an increase of self-absorption with the increase of the laser energy.

The opacities and SA coefficients of the seven Mn I lines here considered can be calculated using Eq. (25); some relevant results are reported in Fig. 7.

4. Discussion

The variation of the self-absorption with the acquisition delay depends on the growth of plasma dimensions, on the decrease of plasma temperature and on the atoms–ions equilibrium, all the three effects being strictly interrelated during the plasma dynamic expansion. The increase of dimensions of the plasma affects the SA coefficient in the growth of the optical path l and in the decrease of the number density $n \propto 1/l^3$, the net effect being a reduction of self-absorption ($k(l) \cdot l \propto 1/l^2$). On the contrary, the cooling of the plasma tends to increase the population of the lower atomic energy levels in proportion to that of the higher levels and thus to enhance the self-absorption of the lines. On the other hand the plasma temperature variation leads also to a shift of the atoms–ions equilibrium, which is however strongly dependent on the plasma electron density according to the Saha equation.

It is clear from Figs. 6 and 7 that the SA coefficient at the different wavelengths decreases and then the plasma opacity dramatically increases in double pulse configuration, for both neutral and ionized Mn lines. In those conditions, the error in the determination of the absolute value of the plasma opacity can be quite high. In fact, although the treatment of self-absorption effects here presented is quite general, under the hypotheses of plasma homogeneity and Local Thermal Equilibrium, from an experimental point of view for obtaining a quantitative estimation of the line opacities the dependence of the right side of Eq. (25) on the $\kappa(\lambda_0)_2 l$ parameter should be strong enough, for making the comparison with the experimental determined value

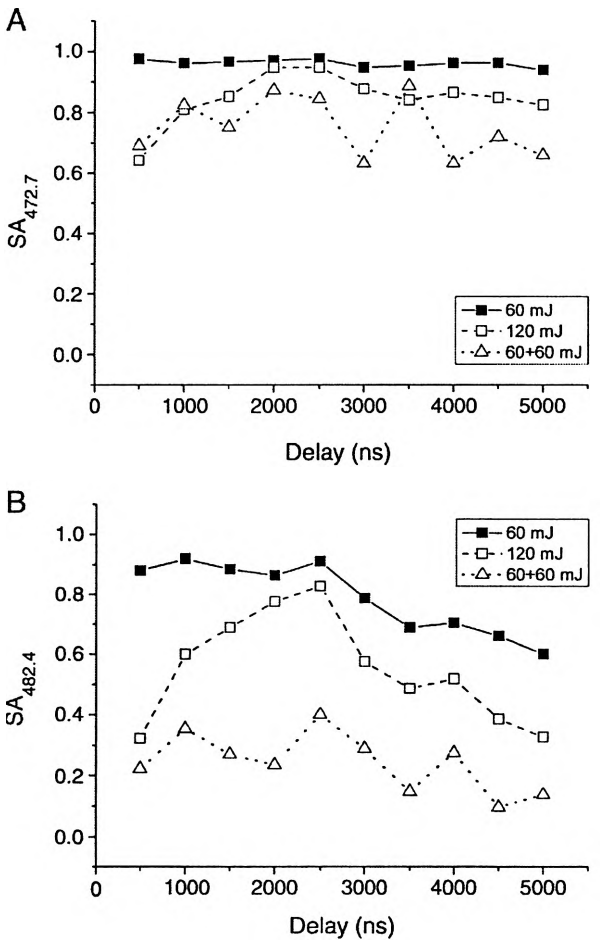


Fig. 7. Time dependence of the self-absorption coefficients SA for some of the Mn I lines considered in this paper (full squares, 60 mJ laser energy; open squares, 120 mJ laser energy; open triangles, 60+60 mJ double pulse measurements). A) Mn I at 472.7 nm, B) Mn I at 482.4 nm.

of the line intensity ratio $\frac{(N_p)_2}{(N_p)_1}$ meaningful. However, we have already shown in Section 2.2.2 that Eq. (25) in the limit $\kappa(\lambda_0)_2 l >> 1$ transforms in

$$\frac{(N_p)_2}{(N_p)_1} = ab^{\beta} \tag{28}$$

i.e. the line intensity ratio (at a given temperature) becomes a constant. Therefore, the determination of the line opacity $\kappa(\lambda_0)_2 l$ from the measurement of intensity ratio becomes impossible. As a consequence, the estimation of $\kappa(\lambda_0)_2 l$ (and $\kappa(\lambda_0)_1 l$ from Eq. (15)) can be obtained only in the limit of small to moderate self-absorption ($\kappa(\lambda_0)_2 l \leq 1$). In the measurements performed in double pulse configuration, it is clear that the condition $\kappa(\lambda_0) l >> 1$ is realized at all time delays for all the lines here considered, therefore the only information we can obtain from the measurements is that all the Mn lines here considered are strongly self absorbed.

However, in single pulse configuration, at least for ionized Mn lines, the increase of plasma opacity with the acquisition delay, at both 60 mJ and 120 mJ laser energy, is well appreciable. Moreover, in the La Plata measurements a clear transition between the low self-absorption to high self-absorption regime is visible at increasing acquisition delays. Since in this condition of irradiation the plasma is strongly ionized ($n^{I}/(n^{I}+n^{II}) \sim 0.1$ during the time window investigated) and the increase in time of the plasma dimensions would tend to lower the opacity, on the basis of what discussed above it is clear that the increase of self-absorption with the acquisition delay is justifiable by the cooling of the plasma.

In the present experimental conditions it is clear that the five Mn II lines belonging to the multiplet centred around 347.0 nm are considerably less self-absorbed than the corresponding lines at 293.3 and 294.9 nm, by about one order of magnitude.

The acquisition delay dependence of the opacities of the Mn I lines considered is more complex and difficult to interpret, being also strongly affected by the atoms–ions equilibrium. It is possible that the initial growth of the self-absorption coefficient (corresponding to a decrease of the self-absorption effect) observed in Fig. 7 in the case of single pulse with energy 120 mJ, is due to the strong decrease of atoms number density due to the initial fast expansion of the plasma. However, it is clear that at all the delays considered the Mn I lines belonging to the multiplet centred around 472 nm are definitely less self-absorbed than the Mn I lines at 478.5 and 482.4 nm. For these lines the condition $\kappa(\lambda_0)_2 l << 1$ is well realized, in single pulse configuration and at the energies used in the Pisa experiment, practically at all the time delays here considered. These lines can thus be good candidates for analytical measurements on Fe–Mn alloys. The results reported above pose some questions on the use of double pulse LIBS method for the analysis of the major components of a given material; in fact, the strong improvement on signal intensity reported in double pulse configuration brings as a side effect a strong increase of the self-absorption effect, which is very difficult to deal with, at the levels measured in the experimental conditions of this paper, in the framework of precise analytical measurements.

5. Conclusions

Starting from the basic equations describing the self-absorption process in a homogeneous plasma, we have derived several analytical relations and devised experimental procedures for the evaluation of self-absorption coefficients (even in the absence of known Stark coefficients), which are important for characterization and control of the experimental conditions in which the analysis is performed. Although the experimental uncertainties and the strong starting hypotheses of the method in many cases do not allow a precise calculation of the self-absorption coefficients, a quick and clear discrimination of the experimental conditions and the emission lines which are less sensitive to self-absorption, and thus are more appropriate for analytical measurements, can be obtained. This estimation, in our opinion, can be very useful in practice because it is fast and do not rely upon any external (not experimental) parameter such as plasma dimensions l, plasma number density or target composition. These results are considered as preliminary for the following study, which will be reported in a forthcoming paper, on matrix effects in LIBS analysis of Fe–Mn alloys.

References

[1] D.A. Cremers, L.J. Radziemski, Detection of chlorine and fluorine in air by Laser-Induced Breakdown Spectrometry, Anal. Chem. 55 (1983) 1252–1256.
[2] L.J. Radziemski, D.A. Cremers, Laser-Induced Plasmas and Applications, Marcel Dekker Inc, New York, 1989.
[3] Y.L. Lee, K. Song, J. Sneddon, in: J. Sneddon, T.L. Thiem, Y.L. Lee (Eds.), Lasers in Analytical Atomic Spectroscopy, VCH Publishers Inc., 1997.
[4] D.A. Cremers, L.J. Radziemski, T.R. Loree, Spectrochemical analysis of liquids using the laser spark, Appl. Spectrosc. 38 (1984) 721–729.
[5] D. Bulajic, G. Cristoforetti, M. Corsi, M. Hidalgo, S. Legnaioli, V. Palleschi, A. Salvetti, E. Tognoni, S. Green, D. Bates, A. Steiger, J. Fonseca, J. Martins, J. McKay, B. Tozer, D. Wells, R. Wells, M.A. Harith, Diagnostics of high-temperature steel pipes in industrial environment by Laser-Induced Breakdown Spectroscopy technique: the LIBSGRAIN project, Spectrochim. Acta Part B 57 (2002) 1181–1192.
[6] A.K. Ray, F.Y. Yueh, J.P. Singh, Laser-Induced Breakdown Spectroscopy of molten aluminium alloy, Appl. Opt. 42 (2003) 2078–2084.
[7] S. Lawson, C.P. Evans, A.I. Whitehouse, J. Wright, J. Young, LIBS — laser eyes for peering into the radioactive zone, Mater. Word 8 (2000) 5.
[8] A.I. Whitehouse, J. Young, I.M. Botheroyd, S. Lawson, C.P. Evans, J. Wright, Remote material analysis of nuclear power station steam generator tubes by Laser-Induced Breakdown Spectroscopy, Spectrochim. Acta Part B 56 (2001) 821–830.
[9] A. Ciucci, V. Palleschi, S. Rastelli, R. Barbini, F. Colao, R. Fantoni, A. Palucci, S. Ribezzo, H.J.L. van der Steen, Trace pollutants analysis in soil by a time resolved Laser-Induced Breakdown Spectroscopy technique, Appl. Phys., B 63 (1996) 185–190.
[10] S.G. Buckley, H.A. Johnsen, K.R. Henken, D.W. Hahn, Implementation of Laser-Induced Breakdown Spectroscopy as a continuous emission monitor for toxic metals, Waste Manage. 20 (2000) 455–462.
[11] R.W. Bogue, Boom time for LIBS Technology, Sens. Rev. 24 (2004) 353–357.
[12] I.V. Cravetchi, M. Taschuk, G.W. Rieger, Y.Y. Tsui, R. Fedosejevs, Spectrochemical microanalysis of aluminium alloys by Laser-Induced Breakdown Spectroscopy: identification of precipitates, Appl. Opt. 42 (2003) 6138–6147.
[13] S. Palanco, L.M. Cabalin, D. Romero, J.J. Laserna, Infrared laser ablation and atomic emission spectrometry of stainless steel at high temperature, J. Anal. At. Spectrom. 14 (1999) 1883–1887.

[14] V. Sturm, L. Peter, R. Noll, Steel analysis with Laser-Induced Breakdown Spectrometry in the Vacuum ultraviolet, Appl. Spectrosc. 54 (2000) 1275–1278.
[15] H. Bette, R. Noll, High speed Laser-Induced Breakdown Spectrometry for scanning microanalysis, J. Phys., D, Appl. Phys. 37 (2004) 1281–1288.
[16] J. Gruber, J. Heitz, N. Arnold, D. Bauerle, N. Ramaseder, W. Meyer, J. Hochortler, F. Kock, In situ analysis of metal melts in metallurgic vacuum devices by Laser-Induced Breakdown Spectroscopy, Appl. Spectrosc. 58 (2004) 457–462.
[17] G.P. Kopitsa, V.V. Runov, S.V. Grigoriev, V.V. Bliznuk, V.G. Gavriljuk, N.I. Glavatska, The investigation of Fe–Mn-based alloys with shape memory effect by small-angle scattering of polarized neutrons, Physica. B + C 335 (2003) 134–139.
[18] T. Schneider, M. Acet, B. Rellinghaus, E. Wassermann, W. Pepperhoff, Antiferromagnetic Invar and anti-Invar in Fe–Mn alloys, Phys. Rev., B 51 (1995) 8917–8921.
[19] A. Borgenstam, M. Hillert, The driving force for Lath and Plate martensite and the activation energy for isothermal martensite in ferrous alloys, J. Phys., IV 7 (1997) C5:23–C5:28.
[20] S.M. Cotes, A. Fernández Guillermet, M. Sade, Gibbs energy modelling of the driving forces and calculation of the fcc/hcp martensitic transformation temperatures in Fe–Mn and Fe–Mn–Si alloys, Mater. Sci. Eng., A Struct. Mater.: Prop. Microstruct. Process. 273–275 (1999) 503–506.
[21] A. Baruj, A. Fernández Guillermet, M. Sade, Effects of thermal cycling and plastic deformation upon the Gibbs energy barriers to martensitic transformation in Fe–Mn and Fe–Mn–Co alloys, Mater. Sci. Eng., A Struct. Mater.: Prop. Microstruct. Process. 273–275 (1999) 507–511.
[22] I.B. Gornushkin, J.M. Anzano, L.A. King, B.W. Smith, N. Omenetto, J.D. Winefordner, Curve of growth methodology applied to laser-induced breakdown spectroscopy, Spectrochim. Acta Part B 54 (1999) 491–503.
[23] C. Aragón, J. Bengoechea, J.A. Aguilera, Influence of the optical depth on spectral line emission from laser-induced plasmas, Spectrochim. Acta Part B 56 (2001) 619–628.
[24] H. Amamou, A. Bois, B. Ferhat, R. Redon, B. Rossetto, M. Ripert, Correction of the self-absorption for reversed spectral lines: application to two resonance lines of neutral aluminum, J. Quant. Spectrosc. Radiat. Transfer 77 (2003) 365–372.
[25] I.B. Gornushkin, C.L. Stevenson, B.W. Smith, N. Omenetto, J.D. Winefordner, Modeling an inhomogeneous optically thick laser induced plasma: a simplified theoretical approach, Spectrochim. Acta Part B 56 (2001) 1769–1785.
[26] J.A. Aguilera, J. Bengoechea, C. Aragón, Curves of growth of spectral lines emitted by a laser-induced plasma: influence of the temporal evolution and spatial inhomogeneity of the plasma, Spectrochim. Acta Part B 58 (2003) 221–237.
[27] D. Bulajic, M. Corsi, G. Cristoforetti, S. Legnaioli, V. Palleschi, A. Salvetti, E. Tognoni, A procedure for correcting self-absorption in calibration free-laser induced breakdown spectroscopy, Spectrochim. Acta Part B 57 (2002) 339–353.
[28] A.M. El Sherbini, Th.M. El Sherbini, H. Hegazy, G. Cristoforetti, S. Legnaioli, V. Palleschi, L. Pardini, A. Salvetti, E. Tognoni, Evaluation of Self-absorption Coefficients of Aluminum Emission Lines in Laser-Induced Breakdown Spectroscopy Measurements, Spectrochim. Acta Part B 60 (2005) 1573–1579.
[29] A. Ciucci, V. Palleschi, S. Rastelli, A. Salvetti, E. Tognoni, New procedure for quantitative elemental analysis by Laser Induced Plasma Spectroscopy, Appl. Spectrosc. 53 (1999) 960–964.
[30] H. Hakkanen, J. Korppi-Tommola, Laser-induced plasma emission spectrometric study of pigments and binders in paper coatings: matrix effects, Anal. Chem. 70 (1998) 4727–4736.
[31] J.M. Anzano, I.B. Gornushkin, S.I. Gornushkin, B.W. Smith, J.D. Winefordner, Effective normalization technique for correction of matrix effects in Laser-induced Breakdown Spectroscopy detection of magnesium in powdered samples, Appl. Spectrosc. 56 (2002) 433–436.
[32] S. Djenize, S. Bukvic, A. Sreckovic, Z. Nikolic, The first measured Mn II and Mn III Stark broadening parameters, New Astron. 11 (2006) 256–261.
[33] L.C. Popovic, M.S. Dimitrijevic, The electron impact broadening parameters in hot star atmospheres: Mn II, Mn III, Ga III, Ge III and Ge IV lines, Astron. Astrophys., Suppl. Ser. 128 (1998) 203–205.
[34] F. Colao, R. Fantoni, V. Lazic, A. Paolini, LIBS application for analyses of martian crust analogues: search for the optimal experimental parameters in air and CO_2 atmosphere, Appl. Phys., A 79 (2004) 143–152.
[35] H. Amamou, A. Bois, B. Ferhat, R. Redon, B. Rossetto, P. Matheron, Correction of self-absorption spectral line and ratios of transition probabilities for homogeneous and LTE plasma, J. Quant. Spectrosc. Radiat. Transfer 75 (2002) 747–763.
[36] M. Friedjung, G. Muratorio, Singly ionized iron as a diagnostic of stellar envelopes. 1. The methods, Astron. Astrophys. 188 (1987) 100.
[37] S.O. Kastner, Clarification and interpretation of the Friedjung–Muratorio self absorption curve method, Astron. Astrophys. 351 (1999) 1016–1020.
[38] S. Chandrasekar, Radiative Transfer, Dover Publications, Inc., New York, 1960.
[39] R.S. Adrain, J. Watson, Laser microspectral analysis: a review of principles and applications, J. Phys., D, Appl. Phys. 17 (1984) 1915–1940.
[40] H.R. Griem, Plasma Spectroscopy, Mc Graw Hill, New York, 1964.
[41] G. Cristoforetti, S. Legnaioli, V. Palleschi, L. Pardini, A. Salvetti, E. Tognoni, Modi: a new mobile instrument for in situ standardless LIBS analysis of Cultural Heritage, in: R. Salimbeni, L. Pezzati (Eds.), Optical Methods for Arts and Archaeology, Proc. SPIE, vol. 5857, 2005, pp. 129–138.
[42] J. Ashkenazy, R. Kipper, M. Caner, Spectroscopic measurements of electron density of capillary plasma based on Stark broadening of hydrogen lines, Phys. Rev., A 43 (1991) 5568–5574.
[43] S. Yalcin, D.R. Crosley, G.P. Smith, G.W. Faris, Influence of ambient conditions on the laser air spark, Appl. Phys., B 68 (1999) 121–130.
[44] M. Corsi, G. Cristoforetti, M. Giuffrida, M. Hidalgo, S. Legnaioli, V. Palleschi, A. Salvetti, E. Tognoni, C. Vallebona, Three-dimensional analysis of laser induced plasmas in single and double pulse configuration, Spectrochim. Acta Part B 59 (2004) 723–735.
[45] G. Cristoforetti, S. Legnaioli, V. Palleschi, A. Salvetti, E. Tognoni, P. Tomassini, Reconstruction of laser-induced plasma spectral emissivity in non-axisymmetric conditions, Spectrochim. Acta Part B 60 (2005) 888–896.

AN AUTOMATIC HIGH-RESOLUTION SCANNING DENSITOMETER APPLIED TO OPTICAL SPECTROSCOPY

A. P. Laquidara

ABSTRACT

A high-resolution digital scanning densitometer was built to record spectral UV-VIS-IR lines on magnetic media from photographic transparencies. The system was assembled with a sliding table measuring machine driven from a PC and a silicon photodiode and A/D converter to record light intensities. A spectroscopic plate or film can be read and recorded with a sampling step of 1.20 μm.

1. INTRODUCTION

In the last three decades, the Centro de Investigaciones Opticas (CIOp), has produced many research works in atomic and molecular spectroscopy using different optical spectrographs, recording stimulated and spontaneous UV-VIS-IR emissions on photographic plates.

Spectral lines are identified visually by comparing photographic records obtained after long periods of exposition. This recording media reaches a very high resolution: about .01 nm/mm.

The use of an automatic plate reading system offers better resolution between lines and easier identification of weaker spectra, printing them on paper for direct eye observation.

Using a **GSIP** precision length measuring machine, usually hand operated, and joining a stepper motor to the fine displacement motion control, the sliding table moves horizontally carrying the film or plate to be read and recorded.

A white light optical beam strikes the bottom face of the film and the light intensity detected on the upper face. The detected signal is sampled with a 12 bit A/D converter and is saved to disk.

The recorded spectra is plotted spanning each slot a hundred times. This magnification between lines allows easier visual identification. A spectroscopic plate 25 cm long may be plotted at a 1nm scale per page, in about a hundred paper sheets size A4.

Centro de Investigaciones Opticas
Comisión de Investigaciones Cientificas de la Provincia de Buenos Aires
Casilla de Correo 124, 1900, La Plata Buenos Aires, Argentina.
E-mail: laquidar@isis.unlp.edu.ar
Received: September 4, 1995. Accepted: May 7, 1996.

2. OPTO-MECHANICAL SETUP

The metrological machine **GSIP** (Societé Genevoise D'Instruments de Physique), mod. MU-214B, is a universal three-dimensional high-precision measuring apparatus that was used in the present project taking advantage of the quality of its linear displacements and ability to connect to a PC to perform the adquisition and control. This avoided the construction of an expensive system of the same mechanical precision.

The machine has a horizontal sliding table 50 cm long and 18 cm wide, with a 40 cm per 11 cm slit. It can be slid manually or by means of a stepper motor up to a distance of 27 cm.

The film is held on the table by a thin glass plate. If the spectra is recorded on a glass plate, this is held on the table by small weights on the edges of the plate.

The light of a 50 W dichroic lamp at the back of the machine is taken by an optical system to the base of the sliding table, lighting the area of the plate to be read.

The machine holds a microscope which slides normally to the table, making an image of the required size on the detector.

The detector optical system is a 10x microscope objective at the bottom of a tube 23 cm long, which makes a real image of the spectroscopic line on a stainless steel slit 50 μm wide by 3 mm height, aligned with the line image, at the opposite end of the tube.

3. MEASUREMENT AND CONTROL INTERFACE

Behind the slit is assembled a silicon photodiode integrated to a I-V variable gain amplifier ranging between 100 KΩ and 10 MΩ and offset adjust. The I-V amplifier output

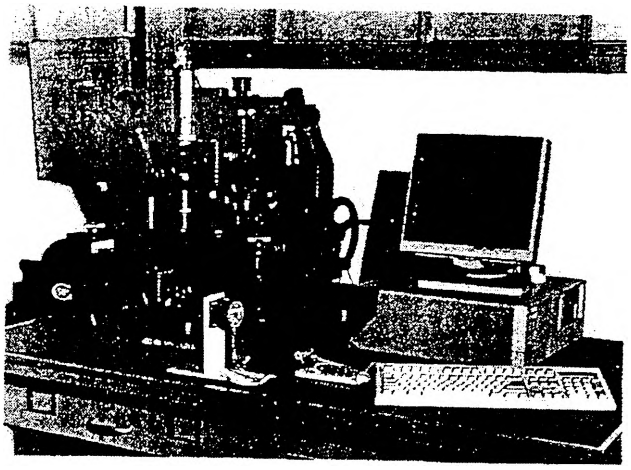


Figure 1. Photograph of the spectroscopic plate reading system.

drives a V-V amplifier stage of gain 130, and limited to a maximum of +5 volts. Both amplifiers are fed from the A/D converter board inside the PC which performs measurement and control.

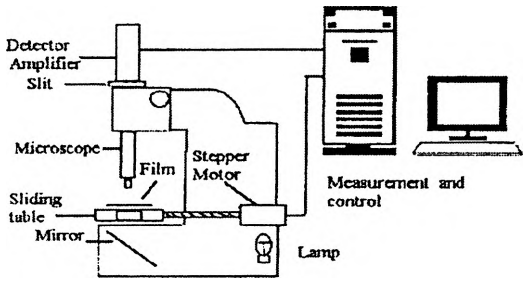


Figure 2. Schematic of the spectroscopic plate reading setup.

Another I/O board inside the PC together with a power supply and an external field switching circuit controls the stepper-motor motion driving the table.

The motor shaft coupled to the fine displacement motion control gives a linear step advance to the table of 1.20 μm, enough to resolve the spectral lines on the plate at a 0.4 nm/mm scale for the visible spectrum. The exact value of the linear dispersion ($\Delta x / \Delta \lambda$) must be computed for each slot of the spectrum.

The mechanical coupling between the fine motion control and the table suffers sliding that reaches a maximum lack of advance of 2.5 μm per each record of 8000 samples, that is, less than 0.026 % of the linear displacement. This lack of advance could be corrected by coupling the table to a linear precision transducer in a closed loop control.

4. SOFTWARE

The plotting mode chosen is the spreadsheet which requires recording of files of 8 KB consecutive samples at a full adquisition and recording time of 90 s per file of almost 10 mm of spectrum on the plate. As well as this, a file is created with the background transparency of the plate, averaged and substracted from each data file for contrast enhancement.

The resultant contrast is over 0.9, limited mainly by the residual noise of the modified file. These are plotted and observed later on the spectrum sector investigated.

The uncertainty noise of the A/D converter does not impair the recorded contrast, and is of +/- 1 LSB. The conversion time per sample is of 60 μs.

Every 8 KB samples the file is closed and the next is opened, avoiding the accumulation of sliding errors, larger than the error mentioned above.

Between every two registers, the zero transparency value is set to its least positive value, ensuring the intensity plotting errors below 5% for each record.

The following programs were written for an IBM PC.

1- **Zero setting:** inicializes the output voltage value of the detector amplifier before the plate logging.
2- **Background intensity:** fixes the reference level of the intensity data files.
3- **Adquisition and control:** saves the spectral intensity data to disk and controls the sliding table motion.
4- **Background substraction:** this program modifies all data files substracting the averaged background intensity of the plate and gives a sequential number to each modified data file for its recognition.

5. SUMMARY OF TECHNICAL CHARACTERISTICS

1- File generation of 8 KB samples in 90 s, equivalent to 9.6 mm of spectral plate or film.

2- Step resolution of 1.20 μm with an error of 0.026 % of linear position for each register, with a spectral dispersion better than 0.4 nm/mm (VIS) for each plotted page.

3- Intensity resolution of +/-5 %.

4- Posibility of substracting the background level from each record to allow the recognition of weak lines.

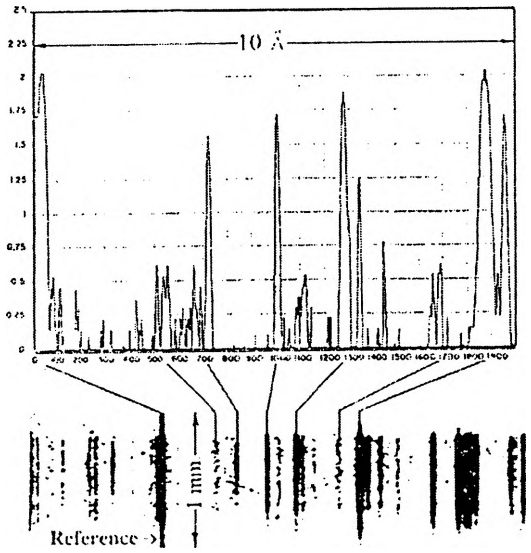


Figure 3. Spectral line logging obtained with the plate reading system.

6. CONCLUSIONS

A spectroscopic plate densitometer was built, adapting an existing machine at CIOp employed in three-dimensional metrology. A high spectral resolution was achieved and a plotting method was developed that simplifies the study and recognition of fine structures.

The open loop operation of the system and the I-V amplifier instability are the limiting factors of the precision of system in its current state.

The resolution reached is better than that of similar apparatus for transparency logging which have 60 μm [1] between samples, and 100 μm [2] between samples, and it allows the printing of spectrum pieces at a scale of 1 nm per page.

REFERENCES

1. A. Abrahamsson, J. Sci. Instruments, **43**, 931-933, (1966)

2. Nguyen-hun Xuong, J. Sci. Instruments (J. of Physics E), Series 2, **2**, 485-489, (1969)

Medición de Gases contaminantes atmosféricos

La experiencia adquirida en estos 30 años tanto en estudios básicos de espectroscopía óptica como en técnicas de medición, llevó a la aplicación de las mismas al estudio de problemáticas concretas de interés mundial, como lo son el llamado agujero de ozono y la contaminación gaseosa atmosférica por emisiones industriales.

Desde mediados de la década del 80 y durante la del 90, ambos temas han estado al tope del interés tanto científico como popular, debido a la concientización general de la problemática ambiental. La Óptica y la Espectroscopía pueden colaborar activamente en la determinación de concentraciones estratosféricas de ozono y troposféricas de otros gases contaminantes. En particular, optamos por desarrollar técnicas de medición que requirieran de instrumental de bajo costo y fácil manipulación, basadas en espectroscopía de absorción diferencial de columna abierta. Los dos trabajos seleccionados ejemplifican las principales tareas realizadas dentro de esta línea de investigación.

El primero trata sobre los resultados de una campaña de medición de radiación UV en el cono sur del continente americano con una red de dispositivos ópticos (7) desplegados en tierra. Cada uno de los dispositivos que conforma esta red incorpora un par de fotodiodos de silicio sensibles al azul (respuesta espectral entre 250 y 900 nm), con óptica de enfoque y sendos filtros interferenciales integrados a ellos, centrados de 300 nm y 313nm. Al detectar la radiación directa del sol a nivel del mar, la gran diferencia en valores de la sección eficaz de absorción del ozono en estas dos longitudes de onda permite, a partir del cociente de las irradiancias medidas y de una cuidadosa calibración, determinar el decrecimiento en el ozono total estratosférico. Los resultados obtenidos coinciden muy bien con los datos satelitales tomados en la misma región y durante el mismo intervalo de tiempo, en el cual se detectaron varios eventos de notable disminución en el espesor de la capa de ozono como así también importantes incursiones del mismo dentro del territorio del cono sur hasta latitudes de 53° Sur.

El segundo de los trabajos seleccionados resume el trabajo realizado en mediciones de gases contaminantes atmosféricos de origen industrial, como el SO2 y el NO2. Como evolución de los dispositivos para medición de ozono, se desarrollaron medidores no dispersivos en UV (NDUV) para detección de estos gases en boca de chimenea, en los que los filtros ópticos fueron debidamente seleccionados para que coincidieran con bandas de absorción de las especies a medir. Para la detección de estos gases a nivel de ambiente urbano, se utilizó la técnica de espectroscopía de absorción óptica diferencial dispersiva (DOAS), que consiste en enviar un haz colimado de luz blanca por una columna abierta de atmósfera de varios cientos de metros y observar con un espectrógrafo en el otro extremo las bandas absorbidas. De la medición de la profundidad de dichas bandas y la aplicación de la ley de Lambert-Beer, es posible determinar la concentración de los gases en cuestión. El trabajo trata sobre una novedosa forma de utilizar esta ley para el posterior tratamiento de los datos y la determinación de las respectivas concentraciones.

Atmospheric trace Gas measurements

The experience in basic optical spectroscopy and related measurement techniques acquired during these 30 years enabled its application to worldwide concern issues such as ozone depletion measurements and atmospheric gas pollution detection.

Since mid 80s and all through the 90s, these problems have been both of scientific and popular interest, mainly due to the growth of global environmental-protection awareness. Spectroscopic and optical methods can be readily used for the determination of ozone depletion and atmospheric pollution measurements. We developed low-cost, user-friendly techniques based on open column differential optical absorption. The two papers selected here show the main activities carried out in this line of research.

The first one deals with ground-based ultraviolet radiation measurements during spring in the southern-hemisphere part of the American Continent, using a network of optical devices deployed in 9 locations in Argentina and Chile.

The devices built for this purpose have been designed to be of low cost and easy to manipulate, in order to implement an extended UV network. The device consists of two EGG

detectors (type DF) incorporating blue silicon photodiodes (spectral response 250-900 nm) and integrated interferential filters (centered at 313 nm and 300 nm, with 10 nm bandwidth). Two quartz based telescopic assemblies and an equatorial mounting (ALSTAR) allow Sun tracking for direct solar-radiation measurement. The relative response of the devices has been carefully calibrated at CIOp.

Due to the great difference (a factor of six) in the absorption cross-section at the selected wavelengths (313 and 300 nm), changes in the irradiance ratio at these wavelengths clearly indicate a decrease in the total ozone amount. Ozone data obtained from the ground stations are compared with total ozone values supplied by the satellite showing a very good agreement.

The second paper exemplifies the work carried out for measurement of atmospheric pollutant gases such as SO2 and NO2. Similarly to those developed for ozone, non dispersive UV (NDUV) devices with appropriate interference filters were constructed and run in a laboratory-based industrial chimney, with very good sensitivity. For urban air quality measurements, differential optical absorption spectroscopy (DOAS) was used. A collimated white light beam is launched, at one end, through a several hundred-meter long atmospheric column and analyzed with a spectrograph at the other end. The absorption bands found and their deepness provide accurate information about the gas species and its concentration through the direct application of Lambert-Beer (LB) law. In particular, the paper shows a novel application of LB to the determination of the concentration of interfering gases.

Published on Europhysics Lett. Vol. 28 (4) pp. 289-293 (1994)

Ground-Based Ultraviolet-Radiation Measurements during Springtime in the Southern Hemisphere

F. JAQUE(1), J. O. TOCHO(2), L. F. DA SILVA(3), G. BERTUCCELLI(4), E. CRINO(5), F. CUSSÓ(1), M. A. DE LAURENTIS(6), J. L. HORMAECHEA(8), G. LIFANTE(1), M. G. NICORA (2), H. F. RANEA-SANDOVAL(4), V. VALDERRAMA(9) and G. D. ZOJA(7)

1. Departamento de Física de Materiales, C-IV, Universidad Autónoma de Madrid 28049 Madrid, Spain
2. Departamento de Física, Universidad Nacional de la Plata and CIOp (CONICET-CIC) - La Plata, Argentina
3. Departamento de Física, Universidad Técnica F. Santa María Casilla 110-V, Valparaíso, Chile
4. Instituto de Física Arroyo Seco - Tandil, Argentina
5. Universidad Nacional de San Luis - San Luis, Argentina
6. Observatorio Astronómico Municipal - Mercedes, Argentina
7. Centro Astronómico - Bariloche, Argentina
8. Estación Astronómica - Río Grande, Argentina
9. Departamento de Matemáticas y Física, Universidad de Magallanes, Punta Arenas, Chile

Abstract - We report the first measurements obtained by a network of UV-B detectors established through Argentina and Chile, at locations covering latitudes extending from 53° S to 18° S. Evidence that UV-B increases are detected at these latitudes during the Austral spring 1993 is presented.

Introduction. - The destruction of the stratospheric ozone layer is generally considered one of the most serious environmental problems. It has been recently published that during October 1998 the ozone hole has been the deepest ever recorded [1]. Reduction of the stratospheric ozone layer was unambiguously detected about two decades ago in the Antarctic continent [2,3]. Since then it has been systematically monitored by different means (satellite, balloon soundings and ground station observations [4-6]. One of the most serious content reduction is the increase of biologically effective ultraviolet doses, particularly the so-called ultraviolet B radiation (280-320 nm) received at the Earth surface, with multiple possible hazards for living species [7]. Despite these consequences, ground stations to check the UV Sun radiation are not very numerous, particularly outside the circumpolar area in the Southern Hemisphere. With the aim of studying whether the ozone depletion over the Antarctic area has extended further, and whether the possibility that UV-radiation increase may begin to affect inhabited regions, a network of UV-B detectors has been established through Argentina and Chile, at locations covering latitudes extending from 53° S to 18° S (fig.1). Here we report the first measurements obtained by this network providing evidence that UV-B increases are detected at these latitudes during the last Austral spring.



Fig.1 - Location of the ground - based UV-B detectors through Argentina and Chile

Experimental results and discussion. - The devices built for this purpose have been designed to be of low cost and easy to manipulate, in order to implement an extended UV network. The device consists of two EGG detectors (type DF) incorporating blue silicon photodiodes (spectral response 250-900 nm) and integrated interferencial filters (centred at 313 nm and 300 nm, whith 10 nm bandwidth). Two quartz based telescopic assemblies and an equatorial mounting (ALSTAR) allow Sun tracking for direct solar-radiation measurement. The relative response of the devices has been carefully calibrated at the Centro de Investigaciones Opticas (CIOp), La Plata, Argentine./p>

Due to the substantial difference (a factor of six) in the absorption cross-section at the selected wavelengths (313 and 3OO nm) [8], changes in the irradiance ratio at these wavelengths clearly indicate a decrease in the total ozone amount. Although the irradiance ratio between these two close wavelengths corrects several effects, such as light scattering by clouds [9], all data presented in this work have been taken in clear days, with high horizontal visibility.

Figure 2a) shows the variation of the total ozone during September 1993 (days 245 to 274 of the year), recorded in Punta Arenas (lat. = 52° S), Chile, with a Brewer spectro-photometer, calibrated in Dobson units. It can be observed that a remarkable depletion in the total ozone between the days 250 to 260 was detected, followed by narrow deeps occurring on the days 270 and 276. The overall ozone reduction registered between the days 248-270 was about 50% of the predepletion values.

Figure 2b) shows (circles) the midday irradiance ratio (R) at 313 nm and 300 nm, taken at the Observatorio Astronómico de Río Grande (lat. = 53° S), Argentina, a locality near Punta Arenas, during the days 246-280 of 1993. As can be observed, this ratio shows a pronounced drop in the R values between the days 250 and 260, followed by narrow deeps on the days 270 and 276. The overall decrease registered between the days 246-270 was about 50% of the predepletion values. These results are in agreement with the evolution of the total ozone measured in Punta Arenas during the same period of time (fig. 2a).

continent during the beginning of the 1993 spring.

It is accepted that ozone depletion in the atmosphere is caused by a series of UV induced photochemical and catalytic reactions involving halogens as well as hydrogen and nitrogen compounds (HO^x and NO^x). The injection of these components, due to the polar-vortex destruction, is generally associated with the recurrent ozone depletion during the Austral spring.

In relation to the UV increase at the Earth surface presented in fig. 2 and 3, the appearance of episodes well localized in time during the days 270 and 276 is apparent. These episodes are of short (few days) duration and appear practically coincident at latitudes as different as in Río Grande (53° S) and Antofagasta (23° S). Therefore, they seem to be inconsistent with a diffusion process of the "ozone hole" from the Antarctica, and other possibilities must be considered.

It is generally accepted that high-intensity (X) solar flares are capable of depositing large amounts of energy in a short time, involving the production of high concentrations of nitrogen oxide and affecting the ozone concentration at different atmospheric altitudes [10-12], so that this possibility must be considered.

An inspection to the solar-activity reports published by the National Oceanographic and Atmospheric Agency [13,14] reveals the absence of high-intensity (X) solar flares, although two moderate solar flares of magnitude Ml.8 on September 27th, and another solar flare (M1.4 intensity) on October 2nd (days 270 and 276) were detected.

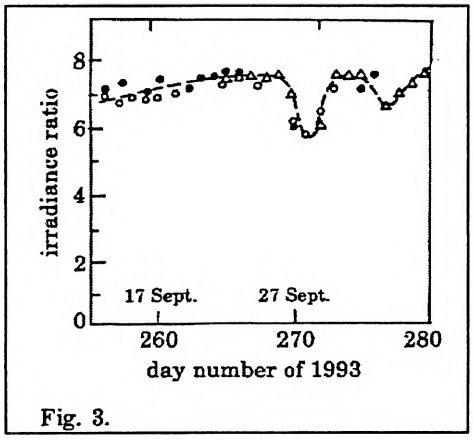


Fig.3 - Evolution of the irradiance ratio at 313 and 300 nm: Valparaíso (Chile), San Luis (Argentina) and Mercedes (Argentina) during the days 256-280 of 1993.

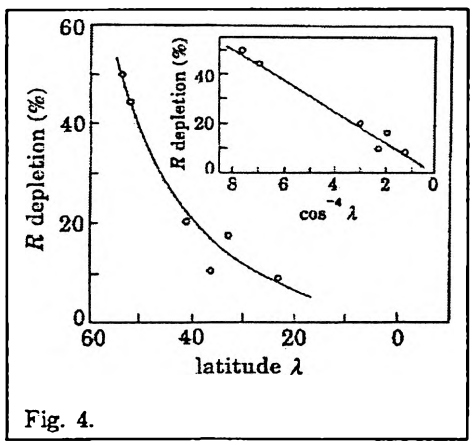


Fig.4 - Dependence of the percentage decrease of the irradiance ratio at 300 nm and 313 nm (R) with the latitude

continent during the beginning of the 1993 spring.

It is accepted that ozone depletion in the atmosphere is caused by a series of UV induced photochemical and catalytic reactions involving halogens as well as hydrogen and nitrogen compounds (HO^x and NO^x). The injection of these components, due to the polar-vortex destruction, is generally associated with the recurrent ozone depletion during the Austral spring.

In relation to the UV increase at the Earth surface presented in fig. 2 and 3, the appearance of episodes well localized in time during the days 270 and 276 is apparent. These episodes are of short (few days) duration and appear practically coincident at latitudes as different as in Río Grande (53° S) and Antofagasta (23° S). Therefore, they seem to be inconsistent with a diffusion process of the "ozone hole" from the Antarctica, and other possibilities must be considered.

It is generally accepted that high-intensity (X) solar flares are capable of depositing large amounts of energy in a short time, involving the production of high concentrations of nitrogen oxide and affecting the ozone concentration at different atmospheric altitudes [10-12], so that this possibility must be considered.

An inspection to the solar-activity reports published by the National Oceanographic and Atmospheric Agency [13,14] reveals the absence of high-intensity (X) solar flares, although two moderate solar flares of magnitude Ml.8 on September 27th, and another solar flare (M1.4 intensity) on October 2nd (days 270 and 276) were detected.

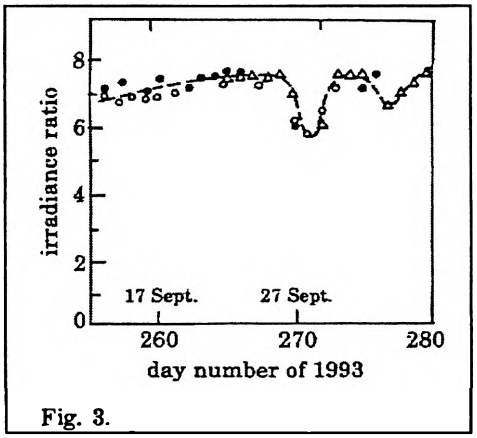


Fig.3 - Evolution of the irradiance ratio at 313 and 300 nm: Valparaíso (Chile), San Luis (Argentina) and Mercedes (Argentina) during the days 256-280 of 1993.

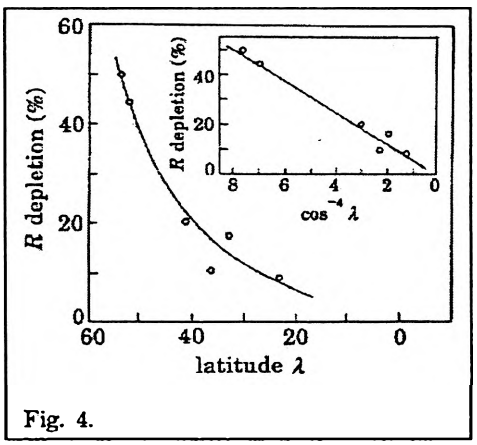


Fig.4 - Dependence of the percentage decrease of the irradiance ratio at 300 nm and 313 nm (R) with the latitude

(lambda), observed around the day 270 of 1993 at the localities of Punta Arenas, Río Grande, Bariloche, Tandil, Valparaíso and Antofagasta. The inset illustrates the power dependence. The solid line represents the least-squares fitting of the data.

Some of these less intense events have also been associated to ozone depletion [11], although the connection of this lower intensity (M) events is not as clear as with the high-energy (X) events, which are occasionally associated with a measurable solar-proton event at the Earth surface (Ground-Level Solar Proton Event).

Therefore, although it cannot be unambiguously stated, the coincidence in time suggests a possible connection between solar flares and the UV-radiation increase. We want to remark also that the ozone depletion here reported on days 270 and 276 of 1993 in Punta Arenas amounts to a 50% of its predepletion value. This is higher than the values previously reported (23% [11] and = 5% [12]) in connection with solar-flare events.

The establishment of a more extensive network, devoted to permanent UV radiation monitoring, covering even higher (equatorward) latitudes than those shown here, would be very convenient to ascertain the origin of the observed UV-radiation increase.

We thank CONICET and CIC-BA (Argentina) and MEC and ICI (Spain) for support. The authors also wish to express their gratitude to Prof. TEITELBAUM and Dr. M. VAZQUEZ for their invaluable suggestions.

References

1. Walker G., *Nature* 365 (1993) 683.
2. Chubachi S., in *Atmospheric Ozone* (Reidel, Dordrecht) 1984, p. 285.
3. Farman J. C., Gardiner B. G. and Shankin J. D., *Nature* 315 (1985) 207.
4. Gleason J. F., Bhartia P. K., Herman J. R., McPeters R., Newman P., Stolarski R. S., Flynn L., Labow G., Larko D., Seftor C., Wellemeyer C., Kohmyr W.D., Miller A.J. and Planet W., *Science*, 260 (1993) 523.
5. Hillsenrath E., Attmannspacher W., Bass A., Evans W., Hagemeyer R., Barnes R. A., Kohmyr W., Mauersberger K., Mentall J., Proffitt M., Robbins D., Taylor S., Torres A. and Weinstock E., *J. Geophys Res.*, 91 (1986) 13137.
6. Frederick J. E. and Weatherhead E. C., *Photochem. Photobiol.*, 56 (1992) 123.
7. McKinley A. F. and Diffey B. L., in *Human Exposure to Ultraviolet Radiation: Risks and Regulations*, edit by W. F. Passchier and B. F. M. Bosnjakovic (Excerpta Medica, Int. Congr. Ser., Amsterdam) 1987, p. 83
8. Molina L. T. and Molina M. J., *J. Geophys. Res.*, 91 (1986) 14501
9. Goody R. M., in *Atmospheric Radiation* (Oxford University Press, New York, N.Y.) 1964, p. 436.
10. Weeks L. H., Cuikay R. S. and Corbin J. R., *J. Atmos. Sci.*, 29 (1972) 1138.
11. Weath D. F., Krueger A. J. and Crutzen P. J., *Science*, 197 (1977) 886.
12. Shumilov O. I., Henriksen K., Raspopov O. M. and Kasatkina E. A., *Geophys. Res. Lett.*, 19 (1992) 1647.
13. *Solar-Geophysical Data prompt reports, NOAA*, Number 590 Part I (1993) 26.
14. *Solar-Geophysical Data prompt reports, NOAA*, Number 591 Part I (1993) 28.

rich2/lp-osa/lp-osa/lp0603/lp8004-03a | reedj | S=3 | 3/25/03 | 13:27 | Art: | Input-1st mke-s, 2nd low

Alternative method for concentration retrieval in differential optical absorption spectroscopy atmospheric gas pollutant measurements

Fabián A. Videla, Daniel C. Schinca, and Jorge O. Tocho

Differential optical absorption spectroscopy is a widely used technique for open-column atmospheric-gas pollution monitoring. The concentration retrieval is based on the fitting of the measured differential absorbance through the Lambert–Beer law. We present an alternative method for calculating the gas concentration on the basis of the proportionality between differential absorbance and differential absorption cross section of the gas under study. The method can be used on its own for single-component analysis or as a complement to the standard technique in multicomponent cases. The performance of the method for the case of cross interference between two gases is analyzed. The procedure can be used with differential absorption cross sections measured in the laboratory or taken from the literature. In addition, the method provides a criterion to discriminate against different species having absorption features in the same wavelength range. © 2003 Optical Society of America

OCIS codes: 010.0010, 010.1120, 280.0280, 280.1120, 300.0300, 300.1030.

1. Introduction

Fn1 Optical sensing techniques have been used during the past decade for environmental studies. Laser- and nonlaser-based long-path absorption methods are particularly advantageous over point-monitoring techniques, since they can perform large area measurements in a single experiment. Differential optical absorption spectroscopy (DOAS) is an open-path, nonlaser-based technique pioneered by Platt, Perner, and co-workers.[1–3] In its original form, light from a high pressure Xe lamp is collimated with a parabolic mirror and launched horizontally into open atmosphere over a distance of several kilometers. The beam is received by a suitable optical device (telescope) and focused in the entrance slit of a spectrometer for wavelength intensity analysis by use of a photomultiplier. The authors[1–3] used a thin spinning metal disc with 100-μm-wide radial slits (rotating slit) placed in the focal plane of the spectrometer. Thus the slit repetitively scanned a short portion of the spectrum where the gas shows absorption features. Consecutives scans are performed, up to 100 scans per second. For scans of less than 10 ms the effect of atmospheric turbulence is small, because its AQ: B frequency spectrum is important only around 0.1–1 Hz. In this way, single and multispecies atmospheric UV-visible absorption spectra could be recorded.

After that, Axelsson, Edner, and co-workers[4–6] used a similar DOAS configuration to measure the concentrations of ozone, sulfur dioxide, nitrogen dioxide, ammonia, and some volatile organic compounds in urban environments over one kilometer path length. Bonasoni, Giovanelli and co-workers[7–9] used a linear photodiode array instead of the photomultiplier, measuring several pollutant gases in both urban and field scenarios, as well as for vertical tropospheric column.

In all of these cases, the concentration is derived either by correlation with laboratory-calibrated absorbance spectra or with synthesized spectra from a previously measured absorption cross section. The algorithm for concentration retrieval relies then on a least-squares fit of the measured differential absorbance spectrum with the reference spectrum. The main point in the DOAS method is the use of the so-called differential cross section, defined as the part

AQ: A F. A. Videla (Departemento Fisicomatematica, Facultad de Ingeneria), D. C. Schinca, and J. O. Tocho (Departemento de Fisica, Facultad de Ciencias Exactas), are with the Universidad Nacional de La Plata and Centro de Investigaciones Opticas, CC124 C P:B1902 WAB, La Plata, Argentina. F. A. Videla's e-mail address is fabianv@ciop.unlp.edu.ar.

Received 14 August 2002; revised manuscript received 5 February 2003.

0003-6935/03/180001-09$15.00/0

© 2003 Optical Society of America

of the absolute cross section that varies rapidly with wavelength.

In this paper we present an alternative method for determining gas concentration in DOAS measurements, using the linear relationship between the area of the measured differential absorbance curve and that of the differential absorption cross-section curve, as taken from the literature. The method can also be used as a complement to the traditional least-squares fit, helping to discriminate among other absorbing gases in a fixed-wavelength range. The case of single- and multiple-component species is analyzed, and a comparison with the standard method is presented. The paper shows experimental results for both cases obtained in a gas test chamber and compares them with concentration values derived from calibrated electrochemical measurements.

2. Theoretical Background

A thorough discussion of the DOAS method can be found in the work by Platt and Platt and Perner.[11] The latter tutorial contains details about basic principles, hardware, and algorithms, recommended for the interested reader. Following it briefly, the absorption of radiation is described by Lambert–Beer's law:

$$I(\lambda) = I_0(\lambda)\exp[-Lc\sigma(\lambda)], \tag{1}$$

where $I_0(\lambda)$ denotes the incident intensity emitted by a suitable light source and $I(\lambda)$ is the radiation intensity transmitted through a layer of thickness L, where the species to be measured is present at the concentration c. The quantity $\sigma(\lambda)$ represents the wavelength-dependent absorption cross section, which is characteristic of each species. The determination of the light path length L is usually trivial. Once these latter quantities are known, the average trace-gas concentration c can be calculated from the measured ratio $I(\lambda)/I_0(\lambda)$:

$$c = \frac{\log\left[\dfrac{I_0(\lambda)}{I(\lambda)}\right]}{\sigma(\lambda)L} = \frac{A(\lambda)}{\sigma(\lambda)L}, \tag{2}$$

where $A = \log(I_0/I)$ denotes the absorbance of the layer of length L. Typical absorbance values recorded in DOAS applications range from 10^{-2} to 10^{-4}. DOAS makes use of the characteristic absorption features of trace-gas molecules along a path of known length in open atmosphere. The problem of determining the true intensity $I_0(\lambda)$, as would be received from the light source in the absence of any extinction, is solved by working with the so called differential absorption, which is defined as the part of the total absorption cross section of any molecule rapidly varying with wavelength in a given interval. F1 Figure 1 illustrates this fact for the case of sulfur dioxide (SO_2),[12] but a similar concept can be applied to the case of other pollutant gases, such as nitrogen dioxide (NO_2) and ozone (O_3). As a general fact, the

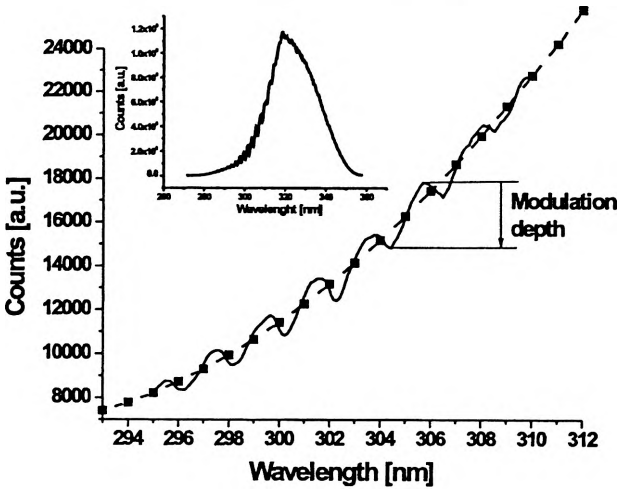


Fig. 1. Part of the raw spectra (solid curve) with interpolating third-degree polynomial (dashed curve). Inset: Typical raw spectra showing the SO_2 absorption modulation in the 300-nm region.

absorption cross section of a given molecular species may be written as the sum of two terms:

$$\sigma_i(\lambda) = \sigma_{i0}(\lambda) + \sigma_i'(\lambda), \tag{3}$$

where $\sigma_{i0}(\lambda)$ represents the monotonously (slow) variation of the cross section with wavelength (due to scattering, for example) and $\sigma_i'(\lambda)$ represents the rapid variation due to an absorption band. Although the absorption spectra of polyatomic molecules may be complicated owing to the presence of numerous closely spaced vibrational–rotational levels,[13] typical spectrographs used in DOAS do not have the necessary resolving power to discriminate the rovibronic bands. So, the meaning of "slowly" and "rapid" are related to the instrument resolution and to the extent of the wavelength range. Thus a differential absorbance can be defined similarly to Eq. (2) as:

$$A'(\lambda) = \log[I_0'(\lambda)/I(\lambda)] = cL\sigma_i'(\lambda), \tag{4}$$

where $I_0'(\lambda)$ is the intensity in the absence of differential absorption.[11] Thus the concentration can be calculated from Eq. (4) with the $\sigma_i'(\lambda)$ taken from the literature (or measured in the laboratory) and fitting $I_0'(\lambda)$ by a suitable polynomial, up to the fifth or sixth order, depending on the selected spectral range.[2,5] After we divide the raw spectrum by this polynomial and take its logarithm, a differential absorbance spectrum (or differential transmission spectrum) is obtained. We can synthesize this spectrum by multiplying $\sigma_i'(\lambda)$ by a suitable concentration-times-length factor [according to Eq. (4)], which is obtained by a least-squares fit.

The residual spectrum generally shows some differential features that may be due to the presence of another species having absorption features in the same spectral region as the former or may arise from

artifacts of the algorithm.[5,6] These artifacts may be introduced by inaccurate matching between the multiple-regression analysis and the actual differential absorbance spectrum, which, after subtraction, yields a residual spectrum showing relatively large structures.[5] This matching process requires shifting up and down in wavelength one of the spectra for precise peak matching.[6] In addition, the reference absorption spectrum must be measured with the same instrumentation or convoluted with the appropriate instrument function to ensure the same resolution for both spectra. This fact makes necessary an accurate determination of the reference concentration to get reliable absorption cross-section values.

An alternative approach is to regard Eq. (4) as a linear parametric relation between the measured differential spectra $[A'(\lambda)]$ and the differential cross section $[\sigma_i'(\lambda)]$. To make this approach effective, the two functions are matched in both wavelength range and spectral resolution. In such a case, Eq. (4) may be integrated from a certain initial wavelength value to a certain final wavelength value to yield:

$$\int_{\lambda_i}^{\lambda_f} A'(\lambda)\mathrm{d}\lambda = cL \int_{\lambda_i}^{\lambda_f} \sigma'(\lambda)\mathrm{d}\lambda. \tag{5}$$

Physically, this equation means that the area under the differential absorbance curve is proportional to the area under the differential cross-section curve. This interpretation is in accordance with the fact that the area under an isolated absorption line remains constant regardless of its width (for a given absorber concentration). If the absorption bands of the gas under study are close enough to each other that they are blended, the above statement may not hold strictly. Nevertheless, since $A'(\lambda)$ and $\sigma_i'(\lambda)$ are matched in spectral resolution (0.1–0.3 nm for a typical DOAS spectrograph), Eq. (5) still holds. In fact, numerical calculations were carried out convoluting $A'(\lambda)$ and $\sigma_i'(\lambda)$ with instrument functions of different widths (covering the range mentioned above). The changes in the resulting spectra do not modify the estimated value of concentration, since the largest width of the instrument function is much less than the width of the bands. For the cases shown in this work and, in general, for almost all gas pollutants that can be measured by DOAS, the combination of band separation, width, and spectral resolution produces negligible blending of the bands. If the lower integral limit in Eq. (5) is kept fixed and the upper limit is taken as a variable parameter, a plot of the values of both integrals for different λ_f will yield a linear plot whose slope is proportional to the actual concentration.

3. Experimental Setup

A. DOAS System

Our DOAS system has been described in detail elsewhere.[14] Briefly, it consists of a 150-W Xe arc lamp placed at the focus of a Newtonian telescope. The collimated beam traverses a long atmospheric path and is collected by another telescope and focused into a spectrograph for wavelength analysis. This setup was used previously to make measurements on SO_2 and NO_2 at a local oil refinery.[15] Since for the present measurements the light path inside the test chamber was about 1 meter, the collimating telescope was removed and the lamp was run at about 70% of its rated power.

Spectrograph

The spectrograph was the same as the one described in a previous work.[13] For high-resolution spectroscopy, an echelle-based spectrograph is preferred over common grating in low order. The main reason is its inherent higher light throughput because of its short focal length. Because the echelle grating has a large groove spacing, it is used at high-order numbers, but it is necessary to provide cross dispersion to avoid an overlapping of diffraction orders. The cross disperser is simply a prism or another grating whose dispersion is at right angles with that of the echelle. The angular dispersion of the cross disperser is usually many times smaller, so the combination of the two elements gives a two-dimensional spectrum format. The cross-dispersion spectrograph used in this work is a Mechelle 900 model from Multichannel Instruments AB (Sweden). The exact position of any wavelength can be determined by use of ray tracing. Thus, for a given wavelength λ, the spectral order m and the focal plane co-ordinates x_c, y_c can be calculated. Recording a spectral image of a calibration source (such as a low-pressure mercury lamp) containing well-defined known spectral lines provides the means for fine calibration. The image has a resolution of 0.23 nm. Although the Mechelle 900 has a built-in pre-exposure command that optimizes exposure time to prevent pixel saturation, the relative intensity ratio between the UV (300-nm) light and near-infrared (900-nm) light of the Xe lamp imposes the use of a UV bandpass filter to cut off most of the visible–NIR Xe emission. This fact also applies to conventional grating-based spectrographs, since the stray light effectively reaching the optical sensor (usually a CCD) is large enough to create a noisy background that masks the weak UV portion of the signal.

C. Test Chamber

The test chamber used in these experiments was constructed at our site and simulates a portion of an industrial chimney. It is a stainless-steel cylinder, 50 cm tall and 50 cm in diameter with internal regulated electrical heaters that can raise the temperature inside the chamber up to 250 °C. It has two pairs of optical ports (25 cm long each) placed opposite to each other through which absorption–transmission experiments can be conducted. Since the length of optical path between these ports was 1 m, the DOAS concentration measurements are given in parts-per-million meter. It also has four other input–output ports for gas inlet, vacuum line, vacuum gauge, and electrochemical probe connector.

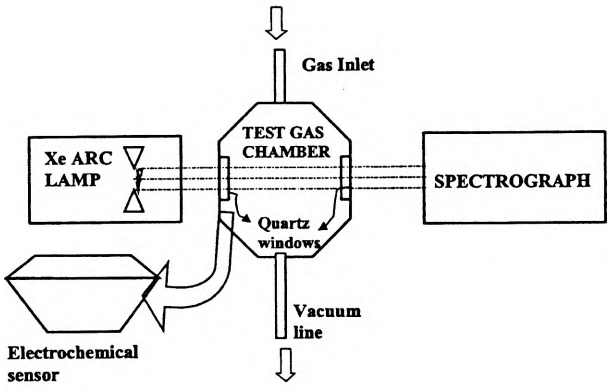


Fig. 2. Experimental setup.

The latter is a TESTO 360 electrochemical sensor capable of measuring SO_2, NO_x, CO, CO_2 and oxygen in the 0–5000 ppm range with an error of 5%. An overall block diagram of the experimental setup is shown in Fig. 2. F2

4. Data Processing

Since uneven sensitivity of the CCD pixels together with a possible lack of smoothness in the intensity spectrum of the Xe arc lamp may introduce fictitious features in the absorption spectrum, a raw spectrum of the lamp in the absence of gases is recorded. A third-order polynomial is fitted and subtracted. The residual difference (positive and negative) is then subtracted from the former raw spectrum to account for the noise features. This procedure is iterated until a smooth lamp spectrum is obtained and saved for future use.

A. Single Component Analysis

The procedure is as follows: A raw spectrum is recorded as shown in the inset of Fig. 1, where it can be seen that the short wavelength side of the transmission profile of the bandpass filter is modulated by the absorption features of SO_2 in the range of 280–320 nm. Only a portion of this spectrum is taken for processing (namely, 295–310 nm), since it contains several peaks usable for concentration retrieval. This spectrum is then matched to the saved smooth lamp spectrum, and the noise is subtracted to eliminate the lamp's features. The differential absorbance spectrum is evaluated according to Eq. (4), where I_0' is a third-order polynomial and I is the matched raw spectrum. At this stage, the areas are calculated and stored for values of λ_f coincident with successive minima under the absorbance curve. This way of taking λ_f values is for ease of calculation, but in principle all values within the wavelength range are equally selectable. An SO_2 library differential cross section is selected and then convoluted with the instrumental function and its areas calculated similarly as the absorbance. This process is illustrated in Fig. 3, where part (a) shows a typical SO_2 absorbance spectrum and part (b) shows a coincident portion of its cross section as taken from Brass- F3

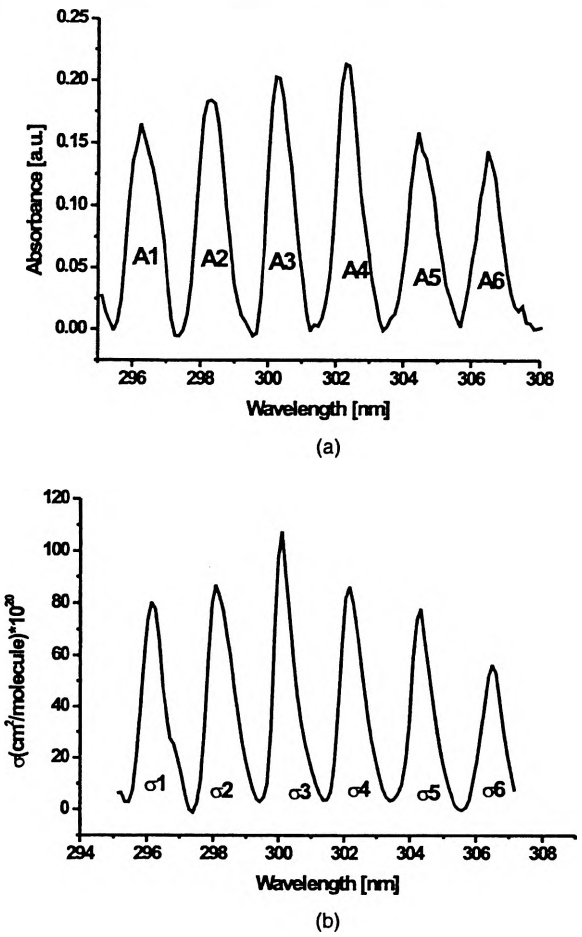


Fig. 3. (a) Typical absorbance SO_2 spectrum. The labeled areas are used for concentration determination. (b) Differential absorption cross section taken from Ref. 12 convoluted with instrument function.

ington[12] convoluted with an instrument function of 0.25-nm width. In each curve, the different areas used for the calculation of Eq. (5) are labeled. Finally, the areas under each absorption band are added to yield

$$\sum_{i=1}^{K} A_i = cL \sum_{i=1}^{K} \sigma_i' + \varepsilon_K, \tag{6}$$

where ε_K is the error, since the left-hand side is a measured magnitude.

By varying K from 1 to n, we obtain n points that can be fitted by a linear regression whose slope is the product of c times L (Fig. 4). It should be noted from Fig. 3 that the index K may take values from 1 to 6 (that is, several bands are taken into account), allowing a reliable regression. F4

B. Multicomponent Analysis

Since the total differential absorbance can be considered as the linear combination of the component differential absorbances, Eq. (5) can be generalized

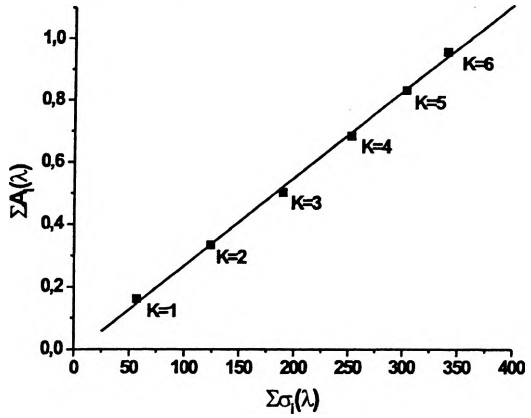


Fig. 4. Linear regression corresponding to Eq. (6). Its slope is proportional to the concentration.

to many species by rewriting its right-hand side as

$$L \sum_{j=1}^{m} c_j \int_{\lambda_i}^{\lambda_f} \sigma_j(\lambda)\mathrm{d}\lambda, \tag{7}$$

where $\sigma_j(\lambda)$ is the absorption cross section of species j, between the wavelengths λ_i and λ_f; c_j is the number density of species j; and m is the number of species present. For the case of two components, $m = 2$, so the difference between the measured total differential absorbance value and the calculated component differential absorbances can be written as

$$\int_{\lambda_0}^{\lambda_f} \mathrm{abs}(\lambda)\mathrm{d}\lambda - L[c_1 \int_{\lambda_0}^{\lambda_f} \sigma_1(\lambda)\mathrm{d}\lambda + c_2 \int_{\lambda_0}^{\lambda_f} \sigma_2(\lambda)\mathrm{d}\lambda] = \varepsilon(\lambda_f), \tag{8}$$

where $\varepsilon(\lambda_f)$ is the error as a function of λ_f. If this parameter takes n values within the selected wavelength range, then Eq. (8) yields a set of n equations whose solution is given in matrix form by[16]:

$$\mathbf{C} = [\mathbf{S}^T\mathbf{S}]^{-1}\mathbf{S}^T\mathbf{A}, \tag{9}$$

where $\mathbf{C}$ is the concentration matrix with elements c_{11}, c_{12}. $\mathbf{S}$ is the $n \times 2$ matrix with elements

$$s_{i1} = \int_{\lambda_0}^{\lambda_k} \sigma_1(\lambda)\mathrm{d}\lambda,$$

$$s_{i2} = \int_{\lambda_0}^{\lambda_k} \sigma_2(\lambda)\mathrm{d}\lambda \qquad k = 1..n,$$

where $n - 1$ is the number of regions to integrate, $\mathbf{S}^T$ is the transpose of $\mathbf{S}$, and $\mathbf{A}$ is the $n \times 1$ matrix with elements

$$a_i = \int_{\lambda_0}^{\lambda_k} \mathrm{abs}(\lambda)\mathrm{d}\lambda.$$

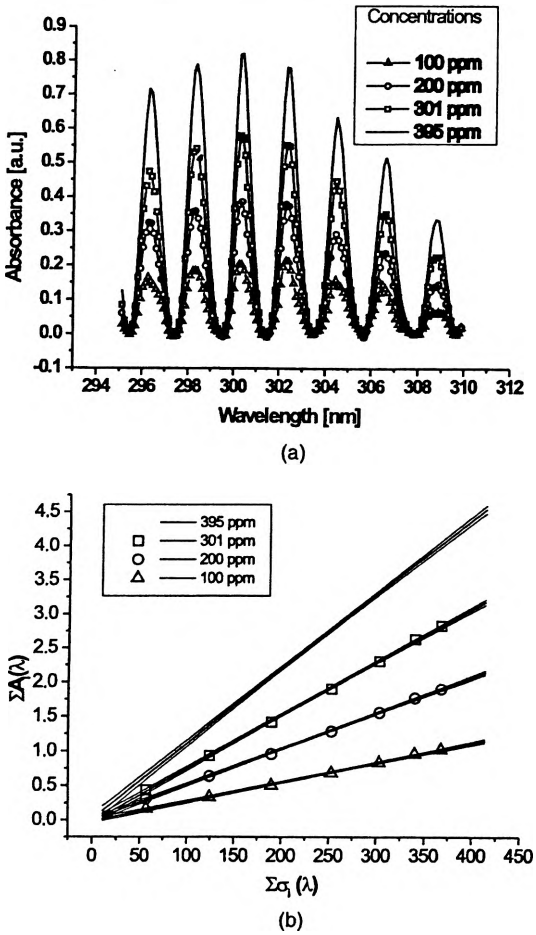


Fig. 5. (a) Differential absorbance curves for different concentration ranges. The numbers in the top right corner are the concentration measured by the electrochemical sensor. (b) Linear regression for the differential absorbance curves of part (a). The confidence interval is shown for each case. The numbers in the top left corner are the retrieved concentration values.

The use of the filter may modify the measurement of the absorbance. If the filter is placed before the absorbing media, the I/I_0 ratio shows the actual modulation depth of the absorption features, in accordance with the Lambert–Beer law. If the filter is placed after the absorbing media (for example, at the entrance slit of the spectrograph), the modulation is modified by a factor that is a function of the filter transmission. In this case, the measured intensity values must be suitably corrected to take into account this departure from the real modulation depth.

5. Results

A. Single-Component Case

This procedure was tested for different SO_2 concentrations diluted in N_2, ranging from 4 to 400 ppm as measured with the calibrated electrochemical sensor. Figure 5(a) shows the differential absorbance spectrum corresponding to four different concentrations with a 100-ppm interval increment. It can be seen F5

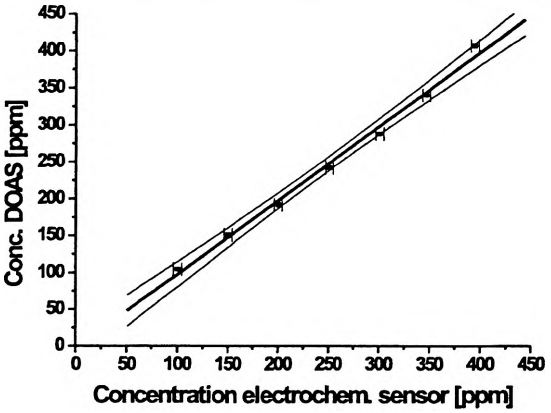


Fig. 6. Comparison between concentration values measured with electrochemical sensor and those retrieved by the integral method for single-component atmosphere.

that there is proportionality between the height of the peaks and the concentration values. If the procedure based on Eq. (6) is applied to each of these absorbance spectra, a family of linear plots is obtained [Fig. 5(b)]. The slope of each curve determines the concentration, as mentioned before. If the concentration values retrieved by DOAS are plotted against the values measured by the electrochemical sensor, it can be seen that a linear regression fits these points (Fig. 6). This shows that there is an excellent agreement between both sets of values, indicating that the integral procedure retrieves concentration values very close to those determined by nonoptical methods. Analogous results are obtained for lower concentrations (Fig. 7).

To test the method for another single gas, pure NO_2 was introduced in the test chamber at different concentrations. It is well known that NO_2 has its maximum differential absorption cross section in the range 430–450 nm and extending with decreasing intensity to both the red and the UV. For reasons that will be clear below, the wavelength range 290–310 nm was chosen. A similar analysis to the SO_2 may be applied to NO_2. Figure 8(a) shows a typical absorption spectrum in this range for a given concentration, and Fig. 8(b) shows the corresponding linear regression.

B. Multicomponent Case

To evaluate the algorithm performance for the cross interference, several mixtures of NO_2 and SO_2 were tested in the chamber. The mixing ratios of these gases span 0 and 100%. Figure 9 shows an example of total differential absorbance for some mixtures and the approximate mixing ratios are (a) SO_2:NO_2 = 1:1.5, (b) SO_2:NO_2 = 1:10, and (c) SO_2:NO_2 = 1:30. Use of Eq. (9) allows us to calculate the individual concentrations, whose values are shown in the bottom right corner of the figures. The dotted curves in Fig. 9 show the calculated differential absorbance with these retrieved values. It can be seen there is a good match between the measured and the calculated curves. The percentual difference with the electrochemical values lies between 1% and 6%. However, it was found that addition of a third gas in Eq. (9) may yield a nonnegative concentration coefficient; despite this, gas was not added to the mixture in the test chamber. This fact was checked including ozone cross section[4,17] (which has a nonnegligible value in the wavelength range used). This possible drawback concerning multiple regression analysis has been mentioned by some authors.[6] To overcome this problem, the integral method can be applied to the resultant spectrum obtained after subtracting from the total differential absorbance a synthesized spectrum corresponding to the component that has the largest N times σ product. Figure 10(a) shows the result of using this approach in the case of the mixture of Fig. 9(a). When a synthesized SO_2 spectrum is subtracted from the total differential absorbance, a resultant spectrum is obtained (inset) that contains features of the other species plus noise. The squares correspond to NO_2 and the circles to O_3. Based on the proportionality between differential absorbance and concentration, it is observed that NO_2 squares are best fitted by a linear regression,

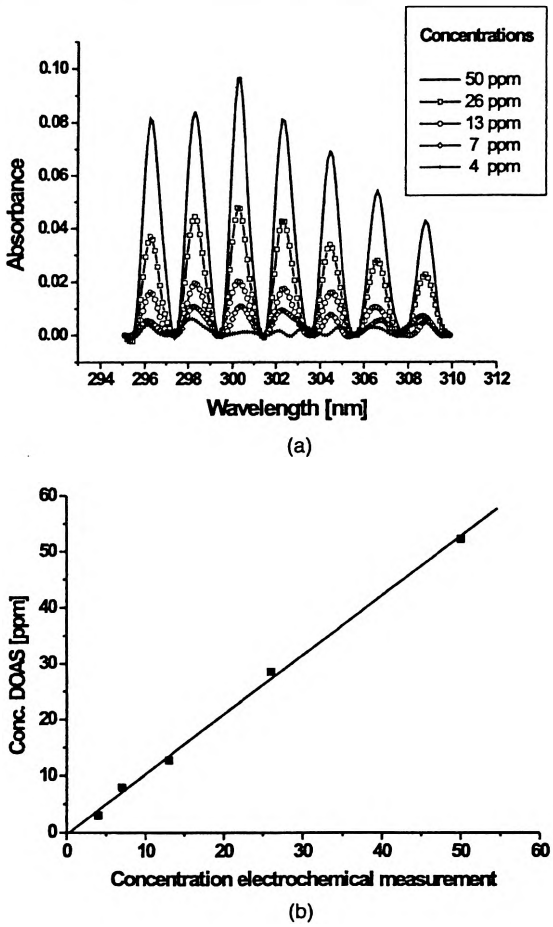


Fig. 7. (a) Differential absorbance curves for low concentration range. (b) Relation between DOAS and electrochemical sensor concentrations for the low concentration range.

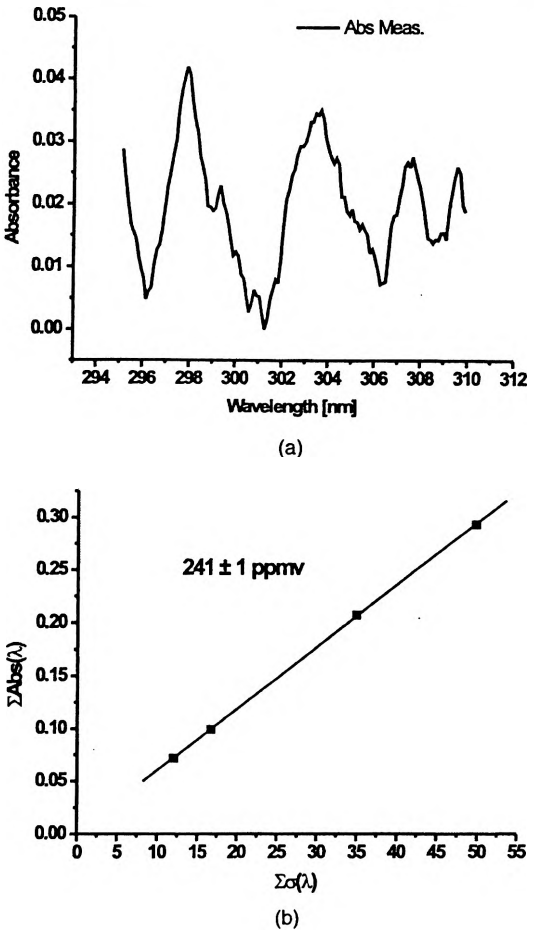


Fig. 8. (a) Differential absorbance spectrum of NO_2 in the 295–310 nm range. The number in the top left corner is the concentration measured by the electrochemical sensor. (b) Linear regression for the differential absorbance curve of part (a). The number in the top left corner is the retrieved concentration.

whereas the O_3 circles show a significant departure from linearity. This establishes a criterion to identify the possible absorbing species present. Figures 10(b) and 10(c) show similar results for other concentration ratios.

F11 Finally, Fig. 11 shows the traditional least-squares method applied to the same mixing ratios used above. The dotted curves represent the calculated differential absorbances with this algorithm. Here also the numbers in the bottom right corner are the retrieved concentrations. It can be seen that the fit is very similar to the one shown in Fig. 9, and the percentual difference with the electrochemical values lies between 1% and 8%. The concentration values retrieved by both methods differ from each other by about 2% to 3%.

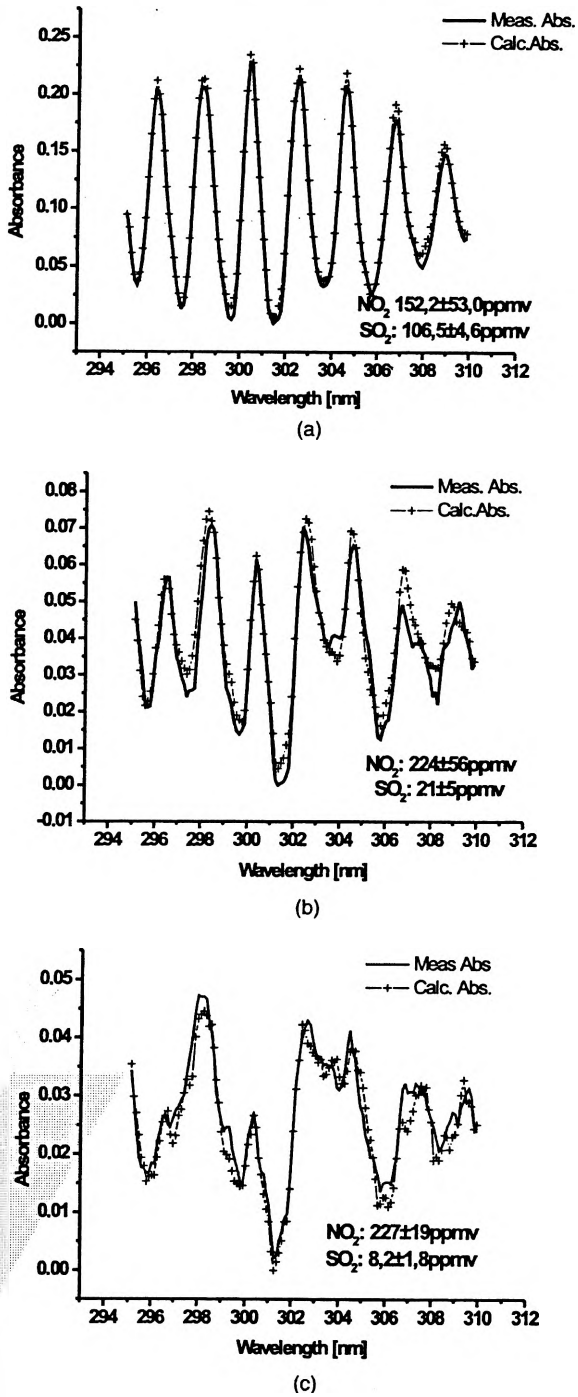


Fig. 9. Measured total differential absorbance (solid curve) and calculated differential absorbance (dotted curve) by use of the concentration coefficients determined by the integral method for different mixing ratios of SO_2 and NO_2 (see text). (a) SO_2, 105 ppm; NO_2, 161 ppm. (b) SO_2, 23 ppm; NO_2, 216 ppm. (c) SO_2, 8 ppm; NO_2, 231 ppm.

6. Conclusions

An alternative method for concentration retrieval in DOAS measurements on the basis of parametric integration of the differential absorbance equation is proposed. The method is tested in a laboratory gas chamber for pure SO_2 and NO_2 in the range of 4–400 ppm over a 1-m optical path. The retrieved concentrations agree with the values measured by a calibrated electrochemical sensor.

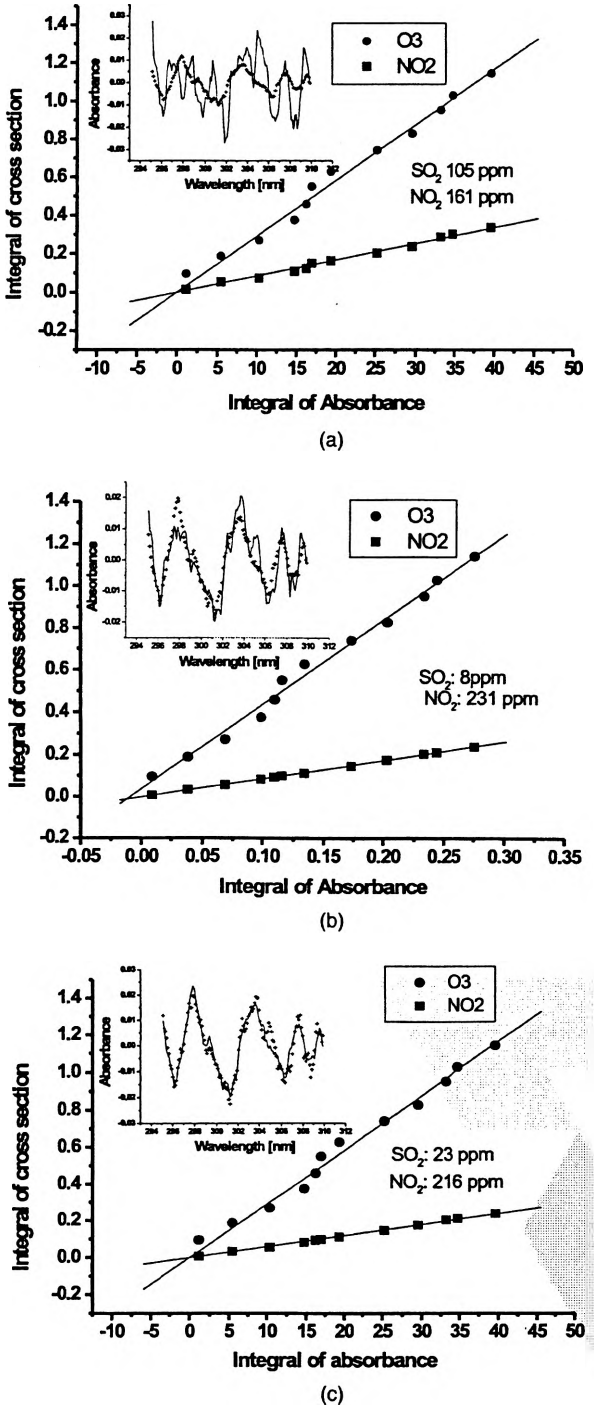


Fig. 10. Linear regression of the values calculated applying Eq. (5) to the resultant spectrum (inset) for the mixtures (a) SO_2, 105 ppm; NO_2, 161 ppm. (b) SO_2, 23 ppm; NO_2, 216 ppm. (c) SO_2, 8 ppm; NO_2, 231 ppm.

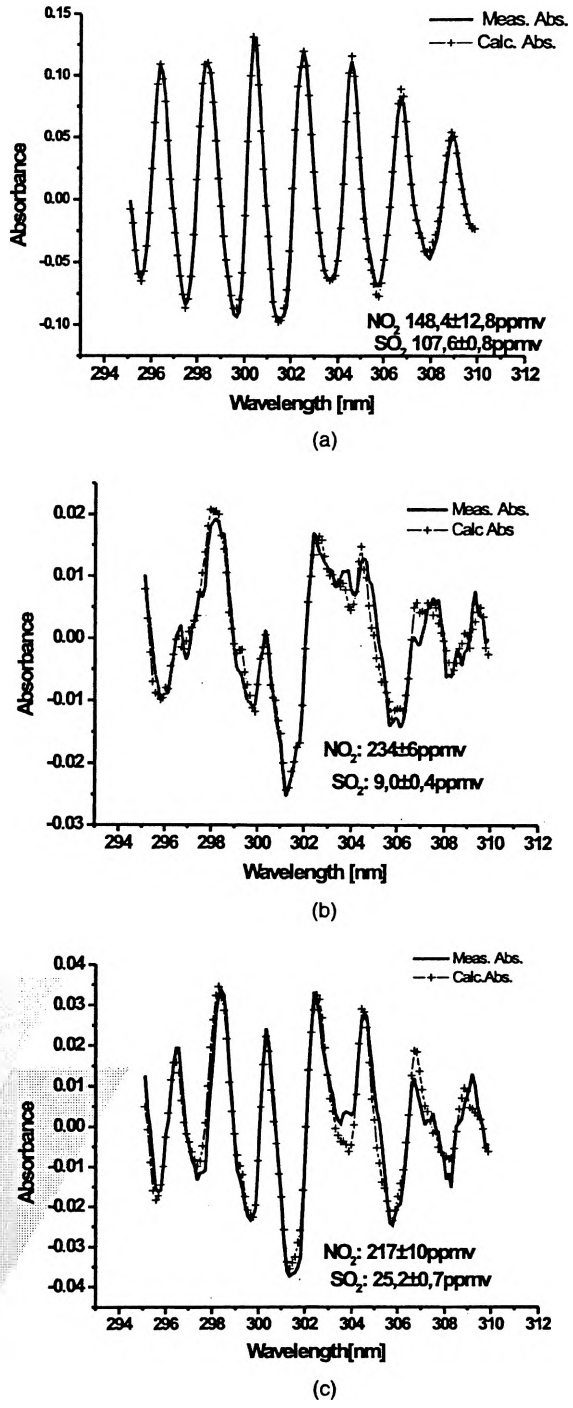


Fig. 11. Measured total differential absorbance (solid curve) and calculated differential absorbance (dotted curve) by use of the standard least-squares method for different mixing ratios of SO_2 and NO_2 (see text). (a) SO_2, 105 ppm; NO_2, 161 ppm. (b) SO_2, 23 ppm; NO_2, 216 ppm. (c) SO_2, 8 ppm; NO_2, 231 ppm.

To expose the method to the cross-interference problem, mixtures of these gases with different mixing ratios were also measured. A multiple-regression analysis applied to the values determined by Eq. (6) yields concentration that agrees with the electrochemical sensor values. Once the resultant spectrum is obtained by subtraction of the main component, the method provides a criterion to identify other species that are probably present in the mixture that absorb in the same wavelength range.

References

1. D. Perner and U. Platt, "Detection of nitrous acid in the atmosphere by differential optical absorption," Geophys. Res. Lett. **6,** 917–920 (1979).
2. U. Platt and D. Perner, "Direct measurements of atmospheric CH_2O, HNO_2, O_3 NO_2 and SO_2 by differential optical absorption in the near UV," J. Geophys. Res. **85,** 7453–7458 (1980). AQ: D
3. U. Platt, D. Perner, and H. Pätz, "Simultaneous measurements of atmospheric CH_2O, O_3, and NO_2 by differential optical absorption," J. Geophys. Res. **84,** 6329–6335 (1979).
4. H. Axelsson, H. Edner, B. Galle, P. Ragnarson, and M. Rudin, "Differential optical absorption spectroscopy (DOAS) measurements of ozone in the 280–290 nm wavelength region," Appl. Spect. **44,** 1654–1658 (1990).
5. H. Edner, P. Ragnarson, S. Spännare, and S. Svanberg, "Differential optical absorption spectroscopy (DOAS) system for urban atmospheric pollution monitoring," Appl. Opt. **32,** 327–333 (1993).
6. H. Axelsson, A. Eilard, A. Emanuelsson, B. Galle, H. Edner, P. Ragnarson, and H. Kloo, "Measurement of aromatic hydrocarbons with the DOAS technique," Appl. Spect. **49,** 1254–1260 (1995).
7. F. Evangelisti, A. Baroncelli, P. Bonasoni, G. Giovanelli, and F. Ravegnani, "Differential optical absorption spectrometer for measurement of tropospheric pollutants," Appl. Opt. **34,** 2737–2744 (1995).
8. G. Giovanelli, P. Bonasoni, F. Evangelisti, and F. Ravegnani, "Ozone ground-based measurements by the GASCOD near UV and visible DOAS system," in *Proceedings of the Quadrennial Ozone Symposium 1992*, R. D. Hudson, ed. (Goddard Space Flight Center, Greenbelt, Md., 1992), pp. 707–710.
9. P. Bonasoni, F. Evangelisti, G. Giovanelli, and F. Ravegnani, "Remote sensing DOAS system for measurements of atmospheric trace gases," Phys. Med. **9,** 304–307 (1993).
10. U. Platt and D. Perner, "Measurements of atmospheric trace gases by long path differential UV/visible absorption spectroscopy," in *Optical and Laser Remote Sensing Techniques*, D. K. Killinger and A. Mooradian, eds., (Springer-Verlag, Berlin, 1983), pp. ●●●–●●●. AQ: E
11. U. Platt, "Differential optical absorption spectroscopy," in *Monitoring by Spectroscopy Techniques*, M. Sigrist, ed. (Wiley, New York, 1994), pp. ●●●–●●●. AQ: E
12. D. J. Brassington, "Sulfur dioxide absorption cross-section measurements from 290 nm to 317 nm," Appl. Opt. **20,** 3774–3779 (1981).
13. G. Herzberg, *Electronic Spectra of Polyatomic Molecules* (Van Nostrand Reinhold, New York, 1966).
14. D. Schinca and J. Tocho, "Development of a DOAS system based on a cross dispersion spectrograph," in *Water, Ground, and Air Pollution Monitoring and Remediation*, T. Vo-Dinh and R. Spellicy, eds., Proc. SPIE **4199,** ●●●–●●●. AQ: E
15. D. Schinca, R. Di Paolo, F. Videla, E. Rodríguez, and J. Tocho, *Medidas en Planta de SO_2 y NO_2 en la Región de La Plata*, (Asociación Física Argentina, Argentina, 1999).
16. E. Lloyd, ed., *Handbook of Applicable Mathematics*, (Wiley, New York, 1984), Vol. VI, Part A, Chap. 8.
17. L. T. Molina and M. J. Molina, "Absolute absorption cross sections of ozone in the 185- to 350-nm wavelength range," J. Geophys. Res. **91,** 14501–14508 (1986).

Fibras Ópticas

Fibras ópticas

Las fibras ópticas son importantes componentes en los sistemas de comunicaciones actuales, permitiendo transmitir por un par de fibras la información que de otro modo necesitaría varios miles de cables de cobre. Su importancia radica en su potencialidad en la transmisión de pulsos luminosos por una guía de unos diez micrones de diámetro por varias decenas de kilómetros sin necesidad de ser regenerados.

Debido a la falta de una base de conocimiento sobre fibras ópticas y sus aplicaciones en el pais, en 1995 iniciamos en el CIOp las actividades del LAMECO (Laboratorio Metrológico para las Comunicaciones Ópticas) por un grupo de investigadores con diversas especialidades dentro de la óptica (óptica espacial, láseres y espectroscopia). Contó con el apoyo de la Comisión de Investigaciones Científicas de la Provincia de Buenos Aires, a fin de generar un laboratorio destinado a brindar servicios a empresas de comunicaciones. Desde entonces se han realizado unos 400 servicios a dichas empresas y entes gubernamentales incluyendo calibración de equipamiento óptico y asesoramiento.

En la fase de investigación, se analizaron e implementaron técnicas de caracterización y metrología de fibras, estudio de medios de ganancia (amplificación óptica en fibras dopadas), desarrollo de láseres de fibras ópticas, diseño y desarrollo de sensores de fibras, y análisis de la propagación de señales luminosas de muy corta duración en dichos elementos. La labor realizada en investigación en los últimos 5 años dio lugar a un número relevante de publicaciones en revistas internacionales especializadas, así como numerosas presentaciones a congresos. Parte de ellas han sido realizadas conjuntamente con investigadores y grupos de trabajo de otros centros inclusive internacionales. Desde el año 2001 se realizan investigaciones conjuntas sobre láseres de fibra y sensores incluyendo un continuo intercambio de investigadores, con el grupo del Profesor Miguel Andrés del Departamento de Física Aplicada, Facultad de Física, Universidad de Valencia, España y desde 2003, luego de realizarse un Convenio de Colaboración CIOp- Fac. de Ingeniería, Universidad Nacional de Mar del Plata, generamos un fuerte apoyo al Laboratorio Láser de esa Facultad. La colaboración se manifiesta en la línea de Sensores de Fibras Ópticas.

En forma paralela se ha dado un fuerte impulso a la formación de recursos humanos. Se impartieron diversos cursos de capacitación teórico prácticos: tres de ellos para personal de las empresas vinculadas con las Telecomunicaciones (convenio CIOp - FOETRA, TELECOM de Argentina, OPTIM S.A. y REYCOM S.A.) y diversos cursos de postgrado para ingenieros y científicos en distintas Universidades Nacionales (La Plata, Corrientes, Comodoro Rivadavia, Bahía Blanca, Gral. Pico y Mar del Plata). Paralelamente, y en forma ininterrumpida, se realizan diversas actividades docentes y de formación de recursos humanos, incluyendo supervisión de tareas vinculadas a Tesis de Doctorado, Maestrías y/o Trabajos de Final de Carrera. Un encuentro relevante fue el Curso Latinoamericano de Capacitación denominado Training course on 'Optical Fibre Communication Networks', La Plata (Argentina), 24 - 28 de octubre 2005, auspiciado por el International Centre for Science and Technology (ICS) de Trieste, Italia y the United Nations Industrial Development Organization (UNIDO), con participación de Profesores extranjeros y participantes de 10 países de Latinoamérica.

Optical Fibers

Optical fibers are important current communication system´s components, that allow transmitting along a single pair of fibers the same amount of information that otherwise would require several thousands of copper cables. Its importance is based on the potential ability for transmitting a light pulse within a ten-micron diameter waveguide along several tens of kilometers without amplification.

In 1995, LAMECO (Laboratorio Metrológico para las Comunicaciones Ópticas) started its activities at CIOp based on a multispecialists researh staff (space optics, laser and spectroscopy), devoted to the development of knowledge and applications of optical fibers. LAMECO was supported by Comisión de Investigaciones Científicas de la Provincia de Buenos Aires and since then, more than 400 services to telecom firms as well as to federal labs were done, including optical equipment calibration and assessment.

As scientific research is concerned, characterization and metrology fiber techniques were implemented, study of doped fiber amplifiers, development of optical fiber lasers and sensors and short pulse fiber propagation. These works gave rise during tha last five years, to several international journals publications and meetings presentations, many of which

were done in collaboration with other research groups. Since 2001, we were visited by Profesor Miguel Andrés from Departamento de Física Aplicada, Facultad de Física, Universidad de Valencia, España and in 2003 we work in collaboration with Laboratorio Láser, Fac. de Ingeniería, Universidad Nacional de Mar del Plata in optical fiber sensors.

Several courses were lectured by LAMECO staff in telecom firms (TELECOM de Argentina, OPTIM S.A. and REYCOM S.A.) and in several national universities (La Plata, Corrientes, Comodoro Rivadavia, Bahía Blanca, Gral. Pico y Mar del Plata), where master and PhD thesis were supervised.

During 24 - 28 october 2005, the Training course on 'Optical Fibre Communication Networks', La Plata (Argentina) was carried out sponsored by International Centre for Science and Technology (ICS) Trieste, Italy and the United Nations Industrial Development Organization (UNIDO), with participation of international professors and Latinamerican attendants.

INSTITUTE OF PHYSICS PUBLISHING JOURNAL OF OPTICS A: PURE AND APPLIED OPTICS
J. Opt. A: Pure Appl. Opt. 5 (2003) S216–S220 PII: S1464-4258(03)56776-9

Q-switching of an erbium-doped fibre laser modulated by a Bragg grating fixed to a piezoelectric

R Duchowicz[1,2], N A Russo[1], E Sicre[3] and M V Andrés[4]

[1] Centro de Investigaciones Opticas, CIOp (CONICET, CIC), La Plata, Argentina
[2] Departamento de Física, Facultad Ciencias Exactas, UNLP, La Plata, Argentina
[3] Universidad Argentina de la Empresa (UADE), Buenos Aires, Argentina
[4] Departamento de Física Aplicada, Universitat de Valéncia, Burjassot, Spain

E-mail: ricardod@ciop.unlp.edu.ar (R Duchowicz)

Received 18 November 2002, in final form 10 March 2003
Published 22 August 2003
Online at stacks.iop.org/JOptA/5/S216

Abstract
The performance of the Q-switched erbium-doped fibre laser with two fibre Bragg gratings as cavity mirrors was theoretically analysed, employing a set of rate equations for the ion populations and the photon flux inside the cavity. The simulation considers a system where the pulsed laser emission is produced by the temporal modulation of a Bragg grating fixed to a piezoelectric and operating in the 1550 nm spectral region. The temporal evolution of different frequency components of the laser emission produced is governed by the instantaneous overlap between the two gratings. Theoretical results are in agreement with previously reported experimental values.

Keywords: Fibre laser, erbium, Bragg grating, Q-switching

1. Introduction

Erbium-doped fibre lasers (EDFLs) have a variety of potential applications, as sources for wavelength division multiplexing (WDM) and soliton communications systems, and in sensor devices, optical time domain reflectometry, non-linear phenomena studies and applications, etc. Continuous-wave, Q-switching and mode-locking laser systems constructed by using doped fibres have been demonstrated. High continuous-wave powers (>100 W) have been achieved with fibre lasers by using the cladding pump technique. In the pulsed operation regime (the Q-switched mode), the energy storage that can be achieved within conventional single-mode erbium-doped fibre limits the maximum energy. The use of fibre Bragg gratings to develop the laser cavity allows one to operate the laser with a narrow linewidth because of the frequency-selective reflectivity of such gratings. They act as high-reflectivity mirrors for the laser emission wavelength, but are transparent to the pump radiation, allowing the obtaining of very low-loss resonators. This has the additional advantage that an all-fibre-in-line laser system can be developed [1–5].

Recently, we reported the performance of a Q-switched erbium-doped fibre laser operating with two fibre Bragg gratings as cavity mirrors where the temporal modulation is performed fixing one of the gratings to a piezoelectric (PZT: $Pb(Zr_xTi_{1-x})O_3$) element [6, 7]. Applying voltage pulses to the PZT, the laser cavity was modulated. By using this simple scheme, a Q-switched laser output has been generated with high laser efficiency of energy conversion. Q-switched laser pulses of 0.5 W peak powers were obtained pumping at 76 mW at 18.5 kHz and an energy conversion efficiency of 26% was obtained. Typical laser emission had temporal widths of 2–3 μs and an optical bandwidth of ~0.1 nm. The results depend on the pumping level of the active medium. In particular, exciting the medium at pump powers larger than six times $P_{p,h}$, where $P_{p,h}$ is the pump power of the laser threshold, produces not an increase in the laser output but the generation of additional laser peaks. A similar scheme has been reported before, but its performance was quite poor [8].

In view of the importance of fibre lasers and of the necessity of having perfect knowledge of the device operation, it is important to obtain a correct description of the laser evolution. So, we analyse here the behaviour of the Q-switched laser by using a general theoretical model based on a homogeneous, three-level approximation of amplification in erbium and compare the results with the behaviour of our Q-

1464-4258/03/050216+05$30.00 © 2003 IOP Publishing Ltd Printed in the UK

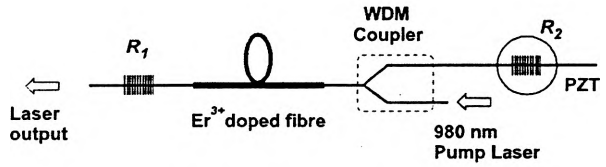


Figure 1. The laser scheme.

switched erbium fibre laser based on a modulation produced by a Bragg grating fixed to PZT. The laser cavity was simulated assuming that its wavelength (frequency) distribution has a different temporal modulation for each component.

2. Theoretical model and results

The system is shown schematically in figure 1. The laser resonator consists of a fibre WDM coupler, a segment of erbium-doped fibre and two fibre Bragg gratings acting as mirrors. In the previous experimental work, we employed as the gain medium 5.5 m of erbium-doped fibre containing 790 ppm Er^{3+} with a core diameter of ~4.8 μm, a numerical aperture (NA) of 0.21 and a confinement factor (Γ) of 0.59. Excitation was produced at 0.98 μm. By means of the pumping action, population from the $^4I_{15/2}$ manifold (level 0) is transferred to the $^4I_{11/2}$ level (level 2). Excited ions in the $^4I_{11/2}$ state decays to the $^4I_{13/2}$ manifold (level 1, with a lifetime of $\tau_1 \approx 10$ ms) in tens of microseconds, mainly in a non-radiative way. Lasing action occurs in the $^4I_{13/2} \rightarrow {}^4I_{15/2}$ transition. In general, the populations are not uniform along the amplifying path. However, for the sake of simplicity we assume that there is uniform volume excitation of the doped fibre. It is also assumed that there is no excited state absorption at the pump wavelength.

In the theoretical comparison, the erbium-doped fibre laser is treated as a three-level homogeneous system. For the continuous laser regime and pumping into the 0.98 μm absorption band, the population in the $^4I_{11/2}$ manifold is negligible in relation to the population in the other levels ($\tau_2 \ll \tau_1$) and the theoretical model may be considered as a two-level approximation. This could not be so for a high-repetition-rate pulsed regime, where the pump period would be of the same order as τ_2. The laser dynamics, in this case, can be described by the usual set of coupled rate equations for the photon number and the normalized populations corresponding to the active levels [1, 9–13]:

$$\frac{\partial \Delta n}{\partial \tau} = \left(P - 1 - \sum_m a_m^- i_m\right) - \left(P + 1 + \sum_m a_m^+ i_m\right)\Delta n + n_2\left(1 - P + \sum_m a_m^- i_m + \frac{\tau_1}{\tau_2}\right) \quad (1)$$

$$\frac{\partial n_2}{\partial \tau} = P - \Delta n\, P - n_2\left(P + \frac{\tau_1}{\tau_2}\right) \quad (2)$$

$$\frac{\partial i_m}{\partial \tau} = (b(a_m^+ \Delta n + a_m^-(1 - n_2)) - \gamma_m(\tau))i_m \quad (3)$$

$$n_0 + n_1 + n_2 = 1 \quad (4)$$

$$\Delta n = n_1 - n_0 \quad (5)$$

where $\tau = t/\tau_1$ with $\tau_1 \approx 10$ ms the decay time of the upper level of the active medium and t the time; i_m is the photon flux spectral density, n_0, n_1, n_2 are the ion populations corresponding to the $^4I_{15/2}$, $^4I_{13/2}$ $^4I_{11/2}$ levels normalized to the total Er^{3+} population and Δn is the population inversion between the $^4I_{15/2}$ and $^4I_{13/2}$ levels, also normalized; P represents the pumping rate normalized to $2\tau_1^{-1}$; $a_m^{+,-} = \tau_1(\sigma_{e,m} \pm \sigma_{a,m})$ with σ_e, σ_a the emission and absorption cross-sections of the gain medium (constants within the Bragg grating influence range); $b = lN/T$ where l is the gain medium length, N the total ion concentration and T the time taken for the light to make one cavity round trip. The decay rate of the laser light in the cavity is given by $\gamma_m(\tau) = -\gamma_0 \ln(R_1 R_2(\tau))$, where $\gamma_0 = \tau_1/T$ is a dimensionless constant, R_1 and R_2 are the mirror reflectivities (Bragg gratings) of the optical cavity and m is the frequency index.

When the PZT is excited, the wavelength distribution of the reflecting grating fixed to it (R_2) starts to oscillate in the spectrum with an amplitude depending of the applied voltage. In order to correlate the experimental behaviour of [7] with theoretical results obtained with this model, we have simulated the reflectivity of the practical gratings (which were characterized in that work by using an optical spectrum analyser) with a Gaussian distribution for the reflectivity of R_1 and a super-Gaussian for R_2. Mathematically we express this as

$$R_1(\lambda) = R_{01} \exp(-((\lambda - \lambda_1)/\Delta\lambda_1)^2) \quad (6)$$

$$R_2(\lambda, \tau) = R_{02} \exp(-((\lambda - \lambda_2(\tau))/\Delta\lambda_2)^8) \quad (7)$$

with

$$\lambda_2(\tau) = \lambda_{02} + \delta\lambda_2 \sin(2\pi f \tau_1 \tau) \quad (8)$$

where λ is the wavelength, λ_1, λ_{02} and $\Delta\lambda_1, \Delta\lambda_2$ are the central wavelength and the bandwidth of each grating reflectivity distribution, $\delta\lambda_2$ is the wavelength modulation amplitude and f is the excitation frequency of the PZT. The set of coupled rate equations (1)–(5) under the cavity conditions given by equations (6)–(8) were solved numerically by using a personal computer with the help of a fourth-order Runge–Kutta integration method.

Typical parameters corresponding to a practical laser system of erbium-doped fibres were employed: $\tau_2 = 10^{-2}$ s, $a_m^- = 0.2 \times 10^{-27}$ m^2 s, $a_m^+ = 2.8 \times 10^{-27}$ m^2 s, $b = 1.4 \times 10^{32}$ m^{-2} s^{-1}, $\gamma_0 = 2 \times 10^7$, $R_{01} = 0.75$, $\lambda_1 = 1540.3$ nm, $\Delta\lambda_1 = 0.12$ nm, $R_{02} = 0.97$, $\lambda_{02} = 1540.0$ nm, $\Delta\lambda_2 = 0.38$ nm, $\delta\lambda_2 = 0.4$ nm and $f = 18.5$ kHz. A value of 590 was taken for the ratio between the time decays (τ_1/τ_2). When a modulated voltage is applied to the PZT, the temporal distribution of R_2 shifts in wavelength as given by equation (6), overlapping periodically with the reflectivity distribution of R_1 (figure 2). The amplitude of this displacement is, in principle, dependent on the PZT voltage input. The overlap time depends on this amplitude, the PZT frequency modulation and the spectral widths of the two gratings.

The evolution of the cavity factor (R_1 R_2) determines the laser operation. Figure 3 shows the wavelength dependence on the temporal evolution of this product. As can be observed, the cavity behaves differently for each laser component, shifting in time (in this case), for the positive edge of the distribution, from lower- to larger-wavelength components. The direction depends on the initial spectral positions of the two gratings. The influence of these temporal differences depends on the modulation amplitude and frequency.

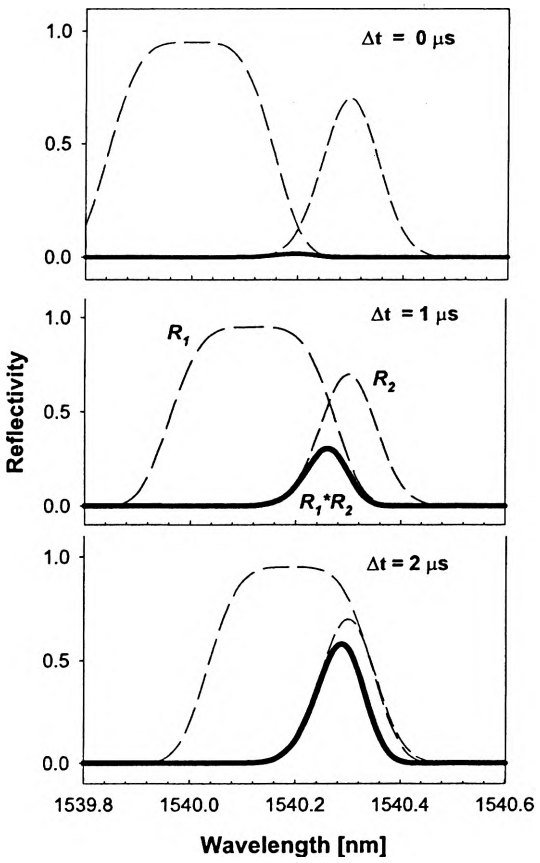


Figure 2. The spectral dependence of the temporal modulation.

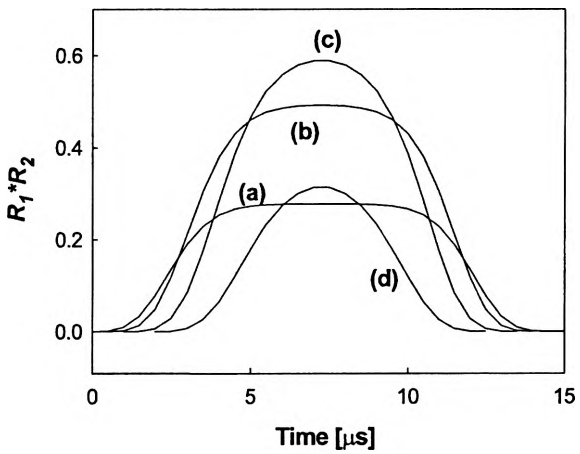


Figure 3. Spectral sweeping of the laser cavity. The spectral distributions correspond to: (a) 1540.23, (b) 1540.26, (c) 1540.30 and (d) 1540.34 nm, respectively.

Figure 4 shows: (a) the PZT modulation voltage with a frequency $f_0 = 18.5$ kHz, (b) the population inversion for the laser transition, (c) the population of the $^4I_{11/2}$ level (n_2) and (d) the laser output, for a pump power $P_p = 4P_{p,h}$.

Figure 5 shows the behaviours obtained for the laser operation under different continuous pumping conditions. By using the above-mentioned parameters in the model resolution, we have observed that: at P_p-values larger than $P_{p,h}$ and

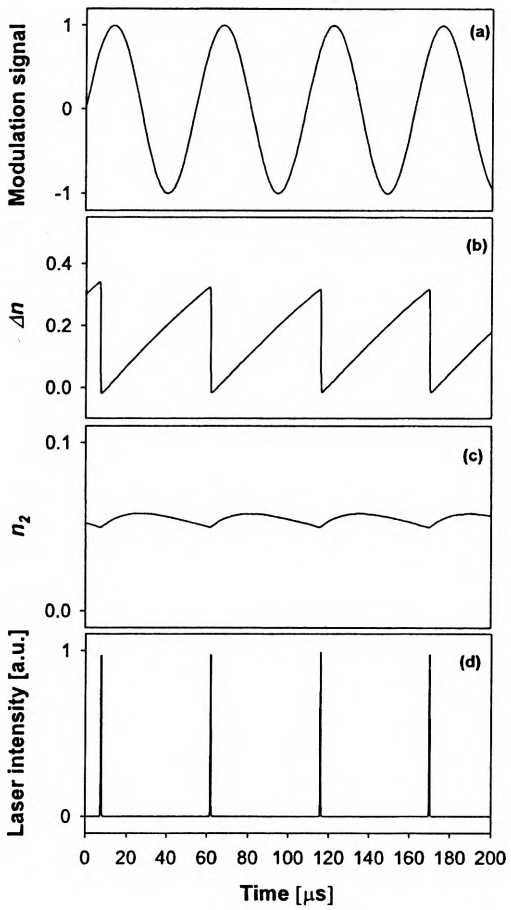


Figure 4. Numerical simulation with $P_p = 4P_{p,h}$: (a) the normalized PZT modulation signal at $f_0 = 18.5$ kHz; (b) population inversion for the laser transition (Δn); (c) population of the $^4I_{11/2}$ level (n_2); and (d) normalized laser output.

smaller than $\sim 2P_{p,h}$, lasing occurs in an unstable regime with a frequency $f < f_0$; at $\sim 2P_{p,h} < P_p < \sim 6P_{p,h}$, PZT governs the laser oscillation and we had a stable regime with $f = f_0$; and when the pump excitation increases to above $6P_{p,h}$, the laser output does not increase and the laser operation becomes unstable with the appearance of additional laser peaks ($f > f_0$). The experimental limit for stable operation was found to be lower ($P_p \approx 5P_{p,h}$) than the theoretical one. The general characteristics described using this model are in agreement with the experimental behaviour of the Q-switched laser described in [7].

For comparison, figure 6 shows typical experimental pulsed laser emission, obtained with the laser system described in [7], as well as the modulating signal at 18.5 kHz repetition rate measured for the PZT. Theoretical values of the temporal pulse width obtained from the model at 18.5 kHz (~ 1 μs) are close to the experimental ones. This value is approximately constant in the region of stable operation.

Figure 7 shows the spectral evolution of one of the pulses when the laser operates at 18.5 kHz. A very small frequency shift of the maximum occurs before a 'broadband' distribution is achieved. The temporal distributions (a), (b), (c), (d) and (e) correspond to the wavelengths 1540.20, 1540.23, 1540.26, 1540.30 and 1540.34 nm, respectively.

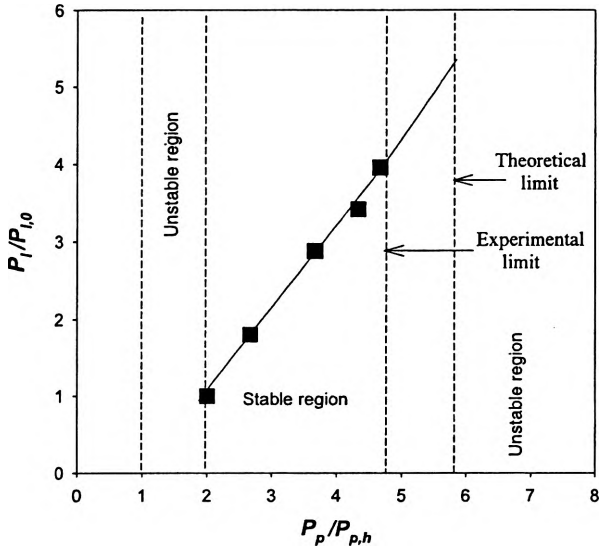


Figure 5. Laser output behaviour under different pump conditions. P_L and $P_{L,0}$ are the laser output power at an arbitrary pump power and with the lowest pumping for stable operation, respectively. The solid line represents the theoretical results and square points are experimental data.

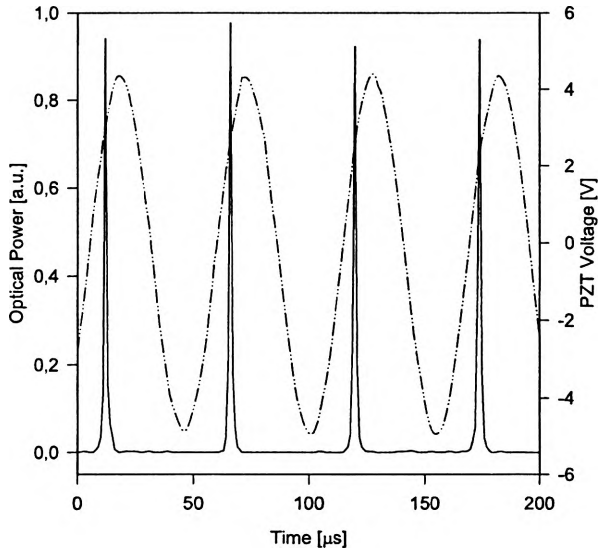


Figure 6. The experimental PZT modulation voltage and laser intensity evolution.

At larger frequencies ($f \gg f_0$), the frequency shift starts to become more important and the pulses are chirped, due to the faster frequency oscillation of the cavity. A complementary experimental study of the spectro-temporal behaviour will be carried out in the near future. Figure 8 shows the agreement between the theoretical and the experimental spectral distributions obtained in the 1540 nm region for the emission of the Q-switched laser. The asymmetry observed in both curves appears also when the laser system operates at 1530 and 1554 nm. The spectral pulse width depends on the spectral characteristics of both gratings and, particularly, on that of the grating with the narrow spectral width. Differences between theoretical and experimental curves are due to imperfections

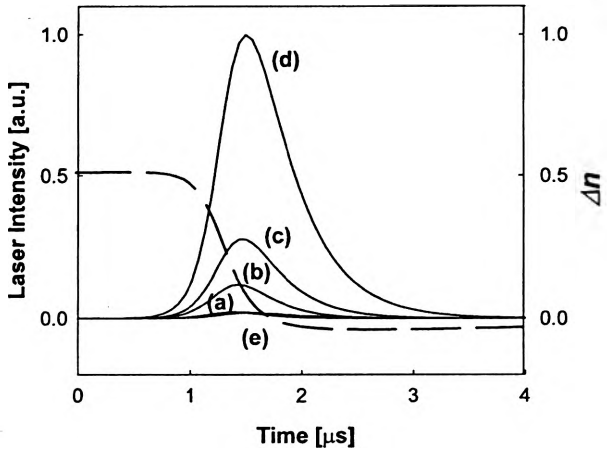


Figure 7. Evolution of the laser emission (theoretical) for several frequency components (solid curves): the temporal distributions of (a), (b), (c), (d) and (e) correspond to the wavelengths 1540.20, 1540.23, 1540.26, 1540.30 and 1540.34 nm, respectively. The normalized population inversion is also shown (dashed curve).

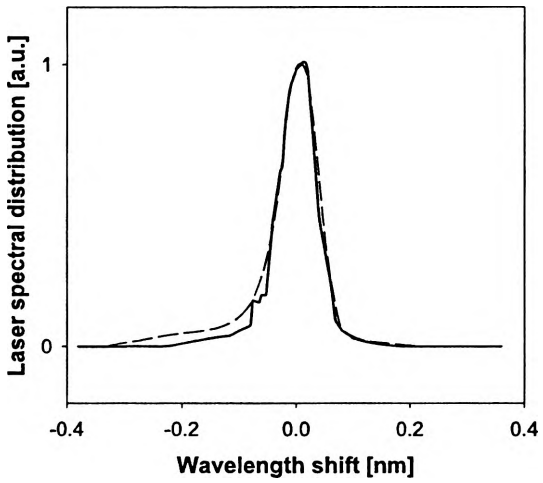


Figure 8. Spectral distributions of the laser emission: theoretical (dashed curve) and experimental (solid curve).

of the spectral grating distributions used in the experimental system.

In [7], the PZT was modulated by a square or sinusoidal voltage wave. In both cases, the laser system was always modulated at $f_0 = 18.5$ kHz, because PZT works better at its resonance frequency. Also, other frequencies have harmonics coincident with this value (18.5 kHz). Because of this, under continuous optical excitation and with square voltage pulses applied to the PZT, the laser behaves similarly for frequencies $f = f_0/n$ (where n is an integer). When the pump excitation was also modulated, the excitation time could only be increased by 10–15% due to the PZT resonance. In these conditions, the laser output was increased by a factor ~2 and the temporal width was reduced by the same factor.

3. Conclusions

A Q-switched fibre laser system actively modulated by using a Bragg grating fixed to PZT was theoretically analysed employing a three-level scheme for the erbium-doped fibre and

a wavelength dependence for the temporal modulation. In our model, we assume that the cavity length is large enough (some metres) that thousands of modes are simultaneously excited. Therefore the wave patterns between different waves can become sufficiently complex that many of the cross-coupling effects tend to be washed out on average, with the result that only the averaged intensity of all the waves is significant [11]. Results obtained with this scheme show several characteristics of the laser operation and they are in good agreement with experimental data previously reported [7].

Acknowledgments

This work was supported by the Consejo Nacional de Investigaciones Científicas y Técnicas (CONICET), the Universidad Nacional de La Plata (UNLP), the Agencia de Investigaciones Científicas, the Comisión de Investigaciones Científicas de la Provincia de Buenos Aires (CIC) and the Universidad Argentina de la Empresa (UADE, Buenos Aires) of Argentina; and by the Project AECI2001-IB-03 of Agencia Española de Cooperación Internacional (Spain).

References

[1] Desurvire E 1994 *Erbium-Doped Fiber Amplifiers. Principles and Applications* (New York: Wiley)
[2] Barnes W L 1993 *Rare Earth Doped Fibre Lasers and Amplifiers* ed M J F Digonnet (New York: Dekker) p 375
[3] Dominic V, MacCormack S, Waarts R, Stevens S, Bicknese S, Dohle R, Wolak E, Yeh P S and Zucker E 1999 *CLEO'99: Conf. on Lasers and Electro Optics* (Washington, DC: Optical Society of America) p 578
[4] Mizrahi V, DiGiovanni D J, Atkins R M, Grubb S G, Park Y K and Delavaux M P 1993 *J. Lightwave Technol.* **11** 2021
[5] Sejka M, Varming P, Hubner J and Kristensen M 1995 *Electron. Lett.* **31** 1445
[6] Russo N A, Duchowicz R, Mora J, Cruz J L and Andrés M V 2001 *Proc. SPIE* **4419** 86
[7] Russo N A, Duchowicz R, Mora J, Cruz J L and Andrés M V 2002 *Opt. Commun.* **210** 361
[8] Imai T, Komukai T, Yamamoto T and Nakazawa M 1996 *Japan. J. Appl. Phys.* 2 **35** L1275
[9] Lou L and Chu P L 1999 *Opt. Commun.* **161** 257
[10] Lou L G and Chu P L 1997 *Opt. Lett.* **22** 1174
[11] Siegman A E 1986 *Lasers* (Oxford: Oxford University Press)
[12] Digonnet M J F 1990 *IEEE J. Quantum Electron.* **26** 1786
[13] Lou L G and Chu P L 1998 *Opt. Commun.* **149** 307

Available online at www.sciencedirect.com
SCIENCE DIRECT®
Optics Communications 244 (2005) 315–319
OPTICS COMMUNICATIONS
www.elsevier.com/locate/optcom

High-repetition rate acoustic-induced Q-switched all-fiber laser

D. Zalvidea [a], N.A. Russo [a], R. Duchowicz [a,b], M. Delgado-Pinar [c], A. Díez [c,*], J.L. Cruz [c], M.V. Andrés [c]

[a] *Centro de Investigaciones Opticas, CIOp (CONICET, CIC), La Plata, Argentina*
[b] *Departamento de Física, Fac. Ciencias Exactas, UNLP, La Plata, Argentina*
[c] *Departamento de Física Aplicada, ICMUV, Universidad de Valencia, Dr. Moliner 50, 46100 Burjassot, Spain*

Received 20 May 2004; received in revised form 9 September 2004; accepted 10 September 2004

Abstract

We report a high-repetition rate actively Q-switched all-fiber laser. The acousto-optic interaction controls the coupling between co-propagating core and cladding modes and is used to modulate the optical losses of the cavity, which permits to perform active Q-switching. Using 1.4 m of 300 ppm Er-doped fiber and a maximum pump power of 120 mW, we have obtained up to 1 W peak power pulses, with a pulse repetition rate that can be continuously varied from 1 Hz to 120 kHz and a pulse width that changes from 70 ns to 2.2 μs.
© 2004 Elsevier B.V. All rights reserved.

PACS: 42.55.W; 42.60.G
Keywords: Fiber lasers; Q-switching

1. Introduction

The development of new fiber optic laser systems is of permanent interest in the optical field, especially on the communication spectral window. In particular, erbium-doped fiber lasers have shown a variety of potential applications, such as sources for WDM and soliton communications systems, medicine, sensing and spectroscopy. In order to produce an erbium-doped Q-switched laser many different approaches can be employed. Passive Q-switching can be obtained by using a saturable absorber constructed by inserting a segment of samarium-doped fiber into a ring cavity [1]. Active Q-switching was performed using an electro-optic modulator, an acousto-optic modulator (AOM), or an intensity modulator based in the transmission of a coupler in the cavity [2–4].

On the other hand, U-V written fiber Bragg gratings (FBGs) as a reliable fiber technology has

* Corresponding author. Tel.: 34 963983431; fax: 34 963983146.
E-mail address: antonio.diez@uv.es (A. Díez).

0030-4018/$ - see front matter © 2004 Elsevier B.V. All rights reserved.
doi:10.1016/j.optcom.2004.09.040

generated very important advances in the development of fiber-based devices and systems. In particular, FBGs can be used as all-fiber mirrors to define a Fabry–Perot cavity. The laser emission wavelength is, in this case, determined by the Bragg wavelengths of the fiber gratings. Many designs of fiber lasers for optical communications, making use of fiber gratings to the resonant cavity, have been previously reported [5].

In a previous work, we demonstrated active Q-switching of an erbium-doped fiber laser that employs a pair of fiber Bragg gratings as reflective mirrors. The laser operation was based on modulating the Bragg wavelength of one grating fixed to a piezoelectric ceramic tube. By using this very simple scheme, we obtained a Q-switched laser in the erbium spectral gain region with a high laser efficiency of energy conversion. Pumping at 76 mW and operating the laser at 18.5 kHz, an efficiency of 26% was achieved [6,7].

Recently, Liu and co-workers [8] demonstrated an actively Q-switched fiber laser in which an acousto-optic-based fiber attenuator [9,10] placed inside the cavity was employed to actively control the cavity losses. Microbending induced in the fiber by a flexural acoustic wave produces resonant coupling between the fundamental core mode and cladding modes, which are rapidly attenuated by the fiber coating [11]. Pulses of several μJ per pulse, 150 ns wide and a repetition rate of up to 5 kHz was reported.

In this paper, we report an optimized design of a Q-switched all-fiber laser based on the idea reported by Liu and co-workers [8]. We have included two modifications to Liu's design to improve the performance of the system. First, we used photosensitive erbium-doped fiber, so that the FBG used as reflective elements were written in the active fiber itself, giving rise to a splice-less laser cavity. Second, to enhance the efficiency of the acousto-optic attenuator, it was made on a section of fiber that was tapered down using a fusion-and-pulling technique. This allows making acousto-optic attenuators as efficient as the one used in [8], which was made using HF etching, but with smaller reductions of the fiber diameter. This is relevant to the performance of the Q-switched laser, i.e. the maximum repetition rate achievable, since the time response of the attenuator shortens as the fiber diameter increases due to the dependence of the acoustic velocity with the diameter [11].

We demonstrate a Q-switched laser with up to 1 W peak power, pulses from 70 ns to 2.2 μs wide, and a pulse repetition rate that can be continuously varied from 1 Hz to 120 kHz.

2. Experimental setup and results

Fig. 1 shows a schematic diagram of the Q-switched erbium-doped fiber laser. The fiber used in the experiments was an erbium-doped germanosilicate fiber containing 300 ppm Er^{3+}, with a cut-off wavelength of 965 nm, and a numerical aperture (NA) of 0.23. Two Bragg gratings, FBG1 and FBG2, were written on the core of the Er^{3+}-doped fiber by UV exposure using a doubled argon laser and a uniform period phase mask, to define a cavity of 140 cm in length. The fiber was hydrogen loaded to enhance its photosensitivity. The Bragg wavelength of both FBGs was 1546.6 nm. The reflectivity of FBG1 and FBG2 was 60% and 99%, respectively, and the bandwidth was 0.15 and 0.25 nm.

The acousto-optic attenuator was implemented on the Er^{3+}-doped fiber itself. Flexural acoustic waves were imposed on the fiber using a piezoelec-

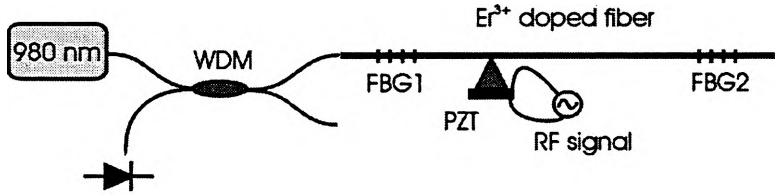


Fig. 1. Experimental setup.

tric transducer (a PZT ceramic disc of 1 cm diameter) driven by a RF signal, and an aluminum horn (see Fig. 1). The acousto-optic interaction takes place in a section of 8 cm long of the Er^{3+} fiber. To enhance the acousto-optic interaction, this section of fiber was tapered down from 125 to 80 μm in diameter using a standard fusion-and-pulling tapering technique [12]. We found that resonant coupling between the fundamental core mode LP_{01} and the LP_{12} cladding mode occurred at around 1.55 μm when the frequency of the RF signal was 1.2 MHz. Fig. 2 shows an example of the transmission spectrum of the fiber when an RF signal of 1.201 MHz and an amplitude of 15 V was applied to the piezoelectric. An attenuation peak centered at 1546.6 nm (i.e., the Bragg wavelength of the FBGs) as deep as 16 dB is observed. The inset of Fig. 2 shows the tunability of the dip with the frequency of the RF signal. Coupling from the LP_{01} to other cladding modes was also observed for other frequencies. Measurements shown in Fig. 2 were done before the FBGs were written.

Fig. 3 shows the time response of the acousto-optic attenuator. For this experiment, the fiber was illuminated using a laser diode tuned at the acousto-optic resonant wavelength and the FBGs were detuned to avoid reflections from them. Fig. 3(a) shows the electrical signal applied to the piezoelectric transducer and Fig. 3(b) shows the corresponding optical transmission. The switching time, i.e., the time that the signal takes to change from 100% to 0%, is about 50 μs. This value is an order of magnitude shorter than the best value reported in [8]. A delay of 30 μs between the electrical and the optical signals is also observed, which is caused by the overall system that generates the acoustic wave.

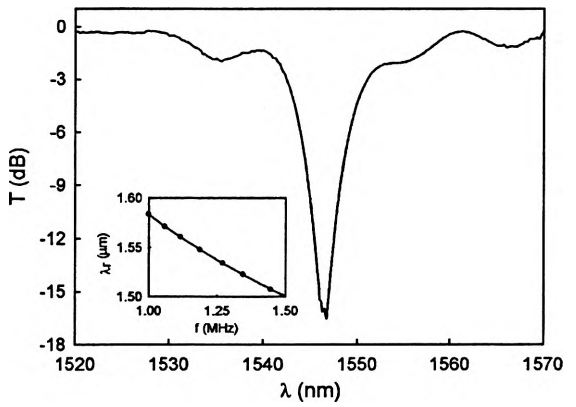


Fig. 2. Transmission spectrum when an electrical signal of 15 V and 1.201 MHz is applied to the piezoelectric. The dip is caused by the resonant coupling between the LP_{01} core mode and the LP_{12} cladding mode. Inset: acousto-optic resonant wavelength λ_T as a function of the RF frequency.

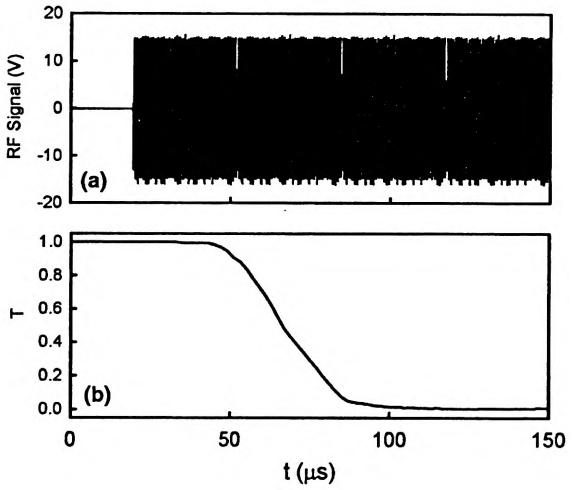


Fig. 3. Time response of the acousto-optic process. (a) Electrical signal applied to the piezoelectric and (b) light transmission.

The active medium was pumped through a WDM coupler using a pigtailed semiconductor laser diode (980 nm, 125 mW of maximum optical power). The optical output from FBG1 was detected using a 125 MHz bandwidth InGaAs photodetector. The efficiency of the fiber laser in CW operation (without acoustic excitation) was about 5% and the threshold was 4 mW.

To perform Q-switching, the RF signal was amplitude modulated by a rectangular wave of variable frequency and duty cycle. This modulation produced on–off periods of the acoustic wave being imposed to the fiber, which results in a modulation of the cavity losses at the laser emission wavelength.

Fig. 4 shows an example of the laser system running at 10 kHz. Fig. 4(a) is the laser signal and Fig. 4(b) shows the modulation signal. The duty cycle was adjusted to optimize the amplitude and the stability of the pulses. Fig. 4(c) shows the performance of the fiber attenuator under the same

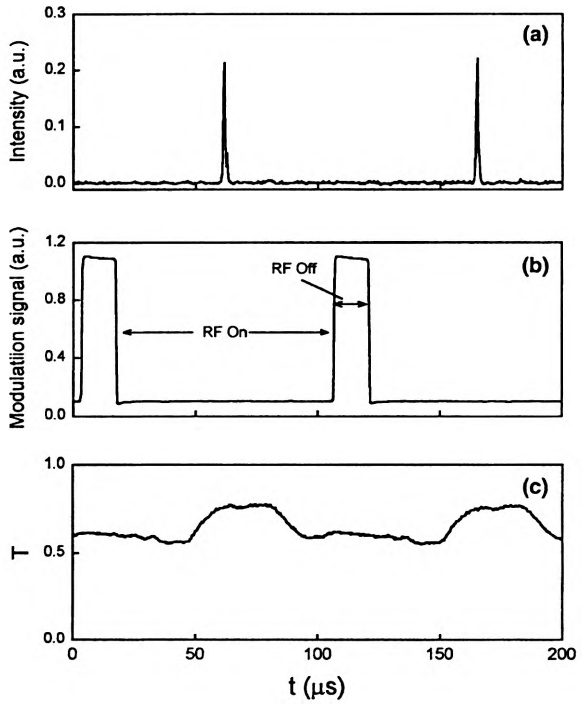


Fig. 4. (a) Laser output when operating at 10 kHz. (b) Corresponding modulation signal. (c) Light transmission under the same piezoelectric excitation.

piezoelectric excitation. This measurement was done in a similar way as in Fig. 3 (with no pump and detuning the FBGs to avoid reflections), and it shows that just a few percent of attenuation change is enough to generate Q-switching. Fig. 5 shows an example of the laser operating at 120 kHz. Higher repetition rates could be attainable by reducing the time response of the acousto-optic attenuator. This could be achieved, for example, by shortening the length of the acousto-optic attenuator, provided that enough acoustic power is available to obtain the required attenuation level to perform Q-switching.

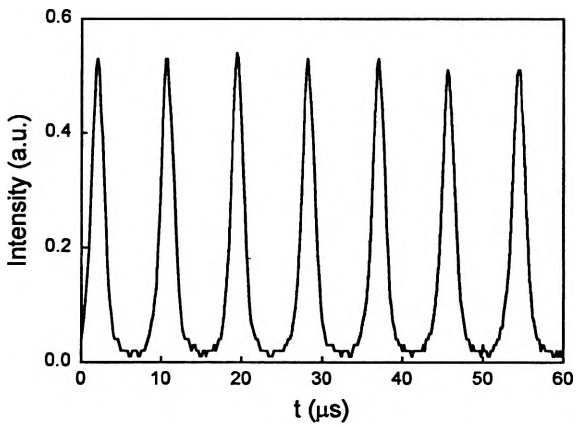


Fig. 5. Laser output when operating at 120 kHz.

Fig. 6(a) gives the output peak power of the Q-switched laser pulses against the continuous pump power, for several repetition frequencies. Pulses of up to 1 W were obtained at low frequencies. Pulse-to-pulse fluctuation of the peak power was typically about 5%. Fig. 6(b) gives the peak power and the pulse width as a function of the repetition rate, when pumping at 85 mW. Around 1–2 kHz the peak power starts to decrease significantly and the pulse width to increase, as expected for a medium with an upper-level effective lifetime of 1 ms. Pulses from 70 ns to 2.2 μs wide were obtained. The long microsecond pulses at high-repetition rates may limit the use of the system in some applications. Shorter pulses could be obtained by reducing the length of the laser cavity and also by improving the time response of the acousto-optic modulator.

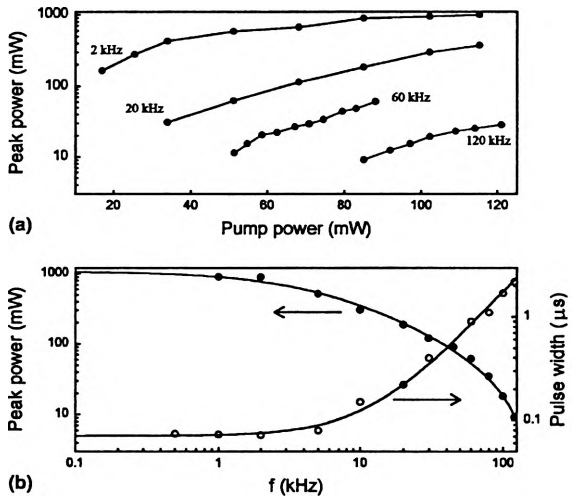


Fig. 6. (a) Optical peak power versus continuous pump power, for several pulse repetition frequencies. (b) Optical peak power and pulse width against pulse repetition frequency when pumping at 85 mW.

3. Summary

In summary, we have reported a high-repetition rate acoustic-induced Q-switched all-fiber laser. A single piece of Er^{3+}-doped germanosilicate fiber has been employed to make the laser, writing the FBGs and performing the modulation of the cavity losses in the fiber itself. Q-switching was performed by controlling the optical losses in the Er^{3+} fiber by coupling light from the core mode to cladding modes using flexural acoustic waves. The active Q-switching can be operated continuously from 1 Hz to 120 kHz and the pulse width changes from 70 ns to 2.2 μs. Using 1.4 m of 300 ppm Er-doped fiber and pumping powers lower than 120 mW, up to 1 W peak power pulses were achieved at 2 kHz repetition rate.

Acknowledgments

This work was financially supported by the Ministerio de Ciencia y Tecnología of Spain (Grant TIC2002-04527-C02-01), NKT Research & Innovation and the Generalitat Valenciana (grupos03/227). R. Duchowicz, N.A. Russo and D. Zalvidea acknowledge financial support from the Consejo Nacional de Investigaciones Científicas y Técnicas (CONICET), the Facultad de Ciencias Exactas, Universidad Nacional de La Plata and the Comisión de Investigaciones Científicas de la Prov. de Buenos Aires (CIC), Argentina.

References

[1] L. Luo, P.L. Chu, Opt. Commun. 161 (1999) 257.
[2] H.H. Kee, G.P. Lees, T.P. Newson, Electron. Lett. 34 (1998) 1318.
[3] P. Roy, D. Pagnoux, L. Mouneu, T. Midavaine, Electron. Lett. 33 (1997) 1317.
[4] A. Chandonnet, G. Larose, Opt. Eng. 32 (1993) 2031.
[5] V. Mizrahi, D.J. DiGiovanni, R.M. Atkins, S.G. Grubb, Y.K. Park, M.P. Delavaux, J. Lightwave Technol. 11 (1993) 2021.
[6] N.A. Russo, R. Duchowicz, J. Mora, J.L. Cruz, M.V. Andrés, Opt. Commun. 210 (2002) 361.
[7] R. Duchowicz, N.A. Russo, E. Sicre, M.V. Andres, J. Opt. A 5 (2003) 5216.
[8] D.W. Huang, W.F. Liu, C.C. Yang, IEEE Photon. Technol. Lett. 12 (2000) 1153.
[9] D.W. Huang, W.F. Liu, C.W. Wu, C.C. Yang, IEEE Photon. Technol. Lett. 12 (2000) 176.
[10] H.S. Kim, S.H. Yun, I.K. Kwang, B.Y. Kim, Opt. Lett. 22 (1997) 1476.
[11] T.A. Birks, P.St.J. Russell, D.O. Culverhouse, J. Lightwave Technol. 14 (1996) 2519.
[12] R.P. Kenny, T.A. Birks, K.P. Oakley, Electron. Lett. 77 (1991) 1654.

Available online at www.sciencedirect.com
ScienceDirect
Optics Communications 275 (2007) 94–103
OPTICS COMMUNICATIONS
www.elsevier.com/locate/optcom

Periodic pulse train conformation based on the temporal Radon–Wigner transform

Christian Cuadrado-Laborde [a,*], Pablo Costanzo-Caso [a], Ricardo Duchowicz [a], Enrique E. Sicre [b]

[a] Centro de Investigaciones Opticas (CIOp), Casilla de Correo 124, 1900 La Plata, Argentina
[b] Centro de Estudios Avanzados (CEAV), Universidad Argentina de la Empresa, Chile 1192, 1073 Buenos Aires, Argentina

Received 22 November 2006; received in revised form 8 March 2007; accepted 12 March 2007

Abstract

By using the Radon–Wigner transform (RWT), we analyze the temporal selfimaging or Talbot effect for producing well-conformed pulse trains with variable repetition rates and duty-cycles. The relationships linking the selfimaging conditions with the fractional orders of the RWT are first obtained for unchirped pulse trains. Then, we extend the analysis to chirped pulse sequences by deriving the conditions to be fulfilled by an equivalent unchirped pulse train producing the same selfimage irradiances. This result becomes relevant for observing well-defined high order fractional selfimaging, which are of interest due to their repetition rate multiplication. Besides, the effect of the finite extension of the pulse train on the selfimage quality is analyzed and a condition is found for relating the required minimum pulse number with the chirp parameter of the pulses.
© 2007 Elsevier B.V. All rights reserved.

Keywords: Pulse propagation; Temporal Talbot effect; Phase-space signal representations

1. Introduction

The development of techniques for the analysis and synthesis of ultrashort optical pulses has become of most importance in the field of optical communications, photonic signal processing and ultrafast optics. The characterization of the optical pulses can be performed from direct interferometric measurements in different domains such as time (t), frequency (v) or in a combined phase-space domain (t, v). Signal analysis using phase-space representations, like the Wigner distribution function (WDF), has been successfully applied to describe the system properties in several spatial optics applications [1–3]. Related with the WDF, a formalism based on the fractional Fourier transform (FRT) was developed in recent years to describe the properties of many optical devices in the spatial domain [4–10]. The FRT of a given optical signal can be also considered as a dual phase-space signal representation where the fractional order p varies from zero (only space information) to one (pure spatial frequency information). Several optical devices were proposed for implementing the spatial FRT, either through guided light transmission in a medium having a quadratic refractive index profile [4] or by combining lens action and free-space propagation [5]. Besides, an alternative interpretation of the FRT was given in connection with the Radon–Wigner transform (RWT) [7]. The RWT is obtained by performing a phase-space coordinate rotation of the WDF associated with the signal followed by a projection of this rotated WDF into the spatial frequency axis. An optical setup was proposed to implement the RWT of a one-dimensional input signal employing a varifocal lens device [9]. The RWT was successfully applied in signal processing as e.g., in the analysis and synthesis of multicomponent linear FM signals [11,12] and for enhancing resolution in ultrasound imaging [13].

* Corresponding author.
E-mail addresses: claborde@ciop.unlp.edu.ar (C. Cuadrado-Laborde), ricardod@ciop.unlp.edu.ar (R. Duchowicz), esicre@uade.edu.ar (E.E. Sicre).

0030-4018/$ - see front matter © 2007 Elsevier B.V. All rights reserved.
doi:10.1016/j.optcom.2007.03.021

On the other hand, the space–time duality theory was developed based on the analogy existing between the properties of quadratic-phase filters and Fresnel transforms in the spatial domain and the time impulse responses of different dispersive media and the frequency modulation of time-varying pulses in guided light transmission [14–18]. In this way, well known concepts and experiments developed in the framework of spatial optical systems can be transferred to the temporal domain thereby providing new ways for analyzing and processing time optical signals. Among several applications (as e.g., spectrum analyzers, temporal microscopy and pulse compression), temporal selfimaging or Talbot effect was implemented in order to produce periodic pulse trains with minimum distortion and different repetition rates [19–26]. Although selfimaging is a linear phenomenon, it has been also applied in connection with some nonlinear phenomena, such as Raman pulse compression [27], soliton generation [28] and cross-phase modulation [29].

In this paper we analyze the pulse trains conformation, which is produced from a proper combination of dispersive transmission and phase modulation applied to a periodic input signal, by employing an approach based on the temporal RWT and its connection with temporal selfimaging. To this end, we generalize a previously reported optical implementation of the RWT that is based on the space–time analogy and the theory of temporal imaging [30]. In that work, a relationship for obtaining the fractional orders p for which the FRT's coincide with a certain selfimaging condition was derived for the particular case of unchirped periodic pulse trains. Now, we extend the RWT signal description for analyzing pulse train conformation in the more realistic case of finite periodic pulse trains where the individual pulses are frequency chirped. The new conditions, for obtaining the fractional orders for which selfimages can be found, are derived by performing the analogy between our chirped pulse train and the equivalent unchirped pulse train, which would produce the same RWT at the specific fractional orders associated with selfimaging. The role of this unchirped pulse train is rather similar to the equivalent dispersion line which was used by Chantada et al. [31] in the spectral analysis of the temporal Talbot effect, without considering time lens action. We also investigate the relation between the number of pulses N that is required for obtaining a well-defined selfimage and the spectral content of the pulse trains. It is derived a relationship between N and the pulse chirp parameter which is corroborated in the numerical simulations.

In Section 2, we summarize the basic definitions of the FRT and the RWT in the spatial domain, together with the link between the FRT and the general spatial selfimaging. In Section 3, we introduce an optical definition of the RWT in the temporal domain. In Section 4, we analyze the temporal selfimaging by using the RWT formalism. The general relationships for producing integer and fractional selfimages of a finite, periodic chirped pulse train are obtained here. In Section 5, some numerical simulations are shown which illustrate the derived results. As we shall see, the previously found relationship between p and selfimaging, for the case of unchirped pulses, can be approximately applied for obtaining integer selfimages of an input chirped pulse train with small distortions. However, for the case of fractional selfimaging (which is of interest due to its repetition rate multiplication capability), the general relationships obtained here should be used for observing well-conformed pulse trains.

2. FRT and selfimaging: definitions and basic relationships in the spatial domain

The FRT can be defined explicitly in standard notation as an integral transform [4,5,10] as well as in several different ways [10]. We prefer to use the definition which involves a given rotation in the phase-space plane of the WDF [7,10]. The FRT of a given signal $u_0(x)$ can be found by performing the following steps

$$u_0(x) \to W_0(x,v) \to \widehat{R}_\phi[W_0(x,v)] \to |u_p(x)|^2 = \int_{-\infty}^{\infty} \widehat{R}_\phi[W_0(x,v)]\mathrm{d}v, \tag{1}$$

being

$$W_0(x,v) = \int_{-\infty}^{\infty} u_0\left(x+\frac{x'}{2}\right) u_0^*\left(x-\frac{x'}{2}\right) \exp(-2\pi i v x')\mathrm{d}x', \tag{2}$$

the WDF associated to the input signal, which is a dual signal representation defined in a phase-space: spatial coordinate (x) vs. spatial frequency (v). In Eq. (1), $\widehat{R}_\phi$ is the rotation operator acting on the WDF which changes $(x,v) \to (x',v') = (x\cos\phi - v\sin\phi, v\cos\phi + x\sin\phi)$, being $\phi = p\pi/2$. Thus, the FRT modulus squared of $u_0(x)$ is obtained: (i) by passing to the WDF domain, (ii) rotating the WDF by an angle ϕ and (iii) by performing a projection into the spatial frequency axis. As these two last steps represent the Radon transform of a signal, $|u_p(x)|^2$ is also called the Radon–Wigner transform (RWT) of $u_0(x)$.

The FRT of a given one-dimensional space signal $u_0(x)$ can be optically implemented by properly combining lens action and light propagation. This combination can be performed either in a distributed or in a tandem way. In the first case, light transmission in a guided medium having a quadratic refractive index profile (like a GRIN medium) originate the successive FRT's of increasing fractional order p [4]. We focus our attention in the second approach where Lohmann proposed two simple setups for obtaining the FRT [5]. In one of them, the input signal $u_0(x)$ is illuminated by a monochromatic plane wave of wavelength λ, then interacts with a first lens of focal length f, then it propagates by a distance z, and it again interacts with a second lens having the same focal length f. The amplitude distribution after the second lens, which can be expressed as a proper scaled Fresnel integral, becomes the FRT of the input object being denoted as $u_p(x) = \Im^{(p)}\{u_0(x)\}$ where $0 < p < 1$. The geometrical parameters are related with p as

$$z = f_0 \sin\left(\frac{p\pi}{2}\right), \tag{3a}$$

$$f = \frac{f_0}{\tan(p\pi/4)}, \tag{3b}$$

being f_0 a scaling factor. If $p = 0$ the FRT becomes $u_0(x)$, and if $p = 1$ the FRT becomes the normal Fourier transform of $u_0(x)$. For other values of p, the FRT exhibits both, mixed space and spatial frequency information about the input signal. As we are mainly interested in the light irradiance, $|u_p(x)|^2$ is the magnitude to be considered. As it was proved in [7], $|u_p(x)|^2$ displayed in a two-dimensional domain (x,p) becomes the RWT of the object $u_0(x)$. The RWT is a bilinear, phase-space signal description which is very useful in signal processing [11–13]. Thus, if a RWT display is obtained for $0 < p < 1$, the information about the input signal $u_0(x)$ continuously changes from a spatial representation ($p = 0$) to a pure spatial frequency description ($p = 1$).

The free-space diffraction originated by an input object under spherical illumination is closely related to the FRT production, as it was demonstrated in [9]. In the FRT setup described above, the first lens generates the spherical wave being the only difference with free-space diffraction the second lens action introducing a quadratic-phase factor. However, this effect is not relevant since the irradiance is the magnitude to be analyzed. Thus, if we choose the output plane placed immediately behind the second lens and we select the radius of the illuminating spherical wave $R = f$ and the propagation distance z accordingly with Eq. (3), the output irradiance $I_{out}(x)$ can be written as

$$I_{out}(x) = |\Im^{(p)}\{u_0(x)\}|^2 = |u_R(x;z)|^2, \tag{4}$$

where $u_R(x;z)$ is the Fresnel pattern diffracted by $u_0(x)$ a distance $z = f_0 \sin(p\pi/2)$ when the object is illuminated with a spherical wave of radius $R = f = f_0/\tan(p\pi/4)$. In the particular case of a periodic object $u_0(x) = t(x;d)$ (being d the spatial period), if $t(x;d)$, located at $z = 0$, is illuminated with a spherical wave converging to $z = R$, selfimages appear at the distances $z = sMd^2/\lambda$, being $M = (R - z)/R$ and $s = n/m$, where n and m are integers (see e.g., [21]). Two kind of selfimaging should be distinguished: (i) integer or Talbot selfimages, for which $s = n$ (i.e., $m = 1$), having periods $M \times d$, and (ii) fractional or sub-Talbot selfimages, for which n and m are coprime integers and $m \geqslant 2$, having periods $M \times d/m$. From these Talbot conditions, and by taking into account Eq. (4), the relationship between the selfimage patterns of $t(x;d)$ and the FRT is obtained as

$$|\Im^{(p)}\{t(x;d)\}|^2 = |t(x;d_T)|^2, \tag{5}$$

where the specific values $p = p_S$ for which Eq. (5) is satisfied are given by

$$p_S = \frac{2}{\pi}\tan^{-1}\left(\frac{sd^2}{\lambda f_0}\right), \tag{6}$$

and the selfimage period d_T results as

$$d_T = \frac{d}{m}\cos\left(\frac{p_S\pi}{2}\right). \tag{7}$$

Eqs. (5)–(7) include both fractional and integer selfimaging. The fractional orders associated with the integer selfimage conditions are derived from Eq. (6) by placing $m = 1$. Thus, for the fractional orders obtained from Eq. (6), the irradiance of the FRT (or equivalently, the RWT) becomes identical to demagnified replicas of the input periodic object with a period d_T given by Eq. (7). In the next section, we extend the RWT definition to the temporal domain for analyzing pulse train transmission in dispersive media using the space–time optical analogy. Pulse trains having a constant repetition rate are the equivalent time signals to the periodic objects of the spatial domain.

3. Temporal Radon–Wigner Transform (RWT)

The space–time duality theory is based on the mathematical analogy existing between the impulse response functions associated with spatial and temporal optical components. By using this analogy, pulse transmission devices can be developed having the same properties in the time domain that those having the amplitude distributions produced by the "analogue" or spatial counterparts [14–17]. In the temporal domain, a time lens introduces a quadratic-phase modulation into the time-varying signal. Besides, a dispersive medium (up to the first-order) has associated a quadratic-phase spectral response with a mathematical expression similar to that found in spatial Fresnel diffraction. In this way, through a suitable combination of dispersion and quadratic-phase modulation into the propagating pulses, time-domain analogues of a spatial imaging system can be synthesized. The equivalencies between spatial optics experiments and guided pulse propagation in dispersive media can be established in the following way

$$\lambda z \Longleftrightarrow 2\pi\Phi_{20}, \tag{8a}$$

$$\frac{2\pi}{\lambda f} \Longleftrightarrow \phi_{20}. \tag{8b}$$

In Eq. (8), z and f are the free-space propagation distance and the focal length, respectively, of the spatial optical system. Besides, Φ_{20} is the second-order dispersion coefficient of the medium where the pulses are transmitted (specified at the working central frequency $\omega = \omega_0$) and ϕ_{20} is the quadratic phase modulation factor associated with the time lens. The symbol $\Longleftrightarrow$ means that the magnitudes of the left side (spatial parameters) should be replaced by the magnitudes of the right side (time parameters) in order to produce the same impulse response (in case of spatial and time lenses) or the same transfer function (in case of Fresnel diffraction and dispersive pulse transmission).

The optical production of the spatial RWT was discussed in Section 2. By using Eq. (8), a photonic device for obtaining the temporal RWT associated with a time-varying signal $u_0(t)$ is shown in Fig. 1. The input light pulse first interacts

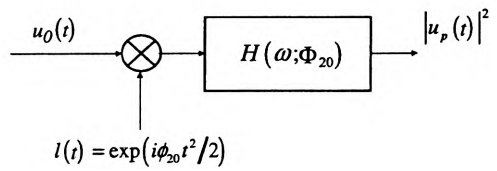


Fig. 1. Scheme of the optical device proposed to implement the temporal RWT. The input signal $u_0(t)$ is first phase modulated by $l(t)$ and then it is transmitted by the dispersive component having the transfer function $H(\omega) = \exp(i\Phi_{20}\omega^2/2)$. The output optical power is $|u_p(t)|^2$.

with a quadratic-phase modulator (having a phase modulation factor ϕ_{20}) and then with a dispersive medium having a second-order dispersion coefficient Φ_{20}, after which the resulting pulse is detected as $P_{\text{out}}(t) = |u_p(t)|^2$. It should be noted that as we are only interested in the signal irradiance (for producing the RWT), the second time lens that would be required for correcting the phase term of the FRT is not needed. Now, by applying Eqs. (3) and (8), the time-domain relationships linking the setup parameters Φ_{20} and ϕ_{20} with the fractional order p of $|u_p(t)|^2 = |\Im^{(p)}\{u_0(t)\}|^2$ result as

$$\Phi_{20} = \frac{\lambda\sigma_0}{2\pi}\sin\left(\frac{p\pi}{2}\right), \tag{9a}$$

$$\phi_{20} = \frac{2\pi}{\lambda\sigma_0}\tan\left(\frac{p\pi}{4}\right), \tag{9b}$$

where σ_0 is a scaling factor having dimensions of ps^2/nm rad. Thus, if the setup parameters Φ_{20} and ϕ_{20} are varied accordingly with Eq. (9), FRT modulus squared with a varying fractional order p are obtained from $P_{\text{out}}(t)$, i.e.,

$$P_{\text{out}}(t) = |\Im^{(p)}\{u_0(t)\}|^2 = \text{RWT}_{\phi=p\pi/2}\{u_0(t)\}, \quad 0 \leqslant p \leqslant 1, \tag{10}$$

Finally, two features should be kept in mind in the observation of the RWT displays of this work. First, since the set up parameters should be continuously changed to obtain $P_{\text{out}}(t) = |u_p(t)|^2$, for varying p, the temporal RWT of the input signal is sequentially produced. Second, there is a pulse delay effect that directly depends with p (through Φ_{20}, see Eq. (9a)) which, if it is not compensated, would originate a shear display of the RWT [30]. Therefore, to facilitate the comparison between different fractional orders p, all RWT displays of this work were temporally aligned with the input, and thus they do not show this shear effect.

If the complete temporal RWT is to be photonically realized, it should be taken into account that the setup parameters Φ_{20} and ϕ_{20} are continuously changed accordingly with Eq. (9) for obtaining $P_{\text{out}}(t) = |u_p(t)|^2$ for varying p. Therefore, the complete RWT display of the input signal can only be sequentially produced and it would require a dispersive medium with a well-controlled second-order coefficient and time lenses with different phase modulation factors. By this reason, we propose a numerical implementation of the RWT in order to achieve the whole display ($0 < p < 1$) for signal analysis purposes and, when a particular value $p = p_0$ is selected depending on the pulse transmission required application, the optical device is only once implemented with the parameters Φ_{20} and ϕ_{20} obtained from Eq. (9) by replacing $p = p_0$.

4. Periodic pulse train conformation with different repetition rates

A very important application related with the spatial–temporal analogy is the temporal selfimaging or Talbot effect where conformation of periodic pulse trains having different repetition rates can be achieved by properly combining signal phase modulation (or time lens action) with pulse transmission in guided dispersive media [19–29]. Although this subject was extensively treated by many authors, there are several features that can be conveniently analyzed employing the RWT approach.

By using the photonic device sketched in Fig. 1, and by considering as input signal $u_0(t)$ a sequence of N pulses having a pulse width T_0 and a repetition period T_1, the output optical power becomes $P_{\text{out}}(t) = |\Im^{(p)}\{u_0(t)\}|^2$, whenever the setup parameters Φ_{20} and ϕ_{20} are related with p in accordance with Eq. (9). Besides, by taking into account Eqs. (5)–(7) linking the selfimage patterns and the FRT of a periodic spatial object, a temporal analogue condition can be found as

$$P_{\text{out}}(t) = |\Im^{(p)}\{u_0(t)\}|^2 = |u_0(t/M)|^2, \tag{11}$$

where the selfimage magnification factor M is given by

$$M = \frac{\cos(p_S\pi/2)}{m}. \tag{12}$$

The specific values $p = p_S$ for which the FRT becomes a temporal selfimage, as given by Eq. (11), can be found by transforming Eq. (6) to the time domain, so resulting

$$sT_1^2 = \lambda\sigma_0\tan\left(\frac{p_S\pi}{2}\right), \tag{13}$$

where, as in the spatial case, $s = n$, with $n = 1, 2, 3, \ldots$, for the integer or Talbot selfimages and $s = n/m$ (being n and m coprime integers and $m \geqslant 2$) for the fractional or sub-Talbot selfimages. The main difference between integer and fractional selfimaging, as replicas of the input pulse train, are: (i) the repetition rates are $T_1 x \cos(p_S\pi/2)$ and $T_1/mx\cos(p_S\pi/2)$ for integer and fractional selfimages, respectively, and (ii) the duty-cycle T_0/T_1 remains unchanged for the integer selfimages while it is multiplied by m for the fractional selfimages. In this way, if the whole RWT display is generated from a given input pulse train $u_0(t)$, output pulse trains having different repetition rates, and equal or different duty-cycles, can be produced by choosing the setup parameters Φ_{20} and ϕ_{20} in accordance with the selected values of p_S.

For establishing the spatial–temporal selfimaging analogy, periodicity becomes an essential condition. In the spatial domain, a finite object may easily have $N \cong 10^3$

diffracting lines, being its space-bandwidth product large enough for considering it as a periodic object. In this case, a large number of well-defined selfimages can be observed. The situation is completely different in the temporal domain. Although pulse trains having constant repetition rate and time duration long enough as to be considered a periodic time signal can be implemented, the actual number N of consecutive pulses which can be phase-modulated by a practical time lens and/or spectral overlapped by the employed dispersive medium is rather limited. By this reason, it is very important to establish the minimum number of pulses $N = N_0$ in order to obtain well-formed temporal selfimages. This question was first analyzed by Azaña [26]. By considering the total time-bandwidth product K_{env} associated with the envelope of the pulse train, the selfimaging conditions and the relation $N \approx \Delta t_{\text{env}}/T_1$, being Δt_{env} the total temporal duration of the pulse train, they derive the following inequality

$$N_0 \gg \frac{K_{\text{env}} s T_1}{2\pi T_0}, \tag{14}$$

where $s = n/m$ characterizes the selfimage. Basically, this relation states that N_0 should be large enough as compared with the reciprocal of the pulse train duty-cycle. We here analyze this question choosing as periodic input signal $u_0(t)$ a pulse train of N Gaussian-profile pulses, with repetition rate T_1, which can be expressed as

$$\begin{aligned} u_0(t) &= A_0 \sum_{k=-N/2}^{N/2} \exp\left[-\frac{(1+\mathrm{i}C)}{2T_0^2}(t-kT_1)^2\right] \\ &= \operatorname{rect}\left(\frac{t}{NT_1}\right) \times \sum_{q=-\infty}^{\infty} a_q \exp(\mathrm{i}2\pi q t/T_1), \end{aligned} \tag{15}$$

where A_0 is the pulse maximum amplitude, T_0 is the half-width (measured at $1/e$ decay in power), C is the chirp parameter and $\operatorname{rect}(t/\Delta t) = 1$ in a time interval $\Delta t \cong NT_1$. The Fourier coefficients a_q become

$$a_q \cong a_0 \exp\left[-\frac{2\pi^2 T_0^2}{(1+\mathrm{i}C)T_1^2} q^2\right]. \tag{16}$$

In the spatial selfimaging, the so-called "walk-off" effect or lack of in-phase interference due to the spatial separation of the several diffracted orders, determines the maximum number of observable selfimages. Basically, the maximum selfimage distance z_T is limited by the relationship $\tan\alpha_c = Nd/z_T \cong q_c\lambda/d$, being Nd the spatial extent of the finite periodic object, q_c the maximum diffracted order that is present in the selfimage and α_c the angle subtended with the optical axis which satisfies the grating condition $d\sin\alpha_c = q_c\lambda$. By translating this result to the temporal domain, by using Eqs. (8a) and (9a), we obtain

$$N_0 \cong \frac{q_c \lambda \sigma_0}{T_1^2} \sin(\pi p_S). \tag{17}$$

As $|a_q|^2$ is the optical power of the q-diffracted order, we limit the infinite Fourier expansion of Eq. (15) to a finite Fourier series up to a maximum order q_c such as $|a_{q_c}/a_0|^2 \cong 0.1$, i.e., we neglect all the orders $q > q_c$ having optical powers lower than 10% of that associated with the zero-order. This criterion yields to different results depending on the shape of the individual pulses but it becomes adequate for slow-varying functions like Gaussians. Thus, q_c can be derived, by using Eq. (16), from the condition

$$\left|\frac{a_{q_c}}{a_0}\right|^2 \cong \exp\left[-\frac{4\pi^2 T_0^2}{(1+C^2)T_1^2} q_c^2\right] \cong 0.1. \tag{18}$$

For a duty-cycle $T_0/T_1 = 0.05$, it can be obtained $q_c = 5$ for $C = 0$ and $q_c = 30$ for $C = -6$. This means that the pulse number N of the chirped pulse train should be increased by a factor $|C|$ as compared with the unchirped pulse train for obtaining the same selfimage quality. This fact will be further illustrated in the next section where some examples were presented. Now, we are interested in deeper analyze the selfimage formation when pulse chirping is present by taking advantage of the RWT formalism. As the procedure for obtaining the RWT, as shown in Fig. 1, consists of a quadratic-phase modulation of the input signal $u_0(t; C)$ by a time lens $l(t)$ followed by dispersive propagation (which is mathematically equivalent to delay the signal spectrum by a quadratic transference function $H(\omega)$), we can express the output amplitude as

$$\begin{aligned} u_{\text{out}}(t) &= [u_0(t)l(t)] \otimes h(t) \\ &= [u_0(t)\exp(\mathrm{i}\phi_{20}t^2/2)] \otimes \exp(-\mathrm{i}t^2/2\Phi_{20}), \end{aligned} \tag{19}$$

being $h(t) = \Im^{-1}\{H(\omega)\}$ the impulse response associated with the dispersive component and $\otimes$ denotes convolution. By calculating Eq. (19), it can be written as

$$\begin{aligned} u_{\text{out}}(t) \cong K &\exp\left[-\mathrm{i}\left(1-\frac{1}{1-\Phi_{20}\phi_{20}}\right)\frac{t^2}{2\Phi_{20}}\right] \\ &\times \sum_{q=-\infty}^{\infty} \exp\left[-\frac{2\pi^2 T_0^2}{(1+C^2)T_1^2} q^2\right] \\ &\times \exp\left[\mathrm{i}\frac{2\pi^2}{T_1^2}\left(\frac{CT_0^2}{1+C^2}+\frac{\Phi_{20}}{1-\phi_{20}\Phi_{20}}\right)q^2\right] \\ &\times \exp\left[\mathrm{i}\frac{2\pi q t}{(1-\phi_{20}\Phi_{20})T_1}\right], \end{aligned} \tag{20}$$

where K is a complex constant and the approximation $\Delta t \cong NT_1 \gg T_0$ was used. Thus, the RWT associated with the chirped pulse train can be obtained from Eq. (20) as

$$P_{\text{out}}(t) = |\Im^{(p)}\{u_0(t; C)\}|^2 \cong \left|K \sum_{q=-\infty}^{\infty} b_q \exp\left[\mathrm{i}\frac{2\pi q t}{MT_1}\right]\right|^2, \tag{21}$$

being

$$\begin{aligned} b_q = &\exp\left[-\frac{2\pi^2 T_0^2}{(1+C^2)T_1^2} q^2\right] \\ &\times \exp\left[\mathrm{i}\frac{2\pi^2}{T_1^2}\left(\frac{CT_0^2}{1+C^2}+\frac{\Phi_{20}}{1-\phi_{20}\Phi_{20}}\right)q^2\right], \end{aligned} \tag{22a}$$

$$M = 1 - \phi_{20}\Phi_{20}, \tag{22b}$$

and the parameters Φ_{20} and ϕ_{20} are varied accordingly with Eq. (9) for obtaining the whole RWT display for $0 < p < 1$.

Let us now investigate the relationship between the RWT, as given by Eq. (21), and the selfimaging formation. For the particular case of an unchirped pulse train, this relationship was previously given by Eqs. (11)–(13). Thus, we reformulate the problem in the following way. We analyze the properties of the unchirped pulse train $\hat{u}_0(t; C = 0)$ that would produce the same RWT for selfimaging as it is given by the output irradiance of Eq. (21). If $\widehat{T}_1$ and $\widehat{T}_0$ denote the repetition rate and pulse width of $\hat{u}_0(t; C = 0)$, then the output irradiance can be obtained by properly using Eqs. (21) and (22) with $C = 0$, i.e.,

$$P_{\text{out}}(t) = |\Im^{(p)}\{\hat{u}_0(t; C = 0)\}|^2 \cong \left| K \sum_{q=-\infty}^{\infty} \hat{b}_q \exp\left[i \frac{2\pi q t}{\widehat{M}\widehat{T}_1} \right] \right|^2, \tag{23}$$

where $\hat{b}_q$ and $\widehat{M}$ are now given as

$$\hat{b}_q = \exp\left[-\frac{2\pi^2 \widehat{T}_0^2}{\widehat{T}_1^2} q^2 \right] \exp\left[i \frac{2\pi^2 \widehat{\Phi}_{20}}{\widehat{M}\widehat{T}_1^2} q^2 \right], \tag{24a}$$

$$\widehat{M} = 1 - \hat{\phi}_{20}\widehat{\Phi}_{20}, \tag{24b}$$

where the unknown values of $\widehat{\Phi}_{20}$, $\hat{\phi}_{20}$, $\widehat{T}_1$ and $\widehat{T}_0$ are to be determined by equalizing Eqs. (23) and (21), since the same output irradiance was required. From this condition, we derive the following three relationships

$$M T_1 = \widehat{M}\widehat{T}_1, \tag{25a}$$

$$\frac{1}{1 + C^2}\left(\frac{T_0^2}{T_1^2}\right) = \frac{\widehat{T}_0^2}{\widehat{T}_1^2}, \tag{25b}$$

$$\frac{C}{1 + C^2}\left(\frac{T_0^2}{2T_1^2}\right) + \frac{\Phi_{20}}{2MT_1^2} = \frac{\widehat{\Phi}_{20}}{2\widehat{M}\widehat{T}_1^2}. \tag{25c}$$

By using Eq. (25), we intend to solve the following question. We have two different pulse trains: (i) one chirped $u_0(t; C)$ having known parameters $(T_1, T_0, C \neq 0)$ for which the fractional orders p_S associated to the selfimages are unknown; (ii) a second unchirped pulse train $\hat{u}_0(t; C = 0)$, with $\widehat{T}_1$ and $\widehat{T}_0$ as unknown parameters, for which the fractional order $\hat{p}_S$ corresponding to a selfimage condition can be obtained from Eq. (13) (since $C = 0$), i.e.,

$$\hat{p}_S = \frac{2}{\pi} \tan^{-1}\left(\frac{s\widehat{T}_1^2}{\sigma_0 \lambda} \right), \tag{26}$$

Unfortunately, Eq. (26) can not be solved since $\widehat{T}_1$ is unknown. However, by returning to the previous heuristic analysis (Eqs. (15)–(18)), we conclude that the main difference between chirped and unchirped pulse trains for producing selfimaging lies in the number of required Fourier coefficients rather than periodicity. Hence, we introduce the condition $\widehat{T}_1 \cong T_1$, approximation which is to be justified from the results shown in the next section. Now, we can solve Eq. (26) for obtaining $\hat{p}_S$. By using Eqs. (25a) and (25c), together with Eq. (9), we derive the following relationship to found the values of p_S

$$\tan\left(p_S \frac{\pi}{2}\right) = \tan\left(\hat{p}_S \frac{\pi}{2}\right) - \frac{C}{1 + C^2}\left(\frac{2\pi T_0^2}{\sigma_0 \lambda}\right). \tag{27}$$

Finally, from Eq. (25b) it results

$$\frac{T_0^2}{1 + C^2} = \widehat{T}_0^2. \tag{28}$$

Thus, we arrive to the following result: The selfimages produced by a chirped Gaussian pulse train $u_0(t; C)$, with pulse width T_0 and repetition rate T_1, which are observed at $p = p_S$ in its RWT display, are the same selfimages originated by an unchirped Gaussian pulse train $\hat{u}_0(t; C = 0)$, having the same repetition rate $\widehat{T}_1 = T_1$ and pulse width $\widehat{T}_0 = T_0/\sqrt{1 + C^2}$, obtained at $p = \hat{p}_S$ (derived from Eq. (26) with $\widehat{T}_1 = T_1$) in its corresponding RWT display. The relationship linking p_S and $\hat{p}_S$ is given by Eq. (27) being their main difference the term involving $CT_0^2/\sigma_0\lambda(1 + C^2)$. As we shall see in the next section, for the first selfimage ($s = 1$) and its associated fractional selfimages ($s = 1/m$, with $m \geqslant 2$), with $C = -6$, $\sigma_0 = 1.42$ ps^2/nm rad and $\lambda = 1550$ nm, from Eq. (27) it can be obtained $p \cong 1.001\hat{p}_S$. However, this slight variation in the selected fractional order of the RWT becomes very important for observing or not fractional selfimaging of high repetition rate multiplication ($m > 10$). As a final remark, Chantada et al. recently presented a spectral analysis of the temporal Talbot effect by only employing fiber dispersive lines [31]. The relationships we obtained between Φ_{20} and $\widehat{\Phi}_{20}$ (as given by Eq. (25c)) (or equivalently, between p_S and $\hat{p}_S$ as given by Eq. (27)) using the tandem time lens-dispersive line of Fig. 1, reduce to the equivalent dispersion defined in Eq. (5) of [31], when unitary magnification $M = \widehat{M} = 1$ is considered. For this particular case, from Eq. (25a) it results $T_1 = \widehat{T}_1$ and the relationships given by Eqs. (27) and (28) are obtained without any approximation.

5. Numerical results

We now illustrate the selfimaging formation properties, discussed in the previous section, by analyzing the RWT of the three following Gaussian periodic pulse trains, all of them having a constant repetition rate $T_1 = 40$ ps, pulse width $T_0 = 2$ ps and a mean wavelength $\lambda = 1550$ nm: (i) $N = 21$ pulses, $C = 0$; (ii) $N = 21$ pulses, $C = -6$; (iii) $N = 129$ pulses, $C = -6$. Accordingly with the analysis done after deriving Eqs. (17) and (18), the pulse train (iii), having a pulse number $|C|$ times greater than (ii), should originate the same selfimage quality as compared with the non-chirped pulse train (i). Following the procedure described in Section 3, we numerically compute the RWT for the three pulse trains and the results are shown in Fig. 2a–c as gray level displays. In order to better visualize the behavior of the pulse trains, a time interval of 100 ps is shown for which only three consecutive central

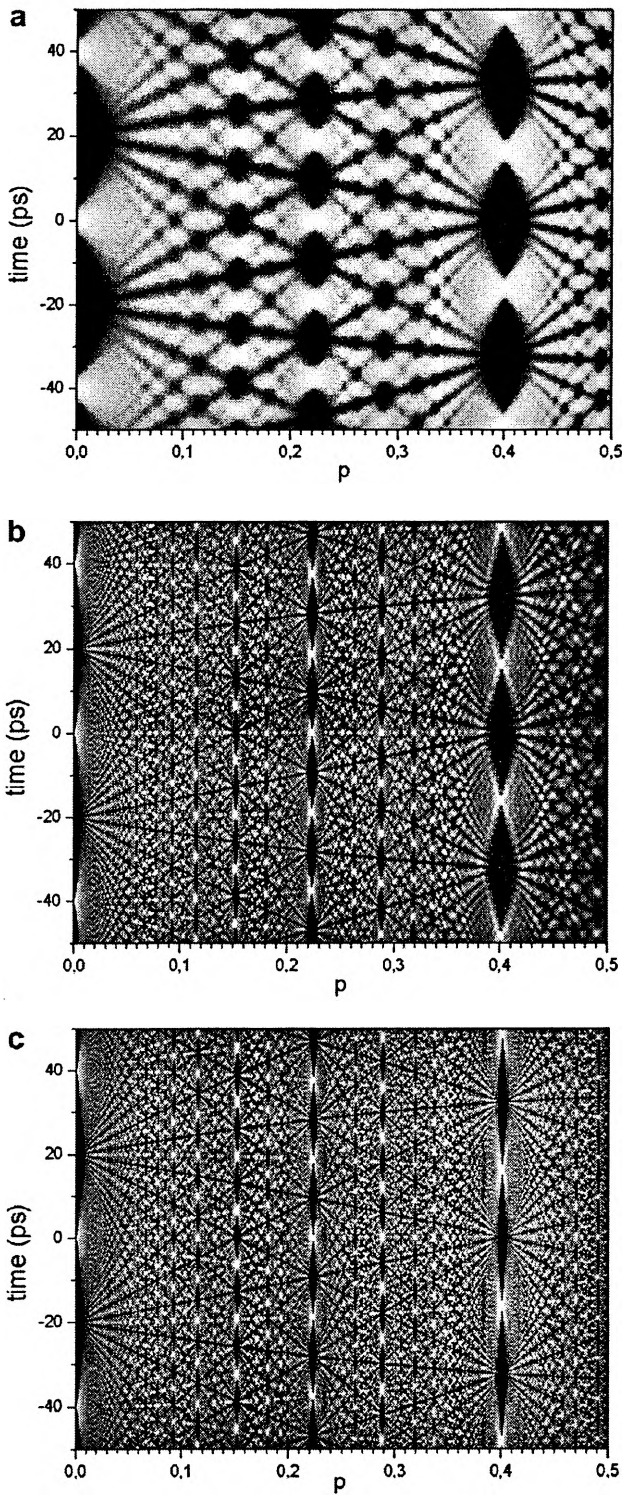


Fig. 2. Gray level displays of the RWT associated with three periodic pulse trains, all of them having a constant repetition rate $T_1 = 40$ ps, a pulse width $T_0 = 2$ ps and a mean wavelength $\lambda = 1550$ nm. In (a) $N = 21$ pulses, $C = 0$; in (b) $N = 21$ pulses, $C = -6$; and in (c) $N = 129$ pulses, $C = -6$. In the three displays, the temporal and fractional order resolutions are $\Delta t = 0.06$ ps and $\Delta p = 0.001$, respectively. For sake of clarity, only three central pulses of the input are shown.

pulses of the input trains can be observed. Besides, for producing well-defined selfimages we restrict the selfimaging orders to be analyzed to the range $0 < p < p_1$, being p_1 the fractional order associated with the first integer selfimage ($s = 1$). For obtaining repetition rate multiplication capability, fractional selfimages are to be also considered for these values of p. For the unchirped pulse train (i), it can be obtained from Eq. (13) $p_1 \approx 0.4004$. By considering this value of p, the RWT displays of Fig. 2 are only shown for $0 < p < 0.5$. Next, we analyze the selfimage irradiances for certain values of the fractional order p. In Fig. 3, the output irradiances $|u_p(t)|^2$ obtained from each RWT display are shown for $p = p_1$. As it is expected, it can be seen in (a) a well-formed selfimage of the pulse train (i) having the repetition period $T_1' = T_1 \times \cos(\pi p_1/2) \approx 32.4$ ps (accordingly with Eq. (12)) and a duty-cycle of 0.05 identical to the input pulse train. In (b), a small distortion in the selfimage of the chirped pulse train (ii) can be observed. Two different distorting effects are present here: the number of pulses should be increased for obtaining a selfimage quality similar to the unchirped case, and the fractional order should be corrected, as it is established by Eq. (27), for chirped pulses. However, as it is shown in (c), the selfimage irradiance of the pulse train (iii), for which the number of pulses is increased by $|C| = 6$, becomes identical to (a) and the mismatch effect in p (due to pulse chirping) is

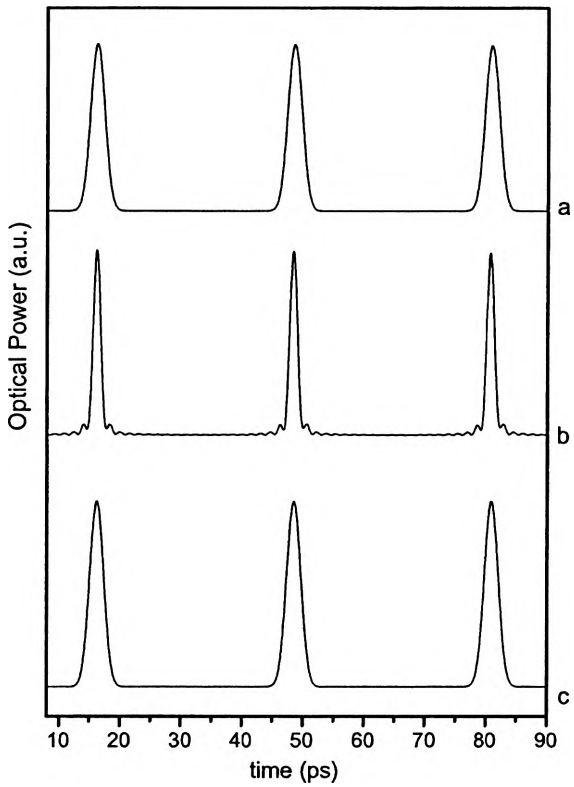


Fig. 3. Output optical powers, associated with the first integer selfimage, obtained from the slices at $p \approx 0.4004$ of each one of the RWT shown in Fig. 2a–c.

negligible. Now, we analyze the irradiances of $|u_p(t)|^2$ for $p \approx 0.0289$. As it can be derived from Eq. (13), this value of p corresponds to the fractional selfimage $s = 1/16$ (i.e., $m = 16$) of the unchirped pulse train (i). The three irradiances are shown in Fig. 4. In (a), the irradiance resembles the input pulse train with a certain distortion level. In this case, the small amount of dispersion Φ_{20} required to obtain $p \approx 0.0289$ is not enough to spectrally overlap the pulses. By inspection of Fig. 2a, it can be concluded that fractional unchirped sefimages can only be observed for $p \geqslant 0.1$. In Fig. 4b and c, the fractional selfimages corresponding to the chirped pulse trains (ii) and (iii) appear severely distorted. In (c), although N is increased by $|C|$ as compared with (b), the mismatch effect in the selection of p (by using Eq. (13) instead of Eq. (27)) becomes relevant. However, as it was discussed after deriving Eqs. (27) and (28), there is an unchirped equivalent pulse train, with repetition period $\widehat{T}_1 = T_1 = 40$ ps and pulse width $\widehat{T}_0 = 2\text{ ps}/\sqrt{1+C^2} \approx 0.33$ ps, which originates the same selfimage irradiances as (ii) and (iii). The RWT of this equivalent pulse train is shown in Fig. 5a, where it can be observed that this display is almost identical to the RWT associated with (iii) (shown in Fig. 2c). To corroborate this equivalence, we derive from Eq. (13) (or equivalently from Eq. (26)) the fractional order for $s = 1/16$ resulting $\hat{p}_S = 0.0289$ (that is the same p as it was used in Fig. 4). By employing Eq. (27), the corrected fractional order associated with $s = 1/16$ for the chirped pulse train results as $p_S \approx 0.0301$. Fig. 5b shows the output irradiance obtained either from the RWT of the chirped pulse train (iii) (shown in Fig. 2c) for $p \approx 0.0301$ or from the RWT of the equivalent unchirped pulse train (shown in Fig. 5a) for $p \approx 0.0289$, so verifying the results found in Section 4. In order to better illustrate the pulse conformation effect, for the chirped and the equivalent unchirped pulse trains, we show in Fig. 6, a small range $0.2218 \leqslant p \leqslant 0.2245$ of the two RWT of Figs. 2c and 5a. This p-range corresponds

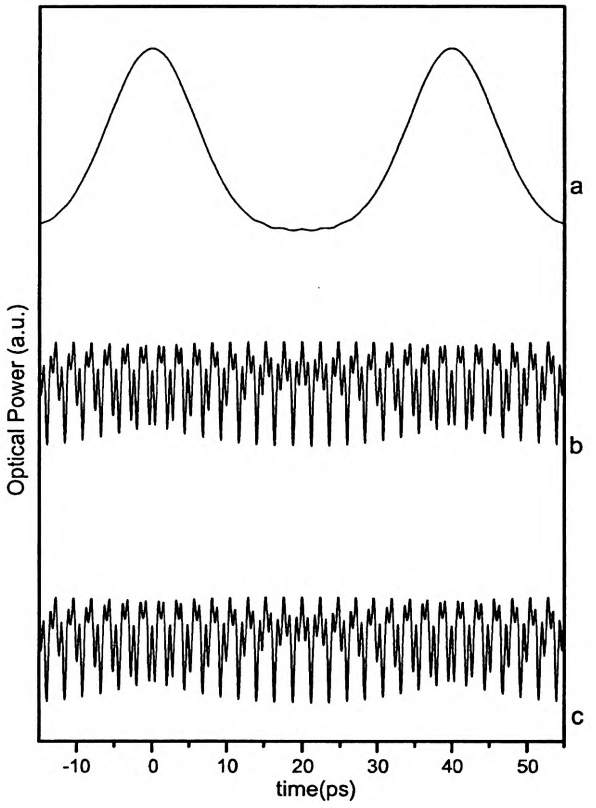


Fig. 4. Output optical powers obtained from the slices at $p \approx 0.0289$ of each one of the RWT shown in Fig. 2a–c. This value of p is associated with the fractional selfimage $m = 16$ of the unchirped pulse train. It can not be observed in (a) (due to the low amount of dispersion Φ_{20} associated with this p), and it is not formed in (b) and (c) due to the shifting effect in the selection of p that should be done for chirped pulses.

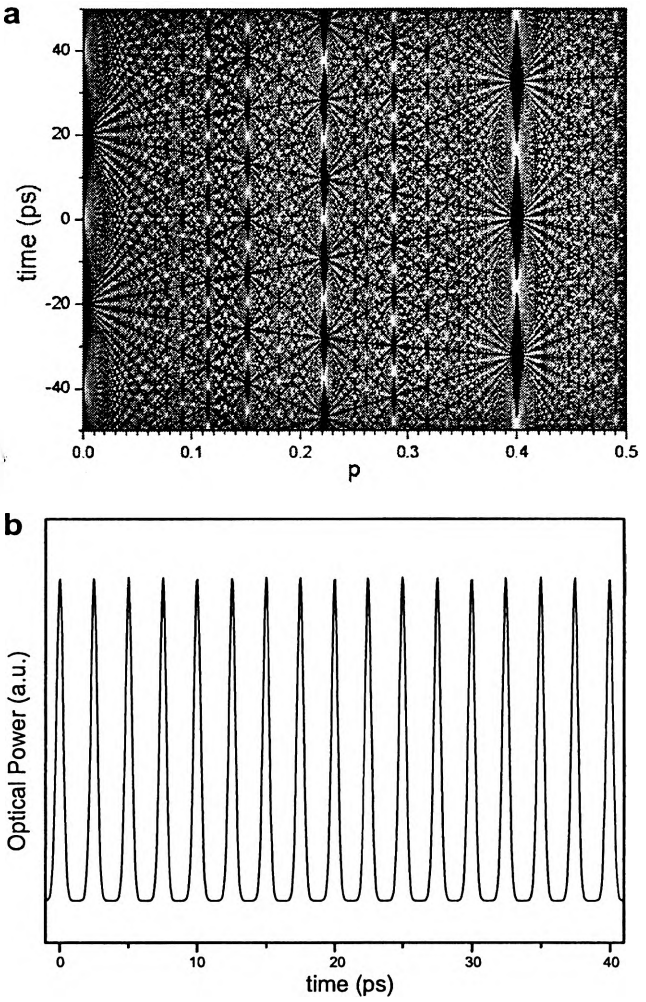


Fig. 5. (a) Gray level display of the RWT corresponding to the equivalent unchirped pulse train (associated with the chirped pulse trains of Fig. 2b and c), having a repetition rate $\widehat{T}_1 = 40$ ps and a pulse width $\widehat{T}_0 \approx 0.33$ ps. The temporal and fractional order resolutions are the same as in Fig. 2 and, for sake of clarity; only three central pulses of the input are shown. (b) Output optical power which can be obtained either from the slice at $\hat{p} \approx 0.0289$ of the RWT shown in (a) or from the slice at the corrected value $p \approx 0.0301$ of the RWT shown in Fig. 2c. Now, a well-defined fractional selfimage $m = 16$ can be observed.

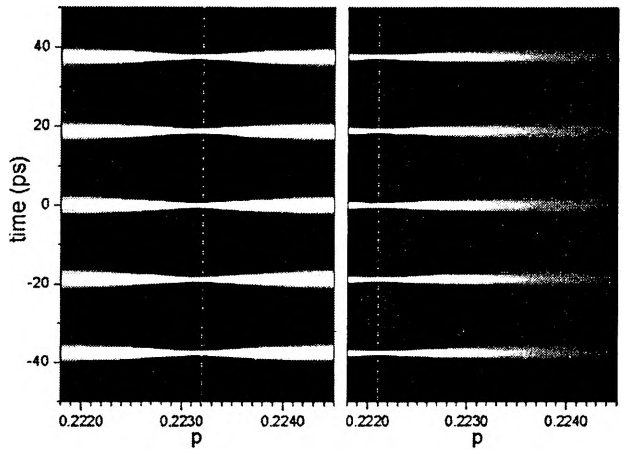


Fig. 6. Enlarged view of the gray level displays of the RWT of Figs. 2c (left side) and 5a (right side). The output optical power corresponding to the fractional selfimage $s = 1/2$ ($m = 2$) can be obtained either from the slice at $\hat{p} \approx 0.2221$ of the RWT (right side) or from the slice at the corrected value $p \approx 0.2231$ of the RWT (left side).

to the fractional selfimage $s = 1/2$ (i.e., $m = 2$). By direct inspection of Figs. 2c and 5a there is no perceptible difference between both RWT displays in the neighborhood of $p \approx 0.22$. However, it can be seen in Fig. 6 that both RWT becomes identical (and so, the associated selfimage irradiances) only for $p_S \approx 0.2232$ (left display, chirped pulses) and $\hat{p}_S \approx 0.2221$ (right display, unchirped equivalent pulses). For other values of p (no satisfying a selfimaging condition), both RWT of Fig. 6 become slightly different. In summary, it can be observed that an additional dispersion is required to observe a selfimage when each optical pulse of the input is chirped, i.e. from $\hat{p}_S \approx 0.2221$ (for $C = 0$) to $p_S \approx 0.2232$ (for $C = -6$). This is so, because when the chirp parameter and the dispersion have opposite signs, the length of the medium can be split in two positive contributions, i.e. $L = L_C + L_T$, assuming that an optic fiber is used as the dispersive medium. The first length of the line (L_C) is used to compress the pulses in the input train individually, and the remaining length of the fiber (L_T) produces the corresponding Talbot selfimage of the compressed pulses train [31].

6. Conclusions

We have presented a method of signal analysis and processing in the time domain based on the RWT description. By employing the space-temporal analogy, a photonic device for producing the temporal RWT was proposed which can be used to originate optical pulses having certain predetermined properties which are of interest in pulse transmission applications in different dispersive media. This approach was applied to analyze several features of the temporal selfimaging or Talbot effect. It was compared the selfimage formation of unchirped and chirped periodic pulse trains. The possibility to obtain, from a certain input periodic train, an output with a higher repetition rate (i.e. selfimages with high fractional order) becomes enhanced by a multiplicative factor ($|C|$), when the input train is chirped. Regarding with the finite extension of the pulse trains, it was found that for obtaining the same selfimage definition, the pulse number of the chirped pulse train should be multiplied by the chirp parameter as compared with the pulse number of the unchirped pulse train. The general relationships linking the pulse train parameters with the fractional orders for which selfimages appear in the RWT were developed for both, unchirped and chirped periodic pulse trains. These results become relevant when fractional selfimages, having high repetition rates, are to be produced since in this case the chirped pulse trains are strongly distorted if they are originated employing the setup parameters associated with the fractional orders corresponding to the similar unchirped condition.

Acknowledgements

This work was supported by Consejo Nacional de Investigaciones Científicas y Técnicas (CONICET – PIP 6156/05), Facultad de Ingeniería, Universidad Nacional de La Plata (UNLP – Project 1106), Secretaría de Ciencia y Técnica (SECyT – PICT03-12502) and Comisión de Investigaciones Científicas (CIC 1114/05). CCL and PCC are fellowships of CONICET and CIC, respectively.

References

[1] M.J. Bastiaans, Opt. Commun. 25 (1978) 26.
[2] M.J. Bastiaans, J. Opt. Soc. Am. 69 (1979) 1710.
[3] H.O. Bartelt, K.H. Brenner, A.W. Lohmann, Opt. Commun. 32 (1980) 32.
[4] D. Mendlovic, H.M. Ozaktas, J. Opt. Soc. Am. A 10 (1993) 1875; D. Mendlovic, H.M. Ozaktas, J. Opt. Soc. Am. A 10 (1993) 2522.
[5] A.W. Lohmann, J. Opt. Soc. Am. A 10 (1993) 2181.
[6] L.B. Almeida, IEEE Trans. Signal Process. 42 (1994) 3084.
[7] A.W. Lohmann, B.H. Soffer, J. Opt. Soc. Am. A 11 (1994) 1798.
[8] S. Granieri, O. Trabocchi, E.E. Sicre, Opt. Commun. 119 (1995) 275.
[9] S. Granieri, W.D. Furlan, G. Saavedra, P. Andrés, Appl. Opt. 36 (1997) 8363.
[10] H.M. Ozaktas, Z. Zalevsky, M. Alper Kutay, The Fractional Fourier Transform with Applications in Optics and Signal Processing, Wiley, 2001.
[11] J.C. Woods, D.T. Barry, IEEE Trans. Signal Process. 4 (1992) 3166.
[12] J.C. Woods, D.T. Barry, IEEE Trans. Signal Process. 42 (1994) 2105.
[13] M.J. Bennett, S. McLaughlin, T. Anderson, N. McDicken, IEEE Trans. Biomedical Eng. 53 (2006) 754.
[14] B.H. Kolner, IEEE J. Quantum Electron. 30 (1994) 1951.
[15] A. Papoulis, J. Opt. Soc. Am. A 11 (1994) 3.
[16] C.V. Bennett, B.H. Kolner, IEEE J. Quantum Electron. 36 (2000) 430.
[17] C.V. Bennett, B.H. Kolner, IEEE J. Quantum Electron. 36 (2000) 649.
[18] J. Azaña, L.R. Chen, M.A. Muriel, P.W.E. Smith, Electron. Lett. 35 (1999) 2223.
[19] J. Azaña, M.A. Muriel, Opt. Lett. 24 (1999) 1672.
[20] J. Azaña, M.A. Muriel, IEEE J. Sel. Topics Quantum Electron. 7 (2001) 728.
[21] J. Azaña, L.R. Chen, J. Opt. Soc. Am. B 20 (2003) 1447.
[22] N.K. Berger, B. Levit, A. Bekker, B. Fischer, IEEE Photon. Technol. Lett. 16 (2004) 1855.

[23] J. Lancis, J. Caraquitena, P. Andrés, M.A. Muriel, Opt. Commun. 253 (2005) 156.
[24] C. Cuadrado-Laborde, P.A. Costanzo-Caso, R. Duchowicz, E.E. Sicre, Opt. Commun. 260 (2006) 528.
[25] S. Longhi, M. Marano, P. Laporta, O. Svelto, M. Belmonte, B. Agogliati, L. Arcangeli, V. Pruneri, M.N. Zervas, M. Ibsen, Opt. Lett. 25 (2000) 1481.
[26] J. Azaña, J. Opt. Soc. Am. B 20 (2003) 83.
[27] D.A. Chestnut, C.J.S. de Matos, J.R. Taylor, Opt. Lett. 27 (2002) 1262.
[28] C.J.S. de Matos, J.R. Taylor, Appl. Phys. Lett. 83 (2003) 5356.
[29] J.A. Bogler, P. Hu, J.T. Mok, J.L. Blows, B.J. Eggleton, Opt. Commun. 249 (2005) 431.
[30] C. Cuadrado-Laborde, P.A. Costanzo-Caso, R. Duchowicz, E.E. Sicre, Opt. Commun. 266 (2006) 32.
[31] L. Chantada, C.R. Fernández-Pousa, C. Gómez-Reino, J. Light. Technol. 24 (2006) 2015.

Física del láser y aplicaciones

Ablación, limpieza y restauración

Fotofísica de moléculas

Láseres de colorantes

Láseres de estado sólido

Láseres gaseosos

Medición tamaño-particulas

Óptica integrada

Pulsos cortos

La física del láser es un área amplia que abarca los estudios básicos de electrónica cuántica, los mecanismos macroscópicos de su funcionamiento, incluyendo el estudio de la interacción material activo-cavidad resonante. Dentro de este marco, el CIOp desarrolló una extensa actividad de investigación en temas básicos como de aplicación del láser. Los primeros abarcaron el estudio de los mecanismos de excitación particulares que daban lugar a la inversión de población en láseres gaseosos iónicos y de moléculas diatómicas, en láseres de colorantes orgánicos en solución y en materiales activos para láseres de estado sólido sintonizables. Los temas de aplicación del láser, tan amplios como pueden ser, se centraron en la macrometrología, micrometrología, restauración y óptica integrada. Cabe aclarar que la presentación de esta área dividida según el estado del material activo es tradicional y se eligió pues representa, en cierta medida, el desarrollo histórico de las líneas de investigación en el tema de física del láser.

Las investigaciones en espectroscopía láser comenzaron hacia finales de la década del 60 en el Laboratorio de Espectroscopía, Óptica y Láser (LEOL) del Dto de Física de la UNLP, por un grupo numeroso de investigadores, muchos de los cuales se convertirían en los investigadores de la línea fundacional del CIOp aproximadamente una década después. Durante esa época y los primeros años del Centro, los estudios se realizaban sobre la espectroscopía de la emisión espontánea y estimulada de nitrógeno molecular (N2) y de xenón (Xe) y su relación con diversos parámetros experimentales como la presión del gas, forma del pulso de corriente, temperatura, etc. El conjunto de datos así obtenidos permitió describir la cinética de población de los niveles de energía involucrados, como base para una descripción teórica del funcionamiento de estos láseres. Es de destacar el caso del láser de Xe que, con diferentes configuraciones de excitación, aun hoy sigue brindando datos accesibles a ser interpretados por modelos de excitación.

Con la llegada del láser de Ar y del láser de colorante sintonizable comerciales hacia fines de los 70, se inaugura una nueva etapa en la línea de espectroscopía láser, en la que ya no se analiza la salida del láser, sino que se lo utiliza como herramienta para estudiar procesos fotofísicos en diversos materiales. En particular, se emprende un estudio sistemático de la fotofísica de moléculas orgánicas de la familia de las cianinas, tanto por su importancia como absorbente saturable para la generación de pulsos ultracortos como por su parecido químico con las moléculas que forman los pigmentos naturales biológicos. Para ello se utilizaron técnicas espectroscópicas de alta relación señal-ruido, como fluorescencia inducida por láser, espectroscopía fotoacústica y lente térmica. Una de las complejidades de los mecanismos de excitación de estas moléculas es la generación de una especie transiente, inducida por absorción de la radiación de bombeo (fotoisómero), que puede retroisomerizar a su especie original. Los resultados experimentales obtenidos fueron interpretados a través de un modelo de excitación y transferencia de población de los niveles de energía de ambas especies, logrando establecer la cinética del fenómeno a partir de procesos radiativos y no radiativos internos. Técnicas similares se aplicaron al estudio de polímeros dopados con colorantes orgánicos, de interés por su potencial uso como material láser sintonizable de estado sólido. En este caso, se lograron establecer los mecanismos básicos de degradación del material por absorción de la radiación de excitación.

A partir de la década del 90 se desarrolla una línea de estudio de propiedades ópticas de sólidos cristalinos dopados con iones de tierras raras o metales de transición con el fin de investigar nuevos materiales para la optoelectrónica y para el campo de láseres sintonizables de estado sólido. Con la llegada al Centro de un láser de Nd:YAG Q-switch con generadores de 2da, 3ra y 4ta armónicas y la posterior adición de un generador óptico paramétrico, se implementaron técnicas como la de bombeo y prueba, fotoacústica de pulso de ns y deflexión térmica para estudiar el rendimiento cuántico de luminiscencia, absorción de estado excitado y acoplamiento electrón fonón de red de los materiales sólidos mencionados. Los estudios se centraron básicamente en dos clases de cristales: haluros alcalinos dopados con tierras raras y niobato de litio dopado con metales de transición, este último por su excelente combinación de propiedades electro-ópticas, acusto-ópticas y no-lineales, que lo hace apto para aplicaciones en Óptica Integrada. En ambos casos, se demostró la posibilidad de determinar el rendimiento cuántico de luminiscencia y otras propiedades fotofísicas midiendo simultáneamente las señales luminiscentes y fotoacústicas para diferentes longitudes de onda.

Finalmente, debemos señalar que las características de trabajo en cualquier rama de la Óptica experimental hacen que surjan aplicaciones concretas de los resultados obtenidos. Así, se han realizado trabajos de aplicación del scattering láser a la determinación de tamaño de partículas, medición de velocidad de fluidos o de superficies en movimiento efecto Doppler láser o interferencia (velocimetría láser), ablación láser de materiales y restauración de piezas de arte o patrimoniales, generación de guías de onda en piezas ópticas (óptica integrada).

Laser Physics and Applications

Laser physics is a wide area of research encompassing basics of quantum electronics, level pumping mechanisms and material-resonant cavity studies through mode interaction. Within this framework, CIOP developed an extended research activity both in basic subjects as well as laser applications. The former include studies of the particular excitation mechanisms responsible for inversion population in pulsed ionic and molecular gas lasers, dye lasers and crystals for tunable solid state lasers. On the other hand, laser applications, as vast as it can be, were addressed through macro and micrometrology, trace analysis, art restoration and integrated optics. Note that the subsections presented here represent mainly the chronological development of the laser physics research lines at CIOp.

Gas laser physics research has been one of the pioneering areas at CIOp, which started when the researching staff still belonged to LEOL, Physics Dept UNLP, many of whom would become founders and pioneers of CIOp. During the first years, the studies aimed to the spontaneous and stimulated molecular nitrogen (N2) emission spectroscopy as well as that of ionic xenon (Xe), together with their relation to experimental parameters such as gas pressure, current pulse, temperature, etc. These data enabled an accurate modeling of their population inversion kinetics. It is worth to note that the Xe laser still yields new data to be interpreted by the proposed modeling.

The purchase of an 5 W argon (Ar) ion laser pumped tunable dye laser by late 70´s opened a new era at CIOp in laser spectroscopy, where the laser were now used as a refined tool to study photophysics of different materials. In particular, cyanine dyes were studied for their importance as saturable absorbers in passive mode-locking and also for their photochemical similarity to natural pigment molecules such as chlorophyll. One of the complexities in the population kinetics of dyes deals with the generation of a transient species induced by the pump photons (photoisomer) that can change back to the original species (backisomerization). Using high signal-to-noise ratio spectroscopies such as laser induced fluorescence, photoacoustics and thermal lensing, the experimental results were interpreted by an excitation and population-transfer model between the corresponding energy levels of original and isomeric species, which helped to establish the kinetics of the different processes. Similar techniques were applied to dye-doped polymers, in which case the basic degradation mechanisms due to optical pumping were established.

Since the beginning of the 90´s, a new line on optical properties of optoelectronic crystals was started around the newly acquired Q-switched Nd:YAG laser with harmonic generators. In particular, rare-earth doped alkali-halide crystals for tunable solid state lasers and transition-metal doped lithium niobate for Integrated Optics applications were studied using several laser spectroscopy techniques such as pump and probe, photoacoustics, excited state absorption and thermal lensing to determine luminiscence quantum yield and electron-phonon coupling.

Finally, it must be remarked that, as a natural consequence of any work in experimental optics, many real applications were derived from the results of the abovementioned studies., particle size determination using optical scattering, laser Doppler velocimetry of fluids and moving surfaces, laser trace element detection, laser ablation of materials, restoration of cultural heritage pieces and fabrication of channeled waveguides in optical active substrates are just some of the applications developed at CIOp.

Ablación, limpieza y restauración con láser

Esta área de trabajo iniciada en 1999 involucra tareas de investigación, desarrollo y servicios en el área de limpieza, restauración, análisis de superficies y caracterización de materiales, utilizando técnicas láser. En particular: limpieza por ablación láser de suciedad superficial de objetos de valor patrimonial, (papeles antiguos, manuscritos, esculturas, piezas de vidrio, metal, tela, cuero); caracterización de composición elemental de materiales por medio de Espectroscopía de Plasmas generados por Ablación Láser (LIBS); desarrollo de métodos e instrumentos para aplicaciones industriales y control de calidad de procesos basados en técnicas ópticas y espectroscópicas, fotoacústicas y de luminiscencia.

El grupo de trabajo que lleva adelante estas tareas es de carácter fuertemente interdisciplinario; es el único en el país que trabaja en temas vinculados a la suciedad superficial utilizando láseres y métodos ópticos, y es uno de los pocos en América Latina y el mundo que realiza investigación desarrollo y servicios en esta temática.

Entre los trabajos más importantes realizados hasta la fecha se pueden destacar los referidos a la medición y caracterización de composición de suciedad superficial, un problema de particular importancia en la industria y la producción. Estos comprenden por un lado la invención de un método y un instrumento para medir in situ y a tiempo real el grado de limpieza de una superficie. Estas invenciones están basadas en ideas originales y únicas a nivel mundial, ya que no existían antecedentes previos ni métodos o dispositivos similares.

Por otro lado se aplicó por primera vez la espectroscopía de plasma inducida por láser (LIBS) para caracterizar la composición de la suciedad superficial. Lo novedoso de la idea introducida en este caso es que el procedimiento empleado permite incluso identificar en forma cuantitativa los componentes de la suciedad, aun en casos en que estos se encuentran como parte constitutiva del sustrato (por ejemplo la cantidad de partículas microscópicas de hierro distribuidas en una capa de grasa o aceite que cubre la superficie de una chapa de hierro).

Otros trabajos realizados comprenden: la invención y patentamiento (Reg. 18/99 CUBA) de un método para la limpieza de vidrios con láser. (Laser cleaning of glassware by opposite incidence); la identificación de trazas de Magnesio y Estroncio y el mapeo de estos elementos en dientes de Homo Sapiens mediante la técnica LIBS, para su empleo como posible indicador alimentario y evolutivo; la determinación de composición elemental de piezas arqueológicas; la limpieza con láser de papeles y manuscritos antiguos y el desarrolló de un método que utiliza procesamiento de imágenes por computadora, para analizar la calidad de este y otros procedimientos de limpieza y la utilización de espectroscopía de plasmas inducida por láser para el control de calidad de recubrimientos superficiales.

Ablation, Cleaning and Restoration with Lasers

The activities in this field started in 1999, involving research, development and services in laser-based methods for cleaning, restoration, surface analysis and material characterization applied to cultural-valued pieces, compositional characterization of laser produced plasmas (LIBS) and development of optical/photoacoustic-based methods and instrumentation for quality contr processes in the industrial area.

Our group is strongly interdisciplinary and it is the only one of its kind in the country and one of a few in Latin America.

An outlook of the most relevant works of this group involve the development and fabrication of a method and instrument for surface dirt compositional characterization applied to the steel industry (patented and currently working in a steel plant), a method for laser glassware cleaning (patent: Laser cleaning of glassware by opposite incidence), Identification of Mg and Sr traces in Homo Sapiens teeth through LIBS technique, element composition determination of archeological pieces, laser cleaning of antique manuscripts and computerassisted image processing for surface cleaning quality control.

Cleaning and characterization of objects of cultural value by laser ablation

Gabriel M. Bilmes[*a], César Freisztav[a], Daniel Schinca[a], Alberto Orsetti[b]
[a]Centro de Investigaciones Opticas (CONICET-CIC) and Universidad Nacional de La Plata, La Plata, Argentina.
[b]Area de Conservación y Restauración, Secretaría de Cultura, Gobierno de la Ciudad de Bs.As. Buenos Aires, Argentina.

ABSTRACT

Surface ablation with nanosecond laser pulses was applied to preservation, cleaning and compositional identification of objects of cultural value. On one hand, treatments of fabrics, coins, bones, and other archeological objects are shown, as well as applications to the preservation of covers, front of books and old manuscripts made in rag paper. Damage fluence thresholds for 17 different XIXth century types of papers, made by processing textiles, were determined. On the other hand, we use the spectroscopic analysis of the plasma generated as a result of laser ablation (LIBS- laser Induced Breakdown Spectroscopy-) for the determination of the elementary composition of unique pieces in anthropology and archaeology. In particular, we show applications to the identification of trace elements in Hominide teeth, of interest concerning the analysis of eating habits. We also apply LIBS to the determination of the composition of acheological objects belonging to different pre-Columbian cultures.

Keywords: Laser ablation; Laser cleaning, LIBS, Art conservation/restoration

1. INTRODUCTION

During the last 20 years optical methods and particularly laser processing of materials and related techniques were increasingly applied to the preservation, cleaning and characterization of objects of cultural value[1-6]. The development of appropiate laser systems and new instruments, together with a better knowledge of the mechanisms involved during the interaction of laser with surfaces, boosted these methods into competitive options respect to traditional ones.

Laser action on materials is strongly dependent on the different parameters involved (i.e. pulse duration, fluence, excitation wavelength, and properties of the surface material). Laser pulses of short duration (below a few ns) and sufficient fluence (energy per unit area) can produce surface ablation.[6], characterized by material extraction, plasma formation (with light emission) and sound emission. It was previously demonstrated[7,8] that sound waves produced during ablation procesess can be used for real time measurement of surface cleanliness, avoiding most of the drawbacks of the traditional methods. The basis of this procedure relies on the fact that the intensity of the sound is proportional to the amount of dirt on the surface, and provides a direct measurement of its cleanliness[9].

Material extraction during laser ablation can be used for surface cleaning. In this case the light emitted by the laser is absorbed by the layer of surface dirt, typically darker than the substrate. In most cases surface dirt can be described as a thin film of organic substances, as oil or grease, in which a more or less homogeneous distribution of particles of different compounds is present. Most of these particles are black, giving the dirt its dark aspect.

Depending on the material, ablation is produced above certain threshold fluence. In cleaning applications the excitation fluence must be appropriate to eliminate the surface dirt without affecting the substrate. Then the excitation fluence must be enough to produce dirt ablation, but it should be below the threshold for substrate ablation. Under this conditions once the surface is cleaned, additional laser shots do not produce any effect.

* gabrielb@ciop.unlp.edu.ar. Casilla de Correo 124, (1900) TE-FAX: 55-221-4712771

Optical Methods for Arts and Archaeology, edited by Renzo Salimbeni, Luca Pezzati, Proceedings of SPIE Vol. 5857 (SPIE, Bellingham, WA, 2005) · 0277-786X/05/$15 · doi: 10.1117/12.612671

The spectral analysis of the plasma generated after laser ablation allows the possibility of determination of material composition. In the last years Laser Induced Breakdown Spectroscopy (LIBS) emerged as one of the most versatile and powerful methods for determination of elementary composition of unique pieces of cultural value[6,10,11]

In a previous work[12] we show that, modyfing the laser fluence, ablation of surface dirt or substrate material can be performed independently. This procedure can be made at real time simultaneously with laser cleaning. On the other hand, using higher fluences, characterization of substrate composition of unique pieces can be performed.

In this work we show examples of application of laser ablation with nanosecond laser pulses for preservation, cleaning and identification of the composition of objects of cultural value.

2. EXPERIMENTAL

A Q-switched Nd: YAG laser with pulse duration of ca. 7 ns (FWHM) operating at different wavelengths λ = 1064 nm, λ = 532 nm and λ= 355 was used working at repetition rates of up to 10 Hz. Excitation fluence was changed by focusing with apropiate lens and by using a neutral density wedge filter to change the energy of the laser pulse. Laser fluences (F) ranging from $0 < F < 4.5$ J/cm^2 were used. Energy was controlled by splitting part of the laser beam to a pyroelectric detector. In order to change the impinging position of the beam, the sample was mounted on a xyz controlled positioning step motor system.

For the LIBS experiments, the spectrum of the plasma was acquired focusing the light by means of a lens to a multimode fiber optic attached to a cross dispersion Echelle spectrometer (Mechelle Multichannel Instruments) with a CCD incorporated camera. Data was sent to a computer and processed with appropriate software that gives the whole spectra covering the 200 to 1100 nm region with a 0.3 nm spectral resolution. This combination enables simultaneous detection of a large spectral range in a single laser shot. To maximize the signal to background ratio we use a spatial screening procedure that allow to collect only light emitted by regions of the plasma far from the surface[12].

3. RESULTS AND DISCUSSION

3.1 Laser cleaning of objects

Figure 1 shows a fragment of fabric *(cáñamo),* of the XIX century, founded in an urban excavation of one of the older houses of the city of Buenos Aires. This fragment was buried and most of the dirt is stacked dust on grease. The traditional methods for cleaning are brushing and vacuum cleaners with suction regulators, but in cases like this one they may destroy the sample. On the contrary, laser cleaning avoids mechanical contact and undesired manipulation of the sample.

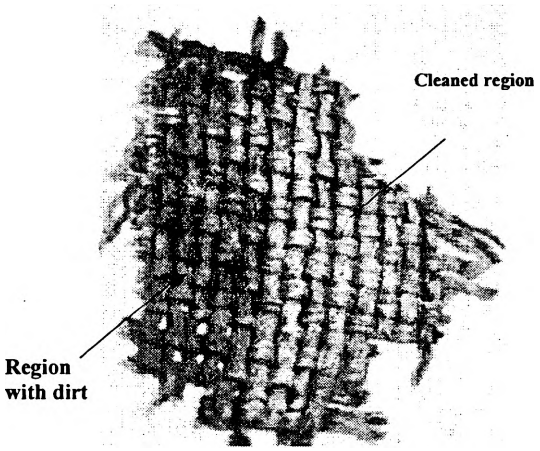


Figure 1. Laser cleaning of fabric of XIXth century.
Origin: urban archeology of the city of Buenos Aires

Figure 2 is an example of laser cleaning of bones. In this case we show the inside face of a calota belonging to a precolumbian craneous. The dirt is mainly composed by particles, grease and stacked earth. Usually the traditional cleaning method is based on neutral detergent wash under controlled humidity, or application of alcohols or other solvents that sometimes affect the material. Laser cleaning is dry, and regions with rough surfaces and weakened zones can be easily treated.

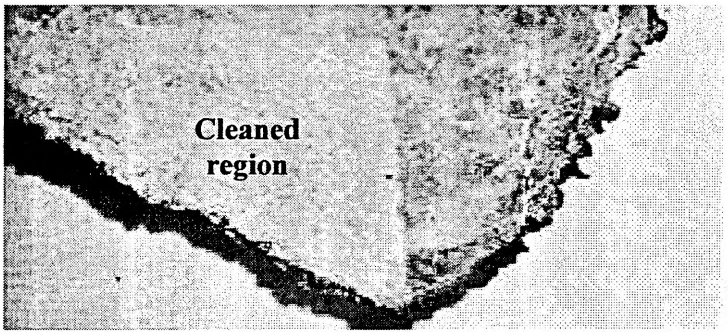


Figure 2. Laser cleaning of a calota of a Precolumbian craneous

Figure 3 shows results of laser cleaning of a coin of 1891. Surface dirt in this case is grease with black particles belonging to manipulation, and oxides. Usually the conventional cleaning is by means of electrolytic or electrochemical baths or acids and alkaline solvents. In some cases these treatments produce erosion of the material, thus altering the shape of the imprinted image.

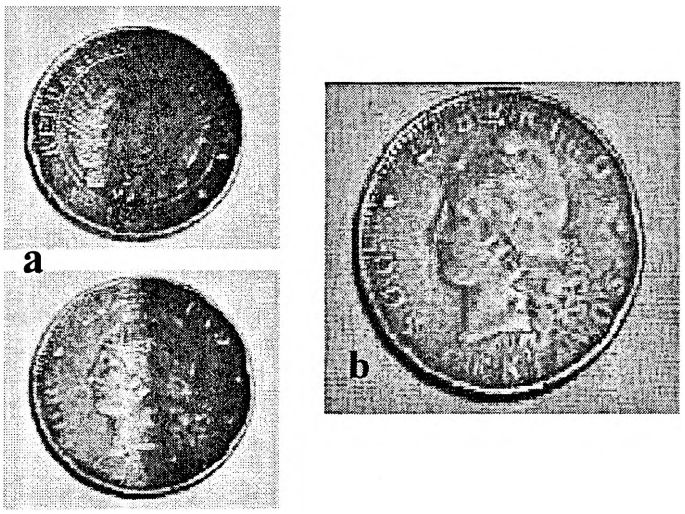


Figure 3: Laser cleaning of a coin of 1891. a) Partial treatment in each face .b) Final state

Laser cleaning of papers and parchments was previously studied showing that treatments require an appropriate knowledge of the type of dirt to be cleaned and the characteristics of the substrate[13-15].

Typical surface dirt in papers, books, and manuscripts are caused by use and manipulation, that produce a thin film of grease with particles of dust, pigments and sometimes candle soot. This is very frequent to find in covers and fronts of books. The traditional cleaning procedure is by means of dry cleaning with softy rubbers or glass fiber pencils.

Sometimes water and another solvents can be used. These cleaning procedures produce abrasion and damage of the material causing loss of its mechanical properties.

Figure 4, 5 and 6 show examples of laser cleaning of covers, front and backs of books (clear rectangles).

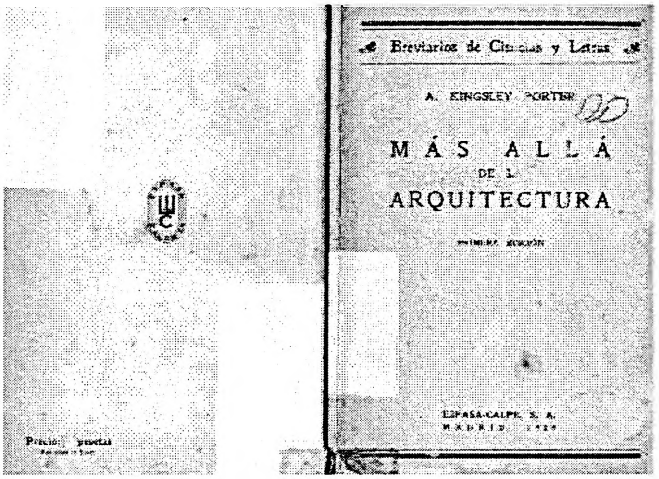


Figure 4. Laser cleaning of cover of books

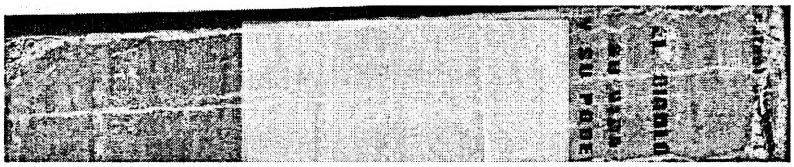


Figure 5. Laser cleaning of a back of a book

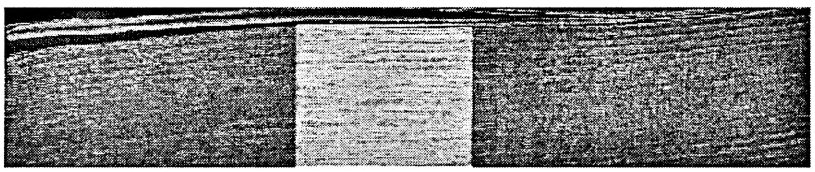


Figure 6. Laser cleaning of edge of a book

Restoration of documents and antique papers usually require cleaning of stains of grease, soot and handling dirt and sometimes ink and pencil writings that must be eliminated. In the case of manuscripts before the XXth century most of them were fabricated by processing textiles (Rag paper). For this type of papers, before laser cleaning, we study the threshold damage fluences as a function of wavelength. We selected a collection of 17 different types of papers belonging to the National General Archive of Argentina. Each sample was treated with increasing values of fluence in different regions of the paper. In each case the energy of excitation and the area was measured. Damage was controlled by microscope inspection.

Damage fluence threshold values c.a. 1, 2,2 and 2,8 J/cm^2 were found for excitation wavelengths of 355, 532, and 1064 nm respectively. Taking into account this result we found that fluences one order of magnitude lower than this values (typically 0,3 J/cm^2) are the best suited for laser cleaning of this type of papers, without any damage of the

substrate. Figure 7 shows examples of laser cleaning of XIXth century manuscripts, made on rag paper, written with ferrogalic inks and covered by a dirt film of candle soot.

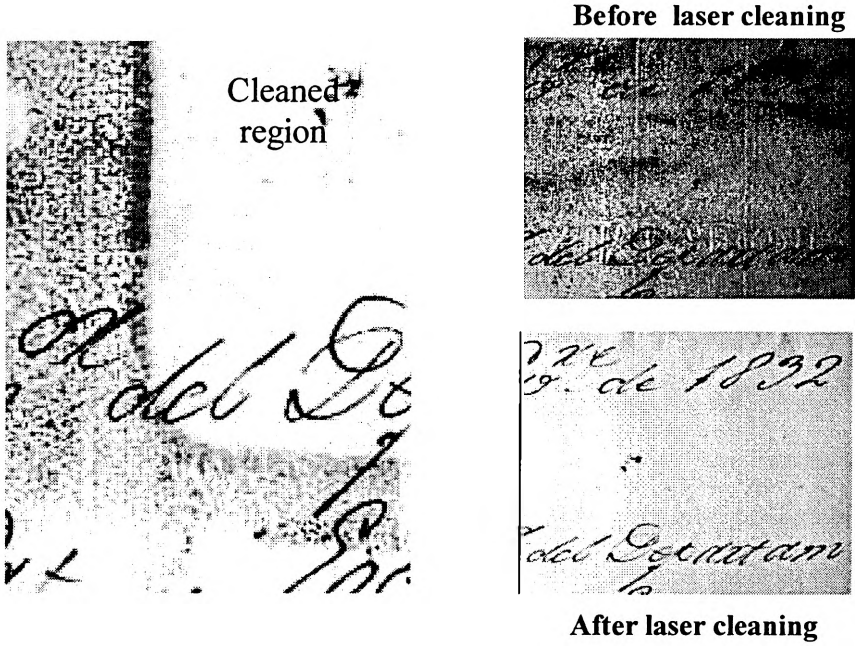


Figure 7: Laser cleaning (□=1064 nm) of a manuscript of XIXth century made in rag paper.

We performed also laser cleaning treatments on other materials like leather of seal, belonging to the Argentine zone of Antarctica and used at the beginning o the XX th century for clothing. In this case the dirt was grease and fungus. In this case laser cleaning allowed the leather to recover its original texture and shine. We also cleaned the inside of glass bottles of the XIX th century by using a method previously described[16].

3.2 Material composition determination

One of the main data retreving pieces in anthropology are teeth, which yield information about alimentary habits and community life conditions of the studied individuals. Trace elements like Mg, Sr, Ba, Cu, Sn, Va are indicative of different feeding diets. Conventional techniques for trace concentration determination imply partial or total destruction of the pieces which in most cases are unique. We show how LIBS is an option for this type of studies, taking advantage of its microdestructive nature and its oustanding posibility of in situ and real time depth profiling.

As part of an ongoing project[17] several neolithic, Middle Ages and current teeth from different geographic regions were analized using the LIBS set up already described. The presence of Ca (I y II) ;K I, Na I, Mg I y Sr (I y II) was searched for and identified in the enamel and dentine spectra. Since Ca is the main constitutive element of teeth, presence of the trace elements relative to Ca can be determined.

Figure 8 show the identification of Sr in dentine and enamel of current and Middle Ages teeth.The shown spectra are typical of a collection of several pieces in each case. As it can be seen in the dentine of the latter there is a noticeable content of Sr compared with its own enamel and dentine and enamel of current teeth, which is low for both.

For the case of the analized neolitic teeth we found that the relation Sr/Ca in dentine is almost twice that of current teeth. The fact that Sr appears in enamel may be related with dietary habits during the early period of growing.

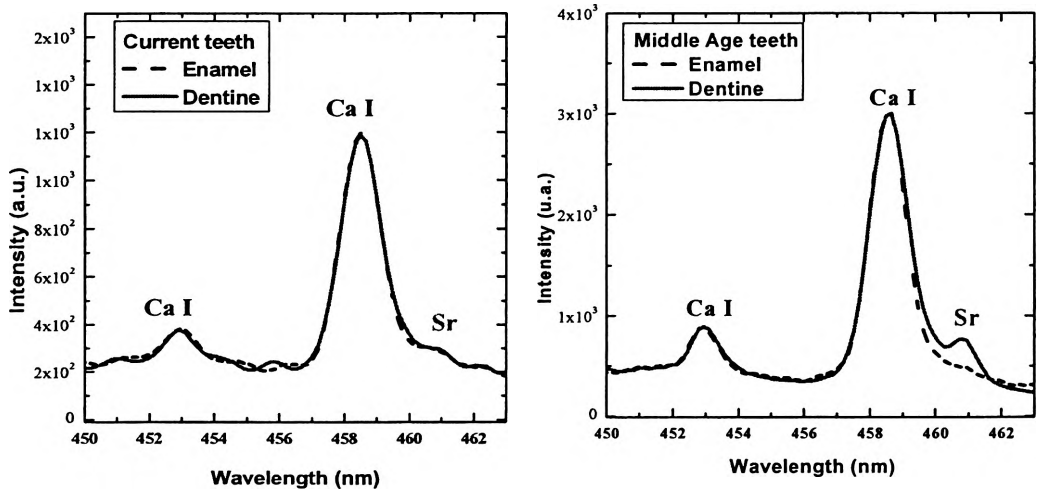


Figure 8. LIBS spectra of current and Middle Ages (south of France) teeth, showing the presence of Sr. Notice the typical Ca I line appearing in both teeth that can be used as reference.

Figure 9 illustrates the depth profiling ability of LIBS. Fig 9a is a photograph of part of an enamel neolitic tooth showing the ablation microdamage produced by increasing number of laser pulses. Figure 9b shows the LIBS spectra obtained for selected number of laser shots (1, 2, 20, 100). Since each shot ablates a layer of material, the correspondig spectrum shows the element content of in-depth zones. Notice the change in the Mg line intensity as a function of depth. This result is important since it indicates that trace elements may be found non uniformly distributed in the piece. This information is usually lost when conventional methods that need special sample preparation are used.

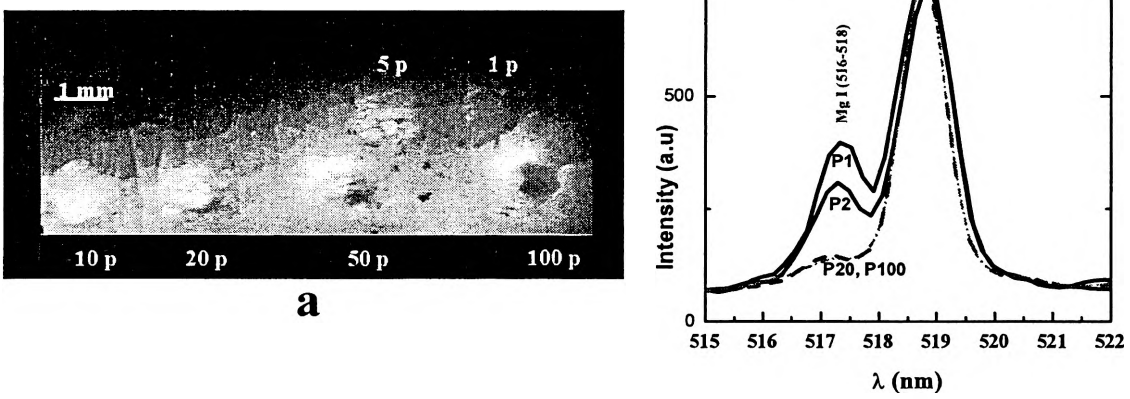


Figure 9. a) Photograph of part of an enamel neolitic tooth showing ablation microdamage as a function of the number of laser pulses (p). b) LIBS spectra corresponding to laser pulses number 1, 2, 20 and 100 impinging on the sample.

Figure 10 shows another application of LIBS, in this case to an archeological piece. The study was aimed to complement a more extensive analysis of a prehispanic bracelet of the Condorhuasi culture from the north of Argentina[18]. Concerning the delicateness of the piece, destructive analysis is prohibitive. In this case the LIBS

technique allowed us to obtain the spectra of the main components of the bracelet by impinging the laser on the edge of a fixing hole, thus making almost imperceptible the microdestruction site. Besides, the use of a cross dispersion spectrograph and the synthesis of the 200-1100 nm spectrum obtained in a single record, allows obtaining the main components with few shots thus reducing the possibility of damage.

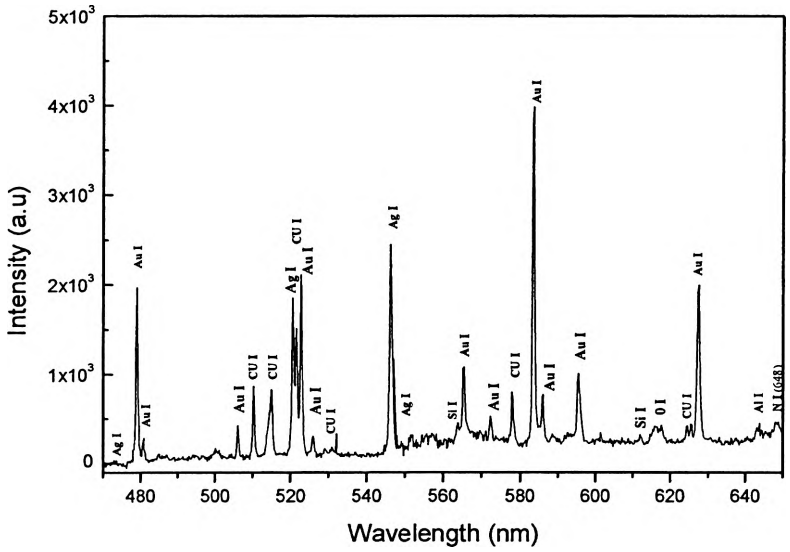


Fig 10. LIBS identification of the composition of a prehispanic bracelet of the Condorhuasi culture from the north of Argentina

REFERENCES

1- J.F. Asmus. *Interdisciplinary Science Reviews* 12, 171, 1987

2- K.G.Watkins, J.H. Lasrson, D.C.Emmony and W.M. Steen. *Proc.Nato ASI on Laser Processing: Surface treatment and film Deposition.* p.907, Kluwer Academic Publishers , 1995.

3- C.Fotakis. *Optics and Photonics news.* p.30, may 1995.

4- Journal of Cultural Heritage. Proc.LACONA III: *Lasers in the conservation of Artworks.* Vol 1. 2000. Elsevier

5- M.Cooper. *Cleaning in conservation: an Introduction.*Butterworth Heinemann, Oxford, 1998.

6- V.Zafiropulos in *Laser Cleaning* . Boris Luk"yanchuk editor. World Scientific 2002.

7- G.M.Bilmes and O.E. Martinez, *Patent AR990627,* Argentina,1999.

8- G.M.Bilmes and O.E. Martinez, *Patent 6.546.784- EEUU.*, 2003.

9- G.M.Bilmes, D.J. Orzi, O.E. Martínez, A. Lencina . *Procc. Optical Measuremets Systems for industrial inspection IV, SPIE International Symposium on Optical Metrology.* 2005

10- D.Anglos *Applied Spectroscopy*, Vol.55, 6, p186A, 2001

11- J.M.Anzano, M.A. Villoria, I.B. Gormushkin; B.W. Smith, J.D. Winefordner *Canadian Journal of Analytical Science and Spectroscopy,* 47, 5, p134, 2002

12- D.J.O.Orzi and G. M. Bilmes, *Applied Spectroscopy* **58**, pp.1475, 2004.

13- W. Kautek, S. Pentzien, P. Rudolph, J. Kruger, E. Konig. *Appl. Surface Science*, p746,1998.

14- J.Kolar, M. Strlic, S. Pentzien, W. Kautek. *Appl. Phys A* 71, 1, p87, 2000.

15- D.Muller-Hess *LACLEPA Workshop* 2000

16- M.Arronte, T. Flores, L. Ponce, G.M. Bilmes, *III LACONA,*1999 and *Patent* 22804/2002, B08B 13/12. Cuba, 2002

17- G.M.Bilmes, D. Schinca F. Ramírez Rozzi, *V Iberoamerican Meeting on Optics and VIII Latin American Meeting on Optics Lasers and their Applications* Porlamar, Isla de Margarita, Venezuela 2004.

18-G.M.Bilmes, D.C. Schinca, M. Garavaglia, G.A.M. Alvarez .*4th Iberoamerican Meeting on Optics and 7th Latin American Meeting on Optics Lasers and their Applications.* Tandil. Argentina.2001

Appl. Phys. B 82, 643–648 (2006)
DOI: 10.1007/s00340-005-2096-7

Applied Physics B
Lasers and Optics

G.M. BILMES[1,✉]
D.J.O. ORZI[1]
O.E. MARTÍNEZ[2]
A. LENCINA[3]

A real time method for surface cleanliness measurement

[1] Centro de Investigaciones Opticas (CONICET-CIC) and Universidad Nacional de La Plata, La Plata, Argentina
[2] Departamento de Física, (FCEyN-Universidad de Buenos Aires) and CONICET, Bs. As, Argentina
[3] Laboratório de Óptica Não Linear, Departamento de Física, Universidade Federal da Paraíba, João Pessoa, Brazil

Received: 13 July 2005/Revised version: 29 September 2005
Published online: 18 January 2006 • **© Springer-Verlag 2005**

ABSTRACT The measurement of surface cleanliness is a significant problem in many industrial and technological processes. Existing methods are based on laboratory procedures, that are not performed in real time, can not be automated, and usually are restricted to a small portion of the sample. In this study we describe a new method for real time measurement of the amount of surface dirt or contamination deposited on a surface. It relies on the ablation of the surface dirt film by means of a short laser pulse, and the subsequent measurement of the emitted sound. The intensity of the sound is proportional to the amount of surface dirt and provides a direct measurement of the cleanliness of the surface. We also developed a reference sample for calibration, based on a uniform distribution of dots printed on white paper. The density and the dot size can be easily modified providing a homogeneous, uniform and reproducible standard for the measurement. Based on this method, we designed, developed and patented the first industrial instrument for on-line determination of the degree of cleanliness of manufactured cold rolled steel plate bobbins.

PACS 79.20.D; 81.70.C; 42.62.

1 Introduction

The measurement of the levels of cleanliness on a surface is a problem of great importance in many industrial and technological processes and in scientific research (fiber optics, plastics, airplane and siderurgical industries, the conservation of pieces of cultural value, in material science, etc.). Usually the main problems are to define what level of cleaning of the surface is necessary for a certain quality standard and how to measure it [1]. Surface dirt deposited on an object may have different origins. It may come from handling, aging, pollution, or could be a consequence of fabrication or industrial procedures. In many cases surface dirt can be described as a dark thin film of organic substances such as oil or grease in which a more or less homogeneous distribution of particles of different compounds is present. Most of these particles are black, giving the dirt a dark aspect. In other cases like in some "clean industries" such as microelectronics, micromechanics, data storage, etc. the main dirt is usually composed of small isolated particles added to the substrate.

Laser cleaning methods have been developed over the last twenty years, including patents and a theoretical understanding of the mechanisms involved [2–7].

Existing methods for surface cleanliness determination of dirt measurements are based, in most of the cases, on laboratory procedures, outside production lines [8, 9], and in special cases they give a direct measurement [10]. Many of them rely on the quantitative analysis of the residues removed by solvent extraction (i.e. by washing) or burned from the surface, or the measurement of the transparency of an adhesive tape that has been stuck and removed from the surface to be tested (tape method) [11].

All these methods have the following drawbacks: they are not performed in real time, and are time consuming; they cannot be automated, and usually they are restricted to a small portion of the sample.

In this study a new method that overcomes all the above mentioned drawbacks is described [12]. The method allows real time measurement of the relative or absolute amount of dirt films present on different types of surfaces. It relies on the ablation of the dirt film by means of a short laser pulse and the subsequent measurement of the emitted sound. The intensity of the sound is proportional to the amount of dirt and provides a direct measurement of the cleanliness of the surface. For the case of cold rolled steel plates, in a previous work we showed that there is an excellent correlation between the acoustic measurements and the standard laboratory methods [13, 14].

Surface dirt can be found on any object, but there is no simple way to produce it in controlled conditions. Therefore, most of the laboratory methods that measure the cleanliness of a surface use an indirect calibration reference. To our knowledge, there are no references samples for calibration purposes, of controlled thickness, particle size, and homogeneity of the dirt distribution. For that reason we developed a dirt reference for calibration purposes based on a uniform distribution of dots printed on white paper. The density of points and their size can be easily modified by a simple computer program, providing a homogeneous, uniform and reproducible standard for dirt measurements.

Based on the method presented above, we designed and patented a commercial instrument named ELMES (Equipo

✉ Fax: 54 221 471 2771, E-mail: gabrielb@ciop.unlp.edu.ar

Láser para Medición de Suciedad) for industrial purposes, that can measure on-line the cleanliness of surfaces [13–16]. The first prototype of this instrument was developed for the siderurgical industry, and was used for the determination of the amount of residual dirt on steel plates after cold rolling. This information is crucial, both for the effectiveness of downstream operations such as galvanizing or painting and as a control of possible malfunctioning of prior stages of the process. This equipment was mounted at the final inspection line of the Ensenada plant of the company SIDERAR of Argentina.

2 Experimental

A schematic of the set up used is shown in Fig. 1. A Q-switched Nd: YAG laser with pulse duration of c.a. 7 ns (FWHM) operating at a wavelength of 1064 nm is directed normal to the sample surface. A neutral density wedge filter is used to change the energy of the laser pulse to produce laser fluences (energy per unit area), F, ranging from $0 < F < 4.5\ \mathrm{J/cm^2}$. For measurements as a function of the excitation area, we change the fluence by modifying the diameter of the laser beam using a focusing lens. A microphone picks up the emitted noise. The detected acoustic signal is registered on an oscilloscope and is correlated with the amount of dirt present on the sample. The pulse energy was measured using an energy meter with a pyroelectric detector, splitting the laser pulse by means of a calibrated beam splitter. Taking into account the non-homogeneous spatial energy distribution of the laser pulse and then the effective area of the laser spot, the fluence values calculated in this work have an estimated uncertainty of c.a. 30%.

The sample can be moved in order to avoid overlapping of successive laser shots. Then, the whole sample can be analyzed giving a statistical measure of the dirt distribution on the surface. It means that not only the mean value, but also its dispersion can be tested. In this way the homogeneity of the surface dirt can be evaluated. When necessary, averaging of several shots, impinging on different sites of a small region of the sample, can be made in order to further increase the signal to noise ratio and subtract background noise.

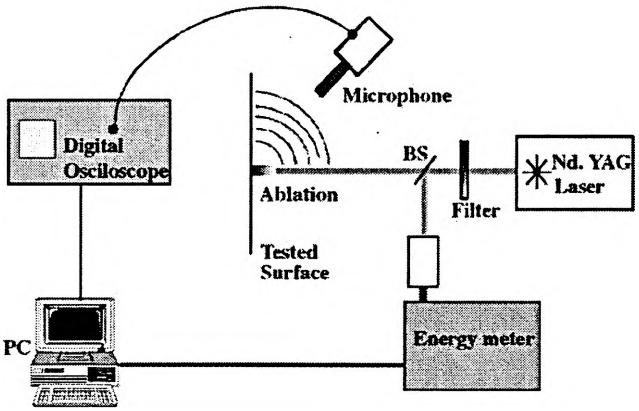


FIGURE 1 Experimental set-up used for real time cleanliness measurements

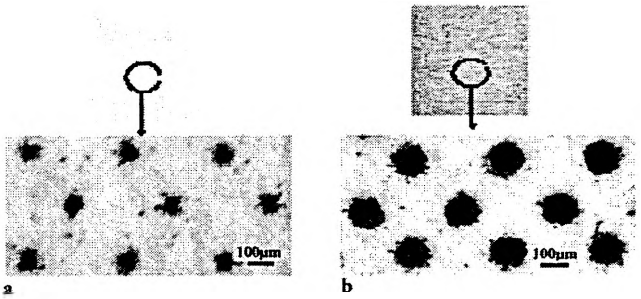


FIGURE 2 Bare eye (*upper*) aspect and microscopic detailed picture (*lower*) of the reference samples used, which are composed by uniform, homogeneous and reproducible distributions of ink points on white paper. (**a**) Point diameter $\Phi = 60 \pm 10\ \mu\mathrm{m}$. (**b**) Point diameter $\Phi = 110 \pm 10\ \mu\mathrm{m}$

Different types of surface dirt were analyzed: dirt produced by hand-manipulation of plastic surfaces; residuals generated during manufacturing of cold rolled steel plates and candle soot deposited on glass substrates.

For opaque samples, such as steel plates, conventional measurements were performed using the tape method. In this case a transparent adhesive tape is stuck to the sample and removed, containing the surface dirt. Afterwards, the tape is stuck to a white paper and the transparency is measured by reflectometry. For transparent substrates (i.e. glass) the transmission of a He-Ne cw laser beam was measured before the ablation of the dirt.

Since it is not possible to produce surface dirt with controlled thickness, size and distribution of the particles that compose the dirt, we decided to develop reference samples. These dirt references can be made easily by means of a simple computer program and a printer. They are composed of a uniform distribution of black ink dots printed on white paper. We used a standard graphic computer program (Corel 9.0) and a HP LaserJet 5100 printer that allow us to change the amount of surface points per square inch ($\mathrm{p/inch^2}$) and the size of the dots, keeping constant the thickness of the distributed ink in the paper. For the experiments presented here we used uniform, homogeneous and reproducible distributions of ink points of two different measured diameters of $\Phi = 60 \pm 10\ \mu\mathrm{m}$ and $\Phi = 110 \pm 10\ \mu\mathrm{m}$, in sets of samples with points densities of: 800 $\mathrm{p/inch^2}$, 1600 $\mathrm{p/inch^2}$, 3200 $\mathrm{p/inch^2}$, 6400 $\mathrm{p/inch^2}$ and 12 800 $\mathrm{p/inch^2}$.

Figure 2 shows a bare eye and a microscopic detailed picture of the reference samples used.

3 Results and discussion

When a laser pulse of suitable fluence and short duration (several ns) impinges on a surface, ablation of the dirt film takes place without damaging the substrate. During ablation, a layer of the dirt film is abruptly expelled from the surface, a weak light pulse is emitted, and a sound that sounds like a 'crack' is produced. When the sound is detected by means of a microphone set at a fixed distance and angle with respect to the impact zone of the plate, a typical signal can be measured as shown in Fig. 3. This figure shows results corresponding to the ablation of a plastic surface with different degrees of cleanliness. As it can be seen the intensity of the sound depends on the amount of dirt and provides a direct

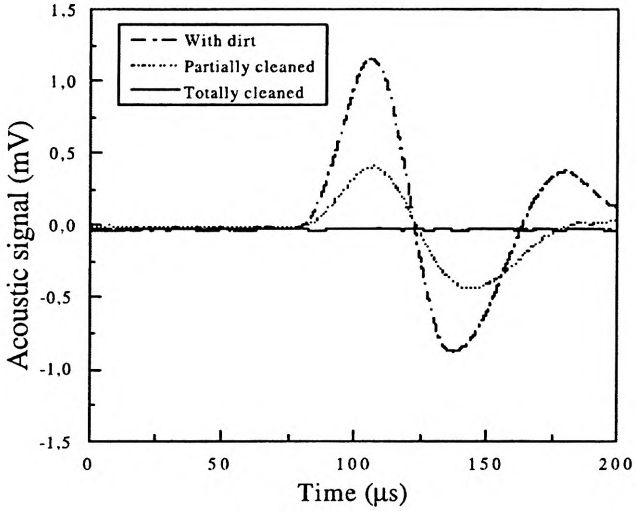


FIGURE 3 Amplitude of the acoustic signals detected by a microphone, corresponding to the ablation of dirt from a plastic surface with different degrees of cleanliness

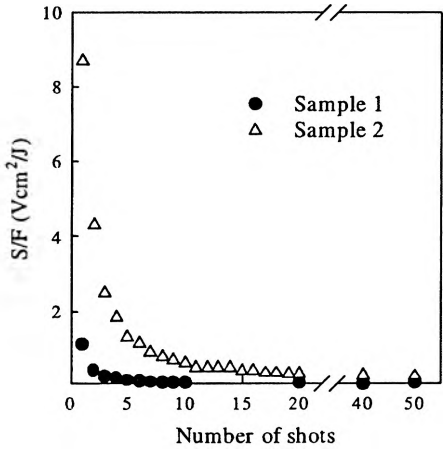


FIGURE 4 Acoustic signal S normalized in fluence F as a function of the number of shots impinging on the same point of the sample. Sample 2 is dirtier than sample 1

measurement of the cleanliness of the surface. We then used the peak-to-peak voltage of the acoustic signal detected by the microphone as a measure of the amount of dirt.

Figure 4 shows the dependence of the peak to peak value of the detected acoustic signal S divided by the laser fluence F as a function of the number of laser shots that impinges on the same point of the surface, for two different samples with different amount of dirt. Sample 2 is dirtier than the sample 1. As can be seen, dirtier samples yield larger values for S/F, and more shots are necessary to clean the surface.

In order to optimize the detection conditions, we studied the response of the microphone as a function of its angular position, performing measurements in two planes perpendicular to the surface. We found a more or less spherical distribution of the emission of sound, which follows the inverse square law. This allows high flexibility for reception designs, provided that the calibration is performed at the final set up configuration.

Taking into account this result and the need in some applications to avoid possible effects of environmental noise, we

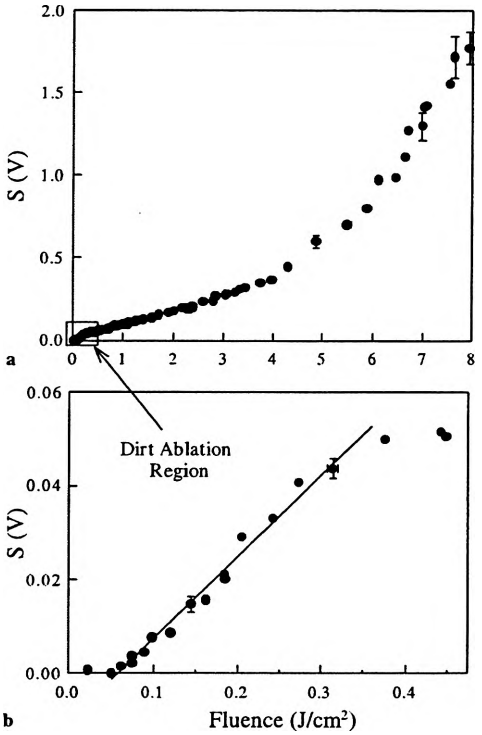


FIGURE 5 (a) peak to peak amplitude of the detected acoustic signal as a function of the laser fluence for a steel plate with dirt residuals generated during manufacturing processes. (b) Shows a detail of the low fluence part of the curve corresponding to the dirt ablation region in which there is no damage of the substrate. An error bar in some measurements corresponds to average (10) values and its uncertainty

improved the directionality of the detection, by mounting the microphone at the end of a small 5 cm long plastic tube.

3.1 *Threshold fluences for dirt ablation and substrate damage*

As is usual in any ablation process, there is a fluence threshold below which there is neither ablation of the dirt nor a detectable acoustic signal. Above this threshold value, ablation of the dirt film occurs and acoustic signals are emitted. For larger values of the fluence, ablation of the substrate can also take place. For a correct measurement of the amount of dirt any influence of the substrate has to be avoided. For that purpose, the laser fluence must be sufficient to produce the ablation of the dirt, but it should be below the threshold for ablation and damage of the substrate.

Figure 5a shows the typical dependence of the detected acoustic signal S as a function of the laser fluence for a dirty surface and Fig. 5b is a detail of the low fluences region. As can be seen, below 0.05 J/cm^2 there is no acoustic signal. Between 0.05 and 0.3 J/cm^2 the acoustic signal grows linearly with the laser fluence and above 0.3 J/cm^2 a plateau is reached. At even higher fluences a new linear region appears between c.a. 1 and 4 J/cm^2. On increasing the fluence a new slope change appears and above 5 J/cm^2 a new linear region is obtained.

Figure 6 shows the dependence of the detected acoustic signal as a function of the number of laser shots. Each curve

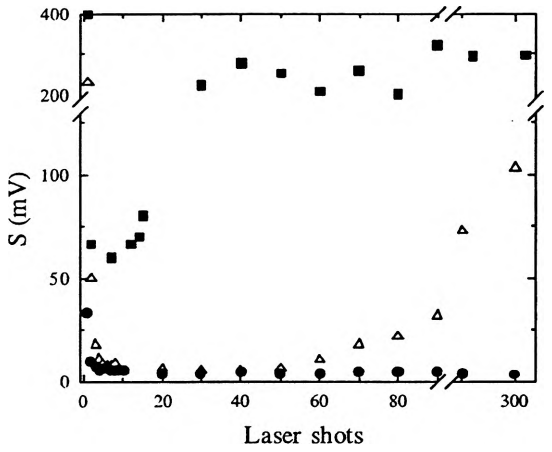


FIGURE 6 Peak to Peak detected acoustic signal as a function of the number of laser shots that impinges on the same point of the sample. (•) $F = 0.2\,J/cm^2$; (Δ) $F = 3\,J/cm^2$; (■) $F = 7\,J/cm^2$ (values are divided by 3 to fit the plot). Sample: steel plate with dirt residuals generated during manufacturing process

corresponds to laser shots of the same fluence, impinging in a fixed area of the sample. It can be seen that for a fluence of $0.2\,J/cm^2$, after a certain number of laser shots no acoustic signal can be detected. At $3\,J/cm^2$ the acoustic signal corresponding to the first shot is higher than that for $0.2\,J/cm^2$ and after that, the acoustic signal decreases from shot to shot but, instead of disappearing, after ca. 50 shots it increases. At fluences of $7\,J/cm^2$, a higher intensity of the acoustic signal is observed for the first shot, and after that, S tends to rapidly reach a constant value.

The behavior shown in Figs. 5 and 6 was found for the different types of dirt samples and substrates studied in this work. It is as expected for an ablation processes and is in very good correlation with time-integrated light intensity plasma emission measurements [17]. We can interpret these results as follows: at lower fluences no surface ablation takes place. Above a threshold value (typically $0.15\,J/cm^2$) dirt ablation takes place. Between this threshold and certain fluence values that depend strongly on the substrate, the acoustic signal S grows linearly as a function of the laser fluence (Fig. 5b). Also, in this region the behaviour of S as a function of the number of laser shots impinging on a fixed area of the sample shows that after a certain number of shots no acoustic signal can be detected (Fig. 6 filled circles). In this fluence region microscopic inspection of the substrate after laser action shows no damage or visible surface modification. This corresponds to what we call the dirt ablation region.

However, for fluence values above the linear region, microscopic inspection of the substrate clearly shows damage produced by ablation. In these cases the laser pulse not only ablates the dirt, but parts of its energy also interacts with the substrate. We can conclude that substrate ablation occurs at higher laser fluences and can be distinguish by abrupt changes in the ratio between the sound intensity and the laser energy (Fig. 5a). These are the cases shown in Fig. 6 (open squares and triangles) for which, after the first shot, each new shot not only removes the dirt but also modifies the substrate.

We also studied the dependence of the acoustic signal, as a function of the excitation area (A) in the dirt ablation region. For that we keep the values of the fluence constant and change the diameter of the beam and the energy of the laser. In these cases linear relationships were found between S and A.

We can conclude that acoustic detection can be used for monitoring the ablation processes real time. Typical ablation curves obtained in this way show fluence thresholds for surface dirt ablation of the order of $0.1\,J/cm^2$, and substrates ablation thresholds of at least one order of magnitude greater than this value. Then, typical fluences between $0.1\,J/cm^2 < F < 0.5\,J/cm^2$ are best suited for the acoustic measurement of surfaces cleanliness. In this fluence region each shot of the laser ablates part of the surface dirt, and completely cleans the surface after a certain number of laser shots, as can be seen in Fig. 6.

3.2 *Comparison between acoustic and standard laboratory measurements*

In order to evaluate the possibilities and advantages of the new method developed in this study we compare measurements of surface cleanliness of different samples, performed by standard techniques relative to the above described acoustic ones. The standard laboratory procedure for that purpose is transmission measurements. For transparent substrates these can be made directly. In the case of opaque substrates the tape method is used.

Figure 7 shows the correlation between the acoustic measurement and the tape method for a cold rolled steel sample with dirt residuals generated during manufacturing processes. The dispersion can be attributed to the inherent uncertainties of the tape test.

Figure 8 shows the correlation for the case of candle soot deposited on glass substrates.

As can be seen in both cases linear relationships were obtained between the sound intensity and the absorbed energy. The reason that the straight lines don't pass through the origin is due to the fact that transmission measurements are sensitive, not only to absorption but also to scattering produced by the wax film that acts as a host for the soot.

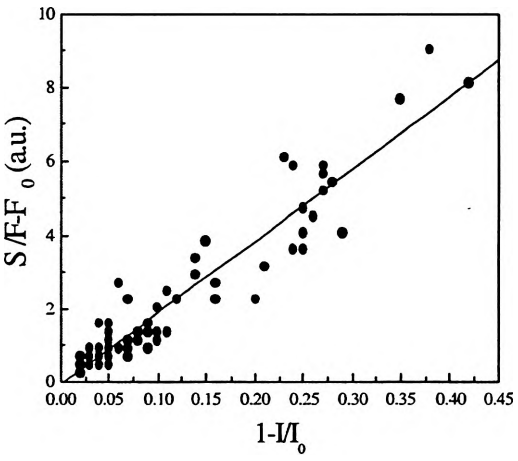


FIGURE 7 Correlation between Tape method and acoustic method. I/I_0 is the reflectivity of the tape over a white paper

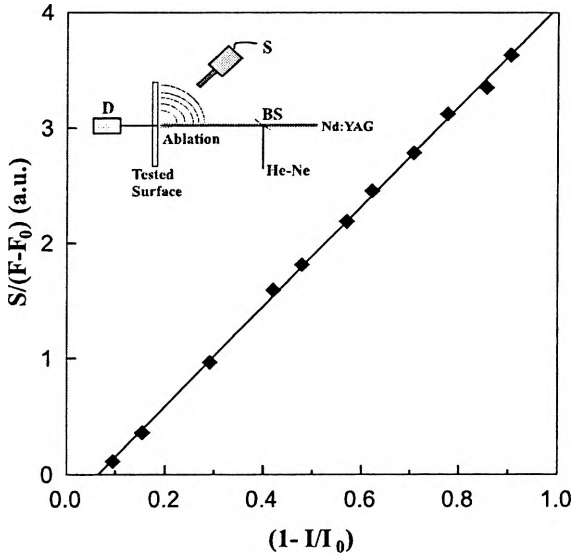


FIGURE 8 correlation between transmission measurements performed with a He–Ne CW laser and acoustic measurements for a sample of candle soot deposited on a glass substrate. *Insert* describes the experimental set-up used for the measurements. D: photodetector; S: microphone and BS: beam splitter

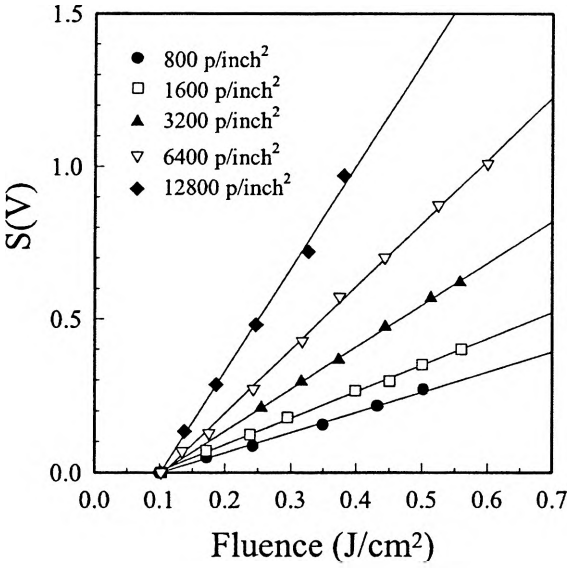


FIGURE 9 Peak to peak amplitude of the acoustic signal S as a function of the laser fluence F for five reference samples made by printing a homogeneous distribution of points of different points density on white paper. Point diameter $\Phi = 60 \pm 10$ μm. Threshold fluence $F_0 = 0.08$ J/cm^2

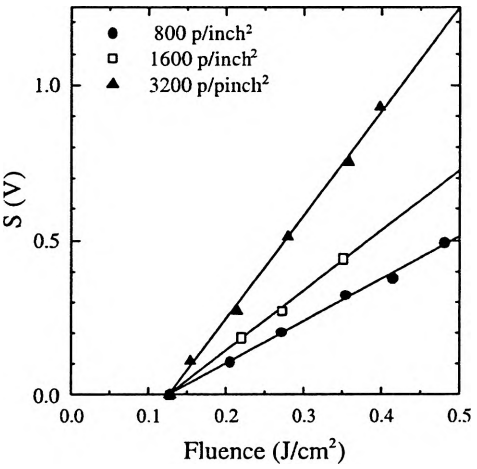


FIGURE 10 Peak to peak amplitude of the acoustic signal S as a function of the laser fluence F for four reference samples made by printing a homogeneous distribution of points of different point density on white paper. Point diameter $\Phi = 110 \pm 10$ μm. Threshold fluence $F_0 = 0.13$ J/cm^2

This result can be described by the following simple expression:

$$S = K(F - F_0)(1 - I/I_0). \quad (1)$$

Where S is the peak to peak amplitude of the acoustic signal; K is a constant that depends on the nature of the dirt film and the detector geometry and sensitivity; F is the fluence; F_0 is the threshold fluence for dirt ablation; I the light transmitted intensity by the tape or the substrate plus dirt, and I_0, the light transmitted intensity of the tape or the substrate without dirt.

The transmission coefficient I/I_0 contains the information on the particle concentration through the Beer's law:

$$I/I_0 = e^{-\sigma \mathrm{Nd}} = e^{-\sigma \eta_s}, \quad (2)$$

where σ is the average particle cross section, N the particle concentration, d the thickness and η_s the particle surface density

3.3 *Characterization of dirt reference samples*

Figures 9 and 10 shows the dependence of the peak to peak amplitude of the acoustic signal S as a function of the laser fluence for references samples made by printing a homogeneous distribution of dots (Point diameter $\Phi = 60$ μm and $\Phi = 110$ μm) of different point density on white paper, as previously described. A linear relationship S vs. F was observed for all the samples. Threshold fluences $F_0 = 0.08$ J/cm^2 for $\Phi = 60$ μm and $F_0 = 0.13$ J/cm^2 for $\Phi = 110$ μm were determined. Due to limitations in the printing procedure for each point diameter there is a limit to the dot densities that can be used. Above this limit, partial overlapping of points can be produced, and no linear relationship S vs. F is obtained. For the case of $\Phi = 60$ μm dot diameters, limit point densities of 12 800 p/inch^2 were obtained. For dot diameters of 110 μm, the limit point densities for linear behavior were 3200 p/inch^2.

For this case (1) and (2) can be used assuming $\sigma = A$ (the dots are opaque), where A is the point surface. Figure 11 shows the dependence of $S/(F - F_0)$, obtained from the slopes of Figs. 9 and 10, as a function of the point coverage (ie. "dirt absorption") $1 - e^{-\sigma \eta_s}$.

As can be seen from Fig. 11, a linear relationship between the fluence normalized acoustic signal and the dirt absorption was found. The interception at the origin of the corresponding straight line can be interpreted as a constant background signal (S_0). The origin of this signal can be explained by the fact that the paper that acts as a substrate for the printed dots is not completely "clean". Small points produced by the splash of the ink are randomly distributed on the white paper, and dur-

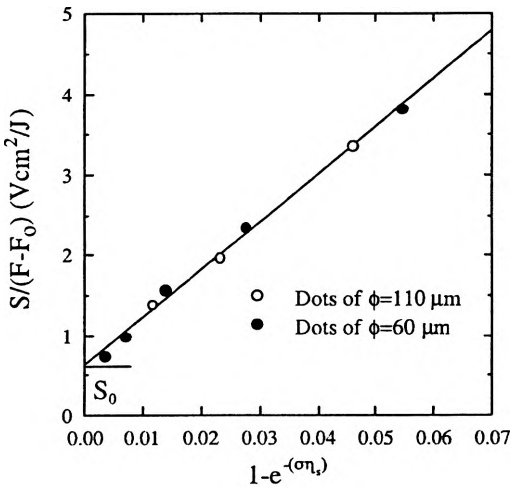


FIGURE 11 Normalized acoustic signal obtained from the slopes of Figs. 9 and 10 as a function of the point coverage

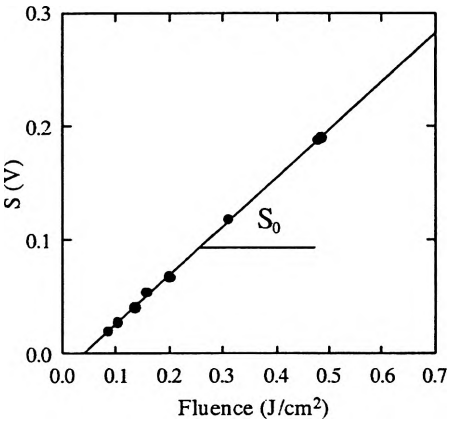


FIGURE 12 Acoustic signal S_0 vs. fluence F of a non-printed region of the dirt reference (white paper printed with dots). The slope represents the background signal, and corresponds to the ordinate interception value of Fig. 11

ing ablation it causes a contribution to the signal produced by the printed distribution of points.

Figure 12 shows the determination of this contribution S_0, performed by measuring the peak to peak amplitude of S as a function of F in a region of the substrate paper without printed dots. As can be seen, the slope of the linear relationship found for S vs. F (0.45 Vcm^2/J) agrees with the ordinate value of Fig. 11. Then, S_0 must be subtracted from S each time that the reference sample is used.

4 Conclusions

We developed a new method for real time measurement of the degree of cleanliness or the amount of dirt of any surface. The method is based on the detection of the peak-to-peak amplitude of the acoustic signal generated after laser ablation of dirt. It overcomes the most important drawbacks of standard techniques improving quality and reliability, allowing quality control and the possibility of immediate correction of processing parameters that give rise to inadequate cleanliness of the tested material. Measurements can be performed in real time and automatically, avoiding uncertainties arising from manual and laboratory operation, required in standard methods. Due to the speed of the technique, multiple measurements allow the determination not only of the average dirt content but also its standard deviation in one or different regions of the surface sample. A distribution map of the main dirt can then be obtained.

We also presented a standard reference of dirt that uses printed dots on white paper, of known size and density. This reference can be used for calibration purposes and to study, in a controlled way, the physical bases of the method.

Finally, an analytical expression was found for the acoustic signal generated after laser ablation, as a function of the laser fluence and the surface dirt parameters.

REFERENCES

1 T. Berdinskikh, H. Tkalec, Photonics Spectra, **38**, 66 (2004)
2 E.Y. Assendel'ft, V.I. Beklemyshev, I.I. Makhonin, N.Y. Petrov, A.M. Prokhorov, V.I. Pustovoy, Sov. Tech. Phys. Lett. **14**(6), 444 (1988)
3 A.C. Tam, W.P. Leung, W. Zapka, W. Ziemlich, J. Appl. Phys. **71**, 3515 (1992)
4 Y.F. Lu, W.D. Song, B.W. Ang, D.S.H. Chan, T.S. Low, Appl. Phys. A **65**, 9 (1997)
5 V. Zafiropulos, C. Fotakis, Lasers in the conservation of painted artworks, Chap.6 In: *Laser in Conservation: an introduction*, ed. by M. Cooper (Butterworth Heineman, Oxford 1998)
6 Y.W. Zheng, B.S. Luk'yanchuk, Y.F. Lu, W.D. Song, Z.H. May, J. Appl. Phys. **90**, 2135 (2001)
7 B. Luk'yanchuk (Ed.), Laser Cleaning and references therein. In: *Optical Physics, Applied Physics and Material Science* (World Scientific 2002)
8 Ford Specification, "Determination of carbon contamination on cold-rolled steel sheets", N° ESB-M2P117-A. The Sumitomo Search **30** (1985)
9 European Commission EUR 18634. Rolling oil distillation and thermocracking reactions in HNX and 100% H_2 annealing, technical steel research series, (1996)
10 Method for determining the surface cleanliness with infrared spectroscopy. Patent application. International Appl. Number: WO2004/061438. Boeing Company, US, (2004)
11 Pressure-sensitive tape method. ISO 8502-3/92. International Organization for Standarization. www.iso.org (1992)
12 G.M. Bilmes, O.E. Martínez, método para la determinaciónde suciedad en superficies. Patent AR990627, Argentina (1999)
13 O.E. Martinez, G.M. Bilmes, D.J.O. Orzi, P. Seré, R. Musso, A. Pignotti, Surf. Eng. **18**, 67 (2002)
14 G.M. Bilmes, O.E. Martínez, P. Seré, R. Musso, D.J.O. Orzi,A. Pignotti, Lat. Amer. Appl. Res. **32**, 263 (2002)
15 G.M. Bilmes, O.E. Martínez, Equipo láser para la medición de suciedad en chapas de acero. Patent P00010124, Argentina (2000)
16 G.M. Bilmes, O.E. Martínez, Laser Apparatus for measuring dirt density on steel plates. Patent 6.546.784-EEUU (2003)
17 D.J.O. Orzi, G.M. Bilmes, Appl. Spec. **58**, 1475 (2004)

Espectroscopía atómica y aplicaciones

Espectroscopía atómica

Contaminantes Atmosféricos

Fotofísica de Moléculas en Solución y Sistemas de Interés Biológico

Esta área de trabajo se lleva a cabo en el CIOp desde mediados de los años 80 y esta referida fundamentalmente al desarrollo e implementación de métodos fotoacústicos y de luminiscencia y su aplicación al estudio de moléculas orgánicas. Desde el año 99 se le ha impreso un fuerte enfoque dirigido al estudio de sistemas de interés en fotobiología.

Además de los trabajos y publicaciones específicas realizados en este campo, el grupo que desarrolla estas temáticas se ha transformado en un referente a escala nacional e internacional en la aplicación de técnicas fotoacústicas y particularmente en el desarrollo de instrumentación fotoacústica. A nivel nacional por ejemplo para grupos de fotoquímica y fotobiología que funcionan en la Facultad de Ciencias Exactas y en la Facultad de Agronomía de la Universidad de Buenos Aires; en la Universidad Nacional de La Plata; en la Universidad Nacional de Córdoba y en la Universidad de Santiago del Estero. A nivel latinoamericano e internacional por haber transferido nuestra experiencia y el equipamiento desarrollado, a grupos de investigación que funcionan por ejemplo en la Universidad Nacional Autónoma de México (UNAM), México; en la Universidad de Santander, Bucaramanga, Colombia; en la Facultad de Ciencias Químicas y Farmacéuticas de la Universidad de Chile y en la Universidad de Angers, Francia. El reconocimiento alcanzado se expresa tanto en las colaboraciones y proyectos conjuntos, como en la contribución realizada al equipamiento de estos grupos (provisión de detectores, amplificadores etc., desarrollados en el CIOp)

Photophysics of molecules in solution and biologic systems

This area of research started at CIOp around mid 80´s and is devoted to the development of photoacoustic and luminescence methods applied to organic molecules studies. Since 1999, it is strongly aimed to the study of photobiologic systems. Besides the specific publication made in the field, our group has grown to be a reference group for the application of photoacoustic techniques and particularly as a developer of photoacoustic instrumentation. This is recognized in collaborations with other research groups working at Facultad de Ciencias Exactas, Universidad Nacional de Buenos Aires, Universidad Nacional de La Plata, Universidad Nacional de Córdoba y Universidad Nacional de Santiago del Estero.

Also, at latinamerican ando verseas levels, where our experience and technology in detectors and amplifiers has been transferred to groups at Universidad Nacional Autónoma de México, Universidad de Santander, Colombia, Universidad de Chile and Universidad de Angers, France.

Conclusion

DBPI is more readily reduced than its parent, perylene, due to the electron-accepting nature of the carboximide substituents in DBPI. The three electron-transfer products of DBPI examined in this paper, $DBPI^{\cdot+}$, $DBPI^{\cdot-}$, and $DBPI^{2-}$, have intense absorption bands in the visible or near-infrared region that make them easy to identify spectroscopically. Practical applications of DBPI or analogous dyes as photosensitizers may be limited to singlet excited-state reactions because of the expected low reactivities of their triplet excited states.

Acknowledgment. The work described herein was supported by the Office of Basic Energy Sciences of the Department of Energy. This is Document No. NDRL-3175 from the Notre Dame Radiation Laboratory.

Photophysical Processes of Polymethine Dyes. An Absorption, Emission, and Optoacoustic Study on 3,3'-Diethylthiadicarbocyanine Iodide

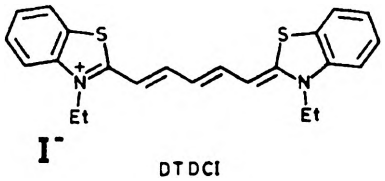
Gabriel M. Bilmes,† Jorge O. Tocho,*,‡ and Silvia E. Braslavsky*,†

Max-Planck-Institut für Strahlenchemie, Stiftstrasse 34-36, D-4330 Mülheim a.d. Ruhr, FRG, and Centro de Investigaciones Opticas (CIOp), CIC, Casilla de Correo 124, 1900 La Plata, Argentina
(Received: February 15, 1989)

Laser flash photolysis, laser-induced optoacoustic spectroscopy (LIOAS), and fluorescence data were used for the study of the photophysical deactivation processes of excited 3,3'-diethylthiadicarbocyanine iodide (DTDCI). Direct excitation of this molecule in air-saturated methanol solutions at room temperature results in the formation of only one transient species, a photoisomer, the spectrum of which was derived for the 600–680-nm spectral range. The energy content difference between the ground state of the stable form and that of the photoisomer was evaluated, $\Delta E = 0.15 \pm 0.15$ eV, as well as limit values for the photoisomer fluorescence quantum efficiency ($\Phi_f^P < 0.2$) and for the quantum yield for the back-photoisomerization from the first excited singlet state of the photoisomer to the ground state of the stable form ($\Phi_{PN} \leq 0.14$).

Introduction

3,3'-Diethylthiadicarbocyanine iodide (DTDCI) is known as a laser dye for pulsed operation in the region 700–760 nm and as a saturable absorber for mode-locking, when used with cresyl violet and rhodamine 101 lasers.[1,2]



DTDCI

Similar to the case of other cyanine dyes, evidences for a reversible photoisomerization process, produced by irradiation with high fluences, have been reported.[3-6] The lasing and saturable absorption properties of DTDCI are probably closely related to the absorption and emission spectra of the photoisomer (P).

The photoisomerization processes and the general photophysical properties of DTDCI are not sufficiently well-known; e.g., the possibility of the existence of more than one transient species has been postulated.[4]

Conventional and laser flash photolysis experiments have been carried out by various groups. Dempster et al.[3] reported the existence, in ethanol solutions, of a photoproduct, P, and calculated possible limits for its absorption coefficient. Kalittevskaya and Razumova[4] reported that the transient changes in transmission were different for excitation with UV light at 347 nm than for excitation with red light (690 mm). As a consequence, they proposed the existence of two isomers, one (P) generated from the first excited state of the stable form (N) and a second one (M) generated from the first excited state of P. The absorption spectrum calculated for P in this work was quite different from the limits calculated by Dempster et al.[3] Fluorescence studies in different solvents including methanol, performed by exciting with UV light, did not need the postulation of a second photoisomer.[7] Thus, the accepted photoisomerization mechanism through a twisted state, similar to that proposed by Rullière for the photoisomerization of DODCI,[8] was postulated.[7] In addition, there are various values in the literature for the quantum yield of photoisomerization, Φ_{NP}, from 0.015 to 0.5.[3,4,6]

Laser flash photolysis, laser-induced optoacoustic spectroscopy (LIOAS), and fluorescence measurements were used in this work to study the deactivation processes taking place upon excitation of DTDCI in methanol. By means of a simple numerical model to analyze the kinetic processes, the absorption spectrum of P is determined and values for the deactivation parameters of the photoexcited isomer are calculated.

Experimental Section

The experiments were made in methanol–aerated solutions at room temperature. In order to minimize dimerization effects, excitation was always performed with dilute ($\leq 10^{-6}$ M) samples. Methanol was chosen among the alcohols due to the higher stability of the dye in this solvent. The absorption properties of DTDCI in methanol are essentially the same as in other types of organic solvents.

DTDCI was used as supplied by Eastman Kodak. Methanol (Merck) was used as purchased. Absorption spectra were measured with a Cary Model 14 and a Perkin-Elmer Model 356 spectrophotometers. Corrected fluorescence spectra were taken

† Max-Planck-Institut für Strahlenchemie.
‡ Centro de Investigaciones Opticas.

(1) Arthurs, E. G.; Bradley, D. J.; Roddie, A. G. *Appl. Phys. Lett.* **1972**, *20*, 125.
(2) Negran, T. J.; Glass, A. M. *Appl. Opt.* **1978**, *17*, 2812.
(3) Dempster, D. N.; Morrow, T.; Rankin, R.; Thompson, G. F. *J. Chem. Soc., Faraday Trans. 2* **1972**, *68*, 1479.
(4) Kaliteevskaya, E. N.; Razumova, T. K. *Opt. Spectrosc.* (*Engl. Transl.*) **1977**, *43*, 398.
(5) Enikhen, F.; Berezovin, D. N. *J. Appl. Spectrosc.* (*Engl. Transl.*) **1985**, *43*, 865.
(6) Chibisov, A. K. *J. Photochem.* **1976/77**, *6*, 199.
(7) Kasatani, K.; Kawasaki, M.; Sato, H. *Chem. Phys.* **1984**, *83*, 461.
(8) Rullière, C. *Chem. Phys. Lett.* **1976**, *43*, 303.

0022-3654/89/2093-6696$01.50/0 © 1989 American Chemical Society

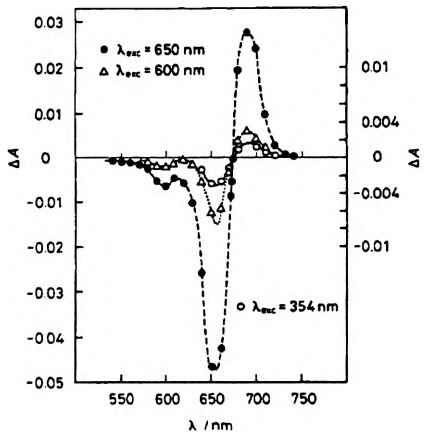


Figure 1. Absorption changes, ΔA, immediately (15 ns) after the excitation of an aerated 10^{-6} M DTDCI/MeOH solution at different excitation wavelengths. The scale on the left corresponds to λ_1 = 650 nm and 600 nm. The scale on the right corresponds to λ_1 = 354 nm.

at 20 °C with a Spex Fluorolog spectrofluorimeter. Rhodamine 101 (Φ_f = 1.0[9]) and cresyl violet (Φ_f = 0.54[10]) were used as references. The solutions of sample and references had matched absorbances at the respective excitation wavelengths. The two references lead to the same fluorescence quantum yield for DTDCI in methanol, $\Phi_f = 0.36 \pm 0.05$, in agreement with the literature data.[11] No corrections for the refractive index difference between methanol and the solvent used for the reference (ethanol) was made.

The nanosecond flash photolysis equipment with optical detection was already described.[12] It consists of a Nd:YAG laser (15-ns pulse duration) either in its third harmonic at 354 nm or when pumping dye lasers (R6G and DCM, Lambda Physik), in its second harmonic at 532.5 nm. The transient absorbance changes were monitored at 90° with respect to the excitation for periods of 1 ms with the pulsed beam of a 150-W Xe arc lamp. The laser energies employed were on the order of 3 mJ for all the measurements. Signal acquisition was performed with a computer-controlled Biomation Model 4500 transient recorder. Signal averaging and handling was performed with an LSI 23/VAX 780 computer system.

The experimental setup for LIOAS was the same as used in ref 13. The excitation source was a flash-lamp-pumped dye laser (Chromatix Model CMX-4). Rhodamine 6G (Exciton) in methanol/water was used for the range 580–620 nm and rhodamine 640 for the region 630–690 nm. The laser beam (1-μs pulse duration, maximum energy 1 mJ, repetition rate 2 Hz), after focusing and passing through a diaphragm, had a diameter of 1 mm ($1/e$ of the maximum intensity) in the sample cuvette. The resolution time of the whole system was 1 μs.[13] In these experiments, $CuCl_2$ in methanol was used as a calorimetric reference. Absorbances of DTDCI and those of the reference were matched to ±0.005 AU.

Results

Flash Photolysis. The transient absorption changes, ΔA, determined after excitation at 354, 600, and 650 nm are shown in Figure 1. The main characteristics observed immediately after the pulse are a difference absorbance minimum at 655 nm, a maximum at 690 nm, an isosbestic point at 675 nm, and a small absorbance decrease in the range 600–630 nm.

The general features of the differential spectra are similar to those reported previously[3,4] for excitation in the orange-red region

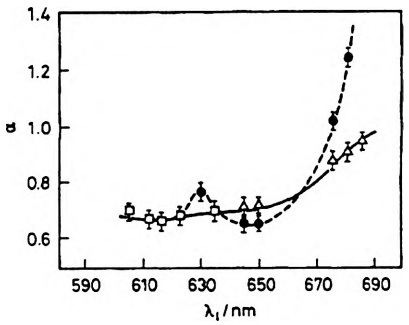


Figure 2. Action spectrum of prompt heat dissipation (α) from photoexcited DTDCI at λ_1 = 605, 612, 617, 625, 630, 645, 650, 675, 680, and 685 nm. Key: excitation energy, (△) 10 μJ and (●) 100 μJ; □, isooptoacoustic points. The fit with the mathematical model gives the full and dashed lines for low and relatively higher energies for the values Φ_{NP} = 0.5, Φ_{PN} = 0.14, and ΔE = 0.15 eV.

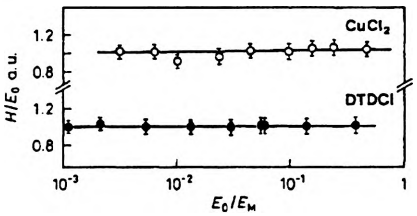


Figure 3. Energy dependence of the normalized heat emission H/E_0 for an isooptoacoustic point for solutions DTDCI/MeOH and $CuCl_2$/MeOH at the same absorbance (A = 0.12) at λ_1 = 610 nm. Maximum laser pulse energy, E_M = 150 μJ.

but different for excitation in the UV region. We found an isosbestic point at λ = 675 nm, independent of the excitation wavelength in contrast to the reports by Kalittevskaya and Razumova.[4] The first-order plot of the decay of the absorption was identical for various detection wavelengths and yielded a rate constant $k = (3.9 \pm 0.7) \times 10^3$ s^{-1}. This value is similar to that obtained by Dempster et al., using laser flash photolysis (k = 4.1 $\times 10^3$ s^{-1}),[3] and somewhat higher than that obtained by Kalittevskaya and Razumova after excitation with red light (k = 2.77 $\times 10^3$ s^{-1}).[4]

LIOAS. As it is usual in these types of experiments,[13,14] the maximum of the amplitude of the first acoustic signal generated after the absorption of the laser pulse was measured for sample (H_{DTDCI}) and reference (H_{CuCl_2}) under the same experimental conditions. The prompt heat, dissipated during the time window of the experiment (1 μs), for different wavelengths and energies of excitation is calculated as $\alpha(\lambda) = H_{DTDCT}/H_{CuCl_2}$. The ratio α was determined for the region 605–680 nm (Figure 2). For each wavelength, the initial absorbances of the sample and reference were matched. Figure 2 shows the dependence of α with the excitation wavelength for two values of constant excitation energies (E_M = 100 and 10 μJ).

The results of Figure 2 can be discussed taking into account the expected signal vs wavelength dependence for a system without an energy-storing species. In such a case, the heat dissipated promptly would have a constant value, independent of excitation wavelength and energy. In our case, as the excitation energy is increased, there is less heat emitted for the region 635–665 nm, while, on the contrary, above 665 nm there is more heat released to the medium than expected. In the region 605–625 nm and at λ = 635 nm, $\alpha = 0.67 \pm 0.05$ was obtained independently of the excitation wavelength and energy. In addition, for this region, the amplitude H_{DTDCI} of the acoustic signal was measured as a function of the energy of the exciting pulse (E_0) in a range of 3 orders of magnitude. The energy-normalized heat emission (H/E_0) for the sample and reference plotted as a function of E_0

(9) Karstens, T.; Kobs, K. *J. Phys. Chem.* **1980**, *84*, 1871.
(10) Madge, D.; Brannon, J. H.; Cremers, T. L.; Olmsted, J. *J. Phys. Chem.* **1979**, *83*, 696.
(11) Roth, N. J. L.; Craig, A. C. *J. Phys. Chem.* **1974**, *78*, 1154.
(12) Ruzsicska, B. P.; Braslavsky, S. E.; Schaffner, K. *Photochem. Photobiol.* **1985**, *41*, 681.
(13) Bilmes, G. M.; Tocho, J. O.; Braslavsky, S. E. *Chem. Phys. Lett.* **1987**, *134*, 335.
(14) Heihoff, K.; Braslavsky, S. E. In *Handbook of Organic Photochemistry*; Scaiano, J. C., Ed.; CRS Press: Boca Raton, FL, 1989, in press.

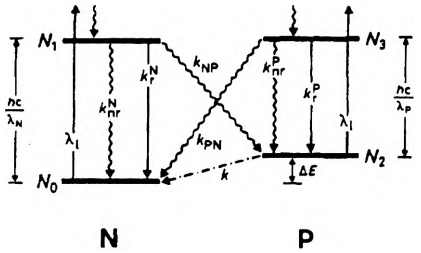


Figure 4. Scheme showing the stable (N) and isomeric (P) forms of DTDCI and the rate constants for the different processes interconnecting both species. The wavy lines represent the processes dissipating heat within the time window of the experiment. See text for the explanation of symbols.

shows no dependence with the energy. Figure 3 shows an example for the case of excitation at 610 nm.

Discussion

The results of flash photolysis show the existence of one transient species that thermally returns to N with a rate constant $k = (3.9 \pm 0.7) \times 10^3\ s^{-1}$. We identify this transient with a photoisomer (P) of N on the basis of the similarity of the spectral difference between these species with those described for the photoisomers of other cyanine dyes (e.g., DODCI[3]). No evidence of other transient species was found at room temperature under our conditions. Thus, the model and the equations employed in ref 13 for the photoisomerization processes of DODCI can be used to analyze the LIOAS results and to evaluate kinetic and spectroscopic parameters of the photoisomerization of DTDCI. Figure 4 shows the scheme employed.

Since $\Phi_{ISC} < 10^{-2}$ was evaluated for DTDCI in ethanol and a series of solvents[3,6] the triplet was not considered in the scheme.

k_{NP} and k_{PN} are the rate constants for isomerization of N ⇌ P and P ⇌ N from the excited states, k is the rate constant for the thermal P ⇒ N isomerization, and k_r^N, k_r^P, k_{nr}^N, and k_{nr}^P are the rate constants for radiative and nonradiative decay from excited N and P, respectively. λ_l is the laser wavelength and λ_N and λ_P are the wavelengths for the 0–0 transitions for N and P, respectively. ΔE is the difference in energy content between N and P.

At the low concentrations used in this work, it is reasonable to assume that radiative or Förster energy-transfer processes between both species can be ruled out, as well as the formation of aggregates.

When DTDCI, initially is in its stable form (N), is excited with microsecond pulses, a phototransformation from N to P (lifetime of excited N, $\tau_1 = 1.38$ ns[15]) takes place. At fluence rates ≥1 kW/cm² and with the strong overlap of the absorption spectra of both species being taken into account, a photochromic system between N and P should be built within the laser pulse duration as suggested by Dempster et al.[3] The energy dependence of the signal (Figure 2) at different λ_l shows a behavior similar to the one we found for DODCI,[13] which was explained also by the establishment of a photochromic equilibrium between N and P within the laser pulse duration. The transient bleaching of the sample observed in flash photolysis (Figure 1) and the loss of heat at higher energies in the LIOAS experiments for wavelengths below 665 nm (Figure i) is thus attributed to the formation of P, which does not thermally return to N during the pulse duration (lifetime of P, $\tau_2 \approx 260$ ps). With the excitation energy in LIOAS experiments being increased, less N is available for the process and the value of α is reduced. For $\lambda_l > 665$ nm, corresponding to the region where the absorption of P becomes important (Figure 1), the increase of the heat emission at higher energies (Figure 2) is due to an increase in the absorbance of the sample during the pulse as a consequence of the buildup of P. It is then reasonable to support the concept that the fluorescence quantum yield of P should be smaller than that of N, in agreement with the proposal by Enikhen and Berezovin.[5]

The lack of dependence of α with the laser energy in the 605–625-nm region and at $\lambda = 635$ nm indicates that these are isooptoacoustic points defined as the wavelengths at which the total energy emitted by the sample as heat does not change upon a chemical or physical perturbation.[16,17] In these points

$$\sigma^N \alpha_N = \sigma^P \alpha_P$$

where σ^N and σ^P are the absorption cross sections of N and P at λ_l and α_N and α_P the nonradiative efficiencies of N and P, respectively. The presence of isooptoacoustic points is further demonstrated by the lack of dependence with laser energy of the normalized heat emission for these wavelengths (Figure 3). Consequently, care should be exercized when analyzing energy dependences of optoacoustic signals, since linear dependencies do not necessarily imply the lack of an additional absorbing species in the system. Extended isooptoacoustic regions may be present in a four-level system.

At very low excitation energies, the population N_2 is negligible with respect to N_0, and the only species absorbing is N. Thus, at the isooptoacoustic points, $\alpha = \alpha_N = 0.67 \pm 0.05$ (from Figure 2). Taking into account the scheme of Figure 4, energy balance considerations lead to

$$\frac{N_A hc}{\lambda_l} = \Phi_f^N \frac{N_A hc}{\lambda_f} + \alpha_N \frac{N_A hc}{\lambda_l} + \Phi_{NP} \Delta E \qquad (1)$$

Φ_f^N and Φ_{NF} are the quantum yields of N fluorescence and N ⇒ P photoisomerization, respectively; λ_f is the wavelength of the fluorescence maximum of N, h is the Planck constant, N_A is the Avogadro constant, and c is the speed of light. With our value of $\Phi_f^N = 0.36$

$$\Phi_{NP} \Delta E = 7.2 \times 10^3\ \text{J mol}^{-1} \cong 0.075\ \text{eV} \qquad (2)$$

is obtained. This value represents the middle point between extremes calculated for various combinations of λ_l (isooptoacoustic points, between 605 and 630 nm) and λ_f and the values for α_N and Φ_f^N with their respective errors. Thus, the range for the product $\Phi_{NP} \Delta E$ is ±100%.

From the same analysis with the same nomenclature as in ref 13, the system of rate equations describing the time evolution of the populations of the states (see Figure 4) can be solved, employing a fourth-order Runge–Kutta numerical method. The heat released promptly by DTDCI and the reference is thus calculated, and the values for α vs λ_l are obtained, fitting this way the experimental data.

The literature value for the lifetime of excited P, $\tau_3 = 0.27$ ns,[18] and $\Phi_f^N = 0.36 \pm 0.05$ (see Experimental Section) were used. Three values for $\Phi_{NP} = 0.5$,[6] 0.12,[3] and 0.03[3,4] were tried with the corresponding ΔE values from 2, and $0 \le \Phi_f^P \le 0.2$ (as suggested in ref 5) were used. The fitting parameters adjusted for the points of Figure 2 were as follows: $B = \sigma^P/\sigma^N$ and Φ_{NP} and $\Phi_{PN} = k_{PN} \tau_3$. In the region of 605–650 nm, the parameter largely affecting the fit is B, especially at the isooptoacoustic points. Changes in the other parameters do not produce important modifications. For the region 650–690 nm, several combinations of the fitting parameters can be used. However, in the isosbestic point, determined by flash photolysis at $\lambda_l = 675$ nm, $B = 1$ and the best fits for 10 and 100 μJ were obtained with $\Phi_{NP} = 0.5$, $\Delta E = 0.15 \pm 0.15$ eV (eq 2), and $\Phi_{PN} \le 0.14$. With these values, B was then adjusted for the whole spectrum and good fits were obtained for low and relatively high energies as shown in Figure 2.

Figure 5 shows the spectrum of P deduced from the calculated values of B, together with the spectrum of N. The spectrum determined for P is within the limits calculated in ref 3.

(15) Sibbett, W.; Taylor, J. R.; Welford, D. *IEEE J. Quantum Electron.* **1981**, *QE-17*, 500.

(16) Bilmes, G. M.; Tocho, J. O.; Braslavsky, S. E. *J. Phys. Chem.* **1988**, *92*, 5958.

(17) Schneider, S.; Coufal, H. *J. Chem. Phys.* **1982**, *76*, 2919.

(18) Sundstrom, V.; Gillbro, T. *J. Chem. Phys.* **1985**, *83*, 2733.

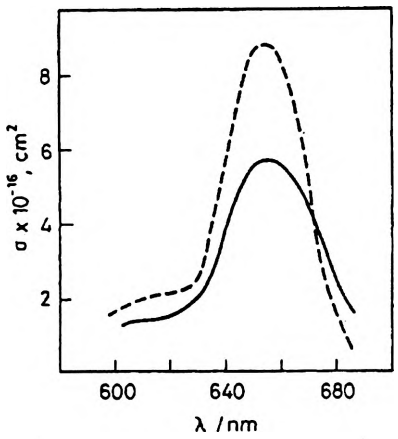


Figure 5. Absorption spectra of the most stable isomer N (--) and the photoisomer P (—) of DTDCI. The latter spectra is derived from the optoacoustic measurements (see text).

The strong superposition of the spectra in both isomers was also confirmed by means of fluorescence measurements. With DTDCI being excited at 650 nm with the flash-lamp-pumped dye laser and various fluences (from 8.5 to (4×10^3) kW/cm^2) being used, no changes were observed in the emission spectra, with respect to conventional fluorescence measurements.[19] For the same conditions of excitation, other cyanine dyes, for which the absorption spectra of both isomers are not so strongly superimposed, show important variations in the fluorescence spectra, depending on the wavelength and excitation energy, due to the emission of both species.[20]

The evaluation of the photophysical parameters for the photoisomerization of DTDCI is less precise than for the case of DODCI,[14,16] a cyanine dye with the same polymethinic chain but just a different heteroatom (S instead of O) in the final rings. Some general conclusions can be extracted. Similar to the case of DODCI, the fluorescence quantum yield of the excited isomer of DTDCI seems to be lower than that of excited N and the photoisomerization of N to P is more efficient than the back-photoisomerization $P^* \rightarrow N$. The latter result can be discussed, taking into account that the accepted scheme for the isomerization mechanism of these molecules follows the normal double bond photoisomerization through a twisted intermediate. This was proposed for the case of DODCI, for which twisting constitutes the main radiationless deactivation channel for the excited N,[8] while internal conversion without passing through the twisted state is the main deactivation channel for excited P.[16] This conclusion was derived from the fact that the branching ratio from the twisted state to N and P has to be the same, independent of the origin of this state, and has been later confirmed by Rentsch et al.[21] and Zhu and Harris.[22]

For the case of DTDCI, the situation cannot be defined so accurately. When, in analogy with DODCI, no direct internal conversion from excited N is assumed and a value $\Phi_{NP} = 0.5$ is used, a value of 0.8 is obtained for the branching ratio to P from the twisted state, when it is arrived from excited N. This value is the same as that from excited P with use of $\Phi_{PN} = 0.14$. This means that, under this assumption, in this case excited P deactivates by passing through the twisted state. However, it is not clear yet that this assumption is valid for DTDCI. More data, especially temperature-dependent photoisomerization quantum yields, are needed to completely understand the mechanisms of deactivation of excited N and excited P in DTDCI.

Additional differences between DTDCI and DODCI are as follows: (i) In the former, the ground state energy of P is much lower than in the latter; i.e., it is only slightly above N. (ii) The spectra of N and P overlap more for DTDCI than for DODCI.

Conclusions

The photophysical behavior of DTDCI can be explained in terms of a reversible photoisomerization process between two configurational isomers. No evidence was found for the presence of an additional isomer in methanol as had been suggested by Kaliteevskaya and Razumova.[4]

Using LIOAS and a simple scheme connecting the stable form and its photoisomer, we can calculate the absorption spectrum for the photoisomer and limits for its fluorescence quantum yield ($\Phi_f^P < 0.2$) and the quantum yield for back-photoisomerization from the first excited singlet state of this species to the ground state of the stable form ($\Phi_{PN} \leq 0.14$).

The application of LIOAS to the study of this system has resulted in a better resolved absorption spectrum of both species than that resulting from conventional and laser flash photolysis. No region shows absorption of one species alone, and it is not possible to use the method developed in ref 16 to obtain the energy content of the less stable isomer. Fitting the photoacoustic data permitted us to estimate $\Delta E = 0.15 \pm 0.15$ eV. The use of the data at the isooptoacoustic points has lead to the evaluation of spectroscopic and kinetic parameters of a photoisomer with optical properties very similar to those of the parent compound. This further demonstrates the potential of the LIOAS technique.

Acknowledgment. We are indebted to Professors K. Schaffner (MPG) and M. Garavaglia (CIOp) for their support and interest. The fruitful discussions with Dr. H. F. Ranea-Sandoval and the help of S. Nonell (MPG) and C. Colombano (MPG) are greatly acknowledged. J.O.T. is a member of Consejo Nacional de Investigaciones Científicas y Técnicas (CONICET, Argentina), and G.M.B. is partial recipient of a CONICET fellowship.

Registry No. DTDCI, 514-73-8.

(19) Scaffardi, L. To be published.
(20) Scaffardi, L.; Bilmes, G. M.; Schinca, D.; Tocho, J. O. *Chem. Phys. Lett.* **1987**, *140*, 163.
(21) Rentsch, S.; Döpel, E.; Petrov, V. *Appl. Phys. B* **1988**, *46*, 357.
(22) Zhu, X. R.; Harris, J. M. *Chem. Phys.* **1988**, *124*, 321.

Appl. Phys. B 66, 245–249 (1998)

Applied Physics B
Lasers
and Optics
© Springer-Verlag 1998

Photoacoustic characterization of phase transitions in amorphous metal alloys

D.J. Orzi[1], G.M. Bilmes[1], J.O. Tocho[1], N. Mingolo[2], O.E. Martínez[3]

[1] Centro de Investigaciones opticas (CIC-CONICET) and Universidad Nacional de La Plata, C.C.124, 1900, La Plata, Argentina
Fax: +54-21/71-2771, E-mail: postmaster@ciop.edu.ar)
[2] Departamento de Física, Facultad de Ingeniería, UBA, Paseo Colón 850, 1063 Buenos Aires, Argentina
(Fax: +54-1-331-0129, E-mail: nmingol@aleph.fi.uba.ar)
[3] Departamento de Física, FCEyN-UBA, Pabellón 1, Ciudad Universitaria, 1428 Buenos Aires, Argentina
(Fax: +54-1-782-7647, E-mail: oem@df.uba.ar)

Received: 24 February 1997

Abstract. In this work a pulsed laser photoacoustic technique is employed in amorphous alloys for the characterization of crystallization temperatures and the determination of the activation energies for the transitions. It is shown that the changes produced in the photoacoustic signal generated by low energy laser pulses (< 200 μJ), is a sensitive probe for detecting the crystallization of a metallic amorphous sample. A piezoelectric transducer attached to the sample by means of a glass substrate was used for the acoustic detection. The developed technique has the advantages of requiring a minimum amount of sample, with no special sample preparation or conditioning. In order to demonstrate the validity of the technique, it was applied to the study of the crystallization processes of the amorphous Mg-Zn alloy, comparing the result with respect to resistivity measurements.

PACS: 78.20; 61.40; 64

The stability of amorphous metals can be determined by thermal measurements. When an amorphous metal is heated above its glass transition temperature, it undergoes first a second order glass to undercooled liquid transition and afterwards a first order liquid to crystal transition [1, 2]. The structural changes are usually detected by X-ray or neutron diffraction, scanning calorimetry or electrical resistivity measurements. The stability of the amorphous phase and the activation energies for the transitions are determined by the kinetics of transformation, that is, the delay before the transition takes place, after heating above the critical temperature. When isothermal annealing is used, the activation energy is determined from Arrhenius plots and at constant heating rates from Kissinger plots [3]. In this work a new technique for the determination of phase transition in metal alloys, based on the photoacoustic effect is presented. Photoacoustics is related to the phenomena of the generation of acoustic waves in a medium after interaction with modulated or pulsed electromagnetic radiation. One interesting property of the phenomena, is that the photoacoustic signal generated, depends on the thermoelastic parameters of the medium (thermal expansion, sound velocity, heat capacity, etc.), magnitudes that change greatly in a phase transition, hence, structural changes can be easily determined in realtime by monitoring the changes in the photoacoustic signals. Prior work related to photoacoustic characterization of phase transitions relies on the use of a chopped lamp or a CW low power laser and a gas cell with a microphone [4]. This technique requires a very small volume of gas contacting the sample and the microphone [5]. This requirement is difficult to achieve as the microphone must be placed far from the sample, outside the temperature controlled region, leading to sophisticated designs [6, 7].

In this work a pulsed laser photoacoustic technique is employed. Pulsed laser generation of acoustic waves in the condensed phase, has been widely used for the characterization of materials [8]. Here, the laser excitation of the sample acts only as a source of acoustic waves, then the energy of the pulse must be always sufficiently low to avoid heating or surface changes. As the detector used is a piezoelectric transducer contacting the sample by means of a glass substrate, it can be easily placed outside the oven without any special requirement in the design.

In order to demonstrate the validity of the technique developed, it was applied to the study of the crystallization processes of the amorphous Mg-Zn alloy ($Mg_{70}Zn_{30}$). This alloy was selected because it has been thoroughly studied and the large number of prior publications allows a reliable comparison with the results. It presents a eutectic at the composition used, and has a high temperature equilibrium phase $Mg_{51}Zn_{20}$ (denoted as Mg_7Zn_3) that has been characterized by Higashi [9]. The sample becomes amorphous after rapid cooling from the melt [10, 11] with a short range order similar to that of the $Mg_{51}Zn_{20}$ crystalline phase [12–14]. According to Andonov [15] it is actually described by the coexistence of a disordered phase similar to the liquid state and better organized aggregates which are not yet crystallized. The amorphous phase is only marginally "stable" [16] and different authors have found somewhat different transition temperatures, depending on the thermal history of the material [7, 17]. The crystallization upon heating has been described

by several authors [10, 11, 13, 18, 19], and the activation energy for crystallization has been determined [11, 18].

In characterizing this new technique, electrical conductivity and photoacoustic signals were simultaneously measured during different thermal cycles of the samples in the range between room temperature and 560 K, identifying completely the most important phase transitions that take place in this material. Activation energies of the transition as well as the sound velocity in the amorphous and crystalline phase were also measured.

Generation of photoacoustic signals and changes as a function of temperature, are discussed in terms of the changes in the thermodynamic parameters of the samples.

1 Experimental

The experimental setup used is shown in Fig. 1. The excitation source was the second harmonic ($\lambda = 532$ nm) of a Q-switched Nd^{3+}-YAG laser, providing 7 ns width pulses at a repetition rate of 10 Hz and attenuated to less than 200 μJ to avoid excessive heating of the material. The samples were ribbons 20 μm thick, 1 mm wide, and pieces around 1 mm long were cut and pressed between an L-shaped glass substrate and a glass cover, to ensure good acoustical contact ("sample holder"). The short arm of the substrate was located inside a temperature controlled oven, and the end of the large part outside it, attached with glue to the acoustic transducer. The latter was a cylindrical ceramic piezoelectric detector (PZT) 4 mm in diameter and 4 mm long. The substrate was L-shaped in order to avoid spurious acoustic signals produced by scattered light absorbed at the surface of the transducer [20]. The peak to peak amplitude of the first detected acoustic oscillation (H) was monitored as a function of the temperature. The acoustic signals were amplified (×800), and afterwards processed by a storage digital oscilloscope that sampled at 100 Msamples/sec with 8–bit resolution per point.

The temperature of the oven could be controlled between room temperature and 560 K using heating rates between 1 K/min and 15 K/min. The temperature of the sample was measured by a thermocouple, mounted on the glass substrate at a distance of a few millimetres from the sample. Energy measurements (E) were performed with a pyroelectric detector, sampling the pulse using a glass plate as the beam splitter. The four probe method was used for the measurement of the resistivity (R), using samples 10 mm long and electric contacts made by pressing copper foils.

Automatic and simultaneous measurements of the amplitude of the acoustic signal, energy of the pulse, temperature, and resistivity, were made by taking 32 averages every 10 seconds. The data were stored in the computer for further processing.

The samples ($Mg_{70}Zn_{30}$ near eutectic composition), were manufactured by the melt spinning technique [21], and X-ray diffraction spectra were taken to verify that the material was initially amorphous.

Figure 2 shows the changes observed in the acoustic signal at three different temperatures (290 K, 423 K and 523 K). The registered signal is the result of the response of the detector to all the waves, including reflections, and presents a characteristic "ringing" of the piezoelectric crystal. Hence, the selection of the part of the signal used to measure, must

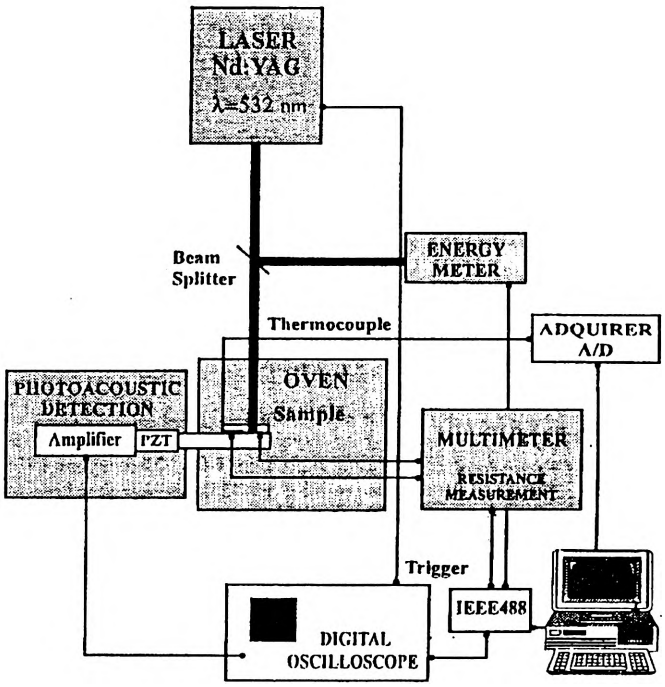


Fig. 1. Experimental set-up used for the photoacoustic detection. Automatic and simultaneous measurements of the amplitude of the acoustic signal, pulse energy, temperature, and resistivity, were made by taking 32 averages every 10 seconds. The data was stored in the computer for further processing

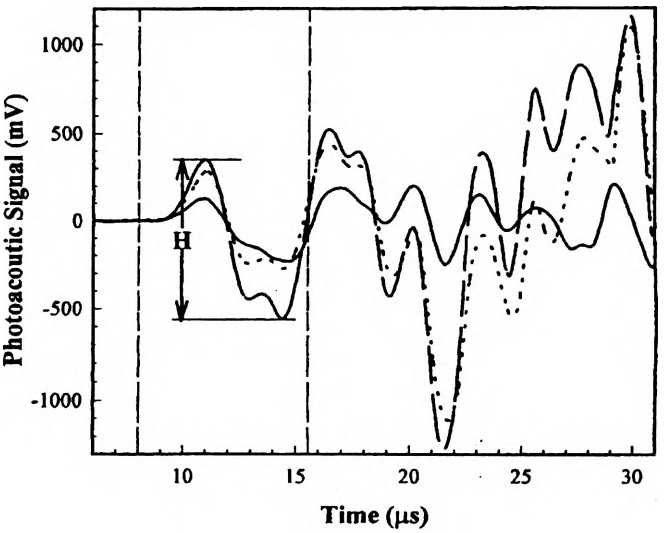


Fig. 2. Time dependence of the photoacoustic signal at different temperatures. (*solid*) 290 K, (*short dash*) 423 K; (*long dash*) 523 K. The change in the shape is evident, and the peak to peak amplitude of the first oscillation is taken as the photoacoustic signal H

be made carefully. It is clear that, with the exception of the first part of the signal, the rest not only changes in amplitude but also in shape, probably due to interference effects between different acoustic waves, deformations of the sample, etc. Taking this into account, the peak to peak amplitude of the first oscillation was used as the photoacoustic signal H, and was divided by the laser pulse energy (E) to compensate the shot to shot laser fluctuations.

2 Results

Figure 3 shows a simultaneous measurement of the normalized photoacoustic signal H/E and the resistance R as a function of the temperature, performed by heating the samples at a rate of 9 K/min. In both cases strong changes were observed above 360 K (an increase of H/E; decrease of R), corresponding to the crystallization of the sample, as it was previously reported in the literature [10, 11, 13, 18]. After heating to 570 K, the sample was cooled to room temperature, showing the irreversibility of the transition. Successive temperature cycles of heating and cooling showed no further changes, confirming complete crystallization. Thermal cycles performed from room temperature to 410 K (after the first transition), showed a similar behaviour consistent with a complete crystallization also at this stage. Hence two transition temperatures can be easily identified, one around 370 K and the other around 470 K.

To determine the reproducibility of the measurements, experiments were performed with the same heating rate with different pieces of the same ribbon. Similar curves were obtained with a reproducibility within 5% of the values of the transition temperatures

The activation energies for the crystallization processes were estimated by the Kissinger "peak shift" method [3, 11]. This procedure involves plotting $\log(T_i^2/v)$ as a function of $1/T_i$, where T_i is the temperature of the transition, and v is the heating rate. The slope of the straight line obtained gives the activation energy of the transition.

Two activation energies were estimated, corresponding to the two steps of the crystallization. Figure 4 shows Kissinger plots corresponding to the data obtained for different heating rates between 1 K/min and 15 K/min. The activation energies obtained for the two transitions are $E_1 = 153$ kJ/mole, and $E_2 = 92$ kJ/mole.

One of the possible sources of variation in the photoacoustic signal is a change in the sound velocity, a parameter that has not been measured previously for this alloy. With the aim of establishing the importance of the different parameters in this change, the sound velocity was determined before and after the crystallization of the sample. This was performed outside the oven by measuring the arrival time of the acoustic signal after the laser shot, as a function of the distance between the laser spot and the transducer. Figure 5 shows that the sound velocity in the amorphous phase (4767 ± 50 m/s) is 15% smaller than in the crystalline phase (5562 ± 77 m/s).

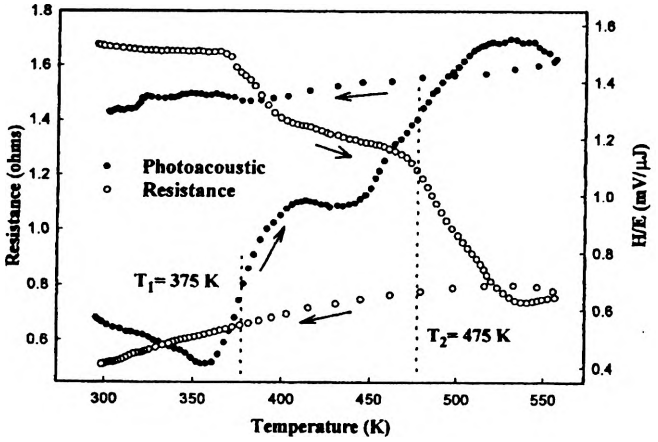


Fig. 3. Simultaneous measurement of resistance (R) and normalized photoacoustic signal (H/E), as a function of temperature for a $Mg_{70}Zn_{30}$ alloy. Arrows show the heating (→) and cooling (←) cycles respectively. The heating rate was 9 K/min. Two transitions appear. The transition temperature was taken at the half point of the signal change, as shown

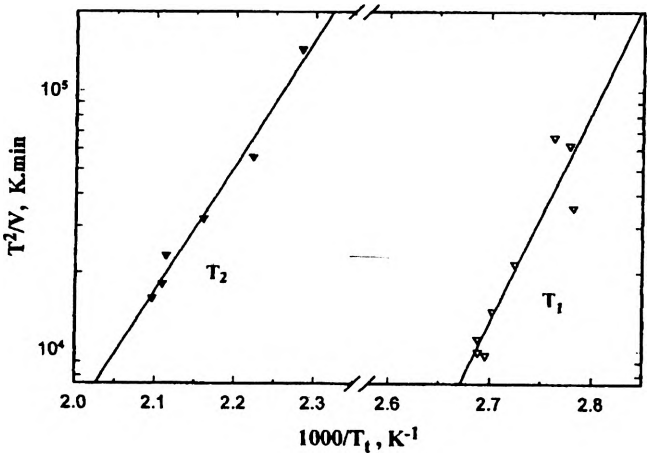


Fig. 4. Kissinger plots for the two steps of the crystallization processes of $Mg_{70}Zn_{30}$. The slope gives the corresponding activation energies, and the values obtained are $E_1 = 153$ kJ/mole, and $E_2 = 92$ kJ/mole

3 Discussions

The origin of the acoustic signal is the pressure wave generated by the local heating of the material, after absorbing part of the laser energy. The signal detected depends in a complicated manner on the excitation-detection geometry conditions of the experiment, and both the surface and bulk waves are coupled to the detector. From the treatment performed by Bunkin et al. for the thermo-optical generation of acoustic waves in a solid [22], the following general expression for the amplitude of the acoustic pulse as a function of the thermo-elastic parameters of the media can be deduced:

$$H = \frac{\beta E}{\rho C_p} F(\tau, D), \tag{1}$$

where β is the volume thermal expansion coefficient, C_p is the heat capacity at constant pressure, E is the absorbed laser pulse energy, ρ is the density, F is a function of the temporal and spatial shape of the laser pulse and the geometry of the detection; τ is the laser pulse duration, and $D = 2c_s\tau Z/a^2$ is the acoustic diffraction parameter, with c_s the sound velocity; Z the distance between the acoustic source and the detector, and a the diameter of the illuminated region.

From (1), changes in the acoustic signal can be expected from changes in the sound velocity, the alloy density, the expansion coefficient or the heat capacity. The small change measured in the sound velocity, together with the smooth dependence of F with D, cannot explain the large variations observed in the acoustic signal. The change in the density between the glass, crystal and liquid is also very small [14, 15].

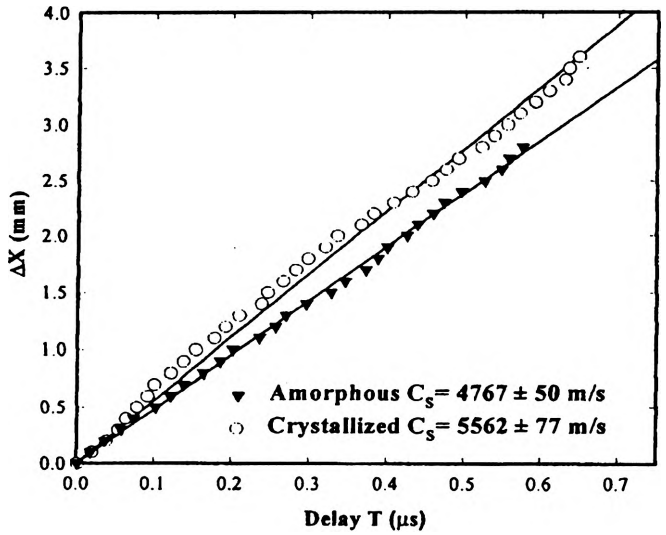


Fig. 5. Sound velocity determination in the amorphous and crystalline phase. The delay in the arrival of the acoustic signal was determined as a function of the distance between the laser spot and the position of the transducer

During a glass to undercooled liquid transition, C_p and β are expected to increase upon heating, and conversely C_p and β should decrease in the undercooled liquid to crystal transition [1, 2]. Hence from (1), the sign of the change in the photoacoustic signal will depend on which of the two magnitudes has a larger relative change.

It is convenient at this stage to summarize prior results obtained by other authors with this alloy. The crystallization upon heating has been described by several authors [10, 11, 13, 18, 19], showing first a crystallization transition around 360 K, reflected by a decrease of the order of 10% in the electrical resistivity [11, 13, 18], and two peaks in DSC experiments [10, 19]. Smaller crystallization temperatures were found by Schaal [23] using small angle X-ray scattering and very slow heating rates (0.375 K/min). This first doublet is associated with the polymorphous crystallization of very fine grained $Mg_{51}Zn_{20}$ which is highly defective, and a subsequent recrystallization process to more perfect grains. A much smaller DSC peak occurs at higher temperature (around 500 K) due to the precipitation of some Mg.

From the photoacoustic results, the first transition can be assigned to the material crystallization to $Mg_{51}Zn_{20}$ (detected as a doublet by DSC [11, 13, 18]). Our results with the electrical resistivity are similar to those previously published [10, 19], validating our interpretation of the photoacoustic signal changes. From Eq. (1), the increase of the photoacoustic signal upon crystallization indicates that the change in C_p is the dominant mechanism involved in this transition. This is consistent with the results reported in [15], where no important change in the thermal expansions in this temperature range were found during their diffraction studies.

From prior work, the activation energies of the two peaks of the DSC doublet were found to be 160 kJ/mole and 120 kJ/mole [11]. Shiotani et al. [18] determined the activation energy for different compositions between 69 at.% and 72 at% of Mg by Arrhenius plots using the electrical resistivity changes, yielding values between 150 kJ/mole and 130 kJ/mole. Calka [16] showed that the activation energy depends on the composition and aging of the sample. With our technique only one activation energy $E_1 = 153$ kJ/mole was determined with a value consistent with prior works.

The second transition detected corresponds to the segregation of Mg, as reported by several authors [10, 11, 13, 18, 19]. The activation energy for this transition has not been previously reported.

It was not possible to determine the glass transition from our measurement, probably due to its proximity to room temperature. The small decrease in the photoacoustic signal between room temperature and 350 K can be attributed to the increase in C_p during the glass transition, but this result was not repetitive enough for an unambiguous assignment. This coincides with previous findings, that showed that when scanned with DSC the endothermic glass transition is either absent or extremely weak [10].

The photoacoustic signal increases by a factor of two in the first transition while the electrical resistivity decreases by only 15%, showing a larger sensitivity of the new method for this amorphous to crystalline transition. This feature arises from the large change in C_p for these transitions. For the crystal-crystal transition, the sensitivities are similar, showing a 50% relative change in both magnitudes.

4 Conclusions

It has been shown that the changes produced in the photoacoustic signal generated by low energy laser pulses (less than 200 μJ), is a sensitive probe for detecting the crystallization of a metallic amorphous sample.

The developed technique has the following advantages over other competitive methods. A minimum amount of sample is required, and it can be solid or a powder. Due to the focusability of the laser and the negligible penetration depth of the light, small area, thin amorphous layers can be studied. No special sample preparation or conditioning is necessary. No contacts are soldered or glued and no special shape is required.

In the particular case of the alloy studied, the sensitivity of the photoacoustic measurements was higher than that obtained with electrical resistivity measurements.

Inspite of the high sensitivity of the technique, the Nd^{3+}-YAG pulsed laser used can be replaced by smaller compact lasers such as diode pumped systems. In this way, the developed method can be converted in a very simple, compact system, to be used for *in situ* studies and incorporated into larger equipment such as electron microscopes, X-ray diffractometers, or scanning calorimeters.

Acknowledgements. The authors wish to thank Dr. M.E. de la Cruz for providing the melt-spinning equipment for the production of the samples, and Eng. N. Martinez for the resistivity measurement equipment. This work was carried out with partial support from the Universidad de Buenos Aires and from the Universidad Nacional de La Plata.

References

1. G.W. Scherer: *Glass formation and relaxation* in Mater. Sci. Technol. Vol.9, ed. by R.W. Cahn, P. Haasen, E.J. Kramer (VCH, New York 1991)
2. H. Baxi, T.B. Massalski: Mater. Sci. Eng. **97**, 291 (1988)
3. H.E. Kissinger: J. Res. Nat. Bur. Stand. **57**, 217 (1956)

4. M.A. Siqueira, C.C. Ghizoni, J.I. Vargas , E.A. Menezes, H. Vargas, L.C.M. Miranda: J. Appl. Phys. **51**, 1403 (1980)
5. H. Vargas, L.C.M. Miranda: Phys. Rep. (Review Section of Physics Letters) **161**, 43 (1988)
6. J. Fernandez, J. Etxebarria, M.J. Tello, A. Lopez Acharri, J. Phys. D: Appl. Phys. **16**, 269 (1983)
7. C. Pichon, M. Le Liboux, D. Fournier, A.C. Boccara: Appl. Phys. Lett. **35**, 435 (1979)
8. See for example: 8th Intenjational Topical Meeting on Photoacoustic and Photothermal Phenomena, Journal de Physique IV, Colloque C7, Vol.4 C7-545-667. (1994)
9. I. Higashi, N. Shiotani, M. Uda, T. Mizoguchi, H. Katoh: J. Solid State Chem. **36**, 225 (1981)
10. A. Calka, M. Madhava, D.E. Polk, B.C. Giessen, H. Matyja, J. Vander Sande: Scripta Metall. **11**, 65 (1977)
11. P. Boswell: Mater. Sci. Eng. **34**, 1 (1978)
12. H. Rudin, S. Jost, H.J. Güntherodt: J. Non-Cryst. Solids **61/62**, 291 (1984)
13. M. Ito, H. Narumi, T. Mizoguchi, T. Kawamura, H. Iwasaki, N. Shiotani: J. Phys. Soc. Jpn. **54**, 1843 (1985)
14. P. Andonov, P. Chieux: J. Non-Cryst. Solids **93**, 331 (1987)
15. P. Andonov, P. Chieux: J. Non-Cryst. Solids **108**, 58 (1989)
16. A. Calka: J. Phys. F: Met. Phys. **16**, 1577 (1986)
17. J.B. Suck, H. Rudin, H.S. Güntherodt, H. Beck: J. Phys. C: Solid State Phys. **14**, 2305 (1981)
18. N. Shiotani, H. Narumi, H. Arai, K. Wakatsuki, Y. Sasa, T. Mizoguchi: Proc. 4th. Int. Conf. on Rap. Quenched Metals, Sendai, Japan, **2**, 667 (1981)
19. T. Matsuda, U. Mizutani: Proc. 4th. Int. Conf. on Rap. Quenched Metals, Sendai, Japan **2**, 1315 (1981)
20. C.K.N. Patel, A.C. Tam: Rev. Mod. Phys. **53**, 517 (1981)
21. R.W. Cahn: *Metallic Glasses* in Mater. Sci. Technol. Vol. 9, ed. by R.W. Cahn, P. Haasen, E.J. Kramer (VCH, New York 1991)
22. F.V. Bunkin, Al.A. Kolomensky, V.G. Mikhalevich: In *Lasers in Acoustics*, Chap. 4, (Harwood Academic Publishers, Switzerland 1991)
23. M. Schaal, P. Lamparter, S. Steeb: Z. Naturforsch. **41a**, 1123 (1986)

PPS
Paper
www.rsc.org/pps

The photophysics of nitrocarbazoles studied by using spectroscopic, photoacoustic and luminescence techniques †

Mariana Mesaros,[a] Sergio M. Bonesi,[b] Maria A. Ponce,[b] Rosa Erra-Balsells *[b] and Gabriel M. Bilmes *[c]

[a] *Centro de Investigaciones Opticas (CONICET-CIC), Casilla de Correo 124, (1900) La Plata, Argentina*
[b] *CIHIDECAR-CONICET, Departamento de Química Orgánica, Facultad de Ciencias Exactas y Naturales, Universidad de Buenos Aires, Pabellón II,3 Ciudad Universitaria, (1428) Buenos Aires, Argentina*
[c] *Centro de Investigaciones Opticas (CONICET-CIC) y Universidad Nacional de La Plata, Casilla de Correo 124, (1900) La Plata, Argentina. E-mail: gabrielb@ciop.unlp.edu.ar*

Received 24th April 2003, Accepted 16th May 2003
First published as an Advance Article on the web 12th June 2003

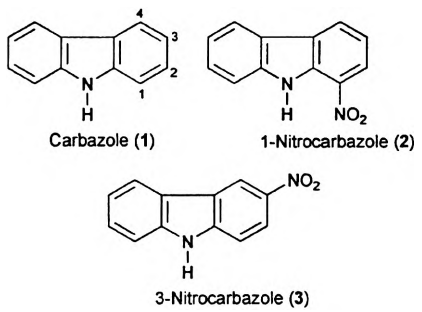
The photophysical behaviour of 1-nitrocarbazol and 3-nitrocarbazol in different organic solvents has been studied by using spectroscopic, luminescence and photoacoustic techniques. Absorption spectra and triplet state transient spectra were recorded and formation quantum yields and lifetimes determined. Phosphorescence emission at 77 K and laser induced luminescence in acetonitrile solution at 298 K for the nitrocarbazoles were studied. Results are discussed in terms of the optimized structure of 1-nitrocarbazole and 3-nitrocarbazole and compared with that of carbazole. The nitro group attached to the carbazole moiety induces important changes in the photophysical behavior of those compounds.

Introduction

As part of a comparative study of the photophysical processes and the photoreactivity of azacarbazoles (β-carbolines)[1,2] and carbazoles[3,4] and their potential use as matrices (photosensitizers) in matrix assisted ultraviolet laser desorption/ionization mass spectrometry (UV-MALDI-MS),[5,6] we decided to examine the behavior of carbazole derivatives. To begin with, nitrocarbazoles were chosen since for aromatic molecules the nitro group as a substituent induces strong modifications on the acid–base properties in the ground and electronic excited states and on the nature (π,π^*; n,π^*), multiplicity (singlet, S_1; triplet, T_1), lifetime (τ_{S1}; τ_{T1}) and efficiency of population (ϕ) of the electronic excited states.[7–10] Thus, after we completed the preparation and full characterization of 1-nitrocarbazole (**2**) and 3-nitrocarbazole (**3**)[11] (Scheme 1), we studied their photostability and their absorption and emission spectra under steady-state conditions.[7]

Both nitrocarbazoles were shown to be stable after irradiation in acetonitrile solution.[7] In experiments of laser desorption/ionization mass spectrometry with an N_2 laser source (λ_{exc} = 337 nm, LD-MS)[5,11] they showed a high efficient desorption/ionization process. They also behaved as efficient photosensitizers (matrix) in UV-MALDI analysis for low molecular mass proteins and for carbohydrates.[5] 1-Nitrocarbazole **2** showed a phosphorescence emission which was weaker than that of 3-nitrocarbazole **3**, while neither compound showed any detectable fluorescence emission in steady-state experiments. Experiments were then coducted by comparing absorption and emission spectroscopy, laser flash photolysis, photoacoustic and laser induced luminescence properties of **2** and **3** relative to **1**.

The results described in the present report show that the presence of the nitro group as a substituent in the carbazole moiety induces different photophysical behaviors in nitrocarbazoles **2** and **3** compared with that of carbazole **1**. Besides, they also show that not only is the presence of the nitro group critical but also its location in the carbazole moiety.



Scheme 1 Structure of the carbazoles studied.

† Dedicated to Professor Silvia Braslavsky, to mark her great contribution to photochemistry and photobiology particularly in the field of photothermal methods.

Experimental

Chemicals and instrumentation

Materials. Spectrograde and HPLC grade cyclohexane, carbon tetrachloride, ethyl acetate, acetonitrile, methanol and acetic acid were purchased from J. T. Baker and were used without further purification.

2-Hydroxybenzophenone, 1-cyanonaphthalene, carbazole and Cresyl Violet were purchased from Aldrich and were recrystallized from ethanol. Ceric ammonium nitrate ($Ce(NH_4)_2(NO_3)_6$; CAN), ammonium ferric(II) sulfate hexahydrate ($(NH_4)_2Fe(SO_4)_2 \cdot 6H_2O$, Mohr salt), EDTA, copper(II) nitrate trihydrate ($Cu(NO_3)_2 \cdot 3H_2O$), sodium nitrite and nitric acid were purchased from Aldrich. Solvents for chromatography and recrystallization were carefully purified and dried before use.[12] Thin layer chromatography (TLC) analysis was performed with aluminium silica gel sheets (0.2 mm layer thickness, silica-gel 60 F254). Products were isolated by preparative thick layer chromatography and column chromato-

 DOI: 10.1039/b304520j

This journal is © The Royal Society of Chemistry and Owner Societies 2003

graphy which was carried out using silica gel 200–400 mesh 60 Å and ethyl acetate and ethyl acetate–ethanol as solvents. Melting points are uncorrected.

Equipment and experimental set-ups. UV absorption spectra were recorded on a Shimadzu UV-1203 UV-visible spectrophotometer and with a Beckman DU 65 spectrophotometer. All the measurements were made with 1 cm stoppered quartz cells at 298 K. Phosphorescence measurements were performed on a Hitachi F-500 spectrofluorometer whose output is automatically corrected for instrumental response by means of a Rhodamine B quantum counter and equipped with a Hamamatsu R 928 photomultiplier tube. The spectra at 77 K were recorded in solid matrices produced by freezing the ethyl ether–isopropanol (1 : 1) solution contained in a cylindrical cell (2 mm path length) with liquid N_2. The concentration of the substrates were 5.0×10^{-5} mol dm^{-3} and the solutions freshly prepared in the solvent mixture at 298 K and degassed with Ar during 10 min before freezing at 77 K. The electronic phosphorescence emission spectra were recorded in phosphorescence mode from 350 to 650 nm at 77 K. The selected excitation wavelength was 320 nm.

The phosphorescence lifetime values (τ_p) were measured in the same apparatus at the maximum phosphorescence emission wavelength. The monoexponential decay curves were acquired on a PC that was interfaced to the spectrofluorometer. Then, the phosphorescence lifetimes were determined by fitting the phosphorescence decay curves with a monoexponential function using the Origin 3.5 program.

The phosphorescence quantum yields (ϕ_p) of the nitrocarbazoles were measured relative to that of carbazole ($\phi_p = 0.24$),[7] which was used as a reference. A simple comparison of the integrated areas under the phosphorescence spectra of the nitrocarbazoles and carbazole yields the ϕ_p values.

Laser flash photolysis experiments were performed by using the third harmonic of a pulsed Nd:YAG laser (Edinburg Laser Flash Photolysis System). The energy of a single 355 nm pulse was monitored with a beam splitter and a pyroelectric energy meter (Laser Precision Corp.). Laser induced transient transmission changes were monitored, perpendicular to the laser beam, by using a Xe arc lamp (ILC UV 33P). The analysing light passed through a 2 nm wide section of the excited sample and was then focused at the entrance slit of a 0.25 mm, doubled grating monochromator (PTI f/4, spectral resolution 3 nm). A photomultiplier (Hamamatsu R 936) and a Tektronix R-7912 transient digitizer interfaced to a PC IBM Asyst. Programs were used to acquire and process the signals. The electronic absorption spectrum of the triplet transient of 3-nitrocarbazole was obtained in Ar degassed acetonitrile solution (substrate concentration: 5.0×10^{-5} mol dm^{-3}) at 298 K. The triplet transient lifetime value (τ_T) of 3-nitrocarbazole was measured with the same apparatus at the maximum absorption wavelength ($\lambda = 575$ nm).

The triplet quantum yield (ϕ_T) values were measured by laser flash photolysis in acetonitrile at 298 K. Benzophenone was selected as the triplet energy donor and as a reference ($\phi_T = 1.0$). 1-Cyanonaphthalene was selected as the triplet energy acceptor. The absorbance of the triplet transient of 1-cyanonaphthalene at 500 nm obtained by photosensitization at 355 nm in the presence of benzophenone was meassured; 1-cyanonaphthalene itself does not absorb at 355 nm. Similarly, the absorbance of the triplet transient of 1-cyanonaphthalene was measured at 500 nm in the presence of the nitrocarbazoles. Taking into account a 100% efficiency of triplet–triplet energy transfer between the triplet energy donors (benzophenone and nitrocarbazoles) and the triplet energy acceptor (1-cyanonaphthalene), a simple ratio of the absorbance values of 1-cyanonaphthalene measured at 500 nm in the presence of the nitrocarbazoles and benzophenone yields the ϕ_T values of nitrocarbazoles.

Photoacoustic measurements were performed by using a Q-switched Nd:YAG laser (Surelite II, Continuum, 7 ns FWHM) operating at the third harmonic ($\lambda = 355$ nm). The diameter of the laser beam was controlled with a focussing lens and a variable pinhole. The laser energy was attenuated using a polarizer and a half wave plate and measured with a pyroelectric detector (RjP-765, Laser Precision Corp.) using a quartz glass as beam-splitter. Sample solutions were contained in a spectrophotometric 1 cm quartz cell. For the detection of the acoustic signals two different piezoelectric transducers were used: a home-made ceramic PZT (4 × 4 mm) attached to a rear wall of the cell and a PVF_2 film of 25 μm width, attached to the bottom of the cell. In both cases the detection was perpendicular to the direction of the excitation beam. Selecting the proper value for the frequency response of the transducers and for the diameter of the beam with the lens-pinhole, the time resolution range for the acoustic measurements was 150 ns to 1.5 μs. The detected acoustic signals were amplified and processed by a storage digital oscilloscope (TDS 3032, Tektronix). Measurements were performed averaging the signals generated by 64 laser shots for better signal to noise ratio. The absorbances of the solutions were checked before and after each set of laser shots.

2-Hydroxybenzophenone was used as a calorimetric reference.[13] For the experiments, sample and reference solution concentrations were matched to absorbance values between 0.1 and 0.2 at the laser wavelength. Signals were also processed mathematically using deconvolution methods, combined with an appropriate kinetic model. Experiments were performed at open air and under controlled atmosphere, bubbling N_2 or O_2 in the solution, during 15 min.

Laser induced luminescence experiments were conducted using the same excitation set-up described for photoacoustic experiments. The spectrum emitted by the sample was recorded by means of an optical fiber attached to a cross dispersion spectrograph (Mechelle Multichannel Instruments, AB) with a CCD incorporated camera. The data was sent to a computer and processed with appropriate software that gives the whole spectra covering the 200 to 1100 nm region with a 0.3 nm spectral resolution. The emission lifetime was measured at the maximum intensity wavelength of the spectrum with a 10 ns resolution photomultiplier.

^{1}H- and ^{13}C-NMR spectra were run in dimethyl sulfoxide-d_6 at 500 MHz. Chemical shifts are reported in ppm values, using tetramethylsilane as internal standard.

Synthesis of nitrocarbazoles

Olah's method. A mixture of copper(II) nitrate trihydrate (200 mg, 0.83 mmol) and acetic anhydride (1.5 ml) was stirred at room temperature for 1.5 h. After that the carbazole (0.72 mmol) was added to the mixture, and stirring was continued for 24 h. Additional copper(II) nitrate trihydrate (100 mg, 0.83 mmol) was added, and stirring was continued for another 24 h. Then methanol (10 ml) was added. After 30 min of stirring volatiles were evaporated *in vacuo*, 20 ml of water were added to the remaining solution, and the mixture was stirred for 30 min. A pH of 14 of the aqueous solution was then set using sodium hydroxide. The aqueous solution was washed with dichloromethane (3 × 15 ml). The combined organic extracts were washed with water (100 ml), and the organic layer was dried over sodium sulfate, filtered and evaporated *in vacuo* to give a solid residue. The residue was separated by flash column chromatography with ethyl acetate–hexane mixtures as eluent.

1-Nitrocarbazole (2). Yellow needles from ethanol, mp 195 °C (lit.[11] 197–198 °C); ^{1}H NMR (dimethyl sulfoxide-d_6): δ 12.15 (br s, 1H, NH), 8.62 (d, 1 H, 4-H, $J = 7.3$ Hz), 8.41 (d, 1 H, 8-H, $J = 8.4$ Hz), 8.31 (dd, 1H, 5-H, $J = 1.1$, 7.8 Hz), 8.24 (d, 1 H,

Table 1 Spectroscopic data of carbazoles in acetonitrile at 298 K under inert atmosphere (Ar) together with the calculated spectroscopic data

Carbazole	λ_{max}(abs)/nm (ε/dm^3 mol^{-1} cm^{-1})			λ_{max}(abs)[a]/nm ($f(S_2-S_0)$[a])	$\Delta\mu$[a]/D	λ_{max}(abs)[a]/nm ($f(S_1-S_0)$[a])	$\Delta\mu$[a]/D
1	260 (90000)	292 (75000)	334 (7800)	274 (0.458)	5.17	288 (0.014)	0.93
2	290 (80000)	300 (100000)	404 (48698)	336 (0.110)	2.81	365 (0.182)	3.76
3	279 (100000)	306 (60000)	366 (45714)	321 (0.292)	2.77	326 (0.111)	2.44

[a] Calculated using the semiempirical ZINDO/S method after HF/3-21G geometrical optimization.

2-H, J = 8.0 Hz), 7.51 (dd, 1 H, 7-H, J = 7.3, 8.4 Hz), 7.35 (dd, 1 H, 3-H, J = 7.3, 8.0 Hz), 7.29 (dd, 1 H, 6-H, J = 1.1, 7.3, 7.8 Hz); ^{13}C NMR (dimethyl sulfoxide-d_6): δ 140.6 (1-C), 132.8 (4-C), 131.6 (9a-C), 130.9 (4a-C), 127.9 (3-C), 127.1 (7-C, 8a-C), 121.6 (2-C), 121.4 (4b-C), 120.5 (5-C), 118.2 (6-C), 112.6 (8-C).

3-Nitrocarbazole (3). Yellow needles from ethanol, mp 215 °C (lit.[11] 215–216 °C); ^{1}H NMR (dimethyl sulfoxide-d_6): δ 12.02 (br s, 1H, NH), 9.15 (d, 1 H, 4-H, J = 1.8 Hz), 8.36 (d, 1H, 5-H, J = 8.0 Hz), 8.29 (dd, 1 H, 2-H, J = 1.8, 8.8 Hz), 7.65–7.58 (m, 2 H, 1-H and 8-H), 8.51 (dd, 1 H, 6-H, J = 6.9, 8.0 Hz), 7.29 (dd, 1 H, 7-H, J = 6.9, 7.7 Hz); ^{13}C NMR (dimethyl sulfoxide-d_6): δ 143.1 (3-C), 140.8 (9a-C), 139.6 (8a-C), 127.3 (7-C), 122.2 (4a-C), 121.9 (4b-C), 121.1 (2-C), 120.9 (5-C), 120.0 (6-C), 116.9 (4-C), 111.7 (1-C), 110.9 (8-C).

Computational details

The ground-state geometries were optimised by *ab initio* calculations (3-21G basis at HF level; Gaussian 98). UV-absorption spectra were calculated by using the ZINDO/S (CI, 6:6) method.

Results and discussion

Absorption, fluorescence and laser flash photolysis measurements at 298 K

The absorption spectra of carbazole **1** and nitrocarbazoles **2** and **3** were recorded in acetonitrile at 298 K and showed three bands at *ca.* 270, 300 and 350 nm (Table 1).

Previously spectroscopic studies and theoretical calculations have been carried out[7,14–16] allowing for unambiguous assignment of the bands located in the 300 and 350 nm regions for carbazole derivatives as ^1L_a (S_2–S_0) and ^1L_b (S_1–S_0) electronic transitions, respectively.

Also, we observed that the absorption spectra of nitrocarbazoles **2** and **3** recorded in acetonitrile at 298 K showed a noticeable bathochromic shift of the ^1L_b band of 70 and 32 nm, respectively, compared to that of carbazole **1**, whereas the ^1L_a band showed a small bathochromic shift of *ca.* 10 nm. These red shifts are a result of the in-plane conjugation of the nitro groups bonded to the carbazole moiety and can be interpreted by the mesomeric effect induced by the nitro group. The oscillator strength $f(S_1$–$S_0)$ and $f(S_2$–$S_0)$ values and the dipole moment ($\Delta\mu$) of the ^1L_b and ^1L_a electronic transitions were calculated from the HF/3-21G optimised ground-state structures of carbazoles using the semiempirical ZINDO/S method and these values are shown in Table 1. The oscillator strength $f(S_1$–$S_0)$ associated to the ^1L_b electronic transition of nitrocarbazoles **2** and **3** are higher than that of carbazole **1** and it may be attributed to an important change in the charge transfer character in the ^1L_b electronic transition and to a noticeable increase of the transition dipole moment ($\Delta\mu$), as can be seen from the predicted ($\Delta\mu$) values of carbazoles **1**, **2** and **3** shown in Table 1. In the case of the S_2–S_0 electronic transition of the nitrocarbazoles **2** and **3** we obtained oscillator strength and transition dipole moment values lower than that of the carbazole **1**. Therefore, we concluded that a smaller change occurred in the charge transfer character in the ^1L_a electronic transition of the nitrocarbazoles **2** and **3** compared to that of the carbazole **1**.

The solvent effect on the absorption spectra of 1-nitrocarbazole and 3-nitrocarbazole was studied and the spectra obtained are shown in Fig. 1. A small bathochromic shift on going from nonpolar to polar solvents was observed. Thus, we concluded that for compounds **2** and **3** the nature of the lowest singlet excited state is most likely to be π,π^* as in the case of carbazole **1**.[7]

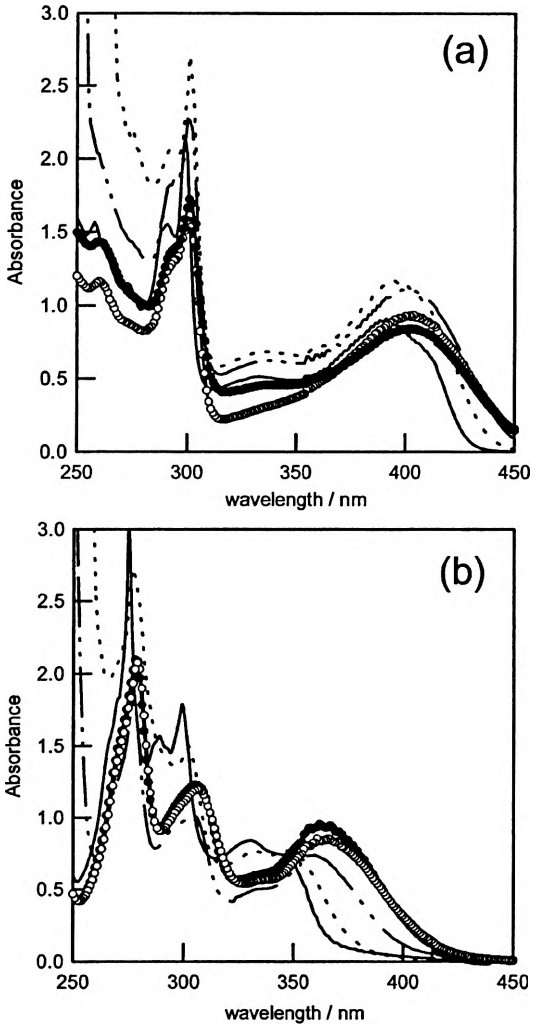


Fig. 1 Electronic absorption spectra of (a) 1-nitrocarbazole (**2**) and (b) 3-nitrocarbazole (**3**) in different solvents: (—) cyclohexane (C_6H_{12}), (· · ·) carbon tetrachloride (CCl_4), (– - -) ethyl acetate ($CH_3CO_2C_2H_5$), (○) acetonitrile (CH_3CN), (●) methanol (MeOH).

Carbazole **1** was a good fluorescent chromophore in acetonitrile at 298 K with ϕ_f = 0.62 and τ_f = 15.1 ns, whereas 1-nitrocarbazole (**2**) and 3-nitrocarbazole (**3**) did not show any fluorescent emission uner similar experimental conditions. Thus, from the electronic excited singlet state one or two radiationless deactivation processes could be operating: (i) an efficient intersystem crossing process, and/or (ii) an efficient release of heat to the medium.

We measured the intersystem crossing quantum yield (ϕ_{isc} or ϕ_T) of the nitrocarbazoles by laser flash photolysis at

Table 2 Intersystem crossing quantum yield (ϕ_T) and triplet lifetime (τ_T) of carbazoles in acetonitrile at 298 K[a]

Carbazole	ϕ_T	τ_T/ns
1	0.38[b]	–
2	0.40 ± 0.04	<10
3	0.50 ± 0.05	500

[a] Measured by laser flash photolysis at λ_{exc} 355 nm under Ar atmosphere. [b] From ref. 7.

λ = 355 nm in acetonitrile, under Ar atmosphere at 298 K. Benzophenone was selected as a reference and as a triplet energy donor, whose ϕ_T value is known (ϕ_T = 1.00).[17–19] 1-Nitrocarbazole (2) and 3-nitrocarbazole (3) were also selected as triplet energy donors whose ϕ_T values are unknown and 1-cyanonaphthalene was selected as a triplet energy acceptor for which a triplet energy value of 2.32 eV had been reported.[18] It is noteworthy to mention that the triplet–triplet energy transfer process between the donors and the acceptor occurs with a quantum efficiency of 1.[19] Table 2 shows the ϕ_T values obtained for carbazole (1), 1-nitrocarbazole (2) and 3-nitrocarbazole (3). The high ϕ_T values obtained indicates that *ca.* 50% of the initial electronic excited S_1 population is involved in the intersystem crossing process $S_1 \longrightarrow T$.

Taking into account that the nitrocarbazoles 2 and 3 are not fluorescent chromophores, the other *ca.* 50% of the absorbed photons should be released to the medium as heat through a radiationless internal conversion pathway from the S_1 state.

In order to characterise the triplet excited state of the nitrocarbazoles 2 and 3, we recorded the electronic absorption spectra of the triplet transients by laser flash photolysis at λ = 355 nm in acetonitrile, under Ar atmosphere at 298 K. Fig. 2 shows the electronic absorption spectra of the 3-nitrocarbazole (3) triplet transient.

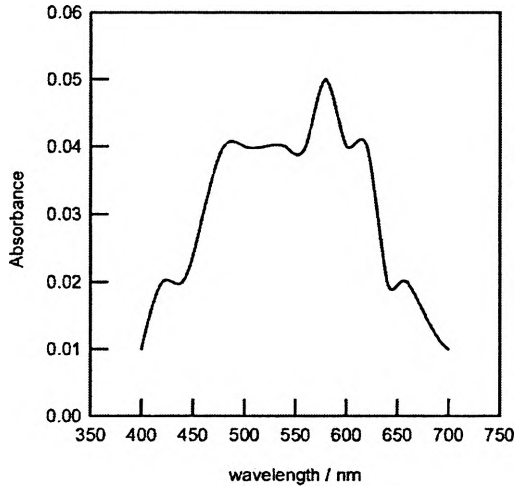


Fig. 2 Electronic absorption spectra of the triplet transient of 3-nitrocarbazole (3) obtained by laser flash photolysis. Solvent: acetonitrile; T = 298 K; atmosphere: Ar; λ_{exc} = 355 nm.

The triplet lifetime (τ_T) of 3-nitrocarbazole was also measured in similar experimental conditions at λ = 500 and 650 nm. At both absorption wavelengths, the triplet transient of 3-nitrocarbazole showed monoexponential decays giving the same τ_T value (Table 2, 500 ns). We also attempted to characterise the triplet transient of 1-nitrocarbazole (2) by laser flash photolysis experiments but no electronic absorption spectra could be detected.

Photoacoustic measurements at 298 K

The peak-to-peak amplitude of the first acoustic pulse (H) detected by the piezoelectric transducers was used to measure the prompt heat released to the medium by the sample after excitation.

Fig. 3 shows the photoacoustic signal amplitude (H) of 1-nitrocarbazole (2) and the calorimetric reference, 2-hydroxybenzophenone, as a function of the excitation fluence (F) measured in different organic solvents at 298 K. In these experiments, the sample and the reference absorbances were matched to the same value.

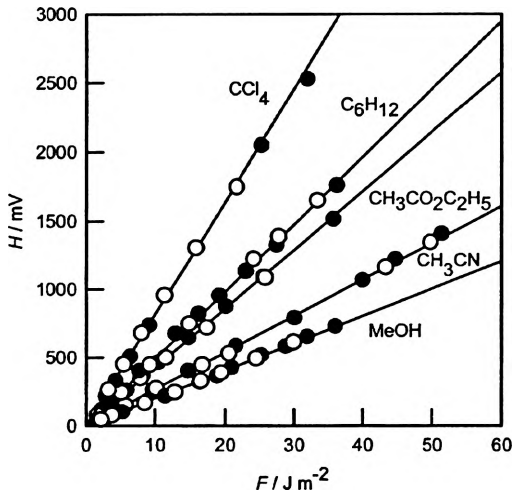


Fig. 3 Amplitude of the photoacoustic signal H as a function of the laser fluence F measured in different solvents; CCl_4 (A = 0.168), C_6H_{12} (A = 0.164), $CH_3CO_2C_2H_5$ (A = 0.151), CH_3CN (A = 0.117), MeOH (A = 0.110); τ_R = 1 μs; (●) 1-nitrocarbazole (2), (○) 2-hydroxybenzophenone (reference).

Linear correlations and good reproducibility of the experimental data were obtained in all the used solvents. No changes in the relationship between sample and reference were observed changing the resolution time of the experiments between 150 ns and 1.5 μs. As can be seen, the same slopes were obtained for the samples and the reference in all cases. These results can be interpreted in terms of the well known eqn. (1) for the photoacoustic signal amplitude:

$$H/F = Ka(1 - 10^{-A}) \quad (1)$$

where K is an experimental constant containing the thermoelastic properties of the solution and instrumental factors, A is the sample absorbance value and a is the fraction of energy released in the medium as prompt heat within the time resolution of the experiment.

Taking into account that for the calorimetric reference, 2-hydroxybenzophenone, a_R = 1 and that the measurements for sample and reference were performed in the same experimental conditions (K is a constant in eqn. (1)), the ratio of the H/F values obtained for sample and reference yields the sample a value. Thus, for the 1-nitrocarbazole (2) a = 1 was obtained when the experimental time resolution ranged from 1.5 μs to 150 ns. The same a value was obtained in the different solvents used (Fig. 3, carbon tetrachloride, cyclohexane, ethyl acetate, acetonitrile and methanol). Then, we assume that 1-nitrocarbazole (2) releases to the medium all the absorbed energy as heat in a time shorter than 150 ns. This result agrees with those obtained by laser flash photolysis experiments and suggests that the triplet transient of 1-nitrocarbazole (2) is short-lived and, after its formation, it decays to the ground state rapidly. Thus, we have roughly estimated for the triplet transient of 1-nitrocarbazole (2) a τ_T value <10 ns (the resolution limit of the laser flash photolysis experiments conducted is 10 ns).

Fig. 4 shows the photoacoustic signal amplitude (H) as a function of the excitation fluence (F) for the case of

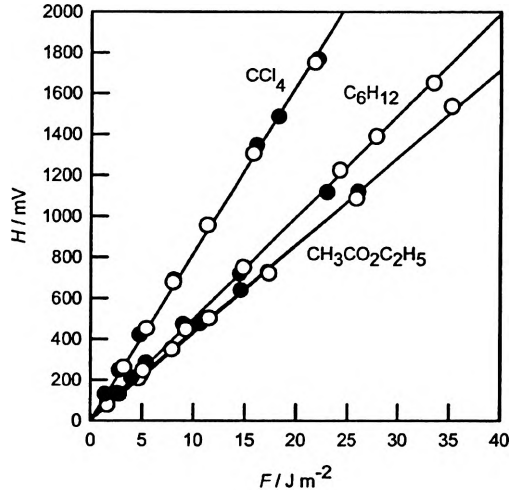


Fig. 4 Amplitude of the photoacoustic signal H as a function of the laser fluence F measured in different solvents; CCl_4 (A = 0.168), C_6H_{12} (A = 0.164), $CH_3CO_2C_2H_5$ (A = 0.151); t_R = 1 μs; (●) 3-nitrocarbazole (3), (○) 2-hydroxybenzophenone (reference).

3-nitrocarbazole (3) by using again 2-hydroxybenzophenone as reference, in cyclohexane, carbon tetrachloride and ethyl acetate solutions, at 298 K. Measurements were conducted under the same experimental conditions described for 1-nitrocarbazole (2). As can be seen, good linear correlations were obtained yielding a = 1 for the three solvents used. It was concluded that when cyclohexane, carbon tetrachloride and ethyl acetate were used as solvents (Fig. 4), 3-nitrocarbazole (3) showed a similar behavior to 1-nitrocarbazole (2) (Fig. 3) releasing to the medium all the absorbed energy as heat in a time shorter than 150 ns.

A comparative study of H as a function of F for 3-nitrocarbazole (3) and for the calorimetric reference in acetonitrile and nethanol, was conducted by using two different piezoelectric transducers. Similar behaviors were observed in both solvents. Fig. 5(a) shows the results obtained when a PVF_2 film with a resolution time (τ_R) of 150 ns was used and Fig. 5(b) shows those obtained with a PZT crystal with a resolution time of 1.5 μs. As it can be seen, in both cases the sample releases to the medium less energy as heat than the reference, showing a quite different behavior than those observed in the other solvents (Fig. 4, carbon tetrachloride, cyclohexane and ethyl acetate). Taking into account eqn. (1), a different value for the H_S/H_R ratio between sample (S) and reference (R) is obtained, depending on the resolution time of the experiment (H_S/H_R = 0.77 for τ_R = 150 ns, and H_S/H_R = 0.88 for τ_R = 1.5 μs). These results can be explained assuming that a transient species with a lifetime between 150 ns and 1.5 μs is formed and it stores part of the absorbed energy. No effect on the 3-nitrocarbazole (3) photoacoustic behavior was observed when the experiments were conducted under different atmospheres (O_2, air, N_2) (see Fig. 5). The absence of an effect due to oxygen in these measurements can be explained taking into account the short lifetime of the involved singlet and triplet states. Then, any possible quenching effect would be of low efficiency and the sensitivity of the photoacoustic method is not sufficient to detect any possible change.

In order to determine the lifetime of the transient storing species and the value of a consistent with this lifetime value, we used a deconvolution method. As it was previously demonstrated,[20,21] when the lifetime of the transient species τ is $\tau_R/5 \leq \tau \leq 5\tau_R$, the observed energy normalised acoustic wave $S(t)$ is a convolution of the system response $R(t)$ and the rate of heat evolution $q(t)$ as shown in eqn. (2):[22]

$$S(t) = H(t)/E(1 - 10^{-A}) = R(t) \oplus q(t) = \int_0^t R(u)q(t-u)\mathrm{d}u \quad (2)$$

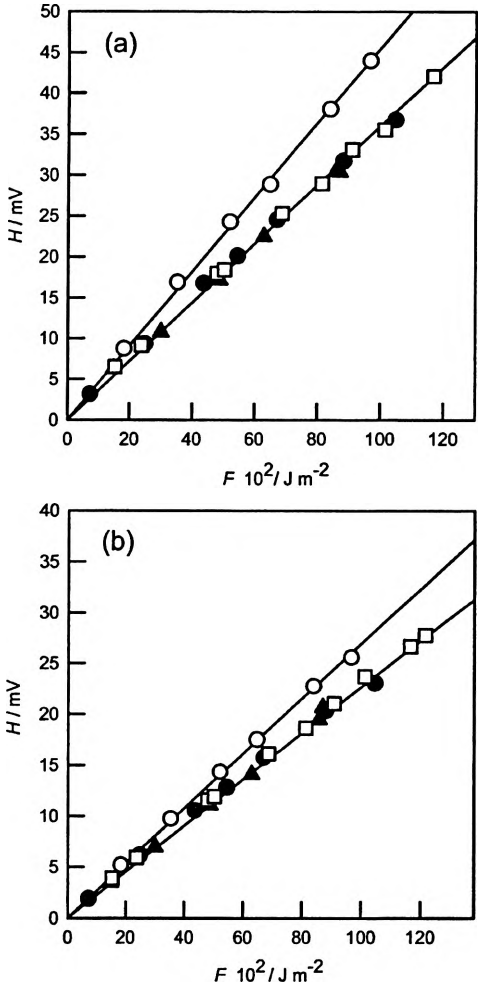


Fig. 5 Amplitude of the photoacoustic signal H as a function of the laser fluence F in acetonitrile and in methanol solutions (absorbance = 0.110); (○) 2-hydroxybenzophenone (reference), (●) 3-nitrocarbazole (3) under air atmosphere, (▲) 3-nitrocarbazole (3) under N_2 atmosphere, (□) 3-nitrocarbazole (3) under O_2 atmosphere. (a) Time resolution t_R = 150 ns, H_S/H_R = 0.77, (b) time resolution t_R = 1.5 μs, H_S/H_R = 0.88.

where $H(t)$ is the observed waveform of the sample and $R(t)$ is the system response which can be determined experimentally by using the calorimetric reference.

Assuming a kinetic decay model with a fast decay and one storing species, and performing the deconvolution by an iterative deconvolution program based on the Lavenberg–Marquardt χ^2 minimisation procedure[22] the values of τ and a can be calculated according to eqn. (3):

$$C(t) = R(t) \oplus ((a/\tau)e^{-t/\tau}) \quad (3)$$

The deconvolution method is best for treating cases where a clear phase shift between the observed waveform for the sample and reference exists. This is the case for 3-nitrocarbazole (3) in acetonitrile and in methanol solutions (see Fig. 6). Resolution of eqn. (3) by deconvolution yielded very good fits for values of τ in the range $350 \leq \tau \leq 650$ ns giving values of a in the range $0.65 \leq a \leq 0.74$. These ranges of values were obtained using sets of waveforms measured with resolution times of 150 ns (see Fig. 6), 1 μs and 1,5 μs. The range of the calculated values for the lifetime of the 3-nitrocarbazole (3) transient species (τ) is in complete agreement with the triplet state value τ_T = 500 ns determined by laser flash photolysis experiments (see Table 2).

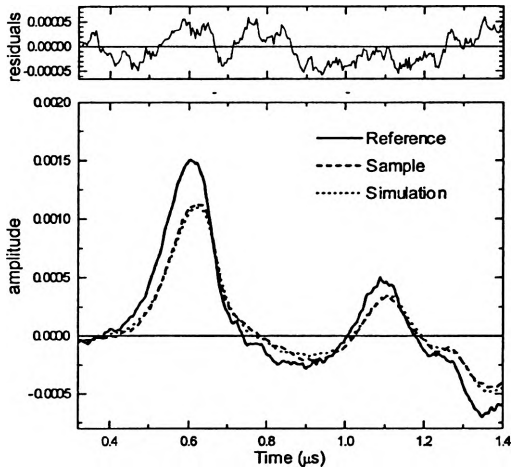


Fig. 6 Acoustic waveforms for 3-nitrocarbazole (**3**) (sample) and 2-hydroxybenzophenone (reference) measured with a piezoelectric PVF_2 film in acetonitrile. Simulation is the best-fit convolution according to eqn. (3). Residuals of the fit are also shown.

A simple energy balance equation[23] can be used to estimate a range for the energy content of the triplet state ($\Delta E(T_1–S_0)$) of 3-nitrocarbazole (**3**) in acetonitrile and in methanol, taking into account that this compound did not show any fluorescence at 298 K:

$$\Delta E(T_1–S_0) = ((1 - a)/\phi_T)E_a \qquad (4)$$

where $\phi_T = 0.50 \pm 0.05$ (see Table 2) is the quantum yield of the triplet formation determined by laser flash photolysis (298 K); the range $0.65 \leq a \leq 0.74$ was determined by photoacoustic measurements and E_a is the absorbed energy at $\lambda = 355$ nm. From eqn. (4) we calculated that, at 298 K, the energy content of the triplet state of 3-nitrocarbazole (**3**) is in the range 1.7 eV $\leq \Delta E(T_1–S_0) \leq 2.8$ eV, leading to a phosphorescence maximum emission in the range $450 \leq \lambda_p(\max) \leq 750$ nm.

Phosphorescence measurements at 77 K

The phosphorescence spectrum of 1-nitrocarbazole (**2**) and 3-nitrocarbazole (**3**) were measured in isopropanol–diethyl ether (1 : 1, v/v) at 77 K. These compounds exhibited structured phosphorescence emission spectra with excitation into the S_1 level (see Fig. 7).

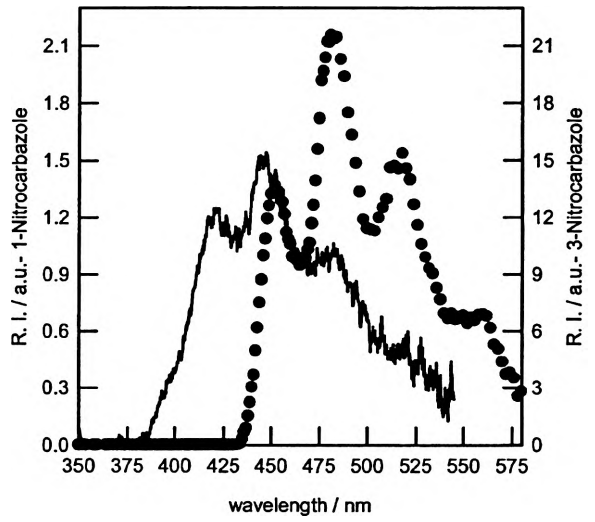


Fig. 7 Phosphorescence spectra of 1-nitrocarbazole (**2**) (—) and 3-nitrocarbazole (**3**) (●) in isopropanol–diethyl ether (1 : 1, v/v) at 77 K.

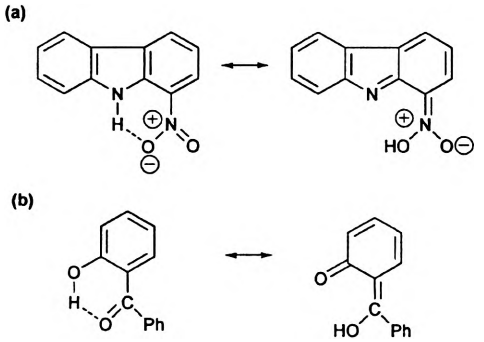
It is interesting to note that the shape and the intensity of both phosphorescence spectra are very similar showing three broad bands which are quite different than those observed for carbazole.[7] Moreover, the structure and the shape of the phosphorescence spectra of compounds **2** and **3** resemble that of the "benzophenone-like" molecules.[9] The experimentally obtained highest relative intensity radiative triplet transition ($\lambda_p(\max)$) of the nitrocarbazoles **2** and **3** are shown in Table 3 together with that of carbazole **1**.

Comparing these data, a noticeable red shift of the $\lambda_p(\max)$ is observed for compounds **2** and **3** which is due to the important mesomeric effect of the nitro group, a strong electron withdrawing substituent group, on the lowest triplet excited state. For 3-nitrocarbazole (**3**) the $\lambda_p(\max) = 480$ nm measured in this experiment ($T = 77$ K), fit in the $\lambda_p(\max)$ range predicted by eqn. (4), where data obtained in photoacoustic and laser flash photolysis experiments ($T = 298$ K), are used (see Discussion section above). It is interesting to point out that due to the influence of the solvent, a red Stokes shift for $\lambda_p(\max)$ can be expected, when the temperature is increased from low values (77 K) to 298 K. Thus, at 298 K the $\Delta E(T_1–S_0)$ value of 2.6 eV would be the upper limit for the energy content of the lower excited triplet state of 3-nitrocarbazole (**3**).

We also measured the phosphorescence lifetime (τ_p) and the phosphorescence quantum yields (ϕ_p) of nitrocarbazoles **2** and **3** in solid matrices at 77 K and the values obtained are shown in Table 3. Therefore, the dynamic properties of the lowest triplet excited states of these compounds were easily calculated and the photophysical parameters obtained, k°_p and k_{nr}, are also shown in Table 3. Finally, the calculated values for the oscillator strength $f(T_1–S_0) = 1.5k^\circ_p\nu^{-2}$, where ν is the wavenumber of the phosphorescence emission, are also included.

At 77 K the deactivation processes of the triplet state (T_1) of carbazole **1**, 1-nitrocarbazole **2** and 3-nitrocarbazole **3** are different. As shown in Table 3, the ϕ_p value of **3** is double (0.47) that of carbazole (0.24) which reflects a greater efficiency of emission from T_1. Thus, the k°_p value accounts for this behaviour and the lowest triplet excited state deactivates preferentially through the phosphorescence emission process while the radiationless process (k_{nr}) occurs competitively to a lesser extent. For 1-nitrocarbazole **2**, the phosphorescence quantum yield (ϕ_p) is very low (0.04) and hence, the deactivation process of the T_1 state occurs preferentially through a radiationless pathway, as can be seen from the k_{nr} value.

This particular behavior observed for the 1-nitrocarbazole **2** can be rationalized as follows. The nitro group is attached to the *ortho* position of the carbazole moiety (C-1) and it is spatially vicinal to the N–H group. Therefore, an intramolecular hydrogen bond is easily formed between the nitro group and the N–H group of compound **2** as shown in Scheme 2(a). The optimized geometry obtained at the HF/3-21G level clearly shows that this



Scheme 2 (a) Intramolecular hydrogen bonding of 1-nitrocarbazole in the ground state (shown left) as the origin of a probable keto-like structure (shown in the right) and a keto–enol-like equilibrium of 1-nitrocarbazole in the electronic excited state. (b) The well known keto–enol-like equilibrium of 2-hydroxybenzophenone.

Table 3 Spectroscopic data and photophysical rate parameters of carbazoles in solid matrices at 77 K

Carbazole	λ_p(max)[a]/nm	$f(T_1-S_0)$[b]	ϕ_p	τ_p/s	k°_p[c]/s^{-1}	k_{nr}[d]/s^{-1}
1	406	1.36×10^{-9}	0.24	7.73	0.055	0.074
2	450	0.53×10^{-9}	0.04	9.0×10^{-4}	105.8	1005.3
3	480	4.0×10^{-9}	0.47	0.159	5.68	0.61

[a] λ_p(max) = λ value at highest relative intensity. [b] Calculated according to the following equation: $f(T_1-S_0) = 1.5k^\circ_p\nu^{-2}$, where ν is the wavenumber of the phosphorescence emission. [c] $k^\circ_p = \phi_p k_p/\phi_p$ [d] $k_{nr} = k_p - k^\circ_p$, where $k_p = \tau_p^{-1}$.

hydrogen bond is possible because of the distance between the involved groups (*ca.* 2.4 Å). This out-of-plane fixed position of the nitro group with respect to the plane of the carbazole moiety could cause the triplet excited state to favour radiationless decay over the competitive phosphorescence emission during its short phosphorescence lifetime (τ_p = 900 μs). This intramolecular hydrogen bond is similar to the well known 2-hydroxybenzophenone intramolecular hydrogen bond and both would be operating, in the electronic excited state, in a similar manner. In Scheme 2 the keto–enol-like equilibrium for 1-nitrocarbazole **2** (a) and for 2-hydroxybenzophenone (b) are represented in a comparative manner. Of course, this intramolecular hydrogen bond is not possible for 3-nitrocarbazole **3** since the nitro group is attached to a different position of the carbazole moiety (C-3).

It is known that oscillator strength $f(T_1-S_0)$ values ranging from 10^{-5}–10^{-9} are characteristic of spin forbidden transitions.[9] Furthermore, electronic transitions of the type T_1 (n, π*) ⟶ S_0 show $f(T_1-S_0)$ values which lie between 10^{-7} and 10^{-8}, k°_p values greater than 1 s^{-1} and k_{isc} values in the range 10^{10}–10^{11} s^{-1}. Organic molecules which show these spectroscopic and photophysical parameters are classified as "benzophenone-like" molecules.[9] It is interesting to mention that the shape and the intensity of the bands in the phosphorescence spectrum is another feature to be taken into account.[9]

As a consequence the comparative analysis of the photophysical parameters (k°_p and τ_p), the shape of the phosphorescence spectra and the oscillator strength values ($f(T_1-S_0)$) allow us to conclude that the lowest triplet excited state of 1-nitrocarbazole **2** and 3-nitrocarbazole **3** is an n,π* electronic state. On the contrary the same analysis for carbazole **1** suggests that the lowest triplet excited state is a π,π* electronic state.

Laser induced luminescence measurements at 298 K

During laser induced optoacoustic experiments (λ_{exc} = 355 nm) in acetonitrile solution at 298 K, the nitrocarbazoles **2** and **3** showed a weak luminescence emission. This luminescence was not observed under the same experimental conditions with carbazole **1**. The spectra registered for both compounds, desplayed in Fig. 8, were measured at the same value of solution absorbance. As can be seen, they are quite similar, with a broad band ranging from 500 to 800 nm with λ_{max} centered at 570 nm. No luminescence emission spectrum of 3-nitrocarbazole (**3**) in cyclohexane, ethyl acetate, carbon tetrachloride or methanol solution was detected. 1-Nitrocarbazole **2** showed the same behavior except for weak luminescence emission in ethyl acetate. This latter spectrum was similar in shape and λ_{max} as that obtained in acetonitrile solution.

Experiments were repeated several times with fresh solutions in purified acetonitrile.[12] The carbazole **1** and the nitrocarbazoles **2** and **3** used were recrystallized, fully characterized and purity carefully controlled by chromatographic methods (see details in the Experimental section).

By adding small amounts of methanol to acetonitrile solutions of compounds **2** and **3** quenching of the luminescence was observed in agreement with the result obtained in methanol solution.

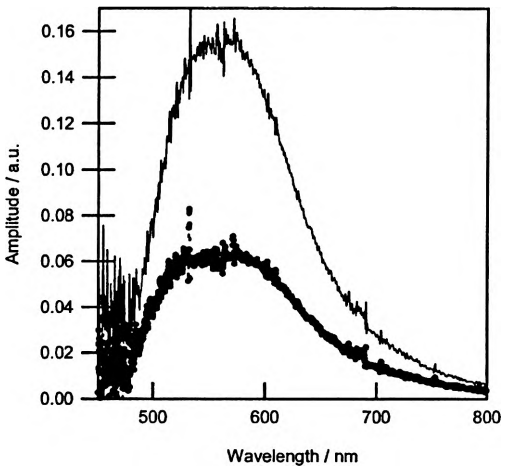


Fig. 8 Laser induced luminescence spectra of 1-nitrocarbazole (**2**) (—) and 3-nitrocarbazole (**3**) (●) obtained using solutions with the same absorbance. Solvent: acetonitrile: λ_{exc} = 355 nm.

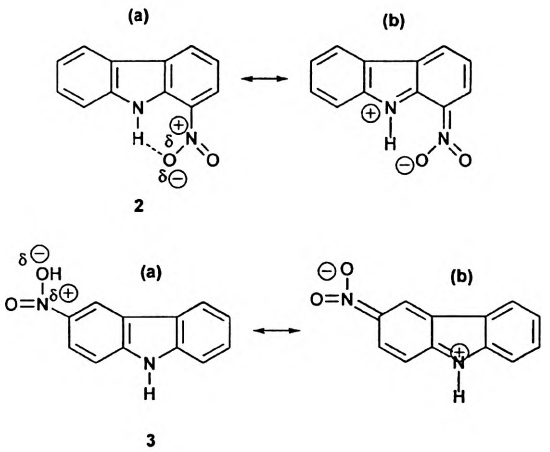
Quantum yield values $\phi_L \leq 10^{-3}$ for the luminescence of nitrocarbazoles **2** and **3** in acetonitrile were estimated, using Cresyl Violet as a fluorescent reference. The same ϕ_L values were estimated under air or N_2 atmosphere.

Experiments were also performed to measure the lifetime of the luminescent species. In all the cases the decay value measured was limited by the resolution time of the detection system used. The lifetime of the luminescent species for compounds **2** and **3** was estimated as <10 ns.

As to the origin of the luminescence observed for compounds **2** and **3** at 298 K, the following considerations must be taken into account: the fluorescent process S_1 ⟶ S_0 can be discarded owing to that in the same solvent, the λ_{max} of the luminescence emission is located *ca.* 300 nm away (red shifted) from the location of the corresponding λ_{max} in the absorption spectrum. The radiative process S_2 ⟶ S_1 can also be discounted as being responsible for the luminescence because under our experimental conditions, λ_{exc} = 355 nm, population of the upper state, S_2, from the energetic point of view is not possible. On the other hand, if we assume that triplet states are involved in this luminescence process (T_n ⟶ T), the heavy atom effect (HAE) should be observed.[9,10] The fact that any luminescence was observed when experiments were conducted in carbon tetrachloride solution, strongly suggests that triplet states would not be involved in these radiative processes. This suggestion is also supported by the estimated lifetime of the luminescent excited states of compounds **2** and **3** (<10 ns) and the fact that these luminescence emissions were observed for both compounds in solution, at 298 K. By the same reason, the radiative process T_1 ⟶ S_0 (phosphorescence) as well as a delayed fluorescence process can be discarded as the mechanisms accounting for the observed luminescences at room temperature. On the other hand, for compound **2** the value of its T_1 lifetime (τ_T) is of similar magnitude or lower than the laser pulse duration (τ_{exc}). For compound **3** τ_T is *ca.* 50 times higher than τ_{exc}. Thus, the radiative emission process T_2 ⟶ T_1, after population of T_2 by absorption of photons at λ = 355 nm, through a T_1 ⟶ T_2 process, can be also discarded. If these processes were the cause of the observed

luminescences, the relative intensity of the 3-nitrocarbazole (3) emission would be higher than that of 1-nitrocarbazole (2), in contrast to the results shown in Fig. 8.

The above considerations suggest that the luminescence observed for compounds 2 and 3 in solution at 298 K, are radiative $S_{1R} \longrightarrow S_0$ processes where S_0 is the ground state of the intact nitrocarbazole compounds and S_{1R} is the lowest singlet excited state of one of the resonance hybrid structures of the same compound whose tentative structure is shown in the Scheme 3. The high permanent dipole created on going from structure (a) to structure (b), would account for the fact that this very low efficiency process is observed only in a highly polar non-protic solvent such as acetonitrile, while methanol quenches it completely because of its protic character. The lack of luminescence in cyclohexane and in carbon tetrachloride solution as well as the very poor luminescence observed in ethyl acetate (for compound 2) support the highly polar structures asigned to the luminescent species (Scheme 3, (b)). Furthermore, this result agrees with the fact that the polar character is higher for compound 3 than for compound 2 (Scheme 3, compare structures (b) for compounds 2 and 3). The above mentioned lack of emission in methanol solution as well as the quenching of the luminescence of nitrocarbazoles 2 and 3 in acetonitrile solution when methanol was added, would account for the very low efficiency photochemical reduction of nitroaromatic compounds in alcoholic–acid mixtures described in the literature.[24,25]



Scheme 3 Structures of nitrocarbazoles 2 and 3 (shown left; structures (a)) and structures of one the corresponding resonance hybrids (shown right; structures (b)).

Finally, it is important to note that due to the extremely low quantum yield of the luminescence emission and its high λ_{max} value, it does not affect too much the results obtained in the present work, particularly those obtained by optoacoustic experiments.

Conclusions

The results obtained in the present work clearly show that the nitro group attached to the carbazole moiety induces changes in the photophysical behavior of the nitrocarbazoles 2 and 3 compared to that of carbazole 1. These results also show that not only the presence of the nitro group itself modifies the photophysical behavior of the nitrocarbazole but the substituent effect depends also on the location of the nitro group in the carbazole ring.

Thus, after excitation of the nitrocarbazoles 2, 3 and carbazole 1 with UV radiation (λ_{exc} = 355 nm) in acetonitrile solution, the lowest singlet excited state S_1 likely of π,π^* nature, is populated (Table 1). From the S_1 state of compounds 1–3, intersystem crossing process $S_1 \longrightarrow T_1$ takes place with an efficiency of *ca.* 50% (Table 2). While in compound 1 the remaining 50% of the absorbed energy is re-emitted as fluorescence, in the case of compounds 2 and 3, the mechanism is a radiationless internal conversion pathway to the S_0 state. From the T_1 state, compound 1 deactivates by phosphorescence and heat through processes of similar efficiency (Table 3, compound 1, $k^o_p = 0.055\ s^{-1}$ and $k_{nr} = 0.074\ s^{-1}$). In the case of nitrocarbazoles 2 and 3 the energy is released to the medium through both processes, but with different efficiency (see Table 3).

The measured lifetime of the lowest triplet state of 3-nitrocarbazole 3 (τ_T = 500 ns) is *ca.* 50 times higher than that of 1-nitrocarbazole 2 (<10 ns). This difference is due to the different location of the nitro group as substituent in the carbazole moiety, that allows the formation of an intramolecular hydrogen bond only in compound 2. As shown in Scheme 2, this structural characteristic allows compound 2 to show a keto–enol-like equilibrium similar to that for benzophenone. Then, it is easy rationalized, as for 2-hydroxybenzophenone, that the preferential deactivation pathway for the T_1 state of compound 2 is through radiationless mechanisms. On the contrary, as is shown in Tables 2 and 3, and in Figs. 3 and 7, for the T_1 state of the 3-nitrocarbazole 3, radiative deactivation through phosphorescence emission is a quite efficient process.

Finally the presence of the nitro group in the carbazole moiety would account for the low efficiency luminescence observed in acetonitrile solutions of compounds 2 and 3 at room temperature (298 K) and the absence of luminescence for carbazole 1 under the same experimental conditions. As shown in Scheme 3, for compounds 2 and 3, the formation of a singlet excited state with the structure of a resonance hybrid with highly polar character explains the results obatined in organic solvents with different polar and protic character.

Acknowledgements

This project was partially financially supported by UBA (X027) and CONICET (PIP 904/98 and PIP1060). We thank Dr F. Quina (Federal University of San Pablo, Brasil) for the use of the Edinburgh OB900 fluorometer, the Hitachi F-500 spectrofluorometer and his generous hospitality. R. E. B. and S. M. B. are research members of CONICET. G. M. B. is a research member of CIC and UNLP, and M. M. has a fellowship from CIC.

References

1 M. C. Biondic and R. Erra-Balsells, Photochemical behavior of β-carbolines. Part 4. Acid-base equilibria in the ground and excited states in organic media, *J. Chem. Soc., Perkin Trans. 2*, 1997, 1323–1328.

2 M. C. Biondic and R. Erra-Balsells, Photochemical behaviour of β-carbolines. Part 5. Ground and excited state interactions between nor-harmane and harmane with alcohols and ethers, *J. Chem. Res., (S)*, 1998, 114–115.

3 S. M. Bonesi and R. Erra-Balsells, Product Study of the Photolysis of N-Acetyl Carbazole in Ethanol and in Dichloromethane Solution. I, *J. Photochem. Photobiol., A: Chem.*, 1991, **56**, 55–72.

4 S. M. Bonesi and R. Erra-Balsells, Outer-Sphere Electron Transfer from Carbazoles to Halomethanes. Reduction Potentials of Halomethanes Measured by Fluorescence Quenching Experiments, *J. Chem. Soc., Perkin Trans. 2*, 2000, 1583–1595.

5 H. Nonami, S. Fukui and R. Erra-Balsells, β-Carboline Alkaloids as Matrices for Matrix-assisted Ultraviolet Laser Desorption Time-of-flight Mass Spectrometry of Proteins and Sulfated Oligosaccharides: A Comparative Study Using Phenylcarbonyl Compounds, Carbazoles and Classical Matrices, *J. Mass Spectrom.*, 1997, **32**, 287–296.

6 H. Nonami, K. Tanaka, Y. Fukuyama and R. Erra-Balsells, β-Carboline Alkaloids as Matrices for UV-Matrix-assisted Laser Desorption/Ionization Time-of-flight Mass Spectrometry in Positive and Negative Ion Modes. Analysis of Proteins of High Molecular Mass, and of Cyclic and Acyclic Oligosaccharides, *Rapid Commun. Mass Spectrom.*, 1998, **12**, 285–296.

7 S. M. Bonesi and R. Erra-Balsells, Electronic spectroscopy of carbazole and N- and C-substituted carbazole in homogeneous media and in solid matrix, *J. Lumin.*, 2001, **93**, 51–74.
8 S. M. Bonesi and R. Erra-Balsells, Electronic spectroscopy of N- and C-substituted chlorocarbazoles in homogeneous media and in solid matrix, *J. Lumin.*, 2002, **97**, 83–101.
9 N. J. Turro, *Modern Molecular Photochemistry*, The Benjamin Cummings Publishing Company, Inc., CA, 1978.
10 J. B. Birks, *Photophysics of Aromatic Molecules*, Wiley Interscience, New York, 1970.
11 M. A. Ponce and R. Erra-Balsells, Synthesis and Isolation of Nitro-β-carbolines Obtained by Nitration of β-Carboline Alkaloids, *J. Heterocycl. Chem.*, 2001, **38**, 1071–1082.
12 D. D. Perrin and W. L. F. Amarego, in *Purification of Laboratory Chemicals*, Pergamon Press, New York, 3rd edn., 1988.
13 Ph. Van Haver, L. Viaene, M. Van der Auweraes and F. C. De Schyver, References for laser-induced optoacoustic spectroscopy using UV excitation, *J. Photochem. Photobiol., A: Chem.*, 1990, **63**, 265–277.
14 N. Mataga, Y. Toriashi and K. Ezumi, Electronic structure of carbazole and indole, and the solvent effects on the electronic spectra, *Theor. Chim. Acta*, 1964, **2**, 158–167.
15 J. R. Huber and J. E. Adams, Effect of the molecular geometry on the electronic structure of aromatic amines. Diphenylamine, iminodibenzyl, acridan and carbazole, *Ber. Bunsenges. Phys. Chem.*, 1974, **78**, 217–233.
16 S. C. Chakravorty and S. C. Ganguly, Polarized absorption spectra of carbazole single crystal, *J. Chem. Phys.*, 1970, **52**, 2760–2762.
17 S. P. Mc Glyn, T. Azumi and M. Kinoshita, in *Molecular Spectroscopy of the Triplet State*, Prentice – Hall Inc., Englewood Cliff, New York, 1969, ch. 6, p. 251.
18 S. L. Murov, I. Carmicheal and G. L. Hug, in *Handbook of Photochemistry*, Marcel Dekker Inc., New York, 2nd edn., 1993.
19 K. Snadros, Transfer of triplet state energy in fluid solutions, *Acta Chem. Scand.*, 1969, **23**, 2815–2829.
20 M. Terazima and T. Azumi, A time-resolved photoacoustic method widht pulsed laser excitation in the condensed phase: the relation between signal intensity and decay-rate constant, *Bull. Chem. Soc. Jpn.*, 1990, **63**, 741–745.
21 C. Martí, O. Jurgens, O. Cuenca, M. Casals and S. Nonell, Aromatic ketones as standards for singlet molecular oxygen photosensitization. Time resolved photoacoustic and near-IR emission studies, *J. Photochem. Photobiol., A: Chem.*, 1996, **97**, 11–18.
22 J. R. Small, L. J. Libertini and E. W. Small, Analysis of photoacoustic waveforms using the nonlinear least squares method, *Biophys. Chem.*, 1992, **42**, 29–48.
23 S. E. Braslavsky and G. E. Heibel, Time resolved photothermal and photoacoustic methods applied to photoinduced processes in solution, *Chem. Rev.*, 1992, **92**, 1381–1410.
24 W. Trotter and A. C. Testa, Photoreduction of 1-nitronaphthalene by protonation in the excited state, *J. Phys. Chem.*, 1970, **74**, 845–847.
25 A. Cu and A. C. Testa, Photochemistry of the nitro group in aromatic heterocyclic molecules, *J. Phys. Chem.*, 1975, **79**, 644–646.

Láseres de Colorante

Los láseres de colorantes orgánicos en solución fueron desarrollados a principios de la década del 70 y se convirtieron en un tema de gran atracción para los investigadores en física del láser a nivel mundial por varios motivos: la complejidad de su cinética de población, su capacidad de sintonía continua de emisión, posibilidad de generar trenes de pulsos ultracortos de luz (picosegundos) y utilidad como absorbente saturable (mode-locking-pasivo). Se excitan ópticamente, pues sus bandas de caen en el UV-azul del espectro, mientras que las de emisión cubren el rango 450 850 nm, dependiendo de la molécula.

El primer láser de colorante en el CIOp funcionó hacia fines de los 70 excitado con el láser de N2 construido también en el Centro. Al poco tiempo se incorporó un láser de colorante comercial sintonizable, bombeado por un láser de Argón.

Una de las complejidades de los mecanismos de excitación de estas moléculas es la generación de una especie transiente, inducida por absorción de la radiación de bombeo (fotoisómero), que puede retroisomerizar a su especie original.

El primer trabajo seleccionado trata sobre la cinética de isomerización de colorantes de la familia de las cianinas (DODCI), utilizando técnicas de fluorescencia y absorción. Se estableció la relación entre la población del fotoisómero y del estado normal en función de parámetros como la fluencia de excitación, temperatura, etc

El segundo trabajo seleccionado avanza sobre el estudio de la retroisomerización del mismo colorante, estableciendo la cinética del fenómeno a partir de procesos radiativos y no radiativos internos.

Dye Lasers

Organic dye lasers in solution were developed at the beginning of the 70´s and were immediately studied worldwide mainly because its tunable emission in the visible, the possibility of making ultrashort laser pulses, the complexity of its population inversion kinetics and its use as saturable absorbers for passive mode locking. In general, the molecule has absorption bands in the UV-visible region and , when excited optically, they emit in the 450-850 nm range, depending on the specific molecule and solvent.

The first dye laser at CIOp worked by the end of the 70´s, excited by the N2 cross-field laser mentioned in the Gas Lasers section. Shortly after, a commercial tunable Ar laser-pumped CW dye laser was acquired, starting a new modern research lines in Laser Spectroscopy.

One of the complexities in the population kinetics of dyes deals with the generation of a transient species induced by the pump photons (photoisomer) that can change back to the original species (backisomerization).

The first selected paper in this section deals with the isomerization kinetics of cyanine dyes (specifically the 3-3´diethyl-oxa-dicarbocianine iodide, shortly known as DODCI), using fluorescence and absorption techniques. A relation between ground state population of normal and photoisomer species and excitation fluence was found.

The second selected paper deals with the determination of the backisomerization rate and the description of the isomerization kinetics based on radiative and non radiative energy level processes.

e)- 7)-

BACK ISOMERIZATION FROM THE EXCITED STATE PHOTOISOMER OF THE LASER DYE 3,3'-DIETHYLOXADICARBOCYANINE IODIDE (DODCI)

Lucía SCAFFARDI, Gabriel M. BILMES, Daniel SCHINCA and Jorge O. TOCHO
Centro de Investigaciones Opticas (CIOp), Comisión de Investigaciones Científicas de la Provincia de Buenos Aires (CIC), Casilla de Correo 124, 1900 La Plata, Argentina

Received 1 May 1987; in final form 14 August 1987

The fluorescence of the first excited state of both the normal (N) and the photoisomer (P) forms of 3,3'-diethyloxadicarbocyanine iodide (DODCI) were analyzed under steady state conditions. Argon ion laser and argon ion pumped dye laser were used for excitation. The long wavelength fluorescence, belonging mainly to the P form, shows a similar degree of polarization as the short wavelength part arising from the N form. The fluorescence spectra of DODCI at different fluences and different wavelengths of laser excitation yielded information about the relative concentrations of the N and P forms. Photoequilibrium between the two species via the excited state of the P form is postulated. The rate constant estimated for the $P^* \rightarrow N$ transition is much lower than the one expected from a model of a twisted state through which all the non-radiative transitions of the P form take place. The value is in agreement with that derived from the previous optoacoustic measurements exciting with higher fluences. The results indicate that stimulated emission and excited state absorption are not important under the conditions of the experiment.

1. Introduction

The study of the photophysics of cyanine dyes has received a great deal of attention in recent years. The main reasons are, on the one hand, their technological use as laser materials or saturable absorbers for mode-locking [1] and, on the other hand, their structural similarity to a variety of natural photobiological systems with polyene structures [2]. 3,3'-diethyloxadicarbocyanine iodide (DODCI) is one of the most extensively studied compounds belonging to this group. The knowledge of its behaviour under high-fluence laser excitation is nowadays of great interest because of its fundamental role in the production of femtosecond optical pulses using the colliding pulse technique [3].

The existence of the DODCI photoisomer (P) transient species produced after singlet excitation of the stable form (N), was established by Dempster et al. [4] by laser flash photolysis. The ground state absorption of P and the isomerization quantum yield were measured and different kinetics parameters, such as excited state lifetime for both forms and fluorescence quantum yield of P were calculated. Afterwards, the photoisomerization process has been studied by several groups. As a result of these studies a consistent model for the isomerization mechanism is well established [5,6].

The values of the kinetic parameters of the N form given by Dempster et al. [4] have been confirmed by direct measurements using picosecond pulse excitation [7–9], but only few studies have dealt with the photophysical properties of the P form.

The present paper is concerned with the photophysical processes undergone by excited P. We present the results of the laser power dependent fluorescence spectra of DODCI under steady state conditions. Polarization of the fluorescence has been taken into account in the measurements, avoiding instrumental artifacts arising from the emission anisotropy of the fluorophores.

2. Experimental

3,3'-diethyloxadicarbocyanine iodide (DODCI) laser dye grade from Kodak was used without further purification. The purity of the dye was checked by thin-layer chromatography on silica plates with dif-

0 009-2614/87/$ 03.50 © Elsevier Science Publishers B.V.
(North-Holland Physics Publishing Division)

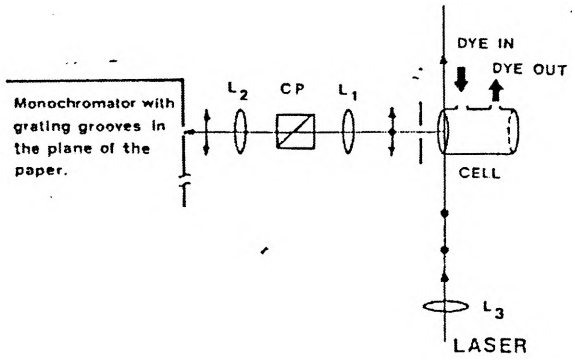


Fig. 1. The experimental apparatus used. Laser is argon ion laser or argon-ion-pumped dye laser. Polarization directions are indicated by dots (•) and double arrows (↕). The focal length of L_3 was 67 mm, while L_1 and L_2 were arranged to focus the fluorescence on the monochromator slit and to illuminate the crystal polarizer CP with low divergence.

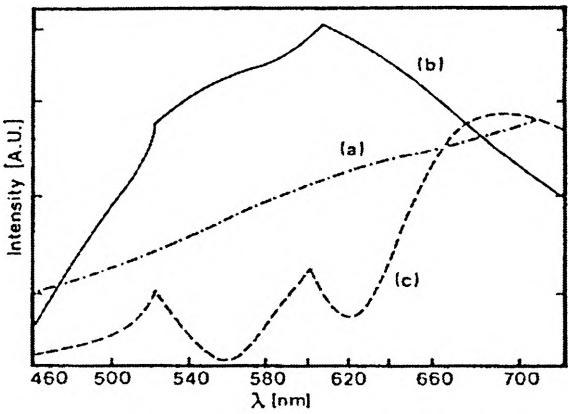


Fig. 2. Calibration of the detection system. (a) is the calibration lamp spectrum, (b) is the response of the system for polarization parallel to the grating grooves and (c) is the response for polarization perpendicular to the grating grooves.

ferent solvents. 10^{-6} M solutions in ethanol (Carlo Erba PA) were used immediately after preparation. The solution was circulated at low rate in a cylindrical optical glass cell (2 cm diameter flat windows, 5 cm length). The excitation light from a cw dye laser tunable between 580 and 620 nm (Spectra Physics 375 with rhodamine 6G) pumped by argon ion laser (SP 165), was focused on the cell by a planoconvex lens (f=67 mm). The excitation beam passed through the cell as near as possible to the observation window to avoid inner filter effects.

The fluorescence was detected at 90° with respect to the direction of the excitation beam. The polarization of the pumping beam was perpendicular to the plane defined by the direction of incidence of the excitation beam and the direction of observation of the fluorescence (fig. 1). Some measurements were carried out by exciting the sample with the most intense lines of the argon ion laser (488 and 514 nm), keeping the same polarization direction.

The spectra were recorded using a 50 cm focal length Ebert mount scanning spectrometer (Jarrell-Ash 82-025) equipped with a Hamamatsu R-466 multialkali photomultiplier connected to a boxcar integrator (PAR 162/163) triggered internally at 1 kHz. The signals were plotted on an X–Y recorder.

The power was varied by changing the current in the ion pump laser, or by attenuating the dye laser beam on the cell with neutral density filters in the low power region, keeping the laser stabilized well over the threshold. The diameter of the spot on the sample was 50 μm as determined by calibrated pinholes. The viewing angle of the fluorescence was properly selected by an iris placed in front of the cell and by the monochromator slit height (5 mm).

It is well known that the response function of a monochromator–photomultiplier system can differ significantly for polarization parallel or perpendicular to the grating grooves [8]. The system was calibrated by use of a standard tungsten lamp. The spectrum of the lamp (a), and the signals registered by the system for polarization parallel (b) and perpendicular (c) to the grating grooves are shown in fig. 2. From these data, the factors to correct the fluorescence spectra taken under controlled polarization conditions are calculated. Due to the smooth dependence of the detection system (fig. 2) for the parallel to the grating grooves polarization, all the spectra were obtained under these conditions. The emission polarization was selected perpendicular to the excitation polarization by means of a crystal polarizer, CP in fig. 1.

3. Results

The fluorescence spectra of DODCI exhibited a strong dependence with both the fluence and the wavelength of the laser excitation. Typical fluorescence spectra excited at 514 and 609 nm with dif-

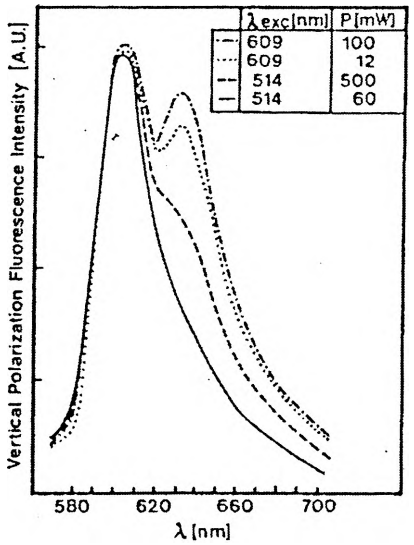


Fig. 3. Typical fluorescence spectra of DODCI with different power and wavelengths laser excitation as indicated. The excitation spot diameter was 50 μm. The spectra are corrected from the technical spectra using the factors taken from fig. 2 for polarization parallel to the grating grooves.

ferent laser powers are shown in fig. 3. The emission intensity is normalized at 595 nm. A laser power of 100 mW corresponds to a fluence of 1.2 kW/cm^2. As the pump power increases, the red fluorescence peak appears and grows in intensity.

The spectra were studied as a function of the rate of ground state absorption by P, $b=a\sigma^P$, where σ^P is the absorption cross section of the P form and a is the photon fluence rate of the excitation. By varying the power and the wavelength of the excitation, the value of b was changed over more than three orders of magnitude. The fluorescence intensities in W cm^{-2} nm^{-1}, I_{640} and I_{603} at 640 and 603 nm respectively, were selected as representative of the P* and N* emission. These wavelengths correspond to the emission peaks of both species [9]. The ratios between the two intensities, I_{640}/I_{603} for different values of b are given in table 1.

Due to the emission polarizer only a fraction of the emitted intensity was detected. The fraction emitted with polarization perpendicular to the polarization direction of the excitation is given by $\frac{1}{2}(1-p)$, where p is the degree of polarization defined as $p=(I_\parallel - I_\perp)/(I_\parallel + I_\perp)$. The degree of polarization for the DODCI normal form p_N was measured at low

Table 1

b (ns^{-1})	$I_{640\,nm}/I_{603\,nm}$	Excitation	
		λ (nm)	P (mW)
10^{-6}	0.31	514	5
1.2×10^{-5}	0.37	514	60
2.4×10^{-5}	0.45	514	120
2.5×10^{-5}	0.44	600	0.6
5×10^{-5}	0.47	514	250
10^{-4}	0.57	514	500
3×10^{-4}	0.64	600	6
6×10^{-4}	0.80	614	6
8.5×10^{-4}	0.79	609	12
10^{-3}	0.81	614	10
2×10^{-3}	0.73	600	50
2.5×10^{-3}	0.83	609	36
3×10^{-3}	0.86	614	30
7×10^{-3}	0.86	609	100

power excitation using a spectrofluorimeter (SLM). In ethanol at room temperature, $p_N=0.17$ was obtained. The degree of polarization of the fluorescence emitted at 700 nm with higher fluence excitation was analyzed with the equipment in fig. 1. Different power and wavelengths in the laser excitation were used and b varied between 10^{-6} and 5×10^{-3} ns^{-1}. The value of p obtained was 0.15 ± 0.04, independent of b. For the higher values of b, most of the intensity comes from the P form at this emission wavelength. The necessity of evaluating the degree of polarization and the use of a polarizer in the detection arise from erratic preliminary results obtained when this factor was not considered.

4. Discussion

It is well established that the photoisomerization of DODCI proceeds via the first excited singlet state [10]. The radiationless deactivation of N* occurs through a short-lived twisted state which branches between the ground stable N, and that of the less stable P. Due to the strong overlap of the absorption of both species, at high fluences the first excited singlet state of P is also populated. P* is responsible of the red fluorescence peak in fig. 3. The mechanism for the non-radiative deactivation of P* is not completely clear. Rullière suggested a similar mechanism than that of N*, that is, a branching between the

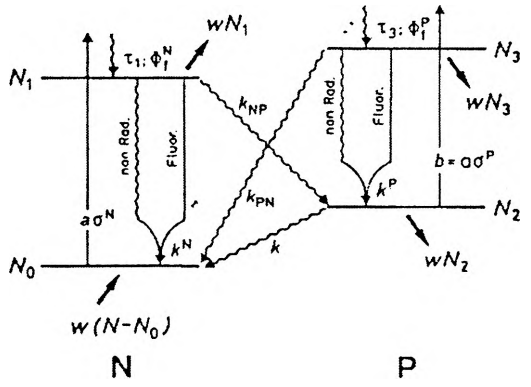


Fig. 4. Four-level scheme used and rate constants for the different processes involved. Non-radiative transitions are indicated by wavy lines. w is the rate constant for the replenishment by the circulation.

direct internal conversion to P and the back isomerization to N [5].

The scheme in fig. 4 was used to model the results in table 1. This scheme is equivalent to Rullière's model in the limit of a very short lifetime for the twisted form [6]. The rate constants of the ground state absorption of N and P are represented by $a\sigma^N$ and $b = a\sigma^P$, respectively. The rate constant for the radiative plus non-radiative transitions between N* and N is given by k^N. For the P form, k^P is the rate constant for the radiative plus the non-radiative transitions between P* and P. The rate constants for the interconnections between the N and P forms are given by k_{NP}, k_{PN} and k as explained in fig. 4. The lifetimes, and the fluorescence quantum yields for the N and P forms are indicated by τ_1, ϕ_f^N, and τ_3, ϕ_f^P, respectively. The change of state population by circulation of the solution is governed by the rate constant w. No triplet state was considered due to the small intersystem crossing yield, $\phi_{ISC} < 0.005$ [4] and the efficient quenching by O_2 in the air-saturated solutions used.

Under these assumptions, the steady state population of the four levels in fig. 4 can be described by the set of rate equations:

$$-a\sigma^N N_0 + kN_2 + k_{PN}N_3 + w(N - N_0) + k^N N_1 = 0\,, \tag{1}$$

$$a\sigma^N N_0 - N_1/\tau_1 - wN_1 = 0\,, \tag{2}$$

$$-bN_2 - kN_2 + k_{NP}N_1 + k^P N_3 - wN_2 = 0\,, \tag{3}$$

$$bN_2 - N_3/\tau_3 - wN_3 = 0, \tag{4}$$

where N_i is the number of molecules in state i as indicated in fig. 4 and the total number of molecules is given by

$$N = N_0 + N_1 + N_2 + N_3. \tag{5}$$

Solving (1)–(5) the ratio of the populations of excited P and N is

$$\frac{N_3}{N_1} = \frac{k_{NP}\,b}{(\tau_3^{-1} + w)(k + w) + b(k_{PN} + w)}. \tag{6}$$

Eq. (6) can be used to simulate the results of table 1. The fluorescence intensity emitted at wavelength λ, in units of W cm^{-2} nm^{-1} by the two species is

$$I_\lambda = [(N_1/\tau_1)\,E_N(\lambda) + (N_3/\tau_3)\,E_P(\lambda)]hc/\lambda\,, \tag{7}$$

where E_N and E_P represents the band shape function in photons/nm, of the fluorescence emitted by N and P respectively, normalized to $\int_0^\infty E_{N,P}(\lambda)\,d\lambda = \phi_f^N, \phi_f^P$. The ratio between the emitted intensities at $\lambda_1 = 640$ nm and $\lambda_2 = 603$ nm can be written as

$$\frac{I_{640}}{I_{603}} = \left(\frac{E_N(640)}{E_N(603)} + \frac{N_3\,\phi_f^P\,\tau_1}{N_1\,\phi_f^N\,\tau_3}\right)\frac{603}{640}, \tag{8}$$

if $E_P(603) = 0$ and $E_P(640)/E_N(603) = \phi_f^P/\phi_f^N$ are assumed due to the similarity of the shape of the fluorescence bands. In order to compare the results of eq. (8) with the measurements of table 1 other fact must be considered: due to the emission polarizer (see fig. 1) the intensities quoted in table 1 are only a fraction of the total intensity emitted. The fraction is governed by the degree of polarization p. From the values of $p = 0.17$ for low power excitation and 0.15 ± 0.04 for high power excitation, it can be assumed that, at room temperature in ethanol, the degree of polarization p for the two isomeric species of DODCI is the same. Under this assumption and introducing (6) in (8), the ratio of the measured intensities at 640 and 603 nm is given by

$$\frac{I_{640}}{I_{603}} = \left(\frac{E_N(640)}{E_N(603)} + \frac{k_{NP}\,b(\phi_f^P\tau_1/\phi_f^N\tau_3)}{(\tau_3^{-1} + w)(k + w) + b(k_{PN} + w)}\right)\frac{603}{640}. \tag{9}$$

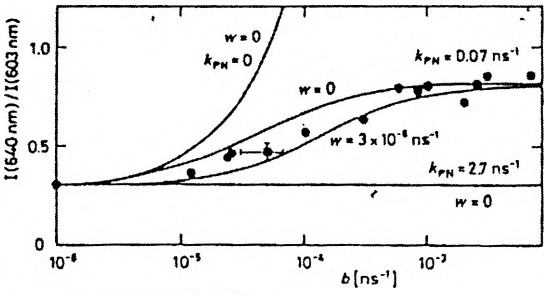


Fig. 5. Fitting of the measurements of table 1 by the expression of eq. (9). The best fitting is obtained for $k_{PN}=0.07$ ns^{-1} and $w\leqslant 3\times10^{-6}$ ns^{-1}. The other parameters in eq. (9) are taken from the literature; the values are given in the text. No connection ($k_{PN}=0$) and strong connection ($k_{PN}=2.7$ ns^{-1}) between P* and N are in disagreement with the experiment.

The values of I_{640}/I_{603} calculated with eq. (9) are given in fig. 5 as a function of b for different values of the rate constant for the back isomerization k_{PN} and the circulation parameter w. The other parameters are taken from the literature [4]: $E_N(640\ nm)/E_N(603\ nm)=0.32$, $k_{NP}=0.07$ ns^{-1}, $\tau_3=0.3$ ns and $k=7.7\times10^{-7}$ ns^{-1}. The values obtained under different excitation conditions are best fitted by $k_{PN}=0.07$ ns^{-1} and $w\leqslant3\times10^{-6}$ ns^{-1}, in agreement with the values used by Bilmes et al. [11] to explain the results from optoacoustic measurements. The value for w assuming homogeneous flow ($w=$ circulation speed/excited volume) is 2×10^{-5} ns^{-1} corresponding to 1 cm^3/s circulation speed and 4×10^{-5} cm^3 excited volume. It is difficult to estimate the exact rate of molecular replenishment due to the turbulent flux near the cell wall; a considerable lower value for w should be expected.

The value $k_{PN}=0$ in fig. 5 corresponds to no conversion from excited P to the ground state of N. A large population of P results and the red fluorescence at 640 nm is overestimated for most of the b values. The value for $k_{PN}=2.7$ ns^{-1} was calculated considering that the radiationless deactivation of N* proceed mainly via a twisted state [5,6], from which a fraction β of molecules undergoes isomerization to the P ground state and $1-\beta$ goes back to the N ground state. The branching ratio $\beta=0.12$ can be estimated from Dempster's measurements [4]. If a similar scheme is assumed for the non-radiative deexcitation of P*, k_{PN} can be calculated from

$$k_{PN}=(1-\beta)\,k_{NR}^{P}=(1-\beta)(1-\phi_f^P)\tau_3^{-1}\,, \qquad (10)$$

For $\phi_f^P=0.07$ [4], eq. (10) yields $k_{PN}=2.7$ ns^{-1}. Such strong conversion would result in a constant value for the emission intensity ratio, showing that no relevant population of P ground state is built up. In this case, the fluorescence would come mainly from the N form, in contrast to the results in figs. 3 and 5.

5. Conclusions

The excitation fluence and wavelength dependence of the fluorescence of DODCI, allowed the determination of the back isomerization (reformation) rate constant for the process starting in the first excited singlet state of the less stable P form. $k_{PN}=0.07$ ns^{-1} was calculated in agreement with recently performed laser-induced optoacoustic measurements [11]. This value is much smaller than that calculated using the model of radiationless deactivation through a twisted state. In contrast to the processes undergone by N, the intramolecular twisting is not the dominant non-radiative process for excited P. Direct internal conversion becomes its main non-radiative process.

Acknowledgement

This work was supported by the Consejo Nacional de Investigaciones Científicas y Técnicas (CONICET) Grant PID: 3901601/85 and by CIC. We thank Professor S.E. Braslavsky of the Max-Planck-Institut für Strahlenchemie, Mülheim, FRG, who continuously encourages our work. We are indebted to Professor M. Garavaglia of CIOp for his support and to Dr. H.F. Ranea-Sandoval for the help in the preparation of the manuscript and fruitful discussions. The degree of polarization of DODCI normal form was determined with Dr. A. Palandini at the Instituto de Investigaciones en Ingeniería Genética, Buenos Aires. LS and JOT are members of CONICET and GMB and DS are supported by CONICET.

References

[1] W. Sibbett, J.R. Taylor and D. Welford, IEEE J. Quantum Electron. QE-17 (1981) 500, and references therein.
[2] O. Isler, ed., Carotenoids (Birkhäuser, Basel, 1971).
[3] J.A. Valdamis and R.L. Fork, IEEE J. Quantum Electron. QE-22 (1986) 112.
[4] D.N. Dempster, T. Morrow, R. Rankin and G.F. Thompson, J. Chem. Soc. Faraday Trans. II 68 (1972) 1479.
[5] C. Rullière, Chem. Phys. Letters 43 (1976) 303.
[6] S.P. Velsko and G.R. Fleming, Chem. Phys. 65 (1982) 59.
[7] D. Magde and M.W. Windsor, Chem. Phys. Letters 27 (1974) 31.
[8] J.M. Miller, ed., Standards in fluorescence spectrometry (Chapman and Hall, London, 1981) ch. 7.
[9] F. Heisel, J.A. Miché and B. Sipp, J. Luminescence 24 (1981) 651.
[10] S.K. Rentsch, Chem. Phys. 69 (1982) 81.
[11] G.M. Bilmes, J.O. Tocho and S.E. Braslavsky, Chem. Phys. Letters 134 (1987) 335.

Dual Laser Excitation of a Photochromic System: Application to DODCI

R. Duchowicz,* L. Scaffardi, R. E. Di Paolo, and J. O. Tocho

Centro de Investigaciones Opticas (CIOP), Casilla de Correo 124, 1900 La Plata, Argentina
(Received: April 23, 1991; In Final Form: August 29, 1991)

A technique based on a combination of pump-and-probe fluorescence and absorption detection was developed in order to obtain the emission parameters of the photoisomeric (P) species of dyes with noncompletely overlapped absorption spectra of P and the starting species (N). Near total population transfer to the ground state of P was achieved using a continuous wave high-fluence pump laser. A pulsed laser probed this population in its absorption region in such a way that the pulsed emission corresponded to fluorescence from P. Absorption measurements allowed us to follow the P population and to establish its relationship with pump fluence and wavelength. The direct monitoring of the P concentration increased the accuracy of the previously reported values for several photophysical parameters. Temperature-dependent fluorescence quantum yield and lifetime, emission spectrum, and Arrhenius parameters of the nonradiative decay processes of P from 3,3′-diethyloxadicarbocyanine iodide (DODCI) are given. The mechanism for the direct transformation between N and P through the singlet excited states of DODCI is re-evaluated.

Introduction

Photoisomerization processes of cyanine dyes have been analyzed through several techniques: flash photolysis,[1,2] picosecond spectroscopy,[3] photoacoustics,[4] thermal grating,[5] laser saturated absorption[6] and fluorescence,[7] absorption and emission spectroscopy with conventional sources,[8] etc. These techniques exhibit a common drawback in the determination of the kinetic parameters of the photoisomeric species P in an indirect way, using a photoisomerization model for the simultaneous fit of several parameters. This procedure leads to an inherent lack of precision. While it can be used for either totally overlapped absorption–emission spectra (DTDCI, merocyanine 540, etc.) or partially overlapped spectra (DODCI, HITCI, etc.), it is only with using time-resolved picosecond spectroscopy that the different contributions can be directly obtained.

Some spectroscopic properties of P in photoisomerizable dyes with partially overlapped spectra have been reported previously.[9,10] These experiments were based on continuous wave (CW) and pulsed excitation of the sample. The CW laser, tuned at the absorption wavelength of the normal (N) ground-state species, produced a stationary population of the P ground state while the second laser (pulsed) probed this population. The pulsed fluorescence arose from P free from interference from the N emission.

In the present work, the measurements were performed at high pump fluence for which the photoequilibrium populations of all levels involved are shown to be independent of this pump fluence. Under this condition (saturation), the analysis of the results is

(1) Dempster, D. N.; Morrow, T.; Rankin, R.; Thompson, G. F. *J. Chem. Soc., Faraday Trans. 2* **1972**, *68*, 1479.
(2) Rullière, C. *Chem. Phys. Lett.* **1976**, *46*, 303.
(3) Sibbett, W.; Taylor, J. R.; Welford, D. *IEEE J. Quantum Electron.* **1981**, *QE17*, 500.
(4) Bilmes, G. L.; Tocho, J. O.; Braslavsky, S. E. *Chem. Phys. Lett.* **1987**, *134*, 335.
(5) Zhu, X. R.; Harris, J. M. *Chem. Phys.* **1988**, *124*, 321.
(6) Bäumler, W.; Penzkofer, A. *Chem. Phys.* **1990**, *142*, 431.
(7) Scaffardi, L.; Bilmes, G. M.; Schinca, D.; Tocho, J. O. *Chem. Phys. Lett.* **1987**, *140*, 163.
(8) Bäumler, W.; Penzkofer, A. *Chem. Phys.* **1990**, *140*, 75 and references therein.
(9) Duchowicz, R.; Scaffardi, L.; Tocho, J. O. *Chem. Phys. Lett.* **1990**, *170*, 497.
(10) Bilmes, G. M.; Tocho, J. O.; Braslavsky, S. E. *J. Phys. Chem.* **1988**, *92*, 5958.

0022-3654/92/2096-2501$03.00/0 © 1992 American Chemical Society

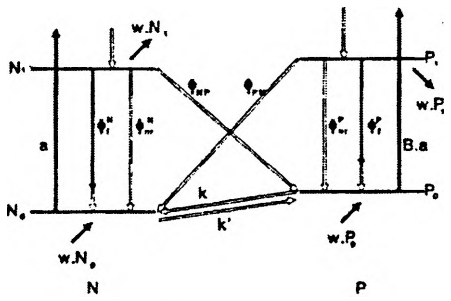


Figure 1. Four-level scheme used for calculation. Nonradiative transitions are indicated with empty lines.

greatly simplified and more reliable. Another modification is the use of a third laser beam as a second probe for the measurement of the P ground-state concentration (P_0) by absorption. Emission of the photoisomer was studied by detection of the fluorescence induced by the pulsed laser as a function of temperature.

This method was applied to DODCI, which has been extensively studied for its importance in pico- and femtosecond pulse generation.[11] Although there is no final evidence about the structure of both isomers of DODCI, it is accepted that a cis–trans isomerization occurs during the transformation N ↔ P. A four-level diagram often is used to study the dynamics of DODCI. This model is of general application and independent of the precise conformation of the N and P isomers.

Figure 1 shows such a diagram where all possible intra- and interisomer transformations are indicated. The notation is given in the Appendix with the corresponding rate equations. When the photochromic system is in equilibrium, the fluence-dependent ground-state population can be expressed (eq A2 of the Appendix) as

$$\frac{P_0}{N} = \frac{\Phi_{NP}a + k'}{(\Phi_{NP} + B\Phi_{PN})a + k + k' + w} \quad (1)$$

For high intensity, $a\Phi_{NP} \gg k + k' + w$, eq 1 can be reduced to

$$\frac{P_0}{N} = \frac{1}{1 + pB} \quad (2)$$

where N is the total population, $p = \Phi_{PN}/\Phi_{NP}$, and $B = \sigma_P/\sigma_N$.

Under this condition, the maximum population of P depends on the excitation wavelength, as a result of the dependence of B with this parameter, and is independent of the laser fluence.

Materials and Methods

3,3'-Diethyloxadicarbocyanine iodide (DODCI), laser grade, Eastman Kodak, in aerated solutions of analytical grade ethanol at low concentrations ($(0.5–3) \times 10^{-6}$ M) were employed in order to avoid dimerization and inner filter effects and to insure a homogeneous concentration of all species along the cell. The solutions were flowed through a standard fluorescence cuvette ($1 \times 1 \times 4$ cm^3) from a reservoir in a thermostatic bath to control the temperature within 0.2 °C. The rate of sample renewal by circulation, w, is related to the flow velocity in the cell, v, and the diameter of the irradiated zone, d; $w = v/d \approx 10^3$ s^{-1} was estimated. Temperatures were measured in the cell by a Cu–constantan thermocouple.

Fluorescence and absorption measurements were simultaneously performed with the setup in Figure 2. For the former, an Ar ion-pumped dye laser (Rhodamine 6G) or the Ar ion laser were focused on the cell. Simultaneously, a Rhodamine 640 flash-lamp-pumped dye laser (Chromatix CMX-4, pulse width = 1 μs, peak energy = 1 mJ, repetition rate = 5 Hz) was aligned in the opposite direction with respect to the CW laser and focused with the lens, L_2, on the same spatial region of the cell. The pulsed fluorescence was detected perpendicularly to the excitation direction. Pulsed and CW laser beam polarizations were perpendicular to the plane defined by the incidence and observation directions. Fluorescence was focused through a system of lenses, L_3 and L_4, on the slit of the Ebert-mount scanning spectrometer (Jarrell Ash 82-025). The fluorescence spectrum was obtained by scanning the emission wavelength. A polarizer oriented at the magic angle[12] was placed between the lenses to eliminate fluorescence contributions arising from temperature-dependent rotational orientation effects. For spectrum correction, a second polarizer, side by side to the former but with vertical transmission, was used, and correction was carried out as in ref 7. Emission was detected using a Hammamatsu R-466 multialkali photomultiplier.

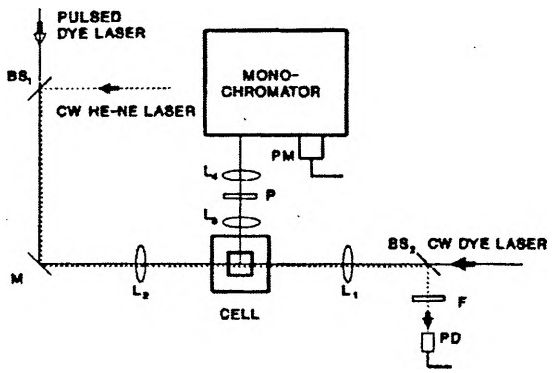


Figure 2. Experimental setup. Fluorescence excitation–detection path is shown by the continuous line, and the absorption path by the dashed line. L_1, L_2, L_3, and L_4 are focusing lenses; P is a polarizer; PM is a photomultiplier; BS_1 and BS_2 are beam splitters; PD is a photodiode; and F is a filter (Schott OG590).

For the absorption measurements, a low-power CW He:Ne laser (632.8 nm) was used instead of the pulsed dye laser (dashed line in Figure 2). A photodiode (Spectra Physics Model 404) measured the He:Ne laser intensity transmitted through the cell with (I_1) and without (I_2) pump beam excitation. The absorption coefficient calculated as $\alpha_P = \ln(I_2/I_1)$ is related to P_0 by

$$\alpha_P = \sigma_P(632.8\text{ nm})P_0 l \quad (3)$$

where l is the length of the cell. It was assumed that the intensity absorbed by the normal species is negligible at this wavelength ($\sigma_P \gg \sigma_N$). Both fluorescence and absorption signals were processed by a Boxcar integrator (EG&G PAR 162-163) and plotted on an Y–t recorder.

Results and Discussion

I. P_0 Population under a Stationary Saturated Regime. Saturation can be defined as the condition for which the absorption of P is independent of the pump fluence. Under this condition, α_P was measured at various pump wavelengths in order to obtain the wavelength dependence of P_0 at photoequilibrium. α_P's values normalized to the value obtained with the pump at the isosbestic point, $B = 1$ ($\lambda_a = 600$ nm for DODCI), are shown in Figure 3. Eqs 2 and 3 can be combined to fit experimental values as

$$\frac{\alpha_P(\lambda)}{\alpha_P(\lambda\alpha)} = \frac{P_0(\lambda)}{P_0(\lambda_a)} = \frac{1 + p}{1 + pB} \quad (4)$$

The best fit was obtained for $p = \Phi_{PN}/\Phi_{NP} = 0.36 \pm 0.06$. B was calculated from σ values from ref 10. The good fit of all data supports the independence of p with the pump wavelength. The value obtained for p allows us to obtain the population of P by using eq 2. From Figure 3 it can be seen that at saturation almost all molecules are converted from N to P for $B < 1$ ($\lambda < 580$ nm), while for $B > 1$ ($\lambda > 600$ nm) back-photoisomerization is an effective channel to return from P to N.

II. Fluorescence Emission under Stationary Saturated Conditions. II.1. P_1 Fluorescence Emission Spectrum. By continuous

(11) Fork, R. L.; Brito Cruz, C. H.; Becker, P. C.; Shank, C. V. *Opt. Lett.* 1987, *12*, 483.

(12) Lessing, H. E.; v. Jena, A. *Chem. Phys. Lett.* 1976, *42*, 213.

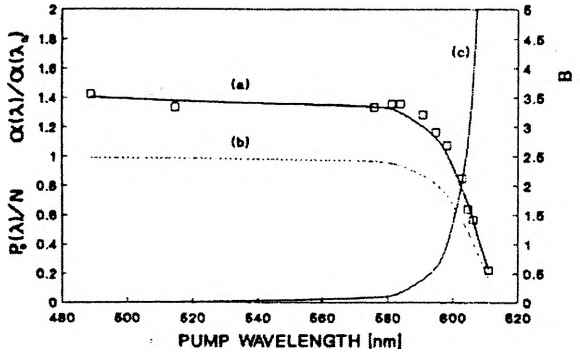


Figure 3. (a) Squares are experimental values of $\alpha(\lambda)/\alpha(\lambda_a)$, a room-temperature absorption ratio obtained from transmition measurements as a function of the excitation wavelength; the solid line corresponds to fitting values calculated using eq 4 (see text). (b) The dashed line represents the ratio of the normalized photoisomer ground-state population to the total population, $P_0(\lambda)/N$ (calculated from eq 2). (c) $B = \sigma_P/\sigma_N$ with values from ref 10.

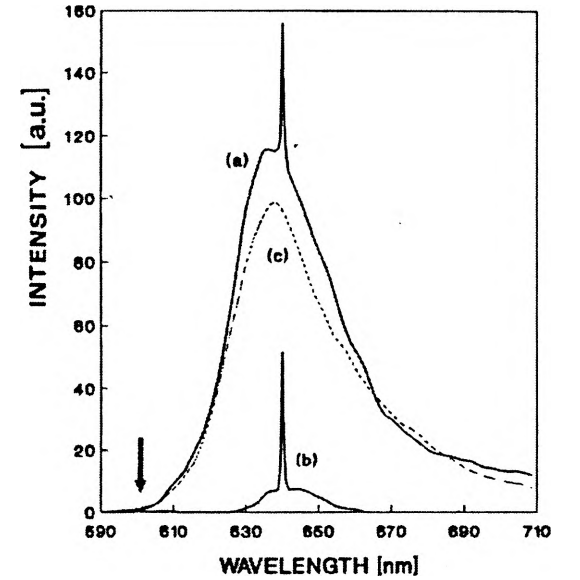


Figure 4. Pulsed fluorescent emission arising from P_1 obtained with (a) the double-excitation method (see text) and (b) the cw pump off. (c) The dashed line is the corrected spectrum. The arrow indicates the position of the emission maximum of the normal species. Spikes are artifacts produced by scattering of the pulsed probe.

excitation of the sample with high fluence (I_0 = 300 W/cm^2) at 580 nm, nearly all molecules are transferred to P_0 at room temperature. For pulsed excitation at 640 nm, since $\sigma_P P_0 \gg \sigma_N N_0$, a pulsed population in P is produced.

Figure 4 shows the pulsed fluorescent signal achieved with this double-excitation technique. The lower curve corresponds to the signal obtained with the CW dye laser off. The arrow indicates the position of the emission maximum of the normal species, whose intensity level is found in this case to be lower than the pulsed noise. The CW signal, arising from N_1 fluorescence when the pump is on, is filtered by the low-impedance (50 Ω) detection system. The spike produced by scattering of the pulsed probe beam was subtracted using pure solvent in the cell in order to correct the spectrum.

II.2. Room-Temperature P_1 Fluorescence Parameters. With the absorption spectrum of the P isomer from ref 10 and the Strickler and Berg formula,[13] the radiative lifetime of the isomeric form was calculated as τ_0^P = 4.0 ns.

In order to obtain the fluorescence quantum yield of P, the emission from the photoisomeric form of DODCI was compared (peak emission, area under spectrum) with the normal species emission of 3,3'-diethylthiadicarbocyanine iodide (DTDCI) selected for its similar absorption–emission properties. The sample was changed to the new dye, the cw pump was turned off, and the same low-energy pulsed excitation was used. An emission ratio of 0.254 was obtained. The absolute value for the fluorescence quantum yield of P was calculated as Φ_f^P (DODCI) = 0.09 ± 0.02 using Φ_f^N (DTDCI) = 0.36 ± 0.05.[14] Φ_f^P results were higher than the value 0.06 ± 0.02 given in ref 10, but they are within the experimental error.

II.3. Analysis of Direct $P_1 \leftrightarrow N_1$ Conversions. The possibility of the direct $P_1 \rightarrow N_1$ conversion[8,15] can be discussed by use the spectrum of Figure 4. The N_1 population can be analyzed in terms of the following processes: direct absorption by N_0 or the absorption by P_0 followed by the passage from P_1 to N_1. The rate of population transferred in the latter case results in a maximum. This fact is due to both the low N_0 population and the small absorption cross section of the normal species at the pulsed-probe wavelength. In other words, N_1 is only populated through the $P_1 \rightarrow N_1$ passage. In this case

$$\frac{dN_1}{dt} = k_{PN}^1 P_1 - \frac{N_1}{\tau_N} \simeq 0 \rightarrow N_1 = k_{PN}^1 \tau_N P_1$$

where stationary conditions for N_1 and P_1 are valid, since the pulse duration is much longer than the excited-state lifetimes. The fluorescence emission ratio between the N_1 and the P_1 emissions is estimated from

$$\frac{I(\lambda_N)}{I(\lambda_P)} = \frac{\dfrac{N_1 E(\lambda_N)}{\tau_N \lambda_N}}{\dfrac{P_1 E(\lambda_P)}{\tau_P \lambda_P}} \simeq \Phi_{PN}^1 \frac{\Phi_f^N}{\Phi_f^P} \rightarrow \Phi_{PN}^1 \simeq \frac{I(\lambda_N)}{I(\lambda_P)} \frac{\Phi_f^P}{\Phi_f^N}$$

where λ_N and λ_P correspond to the maximum emission of each species and $E(\lambda)$ is the line shape of the emissions, which was assumed equal for both species. Taking the intensities ratio as 0.01 and efficiencies ratio as 0.225 (Φ_f^N = 0.4[2] and Φ_f^P = 0.09 obtained in section II.3), $\Phi_{PN}^1 \leq 2.25 \times 10^{-3}$ results, a value that can be neglected in relation to Φ_{PN}.

The direct process $N_1 \rightarrow P_1$ is more difficult to estimate. An overestimated limit can be obtained assuming a two-valley model for the upper potential energy surface of DODCI and an activated process where the depletion of population through the twisted state is neglected. In this case

$$k_{NP}^1 = k_{PN}^1 \exp(\Delta E / k_B T)$$

where $\Delta E = E_N^1 - E_P^1$ is the energy difference between the N_1 and P_1 levels, k_B is the Boltzmann constant, and T is the temperature. The highest value of k_{NP}^1 is obtained using an energy value of ΔE = 770 cal/mol,[8] corresponding to the lower energy difference between the N_0 and P_0 levels reported. At room temperature, $k_{NP}^1 \leq 9 \times 10^{-3}$ ns^{-1} and $\Phi_{NP}^1 \leq 2 \times 10^{-2}$ result. Considering also the decay through the twisted state, these values should be much lower. $P_1 \rightarrow N_1$ and $N_1 \rightarrow P_1$ steps can be ruled out, as a first approach, from the model.

II.4. Temperature Dependence of Fluorescence Quantum Yield and Lifetime. When a P_0 equilibrium population is reached by cw pump at a given temperature, the amplitude of the pulsed fluorescence signal, $I(T)$, can be taken proportional to both the P_0 population and $\Phi_f^P(T)$. P_0 was measured as described before, between 0 and 55 °C; relative values referred to the room-temperature value are given in Figure 5. The fluorescence intensity produced by the pulsed probe at 640 nm was measured in the same temperature range. Φ_f^P was calculated for each temperature as

$$\Phi_f^P(T) = \frac{I(T)}{I(T_0)} \frac{P_0(T_0)}{P_0(T)} \Phi_f^P(T_0) \qquad (5)$$

(13) Strickler, S. J.; Berg, R. A. *J. Chem. Phys.* **1962**, *37*, 814.

(14) Bilmes, G. M.; Tocho, J. O.; Braslavsky, S. E. *J. Phys. Chem.* **1989**, *93*, 6696.

(15) Arthurs, E. G.; Bradley, D. J.; Roddie, A. G. *Chem. Phys. Lett.* **1973**, *22*, 230.

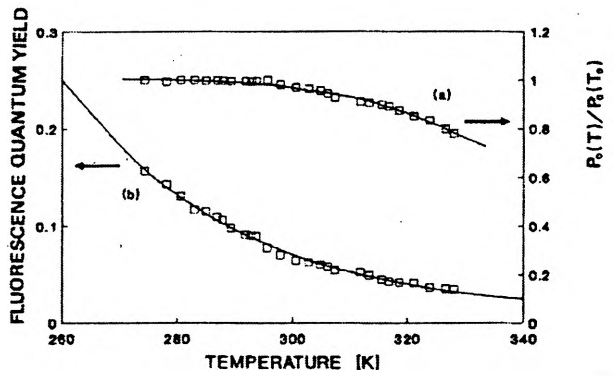


Figure 5. Squares are experimental points of (a) temperature dependence of the P population normalized at room temperature ($P_0(T)/P_0(T_0) = \alpha_P(T)/\alpha_P(T_0)$ was used from eq 3) and (b) temperature dependence of photoisomer fluorescence quantum yield ($\Phi_f^P(T)$) from eq 5. Solid lines are fittings using eq 1 with $a = 3 \times 10^{-4}$ ns^{-1}, $w = 3 \times 10^{-7}$ ns^{-1}, and isomerization constants from refs 9 and 16 as parameters.

The values obtained from 0 to 55 °C are also given in Figure 5. A small departure from saturation can be observed at high temperatures (20% at 50 °C). This fact is due to the increasing value of k ($P_0 \rightarrow N_0$ transformation rate constant) with temperature.

Using $\Phi_f^P(T)$ and the radiative lifetime value obtained in section II.1, the lifetime of P_1 for each temperature can be calculated from

$$\tau_P(T) = \tau_0^P \Phi_f^P(T)$$

From τ_0^P and τ_P, the temperature dependence of the nonradiative processes can be analyzed as follow:

$$k_{nr}^P = 1/\tau_P - 1/\tau_0^P \qquad (6)$$

The results are plotted in the usual fashion (Arrhenius plot) in Figure 6a. The linearity of the plot indicates that only one radiationless process is involved in this temperature range. The activation energy was evaluated as $E_a^P = 5740 \pm 100$ cal mol^{-1}. This value turns out to be similar to those reported for the activation energies of the nonradiative processes from N_1, the isomerization (k_{NP})[16] and the back-isomerization (k_{PN}).[9] No contributions from T-independent nonradiative processes were found.

The nonradiative rate constant can be written as

$$k_{nr}^P = F(\eta) \exp(-E_0^P/RT)$$

where $F(\eta)$ is a universal function of viscosity and E_0^P is the intrinsic molecular barrier height,[16] which is related only with molecular properties. By using different solvents (methanol, methanol–water, ethanol, and 2-propanol), an Arrhenius plot at constant viscosity can be constructed in order to obtain E_0. The results using $\eta = 0.9$ cP and temperature-dependent viscosity value from ref 17 are shown in Figure 6b. An intrinsic barrier $E_0^P = 2830 \pm 200$ cal mol^{-1} was obtained. This result is similar to that obtained for the N_1 nonradiative decay.[16]

Conclusions

Photophysical parameters for the DODCI P species have been obtained using a combination of pump-and-probe fluorescence and absorption methods. Fluorescence quantum efficiencies (Φ_f^P), radiative lifetime (τ_0^P), and lifetime (τ^P) in the range from 0 to 55 °C were obtained with more accuracy than previously reported.[1,16,18] Analysis of the direct exchange between the excited singlet states indicates that the efficiencies for these processes are very low. Therefore, they should be ruled out from the DODCI photoisomerization model.

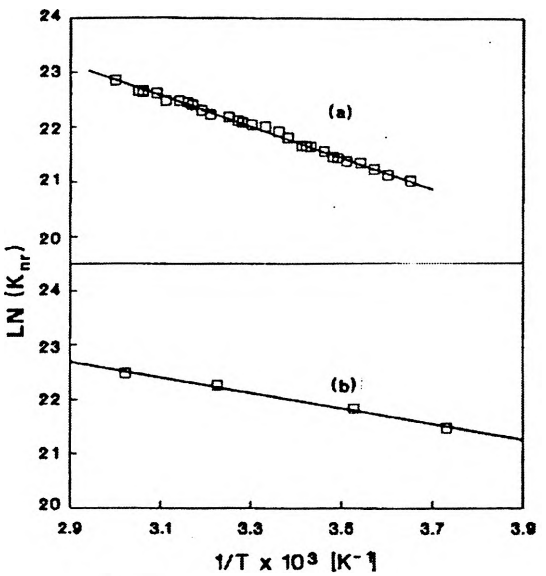


Figure 6. Arrhenius plots of photoisomer nonradiative rate constants in different solvents: (a) ethanol; (b) isoviscosity solutions ($\eta = 0.9$ cP) (methanol, methanol–water, ethanol, and 2-propanol were used).

The ratio between both isomerization quantum yields, $p = \Phi_{PN}/\Phi_{NP}$, was found independent of pump wavelength. This fact is in disagreement with the results of Bäumler and Penzkofer.[6] These authors found p values of 1.35 at short pump wavelengths of 0.25 at the longest wavelength, and of a maximum of 3.5 at 570 nm as a result of the dependence with the excitation wavelength for both transfer efficiencies. The reason for such discrepancies is not clear at the moment. Higher concentrations and a lower pump intensity were used in the above-mentioned paper with respect to those of the present work. With the concentration used in ref 6, inhomogeneous population densities should be present along the cell. This fact was not considered by the authors. In addition, the interpretation of the results obtained below saturation is more difficult and sensitive to the fitting procedure. Furthermore, Velsko et al.[19] have shown that the direct isomerization rate, Φ_{NP}, is independent of pump wavelength.

Working at saturation condition, since fitting is reduced to a minimum, the interpretation of the photoisomerization process is simplified and the results are more reliable. The technique developed can be extended to the other molecules with incomplete overlapping of the absorption spectra.

Acknowledgment. The work was supported by the Consejo Nacional de Investigaciones Cientificas y Tecnicas of Argentina (CONICET) (Grant PID 3-060100/88). R.D., L.S., and J.O.T. are members of the Carrera del Investigador from CONICET and members of Departamento de Fisica of Universidad Nacional de La Plata. R.E.DiP. thanks the Comision de Investigaciones Cientificas de la Provincia de Buenose Aires (CICBA) for a fellowship.

Appendix

Equations for the Calculation of Populations under Photoequilibrium. The scheme of Figure 1 summarizes the four-level kinetic model used here to formulate the set of differential rate equations that leads to eq 1. The direct passage between excited states N_1 and P_1 is ruled out in this analysis by taking into account

(16) Velsko, S. P.; Fleming, G. R. *Chem. Phys.* **1982**, *65*, 59.
(17) *Handbook of Chemistry and Physics*; 62nd ed.; CRC Press: Boca Raton, FL, 1981–1982.
(18) Mialocq, J. C.; Boyd, A. W.; Jaraudias, J.; Sutton, J. *Chem. Phys. Lett.* **1976**, *37*, 236.
(19) Velsko, S. P.; Waldeck, D. H.; Fleming, G. R. *J. Chem. Phys.* **1983**, *78*, 240.

the results of section II.3.

$$\frac{dN_0}{dt} = -(a + w)N_0 + \frac{(1 - \Phi_{NP})}{\tau_N}N_1 + \frac{\Phi_{PN}}{\tau_P}P_1 + kP_0 - k'N_0 + wN$$

$$\frac{dN_1}{dt} = aN_0 - \left(\frac{1}{\tau_N} + w\right)N_1$$

$$\frac{dP_1}{dt} = BaP_0 - \left(\frac{1}{\tau_P} + w\right)P_1$$

$$\frac{dP_0}{dt} = \frac{\Phi_{NP}}{\tau_N}N_1 + \frac{(1 - \Phi_{PN})}{\tau_P}P_1 - (Ba + k + w)P_0 + k'N_0 \quad \text{(A1)}$$

In eq A1, N_0, N_1 and P_0, P_1 are the ground- and excited-state populations of the normal and photoisomer species, respectively, and $N = N_0 + N_1 + P_0 + P_1$. $B = \sigma_P/\sigma_N$, with σ_P and σ_N as the absorption cross section coefficients of the P and N species. $a = I_1\sigma_N$, which is the rate of light absorption, where I_1 is the excitation fluence. w is the rate of sample renewal within the irradiated volume by circulation of the solution. k and k' are the rate constants of the $P_0 \rightarrow N_0$ and $N_0 \rightarrow P_0$ processes, and τ_N and τ_P are the lifetimes of excited states for the normal and photoisomeric species. Φ_{NP} and Φ_{PN} are the quantum yields of $N_1 \rightarrow P_0$ and $P_1 \rightarrow N_0$ isomerization processes.

Under steady-state irradiation conditions and low absorption, the following expression can be obtained:

$$\frac{P_0}{N} = \frac{\Phi_{NP}a + k'}{(\Phi_{NP} + B\Phi_{PN})a + k + k' + w} \quad \text{(A2)}$$

where excited-state populations are taken negligibly small because the pump intensity, I_1, is small compared to the saturation intensity for the excited-state populations, $I = h\nu/\sigma$ which are in the MW/cm^2 region and the depopulation of N_1 and P_1 by circulation ($w \ll 1/\tau_N$; $1/\tau_P$) are neglected.

Láseres de estado sólido

Luego de los primeros estudios generales sobre matrices de estado sólido aptas como medio láser y de la posterior consolidación de materiales como el Nd:YAG para láseres de estado sólido de alta potencia y prolongado rendimiento, el interés en estos temas se centró en la búsqueda de nuevos materiales apropiados para el desarrollo de láseres de estado sólido sintonizables. El tema de láseres de estado sólido se estableció en el ClOp a principios de la década del 90, con el estudio de la fotofísica y mecanismos de población en cristales dopados con iones de tierras raras o metales de transición. La determinación del llamado rendimiento cuántico de fluorescencia, absorción de estado excitado y acoplamiento electrón fonón de red son parámetros fundamentales para la caracterización de estas matrices como posibles materiales láser. Las técnicas usadas para la determinación de estos parámetros fueron luminiscencia inducida por láser, absorción, fotoacústica y termoluminiscencia.

En particular, se desarrolló un método sencillo para la determinación del rendimiento cuántico de fluorescencia, basado en la medida simultánea de la intensidad de luminiscencia y fotoacústica de una muestra para distintas longitudes de onda de excitación. Con estas técnicas se estudiaron diferentes muestras cristalinas, comenzando por haluros alcalinos dopados con iones de tierras raras (KCl:Eu2+, NaCl:Eu2+, KBr:Eu2+ y KI:Eu2+), determinando su rendimiento cuántico para sus posibles emisiones láser en longitudes de onda cortas (región azul-violeta del espectro). También se trabajó en la caracterización de cristales ferroeléctricos como el niobato de litio (LiNbO3), codopado e impurificado con cromo trivalente, de interés por su aplicación en optoelectrónica.

Los trabajos presentados a continuación resumen las actividades realizadas en este tema: el primero estudia la absorción de estado excitado del KCl:Eu2+, determinando su sección eficaz de absorción a dos longitudes de onda analizando las señales de luminiscencia y fotoacústica en función de la fluencia de excitación; los otros dos ilustran un estudio de la eficiencia cuántica de luminiscencia del ión Cr3+ en niobato de litio codopado con óxido de zinc y la influencia del acoplamiento ión-red en los niveles de energía del Cr3+.

After the worldwide general study of solid state matrices potentially useful for laser

Solid State Lasers

media and the consequent establishment of some of them as commercial high power lasers (like Nd:YAG, for instance), research interests pointed for new materials appropriate for solid state tunable lasers.

This line of research started at ClOp by the beginning of the 90´s with the study of the photophysics and population mechanisms of rare-earth/transition-metal doped crystals. In these materials, the fluorescence quantum yield, excited state absorption, and electron-lattice coupling are basic parameters to be determined when looking for possible laser emission. The techniques used for these determinations were laser induced fluorescence, ground state absorption, photoacoustics and thermoluminescence.

A simple method for quantum fluorescence yield based on the simultaneous measurement of luminescence and photoacoustics signals at different excitation wavelengths was developed. With this method, rare-earth doped alkali-halide crystals (KCl:Eu2+, NaCl:Eu2+, KBr:Eu2+ y KI:Eu2+) were studied as potential solid state short wavelength lasers. Ferroelectric crystals like doped lithium niobate (LiNbO3:ZnO:Cr3+) was also extensively studied for its applications in optoelectronics.

The selected papers presented in this section summarizes the activities carried out in this field: the first one deals with the excited state absorption of KCl:Eu2+, determining its cross section for two pump wavelengths, studying luminescence and photoacoustic signals as a function of excitation fluence; the other two deal with the determination of the luminescence quantum yield and electron-phonon coupling in the system LiNbO3:ZnO:Cr3+.

JOURNAL DE PHYSIQUE IV
Colloque C7, supplément au Journal de Physique III, Volume 4, juillet 1994

Excited state absorption in KCl:Eu^{2+}

D. Schinca, J.O. Tocho, E. Rodríguez* and F. Cussó*

Centro de Investigaciones Opticas (CIOp), C.C. 124, 1900 La Plata, Argentina
** Dept. Física de Materiales, Universidad Autónoma de Madrid, Spain*

ABSTRACT: Non-linear behavior with respect to exciting fluence of both photoacoustic and luminescent signals in KCl:Eu(2+) , excited by laser pulses at 355 nm, were analyzed in terms of excited state absorption (ESA). Measured ESA cross-sections for 355 and 420 nm were found to be 1 x 10^(-17) cm^2 and 2.5 x 10^(-18) cm^2 respectively.

1. INTRODUCTION

There is great interest to search for materials to develop tunable solid-state lasers emitting at shorter wavelengths than the present ones. Divalent europium ions in a strong crystalline field has potential for laser operation in the violet and blue spectral regions[1]. However, in some crystalline hosts, (like CaF_2), it was found that strong excited state absorption prevented laser action[2]. Alkali halides can be more appropriate hosts for laser action due to their small Madelung energy at the europium site. In view of this interest, excited state absorption (ESA) measurements have been performed at room temperature in KCl:Eu^{+2} using photoacoustic and luminescence methods.

As it is well known[3], the absorption spectrum of Eu ions in KCl crystals consists in two broad absorption bands attributed to transitions from the $^8S_{7/2}$ ground state of the $4f^7$ configuration, to the $4f^6 5d$ configuration. In cubic symmetry, the crystal field splits the d electron into two e_g and t_{2g} components, which correspond to the observed absorption bands. For sixfold coordination, which is the case for Eu^{+2} ions entering substitutionally for K^+ ions in KCl, the t_{2g} is the low-lying level (fig 1). After excitation of these two bands, a single luminescent band is observed, corresponding to the $t_{2g} \rightarrow 4f^7$ transition. Vibronic relaxation provides strong photoacoustic signals for both excitations.

(*) Member of Com. Invest. Cient. Pcia Buenos Aires (CICBA), Argentina

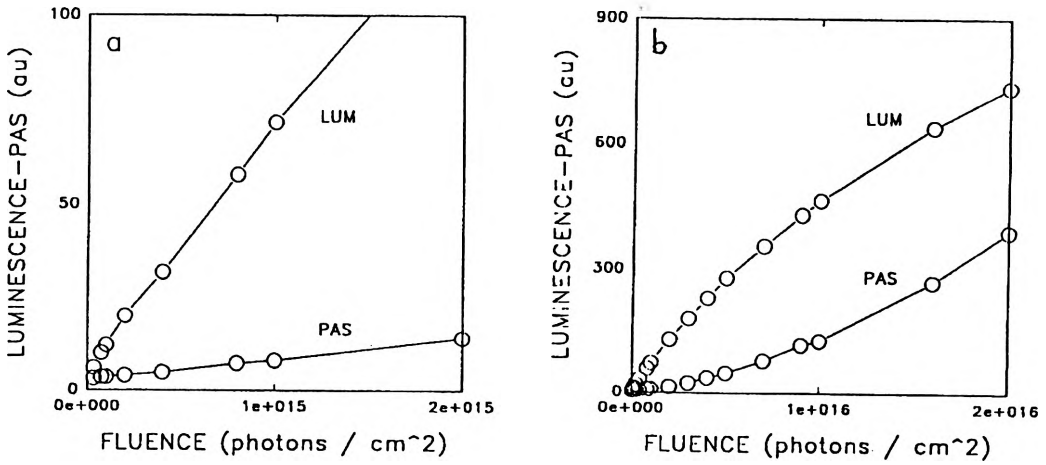


Fig.3: Photoacoustic and luminescence signals, as defined in the text, vs. excitation fluence. (a) linear behaviour at low fluence and (b) non linear behaviour at high fluence.

transition, σ_g and σ_e are the ground and excited state absorption cross sections at 355 nm and q_i values can be calculated from absorption and luminescence spectra. k_p is a constant that relates the heat to the amplitude of the PAS signal and it was calculated to match the experimental results at low fluence (linear region). The third term arises from ESA. Relaxation after this process is assumed to be 100% non- radiative. Each contribution is represented in fig. 4. Best fit of all points by using eq.(1) was obtained for σ_e(355 nm) = $1 \times 10^{-17} cm^2$. Luminescence results could not be fitted using this simple model. LUM saturates more strongly than the predictions given by depletion of the ground state due to excited state population.

We concluded that luminescence is reabsorbed within the excited zone. If σ_e(LUM) represents the ESA cross section for the luminescence wavelength and L, the length of the excited zone in the direction of observation, LUM can be written as:

$$LUM = (1 / L.\sigma_{e(LUM)}). [\ 1 - \exp (- N_1 L \sigma_{e(LUM)})\ ], \qquad (2)$$

with:

$$N_1 = N_0 \sigma_g . [\exp(- \sigma_g F) - \exp(-\alpha \sigma_{e(355)} F)\ ] / (\alpha \sigma_{e(355)} - \sigma_g),$$

where α represents the fraction of ions going from the higher excited state to metastable states. In reference [4], $\alpha = 0.67$ was calculated. Using eq. 2, the best fit of experimental results of LUM was obtained for $\sigma_{e(LUM)} = 2.5 \times 10^{-18}$ cm^2 (fig.5).

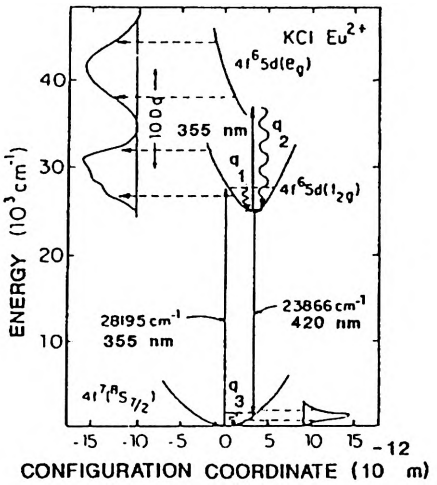


Fig.1: Energy levels of $KCl:Eu^{2+}$. Main excitation and relaxation processes are shown.

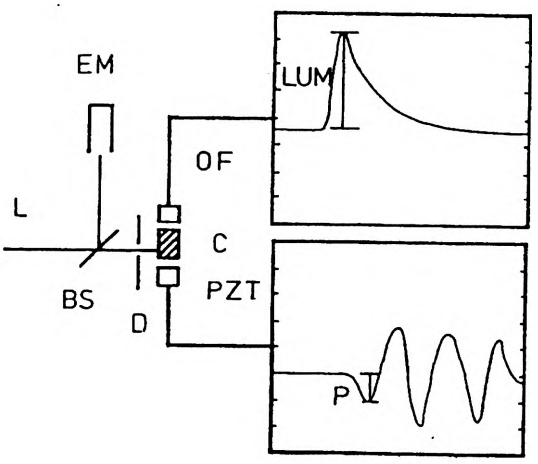


Fig.2: Experimental setup. L laser beam; BS: beam splitter; M:energy meter; D:diaphragm; OF: optic fiber; C: crystal; PZT: piezo transducer; LUM: luminescence signal; P: Photoacoustic signal.

2. EXPERIMENTAL SETUP AND RESULTS

The experimental setup used in this work (fig 2) is similar to that described for the determination of the luminescence quantum yield of this material[4]. Excitation at 355 nm was provided by the third harmonic of a Nd:YAG pulsed laser. The sample, in the form of a rectangular slab of 10 by 5 by 1 mm, with absorbance less than 0.1, was fixed to a PZT detector. Luminescence was collected by an optical fiber and analyzed by a monochromator-photomultiplier system. Both signals were amplified and digitized. Laser pulse energy was measured by using a calibrated pyroelectric detector. The first peak of the photoacoustic signal (PAS) and the maximum of the luminescence signal (LUM) were plotted in terms of incident laser fluence, which could be varied by using a half-wave plate polarizer combination. It is clearly seen in fig.3 that both signals depart from linearity. While LUM tends to saturate, PAS has an opposite behavior.

3. DISCUSSION

By the use of the diagram in fig. 1 we can calculate the amount of prompt heat released after the absorption of the excitation laser pulse with fluence F. The PAS signal can be written as:

$$PAS = k_p[(\sigma_\varepsilon q_1 F) + (\Phi q_3 F) + (\sigma_e(355) q_2 F^2)], \quad (1)$$

where Φ represents the fluorescence quantum yield of the $t_{2g} \rightarrow 4f^7$

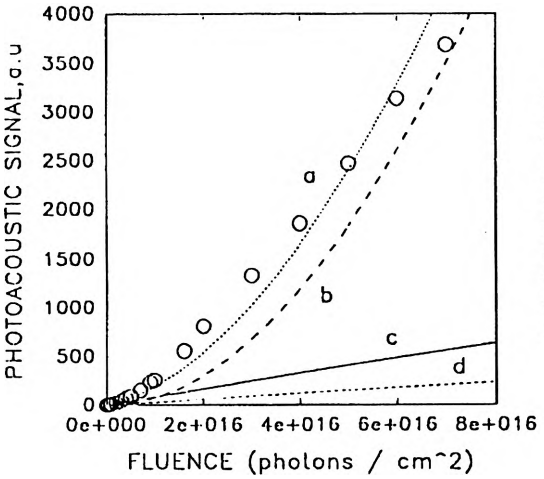


Fig.4:PAS signal vs. fluence. (o) experimental data. Curve (a): total PAS signal; (b): ESA contribution; (c),(d): linear contributions.

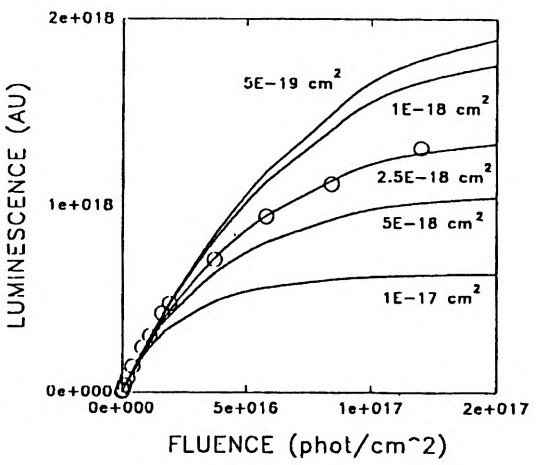


Fig.5: Luminescence signal vs fluence. (o): experimental data.Curves represent eq. (2) for different values of $\sigma_e(420)$.

4. CONCLUSIONS

Non linear behaviour of photoacoustic signals in KCl:Eu^{2+} can be explained in terms of ground state depletion due to excited state absorption at the pump wavelength. The calculated value for λ = 355 nm is in agreement with previously published results [5].

Excited state reabsorption of luminescence must be included in order to explain the strong saturation of luminescence with pump fluence. The obtained value for σ_e(420 nm) seems to be enough to prevent laser action in KCl:Eu^{2+}. This result is in disagreement with calculations made in ref.[6]. No laser action in this material has been reported yet.

5. ACKNOWLEDGMENTS

This work was partially financed by CONICET, Argentina and Agencia de Cooperación Internacional, España.

REFERENCES

1.- Tunable Solid State Lasers II, Eds. A.B. Budgor, L. Esterowtz, and L.G. de Shazer, Springer, Berlin, 1986.
2.- J.F. Owen, P.B. Dorain, and T. Kobayasi, J. Appl. Phys. 52, 1216, 1981.
3.- J.E. Muñoz Santiuste, Ph. D. Thesis, Universidad Autónoma de Madrid, España, 1991.
4.- E. Rodríguez, J.O. Tocho, and F. Cussó, Phys. Rev. B 47, 14049, 1993.
5.- L. Merkle and P. Bandyopadhyay, Phys. Rev. B , 39, 6939, 1989.
6.- L.E. Nagli and M.N. Karklinya, Opt. Spectrosc. (USSR) 67, 832, 1989.

INSTITUTE OF PHYSICS PUBLISHING JOURNAL OF PHYSICS: CONDENSED MATTER

J. Phys.: Condens. Matter 13 (2001) 6577–6583 PII: S0953-8984(01)22081-5

Electron–lattice coupling in congruent Co-doped $LiNbO_3:Cr^{3+}:ZnO$ crystal

G A Torchia[1,2,3], O Martinez Matos[1], P Vaveliuk[1,2] and J O Tocho[1,2]

[1] Centro de Investigaciones Opticas CIC—CONICET, Argentina
[2] Departamento de Física, Facultad de Ciencias Exactas, Universidad Nacional de La Plata, Argentina

E-mail: gustavot@ciop.unlp.edu.ar (G A Torchia)

Received 19 February 2001
Published 13 July 2001
Online at stacks.iop.org/JPhysCM/13/6577

Abstract

The importance of the role of the ion–lattice coupling in determining the energy levels of Cr^{3+} ions in congruent $LiNbO_3$ crystals doped with 2.9% of ZnO is demonstrated in this paper. The Racah parameters: $B = 533\ cm^{-1}$, $C = 3244\ cm^{-1}$ and the crystal-field intensity $Dq = 1527\ cm^{-1}$ were determined and the Tanabe–Sugano diagram was constructed. The characteristics of the absorption and the emission spectra of Cr^{3+} ions in these crystals can be explained in terms of the configurational-coordinate diagram in the harmonic approximation, with good agreement obtained. The Huang–Rhys parameter $S = 6.86$ and the lattice phonon energy $\hbar\omega = 343\ cm^{-1}$ are also reported in this work.

1. Introduction

In the last few years there has been great interest in developing lithium niobate crystals doped with transition metals and rare-earth ions for use in laser and non-linear optics devices. The strong photorefractive effect that lithium niobate presents is a severe drawback as regards laser applications but can be quenched by adding around 5% of MgO or ZnO to the melt. Several examples of high-efficiency lasers based on doubly doped lithium niobate have been reported [1–3].

The Cr^{3+} ion is a good candidate for doping lithium niobate in order to obtain broad-spectrum tunable lasers [4]. It was suggested that Cr^{3+} substitutes for Li^+ in singly doped crystal and it has been proved that most of the chromium ions are found approximately at the Nb^{5+} positions in crystals heavily co-doped with Mg^{2+} or Zn^{2+} [5–10]. Another substitution mechanism has been proposed in which two chromium ions substitute simultaneously for a pair

[3] Author to whom any correspondence should be addressed. Gustavo Adrián Torchia, Centro de Investigaciones Opticas, CC 124, 1900 La Plata (BsAs), Argentina; telephone: (54-221) 484-0280; fax: (54-221) 471-2771.

0953-8984/01/306577+07$30.00 © 2001 IOP Publishing Ltd Printed in the UK

of Li^+ and Nb^{5+} ions to compensate the charge [11]. At both sites the Cr^{3+} experiences a nearly octahedral electric field produced by two planes of O^{2-} ligands. The influence of the crystal field on transition metal ions is very strong because the extended $3d^n$ electron configuration is substantially affected by this field. The energy levels for different d^n electron configurations in a rigid environment with one octahedrally coordinated lattice have been calculated by Tanabe and Sugano [12]. The energy values have been tabulated in terms of the Racah parameters A, B and C and the crystal field Dq. For a $3d^3$ system like chromium in lithium niobate, the energy that results from the Coulomb interaction between the electrons and the interaction between the electrons and the octahedral crystal field are given in table 1. There is a single $^4A_2$ ground state with energy $-15B$ that does not depend on the crystal field; similarly there are only single $^4T_2$, $^2A_1$ and $^2A_2$ states. There are two $^4T_1$ states whose energies can be obtained by diagonalization of the 2×2 matrix shown in the table. Similarly the energy of the ^2E, $^2T_1$ and $^2T_2$ states can be calculated from a matrix also shown in table 1. The lowest-energy ^2E state is important because it is the lowest-energy excited state of many chromium systems that show sharp luminescence (R lines).

Table 1. Matrix elements of the crystal-field and Coulomb interactions and energy levels for the relevant d^3 states in octahedral symmetry, from reference [13].

$$E(^4T_1) = \begin{pmatrix} 10Dq - 3B & 6B \\ 6B & 20Dq - 12B \end{pmatrix}$$

$$E(^2T_2) = \begin{pmatrix} 5C & -3\sqrt{3}B & -5\sqrt{3}B & 4B+2C & 2B \\ -3\sqrt{3}B & 10Dq - 6B + 3C & 3B & -3\sqrt{3}B & -3\sqrt{3}B \\ -5\sqrt{3}B & 3B & 10Dq + 4B + 3C & -3\sqrt{3}B & \sqrt{3}B \\ 4B+2C & -3\sqrt{3}B & -3\sqrt{3}B & 20Dq + 6B + 5C & 10B \\ 2B & -3\sqrt{3}B & \sqrt{3}B & 10B & 20Dq - 2B + 3C \end{pmatrix}$$

$$E(^2T_1) = \begin{pmatrix} -6B+3C & -3B & 3B & 0 & -2\sqrt{3}B \\ -3B & 10Dq + 3C & -3B & 3B & 3\sqrt{3}B \\ 3B & -3B & 10Dq - 6B + 3C & -3B & -\sqrt{3}B \\ 0 & 3B & -3B & 20Dq - 6B + 3C & 2\sqrt{3}B \\ -2\sqrt{3}B & 3\sqrt{3}B & -\sqrt{3}B & 2\sqrt{3}B & 20Dq - 2B + 3C \end{pmatrix}$$

$$E(^2E) = \begin{pmatrix} -6B+3C & -6\sqrt{2B} & -3\sqrt{2B} & 0 \\ -6\sqrt{2B} & 10Dq + 8B + 6C & 10B & \sqrt{3}(2B + C) \\ -3\sqrt{2B} & 10B & 10Dq - B + 3C & 2\sqrt{3}B \\ 0 & \sqrt{3}(2B + C) & 2\sqrt{3}B & 30Dq - 8B + 4C \end{pmatrix}$$

$$E(^4T_2) = 10Dq - 15B$$

$$E(^2A_1) = 10Dq - 11B + 3C$$

$$E(^2A_2) = 10Dq + 9B + 3C$$

$$E(^4A_2) = -15B$$

Purely electronic transitions in perfect crystals have linewidths determined entirely by the lifetime and dephasing mechanisms. The interaction between optically active impurity ions and the vibration of the host lattice is of great importance for understanding optical transitions in real crystals. In this paper we present the absorption and emission characteristics of Cr^{3+} in congruent lithium niobate co-doped with ZnO. The ion–lattice coupling is analysed in terms of the configurational-coordinate breathing model in the harmonic approximation. The Huang–Rhys parameter S and the phonon energy are determined on the basis of this model.

2. Experimental procedure

The samples used in this work were grown by the Czochralski method in the open air, starting with amounts of Li_2O and Nb_2O_5 that ensure congruent concentrations in the crystal. The doping concentrations in the melt were 3% for ZnO and 0.15% for Cr_2O_3. The composition of the crystals was analysed by means of the EXTF (fluorescence total x-ray emission); the results for chromium and zinc ions were 0.1% and 2.9% respectively, normalized to the Nb^{5+} concentration. Congruent crystals have a composition of $Li_{0.945}Nb_{1.05}O_3$ instead of the stoichiometric composition $LiNbO_3$. The samples was cut in slices of 1 mm width, reduced to dice of dimensions $1 \times 4 \times 6$ mm and polished with diamond powders of different diameters.

The optical absorption spectrum was taken at room temperature with a commercial spectrophotometer (Hitachi U-3501). The continuous-wavelength (cw) emission spectrum was taken at room temperature using an argon multiline laser as the excitation source and detecting the light with an AsGaIn (Hamamatsu 751 K) cooled photomultiplier. The luminescence was dispersed by a 0.5 m monochromator (SPEX 5000M) and amplified by a lock-in (EE&G). The absorption and emission spectra were analysed with a multi-Gaussian fitting and the energy levels reported below correspond to peak values of the fitting.

3. Results and discussion

Figure 1 presents the absorption and emission spectra at room temperature for congruent lithium niobate crystals co-doped with Cr^{3+} and ZnO (2.9%). The absorption spectrum shows two broad bands centred at 20 770 cm^{-1} (481 nm) and 15 274 cm^{-1} (655 nm) associated with vibronic transitions of the Cr^{3+}. The band centred at 481 nm is associated with the $^4A_2 \rightarrow {}^4T_1$ transition while the band centred at 660 nm is associated with the $^4A_2 \rightarrow {}^4T_2$ transition; both bands are spin allowed. In this spectrum there are also present three weak peaks centred at 19 607 cm^{-1} (510 nm), 14 705 cm^{-1} (680 nm) and 13 755 cm^{-1} (727 nm) corresponding to the spin-forbidden transitions $^4A_2 \rightarrow {}^2T_2$, $^4A_2 \rightarrow {}^2T_1$ and $^4A_2 \rightarrow {}^2E$ [11]. As can be seen in figure 1, the emission spectrum has a broad band centred at 10 883 cm^{-1} (919 nm); this band was assigned previously to the transition $^4T_2 \rightarrow {}^4A_2$ that corresponds to Cr^{3+} ions at Li^+ sites of congruent lithium niobate crystals because the content of Zn is not sufficient to induce the occupation of the Nb site [6].

From the energy level values obtained, the strength of the octahedral crystal field Dq and the spectroscopic Racah parameters B and C are calculated. The magnitude of Dq is obtained directly from the energy corresponding to the peak of the $^4A_2 \rightarrow {}^4T_2$ absorption band, which is $10Dq$:

$$Dq = [E(^4T_2) - E(^4A_2)]/10 = 1527\ \text{cm}^{-1}. \tag{1}$$

If we write ΔE for the energy difference between the $^4T_2$ and the lowest $^4T_1$ state, which experimentally is the separation between the two strong absorption bands in figure 1, the B-value can be obtained from

$$\frac{B}{Dq} = \left[\left(\frac{\Delta E}{Dq}\right)^2 - 10\left(\frac{\Delta E}{Dq}\right)\right] \Big/ 15\left(\frac{\Delta E}{Dq} - 8\right). \tag{2}$$

For $Dq = 1527\ \text{cm}^{-1}$ and $\Delta E = 5496\ \text{cm}^{-1}$, the result $B = 533\ \text{cm}^{-1}$ is obtained.

The last Racah parameter can be calculated from an approximate expression given by Henderson and Imbusch [14]:

$$C = [E(^2E) - 7.9B + 1.8B^2/Dq]/3.05. \tag{3}$$

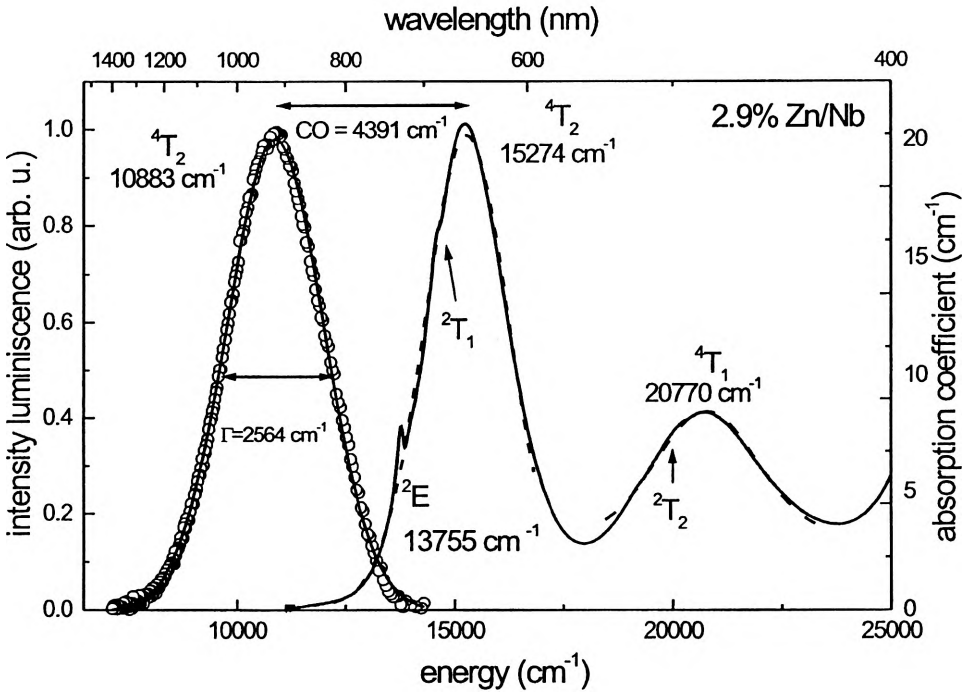


Figure 1. Room temperature absorption and luminescence spectra of Cr^{3+} ions in $LiNbO_3$ (2.9% of ZnO) crystal. The energy values of relevant levels, the Stokes shift (CO) and the FWHM bandwidth (Γ) of the emission band are indicated.

Using the experimental value $E(^2E) = 13\,755\ cm^{-1}$ and the values found previously for Dq and B, the result $C = 3238\ cm^{-1}$ is obtained. More accurate determination of C requires the diagonalization of the 4×4 matrix corresponding to the ^2E states given in table 1. The lowest eigenvalue gives the analytical expression necessary to calculate $C = 3244\ cm^{-1}$ by solving a transcendental equation.

With the Racah parameters found above, the Tanabe–Sugano diagram for the Cr^{3+} ions was constructed. The energy for the most relevant states, taking the energy of the $^4A_2$ state equal to zero, can be calculated by using equations (1)–(3):

$$\begin{aligned} E(^4A_2)/B &= 0 \\ E(^4T_2)/B &= 10/a \\ E(^4T_1)/B &= \{20 + 15a - [(10 + 15a)^2 - 480a]^{1/2}\}/2a \\ E(^2E)/B &= 3.05C/B + 7.90 - 1.80a \end{aligned} \tag{4}$$

where $a = B/Dq$.

The Tanabe–Sugano diagram constructed in this manner for the main spectroscopic states of Cr^{3+} in congruent lithium niobate is presented in figure 2. The vertical broken line represents the appropriate value for Dq/B (2.86) found for this crystal. The diagram presents one important contradiction: the lower-energy excited level in the Tanabe–Sugano representation is the state ^2E while the broad band of luminescence observed experimentally indicates that the lower level must be the $^4T_2$ state. The energy of the ^2E state shows little dependence on the crystal field, similarly to that of the ground state $^4A_2$, so the emission between these levels

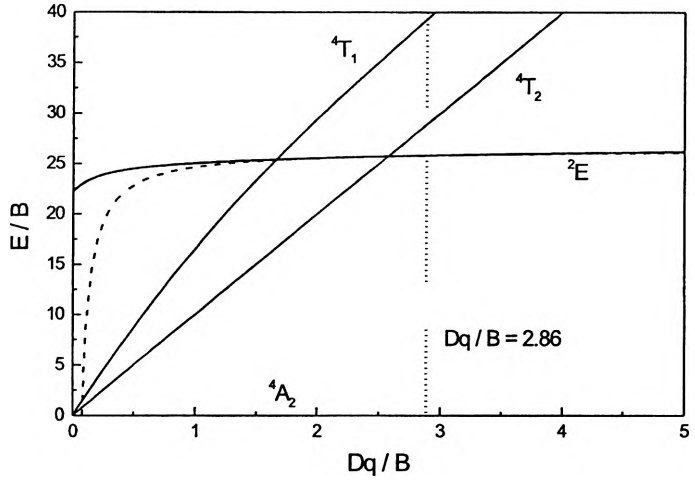


Figure 2. The Tanabe–Sugano diagram for Cr^{3+} in $LiNbO_3$:ZnO (2.9%) crystal corresponding to the experimental values obtained in this work. The solid line for the ^2E level corresponds to the exact diagonalization of the matrix in table 1 while the dashed line is the approximation given by equation (3).

gives a narrow band (R line). The $^4T_2$ state with its greater dependence on the crystal field can give rise to a broad band of luminescence.

Big errors in the crystal-field determination that displace the position of the value of Dq/B enough to invert the positioning of the $^4T_2$ and ^2E energies must be excluded because the absorption spectra are consistent with the diagram of figure 2. To explain the contradiction, the octahedral vibration and the electron–lattice coupling must be considered. As a first approximation, the vibrating environment can be modelled by the single-configurational-coordinate model in the harmonic approximation.

The configurational-coordinate model assumes that the distance Q from the active ion to its first shell of neighbouring ions pulsates harmonically about its equilibrium value Q_0. The vibration energy can be written as $m\hbar\omega$, where m is the number of vibrating quanta and ω is the breathing frequency. As a further approximation, the same breathing frequency is considered for all of the electronic states. The equilibrium values for Q are specific to each electronic state. The departure from the average of Q corresponds to the difference in coupling between the ion and the lattice. The larger the coupling, the larger the difference between equilibrium values. As usual, the difference in electron–lattice coupling is characterized by a dimensionless constant, the Huang–Rhys parameter, S, defined as the number of vibrating quanta excited in the most probable absorption transition.

For the determination of the phonon energy and the Huang–Rhys parameter we used the spectroscopic data of figure 1. The absorption and emission bands from transitions that connect the $^4A_2$ and $^4T_2$ states are approximately Gaussians and mirror images of each other; for this case the Stokes shift, the difference in energy between the absorption and emission band peaks, can be related to S by

$$CO = (2S - 1)\hbar\omega \tag{5}$$

where CO is the Stokes shift. Another equation necessary to calculate the phonon energy and the Huang–Rhys parameter is given by the expression for the bandwidth, which at room

temperature can be written as

$$\Gamma(T) = 2.35\hbar\omega(S\coth(\hbar\omega/kT))^{1/2} \tag{6}$$

where $\Gamma(T)$ stands for the FWHM of the emission band; $k = 0.695\ \text{cm}^{-1}\ \text{K}^{-1}$ is Boltzmann's constant. Using equations (5) and (6) and the values found experimentally for the Stokes shift and the bandwidth ($CO = 4391\ \text{cm}^{-1}$, $\Gamma(T) = 2564\ \text{cm}^{-1}$), we get $\hbar\omega = 343\ \text{cm}^{-1}$ and $S = 6.86$ for $T = 295$ K.

The energy level scheme of Cr^{3+} in congruent lithium niobate crystals is presented in figure 3. The new level diagram shows that the electron–lattice coupling is sufficiently large to explain why the minimum electronic energy of the $^4T_2$ manifold is below the energy of the ^2E state.

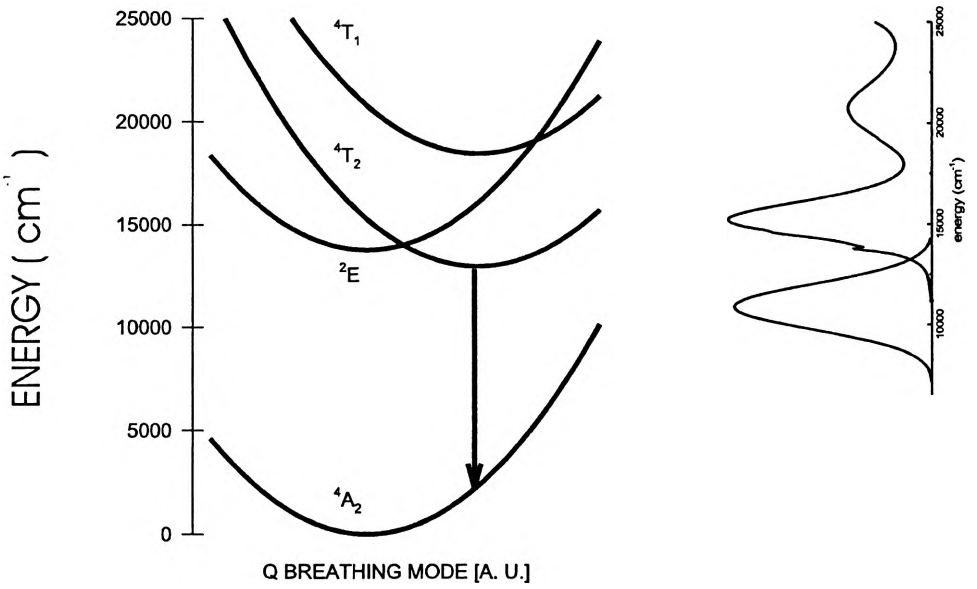


Figure 3. The configurational-coordinate diagram for Cr^{3+} in $LiNbO_3$:ZnO (2.9%) crystal.

4. Conclusions

In this paper we have presented the crystal-field strength, the spectroscopic Racah parameters, the Huang–Rhys parameter and the breathing-mode phonon frequency corresponding to the Cr^{3+} ion in congruent lithium niobate crystal co-doped with 2.9% of ZnO. The crystal-field strength Dq and Racah parameters are found; the values are similar to ones reported previously for other lithium niobate samples [15, 16]; the Huang–Rhys parameter obtained, $S = 6.86$, is identical to that estimated by Weiyi Jia *et al* [11] for a sample of Cr^{3+}:$LiNbO_3$ without specification of the congruency. The breathing phonon energy was determined to our knowledge for the first time for congruent lithium niobate co-doped with Cr^{3+} and Zn^{2+}. This medium-hard phonon (343 cm^{-1}) can be coupled with the TO_3 phonon of the bulk lithium niobate, which was found from Raman measurements at 332 cm^{-1} for a nearly stoichiometric sample at room temperature [17]. Similarly, Ridah *et al* [18] working with congruent samples have found LO phonons at 345 cm^{-1} and TO phonons at 322 and 369 cm^{-1}. Because the

breathing mode at 343 cm^{-1} can be strongly coupled to the bulk phonons, the non-radiative process can compete with the radiative process even for energy gaps over 10 000 cm^{-1}; consequently the fluorescence quantum yield could be low in these crystals. Recently the fluorescence quantum yield of Cr^{3+} at lithium sites in congruent lithium niobate co-doped with ZnO was found to range around 5% [19].

References

[1] Volk T R, Rubinina N M and Wöhlecke V I M 1994 *J. Opt. Soc. Am.* B **11** 1681–7
[2] Jaque D, Capmany J, García-Solé J, Brenier A and Boulon G 2000 *Appl. Phys.* B **70** 11–14
[3] Montoya E, Capmany J, Bausá L E, Kellner T, Diening A and Haber G 1999 *Appl. Phys. Lett.* **74** 3113–15
[4] Qiu Y 1993 *J. Phys.: Condens. Matter* **5** 2041–4
[5] Diaz-Caro J, García-Solé J, Bravo D, Sanz-García J A, López F J and Jaque F 1996 *Phys. Rev.* B **54** 13 042–6
[6] Torchia G A, Sanz-García J A, Díaz-Caro J, Han T and Jaque F 1998 *Chem. Phys. Lett.* **288** 65–70
[7] Torchia G A, Sanz-García J A, López F J, Bravo D, García-Solé J, Jaque F, Gallagher H G and Han T P J 1998 *J. Phys.: Condens. Matter* **10** L341–5
[8] Corradi G, Soethe H, Spaeth J M and Polgár K 1991 *J. Phys.: Condens. Matter* **3** 1901–8
[9] Martín A, López F J and Agulló-López F 1992 *J. Phys.: Condens. Matter* **4** 847–53
[10] Kling A, Soares J C, da Silva M F, Sanz-García J A, Dieguez E and Agulló-López F 1998 *Nucl. Instrum. Methods Phys. Res.* B **136–138** 426–30
[11] Jia W, Liu H, Knutson R and Yen W M 1990 *Phys. Rev.* B **41** 10 906–10
[12] Tanabe Y and Sugano S 1954 *J. Phys. Soc. Japan* **9** 753–66
[13] Sugano S J, Tanabe Y and Kamikura H 1970 *Multiplets of Transition Metal Ions in Crystals* (New York: Academic)
[14] Henderson B and Imbush G F 1989 *Optical Spectroscopy of Inorganic Solids* (Oxford: Oxford Science)
[15] Macfarlane P I, Holliday K, Nicholls J F H and Henderson B 1995 *J. Phys.: Condens. Matter* **7** 9643–56
[16] Camarillo E, Tocho J O, Vergara I, Dieguéz E, García-Solé J and Jaque F 1990 *Phys. Rev.* B **45** 4600–4
[17] Ridah A, Fontana M D and Bourson P 1997 *Phys. Rev.* B **56** 5967–73
[18] Ridah A, Bourson P, Fontana M D and Malovichko G 1997 *J. Phys.: Condens. Matter* **9** 9687–93
[19] Torchia G A, Muñoz J A, Cusso F, Jaque F and Tocho J O 2001 *J. Lumin.* **92** 317–22

ELSEVIER

Journal of Luminescence 92 (2001) 317–322

JOURNAL OF LUMINESCENCE

www.elsevier.com/locate/jlumin

The luminescent quantum efficiency of Cr^{3+} ions in co-doped crystals of $LiNbO_3:ZnO$ determined by simultaneous multiple-wavelength photoacoustic and luminescence experiments

G.A. Torchia[a,*], J.A. Muñoz[b], F. Cussó[b], F. Jaque[b], J.O. Tocho[a]

[a] *Centro de Investigaciones Opticas (CONICET-CIC) and Departamento de Física, Facultad de Ciencias Exactas, Universidad Nacional de La Plata, CC 124, 1900 La Plata, Argentina*

[b] *Departamento de Física de Materiales C-IV, Universidad Autónoma de Madrid, Spain*

Received 1 May 2000; accepted 19 September 2000

Abstract

In this paper, the luminescent quantum efficiency of Cr^{3+} ions in co-doped crystals of $LiNbO_3:ZnO:Cr^{3+}$ is determined by using a method based on simultaneous multiple-wavelength measurement of photoacoustic and luminescence signal after pulsed laser excitation. The quantum efficiency found in this lattice was $(10 \pm 4)\%$. This result was compared with the value found from the study of the lifetime in terms of the temperature of the luminescent levels involved. In this last case, two non-equivalent crystal sites were found for Cr^{3+} ions, and two fluorescence quantum yields were determined. After the estimation of the concentration of each site by electron paramagnetic resonance experiments, the averaged fluorescence quantum yield value was $(9 \pm 2)\%$ in agreement with the previous result. © 2001 Elsevier Science B.V. All rights reserved.

PACS: 43.35U; 78.55; 78.60

Keywords: Photoacoustic spectroscopy; Luminescent quantum efficiency; Cr^{3+}; $LiNbO_3$

1. Introduction

Lithium niobate is a material that combines excellent electro-optic, acousto-optic and non-linear properties with the possibility of rare earth or transition metal doping. This material can be used in bulk or it is possible to prepare low-loss optical wave guides [1,2]. Laser action was obtained in different doping ions and more recently self-frequency doubled action was obtained in lithium niobate doped with Nd or Yb [3,4].

The fluorescence quantum efficiency Φ of a luminescent material is one of the most relevant parameters to have a complete characterisation of a material. While photoacoustic methods have been extensively used in the quantum efficiency

*Corresponding author. Tel.: +54-221-484-0280, fax: 54-221-471-2771.

E-mail address: gustavot@ciop.unlp.edu.ar (G.A. Torchia).

0022-2313/01/$ - see front matter © 2001 Elsevier Science B.V. All rights reserved.
PII: S0022-2313(01)00161-2

determination of gases or liquids [5–7], there are much less examples for solid state materials. Normally, photoacoustic methods use a comparison with one standard material. This procedure is not adequate for quantitative measurements in solid state, because changing the sample may substantially affect the acoustic coupling in the experimental set-up. Some authors have pointed out the possibility of obtaining absolute measurements without standards [8] and this last time an alternative method based on the simultaneous detection of photoacoustic and luminescence signals, after excitation at two different wavelengths, has been proposed by E. Rodriguez et al. [9]. This method called SIMPLE (simultaneous multiple-wavelength photoacoustic and luminescence experiments) relies on the existence of a full non-radiative relaxation, providing an internal reference that can be used for absolute quantum efficiency determination. The harmonics of a Nd:YAG laser were used in the first experiments, with the disadvantage of the necessary coincidence of the Nd:YAG harmonics with the absorption bands of the sample. These difficulties can now be avoided thanks to the appearance of pulsed tunable sources (oscillator parametric MOPO) which can be used for broad excitation in the range 0.4 at 2 μm. This method was applied to the determination of luminescence quantum efficiency of Cr^{3+} ions in co-doped $LiNbO_3$:ZnO crystal. The Cr^{3+} ions in this crystal present two broad absorption bands and can be excited with the MOPO. In relation to Zn co-doping, it should be noted that in this way the photorefractive damage of $LiNbO_3$ is suppressed and therefore this material is adequate for optoelectronic application.

Additionally, a comparison between this method and values found by luminescence lifetime studies in terms of the temperature is reported in this paper.

2. Experimental set-up

The congruent $LiNbO_3$:Cr:Zn crystal used in this work was grown in the Universidad Autónoma de Madrid, by Czochralski's method in an open atmosphere. The Cr^{3+} and Zn^{2+} compositions were determined by EXFT (Fluorescence Total X-ray Emission) calibrated with standard samples. The concentrations of chromium and zinc ions in the crystal were 0.1% and 5.3%, respectively; these measurements were normalised at Nb^{5+} concentrations. The samples were cut in the form of rectangular slabs of approximate dimensions $10 \times 5 \times 1\,mm^3$. Their faces were carefully polished with diamond powder of 1 μm. Continuous wave and pulsed optical and photoacoustic measurements were performed.

Optical absorption was conducted at room temperature by using an Hitachi U-3501 spectrophotometer. Continuous wave (cw) emission was excited with a multiline Argon laser. The fluorescence spectrum was analysed with a 50 cm focal length monochromator (SPEX 5000 M) with a germanium photodiode followed by lock-in amplification.

Pulsed measurements were made with excitation from an optical parametric oscillator (MOPO-730 by Spectra Physics). This source pumped by a Q-Switch neodymium laser provide pulses of 8 ns (FWHM), of approximately 200 mJ from 450 to 690 nm with a bandwidth of $0.1\,cm^{-1}$.

Pulsed fluorescence (LUM) was detected by using the above mentioned monochromator at fixed wavelength of 950 nm but with a different light detector for better time resolution. A Hamamatsu 751 K AsGaIn phototube was used. For the fluorescence quantum yield determinations by simultaneous multiple-wavelength photoacoustic and luminescence experiments (SIMPLE) method, LUM was taken as the maximum of luminescence time resolved signal.

Photoacoustic signal was achieved with a resonant ceramic piezoelectric transducer (PZT), having a bandwidth of 200 kHz. The piezoelectric detector was coupled to the sample with vacuum grease, to optimise the acoustic coupling. To use the SIMPLE method, photoacoustic signal (PAS) was taken as the peak to peak value of the first arrival wave. These considerations make negligible the other contribution originated by reflections on the other face of the sample.

Both signals, photoacoustic (PAS) and LUM were detected simultaneously and registered by

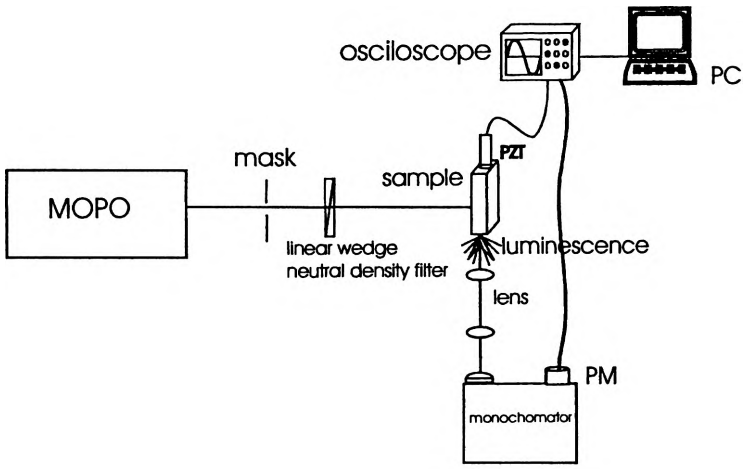


Fig. 1. Experimental set-up used in this work for the measurement of quantum efficiency of Cr^{3+} ions in co-doped $LiNbO_3:ZnO:Cr^{3+}$ crystals by the SIMPLE method.

digital oscilloscope Tektronix 2440. Fig. 1 shows the experimental set-up used in this work.

The whole time-resolved phototube-signal was recorded in order to get the lifetime of the emission level. In this case the sample was cooled from room temperature to liquid helium temperature by using a flux cryostat. PZT was removed for these measurements.

3. Results and discussion

The absorption spectrum of Cr^{+3} ions in co-doped $LiNbO_3:Cr^{3+}:ZnO$, presents two broad absorption bands, centred at 500 nm and 660 nm, when the content of ZnO in the melts is above 7% mol. These bands are associated with the vibronic transitions $^4A_2 \rightarrow {}^4T_1$ and $^4A_2 \rightarrow {}^4T_2$, respectively, of Cr^{3+} ions in $LiNbO_3:ZnO$ congruent crystals [10].

Fig. 2 shows the absorption and emission spectra obtained by cw excitation. A single luminescence wide band is observed independent of the excitation wavelength; therefore the internal non-radiative relaxation between the $^4T_1$ and $^4T_2$ provides a valuable PAS reference for internal calibration. This band is centred at 950 nm with 100 nm of FWHM, corresponding to the vibronic transition of chromium $^4T_1 \rightarrow {}^4A_2$ [10]. In the same figure level diagram is presented, where all radiative and non-radiative processes, corresponding to vibronic transitions of Cr^{3+} into a low crystal field symmetry, are included [11].

For the luminescence conditions found in this ion, two excitation bands and one emission band, the fluorescence quantum efficiency by the SIMPLE technique can be determined. In this method, the fluorescence quantum efficiency (Φ) can be calculated from

$$\Phi = \frac{\lambda_{emi}}{\lambda_L} \frac{\Lambda - \lambda_L/\lambda_H}{\Lambda - 1}, \tag{1}$$

where λ_L and λ_H represent the wavelengths of low and high energy excitation, λ_{emi} is the emission wavelength and Λ represents the ratio between the slope of the linear fit in the graphics PAS against LUM, for each excitation wavelength at low and high energy,

$$\Lambda = \frac{\partial \mathrm{PAS}_{\lambda_{High}}/\partial \mathrm{LUM}_{\lambda_{High}}}{\partial \mathrm{PAS}_{\lambda_{Low}}/\partial \mathrm{LUM}_{\lambda_{Low}}}. \tag{2}$$

Fig. 3 shows the experimental results for the PAS against the LUM signal The crystal of $LiNbO_3:Cr^{3+}:ZnO$ was excited with pulses from the MOPO at 500 nm (λ_{High}) for high energy and 650 nm (λ_{Low}) for low energy. These results clearly show that the relation PAS vs. LUM for different excitation energies from the MOPO was linear.

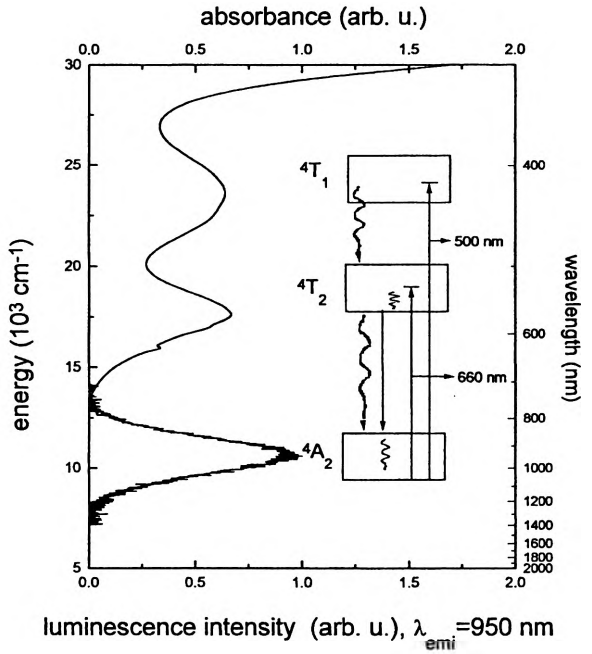


Fig. 2. Absorption and emission (cw) spectra of chromium ions in the $LiNbO_3$: ZnO crystal. The level diagram of Cr^{3+} ions in this crystal is also presented.

After a linear fit for experimental points $\Lambda = 1.35 \pm 0.05$ was determined. By using the expression (1), the fluorescence quantum efficiency of Cr^{3+} ions in co-doped $LiNbO_3$: ZnO crystal was calculated as $\Phi = 10 \pm 4\%$.

The fluorescence quantum yield can be estimated through the analysis of the lifetime of the emission level in terms of the temperature. If sufficiently low temperature values can be achieved, Φ can be calculated from

$$\Phi(T) = \frac{\tau_{exp}(RT)}{\tau_{exp}(LT)}, \tag{3}$$

where the non-radiative transitions probability at low temperature (LT) was taken as null.

Fig. 4 shows the time resolved luminescence signals at low temperature (a) and room temperature (b) of chromium ions in lithium niobate doped with ZnO. Fluorescence was excited by 650 nm pulses and detected at 950 nm. Bi-exponential decay can be attributed to the presence of two non-equivalent sites for Cr^{3+} in $LiNbO_3$.

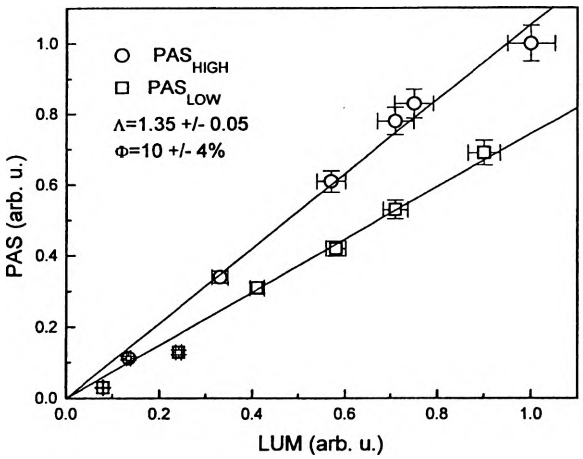


Fig. 3. Photoacoustic (PAS) and luminescence (LUM) signals for different MOPO excitation powers corresponding to different wavelengths.

The fitting gives (8 ± 2) μs and (19 ± 2) μs for the lifetime of Cr^{3+} at LT and (0.4 ± 0.1) μs and (2.3 ± 0.2) μs, at room temperature for both sites. Faster relaxation can be attributed to Cr^{3+} in lithium sites because the lifetime is similar to the measured one in $LiNbO_3$ without doping. Other lifetimes correspond to Cr^{3+} in niobium sites; this site is induced by the high concentration of Zn^{2+} used in the sample. By using these lifetime values in the expression (3) quantum efficiencies of 10 ± 2 and $4 \pm 1\%$ for $Cr^{3+}_{(Nb^{5+})}$ and $Cr^{3+}_{(Li^{+})}$, respectively, were obtained.

The concentration of Cr^{3+} ions in both sites was estimated by Electron Paramagnetic Resonance (EPR) technique. The inset of Fig. 4 shows the EPR spectrum at RT for $LiNbO_3 : Cr^{3+} : ZnO$ (5.3%) obtained with the magnetic field applied perpendicular to the c axis of the crystal with 100 kHz modulation frequency. The two lines of resonance at 1800 and 3500 G were associated with $Cr^{3+}_{(Li^{+})}$ and $Cr^{3+}_{(Nb^{5+})}$, respectively [12]. From the ratio of areas of this spectrum, the concentration ratio of $[Cr^{3+}_{(Nb^{5+})}]/[Cr^{3+}_{(Li^{+})}]$ equal to 4 was calculated.

As the total quantum efficiency luminescence Φ is proportional to the concentration times the quantum efficiency for each chromium site in the crystal, Φ is equal to $(9 \pm 2)\%$, in agreement with the values found by SIMPLE method.

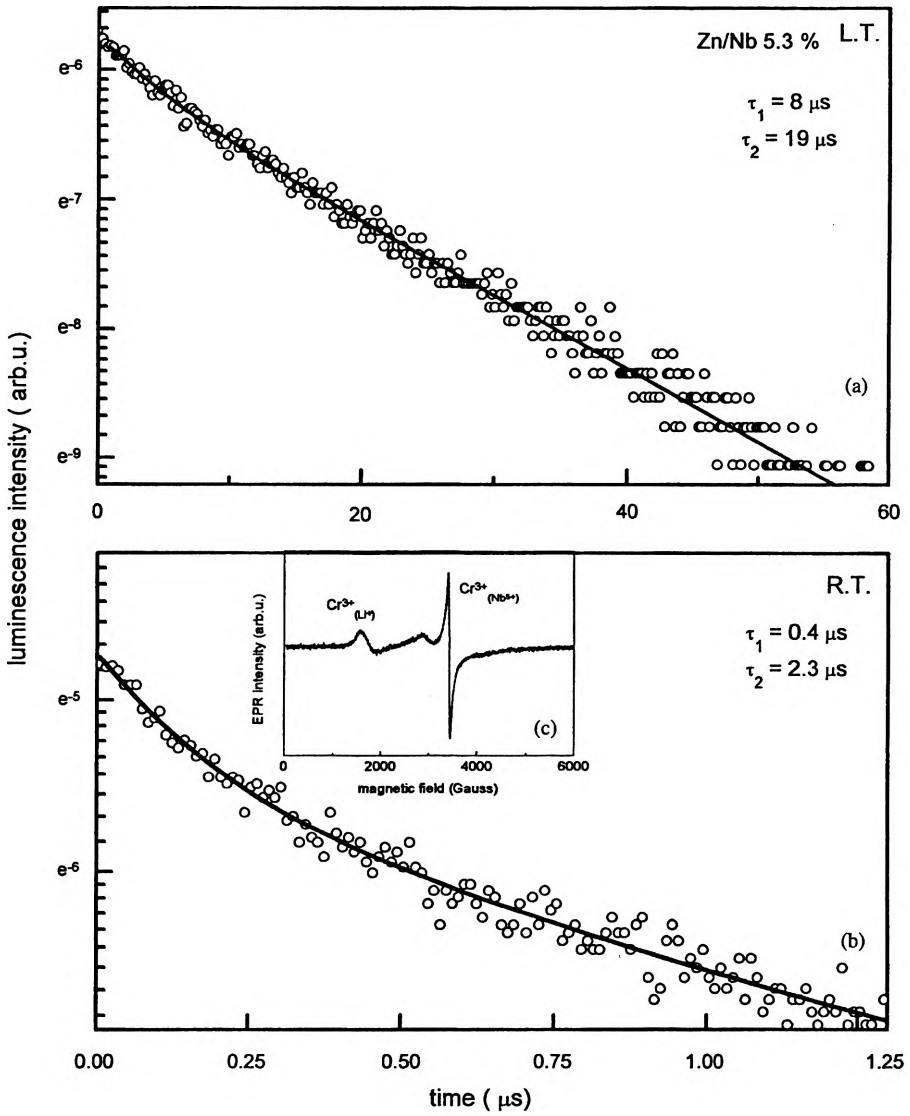


Fig. 4. Logarithmic plots for time resolved fluorescence (950 nm emission, 650 nm excitation) at low temperature (a) and room temperature (b). Bi-exponential fittings are also shown. The two lifetimes are associated to the two centres presented in the crystals. In the inset the EPR spectrum at RT is shown.

4. Conclusions

In this work, the fluorescence quantum efficiency of Cr^{3+} ions in co-doped $LiNbO_3:ZnO:Cr^{3+}$ congruent crystal was obtained. By using SIMPLE method the unresolved crystal sites value was $(10\pm4)\%$, while by lifetime measurements and weighting the two non-equivalent sites found in this crystal, the total fluorescence quantum yield was estimated as $(9\pm2)\%$. Despite the fact that this last method is only approximate because several simplifications must be assumed to justify its validity, the values obtained are comparable. It can be affirmed that the quantum efficiency Φ for the Cr^{3+} ions in ZnO co-doped $LiNbO_3$ congruent crystal is not more than 10%.

In a previous experiment by E. Rodriguez and co-worker a quantum efficiency of 5% was found but for $LiNbO_3:Cr^{3+}$, without ZnO co-doping [13]. Despite the fact that in that case the accuracy was much lower due to the reduced excitation range accessed with a dye laser, the value is in good agreement with the value found here for the luminescence quantum yield of Cr^{3+} in Li sites.

The SIMPLE method in pulsed regime has been proved as a reliable technique for the determination of fluorescence quantum efficiency in a wide range of Φ values and for different ions in several crystal lattices.

References

[1] B. Herreros, G. Lifante, Appl. Phys. Lett. 72 (1998) 531.
[2] W. Solher, Advanced Integrated Optics in LiNbO3 Proceedings of the 11th Annual Conference On European Fibre Communications and Networks (EFOC&N'93), 1993.
[3] D. Jaque, J.A. Sanz-Garcia, J. Capmany, J. Garcia Sole, Appl. Phys. B. 70 (2000) 483.
[4] E. Montoya, J. Capmany, L.E. Bausá, T. Kellner, A. Diening, G. Haber, Appl. Phys. Lett. 74 (21) (1999) 3113.
[5] C.K.N. Patel, A.C. Tam, Rev. Mod. Phys. 53 (1981) 517.
[6] A.C. Tam, Rev. Mod. Phys. 58 (1986) 381.
[7] H. Vargas, L.C.M. Miranda, Phys. Rep. 161 (2) (1988) 43.
[8] D.J. Dunstan, J. Phys. D. 25 (1992) 1825.
[9] E. Rodriguez, J.O. Tocho, F. Cussó, Phys. Rev. B 47 (21) (1993) 14049.
[10] G.A. Torchia, J.A. Sanz-García, J. Díaz-Caro, T. Han, F. Jaque, Chem. Phys. Lett. 288 (1998) 65.
[11] B. Henderson, Imbush Optical Spectroscopy of Inorganic Solids, Oxford Science Publications, Oxford, 1989.
[12] J. Diaz-Caro, J. García-Solé, D. Bravo, J.A. Sanz-García, F.J. López, F. Jaque, Phys. Rev. B 54 (18) (1996) 13042.
[13] E. Rodriguez, L. Nuñez, J.O. Tocho, F. Cussó, J. Lumin. 58 (1994) 353.

Láseres gaseosos

La investigación sobre láseres gaseosos ha sido una de las líneas pioneras en el CIOp, que se comenzó a desarrollar cuando los investigadores aún pertenecían al LEOL, Dto de Física UNLP. Estos láseres funcionan confinando el gas en celdas tubulares a determinada presión y haciendo pasar una corriente (continua o pulsada) por medio de electrodos de geometría apropiada. A principios de la década del 70, uno de los láseres gaseosos que más se estudiaban a nivel mundial era el de nitrógeno molecular (N2), principalmente debido a su alta potencia en el UV (337 nm) cuando se lo excitaba con descargas eléctricas pulsadas de alta tensión y corriente en una configuración transversal a la dirección de ganancia óptica ("campo cruzado"). La experiencia en espectroscopía atómica y molecular y el trabajo sistemático sobre circuitos de descarga confluyeron para dar varios trabajos sobre la relación entre diversas condiciones de excitación y espectroscopía de la salida láser y espontánea. Estos primeros estudios sobre la emisión UV de este láser se extendieron a la emisión en distintas bandas del cercano IR y a la interacción entre los niveles de energía que las generaban. Al escribir estas características en función de las ecuaciones de "rate" que gobiernan la cinética de población de los distintos niveles involucrados, fue posible obtener un conocimiento más profundo de los mecanismos de población en estos tipos de láseres.

Dentro de la línea de láseres gaseosos moleculares, se estudió, con el mismo enfoque, el caso del monóxido de carbono (CO). Las distintas bandas de emisión en el visible de este láser poseen niveles de energía que muestran cierto grado de interacción que pudo estudiarse en base a otro conjunto de ecuaciones de rate que en este caso, contenían un término que daba cuenta de la pérdida de moléculas activas por descomposición química durante la descarga eléctrica.

El primero de los trabajos seleccionados resume el conocimiento alcanzado sobre los mecanismos de inversión de población en láseres de moléculas diatómicas.

El otro láser gaseoso largamente estudiado en el CIOp es el láser de Xenon (Xe) iónico. En este caso, el material activo es Xe que, al ser excitado por una corriente pulsada de varios kiloamperes de pico, genera especies iónicas de distintos grados. El estudio espectroscópico sistemático de la salida multilínea de este láser, que cubre el UV cercano y el espectro visible, asigna a las líneas observadas distinto origen iónico. Una descripción de ecuaciones de rate para este láser, junto con un análisis espectroscópico resuelto en tiempo de las distintas líneas láser observadas, permitió comprender con buena exactitud los mecanismos que llevan a la inversión de población en este láser.

El segundo de los trabajos seleccionados resume las diversas tareas de investigación realizadas con este láser gaseoso.

Gas Lasers

Gas laser physics research has been one of the pioneering areas at CIOp, which started when the researching staff still belonged to LEOL, Physics Dept UNLP. These lasers work when a pulsed or CW current is passed through a tubular cell containing the gas at a definite pressure and temperature. In turn, the cell is confined within an appropriate resonant optical cavity. At the beginning of the 70´s, one of the most studied gas lasers was that of molecular nitrogen (N2), mainly due to its high power UV emission (337 nm) when excited by fast pulsed high current electrical discharges, mainly in transversal configuration ("cross-field"). The experience in atomic and molecular spectroscopy together with a systematic work on low-inductance discharge circuitry allowed the authors to publish several papers on the relation between fine-detail emission spectroscopy and diverse excitation conditions. These first studies on UV emission of the N2 laser extended to other NIR laser emissions and to the interaction between the energy level populations that gave rise to those transitions. This interaction was put in rate equation language and permitted a deeper knowledge of the population mechanisms involved in this type of lasers.

Another molecular gas laser studied was the CO laser in its multiband visible emission. The energy levels that give rise to these emissions also show cascade-type interaction in their populations, which was also studied using the rate-equation formalism. The first selected work presented in this section summarizes the knowledge acquired in this area.

The other largely studied gas laser at CIOP was the Xe laser. When kiloampere peak fast pulse current is passed through a low pressure Xe discharge tube, multiline UV-visible laser emission is obtained. These lines originate from different transient ionic Xe species during the electric discharge. Again, a rate equation approach together with data taken from time resolved spectroscopy of its spontaneous and laser output enabled a comprehensive understanding of its population kinetics.

The second selected work presented in this section summarizes the knowledge acquired with this laser.

J. Quant. Spectrosc. Radiat. Transfer Vol. 41, No. 3, pp. 225–233, 1989
Printed in Great Britain. All rights reserved
0022-4073/89 $3.00 + 0.00
Copyright © 1989 Pergamon Press plc

SPECTROSCOPIC STUDY OF POPULATION INVERSION MECHANISMS IN DIATOMIC-MOLECULE LASERS

L. SCAFFARDI, D. SCHINCA, J. O. TOCHO, and H. F. RANEA-SANDOVAL
Centro de Investigaciones Opticas (CIOp), Casilla de Correo 124, 1900 La Plata (B.A.), Argentina

(*Received* 1 *September* 1987; *received for publication* 13 *July* 1988)

Abstract—Spectral analysis of laser radiation emitted by diatomic molecules and simple theoretical models have allowed us to study population-inversion mechanisms in the u.v. and i.r. for N_2 and visible CO molecular lasers. The technique is readily applicable to other diatomic molecules. Observations of Λ-doubling in N_2 u.v. laser emission and analysis of rotational structure in i.r. laser emission for the same molecule are used to determine the main features of electronic excitation and different channels for population of the laser levels involved. For the visible molecular CO laser, a fit of the rotational intensity distribution of the emitted visible bands was used to determine enhancement mechanisms by which population inversion is achieved in some Q-branch transitions.

INTRODUCTION: OUTLINE OF THE METHOD

An extensive review on N_2 lasers was published recently.[1] Several questions remained unanswered concerning excitation mechanisms, particularly of levels involved in the first positive i.r. band system. In this paper, we present a method that can be applied to any diatomic molecule and allows determination of the relative importance of a proposed mechanism on population inversion between vibrational–rotational levels of different electronic states in the molecule. The method has been applied to the N_2 and CO laser systems, using spectroscopic data derived from analysis of the rotational intensity distribution of the 0–1 i.r. and 0–0 u.v. bands in N_2 and of the 0–5, 0–4, 0–3, and 0–2 visible bands in CO.

Two basic levels of information are needed. First, a high-resolution spectrum is required of the bands under study, from which the intensity distribution of the rotational lines can be reliably obtained. Second, a description is needed of the gain for each individual rotational line; this description is obtained from the theory of spectra for diatomic molecules, which is well established.

In writing the gain equation, proposed mechanisms for level population are included. We have studied participation of two different mechanisms in the population of levels, namely, direct impact excitation by slow electrons in a pulsed discharge and cascade population (and depopulation) by stimulated emission from upper levels.

Basically, we assume that, upon direct collisional excitation by slow electrons of molecules in the ground state, the rotational population is duplicated in the excited states,[2] and there is no possibility for equilibration before the onset of stimulated emission because of the small ratio of radiative to collisional decay times. This approximation eliminates the need of knowing electron–molecule and molecule–molecule collision rates for time-dependent populations. Thus, population variation is adiabatically eliminated. For cascading, the use of optical-transition probabilities and statistical-weight factors allows us to model the process. If other population (depopulation) mechanisms are included, knowledge of their influence on rotational population redistribution is required.

With the specified assumptions, a simulated spectrum can be generated and fitted to observed data by varying parameters that measure the relative importance of different processes. A threshold-gain value is used to define the laser intensity of the simulated lines in the first approximation. Additional information on observed spectra may be used to reject mechanisms and to simplify the analysis, as will be shown for the case of Λ-doubling in the second positive system of N_2.

Three adjustable parameters must be chosen in our examples in order to fit a complete rotational spectrum. This requirement has proved to be highly restrictive and assures good accuracy for the parameters involved.

N_2 LASER

Laser action in molecular nitrogen in the i.r. and u.v. was first obtained by Mathias and Parker[3] and Heard,[4] respectively. Since the lower level of the u.v. transition (2^+ system) is the upper level of the i.r. transition (1^+ system), as shown in Fig. 1, interaction between them may be assumed. Only a few studies deal with this interaction and there is some disagreement concerning the conclusions.[5,6]

Recently, Kruger[7] has studied the interaction between the 1^+ and 2^+ systems by analysing the spontaneous sidelight emission from a discharge tube lasing in the i.r. He was able to reproduce the vibrational intensity distribution of the observed bands by varying a cascade factor f, related to stimulated emission connecting the $C^3\Pi_u$ and the $B^3\Pi_g$ states, in the rate equations. We have studied population mechanisms of the $C^3\Pi_u$, $B^3\Pi_g$, and $A^3\Sigma_u^+$ levels by using a model that simulates the rotational intensity distribution of the 0–1 i.r. laser band at different pressures. We compare this intensity distribution with experimental data.

Discharge tubes of different active lengths and internal diameters were used for both the axial and transverse excitation modes. The tubes were immersed in a liquid-air bath to increase the gain of the stimulated emission. A 3.4-m focal length, Ebert-mount spectrograph with a 600 grooves/mm diffraction grating was used for the spectral analyses. Dispersions in the 1st and 9th diffraction order were 4.8 and 0.22 Å/mm, respectively. A detailed description of the experimental setup has been given elsewhere.[8,9]

While nearly all laser bands present only one output maximum as a function of pressure,[10] the 0–1 i.r. band peaks at two different pressures (see Fig. 2). Since the pressure range used to study the 0–0 u.v. band is the same as that for the low-pressure peak of the 0–1 i.r. band, and the lower level of the u.v. band is the upper level for i.r. emission, it is plausible to assume that the population of the $v = 0$ vibration level of the $B^3\Pi_g$ state is due, in part, to a cascade process from the $C^3\Pi_u$ state and, in part, to an electron-impact process. In this case, inhibition of u.v. emission should affect the low-pressure peak of the i.r. band.

It is apparent from Fig. 2 that inhibition of the feed-back of the u.v. radiation by suitable intracavity filters drastically reduces the intensity of the low-pressure peak of the 0–1 i.r. band, which indicates that the proportion of the cascade population channelled by direct impact excitation is greater at lower pressures. This difference in excitation mechanisms affects the rotational structures of the emission spectra of both peaks, as is shown in Fig. 3. In order to

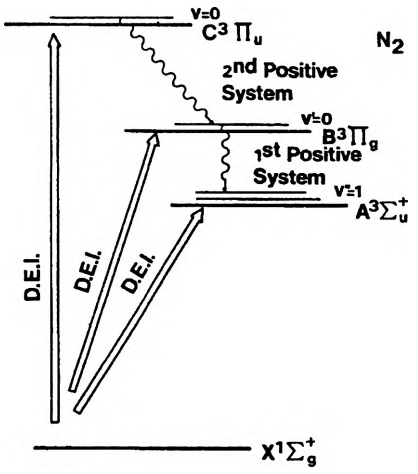


Fig. 1. Partial energy level diagram for a molecular laser.

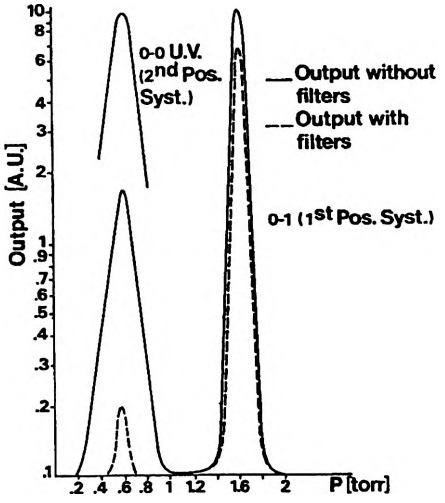


Fig. 2. Output of the 0–1 i.r. laser band vs N_2 pressure, with and without intracavity filters to block the 0–0 u.v. laser band.

simulate these rotational spectra, we assume that the $B^3\Pi_g$ state population is caused, in part, by direct electron impact from the ground state and, in part, by radiative decay from the $C^3\Pi_u$ state. The latter process selectively populates rotational levels of the $v = 0$ vibrational level in the $B^3\Pi_g$ state, thereby destroying population equilibrium. This situation is stationary in the pressure range used since the collision frequency is not sufficiently high to redistribute the population during the time that i.r. laser emission lasts (150 ns).[8]

When a molecule is excited by electron collisions, large changes are not produced in the angular momentum of the system.[11] Therefore, molecules excited by electron impact from the ground state of the B-state show the same population distribution over the rotational level as in the initial state.

The population of the B_J levels caused by cascading can be calculated by using optical selection rules governing the u.v. transitions ($C^3\Pi_u \rightarrow B^3\Pi_g$) and a population for the C-state associated with pure electron impact.[8] The specified rules only allow P and P' ($\Delta J = -1$) or R and R' ($\Delta J = 1$) branches. Since only the $\Delta J = -1$ branches were observed in the u.v. laser spectra, we disregard the R and R' branches in our analysis.

The population of rotational levels in the $v = 0$ vibrational level of the B-state is given by

$$N_J^B = [a_1(2J+1) + a_2 i(P, P')]2^n \exp[-B_x J(J+1)hc/kT], \tag{1}$$

where the first term in the bracket arises from electron impact and the second from cascading. Here, a_1 and a_2 are parameters that determine the ratio between cascading and direct impact. We normalize the population distribution by setting $a_1 + a_2 = 1$ to obtain a purely thermal distribution for $a_2 = 0$: J is the rotational quantum number, B_x the vibrational constant of the ground state, h Planck's constant, c the velocity of light, k Boltzmann's constant, T the rotational temperature, n an integer that has the values 0 or 1 (depending on whether the rotational level is asymmetric or symmetric, respectively), and i the optical transition probability for the P and P' branches given by Kovács[12] when both states belong to Hund's case a for small J values. The population of the $A^3\Sigma_u^+$ state may be assumed to be caused by electron impact from the ground state and is given by an expression similar to that for the B and C populations:

$$N_J^A = (2J+1)2^n \exp[-B_x J(J+1)hc/kT]. \tag{2}$$

The unsaturated gain $G_{JJ'}$ of laser lines is proportional to population inversion and to transition probability. Hence, we may write

$$G_{JJ'} = [N_J^B - (1/a)(g_B/g_A)N_{J'}^A]i_{JJ'}, \tag{3}$$

where $a^{-1} = N_v^A/N_v^B$ is the inverse of the vibrational population inversion, g_B and g_A are the

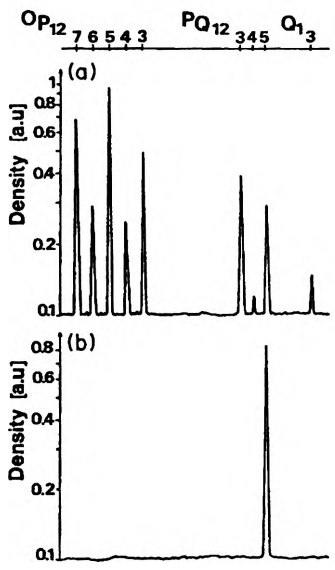


Fig. 3. Microdensitogram of (a) the high-pressure spectrum and (b) the low-pressure spectrum of the 0–1 i.r. laser band.

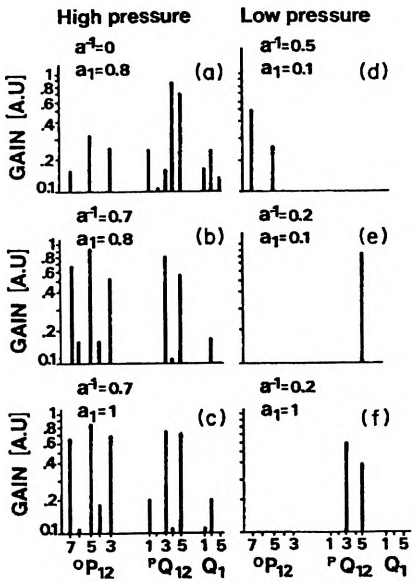


Fig. 4. Simulated spectra of the 0–1 i.r. laser band.

statistical weights of the rotational level, and $i_{JJ'}$ is the optical transition probability for a given rotational transition when the A-state is in Hund's case b.

The relation between laser intensity and calculated gain was obtained by neglecting spontaneous emission. Above the threshold, the intensity is proportional to the gain, i.e., $I \propto (G - G_T)$.[13] Thus, the intensity can be written as

$$I = \begin{cases} 0 & \text{if} \quad G < G_T, \\ 100(G - G_T)/(1 - G_T) & \text{if} \quad G \geqslant G_T, \end{cases} \tag{4}$$

where G is the gain that is normalized to the maximum unsaturated gain $G_{JJ'}$. Since we measure only relative intensities, this maximum was arbitrarily taken as 100.

Using Eqs. (1)–(4), the intensity of the i.r. lines was calculated for different values of the parameters a_1, a, and G_T. Some results are shown in Fig. 4. Figure 4(b) shows the simulated spectrum of the high-pressure peak for optimal values of a_1 and a^{-1}. It is possible to find a threshold value so that only lines with gains above this threshold can be observed experimentally.

It is, however, impossible to find such a value from Fig. 4(c) for which no cascading is assumed. Figure 4(a) shows that if the A-state population is neglected ($a^{-1} = 0$), it is impossible to reproduce the high-pressure spectrum for any value of a_1. This result means that the dependence of the intensity distribution of the laser emission on J does not follow the intensity distribution for spontaneous emission.

Similar results are shown for the low-pressure peak in Figs. 4(d)–(f). Unfortunately, the 0–1 i.r. band only lases in one line, a fact that prevents the accurate determination of best values for a_1 and a^{-1}. Nevertheless, these parameters can be determined to fit such a spectrum. The values for both parameters range from 0 to 0.4, suggesting that there is a lower population of the A-state and a lower proportion of electron impact than in the high-pressure case.

Figure 4(e) shows a simulation of the low-pressure spectrum. However, if either a^{-1} [Fig. 4(d)] or a_1 [Fig. 4(f)] are chosen beyond this range of values, the line of maximum intensity is not the experimentally observed curve.

The optimal parameters show that, in the low-pressure case, cascading contributes 70–90% to the population of rotational levels of the $v = 0$ vibrational level of the B-state, while for the high-pressure case, this contribution amounts to 20%. This result agrees with previously mentioned measurements of Kruger[7] and with the results obtained through u.v. laser-radiation inhibition at low pressures.

LAMBDA-DOUBLING

The observation of the Λ-doublet components in transverse and longitudinal discharge spectra has led to clearer understanding of the excitation mechanisms of the C- and B-states.

Massone et al[8] were the first to observe both Λ-components of the 0–0 u.v. laser band in axial-discharge lasers. The high resolution achieved in the spectra, together with a careful assignment of rotational lines, allowed the authors to discuss some previous conclusions given by Parks et al.[14]

The conclusions in Ref. 14 were that observation of only one of the Λ-components (Π^+) could be explained by a detailed analysis of the electron-collision process. For electron energies much greater than the excitation threshold and in the limit of small momentum transfer, the inelastic electron collision cross section can be expressed in terms of the optical transition probability factor. To show the general consistency of this approximation, the authors of Ref. 14 showed agreement between their calculated gain term and their observation of only one Λ-component.

Fortrat parabolas constructed in accordance with the results of Massone et al are shown in Fig. 5. The dots represent the values found by Parks et al, which were assigned by these authors to a single Fortrat parabola. Analysis of the experimental data of other authors and their own enabled Massone et al to show that the mean energy of electrons in the discharge should be close to the excitation threshold of the C-state (11 eV), indicating that the assumption of high mean electron-excitation energy is not an appropriate mechanism for the C-state excitation.

Later work at our laboratory[9] clearly showed the difference between the 0–0 u.v. laser band spectra obtained in axial and in transversed discharges (see Fig. 6), indicating that in the latter only

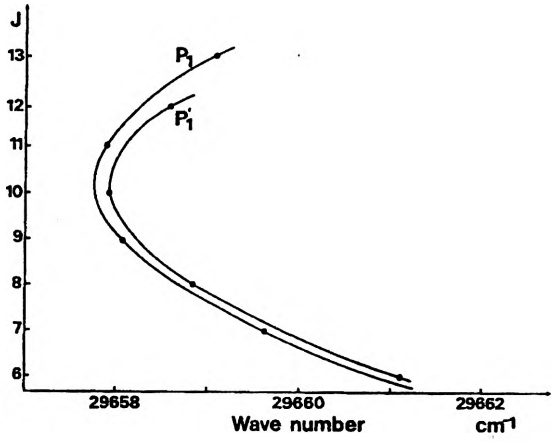


Fig. 5. Partial Fortrat parabolas of the P_1 and P_1' branches of the 0–0 u.v. laser bands. Dots represent the values assigned in Ref. 11 to a single parabola.

the strongest Λ-doublet components are observed. The authors[9] concluded that the doublet may be observed if threshold excitation conditions are better met. This conclusion agrees with the results of Scaffardi et al,[15] who observed both components in axial-type lasers, but only the alternating strong components in superfluorescent emission with the same geometry. The studies of Ranea-Sandoval et al[16] on transverse discharges show growth of the weak Λ-components as the excitation increases. These results are in general qualitative agreement with those of Petit et al,[17] as was noted in Ref. 18. Preliminary gain calculations assuming low mean electron-energy-excitation are in agreement with experimental observations of the Λ-doublets, both in axial and transverse discharges. For low-temperature axial lasers, the best fit of the observed intensity distribution was achieved for an a-value of 1.4; for transverse lasers at room-temperature, the best fit corresponds to an a-value of approx. 1.6.

CO LASER

In this section, we apply our procedure to the study of excitation mechanisms involved in the Ångstrom system laser levels of the CO molecule.

Carbon monoxide laser action can be obtained in three spectral regions: the i.r. (5 μm), the visible (450–700 nm), and the v.u.v. (180–190 nm). While the i.r. emission has been studied extensively (see, for example, Ref. 19), there are few studies dealing with visible[20–23] and v.u.v.[24] emission

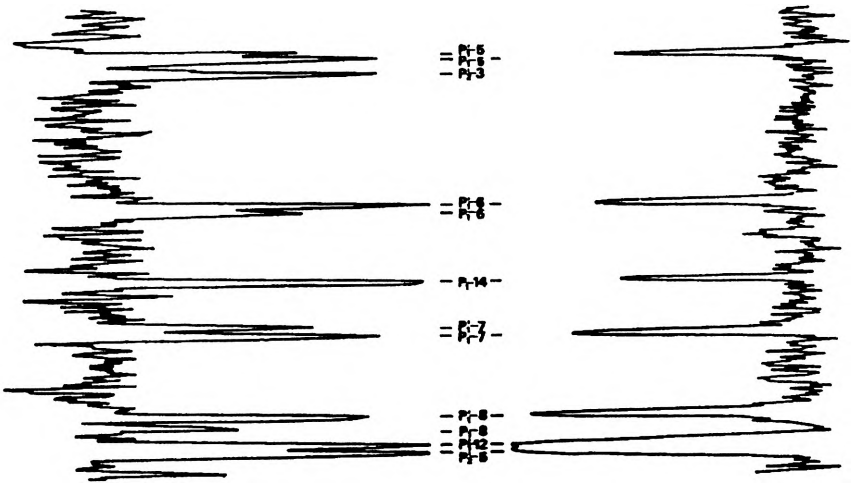


Fig. 6. Microdensitometric traces of a part of the 0–0 (337.1 nm) N_2 laser band. The right-hand and left-hand traces correspond to axial and crossed field discharges, respectively.

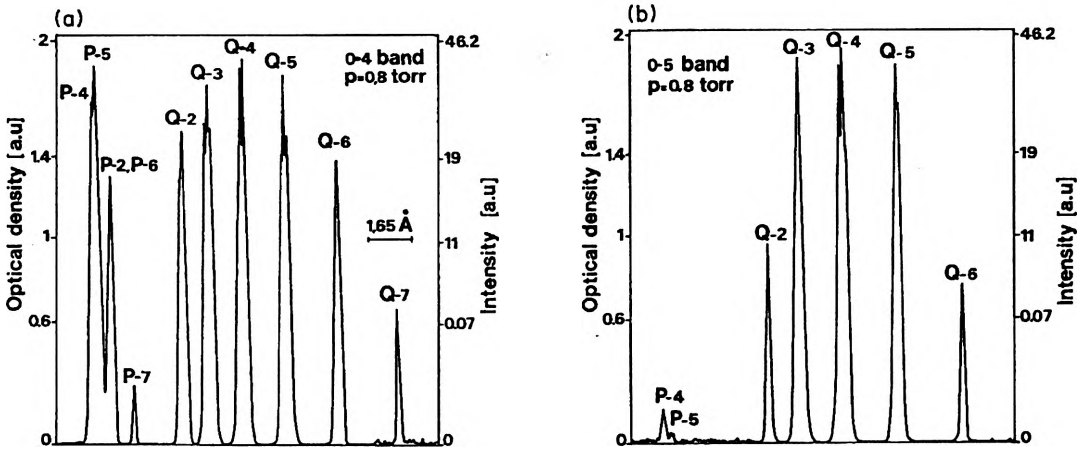


Fig. 7. Microdensitograms of the CO laser bands: (a) 0–4 and (b) 0–5. The dispersion is the same in both cases.

characteristics. Only one of these[21] deals, in a preliminary way, with population inversion mechanisms of the Ångstrom system.

In our experimental apparatus, commercial CO was allowed to flow slowly through an 80 cm long and 10 mm i.d. discharge tube, which was immersed in a liquid-air bath to increase the gain of the transitions.[23] The spectrograph used was the same as that described in the section devoted to the N_2 case. A detailed description of the experimental setup can be found elsewhere.[25,26]

Spectra of the 0–5, 0–4, 0–3, and 0–2 CO visible laser bands, at pressures ranging from 0.6 to 1.3 torr, were recorded.[27] Figure 7 shows two microdensitograms of these bands at optimum pressure. The rotational structure of the bands consisted of only Q- and P-branches. At low pressures, only Q-branch lines were observed.

Simulation of the observed spectra was carried out by calculating the gain of the electronic–vibrational–rotational transitions of interest, based on the following assumptions (see Fig. 8): (a) the $B^1\Sigma^+$ state belongs to Hund's case a.[11] This state is populated by direct electron impact (DEI) from the $X^1\Sigma^+$ ground state.[21] Because of its short lifetime (25 ns),[28] the collision frequency for our pressure conditions is not high enough[8] to equilibrate the population during the time the visible emission occurs (100 ns). Once again, the rotational population distribution duplicates that of the ground state and, therefore, the population of the rotational levels of the B-state may be written as

$$N_J^B = N_v^B(2J+1)\exp[-B_x J(J+1)hc/kT], \tag{5}$$

where N_v^B is the vibrational level population; (b) the $A^1\Pi$ state belongs to Hund's case a.[11] The

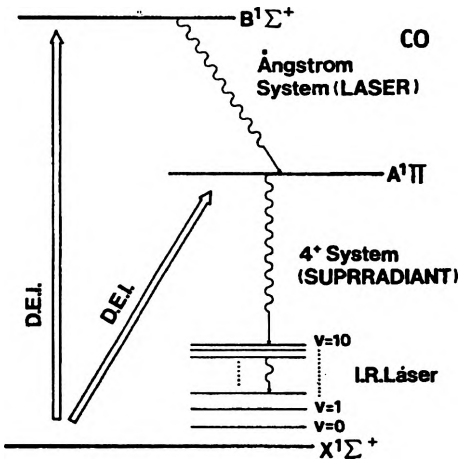


Fig. 8. Simplified energy level diagram of CO.

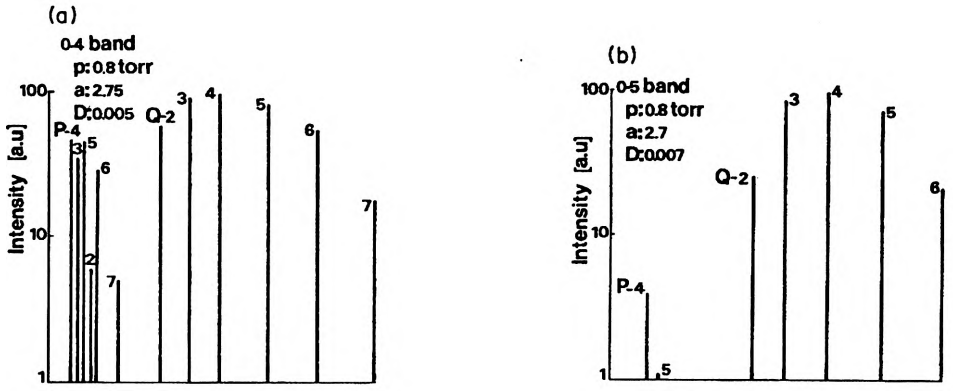


Fig. 9. Simulated spectra of the CO laser bands: (a) 0–4 and (b) 0–5.

$v = 2, 3, 4, 5$ vibrational levels are also populated by DEI from the ground state[21] and duplicate the rotational population distribution because of the short lifetime of the rotational levels (17 ns).[29] Since the A-state is the upper level of the v.u.v. laser transition, it was assumed that its vibrational levels $v = 2, 3, 4, 5$, are depopulated by the v.u.v. radiative transition.

The fact that the v.u.v. laser bands have strong Q-branch, weak R-branch and no P-branch lines[24] suggests that there should be selective depopulation of A-state rotational levels, creating favourable conditions for population inversion of the Q-branch in the visible transition. Thus, the rotational population of the A-state can be written as a combination of DEI and radiative depletion, i.e.,

$$N_J^A = N_v^A[(2J+1)\exp[-B_x J(J+1)hc/kT - 2\Omega^2](1-2(J+1)D)], \tag{6}$$

where N_v^A is the vibrational level population of the A-state, Ω the total angular momentum projection, and D the parameter measuring the porportion of v.u.v. emission. Introducing Eqs. (5) and (6) with the corresponding Hönl–London factor into Eq. (3), we write the gain for the P, Q, and R branch as

$$G_P = (1/2)(J+1)\exp[-B_x J(J-1)hc/kT] - (1/a)\exp[-B_x J(J+1)hc/kT - 2], \tag{7}$$

$$G_Q = (1/2)(2J-1)\exp[-B_x J(J+1)] - (1/a)(1-D(2J+1))\exp[-B_x J(J+1)hc/kT - 2], \tag{8}$$

$$G_R = (1/2)J\exp[-B_x(J+1)(J+2)hc/kT] - (1/a)\exp[-B_x J(J+1)hc/kT - 2], \tag{9}$$

where J is the rotational quantum number of the A-state, and $a = N_v^B/N_v^A$ is the vibrational population inversion ratio.

The observed spectra were simulated by introducing Eqs. (7)–(9) in Eq. (4) and varying the parameters a, D, and G_T. A weighted least-squares method was used in this simulation. The calculated spectra are shown in Fig. 9 and correspond to those of Fig. 7. In each case, the optimal

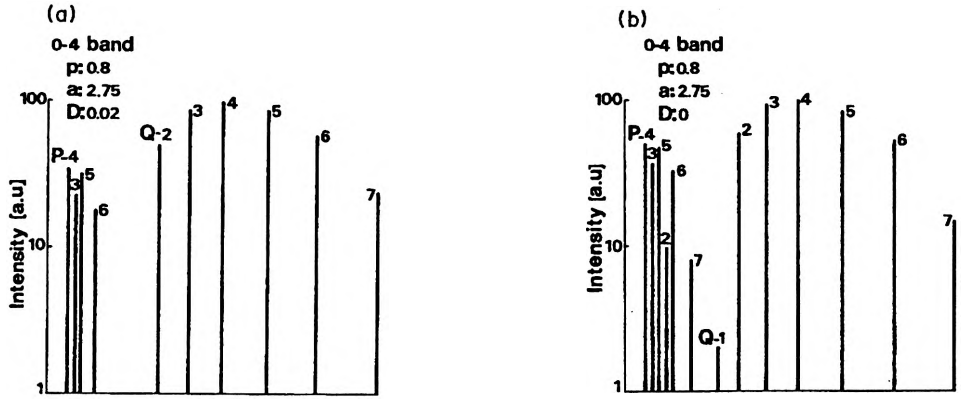


Fig. 10. Simulated spectra of the 0–4 CO laser band for non-optimal a and D parameters.

values of a and D are indicated. For the 0–4 and 0–5 bands, D increases rapidly with pressure, suggesting that depopulation of the lower level enhances the gain of the bands at high pressure.

Simulated spectra calculated for other values of a and D are shown in Fig. 10. For the 0–4 band, a D value above the optimal estimate makes the P-2 and P-7 lines disappear [Fig. 10(a)], while a D value below the optimal results in the appearance of the Q-1 line [Fig. 10(b)]. The method is very sensitive to small changes of a and D, a fact that enables us to obtain an accurate simulation of spectra showing different rotational structures.

These results suggest a strong contribution involving cascading from the 4^+ system to the visible transition gain, especially in the 0–4 and 0–5 bands. This enhancement of the gain of the Q-branch lines of the visible spectra is produced by selective depletion of the lower laser level through v.u.v. radiative transitions.

CONCLUSIONS

Our analysis shows that it is possible to establish quantitatively excitation mechanisms that lead to population inversion in some transitions by using a simple theoretical model that reproduces the spectral intensity distribution. This method is particularly useful for diatomic molecules, for which the large number of rotational lines provides a good deal of information for an accurate fitting of the spectra. The procedure proved to be extremely sensitive to variations of the fitting parameters. Small deviations from optimal values distort the simulated intensity distribution in such a way that it is impossible to reproduce the observed spectra. The assumptions made about populations of the involved levels on excitation simplify gain-theoretical calculations and proved to be a useful approximation for diatomic molecules.

REFERENCES

1. R. S. Kunabenchi, M. R. Gorbal, and M. I. Savadatti, *Prog. Quant. Electron.* **9**, 259 (1984).
2. V. N. Ochkin, S. Yu. Savinov, and N. N. Sobolev, *Soviet Phys. JETP* **48**, 232 (1978).
3. L. E. S. Mathias and J. T. Parker, *Appl. Phys. Lett.* **3**, 16 (1963).
4. H. G. Heard, *Nature, Lond.* **200**, 667 (1963).
5. L. Allen, D. G. C. Jones, and B. M. Sivaram, *Phys. Lett. A* **25**, 280 (1967).
6. M. Garavaglia, M. Gallardo, and C. A. Massone, *Phys. Lett. A* **28**, 787 (1969).
7. J. S. Kruger, Ph.D. Thesis, The American University, Washington, DC (1981).
8. C. A. Massone, M. Garavaglia, M. Gallardo, J. A. Calatroni, and A. A. Tagliaferri, *Appl. Opt.* **11**, 1317 (1972).
9. J. O. Tocho, H. F. Ranea-Sandoval, A. A. Tagliaferri, M. Garavaglia, M. Gallardo, and C. A. Massone, *Nouv. Rev. d'Opt.* **5**, 319 (1974).
10. L. Scaffardi, D. Schinca, J. O. Tocho, H. F. Ranea-Sandoval, and M. Gallardo, *Appl. Opt.* **24**, 22 (1985).
11. G. Herzberg, *Molecular Spectra and Molecular Structure—I. Spectra of Diatomic Molecules*, Van Nostrand-Reinhold, Princeton, NJ (1950).
12. I. Kovács, *Rotational Structure of the Spectra of Diatomic Molecules*, Adam Hilger, London (1969).
13. A. Yariv, *Quantum Electronics*, 2nd edn, Chap. 9, Wiley, New York, NY (1975).
14. J. H. Parks, D. Ramachandra Rao, and A. Javan, *Appl. Phys. Lett.* **13**, 142 (1968).
15. L. Scaffardi, D. Schinca, J. Reyna-Almandos, M. Gallardo, and M. Garavaglia, *Appl. Opt.* **19**, 3590 (1980).
16. H. F. Ranea-Sandoval, J. O. Tocho, M. Gallardo, and M. Garavaglia, *IEEE J. Quantum Electron.* **QE-17**, 295 (1981).
17. A. Petit, F. Launay, and J. Rostas, *Appl. Opt.* **17**, 3081 (1978).
18. H. F. Ranea-Sandoval, J. O. Tocho, M. Gallardo, and M. Garavaglia, *Appl. Opt.* **18**, 1705 (1979).
19. R. M. Osgood, Jr., W. C. Eppers, Jr., and E. R. Nichols, *IEEE J. Quantum Electron.* **QE-6**, 145 (1970) and references therein.
20. L. E. S. Mathias and J. T. Parker, *Phys. Lett.* **7**, 194 (1963).
21. M. G. Cooper and P. K. Cheo, *Appl. Phys. Lett.* **5**, 44 (1964).
22. A. Henry, G. Arya, and L. Henry, *C. R. Acad. Sci.* **261**, 1465 (1965).
23. V. M. Kaslin and G. G. Petrash, *Proceedings P. N. Lebedev Physics Institute*, N. G. Basov ed., Moscow (1975).
24. R. T. Hodgson, *J. Chem. Phys.* **55**, 5378 (1971).
25. D. Schinca, J. O. Tocho, L. Scaffardi, and M. Gallardo, *Optica Pura Apl. (Spain)* **18**, 211 (1985).

26. D. Schinca, H. F. Ranea-Sandoval, L. Scaffardi, and J. O. Tocho, *IEEE J. Quantum Electron.* **QE-22,** 2272 (1986).
27. D. Schinca, L. Scaffardi, and J. O. Tocho, *Appl. Opt.* **25,** 102 (1986).
28. J. Rogers and R. Anderson, *JOSA* **60,** 278 (1970).
29. J. C. Chervenalk and R. Anderson, *JOSA* **61,** 952 (1971).

Excitation Mechanisms and Characterization of a Multi-Ionic Xenon Laser

H. Sobral, M. Raineri, D. Schinca, M. Gallardo, and R. Duchowicz

Abstract—**The emission characteristics of an ultraviolet-visible pulsed multi-ionic xenon laser were studied through time-resolved spectroscopy and the results were interpreted using a collisional-radiative theoretical model. This analysis includes more than 20 laser lines belonging to several ionic species (Xe III–VIII). Depending on the experimental conditions, different temporal distributions of the laser lines and their corresponding spontaneous emissions can be observed. In particular, laser emission presents temporal oscillations near threshold. Pumping processes for the laser transitions have been analyzed by using this model. Relativistic Hartree–Fock calculations of laser level lifetimes and radiative transition probabilities were performed. Experimental laser gain for several transitions were obtained and compared with the theoretical values derived from the calculations.**

Index Terms—**Collisional-radiative model, gas discharge, gas lasers, xenon laser.**

I. Introduction

SINCE THE advent of the laser, capillary discharges have been used to produce laser action in the ultraviolet (UV), visible, and infrared (IR) range [1]–[4]. In particular, low-pressure xenon plasma excited by pulsed high-current–high-voltage electrical discharges produces high-gain laser transitions in the near UV and visible range. This laser output has been used for pumping dye lasers [5]–[7] and for studying injection-locking phenomena in CW dye lasers [8], [9].

Both from a basic and practical point of view, it is important to know which are the levels and ionic species involved in laser emission. Duchowicz *et al.* [10] showed that most visible laser emissions belong to Xe V while UV emissions belong in general to Xe VII. In recent works, most of the unresolved laser lines were attributed to Xe V [11], Xe VII [12], and Xe VIII [13].

Manuscript received December 9, 1998; revised June 7, 1999. This work was supported by the Consejo Nacional de Investigaciones Cientificas y Técnicas (CONICET), by the Comisión de Investigaciones Cientificas de la Provincia de Buenos Aires (CICBA), and by the Facultad de Ciencias Exactas, Universidad Nacional de La Plata.

H. Sobral and D. Schinca are with Centro de Investigaciones Opticas, 1900 La Plata, Argentina. They are also with CICBA, 1900 La Plata, Argentina, and with the Physics Department, Universidad Nacional de La Plata, 1900 La Plata, Argentina.

M. Raineri is with Centro de Investigaciones Opticas, 1900 La Plata, Argentina. He is also with CICBA, 1900 La Plata, Argentina.

M. Gallardo is with the Centro de Investigaciones Opticas, 1900 La Plata, Argentina. He is also with CONICET, 1916 Buenos Aires, Argentina.

R. Duchowicz is with the Centro de Investigaciones Opticas, 1900 La Plata, Argentina. He is also with CONICET, 1916 Buenos Aires, Argentina, and with the Physics Department, Universidad Nacional de La Plata, 1900 La Plata, Argentina.

Publisher Item Identifier S 0018-9197(99)06785-8.

Following another line of research, Papayoanou *et al.* [14] reported on the parametrization of a xenon plasma laser including observations about the temporal distribution of the output. Sasaki and Saito [15] have obtained double-pulsed output when the plasma was excited with a long current pulse. In a previous work [16], we presented experimental results about the temporal evolution of visible laser lines together with a simple model to simulate this behavior. After that, we performed an extensive study on the temporal characteristics of the spontaneous emission of a low-density pulsed discharge plasma. The results were interpreted through a collisional-radiative theoretical model [17].

This paper extends the previous temporal study of the laser emission to more than 20 lines in the UV-visible region. Based on our previous plasma model that considers the population behavior of Xe I–IX species [17], we have now also included stimulated emission terms to take into account different laser transitions. On the basis of this model, we analyze the population mechanisms responsible for most of the classified laser xenon transitions corresponding to Xe III, Xe V, Xe VII, and Xe VIII, in this region. We also performed laser gain analyses for several lines by using level parameters (lifetimes and radiative transition rates) obtained from relativistic Hartree–Fock calculations; these results are compared with the corresponding experimental values.

II. Experimental Setup and Results

The experimental setup is similar to that used in [16]. The discharge tube was 1.3 m long and has a 5-mm bore, with cold electrodes in side arms at the ends. Excitation was achieved using a capacitor bank having an overall capacitance ranging from 100 to 420 nF and charged to a voltage up to 18 kV, which yields peak current pulses of about 3 kA having a temporal width between 1–3 μs full-width at half-maximum (FWHM). Xenon pressure was varied between 5–100 mtorr. The resonant cavity consisted of two multilayer coated spherical mirrors of 1.5-m radius of curvature located in a nearly confocal configuration. The light emitted longitudinally was focused into a 0.5-m focal length scanning monochromator and detected with a UV-visible photomultiplier. Its output was amplified and displayed by a 200-MHz digital oscilloscope and recorded by a plotter.

The temporal study carried out previously in the visible region was extended into the UV region as far as 2000 Å, studying more than 20 transitions corresponding to different ionic degrees (Xe III–VIII).

0018–9197/99$10.00 © 1999 IEEE

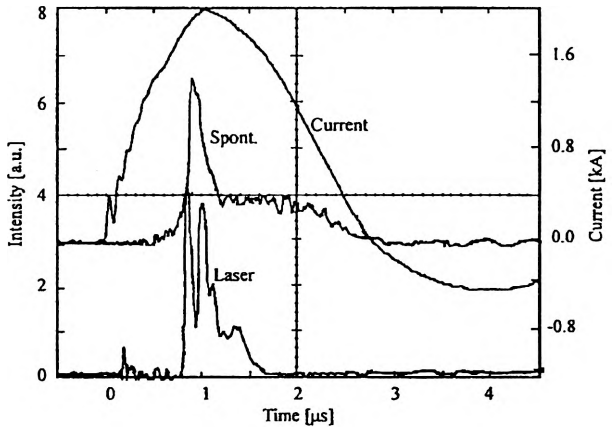


Fig. 1. Oscillation behavior near laser threshold for the $\lambda = 3350.03$ Å transition belonging to Xe VIII; pressure: 12 mtorr.

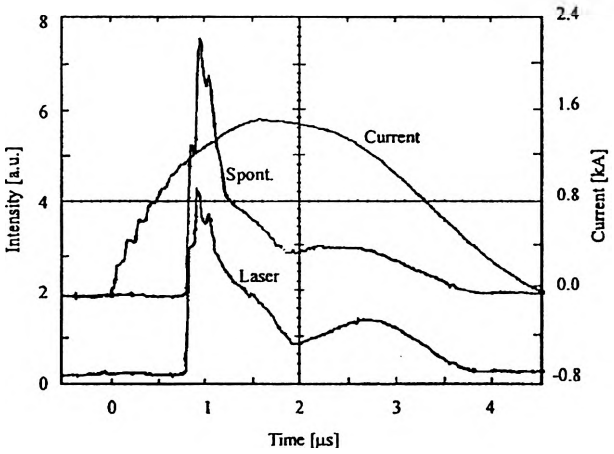


Fig. 2. Temporal distribution for the $\lambda = 3645.48$-Å line (Xe VII); pressure: 10 mtorr.

Depending on the mirror reflectivity and experimental conditions, several ions can lase simultaneously. As the stage of ionization increases, the onset of lasing is delayed further with respect to the beginning of the current pulse. These results were also observed in previous studies of the spontaneous emission [10], [17].

We have analyzed the temporal distribution of the laser and the corresponding spontaneous emission of each line studied under different experimental conditions. In these situations, we removed the output mirror to compare the former (that depends on both the upper and lower laser level population) with the latter (proportional to the upper level population only). Near threshold, laser emission oscillations occurs in most of the observed lines, especially for high ionic degrees. Fig. 1 shows the temporal distribution of the laser emission near threshold for a line belonging to Xe VIII ($\lambda = 3350.03$ Å) together with the corresponding spontaneous emission output and the current pulse for reference. During the temporal region around the spontaneous peak, the laser emission exhibits oscillations. After that, the ion population and the spontaneous and laser emission decay.

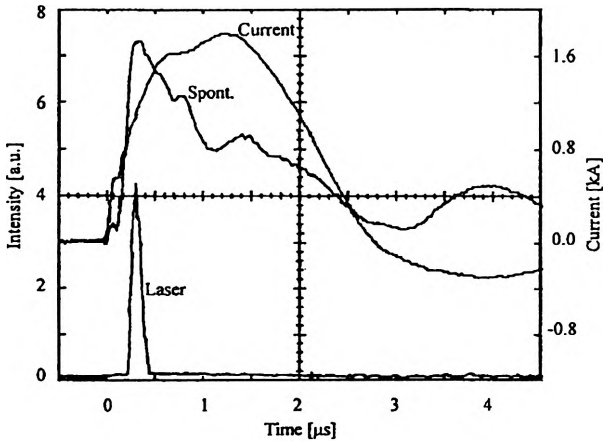


Fig. 3. Spontaneous and laser emission well above threshold for the $\lambda = 4060.45$-Å line (Xe III); pressure: 15 mtorr.

When pumping is increased either by increasing the discharge voltage or by decreasing the pressure, oscillations tend to disappear and laser emission follows the temporal shape of the spontaneous emission. This behavior is shown in Fig. 2 for the 3645.48-Å line (Xe VII), where laser and spontaneous temporal distributions are similar. This particular line presents, when pumping is above threshold, a flat temporal profile during almost all of the current pulse.

Well above laser threshold, the output consists of a single pulse appearing at the beginning of the corresponding spontaneous pulse. The large initial gain obtained under these conditions produces a depopulation of the upper laser level which usually cannot recover to generate a positive population inversion. Fig. 3 shows this behavior for the 4060.45-Å line, belonging to Xe III.

III. Model

The model used to analyze the temporal evolution of the population densities is similar to that used in [17]. If N_j^z is the population density of the jth level of ion z in a plasma with no cavity effects, the set of equations that describe its temporal evolution is the following:

$$\begin{aligned}\left(\frac{dN_j^z}{dt}\right)_{Sp.} &= n_e(t)\sum_{i<j} R_{ij}^z N_i^z - n_e(t)\sum_{k>j} R_{jk}^z N_j^z \\ &\quad - \sum_{i<j}(A_{ji}^z + n_e(t)D_{ji}^z)N_j^z \\ &\quad + \sum_{k>j}(A_{kj}^z + n_e(t)D_{kj}^z)N_k^z - n_e(t)\sum_i S_{ji}^z N_j^z \\ &\quad + n_e(t)\sum_k S_{kj}^{z-1}N_k^{z-1} + n_e(t)\kappa_{d_{0j}}^z N_0^{z+1} \\ &\quad - n_e(t)\delta_{j1}\sum_i \kappa_{d_{ji}}^{z-1}N_j^z \end{aligned} \quad (1)$$

where the electron density n_e can be calculated from the charge balance equation, R_{ij}^z is the excitation rate coefficient from level i to level j of the ion z (corresponding to the $z-1$ times ionized xenon), D_{ji}^z is the deexcitation rate coefficient, A_{ji}^z is the radiative transition rate, S_{ji}^z is the electron-impact

ionization rate from a jth level of the ion z to the level i of the ion $(z+1)$, and $\kappa^z_{d_{kj}}$ is the dielectronic recombination coefficient from the kth level of the ion $z+1$ to the level j of the ion z. The excitation and ionization rates were calculated using the semi-empirical formulas of Van Regemorter and Lotz, respectively, cited in [18]; D^z_{ji} is calculated through its relation with the excitation rate [18] $g_i R^z_{ij} = g_j D^z_{ji} \exp(-\Delta E/T_e)$, where g_i and g_j are the statistical weights of levels i and j, and T_e is the electron temperature. Since our plasma has a moderate electron density [17], the two-body recombination process (dielectronic and radiative recombination) prevails. Both processes can be calculated by Sobelman [18, pp. 118 and 122] and show that dielectronic recombination is the dominant term. We will restrict the number of ions to $z \leq 9$ since no experimental evidence of the existence of Xe X was found under our conditions. The system must also satisfy the initial condition that N^1_1 takes on a value of about 10^{15} cm^{-3} (depending on the filling pressure), while the rest of populations are zero.

When the cavity is taken into account, the temporal evolution of the levels that give rise to laser action are also affected by the stimulated emission terms. If N^z_u and N^z_l represent the population densities for the upper and lower levels corresponding to each laser line, and n^z is the corresponding total number of photons inside the cavity, their temporal evolution must satisfy the following set of equations [19]:

$$\frac{dN^z_u}{dt}_{St.} = \frac{dN^z_u}{dt}_{Sp.} + Kn^z[N^z_l - N^z_u] \quad (2)$$

$$\frac{dN^z_l}{dt}_{St.} = \frac{dN^z_l}{dt}_{Sp.} + Kn^z[N^z_u - N^z_l] \quad (3)$$

$$\frac{dn^z}{dt} = V_c K n^z[N^z_u - N^z_l] + V_c K N^z_u - \gamma_c n^z \quad (4)$$

where γ_c is the inverse lifetime of the photons in the cavity, V_c is the cavity volume, and K is the coupling constant given by

$$K = A^z_{ul}\left(4\pi^2 V_c \frac{1}{\lambda^3}\frac{\Delta\lambda}{\lambda}\right)^{-1} \quad (5)$$

where λ is the wavelength of the transition and $\Delta\lambda/\lambda$ is its relative linewidth.

IV. Spectroscopic Parameters

To analyze the excitation processes that give rise to stimulated emission, the lifetime and transition probability for the main laser transitions in the UV-visible region were calculated. For this purpose, theoretical determinations from relativistic Hartree–Fock (RHF) *ab initio* calculations and energy matrix diagonalization [20] were used. In order to obtain the best values for lifetimes and spontaneous transition probabilities, semi-empirical calculations using energy parameters adjusted from least-squares calculations were performed. Rydberg series interactions were also included for a better fit of the theoretical values of the experimental energy level values.

Under our experimental conditions, we did not observe any Xe II laser lines. For Xe III, RHF calculations were carried out using energy parameters from Persson *et al.* [21]. Although Xe IV laser lines do exist, they appear with weak intensity [22] and seem to be of little practical interest. Despite this fact, the model does take into account the dynamics of these transitions. For Xe V, similar calculations were performed with parameters taken from [11] for the even parity levels and from [23] for the odd parity levels. Spectroscopic results do not show any laser lines belonging to Xe VI. For Xe VII, almost all the experimental energy levels of the $5s4f$ configuration are unknown. In such a case, it is not possible to optimize the parameters using the previously mentioned technique; therefore, *ab initio* calculations were carried out. Since Xe VIII has a single electron out of a closed shell, inclusion of the Rydberg series becomes important [20]. *Ab initio* calculations were also used in this case including the ns and np series up to $n = 15$ and nd and nf series to $n = 12$.

TABLE I
Main Classified Ionic Xenon Laser Transitions in the UV-Visible Region: Theoretical Upper Lifetime τ_3, Lower Lifetime τ_2, and Spontaneous Transition Probability A_{32}

λ [Å][a] (air)	Ion	Classification $E_3 \rightarrow E_2$	τ_3 [ns]	τ_2 [ns]	A_{32} [$10^7 s^{-1}$]
2315.43	VII	$5s4f\ (^2S)^1F_3 \rightarrow 5p^2(^1D)^1D_2$	20.4	0.38	6.0
3246.99	VIII	$6d\ (^1S)^2D_{5/2} \rightarrow 5f\ (^1S)^2F_{7/2}$	3.3	0.37	0.2
3305.96	V	$5s^25p4f\ (^2P)^3G_3 \rightarrow 5s^25p5d\ (^2P)^3F_2$	9.9	0.78	3.0
3330.84	V	$5s^25p4f\ (^2P)^3F_4 \rightarrow 5s^25p5d\ (^2P)^3F_3$	12.0	0.71	4.8
3350.03	VIII	$6d\ (^1S)^2D_{3/2} \rightarrow 5f\ (^1S)^2F_{5/2}$	3.1	0.50	0.1
3645.48	VII	$5s4f\ (^1S)^1F_3 \rightarrow 5p^2\ (^3P)^3P_2$	20.4	0.12	0.5
3803.26	V	$5s^25p4f\ (^2P)^3D_1 \rightarrow 5s^25p5d\ (^2P)^3P_0$	8.3	0.04	1.7
3973.01	V	$5s^25p4f\ (^2P)^3D_1 \rightarrow 5s^25p5d\ (^2P)^3P_1$	8.3	0.04	1.4
4060.45	III	$5s^25p^3(^2p)6p\ ^1D_2 \rightarrow 5s^25p^3(^2p)6s^1P_1$	3.1	0.10	10.0
4305.69	V	$5s^25p4f\ (^2P)^3D_2 \rightarrow 5s^25p5d\ (^2P)^3P_1$	8.6	0.04	1.2
4558.49	V	$5s^25p4f\ (^2P)^3F_2 \rightarrow 5s5p^3\ (^2P)^1P_1$	8.8	0.07	0.5
4954.13	V	$5s^25p4f\ (^2P)^1G_4 \rightarrow 5s^25p5d\ (^2P)^1F_3$	38.3	0.04	1.8
5007.80	V	$5s^25p4f\ (^2P)^3D_3 \rightarrow 5s^25p5d\ (^2P)^1D_2$	9.2	0.05	1.0
5159.08	V	$5s^25p4f\ (^2P)^3F_4 \rightarrow 5s^25p5d\ (^2P)^3D_3$	10.4	0.04	1.0
5260.19	V	$5s^25p4f\ (^2P)^1F_3 \rightarrow 5s^25p5d\ (^2P)^3D_2$	9.5	0.05	0.8
5352.92	V	$5s^25p4f\ (^2P)^3F_3 \rightarrow 5s^25p5d\ (^2P)^3P_2$	9.7	0.04	0.9
5394.62	V	$5s^25p4f\ (^2P)^3F_2 \rightarrow 5s^25p5d\ (^2P)^3D_1$	8.8	0.06	0.6
5955.67	V	$5s^25p4f\ (^2P)^1D_2 \rightarrow 5s^25p5d\ (^2P)^1P_1$	8.2	0.07	0.5

[a] Wavelengths were taken from [24].

Table I shows the results obtained for the main classified transitions in these ions. In general, the spontaneous transition probability is about 10^7–10^8 s^{-1}, and the lifetime of the upper level lies between 3–40 ns, while the lifetime of the lower level is one or two orders of magnitude lower.

V. Pumping Processes

According to [17], we assume that the main excitation and deexcitation processes are radiative and collisional. In order to understand the population inversion mechanisms, the set of equations (1) was solved for typical discharge conditions. RHF *ab initio* calculations were carried out for each one of the ions. They included all the relevant configurations that show interaction with those to which the laser levels belong. From these results, the levels that showed larger oscillator

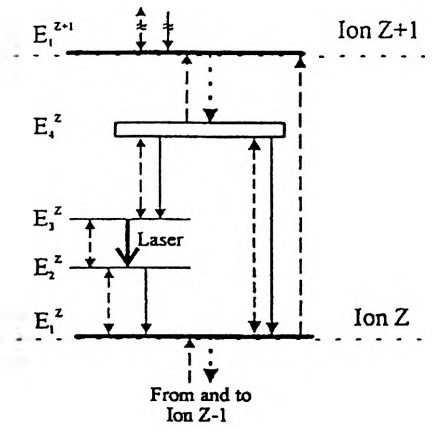


Fig. 4. Simplified laser excitation model energy level scheme. Solid line: radiative decay channels; dotted line: recombination processes; dashed line: collisional excitation–deexcitation and ionization processes.

TABLE II
CALCULATED AND MEASURED LASER GAIN

λ [Å][a] (air)	Measured Gain [dB/m] and {Mirror Reflectivities, Front - Rear [%]}			Calculated Gain [dB/m]
	Ref. [28]	Ref. [14]	This work	
3246.99	-	-	2.8 {70-95}	3.0
3350.03	-	-	2.7 {85-99}	2.7
3645.48	-	-	6.1 {94-100}	6.5
3803.26	-	-	2.5 {93-96}	2.2
4060.45	-	-	2.5 {75-85}	2.5
4954.13	6.3 {88-100}	7.3 {84-99}	6.2 {85-99}	6.1
5007.80	2.3 {88-100}	-	2.6 {85-99}	2.7
5260.19	3.6 {88-100}	4.0 {85-99}	2.9 {85-99}	3.5
5352.92	5.2 {88-100}	6.4 {85-99}	4.5 {85-99}	5.0
5394.62	3.6 {88-100}	4.4 {84-99}	3.6 {85-99}	3.5
5955.67	-	2.7 {75-99}	2.4 {80-99}	2.3

[a] Wavelengths were taken from [24].

strengths with the laser transition levels were determined and their parameters included in equation set (1).

Laser levels are mainly populated by electron impact and cascade recombination, and their relative weights differ for different ions. We will restrict our analysis to the optically allowed transitions since their cross sections maintain a large value for a much broader range than the optically forbidden ones [25]. Besides, calculations show that the upper laser level has a stronger transition probability to the lower laser level than to the rest of the levels. The upper level has also a strong connection with higher levels that populate it, with an oscillator strength value of about unity. Based on these facts, a four-level model turns out to be the most favorable scheme to describe the excitation processes that lead to laser action for the different ions.

Fig. 4 shows a simplified diagram of the excitation mechanisms that give rise to inversion population. Contributions of electronic impact, radiative and collisional decay, and recombination cascade processes were taken into account in all cases for the optically allowed transitions. The population is transferred by electron impact from the ground level of each ion E_1^z to higher excited levels E_4^z. The latter may receive (depending on the configuration) cascade contributions due to recombination processes [18]. E_4^z and E_3^z populations are connected by radiative decay and excitation–deexcitation electron collision processes [17]. Since, in all cases, the E_3^z lifetime is much larger than E_2^z, the population of state 3 exceeds that for state 2. Based on these assumptions, we will analyze in detail some of the laser transitions belonging to different ions.

Calculations showed that the upper laser level of the 4060.45-Å laser line belonging to Xe III is populated mainly by dielectronic recombination from the ground Xe IV level: $5s^25p^3\ {}^4S_{3/2}$.

The upper level E_3 of Xe V laser transitions is filled mainly by cascading from the $5s5p^24f$ and $5s^25p7d$ configurations (E_4), and these are populated by electron impact from the ion ground level in a multistep process.

The upper laser level E_3 of the Xe VII ($5s4f\ {}^1F_3$), is populated both by radiative decay from E_4 and by recombination from the Xe VIII ground level. Our calculations showed that the latter process is dominant for the T_e peak values considered here.

Finally, for Xe VIII, the E_3 levels are mainly populated by a strong radiative decay from the upper configurations, with transition probabilities of the order of $10^{12}\ s^{-1}$. In turn, these levels are populated mainly by recombination from the $4d^{10}$ configuration belonging to Xe IX.

VI. LASER GAIN

The gain coefficient per unit length for different lines appearing in Table II can be calculated using the following relation [26]:

$$G_{32} = \frac{1}{8\pi c}\left(\frac{\Delta\lambda}{\lambda}\right)^{-1} A_{32}\lambda^3 g_3\left(\frac{N_3}{g_3} - \frac{N_2}{g_2}\right) \qquad (6)$$

where A_{32} is the radiative transition rate, N_i and g_i are the density population and the statistical weights corresponding to level i, $\Delta\lambda/\lambda$ is the relative linewidth, and c is the speed of light.

The linewidth is given by Doppler broadening and by collisions between electrons and ions. The former can be calculated from [25], and the latter from an expression proposed by Griem [27]. Under our experimental conditions, calculations show that the last term is dominant.

A_{32} values were obtained from RHF calculations. The population densities N_3 and N_2 were determined by solving (1)–(5) for typical excitation values [17] and including the main levels that interact with each laser level. The electron temperature (T_e) is increased until laser threshold is reached for each line. The population densities T_3 and N_2 obtained under these conditions are introduced in (6).

The small-signal laser gain for the main known transitions was measured in the usual way, introducing a known loss into

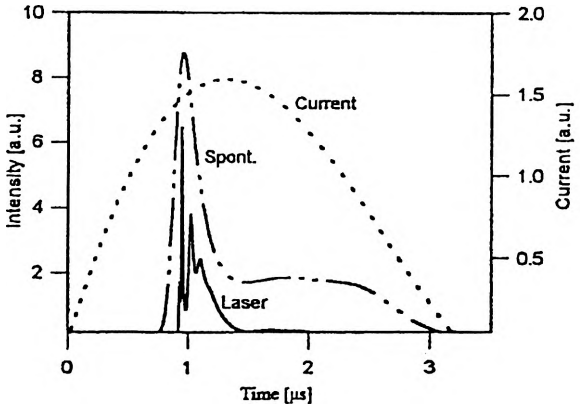


Fig. 5. Calculated temporal distribution of the spontaneous and stimulated emission near threshold for a Xe VIII ($\lambda = 3350.03$ Å) line.

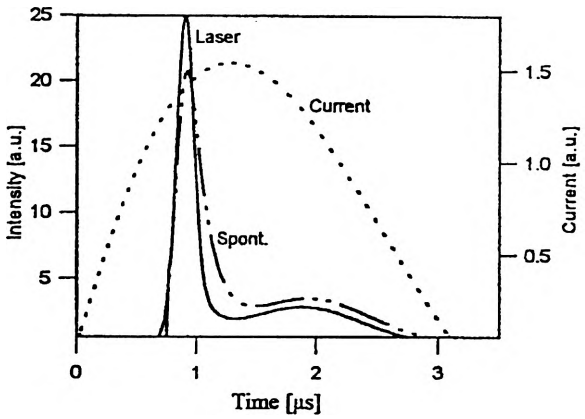


Fig. 6. Calculated output of the spontaneous and stimulated emission for the $\lambda = 3645.48$-Å line belonging to Xe VII.

the cavity until threshold was reached for a particular line. The results can be seen in Table II, together with values from other authors for comparison [14], [28].

Theoretical results are in general agreement with experimental data. For Xe VIII, the spontaneous transition probabilities are lower than those corresponding to other ions, although it is compensated for by the large radiative-collisional decay rate mentioned previously.

VII. Temporal Analysis

In order to analyze the temporal characteristics of the emission, (1) was solved numerically for typical discharge parameters. All the levels that take place in the excitation–deexcitation processes giving rise to laser action were included. The electron temperature is increased until the shape of the calculated spontaneous emission reproduces the experimental results. After that, the stimulated emission terms (2) and (3) were included in (1), and the whole system was solved together with (4) and (5).

Calculations shows that laser oscillations are dependent on the pumping rate of the levels. As expected, they appear near threshold, in agreement with previous work [16]. This fact was more clearly observed in lines belonging to higher ionization stages such as Xe VII and Xe VIII, since, under our experimental conditions, they operate near threshold. This is theoretically supported by the lower transition probability for the upper laser levels belonging to several of these lines. Near threshold, the calculated emission presents a large number of oscillations. This situation holds, for example, when A_{32} is low, as in the typical case for Xe VIII. Fig. 5 shows the temporal evolution of the spontaneous and stimulated emission for the 3350.03-Å line of the Xe VIII. The result agrees with that shown in Fig. 1 for the same line.

When the electron temperature is increased from threshold, oscillations disappear and the stimulated emission follows the temporal shape of the spontaneous emission. This agrees with the fact that the lower laser level radiative decay rate is much larger than that for the upper laser level (Table I). Fig. 6 shows the temporal shape of the spontaneous emission for a Xe VII transition and the 3645.48-Å stimulated emission, reproducing the experimental observation of Fig. 2. Further increases of the electron temperature produce an intense single laser pulse, as was shown in previous works [10], [16].

VIII. Conclusions

The temporal evolution of more than 20 UV-visible xenon laser lines and their corresponding spontaneous emission from a multi-ionic low-pressure plasma is analyzed using time-resolved spectroscopy. RHF calculations on Xe III to Xe IX were carried out to determine spontaneous transition probabilities and lifetimes of relevant levels involved in the laser emission. Results show that the upper laser spontaneous transition rate to the lower laser level is larger than to the rest of the levels. Moreover, the upper level lifetime is one or two orders of magnitude greater than that for the lower state. Using a collisional-radiative model based on electron impact and cascade processes, we studied the dynamics of the plasma. The numerical solution of this model, including the stimulated terms, predict the observed oscillations near threshold which agrees with experimental results. It can also be used to determine the optimum lasing conditions for each line. The results also indicated that, under certain experimental conditions, the strong 3645.48-Å line can also be made to lase in an extended mode, giving rise to a quasi-CW temporal profile, similar to the visible lines reported in [29]. We found in most of the laser lines that both the electron impact and recombination mechanisms are responsible for population inversion. The agreement between experimental small-signal measured gain and the calculated gain values supports the proposed model. The model is being applied to other multi-ionic rare-gas laser systems.

References

[1] W. B. Bridges and A. N. Chester, "Visible and UV laser oscillations at 118 wavelengths in ionized neon, argon, krypton, xenon, oxygen, and other gases," *Appl. Opt.*, vol. 4, pp. 573–580, 1965.

[2] ——, "Spectroscopy of ion lasers," *IEEE J. Quantum Electron.*, vol. QE-1, pp. 66–84, 1965.

[3] P. K. Cheo and H. G. Cooper, "Ultraviolet ion laser transitions between 2300 and 4000 Å," *J. Appl. Phys.*, vol. 36, pp. 1862–1865, 1965.

[4] E. Gallego Lluesma, A. Tagliaferri, C. Massone, M. Garavaglia, and M. Gallardo, "Ionic assignment of unidentified of xenon laser lines," *J. Opt. Soc. Amer.*, vol. 63, pp. 362–364, 1973.
[5] T. W. Hänsch, A. L. Schawlow, and P. Toschek, "Simple dye laser repetitively pumped by a xenon ion laser," *IEEE J. Quantum Electron.*, vol. QE-9, pp. 553–554, 1973.
[6] D. W. Fahey and L. D. Schearer, "A xenon ion pumped blue dye laser," *IEEE J. Quantum Electron.*, vol. QE-14, pp. 220–221, 1978.
[7] L. D. Schearer, "A high-power pulsed xenon ion laser as a pump source for a tunable dye laser," *IEEE J. Quantum Electron.*, vol. QE-11, pp. 935–937, 1975.
[8] J. Pinard and L. Liberman, "A frequency locked, single mode pulsed dye laser. Application to single frequency tunable UV generation," *Opt. Commun.*, vol. 20, pp. 344–346, 1977.
[9] J. Tocho, R. Duchowicz, M. Gallardo, and M. Garavaglia, "Frequency locking in double-pumped dye laser," *IEEE J. Quantum Electron.*, vol. QE-17, pp. 1591–1592, 1981.
[10] R. Duchowicz, D. Schinca, and M. Gallardo, "New analysis for the assignment of UV-visible ionic Xe laser lines," *IEEE J. Quantum Electron.*, vol. 30, pp. 155–159, 1994.
[11] M. Gallardo, M. Raineri, J. Reyna Almandos, H. Sobral, and F. Callegari, "Revised and extended analysis in four times ionized xenon Xe V," *J. Quantitative and Radiative Transfer*, vol. 61, pp. 319–327, 1998.
[12] M. Larsson, A. Gonzalez, R. Hallin, F. Heijkenskjöld, R. Hutton, A. Langereis, B. Nynström, B. Sullivan, and A. Wönnström, "Wavelengths and energy levels of Xe VII and Xe VIII obtained by collision-based spectroscopy," *Phys. Scr.*, vol. 51, pp. 69–75, 1995.
[13] M. Wang, A. Arnesen, R. Hallin, F. Heijkenskjöld, A. Langereis, M. Larsson, C. Nordling, and A. Wönnström, "Collision-based spectroscopy of Xe VIII Rydberg states," *J. Opt. Soc. Amer. B*, vol. 13, pp. 1650–1658, 1996.
[14] A. Papayoanou, R. Buser, and I. Gumeiner, "Parameters in a dynamically compressed xenon plasma laser," *IEEE J. Quantum Electron.*, vol. QE-9, pp. 580–585, 1973.
[15] W. Sasaki and S. Saito, "Double-pulsed output with a Xe IV laser excited by long current pulse discharges," *Appl. Opt.*, vol. 19, pp. 5–6, 1980.
[16] H. Sobral, D. Schinca, R. Duchowicz, and M. Gallardo, "Gain switching and oscillations in a ionic pulsed xenon laser," *Pure Appl. Opt.*, vol. 5, pp. 1011–1019, 1996.
[17] H. Sobral, D. Schinca, M. Gallardo, and R. Duchowicz, "Time dependent study of a multi-ionic xenon plasma," *J. Appl. Phys.*, vol. 85, pp. 69–73, 1999.
[18] I. Sobelman, L. Vainshtein, and E. Yukov, *Excitations of Atoms and Broadening of Spectral Lines*. Berlin, Germany: Springer-Verlag, 1981.
[19] A. Siegman, *Lasers*. Mill Valley, CA: University Sci., 1986.
[20] R. Cowan, *The Theory of Atomic Structure and Spectra*. Berkeley, CA: UC Berkeley, 1981.
[21] W. Persson, C. Wahlström, G. Bertuccelli, H. Di Rocco, J. Reyna Almandos, and M. Gallardo, "Spectrum of doubly ionized xenon (Xe III)," *Phys. Scr.*, vol. 38, pp. 347–369, 1988.
[22] J. Marling, "Ultraviolet ion laser performance and spectroscopy—Part I: New strong noble-gas transitions below 2500 Å," *IEEE J. Quantum Electron.*, vol. QE-11, pp. 822–834, 1975.
[23] A. Tauheed, Y. Joshi, V. Kaufman, J. Sugar, and E. Pinnington, "Analysis of the $5s^25p^2 - (5s5p^3 + 5s^25p5d + 5s^25p6s)$ transitions of four-times ionized xenon (Xe V)," *J. Opt. Soc. Amer. B*, vol. 10, pp. 561–565, 1993.
[24] M. Gallardo and J. Reyna Almandos, private communication.
[25] C. Willett, *Introduction to Gas Lasers: Population Inversion Mechanisms*. Oxford, U.K.: Pergamon, 1974.
[26] M. Pöckl, M. Hebenstreit, T. Neger, and F. Aumayr, "Time-dependent collisional-radiative model for capillary discharge plasmas," *J. Appl. Phys.*, vol. 76, pp. 733–737, 1994.
[27] H. Griem, "Semiempirical formulas for the electron-impact widths and shifts of isolated ion lines in plasmas," *Phys. Rev.*, vol. 165, pp. 258–266, 1968.
[28] W. Simmons and R. Witte, "High-power pulsed xenon ion lasers," *IEEE J. Quantum Electron.*, vol. QE-6, pp. 466–469, 1970.
[29] W. Bridges and G. Mercer, "CW operation of high ionization states in a xenon laser," *IEEE J. Quantum Electron.*, vol. QE-5, pp. 476–477, 1969.

H. Sobral, photograph and biography not available at the time of publication.

M. Raineri, photograph and biography not available at the time of publication.

D. Schinca, photograph and biography not available at the time of publication.

M. Gallardo, photograph and biography not available at the time of publication.

R. Duchowicz, photograph and biography not available at the time of publication.

Medición de Tamaño de partículas

La línea de investigación sobre determinación de tamaño de partículas por scattering óptico comenzó en el CIOp hace más de 15 años cuando se llevaron a cabo la determinación de mediciones de material particulado dieléctrico de una solución con para tratamiento de cueros (¿superficies porosas?) por métodos ópticos. En esa oportunidad, se implementó la técnica de scattering angular a una longitud de onda con polarizaciones paralela y perpendicular al plano de observación. La reproducción de la intensidad observada para distintos ángulos y ambas polarizaciones se ajusta con teoría de Mie, utilizando el radio de las partículas como parámetro de ajuste. Desde entonces, se realizaron actualizaciones al equipamiento tendientes a realizar experiencias con un mayor grado de automatización.

La línea se expandió hacia otros métodos ópticos para la determinación de tamaño de partículas, como la extinción espectral. A diferencia del scattering angular, aquí se mide la variación de intensidad que sufren las distintas frecuencias componentes de un fino haz de luz blanca, luego de atravesar la muestra, con un espectrofotómetro comercial simple. Si las partículas no poseen bandas de absorción en el rango espectral en estudio, la disminución logarítmica de la intensidad en función de la longitud de onda puede relacionarse con el scattering a 0° (forward scattering) y permite determinar el radio de partículas, conociendo el índice de refracción de las mismas y del medio en función de la longitud de onda. Con este método se pudieron determinar radios promedio de partículas componentes de emulsiones para tratamiento de cueros.

Más adelante, se incorporó el método de espectroscopía de backscattering para la determinación de diámetro de partículas dieléctricas en solución. La disposición experimental resulta sencilla y apta para mediciones endoscópicas: una fibra óptica lleva luz a la muestra mientras que otra fibra similar y paralela a la primera recoge la luz dispersada a 180° por la muestra y la envía a un espectrógrafo para su registro. El tratamiento de datos para la determinación del tamaño de las partículas en suspensión utiliza las características variaciones oscilatorias con la longitud de onda que muestra la eficiencia de scattering a 180°, según puede calcularse por scattering de Mie. Como el número de dichas oscilaciones depende de radio de la partícula, fue posible aplicar algoritmos de transformada de Fourier a los espectros obtenidos para la determinación directa del tamaño. Este método permite medir muestras mono y polidispersas en un rango que va desde 0,5 a 60 □m de diámetro.

Más recientemente, el interés se dirigió hacia el estudio de las propiedades ópticas de partículas metálicas nanométricas, tanto por su importancia teórica como por su aplicación práctica como marcadores en experiencias biomédicas. En particular, se estudiaron las propiedades ópticas de nanopartículas de oro de radios inferiores a 3 nm, a través del estudio de los espectros de extinción y su interpretación en base a una modificación de la función dieléctrica para tener en cuenta la limitación del camino libre medio de los electrones de conducción debido a colisiones con el contorno de la misma. Este enfoque se aplicó también a nanopartículas esféricas y nanoalambres de plata, permitiendo la determinación de tamaño medio.

Particle sizing

Particle sizing by optical scattering started at CIOp more than 15 years ago when the size of latex spheres suspended in a porous- surface finisher bath had to be measured by optical means. Angular scattering at one wavelength with two perpendicular polarizations was the method used at that time, and its interpretation was based on Mie theory, where the particle radius was the fitting parameter.

Since then, the line of research expanded to other optical methods for particle sizing, such as spectral extinction. In this method, intensity variations of the different component frequencies of a slim white light beam passing through the sample are measured using a spectrograph and a photodetector (photodiode, CCD array). If the particles have no absorption bands in the spectral range of study, the ratio of output to input intensities can be to forward scattering and allows to determine the particle radii if the refractive index is known as a function of wavelength. With this method, mean radii of particulate matter of emulsions used in the leather industry were determined.

Another method that was also incorporated to optical scattering was the backscattering spectroscopy for dielectric particles sizing suspended in solutions. The experimental setup is simple and suitable for endoscopic measurements: an optical fiber delivers light into the sample while a similar fiber, placed beside and parallel to the first one collects the backscattered light and sends it to spectrograph for wavelength analysis. Theoretical calculation of the backscattering coefficient shows oscillatory behavior with wavelength, depending on particle radius. A Fourier analysis allows to size m o n o a n d polydisperse samples in the range 0,5 to 60 □m diameters.

Recently, research interest headed toward the study of optical properties of metal nanoparticles, both for its theoretical importance and application to biomolecular markers. In particular, optical properties of gold and silver nanoparticles of radius less than 3 nm were studied, introducing a modification to the dielectric function to take into account the limitation in mean free path of the conduction electrons due to collision with the boundaries of the particle. This approach was also applied to silver nanowires, allowing its sizing.

INSTITUTE OF PHYSICS PUBLISHING NANOTECHNOLOGY
Nanotechnology 16 (2005) 158–163 doi:10.1088/0957-4484/16/1/030

Sizing gold nanoparticles by optical extinction spectroscopy

L B Scaffardi[1,3], N Pellegri[2], O de Sanctis[2] and J O Tocho[1]

[1] Facultad de Ciencias Exactas, UNLP and Centro de Investigaciones Ópticas (CIOp), CC124, 1900 La Plata, Argentina
[2] Laboratorio de Materiales Cerámicos, FCEIyA, IFIR, UNR, Rosario, Argentina

E-mail: lucias@ciop.unlp.edu.ar

Received 30 August 2004, in final form 9 November 2004
Published 10 December 2004
Online at stacks.iop.org/Nano/16/158

Abstract
The measurement of optical extinction is used to determine the size of nearly spherical gold nanoparticles suspended in solution, produced by a 'reverse micelles' process. The contrast between the maximum and the minimum in the extinction spectra around 450 and 520 nm shows a linear dependence with the mean radius of the gold particles less than 3 nm; however, the method can be used to size particles up to 7 nm. Experimental results for extinction spectra can be fitted by Mie's theory if the optical constants from bulk material values are modified by introducing the limitation of the mean free path due to collisions of conduction electrons with the boundary of the nanoparticles.

1. Introduction

The determination of particle size in the micron and submicron region has been a subject of increasing interest during recent years. Among the diverse fields of applied sciences that involve this subject, the studies of atmospheric and combustion aerosols, the analysis of interstellar dust, and the characterization of many biological, chemical and physical systems of interest for industrial processes stand out. Materials science is another field of interest where it is recognized that many properties of materials are affected by the size and characteristics of the particles within them. To understand the influence of particles in nature or to control industrial processes involving them it is essential to develop methods to measure their size [1]. Many physical techniques are available, but optical methods are often preferred because they can be non-disturbing, the measurements can be made remotely, and analysis can be very rapid. The optical methods include static and dynamic dispersion; lidar [2, 3]; counters, where the size is correlated with the height of the pulse of light dispersed by the particle; extinction spectrum; and many others. Among them, the spectral extinction method is one of most used because it requires a simple optical disposition like the slight adaptation of a commercial spectrophotometer and it can work in an extended interval of sizes.

[3] Author to whom any correspondence should be addressed.

The spectral extinction method can be easily performed for particles in diluted liquid suspensions. The knowledge of the refractive index for both the particle material and the solvent, as a function of the wavelength, is necessary. As usual, experimental results are fitted by Mie calculations for spherical particles. This method has proved to be very useful for sizing particles in the submicron range, where it can be compared with both transmission electronic microscopy (TEM) and scanning electronic microscopy (SEM) [4]. To deal with the distribution of radius, extinction measurements at a discrete set of wavelengths are performed (multispectral extinction). Inversion of the experimental results to get the distribution of sizes is not a trivial task, but it can be solved by a nonlinear inversion algorithm [5]. As is common for all the optical methods, the range of the radius determined for optical extinction is related to the range of the wavelength used. As an example, when a commercial spectrophotometer with a wavelength range of 300–1100 nm is used, particle sizing over a radius range of 300–1400 nm can be attained.

In particular, measurements of optical extinction as a function of wavelength offer useful information of particle size on the micrometre range. This analysis yields, in general, inaccurate results when the sizes of particles are much smaller than the wavelength, thus making it an unsuitable method to measure particles with radius below 100 nm.

Metal particles constitute one important exception to this rule because the extinction spectra present clear size effects

for radius well below the wavelength. For this reason colloidal solutions of noble metals, like copper, gold and silver, present intense colour that is absent in bulk material. For spherical particles Mie's theory predicts one strong absorbance for small particles at the frequency where $\varepsilon = -[2+(12/5)x^2+\cdots]\varepsilon_m$. Here ε is the complex dielectric function for the particle, ε_m is the dielectric function for the solvent, and x is the size parameter [6]. For vanishing small particles (Rayleigh limit) surface resonance modes can be achieved, and strong extinction is observed at the Fröhlich frequency where $\varepsilon = -2\varepsilon_m$. The size effect on the extinction spectra is explained because, in general, the real part of the dielectric function (ε') is an increasing function of the frequency, and when x increases, the absorption maximum is shifted to longer wavelength. This behaviour is used extensively in sizing metal particles, and is known as the extrinsic size effect on the plasmon band absorption [7]. In particular for gold particles, this method can be applied for a radius in the range 10–100 nm. Below 10 nm, the absorption spectrum peaks near 520 nm become independent of size, except for a varying intensity due to the dependence between the absorption cross section and the volume of the particle.

For small enough metal particles, well in the nanometre region, the extinction spectra show a new size dependence that can be used to characterize the radius. This region, known as the intrinsic size effect, can be studied by assuming that the dielectric function of the bulk must be modified for nanoparticles. The present work deals with gold particles whose radii are included in this region. These particles are used in the development of materials that have acquired great importance during recent years in different areas of scientific research and nanotechnology.

Many of the structures within the human body, such as proteins, are measured in nanometres, making nanotechnology an alluring area of biomedical research. The growing ability of researchers to synthesize nanomaterials opens up the possibility of using synthetic molecules such as biosensors to probe cellular functions. In the optical field, semiconductor and metal nanoparticles are of interest due to their many important applications in the development of optical devices [8, 9]. In the area of semiconductor technology, the band gap of semiconductor nanoparticles can be controlled by the quantum size effect. In addition, it has been reported that the band structure of Si with indirect transition can be changed into that of direct transition by down-sizing of nanoparticles.

Many potential industrial applications of nanoparticles, such as quantum dots and tuneable laser diodes, require extreme monodispersity of particles. The generation of monodisperse nanoparticles is also important for nanoparticle instrumentation development and calibration. The above-mentioned research and development areas need the knowledge of sizing distribution.

Below 10 nm, sizing effects over the dielectric functions open a new window for measurements. This work shows a way to determinate the size of gold nanoparticles in this nanometric region. The theoretical fit of the extinction curves was performed using Mie theory, taking into account a modification of the bulk dielectric function for the case of very small particles.

Extinction measurements with a commercial spectrophotometer can be an alternative simple and economical technique when special electronic microscopy (TEM or SEM) is not available. Recently the possibility to size nanoparticles down to 1 nm by dynamic light scattering techniques was claimed by some manufacturers.

As with other sizing techniques, optical extinction spectroscopy cannot be considered as an absolute or universal method. This work is related to mean size determinations, and no distribution of size was considered. This is an important limitation when it is compared with microscopic measurements that allow mean size and distribution results simultaneously.

2. Experimental section

The gold nanoparticles analysed were synthesized in 'reverse micelles' in water–hydrocarbon phases and isolated with a stabilizer. The solvent was n-heptane and the water was triply distilled. Hydrogen tetrachloroaurate (III) hydrate ($HAuCl_4 \cdot 3H_2O$) (Aldrich, 25 416) was selected as the source of gold. Sodium bis (2-ethylhexyl) sulfosuccinate (AOT, Sigma) was used as surfactant and *N*-[3-(trimethoxysilyl)propyl]diethylenetriamine (Aldrich, 41 334, hereafter ATS) as stabilization agent. The $[H_2O]/[AOT]$ ratio was equal to 6, and it was maintained constant for all samples. The 'pool' size of the 'reverse micelles' was changed by using values of 6, 10 and 20 for the $[ATS]/[Au^{3+}]$ ratio. The gold nanoparticles were formed by photoreduction of the $HAuCl_4$ irradiating the Au^{3+} micellar solutions with light emitted from a mercury high-pressure lamp (maximum intensity at $\lambda = 365$ nm, 400 W). As the photochemistry of gold nanoparticles in reverse micelles depends strongly on the synthesis conditions, experimental conditions were developed such that all samples received the same amount of radiation. In order to remove the nanoparticles from the micellar solution, a water–acetone mixture (3:1 volume ratio) was added to the Au particle micellar solution under strong stirring. The micellar structure broke down and a two-phase separation took place; the upper phase contained the gold nanoparticles dispersed in heptane and the lower phase contained acetone, water and AOT. The nanoparticles were obtained by evaporating the heptane at 70 °C under a pressure of 5 kPa. More details of the preparation of the particles can be found in [10].

There is strong evidence that the particles are capped with the stabilization agent ATS and that this helps to maintain the gold particles in the dispersion state in organic solvents after extraction from that synthesis medium. For this reason samples were dispersed in heptane for the UV–visible extinction measurements. THE Spectra were recorded using a Beckman Spectrophotometer (Model 600), using n-heptane as the reference background. The optical density for 1 cm light pass was kept below one to avoid multiple scattering effects. Experimental refractive index values of heptane for 434, 486, 589 and 656 nm were used [11] to calculate values for other wavelengths with a Sellmeier's dispersion equation.

Transmission electron microscopy (TEM, JEOL 1010, at 80 kV) images were obtained by application of a droplet of the nanoparticle-dispersed heptane solution on carbon coated copper grids. Figure 1 shows TEM images of three samples of gold nanoparticles, ATS-6, ATS-10 and ATS-20. The nanoparticle shape is nearly spherical, but some superposition arising from the sample preparation process is observed in the

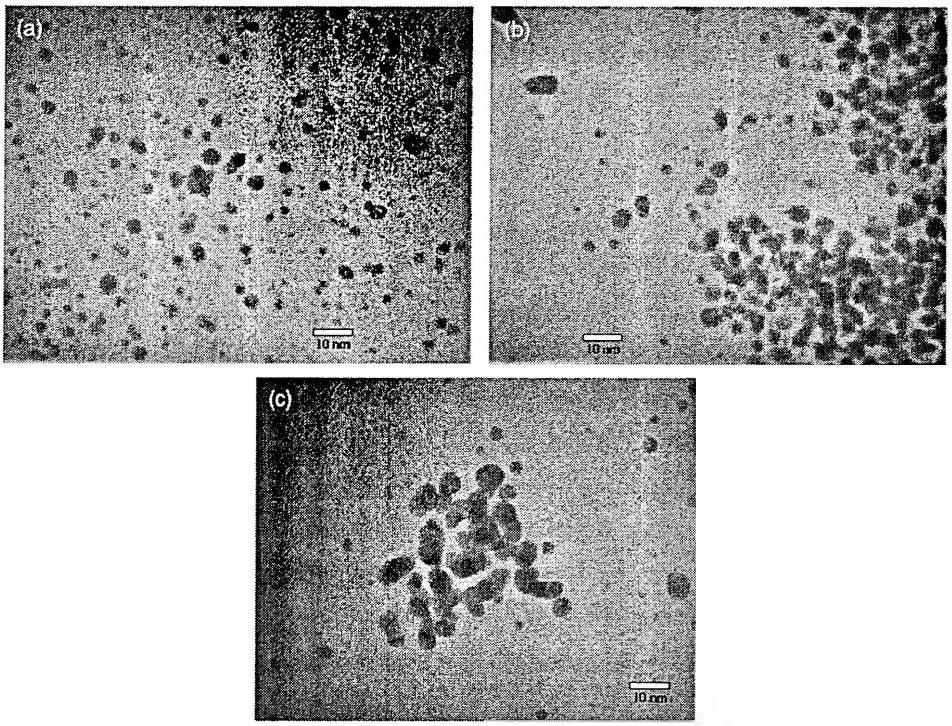


Figure 1. TEM images of (a) ATS-6, (b) ATS-10 and (c) ATS-20 gold nanoparticles samples. From histograms of these images the mean radius was determined as 1.34, 1.58 and 1.96 nm, respectively.

pictures. The mean radius can be determined from statistical analysis from histograms of these pictures, discarding obvious superpositions. As expected, the particle size increased as the amount of stabilizer used in the preparation was increased.

3. Theory and discussion

The optical properties of materials are often described by two sets of quantities: the real and imaginary parts of the *complex refractive index*, $N = n + ik$, and the real and imaginary parts of the *complex dielectric function*, $\varepsilon = \varepsilon' + i\varepsilon''$. These sets are not independent, since they are related by

$$\varepsilon' = n^2 - k^2, \tag{1}$$

$$\varepsilon'' = 2nk. \tag{2}$$

The optical properties for gold used in this work were taken or calculated from experimental values for n and k given by Palik [12]. For real metals where there is a substantial bound electron component, the dielectric function for the bulk can be decomposed into two terms, a free-electron term and an interband, or bound-electron term [6]. The dielectric function is additive, and it can be written as

$$\varepsilon_{\text{bulk}}(\omega) = \varepsilon_{\text{bound-electrons}}(\omega) + 1 - \frac{\omega_p^2}{\omega^2 + i\omega\gamma_{\text{bulk}}}, \tag{3}$$

where ω_p is the bulk plasma frequency and γ_{bulk} is the damping constant in the Drude model. From equation (3), $\varepsilon_{\text{bound-electron}}$ can be calculated by subtracting the free-electron part from $\varepsilon_{\text{bulk}}$. Values for $\omega_p = 1.3 \times 10^{16}$ s^{-1} and $\gamma_{\text{bulk}} = 1.64 \times 10^{14}$ s^{-1} were taken from [13].

For small particles, the plasma frequency is assumed to be independent of the size, while the damping, related to the mean free path for electrons, is strongly affected by the size. In particles smaller than the mean free path of conduction electrons in the bulk metal, the mean free path can be dominated by collisions with the particle boundary [14–16]. The mean free path limitation has been discussed by Kreibig and von Fragstein [14], who considered that the damping constant (the inverse of the collision time for conduction electrons in the Drude theory) is increased due to additional collisions with the boundary of the particle, and it can be written as

$$\gamma(r) = \gamma_{\text{bulk}} + \frac{v_F}{L} = \gamma_{\text{bulk}} + C\frac{v_F}{r}, \tag{4}$$

where v_F is the electron velocity at the Fermi surface, and L is the effective mean free path for collisions with the boundary. The value $v_F = 14.1 \times 10^{14}$ nm s^{-1} was used [13]. There is slight disagreement among various authors about the proportionality constant C between L and the radius r of the particle. C is a constant that includes details of the scattering processes. For isotropic electron scattering $C = 1$ was calculated theoretically; for diffuse scattering its value is reduced to 0.75, while for additional limitations due to the internal grain boundary C can be greater than 1 [17].

Now, the real and the imaginary part of the dielectric function for a particle of radius r, take the form

$$\varepsilon'_{\text{size}}(\omega, r) = 1 - \frac{\omega_p^2}{\omega^2 + \gamma^2(r)} + \varepsilon'_{\text{bound-electron}}, \tag{5}$$

$$\varepsilon''_{\text{size}}(\omega, r) = \frac{\gamma(r)\,\omega_p^2}{(\omega^2 + \gamma^2(r))\omega} + \varepsilon''_{\text{bound-electron}}, \tag{6}$$

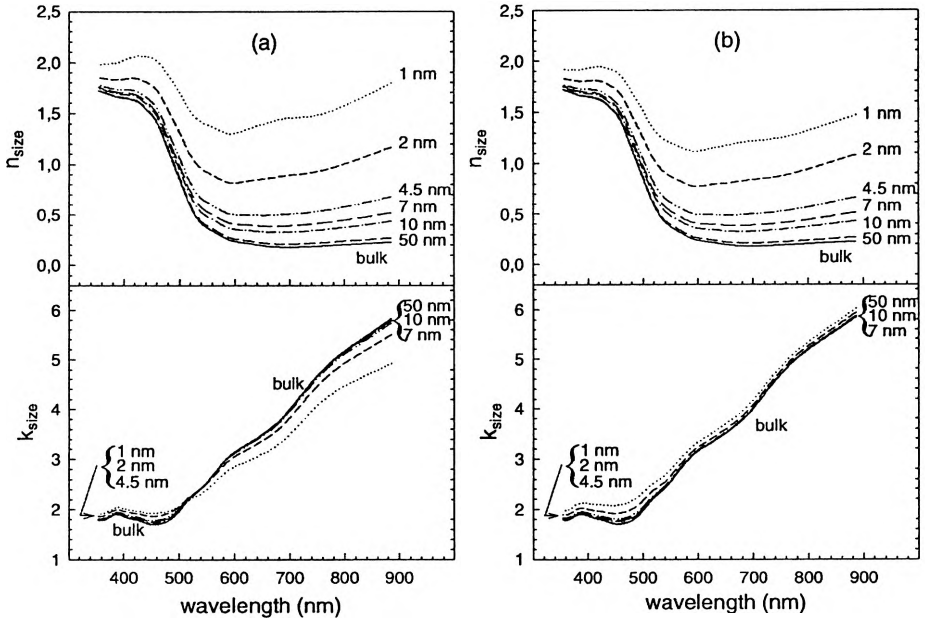


Figure 2. Calculated n_{size} and k_{size} as a function of wavelength for different sizes of gold nanoparticles. (a) Values of ε' and ε'' are corrected for size. (b) Only ε'' is corrected for size while ε' bulk is used for any size.

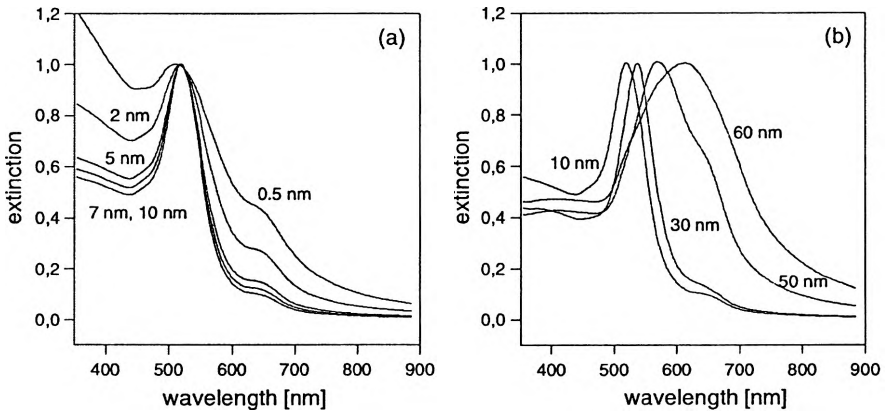


Figure 3. Normalized extinction spectra of gold particles. (a) For small radii the spectral features depend on optical constants calculated with the modification of the electron mean free path. (b) For radii larger than 10 nm, the peak and the width of the spectra are a consequence of the effect of finite size on the Fröhlich resonance.

where the contribution coming from the bound electrons to ε' and ε'' were calculated before. Now the values for the real and the imaginary parts of the refractive index corrected by the size, $n_{size}(\lambda, r)$ and $k_{size}(\lambda, r)$, can be calculated introducing (5) and (6) in equations (1) and (2):

$$n_{size}(\lambda, r) = \{\tfrac{1}{2}[(\varepsilon'^2_{size}(\lambda) + \varepsilon''^2_{size}(\lambda, r))^{1/2} + \varepsilon'_{size}(\lambda)]\}^{1/2}, \quad (7)$$

$$k_{size}(\lambda, r) = \{\tfrac{1}{2}[(\varepsilon'^2_{size}(\lambda) + \varepsilon''^2_{size}(\lambda, r))^{1/2} - \varepsilon'_{size}(\lambda)]\}^{1/2}. \quad (8)$$

Figure 2(a) shows values for n_{size} and k_{size} calculated as a function of wavelength for different sizes of gold nanoparticles. $C = 1.1$ was used in this calculation. The choice of this value for parameter C will be discussed in section 4. It can be seen that n_{size} shows a clear dependence with size up to 10 nm particle radius, while k_{size} tends to the bulk values for smaller radius. Special care must be taken to analyse these optical variables in relation to spectral features in the extinction spectra. For metals, the values for k range between 1 and 10. These are really huge if we recognize that a well absorbing material in the visible has a k value not much greater than 10^{-4} [6]. Additionally, it must be considered that the extinction depends on both the n and k values. In figure 2(b) we show the values for n_{size} and k_{size} calculated when only the imaginary part of the dielectric function is modified in terms of the size, that is, when ε'_{size} was taken as ε'_{bulk}. The reason for this will be discussed later. Mie theory was used to calculate the extinction as a function of the wavelength for different values of the radius. Figure 3 shows the theoretical curves for gold nanoparticles embedded in heptane with radius between 1 and 60 nm. All spectra were normalized to 1 at the wavelength where the maximum of the Fröhlich's resonance occurs.

Figure 3 illustrates the varied optical effects exhibited by small gold metallic particles. In the surface mode region ($r > 10$ nm), the peak and the width of the absorption spectra depend on the radius of the particle; as the radius increases

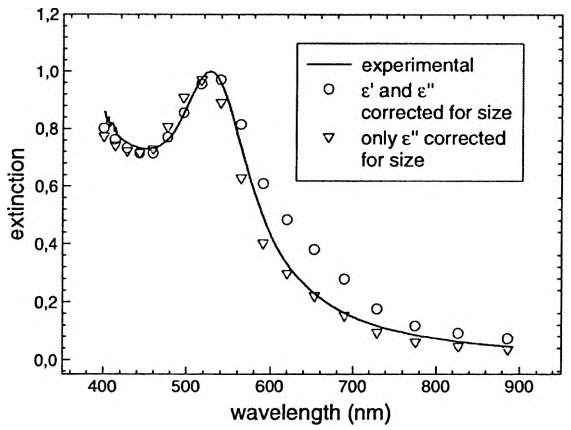


Figure 4. The full curve shows the experimental optical extinction corresponding to the ATS-6 sample as measured with a commercial spectrophotometer. The symbols represent the fitted values (for discrete wavelengths) calculated with Mie theory. Open circles correspond to ε' and ε'' corrected for size. Open triangles correspond to only ε'' corrected for size. The best fit corresponds to a mean radius of 1.5 nm.

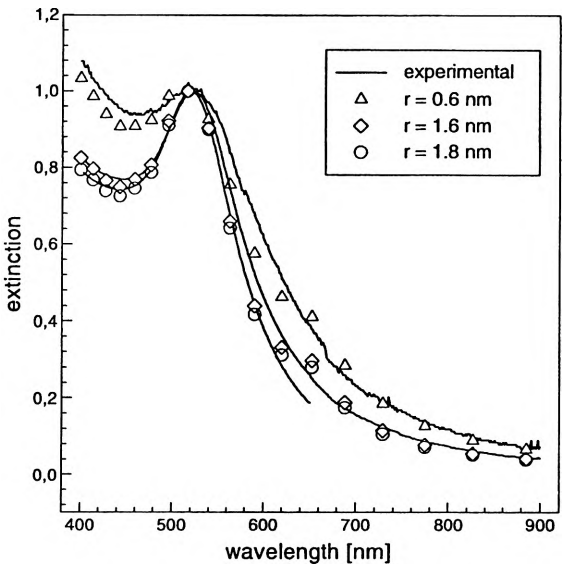


Figure 5. Full curves show experimental optical extinction corresponding to three different gold nanoparticles samples, as measured with a commercial spectrophotometer. The symbols represent the theoretical best fitted values for each case.

beyond 10 nm, the absorption peak broadens and shifts to longer wavelengths. Absorption spectra by particles with radii between about 2.6 and 10 nm peak near 520 nm, and they are independent of size. Below 2.6 nm, the spectra again show a dependence with radius: peaks remain near 520 nm but the contrast between the maximum and the minimum near 440 nm depends clearly on size. All regions can be explained by Mie theory with optical constants calculated with the modification of the electron mean free path.

4. Results

The theoretical extinction curves allow us to perform fits of the spectra corresponding to different samples of gold nanoparticles dispersed in heptane. These curves are calculated for discrete wavelength values for which the refractive index of gold is known from the literature. In figure 4 we show the UV–visible spectra corresponding to sample ATS-6. The theoretical extinction coefficient was calculated with Mie theory for the mean radius of 1.34 nm determined from the TEM images and optical properties given by equations (7) and (8). The C value was changed to fit the results. The best fit corresponded to $C = 1.1$, a value close to that expected from the literature. The fit is good for short wavelengths; however, the calculated values are greater than the experimental values for longer wavelengths. For metals, the real part of the dielectric function evaluated for the bulk is usually used for particles without any modification, while the effect of the mean free path limitation on the imaginary part of the dielectric function is considered [18–20]. When these facts are used to calculate the size-dependent refractive index, the fitting improves. This procedure gives good agreement with the experimental results in gold, but it is not clearly justified. Probably this action hides the size effect on the contribution of the band to band transitions over the dielectric function. This point must be analysed further.

Figure 5 shows the extinction spectrum corresponding to three other samples of gold particles in heptane. For ATS-10 (sample with $[ATS]/[Au^{3+}] = 10$), the mean radius yielded by the TEM image is 1.58 nm, and the best theoretical fit shows a value of 1.6 nm; for ATS-20 (sample with $[ATS]/[Au^{3+}] = 20$), the TEM image shows 1.96 nm for the mean radius, while the best theoretical fit yields a value of 1.8 nm, (8% difference). The spectrum adjusted with a radius of 0.6 nm corresponds to a sample produced with another stabilization agent (AES = 3-(2-aminoethylaminopropyl)trimethoxysilane). This sample (AES-10, with $[AES]/[Au^{3+}] = 10$) shows a shallow spectrum typical of particles smaller than ATS samples. A similar result was obtained with a sample with $[AES]/[Au^{3+}] = 20$; its spectrum, not shown in figure 5, was adjusted with $r = 0.7$ nm. Unfortunately no TEM images for these AES samples are available; however, particles prepared with the AES stabilization agent must be smaller than the equivalent ATS samples. In addition, for particles prepared with one type of stabilization agent, it is expected that the size of the particles increases with the ratio between the amount of stabilization agent and the concentration of gold used. That is, the radius of the particles must be ordered as ATS-20 > ATS-10 > ATS-6 > AES-20 > AES-10.

The contrast between the maximum and the minimum in the extinction spectra, around 520 and 440 nm respectively, can be used to evaluate the size of small gold particles. In figure 6 the theoretical contrast for particles with radius between 0.5 and 5 nm are represented in terms of the size. Good linear dependence can be observed up to 3 nm, but a particle size between 3 and 5 nm can also be determined by using this plot. Experimental results for the contrast measured on five samples of gold nanoparticles are shown; the radii were determined from the fitting of the whole spectrum as was discussed before. The error bars assume a 15% error in the radius determination.

5. Conclusions

We have shown that Mie theory, combined with a suitably modified dielectric function to include the limitation in

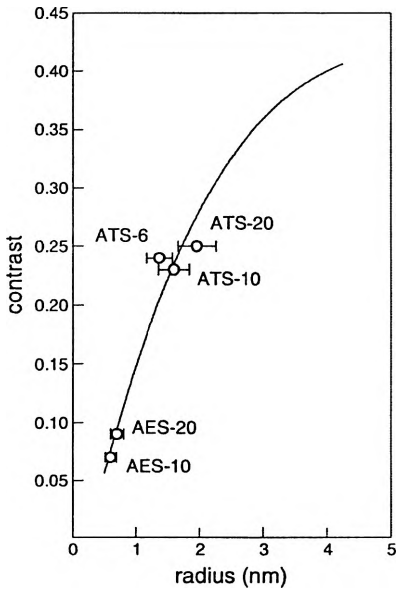


Figure 6. The full curve represents the contrast between the maximum and the minimum in the calculated extinction spectra for gold nanoparticles in terms of their radius. The symbols correspond to the contrast measured in the experimental extinction spectra of AES-10. AES-20, ATS-6, ATS-10 and ATS-20 samples; the radii were assigned from fitting of these spectra (bars assume a 15% error).

the mean free path of conduction electrons, gives very good agreement with experiments performed with gold nanoparticles. The preparation of these particles assures a nearly spherical form and avoids the formation of clusters. Samples were suspensions of well isolated particles in a low concentration where simple scattering occurs.

This work offers a useful tool to determine the mean radius of gold nanoparticles between 0.5 and 5 nm from the analysis of the absorbance measurements performed with a commercial spectrophotometer. Sizing can be performed, within a 15% error, either by fitting the UV–visible spectra or by measuring the contrast between the minimum and the maximum in the 440–520 nm region. For radii between 5 and 10 nm, optical measurements are not useful for sizing gold particles. Over 10 nm the extinction spectra show features well correlated with size, and optical extinction spectroscopy is used extensively in sizing metal particles.

For the small particles used in this work there is a very good agreement between the determination of the radius by optical methods and TEM techniques. The relative errors in the determination of the nanoparticles size were smaller than 15%. Although TEM is the most widely used technique for measuring particle size, it has some disadvantages due to careful sample preparation and the expensive instrument. In such a case, the absorption measurement offers an attractive method to obtain very good results with a low cost.

Acknowledgments

The authors would like to thank Francisco Jaque-Rechea from Universidad Autónoma de Madrid, Spain, for useful discussions, Raúl Trbojevich from LMC Argentina for the sample preparation and Horacio E Troiani from Texas Material Institute USA for the TEM images. This work was performed with the aid of grants PICT 08852 and PICT 12 8300 from Agencia Nacional de Promoción Científica y Técnológica, Argentina, and grant X11/324 from Universidad Nacional de La Plata. Support from CYTED network VIII-E, Project VIII-9 and Subprograma VIII, Project VIII-2 are also acknowledged. The authors are fellows of CONICET, Argentina.

References

[1] Jones A R (ed) 2002 *Special issue: 6th International Congress on Optical Particle Characterization (Brighton, April 2001); Meas. Sci. Technol.* **13** (3) Editorial
[2] Méjean G *et al* 2003 Towards a supercontinuum-based infrared lidar *Appl. Phys.* B **77** 357–9
[3] Mejean G, Kasparian J, Yu J, Frey S, Salmon E and Wolf J-P 2004 Remote detection and identification of biological aerosols using a femtosecond terawatt lidar system *Appl. Phys.* B **78** 535–7
[4] Scaffardi L B, Tocho J O and Yebrin L L 1996 Sizing particles used in the leather industry by light scattering *Opt. Eng.* **35** 52–6
[5] Ferri F, Bassini A and Paganini E 1997 Commercial spectrophotometer for particle sizing *Appl. Opt.* **36** 885–91
[6] Bohren C F and Huffman D R 1998 *Absorption and Scattering of Light by Small Particles* (New York: Wiley)
[7] Link S and El-Sayed M A 1999 Size and temperature dependence of the plasmon absorption of colloidal gold nanoparticles *J. Phys. Chem.* B **113** 4212–7
[8] Kadono K, Sakaguchi T, Miya M, Matsuoka J, Fukumi T and Tanaka H 1993 Optical non-linear property of Au colloid-doped glass and the laser irradiation stability *J. Mater. Sci. Mater. Electron.* **4** 59–61
[9] Brusatin G, Guglielmi M, Innocenzi P, Martucci A and Scarinci G 2000 Materials for photonic applications from sol–gel *J. Electroceram.* **4** 151–65
[10] Trbojevich R, Pellegri N, Frattini A, de Sanctis O and Almeida R M 2002 Preparation and isolation of gold nanoparticles coated with a stabilizer and sol–gel compatible agent *J. Mater. Res.* **17** 1973–80
[11] Huglin M B 1972 *Light Scattering from Polymer Solutions* (New York: Academic)
[12] Palik E D (ed) 1998 *Handbook of Optical Constants of Solids* vol 1 (New York: Academic) pp 286–95
[13] Granqvist C G and Hunderi O 1977 Optical properties of ultrafine gold particles *Phys. Rev.* B **16** 3513–34
[14] Kreibig U and von Fragstein C 1969 The limitation of electron mean free path in small silver particles *Z. Phys.* **224** 307–23
[15] Kreibig U 1974 Electronic properties of small silver particles: the optical constants and their temperature dependence *J. Phys. F: Met. Phys.* **4** 999–1014
[16] Hövel H, Fritz S, Hilger A, Kreibig U and Vollmer M 1993 Width of cluster plasmon resonances: bulk dielectric functions and chemical interface damping *Phys. Rev.* B **48** 18178–88
[17] Alvarez M, Khoury J, Schaaff T, Shafigullin M, Vezmar I and Whetten R 1997 Optical absorption spectra of nanocrystal gold molecules *J. Phys. Chem.* B **101** 3706–12
[18] Doremus R, Kao S and García R 1992 Optical absorption of small copper particles and the optical properties of copper *Appl. Opt.* **31** 5773–8
[19] Doremus R H 1964 Optical properties of small gold particles *J. Chem. Phys.* **40** 2389–96
[20] Doremus R H 1965 Optical properties of small silver particles *J. Chem. Phys.* **42** 414–7

INSTITUTE OF PHYSICS PUBLISHING NANOTECHNOLOGY
Nanotechnology 17 (2006) 1309–1315 doi:10.1088/0957-4484/17/5/024

Size dependence of refractive index of gold nanoparticles

Lucía B Scaffardi[1,2] and Jorge O Tocho[1,3]

[1] CIOp (CONICET-CIC), CC 124, 1900 La Plata, Argentina
[2] Área Departamental de Ciencias Básicas, Facultad de Ingeniería, Universidad Nacional de La Plata, Argentina
[3] Departamento de Física, Facultad de Ciencias Exactas, Universidad Nacional de La Plata, Argentina

E-mail: lucias@ciop.unlp.edu.ar

Received 9 September 2005, in final form 25 November 2005
Published 10 February 2006
Online at stacks.iop.org/Nano/17/1309

Abstract
The extinction spectra of spherical gold nanoparticles suspended in a homogeneous media were measured and the results were adjusted with Mie's theory together with an appropriate modification of the optical properties of bulk material considering the limitation that introduces the size of nanoparticles on the dielectric function. Usually, the contribution of free electrons to the dielectric function is modified for particle size, while the contribution of bound electrons is assumed to be independent of size. This work discusses the separated contribution of free and bound electrons on the optical properties of particles and their variation with size for gold nanoparticles. The effects of dielectric function and its changes with size on extinction spectra near plasmon resonance are considered. The damping constant for free electrons was changed with size as usual and a scattering constant of $C = 0.8$ was used. For the bound electron contribution, two different models were analysed to fit the extinction spectra: on the one hand, the damping constant for interband transitions and the gap energy were used as fitting parameters and on the other, the electronic density of states in the conduction band was made size-dependent. For the first model, extinction spectra corresponding to particles with radius $R = 0.7$ nm were fitted using two sets of values of the energy gap and damping constant: $E_g = 2.3$ eV and $\gamma_b = 158$ meV/$\hbar$ or $E_g = 2.1$ eV and $\gamma_b = 200$ meV/$\hbar$. For the second model, a simple assumption for the electronic density of states and its contribution to the dielectric function in terms of size allowed to adjust extinction spectra for all samples explored (from 0.3 to 1.6 nm radius). This last model uses only one parameter, a scale factor $R_0 = 0.35$ nm, that controls the contribution of the bound electrons in nanoparticles. Contrast between the maximum and the minimum in the extinction spectra near the resonance at 520 nm or alternatively the broadening of the plasmon band can be used to determine the size of gold nanoparticles with radius smaller than 2 nm.

1. Introduction

Metal nanoparticles show very complex and interesting optical properties known from the beginning of the last century. Recent advances in the production, manipulation and measurements on the nanometre scale have revitalized this field in recent years. Applications of nanoparticles to biological sensors [1] and optoelectronic devices, among others, are now receiving increasing attention. Guiding light in integrated optical systems and interfacing with electronic components remain important challenges for research and development today. Nanostructured metals are believed to

be one of the key components of such future optoelectronic devices [2].

One of the most characteristic features encountered in metal nanoparticles is electromagnetic resonances due to collective oscillations of the conduction electrons named 'plasmons'. Plasmons excited by light lead to strong light scattering and absorption together with an enhancement of the local electromagnetic field. Plasmon modes in metals such as gold and silver fall in the visible spectral region. The spectral characteristics of plasmons have been used frequently to characterize the size of gold nanoparticles in the range 10–100 nm radius [1].

Recently, we have shown a method for sizing gold nanoparticles below 7 nm by fitting extinction spectra with Mie's theory together with a conveniently modified bulk refractive index [3]. The modification follows the idea of Kreibig and von Fragstein [4], who considered that the damping constant in Drude's model is increased due to additional collisions of free electrons with the boundary of the particle. This fact produces a size dependence of the dielectric function and consequently of the refractive index. As usual, the real part of the dielectric function evaluated for the bulk was used without any modification, but the effect of size limitation on the imaginary part of the dielectric function was considered. Recently, Arbouet *et al* [5] made similar assumptions: only free electrons were considered and only the imaginary part of the dielectric function was modified by size.

For noble metals, transitions of bound electrons to conduction levels contribute appreciably to the dielectric function. Recently, Pinchuk *et al* [6] have analysed the influence of interband electronic transitions on the frequency, amplitude and bandwidth of the surface plasmon resonance in small metal clusters in the Rayleigh approximation. Their theoretical results for silver and gold, including the interband transitions in the model, lead to a more reasonable value for the plasmon bandwidth, although the experimental results are still different from calculated values.

The size effect over the dielectric function will be studied further in this work in order to analyse the influence on the extinction spectra of gold nanoparticles. Both free and bound electron contributions will be considered and the values of the different parameters involved in the model will be determined.

2. Experimental section

The gold nanoparticles used in this work were synthesized as 'reverse micelles' in water–hydrocarbon phases and isolated with a stabilizer. Details of the preparation of the particles can be found elsewhere [7]. The particles are capped with the stabilization agent and this fact helps to maintain the gold particles in a dispersion state in organic solvents. For this reason samples were dispersed in heptane for the UV–visible extinction measurements.

Extinction spectra of a suspension of gold nanoparticles in heptane were recorded between 300 and 900 nm using a Beckman Spectrophotometer (Model 600). The optical density for a 1 cm light path was kept below one to avoid multiple scattering effects. The spectrum for a gold sample named ATS-6 is shown in figure 1. The insets show a TEM image (JEOL 1010, at 80 kV) of this sample and the corresponding

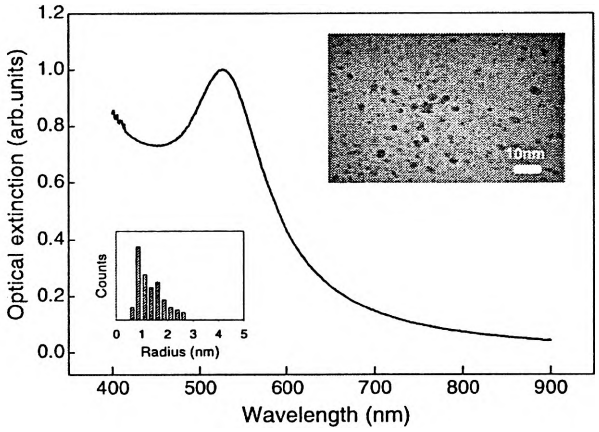


Figure 1. Optical extinction spectra and TEM image of gold ATS-6 sample ($R = 1.3$ nm).

histogram. The nanoparticle shape is nearly spherical. The mean radius was determined from statistical analysis of the histogram of this picture discarding obvious superposition. For this sample, the mean radius was determined as 1.3 nm.

Optical extinction spectra of other samples corresponding to particles prepared with different stabilization agents ATS, *N*-[3-(trimethoxysilyl) propyl] diethylenetriamine (Aldrich Tech.), AES, 3-(2-aminoetilaminopropil) trimethoxisilane) (Aldrich, 97%); and APS, 3-aminopropyltrimethoxysilane (Aldrich, 97%); were measured. Particles prepared with APS and AES are expected to be smaller than samples prepared with ATS, that range between 1.3 and 1.9 nm radius. Spectra of some of them will be shown in section 4, where the main feature is a reduction in the contrast between the maximum at the plasmon band and the minimum near 440 nm in the extinction. Unfortunately, no good microscopic images of all the samples are available, due mainly to coalescence when they were prepared for observation.

3. Theoretical framework

For noble metals, where there is a substantial bound electron component, the dielectric function for the bulk can be decomposed into two terms, a free electron term and an interband, or bound electron, term [8]. Since the dielectric function is additive, it can be written as

$$\varepsilon_{\text{bulk}}(\omega) = \varepsilon_{\text{bound-electrons}}(\omega) + \varepsilon_{\text{free-electrons}}(\omega). \quad (1)$$

For bound electrons, the complex dielectric function can be calculated taking into account the interband transitions from the d-band to the conduction sp-band near the L point in the Brillouin zone of gold [9]. Inouye *et al* [10] have shown a simplified expression of this calculation assuming that the curvature of the d-band can be ignored. The following expression, where a misprint in the original paper is corrected, will be used throughout this work:

$$\varepsilon_{\text{bound-electrons}}(\omega) = Q_{\text{bulk}} \int_{\omega_g}^{\infty} \frac{\sqrt{x-\omega_g}}{x}[1 - F(x,T)] \times \frac{(x^2 - \omega^2 + \gamma_b^2 + \mathrm{i}2\omega\gamma_b)}{(x^2 - \omega^2 + \gamma_b^2)^2 + 4\omega^2\gamma_b^2}\,\mathrm{d}x, \quad (2)$$

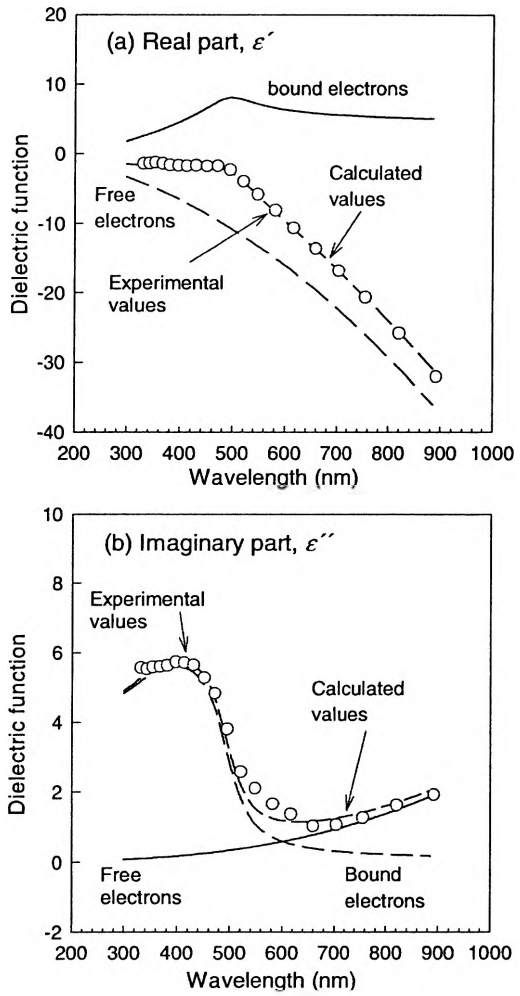


Figure 2. Dielectric function for bulk gold calculated with equations (1), (2) and (3) (lines) and experimental values (hollow circles) from Johnson and Christy [11]. The fitting parameters used are given in table 1.

where $\hbar\omega_g$ is the gap energy (E_g) for gold; $F(x, E_F, T)$ is the Fermi energy distribution function of conduction electron of energy $\hbar x$ at the temperature T with Fermi energy E_F; γ_b represents the damping constant in the band to band transition and Q_{bulk} is a proportionally factor.

The complex dielectric function for the free electrons can be written as usual:

$$\varepsilon_{free-electrons}(\omega) = 1 - \frac{\omega_p^2}{\omega^2 + i\gamma_{free}\omega}, \tag{3}$$

where ω_p is the bulk plasma frequency and γ_{free} is the damping constant (the inverse of the collision time for conduction electrons) in the Drude model.

Figure 2 shows the results of our calculations for the bulk dielectric function using equations (1)–(3). For the free electron contribution, values given by Johnson and Christy [11] and Granqvist *et al* [12] for γ_{free} and ω_p, respectively, were used. For the bound electron contribution, the damping constant γ_b given by Inouye *et al* [10] was used. Other parameters in equation (2), such as Q_{bulk}, E_g and E_F, were adjusted to fit the experimental values for bulk gold. The experimental optical properties for gold were taken from Johnson and Christy [11]. This dielectric function yields n and k values similar to those given by Palik [13]. All the parameters used in this work for bulk gold are summarized in table 1.

For metallic particles, the plasma frequency ω_p can be calculated from

$$\omega_p^2 = \frac{N/V}{m\varepsilon_0}e^2, \tag{4}$$

where N is the amount of free electrons in a volume V, m is the effective mass of an electron (near the free electron mass in the case of gold) and e and ε_0 have the usual meaning. Each atom of gold contributes with one free electron to N and the density N/V remains constant for different sizes. For this reason the plasma frequency ω_p is assumed independent of the size. However, the damping, related to the mean free path for free electrons, is strongly affected by the size. In particles smaller than the mean free path of conduction electrons in the bulk metal, the mean free path is dominated by collisions with the particle boundary [4, 12, 14, 15]. For small particles, the damping constant for the free electron contribution is increased due to additional collisions with the boundary of the particle, and it can be written as

$$\gamma_{free}(R) = \gamma_{bulk} + C\frac{v_F}{R}, \tag{5}$$

where v_F is the electron velocity at the Fermi surface and R is the radius of the particle. A value $v_F = 14.1 \times 10^{14}$ nm s^{-1} was used in the calculations [12]. C is the scattering constant that includes details of the scattering processes. Its actual value is not free from controversy; values from 0.1 to 2 have been theoretically justified [16].

For the contribution of bound electrons, no functional form is known to change the parameters in equation (2) as a function of the size of the particle. However, we can assume that, similarly to the change made in the damping constant for the free electron contribution, the value of γ_b can be made size dependent. Besides that, E_g can change also with size. Alternatively, Logunov *et al* [17] introduced the idea that the electronic density of states is different for nanoparticles of different size. This fact affects equation (2), where part of the integrand is just the density of states in the upper band. Since small particles have larger spacing between electronic states, it is valid to conclude that the density of states will be smaller for very small nanoparticles. We propose to take account of this fact by changing the proportionality factor Q_{bulk} in the contribution of bound electrons from its value accepted for the bulk to $Q_{size} = Q_{bulk}[1-\exp(R/R_0)]$, where R is the radius of the particle and R_0 is the scale factor, that represents the range for which the density of states can be considered to reach the value of the bulk.

To calculate the optical extinction spectra corresponding to the studied small gold nanoparticles we assumed that only the dipole absorption in the Mie calculation contributes to the cross section [8, 18],

$$\sigma(\lambda, \text{size}) \propto \frac{R^3 n_0^3 \varepsilon''_{size}/\lambda}{(\varepsilon'_{size} + 2n_0^2)^2 + (\varepsilon''_{size})^2}, \tag{6}$$

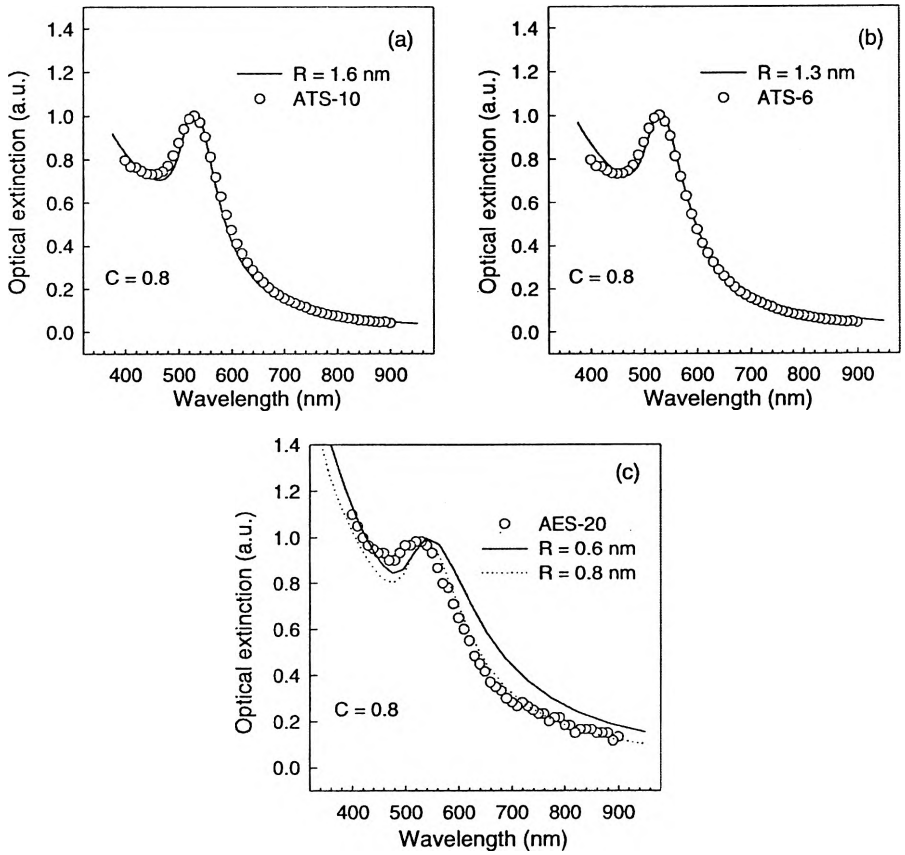


Figure 3. Optical extinction spectra for three samples: (a) ATS-10, (b) ATS-6 and (c) AES-20. Hollow circles correspond to experimental results and lines represent the fits obtained using the parameters for the bulk given in table 1 and $C = 0.8$. Good agreement with experimental spectra can be seen in (a) and (b), for 1.6 and 1.3 nm radii, respectively. However, for smaller radii, (c), no good fit can be obtained for any particle radius using parameters for the bulk.

Table 1. Optical parameters of bulk gold used and determined in this work.

Parameter	Symbol	Value	Reference
Plasma frequency	ω_p	13×10^{15} Hz	Granqvist
Dumping constant for free electrons	γ_{bulk}	1.1×10^{14} Hz	Johnson and Christy
Coefficient for bound electron contribution	Q_{bulk}	2.3×10^{24}	This work
Gap energy	E_g	2.1 eV	This work
Fermi energy	E_F	2.5 eV	This work
Damping constant for bound electrons	γ_b	158 meV/$\hbar$ (2.4×10^{14} Hz)	Inouye

where n_0 is the refractive index of the medium (heptane) and λ is the wavelength for frequency ω. The experimental refractive indices of heptane for 434, 486, 589 and 656 nm were used to calculate values for other wavelengths with Sellmeier's dispersion equation [19].

4. Results

The optical extinction spectra for three samples (ATS-10, ATS-6, and AES-20) are shown in figure 3, together with calculated spectra. For these theoretical fits, we consider that the real (ε') and imaginary (ε'') parts of the dielectric function are composed by addition of the bound electron contribution corresponding to the bulk and the free electron contribution corrected for size through the damping constant.

The fits shown in figure 3 were obtained using the parameters accepted for the bulk given in table 1 and $C = 0.8$. A good agreement with the experimental spectra can be seen in figures 3(a) and (b), where 1.6 and 1.3 nm radius were used respectively. These values were obtained by TEM, as mentioned in a previous work [3]. The optical extinction spectrum depicted in figure 3(c) shows a less pronounced contrast than in the previous ones, indicating that it corresponds to smaller particles. However, it was not possible to find a good fit for any particle radius. For $R = 0.8$ nm, the long wavelength tail is well adjusted but the short wavelength region is not. For $R = 0.6$ nm, the fit is slightly improved in the short wavelength region but it is quite bad in the tail. Unfortunately, a microscope image is not available for this sample but its radius was determined by a fitting procedure in a previous work as 0.7 nm [3].

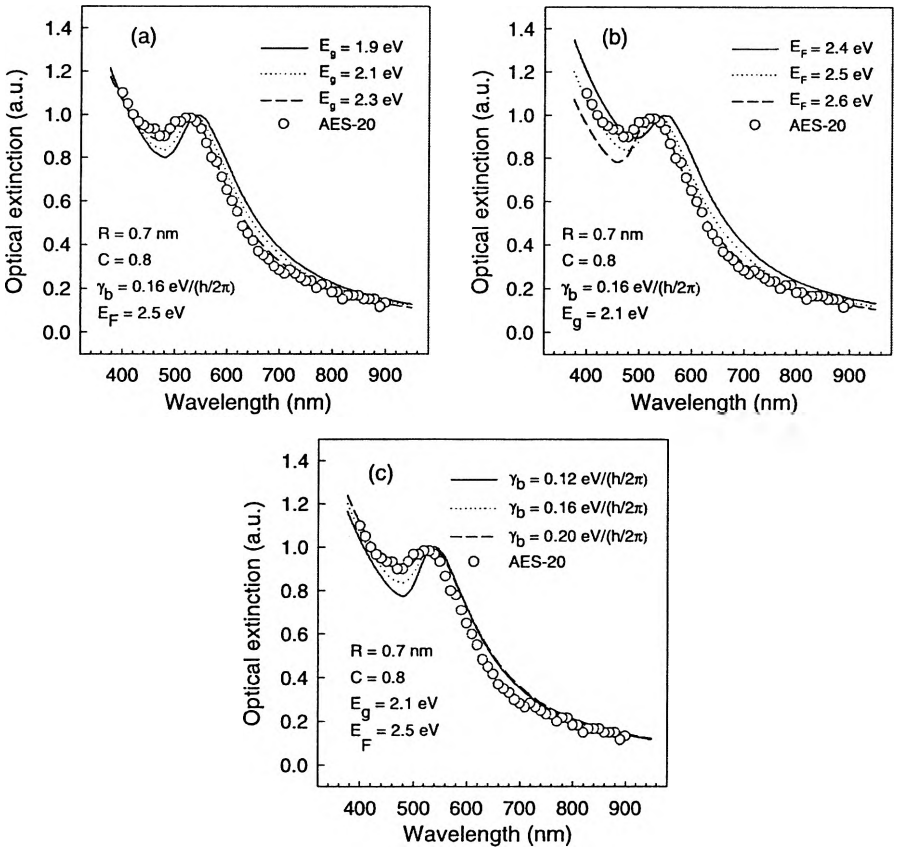


Figure 4. Influence of different parameters for bound electrons on the extinction spectra of small gold nanoparticles: (a) the energy gap (E_g), (b) the Fermi energy (E_F) and (c) the damping (γ_b).

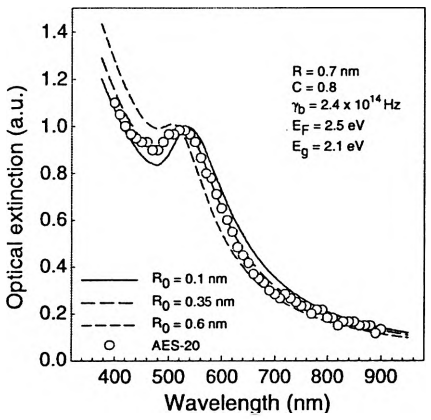


Figure 5. Optical extinction spectra of AES-20 gold nanoparticles. The fitting values correspond to different R_0 values, $C = 0.8$, and other parameters are for bulk gold. The best fit corresponds to $R_0 = 0.35$ nm.

It can be argued that, for the smallest particles, it is necessary to include some size-dependent correction to the contribution of the bound electrons in the dielectric function. In order to study the influence of the different parameters involved in the extinction spectra of gold nanoparticles, we explore the changes introduced by different values of E_g, E_F, and γ_b of equation (2) over the extinction spectra given by equation (5). A radius of 0.7 nm was assumed in this calculation. Experimental results for sample AES-20 are included in figure 4 for reference. Figure 4(a) shows the influence of E_g on both the position of the maximum of the extinction spectra and its contrast. We can observe that the position of the maximum is slightly shifted to lower wavelengths when E_g is increased from its bulk value. Simultaneously, the contrast is reduced. Reasonably good fitting was obtained for $E_g = 2.3$ eV. Figure 4(b) shows the effect of E_F on the positions of the maximum and minimum in the extinction spectra: when E_F increases, both extremes are noticeably shifted to lower wavelengths. No good fit can be obtained by changing only this parameter. Figure 4(c) shows the behaviour of the extinction spectra when γ_b is varied within a certain range. For wavelengths larger than that of the maximum, the spectra are not altered, while for smaller wavelengths different contrast values are observed. By increasing γ_b from its bulk value to 0.20 eV/$\hbar$, the fit is improved in the short wavelength part of the spectra, although the fit for the tail is not good.

The results of figure 4 show that extinction spectra of small gold nanoparticles can be adjusted reasonably well assuming that the Fermi energy is similar to the bulk value but the gap energy or alternatively the damping constant must be increased from its bulk values. For particles with $R = 0.7$ nm, best fits were obtained for two sets of values, $E_g = 2.3$ eV and

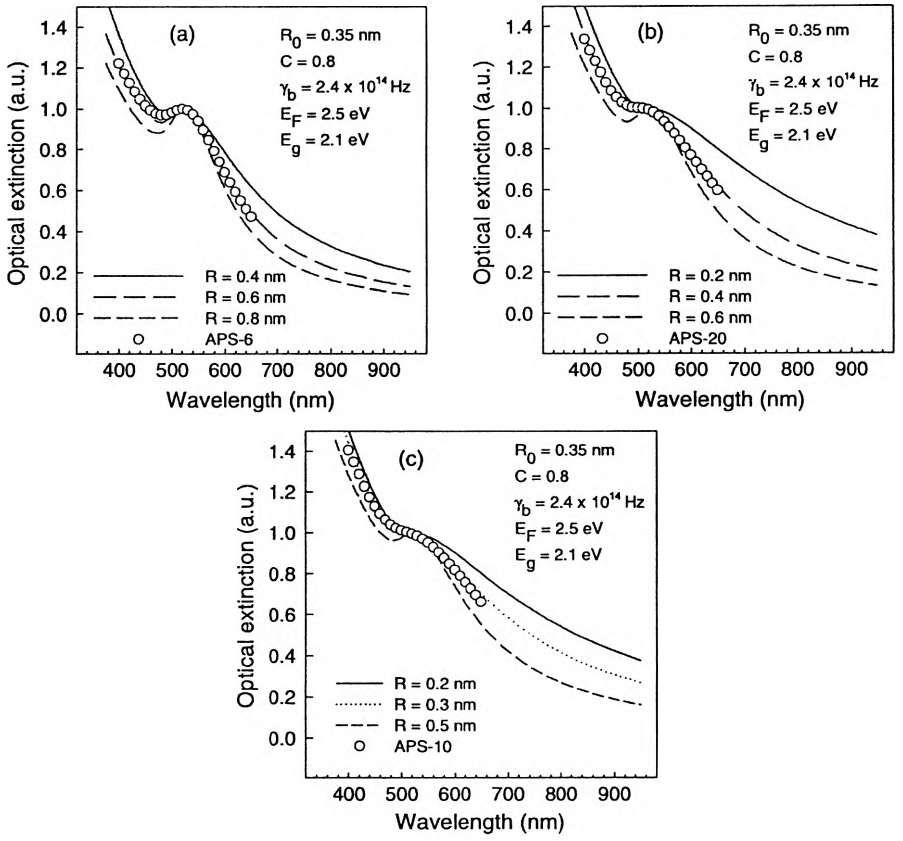


Figure 6. Optical extinction spectra (hollow circles) and fitting results (lines) for APS samples. Best fits correspond to: (a) radius 0.6 nm for APS-6; (b) radius 0.4 nm for APS-20 and (c) radius 0.3 nm for APS-10.

Table 2. Optical parameters of gold nanoparticles used and determined in this work.

Parameter	Symbol	Value
Scattering constant	C	0.8
Gap energy and damping constant for bound electrons (R = 0.7 nm)	E_g, γ_b	E_g = 2.3 eV, γ_b = 158 meV/$\hbar$ E_g = 2.1 eV, γ_b = 200 meV/$\hbar$
Coefficient for bound electrons contribution	Q_{size}	$2.3 \times 10^{24} \times [1 - \exp(R/R_0)]$ R_0 = 0.35 nm

γ_b = 158 meV/$\hbar$ (bulk) or alternatively for E_g = 2.1 eV (bulk) and γ_b = 200 meV/$\hbar$.

As was mentioned in section 3, there is another model used to calculate the influence of the size over the contribution of the bound electrons on the dielectric function. Small particles with larger spacing between electronic states have smaller density of states than larger particles that resemble the bulk material. This fact can be taken into account by making the proportionality factor Q_{size} a function of the size in the form

$$Q_{size} = Q_{bulk}\left[1 - \exp\left(\frac{R}{R_0}\right)\right], \qquad (7)$$

where R is the radius of the particle and R_0 is a scale factor. This expression can be introduced in equation (2) to calculate the contribution of the bound electrons to the dielectric function, and its results are then used in equation (6) to calculate the extinction spectra. Results for sample AES-20 with particles of 0.7 nm radius are shown in figure 5.

Excellent fit was obtained for R_0 = 0.35 nm.

Table 2 summarizes the optical parameters used to adjust the experimental spectra of gold nanoparticles by the two models proposed in this work. The expression given by equation (7) suggests that, for particles with radius bigger than 3 R_0, the correction over Q_{bulk} is negligible. This fact was checked over the bigger nanoparticles (R = 1.6 and 1.3 nm) where the fitting spectra did not show any modification relative to data shown in figure 3. By using this last model, that modifies the density of electronic states in the conduction band according to the size of the nanoparticles, it was possible to fit the extinction spectra of other samples prepared with a different surface modifier, namely APS. The results are shown in figure 6, where it is clearly seen a small contrast in the extinction spectra that predicts the presence of very small

particles. The best fit corresponds to $R = 0.6$ nm (APS-6); $R = 0.4$ nm (APS-20) and $R = 0.3$ (APS-10). TEM results for these samples show strong clustering due to coalescence and are not reliable for the determination of size. Optical extinction spectroscopy is well suited for measurements in solution and allows one to obtain good results for sizing very small nanoparticles.

5. Conclusions

In this work we have shown that the extinction spectra of gold nanoparticles can be fitted using Mie's theory, taking into account the dependence of the optical properties with size. While the change with size of the free electron contribution to the dielectric function has been explored in many works, we show for the first time that the bound electron contribution must be modified as well in order to fit extinction spectra of very small nanoparticles. The contribution of electron transitions from the d-band to the conduction band was modelled using the expression given by Inouye *et al* [10]. First, the different parameters of this expression were obtained by fitting the bulk dielectric function as a sum of free electron and bound electron contributions. After that, two different models were used to include the size dependence on the bound electron contribution: one uses the energy gap and the damping constant as adjustable parameters to fit the experimental extinction spectra, and the other changes the electronic density of states in the conduction band in terms of size. The latter model allows one to fit the spectra of all the samples explored. The dependence of the electronic density of states with size proposed in this work is a good representation of the fact that small particles have larger spacing between electronic states, but the proposed mathematical expression ($\propto 1 - \exp(R/R_0)$) is of course not necessarily unique. This expression suggests that for particles with radius larger than 1 nm, the correction over the bound electron contributions in negligible.

We did not observe a fine structure on the optical extinction spectra for any sample. This feature can be explained due to fact that the samples are not strictly monomodal and present a small dispersion around the mean value. This situation does not represent a restriction when the mean radius is to be determined. Contrast between the maximum and the minimum in the extinction spectra near the resonance at 520 nm or alternatively the broadening of the plasmon band can be used to determine the size of gold nanoparticles, as was suggested previously [3].

Acknowledgments

This work was performed with the aid of grants PICT 08852 from Agencia Nacional de Promoción Científica y Técnológica, Argentina, and grants 11/X324 and 11/I104 from Universidad Nacional de La Plata. The authors are fellows of CONICET, Argentina. The gold nanoparticles were synthesized in the Laboratorio de Materiales Cerámicos, FCEIyA, IFIR, Rosario, Argentina.

References

[1] Bogatyrev V A, Dykman L A, Khlebtsov B N and Khlebtsov N G 2004 Measurement of mean size and evaluation of polydispersity of gold nanoparticles from spectra of optical absorption and scattering *Opt. Spektrosk.* **96** 128–35

[2] Xia Y, Gates B, Yin Y and Lu Y 2000 Monodispersed colloidal spheres. Old materials with new applications *Adv. Mater.* **12** 693–713

[3] Scaffardi L B, Pellegri N, de Sanctis O and Tocho J O 2005 Sizing gold nanoparticles by optical extinction spectroscopy *Nanotechnology* **16** 158–63

[4] Kreibig U and Fragstein C V 1969 The limitation of electron mean free path in small silver particles *Z. Phys.* **224** 307–23

[5] Arbouet A, Christofilos D, Del Fatti N, Vallée F, Huntzinger J R, Arnaud L, Billaud P and Broyer M 2004 Direct measurement of the single-metal-cluster optical absorption *Phys. Rev. Lett.* **9** 127401/1–4

[6] Pinchuk A, von Plessen G and Kreibig U 2004 Influence of interband electronic transitions on the optical absorption in metallic nanoparticles *J. Phys. D: Appl. Phys.* **37** 3133–9

[7] Trbojevich R, Pellegri N, Frattini A, de Sanctis O and Almeida R M 2002 Preparation and isolation of gold nanoparticles coated with a stabilizer and sol–gel compatible agent *J. Mater. Res.* **17** 1973–80

[8] Bohren C F and Huffman D R 1998 *Absorption and Scattering of Light by Small Particles* (New York: Wiley)

[9] Rosei R, Antonangeli F and Grassano U M 1973 d bands position and width in gold from very low temperature thermomodulation measurements *Surf. Sci.* **37** 689–99

[10] Inouye H, Tanaka K, Tanahashi I and Hirao K 1998 Ultrafast dynamics of nonequilibrium electrons in a gold nanoparticle system *Phys. Rev.* B **57** 11334–40

[11] Johnson P B and Christy R W 1972 Optical constants of the noble metals *Phys. Rev.* B **6** 4370–9

[12] Granqvist C G and Hunderi O 1977 Optical properties of ultrafine gold particles *Phys. Rev.* B **16** 3513–34

[13] Palik E D (ed) 1998 *Handbook of Optical Constants of Solids* vol 1 (New York: Academic) pp 286–95

[14] Kreibig U and von Fragstein C 1969 The limitation of electron mean free path in small silver particles *Z. Phys.* **224** 307–23

[15] Kreibig U 1974 Electronic properties of small silver particles: the optical constants and their temperature dependence *J. Phys. F: Met. Phys.* **4** 999–1014

[16] Alvarez M M, Khoury J I, Schaaff T G, Shafigullin M N, Vezmar I and Whetten R L 1997 Optical absorption spectra of nanocrystal gold molecules *J. Phys. Chem.* B **101** 3706–12

[17] Logunov S L, Ahmadi T S, El-Sayed M A, Khoury J T and Whetten R L 1997 Electron dynamics of passivated gold nanocrystals probed by subpicosecond transient absorption spectroscopy *J. Phys. Chem.* B **101** 3713–9

[18] Doremus R, Kao S and García R 1992 Optical absorption of small copper particles and the optical properties of copper *Appl. Opt.* **31** 5773–8

[19] Huglin M B 1972 *Light Scattering from Polymer Solutions* (New York: Academic)

Visible and near-infrared backscattering spectroscopy for sizing spherical microparticles

Lucía B. Scaffardi, Fabián A. Videla, and Daniel C. Schinca

Scattering is a useful tool for the determination of particle size in solution. In particular, spectroscopic analysis of backscattering renders the possibility of a simplified experimental setup and direct data processing using Mie theory. We show that a simple technique based on near-infrared (NIR) backscattering spectroscopy together with the development of the corresponding algorithm based on Fourier transform (FT) and Mie theory are a powerful tool for sizing microparticles in the range from 8 to 60 μm diameter. There are three wavelength intervals in the NIR, within which different diameter ranges were analyzed. In each one, the FT yields a coarse diameter value with an uncertainty dependent on the wavelength range. A more accurate value is obtained by further applying cross correlation between experimental and theoretical spectra. This latter step reduces the uncertainty in diameter determination between 30% and 40%, depending on wavelength interval and particle diameter. These results extend previous information on visible backscattering spectroscopy applied to sizing microparticles in the range between 1 and 24 μm diameter. This technique could be the basis for the construction of a portable and practical instrument. © 2007 Optical Society of America

OCIS codes: 300.0300, 290.1350, 300.6340, 120.5820.

1. Introduction

Size characterization of particulate material in solution is important for quality control processes in pharmacological, paint, cement, cosmetic, and pesticide industries, among others. Different optical techniques based on light scattering have been developed and applied to sizing particles due to their ease of use and noninvasive nature. Some are based on measurements of angular scattering at a fixed wavelength,[1,2] while others use dynamic light scattering,[3] working with a fixed angle and a fixed wavelength. Also, some authors addressed the problem of sizing particles in solutions, in laboratory phantoms, and in biological specimens using light scattering spectroscopy methods.[4–6]

In particular, optical backscattering spectroscopy shows advantages over fixed wavelength multiangle scattering measurements. On the one hand, it offers an instrumental advantage, since it may be ensembled endoscopically in a simple and compact way. On the other hand, the rich dependence of the theoretically calculated backscattering coefficient on wavelength and particle diameters can be used for particle sizing.

Previously,[4] we reported the use of visible backscattering spectroscopy for sizing particles in the 1–24 μm diameter range. Briefly, the analysis was based on the characteristic oscillatinglike nature of the backscattering spectrum when a beam of white light is incident on a suspension of particles, as can be seen in Fig. 1 for a set of calibrated latex particles of 5, 8, 10, and 20 μm nominal diameters.

In general, the spectra consist of a slowly wavelength-varying part, modulated by a rapidly varying signal. The former represents the combined response of the white lamp spectrum and the sensitivity curve of the detector, while the latter represents the wavelength dependence of the backscattering coefficient. Since this dependence is characteristic for each

The authors are with the Centro de Investigaciones Ópticas (CONICET-CIC), Camino Centenario y 506, 1897 La Plata, Argentina. The authors are also with the Área Departamental de Ciencias Básicas, Facultad de Ingeniería, Universidad Nacional de La Plata, Argentina. L. B. Scaffardi is also with the Carrera de Investigador Científico, Consejo Nacional de Investigaciones Científicas y Técnicas (CONICET), Argentina. F. A. Videla is also with the Departamento de Electrotecnia, Facultad de Ingeniería, Universidad Nacional de La Plata, Argentina and the Carrera de Profesional de Apoyo, Comisión de Investigaciones Científicas y Técnicas de la Provincia de Buenos Aires (CICBA), Argentina. D. C. Schinca (daniels@ciop.unlp.edu.ar) is also with the Carrera de Investigador Científico, Comisión de Investigaciones Científicas y Técnicas (CONICET), Argentina.

Received 18 April 2006; revised 3 August 2006; accepted 25 August 2006; posted 30 August 2006 (Doc. ID 69958); published 15 December 2006.

0003-6935/06/010067-09$15.00/0

© 2007 Optical Society of America

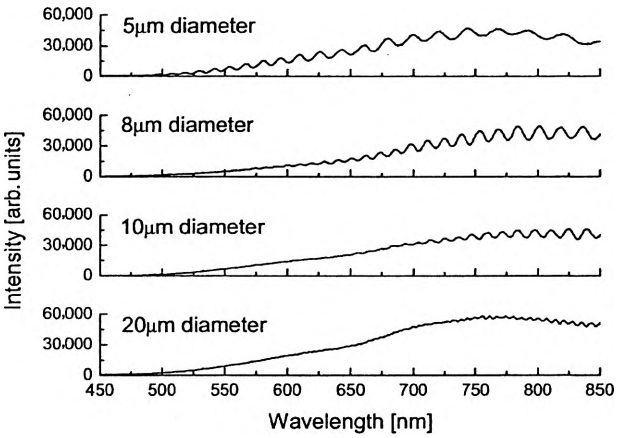


Fig. 1. Experimental raw backscatter spectra for monomodal samples of 5, 8, 10, and 20 μm latex particle diameters suspended in water.

diameter, it may be used for particle sizing. The number of maxima for a fixed wavelength interval is related to the particle's diameter. Thus if a certain wavelength interval is chosen based on inspection of the backscattering spectra, its frequency content can be determined by Fourier transform (FT) analysis. The oscillating nature of the backscattering signal as a function of wavelength, suggests that its FT should have a relatively sharp maximum whose position should be related to particle diameter. These experimental FTs agree with those obtained from calculated backscattering coefficients using Mie theory and allow for plotting a calibration curve between the FT maximum and the particle diameter. This curve allows for knowing, as a first step, the different particle sizes present in a given sample. Since the FWHM of the FT curve sets a limit on diameter resolution, a second step based on local cross correlation between experimental and theoretical spectra allows for improvement in the accuracy of diameter determination. That work was devoted to sizing particles of diameters between 1 and 24 μm using the visible wavelength interval of 600–730 nm. In its conclusions, it was mentioned that the technique could also be used to measure larger particles if the working spectral interval was adequately shifted to NIR wavelengths, based on the observed fact that the oscillations tend to appear more to the IR as the particle diameter increases. Moreover, it was also mentioned that in this new interval a new calibration curve should be determined according to the procedure described in the cited reference.

Here we extend the application of the backscattering spectroscopy technique to size larger particles and present new experimental backscattering spectra obtained in three NIR wavelength intervals for particles with increasing diameters (20, 30, and 50 μm). Our approach basically consists of the application of a simple algorithm to relate the FT maximum of the white-light backscattering spectrum to particle diameter. To increase the accuracy, a second step with cross correlation between experimental and calculated spectra is applied. The FT of experimental signals coming from scatterers have also been successfully applied to fixed wavelength multiangle scattering (FWMS)[7] for heptane spherical droplets between 10 and 100 μm. Recently, Semyanov *et al.*[8] also used FWMS FT to size polystyrene spherical particles ranging from 1.2 to 27.2 μm for different refractive index values.

2. Experimental

Figure 2 shows the experimental arrangement, which is similar to the one used in a previous work[4]: light from a quartz–tunsgten–halogen lamp (visible and NIR) is focused on the cell containing the sample through a delivery optical fiber of 200 μm core diameter. The backscattering light is collected by a similar optical fiber (collection) positioned close and parallel to the delivery fiber (separation of the fiber cores between 300 and 500 μm), both immersed in the sample. The collection fiber is connected to an echelle spectrograph multichannel instrument, which is sensitive in the interval of 200–1100 nm (Apogee CCD camera) with a constant resolution of 0.3 nm. The setup of the fibers (distance between fibers and depth when immersed in the sample) leads to a maximum collection cone of approximately 3° from the backward direction. The wavelength intervals studied in this work cover three NIR regions: 750–850, 1060–1100, and 1110–1150 nm. Standard calibrated monodisperse latex spheres suspended in pure filtered water were used as samples. The nominal calibrated diameters of the particles used were 5, 8, 10, 20, 30, and 50 μm, traceable to the standard meter through the National Institute of Standards and Technology, as stated by the manufacturer. All the samples were manufactured by Duke Scientific Corporation except for the 1 μm diameter particles, which were manufactured by Seradyn. The sample cell was a 10 cm long and a 1.0 cm diameter cylinder with an inner flat black coating to avoid wall reflections to reach the collection fiber. The experimental spectra were made free from instrument-dependent features by normalizing to a white reflectance spectrum taken as a reference. Simple scattering was achieved provided that concentration of solids used for the measure-

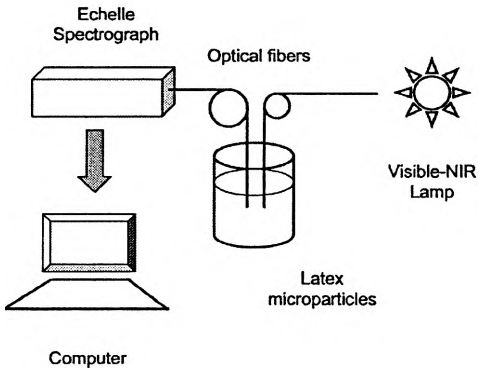


Fig. 2. Experimental setup.

ments ranged from 10^{-4} to 10^{-5} g/cm^3. This condition was always met in our experiments.

3. Results

For a better analysis of the spectra, it is convenient to take off the slowly varying component by subtracting an appropriate polynomial that mimics the quartz–tungsten–halogen spectrum. This procedure is similar to the one used in atmospheric gas pollutant detection using differential optical absorption spectroscopy.[9–11] Thus the raw spectra are transformed into ac-component spectra, as seen in Fig. 3(a) for 8, 10, and 20 μm particle diameter monodispersed samples in the 750–850 nm wavelength interval. Two features can be observed: first, the oscillations are almost sinusoidal, and second, the number of maxima (and minima) increases as the diameter increases.

It can be observed in Fig. 1 and in Fig. 3(a) that the period of the oscillations increases with increasing wavelength. This fact is due to the dependence of the scattering coefficient on Bessel and Hankel functions.[12] When the spectra are plotted versus the wavenumber, an almost constant oscillation period is observed, which is more appropriate for FT calculation. All the FT shown in this paper are applied to spectra plotted versus the wavenumber, although, for visualization purposes, the spectra will be shown in the wavelength scale, which is the conventional way that a spectrometer yields information.

In these conditions, if FTs are calculated on the above spectra, two facts can be observed: first, they will show a distinct maximum located at a specific frequency value for each sample, and second, this maximum will shift to larger frequencies as the diameter increases. These behaviors are shown in Fig. 3(b), where the FT of the different spectra shown in Fig. 3(a) (previously plotted as a function of the wavenumber) were calculated with the fast FT algorithm. It can be seen that the curves are almost single peaked, and its position increases monotonically as the particle diameter increases.

For the case of multimodal samples, the different components contribute to the total backscattering intensity, yielding a spectrum that, in general, may not have an almost sinusoidal shape. Figure 4(a) corresponds to the experimental spectrum obtained for a

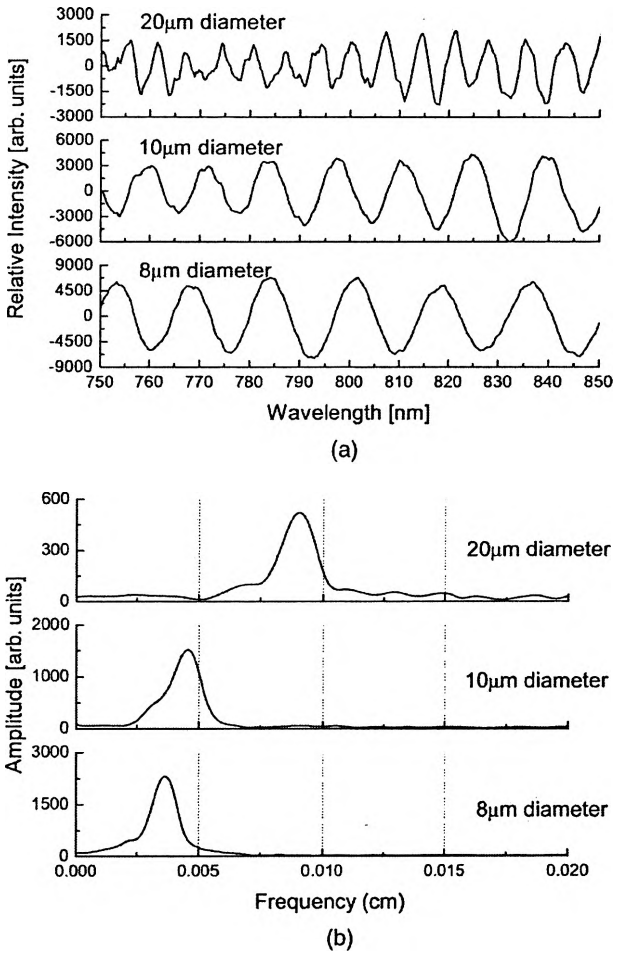


Fig. 3. (a) Experimental baseline-corrected backscattering spectra for monomodal samples of 8, 10, and 20 μm latex particle diameters suspended in water. (b) FT of the spectra of (a).

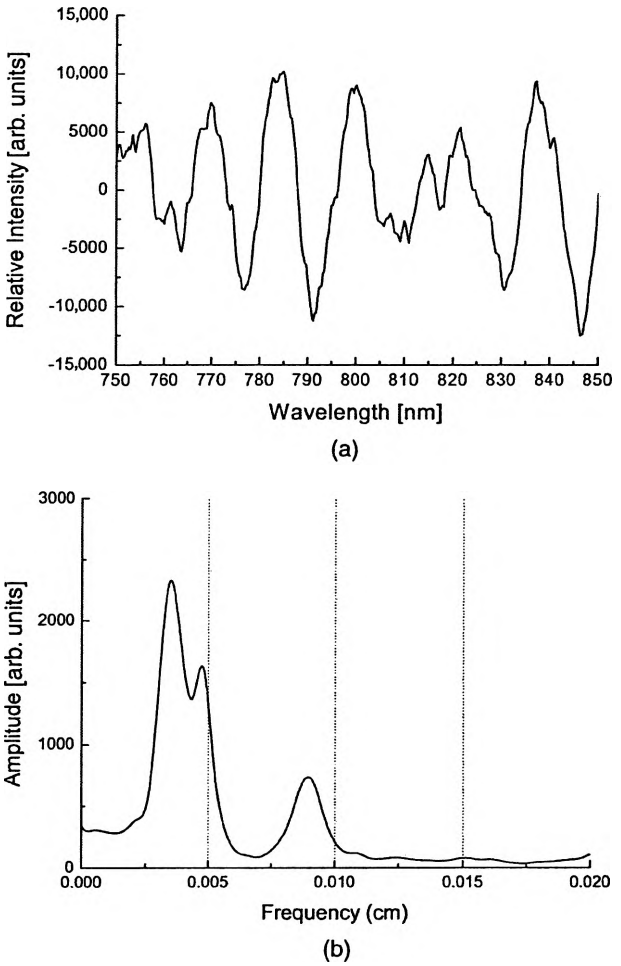


Fig. 4. (a) Experimental backscattering spectrum for a multimodal sample consisting of a mixture of latex particles of 8, 10, and 20 μm diameters suspended in water. (b) FT of the spectra of (a).

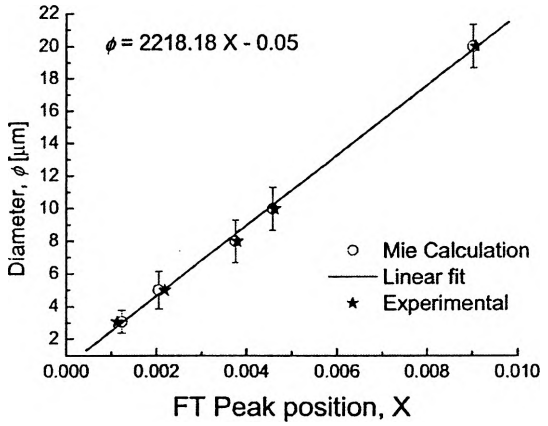


Fig. 5. Relation between the particle diameter and the FT peak position for five diameter values corresponding to spectra in the 750–850 nm range. Open circles correspond to theoretical calculations. Filled stars correspond to experimental values for the same diameters. The linear fit is on theoretical values.

mixture sample of 8, 10, and 20 μm diameter particles. When the FT is applied directly to this backscattering spectrum [Fig. 4(b)], three peaks can be observed, indicating the three sizes present in the sample. Note that the position of the three peaks coincides with the position of the FT maximum for each monomodal spectrum [Fig. 3(b)]. These results are similar to those obtained when studying smaller particles in the 600–730 nm visible interval.[4]

Nominal diameters (3, 5, 8, 10, and 20 μm) of the particles given by the manufacturer may be plotted versus the maxima of the FT of theoretical backscattering efficiency spectrum (open circles, Fig. 5). It can be seen that the results may be fitted by a linear regression. Filled stars represent FT peaks of experimentally monomodal measured backscattering spectra for the same diameters. Note that they lay on the same linear regression curve. This regression may then be used to determine particle diameter (ϕ) from the FT peak position (X). The slope transforms the X value (measured in centimeters) in appropriate units for ϕ to be measured in nanometers. The error bars (approximately ±1.3 μm) for each diameter in the figure represent the uncertainty given by the FWHM of the corresponding FT peak. This determination may be considered as a coarse approximation to a more precise value of the particle diameter.

For the improvement of accuracy in an experimental case, diameter determination should consist of a two-step process: first, a coarse value is taken from the FT maximum of the experimental spectrum, and second, a local approximation is taken to a more accurate value applying a cross-correlation algorithm between the experimental spectrum and the calculated ones within the FWHM range of the FT peak. In our case, integral correlation is formally expressed as

$$C(\varphi) = \int_{\lambda_{low}}^{\lambda_{high}} I_{exp}(\lambda, d_{FT}) I_{MIE}(\lambda, d_{FT} + \varphi) d\lambda,$$

where the limits of the integral correspond to the lowest and highest values of the chosen NIR interval wavelength, I_{exp} is the experimentally obtained spectrum, d_{FT} is the value of the diameter calculated by FT (coarse approximation), I_{MIE} is the spectrum

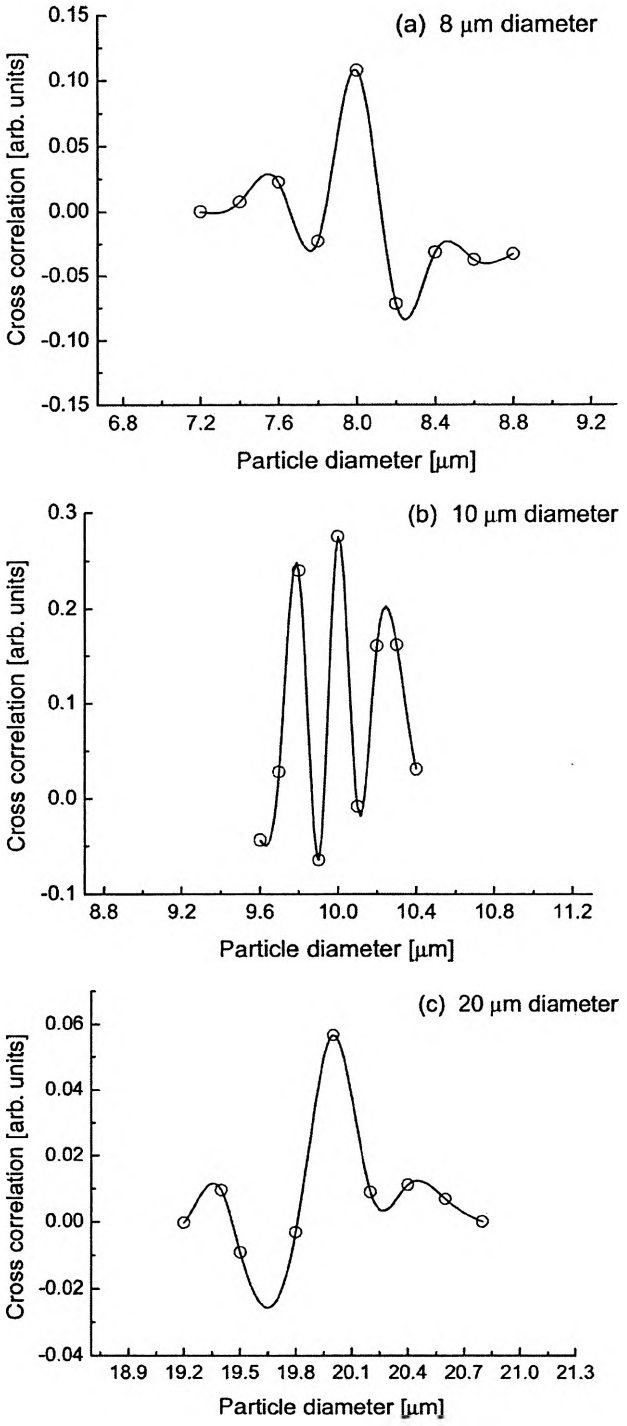


Fig. 6. Cross-correlation results between the mixture spectrum of Fig. 4(a) and calculated monomodal spectra for several diameters at approximately (a) 8 μm, (b) 10 μm, and (c) 20 μm. The span of the horizontal axis corresponds to the uncertainty given by the FWHM of the FT curve.

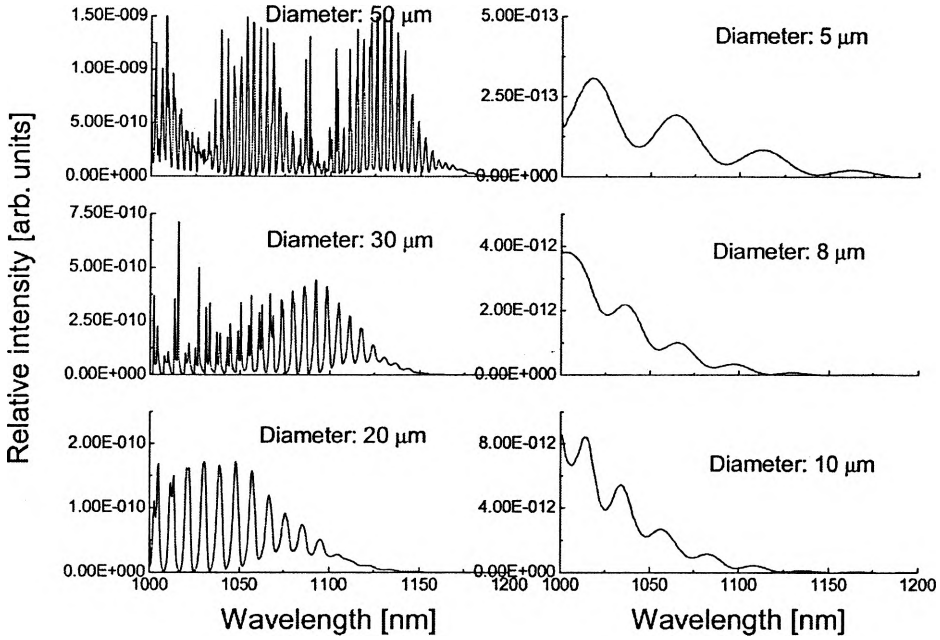


Fig. 7. Calculated backscattering coefficients for different spherical particles as a function of wavelength.

obtained by means of Mie theory, λ is the wavelength, and φ is the diameter increment around d_{FT} (delay).

I_{MIE} for spherical particles is calculated by Mie theory[13] as a function of wavelength. This calculation is based on the code given by Bohren and Huffman,[12] where the wavelength dependence of the refractive index of water and particle material was taken into account by[1]

$$n_w(\lambda) = 1.324 + 3046/\lambda^2 \quad \text{for water,}$$

$$n_p(\lambda) = 1.59 + 15 \times 10^3\,(1/\lambda^2 - 1/589.32^2)$$
for polystyrene particles.

Several I_{MIE} backscattering spectra are calculated for diameter values at approximately d_{FT} in an interval covering the FWHM of the FT peak. The largest correlation value for zero delay is then taken as the most probable diameter.

To check the usability of this technique, cross correlation was applied to each peak for the multimodal sample of Fig. 4(a). In this case, λ_{low} and λ_{high} correspond to 750 and 850 nm, repectively. Figure 6 shows these results, where the span of the horizontal axes corresponds to the uncertainty interval derived from the FWHM of the corresponding FT curves. Note that, although the correlation values for each diameter have a sharp absolute maximum within the FWHM range, coincident with the value given by the manufacturer, there are also other lower relative maxima, mainly due to the functional form of the calculated backscattering coefficients in this wavelength interval. This fact settles a criterion for determining the correlation width, that includes these maxima as the new uncertainty in diameter value. It

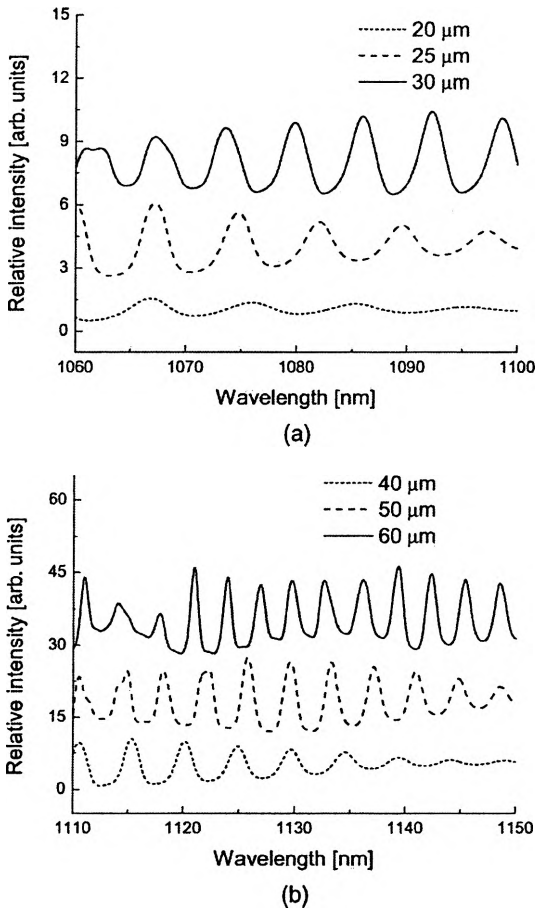


Fig. 8. Calculated backscattering intensity for (a) 20, 25, and 30 μm particle diameters between 1060 and 1100 nm and (b) 40, 50, and 60 μm particle diameters between 1110 and 1150 nm.

can be observed that this FWHM of the correlation is still narrower than that of the FT. This procedure reduces the uncertainty on the diameter determination in ~35% in this region.

For larger particles, it is interesting to analyze the spectra of theoretical backscattering coefficients calculated in a wavelength interval that extends farther into the NIR. The backscattering efficiency for spherical particles as a function of wavelength can be calculated using the codes given by Bohren and Huffman[12] and Laven.[14] Figure 7 shows an example of such calculations for different sphere diameters (5, 8, 10, 20, 30, and 50 μm). It can be seen that, as the diameters increase, the backscattering efficiency spectrum extends farther into the NIR. Inspection of the spectra shows that there are wavelength intervals that comprise almost equally spaced oscillation features, typical for each diameter, thus suggesting an almost single-peaked FT spectrum. These wavelength intervals may coincide for a certain range of diameters, but must be changed if larger particle diameters are to be analyzed. In particular, from 20 to ~35 μm diameter, a suitable wavelength interval seems to be ~1060–1100 nm, while for diameters between 35 and 60 μm, the most suitable interval is in the range of 1110–1150 nm.

Figure 8 shows the calculated backscattering efficiency spectrum for particle diameters of (a) 20, 25, and 30 μm and (b) 40, 50, and 60 μm. They are grouped into two different wavelength intervals (as stated above), both of the same length. In each group, it can be seen that the curves differ in the number of maxima. When the FT of these spectra (taken as a function of the wavenumber) are calculated, their maxima fall in different positions, as shown in Figs. 9(a) and 9(b). Each FT spectra shows a distinct maximum that shifts to larger values as the particle diameter increases. The secondary maxima account for the slight modulation in the amplitude of the scattering coefficients in the analyzed wavelength interval. Similar to what was shown for the interval of 750–850 nm, the functional relation between the position of the FT peaks and the corresponding particle

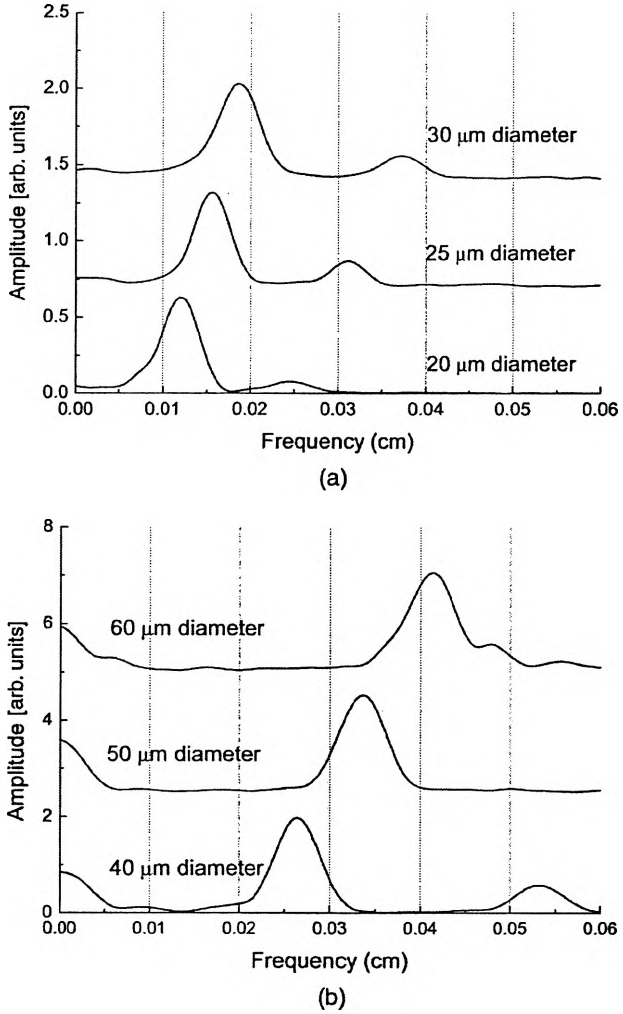


Fig. 9. FT of spectra of (a) Fig. 8(a) and (b) Fig. 8(b).

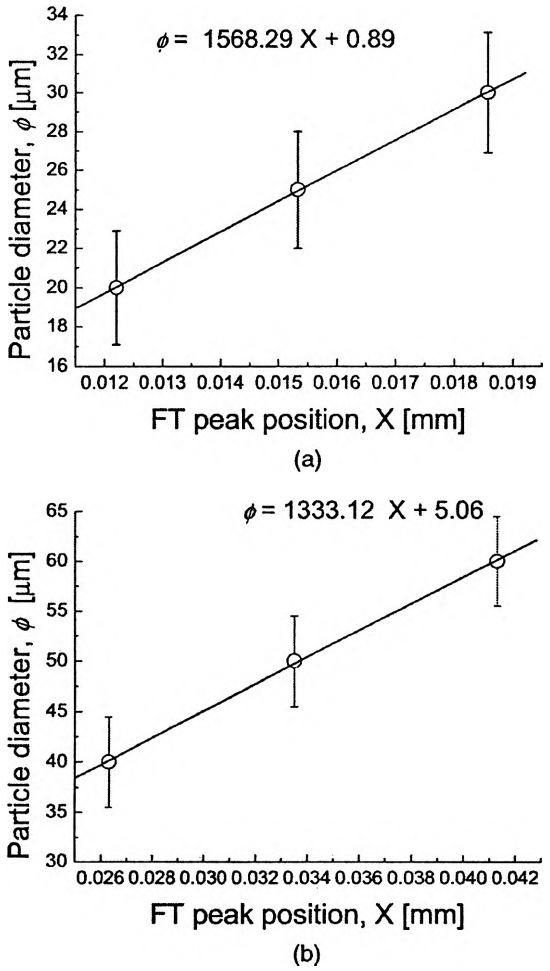


Fig. 10. Particle diameter versus FT peak position for (a) 20, 25, and 30 μm particle diameters (circles with error bars) and linear regression (line) for the 1060–1100 nm range and (b) 40, 50, and 60 μm particle diameters (circles with error bars) and linear regression (line) for the 1110–1150 nm range. The error bars represent the uncertainty given by the FWHM of the FT curve.

diameter in these new ranges may be fitted by a linear regression for particle diameters between 20 and 35 μm, and by another linear regression between

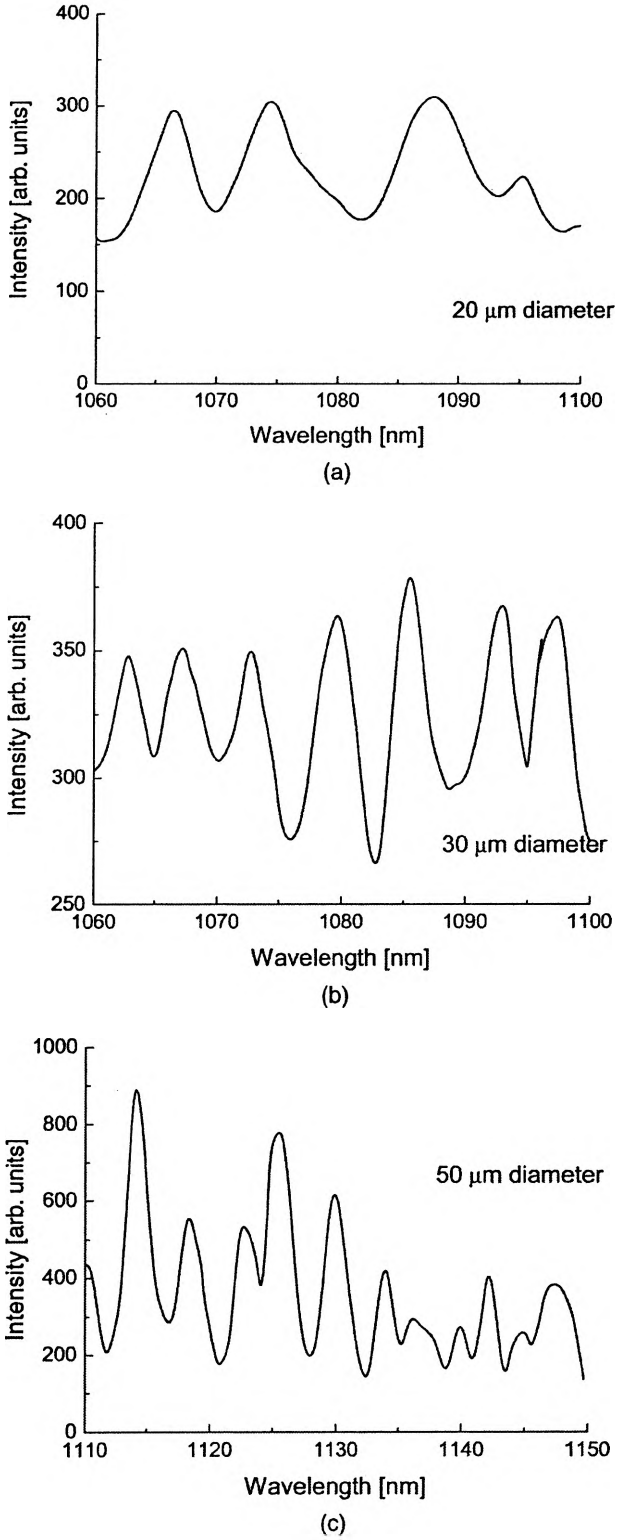


Fig. 11. Experimental backscattering spectrum. The data were processed according to the guidelines described in the text.

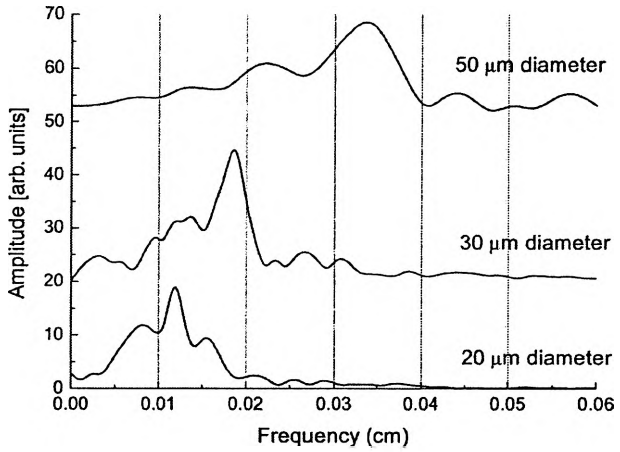


Fig. 12. Stacked FT of the experimental spectra of Fig. 11.

35 and 60 μm, each with its own slope and error bars given by the FWHM of the corresponding FT peaks. Such curves are depicted in Figs. 10(a) and 10(b) for the wavelength intervals of 1060–1100 nm and 1110–1150 nm, respectively. To test the method in these two NIR intervals, we recorded experimental backscattering spectra for samples of 20, 30, and 50 μm nominal diameter particles, using the instrumental setup described previously. The selected wavelength intervals coincide with those shown in Figs. 8(a) and 8(b). Unfortunately, these wavelengths are at the edge of the sensitivity curve of our detector (silicon CCD), where the signal-to-noise ratio is very poor.

To enhance the useful signal, the CCD background noise was first subtracted from the raw backscattering spectra and then displayed as a function of the wavenumber. The remaining high-frequency noise was almost removed by smoothing with a seven-point moving average and then cor-

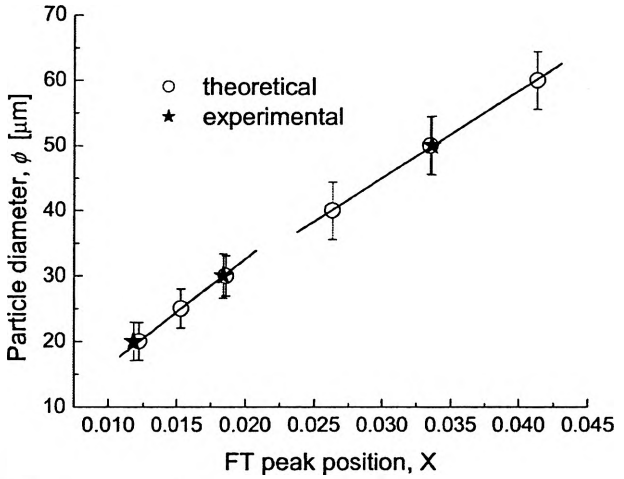


Fig. 13. Comparison of the particle diameter versus the FT peak position relation for calculated 20–60 μm particle diameters (circles with error bars) and experimental 20, 30, and 50 μm particle diameters.

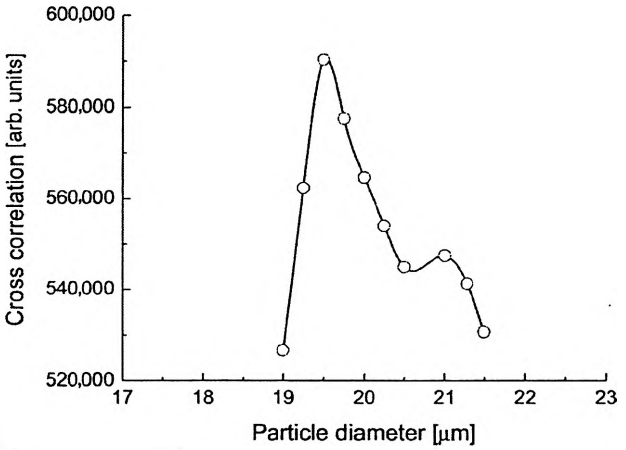


Fig. 14. Correlation values for backscattering spectrum corresponding to a 20 μm nominal diameter. The span of the horizontal axis corresponds to the uncertainty interval derived from the FWHM of the FT curve.

rected by subtracting a suitable slowly varying baseline. At this step, the signal is almost free from its dc component and only rapidly wavelength varying ac components are present, which can be explored using the FT. In fact, all the FT obtained in this work were applied to signals processed in this way. Figures 11(a)–11(c) show the obtained spectra for 20, 30, and 50 μm particle diameters, respectively. It can be seen that, in general, the sequence of peaks and valleys correspond to those calculated for the backscattering efficiency coefficient depicted in Fig. 7, although the whole signal seems to be modulated by a slowly varying noise.

Figure 12 shows the stacked FT for the three experimental backscattering spectra of Fig. 11. Note that, in spite of the noisy signals, the FT spectra still show distinct peaks that agree well with those corresponding to theoretical calculations.

These peak values (with their corresponding error bars) are shown in Fig. 13, together with the FT peak values derived from the Mie calculations, taken from Fig. 10. It can be seen that the experimental values lay well within each linear fit.

Again, the observed linear relation between the FT maxima and the particle diameter may be used as a first approach to determine the diameter of particles in a sample at these wavelength intervals. Following the previously described procedure, at this point the cross-correlation technique may be applied. Results for 20 μm nominal diameter particles are shown in Fig. 14 for the wavelength interval of 1060–1100 nm. The span of the horizontal axis has been set equal to the error given by the FWHM of the corresponding FT. It can be observed that a correlation maximum appears for a certain diameter value, very close to that obtained by the FT. The uncertainty width reduces to ~33% of that corresponding to the FT. However, this reduction is not as good as in the case of smaller particles (1–20 μm diameter) analyzed in the visible range.[4]

Thus the calibration curves obtained for the three analyzed spectral intervals allow, in general, for the solving of any multimodal sample having particles between a 3 and 60 μm diameter. If the sample contains a mixture of small, medium, and large particles, they will contribute to different spectral intervals. The FT calculated for each interval will yield peaks corresponding to the different particles present in the sample which, in turn, can be explored using the correlation step.

As mentioned in Section 1, other authors[6] analyzed small biological particles (hundreds of nanometers in diameter) using light scattering spectroscopy. They worked with least-squares techniques for size distribution determination and achieved a reduction in uncertainty compatible with the diameter range studied. In the case of larger particles, as the ones considered in this work (tens of micrometers), the FT yields a satisfactory first approach to size determination in multimodal samples. A finer approach using cross correlation reduces the uncertainty by ~30%, which is acceptable for this diameter range.

Finally, considering the results obtained in the previous work for the visible 600–730 nm region,[4] there

Table 1. Spectral Intervals and Particle Diameters Analyzed with Backscattering Spectroscopy Using FT and Cross Correlation[a]

Spectral Range of Analysis (nm) [λ_{low}, λ_{high}]	Range of Diameters [ϕ_i, ϕ_f], [μm]	FT Linear Regression X = FT Peak Position [cm] ϕ = Diameter [μm]	Uncertainty in FT Linear Regression [μm]	Mean Uncertainty after Cross Correlation [μm]
[600, 730][b]	[0.5, 10]	$\phi = 2340.11X + 0.04$	±0.7	±0.025 (±0.030)
[750, 850][c]	[10, 20]	$\phi = 2218.18X - 0.05$	±1.3	±0.50 (±0.10)
[1060, 1100][c]	[20, 35]	$\phi = 1568.29X + 0.89$	±3	±1 (±0.16)
[1110, 1150][c]	[35, 60]	$\phi = 1333.12X + 5.06$	±4.4	±1.47 (±0.51)

[a]Results in the first row are from a previous work.
[b]Reference 4.
[c]This work.

are four wavelength intervals that can be used for particle sizing with backscattering spectroscopy in the visible and NIR.

Table 1 summarizes the overall results. Column 1 shows the spectral interval of analysis. Column 2 shows the diameter range that is best measured in the corresponding spectral interval (linear piecewise representation). Column 3 shows the linear regressions corresponding to the different wavelength intervals analyzed, which allow for calculation of the diameter of the particles in a first approach, together with the corresponding uncertainties. Column 4 shows the mean uncertainty due to FT linear regression. Column 5 shows the mean uncertainties after applying cross correlation. Both mean uncertainties represent the average errors for the different diameter values within the specified range. The specific uncertainty shows an increasing trend as the diameter increases. In this last column, the mean uncertainties given by the manufacturer are shown in parentheses for comparison purposes.

4. Conclusions

We have shown that it is possible to size microparticles in the range of 20–60 μm diameters in a reliable and simple way using NIR backscattering spectroscopy. It has been demonstrated that the FT of the scattering spectra has a characteristic maximum, whose position is linearly related to the particle's diameter within a specific wavelength interval. A first approximation to particle diameter may be obtained through this linear relation. To improve determination accuracy, a cross-correlation technique between calculated and experimental spectra was applied. This improvement is range dependent, thus forcing a trade-off between sizing capability and accuracy. Together with the results obtained in a previous work on visible backscattering spectroscopy, the improvement due to correlation is very good for a 0.5–10 μm particle diameter in the visible interval (3.5%), good for a 10–20 μm particle diameter in the 750–850 nm interval (38%), and acceptable for a 20–60 μm particle diameter in the 1060–1100 nm and 1110–1150 nm intervals (33%). Overall, the method yields reasonable accuracy when compared with that of the manufacturer. This method could be used to construct a portable and practical measurement instrument. The possible disadvantages of measuring in the NIR range beyond 1000 nm with a CCD sensor may be overcome by using a NIR sensitive array such as, for example, InSb.

This work was partially supported by research project 11/I104 from Facultad de Ingeniería, Universidad Nacional de La Plata. This work is the basis of a pending patent, P050101083, INPI, Argentina.

References

1. L. B. Scaffardi, J. O. Tocho, L. L. Yebrin, and C. S. Cantera, "Sizing particles used in the leather industry by light scattering," Opt. Eng. **35,** 52–56 (1996).
2. G. Gouesbet and G. Gréhan, eds., *Optical Particle Sizing* (Plenum, 1988).
3. B. Chu, *Laser Light Scattering: Basic Principles and Practice* (Academic, 1991).
4. F. Videla, D. Schinca, and L. B. Scaffardi, "Sizing particles by backscattering spectroscopy and Fourier análisis," Opt. Eng. **45,** 048001 (2006).
5. J. Mourant, T. Fuselier, J. Boyer, T. Johnson, and I. Bigio, "Predictions and measurements of scattering and absorption over broad wavelength ranges in tissue phantoms," Appl. Opt. **36,** 949–957 (1997).
6. H. Fang, M. Ollero, E. Vitkin, L. M. Kimerer, P. B. Cipolloni, M. M. Zaman, S. D. Freedman, I. J. Bigio, I. Itzkan, E. B. Hanlon, and L. T. Perelman, "Noninvasive sizing of subcellular organelles with light scattering spectroscopy," IEEE J. Sel. Top. Quantum Electron. **9,** 267–276 (2003).
7. S. Min and A. Gomez, "High-resolution size measurements of single spherical particles with a fast Fourier transform of the angular scattering intensity," Appl. Opt. **35,** 4919–4926 (1996).
8. K. Semyanov, P. Tarasov, A. Zharinov, A. Chernyshev, A. Hoekstra, and V. Maltsev, "Single-particle sizing from light scattering by spectral decomposition," Appl. Opt. **43,** 5110–5115 (2004).
9. D. Perner and U. Platt, "Detection of nitrous acid in the atmosphere by differential optical absorption," Geophys. Res. Lett. **6,** 917–920 (1979).
10. H. Edner, P. Ragnarson, S. Spannare, and S. Svanberg, "Differential optical absorption spectroscopy (DOAS) system for urban atmospheric pollution monitoring," Appl. Opt. **32,** 327–333 (1993).
11. F. A. Videla, D. C. Schinca, and J. O. Tocho, "Alternative method for concentration retrieval in differential optical absorption spectroscopy for atmospheric-gas pollutant measurements," Appl. Opt. **42,** 3653–3661 (2003).
12. C. F. Bohren and D. R. Huffman, *Absorption and Scattering of Light by Small Particles* (Wiley, 1983).
13. G. Mie, "Beitrage zur Optik trüber Medien speziell kolloidaler Metallösungen," Ann. Phys. **25,** 317–445 (1908).
14. P. Laven, MiePlot, 2005, *http://www.philiplaven.com/mieplot.htm*.

Óptica Integrada

La Óptica Integrada trata principalmente del manejo de la luz (fotones) en dimensiones micrométricas con el fin de manipular señales fotónicas, ya sea de forma activa o pasiva, a través de circuitos ópticos basados en guías de onda acanalada. En estos circuitos, la luz juega el mismo papel que electrones y huecos en la microelectrónica. En los últimos años, mediante escritura láser con pulsos ultracortos intensos, es posible agilizar y abaratar la fabricación de cualquier dispositivo óptico integrado mediante la escritura directa (dispositivos pasivos: divisores de haz, acopladores, interferómetros Mach Zehnder, dispositivos activos: amplificadores, láseres etc.). El ClOp está explorando una línea de investigación focalizada en estos temas concretos donde principalmente se están caracterizando nuevos dispositivos integrados obtenidos por escritura láser en materiales usualmente utilizados como emisores de luz (láser) de estado sólido como así también en regeneradores (amplificadores ópticos) de señal para comunicaciones ópticas. Como ejemplo podemos mencionar, Nd:YAG , Nd.LiNbO3 o Er-Yb:Glass entre otros.

Integrated Optics

Integrated optics deals mainly with the management of light (photons) within micrometric regions, with the aim to control this kind of optical signals either by means of active or passive optical circuits based on channel waveguides. In these devices, the light plays the same role that the electrons and holes do in microelectronics. By using ultrashort intense pulse laser writing, in the last years it has been possible to fabricate optical circuitry including passive (splitters, couplers, Mach Zehnder interferometers) and active devices (lasers, amplifiers) in fast way and at low cost. In this sense, the ClOp has addressed its research goals to the optical characterization of new integrated devices obtained by means of laser writing in different substrates commonly used as light coherent emitter (lasers) or signal regenerator (optical amplifiers) for optical communications. For instance, we can show Nd:YAG, Nd:LiNbO3 or Er-Yb:Glass etc.

Appl. Phys. B 80, 535–539 (2005)
DOI: 10.1007/s00340-005-1739-z

Applied Physics B
Lasers and Optics

O.M. MATOS[1]
G.A. TORCHIA[2]
G.M. BILMES[3,4,✉]
J.O. TOCHO[4,5]
H.F. RANEA-SANDOVAL[6]

On the origin of the acoustic signals generated in KDP by pulsed UV laser excitation

[1]Departamento de Óptica, Universidad Complutense de Madrid, 28400 Madrid, Spain
[2]Departamento de Física de Materiales C-IV, Universidad Autónoma de Madrid, 28049 Canto Blanco, Madrid, Spain
[3]Facultad de Ingeniería, Universidad Nacional de La Plata, Argentina
[4]Centro de Investigaciones Ópticas (CONICET-CIC), CC 124, 1900 La Plata, Argentina
[5]Departamento de Física, Facultad de Ciencias Exactas, Universidad Nacional de La Plata, Argentina
[6]Instituto de Física 'Arroyo Seco', Facultad de Ciencias Exactas, Universidad Nacional del Centro de la Provincia de Buenos Aires, Pinto 399, B7000GHG Tandil, Argentina

Received: 25 August 2004 / Final version: 10 December 2004
Published online: 24 February 2005 •
© Springer-Verlag 2005

ABSTRACT The origin of the acoustic signals that are generated in the bulk of a KDP crystal during irradiation with short UV laser pulses is determined. The generation of these signals by excitation with moderate or high optical fluences is linked to the evolution of the population of point defects that is generated in the crystal by absorption of two UV photons. These defects are bleached due to their efficient linear absorption of UV radiation, and their non-radiative relaxation is shown to be the origin of the acoustic signals. The rate constants for the different processes involved in both the linear and the non-linear interactions were determined from the experiments presented here. Characteristic values for the quantum efficiency for the generation of defects, $\eta_F = 0.95 \pm 0.05$, and for the quantum efficiency for bleaching of defects, $\eta_B = 0.065 \pm 0.005$, were obtained for 266-nm laser radiation. The model developed for the intensity of the acoustic signals reproduces the experimental facts with very good accuracy.

PACS 42.65.Ky; 43.35.Ud; 78.20.Hp

1 Introduction

Laser-induced generation of acoustic signals in solids has been used as a tool for the study of several physical phenomena [1, 2]. Acoustic signals produced in a potassium dihydrogen phosphate (KDP) crystal after excitation with $\lambda = 266$-nm pulses were previously demonstrated, and a method for the orientation of non-linear crystals based on the generation of these photoacoustic signals (PS) was proposed in Ref. [3]. PS can be detected with a piezoelectric transducer (PZT) without the need of an amplifier, thus indicating that the conversion efficiency of optical into acoustic energy is fairly high. Recently [4], we have been working on the characterization of PS in KDP showing that transient defects in the crystal are responsible for the acoustic emission. After the KDP crystal has been irradiated with UV light, gray spots are formed in the bulk of the crystal indicating that defects have been formed during the laser irradiation. The lifetime of these defects can be easily determined by using a photoacoustic method developed in Ref. [5], instead of the usual optical way.

In Ref. [3], the main features of the mechanism responsible for the signal generation were suggested. When trying to fit the amplitude of the PS generated for different intensities of UV radiation, however, non-physical values for the linear and for the two-photon absorption coefficients were found. In Ref. [5], it has been shown that if KDP is irradiated simultaneously with 532- and 266-nm radiation, the PS generation is mainly due to the linear absorption of 532-nm radiation by defects that were generated by the UV radiation. This turns out to be a common experimental situation when KDP is used as a non-linear crystal for second-harmonic generation from 532 to 266 nm. In the last few years, KDP crystals were used as a non-linear medium to generate the UV radiation necessary for fusion experiments with inertial confinement, like the Nova laser or the National Ignition Facility at Lawrence Livermore National Laboratory [6, 7]. Defect characteristics, such as their formation, evolution, and light-absorption mechanisms, are a major concern for fusion experiments.

For UV irradiation, it is accepted that defects are produced by two-photon absorption as an electron–hole pair is produced in the material. The pair relaxes partially and both the electron and the hole can be stabilized in a variety of positive and negative traps, as is common for color centers in alkaline halides. Besides that, there is no definitive identification of the nature of the traps. The involvement of the $PO_4H_2^-$ group in the optically active centers is generally accepted [8–17]. A hole localized at one oxygen near a proton vacancy in the basic unit (PO_4H^-), a self-trapped hole at the basic unit (PO_4H_2), and a neutral hydrogen H^0 localized near the basic group ($PO_4H_3^-$) were proposed as the cause of the coloration of KDP in Refs. [8–17].

The generation and bleaching of transient point defects are both associated with different processes involving the

✉ Fax: +54-221-471-2771, E-mail: gabrielb@ciop.unlp.edu.ar

interaction between radiation and the KDP structure; in this study we analyze their relative contributions to the PS. We developed a model, called the 'two-step' model, in which all possible channels involved in the point-defect dynamics are considered. We have determined the quantum efficiency for formation and bleaching of point defects by means of a fitting procedure with this model using two parameters very well known in the literature. These two parameters provide useful information about the behavior of the PS at different excitation fluences, as a function of time and history of the crystal.

2 Theoretical model

2.1 *Two-step model*

The proposed mechanism for PS generation in a KDP crystal irradiated with pulsed UV light with photons of energy $\hbar\omega$ was developed with the aid of the energy diagram depicted in Fig. 1.

We call it a 'two-step' mechanism because the PS generation is due to the heat released in two interconnected processes: linear and non-linear UV absorption with generation of transient defects (step A) and the later, linear absorption of the defects at the same wavelength (step B).

Energy involved in linear absorption in KDP is relaxed completely in a non-radiative way, while only a fraction of the energy absorbed in the two-photon process contributes to the PS, because part of its energy is consumed generating the defect. This fact is represented in Fig. 1 displaying the ground energy level of the defect inside the gap, E_D, relative to the valence band. Transient defects observed in KDP have a lifetime of several seconds, and their relaxation does not contribute to the acoustic signal in cases in which detection is performed with a technique sensitive only to prompt energy dissipation.

Calling $I(x,t)$ the intensity of the UV pulse inside the KDP sample at depth x (measured from the side that is exposed to the laser) and at time t, the amount of heat released, after linear and non-linear absorption, in a time window less than the ground-state lifetime of the defects (step A), can be written as

$$H_A = \iint [\alpha\hbar\omega + (\beta/2)(2\hbar\omega - \eta_F E_D)I(x,t)]I(x,t)\,dx\,dt, \tag{1}$$

where α and β are the linear absorption coefficient and the two-photon absorption coefficient of KDP at frequency ω, respectively, and η_F is the quantum efficiency for defect generation by UV two-photon absorption.

In step B a defect absorbs one UV photon that excites it from the ground to an excited state situated within the conduction band. Non-radiative de-excitation from this excited state generates acoustic waves. This de-excitation bleaches the defects with a probability η_B, causing a PS contribution proportional to $\hbar\omega + E_D$. On the other hand, if the defect is not bleached, the relaxation to its fundamental state proceeds with a probability $1 - \eta_B$, resulting in a PS contribution proportional to $\hbar\omega$.

If $N(x,t)$ is the concentration of point defects at a sample depth x at time t, the heat produced in step B is

$$H_B = \iint \sigma(\hbar\omega + \eta_B E_D)N(x,t)I(x,t)\,dx\,dt, \tag{2}$$

where σ represents the absorption cross section for defects for light with an energy $\hbar\omega$. The total heat released can be calculated by adding the contributions (Eqs. (1) and (2)), and results in

$$\mathrm{PS} \propto \iint [\alpha\hbar\omega + (\beta/2)(2\hbar\omega - \eta_F E_D)I(x,t) + \sigma(\hbar\omega + \eta_B E_D)N(x,t)]I(x,t)\,dx\,dt. \tag{3}$$

It is obvious that Eq. (3) can be integrated to obtain the PS after the space–time dynamics of $N(x,t)$ and of $I(x,t)$ are solved. The equations describing such evolution during each UV pulse are

$$\frac{\partial I(x,t)}{\partial x} = -[\alpha + \sigma N(x,t)]I(x,t) - \beta I^2(x,t), \tag{4a}$$

$$\frac{\partial N(x,t)}{\partial t} = \frac{\eta_F \beta I^2(x,t)}{2\hbar\omega} - \frac{\eta_B \sigma N(x,t)I(x,t)}{\hbar\omega}. \tag{4b}$$

These equations describe three mechanisms for the attenuation of the incident UV pulse: the linear and the non-linear absorption by bulk KDP, and the linear absorption by defects.

Defects are generated by two-photon absorption and bleached by radiation with efficiencies η_F and η_B, respectively. Between consecutive UV pulses, defects relax following quite complicated kinetics that is not completely understood. However, experiments with the same sample showed that, after a few seconds, the defect population was reduced only slightly [4, 5]. Hence, in the analysis of the PS due to the irradiation by a train of UV pulses separated for a few seconds, we can assume that the amount of defects that will survive until the next pulse is the same as that at the end of the previous pulse.

Equations (3) and (4) can be solved numerically to obtain the PS for different UV energies. For all the parameter regions inspected, and for pulse energies of less than 20 mJ focused on

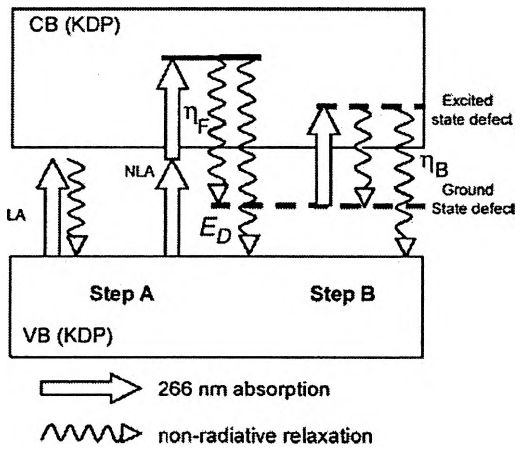


FIGURE 1 Model for photoacoustic signal generation. *LA*: linear absorption by KDP; *CB*: conduction band; *VB*: valence band. *Step A*: generation of defects by two-photon absorption. *Step B*: linear absorption by defects. *Straight arrows* represent the absorption of one photon. *Wavy arrows* represent non-radiative decay

a spot of 1-mm diameter, we have found that the UV intensity predicted by our model is attenuated only very slightly along the pump beam. In a first approximation we can, therefore, assume that the intensity is uniform inside the crystal, that is

$$I(x,t) = I_0, \quad \forall x, t < \tau, \tag{5}$$

where I_0 is the intensity at the surface at $x = 0$ and τ is the duration of the UV pulse. Under this assumption, Eq. (4b) can be solved exactly, giving the density of defects formed during the first pulse, which is

$$N_1(t) = (P/Q)[1 - \exp(-Pt)], \tag{6}$$

with $P = \eta_B \sigma I_0/\hbar\omega$ and $Q = \eta_F \beta \sigma I_0^2/2\hbar\omega$.

The density of defects at the end of the first pulse is $N_1 = (P/Q)[1 - \exp(-P\tau)]$. Thus, the density of defects during the pulse number n in a pulse train is

$$N_n(t) = N_1 + N_{n-1}\exp(-Pt). \tag{7}$$

The time evolution of the density of defects during the UV irradiation can then be introduced in Eq. (3). Under these conditions the acoustic signal produced by the nth UV pulse is described as

$$\mathrm{PS}(n) = \mathrm{PS}(n-1) + K(\sigma/Q)(\hbar\omega + \eta_B E_D)N_1^2 \times \exp[(2-n)\tau P], \tag{8}$$

where the PS due to the first pulse is

$$\mathrm{PS}(1) = K\{\alpha\tau\hbar\omega I_0 + (\beta/2)(2\hbar\omega - \eta_F E_D)\tau I_0^2 + \sigma(Q/P^2) \times (\hbar\omega + \eta_B E_D)[\tau P + \exp(-\tau P) - 1]\}L, \tag{9}$$

with L being the length of the crystal and K an arbitrary constant reflecting all the instrumentation parameters such as the efficiency for the transformation from heat to acoustic energy, the sensitivity of the acoustic transducer, etc.

2.2 *Numerical simulations*

To fit experimental results with the model presented above, we face the well-known difficulty shared by all the photoacoustic methods: an absolute calibration of the PS is extremely difficult. Thus, the criterion we used to assess the quality of the fit of our results was the ratio of the predicted photoacoustic signal and its value after an infinite number of pulses, which we call the *asymptotic value* of the PS, and compare it with the experimentally determined ratio.

We restricted the analysis to the variation of the defect-formation probability and the defect-bleaching probability, using accepted values for the linear absorption coefficient (α for KDP and σ for the defects) and the two-photon absorption coefficient (β for KDP) at 266 nm, taken from Ref. [16].

The value for E_D can be estimated from the absorption spectrum of the defects. As the defects do not absorb at wavelengths longer than approximately 700 nm, we can safely use $E_D = 3 \times 10^{-19}$ J over the valence band of KDP, as in Ref. [4].

In Fig. 2 the evolution of the amplitude of the PS is shown as a function of the number of pulses in the train. In each case the PS signal was normalized to its asymptotic value that corresponds to the maximum value reached. Errors for the different parameters included in the model were considered.

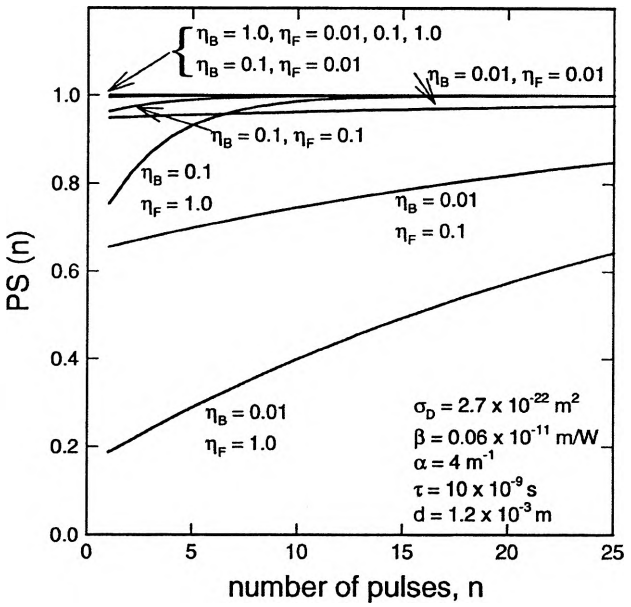


FIGURE 2 Calculated photoacoustic signal amplitude as a function of the number of pulses (n) for different values of η_F and η_B

The results of Eqs. (8) and (9) can be represented for different parameters. It is clear that a no-defects case (η_F close to zero) should give a constant signal from the first pulse on. Similar results should be obtained with strong bleaching (η_B close to 1) independent of the η_F value. On the other hand, low bleaching efficiencies correspond to a slow growing of the PS and a much stronger contrast between the first-pulse signal and the asymptotic value will be found.

The calculated amplitude of the PS from the very first pulse and the asymptotic value of the amplitude are shown as a function of the energy of the UV pulses in Fig. 3.

In this case, the PS is normalized to 1 for the asymptotic value for 10-mJ pulse energy. The difference between the PS for the first pulse and the asymptotic value is obvious and depends mainly on the bleaching efficiency.

3 Experimental results

We have performed experiments to study three aspects of the PS: their dependence on UV laser pulse energy, the relation between the PS and the quantity of defects generated by one pulse, and the accumulative effects of successive pulses on the value of the amplitude of the PS. Excitation was performed using the fourth harmonic of a Nd^{+3}:YAG laser of 10-ns pulse duration in a train of pulses each separated by 1.5 s. The UV pulse radiation passes through a 1.2-mm-diameter pinhole before striking the KDP crystal (see inset in Fig. 4). This was a fresh KDP crystal with a size of $1 \times 1 \times 0.5\,\mathrm{cm}^3$, cut for second-harmonic generation of 1060-nm radiation.

The signal from a 200-kHz-bandwidth PZT transducer, glued directly to the crystal, was recorded, without amplification, by a digital oscilloscope. The amplitude of the

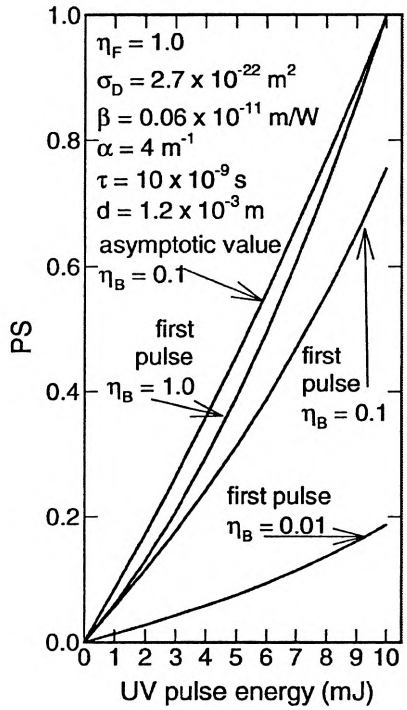


FIGURE 3 Calculated photoacoustic signal amplitude normalized for the asymptotic value for a 10-mJ pulse: comparison between the first-pulse PS and its asymptotic limit, for different values of the bleaching efficiency (η_B)

first resonant peak of the ringing was taken as representative of the PS generated in the bulk, as is common.

Figure 4 shows the evolution of the experimental PS (circles) with accumulative UV laser pulses, each one with an energy of 9.9 mJ. The PS grow, approaching an asymptotic level after irradiation with tens of UV pulses.

At the beginning of the experiment the crystal was defect-free, but afterwards the sample had gray defects. This fact, together with the sigmoid character of the curve of Fig. 4,

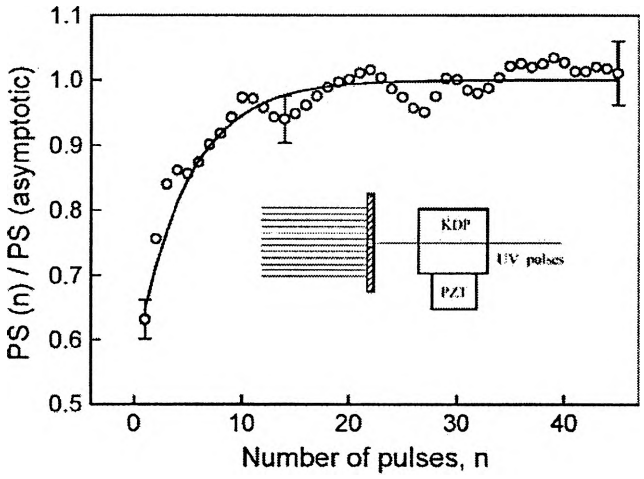


FIGURE 4 Photoacoustic signal as a function of the number of pulses. Crystal starts without defects. Signal is normalized for the mean asymptotic value at the maximum energy of 9.9 mJ per pulse. *Full line* represents the result of Eq. (6) with the parameters indicated in Table 1. The experimental set-up is indicated in the *inset*

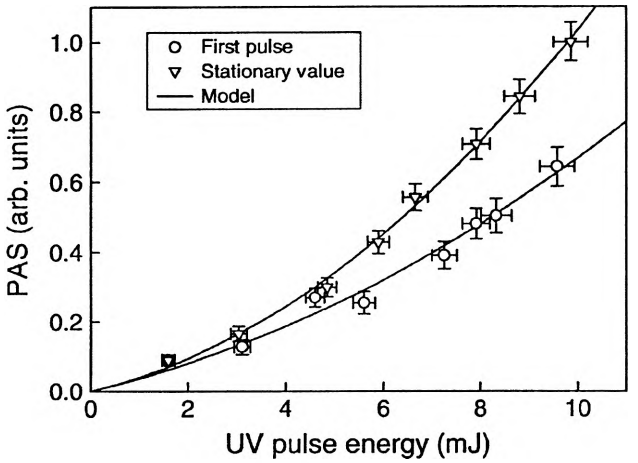


FIGURE 5 Photoacoustic signals corresponding to the first pulse (*circle*) and the stationary level reached after several pulses 1.5-s apart (*square*) vs. the energy of the UV pulse. *Full lines* represent the results of Eqs. (8) and (9), using the parameters of Table 1

suggests that the dependence of the PS on the number of pulses is determined by the growth of the number of defects present in the sample until a stationary level is reached. This asymptotic level is reached when the amount of defects generated by each UV pulse is equal to the number of defects bleached during the pulse.

Figure 5 displays measurements of the amplitude of the normalized PS as a function of the UV pulse energy, performed while maintaining the other experimental conditions unchanged.

Open circles represent the experimental PS observed for single excitation pulses. Open squares represent the stationary level reached after several (typically 40 pulses would be required to reach the asymptotic value) pulses 1.5-s apart. Values for stationary level signals are averaged over several pulses. All the results are normalized to the asymptotic value corresponding to the maximum energy used (9.9 mJ). There is a growing difference between the PS due to the first pulse and the corresponding stationary value.

The fitting procedure described in Sect. 2.2 yields the continuous lines that are shown in both figures, Figs. 4 and 5. The complete set of parameters used to draw the fitting curves is summarized in Table 1.

From the fitting procedure we determined the quantum efficiency for the formation of point defects in KDP as $\eta_F = 0.95 \pm 0.05$, and for the quantum efficiency for bleaching of defects as $\eta_B = 0.065 \pm 0.005$ for 266-nm pulsed laser irradiation.

Finally, we used the experimental data depicted in Fig. 5 (circles and triangles) and the fitting procedure based on the above model to explore the influence of the processes involved

α (cm^{-1})	β (cm^{-1}/GW)	η_F (dimensionless)	η_B (dimensionless)	σ ($\times 10^{-18}$ cm^{-2})
0.03	0.085	1	0.065	3.7

TABLE 1 Parameter values used for the best of fits to the experimental results are listed

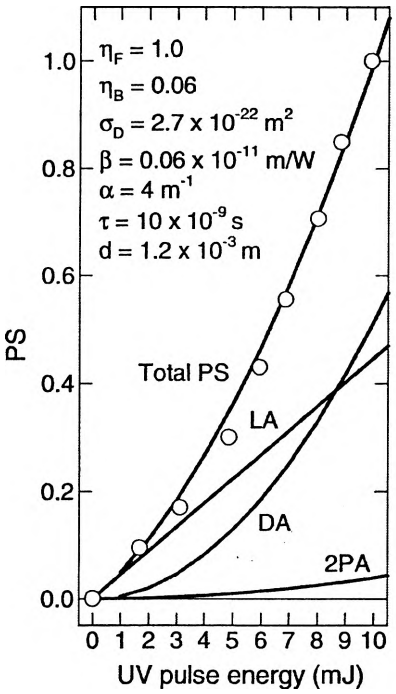


FIGURE 6 Comparison between different model assumptions and experimental data: the *open circles* are experimental data that correspond to the stationary level reached after several pulses as depicted in Fig. 5. *LA*: linear absorption of KDP; *2PA*: two-photon absorption of KDP; *DA*: linear absorption of defects

in the generation of the acoustic signal, namely the linear absorption of KDP, the two-photon absorption of KDP, and the linear absorption by defects.

Results are shown in Fig. 6, and the interpretation is as follows: the shown fit indicates that at low laser fluences the signal will be mainly produced by the linear absorption of KDP, while at higher fluences the main contribution to the signal is produced by the defects that relax non-radiatively after a linear absorption process.

4 Conclusions

In this study we present, for the first time to our knowledge, an analytic expression for the relative photoacoustic signal generated in KDP irradiated by nanosecond UV pulses. We verify the assumption of a 'two-step' model by fitting the experimental results corresponding to irradiation by one UV pulse on a clear crystal, and the signals corresponding to irradiation by consecutive pulses in a train. The quantum efficiency for the generation of defects by two-photon absorption and the quantum efficiency for the bleaching of defects after absorption of one 266-nm photon are derived with this model from the experimental data. The values we have obtained are in good agreement with those reported in the literature, which were determined with completely independent experiments [11].

We conclude that defect dynamics is the cause of the acoustic signal. Irradiation with relatively low fluence pulses shows that the main acoustic contribution is due to the non-radiative decay of excited states of defects after they absorb the UV radiation. Consequently, the PS intensity as a function of the pump fluence scales with the number of defects.

The predictions from this simple model are almost identical to the ones obtained solving the space–time evolution of the different fields involved, described by Eqs. (1)–(3), and describe with very good accuracy the experimental results. This model can be used as a basis to reproduce the PS produced by phase matching second-harmonic generation from 532 to 266 nm in KDP crystals. The results presented herein are useful for studies of other crystals used in non-linear processes.

ACKNOWLEDGEMENTS This work was partially supported by FOMEC, CONICET, ANPCYT, UNCPBA, and UNLP. OEM is a Fellow of FOMEC; GMB is a member of the Carrera del Investigador Científico CIC-BA; JOT and HFRS are both members of the Carrera del Investigador Científico CONICET.

REFERENCES

1 C.K.N. Patel, A.C. Tam, Rev. Mod. Phys. **53**(3), 517 (1981)
2 A.C. Tam, Rev. Mod. Phys. **58**(2), 381 (1986)
3 J.O. Tocho, G.M. Bilmes, H.F. Ranea-Sandoval, Appl. Phys. B **69**, 473 (1999)
4 O.M. Matos, PhD Thesis, Universidad Nacional de La Plata (2002)
5 O.M. Matos, G.A. Torchia, G.M. Bilmes, J.O. Tocho, Phys. Rev. B **69**, 224 102 (2004)
6 P. Weiss, Science **275**, 1569 (1997)
7 J. Glanz, Science **277**, 304 (1997)
8 K. Tsuchida, R. Abe, M. Naito, J. Phys. Soc. Jpn. **35**(3), 806 (1973)
9 J.A. McMillan, J.M. Clemens, J. Chem. Phys. **68**(9), 3627 (1978)
10 E. Dieguez, J.M. Cabrera, J. Phys. D: Appl. Phys. **14**(1), 91 (1981)
11 S.G. Demos, M. Yan, M. Staggs, J.J. De Yoreo, H.B. Radowsky, Appl. Phys. Lett. **72**, 2367 (1998)
12 L.N. Ogorodnikov, V.Y. Yakovlev, B.V. Shul'gin, M.K. Satybaldieva, Phys. Solid State **44**, 880 (2002)
13 S.D. Setzler, K.T. Stevens, L.E. Halliburton, M. Yan, N.P. Zaintseva, J.J. De Yoreo, Phys. Rev. B **57**, 2643 (1998)
14 E. Dieguez, J.M. Cabrera, F. Agulló-López, J. Chem. Phys. **81**, 3369 (1984)
15 J.-T. Yu, S.-H. Lou, J. Phys. Soc. Jpn. **62**, 3294 (1993)
16 C.D. Marshall, S.A. Payne, M.A. Henesian, J.A. Speath, H.T. Powell, J. Opt. Soc. Am. B **11**, 774 (1994)
17 J.E. Davis, R.S. Hughes, H.W.H. Lee, Chem. Phys. Lett. **207**, 540 (1993)

Spatial Modulation of Linear and Quadratic Susceptibilities in Lithium Niobate Crystals by Using Femtosecond Laser Pulses

G. A. TORCHIA,[1,2,*] C. MÉNDEZ,[1]
J. R. VÁZQUEZ DE ALDANA,[1] D. DELGADO,[1] I. ARIAS,[1]
AND L. ROSO[1]

[1]Optics Group—Applied Physics Department, Universidad de Salamanca, Plaza de la Merced s/n 37008 Salamanca, Spain
[2]Centro de Investigaciones Ópticas (CIC-Conicet), C.C. 124, 1900 La Plata, Argentina

QUERY SHEET

Q1: Au: Please provide keywords.
Q2: Au: Is shortened title on top of page correct?
Q3: Au: Please cite Figure 4 in text.

Ferroelectrics, 333:1–6, 2006
Copyright © Taylor & Francis Group, LLC
ISSN: 0015-0193 print / 1563-5112 online
DOI: 10.1080/00150190600700634

Taylor & Francis
Taylor & Francis Group

Spatial Modulation of Linear and Quadratic Susceptibilities in Lithium Niobate Crystals by Using Femtosecond Laser Pulses

G. A. TORCHIA,[1,2,*] C. MÉNDEZ,[1]
J. R. VÁZQUEZ DE ALDANA,[1] D. DELGADO,[1] I. ARIAS,[1]
AND L. ROSO[1]

[1]Optics Group—Applied Physics Department, Universidad de Salamanca, Plaza de la Merced s/n 37008 Salamanca, Spain
[2]Centro de Investigaciones Ópticas (CIC-Conicet), C.C. 124, 1900 La Plata, Argentina

In this work we present the spatial control of the linear susceptibility (χ_1) in Lithium Niobate crystals by means of infrared (800 nm) femtosecond interaction. Diffraction gratings have been performed on the surface (relief) and inside (phase) of these samples by femtosecond laser writing. Also we have performed a spatial control of the quadratic susceptibility (χ_2) by direct writing of a pattern of ferroelectric domains on the surface of z cut substrates by using the second harmonic femtosecond pulses (400 nm). Finally, efficient photonic devices for second harmonic generation via quasi phase matching could be obtained following the experimental procedure presented in this work.

Keywords Q1

Introduction

During last years, femtosecond laser writing have represented an important tool to make photonic structures because of the simplicity, fast procedure and low cost to make integrated devices by using one step process [1–4].

The aim of these procedures deals on the interaction of femtosecond pulses with transparent materials giving rise to ionization processes. Focusing high intensity (10^{13} W/cm^2) laser on the surface of transparent materials, for fluences above the ablation threshold, ionization process due to the multiphoton absorption takes place in the medium. For this energy regime, the material begins to be removed from the surface of the sample. On the other hand, focusing high intensity lasers inside transparent samples, and depending of the energy range used in the experiments, the observed phenomenon can be identified as follow: 1) for laser intensities below damage threshold, it is possible to obtain a weak refractive index increment (about 10^{-3}) at the focusing region. This fact can be associated with the formation of colour centres and high density regions at the interaction zone; 2) for intensities above damage threshold, filaments due to Kerr effect can be observed whose length is

Paper originally presented at IMF-11, Foz do Iguaccu, Brazil, September 5–9, 2005; received in final form
*Corresponding author. E-mail: gtorchia@usal.es

large compared with the Raleigh zone from the focused beam. In this case, previous to the initial part of the filament, an important guiding region is also obtained [7].

Different 3D photonic devices have been recently reported by femtosecond laser writing in fused silica and other glass materials like fluoride, garnets and Ge-silica samples [8].

Addressing this type of photonic devices fabrication method for the use of electro-optic crystals like Lithium Niobate substrates it is possible boostering its application for optical communications such as splitters, Mach Zehnder interferometers, modulators, switches, erbium doped waveguides amplifiers (EDWAS), etc.

In this work we show the spatial control of the linear susceptibility (χ_1) trough of the fabrication of diffraction gratings on the surface (relief) and inside (phase) Lithium Niobate crystals by means of the direct femtosecond laser writing. Also it is presented the spatial control of quadratic susceptibility (χ_2) inducing the ferroelectric domains by using femtosecond writing at 400 nm on $-$ z face of $LiNbO_3$ substrates.

Experimental Procedure

The laser source to make the femtosecond laser writing was a Ti:Saphire laser at 800 nm from Spectral Physics with 120 fs pulse width, 1 KHz repetition rate and up to 1 mJ energy delivered. The laser writing was made by using the experimental set-up shown in Fig. 1. The femtosecond infrared radiation was focused to the sample by means of the microscope objective 10× after passing through a 3 mm pinhole to get a cleaner beam. The sample was mounted on micro-positioning stages which are controlling by a PC. The minimal displacement from these stages is 0.5 μm. The diffraction gratings have an area of 4 mm^2 and a 10 μm pitch. To make the ablation groove, the writing laser was focused on the surface of the samples while for the phase gratings fabrication process, the laser was focused without pinholes, by using 20× and 40× microscope objectives at 200 μm below the surface of the z-cut $LiNbO_3$ substrates.

Finally, to get a spatial control of χ_2, inducing the ferroelectric domains inversion by laser writing, the infrared femtosecond laser was doubled by using a Beta Barium Borate (BBO) non linear crystals cut to achieve 400 nm at the output to make this process. The *optical poling* [9] was performed by focusing the blue radiation on the $-$ z face of the sample by means the experimental set-up shown above. The z-cut $LiNbO_3$ crystal was impinged with blue radiation at energies below the ablation threshold. In order to reveal the ferroelectrics domains, after blue laser interaction, the sample was kept in HF solution during 1 hour.

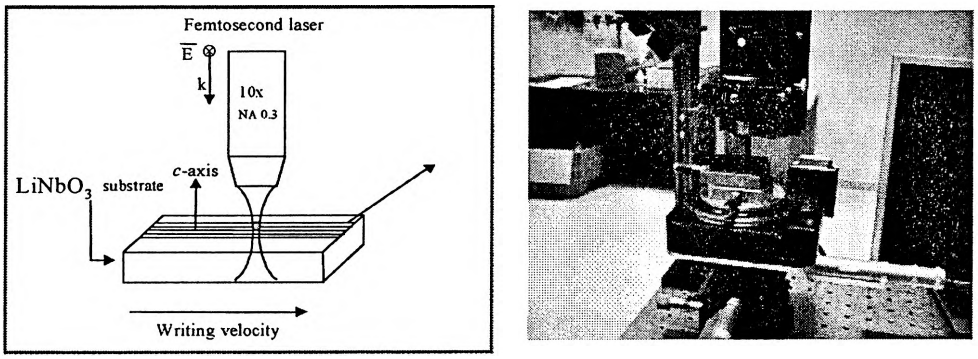
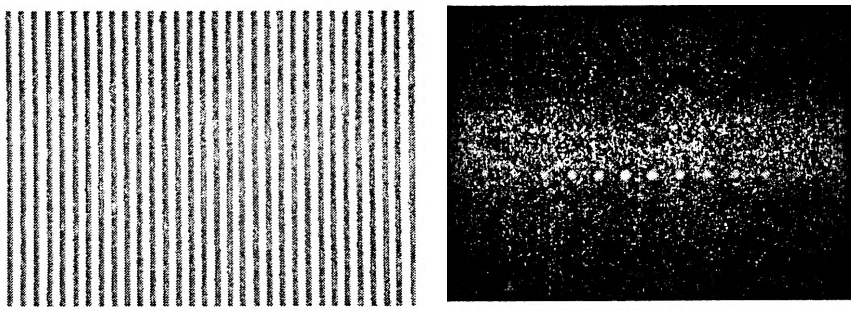


Figure 1. Experimental set up to perform the femtosecond laser writing on the z-cut Lithium Niobate substrates.



(a) (b)

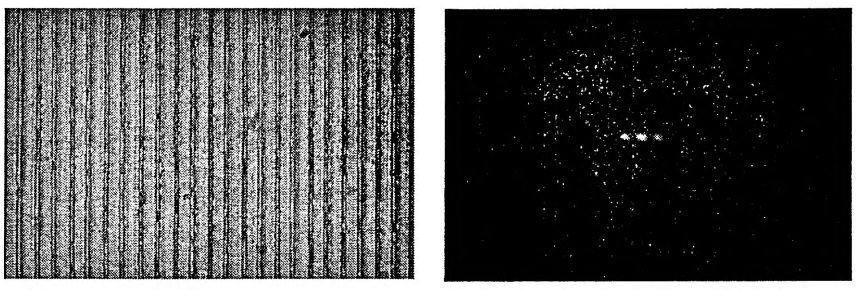
Figure 2. (a) Optical microscope photograph (working in reflection) of the relief diffraction grating fabricated by femtosecond laser writing. (b) He-Ne diffraction pattern from this grating.

Results and Discussion

Ther ablation gratings were made by impinging fluences of 1 J/cm^2, sligthy above the ablation threshold (0.7 J/cm^2). Figure 2a shows a photograph taken with microscope (working in reflection) of the relief grating performed at the surface of $LiNbO_3$ crystals by femtosecond laser radiation. As it can be seen, on the dark region have been carried out the ablation process and the material was removed over these regions. On the other hand, the white regions correspond to non-irradiated zones. The depth and width of the ablation channels are 5 μm and 6 μm respectively, while the pitch of the grating was set to be 10 μm. Due to fabrication process, these gratings have a high refractive index contrast which is about 50% ($\Delta n = 1.2$). In order to characterize the diffraction behaviour of these photonic structures, a He-Ne laser at 632.8 nm was used at normal incidence for testing the device. A diffraction pattern with high orders were observed, as it is illustrated in Fig. 2b. The intensity of these diffraction orders show a very smooth decrease for consecutive orders. This fact can be related to the high refractive index contrast for the fabricated ablation gratings.

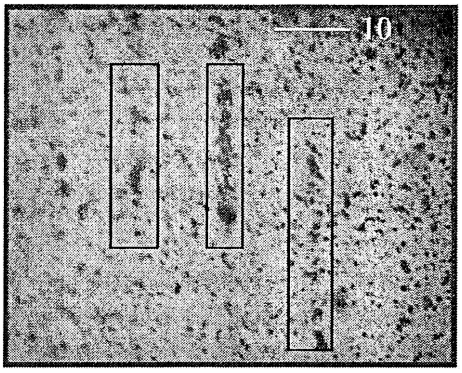
Figure 3a presents the optical contrast microscope image corresponding to phase grating recorded inside the Lithium Niobate crystal. As it can be seen the irradiated regions shows a thinner width (2–3 μm) than that observed for ablation gratings (6 μm).

From these gratings a lower diffraction efficiency has been observed which can be associated to the weaker index increment for the experimental conditions performed. In



(a) (b)

Figure 3. Optical microscope photograph (taken in trasnmision) pf the phase grating written inside of Lithium Niobate crystals by femtosecond laser pulses.



Q3

Figure 4. Ferroelectric domains induced by 400 nm femtosecond writing after revealing in HF solution.

our experiments, the induced index increment can be estimated to be $\Delta n = 10^{-3}$ which originates a refractive index spatial modulation up to 0.2%. In spite of the low refractive index increment, an important diffraction pattern from the 1 D photonic structures is obtained, as it is shown in Fig. 3b. It can be seen that high intensity orders reach up to ± 1, and an appreciable decrease of intensity for the following orders is also observed. Moreover, for a similar refractive index increment induced in the Lithium Niobate crystal, efficient waveguides can been obtained by using several fabrication techniques [10].

In order to control the spatial distributions of the ferroelectric domains in a z cut lithium niobate substrate, the femtosecond laser writing process by using a wavelength of 400 nm for energies below to the ablation threshold was conducted. The blue irradiated regions, after keeping the sample on HF solution during 1 hour, show a clear intensified domain patters on the surface of lithium niobate, as it is illustrated in Fig. 5. The surrounding regions to written tracks, also present some revealed ferroelectric domains which are due to the non monodomain initial sample.

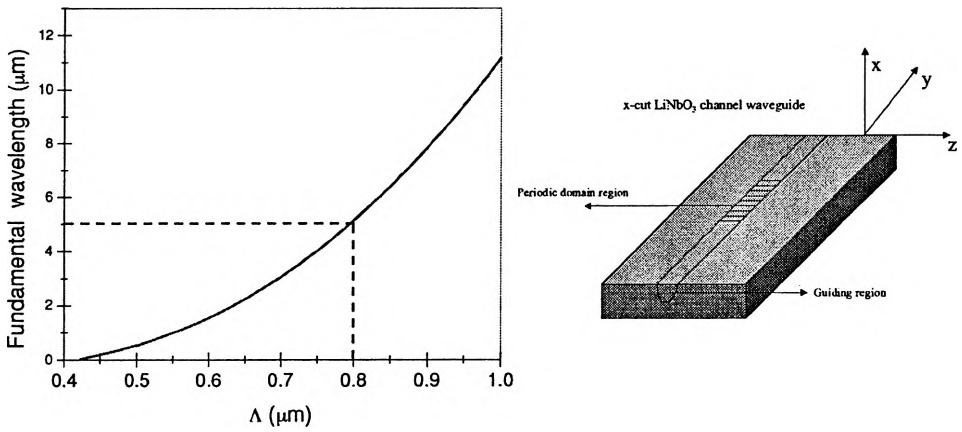


Figure 5. Dependence of the fundamental wavelength as a function of the length (Λ) of periodic domain structure to achieve Second Harmonic Generation (QPM) via Quasi Phase Matching for TE->TE conversion in x-cut LNB crystals.

As it can be clearly observed from the figure, the region where the ferroelectric domains (denoted by hollow oblong) have been revealed correspond to the written tracks. From these preliminary results we can show that it is possible to obtain a spatial control of the ferroelectrics domains on the $LiNbO_3$ surface by writing the desired period structure with blue femtosecond laser pulses.

Further works will be addressed to describe the mechanisms involved in the phenomenology of ferroelectric domain orientation on the surface of lithium niobate crystals induced by using blue femtosecond radiation.

By combining the spatial control of quadratic susceptibility (χ_2) and writing a waveguiding region at the same region of the material, it is possible to make powerful integrated devices in waveguide configuration. In order to do this, a periodic ferroelectric structure on the surface or inside of x-cut or y-cut lithium niobate waveguides can be performed. For instance, to get second harmonic generation via quasi phase matching at 800 nm as fundamental wavelength it is necessary a ferroelectric periodic structure ranged between 5–10 μm, depending on the polarization state for both traveling waves inside the waveguides.

Figure 5 shows the dependence of the fundamental wavelength as a function of the of lattice pitch for quasi phase matching process. For efficient conversion, the second harmonic generation in lithium niobate crystals uses the highest second harmonic coefficient d_{33}, in this case x-cut or y-cut samples should be used [11]. A particular case, the fundamental and the second harmonic waves should be TE (ne, extraordinary index) polarized as it is sketched in the inset of Fig. 5.

Conclusions

In this work we present the spatial control of the linear susceptibility (χ_1) on the surface of Lithium Niobate substrates by means of femtosecond laser writing. In order to do that, efficient diffraction gratings either on the surface (relief) or inside (phase) of LNB crystals have been conducted.

Preliminary results of *optical poling* on the surface of Lithium Niobate crystals by writing at 400 mn also has been obtained. A spatial control of 1 μm of period of the quadratic susceptibility (χ_2) could be reached.

From the above experimental procedure we can fabricate integrated waveguides for second harmonic applications via the quasi phase matching in Lithium Niobate substrates by means of femtosecond laser writing.

Acknowledgements

This work has been partially supported by the European community under contract n° HPMD-CT-2001-00115 and the Spanish Ministerio de Ciencia y Tecnología grant n° BFM-2002-00033.

References

1. K. M. Davis, K. Miura, N. Sugimoto, and K. Hirao, Writing waveguides in glass with a femtosecond laser, *Opt. Lett* **21**, 1729 (1996).
2. D. Homoelle, S. Wielandy, A. L. Gaeta, N. F. Borrelli, and C. Smith, Infrared photosensitivity in silica glasses exposed to femtosecond laser pulses, *Opt. Lett.* **24**, 1311–1313 (1999).
3. A. M. Strelsov and N. F. Borrelli, Study of femtosecond laser written waveguides in glasses, *J. Opt. Soc. Am.* B **19**, 2496–2504 (2002).

4. A. Salamina, N. T. Nguyen, M. C. Nadeau, S. Petit, S. L. Chin, and R. Vallé, Writing optical waveguides in fused silica using 1 kHz femtosecond infrared pulses, *J Appl. Phys.* **93**, 3724–3728 (2003).
5. A. M. Strelsov and N. F. Borrelli, Study of femtosecond laser written waveguides in glasses *J. Opt. Soc. Am.* B **19**, 2496–2504 (2002).
6. M. Will, S. Nolte, B. N. Chichkov, and A. Tunnermann, Optical properties of waveguides fabricated in fused silioca by femtosecond laser pulses, *App. Opt.* **41**, 4360–4364 (2002).
7. J. Siegel, J. M. Fernandez-Navarro, A. Garcia-Navarro, V. Diez-Blanco, O. Sanz, J. Solis, F. Vega, and J. Armengol, Waveguide structures in heavy metal oxide glass written with femtosecond laser pulses above the critical self-focusing threshold, *Applied Physics Letters* **86**, 121109–121113 (2005).
8. S. Nolte, M. Will, J, Burghoff, and A. Tunnermann, Femtosecond waveguide writing: A new avenue to three-dimensional integrated optics, *App. Phys.* A **77**, 109–111 (2003).
9. C. L. Sones, C. E. Valdivia, J. G. Scott, S. Mallis, R. W. Eason, D. A. Scrymgerour, V. Gapalan, T. Jungk, and E. Soergel, Ultraviolet laser induced sub-micron periodic domain formation in congruent udoped lithium niobate, *Appl. Phys.* B 80 (2005).
10. G. Lifante: *Integrated Photonics: Fundamentals* (J. Wiley & Sons, U.K. 2003).
11. E. Cantelar, G. A. Torchia, J. A. Sanz-García, P. L. Pernas, G. Lifante, and F. Cussó, Red, green, and blue simultaneous generation in aperiodically poled Zn-diffused $LiNbO_3$: Er^3/Yb^3 nonlinear channel waveguides. *Appl. Phys. Lett.* **83**, 2991–2993 (2003).

Pulsos ultracortos de luz

Sin duda entre los record alcanzados gracias al láser se debe dedicar un capítulo a la obtención de pulsos de muy corta duración. En el momento de la invención del láser no se disponía de mecanismos confiables para generar pulsos de luz con duración de nano segundos (10-9 s). Los láseres de "pulso gigante" o "Q- switch" y ciertos láseres pulsados como el de nitrógeno molecular, permitieron disponer de pulsos de ns bien temprano en la década de 1960. La generación de pulsos ultracortos de luz, pulsos con duración de pico segundos (ps, 10-12 s) o femto segundos (fs, 10-15 s) fue posible mediante la introducción de la técnica conocida como "mode locking". Los colorantes orgánicos jugaron un papel muy importante en la primera parte del desarrollo de los láseres de pulsos ultracortos ya sea suministrando el medio activo del láser o bien participando en el mode locking a través de la característica de absorción saturable, un mecanismo mediante el cual un material se vuelve más transparente cuando se ilumina con alta intensidad. Las cianinas isomerizables mencionadas en otras áreas de este capítulo son un buen ejemplo de este comportamiento.

El primer trabajo seleccionado se refiere a la observación de reflexión con conjugación de fase en una celda de mode locking. El fenómeno de conjugación de fase es extremadamente importante en Óptica donde se utiliza para corregir deformaciones en los frentes de onda. Es interesante mencionar que este trabajo puede considerarse como un antecedente de la técnica "colliding-pulse modelocking" que fue introducida por Fork, Greene and Shank en 1981 y que condujo a la obtención por primera vez de pulsos de menos de un ps de duración.

El segundo trabajo muestra como el conocimiento de las características fotofísicas del absorbente saturable, junto a las del medio activo y a la geometría de la cavidad resonante, permiten predecir el comportamiento de un laser CPM que genera pulsos por debajo del ps.

Actualmente los pulsos ultracortos de luz vuelven a ser tema de trabajo en el CIOp. Un grupo dedicado a la Física y a la Tecnología de las fibras ópticas trabaja en el desarrollo de nuevas fuentes de pulsos ultracortos y en el estudio de la propagación de los mismos en los dispositivos utilizados en esta especialidad. Mediante una colaboración con la Universidad de Salamanca, investigadores del CIOp realizan modificaciones en materiales utilizando pulsos de fs con niveles de intensidad elevados. Alcanzado ya un grado muy alto de confiabilidad en la operación de láseres comerciales de fs, el Centro pretende incorporar una estación de micromaquinado láser que permita alcanzar una resolución espacial cien veces mayor que la que tenemos actualmente con un láser continuo de CO2.

Ultrashort light pulses

Within the records reached thanks to the laser a chapter must be dedicated to the generation of pulses of very short duration. At the moment of the invention of the laser it was not easy to obtain pulses of light with duration less than 10 ns (10-9 s). "Q- switch" lasers and certain molecular lasers allowed to obtain pulses of ns well early in the decade of 1960. The generation of ultrashort light pulses, pulses with duration of ps (10-12 s) or fs (10-15 s) was possible by means of the "mode locking" technique The organic dyes played a very important role in the first part of the development of the lasers of ultrashort pulses either providing the gain medium or participating in mode locking through the saturable absorption characteristics, a mechanism by means of which a material becomes more transparent when it is illuminated with high intensity. Cyanines, already mentioned in other works performed at CIOp, are a good example of this behavior.

The first selected work talks about to the observation of a "phase conjugated wave" in the reflection in a mode locking cell inside a laser. Phase conjugation is extremely important in Optics where it is used to correct deformations in wave fronts. He is interesting to mention that this work can be considered as an antecedent of the technique "colliding pulse modelocking" (CPM) that was introduced by Fork, Greene and Shank which, in 1981, enabled sub-100 fs pulses to be produced from a dye laser. and which it lead for the first time to the obtaining of pulses of less of ps of duration.

The second work shows like knowledge of the Photophysics of the saturable absorbent used in mode locking and the other laser characteristics, allow to predict the behavior of a CPM laser that generates pulses below ps.

At present, ultrashort light pulses return to be subject of work in the CIOp. A group dedicated to the Physics and the Technology of optical fibers works in the development of new sources of ultrashort pulses and in the study of the propagation of such pulses in different devices used in this specialty. By means of a collaboration with the University of Salamanca, researchers of CIOp make modifications in materials using pulses of fs with high levels of intensity. Nowdays, when the operation of commercial lasers of fs is well established, the Center tries to incorporate a micromachining laser facility that allows to reach a spatial resolution one hundred times greater than we have at the moment with a continuous CO2 laser.

PICOSECOND PHASE-CONJUGATE REFLECTION FROM ORGANIC DYE SATURABLE ABSORBERS

J.O. TOCHO *, W. SIBBETT and D.J. BRADLEY
Optics Section, Blackett Laboratory, Imperial College, London SW7 2BZ, UK

Received 27 March 1980

Phase conjugation with conversion efficiences of up to 50% has been obtained in DODCI and other saturable absorbers with picosecond pulses from a mode-locked dye laser. Reflectivity shows a quadratic dependence on pump intensity up to ~ 500 MW cm^{-2}.

1. Introduction

Phase conjugation reflection [1] by degenerate nonlinear mixing [2] involving local saturation of absorption [3,5] or gain [6,7] has been experimentally demonstrated in gaseous, solid and liquid media. These experiments have employed a Q-switched ruby laser pumping a saturable dye solution [2], a CW argon ion laser interacting with a ruby crystal [3], pulsed CO_2 lasers using germanium [4] and SF_6 [5] as saturable absorbers, and a pulsed dye laser pumping atomic sodium vapour [6]. Nonlinear mixing within the laser gain medium has been obtained with pulsed CO_2 [7] and Nd-YAG lasers [8]. Wavefront conjugation has been produced with picosecond pulses using stimulated Raman and Rayleigh Wing Scattering in benzene and cyclohexane [9], and the nonlinear Kerr effect in CS_2 [10]. We report achievement of high efficiency (up to 50%) phase conjugation reflection in organic dye saturable absorbers, produced by a train of picosecond pulses from a passively mode-locked flashlamp pumped dye laser. As with ruby [3,10] the conjugate pulses can be efficiently generated with broad-band and thus ultrashort duration, pumping pulses but since the lifetime of the excited electronic level of a dye is ~1 ns (compared with 4 ms for ruby) the transistory hologram creates is more suitable for rapid real-time holography and signal processing [1].

* Permanent address: Centro de Investigaciones Opticas, Casilla de Correo 124, 1900 La Plata, Argentina.

2. Experimental

A flashlamp passively mode-locked dye laser [11] generated a 1.2 μs train of pulses of duration ~5 ps at the centre of the train and with ~50 μJ of energy in each pulse. The laser was tuned to operate at 605 nm where mode-locking is optimum [12]. The pulses are separated by the 5 ns round-trip time of the laser cavity and the output was more than 95% polarized in the horizontal plane. A beam-splitter (BS1 in fig. 1) devided the laser beam to generate pulses of high intensity I_1 for pumping and low intensity I_2 probe pulses. The times of arrival of the pulses of each pair at the saturable absorber dye cell were controlled by varying the lengths of the prism optical delay lines. The interaction cell was of the type used in passively mode-locked dye-lasers [11] with a 100% reflectivity mirror immersed in the dye. The mirror was aligned to retroreflect the incident pumping beam so as to provide counter propagating, pump pulses for phase conjugation. The probe beam pulses were arranged to arrive at the cell at the same time as the pumping pulses. The resulting phase-conjugate reflected pulses were detected by a fast photodiode (ITL type FD125), after passing through the 50% reflectivity beamsplitter BS2. Alternatively, the reflected beam profile could be photographed with a lensless camera back, C, using another beamsplitter BS3. Neutral density filters, ND, were used to attenuate the pump and probe beams. When a half-wave plate was placed in

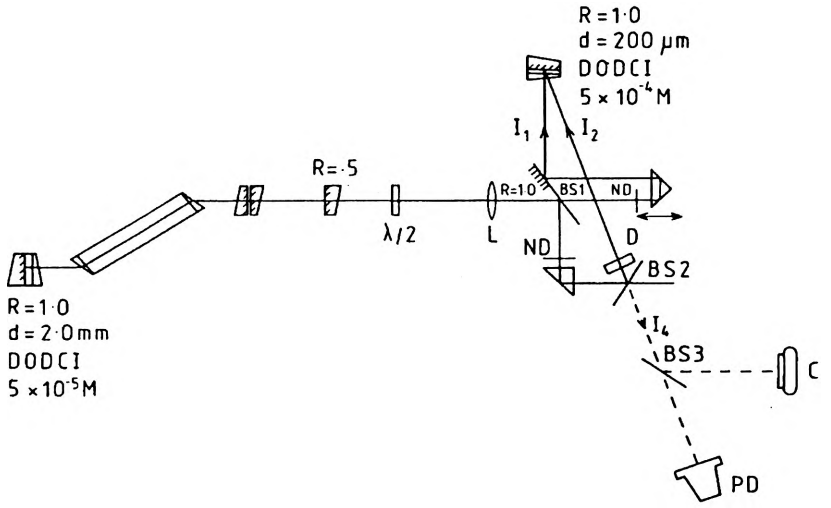


Fig. 1. Experimental arrangement.

the laser beam the plane of polarization was rotated. In this way two values for the ratio of the probe and pump beam intensities, I_2/I_1 were obtained. For horizontal polarization $I_2/I_1 = 0.009$ and for vertical polarization this ratio had the value 0.085.

The pulses were focused into the 200 μm thick dye layer by a 35 cm focal length lens, L, to give a peak pump intensity of ~500 MW cm^{-2}, in an area of ~1 mm diameter. To confirm that phase conjugation was occurring a cylindrical lens of 15 cm focal length was placed in the probe beam path at D. Solutions of DODCI, DQTCI and Oxazine 1, all absorbing at the dye laser wavelength, in a range of solvents (ethanol, methanol, and glycerol) were employed in the dye cell. The results were found to be independent of the solvent employed and phase conjugate reflectivity was produced by all three saturable absorbers. Most of the work was carried out with DODCI dissolved in ethanol and the results obtained with this dye are reported.

3. Results

To obtain backward wave reflectivity it was necessary to ensure that the difference in time of arrival of the object and pump pulses at the absorber cell was kept less than the coherence time of the laser beam. Fig. 2 shows the variation of reflected intensity as a function of the delay between the object and pump pulses. This is effectively a method of measuring the temporal coherence function of the laser beam [13]

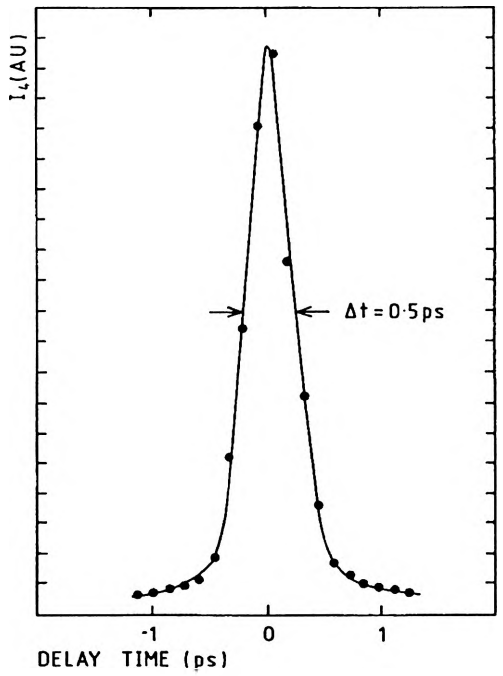


Fig. 2. Variation of reflected intensity I_4 (arbitrary units) with delay between arrival of pump and probe pulses at DODCI cell.

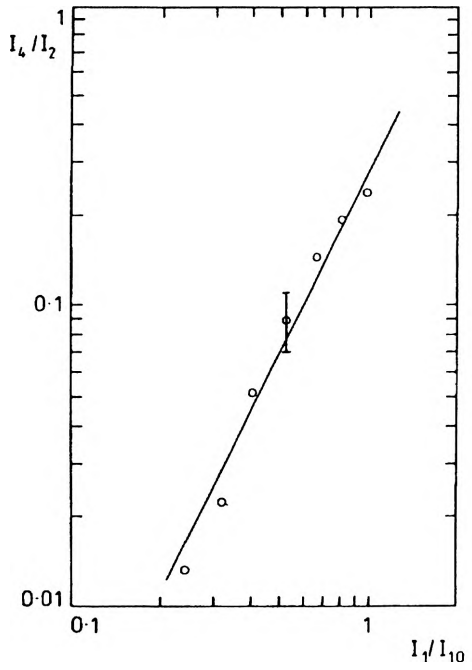


Fig. 3. Plot of phase conjugate reflectivity R as a function of pump intensity I_1 (normalized to maximum pump intensity I_{10} = 480 MW cm^{-2}). I_2 = 5 MW cm^{-2}.

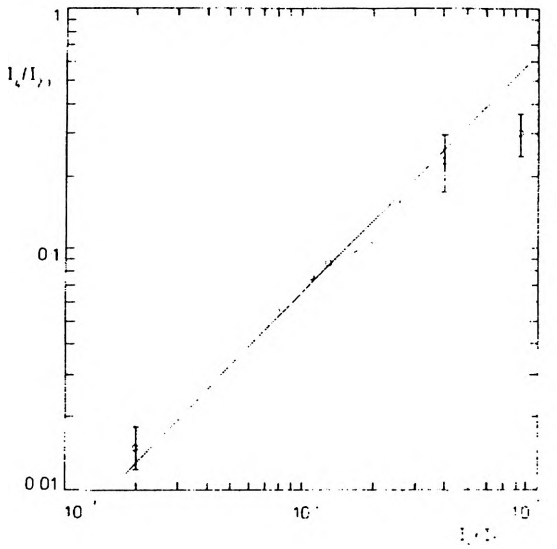


Fig. 4. Plot of phase conjugate reflected intensity I_4 (normalized to maximum probe intensity I_{20} = 36 MW cm^{-2}) as function of probe intensity I_2 (normalized to pump intensity I_1 = 440 MW cm^{-2}).

and the half-width of 0.5 ps gives the value of the coherence time. The spectral bandwidth of the pulse train was measured to be 2.3 nm which corresponds to a coherence time (or pulse duration for bandwidth-limited pulses) of 0.22 ps for gaussian shaped pulses. The discrepancy probably arises from spectral broadening due to self-phase modulation when the laser is pumped above threshold [14]. This broadening increases monotonically along the pulse train so that the recorded time-integrated bandwidth largely comes from pulses towards the end of the pulse train. Thus fig. 2 gives an average coherence time for the whole pulse train.

The reflectivity as a function of pump intensity is plotted in fig. 3 for horizontally polarized light. The maximum pump intensity employed was well above the saturation intensity $I_{sat} \sim 250$ MW cm^{-2} of DODCI for 5 ps pulses at 605 nm. The theory of conjugate-wave generation by nonlinear mixing has been treated for two-level [15] and three-level [3] absorbing media. Since the relaxation rates within the electronic singlet bands of the saturable absorber dye molecules are rapid ($\sim 10^{12}$ s^{-1}) it is possible to apply the two-level theory of [15] if triplet state population and absorption to higher singlet and triplet levels are neglected. Then the reflectivity R can be shown [3,15] to be proportional to $I_1^2 \exp(-2\alpha d)(1-\exp(-2\alpha d))^2$ where d is the dye cell thickness and α is the absorption coefficient. The expected quadratic dependence of reflectivity upon intensity is shown in fig. 3 up to the maximum pump intensity employed of ~500 MW cm^{-2}. The corresponding value for the backward wave reflectivity was then ~30%. In fig. 4 the reflected intensity for vertically polarized light is plotted as a function of the probe intensity for a constant pump intensity of ~450 MW cm^{-2}. The output intensity is seen to increase linearly with the object wave intensity until this approaches 17 MW cm^{-2}, corresponding to an output power of ~8 MW cm^{-2}. Before saturation sets in the power reflectivity is ~50%. The dependence of reflectivity upon the DODCI concentration is shown in fig. 5, measured for a pump intensity and a probe intensity similar to that used for fig. 4. The experimental points are seen to be a good fit to the theoretical function $\exp(-2\alpha d)(1-\exp(-2\alpha d))^2$ for the experimental parameters employed. At dye concentrations below the optimum value of 5.5 ×

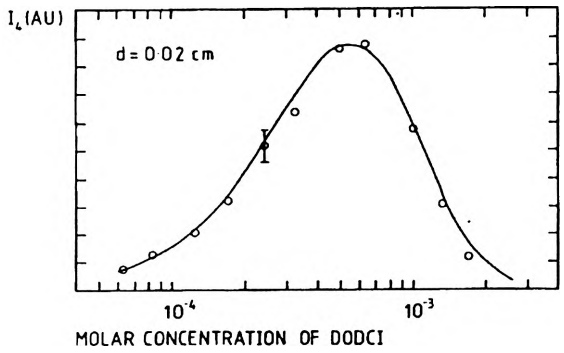


Fig. 5. Plot of reflected intensity I (in arbitrary units) as function of DODCI molar concentration for pump and probe intensities similar to fig. 4. The smooth curve corresponds to the theoretical relationship $I_4 \propto \exp(-2\alpha d)(1-\exp(2\alpha d))^2$ $\alpha = n\epsilon$; n = molar concentration, ϵ = extinction coefficnet (0.5×10^5 M^{-1} cm^{-1} at 605 nm) and d = 0.02 cm (the cell thickness).

10^{-4} M the coupling constant for nonlinear mixing is low [15] and the intensity of the backward wave is reduced. For higher dye concentrations the efficiency also drops because of increasing absorption of all the waves. For the optimum dye concentration but with a cell of 1 mm thickness there was a considerable decrease in efficiency (to ~5% reflectivity).

Confirmation of wavefront phase conjugation in the backward reflected pulses is given by the photographs of the beam profiles of fig. 6. While the cylindrical lens distorter has only a minor effect on the beam profile reflected from the dye cell, replacing this with a plane mirror produces a major change. Phase-conjugate reflection has also been obtained when the dye laser was not mode-locked. The reflected laser pulse had a duration ~270 ns which was much shorter than the expected value of 870 ns for the 1.5 μs pumping duration. This was probably due to the effect of photoisomer generation [16].

In conclusion our results show that saturable absorber dyes can be employed for efficient phase-conjugation of broad-band laser pulses. With a wide range of dyes absorbing in the ultra-violet, visible and near-IR, backward conjugation of picosecond laser pulses can thus be easily obtained throughout these spectral regions. Optimum conditions can be readily achieved by simply adjusting the dye concentration and the cell thickness.

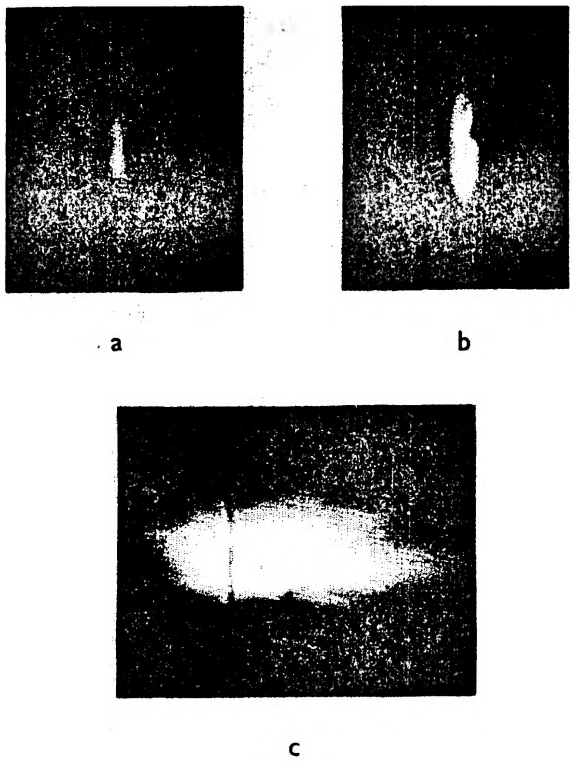


Fig. 6. (a) Reflected phase conjugate beam profile recorded on film in camera-back (C of fig. 1) with X 3 attenuation. (b) Reflected phase conjugate beam with 15 cm focal length cylindrical lens distorter with no attenuation. (c) Reflected beam with distorter when DODCI cell was replaced by plane mirror for X 10 attenuation.

We are pleased to acknowledge financial support from the Science Research Council and one of us (J.O.T.) is supported by the Consejo Nacional Investigaciones Cientificas y Técnicas de la República Argentina.

References

[1] A. Yariv, I.E.E.E.J., Quant. Electron QE-14 (1978) 650; QE-15 (1979) 524, and references therein.
[2] B.I. Stepanov, E.V. Ivakin and A.S. Rubanov, Sov. Phys. -Dokl. 16 (1971) 46.
[3] P.F. Liao and D.M. Bloom, Optics Lett. 3 (1978) 4.
[4] E.E. Bergmann, I.G. Bigio, B.J. Fledman and R.A. Fisher, Optics Lett. 3 (1978) 82.
[5] R.C. Lind, D.G. Steel, J.F. Lam and C.R. Guilionoa, Appl. Phys. Lett. 34 (1979) 457.

[6] D.M. Bloom, P.F. Liao and N.P. Economon, Optics Lett. 2 (1978) 58.
[7] R.A. Fisher and B.J. Feldman, Optics Lett. (May, 1979).
[8] A. Tomita, Appl. Phys. Lett. 34 (1979) 463.
[9] A.D. Kudriavtseva, A.I. Sokolovskaia, J. Gazengel, N. Phu Xuan and G. Rivoire, Optics Comm. 26 (1978) 446.
[10] D.M. Bloom, C.V. Shank, R.L. Fork and O. Teschke, Springer Series in Chemical Physics 4, Picosecond phenomena (1978) p. 96.
[11] D.J. Bardkey, in: Topics in applied physics, 18 Ultrashort light pulses, ed. S.L. Shapiro (Springer Verlag, Heidelberg, 1977) pp. 17–81.
[12] D.J. Bradley, Optical and Quantum Electronics 6 (1974) 25.
[13] H.J. Eichler, U. Klein and D. Langhams, Appl. Phys. 21 (1980) 215.
[14] E.G. Arthurs, D.J. Bradley and A.G. Roddie, Appl. Phys. Lett. 19 (1971) 428.
[15] R.L. Abrams and R.C. Lind, Optics Lett. 2 (1978) 94.
[16] E.G. Arthurs, D.J. Bradley and A.G. Roddie, Appl. Phys. Lett. 20 (1972) 125.

PARAMETERS THAT DETERMINE THE WAVELENGTH OF A PASSIVE MODE-LOCKED DYE LASER

J.L.A. CHILLA, P.L. PERNAS, O.E. MARTINEZ
Division Fisica del Solido, Comision Nacional de Energia Atomica, 1429 Buenos Aires, Argentina

and

J.O. TOCHO
Centro de Investigaciones Opticas, CIC, 1900 La Plata, Argentina

Received 25 November 1988; revised manuscript received 21 April 1989

We introduce a new stability criterion that should be added to previous theoretical models of passive mode locked lasers in order to predict emission wavelength, which is to require that the pulse spectrum reproduces itself after one transit. The CPM laser consisting of rhodamine 6G as gain medium and DODCI as saturable absorber is studied. The relative population balance of the fundamental and photoisomer species of the DODCI are computed as a function of the pulse energy and wavelength. The necessity of a spectral stability criterion follows from the dependence of the gain profile on the pulse parameters. Use of the criterion is shown to agree with previous experimental results, such as the red spectral region of emission and dependence of emission wavelength on absorber concentration. This criterion is expected to be an useful tool in order to select other dye combinations and predict the laser behavior.

1. Introduction

Passive mode-locking of a CW dye laser was first demonstrated in 1972 [1] and the original choice of dyes, Rhodamine 6G as the gain medium and DODCI as the saturable absorber has been commonly used since then.

The primitive cavity designs were tunable, but the bandwidth limitation introduced by the tuning element prevented the obtention of the shortest pulses. Further designs led to pulses in the subpicosecond regime using the colliding pulse scheme [2]. The control of the group velocity dispersion through prisms [3,4] gave rise to even further pulsewidth reduction down below 30 fs [5]. It was also found that CPM systems presented an emission wavelength determined primarily by the absorber concentration [6].

Theoretical investigations were first conducted by New [7]. He showed the need to meet several stability criteria, such as requiring a net gain for the peak of the pulse but with net loss at both leading and trailing edges. Analytical solutions for the equations describing the behavior of passively mode-locked dye lasers were given by Haus [8] who also introduced an additional condition to satisfy the self starting requirements [9]. In more recent works Martinez et al. [10] and Haus et al. [12] included frequency modulation terms that gave rise to new analytical solutions. These solutions consisted of chirped pulses that depended on the group velocity dispersion and other frequency pulling terms. In these works the closed form solutions could be found after assuming the wavelength of emission of the laser. The model showed a good description of the behavior of the Rhodamine 6G-DODCI combination of dyes, but cannot be used to predict the behavior of other dye combinations unless the emission wavelength is determined independently.

A straightforward approach to this problem would be simply to choose the wavelength were net gain is maximum, but saturation of dyes makes gain very

0 030-4018/89/$03.50 © Elsevier Science Publishers B.V.
(North-Holland Physics Publishing Division)

sensitive to changes in pulse features. This can be seen in fig. 1(a), which shows how the shape of the gain profile changes for different pulse energies, shifting the position of the maximum about 20 nm by increasing the degree of saturation. A subtler way in which the degree of saturation changes arises from changes in pulse wavelength. This alters the saturation energies, by changing the cross sections of the dyes as seen by the pulse. For a pulse wavelength of 580 nm, gain saturation energy is 2.1 mJ/cm^2, DODCI's is 0.21 mJ/cm^2 and photoisomer's is 4.8 mJ/cm^2, while for 620 nm same species saturation energies are 3.4, 2.7 and 0.24 mJ/cm^2 respectively.

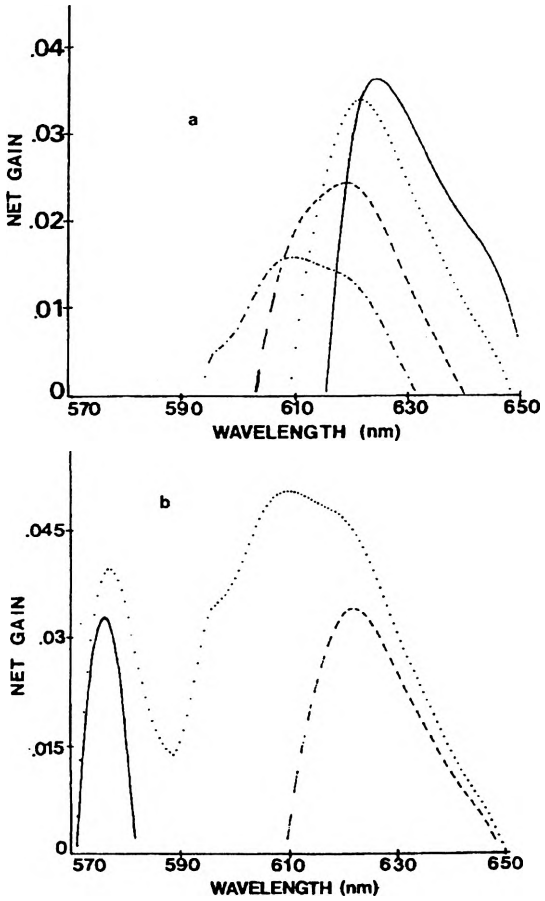


Fig. 1. (a) Net gain at the peak of the pulse for fixed wavelength (620 nm) and different energies (solid 2 nJ, dots 4 nJ, dashed 6 nJ and dash-dot 8 nJ). (b) Net gain at the peak of the pulse for fixed energy (4 nJ) and different wavelengths (solid 580 nm, dots 615 nm and dashed 620 nm).

This effect gives the dramatic result shown in fig. 1(b), where net gain is displayed for three pulse wavelengths. It is clear then that we must ask for self consistency in our model.

In this work we will try to introduce a new stability criterion that should be added to previous models in order to obtain a self consistent solution that also predicts the wavelength of the pulse to be emitted. This criterion is simply to request that the pulse spectrum repeats itself after each transit. In order to take into account this simple condition, one must consider the dependence of the dyes population inversions on the pulse energy and wavelength. This dependence should be added in a self consistent manner to the model that predicts the wavelength. In this work we will simplify this condition to requesting that the emission wavelength is such that the gain spectrum has a maximum at such wavelength after saturation by half of the pulse (pulse peak). Small signal gain is unimportant, as it only represents loss at the leading edge of the pulse. The starting wavelength may be different from the operating one, but as the pulse builds up from noise, the wavelength shifts to maximum gain at the peak of the pulse. Actually this is only a first estimate on the wavelength because, as shown by Martinez et al. [11], some frequency pulling might be necessary to achieve a stable solution with a chirped pulse. As such terms will only introduce a minor shift in the wavelength in typical operating conditions [12] it will not change the fundamental features presented here. Assuming typical energies for the pulse, we will use this criterion to predict the dependence of the emission wavelength on different parameters such as dye concentration, pump power and relative focusing on the gain and absorber dyes. Parameter ranges where stable solutions are found can also be predicted in this manner. The examples discussed will assume that Rhodamine 6G and DODCI are used as gain and absorber respectively (curves from [13] and [14]), and values of parameters of a typical CPM ring laser [5], such as a beam waist radius of 10 μm in the gain jet. Unless stated otherwise, a pulse energy of 6 nJ is assumed, and a spot area three times smaller in absorber jet.

2. Steady state regime

In order to compute net gain at the peak of the pulse, one must take in account the cross sections of the involved processes and the saturation dependent population of the states of the three dyes in the system (R6G, DODCI and its photoisomer). Both absorption and amplification are proportional to the population difference of the respective medium, being in the proportionality factor (the cross sections), where the wavelength dependence of the gain profile appears. We will derive expressions for the population inversion per unit area, including in such way the path traversed through the medium. During the passage of the pulse this population difference evolves after the following expression. Detailed derivation can be found in ref. [8],

$$n = n_0 \exp[-2U(t)/U_s] . \quad (1)$$

Here $U(t)$ is the cumulative energy of the pulse up to time t and U_s is the saturation energy. The factor 2 accounts for the pulse being so short (less than 100 fs) that no relaxation occurs during the passage of the pulse [15], but should be dropped if modeling a picosecond system. Between the passage of two successive pulses, population difference grows asymptotically to a certain value with a proper time constant. Populations at the arrival of the pulse are determined from requirement of a steady state regime.

The gain medium is the simplest, in steady state regime, pumping between the passage of two successive pulses exactly compensates the depletion of excited state population produced by the preceding pulse. This depletion depends on the energy and color of the pulse. A yellow pulse will decrease excited state population more efficiently than a red one of equal energy,

$$n_i = \frac{t I_p [1-\exp(-T/2t)]}{[1-\exp(-T/2t)][1+\exp(2U/U_1)]/2} . \quad (2)$$

Here n_i is the excited state population at the arrival of the pulse, U is the pulse energy, t is relaxation time for Rhodamine 6G and U_1 is its saturation energy. T is the period of the mode-locked pulse train, and I_p is the pump power.

Population of the DODCI can be transferred to the photoisomer by the pulse and population of photoisomer also experiences back isomerization [16]. Fig. 2(a) depicts the path by which such mixing of populations occurs. It is a simplification of the real processes that take place and involve a short lived twisted state. Absorption of energy during the passage of the pulse causes transition of both species to their excited levels. As the pulse is very short, all other processes may be neglected during the pulse, but they are important between the passage of two successive pulses. Desactivation from excited states with time constants as defined in the figure include both radiative and non-radiative processes. A very complete and recent description of DODCI can be found

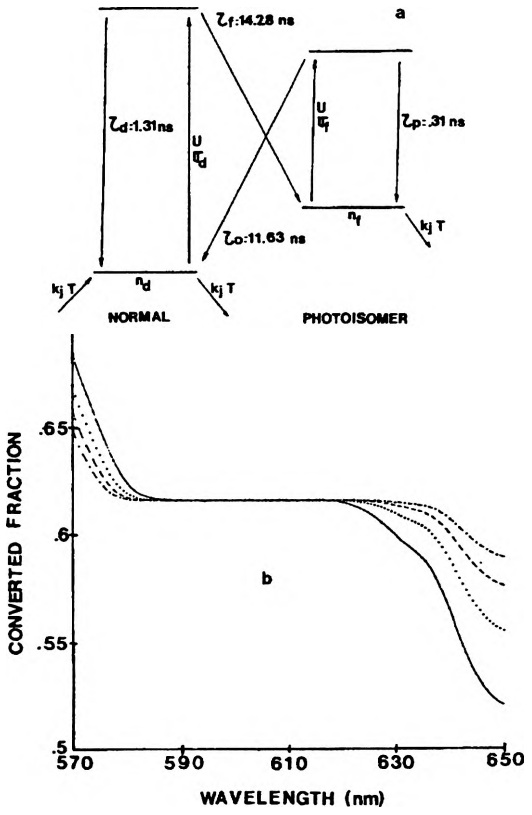


Fig. 2. (a) Simplified diagram of levels and transitions of the saturable absorber DODCI and its photoisomer. Time constants used in computation are defined. (b) Fraction of DODCI concentration that is converted to photoisomer as a function of pulse wavelength for different pulse energies (solid 6 nJ, dots 8 nJ, dashed 10 nJ and dash-dot 12 nJ).

in ref. [17]. Ground states are also affected by the circulation of the dye solution, which tends to increase normal species population.

When the laser is working, a fraction of the absorber concentration will be converted to the photoisomer form. Restricting our attention to ground state of normal form, and requiring its population not to change after one transit, an expression can be found for the converted fraction as a function of the energy and wavelength of the incoming pulse,

$$\frac{n_f}{n_d+n_f} = \frac{[1-\exp(-2U/U_d)]\tau_d}{2(\tau_d+\tau_f)} \times\left(k_j T+\frac{[1-\exp(2U/U_f)]\tau_p}{2(\tau_0+\tau_p)} + \frac{[1-\exp(-2U/U_d)]\tau_d}{2(\tau_d+\tau_f)}\right)^{-1}. \quad (3)$$

n_d and n_f are the population of normal and photoisomer species respectively, U_d and U_f are their saturation energies (wavelength dependent) and k_j accounts for the apparent relaxation due to dye renewal in the jet. Typical values give relaxation times around 700 ns. A plot of numerical computation of this expression is displayed in fig. 2(b) as a function of wavelength for different pulse energies. It can be seen that in the zone where both the photoisomer and the normal species saturate, converted fraction takes the value 0.616, regardless the wavelength and the energy of the pulse. When only one of the species is saturated, the converted fraction becomes more sensitive to the incoming pulse. For a yellow pulse, DODCI converts very efficiently to the photoisomer, but back isomerization is not so efficient because of the smaller cross section of the photoisomer in that wavelength. Converted fraction approaches both saturated value only for pulses with larger energies. An analogous but inverted situation rises when the pulse is red.

3. The criterion

From the preceding discussion, it is clear that net gain in the peak of the pulse will depend very strongly on the pulse that is travelling in the cavity. This can be seen in fig. 1(b), where the net gain is displayed as a function of wavelength for pulses of fixed energy and three different wavelengths. If the pulse is yellow, a maximum appears around 580 nm, while with a red pulse the maximum is around 620 nm. For pulse wavelength between these, both maxima are present. The exact positions of these maxima are very sensitive to the energy and wavelength of the incoming pulse. The dependence on pulse energy is shown in fig. 1(a). Keeping the wavelength fixed at 620 nm, a larger pulse energy shifts the position of the maximum gain to shorter wavelength.

If a steady state regime is to be achieved, with a pulse of well defined energy and wavelength, the position of the maximum of net gain at the peak of the pulse must coincide with the wavelength of the pulse, otherwise a frequency pulling term would appear and the pulse would not repeat itself after a transit. This condition represents a stability criterion on emission wavelength, and severely restricts the possible emission wavelengths of the system. An immediate representation that will help to make clear the influence of the different parameters is shown in fig. 3. The position of the maximum for a fixed pulse energy is plotted as a function of the pulse wavelength for different sets of parameters. It can be easily seen that there is only one wavelength that fulfills our stability criterion; the one where each curve intersects the diagonal near 620 nm. Crossing the diagonal from upside ensures stability against perturbation of the system, as can be understood considering that a perturbation of either sign shifts maximum position as to produce a restoring frequency pulling.

It should be noted, however, that this only means a possible emission wavelength of the system. In order to predict emission wavelength the criterion must be used in conjunction with a model that predicts the rest of the features of the steady state solution, such as pulse energy (for example [11], completed in a self consistent way). We study the effect of different parameters of the laser system upon the emission wavelength, as given by the criterion for fixed pulse energy i.e. we are disregarding changes in the pulse caused by the parameter we are varying. If taken in account, that would change the exact dependence of emission wavelength upon laser parameters, but not the fundamental features presented here.

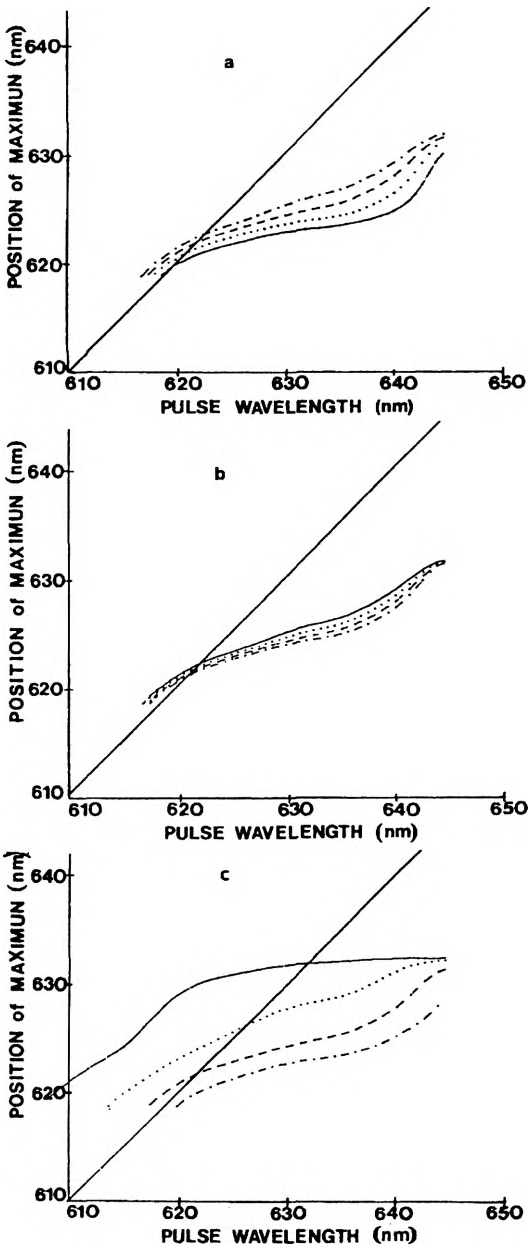


Fig. 3. Representation of stability criterion. Position of maximum gain as a function of the pulse wavelength. Stable wavelength is the one where the curve intersects the diagonal. (a) Effect of absorber concentration. Curve of maxima for different absorber concentration (solid 3.0, dots 3.6, dashed 4.2, dash-dot 4.8×10^{15} l/cm^2). (b) Effect of pump power. Curve of maxima for different pump powers (solid 2.86, dots 3.04, dashed 3.22, dash-dot 3.40×10^{23} phot/cm^2/s). (c) Effect of relative focusing. Curve of maxima for different relative focusing in the gain and absorber medium (focusing ratio: solid 1, dots 2, dashed 3, dash-dot 4).

4. Dependence on laser parameters

Any change in laser parameters alters the position of the maximum gain for given pulse energy and wavelength, and thus changes the shape of the curve of maxima. The modified curve will intersect the diagonal in some different wavelength, or may not intersect it at all. This means the system would not work for such particular choice of parameters.

It is well known, though it was rather surprising at first, that the emission wavelength of the passive mode locked dye laser is determined primarily by the concentration of the absorber dye [6]. Fig. 3(a) shows how the curve of the maxima is affected by the concentration of DODCI. Increasing the absorber concentration shifts the only stable operating wavelength further to the red. This behavior can be interpreted as follows: for a red pulse the photoisomer is deeply saturated because of its larger cross section, and its absorption at the peak of the pulse may be neglected. Absorption of the normal species is still important, as it saturates near the peak of the pulse. Increasing absorber concentration increases the loss for the short wavelength side and thus shifts the maximum to longer wavelength. For a sufficiently small absorber concentration, the curve of maxima keeps below the diagonal and no stable solution is found near 620 nm, but another one is found around 580 nm.

In fig. 3(b) we study the effect of pump power. Increasing pump power shifts down the curve of maxima. This behavior offers a new interpretation for bistability reported on CPM systems [18]. For a given absorber concentration they increase pump power until the curve of maxima is pushed below the diagonal and laser wavelength jumps to yellow, where the threshold for continuous operation has been surpassed. In that situation the fraction of DODCI concentration that is converted to the photoisomer is larger than the one in the mode locked regime. Increased absorption in the red thus prevents the laser from jumping to red again, even if pump power is lowered below the point where the first transition occurred.

Another parameter that affects emission wavelength is the relative focusing on the gain and absorber. As it can be seen in fig. 3(c) (focusing ratio is defined as gain beam area over absorber beam

area), stronger focusing in the absorber shifts the emission wavelength to orange. As discussed in connection with fig. 3(a), we are only interested in absorption by the normal species of DODCI. Strong focusing favours saturation with an overall effect of decreasing absorber concentration at the peak of the pulse.

5. Conclusion

In conclusion we have shown the need of an additional stability criterion on emission wavelength of passive mode-locked dye lasers, consisting in requesting the pulse spectrum to repeat itself after each transit. Self consistency is essential because the spectral profile of the net gain depends dramatically upon pulse features as energy and central wavelength. Influence of different laser parameters according to this new criterion is shown to agree with reported behavior. In order to give detailed dependence of emission wavelength upon laser parameters, the criterion should be used in conjunction with a model that predicts pulse features from this parameters. Nevertheless, this criterion alone can be useful to predict possible emission wavelength of new and yet not experimented gain/saturable absorber dye combinations, and with minor modifications it would be suitable for the case of femtosecond hybrid mode locked lasers.

References

[1] E.P. Ippen, C.V. Shank and A. Dienes, Appl. Phys. Lett. 21 (1972) 348.
[2] R.L. Fork, B.I. Greene and C.V. Shank, Appl. Phys. Lett. 38 (1981) 671.
[3] O.E. Martinez, J.P. Gordon and R.L. Fork, in: Ultrafast Phenomena IV (Springer Verlag, New York, 1984) p. 7.
[4] R.L. Fork, O.E. Martinez and J.P. Gordon, Optics Lett. 9 (1984) 150.
[5] J.A. Valdmanis and R.L. Fork, IEEE J. Quantum Electron. QE-22 (1986) 112.
[6] J.J. Fontaine, W. Dietel and J.C. Diels, IEEE J. Quantum Electron. QE-19 (1983) 1467.
[7] G.H.C. New, IEEE J. Quantum Electron. QE-10 (1974) 115.
[8] H.A. Haus, IEEE J. Quantum Electron. QE-11 (1975) 736.
[9] H.A. Haus, IEEE J. Quantum Electron. QE-12 (1976) 169.
[10] O.E. Martinez, R.L. Fork and J.P. Gordon, Optics Lett. 9 (1984) 156.
[11] O.E. Martinez, R.L. Fork and J.P. Gordon, J. Opt. Soc. Am. B 2 (985) 753.
[12] H.A. Haus and Y. Silberberg, J. Quantum Electron. QE-22 (1986) 325.
[13] F.P. Schafer, in: Dye lasers (2nd Ed., Springer Verlag, 1977).
[14] D.N. Dempster, T. Morrow, R. Ranken and G.F. Thompson, J. Chem. Soc. Faraday II, vol 68 (1972) 1479.
[15] A.M. Weiner and E.P. Ippen, Chem. Phys. Lett. 114 (1985) 456.
[16] L. Scaffardi, G. Bilmes, D. Schinca and J. Tocho, Chem. Phys. Lett. 140 (1987) 163.
[17] S. Rentsch, V.W. Grummt and D. Khetchinashwili, Laser Chem. 7 (1987) 261.
[18] G.R. Jacobovitz, C.H. Brito Cruz, N.P. Mansur and M.A. Scarparo, Optics Comm. 59 (1986) 233.

Óptica física y aplicada

Holografía

Metrología optoelectrónica

Óptica fisica y propagación de ondas

Procesamiento fotorrefractivo

Speckle digital

Speckle dinámico

Speckle modulado

Óptica Física y Aplicada

Desde sus inicios se ha generado en el CIOp un gran interés y se han dedicado muchos esfuerzos a las investigaciones en óptica física y sus aplicaciones.
Así, los primeros hologramas hechos en la Argentina (y aún en Sud América) fueron realizados por un grupo de investigadores que más tarde formaría parte del CIOp, a partir de 1977.

En el caso de la propagación de ondas electromagnéticas en distintos medios y el análisis de la coherencia se han empleado en el CIOp diferentes herramientas matemáticas para describir estos fenómenos, entre ellas la transformada fraccionaria de Fourier, la función distribución de Wigner, las funciones de Walsh y la transformada wavelet.

El análisis de la granularidad óptica ó speckle y su empleo en aplicaciones metrológicas fue también un tema relevante desde principios de los 80´s. En particular, la modulación interna del speckle obtenida mediante sistemas ópticos de múltiples aperturas, las cuales pueden modificarse en una secuencia de múltiples exposiciones, permitieron desarrollar novedosas aplicaciones poniendo en evidencia las ventajas relativas de la propuesta

La llegada del procesamiento digital en el campo de la óptica trajo aparejado nuevas posibilidades y la Interferometría Digital de Diagramas de Speckle (IDDS) es una línea de investigación que se remonta a los primeros trabajos en la metrología speckle desarrollados en el Centro. En este marco, la holografía digital, los sistemas ópticos virtuales, y más recientemente la encriptación y validación opto-digitales aprovecharon los avances del speckle digital.

El efecto fotorrefractivo ocurre al cambiar el índice de refracción en un medio debido a la propagación luminosa no uniforme. Las investigaciones en este tema se iniciaron en el CIOp en 1987, siendo el primer laboratorio que lo hizo en el país, realizándose originales contribuciones en procesamiento de imágenes. El speckle, a pesar de su naturaleza en volumen, se había utilizado sólo según un enfoque bidimensional. Dentro de la metrología speckle en tiempo real se aprovechó la conjunción del registro fotorrefractivo en volumen y las características tridimensionales del speckle, para desarrollar aplicaciones que incluyeron la conjugación de fase y la amplificación óptica.

En otro aspecto, el estudio de la evolución temporal de los patrones de speckle puede proporcionar una herramienta interesante para caracterizar los parámetros implicados en procesos transitorios biológicos e industriales. Desde 1996, se han hecho muchos esfuerzos en el CIOp para asignar los números que caracterizan esta actividad del biospeckle. .Además de proponerse modelos numéricos, se han realizado varios algoritmos para caracterizar en forma cualitativa la actividad dinámica del patrón de speckle así como herramientas de medidas cuantitativas. De este modo, se han desarrollados satisfactoriamente en el CIOp diversas técnicas del biospeckle orientadas a la caracterización de tejidos biológicos y de procesos industriales.

Es conocido que las medidas de superficie utilizando métodos ópticos en escala macro ó microscópica son relevantes en aplicaciones industriales por ser no-invasivas y por su velocidad al efectuarse la medida. Este tema también fue abordado en el CIOp desde los primeros años, desarrollándose varias técnicas opto-electrónicas para medir rugosidad de superficies, velocidad, índice de refracción, distancias, desplazamientos, deformaciones, fisuras, contorneado, etc.

Optical Physics and its applications

The research in optical physics and its applications has been actively generated since the early beginning at CIOp.
An interesting case is that the first holograms made in Argentina (even in South America) were devised and produced by a group of researchers that later on conformed CIOp in 1977.
In optical wave propagation and coherence of the light analysis much effort has been devoted to the development of several approaches for the description of these subjects by using different tools as the fractional Fourier transform, the Wigner distribution function, the Walsh functions and the wavelet transform.

The use of speckles for metrological application was also of great interest at CIOp since the early 80´s. In particular, the internal modulation of the speckles achieved through an optical system whose pupil consists of multiple apertures in which the pupil changes between exposures were widely studied. Applications were developed demonstrating the possibility of carrying out a variety of experiments which can not implemented otherwise.

The advent of the digital processing in the optical domain brought new possibilities and Digital Speckle Pattern Interferometry (DSPI) traces back to the first papers developed in metrology by means of speckle patterns. In this frame, digital holography, Virtual Optical Imaging Systems (VOIS), and more recently opto-digital encryption and validation profited from digital speckle advances.

Photorefractive effect takes place when a refractive index change is produced in a material due to non uniform light distribution and, therefore, it is possible to register dynamic holograms in real time and with a high fidelity. Photorefractive studies start at CIOp in 1987 being the first laboratory in Argentina to initiate this line of research. Several original real time image processing techniques were produced. In speckle metrology has been taking advantage of the photorefractive material volume and the three-dimensional nature of speckles to produce very innovative research. In particular, applications that include phase conjugation and image amplification have been carried on.

The study of the temporary evolution of the speckle patterns may provide an interesting tool to characterize the parameters involved in both biological and industrial transient processes. Since 1996, many efforts have been carried out at CIOp, to assign numbers that characterize this biospeckle activity and that correlate favourably with alternative measurement methods of interest for the experimenter. Several algorithms to characterize cualitatively the dynamic speckle pattern activity as well as quantitative tool measurements have been developed. Numerical models were also proposed. In this way, bio-speckle techniques oriented to the characterization of biological tissues and industrial processes were developed at CIOp.

It is well known that surface optical measurements on the macro and microscopic scale is very important for industrial applications because of non contact operation mode, fast measurement speed and damage free data acquisition. Since the early years at CIOp, several optoelectronic techniques have been developed in order to measure surface roughness, velocity, refractive index, distances, displacements, deformations, cracks, contouring, etc

Holografía en el CIOp

Los primeros hologramas hechos en la Argentina (y aún en Sud América) fueron realizados en 1969 en el Laboratorio de Espectroscopia, Óptica y Láser (LEOL) de la Facultad de Ciencias Exactas de la Universidad Nacional de La Plata, grupo que vendría luego a constituir el Centro de Investigaciones Opticas (CIOp), a partir de 1997. Los hizo el entonces Licenciado José Lunazzi, dirigido por el Dr. Mario Garavaglia. Se trataba de pequeños hologramas de los tipos conocidos como de Gabor y de Leith y Upatnieks y otras geometrías ideadas por esos investigadores.

Un año más tarde se incorporó al grupo el entonces alumno de Licenciatura Héctor Rabal y un poco más tarde los Licenciados Lía Zerbino y José Calatroni.

En esos primeros años se reprodujeron las principales técnicas holográficas conocidas hasta ese momento agregando holografía en el plano imagen y microscopía holográfica.

A partir de esa época, algunas experiencias de holografía comenzaron a ser incluídas como trabajos de laboratorio para alumnos de cuarto año de Licenciatura en Física.

A continuación se desarrollaron experiencias de interferometría holográfica por doble exposición y a tiempo real por revelado in situ para la medida de deformaciones (años 1972-1973).

Las Tesis Doctorales de Lía Zerbino y de Héctor Rabal, presentadas en 1978, incluían desarrollos sobre aspectos holográficos de algunos registros interferométricos obtenidos con el interferómetro de Fabry Perot.

En el año 1979 se desarrolló en el CIOp el Seminario sobre Óptica de Fourier (CONICET-NSF) con la participación entre otros de Emmet. Leith, uno de los pioneros de la holografía y de Joseph Goodman, James Wyant, Charles Vest, Silverio Almeida.

A partir de 1979 se desarrollaron otras Tesis Doctorales con contenidos de holografía, como las de Enrique Sicre, Néstor Bolognini, Roberto Torroba y Nora Rodríguez.

En el año 1981, tres investigadores alemanes, K. Wanders, H. Steinbischler y G. Schweiger dictaron un curso sobre holografía con experiencias que fue uno de los precursores del Curso Láser y Óptica en Ingeniería (LOI).

El interés por la holografía se vio acentuado por la visita del Profesor Jean Charles Vienot de la Universidad de Besançon, Francia, quien dictó un curso sobre ese tema en noviembre y diciembre de 1983.

Este mismo profesor volvió a visitar el Ciop en otras oportunidades manteniendo el intercambio de informaciones de interés en este tema.

Lo mismo sucedió con las visitas del Prof. Maurice Françon de la Universidad de Paris VI, Francia, quien dictó dos cursos sobre los avances que se iban produciendo en holografía y técnicas conexas hasta el año 1982.

En 1986, H. Rabal, R. Torroba y M. Garavaglia publicaron un trabajo sobre una nueva forma de registro de hologramas arco iris.

En 1989 se publicó un trabajo de divulgación sobre fenómenos naturales con comportamiento similar a la holografía.

Debido al creciente interés público en la holografía se dictaron tres cursos teórico-prácticos de divulgación para el público en general. El "Primer Curso Introductorio de Holografía" realizado en el CIOp con el auspicio de la Comisión de Investigaciones de la Prov. de Buenos Aires junio de 1989, fue repetido en agosto y octubre como Segundo y Tercer Curso respectivamente.

Durante 1990 y 1991, el Licenciado Ricardo Arizaga trabajó conjuntamente con artistas plásticos en la implementación del uso de la holografía para desarrollar ó registrar objetos de arte.

Los holografistas profesionales Ken Harris y Kevin Brown en el año 1992 en cooperación con N. Bolognini, R. Arizaga y H. Rabal participaron en la realización de algunos hologramas H2 y arco iris de esculturas de Marta Minujin.

A partir de 1991 se comenzó a desarrollar en el CIOp la interferometría holográfica digital (DSPI) y se realizaron algunas experiencias de luz en vuelo y contorneado empleando fuentes de baja longitud de coherencia (1993). Asimismo, se publicó un artículo con la explicación de una imagen aparentemente anómala que se observaba en holografía de Fresnel.

Es interesante mencionar que en 1999, H. Rabal y R. Arizaga realizaron el único holograma revelado con café instantáneo del que se tenga noticias.

Finalmente debe mencionarse que la holografía analógica y digital es tema de interés permanente en el CIOp y forma parte de algunas líneas de investigación que se llevan adelante, como por ejemplo, la holografía en medios de volumen reciclables.

Holography at ciop

The first holograms made in Argentina (even in SouthAmerica) were devised and produced in 1969 at Laboratorio de Espectroscopía Óptica y Láser (LEOL), Faculty of Science, National University of La Plata. Those holograms were done by Licenciate José Lunazzi under the guidance of Dr. Mario Garavaglia. The holograms of small size were of different types: Gabor, Leith and Upatnieks as well as other configurations conceived by both researchers. In 1970 the student Héctor Rabal and the Licenciates Lía Zerbino and José Calatroni joined the group.

It should be pointed out that further on the LEOL group constituted the Centro de Investigaciones Opticas (CIOp) in 1977.

The main holographic techniques just known in those early years were also reproduced at CIOp. For instance, image holography and holographic microscopy. Besides, some holographic experiences were included in undergraduate courses as laboratory work for students in the last year of the Physics Licenciate Career. Furthermore, in 1973, some projects were carried on concerning experimental arrangements with double exposure holographic interferometry and real time ("in-situ") holography applied to deformation measurements.

Doctoral Thesis of Lía Zerbino and Héctor Rabal issued in 1978 included some development related with holographic features of Fabry Perot interferometer measurements. In 1979 took place at CIOp the Fourier Optics Workshop under the agreement of CONICET and National Science Foundation, USA, with the participation of highly qualified researchers and lecturers as Joseph Goodman, James Wyant, CharlesVest, Christ Dainty, Silverio Almeida and Emmet Leith, one of the pioneering researcher on holography.

From 1979, several Doctoral Thesis mainly devoted to holography (Enrique Sicre, Néstor Bolognini, Roberto Torroba, Nora Rodriguez) were carried on.

In 1981 German researchers, K. Wanders, H. Steinbischler and G. Schweiger dictated a practical and theoretical holography course that could be considered a preceding step to the "Láser y Óptica en Ingeniería" course.

Professor Maurice Francon from Paris IV University visited CIOp in 1982 and dictated two courses about the recent progress on holography and related techniques. The increasing appeal to holography projects was also encouraged by the visit of Professor Jean Charles Vienot of Besancon University who dictated a two months course on holography in 1983. Afterwards, Professor Vienot visited CIOp several times, keeping up a continuous up-to-date on the subject.

This maintained interest renders good results. In 1986, a new arragement concerning rainbow holography was developed by CIOp researchers. Three years later, in was published a contribution were it was stated that some natural phenomena exhibited an holographic behaviour.

At that time, the public interest in holography prompted to spread out the basic principles and practical approaches on the subject. Therefore, a First Introductory Holography Course that includes a basic theory and practical demonstrations devoted to an audience without a scientific background was conducted at CIOp in June 1989. The course was supported by Comisión de Investigaciones Científicas de la Provincia de Buenos Aires (CICBA). Success in people attendance causes to repeat the course twice that year.

During 1990 and 1991 cooperative activities between artists and CIOp researchers leaded to some interesting developments in display holography.

In 1992, professional holographers Ken Harris and Kevin Brown in cooperation with Ricardo Arizaga, Héctor Rabal and Néstor Bolognini made holographic versions of Marta Minujin's sculpture pieces in a rainbow type format.

I t should be pointed out that in 1999, H. Rabal and R. Arizaga made a hologram that was developed with black coffee. It seems to be the first time this chemical procedure was employed.

By going back to 1991, "light in flight" experiments and contouring holography with low coherent sources were implemented. Also that year, digital holographic interferometry started at CIOp and a permanent interest remains in this field.

At present, holography is a main subject in different research lines, for example, dynamic holography in volume media.

volumen 1 1974 número 2

comunicaciones

asociación física argentina

MEDICIÓN DE LA DEFORMACIÓN DE UNA BARRA METALICA POR MEDIO DE LA HOLOGRAFÍA INTERFEROMÉTRICA

J.A.E.Calatroni, J.J.Lunazzi, H.J.Rabal, M.J.Garavaglia

Dpto. de Física , Fac. de Ciencias Exactas ,Universidad Nacional de La Plata , C.C. 67 La Plata .

Una barra metálica sostenida por uno de sus extremos es sometida primeramente a la acción de su propio peso, y luego a la de una sobrecarga; en ambos casos se realiza una toma holográfica de modo que ambas tomas se superponen sobre una misma placa.

La reconstrucción de este holograma de doble exposición crea figuras de interferencia que corresponden a la diferencia entre ambas posiciones de la barra. Se logra de este modo medir con precisión interferométrica la deformación de una barra metálica cualquiera,aunque esta no haya sido preparada ópticamente como lo sería en el caso de una medición interferométrica común.

Este estudio se completó con el procedimiento que consiste en superponer la reconstrucción holográfica con la imagen directa de la barra. De este modo la interferencia es vista en el mismo instante que se produce, y este procedimiento simultaneo permite además observar los efectos de una variación continua de la deformación de la barra.

Con el objeto de aplicar las técnicas de la holografía interferométrica al estudio de la deformación de un modelo mecánico se utilizó una barra metálica de 193 x 21,5 x 4 mm^3 sometida a esfuerzos de flexión.

La deformación se realizó aplicando a un extremo de la misma una sobrecarga de 330 grs. El otro extremo fue amordazado en una morsa y se realizaron hologramas interferométricos por doble exposición en la zona de sujeción de la barra. Esta técnica requiere la superposición de dos tomas holográficas en una misma placa: una de ellas correspondiente al modelo sin sobrecarga y la otra al modelo deformado por la sobrecarga.

Es así como en el proceso de reconstrucción holográfica se obtienen dos imágemes muy similares pues la deformación es de unos pocos micrones; estas imágenes corresponden a frentes de onda coherentes porque han sido reconstruidos con el mismo haz de luz láser y es por esto que se produce interferencia entre ambas de manera tal que la imagen del objeto se ve cubierta con un sistema de franjas de interferencia caracteristico de la deformación que ha tenido lugar.

De la observación de estos hologramas se concluyó inmediatamente que el soporte requería condiciones de mayor rigidez puesto que las franjas de interferencia se extendían sobre él, por lo que se diseñó el dispositivo dibujado en la fig. 1; este fue sujetado firmemente a una base de cemento que descansa sobre terreno firme a 3 m de profundidad (se trata de una base ubicada en un subsuelo y aislada en sus contornos del resto del edificio)

Fué necesario, para lograr condiciones extremas de estatismo, construir un portaplaca que pudiera sujetarse en el mismo soporte que la barra

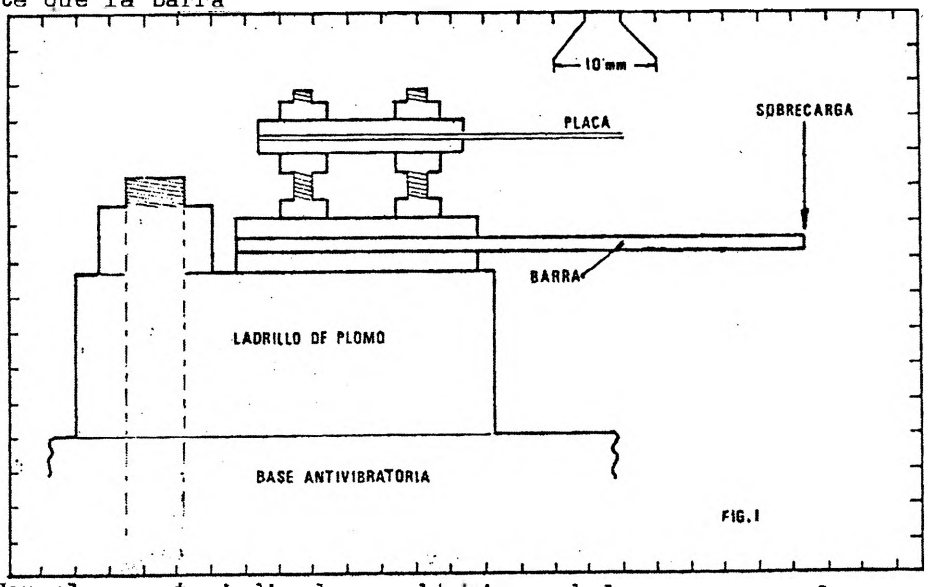


FIG. 1

Con el soporte indicado se obtuvieron hologramas como los esquematizados en las fig. 2 y 3; para ello se utilizó un láser de He-Ne de 2 mW (con esta potencia pudimos realizar hologramas de dimensiones no mayores que las indicadas en las figuras).

En estos hologramas la presencia de franjas oscuras de interferencia señala puntos cuyo desplazamiento, relativo al de la franja oscura adyacente, ha sido de aproximadamente media longitud de onda. El valor exacto de este desplazamiento depende en cada caso de la posición que tuvieron el láser, la barra, la placa (al realizar la toma) y además, el punto de observación en la reconstrucción, pero siempre es del orden de $\lambda / 2$. En el holograma correspondiente a la fig. 2 la concentración de franjas aumentaba hacia la derecha, donde estaba centrada la sobrecarga, debido a que en esa región la deformación era mayor. Además, se observaron unas pocas franjas en la región amordazada lo que constituye una prueba de lo dificultoso que es aproximarse a condiciones de rigidez que impliquen desplazamientos menores que $\lambda / 2$ (0,3 μm para un láser de He-Ne) en sujeciones como la empleada.

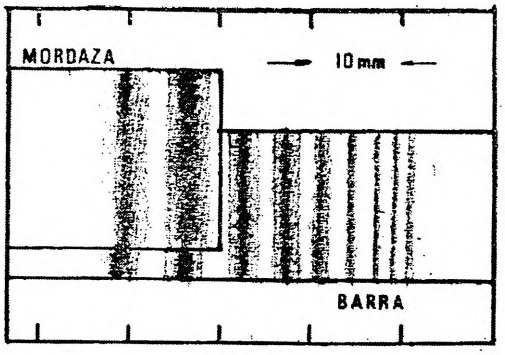


FIG.2

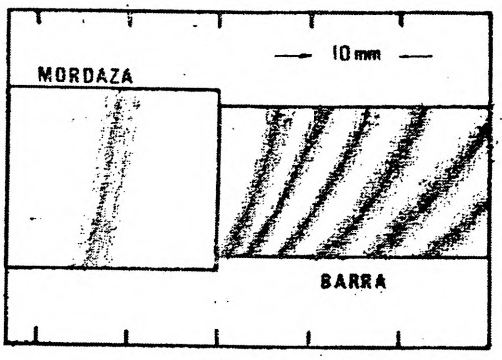


FIG.3

El holograma de la figura 3 fué obtenido cuando la sobrecarga se aplicó levemente desplazada hacia el extremo inferior derecho de la barra y esto produjo la inclinación de las franjas.

A fin de poder hacer este estudio contando con la posibilidad de variar de manera continua la deformación de la barra empleamos la técnica denominada holointerferometría simultanea ("real-time"). Esto consistió en realizar una única toma de la barra sin sobrecarga, la que sirve como toma patrón. La placa es revelada en el lugar de la toma y al reconstruir el holograma se produce interferencia entre la imagen reconstruida por el holograma y la imagen directa de la barra.

Podemos entonces deformar al objeto y ver las franjas interferenciales en el mismo instante en que la deformación es producida; se observan algunas franjas de interferencia residuales que se deben a que el holograma patrón reconstruye una imagen levemente diferente a la del objeto, debido principalmente a efectos de encogimiento de la emulsión fotográfica durante el revelado y a variaciones térmicas; en nuestro caso, habiendo tomado las precauciones debidas, el número de franjas residuales fue pequeño frente al número de franjas útiles.

Los hologramas que se obtuvieron con estas técnicas fueron similares a los obtenidos por medio de la doble exposición. Naturalmente, tienen la ventaja de permitir observar diferentes deformaciones en la muestra con un único holograma; sin embargo son de realización dificultosa.

Concluimos así que las técnicas expuestas son de real importancia por cuanto permiten mediciones no destructivas con precisiones interferométricas de modelos cuyo tamaño está limitado por la potencia del láser empleado. Pensamos continuar estos estudios con el objeto de sistematizarlos a fin de emplearlos en experiencias que no sean exclusivamente las del laboratorio y puedan ser aplicadas a la tecnología.-

Light-in-flight digital holography display

H. Rabal, J. Pomarico, and R. Arizaga

We present a digital speckle-pattern interferometric setup that can be operated at TV frame rates (30 ms) to display the locus of the points at which the optical-path difference between the reference and object beams is within the coherence length. Experimental results are shown.

Key words: Light in flight, digital speckle-pattern interferometry.

In 1978 Abramson[1] demonstrated a method called light-in-flight holography to display the locus of the zero optical-path difference (OPD) between the object and the reference beams of a holographic setup. He used the short coherence length of an argon-ion laser without an intracavity étalon. A picosecond laser was also used for this purpose.[2] A similar method had been proposed by Boden *et al.*[3] and Denisyuk *et al.*[4]

On the other hand, digital speckle-pattern interferometry (DSPI) has developed as a powerful tool to perform several operations usually associated with holographic interferometry in the image plane; thus this method is also called digital holography. Deformation measurements and generation of contours of three-dimensional objects are some examples.[5,6] A review of some of these applications can be found in Ref. 7, but a profusion of recent developments exists in the literature.

In its basic form the image of an object with a superposed coherent background is registered by a TV camera and then digitized and stored in a frame memory. Subsequent images are subtracted from the initial image, and the square or the modulus of the difference is shown on a monitor. A phase change between the reference and the object waves is introduced between the first and the final observed states. It can be produced, for example, by a deformation of the object or by a change in the illumination conditions. If this phase difference on the image is slowly varying on areas comprising several pixels, then the same speckle pattern is present in both images in regions in which the phase difference is 2π or congruent values. In these regions, subtraction produces a dark area in the result. Other phase delays modify the resulting speckle pattern, and the subtraction gives a nonzero response. Fringes are thus obtained in the subtracted image showing the locus of constant phase difference. High resolution inherent to analog holography is not required here. Only the speckle grains must be barely resolved by the imaging system. Three-dimensional image formation is sacrificed, but operation at TV frame rates without chemical developing is obtained as a trade.

We describe now how a DSPI experiment can be modified to obtain a light-in-flight display. Figure 1 shows the experimental setup. A cw argon-ion-laser-pumped Rhodamine 110 dye laser is employed ($\bar{\lambda}$ = 550 nm). A piezoelectrically driven mirror (PEM) is used to introduce a π-phase shift in the reference beam between the two exposures. Lens L conjugates the focal point of the beam expander, E, in the front focal plane of the imaging system of the CCD camera, thus producing a plane wave on the detector array. The image registered by the detector is the superposition of a speckle pattern and a uniform background produced by the reference beam.

For all image places in which the OPD is greater than the coherence length of the light the phase shift is of no consequence. At these points the superposition is incoherent; therefore a phase shift in the reference beam does not change the measured intensity, and subtraction produces a dark output at these points.

In regions in which the superposition is coherent, interference fringes are produced. These fringes are substituted by the complementary ones when the phase shift is introduced and the observed speckle pattern changes. Though the actual fringes are not resolved by the TV camera, subtraction in these

The authors are with the Centro de Investigaciones Opticas, Casilla de Correo 124, La Plata, 1990, Argentina.

Received 12 March 1993; revised manuscript received 19 November 1993.

0003-6935/94/204358-03$06.00/0.

© 1994 Optical Society of America.

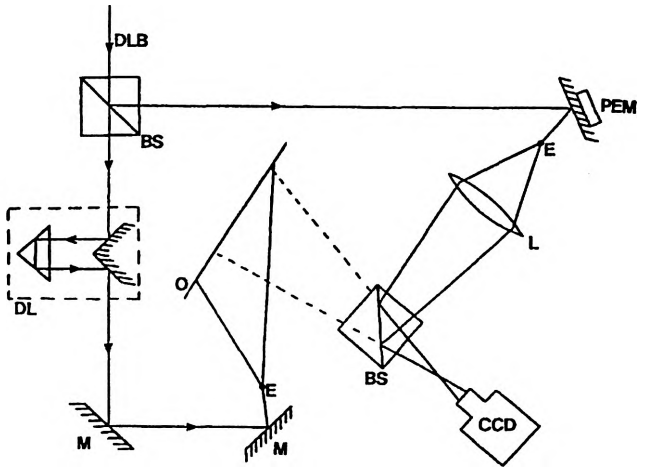


Fig. 1. Experimental setup: DLB, dye laser beam; BS's, beam splitters; M's, mirrors; E's, beam expanders; O, plane object; L, lens; PEM, piezoelectrically driven mirror; DL, delay line (optional); CCD, TV camera connected to a frame grabber a and computer.

regions produces a nondark result depicting the locus at which the OPD is within the coherence length.

A delay line (DL) in one of the beams can be used to change the place at which the object wave front differs in optical path with the reference wave front by less than the coherence length, thus producing a different contour. It can be seen that a sharp transition from coherent to incoherent in the light source as a function of OPD is desirable for a well-defined intersection of the wave front with the object.

Usually a spherical reference beam emerging from the center of the diaphragm is used to illuminate the whole image in DSPI systems. This configuration also leads to a light-in-flight display. Nevertheless, using a plane wave a as reference beam is more appropriate because then all of the path difference in the interference pattern can be attributed to the object beam. Only then can the display show the propagation of the object wave accurately.

The f-number of the camera lens was set at a relatively high value ($f = 11$) so that speckle grains could be resolved by the CCD array. This geometry introduces a certain amount of vignetting, but with a long enough focal length (in our case, 135 mm) in the imaging lens, the best part of the CCD detector area (roughly 1 cm × 1 cm) can be illuminated.

As the experiment is performed in the image plane, it is not necessary to use an object-to-reference-beam intensity ratio greater than 1. This ratio was used in our experiment.

The geometrical aspects of this experiment can be easily understood in terms of the holodiagram.[8] The two foci of the ellipsoids are in this case the focal point of E, the origin of the beam illuminating the object, and the center of the image-forming lens (Fig. 1).

Figure 2 shows the experimental result obtained for the intersection of a spherical wave front with a plane object. The holodiagram constants for this

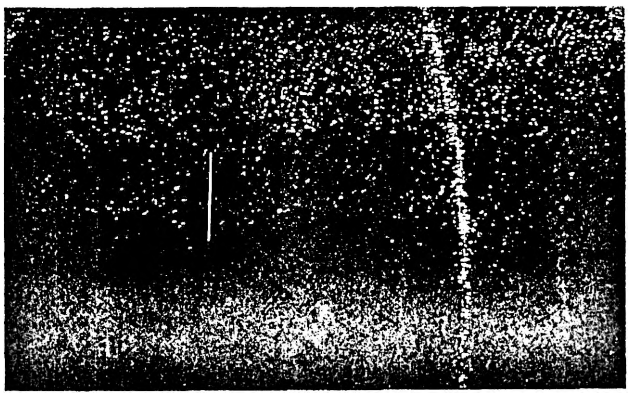
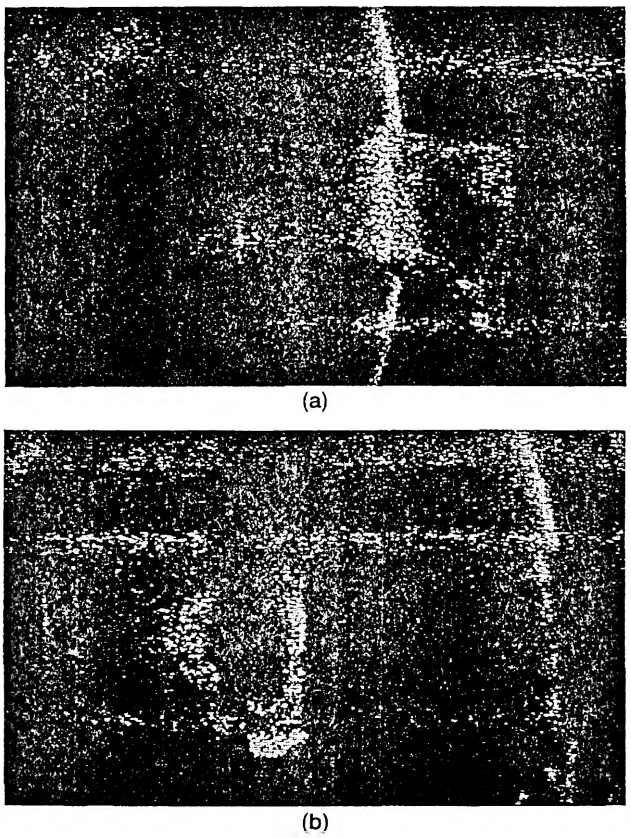


Fig. 2. Intersection of a spherical wave front with a plane-tilted object.

experiment are $k \cong 1.15$ ($\alpha \cong 30°$) and k^* nominally infinite ($\beta \cong 0$)[2-8]; 2α is the angle between illumination point E and the observation point defined by the center of the lens as seen from a generic object point, and 2β is the angle between the object beam and the reference beam at the CCD array plane.

A small parallel glass plate was then introduced in the central region of the object, and the wave front showed its presence by a delay corresponding to ~4 ps. The results are shown for two different positions of the delay line in Fig. 3.



(a)

(b)

Fig. 3. Intersection of a spherical wave front with the same object after passing through a small parallel glass plate for two different positions of the delay line.

An adequately designed Michelson interferometer acting simultaneously as a beam splitter and as a delay line could be used to obtain two bright lines. A Fabry–Perot interferometer could also be used to increase the number of lines.

We have proposed and demonstrated a DSPI experiment to depict the locus of the intersection of an object with an evolving wave front. Although it is intrinsically a sequential method, it can be implemented at a TV frame rate without chemical processing of a holographic plate. The position of the wave front can be changed by the adjustment of a delay line.

This work was supported by Consejo Nacional de Investigaciones Científicas y Técnicas grant PID 3-071700/88 and a grant from Fundación Antorchas. We thank the Laser Group of the Centro de Investigaciones Opticas for providing the dye laser. J. Pomarico is a Fellow of the Comisión de Investigaciones Científicas de la Provincia de Buenos Aires.

References and Notes

1. N. Abramson, "Light-in-flight recording by holography," Opt. Lett. **3**, 121–123 (1978).
2. N. Abramson, "Light-in-flight recording: high-speed holographic motion pictures of ultrafast phenomena," Appl. Opt. **22**, 215–232 (1983).
3. F. Boden, H.-D. Reidenbach, and G. Köppen-Borgstedt, "Gated viewing by holographic range gating," Optik **51**, 199–212 (1978).
4. Yu. N Denisyuk and D. I. Staselko [Appl. Opt. **31**, 1682–1684 (1992)] claimed that the method was previously developed by them in 1969.
5. J. Butters, R. Jones, and C. Wykes, "Electronic speckle pattern interferometry," in *Speckle Metrology*, R. Erf, ed. (Academic, New York, 1978), pp. 111–158.
6. N. Bolognini, H. Rabal, and R. Torroba, "Single-beam digital holographic contouring," Appl. Opt. **31**, 1009–1011 (1992).
7. J. R. Tyrer, "A critical review of recent developments in electronic speckle pattern interferometry," in *Holographic Nondestructive Testing*, C. M. Vest, ed., Proc. Soc. Photo-Opt. Instrum. Eng. **604**, 95–99 (1986).
8. N. Abramson, "The holo-diagram. VI. Practical device in coherent optics," Appl. Opt. **11**, 2562–2571 (1972).

Metrología empleando Técnicas Optoelectrónicas

Medidas de superficie utilizando métodos ópticos tanto a escala macroscópica como microscópica son muy importantes tanto en aplicaciones industriales como científicas. Las ventajas de estos métodos son la velocidad de medida, son no invasivos y no hay contacto con la superficie estudiada. Se utilizan distintos principios físicos tales como el tiempo de vuelo, medida de la fase, técnicas moiré, triangulación, proyección de franjas, microscopía confocal, interferometría, holografía, speckle, etc.

Desde los primeros años del CIOp, varias aplicaciones han sido desarrolladas para medir rugosidad de superficies, velocidad, índice de refracción, distancias, desplazamientos, deformaciones, fisuras, contorneado, etc.

En particular, varios métodos han sido propuestos para medir parámetros estadísticos asociados con los perfiles de una superficie difusora, usando propiedades de la luz "scattereada" de la superficie y dependiendo del valor de r.m.s. de la misma. El rango medido es de 1 a 30 micrones.

Métodos ópticos sin contacto con las muestras son particularmente apropiados en aplicaciones industriales para medida de velocidad de una superficie rugosa. Se han propuesto varios métodos para un rango de medidas de 0 a 40 m/s.

Usando técnicas interferométricas, se analizaron superficies líquidas volátiles y no volátiles. Además de los contenedores de paredes planas, se estudiaron recipientes con paredes cilíndricas y toroidales. Se demostró la validez de las aproximaciones utilizadas.

Se han desarrollado métodos ópticos para medida de distancias basadas en el efecto moiré. Distancias del orden de cientos de metros fueron medidas con una incerteza del 2%.

Metrology by using optoelectronic techniques

Optical measurement of surfaces on the macro and microscopic scale is becoming very important for scientific and industrial applications. The advantage of optical methods is non contact operation mode, the measurement speed and the damage free data acquisition. Different physical principles are used like time of flight, phase measuring as well as moiré techniques, triangulation, fringe projection, confocal microscopy, interferometry, holography, speckle, etc.

Since the early years at CIOp, several optical applications have been developed in order to measure surface roughness, velocity, refractive index, distances, displacements, deformations, cracks, contouring, etc

In particular, several optical methods have been proposed in order to measure the statistical parameters associated with the height profile of diffuser surfaces, using the properties of scattered light, and depending on the r.m.s. roughness value of the inspected surface. The r.m.s. surface roughness measuring range is 1-30 microns.

Also, optical non-contacting methods are particularly appropriate for measuring the velocity of moving rough surfaces in industrial applications. We have proposed different speckle methods for measuring the linear velocity of a moving diffuse object. The measuring range is 0-40 m/s.

A fruitful approach to the studies of a liquid free surface was demonstrated. Using optical interferential techniques, the free surface of nonvolatile and volatile confined liquids were analyzed. Various wall container types were investigated. Besides the classical plane wall, experiments were performed by using cylindrical and toroidal walls.

An application for distance measurements based on the moiré optical technique was developed. Hidden grids from the photocopy process were used to produce moiré patterns. Distances in the range of hundred meters were measured with an uncertainty of 2%.

INTERNATIONAL JOURNAL OF OPTOELECTRONICS, 1990, VOL. 5, NO. 5, 389–395.

Surface roughness measurement through a speckle method

NÉLIDA A. RUSSO†, NÉSTOR A. BOLOGNINI‡, ENRIQUE E. SICRE‡ and MARIO GARAVAGLIA‡

Centro de Investigaciones Opticas (CIOp), C. Correo 124, 1900 La Plata, Argentina

(*Received 8 February 1990; accepted 29 March 1990*)

Abstract. An optical approach for real-time measurement of statistical parameters associated with rough surfaces is proposed. Two crossed-polarized, partially correlated, speckle patterns originated from a surface under different illumination conditions are recorded on a linear photodiode array. The r.m.s. surface roughness is related to the correlation degree between both speckle patterns, which in turn is derived by processing the detected intensity distribution. Some experimental results are shown in order to illustrate this technique.

1. Introduction

Several optical methods have been proposed in order to measure the statistical parameters associated with diffuser surfaces using the properties of scattered light. Depending on the r.m.s. roughness value of the inspected surface, two different approaches seem to be appropriate. For surfaces having a r.m.s. roughness from 0·01 to about 2 μm, the methods based on Beckmann's model for the light scattering distribution provide a non-contacting roughness measurement through a transference curve optical-to-mechanical parameter, which depends on the machined type of the surface [1–4]. For a more restricted range (r.m.s. from 0·05 to 0·25 μm), Asakura *et al.* [5–8] proposed a method in which the roughness value is obtained by measuring the average contrast of the image speckle pattern originated from the surface under coherent illumination, and varying the imaging conditions of the optical system.

On the other hand, for larger surface roughness, in the range 1–30 μm, a different approach, in which the surface information can be derived from the correlation properties of the speckle patterns produced by the surface under different illumination conditions, gives better results. Léger *et al.* [9] analyzed the correlation degree of two speckle patterns originated by the test surface, each one obtained from a light beam having slightly different angles of incidence. Both speckle patterns are successively recorded by double exposure on the same photographic plate. In a second step, by performing an optical Fourier transform of the developed plate, Young's interference fringes are produced. They derived a theoretical relationship between the visibility of these fringes, and the values of the surface roughness and the several geometrical parameters involved. Based

†Fellowship of the Comisión de Investigaciones Científicas de la Provincia de Buenos Aires (CIC).
‡Member of the Consejo Nacional de Investigaciones Científicas y Técnicas (CONICET).

0952-5432/90 $3.00 © 1990 Taylor & Francis Ltd.

on this principle, they proposed a method where the surface is simultaneously illuminated by two coherent light beams with different and variable angles of incidence through an afocal lens system [10]. A Michelson interferometer is used in order to collect and combine the speckle patterns formed by the scattered light beams in two different directions. It is shown that the resulting speckle pattern diffraction at infinity is partially correlated, and from the visibility of the interference fringes that are obtained the roughness value of the surface can be derived.

In order to get a real-time measurement for practical cases, the above mentioned procedure becomes rather difficult to implement. For this reason, in this paper we propose a speckle correlation method employing an optical arrangement which is suitable for performing fast and continuous measurements of surface roughness. These changes are considered taking into account industrial environmental conditions, so that the influence of factors such as misalignments or vibrations on the system performance is minimized. The signal processing algorithm used by the optoelectronic system can yield a measuring rate of about ten roughness values per second.

In section 2, a description of the method is presented, and a discussion of the influence of the several parameters involved on the measuring accuracy follows. Next, in section 3, some experimental results obtained by using plane-ground comparison standards are shown to illustrate this approach. Finally, in section 4, we summarize the advantages and limitations of this method.

2. Principle of the method

As shown in figure 1, the coherent light beam emerging from the laser source is split into two crossed-linear polarized light beams by the polarizing cube beamsplitter PBS. Both light beams are combined by the beamsplitter BS, in such a way that the surface S under study is simultaneously illuminated by two light beams, Σ_1 and Σ_2, with angles of incidence θ_1 and $\theta_1+\Delta\theta_1$. The angular separation $\Delta\theta_1$ between Σ_1 and Σ_2 can be selectively changed by rotating the mirror M_2. The motion of the mirror is synchronized with the output of a camera LG_1, provided with a linear photodiode array, which measures $\Delta\theta_1$ through the

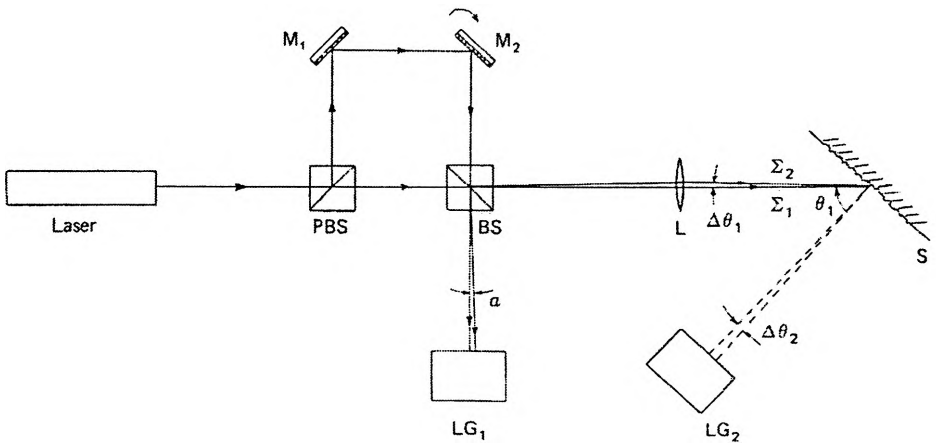


Figure 1. Optical system configuration.

relationship $\alpha = m\,\Delta\theta_1$, m being the magnification of the lens L. As the illuminating beams Σ_1 and Σ_2 have crossed-linear polarization states, two (non-interfering) speckle patterns are scattered by the surface S. If we choose the normal to the surface as the viewing direction (i.e. $\theta_2 = 0$), then the whole intensity distribution detected by a second linear camera LG_2 can be considered as the speckle pattern originated only by Σ_1, and a shifted version of that speckle pattern by an amount $\Delta\theta_2$, originated by Σ_2, and where

$$\Delta\theta_2 = \cos\theta_1\,\Delta\theta_1\,. \tag{1}$$

In addition, the intensity distribution of each individual speckle pattern also changes, so that their correlation degree decreases as $\Delta\theta_1$ increases. As was established in [9], if a recording of such intensity distribution were Fourier transformed, Young's fringes would appear with a visibility V given by

$$V = \exp\left[-(2\pi R_s \sin\theta_1\,\Delta\theta_1/\lambda)^2\right], \tag{2}$$

R_s being the standard height deviation of the surface. It is to be noted that equation (2) was derived under the assumption of a normally distributed surface.

In the case examined, an interference fringe pattern is not produced, so equation (2) cannot be directly applied to obtain the roughness value of the surface. However, since we want to relate the correlation degree between the scattered speckle patterns with a roughness parameter, the Fourier transformation which would originate the interference fringes is replaced by a simplified one-dimensional autocorrelation product of the intensity detected by the linear photodiode array. This operation also takes into account the statistical behaviour of the partially correlated speckle patterns. Thus, a transference curve can be obtained from which the roughness value is measured, with θ_1 and $\Delta\theta_1$ as known geometrical parameters.

If the camera LG_2 is located at a distance D from the surface S, far enough away for the Fraunhofer approximation to be valid, then the linear separation Δx between both speckle patterns at the plane of the photodiode array becomes

$$\Delta x = D\cos\theta_1\,\Delta\theta_1\,. \tag{3}$$

Therefore, the detected intensity distribution consists of a collection of speckle pairs, with a speckle separation for each pair given by equation (3), and with an average value size δx for each individual speckle grain:

$$\delta x \simeq 1{\cdot}22\,\lambda D/a\,, \tag{4}$$

where a is the diameter of the illuminated area of S. If N is the number of photodiodes in the array, and Δx_0 is the spacing between adjacent photodiodes, the two following conditions should be fulfilled in order to get enough spatial resolution for processing the speckle intensity

$$\Delta x > \delta x \gg \Delta x_0, \qquad N\Delta x_0 \gg \Delta x\,. \tag{5}$$

In this case, the information content of each speckle grain can be recovered, and furthermore, several speckle pairs can be adequately processed.

As was previously stated, for measuring the correlation degree between both crossed-linear polarized speckle patterns, a one-dimensional autocorrelation operation $W(x)$ of the resulting intensity distribution is performed. From $W(x)$, we are only interested in the value that this function takes when $x = \Delta x$; (the

speckle pattern separation). Taking into account the sampling nature of the recording procedure, the algorithm employed in order to carry out the intensity processing is a discrete autocorrelation operation which can be expressed as

$$W_k = \sum_{i=1}^{N} I_i I_{i+k} . \tag{6}$$

In equation (6), the following assumption is made: $I_j = 0$, if $j > N$; and the value of $k = \Delta x/\Delta x_0$ is selected so as to be an integer.

Now, we want to relate the intensity autocorrelation W_k with a surface roughness parameter in a similar way as was theoretically established by equation (2) for the case of the fringe visibility V. If we consider only one speckle pair from the detected intensity, the normalized autocorrelation $W = W_k/W_{k-0}$ can be thought as proportional to the quotient between the transmittance values associated with each speckle grain. In turn, this quantity is responsible for the contrast of the fringe pattern which the speckle pair would originate under Fourier transformation. Thus, it can be concluded that, as in the case of the interference fringes, a relationship: $W = W(R_s;\theta_1;\Delta\theta_1)$ can be stated, and where the specific function dependence is given, in each particular case, by the statistical behaviour of the surface. For a Gaussian distribution, such a relationship takes the form of an exponential function. Therefore, with a fixed value of θ_1, the surface roughness parameter is obtained through the transference curve $W = W(R_s;\theta_1;\Delta\theta_1)$, the value of $\Delta\theta_1$ being selected (by rotating the mirror M_2) in such a way that the measured autocorrelation value of W falls in the maximum change domain of the curve.

In the next section, we show some experimental results in order to illustrate the discussed method. Now, we analyse the influence of external features on the optical arrangement, such as surface vibration and tilt, on the system performance. We start by considering a vibration motion in the direction joining the surface S with the camera LG_2, with an amplitude A_z and a frequency ν. If ν_0 is the scanning frequency of the photodiode array, two cases can be considered: $\nu_0 \gg \nu$, and $\nu_0 \leqslant \nu$. In the first one, since the detection process takes place in a time interval very short compared with that associated with the surface oscillation, the roughness measurement is not affected by the vibration motion. In the second case, since the measuring time is comparable with the oscillation time, the value of A_z should be less than the average longitudinal size of the speckle grains δ_z in order that the roughness measurement should not be greatly affected by the surface vibration. Thus: $A_z < \delta_z \simeq \lambda D^2/a^2$. In most practical cases, this condition is satisfied since 1 mm $< \delta_z <$ 5 mm.

For the case of surface tilting, equation (1) should be replaced by

$$\Delta\theta_2' = \cos\theta_1 \, \Delta\theta_1 \, (1 - \tan\theta_1 \, \delta\theta_1) . \tag{7}$$

where now $\theta_1 + \delta\theta_1$ is the angle of incidence for the Σ_1 light beam. Therefore, the speckle patterns separation changes in the following way

$$\frac{\Delta x'}{\Delta x} = 1 - \tan\theta_1 \, \delta\theta_1 . \tag{8}$$

For a tilt angle $\delta\theta_1 = 2°$, and $\theta_1 = 45°$, the separation between the speckle patterns changes 3·5 %.

3. Experimental results

The optical arrangement shown in figure 1 was implemented in order to test this method. The light source was a 2 mw He–Ne laser, $\lambda = 0{\cdot}633$ μm. Two linear cameras LG_1 and LG_2 were used, each one provided with a 512×1 photodiode array. The spacing between adjacent photodiodes was: $\Delta x_0 = 13$ μm. and the scanning time was 200 μ s. The distance D between the camera LG_2 and the surface S was selected as $D = 170$ mm, and the diameter of the illuminated area of S was $a = 2$ mm. Therefore, speckle grains with an average size $\delta x = 65$ μm are detected by the photodiode array. In these conditions, the validity of equation (5) is established, and the spatial resolution of the detector is enough for processing the speckle pattern information. In figure 2, the double speckle pattern intensity for the case of a surface having an arithmetic roughness value $R_a = 12{\cdot}5$ μm is shown. In order to verify the system performance, Rugotest plane-ground comparison standards were employed with the following R_a roughness values: 1·6 μm, 3·2 μm, 6·3 μm, 12·5 μm and 25 μm. In figures 3, 4 and 5, the measured autocorrelation parameter W is plotted against the angular separation $\Delta\theta_1$ (expressed in arc min), for the roughness values $R_a = 3{\cdot}2$ μm, 6·3 μm and 25 μm, respectively. Finally, in figure 6, the autocorrelation value W measured for varying surface roughness is shown for a constant angular separation $\Delta\theta_1 = 30'$.

4. Conclusions

A speckle correlation method for the real-time measurement of surface roughness parameters is proposed. Two, non-interfering, partially correlated speckle patterns are simultaneously detected by a linear photodiode array. Their correlation degree depends on the surface roughness, and on the geometrical configuration of the optical system. From the speckle intensity autocorrelation, the roughness value of the surface is obtained. Some advantages of this method

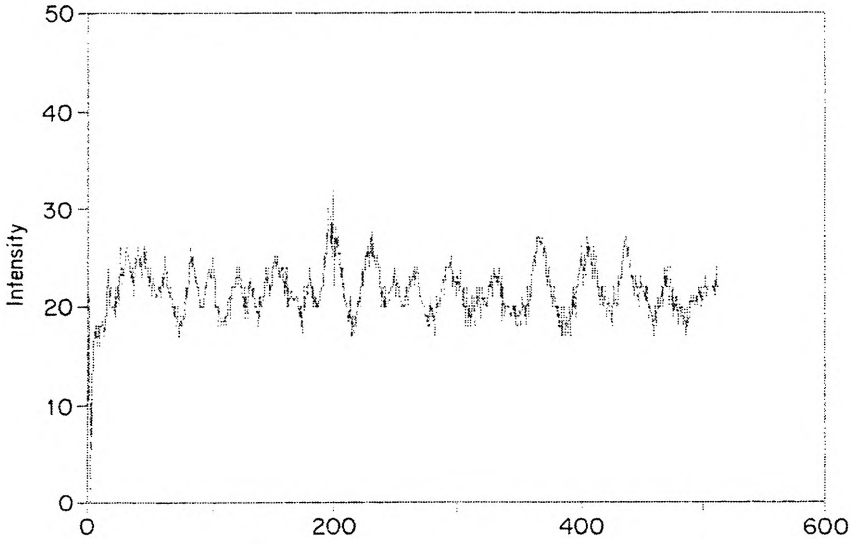


Figure 2. Intensity distribution of a recorded double speckle pattern.

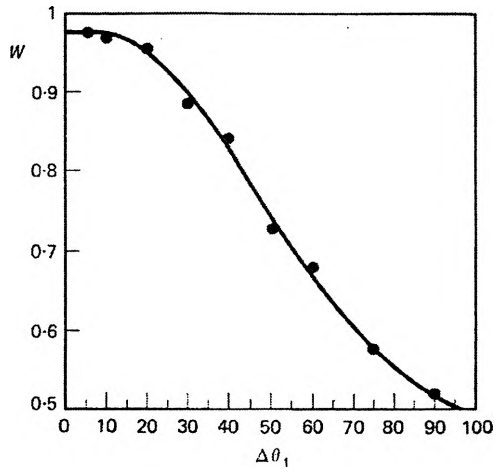


Figure 3. Normalized autocorrelation W measured for several values of $\Delta\theta_1$, for a surface roughness $R_a = 3{\cdot}2$ μm.

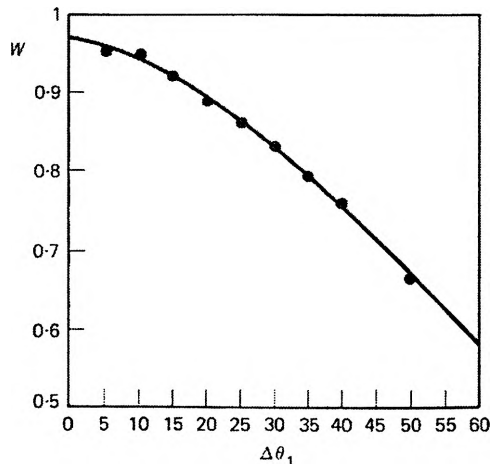


Figure 4. Normalized autocorrelation W measured for several values of $\Delta\theta_1$, for a surface roughness $R_a = 6{\cdot}3$ μm.

are: simple optical implementation which can be easily adapted for industrial applications, continuous real-time measuring capability up to about ten measurements per second, and low sensitivity to misalignments. The main disadvantage arises from the fact that a one-dimensional autocorrelation operation is performed (instead of a two-dimensional one), and hence, the signal-to-noise ratio obtained is not very high.

Acknowledgment

The work was supported by CONICET (grant PID 3-065400/88).

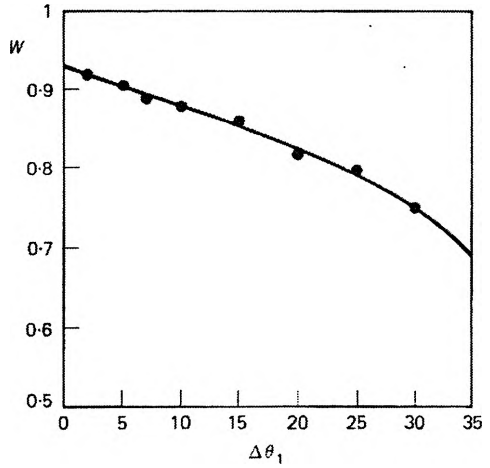


Figure 5. Normalized autocorrelation W measured for several values of $\Delta\theta_1$, for a surface roughness R_a = 25 μm.

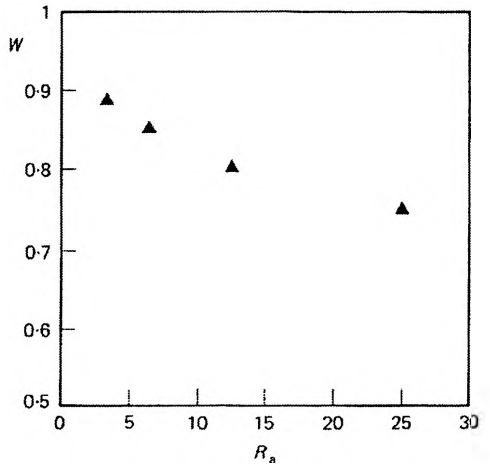


Figure 6. Normalized autocorrelation W against R_a for an angular separation $\Delta\theta_1$ = 30'.

References

[1] Beckmann, P., 1967, *Progress in Optics* VI, edited by E. Wolf (Amsterdam: North Holland), p. 55.
[2] Chandley, P. J., 1976, *Opt. quant. Electron.*, **8**, 323.
[3] Chandley, P. J., 1976, *Opt. quant. Electron.*, **8**, 329.
[4] Brodmann, R., Gerstorfer, O., and Thurn, G., 1985, *Opt. Engng*, **24**, 408.
[5] Fujii, H., and Asakura, T., 1974, *Optics Commun.*, **11**, 35.
[6] Ohtsubo, J., and Asakura, T., 1976, *Optik*, **45**, 65.
[7] Fujii, H., Asakura, T., and Shindo, Y., 1976, *J. opt. Soc. Am.*, **66**, 1217.
[8] Fujii, H., and Asakura, T., 1977, *Optics Commun.*, **21**, 80.
[9] Léger, D., Mathieu, E., and Perrin, J. C., 1975, *Appl. Optics*, **14**, 872.
[10] Léger, D., and Perrin, J. C., 1976, *J. opt. Soc. Am.*, **66**, 1210.

Optical interferometric studies of a confined liquid free surface: meniscus-effect compensation and time evolution of the surface

Lea V. Bourimborde
Alejandro Tonso
Lía M. Zerbino
Mario Garavaglia
Centro de Investigaciones
Opticas (CONICET-CIC)
Casilla de Correo 124
La Plata 1900, Argentina
E-mail: postmaster@ciop.edu.ar

Abstract. A fruitful approach to the studies of a liquid free surface is demonstrated. Using optical interferential techniques, the free surface of nonvolatile and volatile confined liquids is analyzed. Various wall container types are investigated. Besides the classical plane wall, experiments are performed by using cylindrical and toroidal walls. In these last cases, the meniscus effect that affects the free surface of the liquid is compensated. Then, it is possible to obtain completely flat free surfaces of liquids up to 80% of their total. Interferometric experiments are also described to measure the inclination of the site with respect to the local horizon, represented by the liquid flat free surface, and to follow the temporal evolution of such free surfaces affected by different conditions.

Subject terms: optical interferometry; optical free surface; meniscus compensation; optical liquid level.

Optical Engineering 35(1), 70–75 (January 1996).

1 Introduction

As is well established, the free surface of a confined liquid is not a plane. In the case of a container of large dimensions, however, it is possible to consider that a small portion of the free surface be planar. To some extent, this small portion is located at the central part of the entire liquid surface.

Nevertheless, in some particular and practical situations it is convenient or necessary that all of the free surface be a plane, in spite of the fact that the container had small dimensions. These cases are present in the studies of aged liquid surfaces or evaporation produced at liquid surfaces. In addition, planar free surface of liquids are important factors in the design and development of high accuracy levels.

Various optical methods were introduced to experimentally analyze the different physical phenomena that occur at the interface of two media. Holographic interferometry,[1] differential interferometry,[2] and ultrasonic holography[3] can be cited as examples. The free surface of a liquid has also been used as a metrological reference surface.[4–6]

In this paper, we offer

1. a new experimental solution to obtain plane free surfaces of confined liquids in small containers
2. the use of such an approach in the development of an optical device of very small dimensions to check in a real-time mode the flatness of the liquid free surface
3. the possibility to follow up the temporal evolution of the free surface of a confined volatile liquid due to its evaporation
4. the possibility to follow up the changes in the horizontal position of small pieces in a real-time mode.

The experimental results obtained with the liquid-optical device are the magnitude, the direction, and the sign of the angular changes of the liquid surface. The threshold of the sensitivity of the overall device is $\Delta = \pm 7 \times 10^{-6}$ rad.

As a first step, a container with toroidal borders confining nonvolatile liquids was studied. A loading tube serves to load

Paper ARG-12 received Apr. 18, 1995; revised manuscript received May 29, 1995; accepted for publication May 30, 1995.
© 1996 Society of Photo-Optical Instrumentation Engineers. 0091-3286/96/$6.00.

and unload the liquid into the cavity of the container. The loading process was followed by optical interference and the interferometrical information was real-time recorded and each image was digitally processed.

The free surface of the liquid can be considered as a phase object and then the monochromatic light reflected and refracted on it contain information related with its topography. Such information can be revealed by simple interferential techniques.

The dynamic analysis of such optical information, however, presents a high degree of complexity, because it is necessary to control a large number of experimental parameters to achieve quantitative evaluations of acceptable quality.

2 Description of the Experimental Method

The topological shape of the free surface of a confined liquid depends on the equilibrium of the gravitational and capillary forces. Formally, they depend on the capillary constant a value and the contact angle formed between the liquid surface and the container wall. In the case of a plane vertical wall, the profile of the liquid free surface is expressed as

$$x=\frac{a}{\sqrt{2}}\cosh^{-1}\left(\frac{\sqrt{2a}}{y}\right)-a\left(2-\frac{y^2}{a^2}\right)^{1/2}+x_0 ,$$

where x_0 is determined taking into account that $(dy)/(dx) = -\cot\theta$ at $x=0$, and that y vanishes at $x\to\infty$ (Ref. 7).

Nevertheless, it is impossible to develop a plane liquid free surface using plane vertical walls because of the influence of meniscus. Because of that, to obtain a plane liquid free surface it is necessary to introduce a cylindrical wall. Figure 1 answers this question. If the level of the liquid inside of the container is equal to h, its free surface will form with the geometrical tangent to the cylinder an angle α whose value will be equal to Θ. In that case, the influence of the meniscus is compensated by the wall, and the liquid free surface will be completely flat.

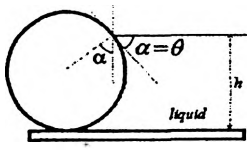


Fig. 1 When the surrounding walls have cylindrical shape, it is possible that $y=0$ (horizontality) when $\alpha=\theta$.

If the level of the liquid is lower or higher than h, the shape of the surface will appear as concave or convex according to the wetting function of the liquid-cylinder interface.

Assuming that the topological shape of the free surface is flat, it is possible to use it as a horizontal reference plane. Then, a container whose bottom is a transparent optical plane-parallel window can serve as an interferometrical level. Figure 2 describes the experimental setup.

The He-Ne laser and the inverted telescope with spatial filter provide a well-collimated monochromatic light beam. By using a front surface mirror, the plane wave illuminates the liquid container from the top. A beamsplitter collects the light waves coming from the free liquid surface and from first plane optical surface at the bottom of the container. A CCD TV camera captures the interference between both waves, sending the signal to the real-time image processor.

The liquid container is a 70- × 50-mm plastic rectangular cavity, whose walls are formed by cylindrical glass rods 8 mm in diameter. The container is sealed at its bottom by a plane parallel glass plate 10 mm thick and $\lambda/10$ flat. The entire container is located on a platform that is horizontally aligned using appropriate fine screws. Inside the described cavity, the toroidal ring is mounted, simply supported by the bottom glass plate. The dimensions of the toroidal ring are 5.4 mm for section diameter and 16.8 mm for the inner diameter.

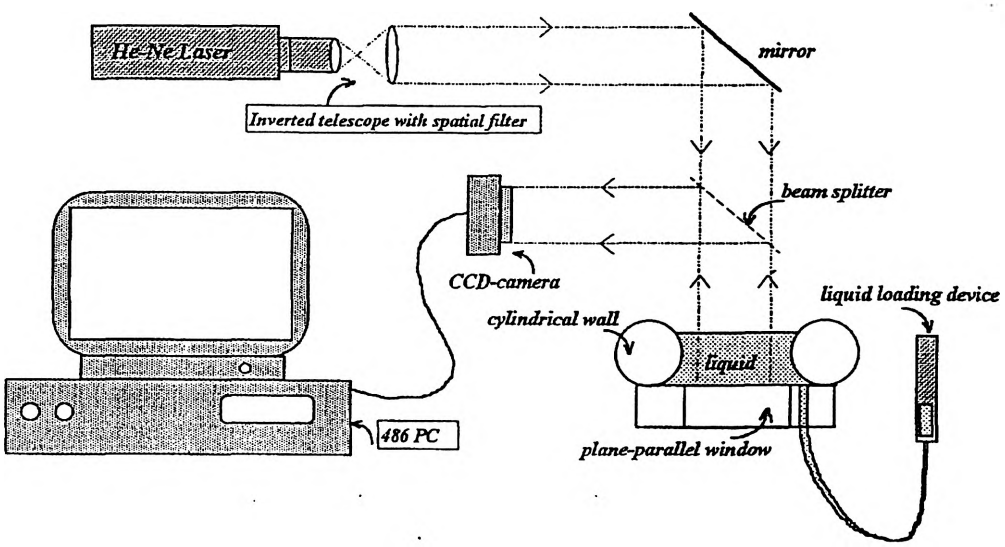


Fig. 2 Experimental setup.

The platform is conveniently isolated to avoid mechanical perturbations. It was designed and constructed as a hydraulic device to load and unload liquid to or from the container, respectively, which enables changes in the liquid free level surface with an accuracy $\Delta h = \pm 100$ nm, without perturbing the surface.

The different kind of experiments and measurements were performed using silicone oil (Dow Corning Fluid 350). At 25°C it has the following physical characteristics: viscosity = 350 cS, density = 0.97 g/cm^3, refractive index = 1.403, and surface tension = 21.1 dyn/cm (Ref. 8).

As long as the container is loading with the liquid, the free surface adopts different topologies: concave, plane, and convex, as shown in Fig. 3. Such surfaces act as mirrors that change shape according to the liquid level. When h reaches the appropriate value to compensate the meniscus effect making $\alpha = \theta$, the free liquid surface will be flat. This position is considered to be the setting point of the device. If the base platform on which the device is mounted adopts the horizontal position, the interference fringes that are observed while the free liquid surface shape is modified by loading liquid into the container appear as a symmetric pattern. This fact is assumed as to be the best criteria to fill the container until α is equal to θ. In addition, near the setting point, the fringes in the interference pattern become wider and more and more spaced, but they always maintain their symmetry.

3 Experimental Results

As mentioned before, when the liquid entering the container adopts level positions deeper or higher than h, the free surface looks like concave or convex mirrors. Then, the interference pattern observed on a screen changes according to the amount of liquid loaded into the container, as shown in Fig. 4(a). Figure 4(b) shows pictures of the interference pattern that demonstrate various steps of the loading operation of the container.

Figures 5, 6, and 7 are pictures of the interference pattern produced with the device. In these experiments, those surfaces that are less than 0.633 μm from a geometrical plane are accepted as "flat" surfaces. Obviously, 0.633 μm is the wavelength of the red He-Ne laser used to illuminate the device.

Figure 5 corresponds to the rectangular container 50 mm wide and 70 mm long with vertical plane walls. The interference pattern is deformed because of the lack of flatness along the entire free liquid surface. The zone that can be considered as a plane is less than 28% of the total surface.

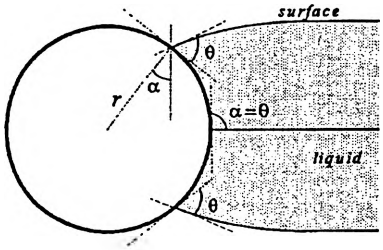
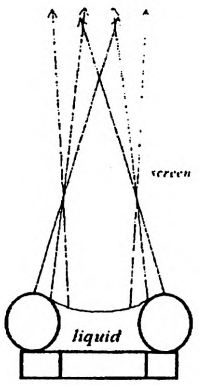
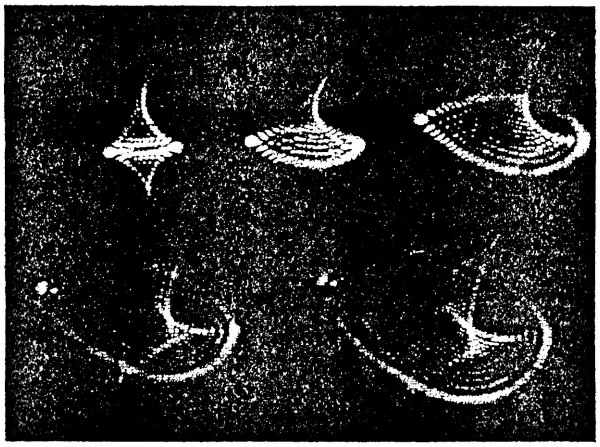


Fig. 3 Depending on the liquid level, the free surface will be concave, plane, or convex.



(a)



(b)

Fig. 4 (a) Free surface looks like a concave mirror. (b) Interference pattern follows the liquid-loading operation.

Figure 6 corresponds to the same sized rectangular container but with circular cylinders acting as walls. In spite of the fact that the liquid level did not reach a high enough altitude h to be $\alpha = \theta$, the zone that is considered a plane is almost 37% of the total surface.

Figure 7 corresponds to the same experimental setup as that of Fig. 6, but the level of the liquid is almost that for

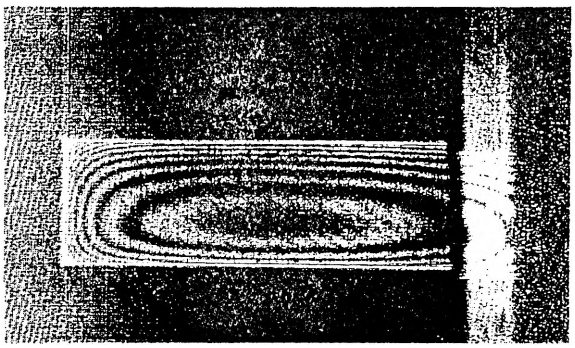


Fig. 5 Interference pattern observed in a plane walled container of rectangular shape. The flat portion of the entire surface is less than 28%.

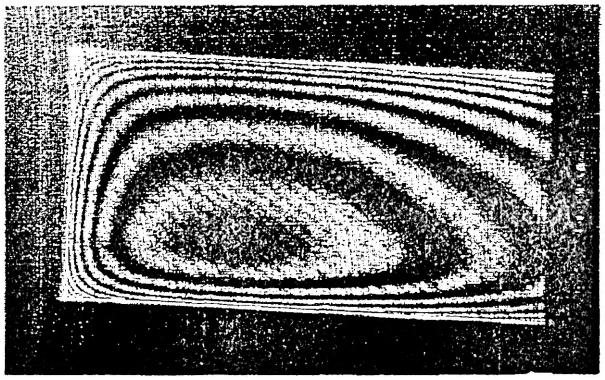


Fig. 6 Interference pattern observed in a circular section walls container of rectangular shape. The flat surface is almost 37%; $\alpha < \theta$.

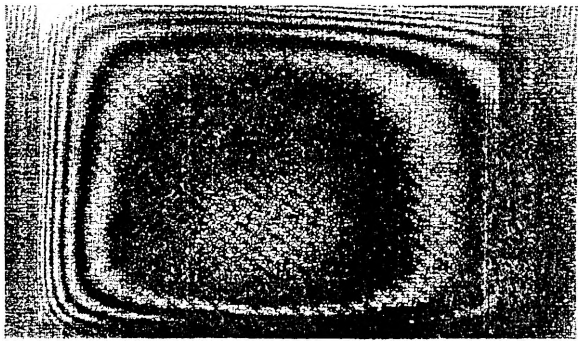
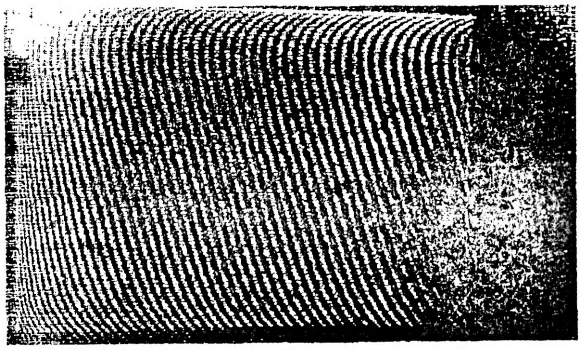
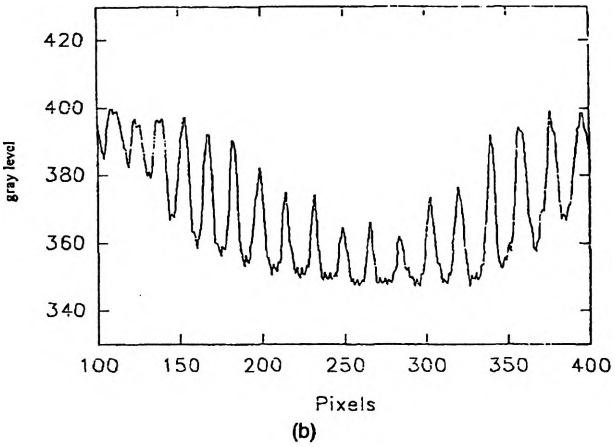


Fig. 7 Same as Fig. 6. The flat surface is 80%; $\alpha \approx \theta$.



(a)



(b)

Fig. 8 (a) Electronic picture and (b) densitometric trace to measure inclination changes of the optoliquid device.

which $\alpha = \theta$ and the effect of the border is compensated to observe a plane free surface. In this case, 80% of the total surface can be considered as a plane. In addition, because this planar zone of the free surface represents the horizontal plane of the site, it was possible to measure the inclination of the optical window at the bottom of the container. The angles of inclination are $\varphi_x = 7.5 \times 10^{-6}$ rad and $\varphi_y = 8.1 \times 10^{-6}$ rad in the x and y directions, respectively.

If the mounting base of the liquid-optical device is arbitrarily inclined, it is easy to measure its lack of horizontality.

Figure 8 is a picture of the interferential pattern observed and its densitometric profile captured by perpendicularly scanning the fringe family. Measurements resulted in inclination of $\varphi = 3.1 \times 10^{-4}$ rad in a direction that forms an angle of 19.5 deg with respect to the x axes.

Figures 9, 10, and 11 correspond to a series of consecutive pictures that demonstrate the temporal evolution of the interferential pattern. Along the time of observation, the effect of the meniscus was compensated by maintaining $\alpha = \theta$. Every picture shows the fringe patterns and their corresponding densitometric traces. Fringes, that are equally spaced by e, are identified by correlative digits representing the interferential order with respect to the center of the patterns, as shown in Fig. 12.

These observations enable us to demonstrate that evaporation is preferentially produced at the middle of the free surface. In fact, comparing the consecutive temporal pictures it is easy to observe that fringes corresponding to equal liquid thickness appeared at distances farther and farther from the center of the pattern. In addition, in these zones of the liquid free surface the distances between fringes are also greater and greater as a function of time. Thus, the evaporation phenomena begin at the middle of the liquid free surface and slowly propagate to the borders of the container, as stated before.

4 Conclusions

A method to compensate the effect of the border to obtain a plane free liquid surface appears to be of great interest in studying the properties of fluids. It enables us to easily perform experiments at the laboratory, on which can be assumed conditions of infinitely extended surfaces by using, in fact, very small containers.

The liquid-optoelectronic device is easy to build and is versatile and flexible to use. It acts as an interferential liquid level, the performance of which represents progress with respect to other liquid levels.[9-11] The proposed device is also very stable from the mechanical point of view and the method has an extended range to observe and measure different kinds of effects with a threshold sensibility at least 10 times greater than others.



(a)

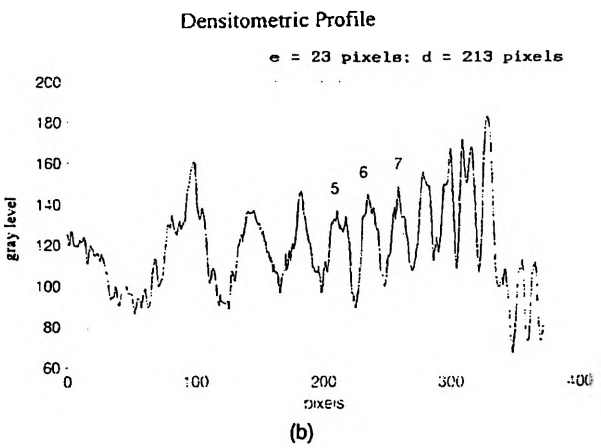


Fig. 9 (a) Electronic picture and (b) densitometric trace. Fringes 5, 6, and 7 are equally spaced.



(a)

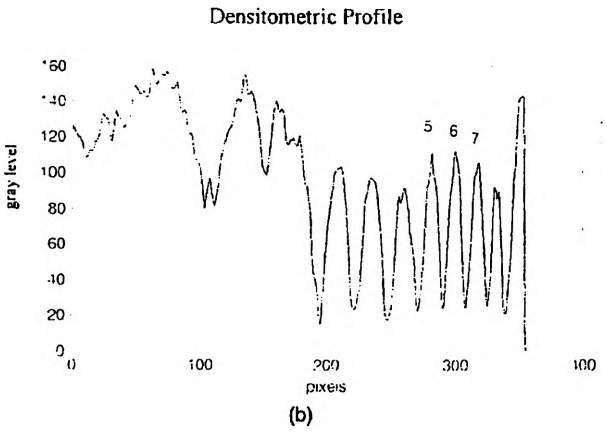


Fig. 10 (a) Electronic picture and (b) densitometric trace. Fringes 5, 6, and 7, which are equally spaced, are moved from the center to the border of the container because of liquid evaporation.

In addition, this device could be employed to measure surface tension, the constant of capillarity, and other interesting parameters of fluids in an ample range of temperature and pressure conditions.

Acknowledgments

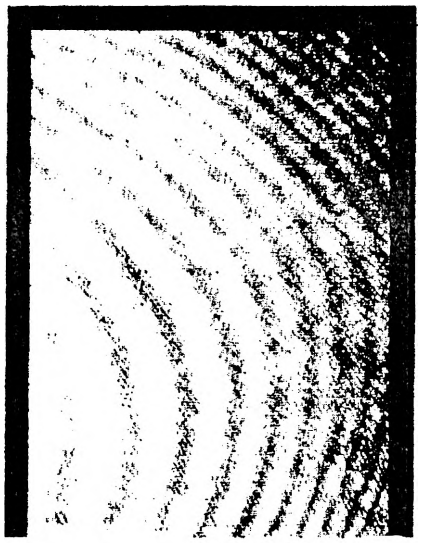
This work was supported by CONICET (Grants PID No. 3071800/91/92 and PID-BID 1116/91).

References

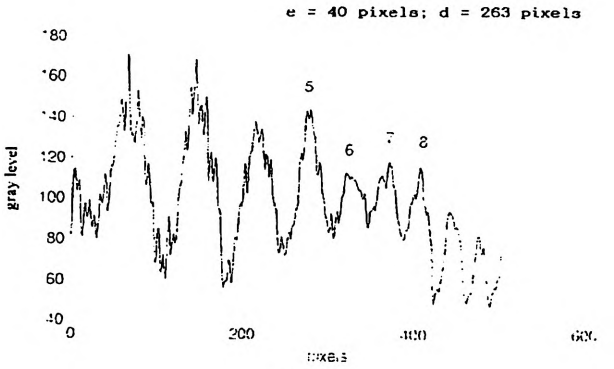
1. K. D. Hinsch, "Holographic interferometry of surface deformations transparent fluid," *Appl. Opt.* **17,** 3101–3107 (1978).
2. A. D. Nikolov, A. S. Dimitrov, and P. Kralchelvsky, "Accuracy of the differential-interferometric measurements of curvature. Experimental study with liquid drops," *Opt. Acta* **33,** 1359–1368 (1986).
3. R. K. Muller and N. K. Sheridon, "Sound holograms and optical reconstruction," *Appl. Phys. Lett.* **9,** 328–329 (1986).
4. S. F. Jacobs and J. G. Small, "Liquid level interferometer," *Appl. Opt.* **20,** 3508–3513 (1981).
5. M. Cervantes, "Liquid level interferometer," *Appl. Opt.* **23,** 3512–3514 (1984).
6. A. Livnat and O. Kafri, "Moire technique for measuring liquid level," *Appl. Opt.* **21,** 2868–2870 (1982).
7. L. D. Landau and E. M. Lifshitz, *Fluid Mechanics,* p. 230–237, Pergamon, London (1959).
8. D. Corning, "Información sobre fluidos de silicona," DOW CORNING, Buenos Aires, Mexico, Miami.
9. W. Jordan, *Tratado General de Topografía,* 3rd ed., pp. 215–229, Gustavo Gili S.A., Barcelona (1961).
10. F. Dominguez Garcia-Tejero, *Topografia General y Aplicada,* 7th ed., pp. 85–94, Dossat, S.A., Madrid (1981).
11. R. E. Davis and F. S. Foote, *Tratado de Topografía,* Aguila S.A. de ediciones (1964). (Translation of *Surveying Theory and Practice,* McGraw-Hill Book Company, New York, Toronto, London) 4th edition.



Lea V. Bourimborde received her MS degree in 1989 from the Universidad Nacional de La Plata, where she teaches physics and is a PhD student. She is involved in research activities at Centro de Investigaciones Opticas (CIOp), Argentina. Her research includes optical signal processing.



(a)



(b)

Fig. 11 (a) Electronic picture and (b) densitometric trace. Fringes 5, 6, 7, and 8, which are equally spaced, are near the border.



Alejandro Tonso received his MS degree in 1988 from the University Nacional de La Plata, where he is presently a PhD student. He has research activities at Centro de Investigaciones Opticas (CIOp), Argentina. He is involved in optical image processing.

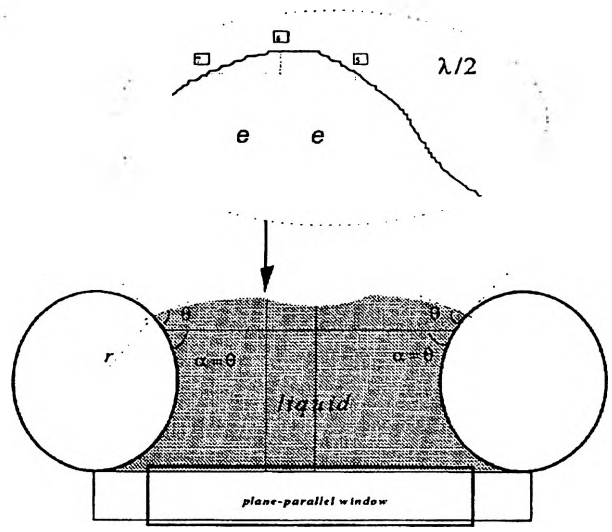


Fig. 12 Fringes 5, 6, and 7, which are equally spaced by *e*, migrate from the center to the border of the container because of liquid evaporation.

Lía M. Zerbino: Biography and photograph appear with the paper "Optical processing by birefringence modulation" in this issue.



Mario Garavaglia received the Licenciado degree in physics from the Universidad Nacional de La Plata (UNLP) in 1960. He spent a postgraduate research stay at Uppsala University, Sweden, in 1964 to 1965, working with Prof. Kjell Bockasten and Prof. Bela Lengyel. He received a PhD in physics from UNLP in 1965. Since 1969 he has been a professor of physics at UNLP and he has directed 20 doctoral theses in physics. In 1977 he founded the Centro de Investigaciones Opticas (CIOp) and was its first director until 1992. He is currently a researcher with CONICET, the Argentinian National Scientific and Technologic Research Council. In 1982 he was a member of the World Health Organization/International Radiation Protection Association task group on Environmental Health Criteria for Lasers. In the same year he was invited by Prof. Dieter Kind, president of the Comité Consultatif pour la Définition du Metre (CDDM), to take part in the seventh session of the CDDM to analyze the ultimate scientific and technologic results and to propose the appropriate wording for the 1983 international definition of the meter based on the constancy of the speed of the light in the vacuum. From 1992 to 1994 he was member of the board of directors of CONICET. He has authored or coauthored more than 100 scientific and technologic papers and four books and holds three patents. Presently he is primarily involved in teaching at UNLP and doing R&D in optics and lasers applications in technology and biomedicine.

ELSEVIER

1 January 1997

Optics Communications 133 (1997) 27–32

OPTICS COMMUNICATIONS

Optical velocimetry based on the spatial correlation of off-axis image speckle patterns

J.A. Pomarico [a], N.A. Russo [a], E.E. Sicre [a], D. Patrignani [b]

[a] *Centro de Investigaciones Opticas, Casilla de Correo 124, (1900) - La Plata, Argentina*
[b] *Departamento de Física, Universidad Nacional del Sur, (8000) - Bahía Blanca, Argentina*

Received 19 February 1996; accepted 19 June 1996

Abstract

A method is proposed for measuring the linear velocity of a moving rough surface. It is based on maximizing the spatial correlation between two laterally shifted image speckle patterns. Besides, an expression of a spatially variant point-spread function is given, which modifies the spatial distributions of the off-axis image speckle patterns.

Keywords: Speckle; Velocimetry; Image formation

1. Introduction

The finite 'mean life' of the speckle pattern is a limitation to be considered for studying moving rough surfaces. For the case of a plane object describing a linear motion, the speckle pattern originating from the surface under coherent illumination encodes information about velocity, roughness, texture, etc. In order to obtain a real-time measurement of such surface parameters, several methods were developed where the speckle intensity distribution is detected and processed following a spatial or a temporal approach [1–13]. In most cases, the speckle pattern is analogically or digitally integrated for performing a correlation operation between successive signals from which the magnitude under study can be derived. The condition to be fulfilled to achieve a reliable measurement becomes: $a/v \gg \tau$, being a the spot diameter of the illuminating beam, v the surface velocity, and τ the detection time, which depends on the detector response, the laser intensity and the optical configuration. However, if the surface velocity is large enough so that the above condition does not fully accomplish, each speckle pattern to be correlated becomes 'blurred', so resulting in a loss of measuring accuracy. Therefore, it is worthwhile for measurement purposes to investigate optical arrangements that allow to record and process high contrast speckle patterns originated from such moving surfaces.

In this paper, we analyze a method where a laser beam is linearly scanned in the same direction of the moving surface. The light scattered from the surface at the different locations of each scan gives rise to laterally shifted speckle patterns, which are uncorrelated unless two conditions are fulfilled: (i) the scanning rate of the laser beam matches the surface velocity, and (ii) the angle of incidence of the laser beam remains constant over the whole scanning region. Therefore, the proposed optical arrangement is designed to satisfy these two conditions in order to achieve a measurement of a spatial correlation pa-

0030-4018/97/$17.00 Copyright 1997 Elsevier Science B.V. All rights reserved.
PII S0030-4018(96)00442-7

rameter between two speckle patterns, from which the surface velocity can be derived. As the employed optical system images on a photodetector the laterally shifted speckle patterns to be correlated, an additional effect should be considered; namely, a spatially variant point-spread function that modifies the measured correlation parameter.

In Section 2, we describe the principle of the method. Then, in Section 3, we derive a general expression for the off-axis spatially variant point-spread function and a particular case is analyzed: a system affected by distortion, which is one of the dominant off-axis aberrations. Finally, in Section 4, the experimental conditions and the range of operation of the method are discussed and some experimental results are presented.

2. Description of the method

By referring to Fig. 1, a scanning laser beam illuminates the moving surface S under study along the x-axis with constant velocity and angle of incidence. This illumination condition is provided by a K–theta lens system [14,15], which consists of a two-element lens that originates an emerging beam parallel to its optical axis, at a distance proportional to the product of the focal length and the angle made by the incident beam. This beam emanates from the front focal point of the lens where a rotating polygon mirror is placed.

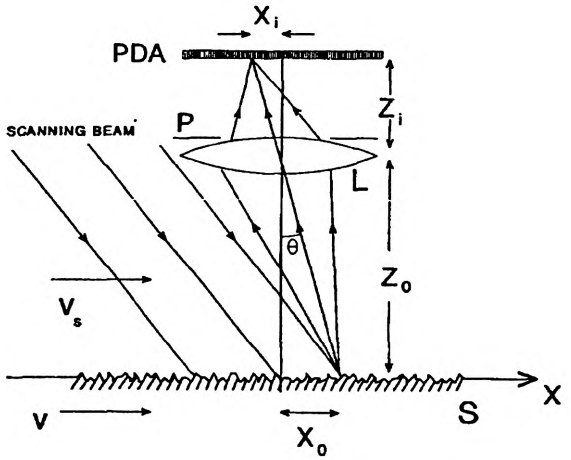


Fig. 1. Experimental setup.

For a certain beam location x_0, the light scattered from S is collected by the optical system L to form an image speckle pattern, centered at $x = x_i = mx_0$, being m the lateral magnification. The intensity distribution recorded by the linear photodiode array PDA is given by the imaging relationship

$$I(x;\, x_i) = \int_{-\infty}^{\infty} p_\theta(x;\, x')\, p_\theta^*(x;\, x'') \times R_s(x';\, x'')\, \mathrm{d}x'\, \mathrm{d}x'', \qquad (1)$$

where $R_s(x';\, x'')$ is a function which depends on the statistical properties of S, and $p_\theta(x;\, x')$ is the point-spread function corresponding to the coordinate $x_i = mz_0 \operatorname{tg}\theta$, being z_0 the distance between L and S.

In a previous work [9], a temporal correlation parameter was defined,

$$\Gamma = 1 - K \sum_{j=1}^{N} |I(x_j;\, t) - I(x_j;\, t+\tau)|, \qquad (2)$$

for the case in which a stationary laser beam illuminates, on-axis, the moving surface. In Eq. (2), $I(x_j;\, t)$ and $I(x_j;\, t+\tau)$ denote the successive (separated by τ seconds) detected intensities by a linear N-photodiode array, and K is a normalization constant. The illuminated zone of the surface changes between two data samples and, consequently, Γ drops as the surface velocity increases. Therefore, a transference curve $\Gamma = \Gamma(v)$ is obtained from which the velocity v can be derived. However, the measuring range using this approach is limited to velocities up to 1 m/s.

For the optical arrangement shown in Fig. 1, we rewrite the parameter Γ given by Eq. (2) in the form of a spatial correlation

$$\Gamma_i = 1 - K \sum_{j=1}^{N} |I(x_j;\, 0) - I(x_j - x_i;\, x_i)|, \qquad (3)$$

where $I(x_j;\, 0)$ and $I(x_j - x_i;\, x_i)$ are the speckle intensities corresponding to the on-axis beam location ($x_i = x_0 = 0$), and to an off-axis situation ($x_i \neq 0$), respectively. The value of x_i should be selected large enough to avoid overlapping between both speckle intensity distributions to be correlated. Taking into account Eq. (3), the relationship $\Gamma_i =$

$\Gamma(x_i)$ defines a curve where Γ diminishes as the value of the coordinate x_i increases. The slope of this curve depends on the difference between the laser scanning velocity v_s and the surface velocity v, reaching a minimum value when the condition $v_s = v$ is met. Under this situation, the illuminated area S remains unchanged over the whole scan, so originating maximum correlation between the on-axis and any of the off-axis image speckle patterns. Thus, for performing a measurement of the surface velocity, the scanning rate of the laser beam (i.e. the scanning velocity v_s) should be varied to obtain the above mentioned condition.

The measuring procedure can be summarized in the following steps: (i) for a given value of v_s, the on-axis ($x_i = 0$) image speckle pattern is recorded and stored; (ii) an off-axis (centered at $x_i \neq 0$) image speckle pattern, corresponding to the same scan, is also recorded and stored. For obtaining maximum measurement sensitivity, x_i is chosen at the extreme of PDA: $x_i = x_{i,\max}$. (iii) The correlation parameter $\Gamma(x_{i,\max})$ is calculated by means of Eq. (3). (iv) The scanning velocity v_s is varied and the steps (i) to (iii) repeated until $\Gamma(x_{i,\max})$ is maximized, and so, $v_s = v$.

In the above description, the maximum attainable value of $\Gamma(x_i)$ never reaches the ideal value of unity due to the variations of the point-spread function of the imaging lens L as the illuminated region of S moves away from the optical axis. In order to give an explanation of this effect, we derive in the following section an expression for this spatially variant point-spread function.

3. Off-axis point-spread function

For simplicity, we perform a one-dimensional treatment. If we consider the line joining the object source point x_0 with the corresponding image point x_i as a new optical axis z', the point-spread function $p(x;\theta)$ can be thought as resulting from the Fraunhofer diffraction pattern of a 'tilted' aperture given by the pupil function $P(\xi)$ of the imaging lens L (see Fig. 1). For the particular on-axis case ($x_0 = 0$, and so $z' = z$), the well-known Fourier transform relationship,

$$p(x;\theta=0) = \exp\left(\frac{i\pi x^2}{\lambda z_i}\right)\int_{-\infty}^{\infty} P(\xi) \times \exp\left(-\frac{2\pi i x\xi}{\lambda z_i}\right) d\xi, \tag{4}$$

is obtained where $z_i = mz_0$ is the image distance. For the general off-axis case ($x_0 \neq 0$), the amplitude distribution $p(x';\theta)$, along a tilted axis x', orthogonal to z', centered at the image point x_i, is still given by the Fourier transform of $P(\xi)$ but in a new set of spatial frequencies which depends on the value of θ [16]. Therefore, all the properties of the Fourier transform can be straightforwardly reformulated for the off-axis case, but calculated in a modified coordinate system. By using the result found in Ref. [16] for the Fraunhofer pattern diffracted by a tilted aperture, we obtain the following expression for the off-axis point-spread function:

$$p(x';\theta) = \int_{-\infty}^{\infty} P(\xi)\exp[-2\pi i\alpha(x')\xi]\, d\xi, \tag{5}$$

where the spatial frequency $\alpha(x')$ becomes

$$\alpha(x') = \frac{\cos\theta\, x'}{\lambda r_i} - \frac{\sin\theta\, x'^2}{2\lambda r_i^2}, \tag{6}$$

being $r_i = z_i/\cos\theta$ the distance between the center of the exit pupil of L and the image point. It should be noted that a quadratic phase term has been neglected in Eq. (5). Hence, the image formation of an off-axis point source can be stated as follows. The Fourier transform which relates the impulse response with the pupil function remains valid but the coordinate axis (i.e. the spatial frequency) changes accordingly with Eq. (6). However, since we are interested to process image information in a fixed recording plane, parallel to the x-axis, Eq. (6) is rewritten as

$$\alpha(x) = \frac{\cos\theta\, x}{\lambda z_i} - \frac{\sin\theta\, x^2}{2\lambda z_i^2} = \alpha_0\left[\cos\theta - \frac{\sin\theta\, x}{2z_i}\right], \tag{7}$$

where $\alpha_0 = x/\lambda z_i$ is the spatial frequency coordinate for the on-axis case. Thus, the point-spread function becomes

$$p(x;\theta) = \int_{-\infty}^{\infty} P(\xi)\exp[-2\pi i\alpha(x)\xi]\,d\xi. \tag{8}$$

Next, we analyze the effect of the impulse response, given by Eq. (8), on the image speckle pattern assuming a pupil function $P(\xi)$ of the form

$$P(\xi) = P_0(\xi)\exp\left[\frac{2\pi i}{\lambda}\frac{W_d}{a}\xi\right], \tag{9}$$

where $P_0(\xi)$ represents a uniform rectangular aperture of width $2a$, and W_d is the Seidel distortion coefficient measured in units of the wavelength λ. By employing Eqs. (7), (8) and (9), the intensity impulse response results in

$$|p(x;\theta)|^2 = (2a)^2\,\mathrm{sinc}^2\left[2a\left(\frac{\cos\theta}{\lambda z_i}x - \frac{W_d}{a\lambda} - \frac{\sin\theta}{2\lambda z_i^2}x^2\right)\right]. \tag{10}$$

As in the on-axis, free aberration case, where the mean width of the point-spread function is $\Delta x_0 = \lambda z_i/a$, in the off-axis situation the corresponding mean width can be derived from Eq. (10) to give

$$\Delta x \simeq \frac{\lambda z_i}{a\cos\theta}\left(1 + \frac{2W_d}{\lambda}\right). \tag{11}$$

Therefore, for increasing values of the angle θ, the extent where the impulse response is significantly different from zero increases proportional to both, $1/\cos\theta$ and the amount of distortion. The effect of other lens aberrations, such as spherical aberration or astigmatism, will further modify the shape of the point-spread function.

An alternative approach to space-variant image formation (by analyzing the effects of shift-variance on the decay of the modulation transfer function of coherent systems) was performed by Tichenor and Goodman [17], who concluded that the isoplanatic region is restricted to object points lying inside a circle of about 1/4 of the aperture radius.

4. Experimental results and discussion

In order to experimentally verify the method proposed in Section 2, we employed the optical setup shown in Fig. 1. A rotating polygon, illuminated by an unexpanded laser beam at the location of the front focal point of a K–theta lens, produces a uniform beam scanning along a direction that coincides with that of the moving surface S. Taking into account the finite length of the linear photodiode array PDA: $l^{(i)} = N\Delta_0$, N being the number of photodiodes and Δ_0 the separation between adjacent photodiodes, a linear illuminated region of S given by $l^{(0)} = l^{(i)}/m$ can be imaged on PDA. In our case, $N = 2048$, $\Delta_0 = 13$ μm, and L is a one-element positive lens of focal length $f = 60$ mm (for which $m = z_i/z_0 = 90$ mm/180 mm = 0.5), so resulting in $l^{(0)} = 53$ mm and $\theta_{max} \simeq 16°$. On the other hand, at a given instant, the laser spot illuminates a region of S having a diameter $\delta x^{(0)} \simeq 2$ mm, producing an image speckle pattern at PDA with a spatial extent $\delta x^{(i)} = m\delta x^{(0)} \simeq 1$ mm. As it was explained in Section 2, the distance x_i between the on-axis and a certain off-axis image speckle pattern should be larger than the extent of each individual speckle distribution for avoiding overlapping when Eq. (3) is used. Thus, in our case, the minimum value of x_i results in $x_{i,min} \simeq \delta x^{(i)} \simeq 1$ mm, and of course the maximum attainable value becomes $x_{i,max} \simeq l^{(i)}/2 = 13$ mm. Besides, as the speckle pattern should be resolved by PDA, each individual speckle grain, having a mean size $\Delta x_i \simeq \lambda z_i/a$ is sampled by more than one photodiode (e.g. 4–5 photodiodes). As $\lambda = 0.633$ μm and $z_i = 90$ mm, this condition requires that the aperture radius becomes $a \simeq 2$ mm. If the detection time of PDA is $\tau = 1$ ms, then the time required to detect a given image speckle pattern becomes $\tau' = \tau/(l^{(i)}/\delta x^{(i)}) = 38$ μs. Thus, for recording a high contrast image speckle pattern, $\tau' < \delta x^{(0)}/v$ should be satisfied, from which the surface velocity to be measured is limited to the range $v < 50$ m/s.

In order to evaluate the influence of both the space-variance and the distortion aberration effects on the image speckle patterns to be correlated, some computer simulations were carried out, which illustrate the results found in Eqs. (10) and (11). As can be derived from Fig. 2, the correlation degree be-

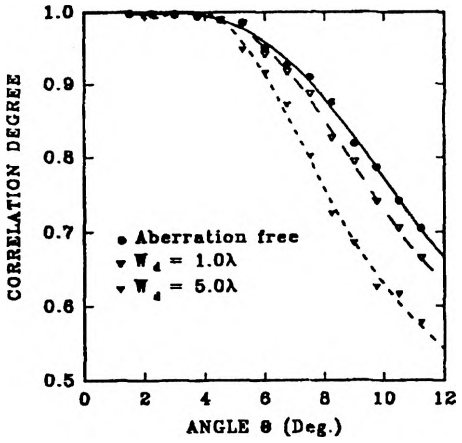


Fig. 2. Influence of space-variance and distortion aberration on the speckle correlation degree.

tween the on-axis ($x_i = 0$) and the successive off-axis ($x_i \neq 0$) image speckle patterns remains almost unchanged for values of $\theta \lesssim 4°$. For larger values of θ, the correlation degree drops, this effect being more noticeable for increasing W_d.

In Fig. 3, the parameter Γ is plotted for different values of x_i. Each measurement is obtained by performing the spatial correlation between the on-axis image speckle pattern and a given off-axis image speckle pattern, centered at x_i, as is defined in Eq. (3). These results were obtained while both the

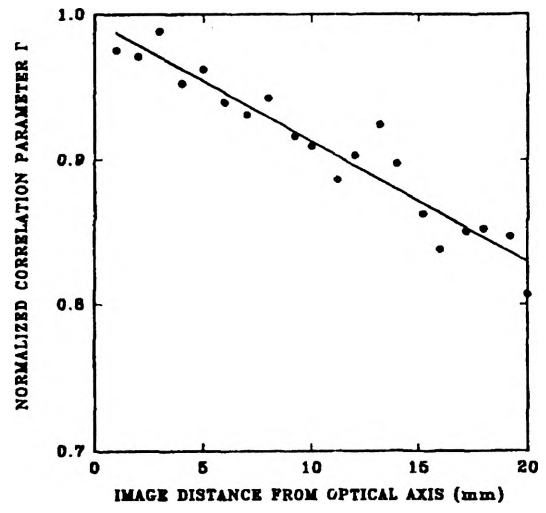


Fig. 3. Experimentally obtained transference curve, Γ_i, in accordance with Eq. (3).

illuminating beam and the portion of the surface S that originates each speckle pattern, remained unchanged. The correlation operation is properly normalized in order to remove the vignetting effect. As can be expected, the speckle correlation parameter diminishes when the illuminated surface is displaced out of the optical axis. However, as was explained in Section 2, in order to achieve the maximum measuring range, the value $\Gamma = \Gamma(x_{i,\max} \cong l^{(i)}/2)$ should be chosen as the reference value to be obtained when the laser scanning velocity v_s is varied to match the surface velocity v.

Next, we analyze the performance of the optical system when surface movements in directions other than the x-axis are considered. If the surface displaces along the z-axis, the condition to be fulfilled for obtaining a reliable velocity measurement along the x-axis is that the 'defocus' effect produced in the image speckle pattern be small enough so as not to modify the correlation parameter Γ. Since the average speckle size along the z-axis becomes $\Delta z_i \cong \lambda(z_i/a)^2 \cong 1.3$ mm, the tolerance for the maximum surface displacement is $\Delta z^{(0)}_{\max} = \Delta z_i/m^2 \cong 5.1$ mm. However, in the lateral direction (y-axis), each individual speckle has an average size $\Delta y_i \cong \lambda z_i/a \cong 60$ μm, so resulting in the maximum allowed displacement $\Delta y^{(0)}_{\max} = \Delta y_i/m \cong 0.12$ mm. Taking into account these restrictions, for practical applications such as in-line monitoring moving strip-type flat rolled products, the measuring system should be properly located close to the contact region cylinder/moving-surface, in order to minimize motions along the y- and z-directions.

Regarding the measurement time, by considering the aquisition time of the signal detected by PDA ($\tau = 1$ ms), the algorithm employed for obtaining the correlation parameter, and an averaging process, a measuring rate of 20 s^{-1} can be achieved.

Acknowledgements

The authors acknowledge the financial support from Fundación Antorchas (Buenos Aires, Argentina) and from Consejo Nacional de Investigaciones Científicas y Técnicas (Argentina), grant PID N 3-065400/88. J. Pomarico also thanks the Facul-

tad de Ingeniería, Universidad Nacional de La Plata. E.E. Sicre and D. Patrignani thank the financial support from Universidad Nacional del Sur (Bahía Blanca).

References

[1] D. Léger, E. Mathieu and J.C. Perrin, Appl. Optics 14 (1975) 872.
[2] D. Léger and J.C. Perrin, J. Opt. Soc. Am. 66 (1976) 1210.
[3] H. Fujii, T. Asakura and Y. Shindo, J. Opt. Soc. Am. 66 (1976) 1217.
[4] M. Kowalczyk and E. Bernabeu, J. Opt. Soc. Am. A 6 (1989) 758.
[5] N. Russo, N. Bolognini, E. Sicre and M. Garavaglia, Int. J. Optoelectron. 5 (1990) 389.
[6] S. Collicott and L. Hesselink, Appl. Optics 31 (1992) 1646.
[7] Y. Aizu, K. Ogino, T. Sugita, T. Yamamoto, N. Takai and T. Asakura, Appl. Optics 31 (1992) 3020.
[8] T. Okamoto, Y. Egawa and T. Asakura, Optics Comm. 88 (1992) 17.
[9] N. Russo, J. Pomarico and E. Sicre, Optics Comm. 90 (1992) 227.
[10] T. Asakura and N. Takai, Appl. Phys. 25 (1981) 179 and references therein.
[11] Q.-C. Zhang, S. Toyooka and I. Yamaguchi, Optics Comm. 101 (1993) 133.
[12] I.A. Popov and L.M. Veselov, Optics Comm. 105 (1994) 167.
[13] T. Okamoto, Y. Egawa and T. Asukura, Opt. Eng. 32 (1993) 10.
[14] R.J. Sherman, Polygonal Scanners: Applications, Performance and Design in Laser Beam Scanning, Ed. G.F. Marshall (Academic Press, New York, 1985).
[15] J. Lawson, Lens where the light rays obey the relation $H = KF\theta$, U.S. Patent 3,973,833, 10 Aug. 1976.
[16] H. Rabal, N. Bolognini and E.E. Sicre, Optica Acta 32 (1985) 1309.
[17] D.A. Tichenor and J.W. Goodman, J. Opt. Soc. Am. 62 (1972) 293.

LASER 1999
METROLOGY

Proceedings of the
International Symposium on
Laser Metrology for
Precision Measurement
and Inspection in Industry

Florianópolis, Brazil
October 13-15, 1999

edited by
Armando Albertazzi Jr.

Promoted by:

The International Measurement Confederation
Technical Committee on Measurement of Geometrical Quantities – TC 14
Laser Measurement Working Group of

The Brazilian Society of Metrology

The International Society for Optical Engineering

Hidden grids, moiré patterns and optoelectronically measurement of distances

Mario Garavaglia and Anibal Pablo Laquidara

Departamento de Fisica, Facultad de Ciencias Exactas y Departamento de Electrónica, Facultad de Ingenieria, Universidad Nacional de La Plata (UNLP), and Centro de Investigaciones Opticas (CONICET-CIC), La Plata, Argentina, Tel/Fax + (54)(221) 471 4341, E-mail: laserlab@pinos.com and garavagliam@ciop.unlp.edu.ar

ABSTRACT

Hidden grids from the photocopy process are used to produce moiré patterns. The method of production of moiré patterns is extended to hidden grids generated in the optoelectronical CCD observations. An application of this moiré is proposed to measure distances.

Keywords: photocopier hidden grids, CCD hidden grids, moiré effect, distance measurement.

1. HIDDEN GRIDS AND MOIRE PATTERNS

Various methods exist to make photocopies of an original image. Photocopies are produced on opaque paper or transparent plastic sheets. The original image can also be a slide that is projected onto the photocopier window or scanned. Each method has its proper form to generate the copied image. In general, matrix of equally or stochastically spaced points or equally spaced lines are employed to reproduce half tones and colours. Figure 1 shows these two types of hidden grids observed under microscope. Also, Figure 1 shows the Fraunhofer diffraction patterns of both grids. The light sources used were a 15 cm long filament lamp and a fluorescent tube.

The matrix of points of the array of lines can be considered as hidden grids that are incorporated to the image through the photocopy process. Hidden grids can be used to encode information into the reproduced image in order to characterize some properties of the original object.

This paper deals with an application of the hidden grids to measure distances in the original object space using the moiré effect to decode the necessary information.

2. PROPOSED METHOD TO MEASURE DISTANCES

Figure 2 shows the geometrical optics principle to form an image through a lens. Let be the object a plane -like a wall- that is perpendicular to the optical axis of the photographic objective O. The optical axis corresponds to the Z-axis of the Cartesian reference system (X, Y, Z). Onto the photographic film, the coordinate system (x, y, z) is the Cartesian reference in the image space. The optical axis corresponds to the z-axis. Points P_1 and P_2 on the wall are reference marks to define the metric in the object space. They are separated a distance D. Points p_1 and p_2 are the images of P_1 and P_2 , which are reproduced without aberrations. If the distance L from the camera objective to the wall is large enough, the distance d from point p_1 to point p_2 on the film can be expressed as $d = f\,D/L$, where f is the focal lenght of the objective. If the photographic camera is rotated an angle α around the z-Z axis, the distance d maintains its value on the film because it is an invariant under rotations.

The proposed method to measure distances requires of two slide pictures of the wall to be photographed. The first one corresponds to the position of the camera on which x-axis and y-axis on the film are parallel to the X-axis and Y-axis on the wall respectively. The second slide picture corresponds to the position of the camera rotated an angle α around the z-Z axis. Transparencies from both slides are prepared in the normal fashion. Each transparency reproduces an enlarged slide image. Points p_1 and p_2 on the slides are reproduced as points p'_1 and p'_2 on the transparencies. If the magnification of the photocopier optical system is M, the distance d' between points p'_1 and p'_2 can be expressed as $d' = Md$. Besides, the superposition of both transparencies generates a moiré pattern. In order to measure distances the superposition must be done in such a way that images of p'_1 and $p'_{1\alpha}$ and p'_2 and $p'_{2\alpha}$ be in coincidence. Then, it is possible to observe moiré fringes generated by transparency-hidden grids rotated through an angle α. So, it means that the moiré pattern decodes the rotation operation that was encoded in transparencies. Figure 3 describes the geometrical situation. If the period of the hidden grid is T_0, the period of the observed moiré fringes results:

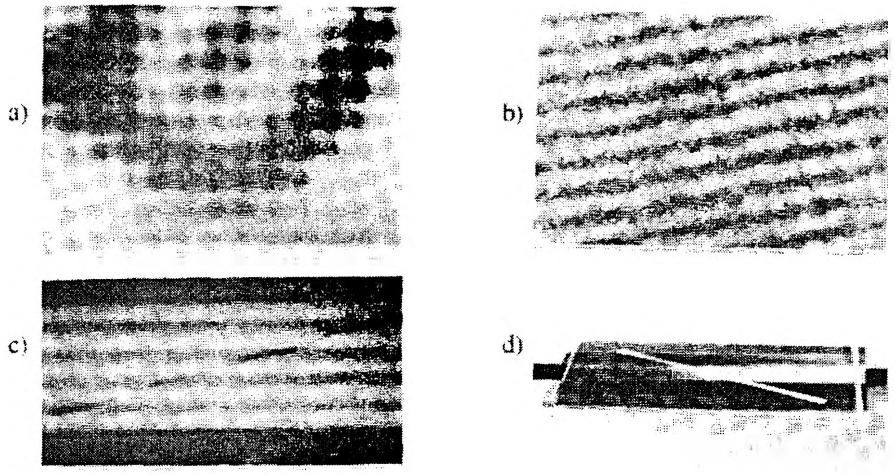


Figure 1. a) Hidden matrix 100 μm x 100 μm point array (Kodak color thermal copier); b) Hidden grid 128 μm spaced lines (Cannon color laser copier); c) Fraunhofer diffraction pattern of the hidden array at a) using a 15 cm long filament lamp as light source (positive), and d) Fraunhofer diffraction pattern of the hidden grid at b) using a fluorescent tube as light source (negative).

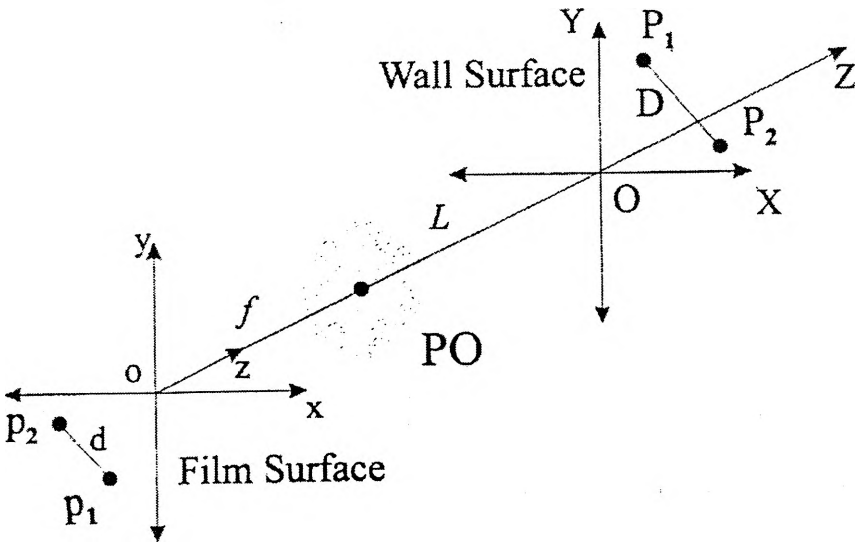


Figure 2. The photographic objective PO forms images p_1 and p_2 onto the film surface from points P_1 and P_2 placed onto the wall surface.

$$T = T_0 / 2 \sin(\alpha/2)$$

Then, the distance d' can be expressed as a function of T. The bisector BB' of hidden grids is perpendicular to moiré fringes. As the segment d' forms an angle β with BB' , it is possible to express d' as a function of T. Taking into account that the positions of points $p'_1 \equiv p'_{1\alpha}$ and $p'_2 \equiv p'_{2\alpha}$ can be placed between moiré fringes, it is necessary to introduce the fractional orders ε_1 and ε_2 of a period in the moiré pattern, as it is shown in Figure 3. Finally, the distance L from the photographic objective to the wall, can be expressed as:

$$L = D\,f\,M\,(\cos\beta) / (n + 1 + \varepsilon_1 - \varepsilon_2)\,T$$

Where n is the number of complete moiré periods contained in d' cos β.
An easy observation of the moiré pattern can be achieved through the Fraunhoffer diffraction pattern of hidden grids. Figure 4 shows the moiré pattern superimposed on the diffraction pattern.

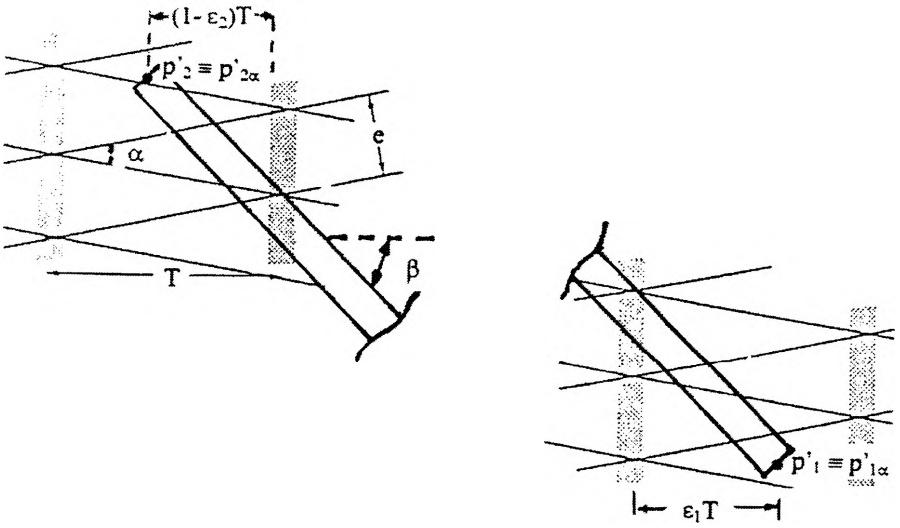


Figure 3. The moiré field positions of the ends of the segment d' corresponding to points $p'_1 \equiv p'_{1\alpha}$ and $p'_2 \equiv p'_{2\alpha}$ are defined by the fractional orders ε_1 and ε_2 with respect to their neighbour left moiré fringes.

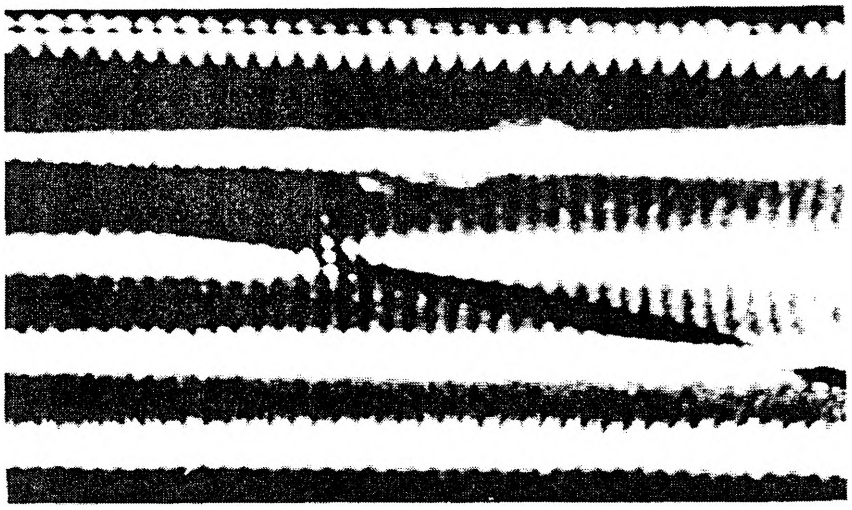
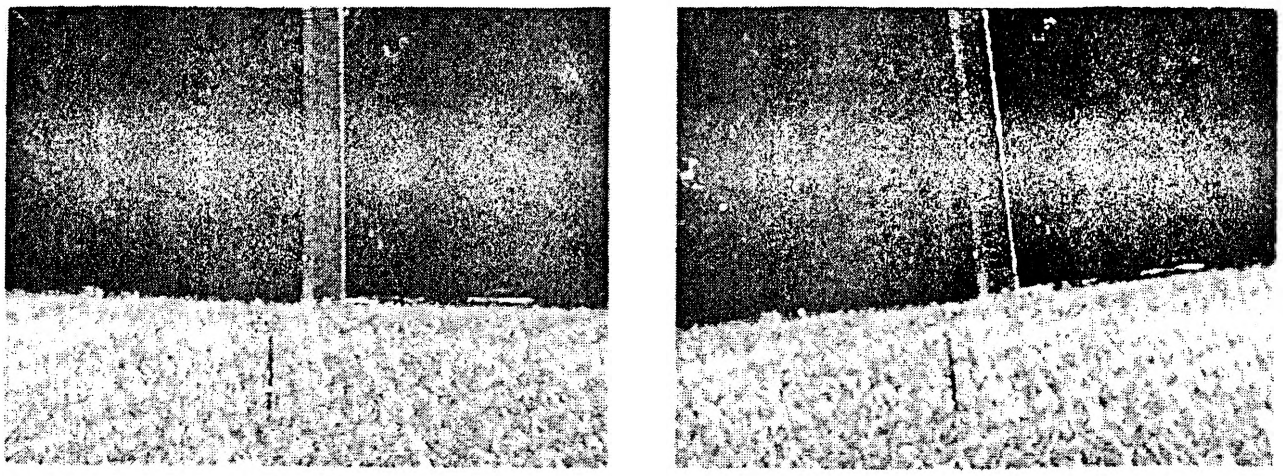


Figure 4. The moiré pattern superimposed on the diffraction patern



a) b)

Figure 5. Water tank of the Campus of Technology at Gonnet photographed from 200 m. a) horizontal view and b) inclined view. Note the three white reference marks on tank columns.

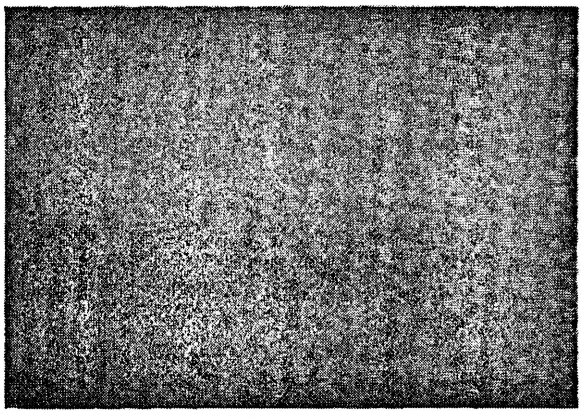
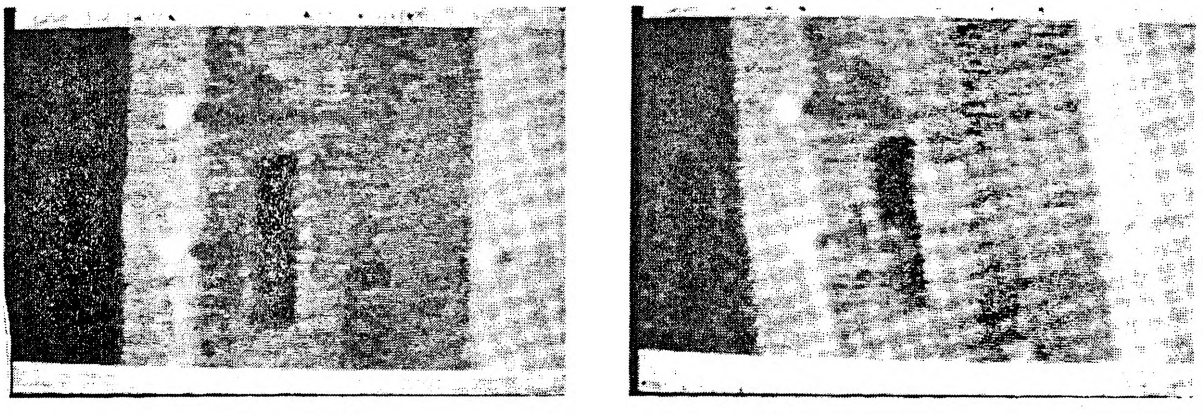


Figure 6. CCD detector microphotograph. Pixels are 8.8 μm x 8.8 μm area.



a) b)

Figure 7. Water tank at Figure 5) captured from 50 m. by the CCD camera and enlarged 8:1 on the screen monitor. a) horizontal view and b) inclined view. Note the pixeled pattern of the image and the three white reference marks.

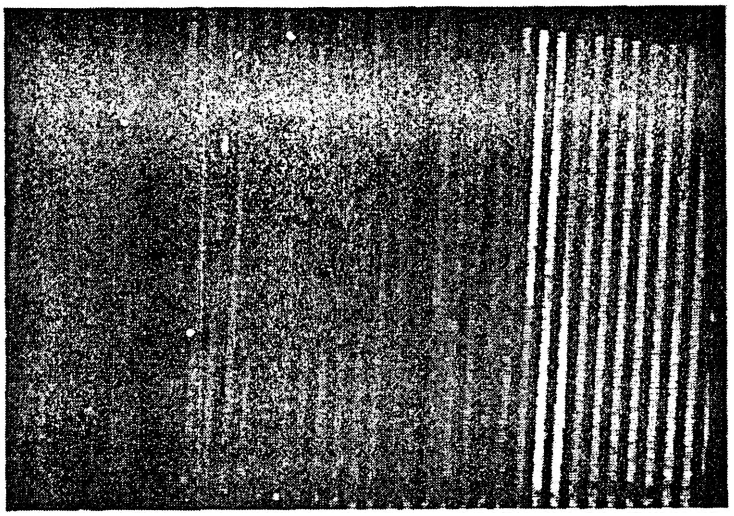


Figure 8.Moiré pattern generated by the electronical superposition of Figures 5 a) and b).

3. CONCLUSION REMARKS AND PROPOSALS

A method to measure distances can be accomplished by using the moiré pattern generated by transparency-hidden grids. However, these types of grids are physically unstable because they suffer the thermal copying processes. More stable and closed grids are observed in CCD optoelectronically captured images. Then, the pure optical method to measure distances can be extended and converted in a pure electronical one. Figure 5 shows a typical view of the CIC – Campus of Technology at Gonnet. Both pictures –Figure 5 a) and b)- were photographed from a distance of 200 m; they were pictured by rotating the camera through the optical z-Z axis an angle of 7.5°. The same pictures al Figure 5 were captured using a CCD camera, whose detector was microscopically observed. Figure 6 shows an enlarged view of a part of the CCD detector. The area of each pixel is 8.8 μm x 8.8 μm. The pixel area of the CCD camera generates an optoelectronical hidden grid. Finally, Figure 7 a) and b) show screen monitor pictures of the campus water tank basis; 8:1 zoom was applied and the pixeled structure of the CCD camera is easily observed.

Figure 8 shows the electronically generated moiré pattern between the information contained in figures 7 a) and 7 b).

A scale scene was defined by three reference marks using three white targets pasted on the concrete columns of the water tank. Following the described moiré procedure between both optoelectronical grids, distances of the order of hundred meters were measured with an uncertainty of 2%.

4. ACKNOWLEDGEMENTS

This work was partially financed by CONICET (PID-BID-CONICET 1116/91 grant) and UNLP (FCE-3711/97)

5. REFERENCE

1. Hidden grids, moiré patterns and measurement of distances.
Mario Garavaglia
III Reunión Iberoamericana de Optica (III RIAO) y VI Reunión Latinoamericana de Optica, Láseres y Aplicaciones (OPTILAS '98), 28 de setiembre a 2 de octubre de 1998, Cartagena de Indias, Colombia, Poster 133.
2. Electronic CD edition by Academia Colombiana de Ciencias Exactas, Físicas y Naturales. ISBN 958-9205-32-1

Óptica Física y Propagación de Ondas

Desde los comienzos del CIOp se ha generado gran interés y se han dedicado muchos esfuerzos a las investigaciones en óptica física, propagación de ondas en distintos medios, estudios de coherencia y se han desarrollado varias aproximaciones usando diferentes herramientas matemáticas para describir estos fenómenos.

Se analizaron las características de un sistema interferométrico de múltiples haces tipo Fabry-Perot. Se calcularon los caminos ópticos y las diferencias de camino entre los haces de luz que interfieren para el caso mas general.

Algunas propiedades de correlación óptica fueron analizadas utilizando los conceptos de la Transformada Fraccional de Fourier. Se obtuvo un filtro insensible a variaciones de escala del objeto utilizando un set particular de órdenes fraccionarios y fue propuesta una configuración óptica para desarrollar la correlación fraccional de manera sensible.

La Transformada Fraccional de Fourier ha sido expresada por medio de la propagación a través de lentes delgadas que producen retardos de fase y fueron encontrados varios sistemas ópticos asociados a este desarrollo. Se propusieron definiciones matemáticas de la convolución y correlación de orden P y fueron verificados teoremas como generalización de las definiciones clásicas.

Se ha utilizado la función distribución de Wigner para analizar la razón de Strehl y la función de transferencia óptica como parámetros de calidad de sistemas ópticos. Para este fin se usaron diferentes funciones pupilas.

Se ha propuesto una generalización del concepto de paridad como una función continua y se ha demostrado que ésta es conservada en la propagación de ondas. Se han discutido las propiedades matemáticas y se ha sugerido una implementación experimental de esta representación óptica.

Se han investigado las propiedades de la luz difractada por una apertura empleando un formalismo basado en funciones de Walsh. Este formalismo, en un esquema de propagación libre ha sido utilizado para describir las propiedades de filtrado espacial en varios dispositivos ópticos.

Se ha investigado sobre la coherencia espacial de primero y segundo orden utilizando interferogramas de Young. El método usa un interferómetro de Michelson a la salida del sistema de doble ranura de Young.

Se ha realizado un estudio para la caracterización de propagación de luz láser a través de medios turbulentos utilizando transformada wavelet. Se utiliza el parámetro H de Hurst y la entropía wavelet normalizada. Esto permite extraer información de procesos estocásticos asociados con la turbulencia dinámica.

Optical Physics and Waves Propagation

The research in optical physics, optical wave propagation and coherence of the light has been actively generated since the early beginning of CIOp. Much effort has been devoted to the development of several approaches using different mathematical tools for the description of these subjects.

Characteristics of multiple-beam interference fringes, as in a Fabry-Perot interferometer with monochromatic light, were analyzed. The optical path and the optical-path difference between interfering beams are calculated for the most general case.

Some properties of optical correlation based on the fractional Fourier transform were analyzed. For a particular set of fractional orders, a filter was obtained that becomes insensitive to scale variations of the object. An optical configuration was proposed to carry out the fractional correlation in a flexible way, and some experimental results were obtained.

Also, the fractional Fourier transform (FRT) has been expressed by means of propagation and thin-lens phase delay operators, and a large number of optical systems associated with it were found. At the same time, the output of optical systems was found in terms of the FRT. Mathematical definitions for the P-order convolution and correlation were proposed as generalizations of the classical ones such that, when the P-order FRT have been applied to them, theorems that generalize the classical convolution and correlation were verified.

An analysis of the Strehl ratio and the optical transfer function as imaging quality parameters of optical elements with enhanced focal length was carried out by employing the Wigner distribution function. To this end, we use four different pupil functions: a full circular aperture, a hyper-Gaussian aperture, a quartic phase plate, and a logarithmic phase mask. A comparison was performed between the quality parameters and test images formed by these pupil functions at different defocus distances.

A generalization of the concept of parity as a continuous function was proposed and showed that is conserved in optical waves propagation. Some properties were commented and a experimental implementation to optically representation was suggested

The free propagation properties of the light field diffracted by an aperture have been investigated by employing a formalism based on the orthogonal and complete set of Walsh functions. This formalism can be used to explain the spatial filtering properties of many optical devices

Spatial partial coherence of first and second order in Young's interferograms has been investigated. The method using a compensated Michelson's interferometer attached at the exit of the Young's slit pair.

A dynamic study for characterization of laser propagation through turbulent media by quantifiers based on the wavelet transform has been developed. It used the Hurst parameter, H, and the normalized total wavelet entropy. This allows us to extract information on the stochastic process associated with the turbulence dynamics.

Interference profiles with multiple spherical waves: general case

L. M. Zerbino, R. Torroba, N. Rodríguez, and M. Garavaglia

Centro de Investigaciones Opticas (CONICET-UNLP-CIC), Casilla de Correo 124, 1900 La Plata, Argentina

Received June 28, 1983; accepted January 10, 1984

Characteristics of multiple-beam interference fringes, as in a Fabry–Perot interferometer with monochromatic light, are analyzed. The optical path and the optical-path difference between interfering beams are calculated for the most general case. Different refractive indices in the inner and outer media, and arbitrary locations of the light source and the point of observation, are taken into account. An expression for the impulse response of the system is given. The results obtained from experimental tests confirm the theoretical predictions.

1. INTRODUCTION

As is well known, the analysis of the interferential processes in different optical structures must include a solution of the geometrical aspect that relates the fringe localization in the interferential pattern with the intensity distribution across it.

In the case of multiple-reflection interferometers, such as the Fabry–Perot interferometer, several kinds of experimental setups were employed. Plane-parallel or spherical mirrors were used in different kinds of scientific or metrological applications.[1–3]

The geometry and the intensity profile of the interference pattern produced by such optical structures are well known for the cases in which mirrors are at normal alignment conditions.

Recently, Brossel[4] and Aebischer[5] researched the geometry and the intensity profile of the interference pattern produced by a misaligned Fabry–Perot interferometer, and Rogers[6] developed a program to compute the profile of multiple-beam Fizeau fringes.

Our paper follows the methodology of Refs. 4–6 but introduces the more general conditions for the calculation of the optical-path difference, the impulse response, and the intensity-profile distribution, as shown in Section 2.

These general conditions are as follows: (1) Three different refractive indices in the entire optical structure are considered. (2) The light source can be placed near the interferometer, which implies the treatment of spherical waves. (3) The observation plane can also be placed near the interferometer. These conditions correspond to the generalization of the two-index case studies by Zerbino[7] and justify the design of a compact device for interferometric holography.[8]

In Section 3 the theoretical results obtained in Section 2 [Eq. (15)] are tested in those limiting cases previously reported, ensuring the consistency of the methodology employed and of the results.

Section 4 describes the experimental test of the theoretical results.

2. CALCULATION OF THE OPTICAL-PATH DIFFERENCE, THE IMPULSE RESPONSE, AND THE INTENSITY-PROFILE DISTRIBUTION

We analyze the optical-path difference as well as the impulse response and the intensity distribution of light in the interferential pattern produced by the most general case of a misaligned Fabry–Perot interferometer.

Optical-Path Difference

To calculate the optical-path difference between rays passing through a misaligned Fabry–Perot interferometer it is necessary to characterize the optical structure under consideration.

We consider a wedge with plane partial reflecting surfaces S_1 and S_2 forming an angle α. Figure 1 shows a cross section

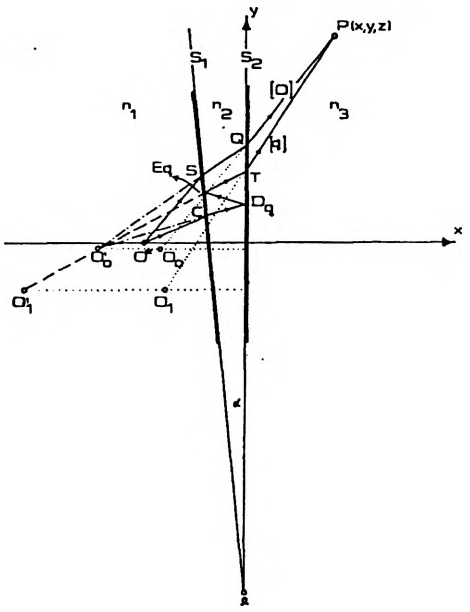


Fig. 1. Cross section of the wedge, showing the O^* real point source and its virtual images.

0740-3232/84/050495-07$02.00 © 1984 Optical Society of America

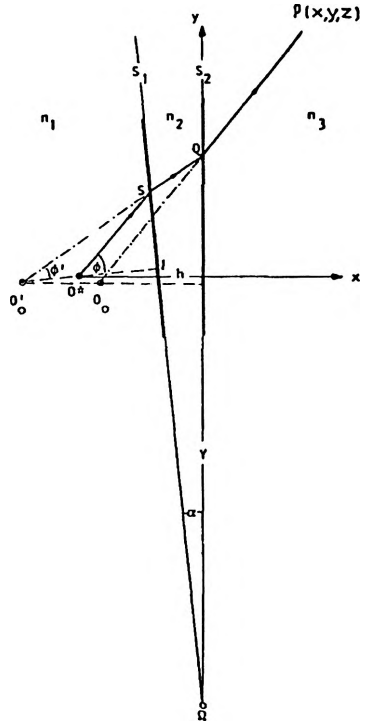


Fig. 2. Schematic diagram of the dihedral angle for the calculation of the positions of the virtual sources.

of the dihedral angle between S_1 and S_2, where Ω is the vertex of α, O^* is a light point source, and n_1, n_2, and n_3 are the refractive indices of the media. We take into account the multiple reflections of rays in the medium characterized by n_2 placed between S_1 and S_2.

There are rays (such as O) that arise from O^* and travel through the wedge without suffering reflections, and there are others (such as q) that are reflected q times on each surface before leaving the cavity.

We determine the difference between the optical-path lengths of rays such as $[q]$ and $[O]$ when both arrive at the same observation point $P(x, y, z)$, interfering with each other. The optical path $\mathbf{r}_q$ for the $[q]$ ray is

$$\mathbf{r}_q = n_1\overline{O^*C} + n_2(\overline{CD_1} + \overline{D_1E_1} + \overline{E_1D_2} + \overline{D_2E_2} + \ldots + \overline{D_qE_q} + \overline{E_qT}) + n_3\overline{TP}; \quad (1)$$

for the $[O]$ ray it is

$$\mathbf{r}_0 = n_1\overline{O^*S} + n_2\overline{SQ} + n_3\overline{QP}. \quad (2)$$

Let O'_0 be the image of the source O^* that is due to the refraction at S_1, and let O'_i be the successive image positions of $O'_0, O'_1, \ldots, O'_{i-1}$ generated by multiple reflections at the surfaces. Also, let O_i be the image of O'_i given by the refraction at S_2. The images $O'_0, \ldots, O'_i$ of the source O^*, which can be interpreted as virtual sources in the medium of index n_2, lie on a circumference of radius l, whose center is Ω, and they are separated from one another by an angular distance 2α. This circumference is in the plane containing the normal to the surface S_1 and the point source O^*, and it is normal to the edge of the wedge (in Fig. 1, the x–y plane).[7]

On the other hand, as O'_1 is an image of O'_0, we can write

$$\overline{O'_0C} + \overline{CD_1} + \overline{D_1E_1} + \overline{E_1D_2} + \ldots + \overline{D_qE_q} + \overline{E_qT} = \overline{O'_1T}.$$

Besides, as is shown in Fig. 2, the segment $\overline{O^*I}$ is parallel to the normal to surface S_1, and we may write for any light ray leaving the source O^* at an angle ϕ

$$\overline{O^*S}\sin\phi = \overline{SI} = \overline{O'_0S}\sin\phi'. \quad (4)$$

Combining Eq. (4) with Snell's law, $n_1 \sin\phi = n_2 \sin\phi'$, produces the following result:

$$\overline{O^*S} = \frac{n_1}{n_2}\overline{O'_0S}. \quad (5)$$

Then, in general, we may write

$$\overline{O'_iQ} = \overline{O_iQ}\frac{n_2}{n_3}, \qquad i = 0, 1, 2\ldots. \quad (6)$$

Going back to Fig. 1 and using Eq. (5) for point C (the intersection with surface S_1), Eq. (3) for a ray that is reflected q times inside the wedge, and Eq. (6) for point T (the intersection with the surface S_2), we find that the length of the optical path $[q]$ is given by

$$\mathbf{r}_q = \frac{n_1^2 - n_2^2}{n_2}\overline{O'_0C} + \frac{n_2^2 - n_3^2}{n_2}\overline{O'_qT} + n_3\overline{O_qP}, \quad (7)$$

and, in the same way, we obtain for the optical path $[O]$

$$\mathbf{r}_0 = \frac{n_1^2 - n_2^2}{n_2}\overline{O'_0S} + \frac{n_2^2 - n_3^2}{n_2}\overline{O'_0Q} + n_3\overline{O_0P}. \quad (8)$$

Let $O^* = (-\rho, 0, 0)$ and $O'_i = (-x'_i, -y'_i, 0)$ be the coordinates of the point light source and their images given by refraction and reflection, respectively, and $O_i = (-x_i, -y_i, 0)$ be the corresponding refraction images of $O'_i = (-x'_i, -y'_i, 0)$.

Then, from Fig. 1 and using Eq. (6), we obtain

$$\overline{O'_0Q} = \frac{n_2}{n_3}\frac{x_0}{x + x_0}\overline{O_0P}, \qquad \overline{O'_qT} = \frac{n_2}{n_3}\frac{x_q}{x + x_q}\overline{O_qP}. \quad (9)$$

Defining the coordinates $T = (x_T, y_T, z_T)$ and $Q = (x_Q, y_Q, z_Q)$, we find it possible to calculate[7]

$$\overline{O'_0C} = \frac{n_2}{n_1}\frac{(\rho - h)\cos\alpha}{x'_q\cos[(2q+1)\alpha] + [z_T^2 + (y_T - y'_q)^2]^{1/2}\sin[(2q+1)\alpha]}\overline{O'_qT},$$

$$\overline{O'_0S} = \frac{n_2}{n_1}\frac{(\rho - h)\cos\alpha}{x'_0\cos\alpha + [z_Q^2 + (y_Q - y'_0)^2]^{1/2}\sin\alpha}\overline{O'_0Q}, \quad (10)$$

where h is the width of the wedge in the x–z plane ($y = 0$).

Points P, T, and Q are not necessarily in the x–y plane because the last expressions are valid for any angle at which light impinges upon the wedge.

Now, in order to calculate both optical paths $[q]$ and $[O]$ and their difference, we must know

(1) The coordinates of the image sources O'_i and O_i as functions of the wedge angle α and the position of O^*.

(2) The coordinates of points Q and T as functions of the positions of the observation point $P(x, y, z)$ and O'_i.

Let h be the width of the wedge in the x–z plane and y be the distance between Ω and the origin of the coordinates, as illustrated in Fig. 2; then

$$h = y \tan \alpha.$$

As we already know that the coordinates of the source are $O^* = (-\rho, 0, 0)$, easy calculations give

$$\left.\begin{aligned} x_0' &= \rho + \left(\frac{n_2}{n_1} - 1\right)(\rho - h)\cos^2 \alpha \\ y_0' &= \left(\frac{n_2}{n_1} - 1\right)(\rho - h)\cos \alpha \sin \alpha \\ z_0' &= 0 \end{aligned}\right\} \text{ for } O_0' = (-x_0', -y_0', 0),$$

$$\left.\begin{aligned} x_q' &= x_0' \cos 2q\alpha + (y - y_0')\sin 2q\alpha \\ y_q' &= y - (y - y_0')\cos 2q\alpha + x_0' \sin 2q\alpha \\ z_q' &= 0 \end{aligned}\right\} \text{ for } O_q' = (-x_q', -y_q', 0),$$

$$\left.\begin{aligned} x_0 &= \frac{n_3}{n_2} x_0' \\ y_0 &= y_0' \\ z_0 &= 0 \end{aligned}\right\} \text{ for } O_0 = (-x_0, -y_0, 0),$$

$$\left.\begin{aligned} x_q &= \frac{n_3}{n_2} x_q' \\ y_q &= y_q' \\ z_q &= 0 \end{aligned}\right\} \text{ for } O_q = (-x_q, -y_q, 0). \tag{11}$$

Points T and Q are defined by the intersections between the y–z plane ($x = 0$) and the segments $\overline{O_qP}$ and $\overline{O_0P}$, respectively; such intersections give

$$\left.\begin{aligned} x_T &= 0 \\ y_T &= y\left(1 - \frac{x}{x + x_q}\right) - y_q\left(\frac{x}{x + x_q}\right) \\ z_T &= z\left(1 - \frac{x}{x + x_q}\right) \end{aligned}\right\} \text{ for } T = (x_T, y_T, z_T)$$

and

$$\left.\begin{aligned} x_Q &= 0 \\ y_Q &= y\left(1 - \frac{x}{x + x_0}\right) - y_0\left(\frac{x}{x + x_0}\right) \\ z_Q &= z\left(1 - \frac{x}{x + x_0}\right) \end{aligned}\right\} \text{ for } Q = (x_Q, y_Q, z_Q). \tag{12}$$

Combining Eqs. (11) and (12) and introducing the result into Eqs. (10) and using Eqs. (9), we can write Eqs. (7) and (8) as functions of $\overline{O_qP}$, obtaining the general expression that is valid for $q = 0, 1, \ldots, p$:

$$\mathbf{r}_q = \overline{O_qP}\left\{\frac{n_1^2 - n_2^2}{n_3} \frac{\frac{n_2}{n_1}(\rho - h)\cos \alpha}{\frac{n_2}{n_3}(x + x_q)\cos[(2q + 1)\alpha] + [z^2 + (y + y_q)^2]^{1/2} \sin[(2q + 1)\alpha]} + \frac{n_2^2 - n_3^2}{n_3} \frac{x_q}{x + x_q} + n_3\right\},$$

where

$$\overline{O_qP} = [(x + x_q)^2 + (y + y_q)^2 + z^2]^{1/2}. \tag{13}$$

Before using this last expression for searching the optical-path difference, we can make several approximations taking into account the different orders of magnitude that play a significant role and then subtract $\mathbf{r}_q$ from $\mathbf{r}_0$.

The order of magnitude of the main parameters involved is as follows:

The width h can measure several millimeters.

The angle α of the wedge is small. It is of the order of 10^{-4}–10^{-3} rad.

$y = h/\tan \alpha \approx h/\alpha \approx 100$ m.

q, the number of reflections, may be several times 10.

$2q\alpha \approx 2 \times 10 \times 10^{-3} \approx 0\ (10^{-2})$.

As we want to obtain a general formula for the optical path that is valid both when the source and the record are at infinity and when the source and the record are near the interferometer, we will consider the possibility that ρ ranges from 10^{-1} m to infinity. Then we can replace $\sin \alpha$ with α and $\cos \alpha$ with 1 and neglect h^2 compared with ρ^2 and also α^2 compared with 1; then Eq. (7) is reduced to

$$\mathbf{r}_q = \overline{O_qP}\left(\frac{n_1^2 - n_2^2}{n_3} \times \left\{\frac{\frac{n_2}{n_3}x_0 - h}{\frac{n_2}{n_3}(x + x_0) + 2qh + [z^2 + (y + y_0)^2]^{1/2}(2q + 1)\alpha}\right\} + \frac{n_2^2 - n_3^2}{n_3} \frac{x_0 + \frac{n_3}{n_2}2qh}{x + x_0 + \frac{n_3}{n_2}2qh} + n_3\right) \tag{14}$$

and $\mathbf{r}_0$ is obtained by replacing q with zero.

After finding the difference between $\mathbf{r}_q$ and $\mathbf{r}_0$ and rearranging terms, we obtain the following expression for the optical path:

$$\delta_q = \frac{n_1^2 - n_3^2}{n_1} \times 2q \left\{ \rho h \frac{n_3}{n_2}\left(\frac{1}{A} - \frac{A}{(x+\rho)^2}\right) + \frac{\rho\alpha y\left[(\rho - 2h)\frac{n_2}{n_1} + h\right]}{(x+\rho)A} - \frac{\rho^2\alpha h y\left[(2q+2)\frac{n_3}{n_1} - \frac{n_3}{n_2} - \frac{n_2 n_3}{n_1^2}\right]}{(x+\rho)^2 A} \right\}$$

$$+ \frac{n_2^2 - n_3^2}{n_2} \times 2q \left\{ \frac{h\alpha y\rho\left[(2q+2)\frac{n_2}{n_1} - 1\right]}{(x+\rho)A} + \frac{hA}{(x+\rho)} \right\}$$

$$- \frac{n_1^2 - n_2^2}{n_2}\frac{n_3^2}{n_1^2} \times 2q \left\{ \frac{(y^2+z^2)^{1/2}\alpha h\rho\left[(2q+2)\frac{n_1}{n_2} - 1\right]}{(x+\rho)A} + \frac{(\rho - h)(y^2+z^2)^{1/2}\alpha\frac{n_1}{n_3}A}{(x+\rho)^2} \right\}$$

$$+ \frac{n_3^2}{n_2} 2q \frac{(\rho + x)h}{A} + n_3 2q\alpha y \frac{\left[(\rho - h)\frac{n_2}{n_1} + h\right]}{A}, \quad (15)$$

where

$$A = [(x+\rho)^2 + Y^2 + Z^2]^{1/2}.$$

Equation (15) represents the optical-path difference between two rays arriving at the same observation point P, one directly transmitted through the wedge and the other transmitted after q reflections inside the wedge, when we make the approximations $h^2 \ll \rho^2$ and $\alpha^2 \ll 1$.

Impulse Response

In the preceding section we calculated the optical path $\mathbf{r}_q$ for light coming from source O^*, having q reflections inside the cavity and reaching observation point P.

The phase difference corresponding to each optical path $\mathbf{r}_q$ is $\phi_q = (2\pi/\lambda)\mathbf{r}_q$, where λ is the wavelength in free space.

Suppose that at plane π^* (see Fig. 3) there is a plane object that is illuminated by monochromatic light. Let $U(O^*)$ be the complex field amplitude of the object at plane π^*, and let $U(P)$ be the complex field amplitude at point π that contains observation point P.

Using the linearity property, we can express the complex amplitude U as function of U^*, that is,

$$U(P) = \iint_{-\infty}^{\infty} U(O^*)h(P, O^*),$$

where $h(P, O^*)$ is the amplitude at P coordinates in response to a point-source object at O^* and h is the impulse response of the optical system.

We calculate the complex amplitude of the field at point P in plane π (refractive index n_3) when the interferometer is illuminated by monochromatic light coming from a point source placed at $O^*(-\rho, 0, 0)$ in plane π^* (refractive index n_1).

As we have already said, the incident field amplitude U_i at point P_I of plane π_I of the system can be written as

$$U_i = A\frac{\exp(ik\mathbf{r}_{0I})}{r_{0I}},$$

where $\mathbf{r}_{0I}$ is the optical path from O^* to $P_I(0, \xi, \eta)$ without reflections inside the instrument and r_{0I} is the geometric distance from O^* (the image of O^* calculated at n_3) to P_I (see Fig. 4).

Let $K(\xi, \eta)$ be the pupil function at plane π_I. The field amplitude U_i' at the output of the system (and also at plane π_I) will be

$$U_i'(\xi, \eta) = AK(\xi, \eta)\sum_{q=0}^{p} t_1 t_2 (r_1 r_2)^q \frac{\exp(ik\mathbf{r}_{qI})}{r_{qI}},$$

where $\mathbf{r}_{qI}$ is $\mathbf{r}_q$ of Eq. (14) for point $P_I \equiv (0, \xi, \eta)$.

As a final step, if we use the Huygens–Fresnel principle, we find that the field amplitude at point P of π is

$$h(x, y, z, -\rho, 0, 0) = \frac{A}{i\lambda}\iint_{-\infty}^{\infty} K(\xi, \eta) \times \frac{\exp(ikn_3 r_I)}{r_I}\left[\sum_{q=0}^{p} t_1 t_2 (r_1 r_2)\frac{e^{ik\mathbf{r}_{qI}}}{r_{qI}}\right]\cos(\bar{n}, \bar{r}_I)\,d\xi\,d\eta,$$

where

$$r_I = [x^2 + (y - \xi)^2 + (z - \eta)^2]^{1/2},$$

$$r_{qI} = [x_q^2 + (y_q - \xi)^2 + (z_q - \eta)^2]^{1/2},$$

and $\mathbf{r}_{qI}$ is given from Eq. (14) for $x = 0, y = \xi$, and $z = \eta$.

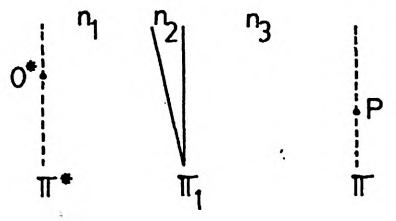


Fig. 3. Diagram showing the positions of the object and observation planes.

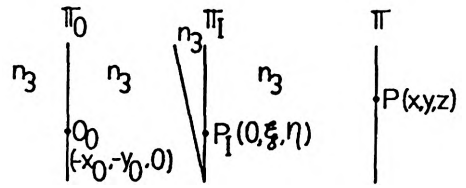


Fig. 4. Diagram of the relative positions of the object and observation planes referring to a medium of index n_3.

Intensity-Profile Distribution

In order to corroborate Eq. (15), we must calculate the transmitted amplitude and intensity through the wedge and the recorded intensity at point P.

Taking into account that observation point P is placed a finite distance from the wedge and supposing that the pupil is large, we can write the transmitted vibrations as

$$A_t = \sum_{q=0}^{p} t_1 t_2 (r_1 r_2)^q \frac{e^{ikr_q}}{r_q} A_i, \tag{16}$$

where $k = 2\pi/\lambda$, r_q is given by Eq. (14), and $r_q = [(x + x_q)^2 + (y + y_q)^2 + z^2]^{1/2}$, where the term e^{ikr_q}/r_q characterizes the spherical wave that reaches point P as coming from point O_q, with

$$\frac{r_0}{r_q} \simeq 1 - \frac{2\epsilon q\alpha}{r_0^2},$$

where

$$\left\{\left(\frac{n_3}{n_2}y\right)^2 + \left[\left(\frac{n_2}{n_1} - 1\right)(\rho - h) + \rho\right]^2\right\} 4q^2\alpha^2 \ll r_0^2$$

and

$$\epsilon = \frac{n_3}{n_2}y(x + x_0) + \left[\left(\frac{n_2}{n_1} - 1\right)(\rho - h) + \rho\right](y + y_0). \tag{17}$$

We can write Eq. (16) as

$$A_t = \left[1 + \sum_{q=1}^{p} (r_1 r_2)^q e^{ik\delta q}\left(1 - \frac{2\epsilon q\alpha}{r_0^2}\right)\right] t_1 t_2 A_i \frac{e^{ikr_0}}{r_0}, \tag{18}$$

where e^{ikr_0}/r_0 is the spherical wave coming from the real light source O^* and reaching point P.

The center of the spherical wave is at point $O_0(-x_0, -y_0, 0)$, and

$$r_0 = [(x + x_0)^2 + (y + y_0)^2 + z^2]^{1/2}.$$

Then the transmitted intensity for monochromatic light can be calculated as

$$I_t = A_t A_t^* = |A_t|^2. \tag{19}$$

With that intensity equation it is possible to plot the theoretical intensity profile for comparison with the experimental microdensitometric record of the interference pattern.

3. ANALYSIS OF LIMITING CASES

Equation (15) reproduces the theoretical expression of δ for the limiting cases already known:

(1) When $\alpha = 0$ and $n_1 = n_2 = n_3 = n$, the optical-path difference given by Eq. (15) take the form

$$\delta_q = 2qn\frac{(x + \rho)h}{[(x + \rho)^2 + y^2 + z^2]^{1/2}}. \tag{20}$$

If the observation point is placed at infinity, we obtain

$$\delta_q = 2qhn\cos\Theta\left\{1 + \frac{\rho(\cos\Theta)^{-1}}{[x^2 + y^2 + z^2]^{1/2}}\right\} \quad \text{for } x \gg \rho \tag{21}$$

and

$$\delta_q = 2qhn\cos\Theta \quad \text{for } x \to \infty, \tag{22}$$

where

$$\cos\Theta = x/[x^2 + y^2 + z^2]^{1/2}.$$

These results correspond to the well-known concentric rings, whose theoretical intensity profile, calculated using Eqs. (18) and (19), is shown in Fig. 5(a).

(2) When $\alpha = 0$, $n_1 \neq n_2 = n'$, and $n_1 = n_3 = n$, the optical-path difference is

$$\delta_q = 2qh\left[\frac{n'(x + \rho)}{(x^2 + y^2 + z^2)^{1/2}} + \frac{(y^2 + z^2)(n'^2 - n^2)}{n'(x^2 + y^2 + z^2)^{1/2}}\right], \tag{23}$$

and, in the case when $x \gg \rho$ and $\rho/(x^2 + y^2 + z^2)^{1/2} \ll 1$, it results in

$$\delta_q = 2qh\left(n'\cos\Theta + \frac{n'^2 - n^2}{n'}\frac{\sin^2\Theta}{\cos\Theta}\right). \tag{24}$$

If the observation is made in a position near the axis ($\sin^2\Theta \ll 1$), the optical-path difference has the expression

$$\delta_q = 2qhn'\cos\Theta, \tag{25}$$

which also corresponds to concentric rings.

(3) When $\alpha \neq 0$ and $n_1 = n_2 = n_3 = n$, the optical-path difference is

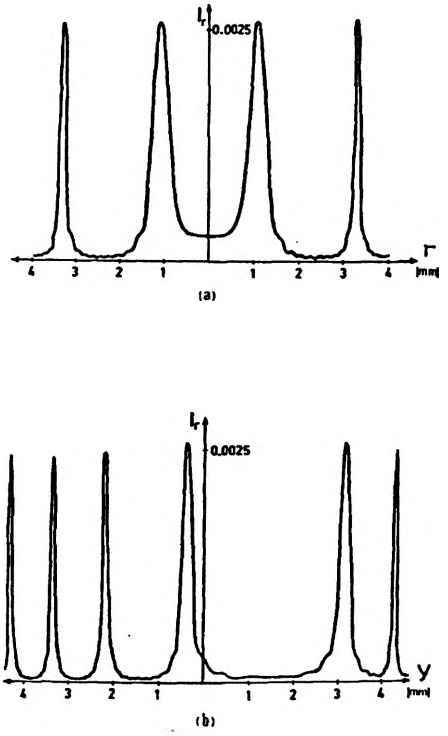


Fig. 5. Computed profiles for $\lambda = 632.8$ nm, $n = n' = 1$, $R = 0.8$, $h = 20$ mm, $\rho = 250$ mm, and $x = 300$ mm, where $r = (y^2 + z^2)^{1/2}$. For the calculations we used $p = 10$ and $I_r = I_t/I_i$: (a) $\alpha = 0$, (b) $\alpha = 2 \times 10^{-4}$ rad. The recording was taken for $z = 0 \Rightarrow r \equiv y$.

$$\delta_q = 2qhn\left[\frac{x+\rho}{(x^2+y^2+z^2)^{1/2}} + \frac{2q\alpha yn\rho}{(x^2+y^2+z^2)^{1/2}}\right], \quad (26)$$

and, for the case when $x \gg \rho$,

$$\delta_q = 2qn\left[h\cos\Theta + \frac{\alpha y\rho}{(x^2+y^2+z^2)^{1/2}}\right] \times\left[1 - \frac{\rho\cos\Theta}{(x^2+y^2+z^2)^{1/2}}\right]. \quad (27)$$

We can also neglect terms in $\rho\cos\Theta/(x^2+y^2+z^2)^{1/2}$, but, in the case of off-axis observation, we must retain the term $\alpha y\rho/(x^2+y^2+z^2)^{1/2}$, obtaining

$$\delta_q = 2qn\left[h\cos\Theta + \frac{\alpha y\rho}{(x^2+y^2+z^2)^{1/2}}\right], \quad (28)$$

which corresponds to interference patterns whose intensity profiles have symmetry only with respect to the z axis, as is shown in Fig. 5(b), which is the theoretical profile for $z = 0$.

We can add a comment for the case of close axis observation. If $y \approx 0$, Eq. (28) coincides with Eq. (22), which means that a small interferometer misalignment does not modify the structure of the central rings. This is also true if $y \approx z \approx 0$ and $n = n_1 = n_3 \neq n_2 = n'$ in Eq. (15). In this case, we again obtain Eq. (22).

4. EXPERIMENTAL RESULTS

The theoretical intensity profiles computed from Eq. (19) were plotted using an IBM/360 computer with a 2250 visual unity. Such plots were compared with the experimental microdensitometric records obtained for typical values of the parameters involved.

Figure 6 is a schematic of the experimental setup used. For the simulation of the light point source O^* we used a cw 1.5-mW He–Ne laser and a beam collimator. Those cases with $n_1 = n_3 \neq n_2$ were tested with a glass fixed interferometer of 7.6-mm width, and those cases with $n_1 = n_2 = n_3$, with an air-scanning Fabry–Perot interferometer. For recording the interference pattern we used Ilford PAN-F film (50 ASA).

The intensity densitometric profiles of the photographic records were scanned with a Grant automatic microdensitometer comparator.

We have observed an adequate coincidence between the theoretical and the experimental profiles. Figures 7(a) and 7(b) and 8(a) and 8(b) reproduce two examples of such coincidence.

The influence of changes in light-source position (ρ coordinate) and the observation plane (x coordinate) on the intensity distribution of interference patterns was also analyzed.

Figure 8(c) shows the experimental profile when $x = 300$ mm and $\rho = \infty$. Compare it with the trace in Fig. 8(b). Figure 8(d) shows the experimental profile when $x = 300$ mm and $\rho = 500$ mm. Compare it with the other experimental traces.

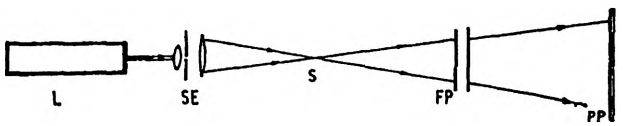


Fig. 6. Experimental setup: L, laser; SE, system of spatial-filter expansor beam collimator; S, light point source; FP, Fabry–Perot interferometer; PP, photographic plate.

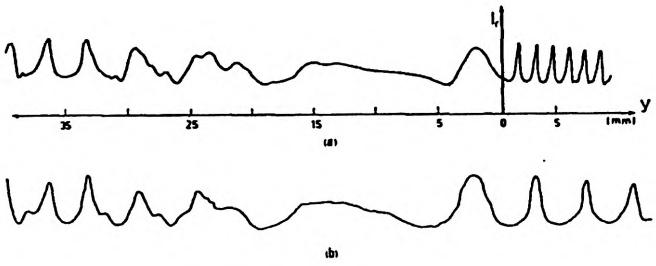


Fig. 7. (a) Theoretical and (b) experimental profiles showing the case $\lambda = 632.8$ nm, $n = 1$, $n' = 1.5$, $h = 7.6$ mm, $R = 0.46$, $p = 10$, $\rho = 250$ mm, $x = 300$ mm, $\alpha = 2 \times 10^{-4}$ rad.; $z = 0 \Rightarrow r = y$. Discrepancies at the right-hand side are due to the mismatch between the microdensitometric record scanning direction and the meridional section of the interference pattern.

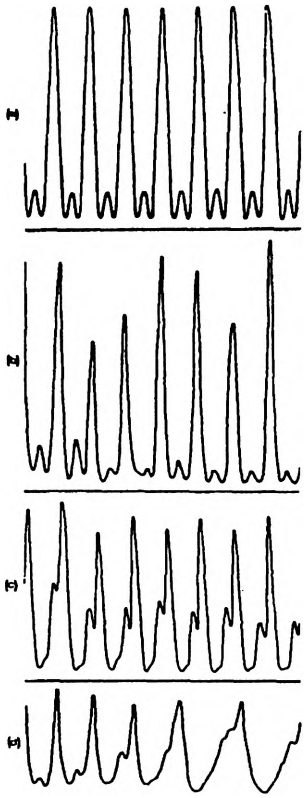


Fig. 8. Panel with different profiles corresponding to $\lambda = 632.8$ nm, $n = n' = 1$, $h = 20$ mm, $R = 0.8$, $p = 10$, $\alpha = 2 \times 10^{-4}$ rad, $z = 0$: (a) and (b) theoretical and experimental profiles for $\rho = \infty$ and $x = 500$ mm, respectively; (c) and (d) experimental profiles for $x = 300$ mm, with $\rho = \infty$ and $\rho = 500$ mm, respectively.

ACKNOWLEDGMENTS

The invaluable support provided by the Subsecretaría de Ciencia y Tecnología, Argentina, is gratefully acknowledged.

REFERENCES

1. K. W. Meissner, "Interference spectroscopy." Part I, J. Opt. Soc. Am. 31, 405–427 (1941); Part II, J. Opt. Soc. Am. 32, 185–210 (1942).

2. J. E. Sears and H. Barrell, "Fundamental standards of length in terms of wave-lengths of light," Phil. Trans. R. Soc. London Ser. A **223**, 143–216 (1934).
3. P. Connes, "Increase of the product of luminosity and resolving power of interferometers by using a path difference independent of the angle of incidence," Rev. Opt. **35**, 37 (1956).
4. J. Brossel, "Multiple beam localized fringes." I. Intensity distribution and localizations; II. Conditions of observation and formations of ghosts," Proc. Phys. Soc. **59**, 224–242 (1947).
5. N. Aebischer, "Calculs de profils dissymétriques observables sur des figures d'interferences en ondes multiples sphériques," Nouv. Rev. Opt. Appl. **2**, 351–366 (1971).
6. J. Rogers, "Fringe shifts in multiple-beam Fizeau interferometry," J. Opt. Soc. Am. **72**, 638–643 (1982).
7. L. M. Zerbino, Doctoral Thesis (Universidad Nacional de La Plata, La Plata, Argentina, 1978).
8. L. Zerbino, H. Rabal, and M. Garavaglia, "Compact device for interferometric holography," Proc. Soc. Photo-Opt. Instrum. Eng. **210**, 188–195 (1979).

JOURNAL OF MODERN OPTICS, 1987, VOL. 34, NO. 10, 1385–1391

Walsh functions: analysis of their properties under Fresnel diffraction

C. COLAUTTI, B. RUIZ, E. E. SICRE and M. GARAVAGLIA
Centro de Investigaciones Opticas (CIC), Casilla de Correo 124, 1900 La Plata, Republic of Argentina

(*Received 8 April 1987; revision received 13 July 1987*)

Abstract. The free-propagation properties of the light field diffracted by an aperture, have been investigated by employing a formalism based on the orthogonal and complete set of Walsh functions. We found an interesting link with the well-known self-imaging phenomenon, which can be used to explain the spatial filtering properties of many optical devices. An experimental result is given in order to illustrate this approach.

1. Introduction

The diffraction properties of most optical imaging systems are properly described in terms of Fourier optics. The input signal of such systems is analysed by considering a linear superposition of sinusoidal functions. After taking into account the effect of the system upon each sinusoidal component, the output signal is obtained by performing a suitable synthesis. However, while the analysis of optical systems is simplified by use of sinusoidal functions (i.e. under coherent illumination, the manipulation of the Fourier spectrum can be performed in a relatively easy way), the interaction between diffracted field and apertures is generally complicated. On the other hand, the analysis and synthesis of systems by means of the Walsh–Hadamard transform play an important role in digital image processing, since the operations are performed by using functions that only take values ± 1. For this reason, they suit computer processing and allow fast algorithms to be developed.

It is clear therefore that these two types of function have a well-defined scope in the field of image processing. However, in spite of their discontinuous nature (which seems not to be a natural representation signal for analogical systems), the Walsh functions have the remarkable property of being cyclically periodic [1], i.e. they can be considered as square-wave functions with step-like amplitude changes occurring at periodical intervals. Since spatial periodicity is a sufficient condition for an object aperture to generate the so-called self-imaging phenomenon [2–5], Walsh functions should behave in free propagation of light in a rather similar way as periodic structures, such as the binary Ronchi grating. In this way, the analysis and synthesis of signals performed in a Walsh scheme can be very useful for studying the properties of certain optical systems where both the free propagation of light and the interaction of aperture and diffracted field are relevant.

We start by analysing the behaviour of the Walsh functions under Fresnel diffraction in accordance with their periodicity properties. This analysis will be extended to a more general aperture synthesized as a linear superposition of Walsh functions. Finally, we illustrate this approach with some experimental results.

2. Properties of Walsh functions under Fresnel diffraction

Inside a certain finite domain $|x|<x_0/2$, the orthogonal and complete set of Walsh functions $\{\mathrm{Wal}_n(x);\ n=1,2,\ldots\}$ can be written as [1]

$$\begin{aligned}\mathrm{Wal}_n(x) &= \prod_{k=0}^{m}[R_k(x)]^{g_k};\quad |x|<x_0/2\\ &= \prod_{k=0}^{m}[\mathrm{sign}\,(\sin(2^k\pi x/x_0))]^{g_k}.\end{aligned}\tag{1}$$

In equation (1), $\{R_k(x)\}$ denotes the set of Rademacher functions, which are periodic square waves of amplitude ± 1, having period $d_k=2^{1-k}x_0$. The integer m is the rank of the binary expansion of n, in which the g_k are the corresponding bits, 0 or 1, i.e. $n=2^m g_m+2^{m-1}g_{m-1}+\ldots+2^0 g_0$. Since the Rademacher functions form an incomplete set, they cannot serve as an appropriate basis for synthesizing any optical signal.

For our purposes, it is more convenient to rewrite the Walsh functions as defined in the entire space domain, and which are restricted to take only 0 or 1 values, instead of ± 1, i.e.

$$W_n(x)=\tfrac{1}{2}[1+\mathrm{Wal}_n(x)]\,\mathrm{rect}\,(x/x_0).\tag{2}$$

Next, we consider a binary aperture with an amplitude transmittance given by the Walsh function as written in equation (2). If it is illuminated with a monochromatic plane wave propagating along the z-axis, the diffracted field amplitude $u_n(x;z)$, in the Fresnel region, becomes

$$u_n(x;z)=\int_{-\infty}^{\infty}W_n(x')\exp[(\mathrm{i}\pi/\lambda z)(x-x')^2]\,\mathrm{d}x'.\tag{3}$$

By using equations (1) and (2), the following expression for $u_n(x;z)$ results:

$$\begin{aligned}u_n(x;z)=\frac{1}{2}\int_{-\infty}^{\infty}\left\{1+K\sum_{k_1}\ldots\sum_{k_m}c_{k_1}^{g_1}\ldots c_{k_m}^{g_m}\exp\left[2\pi\mathrm{i}x'\left(\frac{g_1k_1}{d_1}+\ldots+\frac{g_mk_m}{d_m}\right)\right]\right\}\\ \times\,\mathrm{rect}\,(x'/x_0)\exp[\mathrm{i}(\pi/\lambda z)(x-x')^2]\,\mathrm{d}x',\end{aligned}\tag{4}$$

where K is a normalization constant. In equation (4), we have replaced the Rademacher functions by their corresponding Fourier expansions, namely the coefficients c_{k_i} which are non-zero only for odd values of k_i. Hence, apart from the Fresnel pattern produced by the uniform finite aperture $(-x_0/2,\ x_0/2)$, we obtain

$$\begin{aligned}u_n(x;z)\simeq(K/2)\exp(\mathrm{i}\pi x^2/\lambda z)\sum_{k_1}\ldots\sum_{k_m}c_{k_1}^{g_1}\ldots c_{k_m}^{g_m}\\ \times\exp\left[-\mathrm{i}\pi\lambda z\left(\frac{x}{\lambda z}-\frac{g_1k_1}{d_1}-\ldots-\frac{g_mk_m}{d_m}\right)^2\right]\\ *\,\mathrm{sinc}\left[x_0\left(\frac{x}{\lambda z}-\frac{g_1k_1}{d_1}-\ldots-\frac{g_mk_m}{d_m}\right)\right],\end{aligned}\tag{5}$$

where $*$ denotes convolution.

Next, we analyse the properties of $u_n(x;z)$. If we want to retrieve an amplitude distribution that resembles the Walsh function (as in the self-imaging phenomenon produced by periodic infinite apertures), then it is clear that the effect of the finite size of the aperture on $u_n(x;z)$ should be minimized. To this end, the sinc function

array, denoted $\mathrm{sinc}(x; k_1, \ldots, k_m)$, must be approximated by δ-functions. Therefore, overlap between different sinc functions should be avoided, except when the respective maxima coincide. The mean width of all the sinc functions is $\Delta x = \lambda z / x_0$, and the separation between successive maxima of $\mathrm{sinc}(x; k_p = 1, \ldots, k_{j-1} = 1, k_j, k_{j+1} = 1, \ldots, k_m = 1)$ is $\delta x_j = 2^j \lambda z / x_0$, $p \leqslant j \leqslant m$, for which $R_p(x)$ is the lowest-order Rademacher component that is present in $W_n(x)$. Since $\delta x_j / \delta x_p = 2^{j-p}$, coincidence between the several maxima always occurs, and the minimum distance between adjacent maxima of the whole array becomes $\delta x = \delta x_p = 2^p \lambda z / x_0$. Hence, the validity of the approximation $\mathrm{sinc}(\cdot) \simeq \delta(\cdot)$ is assured whenever $\delta x \gg \Delta x$, or equivalently $2^p \gg 1$. Of course, this condition places a limitation on the lowest-order Rademacher function that can be present in $W_n(x)$. Thus, by assuming $2^p \gg 1$, we obtain

$$u_n(x; z) \simeq (K/2) \sum_{k_p} \ldots \sum_{k_m} c_{k_p}^{g_p} \ldots c_{k_m}^{g_m} \times \exp\left[-2\pi i x \left(\frac{g_p k_p}{d_p} + \ldots + \frac{g_m k_m}{d_m} \right) \right] \exp\left[-i\pi\lambda z \left(\frac{g_p k_p}{d_p} + \ldots + \frac{g_m k_m}{d_m} \right)^2 \right]. \quad (6)$$

It is convenient to rewrite equation (6) in the following way:

$$u_n(x; z) \simeq (K/2) \sum_{k_p} \ldots \sum_{k_{j-1}} \sum_{k_{j+1}} \ldots \sum_{k_m} c_{k_p}^{g_p} \ldots c_{k_m}^{g_m} \times \exp\left[-2\pi i x \sum_{r \neq j} g_r k_r / d_r \right] \sum_{k_j} c_{k_j} \exp(-2\pi i x k_j / d_j) \times \exp\left[-i\pi\lambda z \left(\sum_{r \neq j} g_r k_r / d_r + k_j / d_j \right)^2 \right] \quad (7a)$$

or, equivalently

$$u_n(x; z) \simeq (K/2) \sum_{k_p} \ldots \sum_{k_{j-1}} \sum_{k_{j+1}} \ldots \sum_{k_m} c_{k_p}^{g_p} \ldots c_{k_m}^{g_m} \times \exp\left[-2\pi i x \sum_{r \neq j} g_r k_r / d_r \right] \exp\left[-i\pi\lambda z \left(\sum_{r \neq j} g_r k_r / d_r \right)^2 \right] \times \sum_{k_j} c_{k_j} \exp(-2\pi i x k_j / d_j) \exp(-i\pi\lambda z k_j^2 / d_j^2) \exp\left(-2\pi i \frac{\lambda z k_j}{d_j} \sum_{r \neq j} g_r k_r / d_r \right) \quad (7b)$$

From equations (7), we can derive the conditions to be satisfied in order to obtain a self-image of $R_j(x)$; namely

$$\lambda z k_j^2 / d_j^2 = 2h \quad \text{and} \quad \frac{\lambda z k_j}{d_j} \sum_{r \neq j} \frac{g_r k_r}{d_r} = q; \quad (8)$$

where h and q are positive integers. Both conditions are fulfilled whenever

$$z^{(j)} = 2\alpha x_0^2 / \lambda 2^{p+j-2}, \quad \alpha = 1, 2, 3, \ldots \quad (9)$$

For these values of z, the amplitude distribution given by equation (7) can be considered as a positive self-image of $R_j(x)$, spatially modulated by the remaining defocused Rademacher functions which act as a noise source.

However, by taking into account that

$$z^{(j)} = 2^{m-j} z^{(m)}, \quad p < j < m; \quad (10)$$

i.e. the first self-image of $R_j(x)$ coincides with the $\alpha = 2^{m-j}$ self-image of $R_m(x)$, then at the self-image planes associated with $R_p(x)$, all the Rademacher functions are well-focused. Therefore, for the distances

$$z = \alpha z_0 = 2\alpha x_0^2/\lambda 2^{2p-2}, \quad \alpha = 1, 2, 3, \ldots, \tag{11}$$

we get

$$u_n(x; z) \simeq (K/2)[1 + \mathrm{Wal}_n(x)], \tag{12}$$

which is a positive direct-contrast self-image of the Walsh function $W_n(x)$.

3. Interaction between the light field and an aperture mask: an approach based on Walsh functions

We turn now to the interaction between the light field and a given aperture from the viewpoint of the discussed properties of the Walsh functions. Since they form an orthogonal and complete set within a finite domain, any transparency limited by a certain pupil can be considered as synthesized from Walsh functions, instead of sinusoidal functions. If this transparency is the input object of a system illuminated by a coherent plane wave, then each Walsh component behaves in free propagation in a similar way to that treated in §2. Taking into account the binary nature of these functions, it is rather simple to understand the interaction of the diffracted field with an arbitrary binary aperture placed at a certain distance z (at least in the Kirchhoff approximation, where the product of the light amplitude with the transmittance function of the aperture can be considered for the transmitted field). All the Walsh functions focused at the plane of the aperture mask as positive self-images are transmitted by the system without appreciable distortion or attenuation, while the remaining Walsh components are severely distorted and attenuated. Of course, the interaction is still very complicated for those Walsh components which are not in focus at the plane of the aperture mask. For this reason, it seems appropriate to consider this kind of analysis for all those cases involving several interactions between the diffracted field and the aperture. Thus, if the number of interactions becomes large, the resulting field will be mainly synthesized by the first type of Walsh functions. This approach was used in [6, 7] to explain the spatial filtering properties of some periodic and non-periodic aperture arrangements. However, in such cases, all the apertures were assumed to be synthesized by Rademacher functions which form an incomplete set of periodic functions.

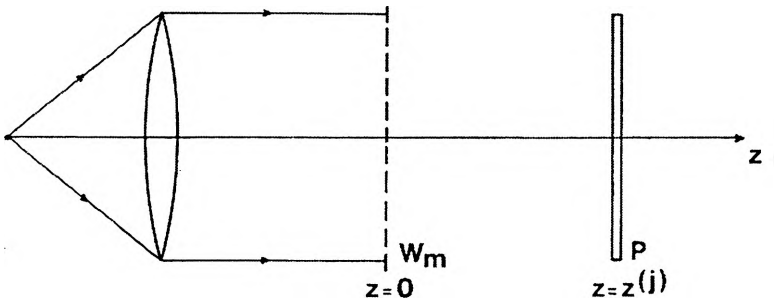
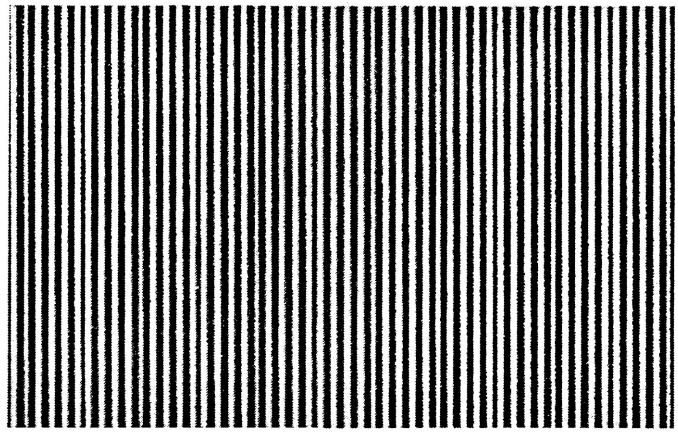
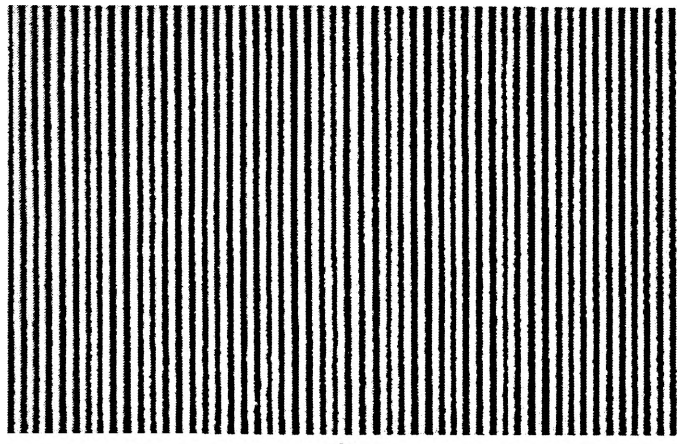


Figure 1. Scheme of the optical device employed for obtaining the self-images of the Walsh functions.

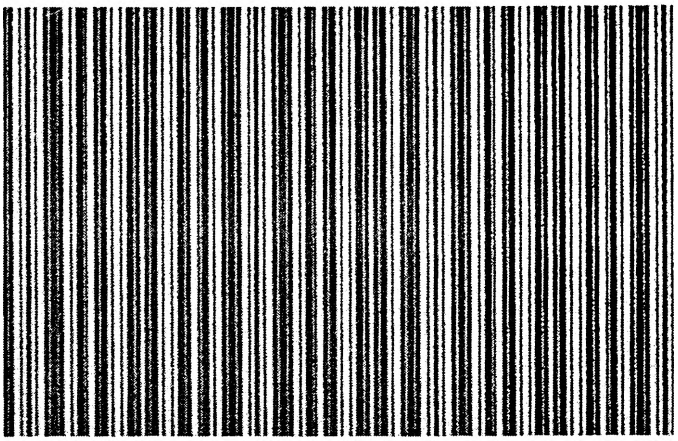


(*a*)

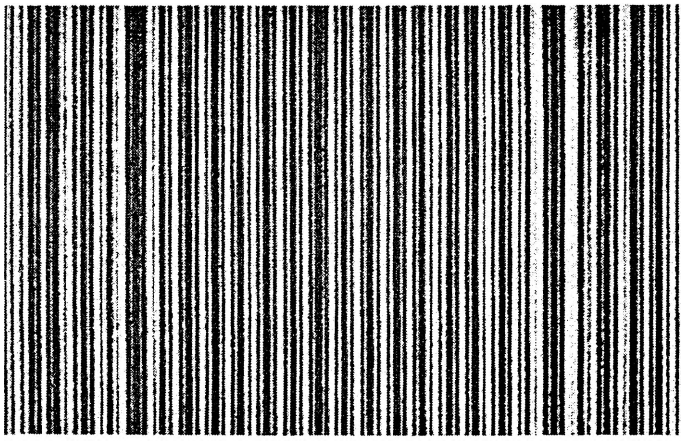


(*b*)

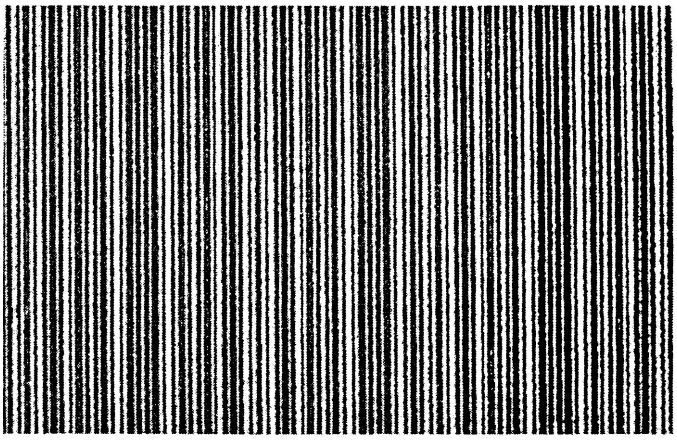
Figure 2. (*a*) Walsh function $\mathrm{Wal}(x) = R_8(x)\, R_9(x)$. (*b*) First self-image of $\mathrm{Wal}(x)$, recorded at $z = 24$ cm.



(*a*)



(*b*)



(*c*)

Figure 3. (*a*) Walsh function $\mathrm{Wal}(x) = R_7(x)\, R_8(x)\, R_9(x)$. (*b*) First self-image of $R_8(x)$, and second self-image of $R_9(x)$, recorded at $z = 24$ cm. (*c*) First self-image of $\mathrm{Wal}(x)$, recorded at $z = 48$ cm.

In order to illustrate the results obtained in § 2, we have synthesized an aperture consisting of a single Walsh function (in the normalized form, as given by equation (2)). When illuminated with a coherent plane wave, the aperture gives rise to the self-imaging phenomenon in accordance with equations (7)–(12) (see figure 1). Figure 2 (*a*) shows the Walsh function composed by two Rademacher functions $R_8(x)$ and $R_9(x)$. Figure 2 (*b*) shows the intensity distribution recorded at the first self-image plane of $R_8(x)$, which coincides with the second self-image plane of $R_9(x)$. Hence, the first self-image of the complete Walsh function can be observed. Figure 3 (*a*) shows the Walsh function composed of three Rademacher functions $R_7(x)$, $R_8(x)$ and $R_9(x)$. In figure 3 (*b*) the first self-image of $R_8(x)$ and the second self-image of $R_9(x)$ are well focused but some artifact noise due to the defocused self-image of $R_7(x)$ can be observed. In figure 3 (*c*), the three Rademacher components are in focus, so producing the first self-image of the complete Walsh function. Owing to the fact that a lower-order Rademacher component is present in the latter case, the approximation involved in deriving equation (6) is not well satisfied, and hence the self-image of the Walsh function exhibits more artifact noise than in the former case.

4. Conclusions

From a mathematical point of view, either a Walsh or a Fourier synthesis can be performed for all classes of finite apertures. Which of these approaches is more suited for synthesis and processing purposes is an open question in the field of digital image systems [8].

For optical systems, we can take into account something resembling a signal-to-noise ratio that characterizes the system. If certain Walsh functions are either perfectly cancelled or transmitted by a binary aperture, their associated energy can be considered as a signal level. The remaining Walsh functions present in the field amplitude (which are defocused at the plane of the aperture) will be severely distorted in transmission, so contributing to a noise level. Therefore, a treatment based on a Walsh approach can be suitably carried out for those cases in which several interactions between the diffracted field and a certain aperture mask occur in such a way that the signal level remains practically unchanged, while the noise level becomes increasingly lower. This is the case of several periodic arrays of apertures, such as the in-line analogue of a Fabry–Perot interferometer.

References

[1] Beauchamp, K. G., 1975, *Walsh Functions and their Applications* (New York: Academic Press).
[2] Winthrop, J. T., and Worthington, C. R., 1965, *J. opt. Soc. Am.*, **55**, 373.
[3] Montgomery, W. D., 1967, *J. opt. Soc. Am.*, **57**, 772.
[4] Montgomery, W. D., 1968, *J. opt. Soc. Am.*, **58**, 1112.
[5] Lohmann, A. W., Ojeda-Castañeda, J., and Streibl, N., 1983, *Optica Acta*, **30**, 1259.
[6] Ojeda-Castañeda, J., and Sicre, E. E., 1983, *Opt. Commun.*, **47**, 183.
[7] Lohmann, A. W., Ojeda-Castañeda, J., and Sicre, E. E., 1984, *Opt. Commun.*, **49**, 388.
[8] Blachman, N. M., 1974, *Proc. IEEE*, **62**, 346.

Fractional Fourier transform description with use of differential operators

B. Ruiz and H. Rabal

Centro de Investigaciones Opticas, Camino Parque Centenario entre 505 y 508, 1897 Gonnet, Argentina, and Casilla de Correo 124, 1900 La Plata, Argentina

Received January 2, 1997; revised manuscript received March 24, 1997; accepted April 21, 1997

The fractional Fourier transform (FRT) is expressed by means of propagation and thin-lens phase delay operators, and a large number of optical systems associated with it are found. At the same time, the output of optical systems is found in terms of the FRT, and the simplicity of the approach is illustrated with two examples. Mathematical definitions for the P-order convolution and correlation are proposed as generalizations of the classical ones such that, when the P-order FRT is applied to them, theorems that generalize the classical convolution and correlation are verified. © 1997 Optical Society of America [S0740-3232(97)01511-1]

Key words: Propagation, optical systems, fractional Fourier transform, convolution, correlation.

1. INTRODUCTION

The fractional Fourier transform (FRT) and its optical implementation have been the subject of considerable attention in recent times: The concept emerged in quantum mechanics and is a generalization of the Fourier transform (FT) with respect to an order P. Fractional-order convolution and correlation have also been defined and optically generated.[1-14]

The FRT is usually defined through integrals that very much resemble the integral representation of scalar diffraction in the Fresnel region. We present here a description of the same transform, that is, one that is equivalent to it, by using differential operators, namely, the propagation operator and the thin-lens phase delay operator (or function).

The use of operators constitutes a powerful symbolic instrument to describe in a comprehensive way the relevant properties of optical systems without being distracted by many details. Very general properties can be highlighted in this way, and adimensional variables are not required.

Differential exponential operators are recognized to be difficult to treat mathematically,[15-19] and this is indeed so, unless the effect of limiting apertures is not considered. If limiting apertures can be separately treated,[19] considerable insight can be gained by using operators. The advantages of our approach with respect to the abstract use of operators[15-19] are that, although one is required to work with infinite series, the explicit physical representation of every mathematical expression is readily present. This is not so when using abstract operators, such as the scaling operator, which is easily defined through its properties but cannot be straightforwardly implemented optically. When it is necessary to use the scaling operator, we put it in at the final step.

In the appendices there are complementary calculations. There we have found explicitly equivalent systems to one given in Ref. 20. In the main text we use the concept of equivalence to find an infinite number of optical systems giving rise to the FRT, which are equivalent to the simplest one. We have used this concept earlier to associate an infinite set of cylindrical systems with the FT.[21]

We begin in Section 2 by reviewing an auxiliary useful concept, that of the q-index FT.[22] This is not a new concept; it can be recognized as an amplitude- and frequency-scaled version of the ordinary FT.[20] Its introduction makes the following mathematical steps easier.

Different equivalent ways to express the FRT, some of them in terms of operators, are proposed in Section 3. The amplitude distribution on an image is then calculated in terms of the FRT in Section 4. In Section 5 some other mathematical definitions of usual operations are given, namely, P-order convolution and correlation. Both intend to be generalizations of classical definitions such that, when the P-order FRT is applied to them, theorems that generalize the classical convolution and correlation are verified.

2. THEORY REVIEW

We are going to use the bidimensional FT in the form[22]:

$$\mathcal{F}_q\{g\}(x, y) = \exp\left(\frac{j\Delta}{2q}\right)\left\{\exp\left(\frac{-jq}{2}\, r^2\right) \times \exp\left(\frac{j\Delta}{2q}\right)[g(x, y)]\right\}, \quad (1)$$

and we are going to call it the q-index ($q > 0$) FT (q-FT), with the operator $\exp(a\Delta)(g) = \Sigma_{n=0}^{\infty}(a^n/n!)\Delta^n(g)$, where $g = g(x, y)$, $\Delta = \partial^2/\partial x^2 + \partial^2/\partial y^2$, $r^2 = x^2 + y^2$, and $j = \sqrt{-1}$. We also have, from Eq. (1), $\mathcal{F}_{-q} = \mathcal{F}_q^{-1} = \mathcal{F}_q^*$.

When $q = 2\pi$, the classical FT is obtained and for $q > 0$ it coincides with the q-index transform defined by[23]

$$\mathcal{F}_q\{g\}(x, y) = \frac{-jq}{2\pi}\int\int_{-\infty}^{\infty} g(u, v) \times \exp[-qj(ux + vy)]\,du\,dv, \quad (2)$$

0740-3232/97/112905-09$10.00 © 1997 Optical Society of America

where the index q includes a scaling factor. In what follows we are going to work with distributions.[24]

For ease, sometimes we use the following notation to describe optical systems: We call $P_z(g)$ the propagation operator applied to g when it is calculated at a distance z, and L_f the function (or operator) that describes the phase delay in a thin lens with focal distance f (positive or negative). That is,

$$P_z(g) = \exp\left(\frac{jz\Delta}{2k}\right)(g), \tag{3a}$$

$$L_f = \exp\left(\frac{-jk}{2f}r^2\right), \tag{3b}$$

with k the wave number of the light. Equation (3a) is equal to the integral expression[25]

$$P_z(g) = \frac{1}{j\lambda z}\iint g(u, v) \times \exp\left\{\frac{jk}{2z}[(x-u)^2 + (y-v)^2]\right\}du\,dv = \frac{1}{j\lambda z}\left[g * \exp\left(\frac{jkr^2}{2z}\right)\right]$$

if we take into account Eq. (B3) in Appendix B with $s = k/2z$ and $\lambda = 2\pi/k$.

The effect of the finite size of the pupil of the lens is not considered here in order to keep the results in a closed form.

If we rewrite Eq. (1) with $q = k/f$ and use Eqs. (3), we obtain the identification of the q-FT with the simple system of Fig. 1 and parameter f:

$$\mathcal{F}_q\{g\} = P_f L_f P_f\{g\}. \tag{4}$$

Expression (1) is also equivalent to[22]

$$\mathcal{F}_q\{g\}(x, y) = j\exp\left(\frac{-jqr^2}{2}\right) \times \exp\left(\frac{j\Delta}{2q}\right)\left[\exp\left(\frac{-jqr^2}{2}\right)g(x, y)\right] \tag{5}$$

and, with the use of Eqs. (3) and $q = k/f$, can be written as

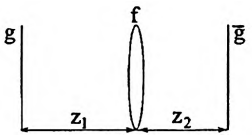


Fig. 1. Optical system to perform the FRT when $z_1 = z_2$.

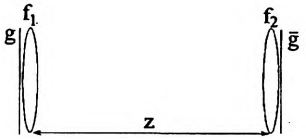


Fig. 2. Optical system to perform the FRT when $f_1 = f_2$.

$$\mathcal{F}_q\{g\} = L_f P_f L_f\{g\}, \tag{6}$$

which identifies the q-FT with the simple system of Fig. 2 and parameter f.

The general setup shown in Fig. 1 is represented by

$$\bar{g} = P_{z_2} L_f P_{z_1}(g), \tag{7}$$

and the setup shown in Fig. 2 is

$$\bar{g} = L_{f_2} P_z L_{f_1}(g). \tag{8}$$

3. FRACTIONAL TRANSFORM: EQUIVALENT DEFINITIONS

We are going to adopt one expression for the FRT, given by Eq. (9), and we shall find different ways to express Eq. (9), which are given by Eqs. (10)–(16). So we have the following for the FRT of order $P = 2\phi/\pi$ ($\phi \neq m\pi$)[12]:

$$\mathcal{F}^P\{g\}(x, y) = \frac{-jk}{2\pi F \sin\phi}\iint_{-\infty}^{\infty} g(u, v) \times \exp\left[\frac{jk(x^2 + u^2 + y^2 + v^2)}{2F\tan\phi}\right] \times \exp\left[\frac{-jk(xu + yv)}{F\sin\phi}\right]du\,dv. \tag{9}$$

By using the q-FT with $q = k/F\sin\phi$ and Eq. (2), we can write Eq. (9) as

$$\mathcal{F}^P\{g\}(x, y) = \exp\left(\frac{jkr^2}{2F\tan\phi}\right) \times \mathcal{F}_q\left\{g\exp\left[\frac{jk(u^2 + v^2)}{2F\tan\phi}\right]\right\}(x, y). \tag{10}$$

Equation (10) is used to calculate the FRT from the FT as in Appendix C.1.

In terms of operators [Eq. (1) or (5)], Eq. (10) is

$$\mathcal{F}^P\{g\}(x, y) = \exp\left(\frac{jkr^2}{2F\tan\phi}\right) \times \mathcal{F}_q\left\{g\exp\left(\frac{jkr^2}{2F\tan\phi}\right)\right\}(x, y). \tag{11}$$

Equation (11) can be represented by the system of Fig. 3 with $f_3 = f_4 = -F\tan\phi$. If $\phi = \pi/2$ in Eqs. (9)–(11), then $\mathcal{F}^1 = \mathcal{F}_q$, where $q = k/F$.

The FRT defined by Eq. (9) is valid for $\phi \neq m\pi$, $m = 0, 1, 2, \ldots$. If $\phi = m\pi$ ($P = 2m$), it is defined as

$$\mathcal{F}^{4m}\{g\} = g, \qquad \mathcal{F}^{4m+2}\{g\} = -g^-,$$

where $g^-(x, y) = g(-x, -y)$.

It can be seen from the last result and Eq. (9) that $\mathcal{F}^P$ is periodic with period 4. It can be proved that it is enough to work with $0 < P < 1$, that is, $0 < \phi < \pi/2$.

Using Eqs. (1) and (11) and Eqs. (5) and (11), we obtained, respectively,

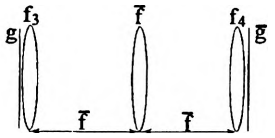


Fig. 3. Optical system equivalent to the systems in Figs. 1 and 2, with the conditions deduced in Appendix A.

$$\mathcal{F}^P\{g\}(x, y) = \exp\left[\frac{jF(1 - \cos\phi)\Delta}{2k \sin\phi}\right]\exp\left[\frac{-jk(\sin\phi)r^2}{2F}\right] \times \exp\left[\frac{jF(1 - \cos\phi)\Delta}{2k \sin\phi}\right](g), \tag{12}$$

$$\mathcal{F}^P\{g\}(x, y) = j\exp\left[\frac{-jk(1 - \cos\phi)r^2}{2F \sin\phi}\right]\exp\left[\frac{jF(\sin\phi)\Delta}{2k}\right] \left\{g \exp\left[\frac{-jk(1 - \cos\phi)r^2}{2F \sin\phi}\right]\right\}. \tag{13}$$

Equations (12) and (13) represent the two simple systems giving the FRT (Figs. 1 and 2).

Equation (9) can also be written as

$$\mathcal{F}^P\{g\}(x, y) = \frac{-jq}{2\pi}\exp\left(\frac{-jkr^2}{2F \cot\phi}\right)\int\int_{-\infty}^{\infty} g(u, v) \times \exp\left\{\frac{jk}{2F \tan\phi}\left[\left(u - \frac{x}{\cos\phi}\right)^2 + \left(v - \frac{y}{\cos\phi}\right)^2\right]\right\}du\,dv, \tag{14}$$

with $q = k/F \sin\phi$.

Equation (14) expresses a convolution. If $h(x, y) = \exp(jkr^2/2F \tan\phi)$, then it can be written as

$$\mathcal{F}^P\{g\}(x, y) = \frac{-jq}{2\pi}\exp\left(\frac{-jkr^2}{2F \cot\phi}\right)(g * h)\left(\frac{x}{\cos\phi}, \frac{y}{\cos\phi}\right). \tag{15}$$

If we use Eq. (B3) from Appendix B, this last equation becomes

$$\mathcal{F}^P\{g\}(x, y) = \frac{1}{\cos\phi}\left\{\exp\left[\frac{-jk \sin(2\phi)}{4F}r^2\right] \times \exp\left[\frac{jF(\tan\phi)\Delta}{2k}\right][g(x, y)]\right\}\left(\frac{x}{\cos\phi}, \frac{y}{\cos\phi}\right), \tag{16}$$

with $\phi \neq (2m + 1)\pi/2$, $m = 0, 1, 2, \ldots$. Equation (16) describes the FRT as a propagation followed by a lens and a change of scale in the output.

Equations (14)–(16) are not applicable to the ordinary FT, that is, when $\phi = \pi/2$. Equation (16) can be used to define the FRT when $\phi = m\pi$ and shows continuity with the above definition.

An important property of the FRT is order additivity. From Eq. (12) it can be seen that $(\mathcal{F}^P)^{-1} = (\mathcal{F}^P)^* = \mathcal{F}^{-P}$. The inverse of the FRT, $(\mathcal{F}^P)^{-1}$, can also be obtained by changing F to $-F$.

4. OPTICAL SYSTEMS AND THE FRACTIONAL FOURIER TRANSFORM

A. Optical Systems Description with the Fractional Fourier Transform

We are going to describe the systems in Figs. 1 and 2 by means of the FRT. Equation (11) lets us write the q-FT in terms of the P-order FRT (P-FRT):

$$\mathcal{F}_q\{g\}(x, y) = \exp\left(\frac{-jkr^2}{2F \tan\phi}\right)\mathcal{F}^P\left\{g \exp\left(\frac{-jkr^2}{2F \tan\phi}\right)\right\}, \tag{17}$$

with $q = k/F \sin\phi$.

For the system in Fig. 1, with $1/f \neq 1/z_1 + 1/z_2$ and Eqs. (A1) and (A2) in Appendix A, we have

$$\bar{g} = \exp\left[\frac{-jkr^2}{2A}(z_1 - f)\right]\mathcal{F}_q\left\{g \exp\left[\frac{-jkr^2}{2A}(z_2 - f)\right]\right\}, \tag{18}$$

with $q = kf/A$, where $A = f(z_1 + z_2) - z_1z_2$.

In Eq. (18) we put $\mathcal{F}_q$ as in Eq. (17) and obtain

$$\bar{g} = \exp\left[\frac{-jkr^2}{2}\left(\frac{z_1 - f}{A} + \frac{1}{F \tan\phi}\right)\right] \times \mathcal{F}^P\left\{g \exp\left[\frac{-jkr^2}{2}\left(\frac{z_2 - f}{A} + \frac{1}{F \tan\phi}\right)\right]\right\}, \tag{19}$$

with $F \sin\phi = A/f$.

If, in Eq. (19), we take $F \tan\phi = A/(f - z_2)$, we obtain the following for the FRT:

$$\bar{g} = \exp\left[\frac{-jk(z_1 - z_2)r^2}{2A}\right]\mathcal{F}^P\{g\}, \tag{20a}$$

with

$$\cos\phi = (f - z_2)/f, \qquad F = A/[z_2(2f - z_2)]^{1/2}. \tag{20b}$$

Equations (20) are not valid, in the real field, for $z_2 \leq 0$ and $z_2 \geq 2f$. For those values it is convenient to work with the classical FT. But if we want to use the FRT, we can separate the last propagation into two successive propagations $z_2 = z + (z_2 - z)$ such that the distance z satisfies Eqs. (20) and the propagation of distance $(z_2 - z)$ can be expressed by means of Eq. (13).

It can be seen from Eq. (20a) that not all output distributions correspond to a FRT. Besides, when only intensity is measured, so that the phase factor produces no effect, the result is always proportional to a squared FRT of a certain order given by Eqs. (20b).

If in Eq. (19) we take $F \tan\phi = A/(f - z_1)$, we obtain

$$\bar{g} = \mathcal{F}^P\left\{g \exp\left[\frac{-jk(z_2 - z_1)r^2}{2A}\right]\right\}, \tag{21}$$

with $\cos\phi = (f - z_1)/f$ and $F = A/[z_1(2f - z_1)]^{1/2}$.

Then Eqs. (20) and (21) are descriptions of the optical system in Fig. 1 by means of the FRT.

B. Equivalent Systems Representing the Fractional Fourier Transform

The FRT can be represented by many optical systems (actually, an infinite number of systems), some of which we are going to describe.

From Eqs. (20) we see that the system in Fig. 1, with a lens at the output with focus $\hat{f} = A/(z_2 - z_1)$, represents $\mathcal{F}^P$. It is shown in Fig. 4.

Conversely, given ϕ and F, there are infinite systems associated with $\mathcal{F}^P$ ($P = 2\phi/\pi$). They are the systems described in Fig. 4, and

$$z_1 = F \tan \phi - f \frac{1 - \cos \phi}{\cos \phi}, \qquad z_2 = f(1 - \cos \phi),$$

$$\hat{f} = fF \frac{\cos \phi}{f \sin \phi - F},$$

with $\phi \neq (2m + 1)\pi/2$.

That is, for each f we have an optical system representing $\mathcal{F}^P$. In general, as the FRT is determined by ϕ and F and the system in Fig. 1 has three free parameters (z_1, z_2, and f), it is possible to choose one of them arbitrarily to represent the FRT. If, for example, we take $z_1 = z_2 = \bar{z}$, then the output lens collapses and Eq. (20a) becomes

$$\mathcal{F}^P\{g\} = \bar{g}, \tag{22}$$

with $\bar{z} = F(1 - \cos \phi)/\sin \phi$ and $f = F/\sin \phi$. Then Eq. (22) coincides with Eq. (12).

Conversely, given the system in Fig. 1, with $z_1 = z_2 = \bar{z}$, the associated FRT has the parameters

$$\cos \phi = (f - \bar{z})/f, \qquad F = A/[\bar{z}(2f - \bar{z})]^{1/2}.$$

As the system in Figs. 1 and 2, with the conditions given in Appendix A, are equivalent, the system in Fig. 2, with a lens of focal length $\bar{f} = f_1 f_2/(f_2 - f_1)$ at the output, represents the FRT. But this means that $f_1 = f_2 = \bar{f}$, so the system in Fig. 2 represents the FRT with

$$\cos \phi = (\bar{f} - z)/\bar{f}, \qquad F = z\bar{f}/[z(2\bar{f} - z)]^{1/2};$$

or, alternatively, the FRT can be represented by the system in Fig. 2 with

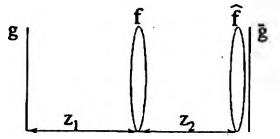


Fig. 4. General optical system to perform the FRT with the parameters given in Subsection 4.B.

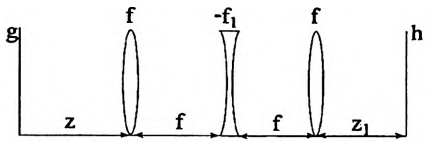


Fig. 5. Optical system described with the FRT in Subsection 4.C.

$$z = F \sin \phi, \qquad \bar{f} = F \sin \phi/(1 - \cos \phi), \tag{23}$$

which coincides with the FRT description in Eq. (13).

Then, from Fig. 4, we can say that a new expression for the P-FRT using operators is

$$\mathcal{F}^P\{g\}(x, y) = \exp\left[\frac{-jk(f \sin \phi - F)}{2fF \cos \phi} r^2\right] \times \exp\left[\frac{jf(1 - \cos \phi)\Delta}{2k}\right] \exp\left(\frac{-jkr^2}{2f}\right) \times \exp\left[\frac{j}{2k}\left(F \tan \phi - f \frac{1 - \cos \phi}{\cos \phi}\right)\Delta\right]\{g\}$$

with any f; this includes as particular cases Eq. (12) ($z_1 = z_2$) and Eq. (13) ($z_1 = 0$).

C. Cascading Systems Description

We can describe the system shown in Fig. 5 as being composed of three FRT cascading systems such as that in Fig. 1; that is, by using Eq. (22) (Ref. 5), we obtain

$$P_{z_1 - z} \mathcal{F}^P \mathcal{F}^{-P_1} \mathcal{F}^P\{g\} = h,$$

with

$$P = 2\phi/\pi, \qquad P_1 = 2\phi_1/\pi, \qquad \cos \phi = 1 - z/f,$$

$$\cos \phi_1 = 1 + (f - z)/f_1, \qquad F = f \sin \phi,$$

$$F_1 = f_1 \sin \phi_1.$$

To be able to apply order additivity, we have to impose the condition that $F = F_1$. This implies that $f_1 = f^2/2(z - f)$, and hence

$$P_{z_1 - z} \mathcal{F}^{2P - P_1}\{g\} = h. \tag{24}$$

In addition, it holds that $2P - P_1 = 2$, and then

$$P_{z_1 - z}\{-g^-\} = h, \tag{25}$$

which implies that the complex system in Fig. 5 with the input g has the same behavior as a propagation of distance $(z_1 - z)$ with the input function $-g^-$.

If $z_1 = z$ in Eq. (25), we have $h = -g^-$, with $f_1 = f^2/2(z - f)$ and f and z arbitrary. Then we can freely take any two parameters (of the four parameters of the system) to obtain $-g^-$ as the image through the system in Fig. 5. That is so because in Eq. (24) with $z = z_1$ there is only one FRT.

If we want to find an alternative system that gives, for any input function g, the output $-g^-$, we put $\mathcal{F}^{2-P} \mathcal{F}^P\{g\} = -g^-$ for any P. This system involves the successive application of the system in Fig. 2 with the parameters given by Eqs. (23) and then the system in Fig. 2 with parameters given by Eq. (23) but with ϕ changed to $\pi - \phi$. This procedure is shown in Fig. 6, where the parameters are

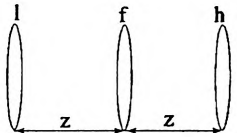


Fig. 6. Optical system to perform $\mathcal{F}^{2-P}\mathcal{F}^{P} = \mathcal{F}^{2}$ with any P, whose elements are analyzed in Subsection 4.C.

$$z = F \sin\phi, \qquad l = F \sin\phi/(1 - \cos\phi),$$
$$f = F \sin\phi/2, \qquad h = F \sin\phi/(1 + \cos\phi)$$

for any F and $\phi(\neq m\pi)$.

5. CONVOLUTION AND CORRELATION

We propose here definitions of convolution and correlation associated with the FRT. In the first place, it is required that they generalize the usual definitions of convolution and correlation in the following sense: For $\phi = \pi/2$, the usual definitions should be obtained. For example, the P convolution must verify a convolution theorem for $\mathcal{F}^{P}$ so that for $\phi = \pi/2$ the theorem associated with the FT should result:

$$\mathcal{F}_q\{g * h\} = (2\pi j/q)\mathcal{F}_q\{g\}\mathcal{F}_q\{h\}. \tag{26}$$

A. Definition of Convolution

We define the P-order convolution between the functions g and h, by using the notation $g \overset{P}{*} h$, as

$$\left(g \overset{P}{*} h\right)(x, y) = \exp\left(\frac{-jkr^2}{2F\tan\phi}\right)\left[g \exp\left(\frac{jkr^2}{2F\tan\phi}\right) * h \times \exp\left(\frac{jkr^2}{2F\tan\phi}\right)\right](x, y), \tag{27}$$

with $P = 2\phi/\pi$. In this definition it can be recognized that there is an external phase correction and that the main operation is a classical convolution between two complex functions, which are those to be fractionally convolved, each with the same quadratic phase modification. This phase modification depends on the operation fractional order and the parameter F.

The external phase correction does not affect intensity measurements but must be taken into account if the field distribution obtained in fractional convolution is used as input to other processing operations.

The expression of the P convolution with use of the propagation operator is obtained from Eq. (27) and Eq. (B3) of Appendix B with $s = k/2F\tan\phi$:

$$\left(g \overset{P}{*} h\right)(x, y) = \frac{j2\pi F\tan\phi}{k}\exp\left(\frac{-jkr^2}{2F\tan\phi}\right) \times \left\{\exp\left[\frac{jF(\tan\phi)\Delta}{2k}\right]\left[g(x, y)h(\alpha - x, \beta - y) \times \exp\left(\frac{jkr^2}{2F\tan\phi}\right)\right]\right\}_{\alpha=x,\beta=y}. \tag{28}$$

In each particular case, the most convenient parameter, s, is chosen so as to make the calculation easy. Then the expression generally used is

$$\left(g \overset{P}{*} h\right)(x, y) = \frac{j\pi}{s}\exp\left(\frac{-jkr^2}{2F\tan\phi}\right)\exp\left(\frac{j\Delta}{4s}\right)\left\{\left[g(x, y)h(\alpha - x, \beta - y) \times \exp\left[\frac{jk}{2F\tan\phi}(r^2 + \tilde{r}^2)\right]\exp(-js\tilde{r}^2)\right\}\right\}_{\alpha=x,\beta=y}, \tag{29a}$$

with $\tilde{r}^2 = (x - \alpha)^2 + (y - \beta)^2$. For example, if $h = \exp(jar^2)$, we choose $s = a + k/(2F\tan\phi) \neq 0$ and obtain, by applying Eq. (13),

$$\left[g \overset{P}{*} \exp(jar^2)\right](x, y) = \frac{j2\pi F\tan\phi}{k + 2aF\tan\phi}\exp\left(\frac{-jkr^2}{2F\tan\phi}\right) \times \exp\left[\frac{jF(\tan\phi)\Delta}{2(k + 2aF\tan\phi)}\right]\left[g(x, y)\exp\left(\frac{jkr^2}{2F\tan\phi}\right)\right] = \frac{j2\pi F\tan\phi}{k + 2aF\tan\phi}\exp\left(\frac{-jkr^2}{F\tan\phi}\right)\mathcal{F}^{P_1}\{g\}, \tag{29b}$$

with P_1 determined by the equations given in Subsection 4.B.

Expression (29b) shows that the P convolution between a function g and a quadratic phase delay is the product of a lens and the P_1-FRT of g. This convolution can be optically obtained by using a lens against the input function transmittance, followed by a free propagation and by a lens with focal length opposite to that of the first one.

From another point of view, this system is shift invariant in a wide sense because the output is the P convolution of the input and the impulse response of the system.

Expression (29b) is valid when $P = 1$, in which case the system reduces to a propagation of distance $z = k/2a$.

B. Convolution Theorem

The P-FRT applied to the P convolution verifies that

$$\mathcal{F}^{P}\left\{g \overset{P}{*} h\right\} = j\lambda F(\sin\phi)\exp\left(\frac{-jkr^2}{2F\tan\phi}\right)\mathcal{F}^{P}\{g\}\mathcal{F}^{P}\{h\}, \tag{30}$$

with $\lambda = 2\pi/k$.

To prove this theorem, we start with $\mathcal{F}^{P}$ as defined in Eq. (11), P convolution as defined in Eq. (27), and $q = k/F\sin\phi$:

$$\mathcal{F}^P\left(g \overset{P}{*} h\right) = \exp\left(\frac{jkr^2}{2F\tan\phi}\right)\mathcal{F}_q\left\{\left(g \overset{P}{*} h\right)\exp\left(\frac{jkr^2}{2F\tan\phi}\right)\right\}$$
$$= \exp\left(\frac{jkr^2}{2F\tan\phi}\right)\mathcal{F}_q\left\{g\exp\left(\frac{jkr^2}{2F\tan\phi}\right) * h\exp\left(\frac{jkr^2}{2F\tan\phi}\right)\right\}.$$

We apply to the last term the classical convolution theorem (26) and again use Eq. (11):

$$\mathcal{F}^P\left\{g \overset{P}{*} h\right\} = \frac{2\pi j}{q}\exp\left(\frac{jkr^2}{2F\tan\phi}\right) \times \mathcal{F}_q\left\{g\exp\left(\frac{jkr^2}{2F\tan\phi}\right)\right\} \times \mathcal{F}_q\left\{h\exp\left(\frac{jkr^2}{2F\tan\phi}\right)\right\} = \frac{2\pi j}{q}\exp\left(\frac{-jkr^2}{2F\tan\phi}\right)\mathcal{F}^P\{g\}\mathcal{F}^P\{h\};$$

thus Eq. (30) is obtained.

C. Definition of Correlation

We define the P-order correlation between the functions g and h, by using the notation $g \overset{P}{\bar{*}} h$ as

$$g \overset{P}{\bar{*}} h = \exp\left(\frac{-jkr^2}{2F\tan\phi}\right)\left[g\exp\left(\frac{jkr^2}{2F\tan\phi}\right) * (-h^-)^*\exp\left(\frac{-jkr^2}{2F\tan\phi}\right)\right]. \quad (31)$$

The asterisk as a superscript indicates conjugation.

D. Correlation Theorem

The P-FRT applied to the P correlation verifies that

$$\mathcal{F}^P\left\{g \overset{P}{\bar{*}} h\right\} = j\lambda F(\sin\phi)\exp\left(\frac{jkr^2}{2F\tan\phi}\right) \times \mathcal{F}^P\{g\}(\mathcal{F}^P\{h\})^*. \quad (32)$$

To prove this theorem, we use the P-FRT defined by Eq. (11) and the convolution theorem (26), with $q = k/F\sin\phi$:

$$\mathcal{F}^P\left\{g \overset{P}{\bar{*}} h\right\} = \exp\left(\frac{jkr^2}{2F\tan\phi}\right)\mathcal{F}_q\left\{g\exp\left(\frac{jkr^2}{2F\tan\phi}\right) * (-h^-)^*\exp\left(\frac{-jkr^2}{2F\tan\phi}\right)\right\}$$
$$= \frac{2\pi j}{q}\exp\left(\frac{jkr^2}{2F\tan\phi}\right) \times \mathcal{F}_q\left\{g\exp\left(\frac{jkr^2}{2F\tan\phi}\right)\right\} \times \mathcal{F}_q\left\{(-h^-)^*\exp\left(\frac{-jkr^2}{2F\tan\phi}\right)\right\}. \quad (33)$$

With the q-FT properties

$$\mathcal{F}_q^* = \mathcal{F}_q^{-1}, \qquad \mathcal{F}_q\mathcal{F}_q\{g\} = -g^-,$$

we obtain

$$\left[\mathcal{F}_q\left\{(-h^-)^*\exp\left(\frac{-jkr^2}{2F\tan\phi}\right)\right\}\right]^* = \mathcal{F}_q^{-1}\left\{-h^-\exp\left(\frac{jkr^2}{2F\tan\phi}\right)\right\} = \mathcal{F}_q\left\{h\exp\left(\frac{jkr^2}{2F\tan\phi}\right)\right\}.$$

Then

$$\mathcal{F}_q\left\{(-h^-)^*\exp\left(\frac{-jkr^2}{2F\tan\phi}\right)\right\} = \left(\mathcal{F}_q\left\{h\exp\left(\frac{jkr^2}{2F\tan\phi}\right)\right\}\right)^*.$$

With the use of Eq. (11), the last equation becomes

$$\mathcal{F}_q\left\{(-h^-)^*\exp\left(\frac{-jkr^2}{2F\tan\phi}\right)\right\} = \exp\left(\frac{jkr^2}{2F\tan\phi}\right)(\mathcal{F}^P\{h\})^*.$$

With this equation and Eq. (11), Eq. (33) results in Eq. (32).

When $\phi = \pi/2$, this correlation theorem is the classical FT correlation theorem, which is what we wanted.

The optical implementation of the correlation can be performed by taking g as input, using a complex holographic filter in the P-Fourier plane, adding the lens given in Eq. (32), and obtaining the result in the $(4 - P)$-Fourier plane.

E. Autocorrelation Theorem

If, in Eq. (31), we take $g = h$, we obtain the P-order autocorrelation. From the correlation theorem results the autocorrelation theorem:

$$\mathcal{F}^P\left\{h \overset{P}{\bar{*}} h\right\} = j\lambda F(\sin\phi)\exp\left(\frac{jkr^2}{2F\tan\phi}\right)|\mathcal{F}^P\{h\}|^2. \quad (34)$$

6. CONCLUSIONS

We have used a description of the Fourier transform (FT) named the q-index FT to analyze the fractional Fourier transform (FRT). When it is used, in operator description, abstract scaling operators do not appear in the middle of system descriptions but, if required, appear only in the final results.

The concept of equivalent optical systems was then used to find an infinite set of systems that represent the FRT. That concept, when applied with the use of operators, results in a set of relations among the parameters (focal lengths and propagation distances), which must be satisfied for the systems to be equivalent. The relations between these parameters and the two parameters that determine the FRT, P and F, were found.

These relations simplify the calculations of the output of any system considered as a cascade and composed of any number of lenses. By considering that both the ϕ and F values can be chosen independently, we can use different focal distances for the lenses in the system. Two application examples were given to illustrate the simplicity of the approach.

The output of a simple optical system with three independent parameters was found in terms of the FRT applied to the input. The output intensity distribution of the system always corresponds to that of a certain FRT.

Some calculations on the FRT and the convolution were given in the appendices.

Mathematical definitions of P convolution and P correlation that generalize the usual ones were proposed and expressed in terms of operators. A physical way to generate a certain P convolution in terms of lenses and propagations was described. More general cases require the use of complex filters, as for example, holographic elements.

APPENDIX A: EQUIVALENCE BETWEEN OPTICAL SYSTEMS

It is possible to prove the equivalence between optical systems with the same number of independent geometrical parameters (the number of propagation distances plus the number of focal distances). In the cases shown in Figs. 1–3, these systems present three nonzero parameters, which are, respectively, (z_1, z_2, f), (f_1, f_2, z), and $(f_3, f_4, \bar{f})$.

The equivalence between the systems in Figs. 1 and 2 is given by[20]

$$z = A/f, \qquad f_1 = A/z_2, \qquad f_2 = A/z_1,$$

or, alternatively,

$$z_1 = zf_1/B, \qquad z_2 = zf_2/B, \qquad f = \frac{f_1 f_2}{B},$$

with $A = (z_1 + z_2)f - z_1 z_2 \neq 0$ and $B = f_1 + f_2 - z \neq 0$, A and B being proportional to the defocusing coefficients associated with the systems in Figs. 1 and 2, respectively.

We are going to find the relations between the parameters to obtain the equivalence of the systems in Figs. 1 and 3.

Thus, given the optical system in Fig. 3, we are going to find f_3, f_4, and $\bar{f}$ such that this system is equivalent to that in Fig. 1. This means that, mathematically,

$$\bar{g} = \exp\left(\frac{jz_2\Delta}{2k}\right)\exp\left(\frac{-jkr^2}{2f}\right)\exp\left(\frac{jz_1\Delta}{2k}\right)(g)$$

$$= \exp\left(\frac{-jkr^2}{2f_4}\right)\mathcal{F}_q\left\{\exp\left(\frac{-jkr^2}{2f_3}\right)(g)\right\}, \tag{A1}$$

with $q = k/\bar{f}$.

We shall prove that

$$\bar{f} = \frac{A}{\bar{f}}, \qquad f_4 = \frac{A}{z_1 - f}, \qquad f_3 = \frac{A}{z_2 - f}. \tag{A2}$$

From Eqs. (A2) we find that

$$f = \frac{\bar{f}f_3 f_4}{f_3 f_4 - \bar{f}^2}, \qquad z_1 = f\left(1 + \frac{\bar{f}}{f_4}\right),$$

$$z_2 = f\left(1 + \frac{\bar{f}}{f_3}\right). \tag{A3}$$

To prove Eqs. (A2), we find the impulse response of the two systems by using the known results[22]

$$\mathcal{F}_q\{\delta(r^2)\} = -jq/2,$$

$$\exp(ja\Delta)[\delta(r^2)] = -\frac{j}{4a}\exp\left(\frac{jr^2}{4a}\right),$$

$$\exp(b\Delta)[\exp(ar^2)] = \frac{1}{1-4ab}\exp\left(\frac{ar^2}{1-4ab}\right),$$

$$4ab \neq 1, \tag{A4}$$

and obtain

$$-\frac{jkf}{2A}\exp\left[\frac{jk}{2A}(f - z_1)r^2\right] = -\frac{jk}{2\bar{f}}\exp\left(-\frac{jkr^2}{2f_4}\right).$$

From this expression it follows that

$$\bar{f} = A/f, \qquad f_4 = A/(z_1 - f),$$

which are the first two equalities in Eqs. (A2).

If we now take $g = 1$ in Eq. (A1) and we use Eq. (A4) and

$$\mathcal{F}_q\{\exp(jar^2)\} = \frac{q}{2a}\exp\left(-\frac{jq^2r^2}{2a}\right),$$

we obtain

$$\frac{f}{f - z_2}\exp\left[-\frac{jkr^2}{2(f - z_2)}\right]$$

$$= -\frac{f_3}{\bar{f}}\exp\left[-\frac{jk}{2f_4\bar{f}^2}(\bar{f}^2 - f_3 f_4)r^2\right].$$

Then it must be true that

$$\frac{f}{f - z_2} = -\frac{f_3}{\bar{f}},$$

and so the third equality in Eqs. (A2) is obtained.

Furthermore, the systems in Figs. 2 and 3 are also equivalent, with

$$\bar{f} = z, \qquad f_3 = \frac{zf_1}{z - f_1}, \qquad f_4 = \frac{zf_2}{z - f_2},$$

or, alternatively,

$$z = \bar{f}, \qquad f_1 = \frac{f_3\bar{f}}{f_3 + \bar{f}}, \qquad f_2 = \frac{f_4\bar{f}}{f_4 + \bar{f}}.$$

APPENDIX B: CONVOLUTION DEFINED BY MEANS OF THE PROPAGATION OPERATOR

To obtain the convolution of two functions expressed by means of the propagation operator, we use Eq. (2) for $\mathcal{F}_s$ and start with the identity

$$(g * h)(x, y) = \frac{j\pi}{s}\mathcal{F}_s^{-1}\left\{\exp\left[\frac{-js}{4}(\xi^2 + \eta^2)\right] \times \mathcal{F}_s\{g(u, v)h(x - u, y - v) \times \exp(-js\bar{r}^2)\}(\xi, \eta)\right\}(x, y), \quad \text{(B1)}$$

with $\bar{r}^2 = (x - u)^2 + (y - v)^2$ and any s. In this equation we insert the $\mathcal{F}_s$ given by Eq. (1), where only the variables x and y appear, and we obtain

$$(g * h)(x, y) = \frac{j\pi}{s}\left(\mathcal{F}_s^{-1}\left\{\exp\left[\frac{-js}{4}r^2\right] \times \mathcal{F}_s\{g(x, y)h(\alpha - x, \beta - y) \times \exp(-js\bar{r}^2)\}\right\}\right)_{\alpha=x,\beta=y}, \quad \text{(B2)}$$

with $\bar{r}^2 = (\alpha - x)^2 + (\beta - y)^2$.

If we use the FT property

$$\mathcal{F}_s\{g \exp(-js^2ar^2)\} = \exp(ja\Delta)\mathcal{F}_s\{g\},$$

the last equation is

$$(g * h)(x, y) = \frac{j\pi}{s}\left\{\exp\left(\frac{j\Delta}{4s}\right) \times [g(x, y)h(\alpha - x, \beta - y) \times \exp(-js\bar{r}^2)]\right\}_{\alpha=x,\beta=y}. \quad \text{(B3)}$$

Observe that it is possible to calculate improper integrals by performing differentiation only. From Eq. (B3) and $h = 1$, we obtain

$$\int\int_{-\infty}^{\infty} g(x, y)dxdy = \frac{j\pi}{s}\left\{\exp\left(\frac{j\Delta}{4s}\right)[g(x, y)\exp(-js\bar{r}^2)]\right\}_{\alpha=x,\beta=y} = \frac{j\pi}{s}\left\{\exp\left(\frac{j\Delta}{4s}\right)[g(\alpha - x, \beta - y) \times \exp(-js\bar{r}^2)]\right\}_{\alpha=x,\beta=y}.$$

APPENDIX C: APPLICATIONS

We give here some calculations to show how our approach gives some results in a very simple way.

1. Fractional Fourier Transform of Some Usual Functions

Using Eq. (11) or (16) and q-FT properties,[22] we obtain

$$\mathcal{F}^P\{\exp(jar^2)\} = \frac{k}{2aF \sin\phi + k\cos\phi} \times \exp\left[\frac{jk(2aF\cos\phi - k\sin\phi)r^2}{2F(2aF\sin\phi + k\cos\phi)}\right],$$

with $2aF\sin\phi + k\cos\phi \neq 0$ and any a, (taking $a = 0$, we obtain $\mathcal{F}^P\{1\}$);

$$\mathcal{F}^P\left\{\exp\left(\frac{-jkr^2}{2F\tan\phi}\right)\right\} = \frac{-j2\pi F\sin\phi}{k}\delta(x, y);$$

$$\mathcal{F}^P\{\delta(x, y)\} = \frac{-jk}{2\pi F\sin\phi}\exp\left(\frac{jkr^2}{2F\tan\phi}\right);$$

$$\mathcal{F}^P\{\delta(r - a)\} = -jqaJ_0(qra)\exp\left[\frac{jk(r^2 + a^2)}{2F\tan\phi}\right],$$

with $q = k/F\sin\phi$;

$$\mathcal{F}^P\{J_0(br)\} = \frac{1}{\cos\phi}J_0\left(\frac{br}{\cos\phi}\right) \times \exp\left[\frac{-j(\tan\phi)(k^2r^2 + F^2b^2)}{2Fk}\right].$$

2. P Convolution of Some Usual Functions

From properties of convolution and Eq. (27), we obtain

$$g \overset{P}{*} \delta(x, y) = g(x, y) \quad \text{for any } P;$$

$$\sum_{-\infty}^{\infty}\delta(x - n, y - m) \overset{P}{*} g(x, y) = \sum_{-\infty}^{\infty} g(x - n, y - m) \times \exp\left\{\frac{-jk}{2F\tan\phi}[n(2x - n) + m(2y - m)]\right\},$$

$$\exp(-ar^2) \overset{P}{*} \exp(-br^2) = \frac{j\pi F\tan\phi}{k + jF(\tan\phi)(a + b)}\exp\left(\frac{-jkr^2}{2F\tan\phi}\right) \times \exp\left\{\frac{(k + j2bF\tan\phi)(jk - 2aF\tan\phi)r^2}{4F(\tan\phi)[k + jF(\tan\phi)(a + b)]}\right\},$$

with $k + jF(\tan\phi)(a + b) \neq 0$.

ACKNOWLEDGMENTS

This work was supported by the Consejo Nacional de Investigaciones Científicas y Técnicas under Proyecto de Investigación y Desarrollo grant 3974/92.

B. Ruiz is also with the Faculty of Astronomic and Geophysic Sciences, Universidad Nacional de La Plata, Paseo del Bosque, 1900-La Plata, Argentina. H. Rabal is also with the Faculty of Engineering, Universidad Nacional de La Plata, 47 y 1, 1900-La Plata, Argentina.

REFERENCES

1. A. Lohmann, "Image rotation, Wigner rotation and the fractional Fourier transform," J. Opt. Soc. Am. A **10**, 2181–2186 (1993).
2. D. Mendlovic and H. Ozaktas, "Fractional Fourier transform and their optical implementation. I," J. Opt. Soc. Am. A **9**, 1875–1881 (1993).
3. H. Ozaktas and D. Mendlovic, "Fractional Fourier transform and their optical implementation. II," J. Opt. Soc. Am. A **10**, 2522–2531 (1993).
4. H. Ozaktas and D. Mendlovic, "Fourier transform of fractional order and their optical interpretation," Opt. Commun. **101**, 163–169 (1993).
5. M. Bernardo and O. Soares, "Fractional Fourier transforms and optical systems," Opt. Commun. **110**, 517–522 (1994).
6. D. Mendlovic, H. Ozaktas, and A. Lohmann, "Graded index fibers, Wigner distribution functions and fractional Fourier transform," Appl. Opt. **33**, 6188–6193 (1994).
7. T. Alieva, V. Lopez, F. Agullo Lopez, and L. Almeida, "The fractional Fourier transform in optical propagation problems," J. Mod. Opt. **41**, 1037–1044 (1994).
8. H. Ozaktas, B. Barshan, D. Mendlovic, and L. Onural, "Convolution, filtering and multiplexing in fractional Fourier domain and their relation to chirp and wavelet transforms," J. Opt. Soc. Am. A **11**, 547–559 (1994).
9. L. Almeida, "The fractional Fourier transform and time-frequency representations," IEEE Trans. Signal Process. **42**, 3084–3091 (1994).
10. P. Pellat-Finet, "Fresnel diffraction and the fractional order Fourier transform," Opt. Lett. **19**, 1388–1390 (1994).
11. P. Pellat-Finet and G. Bonnet, "Fractional order Fourier transform and Fourier optics," Opt. Commun. **111**, 141–154 (1994).
12. D. Mendlovic, Y. Bitran, R. Dorsh, and A. Lohmann, "Optical fractional correlation: experimental results," J. Opt. Soc. Am. A **12**, 1665–1670 (1995).
13. D. Mendlovic, H. Ozaktas, and A. Lohmann, "Fractional correlation," Appl. Opt. **34**, 303–309 (1995).
14. H. Ozaktas and D. Mendlovic, "Fractional Fourier optics," J. Opt. Soc. Am. A **12**, 743–751 (1995).
15. A. Van Der Lugt, "Operator notation for the analysis and synthesis of optical data-processing systems," Proc. IEEE **54**, 1055–1063 (1966).
16. M. Nazarathy and J. Shamir, "Fourier optics described by operator algebra," J. Opt. Soc. Am. **70**, 150–159 (1980).
17. M. Nazarathy and J. Shamir, "First-order optics—a canonical operator representation: lossless systems," J. Opt. Soc. Am. **72**, 356–364 (1982).
18. M. Nazarathy and J. Shamir, "First-order optics: operator representation for systems with loss or gain," J. Opt. Soc. Am. **72**, 1398–1408 (1982).
19. D. Stoler, "Operator methods in physical optics," J. Opt. Soc. Am. **71**, 334–341 (1981).
20. H. Butterweck, "General theory of linear, coherent optical data-processing systems," J. Opt. Soc. Am. **67**, 60–70 (1977).
21. B. Ruiz and H. Rabal, "Cylindrical optical systems and the Fourier transform," Optik (Stuttgart) **106**, 28–72 (1997).
22. B. Ruiz and H. Rabal, "Differential operators, the Fourier transform and its applications to optics," Optik (Stuttgart) **103**, 171–178 (1996).
23. R. Bracewell, *The Fourier Transform and Its Applications* (McGraw-Hill, New York, 1978).
24. Y. Choquet-Bruhat, *Distributions. Theorie et problemes* (Masson, Paris, 1973).
25. J. W. Goodman, *Introduction to Fourier Optics* (McGraw-Hill, New York, 1968).

Optical correlation based on the fractional Fourier transform

Sergio Granieri, Ricardo Arizaga, and Enrique E. Sicre

Some properties of optical correlation based on the fractional Fourier transform are analyzed. For a particular set of fractional orders, a filter is obtained that becomes insensitive to scale variations of the object. An optical configuration is also proposed to carry out the fractional correlation in a flexible way, and some experimental results are shown. © 1997 Optical Society of America

Key words: Optical correlation, space-variant optical processing.

1. Introduction

Among several mathematical operations that can be optically implemented, correlation is one of the most important because it can be used for different applications, such as pattern recognition, aerial imagery, image feature extraction, object localization, etc. Correlation can be performed by use of the Fourier transform property of coherent optical systems, as, for example, with the VanderLugt $4f$ configuration[1] or the joint transform correlator.[2] Since conventional correlation is a shift-invariant operation, the location of the correlator output simply moves if the object translates at the input plane. In many cases this property is necessary, but there are situations in which the position of the object provides an additional encoding feature, and so space invariance can be a drawback. In the search for space-variant optical filters, the fractional correlation,[3,4] which is a generalization of the classical correlation operation that employs the fractional Fourier transform (FRT) instead of the conventional Fourier transform of the signals to be correlated, was recently proposed.

The FRT was defined mathematically by Namias[5] and introduced to optics by Mendlovic *et al.*[6–10] As it was analyzed in Ref. 9, the optical definition of the FRT can be established through a phase–space rotation of the Wigner distribution function. This point of view leads to the development of simple optical devices for obtaining the FRT, but it also emphasizes the dual character of the FRT. Accordingly, the order p varies from $p = 0$ (pure spatial information) to $p = 1$ (pure spectral information). Therefore, a filter that stores information about the FRT ($0 < p < 1$) instead of the ordinary Fourier transform ($p = 1$) can be used to recognize objects with a space-variance degree that depends on the selected value of p.

The purpose of this paper is (i) to define the fractional correlation in a general way in which different orders of the FRT associated with the correlated signals are considered; (ii) to analyze some of its properties, as, for instance, those related to the space-variance degree; and (iii) to demonstrate experimentally the fractional correlation that yields an application to build a filter insensitive to scale changes of the object. With respect to point (iii), a multiple-exposure hologram is employed to work in a parallel way. An optical configuration for performing the fractional correlation in a flexible way is also proposed and experimentally verified.

2. Fractional Correlation

For the following analysis the FRT is obtained by use of the optical setup proposed by Lohmann,[9] which is shown in Fig. 1. In terms of the Fresnel diffraction, the amplitude distribution at the output plane corresponds to the FRT of order p that is associated with the input signal $t(x_0)$, i.e.,

$$\begin{aligned} Up(x) &= \mathcal{F}^{(p)}\{t(x_0)\} \\ &= \exp\left(\frac{i\pi x^2}{\lambda f_0 \tan\phi}\right)\int_{-\infty}^{\infty} t(x_0)\exp\left(\frac{i\pi {x_0}^2}{\lambda f_0 \tan\phi}\right) \\ &\quad \times \exp\left(\frac{-2\pi i x x_0}{\lambda f_0 \sin\phi}\right)dx_0, \end{aligned} \tag{1}$$

The authors are with the Centro de Investigaciones Opticas (CIOp), C.C. 124, 1900 La Plata, Argentina. S. Granieri is also with the Facultad de Ciencias Exactas and R. Arizaga is also with the Facultad de Ingeniería, Universidad de La Plata, La Plata, Argentina.

Received 2 January 1997; revised manuscript received 2 April 1997.

0003-6935/97/266636-10$10.00/0

© 1997 Optical Society of America

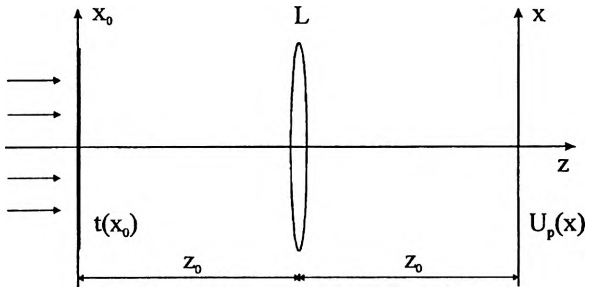


Fig. 1. Optical setup for performing the FRT of $t(x_0)$ for a given fractional order p, where $z_0 = f_0 \tan(p\pi/4)$, $f = f_0/\sin(p\pi/2)$, and f_0 is a scaling factor.

where λ is the wavelength, f_0 is a free-scale parameter, and $\phi = p\pi/2$. For mathematical simplicity, we consider only one-dimensional functions. For a value of $p = 1$, Eq. (1) reduces to the well-known Fourier transform relation. It should be noticed that Eq. (1) can be used as an optical definition of the FRT whenever the Fresnel approximation remains valid. Since the distance z_0 between the lens and the input (or output) plane is given by $z_0 = f_0 \tan(p\pi/4)$, this limitation restricts the lower values of p that can be chosen in Eq. (1). However, as we are interested in optical correlation applications for which the spectral information of the signal becomes relevant, the values of p to be considered are large enough to be able to validate Eq. (1), i.e., $0 \ll p < 1$.

The correlation of two functions $t_1(x)$ and $t_2(x)$ can be defined alternatively in the space or the spectral domain as

$$C_{12}(x) = \int_{-\infty}^{\infty} t_1(x_0) t_2^*(x_0 - x)\mathrm{d}x_0 \tag{2a}$$

$$= \int_{-\infty}^{\infty} \tilde{t}_1(\nu)\tilde{t}_2^*(\nu)\exp(2\pi i\nu x)\mathrm{d}\nu, \tag{2b}$$

where $\tilde{t}(\nu)$ is the conventional ($p = 1$) Fourier transform of $t(x)$. By taking into account the second definition [Eq. (2b)] we propose the following expression as a generalized fractional correlation of $t_1(x)$ and $t_2(x)$:

$$C_{12}^{(p,q,r)}(x) = \mathcal{F}^{(q)}\{\mathcal{F}^{(q)}\{t_1(x_0)\}\mathcal{F}^{(r)*}\{t_2(x_0)\}\}. \tag{3}$$

Equation (3) becomes the standard correlation for the case of $p = -1$, $q = r = 1$.

We next analyze the requirements to be fulfilled by Eq. (3) to get a meaningful fractional-correlation operation. The similarity condition [i.e., the same object in the same location: $t_1(x_0) = t_2(x_0)$] should maximize the correlation output for any value of the fractional orders. To derive an explicit expression for the fractional correlation, we replace the FRT operators in Eq. (3) by their equivalent definitions based on Fresnel integrals, as given by Eq. (1). Thus, we obtain

$$\begin{aligned} C_{12}^{(p,q,r)}(x) = \exp\left(\frac{i\pi x^2}{\lambda f_0 \tan\phi_1}\right) \int_{-\infty}^{\infty} t_1(x_0')\exp\left(\frac{i\pi x_0'^2}{\lambda f_0 \tan\phi_2}\right)\mathrm{d}x_0' \\ \times \int_{-\infty}^{\infty} t_2^*(x_0'')\exp\left(-\frac{i\pi x_0''^2}{\lambda f_0 \tan\phi_3}\right)\mathrm{d}x_0'' \\ \times \int_{-\infty}^{\infty} \exp\left[\frac{i\pi x_0^2}{\lambda f_0}\left(\frac{1}{\tan\phi_1} + \frac{1}{\tan\phi_2} - \frac{1}{\tan\phi_3}\right)\right] \\ \times \exp\left[\frac{-2\pi i x_0}{\lambda f_0}\left(\frac{x}{\sin\phi_1} + \frac{x_0'}{\sin\phi_2} - \frac{x_0''}{\sin\phi_3}\right)\right]\mathrm{d}x_0, \end{aligned} \tag{4}$$

where

$$\phi_1 = p\frac{\pi}{2}, \qquad \phi_2 = q\frac{\pi}{2}, \qquad \phi_3 = r\frac{\pi}{2}. \tag{5}$$

For the purely spectral case $p = -1$, $q = r = 1$ and Eq. (4) gives rise to a sharp correlation peak whenever $t_1(x_0) = t_2(x_0 + \Delta)$, where Δ represents the shift between both correlated functions. For other values of the fractional orders Eq. (4) becomes sensitive to both the locations and the shapes of $t_1(x_0)$ and $t_2(x_0)$. However, the above-mentioned similarity condition, when applied to fractional correlation, requires that the quadratic phase exponential in the inner integral of Eq. (4), which generates a defocus effect, should be eliminated. This situation is achieved whenever the following relation for the fractional orders is satisfied:

$$\frac{1}{\tan\left(p\frac{\pi}{2}\right)} + \frac{1}{\tan\left(q\frac{\pi}{2}\right)} - \frac{1}{\tan\left(r\frac{\pi}{2}\right)} = 0, \tag{6}$$

$$\begin{aligned} C_{12}^{(p,q,r)}(x) = \exp\left(\frac{i\pi x^2}{\lambda f_0 \tan\phi_1}\right) \iint_{-\infty}^{\infty} t_1(x_0')t_2^*(x_0'') \\ \times \exp\left(\frac{i\pi x_0'^2}{\lambda f_0 \tan\phi_2}\right)\exp\left(-\frac{i\pi x_0''^2}{\lambda f_0 \tan\phi_3}\right) \\ \times \delta\left(\frac{x}{\sin\phi_1} + \frac{x_0'}{\sin\phi_2} - \frac{x_0''}{\sin\phi_3}\right)\mathrm{d}x_0'\mathrm{d}x_0''. \end{aligned} \tag{7}$$

The fractional correlation as given by Eq. (7) is restricted to those cases in which the involved orders satisfy Eq. (6). For example, if $q = r$ then $p = \pm 1$, and Eq. (7) becomes the fractional correlation proposed and demonstrated experimentally in Refs. 3 and 4. In this case, Eq. (7) can be rewritten as

$$\begin{aligned} C_{12}^{(-1,q,q)}(x) = \exp\left(\frac{-i\pi\sin(2\phi)x^2}{2\lambda f_0}\right) \int_{-\infty}^{\infty} t_1(x_0')t_2^* \\ \times (x_0' - \sin\phi x)\exp\left(\frac{2\pi i}{\lambda f_0}\cos\phi x x_0'\right)\mathrm{d}x_0', \end{aligned} \tag{8}$$

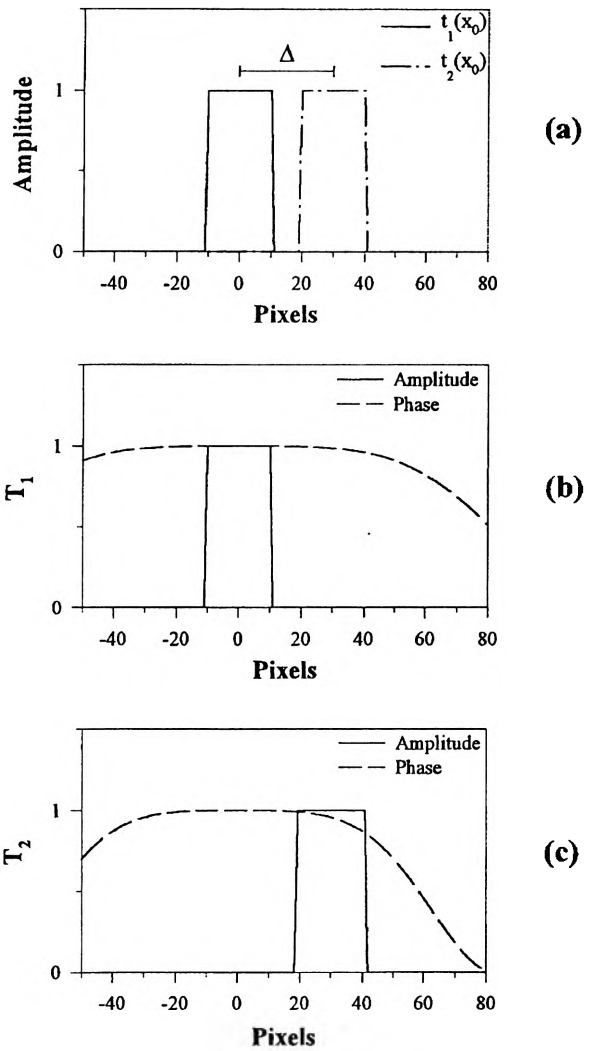


Fig. 2. (a) Object amplitude transmittances $t_1(x_0)$ and $t_2(x_0)$. (b) and (c) Modulus and phase of $T_1(x_0; z_1)$ and $\bar{T}_2(x_0; z_2)$, respectively, for $q = 0.8$ and $r = 0.7$.

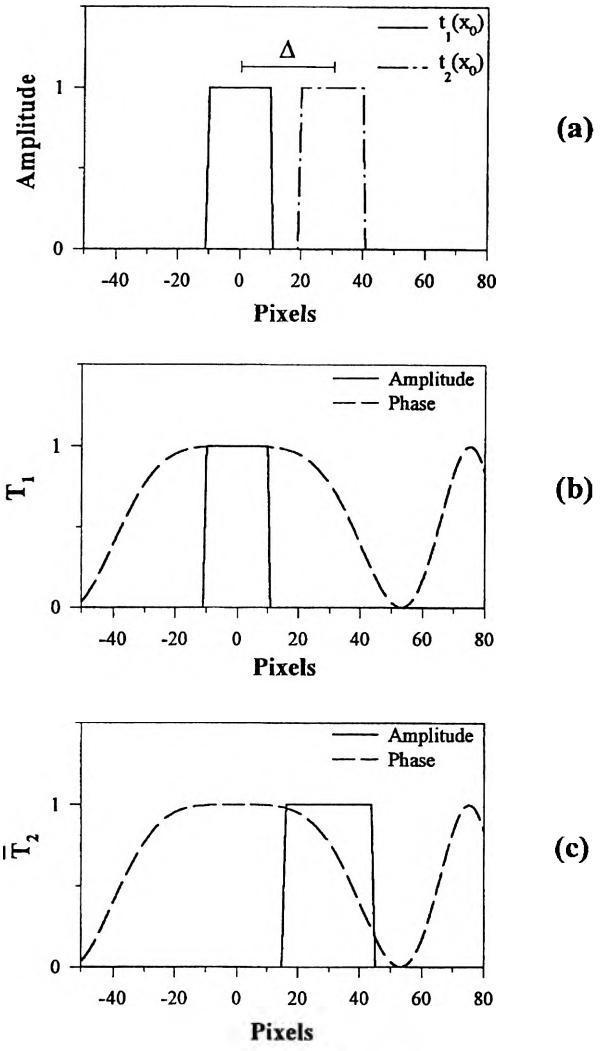


Fig. 3. (a) Object amplitude transmittances $t_1(x_0)$ and $t_2(x_0)$. (b) and (c) Modulus and phase of $T_1(x_0; z_1)$ and $\bar{T}_2(x_0; z_2)$, respectively, for $q = 0.6$ and $r = 0.4$.

or equivalently as

$$C_{12}^{(-1,q,q)}(x) = \int_{-\infty}^{\infty} t_1\left(x' + \frac{\sin\phi}{2}x\right) t_2^*\left(x' - \frac{\sin\phi}{2}x\right) \times \exp\left(\frac{2\pi i}{\lambda f_0}\cos\phi x x'\right) dx' = A_{t_1 t_2}\left(y, \mu = \frac{-y}{\lambda f_0 \tan\phi}\right), \quad (9)$$

where $\phi = (\pi/2)\,q$, $y = \sin\phi x$ and $A_{t_1 t_2}(y, \mu)$ is the cross-ambiguity function,[11] which is a dual phase–space representation coordinate–spatial frequency of the functions $t_1(x_0)$ and $t_2(x_0)$. Thus, the scaled fractional correlation for the several values of q can be found from different slices in the phase–space (y, μ).

This result was pointed out in Ref. 12, where it was analyzed by means of the analogy of optical spatial filters based on the FRT to wavelet transforms and adaptive neural networks. Besides, Eq. (9) means that all fractional correlations, from $q = 0$ (vertical line, $y = 0$) to $q = 1$ (horizontal line, $\mu = 0$) are contained in a single picture display of the ambiguity function.

For the more general case of $q \neq r$, the fractional correlation obtained from Eq. (7) can be rewritten as

$$C_{12}^{(p,q,r)}(x) = \exp\left(\frac{i\pi x^2}{\lambda f_0 \tan\phi_1}\right) \int_{-\infty}^{\infty} T_1(x_0'; z_1) \times \bar{T}_2^*\left(x_0' + \frac{\sin\phi_2}{\sin\phi_1}x; z_2\right) dx_0', \quad (10)$$

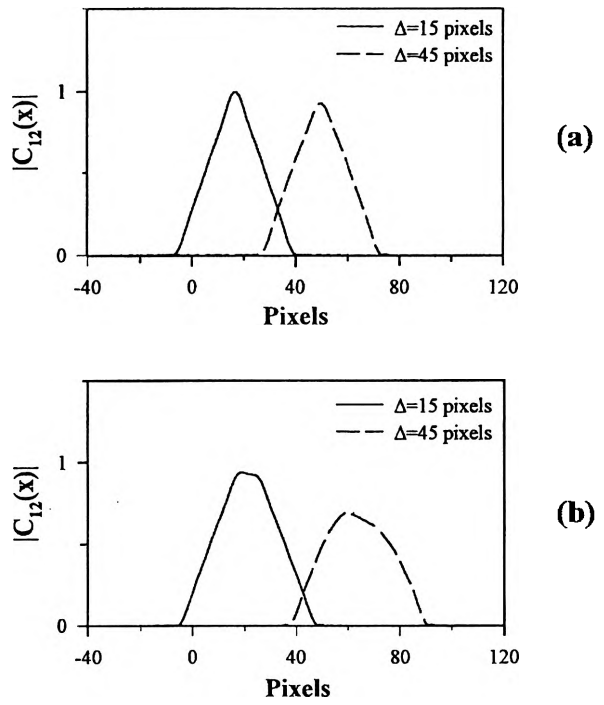


Fig. 4. (a) Normalized fractional correlation for $q = 0.8$, $r = 0.7$, and $p = 0.884$ for two different shifts Δ between $t_1(x_0)$ and $t_2(x_0)$. (b) Normalized fractional correlation for $q = 0.6$, $r = 0.4$, and $p = 0.633$ for two different shifts Δ between $t_1(x_0)$ and $t_2(x_0)$.

where

$$T_1(x_0'; z_1) = t_1(x_0')\exp\left(\frac{i\pi x_0'^2}{\lambda z_1}\right), \qquad z_1 = f_0 \tan \phi_2, \tag{11a}$$

$$\bar{T}_2(x_0'; z_2) = t_2\left(\frac{x_0'}{M}\right)\exp\left[\frac{i\pi}{\lambda z_2}\left(\frac{x_0'}{M}\right)^2\right], \qquad z_2 = f_0 \tan \phi_3, \tag{11b}$$

$$M = \frac{\sin \phi_2}{\sin \phi_3}. \tag{12}$$

The fractional correlation as given by Eq. (10) can be thought as the conventional correlation of two functions: $T_1(x_0'; z_1)$, which is the input signal $t_1(x_0')$ multiplied by a zonal phase factor with focal length z_1, and $\bar{T}_2(x_0'; z_2)$, which is a scaled version of the product between $t_2(x_0')$ and a zonal phase factor with focal length z_2. Taking into account the analogy between the FRT formalism and the Fresnel diffracted fields,[13,14] we find that the fractional correlation [Eq. (10)] is closely related to the space-variant Fresnel transform correlator [see Eq. (7) in Ref. 15].

The positional sensitivity of the fractional correlation is illustrated in Figs. 2 and 3 with a simple example: Terms $t_1(x_0)$ and $t_2(x_0)$ are two identical slits placed at different locations. It can be seen from Figs. 2(b), 2(c), 3(b), and 3(c) how the matching between the zonal phase factors of $T_1(x_0'; z_1)$ and

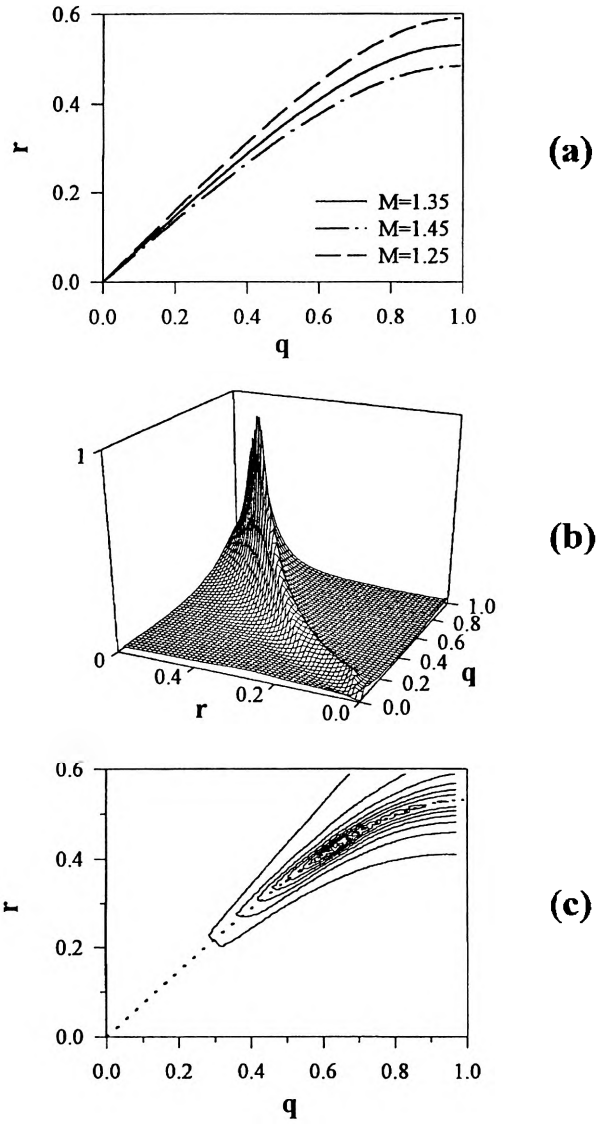


Fig. 5. (a) Curves showing the set of orders (q_0, r_0) that satisfy Eq. (12), i.e., $\sin[q_0(\pi/2)] = M \sin[r_0(\pi/2)]$, for three different values of M. (b) Contour display of $\alpha^{(p,q,r)}$ for the case of $M = 1.35$. (c) Level curves corresponding to the contour plot of (b). The dotted curve represents the theoretical curve of (a) for $m = 1.35$.

$\bar{T}_2(x_0'; z_2)$ depends on the selected values of p, q, and r.

In Fig. 4, the display of $|C_{12}^{(p,q,r)}(x)|$ is shown for two different displacements Δ_1 and Δ_2 between the slit functions $t_1(x_0')$ and $t_2(x_0')$, along with two different sets of p, q, and r. As can be seen from these results, the correlation peak diminishes for increasing values of Δ. In addition, this effect becomes more noticeable for decreasing values of q and r, as should be expected.

The fact that the fractional correlation becomes a conventional correlation between two functions, $T_1(x)$ and $\bar{T}_2(x)$, related to the original signals $t_1(x_0)$ and $t_2(x_0)$, respectively, through a combined phase–

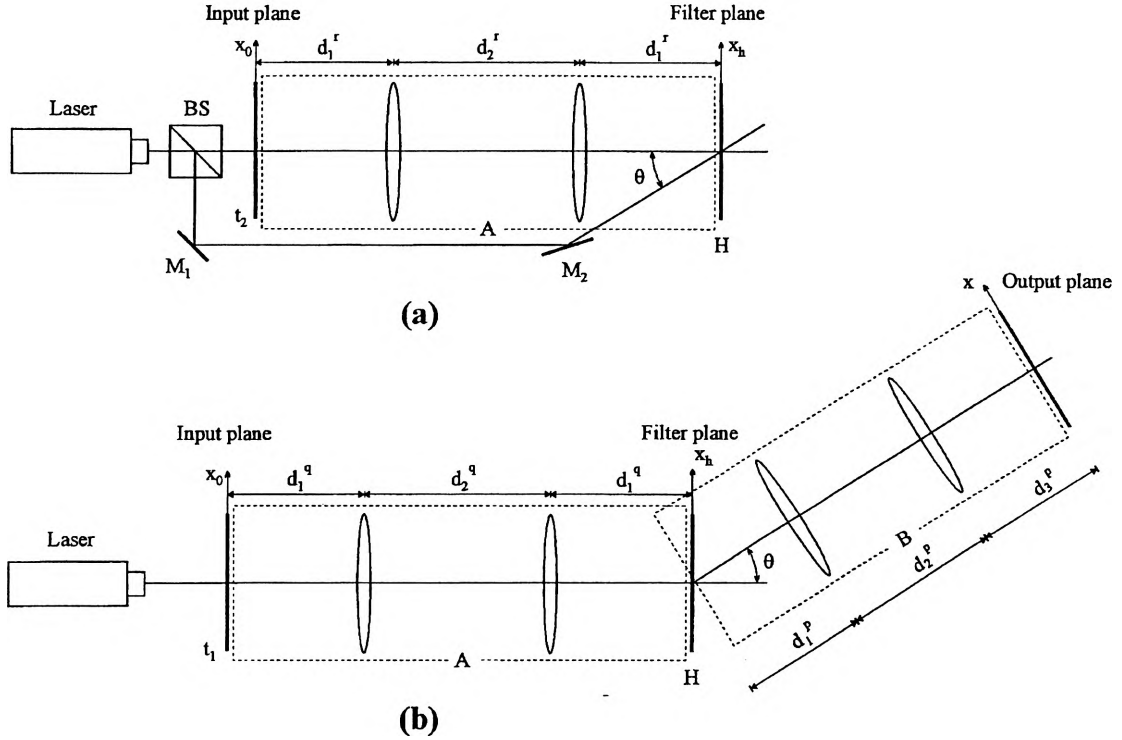


Fig. 6. Scheme of the optical device employed to achieve (a) the filter H, which stores the rth-order FRT of $t_2(x_0, y_0)$, and (b) the fractional correlation $C_{12}^{(p,q,r)}(x, y)$ at the output plane. M, mirror; BS, beam splitter.

scaling transform [given by Eqs. (11)] suggests how a recognition filter insensitive to scale variations of the input object can be implemented by use of this approach. For two functions $t_1(x_0)$ and $t_2(x_0)$ that are placed in the same position and differ by only a certain scale factor, several sets of values (p_0, q_0, r_0) exist for which the fractional correlation $C_{12}^{(p,q,r)}(x)$ becomes the conventional cross correlation of two functions having identical amplitude distributions but slightly different phase factors. This particular set of values (p_0, q_0, r_0) is illustrated in Fig. 5(a) for three different relative magnifications between $t_1(x_0)$ and $t_2(x_0)$. To analyze the behavior of the fractional correlation we define a correlation parameter as

$$\alpha^{(p,q,r)} = \left[\frac{\int |C_{12}^{(p,q,r)}(x) - C_{11}^{(-1,1,1)}(x)| dx}{\int C_{11}^{(-1,1,1)}(x) dx} \right]^{-1}, \quad (13)$$

i.e., it measures the deviation of the fractional correlation between two objects of the same shape but with different magnifications from a conventional autocorrelation of one of these objects for the selected value of the relative magnification M [as given by Eq. (12)].

In Figs. 5(b) and 5(c) the numerical calculation of $\alpha^{(p,q,r)}$ is shown for two slits with a relative magnification of $M = 1.35$. It can clearly be seen that the maxima of $\alpha^{(p,q,r)}$ lie on a curve in the domain of the fractional orders q and r; the curve coincides with that previously illustrated in Fig. 5(a) for the case $M = 1.35$. However, it can be observed that $\alpha^{(p,q,r)}$ diminishes for decreasing values of q and r, a fact that is related to the above-mentioned phase mismatch between $T_1(x)$ and $\bar{T}_2(x)$. In Section 3 we illustrate the developed analysis with some experimental verifications. Therefore, an optical setup that performs the fractional correlation in a flexible way for varying values of p, q, and r could be used to detect objects with magnifications different from that stored in the filter. Recently, Lohmann *et al.*[16] developed a similar analysis to that carried out for obtaining Eq. (7) in connection with the space-variance properties of the fractional correlation for three particular cases.

3. Experimental Results

The scheme of the optical setup employed to perform the fractional-correlation operations is shown in Fig. 6. A holographic filter H stores the FRT of order r associated with the transparency $t_1(x_0, y_0)$ by use of optical system A (with distances adequate to the value of r) and a reference light beam. The whole system A–B becomes a modified $4f$ configuration. In the first step, subsystem A performs the qth-order FRT of $t_2(x_0, y_0)$ in the plane containing filter H, where the distances d_1^q and d_2^q are selected to be $d_1^q = f \tan(\pi q/4) + f$ and $d_2^q = f \sin(\pi q/2) + 2f$, respectively. Behind the filter H subsystem B carries out the pth-order FRT of the amplitude transmitted by H, with distances $d_1^p = f \tan(\pi p/4) + f$ and $d_2^p = f$

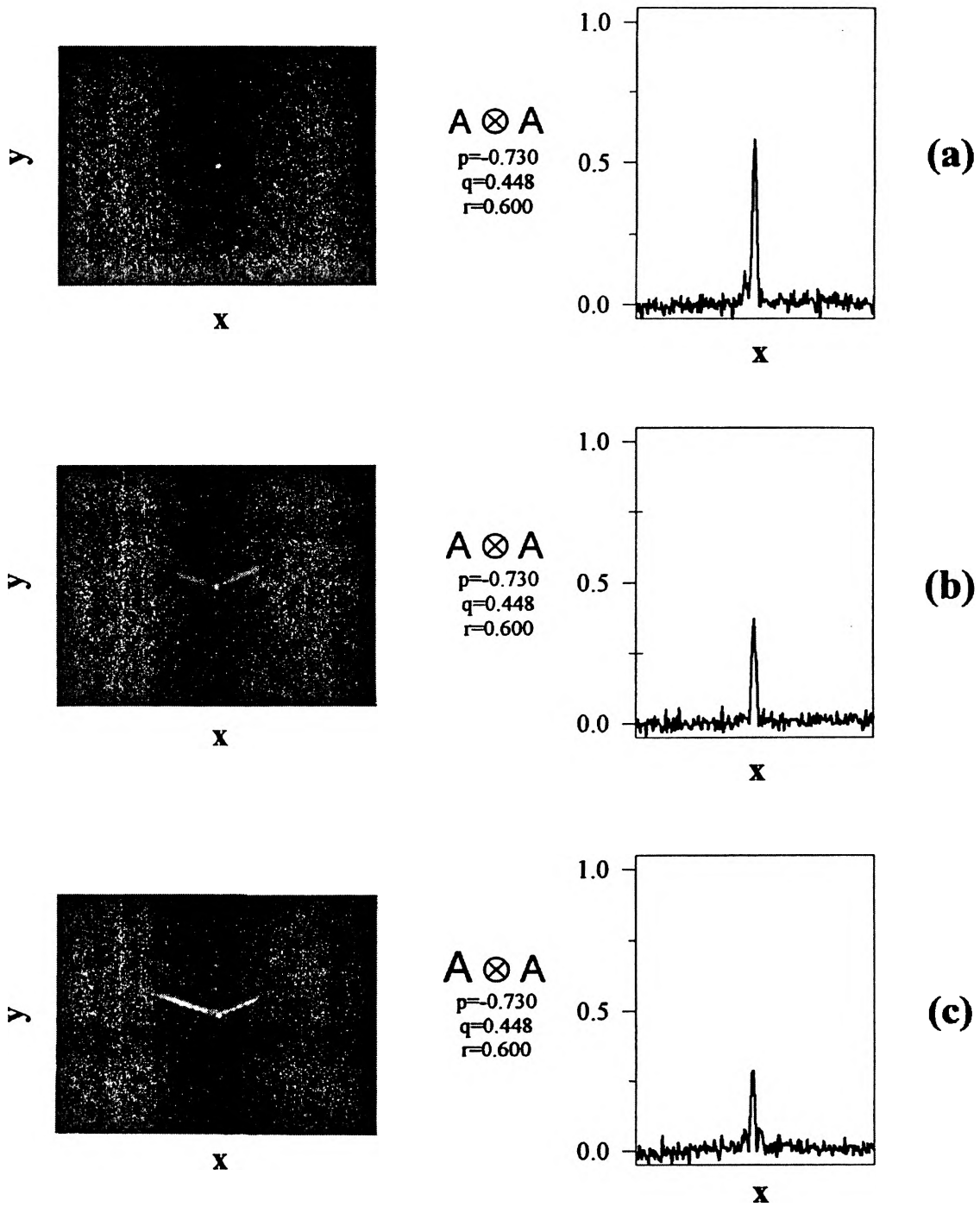


Fig. 7. Fractional correlation between two characters, A, differing by three relative magnifications: (a) $M = 0.80$, (b) $M = 1.00$, and (c) $M = 1.20$. Since the fractional order were chosen to be $p = -0.730$, $q = 0.448$, and $r = 0.600$ [from Eq. (12)], a magnification of $M = 0.80$ results, and so the maximum correlation peak appears in (a).

$\sin(\pi p/2) + 2f$. In this arrangement a fractional correlation $C_{12}^{(p,q,r)}(x, y)$ with arbitrary orders can be obtained by variation of the distances d_1^q, d_2^q, d_1^p, and d_2^p. In addition, the FRT's involved have the same parameter f_0 [see Ref. 17]. Thus, the correlator can easily be adapted to a given object magnification by variation of the orders q and r to select an adequate value of M [Eq. (12)]. A sharp correlation peak is obtained at the output plane of the optical system whenever the objects $t_1(x_0, y_0)$ and $t_2(x_0, y_0)$ differ by this scaling factor M.

In Figs. 7–9 the fractional correlations between two

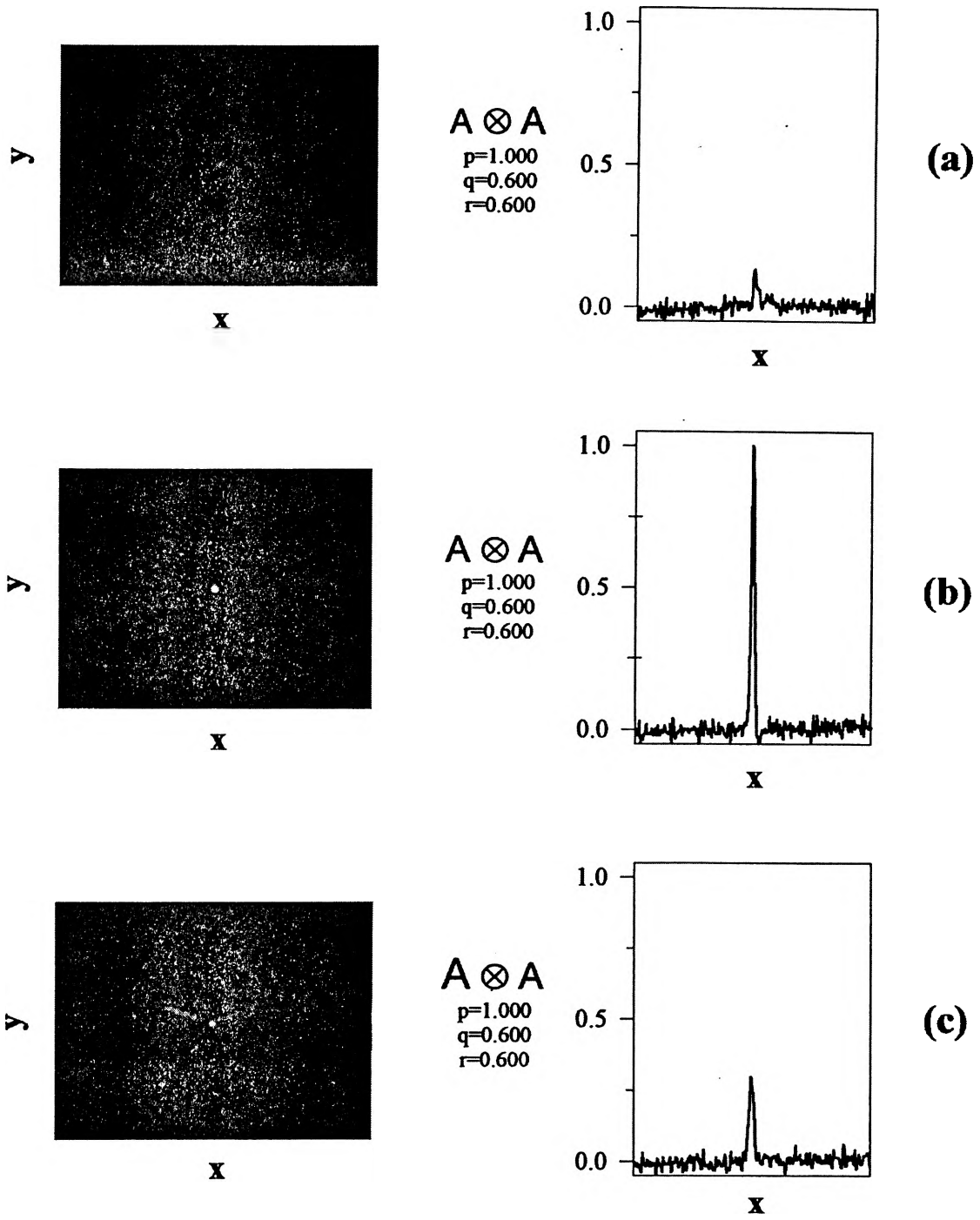


Fig. 8. Fractional correlation between two characters, A, differing by three relative magnifications: (a) $M = 0.80$, (b) $M = 1.00$, and (c) $M = 1.20$. Since the fractional orders were chosen to be $p = 1.000$, $q = 0.600$, and $r = 0.600$ [from Eq. (12)], a magnification of $M = 1.00$ results, and so the maximum correlation peak appears in (b).

identical characters with different magnifications are displayed for three sets of (p, q, r). In each of these figures the maximum of the fractional correlation is obtained for the particular character relative magnification that satisfies Eq. (12). In Table 1 the values of the several distances employed are indicated.

Next, we slightly modify optical device A [Fig. 6(a)] to record a multiple holographic filter H that stores several FRT's of the same object with different fractional orders r. Each recording is performed with a variation of the incident angle θ of the reference light beam. Now the optical correla-

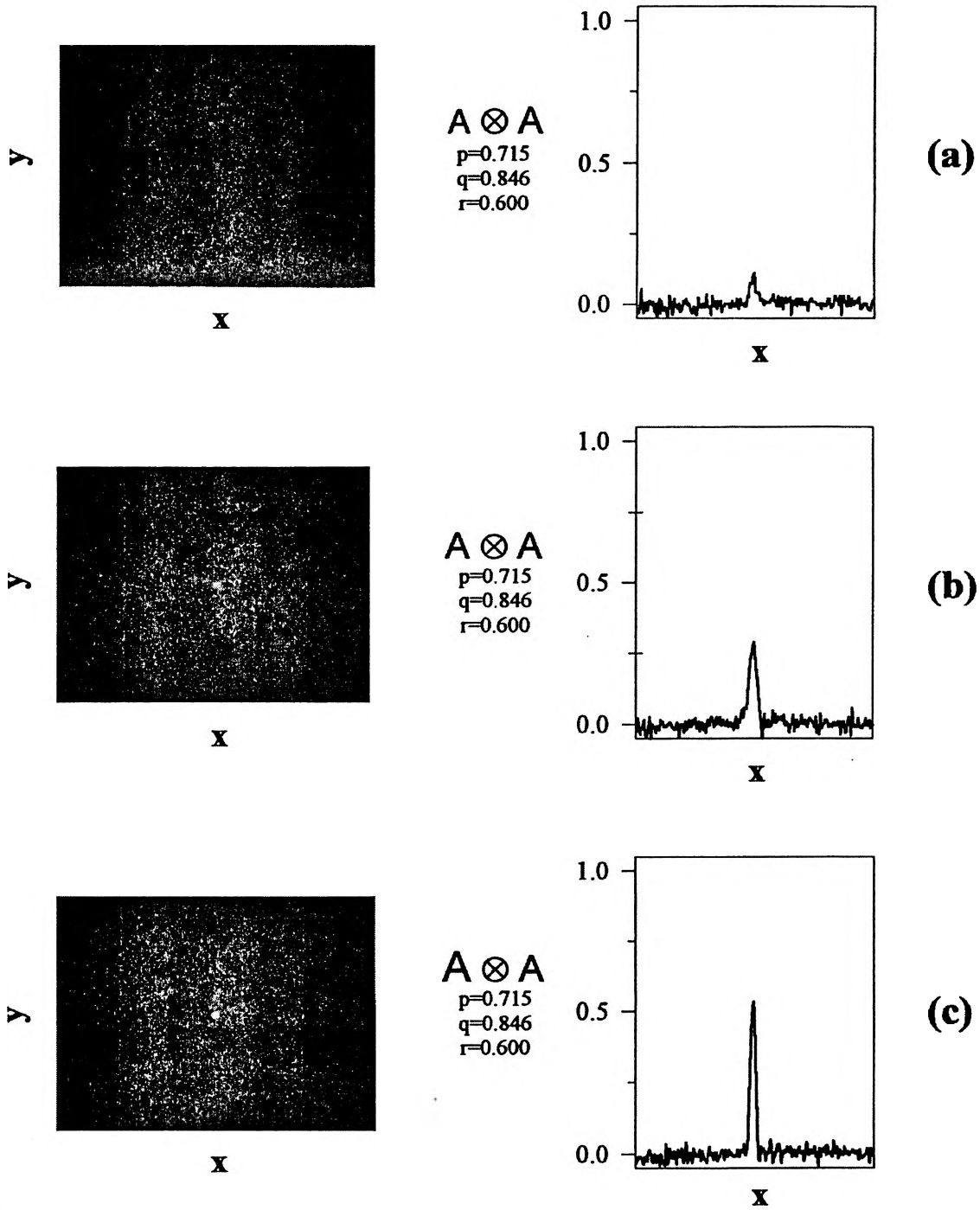


Fig. 9. Fractional correlation between two characters, A, differing by three relative magnifications: (a) $M = 0.80$, (b) $M = 1.00$, and (c) $M = 1.20$. Since the fractional order were chosen to be $p = 0.715$, $q = 0.846$, and $r = 0.600$ [from Eq. (12)], a magnification of $M = 1.20$ results, and so the maximum correlation peak appears in (c).

tor [Fig. 6(b)] works in a rather different way: As the distances d_1^q and d_2^q remain fixed, the distances d_1^p and d_2^p should be selected so as to satisfy the requirements for (p, q, r) established by Eq. (6). This means that a sharp correlation peak appears at the location associated with the angle θ for which the order r (of the FRT stored in the filter) and the order q satisfy Eq. (12). Thus the filter recognizes, at this particular location θ (or spatial coordinate x of the output plane), objects with a scale difference given by this value of M.

In Fig. 10 we show the results obtained from a

Table 1. Values of the Distance d Employed in the Experimental Setup of Fig. 6

	Magnification								
	M = 1.0			M = 0.8			M = 1.2		
Distance	p = 1.000	q = 0.600	r = 0.600	p = −0.730	q = 0.448	r = 0.600	p = 0.715	q = 0.846	r = 0.600
d_1 (*mm*)	200	150.9	150.9	35.4	136.7	150.9	162.9	178.3	150.9
d_2 (*mm*)	300	280.9	280.9	108.8	264.7	280.9	290.2	297.1	280.9

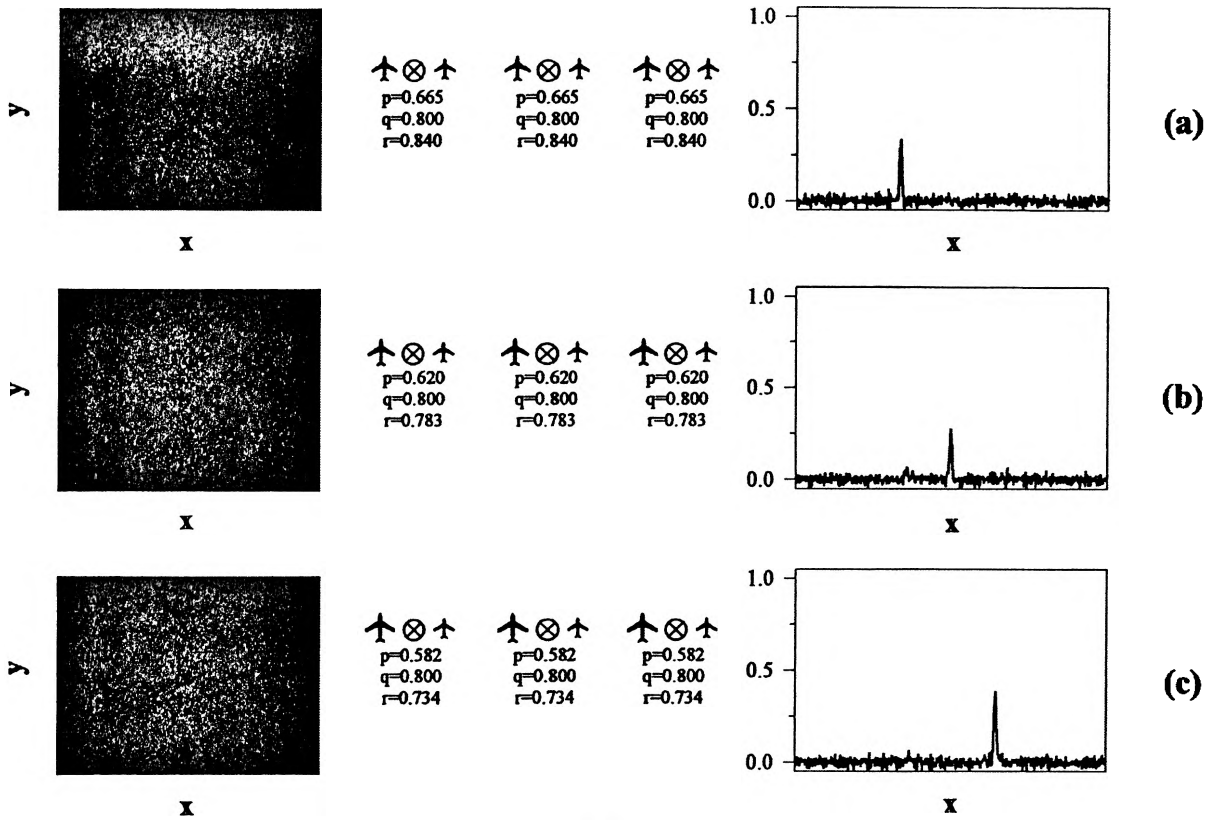


Fig. 10. Intensity distribution obtained at the output plane of the fractional correlator illustrated by Fig. 6 for a multiple-recorded filter H that stores three FRT's of an airplane-shaped object t_2 with the orders r = 0.840, r = 0.783, and r = 0.734. Depending on the magnification M of the input object t_1, the maximum correlation peak is detected at different locations: (a) M = 1.10, (b) M = 1.15, and (c) M = 1.20.

holographic filter that stores three different FRT's of the same object. Figure 10(a) shows the distances d_1^P and d_2^P when they are chosen to yield a value of M = 1.10. Therefore, a sharp correlation peak appears at the location associated with the angle θ corresponding to the stored FRT of the order r = 0.840. In Figs. 10(b) and 10(c), results for the same procedure are shown for achieving M = 1.15 and M = 1.20, respectively. The correlation maxima now appear at the locations corresponding to the stored FRT's of orders r = 0.783 and r = 0.734, respectively. In this way, depending on which magnification of the object $t_1(x_0, y_0)$ is present, the correlation peak is found at different locations in the output plane. Of course, the range of object scales that can be recognized by the filter is limited by the maximum number of FRT's that can be stored in the holographic medium.

4. Conclusions

In this paper we have analyzed the fractional correlation in connection with the space-variance properties of the FRT. It was found that, for specific values of the fractional orders, the fractional correlation becomes insensitive to scale changes of the input object. An optical configuration was proposed for obtaining the fractional correlation in a flexible way. Thus, the orders of the FRT's involved in the fractional-correlation operation can easily be varied to match the filter to any required object magnification.

Financial support from the Consejo Nacional de Investigaciones Científicas y Técnicas (Argentina) is gratefully acknowledged.

References

1. A. Vander Lugt, "Signal detection by complex spatial filtering," IEEE Trans. Inf. Theory **IT-10,** 139–140 (1964).
2. C. S. Weaver and J. W. Goodman, "A technique for optically convolving two functions," Appl. Opt. **5,** 1248–1249 (1966).
3. D. Mendlovic, H. M. Ozaktas, and A. W. Lohmann, "Fractional correlation," Appl. Opt. **34,** 303–309 (1995).
4. D. Mendlovic, Y. Bitran, R. G. Dorsch, and A. W. Lohmann, "Optical fractional correlation: experimental results," J. Opt. Soc. Am. A **12,** 1665–1670 (1995).
5. V. Namias, "The fractional Fourier transform and its applications in quantum mechanics," J. Inst. Math. Appl. **25,** 241–265 (1980).
6. H. M. Ozaktas and D. Mendlovic, "Fourier transforms of fractional order and their optical implementation," Opt. Commun. **101,** 163–169 (1993).
7. D. Mendlovic and H. M. Ozaktas, "Fractional Fourier transforms and their optical implementation: I," J. Opt. Soc. Am. A **10,** 1875–1881 (1993).
8. H. M. Ozaktas and D. Mendlovic, "Fractional Fourier transforms and their optical implementation: II," J. Opt. Soc. Am. A **10,** 2522–2531 (1993).
9. A. W. Lohmann, "Image rotation, Wigner rotation, and the fractional Fourier transform," J. Opt. Soc. Am. A **10,** 2181–2186 (1993).
10. D. Mendlovic, H. M. Ozaktas, and A. W. Lohmann, "Graded-index fiber, Wigner distribution functions, and the fractional Fourier transform," Appl. Opt. **33,** 6188–6193 (1994).
11. A. Papoulis, "Ambiguity function in Fourier optics," J. Opt. Soc. Am. **64,** 779–788 (1974).
12. S. Y. Lee and H. H. Szu, "Fractional Fourier transform, wavelet transform, and adaptive neural networks," Opt. Eng. **33,** 2326–2329 (1994).
13. P. Pellat-Finet, "Fresnel diffraction and the fractional order Fourier transform," Opt. Lett. **19,** 1388–1390 (1994).
14. S. Granieri, O. Trabocchi, and E. E. Sicre, "Fractional Fourier transform applied to spatial filtering in the Fresnel domain," Opt. Commun. **119,** 275–278 (1995).
15. J. A. Davis, D. M. Cottrell, N. Nestorovic, and S. M. Highnote, "Space-variant Fresnel transform optical correlator," Appl. Opt. **31,** 6889–6893 (1992).
16. A. W. Lohmann, Z. Zalevsky, and D. Mendlovic, "Synthesis of pattern recognition filters for fractional Fourier processing," Opt. Commun. **128,** 199–204 (1996).
17. A. W. Lohmann, "A fake zoom lens for fractional Fourier experiments," Opt. Commun. **115,** 437–443 (1995).

ELSEVIER

Optics & Laser Technology 30 (1998) 313–316

Optics & Laser Technology

Spatial partial coherence in Young's interferograms

Román Castañeda[a, 1], Francisco F. Medina[b, *], Mario Garavaglia[c, 2], Lía Zerbino[c]

[a]*Physics Department, Universidad Nacional de Colombia, Sede Medellín, A.A. 3840, Medellin, Colombia*
[b]*Physics Department, Universidad de Antioquia, A.A. 1226, Medellin, Colombia*
[c]*Centro de Investigaciones, Opticas - CIOp, Casilla de correo 124, 1900 La Plata, Argentina*

Received 17 June 1998; received in revised form 12 August 1998; accepted 19 August 1998

Abstract

Young's interferograms with high visibility reveals a high degree of spatial coherence of first order. But, spatially partial coherence of second order can be observed when it interferes itself through a compensated Michelson's interferometer attached at the exit of the Young's slit pair. We show that the patterns at the exit of the Michelson's interferometer are Young's interferograms with modulation fringes, which allow an estimation of the degree of the high order spatial coherence. © 1998 Elsevier Science Ltd. All rights reserved.

Keywords: Michelson's interferometer; Young's interferograms; High order coherence

1. Fundamentals

Fig. 1 shows the experimental setup. A pair of Young's slits, of width a along the x-axis, length $l \gg a$ along the y-axis and separation $b > a$, is illuminated by an He–Ne laser. The mirrors M1 and M2 of a compensated Michelson's interferometer reflect the Young's interference pattern it produces. The reflected patterns will be superimposed at the CCD sensor, which is attached at the exit of the Michelson's interferometer.

The reflected patterns can interfere depending on the tilting angle ϕ, which introduces a relative lateral shift between the patterns. This interference allows us to analyse the coherence patch of the optical field [1]. Indeed, it will produce a modulation of the Young's pattern whose fringe orientation, period and visibility depend on this lateral shift and on the structure of the coherence patch of the optical field.

The intensity distribution of the interferogram at the exit and of a Michelson's interferometer when the optical field is spatially partial coherent [1] is given by

$$I(x,y) = I_1(x,y) + I_2(x-X, y-Y) + 2W_{12}^{(r)}(x,y;X,Y). \quad (1)$$

$I_j(x,y)$ is the intensity distribution of the pattern from the mirror j ($j = 1, 2$); (X,Y) is the relative lateral shift between the patterns reflected by the two mirrors and $W_{12}^{(r)}(x,y;X,Y) = \mathrm{Re}|\mu(x-X, y-Y)E_1^*(x,y)E_2(x-X, y-Y)|$, where Re denotes the real part; $\mu(x-X,y-Y) = |\mu(x-X,y-Y)|e^{i\alpha_{XY}}$ is the complex degree of spatial coherence of the optical field, with $0 \le |\mu(x-X,y-Y)| \le 1$, $\mu(x,y) \equiv 1$ and $\alpha_{XY} = \alpha_{XY}(x-X,y-Y)$; $E_j(x,y)$ is the amplitude distribution of the pattern from the mirror j, and the asterisk denotes complex conjugate.

So, the visibility of such an interferogram [1] will be given by $V = [2\sqrt{I_1(x,y)}\sqrt{I_2(x-X,y-Y)}]/[I_1(x,y) + I_2(x-X,y-Y)]|\mu(x-X,y-Y)|$. Thus, for $I_1(x,y) \approx I_2(x-X,y-Y)$, V will be large inside the coherence patch of the optical field and will be small or zero outside of it.

* Corresponding author. Fax: +57-94-233-0120; e-mail: fmedina@catios.udea.edu.co.
[1] rcastane@perseus.unalmed.edu.co
[2] postmaster@ciop.edu.ar

0030-3992/98/$19.00 © 1998 Elsevier Science Ltd. All rights reserved.
PII: S0030-3992(98)00058-9

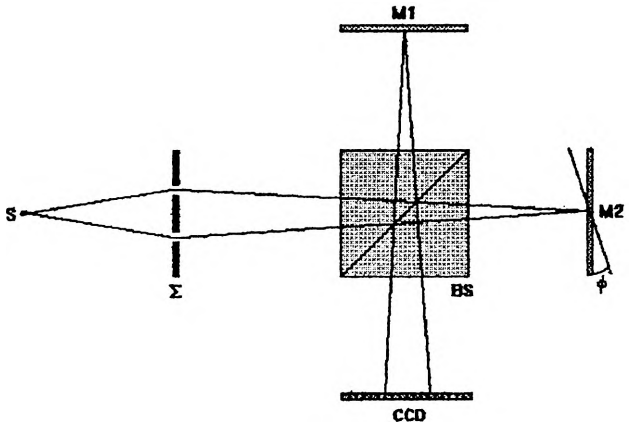


Fig. 1. Experimental setup to obtain an interference pattern from a Young's interferogram.

According to the experimental setup, let us assume that $I_j(x,y)$ represents a Young's pattern of high visibility, which is due to a high degree of first order spatial coherence of the optical field. Therefore, the visibility of the modulation at the exit of the Michelson's interferometer will reveal a spatially partial coherence of second order, due the partial correlation between pairs of corresponding radiators at the interferometer mirrors M1 and M2.

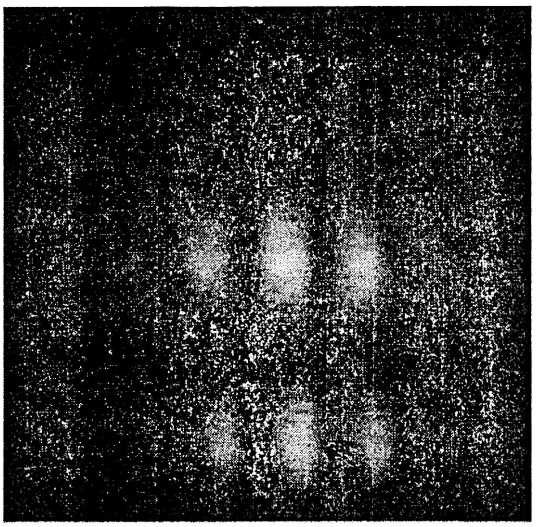
Taking into account that $k = 2\pi/\lambda$, with λ the wavelength and L the optical path length into the compensated Michelson's interferometer [2], we have

$$I_1(x,y) = |E_0|^2 \left(\frac{\sin\left(\frac{ka}{L}x\right)}{\frac{ka}{L}x} \right)^2 \times \left(\frac{\sin\left(\frac{kl}{L}y\right)}{\frac{kl}{L}y} \right)^2 \cos^2\left(\frac{kb}{L}x\right), \tag{2a}$$

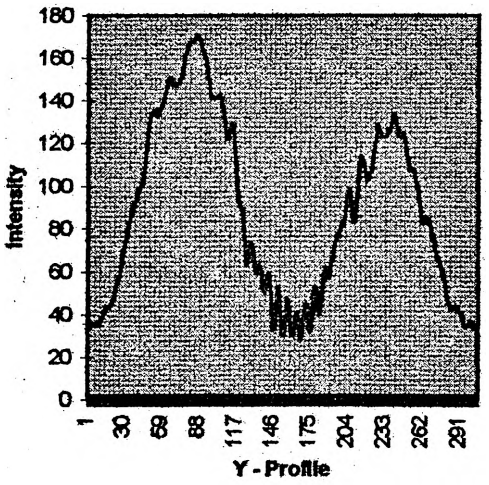
$$I_2(x-X,y-Y) = |E_0|^2 \left(\frac{\sin\left(\frac{ka}{L}(x-X)\right)}{\frac{ka}{L}(x-X)} \right)^2 \times \left(\frac{\sin\left(\frac{kl}{L}(y-Y)\right)}{\frac{kl}{L}(y-Y)} \right)^2 \cos^2\left(\frac{kl}{L}(x-X)\right), \tag{2b}$$

$$W_{12}^{(r)}(x,y;X,Y) = |E_0|^2 |\mu(x-X,y-Y)| \cos\alpha_{XY} \times \left(\frac{\sin\left(\frac{ka}{L}(x-X)\right)}{\frac{ka}{L}(x-X)} \right) \times \left(\frac{\sin\left(\frac{ka}{L}x\right)}{\frac{ka}{L}x} \right) \times \left(\frac{\sin\left(\frac{kl}{L}(y-Y)\right)}{\frac{kl}{L}(y-Y)} \right) \cos\left(\frac{kb}{L}(x-X)\right) \times \cos\left(\frac{kb}{L}x\right). \tag{2c}$$

For $X = Y = 0$ Eqs. (1) and (2a)–(c) yield $I(x,y) = 4\,|E_0|^2 \{\sin[(ka/L)x]/(ka/L)x\}^2 \{\sin[(kl/L)y]/$

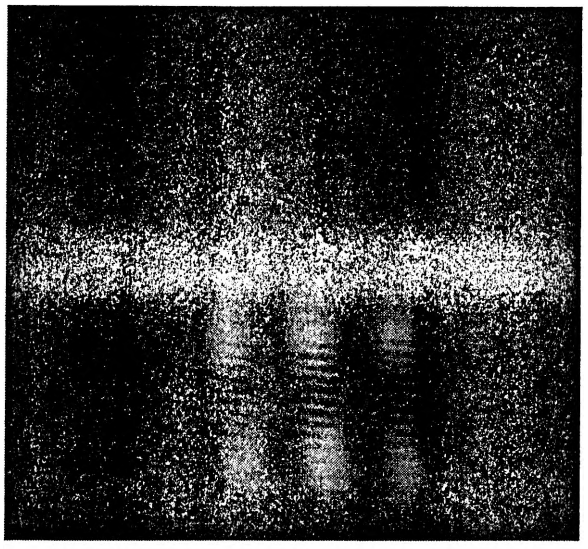


a

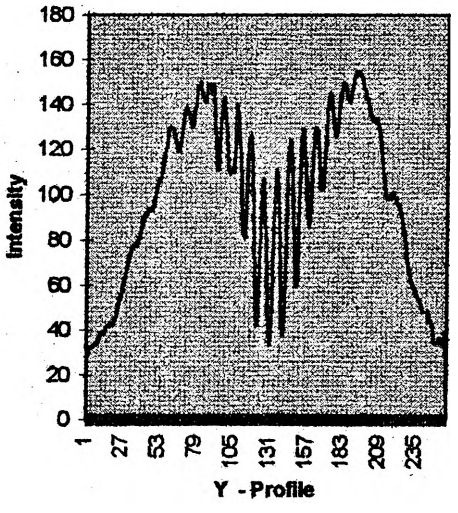


b

Fig. 2. (a) Young's interferograms outside of the coherence patch of the optical field. (b) A vertical profile in (a).



a



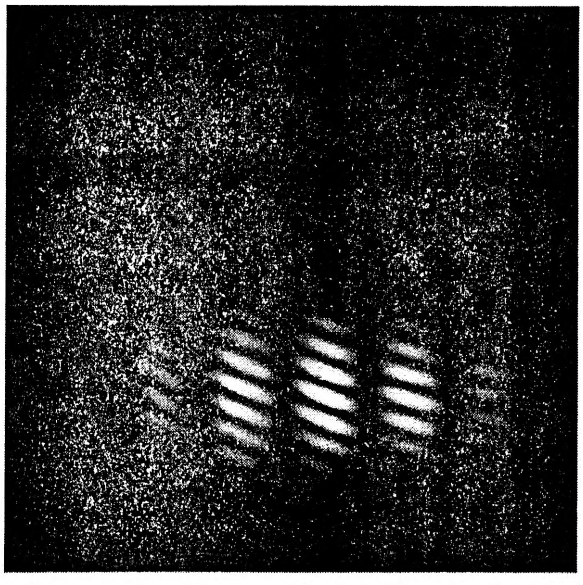
b

Fig. 3. (a) Young's interferograms partially located inside of the coherence patch of the optical field. (b) A vertical profile in (a).

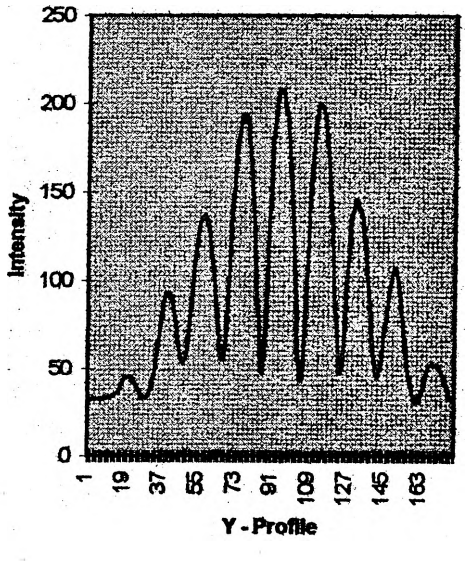
$(kl/L)y\}^2 \cos^2[(kb/L)x]$, which exhibits the same structure as an individual Young pattern without modulation, and allows us to calibrate the Michelson interferometer. The modulation fringes on the Young pattern will be mainly described by the first cosine term in parentheses in expression (3), which is obtained from Eq. (2c), by applying the trigonometric identity for the product of cosine functions [1–3], i.e.

$$\tfrac{1}{2}|\mu(x-X,y-Y)|\cos\alpha_{XY}\left\{\cos\left[\frac{2kb}{L}\left(x-\frac{X}{2}\right)\right]+\cos\left(\frac{kb}{L}X\right)\right\}. \quad (3)$$

If $X < (\lambda L/b)$ expression (3) approaches to $|\mu(x-X, y-Y)|\cos\alpha_{XY}\{\cos^2[(kb/L)x]+(kb/2L)X\sin[(2kb/L)x]\}$. The coefficient of the second term into the parenthesis will be smaller than 1, so that the sinus function can be considered as a perturbation of the cosine squared. In other words, the profile of the modulation fringes (when they appear) will be essentially the cosine squared function.



a



b

Fig. 4. (a) Superimposed Young's interferograms, completely located inside of the coherence patch of the optical field. (b) A vertical profile in (a).

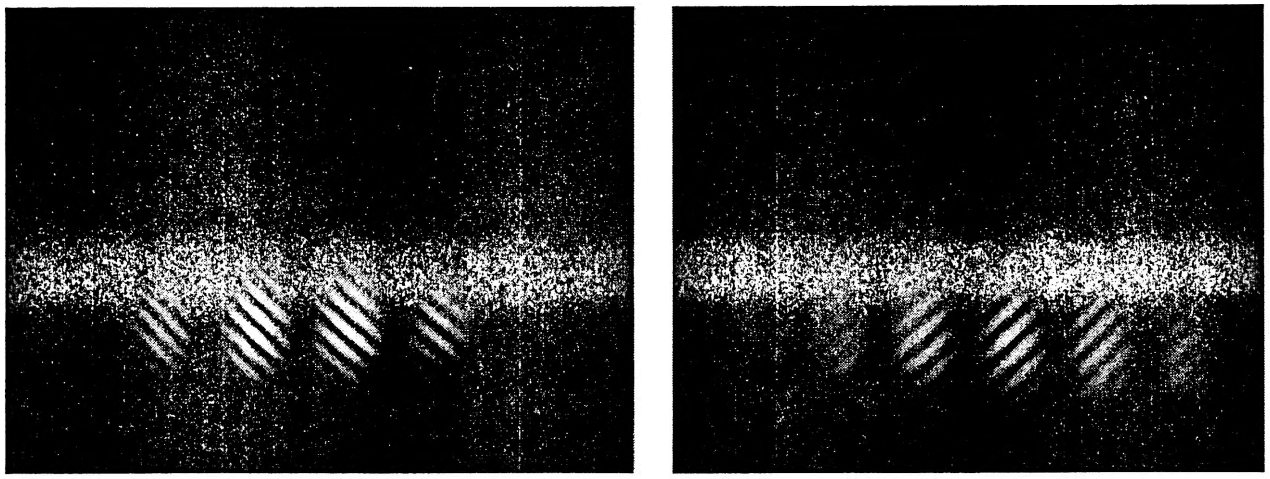


Fig. 5. Superimposed Young's interferograms with (a) left and (b) right horizontal shifts. The histograms of their vertical profiles are similar as in Fig. 4b.

2. Experimental results

Figures 2–5 show the portion of the diffraction central peak of the Young's patterns at the exit of the Michelson's interferometer. The size of the coherence patch of the optical field is of the order of the area of those diffraction peaks, i.e. $|\mu(x-X,y-Y)| \to 1$ inside them.

In Fig. 2a the Y shift is greater than the size of the coherence patch along this axis. As a consequence, $|\mu(x-X,y-Y)| \to 0$. Indeed, there is a low intensity modulation between the superimposed patterns and an absence of modulation into the Young's lobes (Fig. 2b).

The square cosine-like modulation in this region increases significantly when the Y shift becomes smaller, but the lack of visibility is even apparent in the Young's lobes (Fig. 3a and b).

The high visibility of the square cosine-like modulation, i.e. $|\mu(x-X,y-Y)| \to 1$, will be apparent inside the whole Young's lobes as $Y \to 0$ (Fig. 4a and b).

In Fig. 5a and b the Y shift is negligible but not the X shift. After a shift of about two orders of the Young's pattern, i.e. $X \approx 2\lambda L/b$, the expression (3) approaches to $\cos^2([kb/L)x + \alpha_{XY}]$. Thus, the modulation fringes are of high visibility (square cosine-like) and covers the whole Young's lobes. It is also interesting to observe the change in the orientation of the modulation fringes, which is essentially related to the change of sign in the coherence phase α_{XY} when the pattern shift goes from the left to the right.

3. Conclusions

Spatial coherence of second order can be analysed if a Young's pattern interferes itself through a compensated Michelson interferometer. Modulation fringes on the Young's pattern can be observed at the exit of this device, whose visibility provides an estimation of the degree of the high order spatial coherence.

Acknowledgements

The Multipurpose Optical Network (MON), CINDEC (Universidad Nacional de Colombia Sede Medellin) and CODI (Universidad de Antioquia) supported this work.

References

[1] Born M, Wolf E. Principles of optics. 6th ed. Oxford: Pergamon Press, 1993:491.
[2] Goodman JW. Statistical optics. 1st ed. New York: Wiley, 1985:157–236.
[3] Basano L, Pontiggia C. Simple demonstrations for introducing spatial coherence. Am J Phys 1996;64(10):1257–61.

Quality parameters analysis of optical imaging systems with enhanced focal depth using the Wigner distribution function

Dobryna Zalvidea, Cecilia Colautti, and Enrique E. Sicre

Centro de Investigaciones Opticas, P.O. Box 124, 1900 La Plata, Argentina

Received July 12, 1999; revised manuscript received January 10, 2000; accepted January 21, 2000

An analysis of the Strehl ratio and the optical transfer function as imaging quality parameters of optical elements with enhanced focal length is carried out by employing the Wigner distribution function. To this end, we use four different pupil functions: a full circular aperture, a hyper-Gaussian aperture, a quartic phase plate, and a logarithmic phase mask. A comparison is performed between the quality parameters and test images formed by these pupil functions at different defocus distances. © 2000 Optical Society of America [S0740-3232(00)00605-0]

OCIS codes: 100.5070, 110.4850, 110.5100.

1. INTRODUCTION

In recent years several types of optical elements that give rise to well-focused energy distributions along three-dimensional paths have been extensively reported in the literature (see, e.g., Ref. 1). Annular-type apertures acting as apodizers to improve the quality of the point-spread function (PSF) and to increase the focal depth have been studied.[2–8] However, the main drawback of all these methods arises from the fact that both the spatial resolution and the optical power decrease at the image plane. An alternative way to achieve an extended depth of field without using apodizers was reported by Häusler[9] for the case in which focusing can be varied through the image-forming process. In this way, the image field is adequately scanned to produce a well-focused PSF at each image point. Another type of optical system that allows the concentration of energy in a segment of the optical axis is the so-called axilens; such lenses have an associated focal length that varies with the radial coordinate, so their phase retardation functions differ from those of the conventional quadratic phase exponential.[10,11] Therefore, if these phase masks are employed as pupil functions of an imaging optical system, although there is no decrease in the image intensity the resulting PSF becomes relatively broad.

To evaluate the image quality originated by an optical system with a required focal depth, it seems adequate to use different parameters: for example, the Strehl ratio[12] (SR), which gives information about the energy concentration along the optical axis, and the optical transfer function (OTF), which shows the behavior of the optical system for varying spatial frequencies.[13] There are several criteria for specifying the tolerance of an optical system to aberrations or focus error, for example, Rayleigh's criterion,[14] and Marechal's treatment of tolerances.[15] In all these criteria the on-axis image irradiance is the relevant quantity. Hopkins[16,17] has shown that it is possible to extend Marechal's treatment by employing OTF theory to give a tolerance criterion. This method is quite suitable as a merit function in automatic optical design.

The relationships between these image quality criteria and the phase-space representations, namely, the Wigner distribution function[18,19] (WDF) and the ambiguity function,[20] (AF) were employed in several studies to analyze the performance of an optical system with respect to different aberrations and defocus.[21–26]

In a previous paper[27] we proposed a method for obtaining phase retardation functions that give rise to an increase in the image focal depth. To this end, the WDF of a certain aperture with small depth of focus in the image space is sheared in the phase-space domain to originate a new WDF from which its related phase pupil gives rise to a more uniform on-axis image irradiance. In this way, a new phase pupil function with a good performance with respect to defocus, is obtained. A lens axicon with a similar phase function was also proposed by Jaroszewicz and Morales,[28] with use of geometrical optics.

In the present paper we first briefly describe the phase-space formalism and its relationships to different image-quality parameters. In particular, an expression of the SR as a function of the WDF of a bidimensional radially symmetric aperture is obtained for any out-of-focus plane. Then we extend the approach to analyze the relationship between the OTF of this kind of pupil function and the related WDF. We apply this analysis to study the behavior of different phase and amplitude pupil functions[7,11] at various defocus distances.

2. WIGNER DISTRIBUTION FUNCTION: DEFINITIONS AND BASIC RELATIONSHIPS

For a two-dimensional complex-valued function $g(x, y)$, its associated WDF phase-space representation can be alternatively defined from the function itself or from its spectrum $\tilde{G}(\nu, \mu)$ as

0740-3232/2000/050867-07$15.00 © 2000 Optical Society of America

$$W_g(x, y; \nu, \mu) = \int\int_{-\infty}^{+\infty} g\left(x + \frac{x'}{2}, y + \frac{y'}{2}\right) \times g^*\left(x - \frac{x'}{2}, y - \frac{y'}{2}\right) \times \exp[-2\pi i(x'\nu + y'\mu)]\mathrm{d}x'\mathrm{d}y' = \int\int_{-\infty}^{+\infty} \tilde{G}\left(\nu + \frac{\nu'}{2}, \mu + \frac{\mu'}{2}\right) \times \tilde{G}^*\left(\nu - \frac{\nu'}{2}, \mu - \frac{\mu'}{2}\right) \times \exp[2\pi i(x\nu' + y\mu')]\mathrm{d}\nu'\mathrm{d}\mu', \quad (1)$$

respectively. From Eq. (1) it can be deduced that this formalism emphasizes equally the role of the spatial and the spatial-frequency coordinates. This feature makes these distributions especially suitable for describing the behavior of optical imaging systems. Among several properties of these distributions, those that are relevant for analyzing image-quality parameters are the following:

$$W_z(x, y; \nu, \mu) = W_0(x - \lambda z\nu, y - \lambda z\mu; \nu, \mu), \quad (2)$$

$$I(x, y; z) = \int\int_{-\infty}^{\infty} W_z(x, y; \nu, \mu)\mathrm{d}\nu\mathrm{d}\mu, \quad (3)$$

$$t(x, y) = \frac{1}{t^*(0, 0)} \int\int_{-\infty}^{\infty} W_t\left(\frac{x}{2}, \frac{y}{2}; \nu, \mu\right) \times \exp[2\pi i(\nu x + \mu y)]\mathrm{d}\nu\mathrm{d}\mu. \quad (4)$$

Equation (2) states that, under free-space propagation in the Fresnel diffraction region, the WDF associated with the light field is sheared in the phase space only along the spatial coordinates. In Eq. (3) the intensity distribution at a certain plane is found by projecting the WDF onto the spatial-frequency plane. The Fourier transform in Eq. (4) allows recovery of the signal from the WDF.

3. IMAGE-QUALITY PARAMETERS AND THE WIGNER DISTRIBUTION FUNCTION: BASIC THEORY

Let us consider an optical imaging system that can be described by the amplitude PSF. At the image plane ($z = 0$), the PSF is given through a Fourier transform relationship

$$p(x, y; z = 0) = \frac{A}{\lambda f}\exp\left[i\frac{\pi}{\lambda f}(x^2 + y^2)\right] \times \int\int_{-\infty}^{\infty} t(\xi, \eta)\exp\left[-\frac{2\pi i}{\lambda f}(x\xi + y\eta)\right] \times \mathrm{d}\xi\mathrm{d}\eta, \quad (5)$$

where A is the constant incident amplitude, f is the focal length, and $t(\xi, \eta)$ is the complex-amplitude transmittance associated with the exit pupil. By taking into account the WDF definition as given by Eq. (1) and replacing $p(x, y)$, as given by Eq. (5), we find the WDF at the image plane to be

$$W_i(x, y; \nu, \mu) = (\lambda f)^2 W_t\left(x - \lambda f\nu, y - \lambda f\mu; \frac{x}{\lambda f}, \frac{y}{\lambda f}\right), \quad (6)$$

where $W_t(x, y; \nu, \mu)$ is the WDF of the pupil function $t(\xi, \eta)$. Accordingly, with Eqs. (2) and (3), the intensity at a defocused plane ($z \neq 0$) can be found as

$$I(x, y; z) = \int\int_{-\infty}^{\infty} W_i(x - \lambda z\nu, y - \lambda z\mu; \nu, \mu)\mathrm{d}\nu\mathrm{d}\mu = (\lambda f)^2 \int\int_{-\infty}^{\infty} \mathrm{d}\nu\mathrm{d}\mu W_t\left[x - \lambda(f + z)\nu, y - \lambda(f + z)\mu; \frac{x}{\lambda f} - \frac{z}{f}\nu, \frac{y}{\lambda f} - \frac{z}{f}\mu\right]. \quad (7)$$

From Eq. (7), the Strehl ratio versus defocus $S(z)$ can be easily derived as

$$S(z) = \frac{I(0, 0; z)}{I(0, 0; 0)} = K\int\int_{-\infty}^{\infty} \mathrm{d}\zeta_1\mathrm{d}\zeta_2 \times W_t(x - \lambda(f + z)\zeta_1, y - \lambda(f + z)\zeta_2; \zeta_1, \zeta_2), \quad (8)$$

where $\zeta_1 = (-z/f)\nu$, $\zeta_2 = (-z/f)\mu$ are redefined spatial frequencies, and $K = (\lambda f^2/za)^2$, a being the pupil area. Thus, the behavior of the optical imaging system can be visualized through the spatial variation of the function $S(z)$, which in turn is obtained from the summation of the values of $W_i(x, y; \nu, \mu)$ along different lines in the phase space. However, although Eq. (8) provides a complete description of the SR for any plane $z \neq 0$, it involves the manipulation of a function defined in a four-dimensional phase space. If we restrict the analysis to radially symmetric apertures, i.e., $t(\xi, \eta) = t(\rho)$, where $\rho = (\xi^2 + \eta^2)^{1/2}$, then the information content of the phase space $(x, y; \zeta_1, \zeta_2)$ [from which the SR, $S(z)$, is obtained] can be displayed in a modified two-dimensional phase space (x, ζ). To this end, we rewrite the intensity in the neighborhood of the image plane as

$$I(x, y; z) = |p(x, y; z|^2. \quad (9)$$

Then, since the analysis is restricted to radially symmetric apertures, the on-axis intensity is

$$I(0, 0; z) = \left|\int_0^{2\pi}\int_0^{\infty} t(\rho)\exp\left(\frac{i\pi z}{\lambda f^2}\rho^2\right)\rho\mathrm{d}\rho\mathrm{d}\phi\right|^2. \quad (10)$$

We now employ the change of variable $\rho = \rho(\zeta)$, previously introduced in Ref. 7, which transforms any two-dimensional radially symmetric aperture $t(\rho)$, defined for $0 \leq \rho \leq \rho_0$, into a modified one-dimensional pupil function $q(\zeta)$ that is different from zero only in the interval $-1/2 \leq \zeta \leq 1/2$; that is,

$$\left(\frac{\rho}{\rho_0}\right)^2 = \zeta + \frac{1}{2}. \quad (11)$$

Then the on-axis intensity becomes

$$I(0, 0; z) = \int\int_{-\infty}^{\infty} q\left(\zeta + \frac{\zeta'}{2}\right) q^*\left(\zeta - \frac{\zeta'}{2}\right) \times \exp\left(2\pi i \frac{z\rho_0^2}{2\lambda f^2}\zeta'\right) d\zeta d\zeta'. \quad (12)$$

By means of the WDF defined for one-dimensional functions, the SR can be rewritten as

$$S(z) = \int_{-\infty}^{\infty} W_q\left(\frac{\rho_0^2 z}{2\lambda f^2}, \zeta\right) d\zeta. \quad (13)$$

Therefore the SR for radially symmetric apertures can be obtained, for any out-of-focus plane, from a proper spatial-frequency projection of the WDF defined in the two-dimensional phase space that is associated with the transformed pupil function $q(\zeta)$.

As presented by us in Ref. 27, it is possible to obtain phase retardation functions that give rise to an increase in the image focal depth. To this end, the WDF of a certain aperture $t_0(\rho)$, which has an associated small depth of focus in the image space, is transformed through the change of variables in Eq. (11) into a one-dimensional aperture $q_0(\zeta)$ that is conveniently sheared by an amount α in the phase-space domain as follows:

$$W_q\left(\frac{z\rho_0^2}{2\lambda f^2}, \zeta\right) = W_{q_0}\left(\frac{z\rho_0^2}{2\lambda f^2} - \alpha\zeta, \zeta\right). \quad (14)$$

In this way, high-value portions of the original WDF translate toward previously low-value regions, thus producing a compensation effect that smooths the variation of the ζ slices of the WDF from which the axial intensity is achieved. Therefore when this new WDF is introduced into the expression of the SR [Eq. (13)], a more uniform on-axis image irradiance can be accomplished. In Ref. 27 we apply this method to a uniform aperture: $t_0(\rho) = \mathrm{circ}(\rho/\rho_0)$, which was selected because of its simplicity and energy considerations. The enhanced depth-of-focus pupil function that we obtained was

$$t(\rho) = \mathrm{circ}\left(\frac{\rho}{\rho_0}\right) \exp\left\{-i\pi\alpha\left[\left(\frac{\rho}{\rho_0}\right)^4 - \left(\frac{\rho}{\rho_0}\right)^2 + \frac{1}{4}\right]\right\}. \quad (15)$$

Through the change of variables introduced by Eq. (11), the original pupil function $t_0(\rho)$ can be expressed as $q_0(\zeta) = \mathrm{rect}(\zeta)$. Then, when we take into account Eq. (14), the WDF of the transformed pupil function $q(\zeta)$, which originates high focal depth, becomes

$$W_q\left(\frac{z\rho_0^2}{2\lambda f^2}; \zeta\right) = \int q_0\left(\zeta + \frac{\zeta'}{2}\right) q_0^*\left(\zeta - \frac{\zeta'}{2}\right) \times \exp(-i\pi 2\alpha\zeta\zeta') \exp\left(i\pi \frac{z\rho_0^2}{\lambda f^2}\zeta'\right) d\zeta'. \quad (16)$$

In order to characterize a certain amount of defocus Δz where the optical imaging system produces a rather uniform $S(z)$, we restrict the WDF as given by Eq. (16) to take the phase-space values that satisfy

$$\frac{z\rho_0^2}{2\lambda f^2} - \alpha\zeta = 0. \quad (17)$$

Inside this domain the WDF takes the form

$$W_q\left(\frac{z\rho_0^2}{2\lambda f^2}; \zeta = \frac{z\rho_0^2}{2\lambda\alpha f^2}\right) = \int \mathrm{rect}\left(\zeta + \frac{\zeta'}{2}\right) \mathrm{rect}\left(\zeta - \frac{\zeta'}{2}\right) d\zeta' = \begin{cases} -2\zeta + 1 & \zeta \geq 0 \\ 2\zeta + 1 & \zeta \leq 0 \end{cases} \quad (18)$$

It can be seen that $W_q(z\rho_0^2/2\lambda f^2; \zeta = z\rho_0^2/2\lambda\alpha f^2)$ is null for $\zeta \geq 1/2$. Hence for $\zeta = 1/2$ the maximum value of the depth of focus is obtained, i.e. $\Delta z = 2z_{\max}$, where

$$z_{\max} = \frac{\lambda f^2 \alpha}{\rho_0^2}. \quad (19)$$

In this way, if a pupil function with a certain depth of focus is required for a given optical system, it is possible to achieve it by a proper shear in the phase-space domain [by applying Eq. (19)]. It is important to note that this procedure is more general than the scheme expressed by Eqs. (14)–(19), as one can apply it to any other pupil function that has a symmetric WDF, in order to derive a new pupil function that takes into account the original pupil characteristics but with enhanced depth of focus.

Up to now, we have analyzed the behavior of the pupil function by taking into account the energy spread along the optical axis. For this reason, the SR provides an adequate criterion for evaluating the performance of the optical system. However, if we are interested in taking into account the degradation of the image resolution for increasing amounts of defocus, the OTF becomes a more relevant quality parameter. The OTF would allow a better understanding of the spatial-frequency performance of a given pupil function for different defocus values. In the following, we are interested in linking the OTF with the WDF that is associated with the pupil function, in a way that is similar to what we did with the SR. Therefore the OTF of a radially symmetric pupil with a transmittance $t(\rho)$ can be expressed as

$$\mathcal{H}(\nu; z) = \frac{\int_0^{\infty} |p(r'; z)|^2 J_0(2\pi\nu r') r' dr'}{\int_0^{\infty} |p(r'; z = 0)|^2 r' dr'}, \quad (20)$$

where $p(r'; z)$ is the PSF of the pupil with transmittance $t(\rho)$, J_0 is the Bessel function of zero order and the first kind, and ν means the modulus of the normalized spatial frequencies. To link this OTF with the WDF of $t(\rho)$, we first rewrite the squared modulus of the PSF as

$$|p(r';z)|^2 = \left|\int_0^\infty t(\rho)\exp\left(\frac{\pi i}{\lambda}\frac{z}{f^2}\rho^2\right)J_0\left(\frac{2\pi\rho r'}{\lambda f}\right)\rho\,d\rho\right|^2$$

$$= \int_0^\infty\int_0^\infty t(\rho)t^*(\rho')\exp\left\{\frac{\pi i}{\lambda}\frac{z}{f^2}[\rho^2-(\rho')^2]\right\} \times J_0\left(\frac{2\pi\rho r'}{\lambda f}\right)J_0\left(\frac{2\pi\rho' r'}{\lambda f}\right)\rho'\rho\,d\rho\,d\rho'. \quad (21)$$

Then, by employing the change of coordinates introduced in Eq. (11) and replacing Eq. (21) in the expression of the OTF, we obtain

$$\mathcal{H}(\nu;z) = \frac{1}{\int_0^\infty |p(r';0)|^2 r'\,dr'}\int_0^\infty\left\{\int_{-\infty}^\infty\int_{-\infty}^\infty q(\xi)q^*(\xi') \times J_0\left(\frac{2\pi\rho_0}{\lambda f}\sqrt{\xi+\frac{1}{2}}\,r'\right) \times J_0\left(\frac{2\pi\rho_0}{\lambda f}\sqrt{\xi'+\frac{1}{2}}\,r'\right) \times \exp\left[\frac{\pi i}{\lambda}\frac{{\rho_0}^2 z}{f^2}(\xi-\xi')\right]d\xi\,d\xi'\right\} \times J_0(2\pi\nu r')r'\,dr', \quad (22)$$

where $q(\xi)$ is the transformed one-dimensional pupil function. To link this expression with the WDF of the transformed pupil we rewrite Eq. (22) as

$$\mathcal{H}(\nu;z) = \frac{1}{\int_0^\infty |p(r')|^2 r'\,dr'}\int_0^\infty\left[\int_{-\infty}^\infty\int_{-\infty}^\infty q\left(\zeta+\frac{\zeta'}{2}\right) \times q^*\left(\zeta-\frac{\zeta'}{2}\right) \times J_0\left(\frac{2\pi\rho_0}{\lambda f}\sqrt{\zeta+\frac{\zeta'+1}{2}}\,r'\right) \times J_0\left(\frac{2\pi\rho_0}{\lambda f}\sqrt{\zeta-\frac{\zeta'-1}{2}}\,r'\right) \times \exp\left(\frac{\pi i}{\lambda}\frac{{\rho_0}^2 z}{f^2}\zeta'\right)d\zeta\,d\zeta'\right]J_0(2\pi\nu r')r'\,dr', \quad (23)$$

where $\zeta = (\xi+\xi')/2$; $\zeta' = \xi-\xi'$. From the definition of the WDF, we found that

$$\mathcal{H}(\nu;z) = \frac{\int_0^\infty\left[\int_{-\infty}^\infty W_{\hat{q}(\zeta;r')}\left(\frac{{\rho_0}^2 z}{2f^2\lambda};\zeta\right)d\zeta\right]J_0(2\pi\nu r')r'\,dr'}{\int_0^\infty\left[\int_{-\infty}^\infty W_{\hat{q}(\zeta,r')}\left(\frac{{\rho_0}^2 z}{2f^2\lambda};\zeta\right)d\zeta\right]r'\,dr'}, \quad (24)$$

where

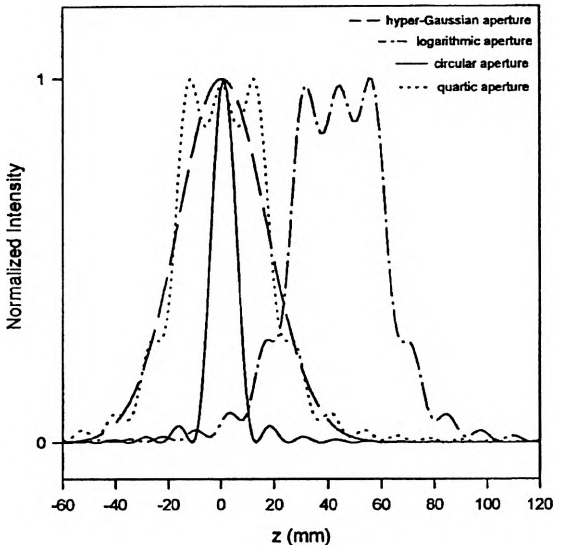


Fig. 1. Normalized intensity of the hyper-Gaussian pupil aperture, the logarithmic phase mask, the circular pupil function, and the quartic pupil function for extended depth of focus, Δz = 60 mm.

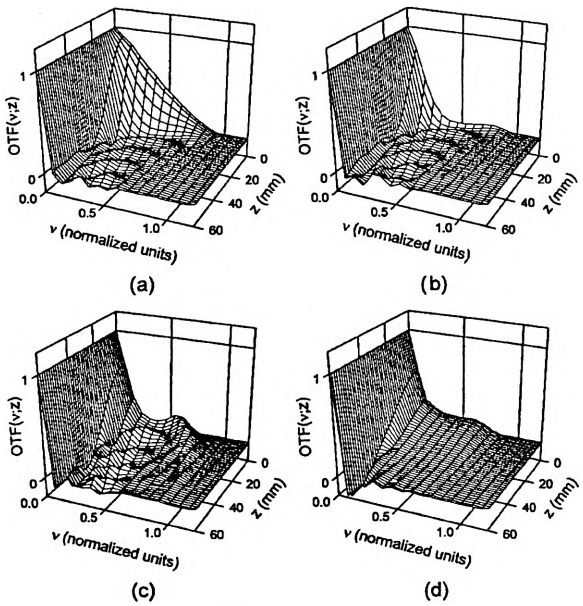


Fig. 2. Optical transfer function of (a) circular pupil function, (b) logarithmic pupil function, (c) quartic pupil function, (d) hyper-Gaussian pupil function for extended depth of focus, Δz = 60 mm.

$$\hat{q}(\zeta;r') = q(\zeta)J_0\left(\frac{2\pi\rho_0}{\lambda f}\sqrt{\zeta}\,r'\right). \quad (25)$$

Every WDF display corresponds to a different $\hat{q}(\zeta, r')$, as is expressed in Eq. (25), where $J_0(\zeta; r')$ acts as a window function for the transformed pupil function $q(\zeta)$, which is related to the original two-dimensional pupil function $t(\rho)$. Each WDF display shows the behavior of $\hat{q}(\zeta,\nu')$ for every z value and for each value of ν', so it would be necessary to evaluate an infinite number of WDF's, one

for each value of ν'. On the other hand, if we analyze the behavior of the transformed pupil function $\hat{q}(\zeta, \nu')$, we see that the zeros of the window function $J_0(\zeta; \nu')$ are fixed, so as ν' increases, ζ decreases; this means that for large ν', $\hat{q}(\zeta, \nu')$ can be approximated by $\hat{q}(\zeta, \nu') \sim q(0)J_0(2\pi\rho_0\sqrt{\zeta}\nu')$, and the contribution of the different WDF's to the OTF in Eq. (25) will be the same when ν' is large enough. In this way, the calculation of $\mathcal{H}(\nu; z)$ is greatly simplified.

It can be seen from Eq. (24) that, in a way similar to what was previously done for the case of the SR, the WDF associated with a one-dimensional modified pupil function provides information about the behavior of the OTF versus defocus. For diverse pupil functions $t(\rho)$, we obtain different $\hat{q}(\zeta, r_0')$, where r_0' is a fixed value of the variable r' that is selected according to the spatial-frequency band to be tested. Then the corresponding WDF's defined in the two-dimensional phase space $[x = (\rho_0{}^2 z)/(2f^2\lambda), \zeta]$ are obtained. In this way, the performances of the different pupil functions can be compared through the rate of variation of these displays along the x coordinate. The tolerance to defocus of the considered pupil functions is determined in a way similar to that for the analysis of $S(z)$, since there is a close resemblance between the ρ expressions in parentheses in Eqs. (13) and (24), which gives the SR.

4. RESULTS

To illustrate the present approach we analyze the SR and the OTF of different pupil functions. We compare the performance of four apertures: two phase pupil functions, the quartic phase plate introduced in Eq. (15), and the logarithmic phase mask,[11] given by

$$t(\rho) = \mathrm{circ}\left(\frac{\rho}{\rho_0}\right)\exp\left[\frac{i\pi{\rho_0}^2}{\lambda\,\delta z}\ln\left(f_0 + \frac{\delta z\rho^2}{{\rho_0}^2}\right)\right], \quad (26)$$

where δz is the focal depth; and two amplitude pupil functions, the hyperGaussian proposed by Ojeda-Castañeda *et al.*,[7]

$$t(\rho) = \mathrm{circ}\left(\frac{\rho}{\rho_0}\right)\exp\left\{-2\pi\gamma\left[\left(\frac{\rho}{\rho_0}\right)^2 - \frac{1}{2}\right]^2\right\}, \quad (27)$$

and the full circular pupil function. The normalized intensities for the four considered cases are shown in Fig. 1. The parameters of the pupil functions have been chosen to give similar depth of focus, and the lower tolerance to defocus of the full aperture can be seen. The corresponding OTF's for different values of z are shown in Fig. 2. For the circular and the logarithmic pupil functions, the OTF's dramatically decrease for out-of-focus planes, thus producing a serious degradation of their imaging capabili-

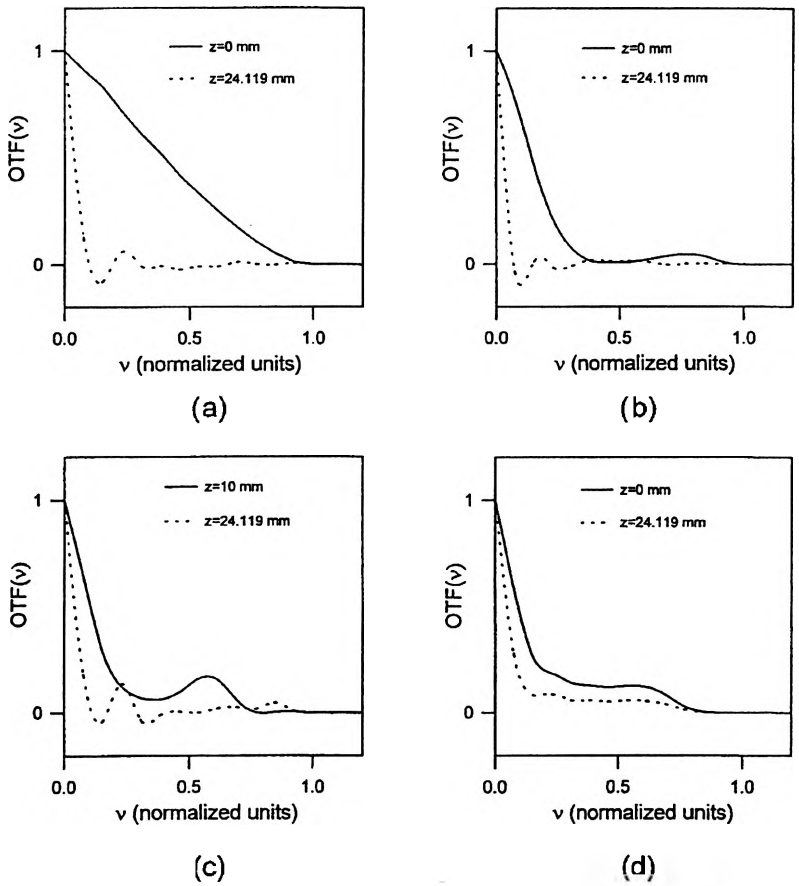


Fig. 3. Cross sections of the OTF of Fig. 2 for $z = 0$ mm and $z = 24.119$ mm. (a) Circular pupil function; some departure from the expected linear decrease (for $z = 0$ mm) due to the computational limitations in data sampling can be observed. (b) Logarithmic pupil function. (c) Quartic pupil function. (d) Hyper-Gaussian pupil function.

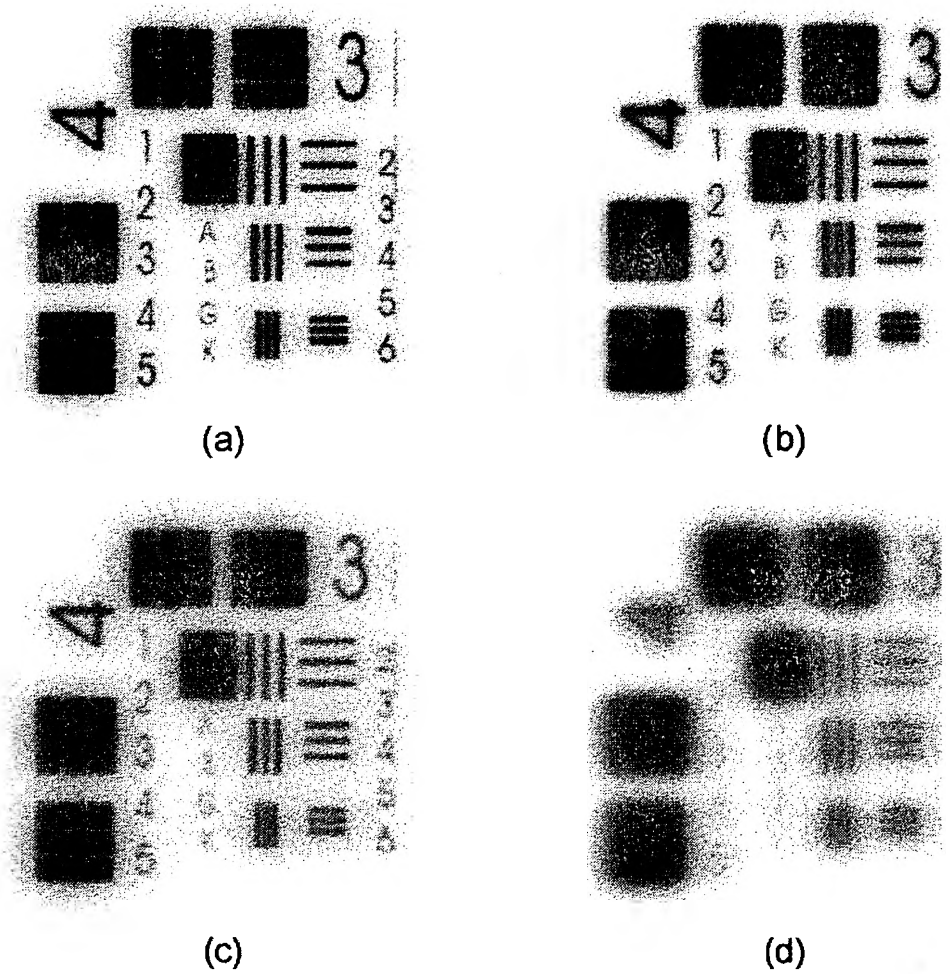


Fig. 4. Images of a test chart with (a) quartic pupil function for $z = 10$ mm, (b) hyper-Gaussian pupil function for $z = 0$ mm, (c) quartic pupil function for $z = 24.119$ mm, (d) hyper-Gaussian pupil function for $z = 24.119$ mm.

ties. The OTF associated with the hyper-Gaussian pupil function shows a smoother decrease than the corresponding quartic aperture, but both of them produce better image quality than the circular and the logarithmic pupil functions. This fact can also be appreciated from Fig. 3. The OTF's associated with the quartic and hyper-Gaussian apertures for $z = 0$ mm and $z = 24.199$ mm show a better performance than for the other two pupils. For the quartic pupil function it can be seen that the cross section of the OTF presents spatial-frequency zones with better image resolution.

In Fig. 4 we compare the performance of the quartic and the hyper-gaussian pupil functions through the simulated images of a test chart for the best in-focus plane ($z = 10$ mm for the quartic pupil and $z = 0$ mm for the hyper-Gaussian pupil function), and for extreme defocus $z = 24.119$ mm. While for in-focus value the quartic and the hyper-Gaussian pupils present similar resolutions, for extreme depth of focus the quartic pupil has a better behavior than the hyper-Gaussian.

5. CONCLUSIONS

In the present paper we studied the SR and the OTF of different phase and amplitude pupil functions for varying defocus. We have linked these quality parameters with the WDF of these pupils. In this way, the SR could be visualized in a single phase-space representation of a one-dimensional modified pupil function. In another procedure, the OTF was analyzed by examination of the different WDF at various defocus distances. From these displays we obtained information directly about the behavior of the OTF criterion and the SR to analyze the image quality produced by four pupil functions with good tolerance to defocus. These relations between the quality parameters and the WDF have important implications in the design of optical imaging systems. Although the expression obtained for the OTF is more difficult to analyze than the equivalent expression for the SR, the present approach reduces calculation time.

Address correspondence to D. Zalvidea at the address

on the title page or by telephone, 54-221-4840280; fax, 54-221-4712771; or e-mail, dobrynaz@odin.ciop.unlp.edu.ar.

REFERENCES

1. L. M. Soroko, "Axicons and meso-optical imaging devices," in *Progress in Optics*, E. Wolf, ed. (Elsevier, New York, 1989), Vol. 27, pp. 109–160.
2. W. T. Welford, "Use of annular apertures to increase focal depth," J. Opt. Soc. Am. **50**, 749–753 (1960).
3. J. T. McCrickerd, "Coherent processing and depth of focus of annular aperture imagery," Appl. Opt. **10**, 2226–2230 (1971).
4. M. Mino and Y. Okano, "Improvement in the OTF of a defocused optical system through the use of shaded apertures," Appl. Opt. **10**, 2219–2225 (1971).
5. M. J. Yzuel and F. Calvo, "A study of the possibility of image optimization by apodization filters in optical systems of residual aberrations," Opt. Acta **26**, 1397–1406 (1979).
6. J. Ojeda-Castañeda, P. Andrés and A. Díaz, "Annular apodizers for low sensitivity to defocus and to spherical aberration," Opt. Lett. **11**, 487–489 (1986).
7. J. Ojeda-Castañeda, E. Tepichin, and A. Pons, "Apodization of annular apertures: Strehl ratio," Appl. Opt. **27**, 5140–5145 (1988).
8. J. Ojeda-Castañeda and L. R. Berriel-Valdós, "Zone-plate for arbitrarily high focal depth," Appl. Opt. **29**, 994–997 (1990).
9. G. Häusler, "A method to increase the depth of focus by two steps image processing," Opt. Commun. **6**, 38–42 (1972).
10. N. Davidson, A. A. Friesem, and E. Hasman, "Holographic axilens: high resolution and long focal depth," Opt. Lett. **16**, 523–525 (1991).
11. J. Sochacki, S. Bará, Z. Jaroszewicz, and A. Kołodziejczyck, "Phase retardation of uniform-intensity axilens," Opt. Lett. **17**, 7–9 (1992).
12. M. Born and E. Wolf, *Principles of Optics* (Pergamon, New York, 1989), pp. 460–464.
13. P. M. Duffieux, *L'intégrale de Fourier et ses Applications à l'Optique* (Imprimeries Oberthur, Rennes, France, 1946).
14. Lord Raleigh, "Investigations in optics with special reference to the spectroscopy," Philos. Mag. **8**, 261 (1879).
15. A. Maréchal, Ph.D. thesis (University of Paris, Paris, 1948).
16. H. H. Hopkins, "The aberration permissible in optical systems," Proc. Phys. Soc. London Sect. B **70**, 449–470 (1957).
17. H. H. Hopkins, "The use of diffraction-based criteria of image quality in automatic optical design," Opt. Acta **13**, 343–369 (1966).
18. M. J. Bastiaans, "The Wigner distribution function applied to optical signal and systems," Opt. Commun. **25**, 26–30 (1978).
19. M. J. Bastiaans, "The Wigner distribution function and Hamilton characteristics of a geometric-optical system," Opt. Commun. **30**, 321–326 (1979).
20. A. Papoulis, "Ambiguity function in Fourier optics," J. Opt. Soc. Am. **64**, 779–788 (1974).
21. K. H. Brenner, A. W. Lohmann, and J. Ojeda-Castañeda, "The ambiguity function as a polar display of the OTF," Opt. Commun. **44**, 323–326 (1983).
22. H. Bartelt, J. Ojeda-Castañeda, and E. E. Sicre, "Misfocus tolerance seen by simple inspection of the ambiguity function," Appl. Opt. **23**, 2693–2696 (1984).
23. J. Ojeda-Castañeda, P. Andrés, and E. Montes, "Phase-space representation of the Strehl ratio: ambiguity function," J. Opt. Soc. Am. A **4**, 313–317 (1987).
24. E. R. Dowsky, Jr., and W. Thomas Cathey, "Extended depth of field through wave-front coding," Appl. Opt. **34**, 1859–1866 (1995).
25. D. Zalvidea, M. Lehman, S. Granieri, and E. E. Sicre, "Analysis of the Strehl ratio using the Wigner distribution function," Opt. Commun. **118**, 207–214 (1995).
26. G. Saavedra, W. D. Furlan, E. Silvestre, and E. E. Sicre, "Analysis of the irradiance along different paths in the image space using the Wigner distribution function," Opt. Commun. **139**, 11–16 (1997).
27. D. Zalvidea and E. E. Sicre, "Phase pupil functions for focal depth enhancement derived from a Wigner distribution function," Appl. Opt. **37**, 3623–3627 (1998).
28. Z. Jaroszewicz and J. Morales, "Lens axicons: systems composed of a diverging aberrated lens and a perfect converging lens," J. Opt. Soc. Am. A **15**, 2383–2390 (1998).

Optik 114, No. 5 (2003) 207–212
© 2003 Urban & Fischer Verlag
http://www.urbanfischer.de/journals/optik

Optik Optics
International Journal for Light and Electron Optics

The parity function in optical waves propagation

Beatriz Ruiz[1], Héctor Rabal[1], Sergio Granieri[2]

[1] Centro de Investigaciones Opticas (CONICET-CIC) P.O. Box 124, 1900 La Plata, Argentina
[2] Deparment of Physics and Applied Optics, Rose-Hulman Institute of Technology, 5500 Wabash Ave., Terre Haute, IN 47803, USA

Abstract. We propose a generalization of the concept of parity as a continuous function and show that it is conserved in optical waves free propagation. Some properties are commented and an experimental implementation to optically generate a representation is suggested.

Key words: Wave propagation – convolution – parity

1. Introduction

Invariant quantities are important powerful tools in many fields of science because they permit to obtain information about the evolution and behavior of systems. As an example, in physics, is well known the utility of momentum, mass, energy, charge, etc., conservation laws. In general, a conservation law is a statement that establishes that a physical magnitude is unchanged (conserved) in an interaction occurring within a closed system. Parity (from Latin *paritas*: equal or equivalent) is a concept appearing in several sciences and even in several branches of physics with related meanings. In mathematics, it designs the property shared by numbers or functions that are both either even or odd. In computer technology the name indicates whether the number of binary ones in a word is odd or even and is usually used for errors detection. In Quantum Mechanics it is the property of a wave function that describes the behavior of a system whose physical coordinates are related by inversion about a center. If parity is even, the wave function is unchanged and if it is odd, the wave function is changed only in sign. Other examples can be found in crystallography, etc. As can be seen, the concept of parity usually assigns a discrete value 1 or −1 to the magnitude it acts upon.

In the usual mathematics definition of parity there is no intermediate state between an even function and an odd function or a function not exhibiting any obvious parity property. Following a similar scope as that that lead Zernike to propose the concept of *degree of coherence*, it would be very convenient if a continuous magnitude related to the concept of parity could be available. Even more if this magnitude could be measured and predicted under current optical situations. Besides, it is an intuitive idea (that can also be demonstrated) that this concept of parity should be conserved by free propagation. If a continuous generalization of the parity can be implemented its conservation could also be expected.

The aim of this paper is to define a more general concept related to parity, named the parity function, applied to optical fields and to demonstrate its conservation under wave field propagation. In section 2, we define the parity function, some properties are established in section 3, and some examples are shown. In section 4 we present an optical setup to obtain the parity function of an optical field.

2. Definition of the parity function

Let us consider a complex scalar field described by a bounded function $f(x)$, where x is the spatial coordinate. For simplicity we are going to consider the spatial dependence to be one-dimensional. The function can be split in its even and odd parts with respect to the coordinate origin as

$$f(x) = f_P(x) + f_I(x), \tag{1}$$

where the even and odd parts are given by

$$f_P(x) = \frac{f(x) + f(-x)}{2}, \tag{2}$$

$$f_I(x) = \frac{f(x) - f(-x)}{2}. \tag{3}$$

The point about which the even and odd parts are defined can be generalized.

Even and odd parts with respect to any arbitrary point x_0 can be written as

$$f_P(x; x_0) = \frac{f(x_0 + x) + f(x_0 - x)}{2}, \tag{4}$$

$$f_I(x; x_0) = \frac{f(x_0 + x) - f(x_0 - x)}{2}. \tag{5}$$

Received 25 March 2003; accepted 15 May 2003.

Correspondence to: H. J. Rabal
Fax: ++54 221 4712771
E-mail: hrabal@volta.ing.unlp.edu.ar

0030-4026/03/114/05-207 $ 15.00/0

The parity (P) of the field $f(x)$ in the point x_0 is defined as

$$P\{f\}(x_0) = \frac{\int |f_P(x;x_0)|^2 \, dx}{\int |f(x)|^2 \, dx}, \tag{6}$$

where the integration interval is the support of $f(x)$ and $0 < \int |f(x)|^2 \, dx < \infty$.

Notice that the denominator is a constant value. So the parity in x_0 is determined by the fraction of total energy contained in the even part of the function.

Eq. (6) can be written, by using eq. (4) and the convolution operator [1], indicated as $\otimes$,

$$P\{f\}(x_0) = \frac{1}{2}\left\{1 + \frac{(f \otimes f^*)(2x_0)}{\int |f(x)|^2 \, dx}\right\}, \tag{7}$$

where * indicates complex conjugation.

After eq. (7), but also from its definition, it can be seen that if $f(x)$ has compact support, then the parity consists of a constant additive term $\frac{1}{2}$ plus a bounded function with compact support. As most pupil functions in optics have compact support, the parity of a plane wave after incidence upon that pupil inherits this property. The parity is then a function generally smoother than (or, eventually as smooth as) the pupil function itself.

For eventual cases in which one (or both) of the integrals in (7) is divergent, the parity is defined

$$P\{f\}(x_0) = \frac{1}{2}\left\{1 + \lim_{A\to\infty} \frac{\int_{-A}^{A} f(x_0+x) f^*(x_0-x) \, dx}{\int_{-A}^{A} |f(x)|^2 \, dx}\right\}, \tag{8}$$

with $\int |f(x)|^2 \, dx \neq 0$.

If both integrals in eq. (8) converge, then eq. (8) and eq. (7) coincide.

Examples

From eq. (7) the following parity functions are obtained

i) $f(x) = \begin{cases} (x+i), & |x| < 1 \\ 0, & |x| > 1 \end{cases}$,

$$P\{f\}(x_0) = \begin{cases} \frac{1}{4}(3 - |x_0|^3), & |x_0| < 1 \\ \frac{1}{2}, & |x_0| > 1 \end{cases}.$$

ii) $f(x) = \begin{cases} \sin^2 x, & |x| < \pi \\ 0, & |x| > \pi \end{cases}$,

$$P\{f\}(x_0) = \frac{1}{2}\begin{cases} 1 + \frac{1}{3\pi}\left[(\pi - |x_0|)(2 + \cos 4x_0) + \frac{3}{4}|\sin 4x_0|\right], & |x_0| < \pi \\ 1, & |x_0| > \pi \end{cases}.$$

iii) If $a = a_1 + ia_2$, $a_1 > 0$,

$$P\{\exp(-ax^2)\}(x_0) = \frac{1}{2}\left(1 + \exp\left(-2\frac{|a|^2}{a_1} x_0^2\right)\right).$$

From eq. (8) the following parity functions are obtained

iv) If $n = 0, 1, 2, \ldots$, $P\{x^n\}(x_0) = \begin{cases} 1, & n \text{ even} \\ 0, & n \text{ odd} \end{cases}$.

v) If $\operatorname{Re} a \neq 0$, $P\{\exp ax\}(x_0) = \frac{1}{2}$.

vi) $P\{\sin x\}(x_0) = \sin^2 x_0$.

vii) $P\{\cos x\}(x_0) = \cos^2(x_0)$.

3. Properties of the parity function

Property 1. The parity function does not change under complex conjugation, as can be seen from eq. (6),

$$P\{f^*\}(x_0) = P\{f\}(x_0). \tag{9}$$

Property 2. The parity function does not change under multiplication of the function f by a complex constant, as can be seen from eq. (6). It is, if $c \in C$,

$$P\{f\}(x_0) = P\{cf\}(x_0), \tag{10}$$

(and then, under general arbitrary phase changes $\exp[i\varphi]$ with φ a constant).

Property 3. If the imparity function I, of the scalar field f in a point x_0 is defined as

$$I\{f\}(x_0) = \frac{\int |f_I(x,x_0)|^2 \, dx}{\int |f(x)|^2 \, dx}, \tag{11}$$

then it is verified that (see Appendix)

$$P\{f\}(x_0) + I\{f\}(x_0) = 1. \tag{12}$$

Property 4. As a consequence of eq. (12), the parity is bounded to the [0,1] interval, it is $P\{f\}(x_0) \leq 1$.

Property 5. If $f(x)$ is even or odd with respect to $x = 0$, then $P\{f\}(x_0)$ is even with respect to 0, as can be seen from eqs. (4) and (6).

Property 6. If $f(x)$ is even with respect to 0, then $P\{f\}(0) = 1$. If $f(x)$ is odd with respect to 0, then $P\{f\}(0) = 0$. So, if an even function has constant parity then its parity is 1, and if an odd function has constant parity then its parity is 0 (see Appendix).

Property 7. For all $a \in \boldsymbol{R}$,

$$P\{f(ax)\}(x_0) = P\{f(x)\}(ax_0), \tag{13}$$

(see Appendix).

Property 8. If f is such that $\int |f|^2 \, dx < \infty$, then $P\{P\{f\}\}(z_0) = 1$. If $\int |f|^2 \, dx = \infty$, in general it is $P\{P\{f\}\}(z_0) \neq 1$, as the case, $P\{\sin x\}(x_0) = \sin^2 x_0$ and $P\{\sin^2 x_0\}(z_0) = \frac{1}{6}(5 + \cos 4z_0))$, shows (see Appendix).

Property 9. If we assume f with $\int |f|^2 \, dx > 0$, then if $P\{f\}(x_0) = \text{constant}$, f has not bounded support (see Appendix).

Examples

viii) From example v), with $\text{Re}\, a \neq 0$, and eq. (12), it verifies $P\{f\} = I\{f\}$.

ix) From examples vi) and vii), and eq. (12) it can be deduced that $P\{\sin x\} = I\{\cos x\}$.

4. Conservation of the parity

Let us consider the free propagation of scalar fields $f(x)$ with $\int |f|^2 \, dx = 1$, along the (mean) direction of the coordinate axis z, and the p-index Fourier Transform of f [2]

$$\Im_p\{f\}(x) = \sqrt{\frac{p}{2\pi}} \int_{-\infty}^{\infty} f(\xi) \exp(-ip\xi x) \, d\xi = F_p(x). \tag{14}$$

Theorem

The necessary and sufficient condition for f and g to have the same parity is

$$F_p(x) \, F_p^*(-x) = G_p(x) \, G_p^*(-x), \tag{15}$$

assuming that the Fourier Transform of f and g exist.

From eq. (7) it follows that the necessary and sufficient condition for f and g to have the same parity is $f \otimes f^* = g \otimes g^*$. Then, by applying the Fourier Transform, eq. (15) is obtained.

Corollary 1 (Conservation of the parity)

If the function g is the function describing the field f after propagation a distance z, then

$$P\{g\}(x_0) = P\{f\}(x_0). \tag{16}$$

By using the fact that $G_p(x)$ is related to $F_p(x)$ by [3]

$$G_p(x) = \begin{cases} \exp\left(ikz\sqrt{1-\left(\frac{px}{k}\right)^2}\right) F_p(x), & \left|\frac{px}{k}\right| < 1 \\ 0, & \left|\frac{px}{k}\right| > 1 \end{cases}, \tag{17}$$

then eq. (15) is verified. It is the functions g and f have the same parity.

Physically, the conservation of the parity function is a consequence of the conservation of energy and indicates that the energy in the even and odd parts of the function is independently conserved after free propagation. Interference between these parts contains no energy.

An example is the plane wave, showing $P = 1$ for every point x_0. This value is trivially conserved with propagation. Other non-diffracting beams are also trivial examples of the parity conservation as, by definition the fields themselves are conserved.

Corollary 2

Assuming both f and g are odd or both are even, the necessary and sufficient condition for f and g to have the same parity is

$$|F_p(x)| = |G_p(x)|.$$

This follows from eq. (15).

Notice that if f is real, (imaginary), by knowing its parity we can get f from

$$\Im_p\{(2P\{f\} - 1)(x_0)\}(2x) = \tfrac{1}{2} F_p(x) \, F_p^*(-x),$$

because the second term is $\frac{1}{2} F_p^2(x)$, $(-\frac{1}{2} F_p^2(x))$.

These definitions and results can be easily generalized to bi-dimensional fields.

5. Optical generation of the parity function

The first step to obtain the parity function of an optical field is the making of a Vander Lugt filter matched to it. It can be done by means of a holographic register or by using a spatial light modulator. Figure 1a shows the set up of a typical Vander Lugt filter [3–5].

If we want the representation of the parity of a function $f(x_0, y_0)$, then the Fourier Transform of the field $f(x_0, y_0)$ is made to form on a holographic plate H, where a coherent reference plane wave is also present, and is given by

$$R(x_1, y_1) = R_0 \exp(-2\pi i y_1 \alpha), \tag{18}$$

with $\alpha = \frac{\sin\theta}{\lambda}$, θ the angle formed by the reference beam with the optical axis and λ the wavelength of the employed light. The transmittance of the filter H, after development with the usual linearity conditions, can be expressed as

$$I(x_1, y_1) = \left| \frac{1}{\lambda d} F(x_1/\lambda d, y_1/\lambda d) + R_0 \exp(-2\pi i y_1 \alpha) \right|^2, \tag{19}$$

where $F(x_1/\lambda d, y_1/\lambda d)$ is the Fourier Transform of the field $f(x_0, y_0)$ performed by the lens L with focal distance d, and where the proportionality constant due to the development process has been omitted for simplicity. Developing the square of the modulus in eq. (19)

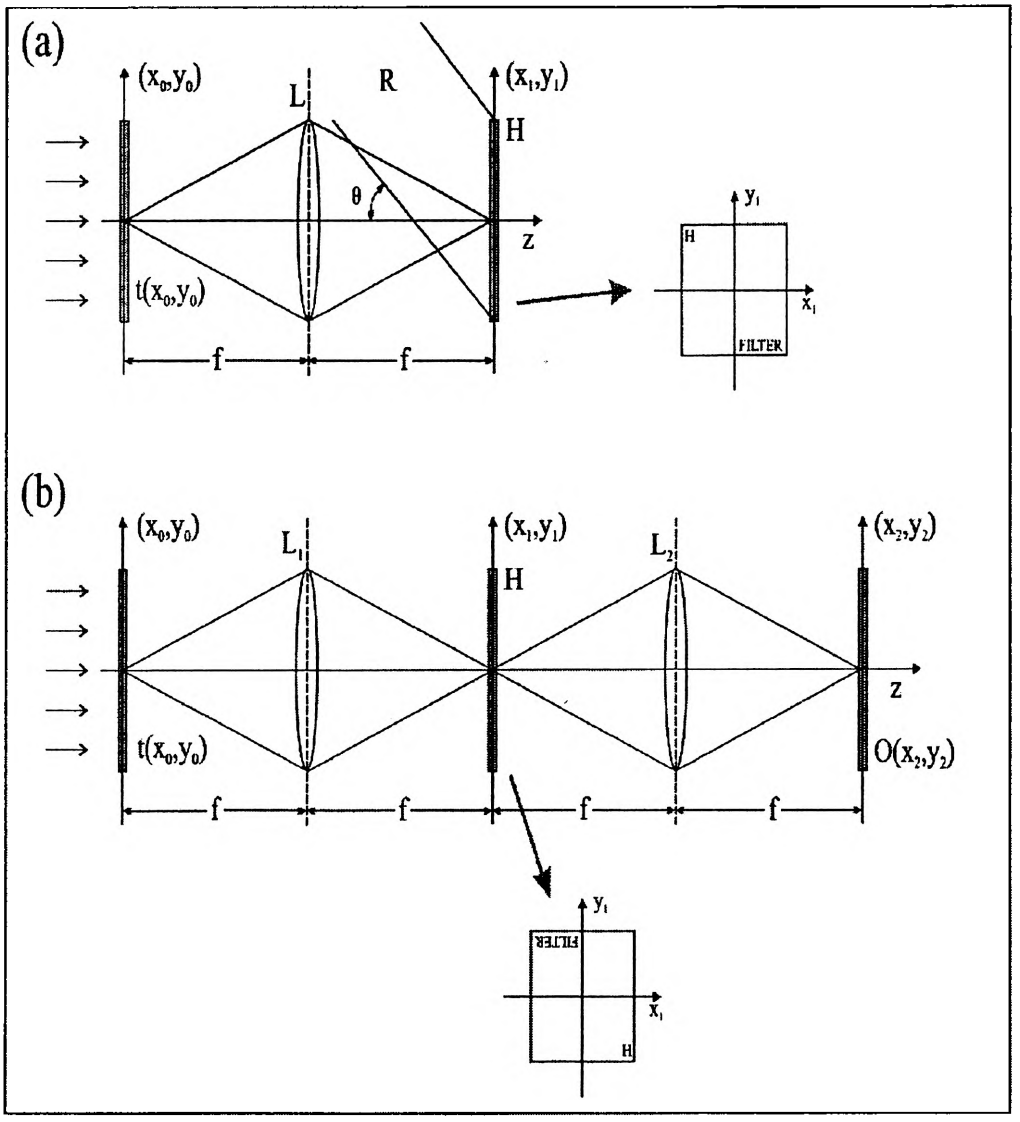


Fig. 1. a) The set-up for the filter construction; b) the generation of the parity function using the matched filter.

we obtain for the filter transmittance,

$$T(x_1, y_1) = R_0^2 + \frac{1}{(\lambda d)^2} |F(x_1/\lambda d, y_1/\lambda d)|^2 + \frac{R_0}{\lambda d} F(x_1/\lambda d, y_1/\lambda d) \exp(2\pi i y_1 \alpha) + \frac{R_0}{\lambda d} F^*(x_1/\lambda d, y_1/\lambda d) \exp(-2\pi i y_1 \alpha). \quad (20)$$

The second step for obtaining an optical version of the parity function is shown in fig. 1b. The filter H is located in the Fourier plane of a 4-d optical processor after an 180° rotation with respect to the coordinates origin. In this way the transmittance function of the filter can be described as

$$T'(x_1, y_1) = T(-x_1/\lambda f, -y_1/\lambda f). \quad (21)$$

If the incoming field to the processor is $f(x_0, y_0)$, then the field immediately behind the filter H due to the first lens L_1, is

$$\frac{1}{\lambda d} F(x_1/\lambda d, y_1/\lambda d)\, T'(x_1, y_1). \quad (22)$$

The second lens L_2 performs the optical Fourier transform of the field represented by the last expression and multiplies by a $1/\lambda d$ factor, so that the field in the output plane of the processor can be expressed as

$$O(x_2, y_2) = R_0^2 f(-x_2, -y_2) + \frac{1}{(\lambda d)^2} f(x_2, y_2) \otimes f^*(-x_2, -y_2) \otimes f(-x_2, -y_2) + \frac{R_0}{\lambda d} f(-x_2, -y_2) \otimes f(x_2, y_2) \otimes \delta(x_2, y_2 + \alpha \lambda d) + \frac{R_0}{\lambda d} f(-x_2, -y_2) \otimes f^*(-x_2, -y_2) \otimes \delta(x_2, y_2 - \alpha \lambda d). \quad (23)$$

The last term in eq. (23) represents, but for a bias term and a multiplicative constant, the parity function of the field $f(x_0, y_0)$ in an inverted coordinates system. Then, if α, the reference wave carrier frequency was chosen high enough so that the last term does not spatially overlap with the others, an optical representation of the parity can be obtained.

6. Conclusions

We have defined and proposed the use of the parity function. We have shown several mathematical properties and its conservation under free propagation in optical fields.

When propagation is not free, i.e. when light interacts with pupils, the value of the parity function is not conserved. There is not a simple expression relating the parity of pupils and the parity of the fields before and after interacting with them.

An optical setup to optically generate a representation using a modified version of the classical Vander Lugt filter was also proposed. The concept can be applied as a tool for help in inverse problems.

Also, by taking as hint the use of parity in computation technology, the variation in the parity function where its conservation is expected can be used as a tool for inducing the presence of alterations in the assumed conditions.

The parity function is only one of a set of magnitudes that can be defined in connection with propagation. A closely connected one, which is the hermiticity function, is under development and will be published elsewhere.

Acknowledgements. This work was partially supported by a CONICET grant PID No. 3974/92 and by Faculty of Engineering, Universidad Nacional de la Plata, Argentina.

Appendix

Property 3

The left hand term in eq. (12) can be written (by using eqs. (6) and (11)) as

$$\frac{\int |f_P(x;x_0)|^2\,dx + \int |f_I(x;x_0)|^2\,dx}{\int |f(x)|^2\,dx}. \tag{A1}$$

By using eqs. (4) and (5), and taking into account that

$$\int f_P(x;x_0)\, f_I^*(x;x_0)\,dx = 0, \tag{A2}$$

due to the orthogonality between functions $f_P(x;x_0)$ and $f_I^*(x;x_0)$, eq. (A1) equals unity.

Property 6

From definition of convolution is

$$(f \otimes f^*)(0) = \int f(x)\, f^*(-x)\,dx = \begin{cases} \int |f(x)|^2\,dx, & f \text{ even} \\ -\int |f(x)|^2\,dx, & f \text{ odd} \end{cases}.$$

From eq. (7) it results

$$P\{f\}(0) = \begin{cases} 1, & f \text{ even} \\ 0, & f \text{ odd} \end{cases}. \tag{A3}$$

Property 7

From

$$\int_{-A}^{A} |f(ax)|^2\,dx = \frac{1}{|a|} \int_{-aA}^{aA} |f(x)|^2\,dx, \tag{A4}$$

and

$$(f(ax) \otimes f^*(ax))(2x_0) = \int f(ax)\, f^*(a(2x_0 - x))\,dx = \frac{1}{|a|} \int f(\xi) f^*(2ax_0 - \xi)\,d\xi,$$

with $\xi = ax$, eq. (13) results.

Property 8

From eq. (6)

$$P\{f\}(x_0) = \frac{1}{2}\left\{1 + \frac{(f \otimes f^*)(2x_0)}{\int |f(x)|^2\,dx}\right\},$$

if we call

$$h(x_0) = \frac{(f \otimes f^*)(2x_0)}{\int |f(x)|^2\,dx},$$

then

$$P\{P\{f\}\}(z_0) = \frac{1}{2}\left\{1 + \frac{[1 + h(x_0)] \otimes [1 + h(x_0)]\,(2z_0)}{\int [1 + h(x_0)]^2\,dx_0}\right\}. \tag{A5}$$

The fact that $\int |f(x)|^2\,dx < \infty$, implies $\lim h(x_0)_{x_0 \to \pm\infty} = 0$, and then $\int h(x_0)\,dx_0$, $\int h^2(x_0)\,dx_0 < \infty$. By using the definition in eq. (6), it is obtained

$$\lim_{A \to \infty} \frac{2A + \int_{-A}^{A} [2h(\xi) + h(\xi)\, h(2z_0 - \xi)]\,d\xi}{2A + \int_{-A}^{A} [h^2(\xi) + 2h(\xi)]\,d\xi} = 1. \tag{A6}$$

Property 9

If we assume that the support of f is bounded, then $0 < \int |f|^2\,dx < \infty$, and there exist at least x, y such that $(f(x) \otimes f^*(x))(x) = 0$, and $(f(x) \otimes f^*(x))\,(y) \neq 0$, then $P\{f\}$ is not constant.

References

[1] Bracewell R: The Fourier Transform and its applications. McGraw-Hill, New York 1978
[2] Ruiz B, Rabal H: Differential operators, the Fourier Transform and its applications to optics. Optik **103** (1996) 171
[3] Goodman JW: *Introduction to Fourier Optics.* McGraw-Hill, New York 1968
[4] Vander Lugt AB: *Radar Lab. Rept.* No. 4594-22-T, Institute of Science and technology, The University of Michigan, Ann Arbor 1963
[5] Vander Lugt A: Signal detection by complex filtering. IEEE Trans. Inf. Theory **IT-10** (1964) 139–145

Available online at www.sciencedirect.com
SCIENCE DIRECT
Physica A 364 (2006) 79–86
PHYSICA A
www.elsevier.com/locate/physa

Characterization of laser propagation through turbulent media by quantifiers based on the wavelet transform: Dynamic study

L. Zunino[a,*], D.G. Pérez[b], M. Garavaglia[a,c], Osvaldo A. Rosso[d]

[a]*Centro de Investigaciones Ópticas (CIOp), CC. 124 Correo Central, 1900 La Plata, Argentina*
[b]*Instituto de Física, Pontificia Universidad Católica de Valparaíso (PUCV), 23-40025 Valparaíso, Chile*
[c]*Departamento de Física, Facultad de Ciencias Exactas, Universidad Nacional de La Plata (UNLP), 1900 La Plata, Argentina*
[d]*Instituto de Cálculo, Facultad de Ciencias Exactas y Naturales, Universidad de Buenos Aires (UBA), Pabellón II, Ciudad Universitaria, 1428 Ciudad de Buenos Aires, Argentina*

Received 10 January 2005; received in revised form 8 August 2005
Available online 19 October 2005

Abstract

We analyze, within the wavelet theory framework, the wandering over a screen of the centroid of a laser beam after it has propagated through a time-changing laboratory-generated turbulence. Following a previous work (Fractals 12 (2004) 223) two quantifiers are used, the Hurst parameter, H, and the normalized total wavelet entropy. The temporal evolution of both quantifiers, obtained from the laser spot data stream, is studied and compared. This allows us to extract information on the stochastic process associated with the turbulence dynamics.
© 2005 Elsevier B.V. All rights reserved.

Keywords: Lightwave propagation; Turbulence; Hurst parameter; Normalized total wavelet entropy

1. Introduction

The purpose of this work is to statistically describe laser beam propagation through time-changing laboratory-generated turbulence. To do so, we analyze data stream corresponding to the centroid position of the laser spot by using two different quantifiers obtained from the wavelet theory: the *Hurst parameter*, H, and the *normalized total wavelet entropy* (NTWS). The former quantifier results from modeling the centroid's coordinates as a *fractional Brownian motion* (fBm) at stationary turbulence strength [1], while the latter has been used for a wider set of stochastic processes—see Ref. [2].

The fBm was discovered by Kolmogorov [3] and defined by Mandelbrot and Van Ness [4] as the only family of processes which are Gaussian, self-similar, and with stationary increments. The normalized family of these gaussian processes, B^H, is the one with $B^H(0) = 0$ almost surely, $\mathbb{E}[B^H(t)] = 0$, and covariance

$$\mathbb{E}[B^H(t)B^H(s)] = \tfrac{1}{2}(|t|^{2H} + |s|^{2H} - |t-s|^{2H}), \tag{1}$$

*Corresponding author.
E-mail addresses: lucianoz@ciop.unlp.edu.ar (L. Zunino), dario.perez@ucv.cl (D.G. Pérez), garavagliam@ciop.unlp.edu.ar (M. Garavaglia), oarosso@fibertel.com.ar (O.A. Rosso).

0378-4371/$ - see front matter © 2005 Elsevier B.V. All rights reserved.
doi:10.1016/j.physa.2005.09.054

for $s, t \in \mathbb{R}$. The power exponent H is also known as the scaling exponent and its range is bounded between 0 and 1. The estimation of this parameter plays a key role modeling an fBm time series. One remarkable property of this family B^H is that the H parameter regulates the presence or absence of memory. In fact, it can be separated into three subfamilies accordingly: long-memory for $\frac{1}{2}<H<1$, memoryless at $H=\frac{1}{2}$ (ordinary Brownian motion), and short-memory in the case $0<H<\frac{1}{2}$. Likewise, the Hurst parameter can be condensed to be the probability of the next increment of the signal having the same sign as the previous increment. Thus, it tunes the trajectory regularity. Fractional Brownian motions are continuous but non-differentiable processes (in the usual sense), and only give generalized spectra $1/f^{\alpha}$ with exponents α between 1 and 3. As a nonstationary process, the fBm does not have a spectrum defined in the usual sense; however, it is possible to define a power spectrum of the form [5]:

$$S_{B^H}(f) = \frac{1}{|f|^{2H+1}}. \tag{2}$$

Remember that this equation is not a valid power spectrum in the theory of stationary processes since it is a non-integrable function in the classical sense.

Several properties evidence that wavelet analysis is well-suited to fBm:

(1) fBm is nonstationary but the wavelet coefficients form a stationary process at each scale [6,7].
(2) fBm exhibits a positive long-range correlation in the range $\frac{1}{2}<H<1$ but wavelet coefficients have a correlation which is highly small as soon as $N>H+\frac{1}{2}$, where N is the number of vanishing moments associated with the mother wavelet $\psi(t)$ [7,8].
(3) The self-similarity of fBm is reproduced in its wavelet coefficients, whose variance varies as a power law as a function of scale j [6,7]

$$\log_2\{\mathbb{E}[C_j^2(k)|_{B^H}]\} \propto -(2H+1)j. \tag{3}$$

These features are due to the fact that the wavelet family $\psi_{a,b}$ is generated by dilations and translations of a unique admissible mother wavelet $\psi(t)$. So, the family itself exhibits scale invariance. It should be noted that the first two properties are valid for any process with stationary increments [9].

In particular these properties are widely used for estimating H or the related spectral exponent $\alpha = 2H+1$ [5,10,11]. Through the *Logscale Diagram* the threefold objective: detection, identification and measurements of the scaling exponent can be achieved [12]. Basically the estimation problem turns into a linear regression slope estimation.

In order to model the time-changing turbulence situation we consider a generalization where the parameter H is no longer constant, but is a continuous function of the time t ($H \to H(t)$). This generalization was introduced in financial research to model the behavior of stock market index time series [13–15]. Also, it was recently used to characterize dynamic speckle or biospeckle [16]. A single scaling exponent would be unable to show the complex dynamics inherent to the data. The constraint of stationary increments is relaxed in this case. *Multifractional Brownian motion* (mBm) [17] was formalized as a class of processes which satisfies these properties.

We calculate the time-dependent Hurst exponent by using the wavelet properties. Provided that variations of H are smooth enough, the signal is divided into i non-overlapping temporal windows and the scaling exponent is calculated for each subset according to the procedure described in Ref. [1]. A sequence of Hurst parameter values is obtained. They give the local scaling exponent around a given instant of time. Artificially mBm were analyzed in order to test the quality of our estimator. In Fig. 1 one can compare the theoretical and experimental results for an mBm with H changing linearly from 0.1 to 0.9 with t. The Matlab code introduced by Coeurjolly [18] was implemented to simulate the mBm. The signal was divided into 64 temporal windows of 512 data points. We used the orthogonal cubic spline functions as the mother wavelet and the resolution levels from $j=-9$ to $j=-1$.

At the same time, the NTWS is also applied to study this time-changing turbulence. Introduced as a measure of the degree of order–disorder of the signal [2], it provides information about the underlying

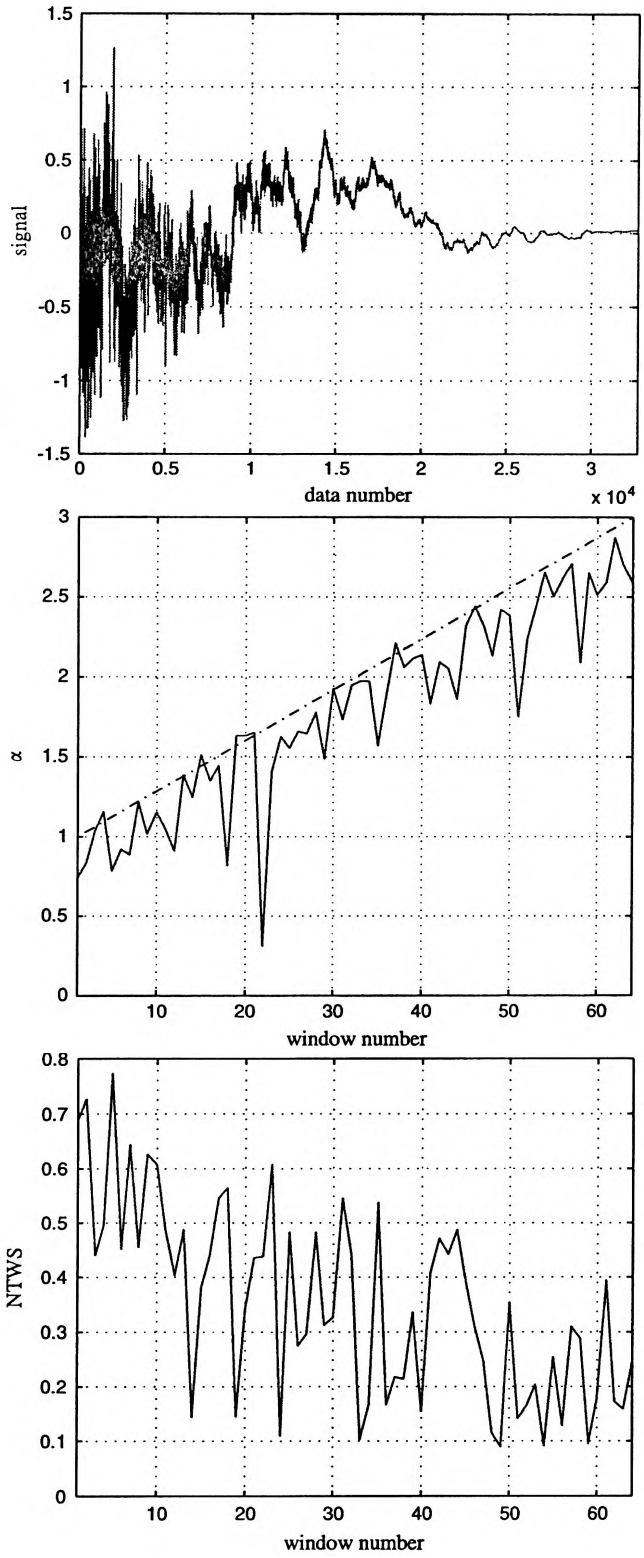


Fig. 1. Top: synthetically generated mBm signal with H changing linearly from 0.1 to 0.9 with t. Middle: theoretical (dashed curve) and measured (continuous curve) Hurst parameter for this simulated mBm. Bottom: measured NTWS.

dynamical process associated with the signal. We define the NTWS as

$$S_{\mathrm{WT}} = -\sum_{j=-N}^{-1} p_j \cdot \ln p_j / S^{\max}, \tag{4}$$

where

$$S^{\max} = \ln N \tag{5}$$

with N the base 2 logarithm of the number of data points and $\{p_j\}$ represent the *relative wavelet energy* (RWE). These are defined as

$$p_j = \mathscr{E}_j / \mathscr{E}_{tot}, \tag{6}$$

with $\mathscr{E}_j = \mathbb{E}[C_j^2(k)]$ being the energy at each resolution level $j = -N, \ldots, -2, -1$ and $\mathscr{E}_{tot} = \sum_{j<0} \mathscr{E}_j$. They yield, at different scales, the probability distribution for the energy. It should be remarked that an orthogonal mother wavelet must be used within this theory—further details can be found in Ref. [1]. Indeed, a very ordered process can be represented by a signal with a narrow band spectrum. A wavelet representation of such a signal will be resolved in a few wavelet resolution levels, i.e., all RWE will be (almost) zero except at the wavelet resolution levels which include the representative signal frequency. For these special levels the RWE will be almost equal to one. As a consequence, the NTWS will acquire a very small, disappearing value. A signal generated by a totally random process or chaotic one can be taken as representative of a very disordered behavior. This kind of signal will have a wavelet representation with significant contributions from all frequency bands. Moreover, one could expect that all contributions will be of the same order. Consequently, the RWE will almost be equal at all resolution levels, and the NTWS will acquire its maximum possible value. Higher values for wavelet entropy means higher dynamical complexity, higher irregular behavior and, of course, lower predictability.

The time evolution of NTWS can be easily implemented. So, it is widely used to study a wide set of nonstationary natural signals. In particular, it was introduced to quantify the degree of disorder in the electroencephalographic epileptic records giving information about the underlying dynamical process in the brain [19], more specifically of the synchrony of the group cells involved in the different neural responses. Also, monthly time series of different solar activity indices (sunspot numbers, sunspot areas and flare index) were analyzed [20,21]. The disorder content of solar cycle activity can be derived by analyzing the wavelet entropy time evolution. Likewise, the dynamic speckle phenomenon mentioned above has also been analyzed by using these wavelet-based entropy concepts [22]. In a recent paper the relation existing between these two quantifiers—H and NTWS—when they are used for analyzing fBm was investigated [23]. Fig. 1 (top and bottom) shows the mBm and its corresponding NTWS, where the same temporal windows, mother wavelet and resolution levels were used.

2. Experimental setup and data acquisition

The experimental measures were performed in a laboratory by producing thermal convective turbulence with two electrical heaters in a row. Three different turbulence intensities were generated by changing the amount of heat dissipated for each electrical heater: normal, soft and hard turbulence. Along the laser path three electronic thermometers sense the air temperature—$T1$, $T2$ and $T3$; see Fig. 2 (bottom). A time series corresponding to the fluctuations of the centroid position of a laser beam's spot (wandering) over a screen, after propagation through this time-changing laboratory-generated turbulence, were recorded with a position-sensitive detector located as a screen at the end of the path. This record consists of 2,500,000 spot beam centroid coordinates' measurements with 500,000 data for each laboratory-generated turbulence condition. Further details of the experiment can be found in Ref. [1]. The temperature and signal records can be observed in Fig. 2. There, it can be observed that the turbulence is increased, and subsequently decreased to recover the initial situation.

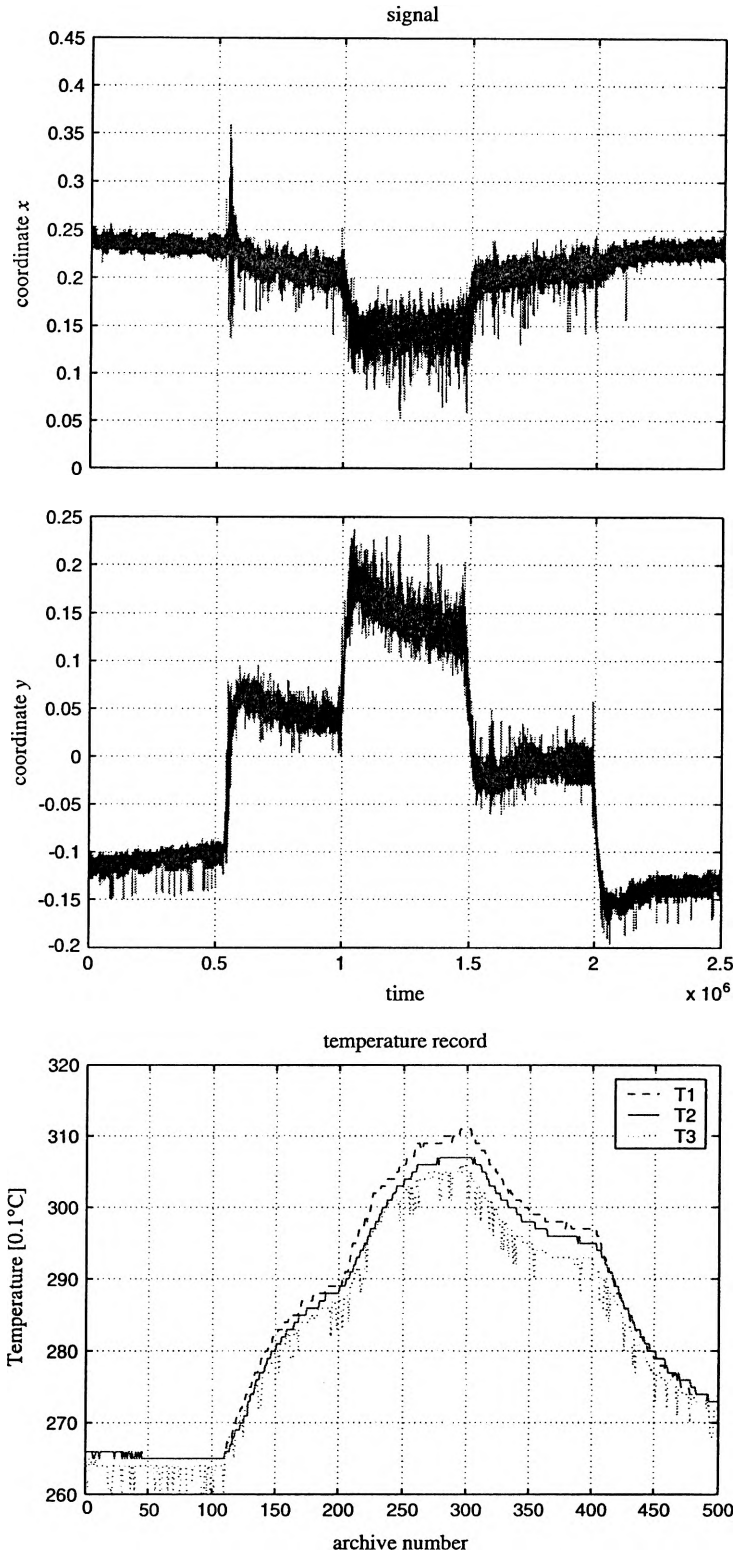


Fig. 2. Experimental records for the x (top) and y (middle) coordinates and the associated temperature record (bottom).

3. Results and conclusions

In the present work, we employ orthogonal cubic spline functions as mother wavelets. Among several alternatives, cubic spline functions are symmetric and combine smoothness in a suitable proportion with numerical advantages. They have become a recommendable tool for representing natural signals [24,25]. The signal was divided into 606 non-overlapping temporal windows of 4096 data points. Resolution levels between $j = -7$ and $j = -3$ were used to calculate both quantifiers. The first two levels ($j = -1$ and $j = -2$) were dropped to reduce the noise introduced by the system, while the lower levels were excluded to reduce nonstationary effects as commented in Ref. [1].

Fig. 3 shows the quantifiers' temporal evolution. Both quantifiers reveal that when the turbulence is normal the detector is not able to resolve position differences, and electronic noise associated with the detector is observed. The NTWS close to one as expected for a signal generated by a totally random process and the α value matches with a white noise. When the turbulence is increased the system changes in an abrupt way—see coordinates' graphs at Fig. 2. It is interesting to observe the transition between the different intensities of turbulence for the signal and its corresponding quantifiers. The Hurst parameter discriminates between the other two increased turbulences. It is possible, in average, to associate a value $\alpha_x = 1.17$, $\alpha_y = 1.04$ for the soft case and $\alpha_x = 1.62$, $\alpha_y = 1.51$ for the hard turbulence. It should be noted that the signal has more regularity for the strongest turbulence. The NTWS diminishes notably showing an increment in the order of the system but it is unable to distinguish between soft and hard turbulence giving values of $\mathrm{NTWS}_x = 0.63$, $\mathrm{NTWS}_y = 0.66$ for the soft turbulence and $\mathrm{NTWS}_x = 0.57$, $\mathrm{NTWS}_y = 0.63$ for the hard turbulence.

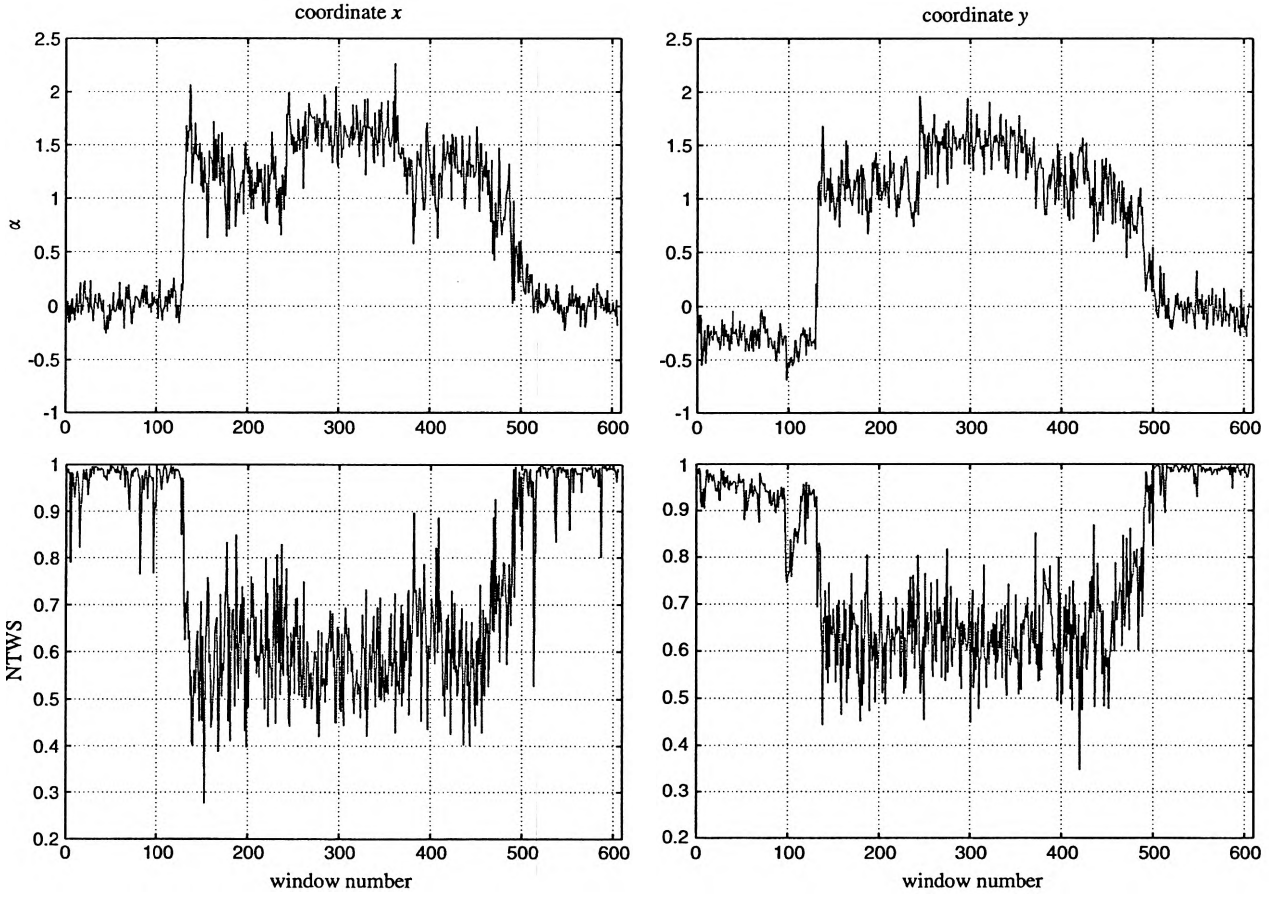


Fig. 3. Quantifiers temporal evolution: α (top) and NTWS (bottom) for the x (left) and y (right) coordinates.

It can be followed by comparing Figs. 2 and 3 that the behavior of the signal is different for both coordinates. Nevertheless, the temporal evolution of the quantifiers is very similar. It can also be observed that the system has a hysteresis effect (see Figs. 2 and 3) as was expected.

The mBm model is justified for modeling the dynamics associated with these processes. We conclude that the associated scaling exponent changes continuously with the turbulence strength. In the future a new generalization will be considered and studied: the *generalized multifractional Brownian motion* (gmBm) [26]. These processes consider that scaling exponent variations may be very erratic and not necessarily a continuous function of time. The latter condition is a strong limitation in turbulence studies where the scaling exponent can change widely from time to time.

Acknowledgements

This work was partially supported by Consejo Nacional de Investigaciones Científicas y Técnicas (CONICET, Argentina) and Pontificia Universidad Católica de Valparaíso (Project No. 123.774/2004, PUCV, Chile).

References

[1] L. Zunino, D.G. Pérez, O.A. Rosso, M. Garavaglia, Characterization of laser propagation through turbulent media by quantifiers based on the wavelet transform, Fractals 12 (2) (2004) 223–233.
[2] O.A. Rosso, S. Blanco, J. Yordanova, V. Kolev, A. Figliola, M. Schürmann, E. Başar, Wavelet entropy: a new tool for analysis of short duration brain electrical signals, J. Neurosci. Method 105 (2001) 65–75.
[3] A.N. Kolmogorov, Wienersche Spiralen und einige andere interessante Kurven im Hilbertschen Raum, The Wiener spiral and some other interesting curves in a Hilbert space, C. R. (Dokl.) Acad. Sci. USSR 26 (1940) 115–118 (German).
[4] B.B. Mandelbrot, J.W.V. Ness, Fractional Brownian motions, fractional noises and applications, SIAM Rev. 4 (1968) 422–437.
[5] A. Peréz, C.E. D'Attellis, M. Rapacioli, G.A. Hirchoren, V. Flores, Analyzing blood cell concentration as a stochastic process, IEEE Eng. Med. Biol. (2001) 170–175.
[6] P. Flandrin, On the spectrum of fractional Brownian motions, IEEE Trans. Inf. Theory IT-35 (1) (1989) 197–199.
[7] P. Flandrin, Wavelet analysis and synthesis of fractional Brownian motion, IEEE Trans. Inf. Theory IT-38 (2) (1992) 910–917.
[8] A.H. Tewfik, M. Kim, Correlation structure of the discrete wavelet coefficients of fractional Brownian motion, IEEE Trans. Inf. Theory 38 (2) (1992) 904–909.
[9] E. Masry, The wavelet transform of stochastic processes with stationary increments and its applications to fractional Brownian motion, IEEE Trans. Inf. Theory IT-39 (1) (1993) 260–264.
[10] P. Abry, D. Veitch, Wavelet analysis of long-range dependent traffic, IEEE Trans. Inf. Theory 44 (1) (1998) 2–15.
[11] S. Soltani, P. Simard, D. Boichu, Estimation of the self-similarity parameter using the wavelet transform, Signal Process. 84 (1) (2004) 117–123.
[12] P. Abry, P. Flandrin, M.S. Taqqu, D. Veitch, Wavelets for the analysis, estimation, and synthesis of scaling data, in: K. Park, W. Willinger (Eds.), Self-similar Network Traffic and Performance Evaluation, Wiley, New York, 2000.
[13] A. Carbone, G. Castelli, H.E. Stanley, Time-dependent Hurst exponent in financial time series, Physica A 344 (1–2) (2004) 267–271.
[14] D.O. Cajueiro, B.M. Tabak, The Hurst exponent over time: testing the assertion that emerging markets are becoming more efficient, Physica A 336 (3–4) (2004) 521–537.
[15] D. Grech, Z. Mazur, Can one make any crash prediction in finance using the local Hurst exponent idea?, Physica A 336 (1–2) (2004) 133–145.
[16] I. Passoni, H. Rabal, C.M. Arizmendi, Characterizing dynamic speckle time series with the Hurst coefficient concept, Fractals 12 (3) (2004) 319–329.
[17] R.F. Peltier, J.L. Vehel, Multifractional Brownian motion: definition and preliminary results, Research Report RR-2645, INRIA, 1995.
[18] J.-F. Coeurjolly, Statistical inference for fractional and multifractional Brownian motions, Ph.D. Thesis, Laboratoire de Modélisation et Calcul-Institut d'Informatique el Mathématiques Appliquées de Grenoble, 2000, http://bibliotheque.imag.fr/publications/theses/2000
[19] O.A. Rosso, M.L. Mairal, Characterization of time dynamical evolution of electroencephalographic epileptic records, Physica A 312 (3–4) (2002) 469–504.
[20] S. Sello, Wavelet entropy as a measure of solar cycle complexity, Astron. Astrophys. 363 (2000) 311–315.
[21] S. Sello, Wavelet entropy and the multi-peaked structure of solar cycle maximum, New Astronomy 8 (2003) 105–117.
[22] I. Passoni, A. Dai Pra, H. Rabal, M. Trivi, R. Arizaga, Dynamic speckle processing using wavelets based entropy, Opt. Commun. 246 (1–3) (2005) 219–228.

[23] D.G. Pérez, L. Zunino, M. Garavaglia, O.A. Rosso, Wavelet entropy and fractional Brownian motion time series, Physica A (2005), in press.
[24] M. Unser, Spline: a perfect fit for signal and image processing, IEEE Signal Process. Mag. 16 (1999) 22–38.
[25] P. Thévenaz, T. Blu, M. Unser, Interpolation revisited, IEEE Trans. Med. Imaging 19 (7) (2000) 739–758.
[26] A. Ayache, J. Lévy Véhel, On the identification of the pointwise Hölder exponent of the generalized multifractional Brownian motion, Stochastic Processes Appl. 111 (2004) 119–156.

Procesamiento Óptico Fotorrefractivo

El efecto fotorrefractivo ocurre cuando se produce un cambio de índice de refracción en un medio transparente debido a la propagación luminosa no uniforme. Este efecto se presenta en materiales: electro-ópticos, fotoconductores y con centros donadores y aceptores de carga. La ventaja primordial de los fotorrefractivos consiste en generar fenómenos no lineales a bajas intensidades de excitación (W/cm2, mW/cm2).

Los fotorrefractivos tienen la habilidad de registrar hologramas en términos de redes dinámicas de índice de refracción y recuperar la información almacenada en paralelo, a tiempo real y con una notable discriminación de la imagen de salida. Estos materiales son muy adecuados para el procesamiento óptico debido a su gran sensibilidad, reversibilidad en su uso, capacidad de multiplexar, de conjugar la fase y amplificar señales ópticas. En particular, han sido utilizados en holografía dinámica y memorias ópticas reversibles.

Las investigaciones en el procesamiento óptico con materiales fotorrefractivos se iniciaron en el CIOp en 1987, siendo el primer laboratorio en abordar esta línea en el país. Los cristales fotorrefractivos han sido utilizados para realizar procesamiento de imágenes y metrología óptica en tiempo real (filtrado renovador, correlación óptica dinámica, realce de imágenes, interferometría Talbot y Lau, memorias holográficas, metrología speckle, encriptación). Dentro de la metrología speckle fotorrefractiva se aprovechó la conjunción del registro en volumen de los medios fotorrefractivos y las características volumétricas del speckle. Cabe destacar que el fenómeno de granularidad óptica ó speckle a pesar de su naturaleza en volumen había sido profusamente utilizado sólo según un enfoque bidimensional.

Fotorrefractive Optical Processing

Photorrefractive effect takes place when a refractive index change is produced in a material due to non uniform light distribution. This effect is observed in electro-optic and photoconductive materials having donor and trap centers. The main advantage of photorefractives consist in producing non linear phenomena under low intensity levels (W/cm2, mW/cm2).

Photorefractives are able to register dynamic holograms in terms of index gratings and to retrieve storage information in parallel, in real time and with a high fidelity. These materials are adequate for image processing due to their high sensitivity, reversibility, multiplexing, phase conjugation and optical amplification capabilities. In particular, it is employed in dynamic holography and reversible optical memories.

Photorefractive image processing research starts at CIOp in 1987 being the first laboratory in our country to initiate this line of research. The photorefractive crystals have been utilized in image processing and optical metrology (novelty filter, dynamic optical correlation, image enhancement, Talbot and Lau interferometry, holographic memories, speckle metrology and encryptation). In photorefractive speckle metrology has been taking advantage from the photorefractive crystal volume features and three-dimensional nature of speckle in very innovative research.

Pseudocoloring with BSO crystals

S. I. Grosz, L. M. Zerbino, and N. Bolognini

Centro de Investigaciones Opticas, CIC, Casilla de Correo 124, 1900 La Plata, B. A., Argentina.

Received 4 April 1989.
0003-6935/90/233337-02$02.00/0.
© 1990 Optical Society of America.

A new pseudocoloring technique is proposed using photorefractive BSO crystals biased under the influence of an externally applied electric field with coherent or incoherent illumination.

Pseudocoloring of gray level information is a technique of introducing false colors into a black and white image. The importance of this operation is based on the human eye's ability to distinguish between different colors more easily than gray levels.

Over the last few years several analogical optical methods have been proposed, involving holographic techniques, halftone screens, and spatial filtering operations. In some cases it is necessary to use a real-time method, which avoids the spatial filtering steps. Several real-time approaches have been implemented.[1–4]

In recent years the photorefractive effect has become the nonlinear optical mechanism of choice for optical image processing. When the light of a suitable wavelength λ_1 is incident on a crystal, photoelectrons are generated, migrate in the lattice, and are subsequently trapped at new sites. The resulting space charge gives rise to an electric field strength distribution in the material, which changes the refractive index via the electrooptic effect.[5] This property allows the simultaneous recording and reading of a given light distribution to be achieved with time constants suitable to real-time operations.[6] Writing and readout beams wavelengths (λ_1 and λ_2, respectively) and intensities must be adjusted according to the absorption band of the photoconductor to ensure that the written image is not erased.

We propose a new pseudocoloring technique using photorefractive BSO crystals biased under the influence of an externally applied electric field with coherent or incoherent illumination.

The experimental setup is depicted in Fig. 1. A gray level transparency to be pseudocolored is placed at plane Π_1, which is illuminated by a monochromatic λ_1 source S_1 through a condensing lens L_1. Lens L_2 images the Π_1 plane on the Π_2 plane and the Π_2' plane through the beam splitters BS_1 and BS_2. Simultaneously, L_2 images Π_2 and Π_2' (by reflection on mirror M) on the Π_3 plane.

The written image (with wavelength λ_1) in the biased BSO (Π_2 plane) induces birefringence due to the photorefractive effect and is read out with the monochromatic λ_2 source S_2 through lens L_2 and polarizer P_3. Polarizers P_1 and P_2 have their polarization axes parallel and the $\lambda/4$ plate with its axis forming an angle of 45° with those of P_1 and P_2. In this way, the reflected image on the BSO face does not reach the Π_3 plane while the direct mirror reflected image will. Thus, with an appropriate orientation of P_3, we produce a contrast reversed image on Π_3 through L_2 when read out with S_2 (λ_2),

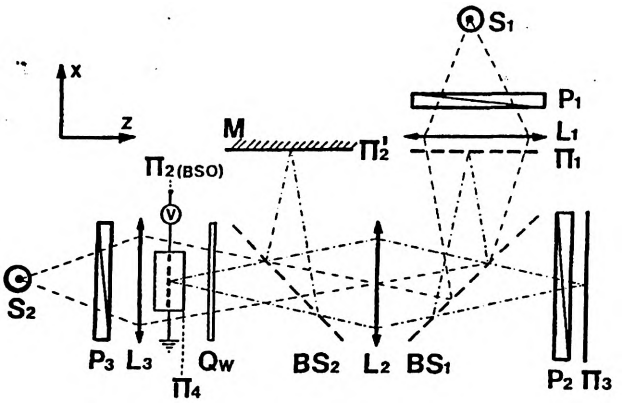


Fig. 1. Experimental configuration of gray level pseudocoloring with BSO crystals: S_1, S_2, illumination sources; P_1, P_2, P_3, polarizers; BS_1, BS_2, beam splitters; L_1, L_3, condenser lenses; L_2, imaging lens; Π_1, gray level transparency plane (input plane); Π_2, BSO image plane; Π_2', mirror M plane; Π_3, pseudocolor image plane (output plane); Π_4, BSO surface plane; QW, $\lambda/4$ plane.

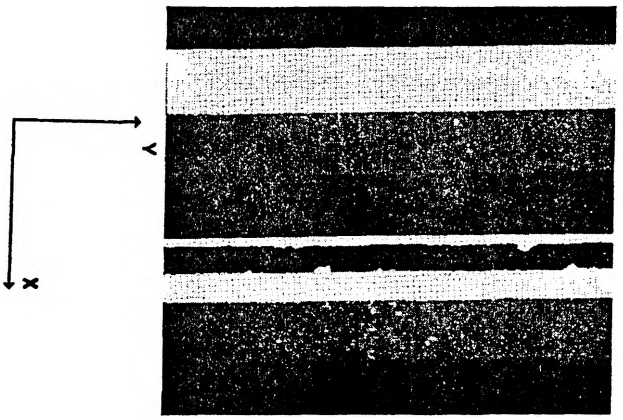


Fig. 2. Gray level original transparency.

the image stored in the BSO crystal. In this way, the direct mirror-reflected image λ_2 superimposed with the photorefractive-induced reversed image gives on Π_3 a pseudocolored image of the original transparency.

Taking into account that the induced birefringence depends on the write-in illumination λ_1 and the applied voltage through the space charge field, a suitable combination of these parameters is necessary to select the resulting colors. A neutral variable density filter was located in front of mirror M for equalizing both intensities (λ_1 and λ_2).

A simplified version is possible without mirror M, beam splitter BS_2, and polarizer P_1. In this case the λ_2 direct contrast image component should be provided by reflection

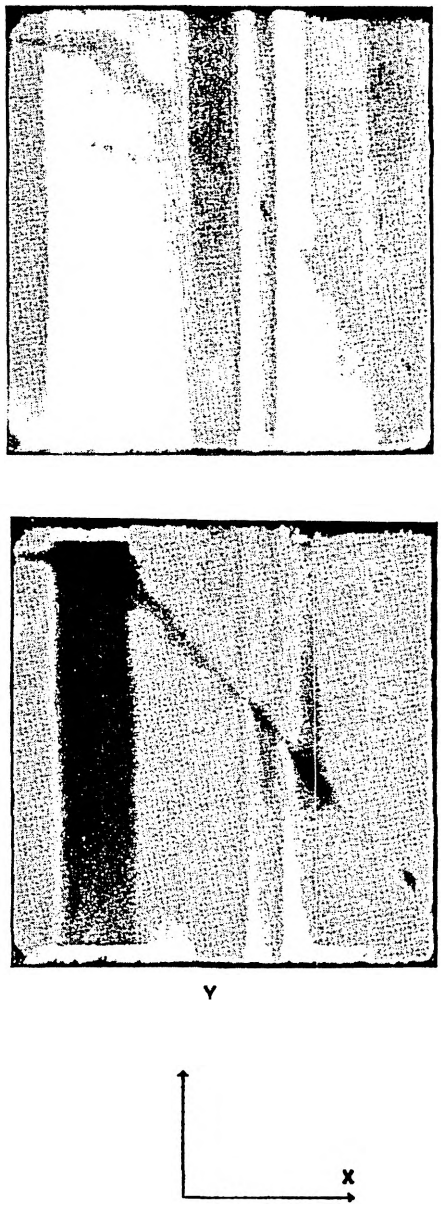


Fig. 3. Black and white pictures of the green (a) and red (b) filtered versions of the pseudocolored image. The faded oblique line across the pictures corresponds to a minute scratch in the crystal surface.

on the BSO surface (Π_4 plane). Nevertheless, in this approach, the equalization also depends on the reflection coefficient of the crystal, and an additional drawback is a misfocusing effect due to the lack of coincidence between planes Π_2 and Π_4. The arrangement of polarizers and mirror M of Fig. 1 provides the λ_2 component at Π_3 plane and eliminates the parasitic misfocused crystal reflection image.

We show an experimental result. In this case the object was a sequence of parallel fringes with different gray levels and widths as shown in Fig. 2. A color picture of the pseudocolored image of this transparency was obtained at the Π_3 plane. Figure 3(a) and (b) are the black and white versions of that colored picture when filtered through a green filter (λ = 5200 Å, $\Delta\lambda$ = 100 Å) and a red filter (λ = 6350 Å, $\Delta\lambda$ = 100 Å), respectively. Both the monochromatic sources S_1 and S_2 were spatially incoherent and were obtained using white light lamps and color filters centered at λ_1 = 5200 Å and λ_2 = 6350 Å, respectively ($\Delta\lambda$ = 100 Å). The BSO crystal of dimensions $Lx = Ly$ = 10 mm; Lz = 3 mm (provided by Sumitomo) was operated with an external bias voltage of ~6 kV.

Clearly, S_1 or S_2 or both could be spatially coherent. In this case, similar results could be expected with the additional effect of a speckled final image.

This work was supported under CONICET PID 3081400.

S. I. G. holds a fellowship from the Comision de Investigaciones Cientificas de la Provincia de Buenos Aires.

L. M. Z. and N. B. are members of the Consejo Nacional de Investigaciones Cientificas y Tecnicas.

References

1. F. T. S. Yu, X. X. Chen, and T. H. Chao, "White-Light Density Pseudocolor Encoding with Three Primary Colors," J. Opt. Paris 15, 55–58 (1984).
2. J. A. Mendez and J. Bescos, "Gray Level Pseudocoloring with Three Primary Colours by Diffraction Grating Modulation Method," J. Opt. Paris 14, 69–73 (1983).
3. R. Arizaga, N. Bolognini, H. J. Rabal, E. E. Sicre, and M. Garavaglia, "Real-Time White Light Pseudocolor Density Encoder," Opt. Commun. 43, 12–17 (1982).
4. J. A. Mendez and M. Nieto-Vesperinas, "Light Scattering by Film Grain Noise: Application to Grey Level Optical Pseudocoloring," Appl. Opt. 22, 2068–2074 (1983).
5. P. Gunter and H. J. Eichler, "Electrooptic and Photorefractive Materials," Springer Proc. Phys. 18, 206–228 (1987).
6. A. Marrakchi, A. R. Tanuay, Jr., J. Yu, and D. Psaltis, "Physical Characterization of the Photorefractive Incoherent-to-Coherent Optical Converter," Opt. Eng. 24, 124–131 (1985).

Self-imaging through incoherent to coherent conversion

María del Carmen Lasprilla A.*
Alexandra Agra Amorim†
Myrian Cristina Tebaldi
Néstor A. Bolognini
Centro de Investigaciones Ópticas, CIOp (CONICET, CIC)
Casilla de Correo 124
1900 La Plata, Argentina
E-mail: postmaster@ciop.edu.ar

Abstract. The self-imaging phenomenon is realized by utilizing an incoherent to coherent converter. For this purpose, a photorefractive BSO crystal that becomes uniformly birefringent due to an external applied voltage is employed. Then, an incoherently illuminated one-dimensional grating that locally modulates the induced birefringence is registered. In the readout process, a linearly polarized plane wave from a He-Ne laser is utilized. The ellipticity of the light exiting the crystal will be determined according to the local birefringence. Then, after passing through a polarizer, the coherent output will reproduce the incoherent input. In this way, under free propagation, coherent replicas of the grating will be obtained.
© *1996 Society of Photo-Optical Instrumentation Engineers.*

Subject terms: self-imaging; real-time image processing; photorefractive crystals.

Paper 19085 received Aug. 18, 1995; accepted for publication Oct. 23, 1995.

1 Introduction

When a periodic transparency (for instance, a Ronchi grating) is illuminated with a monochromatic collimated beam, the grating amplitude transmittance is periodically reproduced along the propagation direction. These replicas under free propagation are called self-images.[1] The spatial frequencies of self-imaging objects have to be discrete and located on the so-called Montgomery rings.[2]

A Ronchi grating of spatial period d fulfills the mentioned condition and therefore generates self-images. It should be mentioned that lateral periodicity of an object is sufficient but not necessary for self-imaging to occur. When the grating transparency is illuminated with a plane wave of wavelength λ, the Fresnel diffraction patterns located at distances $z_T = 2d^2 n/\lambda$ ($n = 1,2,3,...$) from the grating reproduce the input grating.[2,3]

Furthermore, the diffraction patterns located between the transparency and the first self-image are repeated between any two successive self-images. That is, the diffracted field is longitudinally periodic.

Photorefractive crystals such as the sillenites combine real-time response, reversibility, and high sensitivity in the visible portion of the spectrum that make them very attractive for many optical information processing and related applications.[4] In this work, an incoherent to coherent converter arrangement that utilizes a sillenite photorefractive crystal (BSO) to encode a periodic transparency is proposed. To this end, the write-in step is detailed in the following section. Afterwards, we discuss the coherent readout process that allows the replicas of the input to be produced.

2 Theoretical Analysis

Let us consider the experimental setup schematized in Fig. 1. A transparency O, which consists of a grating of binary amplitude with an opening ratio equal to 0.5, is illuminated with a white light source S through the condenser lens L_1. An image of unit magnification of the transparency is obtained in the crystal by means of the lens L_2. The directions $\langle\bar{1}10\rangle$, $\langle 001\rangle$, and $\langle 110\rangle$ of the crystal coincide with the X, Y, and Z axes, respectively (laboratory axes).

The crystal exhibits the linear electro-optic effect. Thus, if a voltage V is applied between $(\bar{1}10)$ faces separated a distance L_x, it becomes uniformly birefringent due to the external field $E_a = V/L_x$. The slow and fast index-induced optical axes are at ± 45 deg with respect to the $\langle\bar{1}10\rangle$ direction. The crystal has a strong photoconductivity in the range of wavelength between 400 and 550 nm. A filter centered at 530 nm ($\Delta\lambda$ ± 3 nm) is placed in front of the white-light source. Under these conditions the light pattern received by the crystal, that is, the Ronchi grating projected by the lens L_2, will create photocharges that will drift due to the external field E_a into the dark regions, where they are trapped. These charges develop a space-charge field that partially compensates the external field in the illuminated areas. In this way, the induced birefringence will be locally modulated according to the light pattern, producing a local change in the ellipticity of the transmitted light.

In order to compute the resulting total internal field E in the crystal, the Kukhtarev equations are employed.[5,6] Considering that the input pattern is a one-dimensional light distribution, a single-spatial-variable approach to these equations is possible:

$$J(x,t) = qD\frac{\partial N(x,t)}{\partial x} + q\mu N(x,t)\left[E_{sc}(x,t) + \frac{V}{L_x}\right], \tag{1}$$

$$\frac{\partial N(x,t)}{\partial t} = g(x) - \frac{N(x,t) - N_D}{\tau} + \frac{1}{e}\frac{\partial J(x,t)}{\partial x}, \tag{2}$$

*Current affiliation: Universidad Industrial de Santander, Departamento de Física, A.A. 678, Bucaramanga, Colombia.
†Current affiliation: Instituto Superior de Engenharia do Porto, Departamento de Física, 4200 Porto, Portugal.

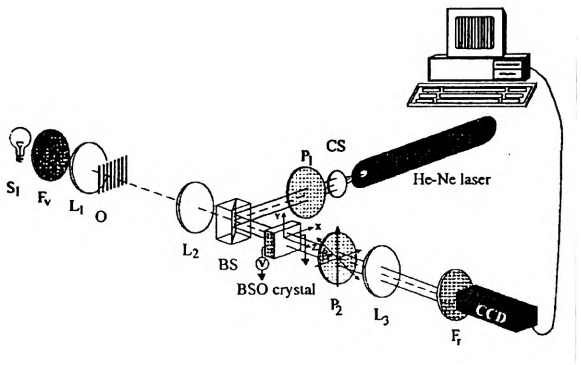


Fig. 1 Experimental setup. S: incoherent source; L_1 and L_2: lenses; F_v: filter centered at 530 nm; O: input transparency (Ronchi grating); BS: beamsplitter; CS: collimated system; F_r: filter centered at 630 nm, P_1 and P_2: polarizers.

where x and t are spatial and temporal variables, respectively, J is the current density, and N is the total free-carrier concentration, which includes the contribution due to the light pattern and the contribution N_D of the free charges in the dark. Furthermore, e is the electron charge, μ is the mobility, τ is the free-carrier lifetime, and D is the diffusion coefficient.

The usual assumption is made that the generation rate $g(x)$ is proportional to the light pattern $I_i(x)$ received by the crystal. That is, $g(x)=g_0 I_i(x)/I_0$, where $I_i(x)/I_0$ is the normalized light intensity and g_0 is proportional to the highest intensity value I_0. Also, the photoinduced space charge field E_{sc} must fulfill

$$\int_{-L_x/2}^{L_x/2} E_{sc}(x,t)\,dx=0. \tag{3}$$

The gradient contribution $\partial N/\partial x$ in the diffusion term of Eq. (1) can be neglected because of the smooth variation of $I_i(x)$ on a microscopic scale. Furthermore, in the steady-state situation $\partial N/\partial t=0$, a constant current density J is of concern.

Under these conditions, from Eqs. (1), (2), and (3), the following total internal field results:

$$E(x)=E_{sc}(x)+\frac{V}{L_x}=\frac{J}{q\mu N(x)}=\frac{V}{KN(x)}, \tag{4}$$

where the expression for $N(x)$ is

$$N(x)=N_D\left[1+\frac{\tau g_0}{N_D}I_i(x)\right]=N_D[1+GI_i(x)] \tag{5}$$

and $G=\tau g_0/N_D$. The value of K is obtained as

$$K=\int_{-L_x/2}^{L_x/2}\frac{dx}{N(x)}. \tag{6}$$

For this configuration, the calculated expression for the modulated birefringence is

$$\delta n(x)=n_0^3 r_{41}E(x), \tag{7}$$

where r_{41} is the electro-optic coefficient and n_0 is the refractive index without induced field.

In the readout or reconstruction process, a collimated Y-direction linearly polarized plane wave from a He-Ne laser is utilized. In order to avoid destructive readout of the stored information, a wavelength that is outside of the spectral sensitivity range of the crystal is employed. Then, let us consider the light amplitude transmitted by the crystal in the readout process. It will be necessary to compute the produced changes in the light ellipticity.

The BSO crystal exhibits rotatory power per unit length $\rho(\lambda)$ (where λ is the wavelength employed for readout), which combines with the induced birefringence modulation $\delta n(x)$. This means that when light of a given ellipticity enters the crystal, in order to evaluate the change in the polarization state, both effects must be computed.

In this case, following the Jones formalism,[7] the following transfer matrix[4] W_C of the crystal written in the coordinate system of the two induced axes results:

$$W_C(x)=\begin{pmatrix}\cos\Delta(x)-i\sin\psi(x)\sin\Delta(x) & -\cos\psi(x)\sin\Delta(x)\\ \cos\psi(x)\sin\Delta(x) & \cos\Delta(x)+i\sin\psi(x)\sin\Delta(x)\end{pmatrix} \tag{8}$$

and

$$\begin{pmatrix}A_x'\\ A_y'\end{pmatrix}=R\left(-\frac{\pi}{4}\right)W_C(x)R\left(\frac{\pi}{4}\right)\begin{pmatrix}0\\ 1\end{pmatrix}=\begin{pmatrix}\sin\Delta(x)\,\exp[i\psi(x)]\\ \cos\Delta(x)\end{pmatrix} \tag{9}$$

where R is the rotation matrix and A_x' and A_y' are the respective output amplitudes in the laboratory axes, and

$$\Delta(x)=L_z\left[\rho^2+\frac{\varphi^2(x)}{4}\right]^{1/2},\quad \psi(x)=\tan^{-1}\left[\frac{\varphi(x)}{2\rho}\right] \tag{10}$$

with

$$\varphi(x)=\frac{2\pi}{\lambda}\delta n(x)=\frac{2\pi}{\lambda}n_0^3 r_{41}E(x). \tag{11}$$

In the experimental setup that is schematized in Fig. 1, the polarizer P_1 is placed with its pass plane parallel to the Y axis, and the polarizer P_2 is oriented with its pass plane making an angle β with respect to the X axis. The Jones matrix of P_2 is

$$\mathscr{P}(\beta)=\begin{pmatrix}\cos^2\beta & \cos\beta\,\sin\beta\\ \cos\beta\,\sin\beta & \sin^2\beta\end{pmatrix}. \tag{12}$$

The transmitted amplitude through the polarizer, considering Eqs. (9) and (12), is

$$\begin{pmatrix}A_x''\\ A_y''\end{pmatrix}=\mathscr{P}(\beta)\begin{pmatrix}A_x'\\ A_y'\end{pmatrix}. \tag{13}$$

Then, the readout intensity $I_c(x,\beta)=|A_x''|^2+|A_y''|^2$ becomes

$$I_c(x,\beta)=\tfrac{1}{2}\,[1-\cos 2\Delta(x)\,\cos 2\beta - \sin 2\Delta(x)\,\sin 2\beta\,\cos\psi(x)]. \tag{14}$$

Finally, the incoherent input $I_i(x)$ has been converted to a coherent output $I_c(x,\beta)$, where the parameter β governs the contrast, as will be detailed in the next section.

3 Experimental Results

A BSO crystal of dimensions $L_x=L_y=10$ mm and $L_z=3$ mm was utilized and a voltage $V=9$ kV was applied between their (110) faces. The intensity of the incoherent grating source was less than 1 mW/cm^2, and a 5-mW He-Ne laser ($\lambda=633$ nm) was employed for the readout beam. The measured rotatory power was $\rho=22$ deg/mm. For the calculation we used[8] $n_0=2.54$, $r_{41}=3.5$ pm/V.

A Ronchi grating of period $d=4$ lines/mm was used as the input transparency. Lens L_2 ($f/6$) images the grating in the crystal with unit magnification. The intensity distribution received in the crystal plane is

$$I_i(x)=I_0\left(\frac{1}{2}+\sum_{m=1}^{\infty}\frac{\sin(\pi m/2)}{\pi m/2}\cos\left(2\pi m\,\frac{x}{d}\right)\right)\operatorname{rect}\left(\frac{x}{L_x}\right), \tag{15a}$$

and the normalized light intensity is

$$t(x)=I_i(x)/I_0. \tag{15b}$$

According to Eq. (7), the received intensity distribution $I_i(x)$ is encoded as a birefringence modulation. In this case, by using Eqs. (4) and (5), the total internal field becomes

$$E(x)=\begin{cases} E_1=\dfrac{2V}{L_x}\left(\dfrac{1+G}{2+G}\right) & \text{if } I_i(x)=0,\\[2ex] E_2=\dfrac{2V}{L_x}\left(\dfrac{1}{2+G}\right) & \text{if } I_i(x)=I_0. \end{cases} \tag{16}$$

Usually $G\gg 1$, and the expression for $E(x)$ reduces to

$$E(x)=\begin{cases} E_1\approx\dfrac{2V}{L_x}=2E_a & \text{if } I_i(x)=0,\\ E_2\approx 0 & \text{if } I_i(x)=I_0. \end{cases} \tag{17}$$

Consider again the intensity received by the crystal, described by Eq. (15a). The periodically striped illuminated regions [$I_i(x)=I_0$] alternate with dark regions of the same width [$I_i(x)=0$]. It follows from Eq. (17) that in the bright striped areas the total internal field drops to a negligible value in comparison with the magnitude of the field in the dark regions, which will increase beyond the external applied value E_a. As a consequence, in view of Eq. (7), the induced birefringence tends to zero in the illuminated regions, while maintaining a nonnegligible value in the dark stripes, that is,

$$\delta n(x)=\begin{cases} \delta n_1=r_{41}n_0^3(2E_a) & \text{if } I_i(x)=0,\\ \delta n_2=0 & \text{if } I_i(x)=I_0. \end{cases} \tag{18}$$

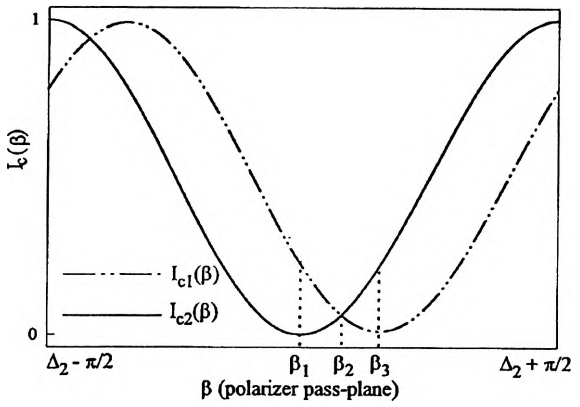


Fig. 2 Transmitted intensity of the polarizer P_2 for the components $I_{c1}(\beta)$ (elliptically polarized) and $I_{c2}(\beta)$ (linearly polarized).

It is clear that $\delta n(x)$ has the same spatial period as $I_i(x)$.

Also, by using Eqs. (10), (11), and (17) we have

$$\varphi(x)=\begin{cases} \varphi_1=\dfrac{2\pi}{\lambda}\,\delta n_1 & \text{if } I_i(x)=0,\\ \varphi_2=0 & \text{if } I_i(x)=I_0, \end{cases} \tag{19a}$$

$$\psi(x)=\begin{cases} \psi_1=\tan^{-1}\left(\dfrac{\varphi_1}{2\rho}\right) & \text{if } I_i(x)=0,\\ \psi_2=0 & \text{if } I_i(x)=I_0, \end{cases} \tag{19b}$$

and

$$\Delta(x)=\begin{cases} \Delta_1=L_z\left[\rho^2+\left(\dfrac{\varphi_1}{2}\right)^2\right]^{1/2} & \text{if } I_i(x)=0,\\ \Delta_2=L_z\rho & \text{if } I_i(x)=I_0. \end{cases} \tag{19c}$$

Thus, when the linearly polarized collimated readout beam propagates through the crystal, it will emerge periodically modulated in its ellipticity. Those parts of the readout beam that pass through the crystal regions where $\delta n\approx 0$ will emerge linearly polarized with the plane of polarization rotated an angle $\Delta_2=\rho L_z$ with respect to that of the entering light. The remaining part of the emerging wave will be elliptically polarized, because it has traveled through the periodic stripes where δn is not negligible (write-in dark regions).

Returning to Eq. (14), we have

$$I_c(x,\beta)=\begin{cases} I_{c1}(\beta)=\tfrac{1}{2}\,(1-\cos 2\Delta_1\,\cos 2\beta-\sin 2\Delta_1 \times\sin 2\beta\,\cos\psi_1) & \text{if } I_i(x)=0,\\ I_{c2}(\beta)=\tfrac{1}{2}\,(1-\cos 2\Delta_2\,\cos(2\beta)-\sin 2\Delta_2 \times\sin 2\beta) & \text{if } I_i(x)=I_0. \end{cases} \tag{20}$$

This expression analyzes the transmitted intensity of polarizer P_2 into two parts: a linearly polarized part of the readout wavefront exiting the crystal, $I_{c2}(\beta)$, and an elliptically polarized part, $I_{c1}(\beta)$. Figure 2 shows $I_{c1}(\beta)$ and $I_{c2}(\beta)$. The phase shift between them depends on the value of δn_1. Then $I_c(x,\beta)$ can be rewritten as

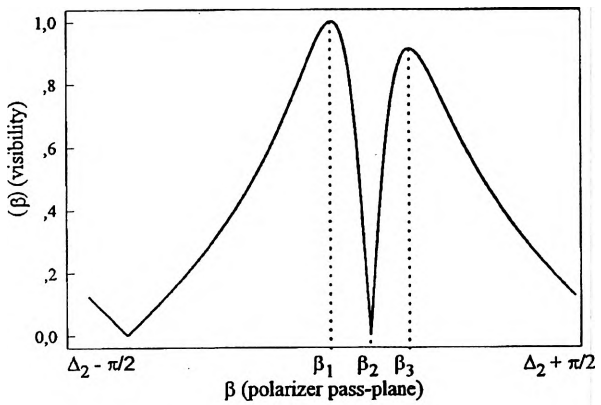


Fig. 3 Visibility of the coherent readout image.

$$I_c(x,\beta)=I_{c2}(\beta)t(x)+I_{c1}(\beta)t\left(x\pm\frac{d}{2}\right). \tag{21}$$

Consider the case $\beta=\beta_1=\Delta_2=L_z\rho$. It means that when the external applied voltage is off ($V=0$), the system is in extinction and no light passes through the analyzer P_2. But if $V\neq 0$, taking into account Eqs. (20) and (21), the following emerging readout intensity results:

$$I_c(x,\beta_1)=I_{c1}(\beta_1)t\left(x\pm\frac{d}{2}\right). \tag{22}$$

That is, the emerging wave of the readout beam will be alternately polarized linearly and elliptically with period d. The analyzer P_2 will block out the linearly polarized parts and will select a component of the elliptically modulated portion of the wavefront. Alternate dark and bright stripes will exit the polarizer. In this way, a coherent contrast-reversed replica of the input is obtained, converting the modulation of birefringence into modulation of transmission. Let us suppose that the spatial coherence of the readout beam is high and that free propagation takes place. In this case the Fresnel intensity distribution along the Z axis will be the same as if the original transparency, shifted a half period, had been located at the position of the polarized P_2.

The visibility of the readout coherent image $I_c(x,\beta)$, defined as

$$\mathscr{V}(\beta)=\left|\frac{I_1(\beta)-I_2(\beta)}{I_1(\beta)+I_2(\beta)}\right|, \tag{23}$$

is displayed in Fig. 3, where it can be observed that the absolute maximum, $\mathscr{V}(\beta)=1$, is reached, because $I_2(\beta_1)=0$.

Let us impose the condition $\mathscr{V}(\beta)=0$. According to the expression (23), this implies equality of the linear and the elliptical components transmitted. The value of β that fulfills this constraint is

$$\beta=\beta_2=\tfrac{1}{2}\tan^{-1}\left(\frac{\cos 2\Delta_1-\cos 2\Delta_2}{\sin 2\Delta_2-\sin 2\Delta_1\cos\psi_1}\right). \tag{24}$$

In this case, taking into account that $t(x+d/2)=1-t(x)$, we obtain

$$I_c(x,\beta_2)=C, \tag{25}$$

so that the output of the polarizer P_2 is uniform.

Another important value of β is that for which $I_{c1}(\beta)$ is minimum. From this condition, $\partial I_{c1}(\beta)/\partial\beta=0$, we have

$$\beta=\beta_3=\tfrac{1}{2}\tan^{-1}(\tan 2\Delta_1\cos\psi_1). \tag{26}$$

Then

$$I_c(x,\beta_3)=I_{c1}(\beta_3)t\left(x+\frac{d}{2}\right)+I_{c2}(\beta_2)t(x). \tag{27}$$

By considering Fig. 2 it is clear that $I_{c1}(\beta_3)\ll I_{c2}(\beta_3)$ and Eq. (27) can be written as:

$$I_c(x,\beta_3)\approx I_{c2}(\beta_3)t(x). \tag{28}$$

In this case, a direct-contrast output is obtained.

As β is rotated from β_1 to β_3, more and more of the linearly polarized parts of the light emerging from the crystal will be transmitted through the analyzer P_2, and less and less of the elliptically polarized parts will be transmitted.

In the three coherent readout images of Fig. 4 the polarizer P_2 was oriented at $\beta=\beta_1$ and the registers were obtained for different longitudinal positions under free propagation. In the following, all distances are measured from the crystal plane. Figure 4(a) displays a contrast-reversed

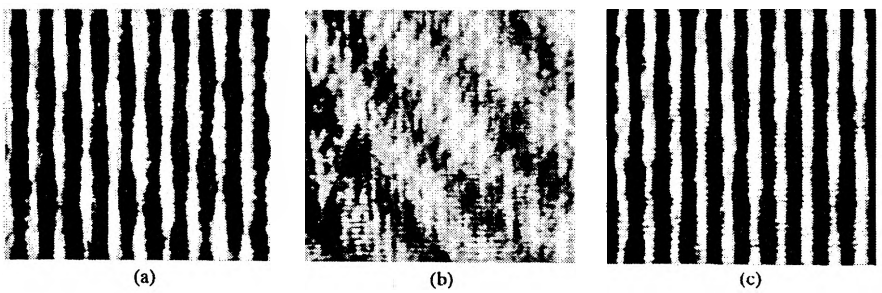
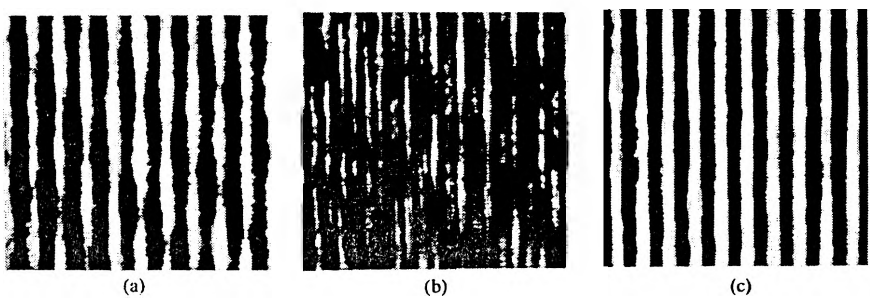


Fig. 4 Self-imaging outputs with the polarizer P_2 oriented at $\beta=\beta_1$: (a) $z=z_T$, (b) $z=5z_T/4$, and (c) $z=3z_T/2$.



(a) (b) (c)

Fig. 5 Coherent readout images at $z=z_T$ with the pass plane of the polarizer P_2 set at (a) $\beta=\beta_1$, (b) $\beta=\beta_2$, and (c) $\beta=\beta_3$.

self-image registered at a distance z_T. Figure 4(b) corresponds to a defocused plane located at $5z_T/4$, while Fig. 4(c) displays a reverse-contrast image with respect to Fig. 4(a) and is obtained at a distance $3z_T/2$.

The pictures displayed in Fig. 5 were registered at the distance z_T for three values of the angle β. Figure 5(a) displays a contrast-reversed self-image obtained when the angle $\beta=\beta_1$. In Fig. 5(b) a defocused image is registered by setting the angle $\beta=\beta_2$, and in Fig. 5(c) a direct-contrast self-image was read out with the angle $\beta=\beta_3$.

By comparison of Fig. 4(a), 4(b), 4(c) with Fig. 5(a), 5(b), 5(c), respectively, it can be seen that a given longitudinal displacement could be comparable to a certain value of β at a fixed plane.

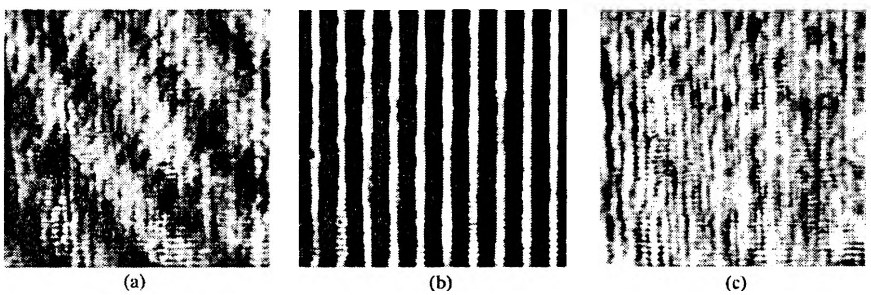
The sequence of Fig. 6 was obtained for values of $\beta=\beta_1,\beta_2,\beta_3$ respectively, in a plane located at $5z_T/4$ from the crystal. This would be comparable to obtaining three registers at distances $z_T/4$ apart from each other, for instance $5z_T/4$, $6z_T/4$, and $7z_T/4$, at a fixed value of $\beta=\beta_1$.

4 Discussion and Conclusions

By observing the visibility curve it can be concluded that an interesting domain runs from β_1 to β_3. To a high-contrast distribution at $\beta=\beta_1$ corresponds a reverse high-contrast version at $\beta=\beta_3$. This could be very useful in certain applications. The converter itself can be planned as a subsystem of an optical device in which control of the visibility is a key point for subsequent processing. In order to achieve this situation, the condition established by Eq. (28) must be fulfilled. This implies a high eccentricity of the elliptical light that originates the component $I_{c1}(\beta)$ [see Eq. (20)], implying a low value for δn_1. As δn_1 increases, $\Delta\beta=\beta_3-\beta_1$ and $I_{c1}(\beta_3)$ increase as well, the visibility in $\beta=\beta_3$ decreases, and this diminishes the system's ability to reverse the contrast of the grating encoded at $\beta=\beta_1$. Let us suppose that the appropriate conditions are fulfilled. Then, for instance, let us suppose that a reference Ronchi grating is placed beyond the polarizer P_2. Hence, the moiré pattern that arises between a readout self-image and a reference grating can be employed to detect phase objects.[9] Furthermore, the contrast control of the self-images could contribute to the easy visualization of those objects. Also, if a birefringent material is located between the analyzer and the reference grating, the shift in the moiré fringes can be used for quantitative determination of the birefringence.

In some circumstances, for subsequent processing, it could be useful to have a Talbot object in the form of an incoherent input, that is, a TV picture, 2-D array, etc. In this case, an incoherent-to-coherent converter as was proposed in this paper could be appropriate.

Some constraints arise from the nature of the converter. It is limited by the crystal response time, which depends on the intensity of the input signal. Furthermore, geometric resolution limitations arise from the write-in imaging system. Also, a compromise must be considered between the increasing of the crystal thickness to improve the sensitivity and the corresponding constraints on the spatial resolution that result. According to the experimental conditions detailed at the beginning of the previous section, the available resolution was 20 lines/mm. Certainly, that can be improved several fold by reducing the crystal thickness (L_z)



(a) (b) (c)

Fig. 6 Coherent readout images at $z=5z_T/4$ with the pass plane of the polarizer P_2 set at (a) $\beta=\beta_1$, (b) $\beta=\beta_2$, and (c) $\beta=\beta_3$.

and increasing the f number of lens L_2. On the other hand, it should be mentioned that because of the finite crystal dimension L_x, the diffracted high harmonics in the readout process gradually "walk off" the zero-order beam and do not take part in the image formation. This inherent drawback in any self-imaging process limits a complete replication of the input.

Finally, we should emphasize the nonholographic nature of the converter, which represents an experimental advantage. A device such as a photorefractive incoherent-to-coherent optical converter (PICOC) could be employed as well, but it has a holographic support[10] that considerably complicates the experimental arrangement. Besides, it lacks flexibility for controlling the contrast of the output.

Acknowledgments

M. C. Lasprilla acknowledges an external fellowship of CONICET (Argentina) and financial support from COLCIENCIAS (Colombia). M. Tebaldi acknowledges an internal fellowship of CONICET. This work was supported by PID 3974/92 of CONICET.

References

1. K. Patorski, "The self-imaging phenomenon and its applications," in *Progress in Optics*, Vol. XXVII, E. Wolf, Ed., Chap. 1, pp. 3–45, North-Holland, Amsterdam (1989).
2. W. Montgomery, "Self-imaging objects of infinite aperture," *J. Opt. Soc. Am.* **57**, 772–778 (1967).
3. R. F. Edgar, "The Fresnel diffraction image of periodic structures," *Opt. Acta* **16**, 281–287 (1969).
4. J. P. Huignard and P. Günter, "Optical processing using wave mixing in photorefractive crystals," in *Photorefractive Materials and Their Applications II*, P. Günter and J. P. Huignard, Eds., Chap. 6, pp. 205–271, Springer-Verlag, Berlin (1989).
5. P. Günter and J. P. Huignard, "Photorefractive effects and materials," in *Photorefractive Materials and Their Applications I*, P. Günter and J. P. Huignard, Eds., Chap. 2, pp. 7–73, Springer-Verlag, Berlin (1989).
6. L. Liu and X. Liu, "Opto-optical switching using field enhancing effect in $Bi_{12}SiO_{20}$," *J. Appl. Phys.* **72**(2), 337–343 (1992).
7. A. Gerrad and J. M. Burch, "Matrices in polarization optics," in *Introduction to Matrix Methods in Optics*, Chap. 4, pp. 179–239, Wiley, London (1975).
8. P. Günter and H. J. Eichler, "Introduction to photorefractive materials," in *Electro-Optical Effects in Dielectric Crystals*, P. Günter, Ed., Part I p. 12, Springer-Verlag, Berlin (1987).
9. J. Ibarra and J. Ojeda Castaneda, "Talbot interferometry: a new geometry," *Opt. Comm.* **96**, 294–301 (1993).
10. A. Marrakchi, A. R. Tanguay, Jr., J. Yu, and D. Psaltis, "Physical characterization of the photorefractive incoherent-to-coherent optical converter," *Opt. Eng.* **24**(1), 124–131 (1985).



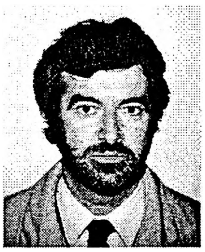
María del Carmen Lasprilla A. completed her MS in physics with a specialization in optics in the Department of Physics, Universidad Industrial de Santander, Colombia, in 1989. She is currently an assistant professor in the same department. She is also a PhD student at the Universidad Nacional de La Plata and does research at Centro de Investigaciones Opticas, Argentina. Her research includes photorefractive devices and optical signal processing.



Alexandra Agra Amorim received a degree in physics (optoelectronics) in 1990 from the University of Porto, Portugal. She held a scholarship at JNICT (CERN project) for 2 years (1990–1992). She has done research at the Vrije Universiteit Brussel and Centro de Investigaciones Opticas. She is preparing the presentation of an MS thesis on nonlinear processing with BSO crystals. She is an assistant in the Physics Department of the Engineering Institute of Porto.



Myrian Cristina Tebaldi received her MS degree from the Universidad Nacional de La Plata in 1994. She teaches physics and is a PhD student at the same university. She is involved in research on real-time image processing at Centro de Investigaciones Opticas, Argentina.



Néstor A. Bolognini obtained his PhD in physics from the Universidad Nacional de La Plata, Argentina, in 1981. He joined the Centro de Investigaciones Opticas in La Plata in 1977. He did research at the University of Stuttgart and Universidad Autónoma de Madrid. His research activities have included speckle techniques, holography, and Fourier optics. He is now involved in image processing using photorefractive materials. He is currently a researcher of CONICET (Nacional Research Council of Argentina), a professor of physics at Universidad Nacional de La Plata, and a PhD thesis adviser.

Available online at www.sciencedirect.com
SCIENCE DIRECT®
Optics Communications 221 (2003) 249–256
OPTICS COMMUNICATIONS
ELSEVIER
www.elsevier.com/locate/optcom

Experimental study of volume speckle in four-wave mixing arrangement

Angel Salazar[a], Myrian Tebaldi[b,*], Néstor Bolognini[b,1]

[a] *Universidad Pontificia Bolivariana, Medellín, Colombia*
[b] *Centro de Investigaciones Ópticas, CIOp (CONICET, CIC) and OPTIMO (Dpto. Fisicomatemática, Facultad Ingeniería, UNLP), P.O. Box 124, La Plata (1900), Argentina*

Received 20 January 2003; received in revised form 2 May 2003; accepted 8 May 2003

Abstract

We study a high frequency modulated speckle pattern in a four-wave mixing arrangement. The three-dimensional nature of the speckles is considered in the phase conjugate reflectivity evaluation which implies to analyze its dependence on the average speckle size. Also, the reflectivity is analyzed in terms of the external applied field, the probe beam ratio, and the pupil aperture diameter of the imaging system that generates the subjective speckle beam.
© 2003 Elsevier Science B.V. All rights reserved.

PACS: 42.30.Ms; 42.30.Va; 42.40.Ht

Keywords: Speckle; Photorefractive BSO crystal

1. Introduction

The photorefractive crystals of the sillenite family have a high photosensitivity and high carrier mobility which permit achievements of fast response time that makes them adequate for real time holography, optical phase conjugation, amplification of weak light signals, and image processing [1–3]. For example, the phase conjugation could be applied to the transmission of optical waves through scattering media such as the atmosphere.

The first experience of phase conjugation in a photorefractive material was done by Huignard et al. [4]. Applications of phase conjugation to nondestructive testing, image processing, and imaging through phase disturbing media have been already demonstrated [5–9]. In [10] a real time double exposure holographic interferometric method of testing phase object by using degenerate four-wave mixing DFWM with photorefractive $Bi_{12}GeO_{20}$ (BGO) crystals has been reported.

As it is well known, when a diffusing surface is illuminated by coherent light, speckles appear in front of the surface. The speckle patterns have important applications in the field of metrology

* Corresponding author. Tel.: +54-221-4840280; fax: +54-221-4712771.
E-mail address: myrianc@ciop.unlp.edu.ar (M. Tebaldi).
[1] Also Facultad de Ciencias Exactas, UNLP, Argentina.

0030-4018/03/$ - see front matter © 2003 Elsevier Science B.V. All rights reserved.
doi:10.1016/S0030-4018(03)01534-7

and image processing [11,12]. Displacements, tilts, and deformations of the input diffuser produce displacements and structural changes in the speckle patterns, which can be analyzed on the basis of the double-exposure imaged speckles, before and after deformation. In previous papers, the use of a thick photorefractive crystal as a speckle recording medium was proposed [13–16]. In [17–19], the storage in a sillenite crystal of low frequency modulated speckle patterns is analyzed. In this case, the image of a coherently illuminated diffuser is formed onto the crystal by an optical system whose pupil consists of two or more identical apertures. In addition, it has been investigated that the features of a multiple exposure specklegram are obtained by using different multiple aperture arrangements for recording [19]. Standard couple wave theory proved to be an adequate theoretical frame to interpret the different experiments mentioned above, which take advantage of the three-dimensional nature of the speckle patterns.

These previous results encourage us to introduce a new experiment where a speckled input signal is high frequency fringe modulated in a four-wave mixing arrangement. The precise knowledge of the speckle pattern recording parameters in BSO constitutes an important feature for image speckle applications. We present an analysis in which the volume speckle nature is accounted for. Three-dimensional speckles must be considered in the phase conjugate reflectivity evaluation which implies to analyze its dependence on the average speckle size. The speckle size can be easily adjusted by modifying the imaging system parameters, in our case, the pupil aperture diameter. We present in this paper an analysis of the reflectivity in terms of the external applied field, the probe beam ratio, and the pupil aperture diameter of the imaging system that generates the subjective speckle beam. Our experimental results are interpreted on the basis of the theoretical calculation proposed in [20].

It should be pointed out that the precise knowledge of the reflectivity behavior leads to the adequate selection of the experimental parameters in speckle applications concerning optical signal processing and metrology.

2. Experimental arrangement and theoretical model

Four wave mixing is a convenient method for the generation of phase conjugated waves. When a signal beam is incident into a nonlinear medium, a fourth beam is generated provided that a pair of counterpropagating laser beams exist in the medium. Referring to the experimental arrangement of Fig. 1, we consider the interaction of four beams in the photorefractive medium which can be schematized as is shown in Fig. 2.

In Fig. 1, the wavefront denoted as A_4 is the signal beam which corresponds to the image of the diffuser R formed onto the photorefractive BSO crystal by lens L_1. A pupil aperture of diameter D is located immediately in front of lens L_1. The parameters Z_0 and Z_C denote the distance from the diffuser to the lens and from the lens to the crystal, respectively. The BSO crystal is cut normal to the $\langle \bar{1}\,1\,0\rangle$ crystallographic direction (transverse electro-optic configuration). Moreover, the directions $\langle \bar{1}\,1\,0\rangle$, $\langle 0\,0\,1\rangle$, and $\langle 1\,1\,0\rangle$ coincide with the XYZ axes, respectively. Let us denote A_i $(i = 1,\ldots,4)$, the amplitudes of the interfering beams. In the crystal, the speckle beam A_4 interferes with the pump beam A_1 so that the three-dimensional image speckle grains are fringe modulated. This intensity distribution generates a space charge field in the crystal due to a charge carrier redistribution.

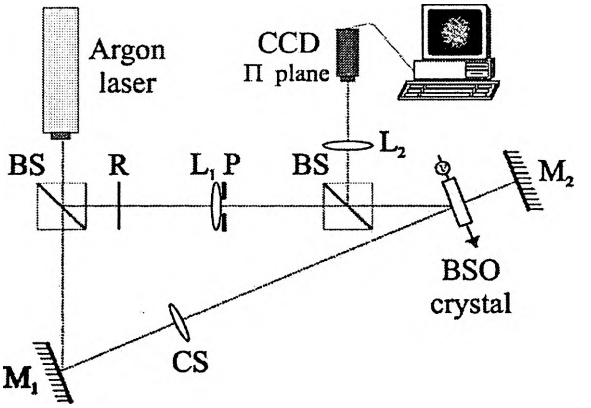


Fig. 1. Experimental set-up: R, diffuser; L_1 and L_2, lenses; CS, collimation system; M_1 and M_2, mirrors; Π, detection plane. The pupil aperture P of diameter D discussed along the text is attached to the lens L_1.

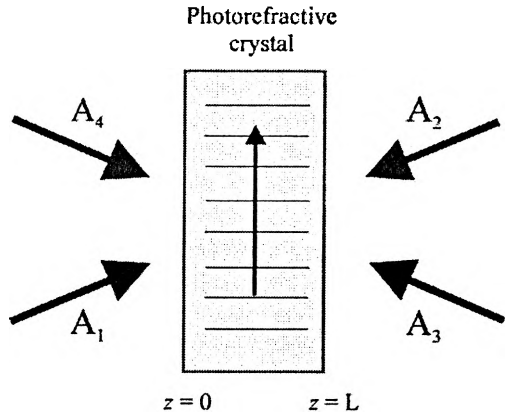


Fig. 2. Transmission grating scheme in a four-wave mixing arrangement.

As a consequence of the linear electro-optical effect that the crystal exhibits, the resulting space charge field produces a refractive index perturbation which replicates and stores the speckle intensity distribution. The transmitted part of beam A_1 is retroreflected by mirror M_2 as beam A_2, so that in the resulting wave mixing inside the crystal, the beam A_3 is generated and is proportional to the conjugate of the image speckle bearing beam A_4. Other index gratings are produced in the wave mixing phenomenon.

The predominance of one grating is common in practical situations due to the space charge field dependence on the grating period, grating orientation, and coherence between the beams. This condition is valid in our case.

An exact solution for the coupling equations is given in [20]. The solution considers only transmission gratings, which implies that the grating associated to $A_1A_4^* + A_2^*A_3$ only couples strongly the beams. This solution considers that the pump beam loses energy in the mixing procedure. By taking into account the conservation laws, it is possible to uncouple the equations and find the amplitudes $A_i(z)$ $(i = 1,\ldots,4)$ throughout the nonlinear medium, which extends between $z = 0$ and $z = L$. After calculation [20], it is possible to obtain the phase conjugate reflectivity R

$$R = \left|\frac{A_3(0)}{A_4^*(0)}\right|^2 = \left|\frac{-2C\tanh(\mu L)}{\Delta\tanh(\mu L) + (\Delta^2 + 4|C|^2)^{1/2}}\right|^2, \quad (1)$$

where

$$\mu = \frac{\gamma(\Delta^2 + 4|C|^2)^{1/2}}{2\sum_{i=1,\ldots,4} I_i}, \quad (2)$$

$$\Delta = I_2 + I_3 - I_1 - I_4 \quad (I_i = A_iA_i^*,\ i = 1,\ldots,4), \quad (3)$$

$$C = A_1A_2 + A_3A_4, \quad (4)$$

and the coupling constant γ is

$$\gamma = \frac{i\pi n_1 \exp(-i\varphi)}{\lambda\cos\theta}, \quad (5)$$

where λ is the wavelength of the beams, θ is the half angle between the incident beams,

$$n_1 = \frac{r_{41}n_0^3E_q}{2}\left[\frac{E_0^2 + E_D^2}{E_0^2 + (E_D + E_q)^2}\right]^{1/2} \quad \text{and}$$

$$\tan\varphi = \frac{E_D(E_D + E_q) + E_0^2}{E_0E_q}$$

[21], r_{41} is the electro-optic coefficient, n_0 is the refractive index at the incident wavelength, $E_D = (kT/q)(2\pi/\Lambda)$ is the diffusion field (T, temperature; k, Boltzmann constant; q, electron charge; $\Lambda = \lambda/2\sin\theta$, grating period), $E_q = (N_Aq/\varepsilon_0\varepsilon_S)(\Lambda/2\pi)$ is the maximum space charge field (N_A, acceptor density; ε_0, vaccum permittivity; ε_S, relative permittivity), and E_0, the external applied field.

By considering the boundary conditions, the parameter $|C|^2$ in Eq. (1) is obtained as a solution of equation

$$\begin{aligned} f(|C|^2) = {} & (|C|^2 - I_1(0)I_2(L))|\Delta\tanh(\mu L) \\ & + (\Delta^2 + 4|C|^2)^{1/2}|^2 \\ & + 4|C|^2|\tanh(\mu L)|^2I_4(0)I_2(L) \\ & + 2|C|^2I_4(0)(\Delta^2 + 4|C|^2)^{1/2} \\ & \times (\tanh(\mu L) + \tanh^*(\mu L)) = 0. \end{aligned} \quad (6)$$

It is convenient to define the probe beam ratio as

$$q = \frac{I_4(0)}{I_1(0) + I_2(L)} \quad (7)$$

and the pump beam ratio as

$$r = \frac{I_2(L)}{I_1(0)}. \quad (8)$$

3. Analysis of the experimental results

In our experimental arrangement the dimension of the BSO crystal is: 10 mm × 10 mm × 10 mm. To perform the theoretical calculation, the parameter values are: $N_A = 0.95 \times 10^{22}$ m^{-3} [2,22], $\varepsilon_S = 56$, $n_0 = 2.63$, $r_{41} = 4 \times 10^{-12}$ m/V. An Argon laser is employed ($\lambda = 514$ nm). The half incident angle is 27.63°. Then, the average grating period is 0.56 μm at $\lambda = 514$ nm.

Let us consider a diffuser that is rough in the scale of the optical wavelength. Under illumination by monochromatic light, the wave transmitted consists of contributions from many different scattering points. The image formed at a given point in the observation plane consists of a superposition of a multitude of amplitude spread functions, each arising from a different scattering point on the surface of the object. As a consequence of the surface roughness the various spread functions add with random phases resulting in a highly complex pattern of interference called speckle. Therefore, the image field is characterized by a randomly varying intensity and phase. The statistical properties of the speckle intensity and phase have been largely studied [11,12].

It should be taken into account that the model detailed in the previous section describes a situation where the beams A_3 and A_4 are uniform. In our case, this situation does not hold. It should be emphasized that the recorder index gratings are random in phase according to the incident speckle distribution. Each of these gratings interacts with the counterpropagating pump beam thus producing a local phase conjugated beam inside each speckle grain with random phase that "remembers" the original local speckle phase. Therefore, the reconstructed beam A_3 is a phase conjugate beam which is a speckle pattern itself governed by the same statistics as the input beam. To consider the statistical behavior, an average amplitude and intensity will be employed in the phase conjugate reflectivity calculations. That is the validity of considering average values and comparing them with the experimental results will be analyzed.

Another feature of the speckle pattern to be taken into account is its volume nature. The average diameter and length of the speckle grains are $\langle S_X \rangle \approx \lambda \cdot (Z_C/D)$ and $\langle S_Z \rangle \approx \lambda \cdot (Z_C/D)^2$, respectively ($D$ is the lens aperture diameter) [11]. Then, the speckle dimensions decrease in proportion as the aperture diameter increases. Owing that Z_C remains fixed along the experiments, the parameter D governs the speckle size.

The phase conjugate reflectivity depends on the parameter L (see Eq. (1)). Usually L coincides with the crystal depth. Note that in the proposed speckle arrangement, the wave mixing is produced inside each speckle grain. Then, in reflectivity theoretical calculation the crystal depth must be replaced by the speckle depth if the speckle grain is shorter than the crystal depth.

In accordance with the experimental arrangement values, let us fix the imaging distance $Z_C = 300$ mm. For instance, for a pupil aperture $D = 2$ mm, the average speckle depth is $\langle S_Z \rangle \approx 11$ mm, whereas for $D = 20$ mm, $\langle S_Z \rangle \approx 0.11$ mm. Therefore, according to the pupil aperture diameter, it should be evaluated which is the correct value of the parameter L in the theoretical model to be utilized, in particular see Eq. (1). For example, let us consider a 10-mm crystal thickness, then for $D = 8$ mm which implies $\langle S_Z \rangle \approx 0.7$ mm, the replacement of the parameter L by the crystal thickness brings an incorrect evaluation of the phase conjugate reflectivity because the speckle length is shorter than the crystal depth. Then, the parameter L in Eq. (1) must be written as

$$L = \begin{cases} \langle S_Z \rangle & \text{if } \langle S_Z \rangle < \text{crystal thickness} \\ \text{crystal thickness} & \text{otherwise.} \end{cases} \tag{9}$$

The total phase conjugate reflectivity is proportional to the phase conjugate reflectivity associated to an individual volume speckle grating. That is to evaluate the total reflectivity, the reflectivity belonging to a single speckle grain must be multiplied by an adequate scale factor related to the density of speckle grains.

Another point to be considered in the experimental data analysis is related with the speckle orientation. It should be noted that the on-axis speckle grains (Z-axis) are oriented along the crystal depth direction, whereas the inclination of

the off-axis speckle grains with respect to the Z-axis changes. Then, the interference between the speckle signal beam and the pump beams generates an ensemble of index gratings which has associated a dispersion $\Delta\vec{K}$ in wave vector space $\vec{K}$ related to $A_1A_4^* + A_2^*A_3$. Note that the dispersion in $\vec{K}$ values depends on the pupil aperture diameter of the imaging lens. Therefore, an ensemble of gratings with different orientations is produced. This behavior is confirmed by observing Fig. 3 where the phase conjugate image beam and the corresponding intensity profile by using pupil aperture diameter $D = 2$ and 5 mm are shown. In both cases, the crystal thickness is 10 mm and the pump beam ratio is fixed at $r = 1.138 \times 10^{-1}$. Note that on an average, the reflectivity profile belonging to $D = 5$ mm is less intense and broadened in comparison with the profile belonging to $D = 2$ mm. This broadening confirms that the diffraction spots corresponding to larger pupil aperture diameters have a higher dispersion in $\vec{K}$ vector space.

The experimental data of this section are obtained from the phase conjugate beam. This beam is itself a speckle distribution. Then, to obtain the experimental data, an average intensity profile is considered.

The experimental probe and pump ratio values are obtained by measuring the average intensity of the beams at the crystal.

On this basis, in the following, different experimental situations are evaluated by considering the dependence of the phase conjugate reflectivity on the parameters that govern the image speckle grain size, the beam intensities, and the external applied field.

3.1. Reflectivity vs. probe ratio

In this case, the pump beam intensities remain fixed as well as the lens pupil aperture diameter, whereas the speckle beam average intensity is modified. By fixing the lens pupil aperture diameter, the speckle size remains unchanged. Let us remember that the probe beam ratio q is defined as the signal (speckle) beam average intensity divided by the sum of both average pump beams, see

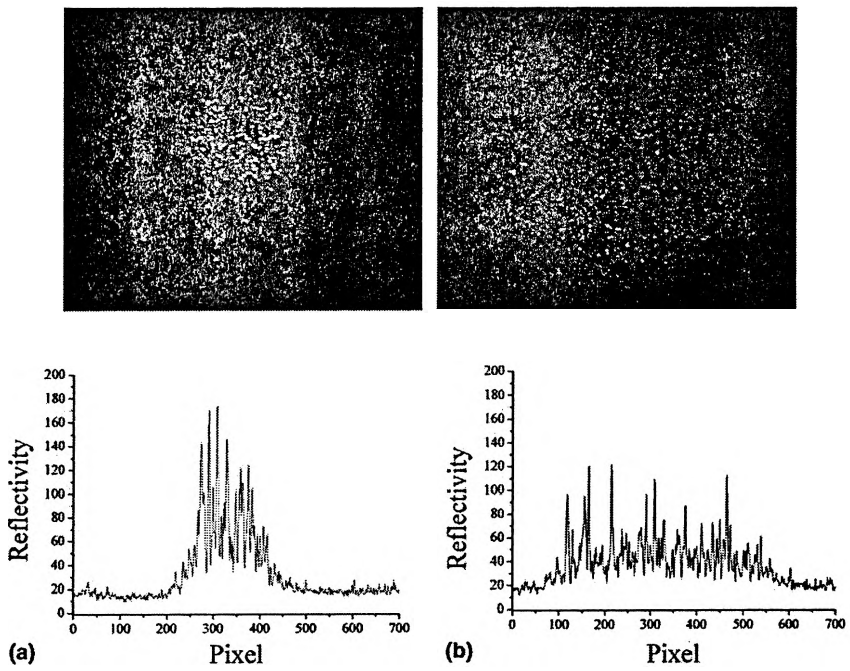


Fig. 3. Phase conjugate reflectivity image beam and their corresponding intensity profile: (a) $D = 2$ mm, (b) $D = 5$ mm ($L = 10$ mm, $r = 1.32 \times 10^{-1}$).

Eq. (7). When the average amplitude of the speckle beam is modified, the grating amplitudes $A_1A_4^* + A_2^*A_3$ change and therefore the modulation of the photorefractive gratings inside the speckle grains change as well.

In Fig. 4, the theoretical and experimental reflectivity values in terms of the probe beam ratio for a 2-mm pupil aperture diameter are shown. In all cases, the crystal thickness is 10 mm. The average pump beams remain unchanged in all the experiments and the pump beam ratio defined as the ratio between the pump beams is fixed at $r = 1.428 \times 10^{-1}$. To determine the experimental probe beam ratio values, the intensities $I_4(0)$, $I_1(0)$, and $I_2(L)$ at the crystal faces are measured. The speckle beam average intensity $I_4(0)$ is modified in our experiments producing a change in the speckle grain modulation. By increasing the speckle beam average intensity $I_4(0)$, both the probe beam ratio and the speckle grain modulation will increase and therefore the conjugate beam intensity $I_3(0)$ increases as well. Experimental results of the phase conjugation reflectivity as a function of the probe beam ratio are shown in Fig. 4. Let us remember that the phase conjugation reflectivity R is obtained as the ratio between the average intensities $I_3(0)$ and $I_4(0)$. It is observed that the phase conjugate reflectivity increases as the probe beam ratio increases. Also, in Fig. 4 a theoretical curve obtained by using Eq. (1) is shown. To perform the theoretical calculations, the parameters values indicated above are used. An agreement between the theoretical curve and experimental data is observed.

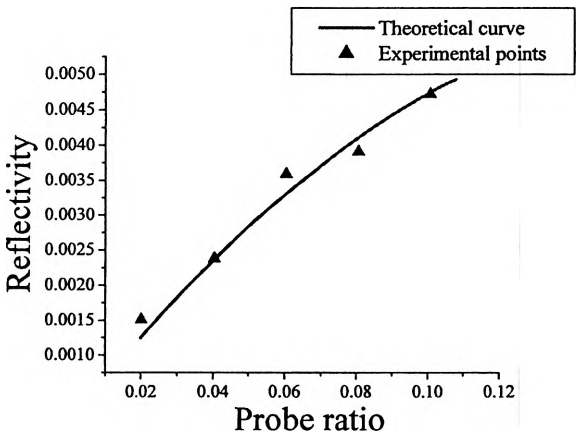


Fig. 4. Phase conjugate reflectivity vs. probe beam ratio q ($r = 1.428 \times 10^{-1}$, $L = 10$ mm, $D = 2$ mm).

3.2. Reflectivity vs. external electric field

In this case, the probe beam ratio remains fixed because neither the pump beams nor the speckle beam average intensity are changed. Also the speckle size remains unmodified. The pump beam ratio is $r = 1.32 \times 10^{-1}$, the probe beam ratio is $q = 0.1$, the crystal thickness L is 10 mm and a 2-mm lens pupil aperture diameter is employed. Under these conditions, Fig. 5 shows the theoretical curve as well as the experimental values of the phase conjugate reflectivity in terms of the applied field which varies between 1 and 8 kV. To perform the theoretical calculations, the same parameters as those employed in the experiments are used. In Fig. 5, it is observed that an applied field increase produces a reflectivity increase. The experimental data almost coincide with the theoretical prediction. However, some discrepancies exist at low field values.

3.3. Reflectivity vs. lens pupil aperture diameter

It is clear that by changing the lens pupil aperture diameter it is possible to vary the speckle

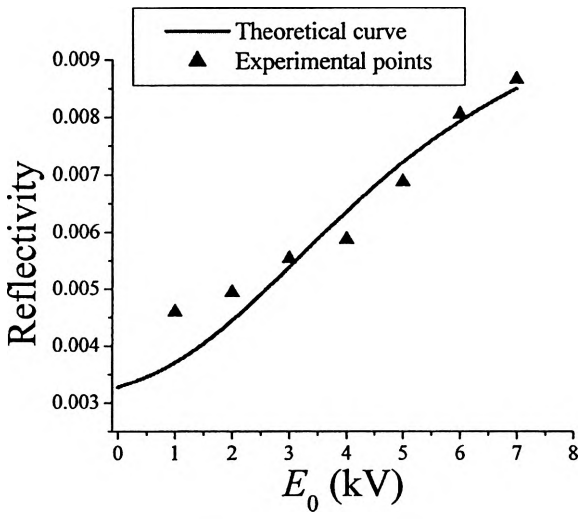


Fig. 5. Phase conjugate reflectivity vs. external applied field ($r = 1.32 \times 10^{-1}$, $q = 0.1$, $L = 10$ mm, $D = 2$ mm).

grain size, in particular the speckle depth and thereby the index grating length that modulates each registered speckle grain. Besides, when the pupil aperture diameter increases, the speckle beam average intensity increases too. So that the probe beam ratio changes. Also, the volume of the speckle grains diminishes and the speckle grain grating length reduces itself, whereas the number of speckle grains increases.

In Figs. 6 and 7, the phase conjugate reflectivity vs. the lens pupil aperture diameter is displayed by setting the pump beam ratio at $r = 1.32 \times 10^{-1}$. In both cases, the BSO crystal thickness L is fixed at 10 mm. In both figures, the theoretical curve and the experimental data are shown. In Fig. 6, no external electric field is applied to the crystal ($E_0 = 0$ kV), whereas in Fig. 7, $E_0 = 7$ kV. As it was mentioned above, if the pupil aperture diameter increases, the average speckle intensity increases and therefore, as the pump beam values remain fixed, the probe beam increases as well. In Fig. 4, it is observed that when the probe beam increases while maintaining the pupil aperture diameter fixed, the reflectivity increases. In Figs. 6 and 7, the probe beam increases but the reflectivity decreases. Note that in these cases, the pupil aperture diameter is not fixed and the decrease is a consequence of the speckle volume diminishing. By comparing both figures, it is apparent that the application of an external applied field increases

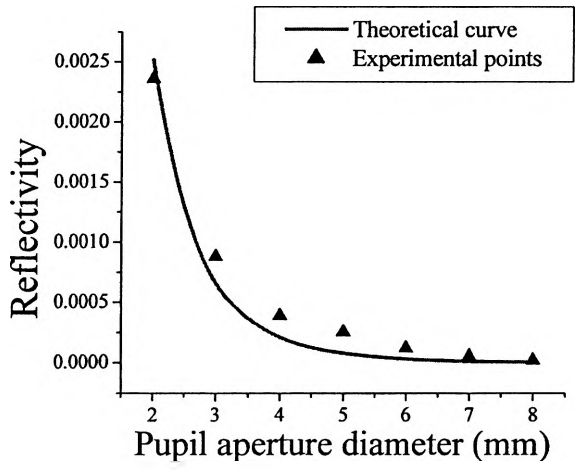


Fig. 6. Phase conjugate reflectivity vs. lens pupil aperture diameter. ($E_0 = 0$ kV, $L = 10$ mm, $r = 1.32 \times 10^{-1}$).

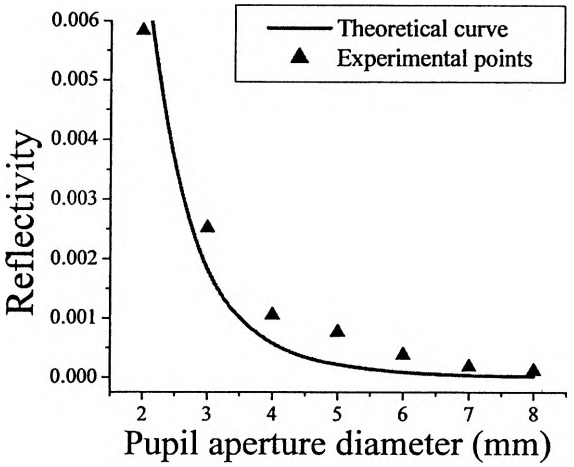


Fig. 7. Phase conjugate reflectivity vs. lens pupil aperture diameter ($E_0 = 7$ kV, $L = 10$ mm, $r = 1.32 \times 10^{-1}$).

the reflectivity, no matter the size of the speckle grain. It is observed that the increase in the aperture diameter and the corresponding decrease in the speckle length produces a reflectivity reduction which takes place independently on the increase in the probe beam ratio. Note that the same speckle size features described in this section are observed in the results of Fig. 3.

4. Conclusions

A four-wave mixing experiment produced in a BSO crystal where the signal beam bears a speckle distribution is analyzed. The speckle grains are fringe modulated due to the interference between the signal and pump beams.

The speckle pattern has a random intensity and phase distribution which leads to a local phase conjugate reflectivity. Besides, the reconstructed beam is a phase conjugate beam which is a speckle pattern itself governed by the same statistics as the input beam.

To consider this point an average amplitude and intensity must be employed in the phase conjugate reflectivity calculations.

Usually, the phase conjugate reflectivity depends on the crystal depth. In our case, the gratings are generated inside the speckle grains. This feature implies that in the theoretical calculation, if

the speckle length is shorter than the crystal depth, then the crystal depth must be replaced by the speckle length in the reflectivity expression.

A standard theoretical model which includes these features describes adequately the phase conjugate reflectivity behavior in terms of different parameters like probe beam ratio, external applied field, and speckle size. The linear model utilized predicts correctly the experimental average values.

The precise knowledge of the reflectivity behavior leads to the adequate selection of the write-in parameters in speckle applications concerning optical signal processing and metrology. An interesting application is related to the optical encryption techniques [9] that can play an important role in holographic memory systems in providing information security. As it is well known an uncorrelated set of reference beams generated by speckle patterns can be used to make it difficult to reconstruct the original beam if the codes are unknown. A possible recovering of the encrypted information could be done by a phase conjugate read out scheme. In this sense, the analysis of a phase conjugate speckle arrangement is a preliminary step to the potential use of this approach in optical encryption arrangement.

Acknowledgements

This research was performed under the auspices of CONICET, Fundación Antorchas and Facultad Ingeniería, Universidad Nacional de La Plata (Argentina). A. Salazar acknowledges the financial support of the Universidad Pontificia Bolivariana of Medellín, Colombia and gratefully acknowledges Prof. Rafael Cabanzo and Prof. Alberto Lencina for many technical discussions.

References

[1] P. Yeh, Introduction to Photorefractive Nonlinear Optics, Wiley, New York, 1993.
[2] P. Huignard, P. Günter, in: P. Huignard, P. Günter (Eds.), Photorefractive Material and their Applications I–II, Springer, Berlin, 1989.
[3] L. Solymar, D.J. Webb, A. Grunnet-Jepsen, The Physics and Applications of Photorefractive Materials, Clarendon Press, Oxford, 1996.
[4] J.P. Huignard, J.P. Herriau, P. Aubourg, E. Spitz, Opt. Lett. 4 (1979) 21.
[5] J.P. Huignard, J.P. Herriau, J.P. Pichon, A. Marrakchi, Opt. Lett. 5 (1980) 436.
[6] J.P. Huignard, H. Rajbenbach, P. Refregier, L. Solymar, Opt. Eng. 24 (1985) 586.
[7] J. Feinberg, Opt. Lett. 8 (1983) 569.
[8] Xiaodi Tan, Osamu Matoba, Tsutomu Shimura, Kazuo Kuroda, Bahram Javidi, Appl. Opt. 39 (2000) 6689.
[9] G. Unnikrishnan, J. Joseph, K. Singh, Appl. Opt. 37 (1998) 8181.
[10] Y.H. Ja, Opt. Laser Technol. 17 (1985) 36.
[11] M. Françon, Laser Speckle and Applications in Optics, Academic Press, New York, 1979.
[12] R.K. Erf, Speckle Metrology, Academic Press, New York, 1978.
[13] H.J. Tiziani, K. Leonhardt, J. Klenk, Opt. Commun. 34 (1980) 327.
[14] H.J. Tiziani, J. Klenk, Appl. Opt. 20 (1981) 1467.
[15] R. Tripathi, G.S. Pati, A. Kumar, K. Singh, Opt. Commun. 149 (1998).
[16] H.J. Tiziani, Opt. Acta 29 (1982) 463.
[17] M. Tebaldi, L. Angel Toro, M.C. Lasprilla, N. Bolognini, Opt. Commun. 155 (1998) 342.
[18] L. Angel, M. Tebaldi, M. Trivi, N. Bolognini, Opt. Commun. 168 (1999) 55.
[19] M. Tebaldi, L. Angel, M. Trivi, N. Bolognini, Opt. Eng. 39 (2000) 3232.
[20] M. Cronin-Golomb, B. Fischer, J.O. White, A. Yariv, IEEE J. Quantum Electron. QE-20 (No. 1) (1984) 241.
[21] N.V. Kukhtarev, V.B. Markov, S.G. Odulov, M.S. Soskin, V.L. Vinetskii, Ferroelectrics 22 (1979) 949.
[22] J.P. Huignard, J.P. Herriau, G. Rivet, P. Günter, Opt. Lett. 5 (1980) 102.

Procesamiento por medio de Speckle Digital

El comienzo de esta línea de investigación en el CIOp se remonta a los primeros trabajos que desarrollamos en la metrología por medio de diagramas de speckle. El speckle es la granularidad óptica característica que surge al momento de iluminar cualquier superficie rugosa con luz de alta coherencia espacial. La llegada del procesamiento digital en el campo de la óptica trajo aparejado nuevas posibilidades, tales como el manejo de los diagramas de speckle mediante software. La correlación digital de diagramas de speckle da lugar a franjas que se interpretan de la misma forma que las franjas obtenidas en la interferometría holográfica clásica. La ventaja más evidente es el procesado de las franjas por computadora, generando los mapas de fase automáticamente, ahorrando tiempo y esfuerzos. La Interferometría Digital de Diagramas de speckle (IDDS) se transformó en una herramienta práctica en la metrología óptica, generando algunas líneas de investigación colaterales. En este marco, la holografía digital, los sistemas ópticos virtuales, y más recientemente la encriptación y validación opto-digitales aprovecharon los avances del speckle digital. Nuestro grupo contribuyó activamente en esta especialidad desarrollando aplicaciones, que incluyen: obtención de líneas de nivel por holografía digital, control y análisis de la visibilidad de franjas digitales, medición del diámetro de fibras ópticas, evolución temporal de diagramas de speckle, codificación digital por polarización, técnicas digitales para la medición de alta precisión de distancias focales, técnicas de moiré digital y sus aplicaciones a la metrología, encriptación y validación digitales.

Digital-speckle processing

The beginning of this research line at CIOp traces back to the first papers we developed in metrology by means of speckle patterns. Speckle is the characteristic optical granularity arising when highly spatial coherent light illuminates any rough surface. The advent of the digital processing in the optical domain brought new possibilities, as the software manipulation of the speckle patterns. Digital correlation of speckle patterns results in fringes with the same interpretation as those obtained by classical holographic interferometry. A straightforward advantage is the fringe computer processing, where phase maps were automatically generated, saving time an efforts. Digital Speckle Pattern Interferometry (DSPI) became a new practical tool in optical metrology, generating some collateral research lines. In this frame, digital holography, Virtual Optical Imaging Systems, and more recently opto-digital encryption and validation profited from digital speckle advances. Our group actively contributed to this field developing application, including: digital holographic contouring, control and analysis of digital fringe visibility, optical fibers core measurements, speckle patterns temporal evolution, digital polarization encoding, digital techniques for high precision measurements of focal lengths, digital moiré techniques and its applications to metrology, digital encryption and validation.

Digital speckle pattern interferometry applied to a surface roughness study

Mario Lehman*
Centro de Investigaciones Opticas (CIOp)
C. C. 124-1900
La Plata, Buenos Aires, Argentina

Juan A. Pomarico
Roberto D. Torroba
Centro de Investigaciones Opticas (CIOp)
C. C. 124-1900
La Plata, Buenos Aires, Argentina
and
Universidad Nacional de La Plata
Facultad de Ingeniería
La Plata, Buenos Aires, Argentina

Abstract. Surface roughness determination is of great interest for many applications. Several methods can be found in the literature, but most of them rely on indirect evaluation of the information, such as photographic techniques. We propose a method to measure surface roughness that takes advantage of digital speckle pattern interferometry for obtaining the data, and of digital image processing for evaluating it. After defining the problem, a theoretical description is presented, and finally it is compared with experimental results, showing good agreement.

Subject terms: digital speckle pattern interferometry; speckle statistics; roughness measurement; interferometry.

Optical Engineering 34(4), 1148–1152 (April 1995).

1 Introduction

Since the fundamental work of Beckmann et al.[1] dealing with the scattering of electromagnetic waves from rough surfaces, their results have been extensively used to obtain information about surface roughness from the scattered light in the far-field region.

The correlation fringes of two speckle patterns, obtained from a rough surface under different angles of illumination, bear information about the roughness. Several optical roughness measurements techniques involve the use of a double-exposure specklegram method. The basic approach is to produce a shift in the incidence angle of the illumination beam between exposures, in order to produce, after a Fourier transformation, a set of interference fringes whose visibility depends on the rms roughness of the scattering surface.[2,3] This technique is known as angular speckle correlation (ASC).

Tribillon[4] showed that the degree of correlation between speckle patterns generated by two different wavelengths depends strongly on the surface roughness. The method based on this effect is known as spectral speckle correlation (SSC).[5]

All of the above-mentioned techniques suffer from the disadvantages of a photographic process, besides introducing a second step in the use of an optical Fourier transform. There also exist statistical methods that derive roughness information from the degree of decorrelation of imaged speckle patterns as a function of the wavelength,[6] where electronic detection and processing replaces the conventional photographic record. Electronic correlation of speckle patterns is currently accomplished by a technique called digital speckle pattern interferometry (DSPI), normally used in various metrological applications.[7–9]

In DSPI a fringe pattern is obtained using video processing by storing an initial reference image of the surface in a frame grabber and then subtracting it from the one being acquired, displaying the modulus of the result on a TV monitor. Fringes, similar to those obtained in holographic interferometry, then appear when a phase change is introduced between the reference image and the subsequent ones. As noted by Wykes,[10] the rms difference of the speckle intensities from different wavelengths is directly related to the degree of speckle correlation.

In this work we apply the DSPI technique on a single-wavelength basis, combined with the ASC method, to show that the visibility of the correlation fringes in this case also depends on the roughness of the object surface. A theoretical approach to the proposed technique is also given.

2 Theoretical Description

Let us suppose the situation sketched in Fig. 1. A plane wave Σ illuminates a rough surface S at an angle of incidence θ with respect to the normal to the surface. In our case, the surface is considered to be formed from a set of n identical scattering elements of random height following a normal distribution of standard deviation σ and zero mean. A CCD camera images the surface on the detector array. A separate reference beam is added to the first one via the beamsplitter BS. Since the DSPI detects a quantity proportional to $|\langle (I_1 - I_2)^2 \rangle^{1/2}|$, we examine how this quantity varies with a tilt of the beam illuminating the surface.

To do that we assume

$$A_1 = A_0 \sum_{j=1}^{n} \exp\left\{\frac{2\pi i}{\lambda}[Z_j(1+\cos\theta)+\phi_0]\right\} + A_R \exp(i\phi_R) \tag{1}$$

*Current affiliation: Universidad de Bahía Blanca, Buenos Aires, Argentina.

Paper 09074 received July 12, 1994; revised manuscript received Nov. 1, 1994; accepted for publication Nov. 1, 1994.
© 1995 Society of Photo-Optical Instrumentation Engineers. 0091-3286/95/$6.00.

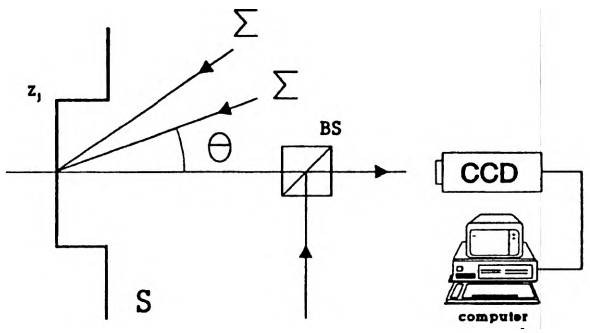


Fig. 1 Schematic representation of two plane waves, Σ and Σ′, illuminating a rough surface at two different angles, θ and θ + Δθ.

to be the field amplitude detected by the CCD array when the surface is illuminated at an angle θ. In this equation the first term denotes the speckle pattern amplitude field, where A_0 is the light amplitude scattered by one element, Z_j is the height of the jth scattering element, and ϕ_0 allows for the constant phase of the incident light. In the second term, A_R is the amplitude of the reference beam and ϕ_R its phase. In the following, all calculations are assumed to be made at the same point (x,y).

Similarly, if the illumination direction is changed by an amount Δθ, the new field amplitude can be described by

$$A_2 = A_0 \sum_{j=1}^{n} \exp\left(\frac{2\pi i}{\lambda}\{Z_j[1+\cos(\theta+\Delta\theta)]+\phi_0\}\right) + A_R \exp(i\phi_R) \ . \tag{2}$$

Equations (1) and (2) can be rewritten as the following more compact expressions:

$$A_1 = A_0 e^{i\phi} \sum_{j=1}^{n} e^{i\alpha Z_j} + A_R e^{i\beta} \tag{3}$$

and

$$A_2 = A_0 e^{i\phi} \sum_{j=1}^{n} e^{i\gamma Z_j} + A_R e^{i\beta} \ , \tag{4}$$

where $e^{i\phi}$ is the common phase term $\exp[i2\pi\phi_0/\lambda]$, A_R is the amplitude of the reference beam, and α and γ are abbreviations for $(2\pi/\lambda)(1+\cos\theta)$ and $(2\pi/\lambda)[1+\cos(\theta+\Delta\theta)]$, respectively.

To obtain $\langle (I_1 - I_2)^2 \rangle$ we need to calculate $\langle I_1^2 \rangle$, $\langle I_2^2 \rangle$ and $\langle I_1 I_2 \rangle$, since

$$\langle (I_1 - I_2)^2 \rangle = \langle I_1^2 \rangle + \langle I_2^2 \rangle - 2\langle I_1 I_2 \rangle \ . \tag{5}$$

Using Eqs. (3) and (4) we obtain

$$I_1 = A_1 A_1^* = A_0^2 \sum_{j=1}^{n} e^{i\alpha Z_j} \sum_{k=1}^{n} e^{-i\alpha Z_k} + A_R^2 + A_0 B e^{i(\phi-\beta)} \sum_{j=1}^{n} e^{i\alpha Z_j} + A_0 A_R e^{-i(\phi-\beta)} \sum_{j=1}^{n} e^{-i\alpha Z_j} \tag{6}$$

and

$$I_2 = A_2 A_2^* = A_0^2 \sum_{j=1}^{n} e^{i\gamma Z_j} \sum_{k=1}^{n} e^{-i\gamma Z_k} + A_R^2 + A_0 A_R e^{i(\phi-\beta)} \sum_{j=1}^{n} e^{i\gamma Z_j} + A_0 A_R e^{-i(\phi-\beta)} \sum_{j=1}^{n} e^{-i\gamma Z_j} \ . \tag{7}$$

Equations (6) and (7) can be reduced to the following expressions:

$$I_1 = A_0^2 \left(n + 2 \sum_{\substack{j=1 \\ j<k}}^{n-1} \cos\alpha(Z_j - Z_k) \right) + A_R^2 + 2A_0 A_R \sum_{j=1}^{n} \cos(\alpha Z_j + \phi - \beta) \ , \tag{8}$$

$$I_2 = A_0^2 \left(n + 2 \sum_{\substack{j=1 \\ j<k}}^{n-1} \cos\gamma(Z_j - Z_k) \right) + A_R^2 + 2A_0 A_R \sum_{j=1}^{n} \cos(\gamma Z_j + \phi - \beta) \ . \tag{9}$$

Squaring Eq. (8) yields

$$\begin{aligned} I_1^2 = {} & A_0^4 n^2 + 4nA_0^4 \sum_{j<k} \cos\alpha(Z_j - Z_k) \\ & + 4A_0^4 \sum_{j<k} \cos^2\alpha(Z_j - Z_k) + A_R^4 \\ & + 8A_0^4 \sum_{\substack{j<k \\ l<m \\ j\neq l,\ k\neq m}} \cos\alpha(Z_j - Z_k)\cos\alpha(Z_l - Z_m) \\ & + 4A_0^2 A_R^2 \sum_{j=1}^{n} \cos^2(\alpha Z_j + \phi - \beta) \\ & + 8A_0^2 A_R^2 \sum_{j<k} \cos(\alpha Z_j + \phi - \beta)\cos(\alpha Z_k + \phi - \beta) \\ & + 2A_0^2 A_R^2 \left(n + 2 \sum_{j<k} \cos\alpha(Z_j - Z_k) \right) \\ & + 4A_0^3 A_R n \sum_{j=1}^{n} \cos(\alpha Z_j + \phi - \beta) \\ & + 8A_0^3 A_R \sum_{j<k} \cos\alpha(Z_j - Z_k)\cos(\alpha Z_l + \phi - \beta) \\ & + 4A_0 A_R^3 \sum_{j=1}^{n} \cos(\alpha Z_j + \phi - \beta) \ , \end{aligned} \tag{10}$$

from which we obtain, taking into account[11] that the mean value of the cosine function evaluates to zero when the phase is uniformly distributed in the interval $[-\pi,\pi]$,

$$\langle I_1^2\rangle = A_0^4 n^2 + 4A_0^4\frac{n^2-n}{4} + A_R^4 + 4A_0^2A_R^2\frac{n}{2} + 2A_0^2A_R^2 n \ . \tag{11}$$

Clearly, since this last expression for $\langle I_1^2\rangle$ does not depend on either α or on γ, the same result holds for $\langle I_2^2\rangle$.

To obtain the third term in Eq. (5) we need now to calculate the mean value of the product $I_1 I_2$:

$$\begin{aligned} I_1 I_2 = A_0^4\Bigg[& n^2 + 2n\Bigg(\sum_{j<k}\cos\alpha(Z_j-Z_k) + \sum_{j<k}\cos\gamma(Z_j-Z_k)\Bigg) \\ & + 4\sum_{j<k}\cos\alpha(Z_j-Z_k)\sum_{j<k}\cos\gamma(Z_j-Z_k)\Bigg] \\ & + A_R^4 + 4A_0^2A_R^2\Bigg(\sum_{j=1}^{n}\cos(\alpha Z_j+\phi-\beta)\sum_{j=1}^{n} \\ & \times\cos(\gamma Z_j+\phi-\beta)\Bigg)\Bigg] + A_0^2A_R^2\Bigg[2n+2\Bigg(\sum_{j<k} \\ & \times\cos\alpha(Z_j-Z_k)+\sum_{j<k}\cos\gamma(Z_j-Z_k)\Bigg)\Bigg] + 2A_0^3A_R \\ & \times\Bigg[\Bigg(n+2\sum_{j<k}\cos\alpha(Z_j-Z_k)\Bigg)\sum_{j=1}^{n}\cos(\gamma Z_j+\phi-\beta) \\ & + \Bigg(n+2\sum_{j<k}\cos\gamma(Z_j-Z_k)\Bigg)\sum_{j=1}^{n}\cos(\alpha Z_j+\phi-\beta)\Bigg] \\ & + 2A_0A_R^3\Bigg(\sum_{j=1}^{n}\cos(\alpha Z_j+\phi-\beta)+\sum_{j=1}^{n} \\ & \times\cos(\gamma Z_j+\phi-\beta)\Bigg) \ . \end{aligned} \tag{12}$$

Taking into account that

$$\cos\alpha(Z_j-Z_k)\ \cos\gamma(Z_j-Z_k) = \frac{1}{2}\Bigg\{\cos\Big[(\alpha+\gamma)(Z_j-Z_k)\Big] + \cos\Big[(\alpha-\gamma)(Z_j-Z_k)\Big]\Bigg\} \ ,$$

the mean value $\langle\cos\alpha(Z_j-Z_k)\ \cos\gamma(Z_j-Z_k)\rangle$ evaluates to

$$\frac{1}{2}\langle\cos(\alpha-\gamma)(Z_j-Z_k)\rangle \ .$$

Taking into account that we assumed a normal distribution with standard deviation σ and zero mean, this last equation can be expressed as

$$\frac{1}{2}\langle\exp[i(\alpha-\gamma)(Z_j-Z_k)]\rangle \ . \tag{13}$$

This ensemble average evaluates to

$$\frac{1}{2}\exp\Bigg(-\frac{1}{2}(\alpha-\gamma)^2\langle(Z_j-Z_k)^2\rangle\Bigg) \tag{14}$$

and $\langle(Z_j-Z_k)^2\rangle = 2\sigma^2(1-r_{jk})$, where r_{jk} is the normalized surface correlation. Since from Eq. (12) we have $j\neq k$, and if the individual steps Z_j are uncorrelated with each other, then Eq. (13) reduces to

$$\frac{1}{2}\exp[-(\alpha-\gamma)^2\sigma^2] \ . \tag{15}$$

With this result, the final expression for $\langle I_1 I_2\rangle$ becomes

$$\begin{aligned} \langle I_1 I_2\rangle = A_0^4\Bigg(n^2 + 2\frac{n^2-n}{2}\exp(-\xi^2\sigma^2)\Bigg) \\ + A_R^4 + 2nA_0^2A_R^2\exp\Bigg(-\frac{\xi^2\sigma^2}{2}\Bigg) + 2nA_0^2A_R^2 \ , \end{aligned} \tag{16}$$

where $\xi=\alpha-\gamma=(2\pi/\lambda)[\cos\theta-\cos(\theta+\Delta\theta)]\approx(2\pi/\lambda)\sin\theta\,\Delta\theta$. From Eqs. (11) and (16) the following expression for $\langle(I_1-I_2)^2\rangle$ can be obtained:

$$\begin{aligned} \langle(I_1-I_2)^2\rangle = 2nA_0^2\Bigg\{(n-1)A_0^2[1-\exp(-\xi^2\sigma^2)] \\ + 2A_R^2\Bigg[1-\exp\Bigg(-\frac{\xi^2\sigma^2}{2}\Bigg)\Bigg]\Bigg\} \ . \end{aligned} \tag{17}$$

The number of scatterers producing the speckle field, n, is very large, and thus $n-1\approx n$. In addition, we suppose that $nA_0^2 = A_S^2$ represents the total light intensity emanating from the surface and A_R can be chosen to be equal to A_S. With these assumptions, the final expression for $\langle(I_1-I_2)^2\rangle$ results:

$$\langle(I_1-I_2)^2\rangle = 2A_S^4\Bigg[3-\exp(-\xi^2\sigma^2)-2\exp\Bigg(-\frac{\xi^2\sigma^2}{2}\Bigg)\Bigg] \ . \tag{18}$$

We are primarily concerned with the determination of the local visibility V_L and its variation with respect to $\Delta\theta$. By using the substitution $\langle(I_1-I_2)^2\rangle = \langle I^2\rangle$, the local visibility is defined as

$$V_L = \frac{\langle I^2\rangle_{\max}^{1/2} - \langle I^2\rangle_{\min}^{1/2}}{\langle I^2\rangle_{\max}^{1/2} + \langle I^2\rangle_{\min}^{1/2}} \ . \tag{19}$$

In practice, it is equivalent to measure the global visibility through the fringe pattern that arises because of the tilt $\Delta\theta$ of the illuminating beam, defined by the equation

$$V = \frac{I_{\max}-I_{\min}}{I_{\max}+I_{\min}} \ , \tag{20}$$

where $I_{\max}$ and $I_{\min}$ are the maximum and minimum intensity values present in the fringe pattern, respectively.

For the case of $\Delta\theta=0$, we have $\langle(I_1-I_2)^2\rangle^{1/2}=0$ (no fringes are present), and Eq. (19) becomes undefined. The corresponding visibility can be taken as one, as for all other cases, having $\Delta\theta\neq0$, lower values are obtained.

Figure 2 shows the variation of the local visibility defined in Eq. (19) versus the rotation $\Delta\theta$ for $\sigma=6.3$ μm.

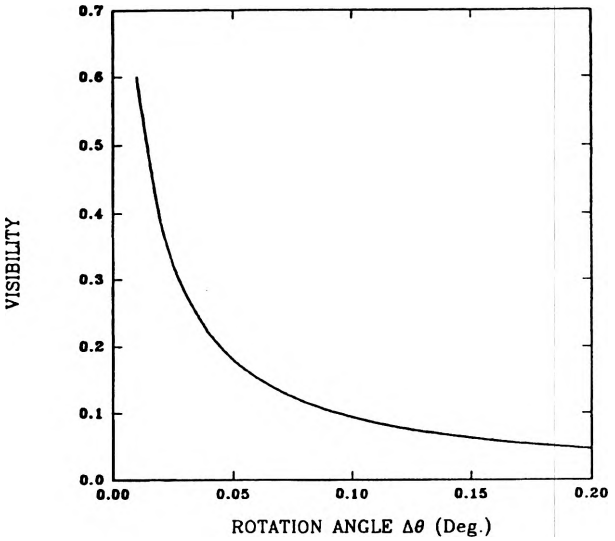


Fig. 2 Theoretical variation of the visibility as a function of the change in the illumination direction, Δθ.

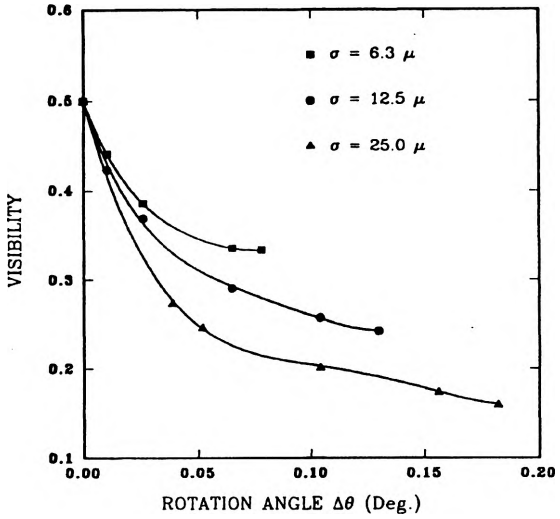


Fig. 4 Visibility of the fringe pattern as a function of Δθ for three different values of the surface roughness. Solid curves represent the best fit to the experimental data.

3 Experimental Results

The experimental arrangement of Fig. 3 was used to reproduce the conditions used in the theoretical approach. A 10-mW HeNe laser beam was divided by the beamsplitter BS1. One of the beams obtained in this way was expanded, collimated, and used to illuminate the rough surface under study at an angle θ with its normal. The second beam was overlapped with the image of the surface, which is a speckle pattern, at the detector array of the CCD camera by using the beamsplitter BS2. It is clear that the optical system does not resolve the individual scatterers. The video signal from the camera is sent to the frame grabber for further processing.

At the frame grabber the following operation, which can be accomplished at near-real-time rates, is performed: a first image of the surface is acquired and stored as a reference, the subsequent images coming from the camera are subtracted from the first one, and the result is then displayed, in modulus, on a TV monitor. If an image is obtained under the same illumination conditions as the reference, then no differences are present between them, and the TV monitor appears dark. On the other hand, when the beam illuminating the surface is rotated by an angle Δθ, a linear phase change occurs, altering the speckle pattern generated by the surface. At points where this phase change equals $2m\pi$, with m an integer, the speckle pattern reproduces itself and the TV monitor shows a dark spot. On the contrary, for phase changes other than $2m\pi$, the subtraction gives a nonzero value and the monitor shows a spot whose gray level varies accordingly to the phase change. Thus the monitor shows a set of fringes immersed in speckle noise and following the zones of constant phase change. Both the spatial frequency and the visibility of these fringes depends on the rotation Δθ of the beam illuminating the surface, as demonstrated above.

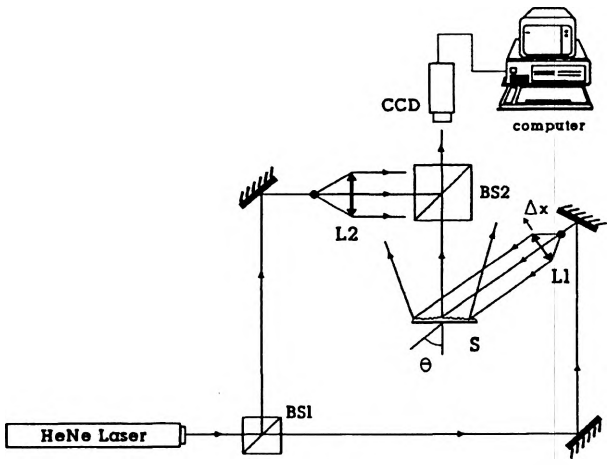


Fig. 3 Experimental DSPI setup for obtaining speckle correlation fringes and measuring the angular variation Δθ.

In our experiment, the rotation Δθ was obtained by a lateral shift Δx of the collimating lens L1, which was mounted on a translator driven by a stepper motor capable of a minimum displacement of 2 μm. Lens L1 was chosen to have a focal length of 22 cm. Thus, the rotation Δθ can be obtained from the simple equation

$$\tan \Delta\theta = \frac{\Delta x}{f} \approx \Delta\theta \ ,$$

with Δx varying from several microns to a few millimeters.

Although this produces not only a rotation but also a displacement of the object beam, using plane waves ensures that all phase changes are only a consequence of the rotation, provided that the whole field of view of the camera (which can always be chosen smaller than the illuminated area) remains unchanged.

The curves plotted in Fig. 4 (fringe visibility as a function of Δθ) were obtained for three different values of the surface roughness, $\sigma = 6.3$, 12.5, and 25 μm, and for $\theta = 19$ deg,

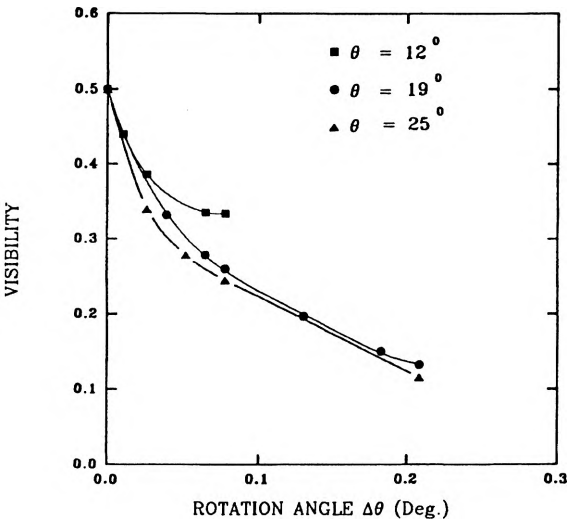


Fig. 5 Best-fit curves for the visibility of the fringe pattern as a function of $\Delta\theta$ for three different values of the initial illumination angle θ and for a fixed value of the surface roughness, $\sigma = 6.3$ μm.

using standard surface roughness test plates. Clearly the visibility drops faster as the roughness increases, as can be expected from Eq. (18). Visibility measurements were carried out using an indirect digital method,[12] where a peak ratio at a Fourier plane is measured, instead of direct fringe visibility analysis. In this way, speckle noise is reduced and the error in the visibility remains around 1.4%.

For a given roughness, if the incidence angle θ of the beam illuminating the surface is changed, the maximum value of $\Delta\theta$ for which a variation in the fringes' visibility can be detected also changes, as illustrated in Fig. 5 for $\sigma = 6.3$ μm and $\theta = 12$, 19, and 25 deg. The sensitivity of the method (which is limited by the fringe density) can thus be controlled by setting the proper value of θ.

For both, Figs. 4 and 5, solid curves represent the best fit to the experimental values.

4 Conclusions

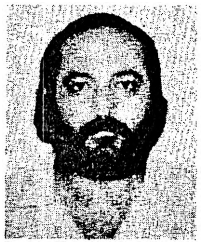
A method for surface roughness determination using digital speckle pattern interferometry has been described theoretically and tested experimentally, showing good agreement. The experimental setup requires an image processor but not sophisticated optical components, making the method suitable, for example, for industrial applications. In addition, the whole process can be accomplished digitally, thus reducing the time needed for a measurement. The range of operation can be controlled by adjusting the parameters.

Acknowledgments

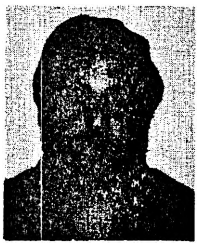
This work was supported by Fundación Antorchas (Argentina), the Alexander Von Humboldt Foundation (Germany), and CONICET PID Nr.:3974/912 (Argentina). We also thank B. Ruiz for her valuable help with the mathematics involved in this work.

References

1. P. Beckmann and A. Spizzichino, *The Scattering of Electromagnetic Waves from Rough Surfaces*, Pergamon, Oxford (1963).
2. D. Léger, E. Mathieu, and J. C. Perrin, "Optical surface roughness determination using speckle correlation technique," *Appl. Opt.* **14**(4), 872–877 (1975).
3. D. Léger and J. C. Perrin, "Real-time measurement of surface roughness by correlation of speckle patterns," *J. Opt. Soc. Am.* **66**(11), 1210–1217 (1976).
4. G. Tribillon, "Correlation entre deux speckle obtenus avec deux longueurs d'onde—application à la mesure de la rugosité moyenne," *Opt. Commun.* **11**(2), 172–174 (1974).
5. B. Ruffling, "Application of speckle-correlation methods to surface-roughness measurement: a theoretical study," *J. Opt. Soc. Am. A* **3**(8), 1297–1304 (1986).
6. D. J. Schertler and N. George, "Roughness determination by speckle-wavelength decorrelation," *Opt. Lett.* **18**(5), 391–393 (1993).
7. C. Joenathan and R. Torroba, "Simple electronic speckle-shearing-pattern interferometer," *Opt. Lett.* **15**(20), 1159–1161 (1990).
8. N. Bolognini, H. Rabal, and R. Torroba, "Single-beam digital holographic contouring," *Appl. Opt.* **31**(8), 1009–1011 (1992).
9. J. Pomarico, R. Arizaga, H. Rabal, and R. Torroba, "Digital holographic contouring," *Opt. Commun.* **98**(4), 257–260 (1993).
10. C. Wykes, "De-correlation effects in speckle-pattern interferometry. 1. Wavelength change dependent de-correlation with application to contouring and surface roughness measurement," *Opt. Acta* **24**(5), 517–532 (1977).
11. J. W. Goodman, "Statistical properties of laser speckle patterns," Chapter 1 in *Laser Speckle and Related Phenomena*, J. C. Dainty, Ed., pp. 9–26, Springer-Verlag, Berlin (1975).
12. J. Pomarico and R. Torroba, "Digital visibility measurements by Fourier analysis," *Optik* **95**(4), 152–154 (1994).



Mario Lehman received his MS degree from the Universidad del Centro de la Provincia de Buenos Aires, Tandil, Argentina, and teaches physics at the Universidad Nacional del Sur, Bahía Blanca. He is working at the Optical Research Center (CIOp) toward his PhD in the field of digital speckle pattern interferometry and optical metrology.



Juan A. Pomarico received his MS and PhD degrees from the University of San Luis, Argentina, in 1985 and 1993, respectively. He teaches physics in the Faculty of Engineering of the University of La Plata and is a researcher at the Optical Research Center (CIOp), La Plata. He has been a research fellow of the German Academic Exchange Service (DAAD) at Stuttgart University (Germany), and of the International Center for Theoretical Physics (ICTP), Italy. His research interests include TV holography and optical metrology.



Roberto D. Torroba received his MS and PhD degrees in physics from the University of La Plata, Argentina, in 1977 and 1982, respectively. He is currently a professor at the Faculty of Engineering of the University of La Plata. Since 1977 he has been in the Optics Group at the Optical Research Center (CIOp), La Plata. He is a member of the Argentinian Research Council (CONICET) and an associate researcher at the International Center for Science and High Technology (ICS), Trieste, Italy. He has been a fellow of the Alexander von Humboldt Stiftung (Germany), the German Academic Exchange Service (DAAD), the Organization of American States, and the Valencian Community (Spain). His current research interests include TV holography and optical metrology.

Digital polarization-encoding technique for optical logic operations

Roberto Torroba, Rodrigo Henao,* and Claudia Carletti

Centro de Investigaciones Opticas, Casilla de Correo 124, La Plata, Argentina 1900

Received July 22, 1996

We implement optical logic operations, using a polarization-encoding architecture based on digital speckle pattern interferometry (DSPI). The method is based on the intensity dependence of DSPI on the rotation of the polarization direction in the paths of the interferometer between acquisition of frames. The 16 two-input logic operations can be achieved and stored in a host computer. This scheme also offers the possibility of creating dynamic logic gates. © 1996 Optical Society of America

In recent years, interest in the design of optical processors has constantly grown. Various methods have been proposed for implementing logic operations. Early versions were based on spatial filtering,[1,2] where the logic gates were characterized by either grating structures or scattering structures. Modern approaches also exploited the use of laser-excited gratings in dye-doped solids.[3] Successful implementations were based on the photorefractive effect, which was extensively studied in connection with optical computing.[4] Photorefractive media were used to encode, transmit, and process information concerning logic operations under different architectures. Some of these techniques used, for example, phase-matched diffraction and holographic interference[5] and multiwavelength encoding and processing.[6] Polarization-encoded optical logic by use of photoinduced gratings in photorefractive crystals[7] is particularly interesting, as such a scheme offers the possibility of creating dynamic logic gates. Including multiwavelength operations in this scheme offers the advantage of spectral parallelism in information processing.[8]

In the last context, the authors' preferences are oriented to make use of the representation of the logic states produced by two orthogonal states of linearly polarized light. Advantages of this approach are that no energy is lost, it is better suited for cascading operations, it requires no filtering or transformations, and it provides not only the result but also the negation of the result. Also, the requirements of intensity equalization and critical alignment are eliminated. Our objective is to use a digital approach based on the polarization-encoding concept as a means to simplify the truth table architectures. In this Letter we propose and demonstrate the implementation of polarization-encoded optical logic in a digital speckle pattern interferometer (DSPI) scheme. The DSPI scheme is a technique widely used in connection with metrological applications that is based on the digital correlation of speckle patterns.[9-11] The basic configuration that we use is shown in Fig. 1.[12] The laser beam is divided in two by a beam splitter, and then each beam is expanded. The input objects, A and B, are made such that they introduce a local change in the polarization direction in each beam. The polarization-modulated beams are brought together to illuminate the surface. This is equivalent to obtaining two different speckle patterns from the same surface, one that serves as a reference wave and the other as an object wave. The resulting speckle pattern is recorded by a CCD camera and then processed with a host computer. The method relies on the speckle correlation concept, in which the correlation operation is performed by subtraction.

The technique combines holographic and speckle interferometry with an in-line reference beam and an image-plane hologram setup, following the methods of double-exposure holography. For comparison, a stored reference frame is continually subtracted from the incoming data. In the standard DSPI procedure, any optical path difference produced by a screen deformation introduces a phase change in the resulting speckle pattern of the actual frame. As a result, speckle correlation fringes are displayed on a TV monitor almost in real time, with the same interpretation as for those fringes obtained by holographic interferometry.

The visibility of such fringes depends on several parameters. Assuming linearly polarized laser light, we

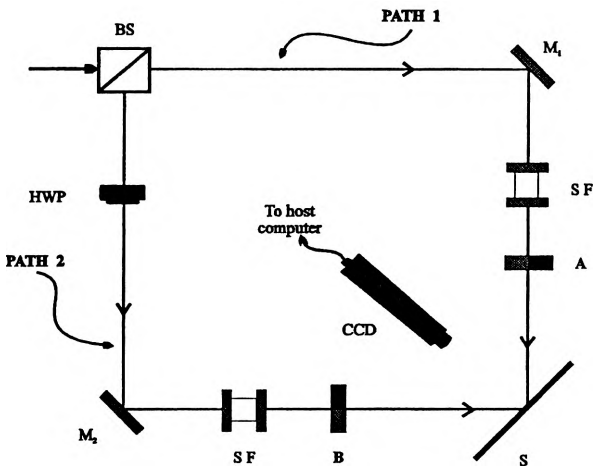
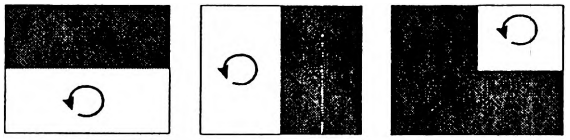


Fig. 1. DSPI setup: BS, beam splitter; M_1, M_2, mirrors; HWP, polarization rotator; SF's, beam expanders; A, B, input objects; S, reference diffusing surface; CCD, charge-coupled device camera.

0146-9592/96/231918-03$10.00/0 © 1996 Optical Society of America



(a) (b) (c)

Fig. 2. Half-wave plate cell arrays in the input objects. (a), (b) Two-input objects. (c) Cell placed in one path of the interferometer. The curved arrows represent the sense of rotation induced by the half-wave plate.

note that, if a rotation is induced in the polarization direction in one path of the interferometer, a decrease in the fringe visibility can be observed.[13] This indicates that the DSPI is polarization sensitive. The mechanism by which the polarization changes are stored in the DSPI has already been studied.[14]

If we denote the intensity distribution in the TV monitor that arises from the operation of a pixel-to-pixel subtraction by $I(x, y)$ and assume that there are no phase disturbances between the reference frame and the actual one, then

$$I(x, y) = 4|A|^2 \sin^2 \Delta\theta \cos \varphi(x, y), \quad (1)$$

where A is the complex amplitude, which is assumed to be constant and equal in both paths, $\varphi(x, y)$ represents the phase of the resulting speckle pattern, and $\Delta\theta$ is the variation of the angle formed by the polarization direction in the stored reference frame with respect to the actual frames. When the directions coincide in both the reference and the actual frames, that is, $\Delta\theta = 0°$ or $\Delta\theta = 180°$, the TV screen is black; otherwise, if $\Delta\theta = 90°$ or $\Delta\theta = 270°$, the screen is white with a speckled background. Thus, after using a digital decoding procedure, we turn the polarization encoding into an intensity display on the TV monitor, which assigns a different intensity level to each recorded polarization rotation according to Eq. (1). The DSPI offers a

Operation	Path 1	Path 2	Experimental Result
0	Without Change	Without Change	
1	Polarization direction rotated 90°	Without Change	
A	Object A	Without Change	
B	Without Change	Object B	
$\overline{A}$	Object A rotated 180°	Without Change	
$\overline{B}$	Without Change	Object B rotated 180°	
A OR B	Object A	Object B and Object C rotated 180°	
$\overline{A}$ OR B	Object A	Object B rotated 180° and Object C rotated 270°	
A OR $\overline{B}$	Object A	Object B rotated 180° and Object C rotated 90°	
A NOR B	Object A	Object B rotated 180° and Object C rotated 180°	
A AND B	Object A	Object B rotated 180° and Object C	
$\overline{A}$ AND B	Object A	Object B and Object C rotated 90°	
A AND $\overline{B}$	Object A	Object B and Object C rotated 270°	
A NAND B	Object A	Object B and Object C	
A EQV B	Object A	Object B rotated 180°	
A XOR B	Object A	Object B	

Fig. 3. Scheme showing how to perform all 16 logical operations and the corresponding experimental results.

means of easily implementing dynamic logic gates. The encoding concept is explained as follows: The two-input objects are array cells made of half-wave plates, as shown in Figs. 2(a) and 2(b). The arrows indicate the direction in which the half-wave plate switches the input direction of the linearly polarized light that is used as illumination source. The shaded areas indicate that no half-wave plate is present. A third array cell, displayed in Fig. 2(c), is placed in one path of the interferometer. This array is used to break the parity generated by rotation combinations that repeat some output results. In all cases, the reference frame is first stored without the object. We obtain the logical level 0 simply by not altering the setup. The TV monitor is black in this case. In the following, all rotations are clockwise. Level 1 is represented by a 90° rotation of the polarization direction in one path of the setup, which is accomplished by the polarization rotator. In this case the monitor screen is white. We display both input A and input B by inserting each separately into any of the interferometer paths. We obtain the negations of input A ($\overline{A}$) and input B ($\overline{B}$) by a 180° rotation of their original positions. The remaining operations are presented by examples. We accomplish operation A XOR B by simultaneously inserting the two input objects, A and B, in their original positions into separate paths of the interferometer. A EQV B is performed with the above configuration but with B rotated by 180°. We obtain the gate A NAND B by maintaining both inputs in their original positions on separate paths of the interferometer but inserting the third array behind B, with the half-wave plate in the upper-right position. By successively rotating this last array by 90°, we get $\overline{A}$ AND B, A OR B, and A AND $\overline{B}$. Rotating B by 180° and rotating C by 0°, 90°, 180°, 270°, we get A AND B, A OR $\overline{B}$, A NOR B, and $\overline{A}$ OR B, respectively. Details of the operations can be found in Fig. 3.

We have proposed and implemented a way to achieve all 16 two-input binary logic gates by a digital polarization-encoding scheme. The method relies on the intensity variations induced in a DSPI arrangement in which the polarization direction is altered with respect to the first reference frame acquired. The entire logic operation can be performed without alterations of the optical setup or auxiliary devices. The technique is independent of diffraction efficiencies and requires no transformations or filtering. The accuracy of the operations does not depend on critical alignment conditions. The intensity throughput is maximum throughout the whole process, as the half-wave plate rotator causes no loss of energy. In our case the signal-to-noise ratio is given in terms of the visibility of the resulting logic gate, which in all cases is approximately 0.6. The principal advantage over a standard electronic gate is the parallelism in processing that can be achieved by use of a more complex matrix as the input object, without the need for multiple operation units. Although we performed our experiments in a non-real-time realization, dynamic logic gates can be easily implemented. By use of a polarization-switchable device as an input object, such as a Pockels cell, near-real-time application can be achieved. The main limitation in the time between operations is set by the frame-acquisition rate of the video equipment.

This study was supported by grants from the Fundación Antorchas (Argentina), the Universidad Nacional de La Plata (Argentina), the Alexander von Humboldt Foundation (Germany), and the Third World Academy of Sciences (93-389 RG/PHYS/LA). R. Henao acknowledges the assistance of the Mutis Programme (Spain) and thanks C. Carletti of the fellowship Becario de la Comision de Investigaciones Cientificas (Argentina).

*Present address, Antioquia Invistigaciones y Recursos en Tecnologia, Apartado Aereo 2073, Medellín, Colombia.

References

1. H. O. Bartelt, A. W. Lohmann, and E. E. Sicre, J. Opt. Soc. Am. A **1,** 944 (1984).
2. A. W. Lohmann and J. Weigelt, Opt. Commun. **52,** 255 (1984).
3. G. R. Kumar, B. P. Singh, K. D. Rac, and K. K. Sharma, Opt. Lett. **15,** 245 (1990).
4. P. Yeh, *Introduction to Photorefractive Nonlinear Optics* (Wiley, New York, 1993).
5. P. Yeh, S. Campbell, and S. Zhou, Opt. Lett. **18,** 903 (1993).
6. W. Wu, S. Campbell, S. Zhou, and P. Yeh, Opt. Lett. **19,** 646 (1994).
7. W. Wu, S. Campbell, S. Zhou, and P. Yeh, Opt. Lett. **18,** 1742 (1993).
8. W. Wu, S. Campbell, and P. Yeh, Opt. Lett. **20,** 79 (1995).
9. M. Lehman, J. Pomarico, and R. Torroba, Opt. Eng. **34,** 1148 (1995).
10. R. Henao, J. Pomarico, N. Russo, R. Torroba, and M. Trivi, Opt. Eng. **35,** 26 (1996).
11. R. Henao, H. Rabal, A. Tagliaferri, and R. Torroba, Opt. Eng. **35,** 63 (1996).
12. C. Joenathan and R. Torroba, Opt. Lett. **15,** 1159 (1990).
13. J. Pomarico, R. Torroba, and N. Bolognini, Optik **99,** 89 (1995).
14. R. Henao, A. Tagliaferri, and R. Torroba, Opt. Commun. **127,** 14 (1996).

Determination of the zero-order fringe position in digital speckle pattern interferometry

Rodrigo Henao, Héctor Rabal, Alberto Tagliaferri, and Roberto Torroba

A method for determining the position of the zero-order fringe in a metrological experiment with digital speckle pattern interferometry is proposed. It is based on an averaging procedure with shifted images obtained before and after a load is applied. This technique is a complement to the phase-shifting methods. Experimental examples are shown. © 1997 Optical Society of America

Key words: Optical metrology, interferometry, speckle, speckle correlation, TV holography.

1. Introduction

Interferometry can be used to produce a fringe pattern that represents the field surface displacement of an object in response to some change in mechanical loading.[1]

Digital speckle pattern interferometry (DSPI) is one of the most modern techniques for depicting such fringe patterns. It combines real-time processing with the flexibility of software handling.[2] DSPI was developed by combining the well-known techniques of holographic and speckle interferometry by using an image hologram setup and following the methods of double-exposure holography. It utilizes a CCD camera interfaced to a computer to process the data. For comparison measurements, a reference frame stored in memory is continuously subtracted from incoming data, and then the intensity difference is displayed. The fringes represent the correlation between the speckle patterns. However, for quantitative purposes, interferograms must be analyzed so that the results can be presented in the required numerical form.[3] Progress has been made in fringe pattern analysis with a number of electronic aids. These devices allowed a substantial improvement in the accuracy of fringe location within an interferogram.

The wide availability of digital image processing equipment prompted a number of studies to investigate different alternatives of automatic interferogram analyzing. Modern techniques have reached a point at which they can provide useful results, especially with phase-stepping methods.[4] By introducing discrete shifts in the position of the fringes, we can calculate the phase map at pixel location (i, j) in a relatively simple way. The phase is changed when a mirror with a computer-controlled piezoelectric translator is moved.

The successful interpretation of an interferogram depends to a great extent on the ability to assign the right order numbers to the fringes. This fringe labeling is used to determine the displacement of a point relative to a certain origin when the sensitivity vector of the experiment is known. Order ambiguity is then a major source of errors, both for displacement measurements and for generating and interpreting contour fringes. Analogical[5] and digital[6] holographic contouring have used multiple illumination sources to modify the fringe structure as a means for reducing order assignment ambiguity.

Another technique for contouring with multiple digital images is to synthesize a particular fringe profile, namely, that of an approximate delta function.[7] That fringe corresponds to the zero-order interference fringe, showing the locus of places with a zero optical path difference between the two illuminating beams. Using such a single-fringe projection, we can eliminate order ambiguity.

We present in this study a method for displaying the fringe of zero displacement by using the same principle. Several illuminating beams are provided for that purpose by the movement of a lens controlled by a stepping motor. A series of images are captured and stored with different object illuminations before and after a load is applied to the object. DSPI fringes are obtained by subtracting the corresponding pairs of images, and the results are then incoherently added, resulting in a single dark fringe showing the

The authors are with Centro de Investigaciones Opticas, Casilla de Correo 124, 1900 La Plata, Argentina.

Received 11 January 1996; revised manuscript received 21 June 1997.

0003-6935/97/102066-04$10.00/0

© 1997 Optical Society of America

locus where no displacement occurred. Accurate repositioning of the lens at its original starting point before object loading is required for the successful application of the method. If this condition is not fulfilled, the dark fringe blurs out its contrast but does not change its position. Experimental verifications of the proposal are presented.

2. Background of the Technique

The basic DSPI equation describing the intensity difference in an image point between a reference frame and the current one is given by[8]

$$\Delta I = 4(I_o I_r)^{1/2} \sin\left(\varphi + \frac{\delta}{2}\right) \sin\frac{\delta}{2}, \tag{1}$$

where I_o and I_r are the intensities of the object and the reference beams, respectively, φ is the random phase of the speckle pattern produced by surface roughness, and δ is the phase change caused by the modified optical path produced, for example, by a displacement between exposures of the corresponding object point. In principle, if the optical system is stable, I_o, I_r, and φ are constants for a given point. Therefore ΔI is a function only of δ. For an object point, $P(x, y, z)$, suffering a displacement, $\mathbf{d} = \mathbf{d}(x, y, z)$, δ is given by[9]

$$\frac{\delta(P)}{2\pi}\lambda = N(P)\lambda = [e_B(P) + e_Q(P)] \cdot \mathbf{d}(P) = \mathbf{S}(P) \cdot \vec{\mathbf{d}}(P), \tag{2}$$

where $N(P)$ is the number of fringes in the image between a fixed point (a point that suffered no displacement between exposures) and P, λ is the light wavelength, e_B is a unit vector from P in the observation direction, e_Q is a unit vector from P in the illumination direction, and $\mathbf{S}$ is the sensitivity vector. We assume the displacements field to be continuous, and we also suppose that in the image a connected path exists between a fixed point and P.

A displacement $\mathbf{d}(P)$ then produces a phase change δ. If it is great enough (corresponding to a phase difference greater than 2π), the intensity ΔI will lie somewhere between the extreme values $I_{\max}$ and $I_{\min}$. This $I_{\min}$ is zero whenever $\delta = 2n\pi$; $n = 0, 1, 2, \ldots$. To construct the phase map, we often require the position of at least one point that suffered no displacement. It is used as an origin for counting fringes to every point of interest. If the sensitivity vector is known, the number of fringes between the origin mentioned and a generic point P determines only one component of the displacement. Three independent equations are required as a minimum for solve for three components of $\mathbf{d}$:

$$N_i(P)\lambda = [eB(P) + e_{Q_i}(P)] \cdot \mathbf{d}(P) = \mathbf{S}_i(P) \cdot \mathbf{d}(P)$$
$$i = 1,2, \ldots, n \quad n > 2. \tag{3}$$

Overdetermined systems combined with the least-squares calculations are usually used to increase the accuracy of the measurement.[9] The sign of every component remains nevertheless ambiguous.

It is evident that the existence of a nondeformed point is not *a priori* warranted. Whole-field displacements have no such a point. Even if such a point exists, it may be located outside the observation field of the experiment. The phase change δ is then measured with $2n\pi$ ambiguity.

When $\mathbf{d} = 0$, $\delta = 0$ for all sensitivity vectors. This is the only case that gives a zero phase shift for such general geometries. That is, the $\mathbf{d} = 0$ locus will be a dark fringe in DSPI, which is obtained through the subtraction of the before and the after states. The converse is true in analogic holography.

If several (in principle, infinite) sensitivity vectors are used, the only dark fringe in the DSPI image common to all observation points, or illuminations or combinations of both, should correspond to the locus $\mathbf{d} = 0$, if it exists. When, as in practice, only a finite number of sensitivity vectors are available, several isolated zero intensity fringes will appear. An *a priori* knowledge of the expected geometry of the displacements could then be used to decide which represents the zero order.

With the technique we propose that a set of images be stored with a progressive increment in the angle directing the object-beam illumination. This increment is obtained by careful movements of a lens controlled by a stepping motor. The illumination directions must be chosen so that every possible displacement produces a phase change, that is, three sensitivity vectors should constitute a basis. Then the load is applied to the object and a similar set of images is recorded, repeating the same illuminating directions of the object beams as before. For each pixel (i, j) the computer assigns a z value to the resulting image calculated as

$$z = \sum_k |(z_k - z_k')|, \tag{4}$$

where z_k is the gray level in the recorded image corresponding to the kth illumination direction before loading, z_k' is the corresponding value after loading,

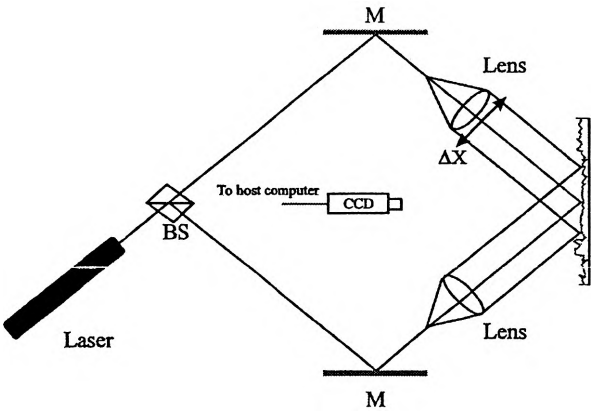
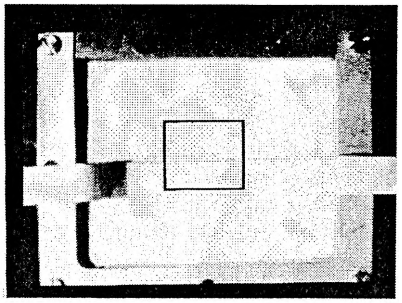
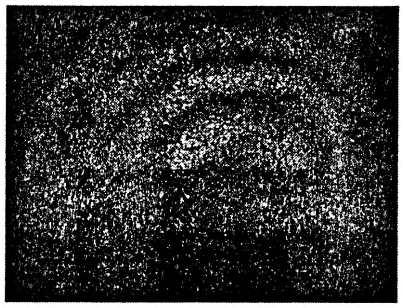


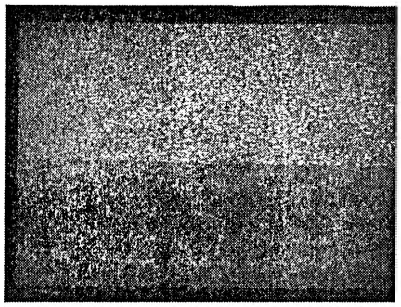
Fig. 1. Experimental configuration used in the technique.



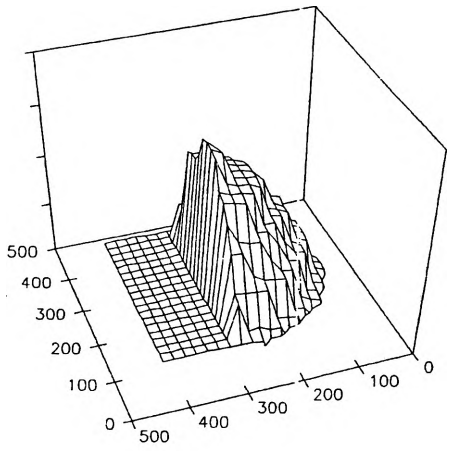
(a)



(b)

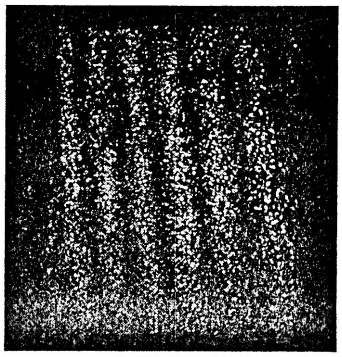


(c)

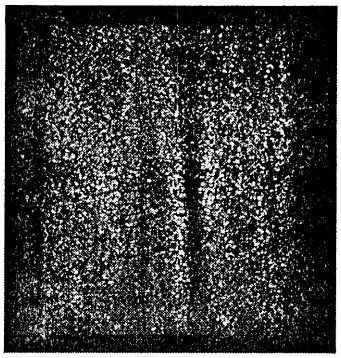


(d)

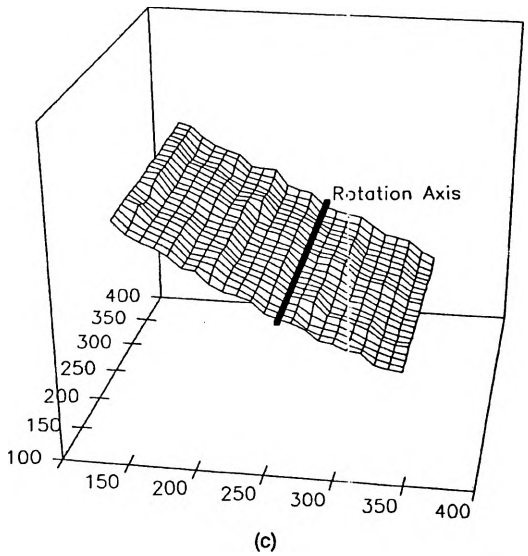
Fig. 2. (a) Clamped metal plate loaded on its center compared with a fixed metal strip. The rectangle indicates the observation area. (b) DSPI display. Result after (c) the averaging procedure and (d) the phase mapping. The metal strip remains black, and the fringes are removed.



(a)



(b)



(c)

Fig. 3. Composition showing (a) the fringe resulting from the rotation of a plate, (b) the zero-order fringe (rotational axis) arising from the digital averaging, (c) the phase-mapping obtained from (a) together with the position of the rotational axis obtained from (b).

and the bars indicate absolute value. The zero-displacement locus does not move during a change in the illumination direction. It plays here the role of the zero-path difference in Ref. 7. Skeletonization of this fringe provides an origin for counting the fringe

in any of the pairs z_k, z_k'. The rest of the fringes move when the illumination direction changes and wash out in the averaging operation.

For a given sensitivity vector there are nonzero displacements that produce a dark fringe in the image, namely, those corresponding to directions perpendicular to that vector. The sensitivity vector set is determined from the observation direction, and the different illumination directions can then be chosen to show a dark fringe corresponding to a subspace of the displacement field, the loci of places that did not move in a certain direction. If, for example, all the sensitivity vectors are contained in a single plane, points with displacements perpendicular to that plane will appear dark in the resulting image. As a consequence, regions obeying a defined property can be highlighted if required for a particular experiment.

3. Experiments

Several experiments were conducted to demonstrate the validity of our proposal. Figure 1 shows the experimental setup. A linear polarized He–Ne laser beam is divided by the beam splitter, BS. One arm serves as a reference beam, and the other is used to illuminate the object through a collimating lens, which is mounted on a stepping motor. This last introduces the required changes in the illuminating beam direction. In all our experiments five image pairs were stored with a step of 30 μm between images.

In the case of Fig. 2 a clamped planar metallic surface, deformed under a load applied from the rear on its center, and an unperturbed metal strip are compared. Figure 2(a) shows the object, and the rectangle indicates the observation area. Figure 2(b) shows the display of the normal DSPI result. The result of applying Eq. (2) to these images is displayed in Fig. 2(c). The metal strip remains totally black, indicating that no deformation occurred to it. The corresponding phase mapping is shown in Fig. 2(d).

In Fig. 3 a plane object is rotated around an axis. In Fig. 3(a) the DSPI interference fringes are shown, whereas Fig. 3(b) shows the actual rotation axis after our procedure is applied. In this example, the axis is the zero-order fringe. Figure 3(c) is the result of the phase mapping of Fig. 3(a) and the position of the rotational axis obtained from Fig. 3(b).

A lack of repeatability of positioning between the acquisition of the reference state and deformed state frames may occur. If such an error introduces an extra optical path of less than $\lambda/2$, no fringe location error appears but a blurring in its contrast. The error depends on the apparatus and the involved setup geometry, but it is not a serious constraint. In our case, s, the maximum error was of 0.05 μm for the whole experiment. This value can be achieved with commercially available equipment. On the other hand, the geometric parameters, like the focal length or the observation angle, can be adjusted to bring the appropriate value for a particular experiment.

4. Conclusions

We have demonstrated the possibility of a zero-order fringe assignment with the aid of DSPI techniques in addition to a multiple-image storing procedure. The proposed method is to some extent complementary with the phase-stepping techniques. Once the zero-order fringe is localized, we can proceed with the standard phase-mapping methods to find the absolute deformation field distribution. The method reported here is suitable only for static loading.

The financial support of the Consejo Nacional de Investigaciones Científicas y Tecnicas (Argentina) and Conselho Nacional de Desenvolvimiento Cientifico e Tecnologico (Brazil) agreement, the Third World Academy of Science grant 93-389, the Alexander von Humboldt Foundation (Germany), Fundación Antorchas (Argentina), and Mutis Program (Spain) is gratefully acknowledged.

References

1. R. Jones and C. Wykes, *Holographic and Speckle Interferometry* (Cambridge U. Press, Cambridge, UK, 1983), Chap. 4, pp. 183–188.
2. K. Creath and G. Slettemoen, "Vibration–observation techniques for digital speckle pattern interferometry," J. Opt. Soc. Am. A **2**, 1629–1636 (1986).
3. D. W. Robison, "Automatic fringe analysis with a computer image processing system," Appl. Opt. **22**, 2169–2176 (1983).
4. D. Robison and D. Williams, "Digital phase stepping speckle interferometry," Opt. Commun. **57**, 26–30 (1986).
5. B. P. Hildebrand and K. A. Haines, "Multiple-wavelength and multiple-source holography," J. Opt. Soc. Am. **57**, 155–162 (1967).
6. J. Pomarico, R. Arizaga, H. Rabal, and R. Torroba, "Digital holographic contouring," Opt. Commun. **98**, 257–260 (1993).
7. R. Arizaga, H. Rabal, M. Trivi, E. Alanis, and G. Romero, "Single fringe contouring," Opt. Commun. **108**, 209–213 (1994).
8. R. Henao, H. Rabal, R. Torroba, and A. Tagliaferri, "Display of the temporal evolution of the speckle patterns," Opt. Eng. **35**, 63–69 (1996).
9. W. Osten and W. Juptner, "Measurement of displacement vector fields based on high-precision phase measurements," in *Interferometry: Techniques and Analysis*, G. M. Brown, M. Kujawinska, O. Y. Kwon, and G. T. Reid, eds., Proc. SPIE **1755**, 162–173 (1992).

Available online at www.sciencedirect.com
SCIENCE DIRECT®
Optics Communications 221 (2003) 43–47
OPTICS COMMUNICATIONS
www.elsevier.com/locate/optcom

Fully digital encryption technique

Ricardo Arizaga[a], Rodrigo Henao[b], Roberto Torroba[a,*]

[a] *Centro de Investigaciones Opticas (CIOp) and OPTIMO, Facultad de Ingeniería, Universidad Nacional de La Plata, C.C. 124, B1902WAB La Plata, Argentina*
[b] *Institute of Physics, Antioquia University, Medellín, Colombia*

Received 12 September 2002; received in revised form 11 March 2003; accepted 24 March 2003

Abstract

We propose an alternative fully digital encryption technique based on using the Fourier transform of the original object to be processed and a speckled reference wave as encryption mask. Once encrypted, the Fourier transform spectrum of the object is holographically stored. The original-data recovering is performed by digital reconstruction using the same encryption mask, which is also holographically stored. Quality of reconstructed data is evaluated as a function of the sensed encrypted data. Computer simulations and experimental results are presented to demonstrate the method.
© 2003 Elsevier Science B.V. All rights reserved.

Keywords: Optical data processing; Information processing; Encryption and validation procedures

1. Introduction

In recent years, several proposals on information security using optical techniques were published [1–6]. Optical encryption have the added property that a large amount of data can be stored or retrieved in parallel and at high speed. The first to be used were techniques related to analog encryption methods based on different correlation architectures [7,8]. These setups can be considered as the basis for the design of real-time optical security devices. Most optical correlators use 2-D input images and are designed around a 2-D optical processing architecture. However, the presence of complex or expensive elements complicates the creation of simple and low-priced devices of this type. These correlators can be used for instance to secure entry systems that identify individuals for access to a restricted area. In security systems, the image, such as a picture of a face or a fingerprint, is used for the same purpose. They include memory units for storing key code images that are used to verify the authenticity of the input image. It is impossible to verify the encoded documents without knowing the key mask that have been used in the encoding. Furthermore, key codes have to be unique to be a full-proof, reliable accurate, ready to implement as well as to meet the goal of putting the counterfeits and frauds to a complete halt.

* Corresponding author. Fax: +54-221-4712771.
E-mail address: robertot@ciop.unlp.edu.ar (R. Torroba).

0030-4018/03/$ - see front matter © 2003 Elsevier Science B.V. All rights reserved.
doi:10.1016/S0030-4018(03)01462-7

The systems are also integrated to a network. If the memory units are stolen or if important data are intercepted by monitoring the transmission line in the network, however, an unauthorized person can extract vital information easily. It is becoming increasingly simple to reproduce the input data of the security system. Therefore, data protection has become necessary. The most preferred method is that of double random phase encryption [9]. In the encryption process input data (positive real-valued image) is multiplied by a random phase function, then Fourier transformed and finally multiplied by another random phase function. We can obtain a decrypted image by first multiplying by the complex–conjugate of the second encoding phase function and taking a Fourier transform. Many related contributions were generated, including the use of a Joint-transform correlator (JTC) [10] or optical arrangements using photorefractive crystals [11]. The content of the proposals was extended to include subjects as stream ciphers [12], other configurations of optical correlators [13], optical memory cards [14], even several optical parameters can be used as encryption–decryption keys, as for example multidimensional keys [15]. In this context, Javidi et al. first introduced digital holography in the field of information securing. This technique has important benefits as enables to store, transmit, and decrypt the encrypted data digitally. Another benefit of the proposed system compared with electronic encryption is that optical processing provides many degrees of freedom for securing information [16].

The setup is a Mach-Zender configuration using the double-encoding phase mask. More recently the proposal was extended to an optical retrieval system for secure real-time display. The images in all these correlators are normally intensity representations.

In this paper, the idea is to present an alternative fully digital technique with a single-random encryption. The object is directly Fourier transformed. At the Fourier plane we place a lensless CCD sensor. We record and simultaneously encrypt the data using an interference with a speckled reference wave. Then a digital hologram of the encrypted object Fourier transform is made, which will be reconstructed also digitally. The decryption key is also recorded as a digital hologram as described in the following section. This second stored frame is sent to all possible clients to be kept as decoding key The retrieval is operated by all-digital means. The whole technique is simpler than the previous ones. Since the process is performed on a CCD camera, the obtained data can be directly transmitted to digital devices or communication lines. Accordingly, the technique has potential for near real-time processing. The influence of the encrypted spectrum content vs the CCD array area is also evaluated. Theoretical explanation, computer simulations and experimental results are presented.

2. Principle of the method and results

In the following, we describe in detail the proposed encryption procedure and the way to experimentally implement it.

Let $i(x,y)$ denote the original image to be encrypted. The proposed experimental setup for the digital encryption is schemed in Fig. 1. A He–Ne laser is used as a coherent light source. A lensless CCD array is directly placed in the lens L Fourier plane. The image of a speckled screen is used as the encryption mask needed for the process. This screen is imaged on the CCD array. Let $s(\mu,\eta)$ denotes the speckle screen at the CCD plane. Precisely, this is the reference wave used in the generation of the digital hologram. If we denote by

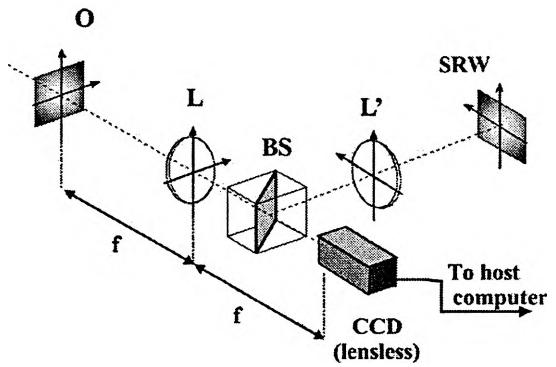


Fig. 1. Setup for the encryption procedure. Laser light illuminates the object to be encrypted O, L transforming lens, SRW speckled reference wave, and CCD lensless sensor array.

$I(\mu,\eta)$ the Fourier transform of $i(x,y)$ at the CCD plane coordinates, the intensity $h(\mu,\eta)$ of the digital hologram created by the interference between these two waves in the Fourier domain is expressed by

$$h(\mu,\eta) = |I(\mu,\eta) + s(\mu,\eta)|^2 = |I(\mu,\eta)|^2 + |s(\mu,\eta)|^2 + I^*(\mu,\eta)s(\mu,\eta) + I(\mu,\eta)s^*(\mu,\eta). \quad (1)$$

Similarly, by removing both the original object and the transforming lens L of the setup and illuminating with a plane wave of uniform unitary amplitude, we get

$$k(\mu,\eta) = |1 + s(\mu,\eta)|^2 = |1|^2 + |s(\mu,\eta)|^2 + s^*(\mu,\eta) + s(\mu,\eta). \quad (2)$$

When extracting the holographic data from Eqs. (1) and (2), retaining the fourth term in both equations and multiplying them, we get $I(\mu,\eta)$. Finally we perform the inverse Fourier transform of this last term for recovering the function $i(x,y)$ and subsequently the original image

$$I(\mu,\eta)s^*(\mu,\eta)s(\mu,\eta) \rightarrow I(\mu,\eta) \Rightarrow FT^{-1}[I(\mu,\eta)] = i(x,y). \quad (3)$$

In Fig. 2, we show a computer simulation of the method. The intensity of the original image 2(a) and its encryption 2(b) are shown. The results of using the right decoding key 2(c) and a wrong key 2(d) are also displayed. The right decoding key can retrieve the original image, but a noise-like image remains by the wrong key.

In Fig. 3, we experimentally demonstrate the procedure. We show the intensity images of 3(a) the input object, 3(b) the encrypted image, and 3(c) the correct digital reconstruction of the input.

The main limiting aspect is the size of the spectrum the CCD array is able to sense. We investigated then the influence of capturing a smaller area of the total encrypted spectrum. In this case we use an algorithm to calculate the mean square error, which is given by

$$\mathrm{Err} = \frac{\sum_{m=1}^{M}\sum_{n=1}^{N}|i(m,n) - i'(m,n)|^2}{M \times N},$$

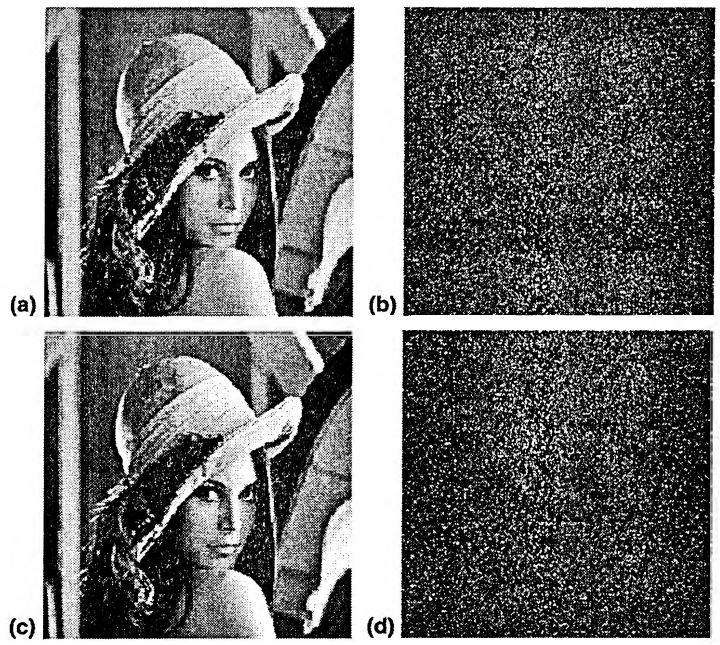


Fig. 2. Results of a computer simulation: (a) original image, (b) encrypted image, (c) retrieved image by the right decoding key, and (d) retrieved image by a wrong decoding key.

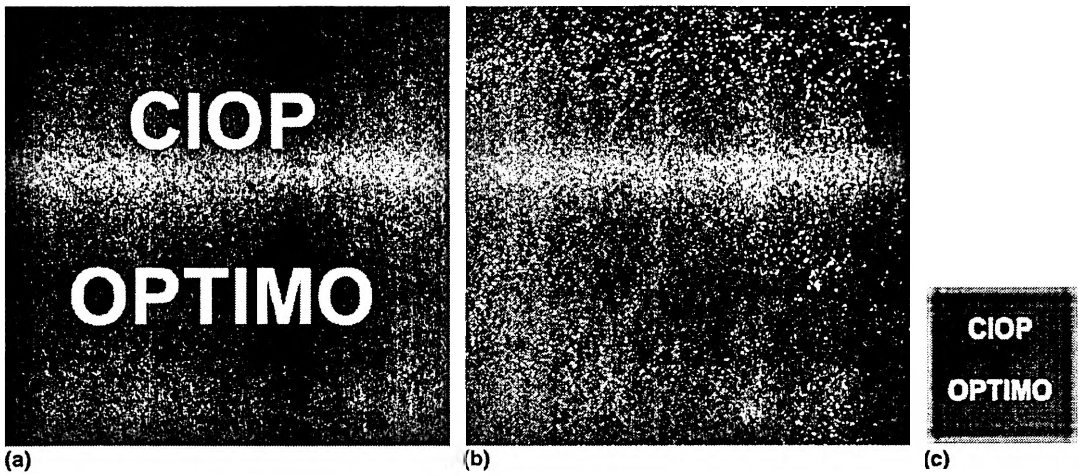


Fig. 3. Experimental results showing (a) the object to be encrypted, (b) the resulting encrypted image, and (c) the reconstructed image after the right decoding process.

where (m,n) are the pixel coordinates, $M \times N$ is the number of pixels of the original image $i(m,n)$, and $i'(m,n)$ is the decrypted information obtained when blocking the area of the CCD sensor.

Evidently, some frequency information is lost due to the limited CCD sensor size. Ideally, all collected data must remain within the CCD array but it depends both on the original image frequency content and on the optical parameters of the imaging system. So, the optical system must be chosen as to fit the object Fourier transform spectrum on the CCD array. On the other hand, for a fixed Fourier spectrum size, a better sensor resolution will only help if lower object frequencies are of importance in recognizing the whole information. In standard conditions, only bulk objects are expected to be recognized.

In the following we investigate the difference in quality of decrypted data when limiting the physical size of the CCD array. In this analysis we use the same test image (same frequency content) and using a varying blocking mask over the CCD array, and centered around it. Actually the problem is the opposite, because the sensor is always the same and the frequency spectrum varies from one object to another, but the situation is illustrated in the same way in our example.

We assume that the Fourier transform field information is properly sampled. Besides we suppose the intensity levels to be adequate to avoid saturation, or they are well above the detector minimum level. In this way, these parameters has little or no influence in the resulting decryption. The optical system we use produces a Fourier transform field whose detectable intensity fits completely into the sensor array without the covering mask in place.

The result are shown in the plot of Fig. 4. This figure shows the mean squared errors as a function of the blocked proportion of the CCD array. When the mean squared error gives around 4×10^3, a visual inspection of the resulting image shows a very poor correlation with the original image. Image

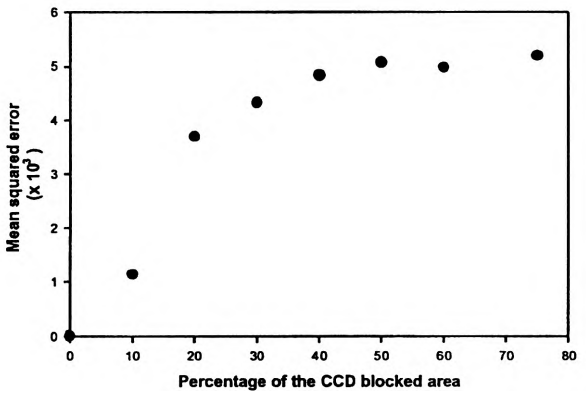


Fig. 4. Plot of the mean squared error versus the proportion of the detector blocked area. It is clearly shown that reconstructed image quickly deteriorates, even when only the 10% of the detector area is blocked.

quality quickly deteriorates as the blocked area increases. As a consequence, care must be taken in choosing the right transforming lens as to fit the object spectrum on the sensor area, although some minor tolerance can be accepted.

Advantages over existing proposals are: (a) there is no need for additional experimental equipment at the decryption stage, (b) it only needs the right decoding key, which is the same for both coding and decoding processes (other methods need the conjugate of the decoding key), (c) is independent of diffraction efficiencies, and (d) requires no filtering

In our case, the signal-to-noise ratio is given in terms of the visibility of the resulting decrypted output.

Acknowledgements

The Grants from CONICET (PICT No. 008/98), from Universidad Nacional de La Plata and CODI-Universidad de Antioquia are gratefully acknowledged.

References

[1] B. Javidi, E. Ahouzi, Appl. Opt. 37 (1998) 6247.
[2] N. Towghi, B. Javidi, J. Opt. Soc. Am. A 16 (1999) 1915.
[3] O. Matoba, B. Javidi, Appl. Opt. 38 (1999) 7288.
[4] X. Tan, O. Matoba, T. Shimura, K. Kinoda, B. Javidi, Appl. Opt. 39 (2000) 6689.
[5] S. Lai, M. Neifield, Opt. C. 178 (2000) 283.
[6] O. Matoba, B. Javidi, Opt. Lett. 27 (2002) 321.
[7] T. Grycewich, B. Javidi, Opt. Eng. 35 (1996) 2519.
[8] L. Muravsky, T. Voronyak, V. Fitio, M. Shovgenyuk, Opt. Eng. 38 (1999) 25.
[9] P. Rèfrègier, B. Javidi, Opt. Lett. 20 (1995) 767.
[10] B. Soon, M. Karim, M. Alam, Opt. Eng. 38 (1999) 39.
[11] G. Unnikrishnan, J. Joseph, K. Singh, Appl. Opt. 37 (1998) 8181.
[12] S. Zhang, M. Karim, Opt. Eng. 38 (1999) 20.
[13] B. Javidi, J. Wang, Opt. Eng. 35 (1996) 2479.
[14] J. Horner, B. Javidi, Opt. Eng. 38 (1999) 8.
[15] O. Matoba, B. Javidi, Opt. Lett. 24 (1999) 762.
[16] B. Javidi, T. Nomura, Opt. Lett. 25 (2000) 28.

Available online at www.sciencedirect.com
SCIENCE DIRECT
Optics Communications 260 (2006) 109–112
OPTICS COMMUNICATIONS
www.elsevier.com/locate/optcom

Multiplexing encrypted data by using polarized light

John Fredy Barrera [a], Rodrigo Henao [a], Myrian Tebaldi [b,*], Roberto Torroba [b], Néstor Bolognini [c]

[a] Grupo de Óptica y Fotónica, Instituto de Física, Universidad de Antioquia A.A. 1226 Medellín, Colombia
[b] Centro de Investigaciones Ópticas (CONICET-CIC) and UID OPTIMO, Facultad de Ingeniería, Universidad Nacional de La Plata, Camino Centenario entre 505 y 508, P.O. Box 124, Gonnet, La Plata 1900, Argentina
[c] Centro de Investigaciones Ópticas (CONICET-CIC), UID OPTIMO, Facultad de Ingeniería and Facultad de Ciencias Exactas, Universidad Nacional de La Plata, P.O. Box 124, La Plata 1900, Argentina

Received 23 September 2005; received in revised form 21 October 2005; accepted 24 October 2005

Abstract

We investigate the feasibility of multiplexing, employing polarized light, a set of security encrypted data. The encryption approach is based on the double random pure-phase enciphering method. Phase conjugation operation is conducted in the reconstruction stage with the aid of a photorefractive crystal which stores the encrypted information. When storing each encrypted image, a polarization change is introduced in the system. This induces decorrelation on the speckle patterns inside the storing medium. We apply this approach for multiple image encryption. We show experimental results that confirm our approach.
© 2005 Elsevier B.V. All rights reserved.

PACS: 42.30.Va; 42.25.Ja

1. Introduction

In the optical field there has been constant efforts on both multiplexed [1] and security encrypted [2] data storage. Securing data in high-capacity storage systems is one of the challenging tasks in order to meet user-requirements in data storage.

Optical data storage presents great advantages over traditional non-optical storage systems with the potentiality of low cost, high storage capacity, high transfer rate, and hardware-based data encryption. To overcome the difficulties concerning the storage means for recording photorefractive crystals have been used.

There are many methods for multiplexing holograms, e.g., wavelength-, shift-, angle-, and phase-coded multiplexing.

Several efforts were performed thanks to the advent of the liquid crystal spatial light modulator (LC-SLM). It has opened up the possibility for dynamic control of amplitude, phase or polarization state of light. The use of LC-SLMs for the spatial control of the state of polarization has already been described and experimentally demonstrated [3].

Several optical systems based on the encryption of information using phase components of wave front have been experimentally demonstrated [4–6]. Polarization has been used for the visualization of the decoded information. Two dimensional encoding of the polarization state of light using a parallel aligned liquid crystal SLM has recently been demonstrated [7]. Unnikrishnan et al. [8] experimentally demonstrated an optical encryption system based on polarization encoding to encrypt binary images. The encryption is done by XOR operation between the image and a random code (key to the encrypted image). The XOR operation is done in the polarization domain of coherent light by using two ferroelectric liquid crystal spatial light modulators. The

* Corresponding author. Tel.: +54 221 4840280; fax: +54 221 4712771.
E-mail address: myrianc@ciop.unlp.edu.ar (M. Tebaldi).

0030-4018/$ - see front matter © 2005 Elsevier B.V. All rights reserved.
doi:10.1016/j.optcom.2005.10.053

information encoded as polarization states of coherent light is converted to intensity variations by using a polarizer. The decryption of the encrypted data are done by a second XOR operation between the encrypted image and the key. Mogensen et al. [9] have proposed an optical encryption and decryption system based on XOR operations using high frame rate ferroelectric liquid crystal spatial light modulators. Tan et al. [10] have proposed a secure holographic memory system with polarization encoding. The polarization state at each pixel is scrambled by a mask (SLM) that changes the polarization state into a random state. Eriksen et al. [11] have proposed a method for spatially encoding the state of polarization in a 2-D wave front with elliptically polarized light controlling both the ellipticity and rotation angle of the major axis of the ellipses. A technique was has also been developed, based on polarization-encoding using digital speckle pattern correlation [12]. In that method, security is twofold by the speckle and polarization characteristics of the procedure. Both encoding and decoding keys are stored digitally.

Recently, an approach for polarization encryption using geometrical phase modification has been proposed. Geometrical phases originate from polarization state manipulation, by using computer-generated space-variant subwavelength gratings (SWG) [13].

In [14], an optical encryption arrangement based on polarization is implemented by using a bacteriorhodopsin film as a polarization sensitive holographic memory. In this case, a single polarization modulation is used to encrypt the data. Reference [15] is an extension of the above paper introducing a double-random polarization encryption that uses two random polarization-modulation masks.

Although several optical encryption arrangements codified the input data in polarization, there have been no working implementations for data multiplexing encryption in the form of polarization encoding. In this paper, we describe a system for optical two-dimensional (2D) multiplexing encoding using the polarization state of light. The proposed technique simultaneously combines double random phase encryption method and polarized behaviour of the encrypted beam. Most of the above mentioned articles use one or two associated SLM, which implies the calibration of such instruments, aside of the additional cost in equipment. In our proposal, we directly used retardation plates, which facilitate the process and lower the costs of the experience.

Our multiplexing proposal has a practical application in optical encryption, increasing the total number of combination possibilities yet improving the robustness of the encryption system.

Another feature to be stressed is precisely the polarization sensitivity. This attribute can be used as a secondary key code to ensure the encryption in case of possible message interception.

Experimental results that confirm our proposal are presented.

2. Description of the method

Fig. 1 shows the basic optical system architecture employed. In this case, multiple encrypted data are stored within a photorefractive holographic memory using the double random phase encoding technique. This technique involves the use of a random pure-phase mask in the input plane R_1 and another R_2 in the spatial frequency plane, thus resulting in the formation of stationary white noise. Generally speaking, the second random pure-phase mask can be located at the Fresnel domain. In our arrangement, besides the two masks, a retardation plate WP_1 is employed to encode the input amplitude data O. Lens L_2 images the encrypted information on a $10\text{ mm} \times 10\text{ mm} \times 10\text{ mm}$ photorefractive BSO crystal. The experimental arrangement is illuminated by Nd-YAG laser operating at wavelength 532 nm with 50 mW output power. The encrypted information is holographically recorded by a reference plane wave. The interference between the encrypted data and the reference beam is obtained inside the crystal volume. The intensity patterns redistribute the photoinduced charges, resulting in an electric field strength at each point, which induces, through the linear electro-optic effect that the crystal exhibits, a corresponding spatial variation of the refractive index. In this way, the input pattern is encoded in terms of the refractive index variation generating index gratings. The angle between the recording beams is 8°.

There is an obvious dependence of the speckle pattern distribution with the polarization of the light source that has been extensively studied by several authors [16–18].

Based on this concept, we introduce a change in the polarization state of the object beam in order to achieve multiplexing. Therefore, for every polarization change the speckle pattern is somehow altered in the same way as a phase change is introduced.

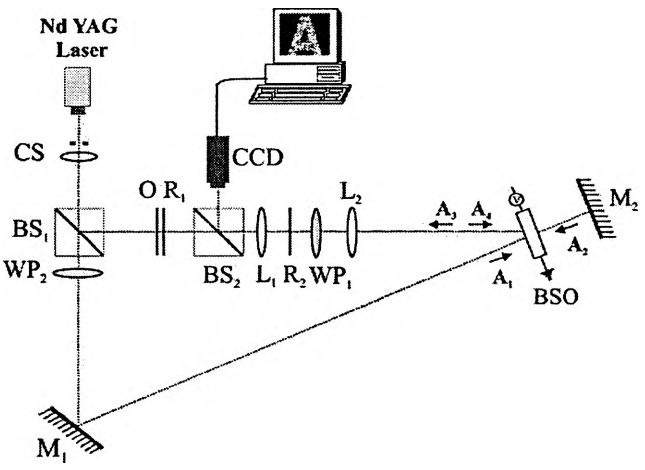


Fig. 1. Optical system architecture to multiple polarization encryption procedure (O: input data; R_1 and R_2: random pure-phase masks; WP_1 and WP_2: retardation plates; BS_1 and BS_2: beam splitters; L_1 and L_2: lenses; CS: collimation system; and M_1 and M_2: mirrors).

Phase conjugation of the reference beam is introduced in the decryption process to read out the data stored in the crystal. Let us denote A_1 and A_4 the amplitudes of the interfering beams. In our set-up, beam A_2 is the transmitted part of beam A_1 retroreflected by mirror M_2. After beam A_2 passes through the crystal, beam A_3 is generated which is proportional to the conjugate of the image bearing beam A_4. Exact cancellation of the phase change introduced in the encryption process is necessary to decrypt the input. Data recovering is observed by a CCD camera according to Fig. 1.

Note that the encrypted information stored in the crystal is essentially a speckle pattern. Each speckle interferes with the reference wave; therefore the speckle pattern is modulated by fringe systems existing in its whole volume. Then, the resulting pattern gives rise to a micro hologram inside each speckle.

It should be emphasized that the registered index gratings are random in phase according to the incident distribution. Each of these gratings interact with the counter-propagating pump beam thus producing a local phase conjugated beam inside each speckle, with a random phase that recognizes the original local speckle phase. The total contribution to the phase conjugation reflectivity is thus produced by each speckle. Therefore, the reconstructed beam A_3 is a phase conjugate beam which is, in turn, a pattern governed by the same statistical behaviour as the input beam.

The recording medium is intensity sensitive and it is not affected by polarization changes. However, in our case the polarization changes modify the intensity distribution of the encrypted pattern which interferes with the reference beam altering thereby the fringe systems and the resulting index grating. In order to maintain the fringe contrast the polarization state of the recording beams must remain unchanged.

Fig. 2 shows the experimental results demonstrating the polarization sensitive of the double random phase encryption arrangement: (a) object to be encrypted, (b) decryption using the right polarization direction, and (c) decryption with a wrong angle of the polarization direction. In this case, the polarization change is introduced by a half wave retardation plate.

Fig. 3(a)–(c) shows the same sequence as described in Fig. 2 but using a quarter wave retardation plate. It should be mentioned that in this case, a 1° rotation of the quarter wave retardation plate is enough to a complete detuning of the right decrypted image. In the half wave retardation plate is necessary a 5° rotation in order to avoid a right decryption. This analysis is useful to assess a correct multiplexing schedule avoiding any cross talk.

A procedure of multiple encryption by using the polarization as a key implies to govern the polarization state of the appropriate device in the successive inputs to be encrypted. The data of the ith stored image can be reconstructed not only if the phase conjugated beam travels through the retardation plate in the adequate orientation, but if it also travels through the second random pure-phase mask R_2 used in the encryption process.

Fig. 4 shows the encryption-decryption procedure for multiple input objects. O_1 and O_2 correspond to the input images, E_1 and E_2: the encrypted images, each one encrypted by using a determined polarization state. The polarization key is a quarter wave retardation plate. As it was established in the experience of Fig. 3, in order to avoid cross talk a 1° retardation plate rotation is introduced. D_1 and D_2: multiple decrypted images by using the correct polarization key.

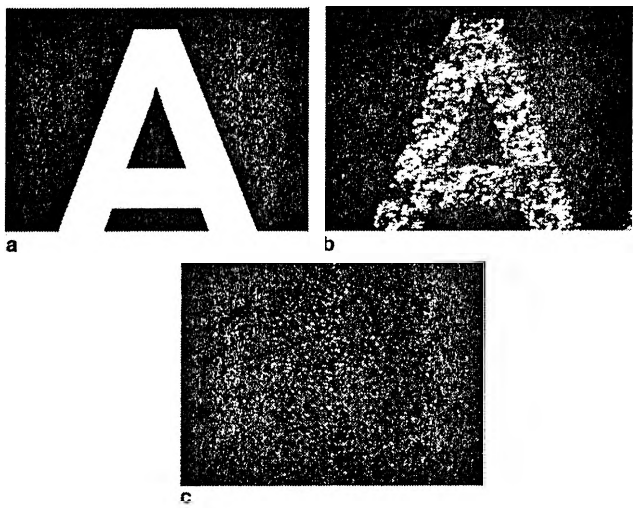


Fig. 2. Experimental results shows (a) object to be encrypted; (b) decryption when the polarization device (half wave retardation plate) is set at the correct polarization state (as in the encrypted procedure); and (c) decryption with a wrong polarization state.

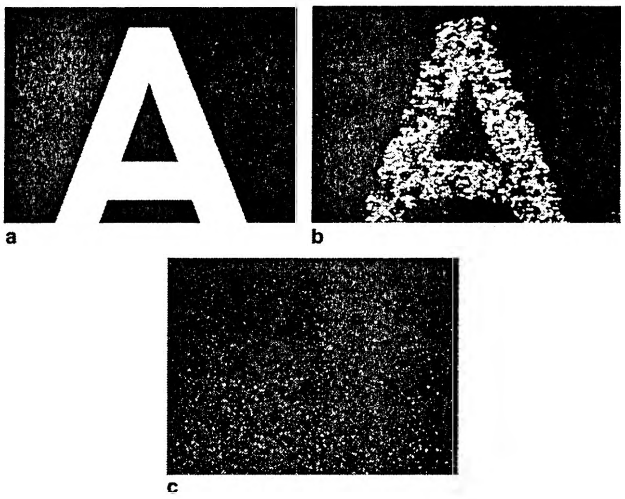


Fig. 3. Experimental results shows (a) object to be encrypted; (b) decryption when the polarization device (quarter wave retardation plate) is set at the correct polarization state (as in the encrypted procedure); and (c) decryption with a wrong polarization state.

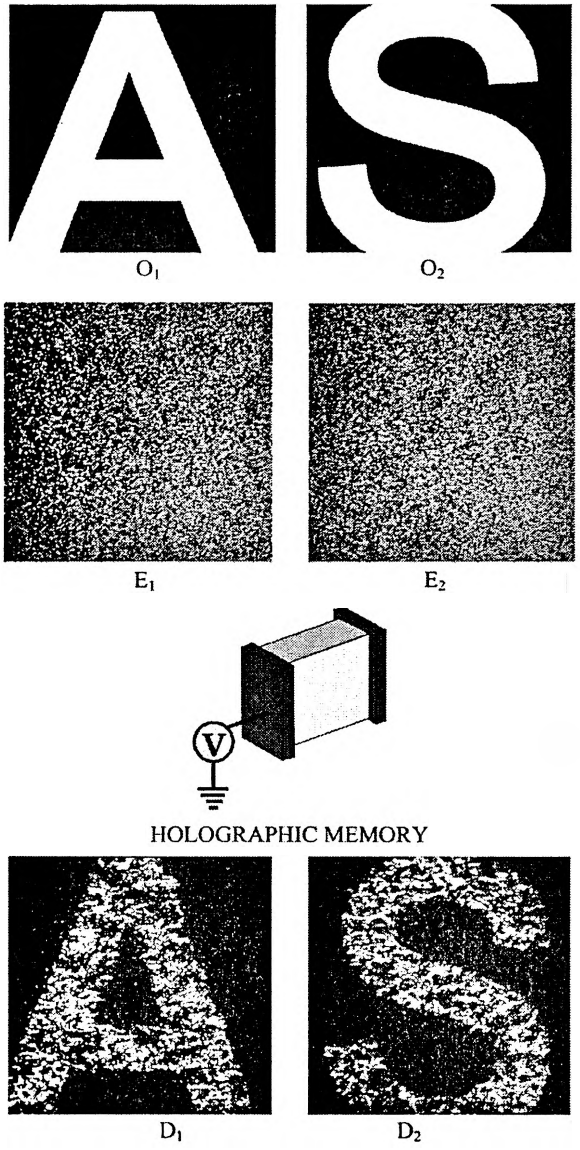


Fig. 4. Multiplexing polarization encryption-decryption procedure (O_1 and O_2: input objects; E_1 and E_2: encrypted images; and D_1 and D_2: decrypted images).

The experiments detailed above clearly confirm that the polarization can be used as unique key to encryption-decryption procedure.

3. Conclusions

In our paper, we propose and demonstrate a polarization encoded encryption system based on a double random pure phase mask technique and retardation plate.

In addition to the exact repositioning required for the random phase mask, for a successful recovering it is essential that a precise retardation plate orientation should be achieved.

It should be emphasized the simplicity and lower costs of the proposed experience in comparison with other polarization arrangements. Our set-up increases the security of the encryption through the introduction of the polarization as an alternative multiplexing encryption key.

To our knowledge this security polarization key is introduced for the first time in a multiple encryption image scheme. Parallel channelling operations are now an open possibility to security optics.

It remains to extensively analyze the sensitivity characteristics of the different polarization schemes.

Summarizing, we settle a new point of view to a multiplexing storing mechanism that expands the possible combinations of encrypted objects with a given optical architecture.

Acknowledgments

This Research was performed under the Auspicious of Colciencias (Colombia), Conicet PIP 2417 (Argentina), Cicpba (Argentina), ANPCYT PICT 12564 (Argentina) and Facultad Ingeniería, Universidad Nacional de la Plata (Argentina).

References

[1] Y. Taketomi, J.E. Ford, H. Sasaki, J. Ma, Y. Fairirnan, S.H. Lee, Opt. Lett. 16 (1991) 1774.
[2] C. Denz, T. Deliwig, J. Lembcke, T. Tschudi, Opt. Lett. 21 (1996) 278.
[3] M. Stalder, M. Schadt, Opt. Lett. 21 (1996) 1948.
[4] P.C. Mogenson, J. Gluckstad, Opt. Commun. 173 (2000) 177.
[5] P.C. Mogenson, J. Gluckstad, Opt. Lett. 25 (2000) 566.
[6] R. Torroba, R. Henao, R. Arizaga, Opt. Commun. 221 (2003) 43.
[7] J.A. Davis, D.E. McNamara, D.M. Cottrell, T. Sonehara, Appl. Opt. 39 (2000) 1549.
[8] G. Unnikrishnan, M. Pohit, K. Singh, Opt. Commun. 185 (2000) 25.
[9] P.C. Mogensen, R.L. Eriksen, J. Gluckstad, J. Opt. A 3 (2001) 10.
[10] X. Tan, O. Matoba, Y. Okada-Shudo, M. Ide, T. Shimura, K. Kuroda, Appl. Opt. 40 (2001) 2310.
[11] R.L. Eriksen, P.C. Mogensen, J. Gluckstad, Opt. Commun. 187 (2001) 325.
[12] R. Arizaga, R. Torroba, Optik 113 (2002) 333.
[13] G. Biener, A. Niv, V. Kleiner, E. Hasman, Opt. Lett. 30 (2005) 1096.
[14] X. Tan, O. Matoba, T. Shimura, K. Kuroda, B. Javidi, Appl. Opt. 39 (2000) 6689.
[15] O. Matoba, B. Javidi, Appl. Opt. 43 (2004) 2915.
[16] J.C. Dainty (Ed.), Laser Speckle and Related Phenomena, Springer, New York, 1975.
[17] J.W. Goodman, Statistical Optics, Wiley, New York, 1978.
[18] J.K. Boger, Opt. Lett. 24 (1999) 611.

Speckle Dinámico

Los objetos iluminados con luz coherente adquieren un aspecto granular peculiar denominado speckle. Si la superficie es ópticamente rugosa evoluciona en el tiempo, la luz dispersada da lugar a un patrón dinámico del speckle y su variación depende de la actividad de la muestra. Las muestras biológicas y otros procesos dinámicos (flujo de sangre, vibraciones, etc.) muestran este comportamiento. El speckle dinámico o biospeckle se puede también observar en procesos industriales no-biológicos, incluyendo el proceso de secado de pinturas, corrosión e intercambio de calor. El aspecto visual del diagrama speckle dinámico es similar a el de un líquido que hierve. Esta actividad ocurre cuando la muestra cambia sus características debido al movimiento de los centros de la dispersión, cambia en el camino óptica debido a las variaciones del índice de refracción, a los cambios de configuración o a la combinación de estas situaciones.

El estudio de la evolución temporal de los patrones de speckle puede proporcionar una herramienta interesante para caracterizar los parámetros implicados en procesos transitorios biológicos e industriales. Desde 1996, muchos esfuerzos se han realizado en CIOp, de asignar los números que caracterizan esta actividad del biospeckle y que correlacionan favorable con métodos alternativos de la medida de interés para el experimentador.

Varios algoritmos se han desarrollado para caracterizar la actividad dinámica del patrón de speckle usando análisis del contraste, acumulación de diferencias entre las imágenes, análisis espacial y temporal del patrón de speckle, entropía basada en wavelets, bandas espectrales temporales, etc.. En estos métodos se presenta una evaluación cualitativa del fenómeno en estudio. Para las medidas cuantitativas, fueron empleados la historia temporal del análisis del patrón de speckle (THSP) con la función del autocorrelation, el momento de la inercia de la matriz de la co-ocurrencia, la función estructura, la variación espacial de la fase y los métodos del histograma de la diferencia. También fueron propuestos modelos numéricos basados en el movimiento de los centros de la dispersión y una valoración de la variación espacial de la fase.

Los usos de las técnicas del biospeckle orientadas a la caracterización de tejidos biológicos y de procesos industriales fueron desarrollados en CIOp. Por ejemplo: viabilidad de semillas, daños en frutas, movilidad de parásitos, detección de hongos, chemotaxis en bacters, procesos de secado de pintura, hydroadsoción en geles, evolución de espumas, etc. Algunos de éstos trabajos fueron realizados en colaboración con grupos de las Universidades de Rosario (IFIR), de Salta, de Centro de la Provincia de Buenos Aires (Tandil), Mar del Plata del CIDEPINT (La Plata), de Universidades de Lavras y de Sao Paulo, Brasil, Católica del Perú (Lima), de Antioquia, Colombia y del Instituto Politécnico, La Habana, Cuba.

Tres publicaciones que ilustran esta línea de investigación se muestran en las páginas siguientes: una aplicación orientada a la caracterización de semillas, un algoritmo propuesto basado en bandas de frecuencia espectral y un display de la actividad obtenida con un modelo numérico basado en la variación espacial de la fase.

Dynamic Speckle

The objects viewed in highly coherent light acquire a peculiar granular appearance named speckle. If the optically rough surface evolves in time, the scattered light gives rise to a dynamic speckle pattern and its variation depends on the activity of the sample. Biological samples and other dynamic processes (blood flow, vibrations, etc.) show this behaviour.

Dynamic speckle or biospeckle can also be observed in non-biological industrial processes, including the drying of paint, corrosion and heat exchange. The visual appearance of the speckle diagram is similar to that of a boiling liquid. This activity takes place when the sample changes its properties due to movement of the scattering centers, changes in the optical path due to variations of refractive index, configuration changes or combination of these situations.

The study of the temporary evolution of the speckle patterns may provide an interesting tool to characterize the parameters involved in both biological and industrial transient processes. Since 1996, many efforts have been carried out at CIOp, to assign numbers that characterize this biospeckle activity and that correlate favourably with alternative measurement methods of interest for the experimenter.

Several algorithms to characterize the dynamic speckle pattern activity using contrast analysis, accumulation of differences between images, spatial and temporal speckle pattern analysis, wavelets based entropy, temporal spectral bands, etc. have been developed. In these methods a qualitative display is presented. For quantitative measurements, the temporal history of the speckle pattern (THSP) analysis with the autocorrelation function, the inertia moment of the co-occurrence matrix, the structure function, spatial variance of the phase and the difference histogram methods were employed. Numerical models based on movement of the scattering centres and an estimation of the spatial variance of the phase was also proposed.

Applications of the biospeckle techniques oriented to the characterization of biological tissues and industrial processes were developed at CIOp. For example: seeds viability, fruits damage, parasite motility, fungi detection, bacterial chemotaxis, drying of paint processes, hydroadsorption in gels, evolution of foams, etc.

Some of these researches were conducted in collaboration with groups of the Universities of Rosario (IFIR), Salta, Centro de la Provincia de Buenos Aires (Tandil), Mar del Plata, CIDEPINT (La Plata), Universities of Lavras and Sao Paulo, Brasil, Católica del Perú (Lima), Antioquia, Colombia and Instituto Politécnico, La Habana, Cuba.

Three published papers that illustrate this research line are shown in the following pages: an application devoted to seeds characterization, a proposed algorithm based on spectral frequency bands and an activity display obtained with a numerical model based on the spatial variance of the phase.

Biosystems Engineering (2003) 86 (3), 287–294
doi:10.1016/j.biosystemseng.2003.08.005
AE—Automation and Emerging Technologies

Available online at www.sciencedirect.com
SCIENCE DIRECT®

Assessment of Seed Viability by Laser Speckle Techniques

Roberto A. Braga, Jr[1]; Inácio M. Dal Fabbro[2]; Flávio M. Borem[1]; Giovanni Rabelo[1]; Ricardo Arizaga[3]; Héctor J. Rabal[3]; Marcelo Trivi[3]

[1]Departamento de Engenharia Agrícola, Universidade Federal de Lavras, (UFLA). CP 37, Campus UFLA, 37200-000, Lavras MG, Brazil; e-mail: roberto@ufla.br
[2]Departamento de Máquinas Agrícolas, FEAGRI, Universidade de Campinas (UNICAMP), Campinas SP, Brazil. e-mail: inacio@agr.unicamp.br
[3]Centro de Investigaciones Opticas (CIC-CONICET) and UID Optimo, Departamento Fisicomatemáticas, Facultad de Ingenieria, Universidad Nacional de La Plata, Argentina; e-mail of corresponding author: rabal@netverk.com.ar

(Received 10 December 2001; accepted in revised form 1 August 2003; published online 13 September 2003)

This work presents a new technique as a potential methodology to analyse seeds. The technology is known as dynamic speckle, or biospeckle, an optical phenomenon produced when active materials, such as biological tissue, are illuminated by laser light. In the present work, the biological activity of seed tissues has been inferred from quantitative and qualitative measurements of their speckle activity. The aim is to show that the biospeckle technique has a potential as a methodology to assess seed viability. One aspect that needs to be investigated is how the water content in the seeds affects bio-speckle activity. An experiment has been performed to determine the effect of humidity in the results. Seed activity for different levels of humidity was determined using quantitative and qualitative methods. Also, in others experiments, viable and non-viable seeds with different specific humidity levels could be classified using the same technique.
© 2003 Silsoe Research Institute. All rights reserved
Published by Elsevier Ltd

1. Introduction

Viability assessment is an important topic for seed production and commercialisation. Many tests have been developed to determine seed vigour and viability, however, these tests are not consistent among themselves, in the sense that they do not yield exactly the same results (Marcos Filho, 1999). Reliability and equivalence of different tests were the main objectives of recent studies (Hampton *et al.*, 1996; Howarth & Stanwood, 1993).

In this context, the evaluation of laser interferometric techniques as tools for seed analysis is worthy of evaluation. One of them is based on the properties of the dynamic speckle, which is a phenomenon occurring when coherent light is scattered by objects exhibiting some type of activity (Rabal *et al.*, 1996). The intensity in each point of the scattering pattern changes in time in a seemingly random fashion, but those intensity variations are related to, and carry information about, the activity in the object. The activity on the object may result in individual scatterers movement, changes in optical paths due to changes in refractive index, or combinations of both. When the phenomenon is observed in samples with biological activity, it is also known as biospeckle (Aizu & Asakura, 1996).

A similar phenomenon is also present in some industrial processes. Many efforts have been devoted to characterise quantitatively the activity, that is to assign numbers that correlate favourably with measurements of the processes of interest (Briers, 1978, 2000; Oulamara *et al.*, 1989; Okamoto & Asakura, 1995). These methods were applied to some extent to transient phenomena, *i.e.* biological activity of botanical specimens (Xu *et al.*, 1995), evaluation of blood flow (Aizu & Asakura, 1992), and drying of paint (Amalvy *et al.*, 2001).

Similar to the tetrazolium test (Howarth & Stanwood, 1993; AOSA, 1983), the dynamic speckle technique aims to generate a map of the seed, identifying areas with different activities. Since it is a new technique, it is necessary to investigate all possible phenomena which might interfere with the desired results, as for example the effect of humidity.

 © 2003 Silsoe Research Institute. All rights reserved
Published by Elsevier Ltd

In this paper, the activity of seeds as inferred from the dynamic speckle patterns generated by them are investigated, with the aim of developing a method for viability assessment.

Two methods are employed in order to evaluate quantitatively and qualitatively the activity of the dynamic speckle patterns. One of them is based on the calculation of the second order moment (moment of inertia) of the co-occurrence matrix in the time history of the speckle patterns (THSP), as proposed by Arizaga *et al.* (1999). The other is a display where the activity of the sample is shown as an image by using a generalised differences (GD) method (Arizaga *et al.*, 2002).

As the seeds must be soaked before testing, the degree of moisture may be an important factor to take into account in the biospeckle measurement. Besides, the presence of water vapour in the path of the light may be a source of error in the measured value of the optical activity. In order to have an estimate of this kind of error, the correlation between dynamic speckle and the moisture level in the seeds was measured.

Then, the information obtained with viable and non-viable biological tissues in presence of moisture was investigated. The studies were based on different experiments that: (a) determined the inertia moment in viable and non-viable seeds during drying; and (b) sorted viable and non-viable seeds into a specific moisture level.

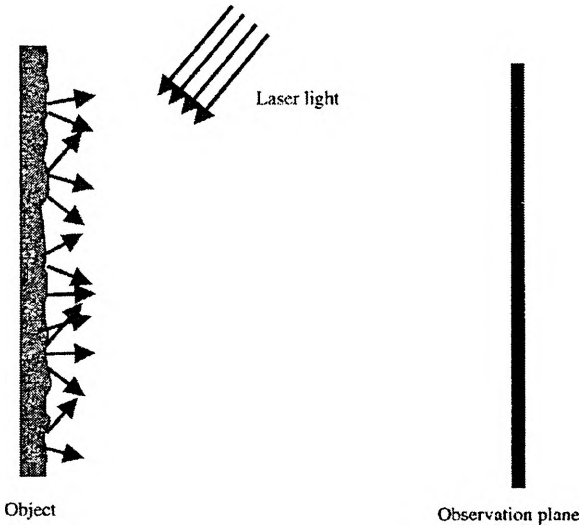
In most cases, different regions of the seeds produce differing levels of activity. Some changes are fast, some are slower and in some regions there are no changes at all. An 'activity image' can be constructed of the sample (the seed in this case) where the dark regions identify low activity and the bright regions denote high activity. The GD method was used to build activity images of seeds and a study of dead (low activity) and live seeds (high activity) is presented. This is convenient for seed viability assessment, since different regions of the seed have distinct importance for its viability.

The paper is organised as follows: Section 2 describes the fundamentals of the speckle phenomenon, and the mathematical tools used in its analysis. In Section 3, we present the experimental procedure, and the application of the method to bean seeds (*Phaseolus vulgaris* L.) is presented. The last section is devoted to discussions and conclusions.

2. Theoretical considerations

2.1. *Fundamentals of the laser speckle phenomenon*

The operation with laser light reveals a perhaps unexpected phenomenon: objects viewed in highly coherent light acquire a peculiar granular appearance. The detailed structure of this granularity bears no obvious relationship to the macroscopic properties of the illuminated object, but rather it appears chaotic and unordered, with an irregular pattern that is best described by the methods of probability theory and statistics. This phenomenon is know as 'laser speckle' (Dainty, 1975). The surfaces of most materials are extremely rough on the scale of an optical wavelength ($\lambda \cong 0{\cdot}6\,\mu m$). When nearly monochromatic light (laser light) is scattered from such a surface, the optical wave resulting at any moderately distant point consists of many components or wavelets, each arising from a different microscopic element of the surface. The distances travelled by these various wavelets may differ by several or many wavelengths if the surface is truly rough. Interference of the coherent wavelets differing in phase results in a granular pattern of intensity that is called speckle. *Fig. 1* shows the physical origin of the



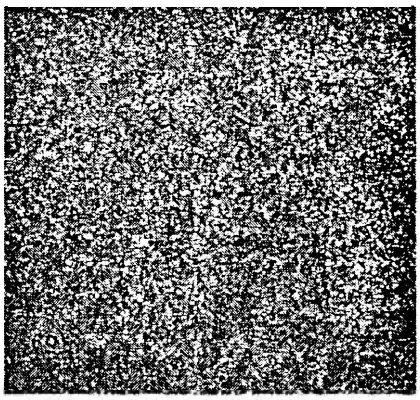


Fig. 1. Speckle pattern

speckle phenomenon and a typical speckle pattern. The object has a rough (unpolished) surface illuminated by laser light and a typical speckle pattern observed at a certain macroscopic distance is also shown.

Dynamic speckle is a phenomenon occurring when laser light is scattered by objects showing some type of activity. It is present in fruits and other biological samples, and some non-biological ones such as the drying of paint. It is due to changes in the phase of light produced by movements of the scatterers, changes in the refractive index, and rotatory power. Contributions from different scatterers beat in the detector producing time variations in local intensity. The visual appearance of the pattern is similar to that of a boiling liquid, so it is sometimes called 'boiling speckle'.

Recently, a method to measure the dynamic activity using the co-occurrence matrix of the time history of speckle pattern (Arizaga *et al.*, 1999), and another one to display the local dynamic activity of the samples was proposed (Arizaga *et al.*, 2002).

2.2. *Moment of inertia of co-occurrence matrix*

A convenient way to show the time evolution of a speckle pattern is that proposed by Oulamara *et al.* For every state of the phenomenon being assessed, 512 successive (digitised) images of the dynamic speckle pattern are registered. A certain column (for example, the middle one) is selected in each of them. Then, a new image is constructed by setting, side by side, the chosen column extracted from the successive patterns. The resulting image is named 'time history of the speckle pattern (THSP)'. Its rows represent different points on the speckle pattern and the columns their intensity in a sequence of regularly spaced time steps. The activity of the sample appears as intensity changes in the horizontal direction, that is, along the rows.

When a phenomenon shows low activity, time variations of the speckle pattern are slow and the THSP shows a horizontally elongated shape. In the limit, when there is no activity, the THSP shows no variation in the horizontal direction. Conversely, when the phenomenon is very active, the THSP shows fast intensity variations that resemble an ordinary spatial speckle pattern.

The THSP is assumed to be representative sample of the state of the phenomenon being assessed when it was registered.

The co-occurrence matrix M_{CO} is defined as

$$M_{CO} = [N_{ij}] \tag{1}$$

where, the entries are the number N of occurrences of a certain intensity value i, that is immediately followed by an intensity value j. This is a particular case of the so-called 'spatial grey level dependence matrices'. It is usually used to characterise texture in images. In the spatial case, its principal diagonal is related to homogeneous regions and the non-zero elements far from it represent high contrast occurrences.

In this work, the variable of interest is time. Then the involved N values are the occurrences of a certain grey value i followed in the next time step by a value j in the THSP as described above.

When the intensity does not change, the only non-zero values of this matrix belong to the principal diagonal. The presence of noise in the illumination source and in the detection precludes this situation.

As the sample shows activity, intensity values change in time, the number N outside the diagonal increases and the matrix resembles a cloud. Nevertheless, this matrix is sparse; it is mostly composed by zero values.

Figure 2 shows the THSP obtained in two extreme cases, high and low activities, and the corresponding co-occurrence matrices. It can be seen that the points in the main diagonal represent no change of intensity while the spread of points out of the diagonal represents time intensity changes. So, if the activity of the biological tissue is low, intensity changes are slow and the only appreciable values of the matrix appear near to the diagonal [*Fig. 2(a)*]. Conversely, if activity is high, the fast intensity changes produce high values far away the principal diagonal of the matrix [*Fig. 2(b)*].

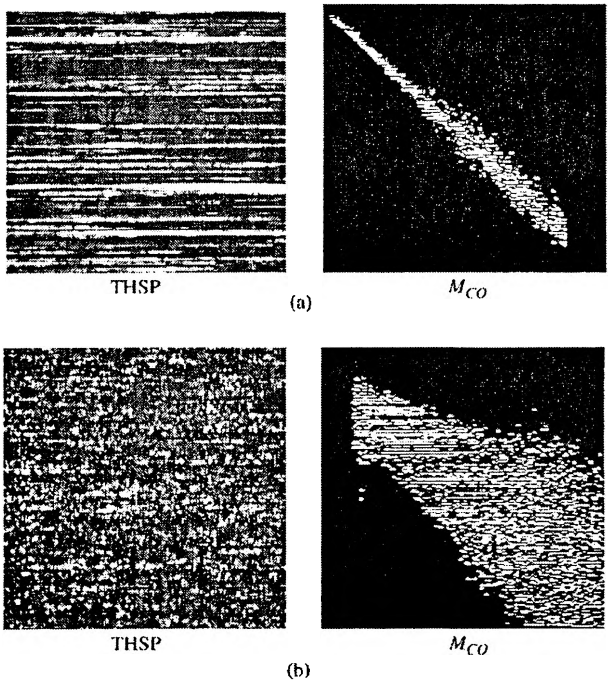


Fig. 2. Time history of the speckle pattern (THSP) and the corresponding co-occurrence matrix (M_{CO}) of: (a) low activity biological material; (b) high activity biological material

In order to obtain a quantitative measure from this matrix, it is necessary first to normalise it. This is done by dividing each row of the matrix by the number of times that the first grey level appeared. The sum of the components in each row then equals to 1.

$$M_{ij} = \frac{N_{ij}}{\sum_j N_{ij}} \tag{2}$$

This modified matrix is named the modified co-occurrence matrix, and it corresponds to a certain generalisation of the histogram. It is an experimental approximation to the transition probability matrix between intensity values in the THSP bearing a certain resemblance to the transition matrix appearing in Markov processes.

A measurement of the spread of the M values around the principal diagonal can be constructed as the sum of the matrix values times its squared row distance to the principal diagonal. This is a particular second-order moment called the moment of inertia M_I of the matrix with respect to that diagonal in the row direction. The name is suggested by the mechanical analogy with that operation. It is

$$M_I = \sum_{ij} M_{ij}(i-j)^2 \tag{3}$$

This measurement is similar to the one currently used in photon correlation spectroscopy, called photon structure function (Chu, 1991).

The occurrences in the diagonal do not contribute to increase the M_I value, while far away M entries add their more heavily weighted values. Similar measurements to this one are used in the discrimination of textures (Allam *et al.*, 1997).

2.3. *Generalised differences method*

When extended regions of a sample are investigated, usually their activity is not uniform. Then, it is sometimes necessary to segment the images according to their activity level. There are several image-processing methods to this end presented by Briers and Webster (1996); Fujii *et al.* (1987), and Konishi and Fujii (1995). Recently, Arizaga *et al.* (2002) proposed that the possibility of intensity changes in different time scales be taken into account by assigning to each pixel in the processed image the value $I'(i,j)$ obtained using the following expression:

$$I'(i,j) = \sum_k \sum_l |I_k(i,j) - I_{k+l}(i,j)| \tag{4}$$

where k and l are indices spanning all the possible numbers of the registered images.

This procedure is called GD. As every $I_k(i,j)$ value is subtracted from all others values in the same location, the result does not depend on the order of appearance of the $I_k(i,j)$ values. With these values, a new image is built where the dark regions identify low activity and the bright regions, the higher ones.

3. Experimental details

The experimental arrangement for both methods is shown in *Fig. 3*, with a low power (10 mW) helium–neon (He–Ne) laser-illuminated sample. By using a charge-coupled device (CCD) camera as detector and a host computer with a frame grabber, the successive sample images were registered, digitised to 8 bits (256 grey levels) and stored. Care was taken so that the speckles were well resolved by the CCD sensor. Very low illuminating intensity was used to minimise the effect of the irradiation on the sample activity. Mean laser illumination was kept constant during all measurements. No appreciable changes in sample reflectivity were observed.

For the co-occurrence matrix analysis, a column of the free propagation speckle pattern was read every 0·08 s, and then, a composite image of 512 by 512 pixels was formed by stacking consecutive columns. Finally, this image was retrieved and the second-order moments of its co-occurrence matrix calculated.

The investigated bean seeds (a total of 450) were kept at five different moisture levels of 13, 20, 30, 37 and 46% wet basis (w.b.), respectively, and were measured with and without a plastic covering film, at three consecutive times. Seeds were treated with an anti-fungi solution of 1:1000 of Captam. The number of replications was three.

Each seed was randomly picked from a set, cut into halves to separate both cotyledons and measured three

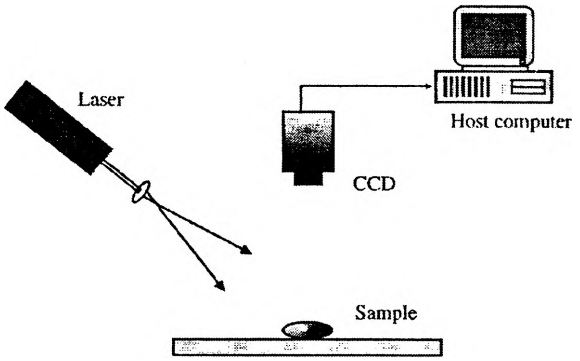


Fig. 3. Arrangement of the seed illumination and image capture: CCD, charge coupled device

consecutive times. The speckle images were then registered, the THSP was constructed and the M_I calculated. Analysis of variance at a probability level of 5% was then applied to the results.

In a further experiment, the seeds were sorted in two types: viable and non-viable. The seeds were verified by the tetrazolium test to confirm the respective batches of non-viable and high vigour bean seeds.

The speckle experiments to sort viable and non-viable seeds were conducted in two ways.

In the first test, two sets of 15 seeds of each kind were soaked for 24 h in germination paper. The THSP was then generated for each one and the M_I of the co-occurrence matrix was obtained.

The second experiment was designed to provide different M_I results during water evaporation in viable and non-viable seeds. Samples were taken from both populations under the same experimental conditions and were soaked in germination paper for 24 h to initiate the germination process. The viable and non-viable seeds were cut into halves and illuminated side by side. The THSP was generated for each one and M_I of the co-occurrence matrix was obtained as before. The initial moisture content of the seeds was 46%, and data were collected during 240 min. The values were averaged from three replicates.

In order to display qualitatively the activity, viable and non-viable seed inspection was also conducted using activity images with the GD method. In this case, the speckled images were not obtained by free propagation but consisted of subjective speckle focused images formed by an objective (focal length $f = 50$ mm). A set of 100 images, each 180 by 480 pixels in size, digitised to 256 grey levels, were registered. After the application of the algorithm described previously, the GD display was obtained. The time required for this process in our image processor (Imaging Technology ITX 151) was less than 2 min.

4. Results and discussion

The analysis of variance (Gomez & Gomez, 1984) was implemented on the M_I results, as transformed by a logarithmic function, to evaluate the influence of the moisture. The results are shown in Table 1. It is possible to observe the significance of the relation between moisture and film at a level of 5%, and also the relation between measurement order and moisture at a level of 1‰.

The analysis of variance of the relation between moisture and film is shown in Table 2. It can be observed that the significance is in the three highest

Table 1
Analysis of variance of ln(inertia moment)

Source of variation	*Degree of freedom*	*Sum of squares*	*Mean square*	*Computed F*	*Significance level*
Moisture	4	52·672	13·168	23·501	0·0000
Film	1	19·901	19·901	35·518	0·0000
Moisture × Film	4	8·733	2·183	3·897	0·0169
Error 1	20	11·206	0·560		
Time	2	0·244	0·122	93·249	0·0000
Time × moisture	8	0·055	0·006	5·265	0·0002
Time × film	2	0·008	0·004	3·128	0·0547
Time × moisture × film	8	0·017	0·002	1·678	0·1340
Error 2	40	0·052	0·001		

Total degree of freedom, 89.
Coefficient of variations 1, % = 21.99.
Coefficient of variations 2, % = 1.06.
Global average, 3.404. Number of observations, 90.

Table 2
Analysis of variance of relation between moisture and film

Source of variation	*Level of moisture*	*Degree of freedom*	*Sum of squares*	*Mean square*	*Computed F*	*Significance level*
Film	13	1	0·000	0·000	0·000	0·9860
Film	20	1	1·050	1·050	1·876	0·1860
Film	30	1	5·343	5·343	9·537	0·0058
Film	37	1	9·511	9·511	16·976	0·0005
Film	46	1	12·727	12·727	22·715	0·0001
Rest		20	11·206	0·560		

levels of moisture (30, 37, and 46% w.b.). This result indicates that evaporation modifies the results in these levels, permitting the conclusion that it is necessary to establish the moisture level before an experiment, and also to determine the best level of moisture required for seed evaluation.

In this case, the results suggest that the levels 23 or 30% w.b. are those where the influence of the evaporation is small or does not exist.

The curves of the averaged results for the relationship between film and moisture are shown in *Fig. 4*. The difference between these curves related to the 'with' and 'without' film conditions can be clearly appreciated. It can be concluded, therefore, that evaporation modifies the M_I results.

Both the viable and non-viable seeds show biospeckle activity after being adequately soaked. It is the moisture that generates an activity measurement not related to the biological sample.

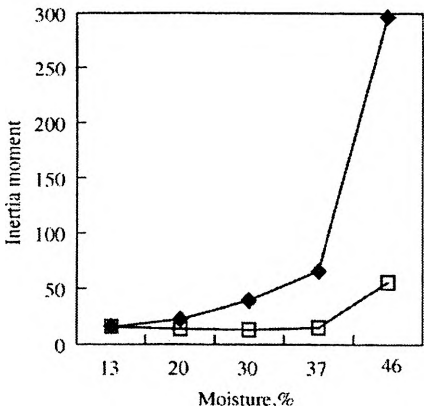


Fig. 4. Curves of the moment of inertia: —□—, with film; —◆—, without film

The results of the first viable/non-viable sorting test are shown in *Fig. 5*. It can be observed that the average of the M_I values for the viable seed set is notably higher than the corresponding value for the non-viable seed set. Only one sample shows anomalous behaviour with respect to the rest in each population. It should be noticed that the 'viable' and 'non-viable' conditions were not assessed by an alternative method and it could be due to misclassification.

The results of the measurement of inertia moment of viable and non-viable seeds as a function of time are shown in *Fig. 6*. In this figure, it can be seen that viable seeds present always greater activity than non-viable seeds. This result shows that the biological activity of the viable beans can be observed even in the presence of water movement and evaporation and could be used to sort the beans according to their viability.

The visual information of viable and non-viable seeds was obtained by using the GD method and the result can be seen in *Fig. 7*. The GD result showed one non-viable seed with a grey level that is clearly lower than that corresponding to the viable seed. This is an indication that viable and non-viable tissues or tissue

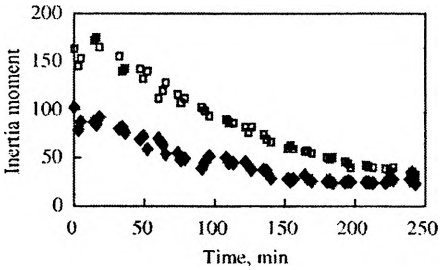


Fig. 6. Time evolution of the inertia moments of: □, viable; and ◆, non-viable beans

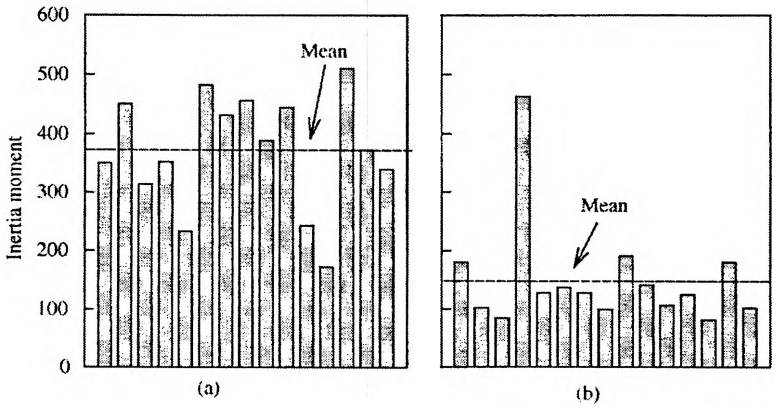


Fig. 5. Activity measurements using the inertia moment method on: (a) potentially viable seeds; and (b) non-viable bean seeds

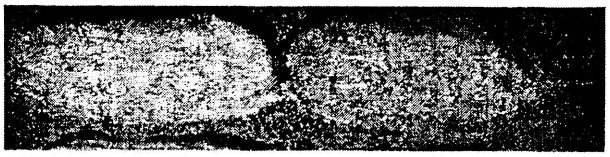


Fig. 7. Viable and non-viable bean seeds display using the generalised differences (GD) method

regions in the same seed with different activities could be distinguished using this type of display.

5. Conclusions

Dynamic speckle techniques were applied to the study of seeds in two series of experiments, one to sort viable and non-viable tissues and the other to investigate the influence of tissue moisture on the measurements.

Two dynamic speckle techniques were employed: the moment of inertia (M_1) of the co-occurrence matrix for the quantitative measurements; and the GD method for qualitative displays.

The experimental results show a significant dependence of the M_1 values on seed moisture content, and this dependence must be taken into account for the application of the dynamic speckle technique. Thus, it was not possible to discriminate between the viable and non-viable material at different moisture contents using the M_1 technique.

It is possible, however, to distinguish between viable and non-viable tissue by quantitative measurements or through a qualitative display, using the GD method.

More extensive validation of the technique is required with greater populations so that statistical tests can be applied to a comparison with actual accepted germination tests. Nevertheless, the proposed technique is simple, relatively cheap and fast, easy to implement and requires only laser and standard digital image processing components. It could be a promising tool to also evaluate other diverse agricultural specimens.

Acknowledgements

Thanks are due to Bruno Botelho Saleh, Monica Fabiana Bento Moreira and Juan Tara for help with the seed preparation and Nelly Cap for computing assistance. This work was supported by the Universidad de La Plata, CONICET and CICPBA (Argentina) and also by Federal University of Lavras, and Universidade Estadual de Campinas (Brazil).

References

Aizu Y; Asakura T (1996). Bio-speckles. In: Trends in Optics (Consortini A, ed.), pp 27–49. Academic Press, London.

Aizu Y; Asakura T (1992). Bio-speckle phenomena and their application to the evaluation of blood flow. Optics and Laser Technology, **23**, 205–219

Allam S; Adel M; Refregier P (1997). Fast algorithm for texture discrimination by the use of a separable ortonormal decomposition of the co-occurrence matrix. Applied Optics, **36**, 8313–8321

Amalvy J; Lasquibar C; Arizaga R; Rabal H J; Trivi M (2001). Application of dynamic speckle interferometry to the drying of coatings. Progress in Organic Coatings, **42**, 89–99

AOSA (1983). Seed Vigour Testing Handbook. Association of Official Seed Analysts, No 32, pp 82–88. Lincoln, NE, USA

Arizaga R; Trivi M; Rabal H J (1999). Speckle time evolution characterization by co-ocurrence matrix analysis. Optics and Laser Technology, **31**, 163–169

Arizaga R; Cap N; Rabal H J; Trivi M (2002). Display of local activity using dynamical speckle patterns. Optical Engineering, **41**, 287–294

Briers J D; Webster S (1996). Laser speckle contrast analysis (LASCA): a nonscanning, full field technique for monitoring capillary blood flow. Journal of Biomedical Optics, **2**, 174–179

Briers J D (2000). Time varying laser speckles for measuring motion and flow. Workshop on Coherent Optics of Ordered and Random Media. Saratov, Russia, 3–6 October 2000. http://optics.sgu.ru/SFM2000/report/Briers

Briers J D (1978). The statistics of fluctuating speckle patterns produced by a mixture of moving and stationary scatterers. Optics and Quantum Electronics, **10**, 364–366

Chu B (1991). Laser Light Scattering Basic Principles and Practice, Chapter 4. Academic Press, Boston.

Dainty J C (ed.) (1975). Laser Speckle and Related Phenomena. Springer Verlag, Berlin

Fujii H; Nohira K; Yamamoto Y; Ikawa H; Ohura T (1987). Evaluation of blood flow by laser speckle image sensing, part I. Applied Optics, **26**, 5321–5325

Gomez K A; Gomez A A (1984) Statistical Procedures for Agricultural Research, 2nd edn, p 680. John Wiley & Sons, New York

Hampton J G; Kahre L; Van Gastel A J G (1996). Quality seed—from production to evaluation. Seed Science & Technology, **24**, 393–407

Howarth M S; Stanwood P C (1993). Tetrazolium staining viability seed test using colour image processing. Transactions of the ASAE, **36**, 1937–1940

Konishi N; Fujii H (1995). Real time visualization of retinal microcirculation by laser flowgraphy. Optical Engineering, **34**, 753–757

Marcos Filho J (1999). Testes de Vigor: Importância e Utilização. [Vigour testing: importance and application.] In: Vigor de sementes:conceitos e testes (Seeds Vigour: Concepts and Testing) (Krzyzanowski F C; Vieira R D; França Neto J B, eds). ABRATES, Londrina, Brazil

Oulamara A; Tribillon G; Duvernoy J (1989). Biological activity measurement on botanical specimen surface using temporal decorrelation effect of laser speckle. Journal of Modern Optics, **36**, 165–179

Okamoto T; Asakura T (1995). The statistics of dynamic speckle. In: Progress in Optics XXXIV (Wolf E, ed.), pp 185–248. Elsevier Science, Amsterdam

Rabal H J; Arizaga R; Cap N; Trivi M; Romero G; Alanís E (1996). Transient phenomena analysis using dynamic speckle patterns. Optical Engineering, **35**, 57–60

Xu Z; Joenathan C; Khorana B M (1995). Temporal and spatial proprieties of the time-varing speckles of botanical specimens. Optical Engineering, **34**, 1487–1502

R00072851_YBENG_272

Decomposition of biospeckle images in temporary spectral bands

G. H. Sendra

Laboratorio Láser, Facultad de Ingeniería, Universidad Nacional de Mar del Plata, Juan B. Justo 4302, Mar del Plata, Argentina

R. Arizaga, H. Rabal, and M. Trivi

Centro de Investigaciones Opticas, Consejo Nacional de Investigaciones Científicas y Técnicas and UID Optimo, Comisión de Investigaciones Científicas de Provincia de Buenos Aires, Facultad de Ingeniería, Universidad Nacional de La Plata, Casilla Correo 124, 1900 La Plata, Argentina

Received December 14, 2004

We present a method of analysis of images of dynamic speckle based on the filtering in frequency bands of the temporary history of each pixel. Butterworth filters are applied to the temporary evolution, and different images are constructed showing the energy in each frequency band. Different degrees of activity of the sample in study, presumably attributed to different origins, are found. The method is exemplified with images of bruising damage in fruits and of biological activity in germinating corn seeds. It is found that the activity in the bruised region of an apple differs from the activity of healthy regions in a certain characteristic frequency range. The activity of the embryo can also be distinguished from that of the endosperm in corn seeds during germination. © 2005 Optical Society of America

OCIS codes: 100.0100, 120.6150, 000.1430.

Dynamic speckle or biospeckle is observed in biological samples illuminated by laser light. The properties and applications of this phenomenon have been treated in the literature.[1–3]

There are several methods for display of speckle pattern activity. Laser speckle contrast analysis,[4] proposed by Briers and Webster, uses the local contrast analysis of the integrated time-varying speckle in a nonscanning full-field technique for monitoring capillary blood flow. In the method of Fujii *et al.*,[5] an image display based on the accumulation of differences between images divided by its average shows a microcirculation map of human skin surface. Konishi and Fujii[6] used the signal-to-noise ratio in a real-time application to visualize a blood flow map of the human retina. The method of Arizaga *et al.*[7] is based on accumulating all possible differences between consecutive and nonconsecutive frames for each pixel of images in a seed analysis application. Recently other approaches were presented to characterization of atherosclerotic plaque by spatial and temporal speckle pattern analysis[8] and to applying time-dependent speckle in holographic optical coherence imaging to the study of tumor tissue.[9]

In the aforementioned methods, the result is a single image that shows a certain measure of the total activity of the sample. In this Letter we propose a method with which to analyze biospeckle activity based on decomposition of images in temporary spectral bands that permits us to obtain several measures with a better-defined meaning, thus adding to a better-detailed characterization of the behavior of the samples.

Most algorithms already developed for activity images discard time information and pool all the information concerning activity measurement in a single measure. Biological phenomena do not exhibit well-defined frequencies, but, in some cases, they differ in the frequency ranges where energy is concentrated. By using the filters in the frequency domain, one can discriminate phenomena in the sample that occur on different time scales. We present some examples to illustrate the methodology, but this technique can be extended to other applications of dynamic speckle in biological samples.

We consider biospeckle image sequences of objects in regions in which different activities are present. It can be observed that the levels of intensity variation of the speckle grains are different in each region. It is possible to find pixels that show fast intensity variations and others that show slow ones or no variations at all. To study these variations and characterize typical times of different regions we can state the analysis in frequencies instead of times.

Fujii *et al.*[10] applied this idea to the measurement of blood flow at a point. We extend its use to a sequence of images. Instead of carrying out a Fourier analysis, we use a bank of filters, implemented in a computer, to find bands that depict different types of activity. In this way, a region with a certain type of activity can be associated with one or several frequency bands.

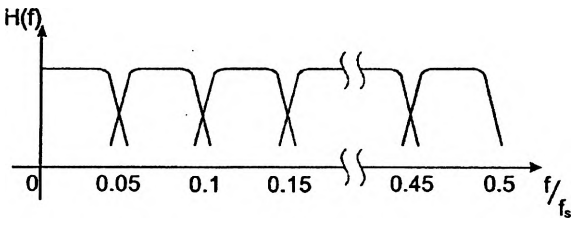


Fig. 1. Frequency bands in the Butterworth filters bank.

0146-9592/05/131641-3/$15.00 © 2005 Optical Society of America

We recorded a sequence of N successive speckle images with a sampling frequency f_s. In this way it was possible to observe how a pixel evolves through the N images. That evolution can be treated as a time series and can be processed in the following way: Each signal corresponding to the evolution of every pixel was used as input to a bank of filters. The intensity values were previously divided by their temporal mean value to minimize local differences in reflectivity or illumination of the object. The maximum frequency that can be adequately analyzed is determined by the sampling theorem and is half of sampling frequency f_s. The latter is set by the CCD camera, the size of the image, and the frame grabber. The bank of filters is outlined in Fig. 1. In our case, ten 5° order Butterworth[11] filters were used, but this number can be varied according to the required discrimination. The bank was implemented in a computer using Matlab software. We chose the Butterworth filter because, in addition to its simplicity, it is maximally flat. Other filters, an infinite impulse response, or a finite impulse response could be used.

By means of this bank of filters, ten corresponding signals of each filter of each temporary pixel evolution were obtained as output. Average energy E_b in each signal was then calculated:

$$E_b = \sum_{n=1}^{N} p_b^2(n), \tag{1}$$

where $p_b(n)$ is the intensity of the filtered pixel in the nth image for filter b divided by its mean value and N is the total number of images. In this way, ten values of energy for each pixel were obtained, each of them belonging to one of the frequency bands in Fig. 1.

With these values it is possible to build ten images of the active object, each one of which shows how much energy of time-varying speckle there is in a certain frequency band. False color assignment to the gray levels in the results would help in discrimination.

Using the proposed method, we performed two experiments: studies of bruising damage in fruits and of biological activity in corn seeds. In the experiments the sample was illuminated by an expanded low-power (10 mW) He–Ne laser. By using a CCD camera as a detector and a host computer with a frame grabber, we registered, digitized, and stored the successive sample images. Care was taken that the speckles were well resolved by the CCD sensor.

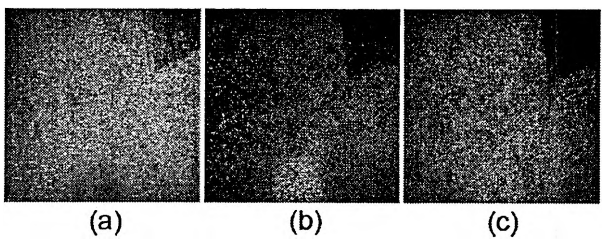


Fig. 2. Results of the apple bruising experiment: (a) first band (0–0.125 Hz), (b) third band (0.250–0.375 Hz), (c) tenth band (1.125–1.250 Hz).

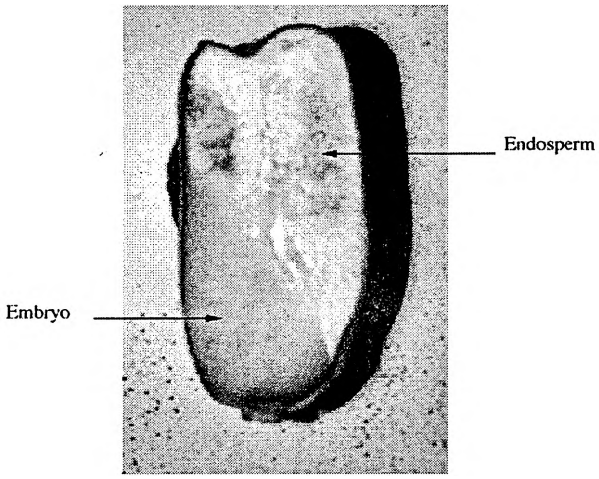


Fig. 3. Incoherent image of a corn seed.

We used a low illuminating intensity to minimize the effect of irradiation on the sample activity. The mean laser illumination was kept constant during all measurements, and no appreciable changes in sample reflectivity were observed.

An apple was bruised[12] by dropping a sphere (diameter, 21.9 mm; weight, 133.6 g) on it from a controlled height (h=20 cm). The bruised region could not be distinguished from the unbruised rest of the apple by visual inspection.

A series of images of dynamic speckle was registered after the blow and the images were processed with the proposed algorithm. An inert object was included as a reference in the upper-right corner of each image. In Fig. 2 we show three representative results. Figure 2(a) corresponds to the lower-frequency band (0–0.125 Hz). The dark zone below represents the bruised region. This means that the activity in this zone and for this frequency band is very low, slightly higher than in an inert region but lower than in a healthy region. Conversely, Fig. 2(b), corresponding to the third band (0.250–0.375 Hz), shows the bruised region with higher activity than in the rest of the apple. Band 10 [1.125–1.250 Hz; Fig. 2(c)] does not show any difference between bruised and healthy regions.

The technique was then applied to images of speckle in corn seeds that had previously been hydrated to start the germination process and had been longitudinally cut in halves. In Fig. 3 an image of seed illuminated by incoherent light is exhibited; the embryo and the endosperm regions can be observed. The six most significant resultant images that correspond to the energy in each band are shown in Fig. 4.

The image of the first band (0–0.1 Hz) shows the bright zone of the endosperm. The embryo, which is the active zone in germination, is dark here because this band emphasizes only the zones of slower activity. The last image represents the highest frequency band reported here (0.5–0.6 Hz). The embryo is bright here, and the endosperm is dark. That is, the embryo shows higher activity in the high frequencies. For higher frequencies than that the results do not show significant differences.

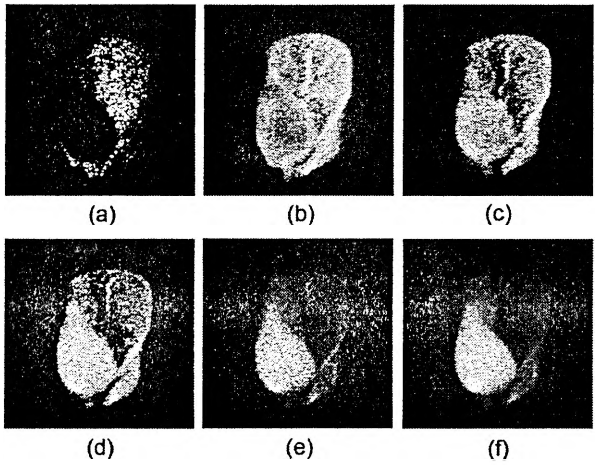


Fig. 4. Results of the corn seed experiment: (a) first band (0–0.1 Hz), (b) second band (0.1–0.2 Hz), (c) third band (0.2–0.3 Hz), (d) fourth band (0.3–0.4 Hz), (e) fifth band (0.4–0.5 Hz), (f) sixth band (0.5–0.6 Hz).

In the intermediate-frequency bands [Figs. 4(b)–4(e)], other regions, such as a riverlike trace in the endosperm, appear bright, probably due to a break but the biological origin of the brightness is not yet certain. It is apparent that in the intermediate-frequency bands the method permits the estimation of the energy that corresponds to several time scales. Several regions can be discriminated by differences in activity.

Adequate interpretation of the meaning of these measures requires learning through experiment to evaluate which activities are normal and which interfere with germination. In these images there seems to be considerable biological information, but its discussion is beyond the scope of this work.

In conclusion, we have proposed the use of temporal filters to identify regions with speckle activity of different possible causes. A bank of filters has been used, and different types of activity have been detected. In this way, regions of the object that show certain types of activity can be associated with one or several frequency bands.

Applications to corn seeds of the onset of germination and to a bruised apple were used as examples. In both cases it was possible to discriminate regions with different types of activity. The interval of frequencies where the apple's bruised region can be distinguished from the healthy regions was identified, and the activities of the embryo and the endosperm in corn seeds were explored.

Compared with existing methods for activity assessment, this method is both quantitative and qualitative as it provides visual information on the several time scales where the various phenomena occur without loss of spatial resolution. Additional information is then obtained, as in all the other displays all the activity information is pooled in a single image. Unfortunately, in its present state the method cannot be implemented in real time.

The technique can be used to segment other types of phenomena in biological samples or in industrial processes (corrosion, drying of paint, vibrations, etc). Each application requires learning and expertise in the phenomenon involved and provides information on the times scales that determine the activity of each region.

This study was partially supported by grants from the Consejo Nacional de Investigaciones Científicas y Técnicas, the Comisión de Investigaciones Científicas de Provincia de Buenos Aires, the Facultad de Ingeniería, Universidad Nacional de La Plata; and the Facultad de Ingeniería, Universidad Nacional de Mar del Plata, Argentina. H. Rabal's e-mail address is hrabal@ing.unlp.edu.ar.

References

1. Y. Aizu and T. Asakura, in *Trends in Optics*, A. Consortini, ed. (Academic, 1996), Chap. 2.
2. T. Okamoto and T. Asakura, in *Progress in Optics*, E. Wolf, ed. (Elsevier Science, 1995), Vol. XXXIV, pp. 185.
3. J. D. Briers, Opt. Eng. **32**, 277 (1993).
4. J. D. Briers and S. Webster, J. Biomed. Opt. **1**, 174 (1996).
5. H. Fujii, K. Nohira, Y. Yamamoto, H. Ikawa, and T. Ohura, Appl. Opt. **26**, 5321 (1987).
6. N. Konishi and H. Fujii. Opt. Eng. **34**, 753 (1995).
7. R. Arizaga, N. Cap, H. J. Rabal, and M. Trivi, Opt. Eng. **41**, 287 (2002).
8. G. J. Tearney and B. E. Bouma, Opt. Lett. **27**, 533 (2002).
9. P. Yu, I. Peng, M. Mustata, J. J. Turek, M. R. Melloch, and D. D. Nolte, Opt. Lett. **29**, 68 (2004).
10. H. Fujii, T. Asakura, K. Nohira, Y. Shintomi, and T. Ohura, Opt. Lett. **10**, 104 (1985).
11. A. V. Oppenheim and R. W. Schafer, *Digital Signal Processing* (Prentice-Hall, 1975), pp. 211.
12. M. Pajuelo, G. Baldwin, H. J. Rabal, N. Cap, R. Arizaga, and M. Trivi, Opt. Lasers Eng. **40**, 13 (2003).

Speckle activity images based on the spatial variance of the phase

Héctor Rabal, Nelly Cap, Marcelo Trivi, Ricardo Arizaga, Alejandro Federico, Gustavo E. Galizzi, and Guillermo H. Kaufmann

We propose the display of the local spatial variance of the temporal variations of the phase as an activity descriptor in dynamic speckle images. The spatial autocorrelation of the speckle intensity is calculated in sliding windows, and an estimation of the variance of the phase variations in each region of the sample is determined. The activity images obtained in this way depict some interesting features and in some cases they could be related to physical magnitudes in the samples. A simulation is presented, and examples corresponding to usual study cases are also shown, namely, fruit bruising and paint drying. © 2006 Optical Society of America

OCIS codes: 110.0110, 110.6150, 030.6140.

1. Introduction

Dynamic speckle or *biospeckle* is a phenomenon occurring when laser light illuminates scattering surfaces with some type of activity.[1,2] For example, fruits, seeds, and painted surfaces subjected to drying show this behavior. The study of the temporal evolution of the speckle patterns may provide an interesting tool to characterize the parameters involved in some biological applications and industrial processes.

The autocorrelation analysis of the intensity as a function of time is a classical method for the characterization of dynamic speckle patterns.[3,4] FWHM is a possible estimator of speckle lifetime and consequently of the local activity. Another approach to analyze the dynamic speckle is given by the generation of the time history of the speckle pattern (THSP) and its characterization using different descriptors. Several algorithms were proposed to give a quantitative measurement of the speckle activity using the THSP.[5,6] Although several methods are effective in some cases, most of them are difficult to associate with physical changes that occur in the sample.

In the activity images corresponding to dynamic speckle, the sizes, shapes, and spatial distribution of the areas of the same gray levels change with time. There are several methods to generate a qualitative display with a speckle pattern activity.[2,7–9] In these cases, a gray level or false color display shows different regions of the samples that allow us to discriminate the differential activity of the scattering surfaces.

Some of the display methods already developed consist of heuristic tools that give little insight into the physical origins that can be attributed to the observed activity. As this estimation is an inverse problem, the causes of the activity most probably cannot be uniquely determined unless some *a priori* knowledge of the phenomenon is available. Nevertheless, under some not very stringent assumptions, estimations of the spatial variance of the phase between consecutive frames can be evaluated, and based on these results, segmentation image displays can also be obtained.

Phase can be easily associated with its physical origins. As a matter of fact, the origin of dynamic speckle phenomena is mainly due to random phase differences, Doppler effect, beating of waves with close frequencies, etc. If the reflectance of an object is constant, temporal variations of the intensity in its speckle patterns are due to phase changes. Therefore if the physical origin of the phase change is known or suspected, the processing leads to additional infor-

H. Rabal (hrabal@ing.unlp.edu.ar), N. Cap, M. Trivi, and R. Arizaga are with the Centro de Investigaciones Ópticas and UID Optimo, Facultad de Ingeniería, Universidad National de la Plata, P. O. Box 124, 1900 La Plata, Argentina. A. Federico is with the Física y Metrología, Instituto Nacional de Tecnología Industrial, P. O. Box B1650WAB, B1650KNA San Martín, Argentina. G. E. Galizzi and G. H. Kaufmann are with the Instituto de Física Rosario (CONICET-UNR), Boulevard 27 de Febrero 210 bis, S2000EZP Rosario, Argentina.

Received 9 December 2005; revised 4 April 2006; accepted 9 May 2006; posted 19 July 2006 (Doc. ID 66474).

0003-6935/06/348733-06$15.00/0

© 2006 Optical Society of America

mation on the underlying phenomena occurring in the sample.

Recently, we presented a numerical simulation that allows for the generation of temporal sequences of 2D dynamic speckle patterns.[10] In this paper we propose an estimation of the spatial variance of the phase from the intensity autocorrelation as a descriptor of the local activity of dynamic speckle images. In the next section, we will briefly describe the theory of the intensity variations in a speckle pattern generated by moving scatterers. Then we will show how an estimation of the spatial variance of phase can be calculated from its intensity autocorrelation. Finally, numerical simulations of a typical experiment will be shown, and the results obtained from two actual experiments on study cases will be presented, namely, the drying of paint on a coin and the presence of bruising in a fruit. In these cases, the knowledge of the height differences in the profile of a coin and the presence of induced bruising in an apple are examples of *a priori* available knowledge that helps to interpret the results.

2. Theory

In this work we have used the same formulation already proposed in Ref. 10 as briefly described below. In this simplified model, the surface of the sample under study is considered to be composed of a set of discrete scattering centers. When coherent polarized laser light with wavelength λ is used for the illumination, the amplitude of the electric field U_0, at a point in the Fresnel region, can be calculated as

$$U_0 = \sum_j a_j \exp(i\phi_j), \tag{1}$$

where a_j and ϕ_j are the amplitude and phase contributions due to the scattering center j. The usual assumptions that lead to the definition of a well-developed speckle pattern are also assumed here.

When the sample shows local activity, the amplitude of the electric field can be written as

$$U = \sum_j a_j \exp[i(\phi_j + \Delta\phi_j)], \tag{2}$$

where $\Delta\phi_j$ is the change in the optical phase because of the activity.

Assuming that a set of K speckle patterns is sequentially acquired at equal time steps, a quantitative measurement of the activity of the underlying process can be obtained through the evaluation of the spatial correlation coefficient $c(k)$ between the first image and the following ones. Considering that the process is piecelike stationary during the acquisition time, $c(k)$ is defined by

$$c(k) = \frac{\langle I(0)I(k)\rangle - \langle I(0)\rangle\langle I(k)\rangle}{\{[\langle I^2(0)\rangle - \langle I(0)\rangle^2][\langle I^2(k)\rangle - \langle I(k)\rangle^2]\}^{1/2}}, \tag{3}$$

where $I(k)$ is the intensity at a point of each temporal frame k and $\langle\ \rangle$ denotes the spatial mean value operator over each speckle image of the sequence.

When the Doppler effect is the dominant cause of the activity, the phase change $\Delta\phi_j$ may be due to an alteration Δh_j in the height of the scattering centers normal to the surface. Then,

$$\Delta\phi_j = (2\pi/\lambda)(1 + \cos\theta_j)\Delta h_j, \tag{4}$$

where θ_j is the angle between the illuminating beam and the observation direction normal to the surface at the scattering center j.

It was demonstrated in Refs. 11 and 12 that the correlation coefficient $c(k)$ decreases exponentially with the variance of the phase change. This result was obtained under the assumption that all amplitude and phase changes of the scattering centers are statistically independent of each other and of the amplitudes and phases of all other scatterers, that the phase change $\Delta\phi_j$ given by Eq. (4) follows a normal distribution with a variance $\sigma^2(\Delta\phi)$, and that there are no changes in the reflectivity of the sample. Consequently, the correlation coefficient can be expressed as

$$c(k) = \exp[-\sigma^2(\Delta\phi)], \tag{5}$$

where the phase change $\Delta\phi$ must be evaluated with respect to the first speckle pattern of the temporal sequence ($k = 0$). Equation (5) holds both for objective and for subjective speckle patterns, as long as the surface roughness and the microstructure variation cannot be resolved. Therefore local estimations of the phase variance can be calculated if the regions where the space average is performed are large enough for the statistics to be effective.

3. Computer Simulation of Time Varying Speckle Patterns

Sequences of time varying speckle patterns can be computer simulated using the method described in Ref. 10. The intensity $I(m, n, k)$ in each speckle pattern point belonging to a given temporal sequence is evaluated from

$$I(m, n, k) = |F^{-1}\{HF[e^{i\phi(m,n,k)}]\}|^2, \tag{6}$$

where $m = n = 0, 1, \ldots, N - 1$ are the pixel coordinates of the CCD detector used to acquire the speckle images, $\phi(m, n, k)$ is an $N \times N$ matrix, which represents the phase distribution of the scattered light from the rough surface; i is the imaginary unit; F and F^{-1} are the direct and inverse Fourier transforms, respectively; and H is a circular low-pass filter with radius r in the Fourier space, which represents the circular aperture of the camera lens and determines the average speckle size of the speckle grains.

The speckle phase $\phi(m, n, 0)$ corresponding to the first frame $k = 0$ is chosen as a matrix with uniform distributed values in the interval $(-\pi, \pi)$. Considering that all scattering centers move randomly up and

down along the direction normal to the surface of the sample, the phase $\phi(m, n, k)$ is evaluated from

$$\phi(m, n, k) = \phi(m, n, k-1) + G(m, n, k) \times \sigma[\Delta\phi(m, n, k-1, k)], \quad k = 1, \ldots, K-1, \tag{7}$$

where $\sigma[\Delta\phi(m, n, k-1, k)]$ is the standard deviation of the phase change between two consecutive speckle patterns, and $G(m, n, k)$ is an $N \times N$ random matrix with Gaussian distributed values having a mean $\mu = 0$, and a standard deviation $\sigma = 1$, which has to be recalculated at every frame k.

Through a simple mathematical derivation, the standard deviation of the phase change between two consecutive speckle patterns $\sigma[\Delta\phi(m, n, k-1, k)]$ can be expressed in terms of the correlation coefficient $c(k)$ of each image with respect to the first frame of the sequence as

$$-\ln[c(k)] = -\ln[c(k-1)] + \sigma[\Delta\phi(k-1, k)]^2. \tag{8}$$

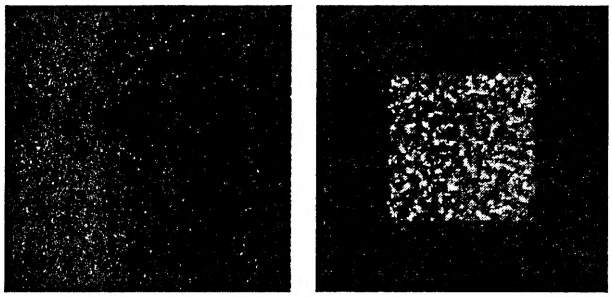
Therefore the sequence of computer simulated speckle patterns generated by Eq. (6) is produced using a phase distribution given by

$$\phi(m, n, k) = \phi(m, n, k-1) + G(m, n, k) \times \sqrt{\ln c(k-1) - \ln c(k)}. \tag{9}$$

The simulation model requires $c(k)$ to be a monotonically decreasing function. This is a limitation of the model, but this is the case that appears at least in several processes such as paint drying and metal corrosion. If this requirement is not verified or due to noise, the term inside the square root of Eq. (9) could be negative in some pixels or regions, and then σ in Eq. (8) will not represent the phase variance. Even when the expression inside the square root of Eq. (9) is not negative, this is not a guarantee that the conditions required for the model are fulfilled. However, we are going to see that even in these cases, the processed image gives some useful qualitative information on the distribution of the activity in the object.

4. Experiments and Results

We used the described numerical model to generate speckle activity images based on the spatial variance of the phase. To test for the possibility of obtaining segmentation images based on the variance of phase changes, we numerically simulated a sequence of active speckle images with different values of the variance in two different regions. Afterward, the simulated speckle patterns were processed as follows: For each pixel of the speckle patterns, the $c(1)$ value was calculated from the first two frames 0 and 1 by means of Eq. (3) using a 5×5 window. The window size is given by a trial and error optimization compromise between statistics and resolution. Large windows reduce spatial resolution and improve variance precision, while the converse is true for small windows.



(a) (b)

Fig. 1. (a) Typical speckle pattern produced by numerical simulation; (b) display of the processed image where the loci of equal σ values are clearly perceived.

The same calculation was performed with the frames 0 and 2 to obtain $c(2)$. A map of $c(1)$ and $c(2)$ was obtained by displacing the window over the speckle patterns. Using these maps, an estimation of the local value of σ was calculated by means of Eq. (8). Then this procedure was repeated for all the consecutive sets of three frames belonging to a given temporal sequence. Finally, the temporal average of the previously computed σ values was evaluated.

The space averaging operation that is applied inside the window and is required in the calculation of the variance is in conflict with high space resolution in the resulting image. The use of a sliding window results in a tiling appearance of the image. To reduce this deleterious effect, we decided to perform the estimation over a set of consecutive frames taken in groups of three and to average the results.

Figure 1(a) shows one of these simulated speckle patterns where the spatial phase variations were set to different values in two square regions. Although no hint of that variation can be observed in the previous image, Fig. 1(b) displays the processed image in which the loci of equal σ values are clearly perceived.

Afterward, we performed several experiments with actual speckle patterns already used in previous works. The temporal sequences of speckle patterns were acquired using the setup shown in Fig. 2. A divergent laser beam ($\lambda = 632.8$ nm, polarized) was used to illuminate the object while a CCD camera acquired the dynamic speckle patterns and a frame grabber digitized and stored the intensity data for each frame. The experimental conditions were: pixel size, 8.4 μm $\times$ 9.8 μm; magnification, 1/3; focal distance of the objective, 50 cm (with added close-up rings); pupil size, 3.1 mm; illumination angle, ~45°. A region wider than the object was illuminated to assure that the object has received uniform illumination.

Then, the spatial correlation evaluated inside the sliding windows was calculated for sets of three consecutive frames as described above. The variance of

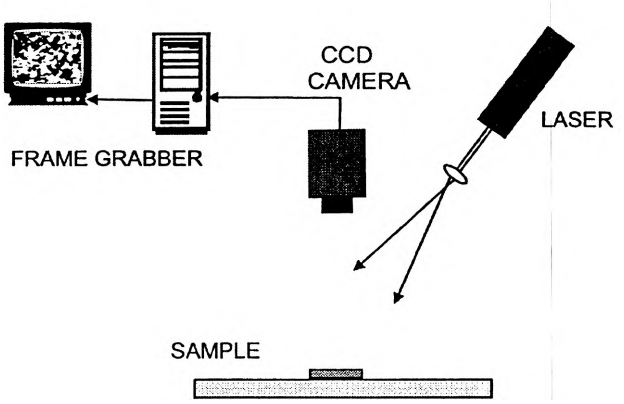
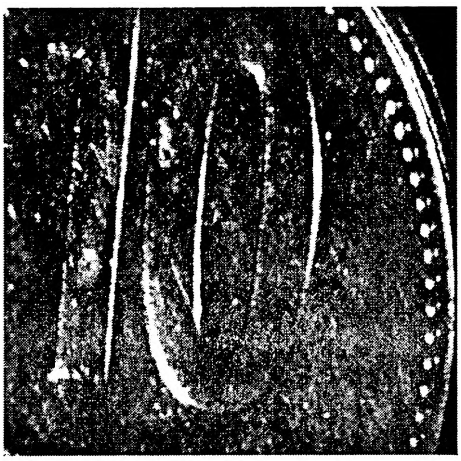


Fig. 2. Experimental setup used to acquire speckle pattern sequences.

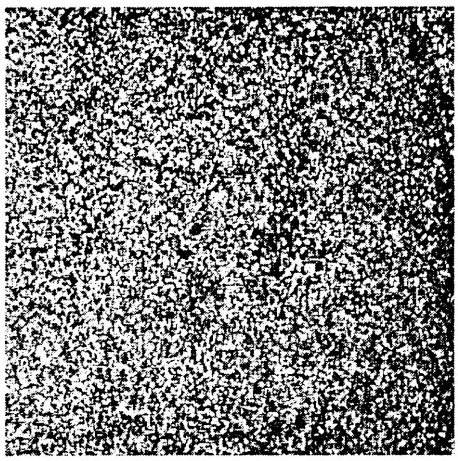
the phase was estimated using Eq. (8), and the activity image was generated using scaled values of the calculated variance. For the assumptions stated in the theory to be valid and the phase variance to be accurately determined, the speckle pattern must be well sampled. This means that the mean speckle size should be greater than the pixel size. This fact was also taken into account both in the numerical simulations and in the experiments. The average speckle size used both in the computer simulation and in the experiments was 2 pixels. Noise in the CCD camera, in the laser source, and in the image processor, limits the performance of the method. Because of the noise, activity changes meaning differences in σ smaller than 0.1 rad cannot be accurately detected.

As explained in Ref. 10, paint drying is a process that was found to be well fitted to apply the described theoretical model. For this reason, one test involved the painting of a coin with a layer of spatial variable thickness due to its relief. It was expected that the paint located in thinner layers, because of the protruding parts of the coin, would dry faster and therefore would be less active than in thicker regions. Figure 3(a) shows the original coin illuminated by incoherent light. One frame of the sequence of speckle patterns is depicted in Fig. 3(b) where no hint of the coin relief can be perceived. Figure 3(c) shows the processed image obtained using the proposed method. Thinner painted regions appear darker than the thicker ones, thus indicating that they are drier and consequently less active and display smaller variance of the phase variations. Note that not only coarse features, such as the numbers on the coin, but also finer detail as on the rim, can also be observed.

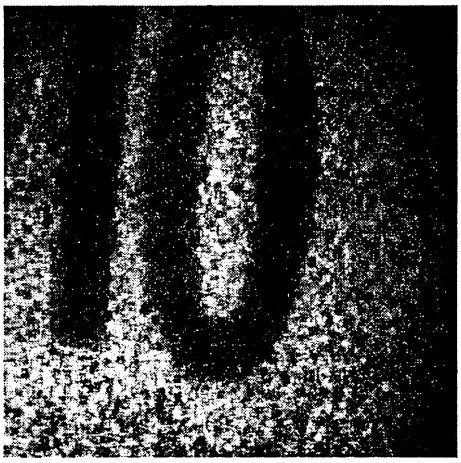
We have also performed a test on a controlled bruising experiment on an apple. This is an object that had previously been used as a case study to evaluate other display techniques.[9,13–15] The object was a region of an apple where intentional bruising was produced by letting a calibrated ball with a diameter of 21.9 mm and a weight of 133.6 g fall from a height of 20 cm. The bruising could not be visually perceived. An inert object (a piece of metal) was in-



(a)



(b)



(c)

Fig. 3. (a) Coin observed under incoherent light illumination; (b) speckle pattern of the coin illuminated by laser light (the imaged area is ~15 mm × 15 mm); (c) display of the processed image where the loci of equal activity corresponding to equal thickness of paint appear as gray levels.

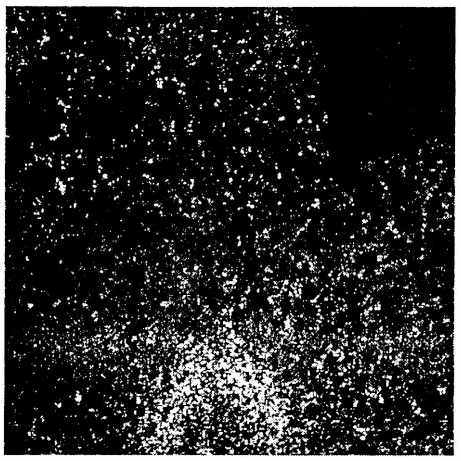


Fig. 4. Display of the activity in a bruised apple experiment (the imaged area is ~20 μm × 20 mm). The upper right corner shows an inert object included as a reference, and it appears dark. The bruised region is in the middle to lower region of the image and appears with a bright rim indicating higher activity than in the healthy regions.

cluded as a reference surface in the upper right corner of the image.

As this phenomenon includes biological tissue, its inner dynamics are poorly known, and it is not to be expected that the conditions of validity of the proposed model be fulfilled. We found that many errors occurred as manifested by obtaining negative values of σ^2. In this case, one out of three pixels showed this behavior. We constructed an image excluding these results, and nevertheless the three regions can be clearly observed as seen in Fig. 4. The inert region appears dark, while the healthy regions of the apple, with intermediate activity, appear in an intermediate gray level. The bruised region located in the middle to bottom of the image appears very bright, indicating higher activity.

The images obtained by applying this methodology are not high-resolution ones, as also happens with some other methods involving spatial windows as, for example, with laser speckle contrast analysis.[2] Speckle activity images show some pixeling and also edge smoothing. Therefore it is expected that edges will not be well resolved. Sharp activity edges are not commonplace in biological tissues so that in most cases this does not constitute a severe limitation. Nevertheless, notice that on the edge that appears on the border between the inert material and the apple in the upper right corner of Fig. 4, the method distinguishes the activity of both regions quite well.

5. Conclusions

In each of the developed methods, to estimate dynamic speckle activity, a different magnitude is calculated and so are the resulting images. Some activity images are sensitive to the temporal signal roughness (Hurst coefficient[14]), some others to entropy,[15] others to the proportion of moving scattering centers,[16] and others to the energy present in different temporal frequency bands,[9] to name just a few. In all cases, the *a priori* knowledge of the phenomenon under study can help in the choice of the method to be used, and an expert in the phenomenon under study helps to discern the best choice.

In the method that we are proposing here, the observed result reflects the spatial variance of the phase if the required conditions are fulfilled. That magnitude can be associated with the velocity of the scattering centers or to refractive index variations or to other physical features of the surface that could be *a priori* known. It gives different information that had not been previously exploited in this context. In some simplified nonbiological examples such as corrosion,[12] the variance of phase can be interpreted as due to the temporal changes in the height of the surface; a well-defined physical property, but biological processes are not so simple and some ambiguity should always be expected.

The phase variance determined from the spatial autocorrelation of the intensity of consecutive frames in a sequence of dynamic speckle patterns can be used as an estimator of its activity, and if some additional information on its origin is available, it can be related to its physical origin. Activity images obtained with the proposed procedure then add to the understanding and segmentation of active regions and can be used for screening of known phenomena when they satisfy the adequate statistics. A compromise between statistical significance of the estimation and spatial resolution in the resulting image display is implicit. However, this effect can be partially alleviated by averaging several sets of consecutive results when the phenomenon is stationary.

Although in many cases the Doppler shift is the main origin of the dynamics, this is not always the case. Refractive index time variations, multiple scattering, and shading are other possible causes, and these effects were not taken into account in the simulations nor were they adequately interpreted in the experimental results, if they were present. Even if the statistical assumptions are satisfied, the variance of the phase still can be attributed to more than one cause.

It should be noted that the computation of $\sigma^2(\Delta\phi)$ involves the ratio of two values of the normalized correlation. In poorly illuminated areas, noise can possibly be boosted, and erroneous values of the variance will be obtained. Therefore care should be taken to maintain a uniform illumination over the whole sample.

The need for using sliding windows limits both spatial and intensity resolutions. Variations in reflectivity were assumed not to be present. Nevertheless, dynamic scattering is known to be a process of many to one; that is, similar effects can be due to different causes. Therefore the present work should be considered as a step forward to obtain more information on the spatial variation of active samples from their speckle patterns.

This research has been supported by Agencia Nacional de Promoción Científica y Tecnológica, Consejo Nacional de Investigaciones Científicas y Técnicas, Comisión de Investigaciones Científicas de la Provincia de Buenos Aires, Red Argentina de Óptica and Universidad Nacional de La Plata, all from Argentina.

References

1. Y. Aizu and T. Asakura, "Biospeckle," in *Trends in Optics*, A. Consortini, ed. (Academic, 1996), Chap. 2.
2. J. D. Briers and S. Webster, "Laser speckle contrast analysis (LASCA): a nonscanning, full field technique for monitoring capillary blood flow," J. Biomed. Opt. **1,** 174–179 (1996).
3. Y. Aizu and T. Asakura, "Biospeckle phenomena and their applications to the evaluation of blood flow," Opt. Laser Technol. **23,** 205–219 (1991).
4. B. Ruth, "Superposition of two dynamic speckle patterns. An application to noncontact blood flow measurements," J. Mod. Opt. **34,** 257–273 (1987).
5. A. Oulamara, G. Tribillon, and J. Dovernoy, "Biological activity measurements on botanical specimen surfaces using a temporal decorrelation effect of laser speckle," J. Mod. Opt. **36,** 165–179 (1989).
6. R. Arizaga, M. Trivi, and H. J. Rabal, "Speckle time evolution characterization by the co-occurrence matrix analysis," Opt. Laser Technol. **31,** 163–169 (1999).
7. H. Fujii, K. Nohira, Y. Yamamoto, H. Ikawa, and T. Ohura, "Evaluation of blood flow by laser speckle image sensing. Part 1," Appl. Opt. **26,** 5321–5325 (1987).
8. R. Arizaga, N. L. Cap, H. J. Rabal, and M. Trivi, "Display of local activity using dynamic speckle patterns," Opt. Eng. **41,** 287–294 (2002).
9. G. H. Sendra, H. J. Rabal, R. Arizaga, and M. Trivi, "Biospeckle images decomposition in temporary spectral bands," Opt. Lett. **30,** 1641–1643 (2005).
10. A. Federico, G. H. Kaufmann, G. E. Galizzi, H. Rabal, M. Trivi, and R. Arizaga, "Simulation of dynamic speckle sequences and its application to the analysis of transient processes," Opt. Commun. **260,** 493–499 (2006).
11. T. F. Begemann, "Optical measurement of deformation fields and surface processes with digital speckle correlation," Ph.D. dissertation (University of Oldenburg, 2002).
12. T. Fricke-Begemann, G. Gülker, K. D. Hinsch, and K. Wolff, "Corrosion monitoring with speckle correlation," Appl. Opt. **38,** 5948–5955 (1999).
13. M. Pajuelo, G. Baldwin, R. Arizaga, N. Cap, H. Rabal, and M. Trivi, "Bio-speckle assessment of bruising in fruits," Opt. Lasers Eng. **40,** 13–24 (2003).
14. I. Passoni, H. Rabal, and C. Arizmendi, "Characterizing dynamic speckle time series with the Hurst coefficient concept," Fractals **12,** 319–329 (2004).
15. I. Passoni, A. Dai Pra, H. Rabal, M. Trivi, and R. Arizaga, "Dynamic speckle processing using wavelets based entropy," Opt. Commun. **246,** 219–228 (2005).
16. J. D. Briers, "The statistics of fluctuating speckle patterns produced by a mixture of moving and stationary scatterers," Opt. Quantum Electron. **10,** 364–366 (1978).

Speckle Modulados

En el CIOp, el empleo del speckle en aplicaciones metrológicas fue un tema de gran interés desde principios de los 80´s. En particular, la modulación interna del speckle producida localizando un arreglo de pupilas de múltiples aperturas en el sistema formador de imagen permitió el desarrollo de diversos métodos de interés metrológico. Así, fueron estudiados los specklegramas obtenidos mediante sistemas ópticos de múltiples aperturas, las cuales pueden modificarse en una secuencia de múltiples exposiciones. Estos arreglos particulares de pupilas permitieron desarrollar novedosas aplicaciones poniendo en evidencia las ventajas relativas de la propuesta. Por ejemplo, se implementaron dispositivos para el multiplexado de imágenes, la fotografía speckle (para la medida de desplazamientos en el plano, rotaciones, etc.) e interferometría speckle (para la caracterización de objetos de fase, etc.).

Desde principios de los 90´s, la incorporación de los materiales fotorrefractivos, como medio de registro, permitieron implementar las técnicas de metrología speckle en tiempo real.

Modulated Speckle

The use of speckles for metrological application has generated a great interest at CIOp since the early 80´s. In particular, the internal modulation of the speckle achieved by locating a multiple aperture pupil mask in front of the imaging lens allows the implementation of several metrological methods. At CIOp the specklegram obtained through an optical system whose pupil consists of multiple apertures in which the pupil change between exposures were widely studied. Applications were developed demonstrating the possibility of carrying out a variety of experiments which can not implemented otherwise. For instance, some developments include image multiplexing, speckle photography (to measure in plane displacements and rotation) and speckle interferometry (to characterize phase objects).

Since 90´s at CIOp the use of photorefractive crystals as recording medium allowed implementing speckle metrology techniques in-quasi-real time and in-situ

Speckle photography with different pupils in a multiple-exposure scheme

Luciano Angel,* Myrian Tebaldi,† Néstor Bolognini,‡ and Marcelo Trivi†

Centro de Investigaciones Ópticas (Consejo Nacional de Investigaciones Científicas y Técnicas–Comisión de Investigaciones Científicas) and Optimo, Departamento de Fisicomatemática, Facultad de Ingeniería, Universidad Nacional de la Plata, La Plata, Argentina, C.C. 124, Correo Central, 1900 La Plata, Argentina

Received April 29, 1999; revised manuscript received August 31, 1999; accepted September 27, 1999

The use of different multiple-aperture pupils for recording each image in speckle photography is proposed. The introduction of suitable spatial frequency carriers, by internally modulating imaged speckles, allows one to selectively isolate or combine the spectral content of different images into spatially separated regions in the Fourier plane. Theoretical and experimental results extend the speckle photography technique to the depiction of several specklegrams of multiple uniform in-plane displacements. In this case, because different pupils are considered for recording, the cross-correlation functions for the amplitudes and intensities in the image plane are calculated on the basis of the statistical properties of the object. Also, the ensemble-average intensity in the Fourier plane is analytically derived, and fringe visibility is investigated. © 2000 Optical Society of America [S0740-3232(00)01701-4]

OCIS codes: 120.0120, 120.3180, 120.3940, 120.6160.

1. INTRODUCTION

Speckle photography is a well-known information-processing technique in which speckle displacement by coherent optical processing is determined.[1] It is based on the introduction of spatial frequency carriers through speckle modulation, which allows the low-frequency spectral components of images to be spread out into the high-frequency region of the Fourier-transform plane. As in other multiplexing approaches to optical image processing and speckle metrology,[1] speckle photography combines speckle modulation and displacement. Speckle photography uses an essentially simpler optical arrangement, has a wider range of measurement, and has less-severe stability requirements than for holographic and speckle interferometry.

Speckle photographic techniques have been implemented in the diffraction field (free-space geometry) and in image configurations, to which only a limited area of the object under illumination contributes.[2] An image obtained through double or multiple displacement of a diffuse object that is generating speckles is recorded. Then the specklegram is analyzed through coherent illumination and Fourier transformation of transmitted light. Two methods[3] are available for speckle photography. One of them consists of a addressing a narrow laser beam on a specklegram point-by point to form Young fringes, whose orientation and spacing can be interpreted in terms of the direction and the magnitude of the diffuser displacement. The orientation of these fringes is normal to the direction of speckle displacement, whereas their spacing is inversely proportional to the magnitude of the displacement. The other method is based on the spatial filtering of a specklegram, which yields the contour lines of speckle displacement along a direction that depends on the position of the filtering aperture in the Fourier plane.

When multiple exposures are made, each of the fields has a correlation area that corresponds to the mean size of the speckles, and object deformation between exposures gives rise to both displacement and decorrelation of laser speckles. Speckle displacement and changes in structure have been investigated by calculation of the cross-correlation functions of speckle intensities before and after displacement. Specifically, the dependence of the speckle correlation properties on the conditions of object illumination and speckle observation as well as on the displacement parameters was theoretically analyzed.[2–6]

To measure accurately the periodicity of the Young fringes obtained in speckle photography, the intensity profile of the diffraction halo is analyzed.[6,7] In an image configuration, the form of the diffraction halo is determined by the aperture function of the recording lens. If the intensity distribution of the imaged speckle pattern is uniform, ergodic, and Gaussian, then the diffraction halo is equal to the power spectrum of the image-plane speckle intensity.[7]

Although an optical system with a single-aperture pupil is usually employed to form the images, some advantage is achieved in speckle photography by use of a multiple-aperture pupil.[8,9] Assuming that the total amount of diffracted light is the same from speckle patterns recorded by a single aperture and by multiple apertures, the amount of diffracted light at the high frequencies selected by the multiple apertures is much greater than the corresponding values from single-aperture recording. Thus multiple apertures yield an increased signal-to-noise ratio and consequently much better fringe resolution.

In this paper we propose the use of different multiple-aperture pupils for recording each image in speckle photography. To our knowledge, this technique was not previously investigated. As we show, this approach has a definite advantage in that it allows selective concentra-

0740-3232/2000/010107-13$15.00 © 2000 Optical Society of America

tion of the spectral components of individual or various speckled images into isolated spots in the Fourier plane. On this basis, a remarkable extension of speckle photography to depict in a single frame several systems of interferometric fringes for different uniform in-plane displacements can be implemented.

When different pupils are employed to form the images, the decorrelation introduced by changing the pupils between exposures must be analyzed. Then the cross-correlation functions of speckle amplitudes and intensities in the image plane are evaluated in terms of the geometric characteristics of the pupils. Finally, expressions for the observed average intensity and fringe visibility in the Fourier plane are derived. Moreover, exact knowledge of these correlation properties is used to optimize fringe visibility.

The fundamentals and the relative benefits of the proposed approach are discussed on the basis of the theoretically predicted features of fringe-modulated diffraction patterns. Also, experimental results that support our analysis are presented.

2. THEORETICAL ANALYSIS

A. Diffuser Properties and Image Formation

Let us consider the experimental setup of Fig. 1(a). A random diffuser, located at the input plane x–y, is illuminated by a collimated laser beam of wavelength λ_W and intensity I_W. This beam impinges perpendicularly on the mean (or smoothed) diffuser surface.

The amplitude transmission function of the diffuser is given by $\zeta(x, y)\exp[i\phi(x, y)]$, where $\zeta(x, y)$ is the macroscopic transmission function and $\exp[i\phi(x, y)]$ is the microscopic one, which is a random phasor related to the diffusing properties of the object. For most diffuser objects, except for observation in the region where the directly transmitted or specularly reflected component is superimposed on the diffused component, the following conditions

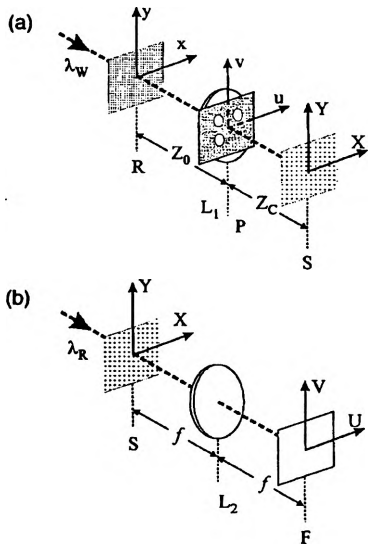


Fig. 1. Experimental setups for (a) recording and (b) analysis of the specklegram. R, diffuser; L_1, imaging lens; P, pupil mask; S's, specklegrams; L_2, Fourier lens; F, Fourier plane.

are satisfied[3]: The phases $\phi(x, y)$ are uniformly distributed over the interval $(-\pi, \pi)$ (i.e., the surface is rough compared with the wavelength) and the phases for two different points are statistically independent of each other (i.e., the elementary scattering areas are unrelated). In addition, the intensity transmission function $|\zeta(x, y)|^2$ has a constant value. In practice, $0 < |\zeta(x, y)|^2 < 1$.

The field amplitude immediately in front of the diffuser, at a time t^k, is given by

$$A_0^k(x, y) = \sqrt{I_W}\zeta(x - x^k, y - y^k) \times \exp[i\phi(x - x^k, y - y^k)], \quad (1)$$

where the vector (x, y) denotes a generic point on the diffuser plane and the vector constant (x^k, y^k) determines the position of the diffuser at that time. This vector in general varies from one exposition to another according to the diffuser displacement.

An image of this input is formed in the X–Y plane by use of a lens L_1 (Fig. 1) located at the u–v plane. To image the input $A_0^k(x, y)$, a dark stop P^k with several apertures is located immediately in front of the lens. This pupil is represented by the function $P^k(u, v)$, which is unity inside the apertures and zero otherwise. Then the image field amplitude is proportional to

$$A^k(X, Y) = \int A_0^k(x, y)K^k(X, Y; x, y)\mathrm{d}x\mathrm{d}y, \quad (2)$$

where

$$K^k(X, Y; x, y) = \int P^k(u, v)\exp\left\{-i\frac{2\pi}{\lambda_W}\left[\left(\frac{x}{Z_0} + \frac{X}{Z_C}\right)u + \left(\frac{y}{Z_0} + \frac{Y}{Z_C}\right)v\right]\right\}\mathrm{d}u\mathrm{d}v \quad (3)$$

is the impulse response of the optical system for the mean object surface. The distances from the diffuser to the lens and from the lens to the image plane are Z_0 and Z_C, respectively.

B. Cross-Correlation Functions for the Image Amplitudes and Intensities

Because of the inherent statistical nature of the experimental situation presented in Subsection 2.A, introduction of the statistical optics formalism is best suited for treating the present problem. Accordingly, the cross-correlation functions for the image amplitudes and intensities are calculated, in terms of which the change in the diffusely transmitted light caused by object displacement can be described.

To this end, let us consider that $A^k(X, Y)$ and $A^l(X, Y)$ represent the image amplitude fields for, in general, two different positions of the diffuser, which are denoted (x^k, y^k) and (x^l, y^l). Also, these images are obtained in general by using two different pupils, $P^k(u, v)$ and $P^l(u, v)$, respectively.

Then, from Eqs. (1) and (2), we obtain the cross-correlation function of the image amplitudes:

$$\langle A^k(X_a, Y_a)[A^l(X_b, Y_b)]^*\rangle \approx I_W|\zeta|^2 \int K^k(X_a, Y_a; x + x^k, y + y^k) \times [K^l(X_b, Y_b; x + x^l, y + y^l)]^* \mathrm{d}x\mathrm{d}y, \quad (4)$$

where the statistical properties of the elementary phasors and the uniformity of the intensity transmission function of the diffuser were considered. The average procedure $\langle\,\rangle$ that is performed over a statistical ensemble of the microscopic structure of the object is introduced to eliminate the speckle-like noise, and it can be physically interpreted as a spatial average over a region of a sufficient extent.[3]

Furthermore, substituting Eq. (3) into Eq. (4) yields

$$\begin{aligned}\langle A^k(X_a, Y_a)[A^l(X_b, Y_b)]^*\rangle &\approx \int\left(\int P^k(u, v)\exp\left\{-i\frac{2\pi}{\lambda_W}\left[\left(\frac{x^k}{Z_0} + \frac{X_a}{Z_C}\right)u + \left(\frac{y^k}{Z_0} + \frac{Y_a}{Z_C}\right)v\right]\right\}\exp\left[-i\frac{2\pi}{\lambda_W Z_0}(xu + yv)\right]\mathrm{d}u\mathrm{d}v\right.\\ &\quad\left.\times\int P^l(u', v')\exp\left\{i\frac{2\pi}{\lambda_W}\left[\left(\frac{x^l}{Z_0} + \frac{X_b}{Z_C}\right)u' + \left(\frac{y^l}{Z_0} + \frac{Y_b}{Z_C}\right)v'\right]\right\}\exp\left[i\frac{2\pi}{\lambda_W Z_0}(xu' + yv')\right]\mathrm{d}u'\mathrm{d}v'\right)\mathrm{d}x\mathrm{d}y\\ &\approx \int\int\left(\int \exp\left\{-i\frac{2\pi}{\lambda_W Z_0}[x(u - u') + y(v - v')]\right\}\mathrm{d}x\mathrm{d}y\right.\\ &\quad\times P^k(u, v)\exp\left\{-i\frac{2\pi}{\lambda_W}\left[\left(\frac{x^k}{Z_0} + \frac{X_a}{Z_C}\right)u + \left(\frac{y^k}{Z_0} + \frac{Y_a}{Z_C}\right)v\right]\right\}\\ &\quad\left.\times P^l(u', v')\exp\left\{i\frac{2\pi}{\lambda_W}\left[\left(\frac{x^l}{Z_0} + \frac{X_b}{Z_C}\right)u' + \left(\frac{y^l}{Z_0} + \frac{Y_b}{Z_C}\right)v'\right]\right\}\right)\mathrm{d}u\mathrm{d}v\mathrm{d}u'\mathrm{d}v'. \quad (5a)\end{aligned}$$

Note that the walk-off of the object points out of the illuminated region causes speckle decorrelation. This effect is included when we consider a finite integration region over x and y in relation (5a). The scope of our analysis concerns mainly those effects that refer to the configuration of the multiple-aperture pupils. To study the decorrelation that is due only to pupil changes between exposures, in the following we disregard the finite dimensions of the diffuser illuminated area. If we assume that the illumination area is large enough, then

$$\int \exp\{-i(2\pi/\lambda_W Z_0)[x(u - u') + y(v - v')]\}\mathrm{d}x\mathrm{d}y = \delta(u - u', v - v'),$$

and relation (5a) reduces to

where

$$P^{kl}(u, v) \equiv P^k(u, v)P^l(u, v),$$

$$(\Delta x^{kl}, \Delta y^{kl}) \equiv (x^l - x^k, y^l - y^k),$$

and $\mathfrak{F}$ indicates a two-dimensional Fourier transform.

Because (x^k, y^k) and (x^l, y^l) represent different positions of the diffuser when it is forming the respective images, it follows that the vector $(\Delta x^{kl}, \Delta y^{kl})$ stands for the relative uniform in-plane displacement that the diffuser undergoes between images. Note that we consider this vector when evaluating the Fourier transform in relation (5b), which implies that the correlation of the field amplitudes is affected by the diffuser displacement.

The function $P^{kl}(u, v)$ can be associated with a pupil P^{kl} whose transmission area corresponds to the transmission area that P^k has in common with P^l. In the following, the function P^{kl} is referred to as the common part of P^k and P^l.

According to relation (5b), the correlation between two speckled images obtained through two different pupils is determined by the common part of the respective pupils and displacements. In particular, if there are no common transmission areas in the pupils $[P^{kl}(u, v) = 0]$, then the speckle patterns are completely uncorrelated; that is, $\langle A^k(X_a, Y_a)[A^l(X_b, Y_b)]^*\rangle = 0$. As expected, this equation demonstrates that the complex amplitudes of waves going through different apertures are statistically independent of one another, because different components of the angular spectrum of scattered light are accepted by the different apertures.

$$\begin{aligned}\langle A^k(X_a, Y_a)[A^l(X_b, Y_b)]^*\rangle &\approx \int\int P^k(u, v)P^l(u', v')\exp\left\{-i\frac{2\pi}{\lambda_W}\left[\left(\frac{x^k}{Z_0} + \frac{X_a}{Z_C}\right)u - \left(\frac{x^l}{Z_0} + \frac{X_b}{Z_C}\right)u'\right]\right\}\\ &\quad\times\exp\left\{-i\frac{2\pi}{\lambda_W}\left[\left(\frac{y^k}{Z_0} + \frac{Y_a}{Z_C}\right)v - \left(\frac{y^l}{Z_0} + \frac{Y_b}{Z_C}\right)v'\right]\right\}\delta(u - u', v - v')\mathrm{d}u'\mathrm{d}v'\mathrm{d}u\mathrm{d}v\\ &\approx \mathfrak{F}\{P^{kl}(u, v)\}\left(\frac{X_a - X_b}{\lambda_W Z_C} - \frac{\Delta x^{kl}}{\lambda_W Z_0}, \frac{Y_a - Y_b}{\lambda_W Z_C} - \frac{\Delta y^{kl}}{\lambda_W Z_0}\right), \quad (5b)\end{aligned}$$

Now we evaluate the average intensity in the image plane by substituting the following for the same point $(X_a, Y_a) = (X_b, Y_b)$ in relation (5b):

$$\langle I^k \rangle = \langle I^k(X, Y) \rangle = \langle A^k(X, Y)[A^k(X, Y)]^* \rangle \approx \mathfrak{F}\{P^k(u, v)\}(0, 0), \quad (6)$$

where $(\Delta x^{kk}, \Delta y^{kk}) = 0$ and $P^{kk}(u, v) = (P^k(u, v)$ were used. Of course, $\langle I^k \rangle$ is a constant.

Moreover, the intensity cross-correlation function that describes the statistical properties of speckle patterns can be derived from the correlation functions of the complex amplitudes. If we assume that $A^k(X, Y)$ and $A^l(X, Y)$ obey the circular Gaussian statistics with zero mean in the complex plane, it follows that

$$\langle I^k(X_a, Y_a) I^l(X_b, Y_b) \rangle = \langle I^k \rangle \langle I^l \rangle + |\langle A^k(X_a, Y_a)[A^l(X_b, Y_b)]^* \rangle|^2, \quad (7)$$

which is realized because the diffuser is rough compared with the wavelength[10] and also because the correlation patch of the complex amplitude directly after being scattered by the object is much smaller than the resolution patch of observation.[2–4]

When the explicit expressions given by relation (5b) and Eq. (6) are substituted into Eq. (7), the cross-correlation function for the intensities in the image plane is

$$\langle I^k(X_a, Y_a) I^l(X_b, Y_b) \rangle \approx \mathfrak{F}\{P^k(u, v)\}(0, 0)\mathfrak{F}\{P^l(u, v)\}(0, 0) + \left| \mathfrak{F}\{P^{kl}(u, v)\}\left(\frac{X_a - X_b}{\lambda_W Z_C} - \frac{\Delta x^{kl}}{\lambda_W Z_0}, \frac{Y_a - Y_b}{\lambda_W Z_C} - \frac{\Delta y^{kl}}{\lambda_W Z_0} \right) \right|^2. \quad (8a)$$

Relation (8a) also can be written as

$$\langle I^k(X_a, Y_a) I^l(X_b, Y_b) \rangle \approx \langle I^k \rangle \langle I^l \rangle \left\{ 1 + \frac{\left| \mathfrak{F}\{|P^{kl}(u, v)|^2\}\left(\frac{X_a - X_b}{\lambda_W Z_C} - \frac{\Delta x^{kl}}{\lambda_W Z_0}, \frac{Y_a - Y_b}{\lambda_W Z_C} - \frac{\Delta y^{kl}}{\lambda_W Z_0} \right) \right|^2}{\int |P^k(\xi, \chi)|^2 d\xi d\chi \int |P^l(\xi', \chi')|^2 d\xi' d\chi'} \right\}, \quad (8b)$$

which reduces to the well-known form of the autocorrelation function of the speckled intensity[10] for $k = l$.

C. Average Intensity Distribution of Diffracted Light

Another important function for describing the properties of speckle is the Fourier transform of the cross-correlation function, whose real part is related to the Young fringes observed in speckle photography.

In the following, the case of a multiple-exposure specklegram through different multiple-aperture pupils is considered. An expression for the average intensity in the Fourier plane is analytically derived on the basis of the statistical properties of recorded speckle distributions.

In the recording process, which is carried out by using the setup depicted in Fig. 1(a), the intensity distributions $I^k(X, Y) = |A^k(X, Y)|^2$ for $k = 1, 2, \ldots N$ are sequentially recorded. The amplitude $A^k(X, Y)$ is given by Eqs. (1)–(3), and a linear recording procedure is assumed for analytical purposes.[4,6–9,11,12] Then the amplitude transmission function of the recorded specklegram can be assumed to be proportional to

$$I(X, Y) = \sum_{k=1}^{N} I^k(X, Y). \quad (9)$$

In accordance with Fig. 1(b), in the analysis the specklegram is located in the X–Y plane and illuminated by a collimated laser beam of wavelength λ_R and intensity I_R, which impinges perpendicularly on the X–Y plane. We assume a general case in which the wavelengths and intensities in the recording and the analysis steps are different; that is, $\lambda_R \neq \lambda_W$ and $I_R \neq I_W$. Afterward, the transmitted light is Fourier transformed by means of lens L_2 (Fig. 1) of focal length f, and the intensity distribution is observed at the U–V focal plane.

Thus the field amplitude in the transform plane is proportional to

$$G_f(U, V) = \sqrt{I_R} \sum_{k=1}^{N} G^k(U, V), \quad (10)$$

where

$$G^k(U, V) = \int I^k(X, Y) \exp\left[-i \frac{2\pi}{\lambda_R f}(XU + YV) \right] dX dY. \quad (11)$$

On this basis, it follows that the cross correlation of the amplitudes in the Fourier plane is

$$\langle G_f(U_1, V_1)[G_f(U_2, V_2)]^* \rangle = I_R \sum_{k,l=1}^{N} \int \langle I^k(X_a, Y_a) I^l(X_b, Y_b) \rangle \times \exp\left(-i \frac{2\pi}{\lambda_R f}(X_a U_1 - X_b U_2 + Y_a V_1 - Y_b V_2) \right) dX_a dY_a dX_b dY_b. \quad (12)$$

Then, when we evaluate this cross correlation for $(U_1, V_1) = (U_2, V_2)$, it follows that the diffuser's ensemble-average intensity in the transform plane is

$$\langle I_f(U, V)\rangle = \langle G_f(U, V)[G_f(U, V)]^*\rangle$$
$$= I_R \sum_{k,l=1}^{N} \int \langle I^k(X_a, Y_a) I^l(X_b, Y_b)\rangle$$
$$\times \exp\left\{-i\frac{2\pi}{\lambda_R f}[U(X_a - X_b) + V(Y_a - Y_b)]\right\} dX_a dY_a dX_b dY_b. \quad (13)$$

Also, the cross-correlation function of intensities can be expressed according to relation (5b) and Eq. (7). Then, by substituting these expressions into Eq. (13), we obtain

$$\langle I_f(U, V)\rangle = \delta(U, V) + \frac{1}{4}\int d(X_a + X_b) d(Y_a + Y_b)$$
$$\times \sum_{k,l=1}^{N} \int \left|\mathfrak{F}\{P^{kl}(u, v)\}\right.$$
$$\times \left.\left(\frac{X' + \Delta X^{kl}}{\lambda_W Z_C}, \frac{Y' + \Delta Y^{kl}}{\lambda_W Z_C}\right)\right|^2$$
$$\times \exp\left[-i\frac{2\pi}{\lambda_R f}(UX' + VY')\right] dX' dY', \quad (14)$$

where $X' = X_a - X_b$, $Y' = Y_a - Y_b$, and for simplicity the constant factor I_R was neglected. In Eq. (14), the vector

$$(\Delta X^{kl}, \Delta Y^{kl}) = -\frac{Z_C}{Z_0}(\Delta x^{kl}, \Delta y^{kl}) \quad (15)$$

is the relative displacement of $A^l(X, Y)$ with respect to $A^k(X, Y)$, where it was assumed that the speckle displacement takes place near the optical axis. The factor $-Z_C/Z_0$ represents the imaging magnification. The $\delta(U, V)$ term in Eq. (14) stands for a brilliant central point in the diffraction field produced by the constant value [see relations (6)] of the product $\langle I^k\rangle\langle I^l\rangle$. The constant factor $\frac{1}{4}\int d(X_a + X_b) d(Y_a + Y_b)$ represents the finite area of the specklegram. In the following, the $\delta(U, V)$ term and the area factor are not considered.

The diffuser displacement causes both speckle displacement and structural changes in the image plane. A double-exposed specklegram for a uniform in-plane displacement consists of many speckle pairs that are mutually independent with respect to shape and position. The two grains that belong to a speckle pair originally are similar but then are displaced from each other. Because of the finite dimensions of the specklegram, unpaired grains appear near the edge of the recording medium. The number of single grains increases as speckle decorrelation in proportion to the image displacement.[13] Similar assertions can be made in connection with a multiple-exposure scheme. In the following, it is assumed that the actual specklegram area is much larger than the characteristic speckle and displacement dimensions, which implies that the decorrelation effect associated with the diffuser displacement becomes negligible. In the process, the limits of the integrals over X' and Y' in Eq. (14) are extended to infinity, becoming a two-dimensional Fourier transform. On this basis, it results that

$$\langle I_f(U, V)\rangle = \sum_{k,l=1}^{N} \mathfrak{F}\left\{\left|\mathfrak{F}\{P^{kl}(u, v)\}\right.\right.$$
$$\times \left.\left.\left(\frac{X + \Delta X^{kl}}{\lambda_W Z_C}, \frac{Y + \Delta Y^{kl}}{\lambda_W Z_C}\right)\right|^2\left(\frac{U}{\lambda_R f}, \frac{V}{\lambda_R f}\right)\right\}$$
$$= (\lambda_W Z_C)^2 \sum_{k,l=1}^{N} \exp\left[-i\frac{2\pi}{\lambda_R f}(U\Delta X^{kl} + V\Delta Y^{kl})\right]$$
$$\times \mathfrak{F}\{|\mathfrak{F}\{P^{kl}(u, v)\}(X, Y)|^2\}(\vartheta U, \vartheta V), \quad (16)$$

where $\vartheta = (\lambda_W Z_C/\lambda_R f)$. In what follows, the proportionality constant value $(\lambda_W Z_C)^2$ is omitted.

In Eq. (16) the summing terms for $k \neq l$ can be separated from those that correspond to $k = l$. By taking into account that $P^{kl} = P^{lk}$, $P^{kk} = P^k$, and $(\Delta X^{kl}, \Delta Y^{kl}) = -(\Delta X^{lk}, \Delta Y^{lk})$, which implies that $(\Delta X^{kk}, \Delta Y^{kk}) = 0$, from Eq. (16) it follows that

$$\langle I_f(U, V)\rangle = \sum_{k=1}^{N} \mathfrak{F}\{|\mathfrak{F}\{P^k(u, v)\}(X, Y)|^2\}(\vartheta U, \vartheta V)$$
$$+ 2\sum_{\substack{k,l=1 \\ (k<l)}}^{N} \cos\left[\frac{2\pi}{\lambda_R f}(U\Delta X^{kl} + V\Delta Y^{kl})\right]$$
$$\times \mathfrak{F}\{|\mathfrak{F}\{P^{kl}(u, v)\}(X, Y)|^2\}(\vartheta U, \vartheta V), \quad (17)$$

where the smooth function

$$\mathfrak{F}\{|\mathfrak{F}\{P^k(u, v)\}(X, Y)|^2\}(\vartheta U, \vartheta V)$$
$$\approx \int |P^k(\xi, \eta)|^2 |P^k(\xi - \vartheta U, \eta - \vartheta V)|^2 d\xi d\eta \quad (18)$$

represents the diffraction halo that corresponds to pupil P^k.[7,10] Then the first term in Eq. (17) describes the overlapping of all the smoothed diffraction halos, each one corresponding to an individual single-exposure recording $\mathfrak{F}\{|\mathfrak{F}\{P^k\}|^2\}$. Note that this term does not contribute to fringe formation. Similarly, the factor $\mathfrak{F}\{|\mathfrak{F}\{P^{kl}\}|^2\}$ in the second term of Eq. (17) can be interpreted in terms of the halos associated with P^{kl}, which are fringe modulated. Note that each pair of pupils P^k and P^l can be associated with an independent contribution to fringe formation, related exclusively to the common part P^{kl} of both pupils and the relative displacement of the respective images. Specifically, spatial frequencies that correspond to a relative displacement $(\Delta X^{kl}, \Delta Y^{kl})$ are observed at the loci of the diffraction halo of P^{kl}. Nevertheless, if the common part of the pupils is null $[P^{kl}(u, v) = 0]$, then no fringe formation can be associated with the kth and the lth recorded images. In summary, the second term of Eq. (17) stands for a rather complex pattern that results from the selective overlapping of elemental fringe-modulated diffraction spots.

To illustrate the previous analysis we consider the particular case of a double-exposed specklegram ($N = 2$). As follows from Eq. (17),

$$\langle I_f(U, V)\rangle = \mathfrak{F}\{|\mathfrak{F}\{P^1(u, v)\}(X, Y)|^2\}(\vartheta U, \vartheta V) + \mathfrak{F}\{|\mathfrak{F}\{P^2(u, v)\}(X, Y)|^2\}(\vartheta U, \vartheta V) + 2\cos\left[\frac{2\pi}{\lambda_R f}(U\Delta X^{12} + V\Delta Y^{12})\right] \times \mathfrak{F}\{|\mathfrak{F}\{P^{12}(u, v)\}(X, Y)|^2\}(\vartheta U, \vartheta V). \quad (19)$$

Observe that fringes are encountered only in those regions of the Fourier plane that coincide with the diffraction halo of the common part of the pupils. It follows that the common part of the pupils determines not only the correlation properties of the two speckled images, as relation (5b) has shown, but also the loci of fringes in the transform plane. In particular, fringes do not appear when two completely uncorrelated speckled images are recorded, that is, when the images are obtained through two pupils P^1 and P^2 for which $P^{12} = 0$.

However, if the same pupil is employed to form both images in a double-exposed specklegram ($P^1 = P^2 = P^{12}$), then Eq. (19) becomes the well-known result,[6–8]

$$\langle I_f(U, V)\rangle = 4\cos^2\left[\frac{\pi}{\lambda_R f}(U\Delta X^{12} + V\Delta Y^{12})\right] \times \mathfrak{F}\{|\mathfrak{F}\{P^1(u, v)\}(X, Y)|^2\}(\vartheta U, \vartheta V), \quad (20)$$

where $\mathfrak{F}\{|\mathfrak{F}\{P^1(u, v)\}(X, Y)|^2\}(\vartheta U, \vartheta V)$ gives the form of the respective diffraction halo [see relation (18)].

D. Pupils with Common and Noncommon Apertures

So far no restriction on the pupils to be employed has been imposed. Besides, it is important at this point to calculate the expressions for the amplitude and intensity cross-correlation functions and the average intensity in the transform plane for equal-aperture pupils that satisfy the conditions specified in the remainder of this subsection.

Each pupil P^k ($k = 1, 2, \ldots N$) to be employed consists of an array of q^k equal apertures represented by the functions $a_n^k(u, v) = a(u - u_n^k, v - v_n^k)$, $n = 1, 2, \ldots q^k$. It is clear that $a_n^k(u, v) = 1$ inside the nth aperture of the pupil P^k and $a_n^k(u, v) = 0$ otherwise. Because the loci of the aperture represented by $a_n^k(u, v)$ are determined by the point (u_n^k, v_n^k), for simplicity we say that the aperture is located at (u_n^k, v_n^k). Furthermore, there is no overlapping between two different apertures of the same pupil, that is, if $n \neq i$ then $a_n^k(u, v)a_i^k(u, v) \equiv 0$. Under these conditions, the pupil function is defined as $P^k(u, v) = \sum_{n=1}^{q^k} a_n^k(u, v)$.

Also, it is assumed that, in a comparison of any pair of pupils P^k and P^l, some of their apertures will coincide exactly, whereas other apertures will not overlap at all. Let the functions $a_n^k(u, v)$ and $a_m^l(u, v)$ represent two apertures that belong to two different pupils ($k \neq l$), where $n = 1, 2, \ldots q^k$ and $m = 1, 2, \ldots q^l$. They are called common apertures if $a_n^k(u, v) \equiv a_m^l(u, v)$ and noncommon apertures if $a_n^k(u, v)a_m^l(u, v) \equiv 0$. Common and noncommon apertures can be identified whenever, for any possible pair of pupils P^k and P^l, the pupil function $P^{kl}(u, v) \equiv P^k(u, v)P^l(u, v)$ results in a similar arrangement of q^{kl} apertures represented by $a_j^{kl}(u, v) = a(u - u_j^{kl}, v - v_j^{kl})$ for $j = 1, 2, \ldots q^{kl}$ ($q^{kl} \leq q^k, q^l$). Points (u_j^{kl}, v_j^{kl}) are those that identify the positions of the common apertures. Finally, it can be written that $P^{kl}(u, v) = \sum_{j=1}^{q^{kl}} a_j^{kl}(u, v)$. Note that $P^{kk} \equiv P^k$, $q^{kk} = q^k$, and $(u_j^{kk}, v_j^{kk}) = (u_j^k, v_j^k)$.

1. Evaluation of Cross-Correlation Functions

For the pupils defined above and from relation (5b) and Eq. (15), the cross correlation for the amplitudes in the image plane is

$$\langle A^k(X_a, Y_a)[A^l(X_b, Y_b)]^*\rangle = \left\{\sum_{j=1}^{q^{kl}} \exp[-i2\pi(u_j^{kl}\eta_{ab}^{kl} + v_j^{kl}\zeta_{ab}^{kl})]\right\} \times \mathfrak{F}\{a(u, v)\}(\eta_{ab}^{kl}, \zeta_{ab}^{kl}), \quad (21)$$

where

$$(\eta_{ab}^{kl}, \zeta_{ab}^{kl}) \equiv (1/\lambda_W Z_C)(X_a - X_b - \Delta X^{kl}, Y_a - Y_b - \Delta Y^{kl}).$$

From Eq. (21) it follows that

$$\langle I^k\rangle = q^k\mathfrak{F}\{a^k(u, v)\}(0, 0) \quad (22)$$

and

$$|\langle A^k(X_a, Y_a)[A^l(X_b, Y_b)]^*\rangle|^2 = \left(q^{kl} + 2\sum_{\substack{i, j=1 \\ (i<j)}}^{q^{kl}} \cos\{2\pi[(u_i^{kl} - u_j^{kl})\eta_{ab}^{kl} + (v_i^{kl} - v_j^{kl})\zeta_{ab}^{kl}]\}\right)|\mathfrak{F}\{a(u, v)\}(\eta_{ab}^{kl}, \zeta_{ab}^{kl})|^2. \quad (23)$$

Then, from Eqs. (7), (22), and (23), the cross correlation of intensities is

$$\langle I^k(X_a, Y_a)I^l(X_b, Y_b)\rangle = q^kq^l[\mathfrak{F}\{a(u, v)\}(0, 0)]^2 + \left(q^{kl} + 2\sum_{\substack{i, j=1 \\ (i<j)}}^{q^{kl}} \cos\{2\pi[(u_i^{kl} - u_j^{kl})\eta_{ab}^{kl} + (v_i^{kl} - v_j^{kl})\zeta_{ab}^{kl}]\}\right)|\mathfrak{F}\{a(u, v)\}(\eta_{ab}^{kl}, \zeta_{ab}^{kl})|^2. \quad (24)$$

2. Evaluation of Average Intensity

If we consider that N images are recorded by use of a set of pupils that satisfy the conditions $P^k(u, v) = \sum_{n=1}^{q^k} a_n^k(u, v)$ and $P^{kl}(u, v) = \sum_{j=1}^{q^{kl}} a_j^{kl}(u, v)$, where the function $a(u, v)$ defines the aperture shape, it follows that

$$\mathfrak{F}\{|\mathfrak{F}\{P^k(u, v)\}(X, Y)|^2\}(\vartheta U, \vartheta V)$$
$$= \mathfrak{F}\left\{\left|\mathfrak{F}\left\{\sum_{j=1}^{q^k} a(u - u_j^k, v - v_j^k)\right\}(X, Y)\right|^2\right\}(\vartheta U, \vartheta V)$$
$$= \mathfrak{F}\left\{\left|\mathfrak{F}\{a(u, v)\}(X, Y)\sum_{j=1}^{q^k} \exp[-i2\pi(Xu_j^k + Yv_j^k)]\right|^2\right\} \times(\vartheta U, \vartheta V)$$
$$= \mathfrak{F}\Bigg\{|\mathfrak{F}\{a(u, v)\}(X, Y)|^2 \times\left(q^k + 2\sum_{\substack{r,s=1\\(r<s)}}^{q^k} \cos\{2\pi[X(u_r^k - u_s^k) + Y(v_r^k - v_s^k)]\}\right)\Bigg\}(\vartheta U, \vartheta V), \tag{25a}$$

and similarly

$$\mathfrak{F}\{|\mathfrak{F}\{P^{kl}(u, v)\}(X, Y)|^2\}(\vartheta U, \vartheta V)$$
$$= \mathfrak{F}\left\{|\mathfrak{F}\{a(u, v)\}(X, Y)|^2\left(q^{kl} + 2\sum_{\substack{r,s=1\\(r<s)}}^{q^k} \cos\{2\pi[X(u_r^{kl} - u_s^{kl}) + Y(v_r^{kl} - v_s^{kl})]\}\right)\right\}(\vartheta U, \vartheta V). \tag{25b}$$

By substituting Eqs. (25) into Eq. (17) and rearranging the summing terms, we obtain finally, the average intensity,

$$\langle I_f(U, V)\rangle = \langle I_f^0(U, V)\rangle + \langle I_f^L(U, V)\rangle, \tag{26}$$

where

$$\langle I_f^0(U, V)\rangle = \left\{\sum_{k=1}^{N} q^k + 2\sum_{\substack{k,l=1\\(k<l)}}^{N} q^{kl}\cos\left[\frac{2\pi}{\lambda_R f}(U\Delta X^{kl} + V\Delta Y^{kl})\right]\right\} \times \mathfrak{F}\{|\mathfrak{F}\{a(u, v)\}(X, Y)|^2\}(\vartheta U, \vartheta V), \tag{27}$$

$$\langle I_f^L(U, V)\rangle = \sum_{k=1}^{N}\sum_{\substack{r,s=1\\(r\neq s)}}^{q^k} \mathfrak{F}\{|\mathfrak{F}\{a(u, v)\}(X, Y)|^2\} \times (\vartheta U + u_r^k - u_s^k, \vartheta V + v_r^k - v_s^k) + 2\sum_{\substack{k,l=1\\(k<l)}}^{N}\cos\left[\frac{2\pi}{\lambda_R f}(U\Delta X^{kl} + V\Delta Y^{kl})\right] \times \sum_{\substack{r,s=1\\(r\neq s)}}^{q^{kl}} \mathfrak{F}\{|\mathfrak{F}\{a(u, v)\}(X, Y)|^2\} \times (\vartheta U + u_r^{kl} - u_s^{kl}, \vartheta V + v_r^{kl} - v_s^{kl}). \tag{28}$$

By defining the function

$$\aleph(U, V) \equiv \mathfrak{F}\{|\mathfrak{F}\{a(u, v)\}(X, Y)|^2\}(\vartheta U, \vartheta V) \tag{29}$$

it is possible to write the average intensities given by Eqs. (27) and (28) as follows:

$$\langle I_f^0(U, V)\rangle = \left\{\sum_{k=1}^{N} q^k + 2\sum_{\substack{k,l=1\\(k<l)}}^{N} q^{kl}\cos\left[\frac{2\pi}{\lambda_R f}(U\Delta X^{kl} + V\Delta Y^{kl})\right]\right\}\aleph(U, V), \tag{30}$$

$$\langle I_f^L(U, V)\rangle = \sum_{k=1}^{N}\sum_{\substack{r,s=1\\(r\neq s)}}^{q^k} \aleph(U - U_{rs}^k, V - V_{rs}^k) + 2\sum_{\substack{k,l=1\\(k<l)}}^{N}\cos\left[\frac{2\pi}{\lambda_R f}(U\Delta X^{kl} + V\Delta Y^{kl})\right] \times \sum_{\substack{r,s=1\\(r\neq s)}}^{q^{kl}} \aleph(U - U_{rs}^{kl}, V - V_{rs}^{kl}), \tag{31}$$

where

$$(U_{rs}^k, V_{rs}^k) \equiv (\lambda_R f/\lambda_W Z_C)(u_s^k - u_r^k, v_s^k - v_r^k),$$
$$(U_{rs}^{kl}, V_{rs}^{kl}) \equiv (\lambda_R f/\lambda_W Z_C)(u_s^{kl} - u_r^{kl}, v_s^{kl} - v_r^{kl}).$$

The function $\aleph(U, V)$ is proportional to the ensemble-average intensity distribution of the diffraction halo for a single-exposed speckle pattern recorded through a pupil consisting of only one of the apertures.

For example, if the pupil consists of circular apertures of diameter D, then

$$\aleph(U, V) = \frac{D^2}{2}\left\{\cos^{-1}\left(\frac{2\rho}{D'}\right) - \left(\frac{2\rho}{D'}\right)\left[1 - \left(\frac{2\rho}{D'}\right)^2\right]^{1/2}\right\} \times \mathrm{cyl}\left(\frac{\rho}{D'}\right), \tag{32}$$

where

$$\rho = \sqrt{U^2 + V^2}, \qquad D' = (2f/Z_C)(\lambda_R/\lambda_W)D,$$
$$\mathrm{cyl}(\rho/D') = \begin{cases} 1 & \text{if } 0 \leq \rho \leq D'/2 \\ 0 & \text{otherwise} \end{cases}$$

In this case $\aleph(U, V)$ stands for a (smoothed) circular diffraction spot of diameter D', centered at the origin of the U–V plane. In addition, the function $\aleph(U - \alpha, V - \beta)$ represents a spot that is similar but centered at the point (α, β).

3. Diffraction Patterns with Common and Noncommon Spots

In speckle photography applications through multiple-aperture pupils, some advantage can be had if separated diffraction spots are observed in the Fourier plane, for example, for avoidance of cross-talk effects in a variety of image multiplexing approaches and for noise reduction by

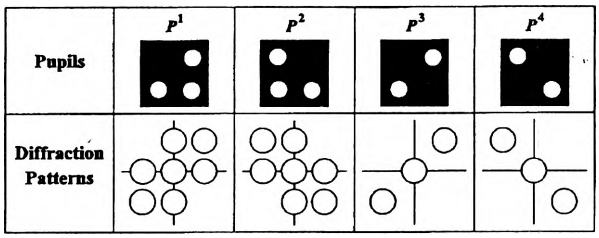


Fig. 2. Diffraction pattern schemes corresponding to the four pupils employed.

spatial filtering in the transform plane. This condition can be fulfilled by proper design of the pupils, as is assumed in the following.

It is convenient to impose another condition: Let us assume that comparison of the two diffraction patterns corresponding to any pair of the pupils to be employed shows that the loci of some spots of one diffraction pattern coincide exactly with some diffraction spots of the other pattern, while the remaining spots do not overlap at all. To illustrate this point, in the first row of Fig. 2 four pupils are schematized, meanwhile in the second row the respective diffraction patterns are depicted. By observing the diffraction patterns that belong to pupils P^1 and P^2, we can see that the spots located along the horizontal and vertical axes are common spots, whereas the lateral spots centered on the diagonals are not shared and are therefore called noncommon spots. Of course, the zero order is always a common diffraction spot, irrespective of the pattern observed. In the same sense in which the common and noncommon apertures were defined for the pupils, in this context it is assumed that common and noncommon spots can be identified when any pair of diffraction patterns is observed for the pupils.

In summary, the shapes of all the apertures of the pupils are identical; for any pair of pupils, common and noncommon apertures can be associated with them; the diffraction pattern corresponding to each pupil consists of separated spots; and common and noncommon diffraction spots can be associated with any pair of the diffraction patterns that the pupils individually generate.

The advantage of using different multiple-aperture pupils that satisfy these working conditions is that we can thus selectively isolate or combine the spectral information of several multiplexed images in separate zones of the diffraction plane.[11] For example, in the case of a double exposure through pupils P^1 and P^2 of Fig. 2, the spectral amplitude components for both exposures are added into the common diffraction spots, while in the noncommon spots their individual spectra are isolated.

4. *Features of the Diffracted Spots*

In this subsection the average expressions $\langle I_f^0(U, V)\rangle$ and $\langle I_f^L(U, V)\rangle$ in Eqs. (30) and (31) are interpreted on the basis of the detailed working conditions. Also, the average intensity of the diffraction spots is analytically obtained and the fringe visibility is analyzed.

As a starting point, note that the location of the spot $\aleph(U-\alpha, V-\beta)$ is unambiguously determined by the point (α, β), and, in this sense, we say that this spot is located at (α, β). Moreover, the spots represented by $\aleph(U-\alpha, V-\beta)$ and $\aleph(U-\sigma, V-\omega)$ coincide only if $\alpha = \sigma$ and $\beta = \omega$ [see Eq. (29)].

Observe that the average intensity $\langle I_f^L(U, V)\rangle$ results from the overlapping of all those spots represented by $\aleph(U-\alpha, V-\beta)$ with $(\alpha, \beta) \neq 0$. This is because the inequality $r \neq s$ implies both that $(U_{rs}^k, V_{rs}^k) \neq 0$ and that $(U_{rs}^{kl}, V_{rs}^{kl}) \neq 0$. Furthermore, for each term of the form $\aleph(U-\alpha, V-\beta)$ in Eq. (31) there is always another term of the form $\aleph(U+\alpha, V+\beta)$ because $(U_{rs}^k, V_{rs}^k) = -(U_{sr}^k, V_{sr}^k)$ and $(U_{rs}^{kl}, V_{rs}^{kl}) = -(U_{sr}^{kl}, V_{sr}^{kl})$. Then the intensity $\langle I_f^L(U, V)\rangle$ results from the overlapping of those spot pairs that are symmetrically located with respect to the origin of the U–V plane, whereas all the terms in Eq. (30) are located at $(\alpha, \beta) = 0$. It can be concluded that $\langle I_f^L(U, V)\rangle$ represents the average intensity distribution for the lateral diffraction spots and that $\langle I_f^0(U, V)\rangle$ represents the zero-order contribution in the Fourier plane.

Let us define the numbers $q_{\alpha\beta}^k$ and $q_{\alpha\beta}^{kl}$ as follows: For a given spot located at $(\alpha, \beta) \neq 0$, $q_{\alpha\beta}^k$ is the number of aperture pairs in the pupil P^k for which $(u_s^k - u_r^k, v_s^k - v_r^k) = (\lambda_W Z_C/\lambda_R f)(\alpha, \beta)$ or, equivalently, $(U_{rs}^k, V_{rs}^k) = (\alpha, \beta)$. Similarly, for $(\alpha, \beta) \neq 0$, $q_{\alpha\beta}^{kl}$ is the number of common aperture pairs in the pupil P^{kl} for which $(U_{rs}^{kl}, V_{rs}^{kl}) = (\alpha, \beta)$. Also, for $(\alpha, \beta) = 0$, $q_{\alpha\beta}^k$ and $q_{\alpha\beta}^{kl}$ are the numbers of apertures in the pupils P^k and P^{kl}, respectively.

On the basis of these definitions, Eqs. (26), (30), and (31) are written in a compact form that exhibits the main features of speckle photography through different multiple-aperture pupils but is easier to interpret and more useful in practical situations. After rearranging terms, we find the average intensity of the diffraction spot located at (α, β) in the Fourier plane:

$$\langle I_{\alpha\beta}(U, V)\rangle = \left\{ \sum_{k=1}^{N} q_{\alpha\beta}^k + 2 \sum_{\substack{k,l=1 \\ (k<l)}}^{N} q_{\alpha\beta}^{kl} \cos\left[\frac{2\pi}{\lambda_R f}(U\Delta X^{kl} + V\Delta Y^{kl})\right] \right\} \times \aleph(U-\alpha, V-\beta). \tag{33}$$

The first term of Eq. (33) is not associated with fringe formation in the spot at the position (α, β). The number $q_{\alpha\beta}^{kl}$ in the second term is a weighting factor that determines the magnitude of the contribution of the pupil P^{kl} to fringe formation. However, only for the zero order are the numbers $q_{\alpha\beta}^k$ and $q_{\alpha\beta}^{kl}$ proportional to the aperture transmission areas of the pupils P^k and P^{kl}, respectively.

For simplicity, let us consider the case of a double-exposed specklegram. Equation (33) becomes

$$\langle I_{\alpha\beta}(U, V)\rangle = \left\{ q_{\alpha\beta}^1 + q_{\alpha\beta}^2 + 2q_{\alpha\beta}^{12} \cos\left[\frac{2\pi}{\lambda_R f}(U\Delta X^{12} + V\Delta Y^{12})\right] \right\} \times \aleph(U-\alpha, V-\beta). \tag{34}$$

In each recording step, a fringe-modulated speckle pattern is stored. Although a rather complex system of fringes modulates the speckles, it can be understood in terms of the overlapping of elemental fringe systems.[9,11] All those aperture pairs in the pupil P^k $(k = 1, 2)$ for which $(u_r^k - u_s^k, v_r^k - y_s^k) = (\lambda_W Z_C/\lambda_R f)(\alpha, \beta)$ stand for

an elemental fringe system into the imaged speckles, whose mean spatial period is $p^k_{\alpha\beta} = \lambda_R f'(\alpha^2 + \beta^2)^{1/2}$ and whose orientation is determined by the angle $\theta^k_{\alpha\beta} = \tan^{-1}(\beta/\alpha)$. In the analysis step, light diffracted by this fringe system goes to the spot located at (α, β) in the $U-V$ plane. Then the numbers $q^1_{\alpha\beta}$ and $q^2_{\alpha\beta}$ in Eq. (34) also represent the number of aperture pairs in the respective pupils P^1 and P^2 that are responsible for a spot formation at (α, β).

In the analysis step of the specklegram, light is diffracted by the speckles that were recorded in both the first and the second exposure. The shape and relative position of the apertures in the pupils control the spectral content of light spread out by the diffuser that is recorded. Only if both numbers $q^1_{\alpha\beta}$ and $q^2_{\alpha\beta}$ are not zero do the spectral components of both images overlap in the spot at point (α, β). Nevertheless, for fringe formation it is not enough that an overlapping of the spectral content of both images occurs, because fringes appear only in the loci of the diffraction halo that corresponds to the common part of the two pupils, where $q^{12}_{\alpha\beta} \neq 0$. In fact, the overlapping of spectral components into a given spot depends on the internal modulation of the imaged speckles, irrespective the correlation properties of the recorded speckle distributions. However, correlation between modulated speckles that diffract light into a given spot depends on the number of common aperture pairs in the pupils that contribute to their internal modulation. Furthermore, for a given diffraction spot, parts of the spectral information accepted by the pupils coincide if there are common aperture pairs in the pupils associated with that spot formation. However, when no such common apertures exist, the spectral components that correspond to different recordings are not related to each other. When different multiple-aperture pupils are employed, it is possible that the spectra associated with common and noncommon apertures are concentrated in a determined spot. In this case, the information that corresponds to noncommon apertures does not contribute to fringe formation, thus reducing the visibility of the correlation fringes. In consequence, a judicious selection of the pupils is most important to ensure that the spectral information in different spots corresponds solely to diffracted light associated with the aperture pairs that the pupils have in common.

Figure 3 depicts the average intensity profile given by Eq. (34) along an axis that is parallel to the U axis and passes through the spot centered at (α, β). For plotting, circular apertures were considered [see Eq. (32)].

Fringe visibility is defined as[6,12]

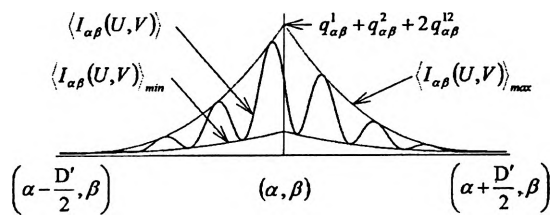


Fig. 3. Average intensity profile for a spot centered at (α, β) in the $U-V$ plane.

$$\mathcal{V}_{\alpha\beta} = \frac{\langle I_{\alpha\beta}(U, V)\rangle_{max} - \langle I_{\alpha\beta}(U, V)\rangle_{min}}{\langle I_{\alpha\beta}(U, V)\rangle_{max} + \langle I_{\alpha\beta}(U, V)\rangle_{min}}, \tag{35}$$

where the intensities $\langle I_{\alpha\beta}(U, V)\rangle_{max}$ and $\langle I_{\alpha\beta}(U, V)\rangle_{min}$ are the envelopes (also plotted in Fig. 2) given by

$$\langle I_{\alpha\beta}(U, V)\rangle_{max} = \{q^1_{\alpha\beta} + q^2_{\alpha\beta} + 2q^{12}_{\alpha\beta}\}\aleph(U - \alpha, V - \beta), \tag{36a}$$

$$\langle I_{\alpha\beta}(U, V)\rangle_{min} = \{q^1_{\alpha\beta} + q^2_{\alpha\beta} - 2q^{12}_{\alpha\beta}\}\aleph(U - \alpha, V - \beta). \tag{36b}$$

Then, according to Eqs. (36), the visibility is

$$\mathcal{V}_{\alpha\beta} = 2\frac{q^{12}_{\alpha\beta}}{q^1_{\alpha\beta} + q^2_{\alpha\beta}}. \tag{37}$$

Note that, as is well known, $0 \leq \mathcal{V}_{\alpha\beta} \leq 1$ because $q^{12}_{\alpha\beta} \leq q^1_{\alpha\beta}, q^2_{\alpha\beta}$. The visibility is null ($\mathcal{V}_{\alpha\beta} = 0$) at the point (α, β) whenever $q^{12}_{\alpha\beta} = 0$. In particular, if the pupils have no common apertures [$P^{12}(u, v) = 0$], then no correlation exists and the visibility fades out. However, if the pupils coincide, then $P^{12}(u, v) = P^1(u, v) = P^2(u, v)$ and $q^{12}_{\alpha\beta} = q^1_{\alpha\beta} = q^2_{\alpha\beta}$. As expected, in this case Eq. (34) reduces to Eq. (20), and the predicted visibility reaches unity for all the spots. In general, we have partially correlated speckle images, and visibility values are less than 1. In particular, if $q^1_{\alpha\beta} = q^2_{\alpha\beta}$, then $\mathcal{V}_{\alpha\beta} = q^{12}_{\alpha\beta}$.

3. EXPERIMENTAL RESULTS

In this section the validity of Eqs. (33), (34), and (37) is analyzed. The procedures implemented are detailed in the following.

A. Double-Exposed Specklegrams

We recorded each imaged speckle distribution by using the conventional experimental arrangement shown in Fig. 1(a). A diffuser was illuminated by a collimated Ar-laser beam ($\lambda_W = 514$ nm) and imaged onto the $X-Y$ plane. In this plane a CCD TV camera was located to capture and then to digitize the image. The distances from the diffuser to the lens and from the lens to the camera were set to $Z_0 = 138$ mm and $Z_C = 382$ mm, respectively. Pupil masks with circular holes of diameter $D = 4.8$ mm and centered at the vertices of a square $d = 9.2$ mm on a side were used. The digitized images were multiplexed to simulate the in-plane displacement between them. Also, the process of analysis was digitally simulated by use of a fast-Fourier-transform (FFT) algorithm.

Each row in Figs. 4–6 corresponds to a double-exposed specklegram obtained by use of the pupils shown schematically in the first column. In each case, for the second exposure an actual uniform horizontal in-plane displacement of the diffuser (40 μm) was simulated. The displacement in the image plane ($\approx$125 μm) is larger than the average image speckle size ($\approx$50 μm). Because no structural change of speckle patterns attributable to displacement is introduced, decorrelation is due only to the pupil change. A conventional FFT algorithm was employed to simulate the analog analysis process presented in Fig. 1(b). From the FFT data, the modulus of the Fourier transform $[I_f(U, V)]^{1/2}$ is calculated. Each image in

the second column in Figs. 4–6 represents the $\ln\{1 + [I_f(U, V)]^{1/2}\}$ data. Also, the thick profiles of the third column correspond to the horizontal upper and central spots of the respective low-pass-filtered $[I_f(U, V)]^{1/2}$ images. For all the thick profiles in Figs. 4–6 the maximum

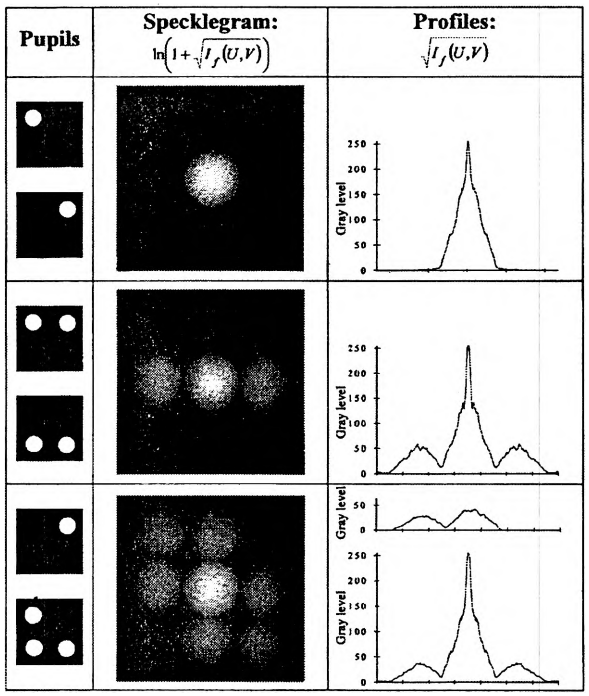


Fig. 4. Double-exposed specklegrams through pupils without common apertures.

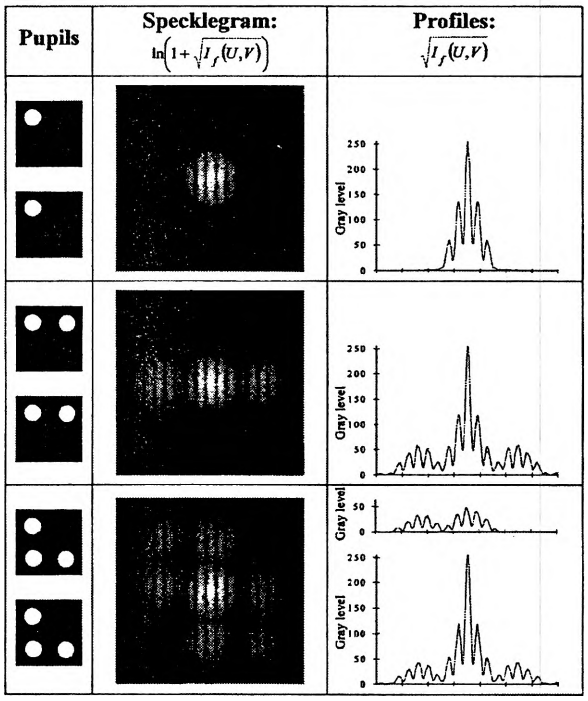


Fig. 5. Double-exposed specklegrams through identical pupils.

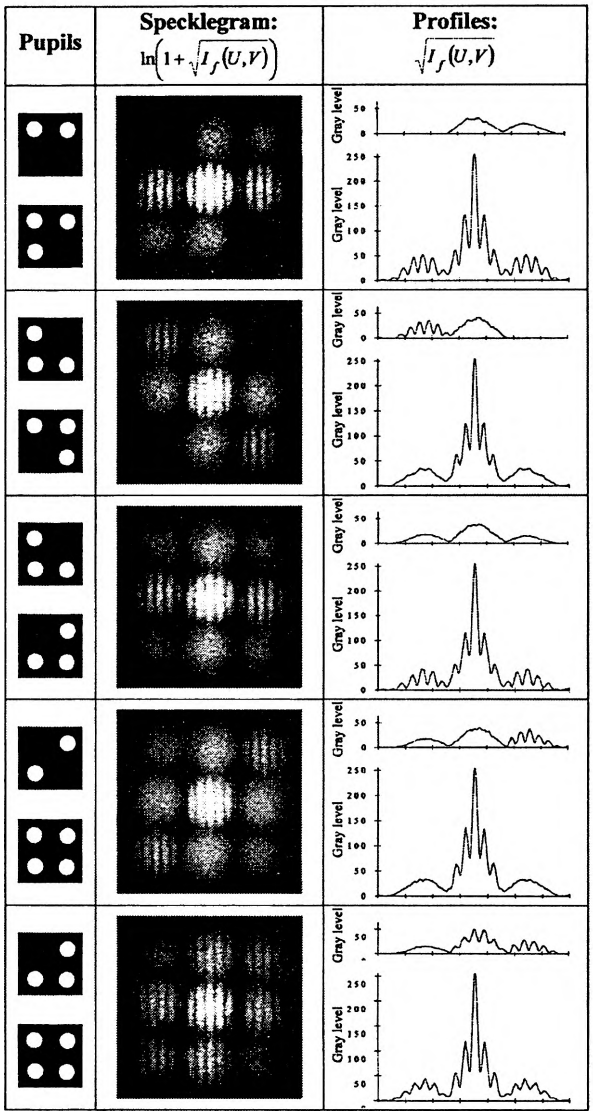


Fig. 6. Double-exposed specklegrams through pupils with common and noncommon apertures.

value was set to the same gray level. This implies that the peak values of lateral spots are diminished in proportion to the absolute peak values of the corresponding central spots. Note that smoothed profiles are obtained because of the averaging effect of both the low-pass-filtering operation and the selection of a rather thick region for sampling. This effect is equivalent to statistical averaging over an ensemble of diffusers. Circular spots are observed in the Fourier plane, as expected, when pupils with circular apertures are used [see Eq. (32)].

The results of Fig. 4 confirm that no fringes are observed ($\mathcal{V}_{\alpha\beta} = 0$) in the transform plane when the two recorded speckle patterns are completely uncorrelated: $\langle A^1(A^2)^* \rangle = 0$. This is so because the two pupils in each row of this figure have no common apertures ($P^{12} = 0$).

Figure 5, however, shows some typical results for uniform in-plane displacements in speckle photography.[8] The optimum fringe visibility for all the spots is observed

because in this case the two pupils coincide ($P^1 = P^2 = P^{12}$) and in consequence the speckle patterns are fully correlated. Observe that, although the theoretically predicted visibility equals unity (irrespective of which spot is of concern), the actual experiments show values that are always less than unity. This result is a consequence of several effects, and some of them are as follows. In practice, the recording procedure is not linear[7]; also, electronic noise is of concern,[14] mainly because of the high dynamic range of the intensity distribution of a Gaussian speckle, whose most probable value is zero. Also, an integrated (or smoothed) speckle pattern is recorded because of the finite area of the detector array in the CCD camera.[10] However, when a speckle pattern is digitally displaced, a portion of the original pattern goes out of and another portion enters into the new frame, as occurs when an actual object displacement takes place between expositions. In consequence, after the two speckle patterns are added, the number of pairs of corresponding speckles within the image frame decreases as the displacement increases. This effect cannot be eliminated and stands for a reduction of interferometric fringe visibility.[6,12] Furthermore, some drawbacks are related to finite areas of integration and digital operations, such as local saturation when speckle patterns and approximations of the FFT algorithm are added.

In Fig. 6 some results obtained by use of two different multiple-aperture pupils are illustrated. In each case, isolated common and noncommon diffraction spots can be identified by comparison of the respective diffraction patterns. Points $(0,0)$, $\pm(d',0)$, $\pm(0,d')$, $\pm(d',d')$, and $\pm(d',-d')$, where $d' = d(\lambda_R f/\lambda_W Z_C)$, denote the generic positions for the spot centers. For simplicity, let us define $d^+ = -d^- = d'$. In the following, only one spot for each pair of lateral spots is considered, because two spots located symmetrically with respect to the origin have the same characteristics.

As an example, let us analyze in detail the specklegram depicted in the fourth row of Fig. 6. Light into the spot at $(d^+, 0)$ carries only the spectral content of the image recorded with the four-aperture pupil ($q^1_{d^+0} = 0$ and $q^2_{d^+0} = 2$), and no fringes are observed because the pupils have no common aperture pairs responsible for that spot formation ($q^{12}_{d^+0} = 0$, then $\mathcal{V}_{d^+0} = 0$). The spot located at $(0, d^+)$ exhibits the same features ($q^1_{0d^+} = q^{12}_{0d^+} = 0$, $q^2_{0d^+} = 2$ and $\mathcal{V}_{0d^+} = 0$) as in the previous case, which is apparent when one compares the respective thick profiles for the spots at $(d^+, 0)$ and $(0, d^+)$. Moreover, for the spot at (d^-, d^+), similar conclusions can be established, in that no fringes are observed ($q^1_{d^-d^+} = q^{12}_{d^-d^+} = 0$ and $q^2_{d^-d^+} = 1$). Besides, the average intensity in this spot is lower (one half) than in the spots at $(d^+, 0)$ and $(0, d^+)$, as one can observe in the corresponding thick profiles. For the spot at (d^+, d^+), the spectral content of both the first and the second images are overlapped ($q^1_{d^+d^+} = q^2_{d^+d^+} = 1$). Furthermore, fringes are observed there because the common part of the pupils includes one pair of apertures associated with this spot formation ($q^{12}_{d^+d^+} = 1$). As results when the same pupils are used for recording, for this spot it holds that $\langle I_{d^+d^+}(U, V)\rangle = 4\cos^2(\pi U\Delta X^{12}/\lambda_R f)\aleph(U - d^+, V - d^+)$, and the predicted visibility is unity. Thick profiles show that fringe modulations for this spot and for the lateral spots in Fig. 5 are comparable. In the zero order the spectra of both images are overlapped ($q^1_{00} = 2$ and $q^2_{00} = 4$), and fringes are observed because the pupils have two apertures in common ($q^{12}_{00} = 2$). Besides, $\mathcal{V}_{00} = 2/3$ because not all the apertures are shared by the pupils. In this case $\langle I_{00}(U, V)\rangle = \{6 + 4\cos(2\pi U\Delta X^{12}/\lambda_R f)\}\aleph(U, V)$.

In the specklegram of the fifth row in Fig. 6, more than one pair of lateral diffraction spots are fringe modulated. Also, only the spots located at (d^+, d^+) and (d^-, d^-) exhibit optimum visibility. For the spots at $(0, \pm d^+)$ and $(\pm d^+, 0)$ the predicted visibility is 2/3; for the zero order it is 6/7. From a comparison of the thick profiles for the spots at (d^+, d^+) and $(0, d^+)$ it is apparent that fringe modulation is greater in the former spot.

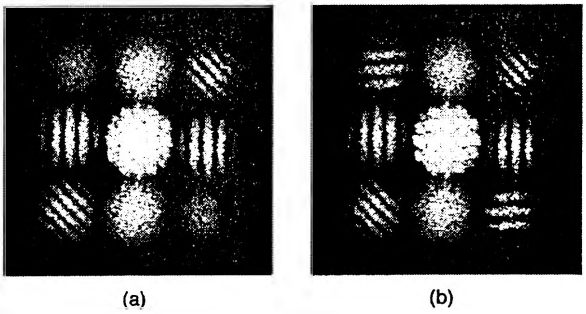
As a consequence of the pupil selection, for each specklegram presented in Fig. 6 there is one pair of lateral diffraction spots where fringe visibility reaches its highest value. This is important because the zero order always contains the spectral information of both images and because high visibility is useful for accurate measurement of displacements in speckle photography.[6,12]

We note that the predicted fringe visibility for the zero order in the specklegrams in Fig. 6 is always less than unity, which is apparent when one compares the thick profiles for the zero order in Figs. 5 and 6. Besides, fringe modulation for all those lateral spots whose visibilities reach their maximum is similar for the experiments illustrated in both figures.

B. Multiple-Exposed Specklegrams

Examples of interferometric fringes achieved by multiplexing three and four modulated speckle distributions are depicted in Figs. 7(a) and 7(b), respectively. Between images, diffuser uniform in-plane displacements were simulated. We obtained the images in Fig. 7 by following the same procedure as for Figs. 4–6. There, the respective normalized versions of the function $\ln\{1 + [I_f(U, V)]^{1/2}\}$ are depicted.

For Fig. 7(a) we recorded three images by using the pupils P^1, P^2, and P^3 represented in Fig. 2. Between the first and the second images, a horizontal 40-μm diffuser displacement was simulated. A vertical 40-μm diffuser displacement was simulated between the second and the third images also. Thus the third image was displaced



(a) (b)

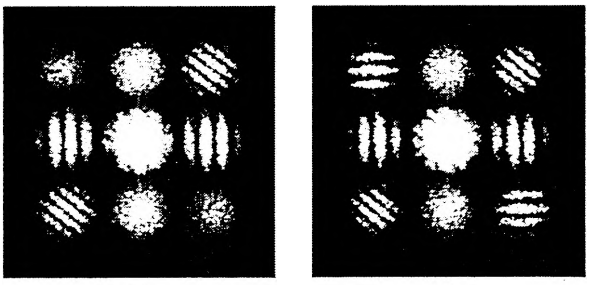
Fig. 7. (a) Triple-exposed and (b) quadruple-exposed specklegrams for different uniform in-plane displacements between images recorded through the pupils illustrated schematically in Fig. 2.

both horizontally and vertically with respect to the first image. Then it holds that $\Delta X^{12} = \Delta X^{13} = \Delta Y^{13} = \Delta Y^{23} \equiv \Delta$ and $\Delta Y^{12} = \Delta X^{23} = 0$. Note that no fringes appear in the spot at (d^-, d^+) because only light diffracted by the pupil P^2 goes there ($q^1_{d^-d^+} = q^3_{d^-d^+} = 0$ and $q^2_{d^-d^+} = 1$). Similarly, there are no fringes into the spot located at $(0, d^+)$. In this case the spectra of both the first and the second images go there ($q^1_{0d^+} = q^2_{0d^+} = 1$). Nevertheless, there are no common aperture pairs in the pupils P^1 and P^2 that are responsible for that spot formation ($q^{12}_{0d^+} = 0$). For the spot at $(d^+, 0)$, only the two common apertures of the pupils P^1 and P^2 are responsible for the light diffracted into this spot ($q^1_{d^+0} = q^2_{d^+0} = q^{12}_{d^+0} = 1$ and $q^3_{d^+0} = q^{13}_{d^+0} = q^{23}_{d^+0} = 0$). It follows that the average intensity is $\langle I_{d^+0}(U, V)\rangle = 4\cos^2(\pi U\Delta/\lambda_R f)\aleph(U - d^+, V)$. Observe that fringe orientation corresponds to the horizontal displacement between the first and the second images and that the predicted visibility is optimum ($\mathcal{V}_{d^+0} = 1$) for this spot. In a similar way we can interpret the fringes in the spot centered at (d^+, d^+) by considering that only the spectra of the first and the third images are overlapped into the spot. Also, the visibility reaches its highest value, but the period and the orientation of the fringes correspond to the relative displacement between the first and the third images. In this case the intensity is $\langle I_{d^+d^+}(U, V)\rangle = 4\cos^2[\pi(U + V)\Delta/\lambda_R f]\aleph(U - d^+, V - d^+)$. Finally, in the central spot the spectra of the three images are overlapped ($q^1_{00} = q^2_{00} = 3$ and $q^3_{00} = 2$). Furthermore, a rather complex spatial modulation appears because horizontal, vertical, and diagonal fringes are also overlapped there ($q^{12}_{00} = q^{13}_{00} = 2$ and $q^{23}_{00} = 1$). From Eq. (33), the corresponding intensity is

$$\langle I_{00}(U, V)\rangle = \{8 + 4\cos(2\pi U\Delta/\lambda_R f) + 2\cos(2\pi V\Delta/\lambda_R f) + 4\cos[2\pi(U + V)\Delta/\lambda_R f]\}\aleph(U, V).$$

In Fig. 7(b) a fourth image was added to the previous three images. We recorded the fourth image by using the pupil P^4 of Fig. 2. The third and fourth images were equally displaced with respect to the first; that is, no relative displacement between the last two images is of concern. Nevertheless, a new system of fringes appears in the spots centered at $\pm(d^-, d^+)$ as a consequence of the overlapping of the spectral components of the second and the fourth images, exclusively. In fact, these (horizontal) fringes are related to the relative vertical displacement between the respective images. Also, the theoretical visibility value is 1, and no change in the other lateral spots is introduced when the fourth image is added. Of course, the zero order contains spectral components that belong to the four images.

To obtain Fig. 8 we carried out real experiments. In this case, a conventional photographic procedure for recording the specklegrams and coherent-optical processing for analyzing them were implemented (instead of the digital procedures employed before). The diffuser was illuminated by a collimated He–Ne laser beam ($\lambda_W = 633$ nm) and imaged onto a high-resolution holographic film (Agfa-Gevaert 10E75). As before, the distances from the diffuser to the lens and from the lens to the film were set to $Z_0 = 138$ mm and $Z_C = 382$ mm, respectively. For recording, the same sequential procedure and geometric parameters of the pupil masks were maintained. Between the first and the second and between the second and the third images a horizontal 40-μm and a vertical 45-μm in-plane diffuser displacement, respectively, was introduced. In Fig. 8(a) a three-exposure specklegram is shown; for Fig. 8(b) an additional exposure was made. There was no relative displacement between the third and the fourth images. To analyze the specklegrams we employed a coherent analogical Fourier-transform procedure. Observe that similar results are obtained in the real experiments and the simulated cases, as is apparent from a comparison of Figs. 7 and 8.



(a) (b)

Fig. 8. (a) Triple-exposed and (b) quadruple-exposed real experiments for different uniform in-plane displacements between images.

In summary, in this experiment the fringe-modulated lateral diffraction spots correspond to three independent double-exposed specklegrams with optimum visibility and for different relative displacements. Only four recording steps are needed, and relative displacements between nonconsecutive images are depicted. Note that because the last two images were displaced by the same amount in this experiment, redundancy in fringe information occurs in Fig. 8(b). However, this could be used to achieve more accurate fringe measurements.[8]

In the context of speckle photography we have restricted ourselves to demonstrating the application of uniform in-plane displacements. Nevertheless, a similar procedure could be carried out for analysis of a general in-plane displacement distribution. To illustrate this, let us assume that four images are recorded with the same procedure as for Fig. 8(b), except that the diffuser is rotated between exposures. In this case no interference fringes will be observed at the transform plane when an expanded laser beam is employed to analyze the specklegram. However, two approaches (one pointwise and one whole field) are possible to measure local displacements.[3]

If we probe each small region of the specklegram point by point with a narrow laser beam, then straight equispaced Young fringes will be observed in the diffraction spectrum.[12] Besides, as in Fig. 8(b), three different systems of fringes will appear in the lateral diffraction spots, depicting different displacements at the same region of the input plane. Note that this approach has no practical meaning in the case of a multiaperture arrangement through the same pupil for recording, as is pointed out in Ref. 8.

On the other hand, isothetic fringes could be generated by optical filtering of specklegrams. In this case, an opaque mask with a small aperture is located onto a fringe-modulated diffraction spot, and light passing through the aperture is in turn Fourier transformed.[8] In our approach light from different spots carries spectral information about different rotations, which implies that isothetics obtained from each spot will depict equal displacement components for a different in-plane rotation. Although it is beyond the scope of this paper, with a proper recording schedule with different multiaperture pupils it is possible to obtain in a single frame independent isothetic fringes of equal sensitivity and thus to measure different general in-plane displacement distributions.

4. CONCLUSIONS

We have proposed a multiplexing method for speckle photography that uses different multiple-aperture pupils for recording. It was shown that the introduction of proper spatial frequency carriers through the internal modulation of speckles allows selective concentration of the spectral components of individual or various images into isolated spots in the Fourier plane.

Both theoretical and experimental results obtained extend the speckle photography technique to depict simultaneously in a single frame several systems of interferometric fringes related to a series of uniform in-plane displacements between images. Also, a comparison of relative displacements between nonconsecutive recorded images is possible.

The cross-correlation functions of the amplitudes and intensities of speckled patterns generated by different pupils and by a diffuser uniform in-plane displacement between images were computed. On this basis, the correlation between images is determined by the spectral components of light admitted by the two pupils and displacements. Each pair of pupils can be associated with an independent contribution to fringe formation, which depends on the transmission area that the two pupils have in common.

The theoretical predictions thus obtained become a relevant tool for designing the recording routine and the set of pupils for the experiment to optimize fringe visibility for accurate measurements. Moreover, the highest visibility value is achieved, as when the same pupil is used for recording.

On the other hand, by proper selection of the different multiple-aperture pupils for recording, fringe-modulated speckle patterns with predetermined correlation properties and interferometric fringes with variable visibility can be generated.

The multiplexing technique with the use of different multiple-aperture pupils is not restricted to the transmission arrangement geometry; it could also be used for a properly illuminated rough reflecting surface.

Although in this paper we have analyzed only the use of different multiple-aperture pupils for uniform in-plane displacement measurements in speckle photography, applications can be implemented with this approach, for both real-time image processing[11] and metrology. In particular, real-time speckle photography through recording by different multiple-aperture pupils for strain analysis is currently being investigated.

ACKNOWLEDGMENTS

This research was performed under the auspices of the Consejo Nacional de Investigaciones Científicas y Técnicas, Comisión de Investigaciones Científicas de la Provincia de Buenos Aires, Faculty of Engineering, National University of La Plata (Argentina). L. Angel acknowledges support from the Consejo Nacional de Investigaciones Científicas y Técnicas (Argentina) and Instituto Colombiano para el Desarrollo de la Ciencia y la Tecnología, "Fransisco José de Caldas" (Colombia).

Address correspondence to N. Bolognini at postmaster@ciop.edu.ar.

*Permanent address, Universidad Eafit, Medellín, Colombia.

†Also with Facultad de Ingeniería, Universidad Nacional de La Plata, La Plata, Argentina.

‡Also with Facultad de Ciencias Exactas, Universidad Nacional de La Plata, La Plata, Argentina.

REFERENCES

1. M. Françon, "Information processing using speckle patterns," in *Laser Speckle and Related Phenomena*, J. C. Dainty, ed. (Springer-Verlag, New York, 1975), pp. 171–202.
2. I. Yamaguchi, "Speckle displacement and decorrelation in the diffraction and image fields for small object deformation," Opt. Acta **28**, 1359–1376 (1981).
3. I. Yamaguchi, "Fringe formations in deformation and vibration measurements using laser light," in *Progress in Optics*, E. Wolf, ed. (North-Holland, Amsterdam, 1985), Vol. XXII, pp. 271–339.
4. D. W. Li, J. B. Chen, and F. P. Chiang, "Statistical analysis of one-beam subjective laser-speckle interferometry," J. Opt. Soc. Am. A **2**, 657–666 (1985).
5. M. Sjödahl, "Calculation of speckle displacement, decorrelation, and object-point location in imaging systems," Appl. Opt. **34**, 7998–8010 (1995).
6. G. H. Kaufmann, "Numerical processing of speckle photography data by Fourier transform," Appl. Opt. **20**, 4277–4280 (1981).
7. R. Meynart, "Diffraction halo in speckle photography," Appl. Opt. **23**, 2235–2236 (1984).
8. F. D. Chiang and R. P. Khetan, "Strain analysis by one-beam laser speckle interferometry. 2. Multiaperture method," Appl. Opt. **18**, 2175–2186 (1979).
9. Y. Y. Hung, R. E. Rowlands, and I. M. Daniel, "Speckle-shearing interferometric technique: a full-field strain gauge," Appl. Opt. **14**, 618–622 (1975).
10. J. W. Goodman, "Statistical properties of laser speckle patterns," in *Laser Speckle and Related Phenomena*, J. C. Dainty, ed. (Springer-Verlag, New York, 1975), pp. 11–76.
11. L. Angel, M. Tebaldi, M. Trivi, and N. Bolognini, "Optical operations based on speckle modulation by using a photorefractive crystal," Opt. Commun. **168**, 55–64 (1999).
12. K. Nakagawa, T. Takatsuji, and T. Minemoto, "Measurement of the displacement distribution by speckle photography using a BSO crystal," Opt. Commun. **76**, 206–212 (1990).
13. K. Nakagawa and T. Minemoto, "Readout properties of the specklegram recorded in photorefractive $Bi_{12}SiO_{20}$ crystal," Appl. Opt. **30**, 2386–2392 (1991).
14. S. Bosco and M. Trivi, "Correlation-like algorithm for superresolution analysis," Opt. Commun. **115**, 444–448 (1995).

Phase-object analysis with a speckle interferometer

Luciano Angel

Departamento de Ciencias Básicas, Universidad Escuela de Administración, Finanzas y Tecnología, Medellín, Colombia

Myrian Tebaldi, Marcelo Trivi, and Nestor Bolognini

Centro de Investigaciones Ópticas (Consejo Nacional de Investigaciones Científicas y Técnicas-CIC) and Unidad de Investgación y Desarollo OPTIMO (Facultad Ingnenieńá, Universidad Nacional de La Plata), La Plata 1900, Argentina

Received October 31, 2001

We describe the characteristics of a double-exposure specklegram obtained through a double-aperture system, by introduction of a wedge in front of one aperture in one exposure. It is assumed that a uniform displacement of the diffuser is produced between exposures. The average intensity distribution and visibility of the interferometric fringes in the Fourier plane are analyzed. An alternative interferometric technique for phase-object detection is proposed. © 2002 Optical Society of America

OCIS codes: 120.6160, 120.5050.

Several techniques for image processing and metrology by introduction of frequency carriers into a random diffuser have been implemented. Some of these proposed techniques are based on internal modulation of speckles, which can be achieved by location of a mask with two or more apertures in front of the imaging lens.[1,2] In some applications the number of apertures or the aperture shape of the optical system is modified between exposures.[3,4] Also, the use of several multiaperture shearing interferometers has been proposed.[5] In those arrangements the pupil of the optical system does not change between exposures. In Ref. 2, a method for image subtracting was reported that uses a uniform plate to control the phase of the wave passing through one of the apertures in a double-aperture system.

In this Letter we analyze the properties of a double-exposed specklegram generated through a double-aperture system by assuming that a wedge is located front of one of the apertures in one exposure. A comparison between theoretical simulations and experimental results is presented by consideration of a parallel plate and a wedge.

The setup for recording is schematized in Fig. 1(a). The diffuser, R, is illuminated by a laser beam of wavelength λ_W and imaged in the $x-y$ plane by lens L_1. Z_0 and Z_C are the distances from the diffuser to the lens and from the lens to the image plane, respectively. A pupil mask with two identical apertures is located in front of the lens. In the second exposure a wedge is introduced in front of one of the pupil apertures. Furthermore, an in-plane displacement of the diffuser is introduced between exposures. This displacement is necessary to generate correlation fringes in the Fourier plane.

The loci of the apertures are given by

$$a_j(u,v) = a(u-u_j, v-v_j) = \begin{cases} 1 & \text{inside the } j\text{th aperture} \\ 0 & \text{otherwise} \end{cases}, \quad j = 1,2,$$

fines the distance between the aperture centers. On this basis, the pupils employed are given by $P^1(u,v) = a(u-u_1, v-v_1) + a(u-u_2, v-v_2)$ and $P^2(u,v) = a(u-u_1, v-v_1) + t\exp[i(\gamma+\tau u)]a(u-u_2, v-v_2)$, where t and $\gamma + \tau u$ represent the real amplitude transmission and the linear phase shift introduced by the wedge, respectively. We consider the u axis to be perpendicular to the thin edge of the wedge.

Analysis of the specklegram is carried out with the arrangement depicted in Fig. 1(b). The specklegram is illuminated with an expanded laser beam of wavelength λ_R, and the transmitted light is Fourier transformed through lens L_2 of focal length f. If a pupil with square apertures of side D is utilized, then the average intensity in the Fourier plane (U, V) results:

$$\langle I(U,V)\rangle = \langle I^0(U,V)\rangle + \langle I^{+1}(U,V)\rangle + \langle I^{-1}(U,V)\rangle, \tag{1}$$

where

$$\langle I^0(U,V)\rangle = KD^2 \operatorname{trian}\left(\frac{\vartheta U}{D}\right)\operatorname{trian}\left(\frac{\vartheta V}{D}\right) \times \{3 + t^4 + 2[1 + t^4 + 2t^2\cos(\vartheta\tau U)]^{1/2} \times \cos\left[\frac{2\pi}{\lambda_R f}(U\Delta X^{12} + V\Delta Y^{12}) - \Phi(U)\right]\}, \tag{2}$$

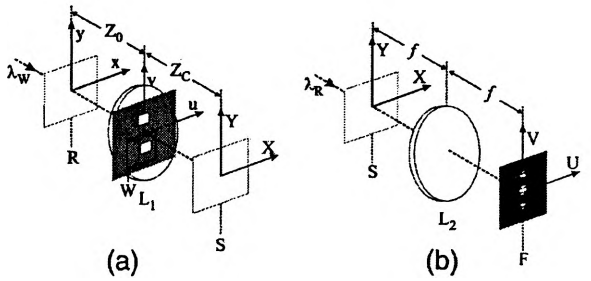


Fig. 1. Experimental setup: S's, specklegram image planes; F, Fourier plane; L_1 and L_2, lenses. See text for other definitions.

0146-9592/02/070506-03$15.00/0 © 2002 Optical Society of America

$$\langle I^{\pm 1}(U,V)\rangle = KD^2 \operatorname{trian}\left(\frac{\vartheta U \mp u_{12}}{D}\right)\operatorname{trian}\left(\frac{\vartheta V \mp v_{12}}{D}\right) \times \left(1 + t^2 + 2t \operatorname{sinc}\left\{\frac{\tau D}{2\pi}\left[1 - \frac{\vartheta U \mp u_{12}}{D} \times \operatorname{sign}(\vartheta U \mp u_{12})\right]\right\}\cos\left\{\frac{2\pi}{\lambda_R f}\left[U\left(\Delta X^{12} - \frac{\lambda_W Z_C}{4\pi}\tau\right) + V\Delta Y^{12}\right] \mp \gamma \mp \frac{u_1 + u_2}{2}\tau\right\}\right), \quad (3)$$

where $\langle I^0(U,V)\rangle$, $\langle I^{+1}(U,V)\rangle$, and $\langle I^{-1}(U,V)\rangle$ are the average intensity distributions corresponding to the zero and the (+1) and (−1) diffracted orders, respectively, and K is a constant. The vector $(u_{12}, v_{12}) = (u_2 - u_1, v_2 - v_1)$ represents the relative position of the apertures, $(\Delta X^{12}, \Delta Y^{12})$ is the relative displacement between the diffuser images and $\vartheta = \lambda_W Z_C/\lambda_R f$. Note that $(\Delta X^{12}, \Delta Y^{12}) = -(Z_C/Z_0)(\Delta x^{12}, \Delta y^{12})$, where $(\Delta x^{12}, \Delta y^{12})$ is the diffuser displacement. Furthermore, the phase term $\Phi(U) = \tan^{-1}[t^2 \sin(\vartheta\tau U)]/[1 + t^2 \cos(\vartheta\tau U)]$ is introduced in Eq. (2).

From Eqs. (2) and (3) it follows that the fringe visibility for the zero and diffracted orders are

$$\mathbf{V}^0(U) = \frac{2}{3 + \tau^4}[1 + t^4 + 2t^2 \cos(\vartheta\tau U)]^{1/2}, \quad (4a)$$

$$\mathbf{V}^{\pm 1}(U) = \frac{2t}{1 + t^2}\left|\operatorname{sinc}\left\{\frac{D\tau}{2\pi}\left[1 - \frac{\vartheta U \mp t_{12}}{D} \times \operatorname{sign}(\vartheta U \mp u_{12})\right]\right\}\right|. \quad (4b)$$

Let us consider a specklegram obtained through a parallel plate located in front of one aperture in the second exposure. Here the dihedral angle of the wedge is null, i.e., $\tau = 0$. In this case, in Eqs. (2) and (3) we must have $\tau = 0$ and $\gamma \neq 0$. The cosine terms in Eqs. (2) and (3) stand for the interferometric fringes observed in the diffracted orders. The presence of factor γ in the cosine function of Eq. (3), which corresponds to the lateral orders, modifies the interferometric-fringe modulation. Note that the amount γ determines the interferometric-fringe shifting in the Fourier plane. The minus sign in Eq. (3) is applied to the (+1) order and the plus sign to the (−1) order. Then, the fringe is shifted in opposite directions in the (+1) and (−1) orders. The interferometric fringes experience a global shift, which is produced in opposite directions in the lateral orders, while the zero order is not affected.

Furthermore, when a parallel plate ($t_2 = t$) is introduced in the second exposure, the visibility of the fringes is determined only by the transmission of the plate employed.

Let us compare the theoretical average intensity distribution in the Fourier plane obtained by use of Eqs. (2) and (3) with the experimental results. The setup shown in Fig. 1 is employed and the parameters are $t = 0.8$, $\gamma = \pi$, $\lambda_R = 633$ nm, $\lambda_W = 514$ nm, $D = 3.8$ mm, $Z_C = 485$ mm, $d = 10$ mm, $f = 100$ mm, $\Delta X^{12} = 0$, and $\Delta Y^{12} = 142 \times 10^{-3}$ mm. The displacement, ΔX^{12} and ΔY^{12}, was done with a precision translation stage within 1-μm accuracy. Note that the centers of the pupils belong to the v axis. See also the coordinate axis attached to the results.

The results of Figs. 2(a) and 2(b) were experimentally obtained by use of a conventional recording scheme without and with a parallel plate in front of one of the pupil apertures in the second exposure, respectively. These experimental results can be compared with the theoretical simulations of Figs. 2(c) and 2(d), obtained by use of Eqs. (2) and (3), corresponding to the average intensity of the zero and the lateral orders. The same parameters are employed as in the experimental case. There is apparent agreement between results.

Let us analyze the interferometric fringes that result when a wedge whose dihedral angle is not null ($\gamma \neq 0$ and $\tau \neq 0$) is used in the second exposure. When the diffuser displacement and the thin edge of the wedge are parallel, Eq. (3) predicts that the fringes will tilt. This fringe rotation is accompanied by increasing spatial frequency. This phenomenon is confirmed by the results shown in Fig. 3. The magnitude of this rotation increases as the τ value increases. Note that if the wedge is introduced in the first exposure rotation in the opposite direction is produced. The angle between the fringes and the U axis is given by $\alpha = \tan^{-1}(\lambda_W Z_C \tau/4\pi\Delta Y^{12})$.

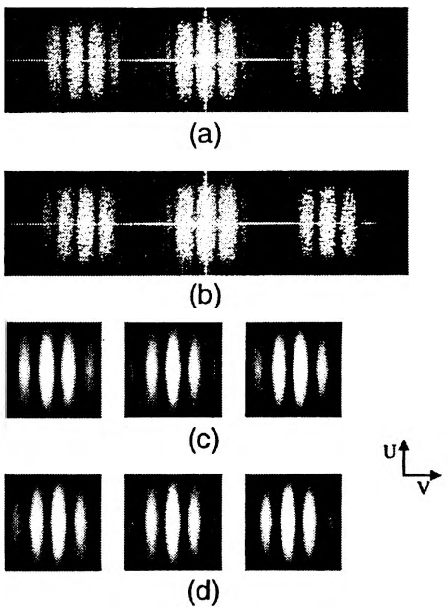


Fig. 2. Experimental results (a) without and (b) with a parallel plate in front of one aperture in the second exposure and (c) and (d) the corresponding theoretical simulations. The center images in (c) and (d) represent the zero order, and the left and right images represent the (−1) and (+1) orders, respectively.

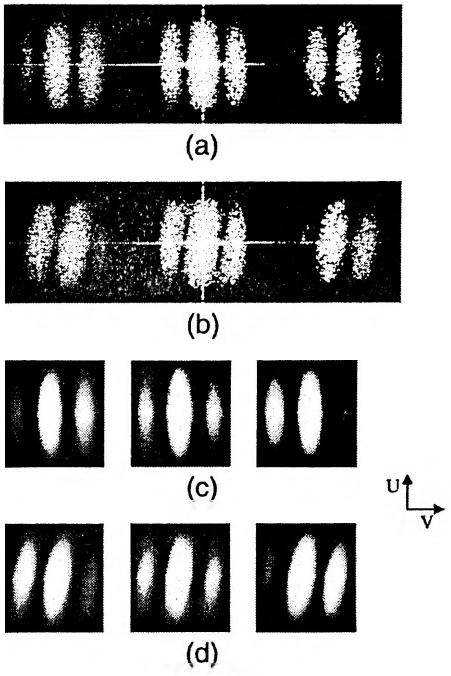


Fig. 3. Experimental results (a) without and (b) with a wedge in front of one aperture in the second exposure and (c) and (d) the corresponding theoretical simulations. The thin edge wedge and the diffuser displacement are parallel. The central images in (c) and (d) represent the zero order, and the left and right images represent the (−1) and (+1) orders, respectively.

Another phenomenon is the appearance of an amplitude modulation of the fringes that diminishes its visibility: This fact is described by the term $2t\ \mathrm{sinc}((\tau D/2\pi)\{1 - [(\vartheta U \mp u_{12})/D]\mathrm{sign}(\vartheta U \mp u_{12})\})$ in Eq. (3). As far as τ increases, visibility in the diffracted-order centers decreases. When the magnitude of τ increases further, the visibility decreases until a null value is reached along one or several lines running parallel to the edge of the wedge. It should be pointed out that the fringe visibility decreases as τ and the angle α increase. The interferometric-fringe visibility at the central point of each diffracted order is $\mathbf{V}^{\pm 1}(\mp d') = (2t)/(1 + t^2)|\mathrm{sinc}(D\tau/2\pi)|$. As a consequence, the visibility drops to zero at the center of the diffracted order, provided that $\tau D = m2\pi$, for $m = \pm 1, \pm 2, \ldots$. To prevent the visibility of the diffracted orders from decreasing below a certain value, we must impose the condition that the magnitude of τ does not exceed a limit defined in terms of the remaining experimental parameters. For example, for a minimum visibility higher than $-t/(1 + t^2)$, it must hold that $D|\tau|/2\pi < 0.6$. In our case, $D = 3.8$ mm, then $|\tau| < 992\ \mathrm{m}^{-1}$. Note that the wedge dihedral angle is $\beta = \tan^{-1}[\tau\lambda_W/(n - 1)2\pi]$, where n is the refractive index of the wedge. Then, if $n = 1.5$ and $\lambda_W = 514$ nm and $|\tau| < 992\ \mathrm{m}^{-1}$, dihedral angle β must be less than 33.5 arcsec.

In Fig. 3 we show the average intensity distribution in the Fourier plane obtained by introduction of a wedge in the second exposure ($\gamma = 0.6$ and $\tau = 750\ \mathrm{m}^{-1}$) so that the thin edge wedge and the diffuser displacement are parallel. The results of Figs. 3(a) and 3(b) are obtained without and with introduction of a wedge in front of one aperture in the second exposure by a conventional recording scheme, respectively. The parameters employed are $t = 0.8$, $\gamma = 0.6$, $\tau = 750\ \mathrm{m}^{-1}$, $\lambda_R = 633$ nm, $\lambda_W = 514$ nm, $D = 3.8$ mm, $Z_C = 485$ mm, $d = 10$ mm, $f = 100$ mm, $\Delta X^{12} = 0$, and $\Delta Y^{12} = 94 \times 10^{-3}$ mm. These experimental results can be compared with the theoretical simulations [Figs. 3(c) and 3(d)] corresponding to the average intensity of the zero and the lateral orders obtained by use of Eqs. (2) and (3) and the same parameters as in the experimental case. With the parameters of Fig. 3, the resulting angle α is 9°.

In our method the phase object is characterized as changes of correlation fringes. To this purpose, the average intensity and visibility of these fringes in the Fourier plane were evaluated. We discussed the phenomena observed in the diffracted orders and compared the results with those obtained with a conventional double-exposed specklegram. The changes in the interferometric fringes can also be evaluated in terms of the parameters that define the phase object employed in each experiment. It should be pointed out that this method can be performed in real time by use of a photorefractive crystal as a recording medium.[4]

This interferometer is well suited to measurement of very small angles concerning phase objects. For instance, the time-varying thickness map of vertical soap films could be analyzed.[6] This study gives information on the nature and range of the intermolecular forces that are responsible for the film formation. This experiment is implemented by storage of a reference speckle image in a buffer memory. Afterward, the evolution of the film can be displayed by real-time addition of the successive status of the speckle pattern and the reference image. By application of a real-time fast Fourier-transform algorithm to the resulting pattern, the correlation fringes are obtained and the film formation can be monitored.

M. Tebaldi's e-mail address is myrian@odin.ciop.unlp.edu.ar.

References

1. D. Duffy, Appl. Opt. **11,** 1778 (1972).
2. H. Rabal, N. Bolognini, E. Sicre, and M. Garavaglia, Opt. Commun. **34,** 7 (1980).
3. M. Tebaldi, L. Angel, M. Trivi, and N. Bolognini, Opt. Commun. **168,** 55 (1999).
4. L. Angel, M. Tebaldi, N. Bolognini, and M. Trivi, J. Opt. Soc. Am. A **17,** 107 (2000).
5. R. Mohanty, C. Joenathan, and R. Sirohi, Appl. Opt. **24,** 3106 (1985).
6. V. Greco and G. Molesini, Sci. Technol. **7,** 96 (1996).

Modulated speckle simulations based on the random-walk model

A. Lencina and P. Vaveliuk

Laboratório de Óptica Não Linear, Departamento de Física, Centro de Ciências Exatas e da Natureza, Universidade Federal da Paraíba, Brasil

M. Tebaldi

Centro de Investigaciones Ópticas, Consejo Nacional de Investigaciones Científicas Técnicas, CIC, and Facultad Ingenieria, Universidad Nacional de la Plata, Argentina

N. Bolognini

Centro de Investigaciones Ópticas, Consejo Nacional de Investigaciones Científicas Técnicas, CIC, and Facultad Ciencias Exactas, Universidad Nacional de la Plata, Argentina

Received December 2, 2002

The random-walk model is employed to simulate modulated speckle patterns. We demonstrate that the geometrical image approximation fails to describe the modulated speckle pattern. A new approach to analyzing this phenomenon is proposed. The validity of the approximations employed is verified by comparison of the simulation with the experimental results. Speckle metrological applications and phase measurement techniques could be improved by taking advantage of this model. © 2003 Optical Society of America

OCIS codes: 070.2580, 110.1220, 110.2990, 110.6150.

Computational developments over the past few years offer new possibilities for the random-walk model. This model allows a physical magnitude to be described as a finite sum of random phasors and is usually utilized to describe several effects involved in the propagation of electromagnetic waves.[1] As is well known, speckles are generated when multiple sources of interference scatter from a diffusing object illuminated by coherent light.[2] Then the diffuser can be assumed to be an ensemble of scattering elements with any distribution of shape, position, and phase. In speckle applications a continuous model for the speckle field is used, thereby restricting the results to mean values. We believe that the random-walk model could help in understanding and lead to a further analysis of the phenomenon based on a point-by-point approach. In particular, we propose using the random-walk model to revise the analysis of the modulated speckle pattern that appears in several metrological applications.[3,4] The speckle simulation can be used to test the geometrical image approximation and to verify its validity. In particular, we find that the approximation fails to describe thoroughly the modulated speckle pattern. Therefore we propose a new approach to analyzing this phenomenon.

In the proposed experimental setup a laser beam of wavelength λ impinges on the diffuser (x-y plane). An image of the diffuser is formed in the X-Y plane by use of a lens of focal length f. A pupil mask with several identical apertures a_h (where $h = 1, 2, \ldots, n$) is located immediately in front of the lens. There is no overlap between two different apertures belonging to the same pupil. Note that the line that joins a particular aperture center and the point that results from the intersection between the optical axis of the imaging system and the pupil mask plane forms an angle α_h with the horizontal axis (u axis). Also, the center of the aperture a_h is located at a distance d_h from the optical axis of the system. Z_0 and Z_C denote the distance from the diffuser to the lens and from the lens to the image plane, respectively. Let us introduce an experimental result to provide a basis for our theoretical approach. In Fig. 1(a) a magnified speckle pattern obtained in the X-Y plane is shown. The image is generated by use of a double-aperture pupil with circular holes of diameter $D = 4.8$ mm and separated a distance $d = 9.2$ mm. The parameters are $\lambda = 514$ nm, $Z_0 = 138$ mm, and $Z_C = 382$ mm.

Let us analyze theoretically the amplitude distribution in the image plane. The speckle image field

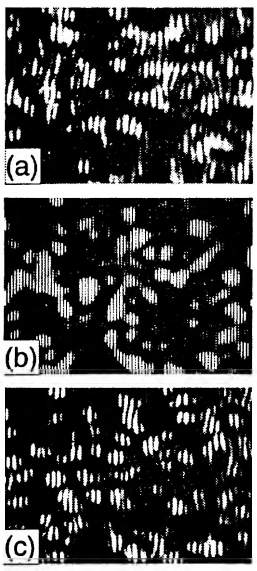


Fig. 1. (a) Experimental modulated speckle pattern. Theoretically modulated speckle pattern obtained by use of (b) geometrical image approximation and (c) local phase approximation.

0146-9592/03/191748-03$15.00/0 © 2003 Optical Society of America

in the X-Y plane obtained by use of the Rayleigh–Sommerfeld expression (see Ref. 5) is given by

$$U_i(X,Y) = \iiiint U_0(x,y)\frac{\exp(-jkR)}{\lambda R}P(u,v) \times \exp\left[j\frac{k}{2f}(u^2+v^2)\right]\frac{\exp(-jkR')}{\lambda R'}\mathrm{d}x\mathrm{d}y\mathrm{d}u\mathrm{d}v, \quad (1)$$

where $k = 2\pi/\lambda$, $j = \sqrt{-1}$, $R^2 = Z_0^2 + (v-y)^2 + (u-x)^2$, and $R'^2 = Z_C^2 + (v-Y)^2 + (u-X)^2$.

To generalize, let us consider a multiple-aperture arrangement. In this case the pupil function in Eq. (1) consists of a sum over all the apertures; that is, $P(u,v) = \sum_{h=1}^{n} a_h(u - d_h\cos\alpha_h, v - d_h\sin\alpha_h)$. Let us replace the explicit pupil function in Eq. (1) and introduce a variable change $u_h = u - d_h\cos\alpha_h$ and $v_h = v - d_h\sin\alpha_h$ for each aperture. Besides, by considering the well-known paraxial approximations ($Z_0 \gg d_h, u_h, v_h$ and $Z_C \gg d_h, u_h, v_h$), we get

$$U_i(X,Y) = \frac{1}{\lambda^2 Z_0 Z_C}\sum_{h=1}^{n}\iiiint U_0(x,y)a_h(u_h,v_h) \times \exp\left\{\frac{-jk}{2Z_C}[(d_h\sin\alpha_h - Y)^2 + (d_h\cos\alpha_h - X)^2]\right\} \times \exp\left\{\frac{-jk}{2Z_0}[(d_h\sin\alpha_h - y)^2 + (d_h\cos\alpha_h - x)^2]\right\} \times \exp\left\{jk\left[u_h\left(\frac{x}{Z_0}+\frac{X}{Z_C}\right) + v_h\left(\frac{y}{Z_0}+\frac{Y}{Z_C}\right)\right]\right\} \times \exp\left\{jk\left[\frac{d_h^2}{2f} - (Z_0+Z_C)\right]\right\}\mathrm{d}x\mathrm{d}y\mathrm{d}u_h\mathrm{d}v_h. \quad (2)$$

Note that Eq. (2) explicitly shows the coordinate system variable associated with each aperture. At this point it is important to analyze the square phase terms in Eq. (2). The term $\exp\{-jk[(d_h\sin\alpha_h - Y)^2 + (d_h\cos\alpha_h - X)^2]/2Z_C\}$ is relevant because it depends on the summation index. In a previous paper, when a single-aperture pupil was considered, this term went out of the integral and vanished if the intensity evaluation was done. The second square term to be analyzed is $\exp\{-jk[(d_h\sin\alpha_h - y)^2 + (d_h\cos\alpha_h - x)^2]\}/2Z_0$. In previous studies,[6] for instance, this term was disregarded because a geometrical image approximation was done. In this approach the light amplitude at coordinates (X,Y) must consist of contributions from a tiny region of the object space, centered at the ideal geometrical object point. If within that tiny region the argument of $\exp[jk(x^2+y^2)/2Z_0]$ changes by no more than a fraction of a radian, then the approximation $x \cong X/M$ and $y \cong Y/M$, where M is the image magnification, is used. The random-walk model is an adequate tool[7] for obtaining an explicit expression of the amplitude field. In this model the speckle field $U_0(x,y) = \sum_{q=1}^{r} U_q(x,y)\exp(j\phi_q)$ consists of a sum of r discrete field amplitudes $U_q(x,y)$ with phase ϕ_q, which contribute to the image speckle field formation. These discrete field components are small spots with random amplitude, phase, and position (x_q, y_q).

At this point, to evaluate the image field, the random-walk model is introduced. In this evaluation the approximations concerning the second square term[6] detailed above are taken into account. In this case, by neglecting the phase terms that go out of the integrals and sums, the amplitude field becomes

$$U_i(X,Y) = \frac{1}{\lambda^2 Z_0 Z_C}\sum_{q=1}^{r}\sum_{h=1}^{n}U_{qh}(X,Y) \times \exp\{j[\phi_q + \phi_h(X,Y)]\}, \quad (3)$$

where

$$\phi_h(X,Y) = \frac{-2kd_h}{Z_C}(Y\sin\alpha_h + X\cos\alpha_h), \quad (4)$$

$$U_{qh}(X,Y) = \iint \mathrm{d}x\mathrm{d}y U_q(x,y)A_h(x,y;X,Y), \quad (5)$$

$$A_h(x,y;X,Y) = \iint a_h(u_h,v_h) \times \exp\left\{jk\left[u_h\left(\frac{x}{Z_0}+\frac{Y}{Z_C}\right) + y_h\left(\frac{y}{Z_0}+\frac{Y}{Z_C}\right)\right]\right\}\mathrm{d}u_h\mathrm{d}v_h. \quad (6)$$

Let us evaluate the intensity. A double-aperture pupil system is considered. Both apertures are identical and are separated by a distance d symmetrically with respect to the optical axis. The line joining the apertures is horizontal. Therefore the value of the angle α_h that corresponds to each aperture is $\alpha_1 = 0$ and $\alpha_2 = \pi$, respectively. In this case the intensity can be written as

$$I_i(X,Y) = \frac{2}{(\lambda^2 Z_0 Z_C)^2}\left[1+\cos\left(\frac{2kdX}{Z_C}\right)\right] \times \left[\sum_{q=1}^{r}U_q^2 + 2\sum_{q=1}^{r-1}\sum_{s>q}^{r}U_qU_s\cos(\phi_q - \phi_s)\right]. \quad (7)$$

This theoretical intensity pattern is depicted in Fig. 1(b). In this case the same parameters as in Fig. 1(a) are employed. In the random-walk model the speckle field in the diffuser plane originates from r points, each one with associated amplitude, phase, and position. In this case the image area is ≈ 0.53 mm^2, and the area of each speckle is ≈ 0.0025 mm^2. Under this condition approximately 200 speckles are necessary to fulfill the corresponding region. Nevertheless, to ensure Gaussian behavior, we include 600 speckles in our simulations. In the model the speckles are uniformly and randomly distributed in the x-y plane and have random amplitudes in the range $[0,1]$. Also, to ensure a fully developed speckle regime, the phases are assumed randomly and uniformly distributed in the range $[-\pi,\pi]$. It should be mentioned that the random values in the simulations are obtained by use of the Mathematica software package that employs the Marsaglia–Zaman subtract-with-borrow (SWB) generator.[8]

It should be noted that the fringe frequency that modulates the speckle pattern obtained by use of Eq. (7) [Fig. 1(b)] differs from the experimental case

[Fig. 1(a)]. A simple geometrical analysis shows that the spatial frequency for a double-aperture system is $|\mathbf{K}| = kd/Z_C$. However, from Eq. (7) the spatial frequency is $|\mathbf{K}'| = 2kd/Z_C$, which confirms the discrepancies between the results of Figs. 1(a) and 1(b). Also, it is observed that the fringe modulation phase in the theoretical pattern does not depend on the speckle position. This behavior does not coincide with the experimental result. These discrepancies have motivated us to make a further analysis. Let us reinterpret the approximations in the second square term $\exp\{-jk[(d_h \sin \alpha_h - y)^2 + (d_h \cos \alpha_h - x)^2]/2Z_0\}$, where now the geometrical image approximation is removed.

We have an explicit expression for the field $U_0(x,y) = \sum_{q=1}^{r} U_q(x,y)\exp(j\phi_q)$. This field is discrete and implies evaluation of the integration in each spot [see Eq. (2)]. Besides, because of its small size, it is valid to fix a local phase value by assuming a low-phase variation in it. This local phase implies replacing (x,y) by (x_q,y_q) in the square term mentioned.

The intensity applied to an identical system, as in Eq. (7), under the conditions detailed above and neglecting phase terms that go out of the integrals and sums yields

$$
\begin{aligned}
I_i(X,Y)\frac{(\lambda^2 d_0 d_i)^2}{2} = {} & \sum_{q=1}^{r} U_q^2\left\{1+\cos\left[kd\left(\frac{x_q}{Z_0}+\frac{X}{Z_C}\right)\right]\right\} \\
& + \sum_{q=1}^{r-1}\sum_{s>q}^{r} U_q U_s \cos\left[\phi_q - \phi_s \right. \\
& \left. + \frac{k}{2Z_0}(y_q^2 - y_s^2 + x_q^2 - x_s^2)\right] \\
& \times\left\{\cos\left[\frac{kd}{2Z_0}(x_q - x_s)\right]\right. \\
& \left. + \cos\left[kd\left(\frac{x_q + x_s}{2Z_0}+\frac{X}{Z_C}\right)\right]\right\}. \qquad (8)
\end{aligned}
$$

By use of Eq. (8) a new theoretical intensity pattern is obtained. This result is depicted in Fig. 1(c). The same parameters as in Fig. 1(b) are used. It is apparent that Figs. 1(a) and 1(c) exhibit similar features. Note that the fringe frequency coincides in both figures and a local phase behavior as in the experimental case is observed in Fig. 1(c).

In this study we demonstrate that by use of the random-walk model and with a new approach for the optical model, it is possible to simulate modulated speckle patterns whose behavior coincides with the experimental results. The analysis is general and could be applied to more complex aperture pupils. In Ref. 9 a peculiar type of speckle pattern was reported. These speckles present a clustering appearance consisting of many chains of speckle grains. This feature is attributed to the circular symmetry of the ring-slit aperture employed. The dynamic of clustering could be analyzed by applying the proposed model to an optical system that gradually increases the circular symmetry of the pupil apertures. To this end, a ring-slit pupil aperture can be synthesized by circular aperture pairs placed along a diameter of the ring. Also, the versatility of the random-walk model allows for the simulation of speckle patterns with different statistical properties in terms of the statistical properties of the diffuser field.

This approach, which yields a more precise description of the speckles' local behavior, could be useful in controlling the diffuser features, for instance, its statistics (fully developed or Gaussian) and surface roughness. Note that in the speckle photography technique a Fourier plane analysis of the specklegram is done. This approach is basically followed in Ref. 10 and does not allow local phase changes due to the presence of complex phase objects in the pupil plane to be determined.[10] Nevertheless, the information needed to determine these local changes is present in the specklegram. In this study a theoretical model that shows the local behavior of the modulated fringe distribution has been outlined. Let us introduce a complex phase object in the pupil plane, and let us suppose that the statistics of the diffuser are known. Under these conditions that theoretical knowledge allows us to interpret and determine the local phase changes introduced by the object that have taken place by analyzing the modulated fringes in the image plane and comparing them with the situation without the phase object. In summary, our approach provides a tool for determining any local phase change by analyzing the image plane. Finally, it is clear that this approach could be applied in another range of the electromagnetic spectrum where the output of the system is statistically ruled and behaves like speckle structures.

A. Lencina's e-mail address is agl@fisica.ufpb.br.

References

1. A. Zardecki, *Inverse Source Problems*, H. P. Baltes, ed. (Springer-Verlag, Berlin, 1985), p. 155.
2. J. C. Dainty, ed., *Laser Speckle and Related Phenomena* (Springer-Verlag, Berlin, 1975).
3. M. Tebaldi, A. Lencina, and N. Bolognini, Opt. Commun. **202,** 257 (2002).
4. L. Angel, M. Tebaldi, M. Trivi, and N. Bolognini, Opt. Lett. **27,** 506 (2002).
5. R. P. Khetan and F. P. Chiang, Appl. Opt. **15,** 2205 (1976).
6. J. W. Goodman, *Introduction to Fourier Optics* (McGraw-Hill, New York, 1996), p. 111.
7. E. Jakeman, Opt. Eng. **23,** 453 (1984).
8. G. Marsaglia and A. Zaman, Ann. Appl. Probab. **1,** 462 (1991).
9. K. Uno, J. Uozumi, and T. Asakura, Opt. Commun. **114,** 203 (1995).
10. M. Tebaldi, L. Ángel, M. Trivi, and N. Bolognini, J. Opt. Soc. Am. A **20,** 116 (2003).

Patentes, desarrollo de instrumentos y servicios

Patentes

Instrumentos

Servicios

Patentes, Desarrollo de Instrumentos y Servicios

Desde sus comienzos, el CIOp se caracterizó por incluir dentro de sus actividades, aplicaciones surgidas de sus líneas de trabajo de investigación básica a problemáticas de interés industrial o de organismos oficiales del ámbito de las pequeñas y medianas empresas. Algunas de dichas aplicaciones se basan en las distintas propiedades del láser (como direccionalidad, monocromaticidad, coherencia, potencia, sintonía), mientras que otras surgen como corolario de trabajos de investigación sobre procesamiento de información óptica publicados en revistas de la especialidad. Este perfil, que el CIOp ha mantenido durante estos 30 años y es uno de sus objetivos fundacionales, apunta a volcar a la comunidad los resultados de la experiencia de sus investigadores y profesionales de apoyo en el área de la Óptica y el láser. Como resultado de esta línea, se han desarrollado instrumentos y técnicas de medida, se han publicado patentes y se han brindado servicios. La experiencia adquirida en espectroscopía se volcó en el desarrollo de medidores ópticos basados en espectroscopía de absorción diferencial en columna abierta para la determinación de concentración de ozono estratosférico (agujero de ozono), medidor no-dispersivo UV de gases contaminantes en boca de chimenea (NDUV), determinación de calidad de aire urbano (DOAS) y medidores de reflectancia espectral de cultivos. También se ha desarrollado un equipo láser para el estudio de la cinética de cristalización isoterma en aceites hidrogenados de interés en la industria alimenticia, basado en la medición de la actividad óptica de estos compuestos y un sistema de medición láser de nivel de llenado de silos de uso agronómico basado en el uso de técnicas de óptica geométrica por triangulación.

Algunos de los dispositivos desarrollados han culminado en patentes de invención, como por ejemplo, el medidor láser de limpieza de superficies metálicas (ELMES), la técnica de espectroscopía de backscattering para medición de tamaño de partículas en suspensión, el desarrollo de un kit educativo sobre experimentos de Óptica y Láser y el desarrollo de estereogramas láser. En lo que respecta a técnicas de medida, se desarrollaron métodos para la generación de planos, alineación de grandes componentes (bancada de motor de barcos, álabes de turbinas en plantas de gas natural), espectroscopía de lámparas de uso domiciliario y para laboratorios medicinales, validación de granulómetro láser para la medición de tamaño de partículas en la industria farmacéutica. Finalmente, cabe mencionar la generación de servicios tanto para la comunidad científica como para el ámbito industrial, como el láser de corte, servicio de calibración de diodos láser y fibras ópticas para comunicaciones ópticas y monitoreo de pozos petrolíferos de extracción secundaria con trazadores fluorescentes.

Patents, Instruments and services

Since its early days, CIOp focused on applications for solving engineering or industrial problems directly derived from its research activities in Optics and Lasers. Some of these applications were based on laser properties such as coherence, monochromaticity, high power, directionality and tunability while others were born as spin-offs from the work on optical data processing, speckle interferometry and optical correlators. These activities are one of its foundation objectives and aim to return to the community the results of its scientific work and the experience of its research teams in Optics and Lasers. The experience acquired in Optical Spectroscopy made possible the development of optical detectors for stratospheric ozone concentration, non-dispersive UV (NDUV) detector of gas emissions in chimneys, urban air quality and green-plants spectral reflectance, all based on open column differential optical absorption spectroscopy. Besides, portable laser-based instruments for food-hydrogenated-oil crystallization kinetics studies and for seed-container filling measurement were developed and successfully installed. Some of the devices ended in an invention patent, like the metallic surface-cleanliness laser detector (ELMES), the backscattering spectroscopy technique for sizing suspended microparticles, the school-level optics and laser education kit and the development of laser stereograms. As measurement techniques are concerned, methods for plane generation and big machines alignment were developed, as well as spectroscopy of home-use and medical labs lamps, validation of a laser granulometer for sizing particles in the pharmaceutical industry. Finally, services for third-parties were implemented such as the high power laser cut service for the steeling industry, diode laser and optical fiber calibration service for communication firs and fluorescence-based monitoring of secondary oil extraction field for the oil refinery industry.

Método para la determinación de suciedad en superficies

Inventores: Gabriel M. Bilmes y Oscar E. Martinez. Tipo: Patente de Invención Registro Nro: AR9906271. Fecha presentación: 9-12-99. País: Argentina. Fecha de resolución: 23-06-06. Fecha de vencimiento: 09-12-2019. Titular/es del Registro: CONICET-CIC-UNLP-UBA.

La presente invención trata de un método que permite determinar, a tiempo real, el grado de suciedad relativo o absoluto (si se usa un patrón adecuado) de cualquier superficie en la que la capa de suciedad sea de un espesor no mayor a 100 □m. El método que se presenta utiliza una fuente de luz capaz de producir la ablación óptica de una porción mínima de la capa de suciedad y un micrófono que detecta el sonido producido durante la ablación. La idea principal del método inventado, es que el sonido medido es creciente con el grado de suciedad de la superficie.

Laser Apparatus for measuring dirt density on steel plates

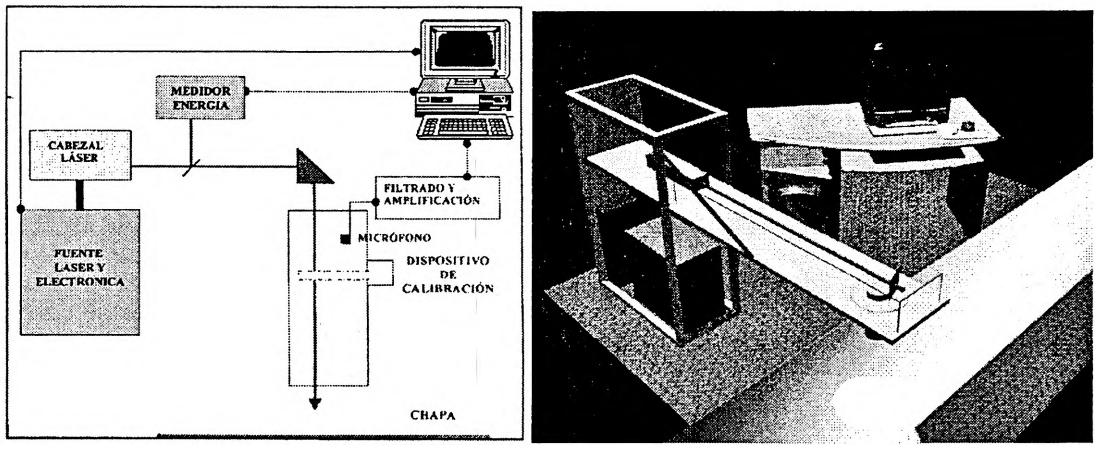
Inventors: G. M. Bilmes and O. E. Martinez.
Country: USA (Pat: 6.546.784- Date: 15-4-2003 Expiration-Date: 15-4-2021).Owners: CONICET-CIC-UNLP-UBA.

The invention is an apparatus that measures dirt density on steel plates, characterized by including a pulsed laser that impinges on the inspected plate, and a microphone that detects the sound produced by the sudden ablation of the dirt, the amplitude of the microphone signal being the measure of the dirt on the plate. The microphone is connected to an electronic signal processing system, which is a computer or a programmed digital processor that determines the average value and standard deviation of the signal over the number of hits specified by the operator.

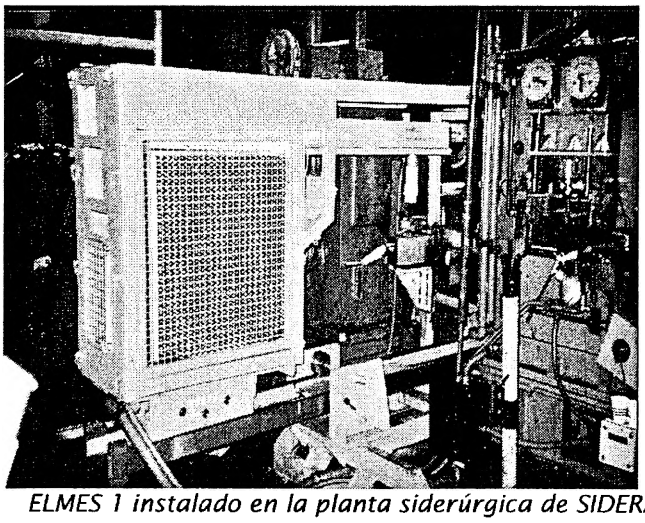
Equipo láser para la medición de suciedad en chapas de acero

Inventores: G. M. Bilmes y O. E. Martinez. Tipo: Patente de invención.
País de registro: ARGENTINA (Registro Nro: P000101241. Fecha:12-3-2000).

La presente invención trata de un equipo capaz de medir la suciedad presente en la superficie de chapas de acero laminadas. Dicha medición puede realizarse directamente sobre la laminadora (con chapa en movimiento), o en una inspección sobre muestras de la misma. El equipo consta de un láser pulsado, los dispositivos ópticos para direccionarlo hacia la chapa que se desea medir, un detector acústico (micrófono) y la electrónica asociada para el control y el procesamiento de la señal. El equipo motivo de la presente patente se basa en el hecho de que la suciedad de la superficie esta formada por una película de grasa o aceite y partículas de diferentes compuestos. Si se hace incidir un pulso de suficiente fluencia (energía por unidad de superficie) y corta duración (~ 10 ns) de un láser, se produce un calentamiento violento de la película que cubre la superficie hasta su evaporación. Durante este proceso las partículas son bruscamente expulsadas de la chapa, junto con restos de aceites u otros fluidos. Diversos fenómenos se producen como consecuencia de la interacción del pulso del láser con la película que cubre la superficie. Uno de ellos es sonido, que se aprecia como un chasquido cuya intensidad depende del nivel de suciedad. La intensidad de dicho sonido es utilizada como medición de la suciedad expulsada, que resulta creciente con el aumento de la suciedad presente en la chapa. Para ello se coloca a una distancia adecuada del punto de impacto del láser sobre la chapa, un micrófono conectado a un sistema de procesamiento de la señal. El procesamiento requerido es la determinación de la amplitud de la señal sonora originada por la expulsión de la suciedad.



Esquema del Elmes: Equipo láser para medición de suciedad



ELMES 1 instalado en la planta siderúrgica de SIDERAR, Ensenada -Buenos Aires-Argentina

Laser Apparatus for measuring dirt density on steel plates

Inventors: G. M. Bilmes y O. E. Martinez..
Country: ARGENTINA (Reg. Nº: P000101241. Date:12-3-2000).

The invention is an apparatus that measures dirt density on steel plates. The measurement can be done directly on the sliding plate or during routine sample inspection. The system consist of a pulsed laser, beam steering optics that makes the laser impinge on the inspected plate, and a microphone that detects the acoustic signal. The microphone is connected to an electronic signal processing system, which is a computer or a programmed digital processor. Since the surface dirt is mainly formed by a thin layer of grease with suspended carbon particles, a high fluence short duration (10 ns) laser pulse produces a sudden evaporation of this layer and a rapid ejection of its compounds. The generated sound blast is detected by the microphone and its intensity isa measure of the dirt amount in the sampled point.

Procedimiento analítico y disposición para determinar el tamaño de partículas suspendidas en un medio líquido

Inventores: L. Scaffardi, F. Videla y D. Schinca
Patente en trámite (CONICET-UNLP-CIC): (acta N° P050101083)

El análisis espectroscópico de la luz retrodispersada por una muestra es una técnica óptica que permite la determinación de tamaño de partículas en suspensión a tiempo real y en forma no destructiva en industrias farmacológicas, alimenticia, etc. La invención es aplicable en diversas áreas industriales relacionadas con la manufactura de productos basados en la utilización de material particulado. Puede utilizarse como técnica de control de calidad en línea de producción en la actividad farmacológica (fabricación de medicamentos), en el desarrollo de emulsiones para el tratamiento del cuero (industria de la curtiembre), industria alimenticia, moliendas, pesticidas, pinturas, pigmentos, etc. Además, tiene particular aplicación en la discriminación de tamaños de partículas en muestras multimodales.

La técnica por excelencia para la determinación de tamaño de partículas es la microscopía. Esta puede ser de tipo óptica (para tamaños con límite inferior a 5 micrómetros) o de tipo electrónica (para tamaños hasta 0,01 micrómetro). Ambas modalidades, en particular ésta última, poseen como desventaja la necesidad del acondicionamiento previo de la muestra para su posterior medición, como así también el requerimiento de la realización de un número grande de observaciones para asegurar una estadística razonable.

Las técnicas ópticas basadas en la dispersión (*scattering*) de luz evitan estos inconvenientes y permiten una medición a tiempo real. La medición de *scattering* a ángulo fijo de 180° (retro-dispersión o *backscattering*) y a distintas longitudes de onda posee una versatilidad mayor, ya que simplifica la arquitectura del dispositivo experimental, ampliando de manera importante el rango de radios hasta más allá de 10 μm.

El presente invento comprende un procedimiento y una disposición para determinar o predecir tamaños de partículas entre 0,2 y 12 μm de radio en suspensión líquida basado en el análisis espectroscópico de la retrodispersión de luz. La técnica del presente invento consiste en la adquisición de señales de *backscattering* con FO y registro de su espectro en función de la longitud de onda con un espectrógrafo de dispersión cruzada, de manera similar a la descrita por los autores. Se envía a la muestra un haz de luz blanca por medio de una fibra óptica. Otra fibra óptica similar a la primera, colocada cercana y paralelamente a la misma (geometría endoscópica), colecta la luz retrodispersada por la muestra y la envía a un espectrógrafo para su análisis en longitud de onda.

El punto novedoso consiste en el desarrollo de un nuevo procedimiento o algoritmo basado en el cálculo de la transformada de Fourier (TF) de los espectros experimentales y su comparación con las transformadas de Fourier de los espectros de eficiencia de *backscattering* calculados con teoría de Mie, lo que permite generar una curva de calibración para radios comprendidos en el rango 0,2 - 12 μm. Para aumentar la exactitud en la determinación del tamaño, se realiza una correlación cruzada entre las curvas de Mie para diferentes radios y la señal experimental, dentro del ancho medio de cada máximo de la transformada de Fourier experimental. La aplicación de la transformada de Fourier permite discriminar diferentes componentes en muestras multimodales, mientras que la exploración por correlación dentro de cada máximo permite ajustar la exactitud en la determinación del radio de cada especie presente.

Analytical procedure for sizing particles suspended in a liquid medium

Inventors: L. Scaffardi, F. Videla y D. Schinca
Patent pend.: (N° P050101083)
Owners: (CONICET-UNLP-CIC)

Backscattering spectroscopy allows sizing particles in suspension on a real-time and noninvasive basis for pharmacological, food and other industries. The invention is of applicability as on-line quality control technique for industries related with the manufacture of particulate-material based products such as leather finishing, paint fabrication, pesticides and others.

Microscopy is the most developed technique for particle sizing. In its both forms, optical or electronic, possess the drawback of sample conditioning prior to measurement and a large number of observation for reliable statistics. Optical techniques based on scattering overcome these limitations and convey a simpler experimental setup when it comes to specific site measurements.

The current invention comprises a procedure and device to determine particle sizes 0.2 and 12 μm radius in liquid suspension based on the spectroscopic analysis of the light backscattered from a sample. The white light is delivered and collected at 180° by two similar optical fibers, deployed in an endoscopic geometry, and recorded in a spectrograph.

The new approach consists in the development of a Fourier-transform based algorithm with which the experimental spectra are processed. Accuracy increase is possible through a further application of a cross-correlation algorithm between obtained spectra and theoretically calculated backscattering efficiencies. The method is also applicable to multimode samples with several particle sizes.

Detección de actividad biológica usando speckle dinámico

Uso do bio-speckle laser como quantificador de atividade biológica: medidor de umidade, identificador de fungos em sementes e quantificador de atividade em sêmen animal

Inventores: R. Alves Braga Júnior, G. Rabelo, H. J.Rabal, M. Trivi, R. Arizaga. Registro Nro. PI 03019268. Instituto Nacional da Propiedade Industrial, Brasil. 2003. En colaboración Universidad Federal de Lavras (MG) Brasil.

Método implementado em microcomputador para captura e procesamento de imagem do biospeckle laser e uso

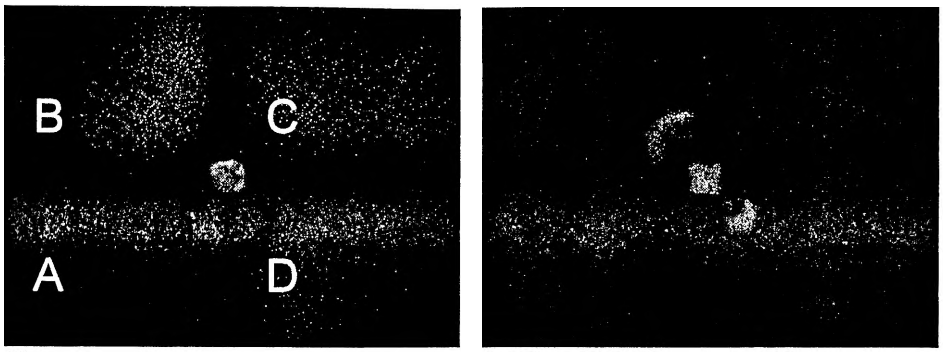
Inventores: R. Alves Braga Júnior, G. Rabelo, H. J.Rabal, M. Trivi, R. Arizaga. Instituto Nacional da Propiedade Industrial, Brasil. En trámite. 2005. En colaboración Universidad Federal de Lavras (MG) Brasil.

Método de detección de respuestas quimiotácticas por speckle dinámico

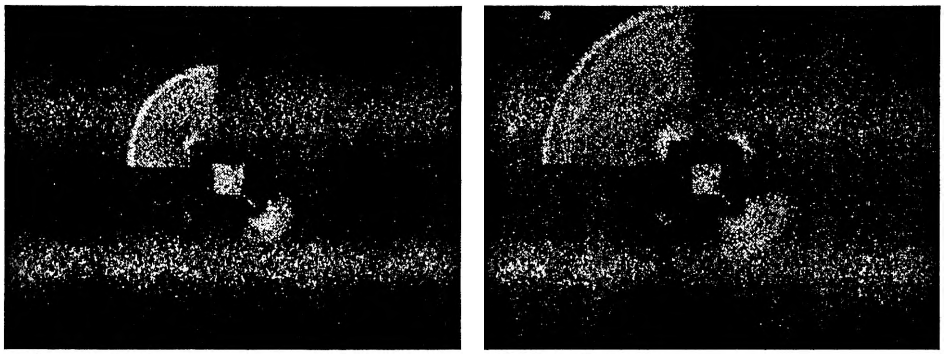
Inventores: S. Murialdo, G. Sendra, H. Rabal, R. Arizaga, M. Trivi. Registro Nacional de Propiedad Intelectual (Argentina) Solicitud registrada bajo el nº de acta: P060104012. 2006. En colaboración con Facultad de Ingeniería, Universidad de Mar del Plata.

La técnica de speckle dinámico o biospeckle ha demostrado ser una herramienta rápida y eficaz para estudiar actividad biológica. En el CIOp se han realizado varios trabajos orientados a la aplicación de esta técnica en el estudio de la viabilidad de semillas, daños en frutos, movilidad de parásitos, presencia de hongos en vegetales, quimiotaxis en bacterias, etc. Además de las comunicaciones en Congresos y publicaciones en revistas de la especialidad, estos desarrollos dieron lugar a las tres patentes precedentes.

Como ejemplo se muestra el estudio realizado mediante biospeckle de la evolución temporal del comportamiento quimiotáctico de bacterias *Pseudomonas aeruginosa* para distintos atractores: (A) Control negativo (agar-agar), (B) Peptona, (C) Glutamato, (D) Glicerol



0hs 16hs. después



22hs. después 28hs. después

Biological activity detection by biospeckle techniques

Using the biospeckle laser as biological activity quantification: moisture measurements, fungi in seeds detection and semen

Inventors: R. Alves Braga Júnior, G. Rabelo, H. J.Rabal, M. Trivi, R. Arizaga. Register Nro. PI 03019268. National Institute of Industrial Patents (Instituto Nacional da Propiedade Industrial), Brazil. 2003. Collaboration with Universidad Federal de Lavras (MG) Brazil.

Microcomputer method implementation for biospeckle laser image processing

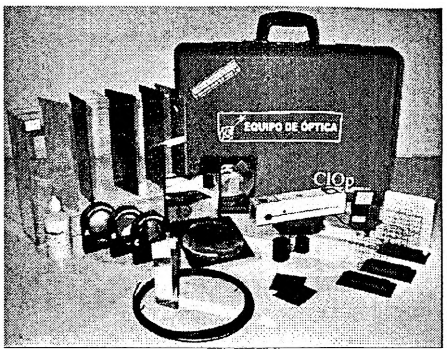
Inventors: R. Alves Braga Júnior, G. Rabelo, H. J.Rabal, M. Trivi, R. Arizaga. National Institute of Industrial Patents (Instituto Nacional da Propiedade Industrial), Brazil. 2005. Patent pending. Collaboration with Universidad Federal de Lavras (MG) Brazil.

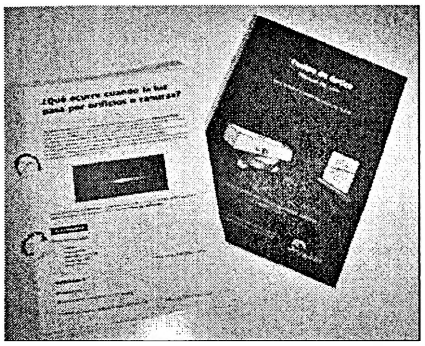
Detection of chemotaxis responses by dynamic speckle method

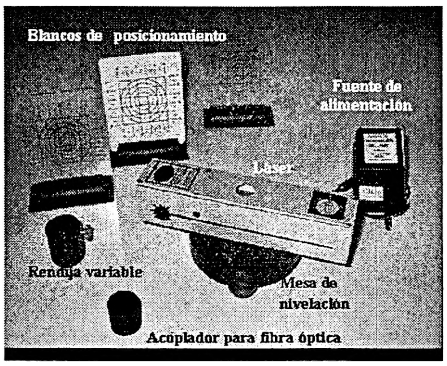
Inventors: S. Murialdo, G. Sendra, H. Rabal, R. Arizaga, M. Trivi. National Institute of Patents (Registro Nacional de Propiedad Intelectual) Argentina. Request: P060104012. 2006. Collaboration with Facultad de Ingenieria, Universidad de Mar del Plata.

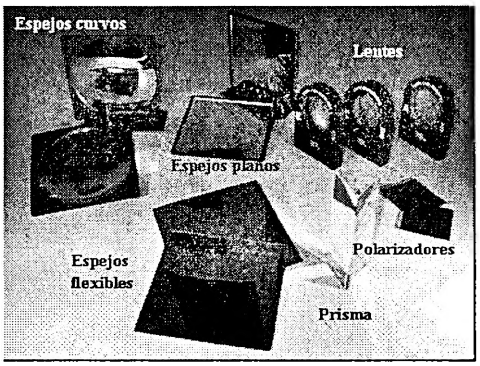
Biospeckle carries useful information about the biological and physiological activity of the biological samples. Many efforts have been developed at CIOp to assign quantities that characterize this activity. Several works were oriented to the applications of this technique to seeds viability, fruits damage, parasite motility, fungi detection in vegetables, bacteria chemotaxis, etc. Besides several publications in Journals and Congress participations, these developments gave rise to three patents.

The figures show a biospecke technique application to the temporal evolution detection of the chemotaxis response for different chemoattractants: A) none (negative control, agar-agar), B) peptone, C) glutamate and D) glycerol









Instrumento láser mejorado

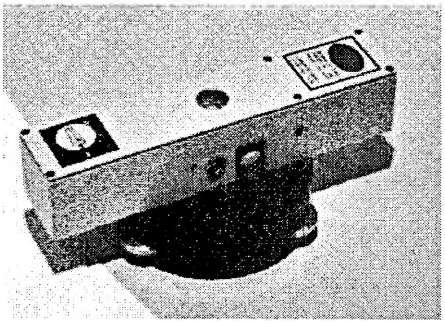
Inventores: G.M. Bilmes, N. Bolognini, M. Gallardo, J.O. Tocho y M. Trivi.
Tipo: Modelo de Utilidad. Registro Nro: M 990106740. Fecha: 23-12-99. País: Argentina.
Titular/es del Registro: ClOp-MCEN.

La invención consiste en un instrumento manual y portátil, de construcción sencilla, robusta y de relativamente bajo costo, que resuelve el problema de generar líneas y planos de referencia, tanto horizontales, empleadas para nivelar y alinear objetos, como verticales, empleadas para alinear y aplomar objetos, mediante la utilización de un rayo de luz laser y en un método para proporcionar la alineación de la dirección del rayo laser respecto de las caras del instrumento. El instrumento básicamente puede ser empleado en trabajos de construcción de obras civiles, de mecánica, de carpintería o en otras actividades semejantes.

Improved Laser Instrument

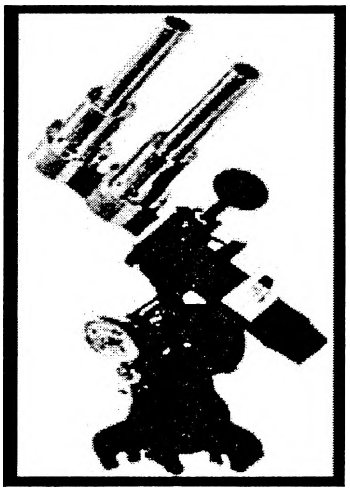
Inventors: G.M. Bilmes, N. Bolognini, M. Gallardo, J.O. Tocho y M. Trivi.
Type: Usage model. Register N°: M 990106740. Date: 23-12-99. Country: Argentina.
Owners: ClOp-MCEN.

The invention consists in a rugged, simple, portable low cost laser based that addresses the problem of generating planes and lines of reference, both horizontal and vertical for alignment of objects, together with a method for aligning the laser beam with the faces of the instrument. It can be used in the building industry, metal machining and carpenter manufacturing.



Medidores de ozono

El deterioro de la capa de ozono observada en los últimos años implica un aumento de la radiación ultravioleta que llega a nivel del mar comprendida entre 290 y 310 nm (UVB). La exposición prolongada a esta radiación produce daños comprobados sobre la vida animal y vegetal. Desde principios de los 80, se incrementaron los registros de la evolución de la capa de ozono a través de técnicas diversas (globos, estaciones en tierra, satélites), mayoritariamente sobre el continente antártico. De aquí se planteó la necesidad de contar con conjuntos de mediciones a latitudes menores que abarquen zonas pobladas, obtenidas por instrumentos en tierra.



A principios de la década del 90, se diseñaron y construyeron (en colaboración con la Universidad Autónoma de Madrid) 15 medidores terrestres de bajo costo y fácil manipulación, de forma de ubicarlos a modo de red de monitoreo de radiación UV en diversas latitudes del cono sur de América (Argentina y Chile). Los medidores están basados en la técnica de absorción diferencial, usando pares de fotodiodos de sensibilidad aumentada en UV, con filtros ópticos interferenciales en 300 nm y 315nm, a los que les llega la radiación solar directa, colimada por sendas lentes de cuarzo. Como la sección eficaz de absorción del O_3 es unas siete veces mayor en la primera banda respecto de la segunda, el cociente de la salida amplificada de cada fotodiodo es función de la concentración total de O_3 en la columna atmosférica observada.

Durante los años 1993 y 1994 se llevó a cabo una campaña de medición de la columna de ozono con esta red de monitoreo, ubicando los medidores ópticos en Río Grande, Bariloche, Tandil, la Plata, Mercedes, San Luis, Salta, Arica, Antofagasta, Rosario Carmen de Patagones, Mar del Plata y Valparaíso, entre el paralelo 23 Sur y 54 Sur. Así, se demostró, por ejemplo, que en la primavera del 93, la destrucción de la capa de ozono llegó a latitudes cercanas a 23 Sur (Antofagasta) indicando que el daño llegó a poblaciones importantes como Buenos Aires y Santiago de Chile. Los datos del resto de la campaña se relacionan muy bien con los satelitales. Con un diseño similar, se construyeron y probaron medidores de aerosoles y de cantidad de agua precipitable.

Ozone optical detectors

The increase of the ozone hole observed during the last years increases directly the ultraviolet radiation that reaches soil level, particularly that in the range between 290 nm and 310 nm (UVB). Prolonged exposure to this radiation is seriously hazardous for the majority of the living species, including humans. Since the beginning of the 80´s, records of the ozone layer evolution using different techniques (balloons, satellites, earthborn stations) have increased, the majority of which are over the Antarctic continent. There has been a need to have records of UVB radiation at lower latitudes where many populated regions are placed.

At the beginning of the 90´s, 15 low cost, user friendly UVB detectors were constructed in collaboration with Universidad Autónoma de Madrid. They were placed in different latitudes in Argentina and Chile so as to form a monitoring network. The detectors are based in differential absorption method, using UV sensitive photodiodes placed behind optical interferential filters at 300 nm and 315 nm. Both pieces are encapsulated inside a cylindrical housing containing a quartz lens for solar radiation collimation. Since ozone absorption cross section is about seven times larger for the first band than for the second, the ratio of the outputs is a function (calibrated at ClOp) of the total ozone concentration.

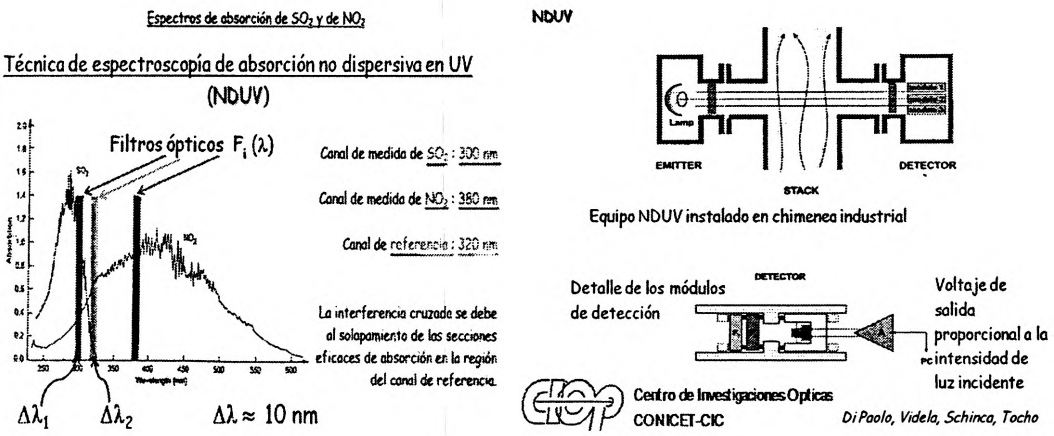
During 1993 and 1994, an extensive campaign was carried out with the detectors placed at these locations: Río Grande, Bariloche, Tandil, la Plata, Mercedes, San Luis, Salta, Arica, Antofagasta, Rosario Carmen de Patagones, Mar del Plata and Valparaíso, between lat. 23 S and 54 S. As a main result, it can be pointed out that during spring 1993, ozone hole reached low latitudes as 23 S (Antofagasta, Chile), indicating that large populations like Buenos Aires and Santiago de Chile could be easily reached. A similar detector's design was used to remotely measure aerosols and precipitable water content.

Medidor de contaminante en chimenea y ambiente urbano

A mediados de la década del 90 y continuando con la experiencia adquirida en la medición de ozono total por métodos ópticos de absorción diferencial, se encaró un proyecto dedicado a desarrollar técnicas y dispositivos ópticos para le detección de contaminantes gaseosos atmosféricos por emisiones industriales.

Así, se diseñó y construyó un medidor no-dispersivo ultravioleta (NDUV) para la determinación de concentraciones de gases testigo SO_2 y NO_2 en boca de chimenea, donde las concentraciones usuales son del orden de varios cientos de ppm. Como puede verse en la figura de la izquierda, los canales ópticos de medida (300nm y 380 nm) coinciden con valores altos de la sección eficaz de absorcion del SO_2 y del NO_2 respectivamente, mientras que para el canal de referencia (320 nm), estos valores son menores. Cada módulo de medida consiste de una sección de filtros ópticos pasabanda e interferenciales que seleccionan la banda a medir, seguidos de un fotodiodo de alta sensibilidad en el UV, funcionando en el modo corriente con amplificador.

Como puede verse en la figura de la derecha, el dispositivo se acopló a una celda de ensayo tipo chimenea, en la que se inyectaban concentraciones conocidas de los gases a medir a los efectos de calibrar y caracterizar la respuesta del los medidores.



Para el caso de ambiente urbano, las concentraciones a medir son mucho menores, por lo que se requiere mayor sensibilidad. Así, se debe recurrir a mediciones dispersivas (espectroscopía de absorción diferencial o DOAS), en las que se puedan registrar con alta resolución las bandas de absorción del gas a medir.

El método DOAS se basa en la aplicación de la ley de Lambert-Beer, que adopta la expresión de la ecuación (1) para las bandas de absorción rápidamente variables con la longitud de onda.

$$I(\lambda) = I_0'(\lambda) \cdot e^{[-L(\sum_i \sigma_{i\ \text{rápida}}(\lambda)\, c_i)]} \qquad (1)$$

$I_0'(\lambda)$: intensidad en ausencia de absorción diferencial

$\sum_i \sigma_{i\ \text{rápida}}(\lambda)\, c_i$: sumatoria de sección eficaz i-ésima con variación rápida multiplicada por la concentración de la especie i-ésima

Un esquema de la disposición experimental utilizada se muestra en la figura 1. La figura 2 muestra una foto del sistema telescópico de colimación (rojo) y de recepción (negro).

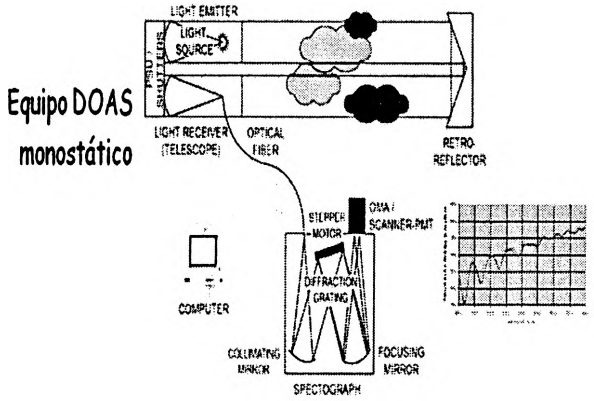


Figura 1

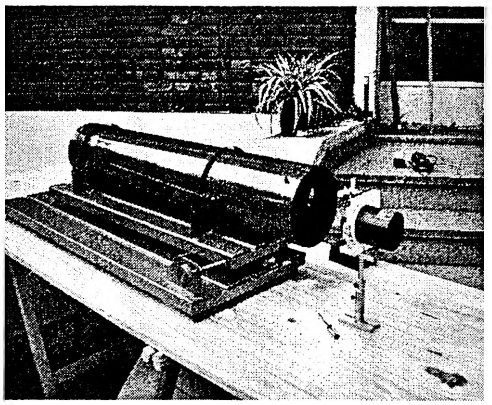
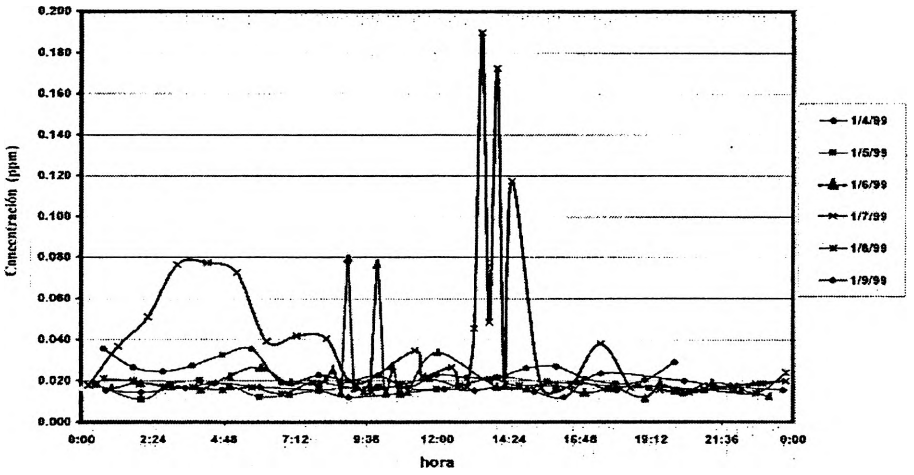


Figura 2



Concentración horaria típica de SO2 durante la campaña 1999 en Destilería Repsol-YPF, Ensenada, partido de La Plata.

Gas pollution detector for chimneys and urban air

During mid 90´s, a project devoted to develop optical and spectroscopic techniques and devices for atmospheric gas pollution from industrial origin started at CIOp. One of the main goals was the design and construction of a non-dispersive ultraviolet optical detector (NDUV) for concentration determination of SO2 and NO2 directly in chimney emissions, where typical values are about hundreds of ppm.

As it can be seen in the left hand-side figure, the optical measurement channels at 300 nm and 380 nm coincide with high absorption cross section values of SO2 and NO2 respectively, while the reference channel at 320 nm is placed at lower values. Each module has narrow passband optical interferential filters for appropriate wavelength selection, followed by a UV sensitive photodiode and an amplifier.

As it can be seen in the right hand-side figure, the portable device was coupled to a chimney-like stainless steel cell, where known concentration of both gases were injected and measured for calibration purposes.

For the case of urban air quality control, pollutant concentrations are typically moch smaller than in the case of chimneys, so dispersive measurements (differential optical absorption spectroscopy, DOAS) have to be used. DOAS method is based on the application of the Lambert-Beer law (equation 1), for absorption bands rapidly varying with wavelength.

$I(\lambda) = I_0'(\lambda) \cdot e^{[-L\sum_i(\sigma_{i\ rápida}(\lambda)\, c_i)]}$ (1)

$I_0'(\lambda)$: *intensity in the absence of differential absorption*

$\sum_i(\sigma_{i\ rápida}(\lambda)\, c_i)$: *sum of rapidly varying i-th species absorption cross section times i-th species concentration*

Figure 1 shows the experimental setup, while figure 2 is a snapshot of the collimation telescope (red)and the collection telescope (black).

Sistema de medición de nivel de llenado de silos de uso agronómico

Entre los años 1999 y 2000 se desarrolló un equipo prototipo para la implementación de un sistema medidor de nivel de llenado de silos agronómicos, principalmente dirigido a ser utilizado en aquellos almacenajes destinados a contener cereales. Este emprendimiento fue encomendado primeramente por la empresa **LOOP S.A.**, siendo finalizado bajo el patrocinio de la empresa **SUPERTEC S.A.**. El grupo de trabajo tuvo como integrantes principales al Doctor Enrique Eduardo. Sicre y al Ing. Eduardo Emilio. Grumel, siendo asistidos en la primera etapa del desarrollo por el Dr. Juan Antonio. Pomarico, la Ingeniera Nélida Araceli. Russo, la Calculista Científica Nelly Lucía. Cap y el Asistente Técnico Guillermo Fischer, siendo partícipe de la segunda etapa el Ing. Enrique. Orellana.

El sistema debía cubrir el rango de 1 a 25 m, con un error no mayor a los 5 cm. en todo el intervalo de medición, siendo indispensable la utilización de técnicas ópticas ya que los sistemas por ultrasonido no resultaban adecuados en las condiciones adversas que se encuentran al momento del llenado de los silos y los sistemas utilizados hasta ese momento dependían en demasía de la componente humana (estaban basados en la lectura de marcas hechas en una cuerda de esparto). Por otra parte, dicho sistema no debía basarse en la medición del tiempo de luz en vuelo, ya que tales equipos resultaban de un costo prohibitivo para las empresas contratantes.

Breve descripción del equipo desarrollado

El sistema optoelectrónico implementado utiliza un láser de diodo semiconductor que irradia en la zona del infrarrojo (específicamente, la longitud de onda es de 765 nm y la potencia irradiada de 35 mW) y un arreglo lineal de fotodiodos acoplados por carga (PCCD) como elemento sensor, estando controlada la toma de datos y la presentación de las medidas por un microcontrolador dedicado.

El método de medición hace uso de técnicas de óptica geométrica por triangulación; para ello, el haz de luz láser impacta sobre el objeto (cereales almacenados) cuya distancia al medidor se desea determinar, formando por tanto un punto irradiante. El sub-sistema óptico incorporado forma imagen de tal punto sobre el sensor, estando la posición del punto imagen directamente relacionada con la distancia incógnita. A fin de poder cubrir el rango de distancias requerido, se crearon dos caminos ópticos perfectamente diferenciados, cada uno de los cuales tiene actuación preponderante en un determinado intervalo de distancias (un camino destinado a medir distancias consideradas cortas y otro para las distancias largas). Hay una zona en la que ambos caminos ópticos actuarán simultáneamente, por lo cual hubo que implementar algoritmos de procesamiento que permitieran discernir la verdadera posición del objeto.

El equipo se entregó a la empresa patrocinante en el mes de Febrero de 2001, quedando a criterio de dicha compañía todo lo que atañe a la faz comercial de este emprendimiento.

Measuring system of filling level of storage containers for agronomics use

*Between years 1999 and 2000 a prototype for the implementation of a measuring system of filling level of storage containers was developed, mainly directed to being used in those storages destined to contain cereals. This development was firstly entrusted by the company **LOOP S.A.**, being finalized under the sponsorship of the company **SUPERTEC S.A.**. Enrique Eduardo. Sicre and Eduardo Emilio. Grumel were the main members of the workgroup, being attended in the first stage of the development by Juan Antonio. Pomarico, Nélida Araceli.*

Russo, Nelly Lucía. Cap and Guillermo Fischer, contributing to the second stage Enrique. Orellana.

The system had to cover the measurement interval between 1 to 25 m, with a non greater error to 5 cm. in all indicated interval. The use of optical techniques was essential since the systems by ultrasound were not suitable in the adverse conditions that are at the time of the filling of the containers and the systems used until that moment depended too much on the human component (they were based on the reading of marks done in a jute cord). On the other hand, this system did not have to be based on the measurement of the time of light in flight, since such equipment was from a prohibitive cost for the contracting companies.

Brief description of the developed equipment

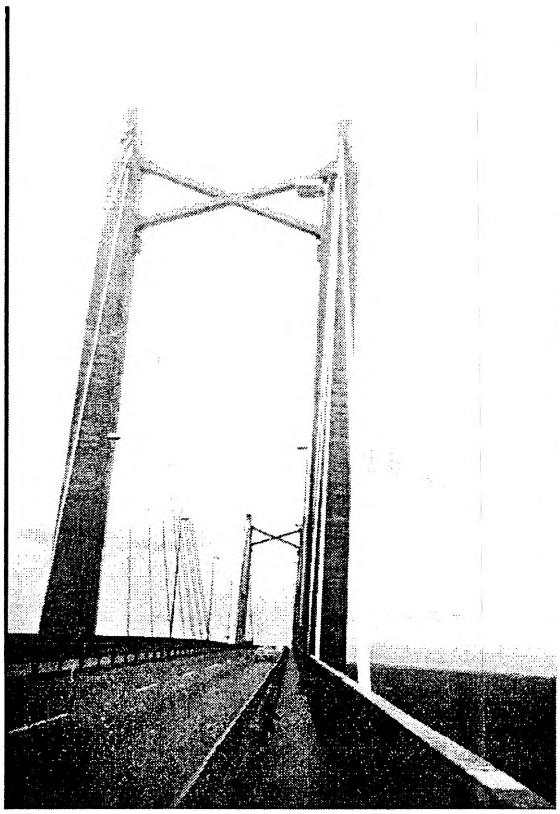
The optoelectronic system uses a semiconductor diode laser that radiates in the infrared zone (specifically, the wavelength is 765 nm and the radiated power is 35 mW) and a Charge Coupled Photodiodes Array (CCPD) like sensorial element, being controlled the data acquisition and the measures display by a dedicated microcontroller.

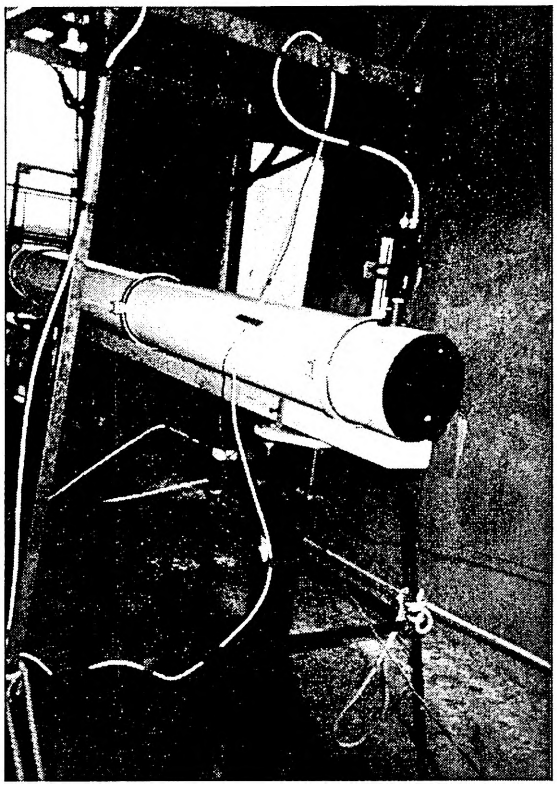
The measurement method makes use of techniques of geometric optics by triangulation; for it, the laser beam hits on the object (stored cereal grains) whose distance to the measuring system is desired to determine, forming therefore a radiant point. The incorporated optical subsystem forms image of such point on the sensor, being the position of the image point directly related to the searched distance. In order to be able to cover the required interval, two perfectly differentiated optical ways were created, each one of which it has preponderant performance in a certain interval of distances (a way destined to measure considered distances short and another one for the long distances). There is a zone in which both optical ways will act simultaneously, thus was necessary to implement processing algorithms that allowed to discern the true position of the object.

The equipment was given to the sponsor company in February of 2001, having left criterion of this company everything what concerns to the commercial face of this development.

Medición de deformaciones en puentes

Se realizaron diversos servicios de alineación y medición de deformación de grandes estructuras entre los que pueden destacarse los siguientes:
Medición de desplazamientos verticales de complejo Vial Ferroviario Zárate-Brazo Largo, bajo la acción del paso de trenes de carga. Trabajo realizado por personal del CIOp, solicitado por Caminos del Río Uruguay S.A. (CRUSA) y Vialidad Nacional. Realizado entre el 11 y el 14 de junio de 1996. La medición fue realizada sobre una plataforma rígida solidaria a una de las columnas donde van fijos los obenques que sostienen al puente. Un sistema de dos diodos láser fueron fijados a la parte inferior en el centro del puente donde se suponía la deflexión sería de mayor valor. Mediante un sistema óptico formado por un telescopio reflector de 2 m de focal y una cámara CCD se registraron y midieron los desplazamientos verticales de la parte central del puente colgante. Se registraron desplazamientos verticales de entre 10 y 20 cm cuando la carga debida al paso del ferrocarril era mayor. Cabe destacar que las mediciones fueron obtenidas con un error no mayor de 0,1 mm siendo mediciones remotas a larga distancia ya que el emisor y el detector estaban separados 170 metros.
Con similares características se realizaron mediciones en:
Puente Internacional Paso de los Libres-Uruguayana, deflexiones verticales debidas a la acción del paso de camiones con carga preestablecida. Trabajo realizado por personal del CIOp, fue solicitado por Vialidad Nacional y se realizó el 29 y 30 de noviembre de 1996.
Puente de la avenida 25 sobre el arroyo "El Gato" en la La Plata. Trabajo solicitado por el Ente Conurbano Bonaerense. Realizado el 5 de enero de 1998





Measurement of deformations in bridges

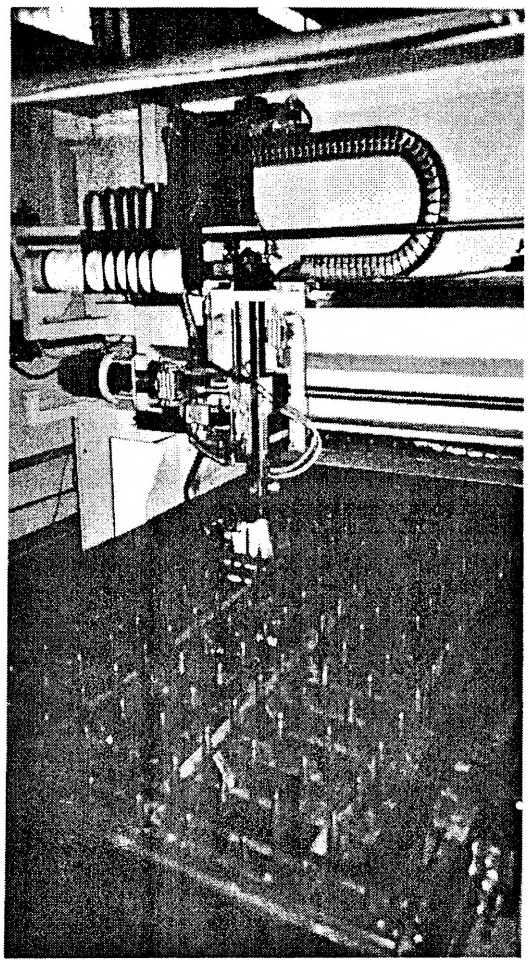
Vertical displacement measurements produced by cargo trains over the Zárate-Brazo Largo railway-road bridge were carried out by CIOp personnel, supported partially by Caminos del Río Uruguay S.A. (CRUSA) and Vialidad Nacional during 11 and 14 of june, 1996. The measurements were conducted over a rigid platform attached to a bridge column. A couple of laser diodes, separated 170m, were attached to the lower part of the center of the bridge, where deformation were expected to be largest. Using a 2m focal length telescope and a CCD camera, 10 to 20 cm vertical displacements were measured when the train passed along. These measurements had an estimated error not larger than 0,1 mm.
Similarly, heavy -truck induced vertical deflections were measured in Puente Internacional Paso de los Libres-Uruguayana, between 29 and 30 november 1996 and also on 25th Ave.bridge,over "El Gato" creek, supported by Ente Conurbano Bonaerense, on January 5, 1998.

Sistema para cortar placas planas mediante laser

El Laboratorio de Procesamiento Láser del CIOp dispone de una máquina MAZAK, SUPER TURBO X48, HI-PRO, que consiste, básicamente, en una fuente láser de potencia, ensamblada con una mesa de Control Numérico, ambas de tipo industrial. Esta combinación permite realizar cortes sobre placas planas de hasta 1220mm x 2440mm con resolución de 1µm en los desplazamientos y con velocidades de corte que llegan a los 2m/min.

El Láser es gaseoso (CO_2, λ= 10,3µm), de flujo axial y excitado por alta tensión. Su máxima potencia lumínica es de 1.500W a régimen continuo y puede funcionar en forma ininterrumpida, salvando las instancias de mantenimiento y reposición de insumos.

Con estas características, pueden cortarse placas planas de: aceros al carbono 1010 al 1090, en espesores de 0,5mm a 4,76mm; aceros inoxidables: 304, 316l, 410, 420 y 430, en espesores de 0,5mm a 5mm; titanio, en espesores de 3mm a 6mm; alpaca, en espesores de 3mm a 6mm; acrílicos, delrin, terciados, maderas y fibrofacil, en espesores de 3mm a 20mm; cuero, fibrocemento; etc.



Este sistema se incorporó al CIOp en el año 1.994. Fue una de las dos primeras máquinas radicadas en nuestro país y la primera en el ámbito local. El objetivo de tal acción puede resumirse en:

- Introducir en la región un servicio de alta tecnología, hasta el momento desconocido por la amplia mayoría de los potenciales usuarios a nivel empresarial.
- Difundir las aplicaciones específicas del corte láser, entendiendo por tal aquellos casos donde el uso de cualquier otra tecnología resulte más costosa o insatisfactoria.
- Promover el uso masivo del servicio, a partir de una política de asistencia técnica completa a los interesados, sin establecer cantidades mínimas de producción y asegurando la atención a todo cliente, sea este grande o pequeño.
- Contribuir a mejorar la calidad de los productos industriales locales y ampliar sus prestaciones en función de las mejoras que ocasiona esta tecnología.
- Capacitar técnicos y profesionales en el uso, mantenimiento y desarrollo de técnicas relacionadas con el servicio.
- Crear una cartera de clientes, que incentive inversiones orientadas a incorporar nuevas y mejores máquinas en la región.
- Desarrollar tareas de investigación, dentro del marco científico de la institución, a partir de la posibilidad que genera contar con una fuente láser de este tipo.

Poco más de diez años de funcionamiento con esta orientación, pueden resumirse en los siguientes puntos:

- Se realizaron servicios de corte láser durante más de 12.000 horas.
- Se atendieron a más de 500 solicitantes del servicio.

- Algunos grandes clientes, compraron sus propias máquinas, dejando de requerir el servicio, cuando sus gastos anuales, relacionados con el corte láser, llegaron al orden del 20% del valor de la máquina.
- El LPL-CIOp es referente nacional en temas relacionados con el corte láser. Actualmente funcionan en el país en el orden de 25 máquinas afines.
- Han visitado el Laboratorio más de 8000 personas entre empresarios, profesionales, docentes, estudiantes, trabajadores en general y vecinos, pudiendo tomar contacto directo con tecnología moderna.
- Los servicios del LPL-CIOp, llegan a lugares tan distantes de su ámbito de prestación, La Plata, como Mar del Plata, Neuquén, Rosario, Mendoza y Bariloche.

Laser Cutting System on Flat Sheets

The CIOP's Laboratory of Laser processing (LPL-CIOp), has a MAZAK machine, SUPER X48 HI-FOR that consists, basically, in a laser power source, assembled with a Numeric Control table, both of industrial type. This combination allows to carry out cuts over flat sheets of up to 1220mm x 2440mm with resolution of 1µm in the displacements and with cut velocities that arrives at the 2m/min.
The Laser is gassy (CO2. = 10,3µm), of axial flow and is excited by high tension. Their maxim ligth power is 1.500W to continuous wave and it can work in uninterrupted form, saving the maintenance instances and reinstatement of inputs.

With these characteristics, it is possible to cut flat sheets of: carbon steels 1010 to 1090, in thickness from 0,5mm to 4,76mm; stainless steels: 304, 316l, 410, 420 and 430, in thickness from 0,5mm to 5mm; titanium, in thickness from 3mm to 6mm; German nickel, in thickness from 3mm to 6mm; acrylic, delrin, wood and fibrofacil, in thickness from 3mm to 20mm; leather; etc.

- *This system was incorporated to the CIOp in 1.994. It was one of the first two machines introduced in our country and the first one in the local environment. The target of this, can be summarized at:*
- *Introduce in the region a high-technology service, until the moment unknown by the wide majority of the potential users at companies level.*
- *Diffuse the specific applications of the cutting laser, pointing to those cases where the use of any other technology is more expensive or less satisfactory.*
- *To promote the massive use of the service, with a starting politics of complete technical support to the interested parties, without establishing minimum quantities of production requirements and assuring the attention to all client, be this big or small.*
- *Contribute to improve the quality of the local industrial products and to enlarge their benefits, in function of the improvements generated by this technology.*
- *qualify technicians and professionals in the use, maintenance and development of techniques in relation with the service.*
- *Create a group of clients that motivates oriented investments to incorporate new and better machines in the region.*
- *Develop investigation tasks, inside the scientific institution objectives, starting from the possibility that generates to have a laser source of this type.*
- *Little more than ten years of operation with this orientation, they can be summarized in this points:*
- *Were made lasers cut services, during more than 12.000 hours.*
- *Were assisted more than 500 applicants of the service.*
- *Some big clients, bought their own machines, stopping their requirement of service, when their annual expenses, related with the laser cut, arrived near of 20% of the machine value.*
- *The LPL-CIOp is a national reference in topics related with laser cut. At the moment, are working in the country near of 25 similar machines.*
- *Have visited the Laboratory more than 8000 people among managers, professionals, educational, students, workers in general and neighbors, being able to take direct contact with modern technology.*
- *The LPL-CIOp services, arrive to places so distant of his benefit environment, La Plata, as Mar del Plata, Neuquén, Rosario, Mendoza and Bariloche.*

Proyectos Tecnológicos en Metrología Optoelectrónica

Se desarrollaron diversos métodos ópticos e híbridos opto-electrónicos para la medición en continuo y a tiempo real (en intervalos de 10-50 milisegundos) de diferentes parámetros físicos y/o geométricos, asociados con objetos tridimensionales. Las características comunes a todos ellos son: alta precisión, elevada velocidad de procesamiento de los datos, y su naturaleza no contactante. Algunas aplicaciones implementadas fueron: determinación de la rugosidad de superficies difusoras en diferentes rangos de rugosidad (empleando técnicas de speckle, scattering o interferométricas); determinación del estado vibratorio (amplitud y frecuencia) de una superficie; medición de índices de refracción de líquidos; velocimetría óptica mediante correlación de diagramas de speckle; medición de parámetros geométricos (diámetro, ancho, etc.) de objetos 3D. En algunos casos, los estudios realizados se complementaron con ensayos desarrollados en el ámbito industrial, o incluso dieron lugar a la construcción de equipos de medición instalados en compañías tales como SIDERCA S.A.I.C., Propulsora Siderúrgica S.A., SOMISA (San Nicolás, Pcia. de Bs. As.), Molinos Río de La Plata, etc.

Technological projects with opto-electronical metrology

Several optical and hybrid opto-electronic methods for continuous and real-time (at 10-50 ms intervals) measurement of different physical and/or geometric parameters associated with 3D objects, were developed. Their common characteristics are: high precision, high speed data processing, and non-contact nature. The optical arrangements employed can be easily adapted for industrial applications, so that the influence of factors such as misalignments or vibrations on the system performance was minimized. Some implemented applications were: roughness determination of diffusing surfaces (by using speckle, scattering or interferometric techniques) (r.m.s. surface roughness measuring range: 1-30 microns); determination of the vibratory state (amplitude and frequency) of a surface; measurement of the refractive index of liquids; optical velocimetry by means of speckle patterns correlation (in the range 0-40 m/s); measurement of geometrical parameters (diameter, wide, etc.) of 3D-objects. These studies were complemented with tests developed in the industrial environment, and in some cases they gave rise to the construction of measurement equipments installed in companies such as SIDERCA S.A.I.C. (Campana, Pcia. de Bs. As.), Propulsora Siderúrgica S.A. (Ensenada, Pcia. de Bs. As.), SOMISA (San Nicolás, Pcia. de Bs. As.), Molinos Río de La Plata, etc.

Publicaciones
Publications

Publicaciones / Publications

1. L. Zerbino, H. Rabal, M. Gallardo, M. Garavaglia, "Alineación empleando un sistema óptico de enfoque y un láser," Ingeniería e industria 492, 73-81 (1977).

2. L. Zerbino, H. Rabal, J.O. Tocho, H. Ranea Sandoval, M. Gallardo, M. Garavaglia, "El láser y sus aplicaciones en la industria naval," Anales del Laboratorio de Ensayos de Materiales e Investigaciones Tecnológicas, Serie II 378, 43-52 (1978).

3. M. Gallardo, A. Tagliaferri, J. Calatroni, C. Massone, M. Garavaglia, "Espectrómetro de doble paso, simple y económico, para analizar radiación láser," Anales del Laboratorio de Ensayos de Materiales e Investigaciones Tecnológicas, Serie II 379, 53-61 (1978).

4. M. Gallardo, C. Massone, A. Tagliaferri, M. Garavaglia, W. Persson, "$5s^2\ 5p^3\ (^4S)$ nl levels of Xe III," Physica Scripta 19, 538-544 (1979).

5. H. Rabal, M. Garavaglia, "Analisis de figuras moiré empleando grillas interferométricas con perfiles de airy," Revista Brasileira de Física 9, 5-18 (1979).

6. H. Ranea Sandoval, J.O. Tocho, M. Gallardo, M. Garavaglia, "Spectroscopic analysis of the transverse excited $C^3\Pi_u$-$B^3\Pi_g$(0-0) UV laser band of N_2 at room temperature: comments," Applied Optics 18, 1705- (1979).

7. L. Zerbino, H. Rabal, H. Ranea Sandoval, J.O. Tocho, M. Gallardo, M. Garavaglia, "Alineación empleando un sistema óptico de enfoque y un láser: aplicaciones en la industria naval," Ingeniería Naval (España) 524, 48- (1979).

8. M. Gallardo, R. Duchowicz, J.O. Tocho, H. Ranea Sandoval, M. Garavaglia, "A Xenon ion pumped open dye stream laser," IEEE Journal of Quantum Electronics QE-15, 541-542 (1979).

9. P. Burlamacchi, H. Ranea Sandoval, "Characteristics of a multicolor dye laser," Optics Communications 31, 185-188 (1979).

10. G. Bilmes, "Las medidas de tiempo: el proceso de medición y la enseñanza de los sistemas de unidades," Revista de Educación La Obra 4, (1979).

11. G. Bilmes, "Error de medición = equivocación? El concepto de medición y la enseñanza de los sistemas de unidades," Revista de Educación La Obra 5, (1979).

12. R. Arizaga, M.L.F. de Mattiello, "Influenece of retinal locus on the discrimination of colorimetric purity," Color Vision Deficiencies V, 207-210 (1980).

13. E. Sicre, N. Bolognini, H. Rabal, M. Garavaglia, "In plane motion measurements with Fourier lensless holography," Applied Optics 19, 1570-1572 (1980).

14. H. Rabal, N. Bolognini, E. Sicre, M. Garavaglia, "Optical image subtraction through speckle modulated by Young fringes," Optics Communications 34, 7-10 (1980).

15. N. Bolognini, H. Rabal, E. Sicre, M. Garavaglia, "Vibration analysis with Young's fringes modulated speckle," Optics Communication 34, 337-339 (1980).

16. E. Sicre, N. Bolognini, H. Rabal, M. Garavaglia, "Color storage and image processing through Young's fringes modulated speckle," Applied Optics 19, 3262-3263 (1980).

17. L. Scaffardi, D. Schinca, J.G. Reyna Almandos, M. Gallardo, M. Garavaglia, "Laser spectroscopy analysis of N_2 pulsed discharges at low temperatures," Applied Optics 19, 3590-3592 (1980).

18. J.O. Tocho, W. Sibbett, D. Bradley, "Picosecond phase-conjugate reflection from organic dye saturable absorbers," Optics Communication 34, 122-125 (1980).

19. N. Carri, H. Campaña, A. Suburo, R. Duchowicz, M. Gallardo, M. Garavaglia, "Distribution of nerve fibers in the optic nerve of the quail: a laser-degeneration study," European Journal of Cell Biology 22, 1- (1980).

20. R. Arizaga, A. Biondini, "Sistemas de procesamiento de valores triestímulos para el cálculo de coordenadas cromáticas CIE, longitudes de onda y pureza," Luminotecnia 14, 14-18 (1980).

21. M. Abbattista, L. Abbattista, N. Rodriguez, R. Torroba, L. Zerbino, M. Gallardo, M. Garavaglia, "Application of vertical brackets in orthodontial treatments: a laser apeckle study," Lasers and Applications. Springer Series in Optical Physics 26, 279-285 (1981).

22. E. Gallego Lluesma, C. Santos, D. Aspnes, "Optical constants of the oxidation of Nb-Ti alloys," Internal Report, Bell Telephon Laboratories, Murray Hill, Estados Unidos, ? (1981).

23. H. Ranea Sandoval, J.O. Tocho, M. Gallardo, M. Garavaglia, "On the observation of the Lambda-doubling in the O-O UV N/sub 2/ laser band," IEEE Journal of Quantum Electronics QE-17, 295-296 (1981).

24. J.O. Tocho, R. Duchowicz, M. Gallardo, M. Garavaglia, "Frequency locking in double-pumped dye laser," IEEE Journal of Quantum Electronics QE-17, 1591-1592 (1981).

25. N. Bolognini, H. Rabal, E. Sicre, M. Garavaglia, "Rigid body motion measurements with Fourier lensless holography," Applied Optics 20, 2342-2344 (1981).

26. J.O. Tocho, W. Sibbett, D. Bradley, "Thermal effects in phase-conjugation in saturable absorbers with picosecond pulses," Optics Communication 37, 67-71 (1981).

27. E. Sicre, N. Bolognini, M. Garavaglia, "Estudio fotoelástico tridimensional de un prisma rectangular parcialmente cargado utilizando radiación laser," Carta Metrológica 53, 53-58 (1981).

28. H. Rabal, E. Sicre, N. Bolognini, M. Garavaglia, "A speckle method of gray level pseudocoloring," Optics Communications 39, 225-227 (1981).

29. M. Gallardo, J.G. Reyna Almandos, "Xenon lines in the range from 2000 Å to 7000 Å," Centro de Investigaciones Opticas. Monografía científica 1, (1981).

30. P. Mazzinghi, P. Burlamacchi, M. Matera, H. Ranea Sandoval, R. Salimbeni, Vanni, "A 200 w average power, narrow bandwidth, tunable waveguide dye laser," IEEE Journal of Quantum Electronics QE-17, 2245-2249 (1981).

31. E. Sicre, N. Bolognini, H. Rabal, M. Garavaglia, "Color storage and image processing through Young's fringes modulated speckle," Optics in Four Dimensions, 478-482 (1981).

32. L. Zerbino, H. Rabal, H. Ranea Sandoval, J.O. Tocho, A. Laquidara, M. Gallardo, M. Garavaglia, "Aplicaciones del láser a la macrometrología," Carta Metrológica 3, 9- (1982).

33. M. Garavaglia, "Sobre la propuesta de una nueva definición del metro," Carta Metrológica 5, 7-20 (1982).

34. J.G. Reyna Almandos, M. Gallardo, M. Garavaglia, "New spectroscopic results in Xe II, Xe III and Xe IV," Optica Pura y Aplicada 15, 1-18 (1982).

35. R. Buffa, P. Burlamacchi, M. Matera, H. Ranea Sandoval, R. Salimbeni, "High repetition rate efects in XeCI tea lasers," Optics Communications 40, 288-293 (1982).

36. N. Bolognini, E. Sicre, R. Arizaga, H. Rabal, M. Garavaglia, "Pseudocoloring method using two different spatial modulations," Applied Optics 21, 2099-2100 (1982).

37. E. Campitelli, "Aplicación de microcomputadoras an la evaluación de sistemas ópticos," Centro de Investigaciones Opticas. Monografía Científica 2, (1982).

38. N. Carri, H. Campaña, A. Suburo, R. Duchowicz, M. Gallardo, M. Garavaglia, "Two distributions of axons in the optic nerve of quails: a study of nerve degeneration after laser lesions of the retina," Brain Research 246, 302-304 (1982).

39. R. Arizaga, N. Bolognini, H. Rabal, E. Sicre, M. Garavaglia, "Real time white light pseudocolor density encoder," Optics Communications 43, 12-17 (1982).

40. H. Rabal, E. Sicre, N. Bolognini, M. Garavaglia, "Pseudocoloring method for 3-D contouring," Journal of Optics 13, 257-262 (1982).

41. R. Arizaga, N. Bolognini, E. Sicre, Rabal, Garavaglia, "Pseudocoloreado de transparencias blanco y negro por métodos ópticos," Informaciones Científicas XVII, 224 (1982).

42. J. Hansen, F. Meijer, M. Outred, W. Persson, H.O. Di Rocco, "Identification of the $4d^{10}\ 5p^6\ {}^1S_0$ level in Xe III using optical spectroscopy," Physica Scripta, (1983)

43. S. Chavasse, L. Martorelli, "Sobre el diseño de telescopios de dos espejos," Observatorio Astronómico de la Universidad Nacional de La Plata. Serie especial 26, (1983).

44. H. Rabal, E. Sicre, N. Bolognini, R. Arizaga, M. Garavaglia, "Stereograms through a speckle carrier," Applied Optics 22, 881-885 (1983).

45. D. Schinca, L. Scaffardi, M. Gallardo, "Espectroscopia láser en nitrógeno molecular," Optica Pura y Aplicada 16, 27-45 (1983).

46. J. Ojeda-Castañeda, E. Sicre, "Tunable bandstop filter for binary objects: a self-imaging technique," Optics Communications 47, 183-186 (1983).

47. E. Campitelli, "Cálculos ópticos con la TI-59," Revista Argentina de Óptica 68, 22- (1983).

48. M. Garavaglia, "Actualidad e importancia de la metrología: hacia una nueva definición del metro," El QUID de la Ciencia, la Tecnología y la Educación Argentina 2, 539-554 (1984).

49. M. Trivi, N. Bolognini, E. Sicre, H. Rabal, M. Garavaglia, "Color storage and gray level pseudocoloring using a speckle carrier," Applied Optics 23, 341-343 (1984).

50. Alvarez, J.G. Reyna Almandos, J. Meda, "Desarrollo de fósforos luminescentes a los rayos X," Anales del CIDEPINT 1, 63- (1984).

51. Lohmann, J. Ojeda-Castañeda, E. Sicre, "Multiple interaction bandstop filters based on the Talbot effect," Optics Communications 49, 388-392 (1984).

52. L. Zerbino, R. Torroba, N. Rodriguez, M. Garavaglia, "Interference profiles with multiple spherical waves: general case," Journal of the Optical Society of America A 1, 495-501 (1984).

53. J.O. Tocho, H. Ranea Sandoval, R. Duchowicz, M. Garavaglia, "The time-resolved spectrum of a pulsed dye laser," Optical and Quantum Electronics 16, 393-398 (1984).

54. H. Bartelt, A. Lohmann, E. Sicre, "Optical logical processing in parallel with theta modulation," Journal of the Optical Society of America A 1, 944-951 (1984).

55. J. Ojeda-Castañeda, E. Sicre, "Bilinear optical syspems Wigner distribution function and ambiguity function representations," Optica Acta 31, 255-260 (1984).

56. H. Bartelt, J. Ojeda-Castañeda, E. Sicre, "Misfocus tolerance seen by simple inspection of the ambiguity function," Applied Optics 23, 2693-2696 (1984).

57. J. Gomis, C. Cocoz, J. Herbst, E. Gallego Lluesma, "Proyecto de una red integral de comuncaciones para la zona deprimida del Río Salado," United Nations Projects for Development PUND 84/007, ? (1984).

58. R. Duchowicz, M. Garbocci, H. Ranea Sandoval, J.O. Tocho, M. Gallardo, "Macrometrología láser: determinación de movimientos y alineación de turbocompresores en el Complejo General Cerri de Gas del Estado," Boletín Informativo de la Comisión de Investigaciones Científicas de la Provincia de Buenos Aires Septiembre, 6-8 (1984).

59. L. Scaffardi, D. Schinca, J.O. Tocho, H. Ranea Sandoval, M. Gallardo, "Cascade population mechanism in nitrogen lasers," Applied Optics 24, 22-25 (1985).

60. Laquidara, R. Gallardo, M. Garbocci, "Monitor de microdesplazamientos en dos dimensiones," Revista Telegrágica-electrónica 861, 309-310 (1985).

61. E. Sicre, N. Bolognini, M. Garavaglia, "Partial achromatization of the self-imaging phenomenon," Applied Optics 24, 929-930 (1985).

62. N. Rodriguez, R. Torroba, M. Trivi, H. Rabal, M. Garavaglia, "Color image optical operations by a modulated speckle carrier," Optics Communications 54, 262-264 (1985).

63. M. Gallardo, "Espectroscopía espontánea y láser en el CIOp," Boletín del Observatorio Astronómico de La Plata, ? (1985).

64. J. Ojeda-Castañeda, E. Sicre, "Quasi ray optical approach to longitudinal periodicities of free and bounded wavefields," Optica Acta 32, 17 (1985).

65. N. Bolognini, J. Ojeda-Castañeda, E. Sicre, "Interferometry based on the Lau effect: a quasi-ray description," Optica Acta 32, 409 (1985).

66. H. Bartelt, E. Sicre, "Simultaneous height and slope measurement of three-dimensional surfaces," Optics Communications 52, 380- (1985).

67. G. Bilmes, H. Ranea Sandoval, J.O. Tocho, M. Gallardo, "XeCl behaviour in pulsed axial discharges," Optics Communications 54, 91-94 (1985).

68. H. Rabal, N. Bolognini, E. Sicre, "Diffraction by a tilted aperture: coherent and partially coherent cases," Optica Acta 32, 1309 (1985).

69. M. Michalski, E. Sicre, H. Rabal, "Display of the complex degree of coherence due to quasi-monochromatic spatially incoherent sources," Optics Letters 10, 585- (1985).

70. D. Schinca, L. Scaffardi, J.O. Tocho, M. Gallardo, "Visible carbon monoxide pulsed laser," Optica Pura y Aplicada 18, 211-216 (1985).

71. G. Bilmes, H. Ranea Sandoval, J.O. Tocho, "Láseres de colorantes excitados por un láser de nitrógeno: estudios de anchos de línea y técnicas de sintonía," Centro de Investigaciones Opticas. Monografía Científica 3, (1985).

72. L. Zerbino, J. Goedgebuer, "2-D wavelength multiplex correlator," Optics Communications 55, 248- (1985).

73. M. Trivi, N. Bolognini, E. Sicre, H. Rabal, M. Garavaglia, "Speckle stereograms," Applied Physics Series 150, 251- (1985).

74. J.G. Reyna Almandos, F. Bredice, H.O. Di Rocco, M. Gallardo, "Ionic assignment of Xe IV lines," Optica Pura y Aplicada 18, 87-97 (1985).

75. N. Rodriguez, R. Torroba, M. Trivi, H. Rabal, M. Garavaglia, "Color image optical operations by modulated speckle carrier," Optics Communications 54, 262- (1985).

76. G. Bertuccelli, J.G. Reyna Almandos, H.O. Di Rocco, M. Gallardo, "Classified lines in the spectrum of Xe II," Optica Pura y Aplicada 16, 163-169 (1986).

77. H. Rabal, W. Furlan, E. Sicre, "Talbot interferometry with anisotropic gratings," Optics Communications 57, 81- (1986).

78. Colautti, E. Sicre, M. Garavaglia, "Incoherent optical spatial filtering based on the Lau effect," Optics Communications 57, 16-20 (1986).

79. H.O. Di Rocco, J.G. Reyna Almandos, M. Gallardo, W. Persson, "Spectrum of Trebly ionized xenon (Xe IV)," Physical Review A; General Physics 33, 2114-16 (1986).

80. G. Bilmes, H. Ranea Sandoval, J.O. Tocho, "Non-conventional spectroscopic source in rare gas-halide exciplexes studies," Optica Pura y Aplicada 19, 13- (1986).

81. H. Rabal, M. Trivi, E. Sicre, M. Garavaglia, "Stereo enhacement in holographic imaging," Applied Optics 25, 1259-1260 (1986).

82. M. Trivi, E. Sicre, H. Rabal, M. Garavaglia, "Multiple orientated speckle patterns: a study of the contrast," Applied Optics 25, 1260-1261 (1986).

83. H. Ranea Sandoval, M. Gallardo, "Measuring flatness of large tables: New methods," Applied Optics 25, 1370-1371 (1986).

84. M. Garbocci, R. Gallardo, A. Laquidara, R. Fernández, "Control numérico computado de un traslador X-Y en aplicaciones de láseres de potencia," Revista Telegráfica-electrónica 874, 764- (1986).

85. H. Rabal, "Interference fringes produced by anisotropic speckle patterns," Optics Communications 58, 69-72 (1986).

86. A.G. Trigueiros, S. Pettersson, J.G. Reyna Almandos, "Transitions within the n = 4 complex of Kr VII obtained from a theta-pinch light source," Physica Scripta 34, 164-166 (1986).

87. H.O. Di Rocco, M. Gallardo, "Isonuclear sequences in atomic spectroscopy," Optica Pura y Aplicada 19, 39- (1986).

88. H. Ranea Sandoval, M. von Reichenbach, R. Rodriguez, F. Schaposnik, "Phase-locking of lásers with injected signal fluctuations," Optics Communications 59, 39- (1986).

89. J. Ojeda-Castañeda, E. Sicre, "Theta-modulation decoder based on the Lau effect," Optics Communications 59, 87- (1986).

90. N. Rodriguez, R. Torroba, M. Gallardo, M. Garavaglia, "Holographic non-destructive testing by optically generated zone plate," Applied Optics 25, 1908-1911 (1986).

91. M. Roblin, H. Rabal, L. Bernstein, R. Grousson, J. Jonathan, "Determination des excentrements des elements d'un systeme optique para interferometrie speckle," Journal of Optics 17, 233- (1986).

92. H.O. Di Rocco, G. Bertuccelli, J.G. Reyna Almandos, M. Gallardo, "Line shift of singly ionized xenon in high current pinched discharges," Journal of Quantitative Spectroscopy and Radiative Transfer 35, 443-6 (1986).

93. M. Trivi, H. Rabal, N. Bolognini, E. Sicre, M. Garavaglia, "Three-dimensional display through speckle stereograms," Applied Optics 25, 3776-3780 (1986).

94. M. Michalski, H. Rabal, M. Garavaglia, "Operations using fringe projection," Applied Optics 25, 4338-4342 (1986).

95. R. Torroba, H. Rabal, M. Garavaglia, "One step rainbow holography using a spherical mirror," Applied Optics 25, 3288-3290 (1986).

96. A.G. Trigueiros, J.G. Reyna Almandos, "Estudo do espectro do criptonio (Kr III - Kr VII) no vacuo (430-2000 Å) usando um theta pinch como fonte de luz," Revista Brasileira de Aplicaçoes de Vacuo 6, 203-208 (1986).

97. Schinca, L. Scaffardi, J.O. Tocho, "Population mechanism in visible carbon monoxide pulsed laser," Applied Optics 25, 102-106 (1986).

98. Schinca, H. Ranea Sandoval, L. Scaffardi, J.O. Tocho, "Lifetime improvement of visible multiline CO laser," IEEE Journal of Quantum Electronics QE-22, 2272-2274 (1986).

99. C. Colautti, B. Ruiz, E. Sicre, M. Garavaglia, "Walsh functions: analysis of their properties under Fresnel diffraction," Journal of Modern Optics 34, 1385-1391 (1987).

100. S. Grosz, W. Furlan, E. Sicre, M. Garavaglia, "Display of the local spectrum: a pseudocoloring approach," Applied Optics 26, 971-972 (1987).

101. C. Colautti, L. Zerbino, E. Sicre, M. Garavaglia, "Lau effect using circular gratings," Applied Optics 26, 2060-2062 (1987).

102. M. Trivi, E. Sicre, H. Rabal, M. Garavaglia, "Three dimensional display through a speckle pattern recording: information content and storage requirements," Applied Optics 26, 2703- (1987).

103. R. Torroba, M. Garavaglia, "On-axis light distribution in converging spherical waves: general case," Applied Optics 26, 2860-2863 (1987).

104. R. Torroba, M. Garavaglia, "Optically generated zone plates as quasi-Fourier holograms," Optica Pura y Aplicada 20, 83-86 (1987).

105. G. Bilmes, J.O. Tocho, S. Braslavsky, "Laser induced optoacoustic studies of the photoisomerization of the laser dye 3,3' - diethyloxadicarbocyanine iodide (DODCI)," Chemical Physics Letters 134, 335-340 (1987).

106. M. Villagrán Muñíz, M. Gallardo, J.O. Tocho, J. Rocca, "The electron temperature in the plasma of a spark-recombination laser," Journal of Applied Physics 61, 4447-4451 (1987).

107. R. Torroba, R. Arizaga, "White light interferometer for real time phase pseudocoloring," Optics Communications 64, 221- (1987).

108. M. Michalski, H. Rabal, E. Sicre, "Complex degree of coherence due to tilted planar source: a study based on the spectral content of a speckle pattern," Journal of Modern Optics 34, 469-478 (1987).

109. L. Scaffardi, G. Bilmes, D. Schinca, J.O. Tocho, "Back isomerization from the excited state photoisomer of the laser dye 3,3' diethyloxadicarbocyanine iodide (DODCI)," Chemical Physics Letters 140, 163-168 (1987).

110. M. Garavaglia, M. Gallardo, H. Rabal, L. Zerbino, J.O. Tocho, E. Sicre, "Algunas aplicaciones de la óptica y del láser en el control del laminado," Siderurgia 13, 14-17 (1987).

111. M. Michalski, H. Rabal, E. Sicre, "Three dimensional information of a spatially incoherent source from the spectral content of a speckle pattern," Optics Communications 61, 309- (1987).

112. W. Demtröder, R. Duchowicz, J. Gress, H. Foth, R. Kullmer, G. Persch, M. Schwarz, "Laser spectroscopy of molecules and clusters," Physica Scripta T23, 176-183 (1988).

113. G. Bilmes, J.O. Tocho, S. Braslavsky, "Spectroscopic parameters of the DODCI photoisomer from laser-induced optoacoustic spectroscopy," Springer Series in Optical Sciences. Photoacoustic and Photothermal Phenomena 58, 48-49 (1988).

114. G. Bilmes, J.O. Tocho, S. Braslavsky, "Spectrum, energy content, and relaxation mechanism of the photoisomer of the laser dye 3,3' - diethyloxadicarbocyanine iodine: laser induced optoacoustic studies," Journal of Physical Chemistry 92, 5958-5962 (1988).

115. R. Torroba, R. Arizaga, "Lau effect by using speckle patterns," Optik 79, 90- (1988).

116. R. Torroba, R. Arizaga, "Real time pseudocolor encoding of depth using white light processing," Journal of Modern Optics 35, 629- (1988).

117. R. Arizaga, R. Torroba, M. Garavaglia, "Real time pseudocolor phase display by using a grating speckle interferometer," Optics Communications 65, 107-109 (1988).

118. Bredice, J.G. Reyna Almandos, M. Gallardo, H.O. Di Rocco, A.G. Trigueiros, "Revised and extended analysis of the low configurations in Kr III," Journal of the Optical Society of America B 5, 222-235 (1988).

119. W. Persson, C. Wahlstrom, G. Bertuccelli, H.O. Di Rocco, J.G. Reyna Almandos, M. Gallardo, "Spectrum of doubly ionized xenon (Xe III)," Physica Scripta 38, 347-369 (1988).

120. Bredice, M. Raineri, J.G. Reyna Almandos, M. Gallardo, "Classifield lines in the spectrum of Kr II," Spectroscopy Letters 21, 11-17 (1988).

121. Laquidara, M. Gallardo, H.O. Di Rocco, G. Bertuccelli, D. Bertuccelli, "Design of a system for the pulsed Zeeman effect with a nonconventional spectral source," Applied Optics 27, 2371-2373 (1988).

122. Rabal, W. Furlan, M. Garavaglia, "Astigmatic holographic processor for local pattern recognition," Optics Communications 65, 343-346 (1988).

123. S. Grosz, E. Sicre, "Ambiguitty function and OTF theory: an optical coherent approach," Optik 78, 78- (1988).

124. W. Furlan, E. Sicre, M. Garavaglia, "Quasi-geometrical paraxial approach to Franhofer by thick planar objects using phase-space signal representations," Journal of Modern Optics 35, 735-741 (1988).

125. M. Trivi, H. Rabal, "Stereoscopic uses of diffraction gratings," Applied Optics 27, 1007- (1988).

126. M. Trivi, E. Sicre, H. Rabal, M. Garavaglia, "Optical dynamical processing: an approach using birefringent pupils," Optics Letters 13, 259-261 (1988).

127. A.G. Trigueiros, C. Pagan, J.G. Reyna Almandos, "Energy levels of the configurations $4s^24p$, $4s4p^2$, $4s^2$ 4d, and $4s^25p$ in Kr VI, obtained from a theta-pinch light source," Physical Review A 38, 166 (1988).

128. H.O. Di Rocco, G. Bertuccelli, J.G. Reyna Almandos, F. Bredice, M. Gallardo, "Line shifts of Kr II, Kr III, and Xe III in high-current, pinched discharges," Journal of Quantitative Spectroscopy and Radiative Transfer 40, 513-517 (1988).

129. M. Schwarz, R. Duchowicz, W. Demtröder, Ch. Jungen, "Autoionizing rydberg states of Li^2: analysis of electronic-rotational interactions," The Journal of Chemical Physics 89, 5460-5472 (1988).

130. Molesini, G. Puccioni, F. Quercioli, M. Trivi, "La misura meccanica dei raggi di curvatura," Fisica e Tecnologia (Italia) 11, 235- (1988).

131. M. Trivi, N. Bolognini, "Three dimensional display through a speckle pattern: a single exposure method," Applied Optics 27, 2370- (1988).

132. C. Colautti, E. Sicre, M. Garavaglia, "Analysis of the Lau effect using Walsh functions," Optics Letters 13, 1069-1071 (1988).

133. Salinas, E. Colombo, H. Rabal, R. Torroba, "Diffraction by cylindrical pupils," Optik 82, 22-24 (1988).

134. B. Ruiz, "The fractional Fourier transform and the p-index transform," Report on the FFT Tel Aviv University, (1988).

135. R. Torroba, "On the propagation of light from periodic incoherent sources," Optics Communications 67, 95- (1988).

136. R. Torroba, "Zone plates periodicities and Talbot effect," Optik 84, 64- (1988).

137. R. Torroba, "Self-Fourier transforming phenomenon," Optik 80, 113- (1988).

138. H. Rabal, L. Zerbino, J. Ojeda-Castañeda, "Continuous order derivative for optical signals and images," Microwave and Optical Technology Letters 1, 64-67 (1988).

139. G. Molesini, F. Quercioli, M. Trivi, "L'interferometria olografica applicata al restauro," Kermes (Italia) 5, 3- (1989).

140. F. Quercioli, M. Trivi, G. Molesini, M. Melozzi, "An optical probe based on spherical aberration for surfahce figure testing," Optics Communications 71, 11- (1989).

141. E. Gallego Lluesma, "Optoelectronic materials," Optics Communications 71, 11- (1989).

142. H. Rabal, M. Trivi, M. Michalski, M. Garavaglia, "Optical substitution transform," Journal of Modern Optics 36, 597-606 (1989).

143. S. Grosz, W. Furlan, C. Colautti, M. Garavaglia, "Display of phase-space functions by elliptical zone plates," Optics Communications 73, 7-11 (1989).

144. A.G. Trigueiros, M. Machida, C. Pagan, J.G. Reyna Almandos, "The spectroscopic study of radiation produced in a theta-pinch," Nuclear Instruments and Methods in Physics Research A 280, 589-592 (1989).

145. A.G. Trigueiros, S. Pettersson, J.G. Reyna Almandos, M. Gallardo, "A study of the configurations 4s, 4s4d,4p,4s5s and 4s5p in six times ionized krypton, Kr VII," Physics Letters A 141, 135-137 (1989).

146. J.G. Reyna Almandos, "Homogeneización curricular para las carreras de ingeniería en el ámbito nacional y latinoamericano," Physics Letters A 141, 135- (1989).

147. E. Colombo, H. Rabal, C. Kirschbaum, M. Jaen, "Sensibilidad del sistema visual humano al desenfoque," Anales de la Asociación Física Argentina 1, 129-132 (1989).

148. E. Colombo, H. Rabal, "Nitidez y desenfoque: Ajuste de un modelo," Anales de la Asociación Física Argentina 1, 133-136 (1989).

149. Bolognini, R. Duchowicz, L. Scaffardi, M. Trivi, "Estereogramas de objetos en movimiento mediante speckle modulado," Anales de la Asociación Física Argentina 1, 124-126 (1989).

150. G. Bilmes, S. Braslavsky, "Espectroscopía Raman mediante fotoacústica con láseres pulsados," Anales de la Asociación Física Argentina 1, 311- (1989).

151. S. Grosz, L. Zerbino, N. Bolognini, "Pseudocoloreado de niveles de gris en tiempo real," Anales de la Asociación Física Argentina 1, 127- (1989).

152. D. Schinca, H. Mancini, J.O. Tocho, "Medición de densidades de cadmio atómico e iónico y temperatura electrónica en un láser de recombinación de He-vapor de cadmio," Anales de la Asociación Física Argentina 1, 149- (1989).

153. J.O. Tocho, G. Lifante, F. Cussó, "Estudio fotoacústico de la luminiscencia de centros de color," Anales de la Asociación Física Argentina 1, 315- (1989).

154. A.G. Trigueiros, C. Pagan, S. Pettersson, J.G. Reyna Almandos, "Transitions and energy levels in the n=4 complex of Kr V," Physical Review A 40, 3911- (1989).

155. M. Gallardo, F. Bredice, M. Raineri, J.G. Reyna Almandos, "A light source for obtaining spectral of highly ionized gases," Applied Optics 28, 4513-4515 (1989).

156. Salinas, E. Colombo, H. Rabal, R. Torroba, "Difraction by cylindrical pupils," Applied Optics 28, 4513- (1989).

157. H. Rabal, "Early speckle experiments and the display of coherence," Optik 81, 127-128 (1989).

158. M. Gallardo, F. Bredice, M. Raineri, J.G. Reyna Almandos, S. Pettersson, A.G. Trigueiros, "New spectroscopic results in Kr VIII," Applied Optics 28, 5088-5090 (1989).

159. U. Diemer, R. Duchowicz, M. Ertel, E. Mehdizadeh, W. Demtröder, "Doppler-free polarization spectroscopy of the B PI_u-state of Cs_2," Chemical Physics Letters 164, 419-426 (1989).

160. H. Rabal, "El comportamiento holográfico," Revista Ciencia e Investigación Marzo, 153-160 (1989).

161. M. Gallardo, "Alineación, posicionamiento, control y medidas," Láser y Óptica en Ingeniería. Centro de Investigaciones Opticas, 281-309 (1989).

162. Chilla, P. Pernas, O. Martínez, J.O. Tocho, "Parameters that determine the wavelength of a passive mode-locked dye laser," Optics Communications 72, 313-318 (1989).

163. C. Colautti, S. Grosz, E. Sicre, "Code transmission through aberrating media using selfimaging," Optik 82, 144- (1989).

164. Scaffardi, D. Schinca, J.O. Tocho, H. Ranea Sandoval, "Spectroscopic study of population inversion mechanisms in diatomic molecules," Journal of Quantitative Spectroscopy and Radiative Transfer 41, 225-234 (1989).

165. H. Ranea Sandoval, L. Scaffardi, "Distintos tipos de láseres," Láser y Optica en Ingeniería. Centro de Investigaciones Opticas, (1989).

166. Scaffardi, D. Schinca, J.O. Tocho, "The excitation mechanism for the Lambda doubling in the 0-0 UV laser band of N_2," Applied Optics 28, 3698-3701 (1989).

167. G. Bilmes, J.O. Tocho, S. Braslavsky, "Photophysical processes of polymethine dyes. An absorption, emission and optoacoustic study on 3,3'-diethylthiadicarbocyanine iodide (DTDCI)," Journal of Physical Chemistry 93, 6696-6699 (1989).

168. G. Molesini, M. Pires de Souza, F. Quercioli, M. Trivi, "Digital phase-shifting interferometry applied to partially developed speckle fields," Optics Communications 75, 14- (1990).

169. Bolognini, H. Rabal, "Spectrum folding," Optik 84, 113-114 (1990).

170. Duchowicz, L. Scaffardi, R. Di Paolo, J.O. Tocho, "Determinación de parámetros fotofísicos de cianinas utilizando distintas técnicas: aplicación al DODCI ," Anales de la Asociación Física Argentina 2, 118-122 (1990).

171. N. Bolognini, H. Rabal, R. Torroba, "Contorneado a tiempo real empleando DSPI," Anales de la Asociación Física Argentina 2, 163- (1990).

172. Grosz, J. Salcedo Pinzón, N. Bolognini, L. Zerbino, "Filtrado espacial con cristales BSO," Anales de la Asociación Física Argentina 2, 161- (1990).

173. E. Colombo, C. Kirschbaum, H. Rabal, "Calidad de impresos: Ajuste de un modelo," Anales de la Asociación Física Argentina 2, 140-146 (1990).

174. G. Molesini, F. Quercioli, M. Trivi, "Rugosímetros ópticos basados en la aberración cromática y esférica del sistema de enfoque," Anales de la Asociación Física Argentina 2, 168- (1990).

175. G. Molesini, F. Quercioli, M. Pires de Souza, M. Trivi, "Hologramas de reflexión registrados en el infrarrojo y reconstruídos en el visible ," Anales de la Asociación Física Argentina 2, 165- (1990).

176. W. Furlan, H. Rabal, E. Sicre, "Display of the hybrid longitudinal and transversal degree of coherence," Optik 84, 115-117 (1990).

177. G. Bilmes, M. Rohr, S. Braslavsky, "Optoacoustic Raman Gain spectroscopy with pulsed lasers," Springer Series in Optical Sciences. Photoacoustic and Phototermal Phenomena II 62, 354-356 (1990).

178. R. Duchowicz, M. Trivi, L. Scaffardi, N. Bolognini, "Speckle stereograms of moving objects," Applied Optics 29, 1871-1872 (1990).

179. R. Duchowicz, L. Scaffardi, J.O. Tocho, "Relaxation processes of singlet excited state of 3,3'-diethyloxadicarbocyanine iodide (DODCI) photoisomer," Chemical Physics Letters 170, 497-501 (1990).

180. G. Molesini, M. Pires de Souza, F. Quercioli, M. Trivi, "Experimental statistics of partially developed speckle fields," Optics Letters 15, 646- (1990).

181. G. Molesini, M. Pires de Souza, F. Quercioli, M. Trivi, "Experimental statistics of fully developed speckle fields by phase-shifting interferometry," Optics Communications 77, 129- (1990).

182. Bolognini, M. Trivi, "Multiple exposure method through speckle carrier," Optik 85, 153- (1990).

183. M. Trivi, F. Quercioli, M. Pires de Souza, G. Molesini, "Denisyuk holograms recording with a laser diode," Applied Optics, (1990).

184. D. Iriarte, H.O. Di Rocco, M. Raineri, J.G. Reyna Almandos, M. Gallardo, "Oscillator strengths for Xe II transitions," Theochem-Journal of Molecular Structure 69, 253-257 (1990).

185. S. Grosz, L. Zerbino, N. Bolognini, "Pseudocoloring with BSO crystals," Applied Optics 29, 3337- (1990).

186. N. Russo, N. Bolognini, E. Sicre, M. Garavaglia, "Surface roughness measurement through a speckle method," International Journal of Optoelectronics 5, 389-395 (1990).

187. Aramendia, R. Duchowicz, L. Scaffardi, J.O. Tocho, "Photophysical characterization of a photochromic system: the case of merocyanine 540," Journal of Physical Chemistry 94, 1389-1392 (1990).

188. G. Lifante, J.O. Tocho, F. Cussó, "Photoacoustic determination of the luminescent quantum efficiencies of F_2^+ and $(F_2^+)_h$ centres in NaCl:OH^- crystals," Journal of Physics B; Condensed Matter 2, 3035-3040 (1990).

189. B. Wernsman, J. Rocca, H. Mancini, D. Schinca, J.O. Tocho, "Recombination lasers in a flowing negative glow discharge," IEEE Journal of Quantum Electronics 26, 1624-1632 (1990).

190. O. Roveri, G. Bilmes, K. Heihoff, S. Braslavsky, "Laser-induced optoacoustic spectroscopy (LIOAS) of proteins spectrum of bovine serum albumin in the 530-670 nm region," Applied Spectroscopy 44, 1706- (1990).

191. L. Bourimborde, C. Colautti, E. Sicre, "Rotation sensitivity of Lau fringes: a WDF approach," Optik 86, 151- (1990).

192. Torroba, R. Arizaga, "An extension of Lau effect based on OTF theory," Optik 85, 155- (1990).

193. J. Salcedo Pinzón, S. Grosz, L. Zerbino, N. Bolognini, M. Garavaglia, "Real-time spatial selective filtering with BSO crystals," Optik 87, 83-86 (1991).

194. J.G. Reyna Almandos, F. Bredice, M. Gallardo, C. Pagan, H.O. Di Rocco, A.G. Trigueiros, "$5s^25p^2(5d+6s)$ configurations in triply ionized xenon (Xe IV)," Physical Review A 43, 6098-103 (1991).

195. J.O. Tocho, R. Ramirez, J. Gonzalo, "New technique for investigating ferroelectric phase transitions: The photoacoustic effect," Applied Physics Letters 59, 1684-1686 (1991).

196. J.O. Tocho, E. Camarillo, F. Cussó, F. Jaque, J. Garcia Solé, "Optical detection of new Nd^{3+} sites in $LiNbO_3$:Nd," Solid State Communications 80, 575-578 (1991).

197. J.O. Tocho, J. Sanz Garcia, F. Jaque, J. Garcia Solé, "Fluorescence bands of Nd^{3+} sites in $LiNbO_3$:Nd,Mg laser system," Journal of Applied Physics 70, 5582-5586 (1991).

198. R. Di Paolo, L. Scaffardi, G. Bilmes, R. Duchowicz, "Fotofísica de colorantes polimetínicos: estudio del DTCI," Anales de la Asociación Física Argentina 3, 130-133 (1991).

199. G. Bilmes, R. Duchowicz, C. Cabello, "Determinación fotoacústica de espectros de absorción de polvos," Anales de la Asociación Física Argentina 3, 134-137 (1991).

200. H. Rabal, N. Bolognini, "Enfoque geométrico para obtener la visibilidad. Su relación con el teorema de van Cittert-Zernike ," Anales de la Asociación Física Argentina 3, 18- (1991).

201. Grosz, L. Zerbino, N. Bolognini, "Discriminación de las partes dinámicas de una imagen mediante cristales fotorrefractivos," Anales de la Asociación Física Argentina 3, 175- (1991).

202. H. Rabal, E. Colombo, "Propuesta de un modelo de dos canales en la percepción de bordes desenfocados," Anales de la Asociación Física Argentina 3, 185-187 (1991).

203. R. Henao, F. Medina, H. Rabal, M. Trivi, "Medición de desplazamientos tridimensionales mediante interferometría speckle," Anales de la Asociación Física Argentina 3, 188-191 (1991).

204. D. Schinca, M. Murphy, H. Ranea Sandoval, "Espectroscoía optogalvánica y fluorescencia en descargas eléctricas de neón," Anales de la Asociación Física Argentina 3, 145- (1991).

205. J.O. Tocho, L. Núñez, J. Sanz García, F. Cussó, D. Hanna, A. Tropper, S. Field, D. Shepherd, A. Large, "Optical properties of Tm doped $LiNbO_3$ and $LiNbO_3$ (MgO)," Journal de Physique IV 1, 293-296 (1991).

206. J. Garcia Solé, A. Monteil, G. Boulon, E. Camarillo, J.O. Tocho, I. Vergara, F. Jaque, "Site selective spectroscopy of Nd^{3+} and Cr^{3+} sites in $LiNbO_3$ crystals codoped with Mg^{2+} ions," Journal de Physique IV 1, 403-406 (1991).

207. Arizaga, N. Bolognini, W. Furlan, H. Rabal, M. Garavaglia, "An upside down image in Fresnel holography," European Journal of Physiscs 12, 199-200 (1991).

208. L. Bourimborde, W. Furlan, E. Sicre, "Off-axis analysis of the Strehl ratio using the Wigner distribution function," Journal of Modern Optics 38, 1685- (1991).

209. M. Raineri, F. Brédice, M. Gallardo, J.G. Reyna Almandos, C. Pagan, A.G. Trigueiros, "Revised and extended analysis of five times ionized argon (Ar VI)," Physica Scripta 45, 584-589 (1992).

210. E. Camarillo, J.O. Tocho, I. Vergara, E. Dieguez, J. García Solé, F. Jaque, "Optical bands of Cr^{3+} induced by Mg^{2+} ions in $LiNbO_3$:Cr,Mg," Physical Review B; Condensed Matter 45, 4600-4604 (1992).

211. Duchowicz, L. Scaffardi, R. Di Paolo, J.O. Tocho, "Dual laser excitation of a photochromic system: application to DODCI," Journal of Physical Chemistry 96, 2501-2505 (1992).

212. R. Duchowicz, J.O. Tocho, L. Nuñez, F. Cusso, "Estudios espectroscópicos de sitios en $LiNbO_3$:Er y $LiNbO_3$:Er:Mg," Anales de la Asociación Física Argentina 4, 126-128 (1992).

213. M. Tebaldi, N. Bolognini, "Procesador óptico en tiempo real," Anales de la Asociación Física Argentina 4, 129-131 (1992).

214. L. Yebrin, J.O. Tocho, L. Scaffardi, "Determinación de tamaño de partículas poliméricas por distintas técnicas ópticas," Anales de la Asociación Física Argentina 4, 132-137 (1992).

215. D. Schinca, J.O. Tocho, "Luminiscencia del Eu^{2+} en matrices de haluros alcalinos," Anales de la Asociación Física Argentina 4, 110-113 (1992).

216. J.O. Tocho, "Sobre el uso del sistema KC1:Eu^2 para estudiar el contenido de ozono atmosférico," Anales de la Asociación Física Argentina 4, 107-109 (1992).

217. J.O. Tocho, F. Jaque, J. García Solé, E. Camarillo, F. Cussó, S. Muñoz, "Nd^{3+} active sites in Nd:MgO:$LiNbO_3$ lasers," Applied Physics Letters 60, 3206-3208 (1992).

218. D. Schinca, R. Duchowicz, M. Gallardo, "Ionic classification of Xe laser lines: a new approach through time resolved spectroscopy," LAMP Series Report LAMP/92/5, (1992).

219. R. Duchowicz, R. Di Paolo, L. Scaffardi, J.O. Tocho, "Analysis of photoisomerizable dyes using laser absorption and fluorescence techniques," LAMP Reports LAMP/92/6, (1992).

220. M. Schwarz, R. Duchowicz, W. Demtröder, Ch. Jungen, "Autoinozing Rydberg states of Li_2 - Tables," PAPS Documents , JCPSA-89-5460-15, (1992).

221. J.O. Tocho, R. Duchowicz, L. Scaffardi, G. Bilmes, R. Di Paolo, M. Murphy, "Spectroscopic properties of isomerizable cyanine dyes," Trends in Physical Chemistry 3, 31-47 (1992).

222. N. Bolognini, H. Rabal, R. Torroba, "Single beam digital holographic countouring," Applied Optics 31, 1009-1011 (1992).

223. N. Russo, J. Pomarico, E. Sicre, "Optical velocimetry: A method using two shifted speckle patterns," Optics Communications 90, 227-230 (1992).

224. N. Russo, E. Sicre, "Real time measurement of surface roughness through Young's fringes modulated speckle," Applied Optics 31, 4334-4336 (1992).

225. N. Russo, E. Sicre, "optical surface roughness measurements using an image speckle pattern at defocus planes," International Journal of Optoelectronics 7, 773-777 (1992).

226. N. Russo, A. Tonso, E. Sicre, "Liquid refractometry: an approach for a continous measurement," Optics and Laser Technology 25, 109-112 (1992).

227. R. Arizaga, R. Torroba, "Real time orientation pseudocoloring method," Optik 90, 144- (1992).

228. J.O. Tocho, F. Cussó, R. Ramirez, J. Gonzalo, "Laser induced photoacoustic effect during ferroelectric phase-transitions," Photoacoustic and Phototermal Phenomena III, Springer Series in Optical Sciences 69, 631- (1992).

229. M. Gallardo, M. Raineri, J.G. Reyna Almandos, "Classified lines in the spectra of Xe II and Xe III," Spectroscopy Letters 26, 1241-1246 (1993).

230. E. Rodriguez, J.O. Tocho, F. Cussó, "Simultaneous multiple-wavelength photoacoustic and luminescence experiments: A method for fluorescent-quantum-efficiency determination," Physical Review B; Condensed Matter 47, 14049-14053 (1993).

231. L. Nuñez, J.O. Tocho, J. Sanz García, E. Rodriguez, F. Cussó, D. Hanna, A. Tropper, A. Large, "Optical absorption and luminescence of Tm^{3+} -doped $LiNbO_3$ and $LiNbO_3$(MgO) crystals," Journal of Luminescence 55, 253-263 (1993).

232. L. Scaffardi, R. Di Paolo, R. Duchowicz, "Fotofísica del ioduro de 3,3'-dietiltiadicarbocianina (DTDCI)," Anales de la Asociación Física Argentina 5, 187-189 (1993).

233. D. Schinca, R. Duchowicz, H. Sobral, M. Gallardo, "Espectroscopía resuelta en tiempo de un láser iónico de Xe de pulso múltiple," Anales de la Asociación Física Argentina 5, 164-168 (1993).

234. M. Mesaros, J. Etcheverry, M. Marconi, O. Martínez, G. Bilmes, J.O. Tocho, "Detección acústica de umbrales de cambio de fase en metales irradiados con pulsos láser de alta potencia," Anales de la Asociación Física Argentina 5, 179-182 (1993).

235. R. Merlo, N. Bolognini, "Cristales electro-ópticos BSO, BTO y BGO. Peculiaridades d ela birrefringencia inducida," Anales de la Asociación Física Argentina 5, 223- (1993).

236. M.C. Lasprilla, L. Zerbino, N. Bolognini, "Selección a tiempo real de amplitud de frecuencias espaciales," Anales de la Asociación Física Argentina 5, 250- (1993).

237. N. Bolognini, L. Solymar, L. Arizmendi, "Filtrado espacial en la reconstrucción de hologramas de volumen," Anales de la Asociación Física Argentina 5, 229- (1993).

238. R. Arizaga, H. Rabal, M. Trivi, E. Alanís, G. Romero, "Métodos de proyección de una franja," Anales de la Asociación Física Argentina 5, 241-243 (1993).

239. L. Scaffardi, L. Yebrin, J.O. Tocho, C. Cantera, "Medición del radio de partículas por scattering óptico," Anales de la Asociación Física Argentina 5, 262-266 (1993).

240. J.O. Tocho, D. Schinca, "Comportamiento no-lineal de la luminiscencia del $KCl:Eu^{2+}$," Anales de la Asociación Física Argentina 5, 190-193 (1993).

241. S. Bosco, M. Trivi, "Algoritmos sub-pixel para análisis de franjas," Anales de la Asociación Física Argentina 5, 237- (1993).

242. J.O. Tocho, M.G. Nicora, L. Da Silva, T. Badorrey, Cussó, F. Jaque, G. Lifante, "Instalación de medidores de ozono en Argentina y Chile," Anales de la Asociación Física Argentina 5, 502-505 (1993).

243. R. Duchowicz, L. Nuñez, J.O. Tocho, F. Cussó, "MgO-induced effects on the optical properties of Er-doped $LiNbO_3$," Solid State Communications 88, 439-442 (1993).

244. E. Rodriguez, J.O. Tocho, F. Cussó, "Nuevo método de determinación de eficiencias cuánticas de fluorescencia: Aplicación al $KCl:Eu^{2+}$," Optica Pura y Aplicada 26, 744-760 (1993).

245. A.G. Trigueiros, A. Mania, S. Pettersson, J.G. Reyna Almandos, "Core-excited levels of the $4p^4$ configuration of Ge-like Kr V," Physical Review A 48, 3595-3597 (1993).

246. J. Bosnic, J.G. Reyna Almandos, C. Cocoz, "Estudio sobre el funcionamiento de los componentes de un sistema de radiación en el cercano ultravioleta para aplicaciones médicas," Boletín de la Facultad Regional La PLata de la Universidad Tecnológica Nacional 2, 66- (1993).

247. H. Rabal, G. Bilmes, "Double slit camera," Applied Optics 32, 2219- (1993).

248. L. Bernardo, J. Pinto, N. Bolognini, "Apodization in rainbow holography," Optics Communications 95, 215- (1993).

249. D. Sing, F. Bredice, F. Giammanco, M. Vaselli, "Effect of electron velocity distribution on the heating of core by corona in spherical pellet," Contributions of Plasma Physics 33, ? (1993).

250. J. Pomarico, R. Arizaga, R. Torroba, H. Rabal, "Digital holographic contouring," Optics Communications 98, 257-260 (1993).

251. J. Pomarico, R. Torroba, "Color image operations based on white light diffraction experiments (Lau effect)," European Journal of Physics 14, 114-120 (1993).

252. R. Henao, F. Medina, H. Rabal, M. Trivi, "Correlation of two speckle patterns generated by the three dimensional diffuser movement," Optica Pura y Aplicada 26, 583-587 (1993).

253. E. Colombo, H. Rabal, "Un modelo de dos canales para explicar la percepción de la nitidez," Optica Pura y Aplicada 26, 438-444 (1993).

254. R. Henao, F. Medina, H. Rabal, M. Trivi, "Three dimensional speckle measurements with a diffraction grating," Applied Optics 32, 726-729 (1993).

255. P. Torroba, N. Cap, H. Rabal, W. Furlan, "The fractional order mean in image processing," Optical Engineering 33, 529-534 (1993).

256. H. Rabal, M. Trivi, "Sign ambiguity in speckle metrology," Applied Optics 33, 2206-2208 (1993).

257. L. Bourimborde, A. Tonso, C. Colautti, E. Sicre, "Real time measurement of the meniscus shape using the Talbot effect," Optics Communication 102, 397- (1993).

258. P. Andrés, J. Lancis, E. Sicre, E. Bonet, "Achromatic Fresnel diffraction patterns," Optics Communication 104, 39- (1993).

259. R. Duchowicz, D. Schinca, M. Gallardo, "New analysis for the assignment of UV-visible ionic Xe laser lines," IEEE Journal of Quantum Electronics 30, 155-159 (1994).

260. M. Gallardo, M. Raineri, J.G. Reyna Almandos, "Analysis of the 5p6p configuration of Xe V," Zeitschrift fur Physik, D. Atoms Molecules and Clusters 30, 261-264 (1994).

261. E. Rodriguez, L. Núñez, J.O. Tocho, F. Cussó, "Quantum efficiency measurement in solids by photoacoustic and luminescence experiments," Journal of Luminescence 58, 353-355 (1994).

262. L. Nuñez, B. Herreros, R. Duchowicz, G. Lifante, J.O. Tocho, F. Cussó, "Site-selective up-conversion in $LiNbO_3:Er^{3+}$," Journal of Luminescence 60-61, 81-84 (1994).

263. D.J. Orzi, J.O. Tocho, "Photoacoustic studies of glassing processes of metacrylate polymers," Journal de Physique IV 4, C7/245-8 (1994).

264. J.O. Tocho, M. Murphy, E. Rodriguez, F. Cussó, "Simultaneous photoacoustic and luminescence multiple wavelength experiments," Journal de Physique IV 4, C7/405-8 (1994).

265. D. Schinca, J.O. Tocho, E. Rodriguez, F. Cusso, "Excited state absorption in KCl:Eu^{2+}," Journal de Physique IV 4, C7/409-12 (1994).

266. F. Jaque, J.O. Tocho, L. Da Silva, G. Bertuccelli, E. Crino, F. Cussó, M. De Laurentis, J. Hormaechea, G. Lifante, M.G. Nicora, H. Ranea Sandoval, V. Valderrama, G. Zoja, "Ground-based ultraviolet-radiation measurements during springtime in the Southern Hemisphere," Europhysics Letters 28, 289-293 (1994).

267. R. Duchowicz, M. Ferrer, F. Amat-Guerri, R. Sastre, A. Acuña, "A proton-transfer dye laser pumped by the third harmonic of a Nd:YAG laser," Optics Communications 104, 336-338 (1994).

268. L. Nuñez, R. Duchowicz, M. Voda, F. Cussó, "Impurity sites of $LiNbO_3$:Er co-doped with MgO or ZnO," Journal de Physique IV 4, 443-446 (1994).

269. D. Murgida, G. Bilmes, R. Erra-Balsells, "Estudio del efecto de sustituyentes en la formación de tripletes de purinas por espectroscopía fotoacústica," Contribuciones Científicas y Tecnológicas de la Universidad de Santiago de Chile 24, 69- (1994).

270. G. Bilmes, D. Murgida, R. Erra-Balsells, "Photoacoustic determination of energy content and quantum yields of formation of trancient states," Journal de Physique IV, Colloque C7 4, 417- (1994).

271. X. Zeng, M. Vaselli, D. Sing, V. Palleschi, F. Bredice, "Scalling laws considering thermal radiation influence for spherical pinch experiment," Journal of Fusion Energy 13, 39- (1994).

272. J. Pomarico, R. Arizaga, R. Torroba, H. Rabal, "Algorithm to compute spacing of digital speckle correlation fringes," Optik 95, 125-127 (1994).

273. P. Vaveliuk, L. Scaffardi, R. Duchowicz, "Cinética de la molécula colorante DTDCI: análisis de una simple o doble fotoisomerización," Anales de la Asociación Física Argentina 6, 73-77 (1994).

274. P. Vaveliuk, L. Scaffardi, R. Duchowicz, "Desarrollo de láseres de colorantes en matrices sólidas," Anales de la Asociación Física Argentina 6, 78-81 (1994).

275. R. Duchowicz, M. Ferrer, A. Acuña, "Análisis de los procesos de decaimiento del estado triplete de eritrosina," Anales de la Asociación Física Argentina 6, 82-85 (1994).

276. R. Duchowicz, R. Di Paolo, J.O. Tocho, L. Nuñez, B. Herreros, G. Lifante, F. Cussó, "UP-Conversion en $LiNbO_3:Er^{3+}$," Anales de la Asociación Física Argentina 6, 86-89 (1994).

277. D. Schinca, H. Sobral, R. Duchowicz, M. Gallardo, "Estudio de la salida multipulso de un láser iónico de xenon," Anales de la Asociación Física Argentina 6, 37-42 (1994).

278. D.J. Orzi, J.O. Tocho, "Relajación de moléculas de colorantes en películas acrílicas orientadas por campo eléctrico," Anales de la Asociación Física Argentina 6, 90-94 (1994).

279. J. Barraza, E. Colombo, H. Rabal, P. Torroba, "Percepción visual de bordes borrosos: Ajuste del modelo de Cornsweet," Anales de la Asociación Física Argentina 6, 65-69 (1994).

280. E. Alanís, G. Romero, C. Martínez, D. Hoyos, H. Rabal, "Propiedades del bio-speckle producido por muestras de sangre con Tripanosoma Cruzi," Anales de la Asociación Física Argentina 6, 59-64 (1994).

281. R. Mazzei, D. Schinca, "Determinación del tiempo de inducción en SSNTD," Anales de la Asociación Física Argentina 6, (1994).

282. M.G. Nicora, J.O. Tocho, "Medición de ozono total durante la primavera de 1993," Anales de la Asociación Física Argentina 6, 386-390 (1994).

283. J. Pomarico, R. Torroba, "Digital visibility measurements by Fourier analysis," Optik 95, 152-154 (1994).

284. H. Rabal, J. Pomarico, R. Arizaga, "Light-in-flight digital holographic display ," Applied Optics 33, 4358-4360 (1994).

285. E. Colombo, H. Rabal, C. Kirschbaum, M. Jaen, "Assessment of defocused words and physical correlations," Imaging Science and Technology 38, 180-184 (1994).

286. P. Torroba, N. Cap, H. Rabal, "Defocus correction using visibility criterion," Journal of Modern Optics 41, 111-117 (1994).

287. R. Arizaga, H. Rabal, M. Trivi, E. Alanís, G. Romero, "Single fringe contouring," Optics Communications 108, 209-213 (1994).

288. R. Arizaga, H. Rabal, M. Trivi, "Simultaneous multiple-viewpoint processing in digital speckle pattern interferometry," Applied Optics 33, 4369-4372 (1994).

289. H. Rabal, M. Trivi, R. Arizaga, G. Romero, E. Alanís, "Biospeckle activity," Optical methods in biomedical and environmental science 3, 19-22 (1994).

290. M.G. Nicora, J.O. Tocho, "Medición de ozono total durante la primavera de 1993," Anales de la Asociación Física Argentina 6, 386-390 (1994).

291. F. Bredice, M. Gallardo, J.G. Reyna Almandos, A.G. Trigueiros, C. Pagan, "Revised analysis of triply ionized argon (Ar IV)," Physica Scripta 51, 446-453 (1995).

292. C. Pagan, J.G. Reyna Almandos, M. Gallardo, S. Pettersson, G. Cavalcanti, A.G. Trigueiros, "Study of the 4s4p4d and the 4s4p5s configurations of Kr VI," Journal of the Optical Society of America B 12, 203-211 (1995).

293. G. Cavalcanti, F. Luna, A.G. Trigueiros, C. Pagan, M. Raineri, F. Bredice, M. Gallardo, J.G. Reyna Almandos, "Additional results on the Ar V spectrum," Brazilian Journal of Physics 25, 1-6 (1995).

294. M. Gallardo, M. Raineri, J.G. Reyna Almandos, H.O. Di Rocco, D. Bertuccelli, A.G. Trigueiros, "$5s^25p^2(6p + 4f)$ configurations in triply ionized xenon (Xe IV)," Physica Scripta 51, 737-751 (1995).

295. Costela, F. Florido, I. García-Moreno, R. Duchowicz, F. Amat-Guerri, J. Figuera, R. Sastre, "Solid-state dye lasers based on copolymers of 2-hydroxyethyl methacrylate and methyl methacrylate doped with rhodamine 6G," Applied Physics B B60, 383-389 (1995).

296. R. Di Paolo, L. Scaffardi, R. Duchowicz, G. Bilmes, "Photoisomerization dynamics and spectroscopy of the polymethine dye DTCI," Journal of Physical Chemistry 99, 13796-13799 (1995).

297. M. Villagrán Muñiz, C. García Segundo, H. Ranea Sandoval, G. Bilmes, "Photoacoustic methods for real-time measurement of laser beam diameter and position, and for laser cavity alignment," Review of Scientific Instruments 66, 3500-3506 (1995).

298. M. Villagrán Muñiz, C. García Segundo, H. Ranea Sandoval, C. Gogorza, G. Bilmes, "Photoacoustic analysis of stimulated emission in pulsed dye lasers," Applied Physics B; Lasers and Optics 61, 361-366 (1995).

299. J. Pomarico, R. Torroba, N. Bolognini, "Fringe visibility control in DSPI by using a BSO crystal," Optik 99, 89-91 (1995).

300. Grosz, L. Zerbino, N. Bolognini, "Motion detection with BSO crystal. Incoherent approach," Optik 99, 77- (1995).

301. J. Alvarez, N. Bolognini, L. Arizmendi, "Cross-talk in multiplexed holograms using angular selectivity in $LiNbO_3$," Optical Materials 4, 414- (1995).

302. N. Bolognini, L. Arizmendi, L. Solymar, "Spatial frequency filtering in holographic image reconstruction," Applied Optics 34, 243- (1995).

303. Agra Amorim, M. Tebaldi, M.C. Lasprilla, N. Bolognini, "Photorefractive implementation of the Talbot effect and applications," Journal of Optics 24, 133-142 (1995).

304. F. Bredice, I. Deha, F. Giammanco, A. Salvetti, D.P. Singh, M. Vaselli, F. Panarella, S. Del Tredici, "Laser initiated diverging and converging spherical blast waves," Fusion Technology 27, 215- (1995).

305. M. Lehman, J. Pomarico, R. Torroba, "DSPI applied to surface roughness study," Optical Engineering 34, 1148-1152 (1995).

306. J. Pomarico, U. Schnars, H. Hartmann, W. Jüptner, "Digital recording and numerical reconstruction of holograms: A new method for displaying light-in-flight," Applied Optics 34, 8095-8099 (1995).

307. R. Mazzei, D. Schinca, "A new simple method to study the induction time ," Nuclear Instruments and Methods B 103, 79- (1995).

308. J. Lancis, E. Sicre, A. Pons, G. Saavedra, "Achromatic white light selimaging phenomenon: an approach using the Wigner distribution function," Journal of Modern Optics 42, 425- (1995).

309. D. Zalvidea, M. Lehman, S. Granieri, E. Sicre, "Analysis of the Strehl ratio using the Wigner distribution function," Optics Communications 118, 207- (1995).

310. S. Granieri, O. Trabocchi, E. Sicre, "Fractional Fourier transform applied to spatial filtering in the Fresnel domain," Optics Communications 119, 275- (1995).

311. J. Lancis, E. Sicre, E. Tajahuerce, P. Andrés, "White light implementation of the Wigner distribution function with an achromatic processor," Applied Optics 34, 8209- (1995).

312. M. Lehman, J. Pomarico, R. Torroba, "Digital speckle pattern interferometry applied to a surface roughness study," Optical Engineering 34, 1148-1152 (1995).

313. S. Bosco, M. Trivi, "Correlation-like algorithm for superresolution analysis," Optics Communications 115, 444- (1995).

314. M. Tebaldi, M.C. Lasprilla, N. Bolognini, "Optimización de la reconstrucción de imágenes binarias registradas en un cristal BSO," Anales de la Asociación Física Argentina 7, 43-45 (1995).

315. S. Granieri, M.C. Lasprilla, N. Bolognini, E. Sicre, "Space-variant optical correlator based on the fractional Fourier transform: implementation using a photorefractive BGO holographic filter," Applied Optics 35, 6951-6954 (1996).

316. R. Torroba, R. Henao, C. Carletti, "Digital polarization encoding technique for optical logic operation," Optics Letters 21, 1918-1920 (1996).

317. L. Bourimborde, A. Tonso, L. Zerbino, M. Garavaglia, "Optical interferometric studies of a confined liquid free surface: meniscus-effect compensation and time evolution of the surface," Optical Engineering 35, 70-75 (1996).

318. C. Pagan, M. Raineri, F. Bredice, J.G. Reyna Almandos, M. Gallardo, S. Pettersson, G. Cavalcanti, A.G. Trigueiros, "Weighted oscillator strengths for Kr VI spectrum," Journal of Quantitative Spectroscopy and Radiative Transfer 55, 163-168 (1996).

319. H. Sobral, D. Schinca, R. Duchowicz, M. Gallardo, "Gain switching and oscillations in an ionic pulsed xenon laser," Pure and Applied Optics 5, 1011-1020 (1996).

320. J.G. Reyna Almandos, F. Bredice, M. Raineri, M. Gallardo, A.G. Trigueiros, "New energy levels of the Kr III spectrum," Journal of Physics, B 29, 5643-5650 (1996).

578. M.C. Lasprilla, L. Zerbino, N. Bolognini, "Aplicaciones del control de la elipticidad d ela luz transmitida en un medio fotorrefractivo," Anales de la Asociación Física Argentina 6, ? (1996).

578. M. Tebaldi, M.C. Lasprilla, N. Bolognini, "Formación y procesamiento de autoimágenes mediante registros fotorrefractivos," Anales de la Asociación Física Argentina 6, 54-58 (1996).

321. G. Cavalcanti, Gallardo, J.G. Reyna Almandos, J. Gomide, A.G. Trigueiros, "Study of the $3p^4$ configuration in four-times ionized argon, Ar V," Journal of Physics B; Atomic Molecular and Optical Physics 29, 6049-6053 (1996).

322. D.J. Orzi, J.O. Tocho, "Relaxation of induced dichroism in corona-poled doped polymers," Optical Engineering 35, 47-51 (1996).

323. L. Scaffardi, J.O. Tocho, L. Yebrin, C. Cantera, "Sizing particles used in the leather industry by light scattering," Optical Engineering 35, 52-56 (1996).

324. R. Di Paolo, J.O. Tocho, "Polarization anisotropy applied to the determination of structural changes in the photoisomerization of DODCI," Chemical Physics 206, 375-382 (1996).

325. P. Vaveliuk, L. Scaffardi, R. Duchowicz, "Kinetic analysis of a double photoisomerization of the DTCI cyanine dye," Journal of Physical Chemistry 100, 11630-11635 (1996).

326. M. Rosato, J.G. Reyna Almandos, "Métodos ópticos para medición de contaminantes atmosféricos," Revista de Seguridad 348, 12- (1996).

327. D. Murgida, R. Erra-Balsells, G. Bilmes, "New photocalorimetric references or UV excitation," Chemical Physics Letters 250, 198-202 (1996).

328. D. Murgida, G. Bilmes, R. Erra-Balsells, "A photophysical study of purines and theophylline by using laser induced photoacoustic spectroscopy," Photochemistry and Photobiology 64, 777-784 (1996).

329. J. Alvarez, N. Bolognini, L. Arizmendi, "Experimental study of the angular selectivity of volume holograms stored in $LiNbO_3$," Applied Physics B; Lasers and Optics 62, 159- (1996).

330. M.C. Lasprilla, L. Zerbino, N. Bolognini, "Optical processing by modulation of birefringence," Optical Engineering 35, 40- (1996).

331. M.C. Lasprilla, A. Agra Amorim, M. Tebaldi, N. Bolognini, "Self imaging through incoherent to coherent conversion," Optical Engineering 35, 1440-1445 (1996).

332. M. Tebaldi, N. Bolognini, "Experiments with an optical converter," European Journal of Physics 17, 236-243 (1996).

333. R. Henao, J. Pomarico, N. Russo, R. Torroba, M. Trivi, "Multimode optical fiber core measurement by speckle correlation," Optical Engineering 35, 26-30 (1996).

334. H. Rabal, R. Arizaga, N. Cap, M. Trivi, G. Romero, E. Alanís, "Transient phenomena analysis using dynamic speckle patterns," Optical Engineering 35, 57-62 (1996).

335. R. Henao, H. Rabal, A. Tagliaferri, R. Torroba, "Digital display of the temporal evolution of speckle patterns," Optical Engineering 35, 63-69 (1996).

336. R. Torroba, R. Henao, H. Rabal, "Digital implementation of a speckle shadow mask method," Optik 102, 168-170 (1996).

337. H. Rabal, R. Henao, R. Torroba, "Digital speckle pattern shearing interferometry using diffraction gratings," Optics Communications 126, 191-196 (1996).

338. B. Ruiz, H. Rabal, "Differential operators, the Fourier Transform and its application to optics," Optik 103, 171-178 (1996).

339. O. Trabocchi, C. Colautti, E. Sicre, "Diffraction properties of a periodic multiple-aperture system: an approach based on the Walsh functions," Optical Engineering 35, 94- (1996).

340. S. Granieri, M.C. Lasprilla, N. Bolognini, E. Sicre, "Space variant optical correlation based on fractional Fourier transform: implementation by use of a photorefractive BGO holographic filter," Applied Optics 35, 6951- (1996).

341. M. Saint Pierce, C. Carletti, L. Ochoa, R. Torroba, "Frequency color encoding by grating resonance," Optik 102, 18-20 (1996).

342. C. Carletti, R. Torroba, "Color coded logic," Optics Communications 126, 197-201 (1996).

343. R. Henao, A. Tagliaferri, R. Torroba, "Digital polarization sensitive speckle pattern interferometry," Optics Communications 126, 14-19 (1996).

344. R. Henao, M. Trivi, F. Medina, "Extensive parametric dependence of the speckle patterns maximum correlation degree," Optik 102, 137- (1996).

345. E. Crinó, J. Sirur Flores, J.O. Tocho, "Resultados de medidas de ozono total en primavera para San Luis (Argentina) entre 1993 y 1995," Energías Renovables y Medio Ambiente 1, 63-67 (1996).

346. J.O. Tocho, L. Da Silva, G. Lifante, F. Cussó, F. Jaque, "Penetración del agujero de ozono en Sudamérica," Investigación y Ciencia 233, 68-73 (1996).

347. P. Meilán, G. Torchia, R. Duchowicz, N. Carri, M. Garavaglia, "The Rayleigh criteria of resolution in fluorescence microscopy and the observation of sources of different spectral composition," FASEB Journal 10, 4767- (1996).

348. G. Cavalcanti, F. Luna, A.G. Trigueiros, F. Bredice, H. Sobral, R. Hutton, M. Wang, "Vacuum ultraviolet spectrum of six-times ionized xenon, Xe VII," Journal of the Optical Society of America B 14, 2459-2462 (1997).

349. A.G. Trigueiros, A. Mania, M. Gallardo, J.G. Reyna Almandos, "Atomic transitions for Ar VII spectrum in the vacuum ultraviolet (VUV)," Journal of the Optical Society of America B 14, 2463-2468 (1997).

350. J.G. Reyna Almandos, M. Rosatto, S. Marteau, G. Ratto, "Métodos de detección y monitoreo de contaminantes gaseosos y medidas de SO2 en La Plata," Revista de Ciencia y Tecnología de la Universidad Tecnológica Nacional 2, 19-26 (1997).

351. J. Muñoz, E. Rodríguez, J.O. Tocho, F. Cussó, "Luminiscence quantum efficiency of europium aggregates in sodium chloride," Journal of Luminescence 72-74, 233-235 (1997).

352. R. Di Paolo, J.O. Tocho, "Rotational diffusion parameters of cyanine dyes determined by depolarization of luminescence," Journal of Luminescence 72-74, 481-483 (1997).

353. R. Henao, H. Rabal, A. Tagliaferri, R. Torroba, "Determination of the zero order fringe position in digital speckle pattern interferometry," Applied Optics 36, 2066-2069 (1997).

354. B. Ruiz, H. Rabal, "Fractional Fourier transform description with use of differential operators," Journal of the Optical Society of America A 14, 2905-2913 (1997).

355. G. Romero, E. Alanís, H. Rabal, "Estadística del speckle dinámico producido por un difusor rotante y su relación con la velocidad tangencial," Anales de la Asociación Física Argentina 9, 58-62 (1997).

356. D. Pérez, M. Garavaglia, "Efectos temporales de la amplitud de onda turbulenta sobre la función de estructura en un modelo atmosférico estratificado," Anales de la Asociación Física Argentina 9, 442-445 (1997).

357. J. Pomarico, N. Russo, E. Sicre, D. Patrignani, "Optical velocimetry based on the spatial correlation of off axis image speckle patterns," Optics Communications 133, 27-32 (1997).

358. M.C. Lasprilla, S. Granieri, N. Bolognini, "Optical correlator by non-degenerate four wave mixing," Optik 105, 61-64 (1997).

359. S. Granieri, R. Arizaga, E. Sicre, "Optical correlation based on the fractional Fourier transform," Applied Optics 36, 6636-6645 (1997).

360. O. Trabocchi, C. Colautti, G. Saavedra, E. Sicre, "Spatial coherence properties of a multiple aperture system: an analysis based on the walsh functions," Journal of Modern Optics 44, 715-729 (1997).

361. B. Ruiz, H. Rabal, "Cylindrical optical systems and the Fourier transform," Optik 106, 28-32 (1997).

362. Greco, L. Hoffer, G. Molesini, M. Trivi, "Using a programmable interferometer for digital phase-shifting speckle interferometry," Optics and Lasers in Engineering 27, 235-240 (1997).

363. M.C. Lasprilla, M. Tebaldi, N. Bolognini, "Polarization sensitive readout of self-images," Optical Engineering 36, 2216-2224 (1997).

364. J. Pomarico, R. Torroba, "Focal lengths measurements using digital speckle interferometry," Optics Communications 141, 1-4 (1997).

365. L. Scaffardi, R. Di Paolo, R. Duchowicz, "Simultaneous absorption and fluorescence analysis of the DOCI cyanine dye," Journnal of Photochemistry and Photobiology A; Chemistry 107, 185-188 (1997).

366. M. Mesaros, O. Martínez, G. Bilmes, J.O. Tocho, "Acoustic detection of laser induced melting of metals," Journal of Applied Physics 81, 1014-1016 (1997).

367. M. Creus, E. Gallego Lluesma, J. Desimoni, R. Mercader, A. Agudelo, R. Gancedo, J. Marco, "Surface carbon steel product after laser irradiations under different processing conditions," Hyperfine Interactions C 2, 155- (1997).

368. P. Meilán, M. Garavaglia, "Fizeau confocal laser scanning interference microscope," Revista de Física Aplicada e Intrumentacao 12, 126-132 (1997).

369. P. Meilán, M. Garavaglia, "Rayleigh resolution criterion for light sources of different spectral composition," Brazilian Journal of Physics 27, 638-643 (1997).

370. N. Pedrero, A. Hernández, J. Flores, A. García-Borquez, J.O. Tocho, M. Villagrán Muñíz, J. García Solé, S. Murrieta, "Analysis of the optical behaviour of Eu^{2+} ions in CsCl crystals," Physica Status Solidi B 203, 591-598 (1997).

371. M. Rosato, J.G. Reyna Almandos, J. Rípoli, V. Rosato, J. Alberino, S. Marteau, "Mediciones de la calidad de aire en La Plata, Berisso y Ensenada," Revista de la Asociación Argentina de Energía Solar 1, 134-137 (1997).

372. G. Cavalcanti, F. Bredice, R. Hutton, F. Luna, H. Sobral, M. Wang, A.G. Trigueiros, "The vacuum ultra violet (VUV) spectrum of six times ionized xenon, Xe VII ," Journal of the Optical Society of America B 14, 2459- (1997).

373. R. Henao, H. Rabal, R. Torroba, "Dynamical digital speckle pattern shearing interferometry," Optik 105, 13-15 (1997).

374. B. Ruiz, H. Rabal, "The fractional Fourier transform description using differential operators," Journal of the Optical Society of America A 14, 1-9 (1997).

375. G. Saavedra, W. Furlan, E. Silvestre, E. Sicre, "Analysis of the irradiance along different paths in the image space using the Wigner distribution function," Optics Communications 139, 11- (1997).

376. C. Colautti, O. Trabocchi, E. Sicre, "Moiré properties of Walsh functions," Optics and Laser Technology 29, 261- (1997).

377. R. Torroba, R. Henao, C. Carletti, "Polarization encoding architecture for optical logic operations," Optik 107, 41-43 (1997).

378. M. Garavaglia, "La óptica en la Argentina," Optica Pura y Aplicada 30, 85-114 (1997).

379. M. Raineri, J.G. Reyna Almandos, F. Bredice, M. Gallardo, A.G. Trigueiros, S. Pettersson, "Weighted oscillator strengths for Kr III spectrum," Journal of Quantitative Spectroscopy and Radiative Transfer 60, 25-42 (1998).

380. J.G. Reyna Almandos, F. Bredice, M. Raineri, M. Gallardo, A.G. Trigueiros, "Extended analysis of the three-times ionized krypton (Kr IV)," Journal of Physics, B 31, 3129-3136 (1998).

381. M. Rosatto, J. Rípoli, J.G. Reyna Almandos, S. Marteau, J. Alberino, M. Barrera, "La corrosión atmosférica sobre materiales ferrosos como índice de contaminación," Revista de seguridad 357, 37 (1998).

382. J. Rípoli, J.G. Reyna Almandos, V. Rosato, J. Alberino, M. Rosatto, J. Maresca, S. Solari, "Mediciones de dióxido de azufre en aire mediante métodos activos y pasivos," Revista de la Asociación Argentina de Energía Solar 2, 29-31 (1998).

383. R. Henao, J. Pomarico, R. Torroba, "Digital speckle pattern interferometry applied to small rotation measurements," Optik 109, 109-112 (1998).

384. M. Manceñido, G. Pozzi, L. Zunino, L. Zerbino, L. Martorelli, M. Garavaglia, "Observación de perturbaciones en aire mediante técnicas de Moiré y Schlieren," Anales de la Asociación Física Argentina 10, 115-117 (1998).

385. M. Manceñido, G. Pozzi, L. Zunino, L. Zerbino, M. Garavaglia, "Experimentos interferenciales de Young empleando una fuente filamentaria monocromática," Anales de la Asociación Física Argentina 10, 111-114 (1998).

386. L. Baum, V. Laguna Weinberg, J. Cesaretti, J. Martínez, M. Garavaglia, "Difraccion por pupilas fractales y principio de Babinet," Anales de la Asociación Física Argentina 10, 102-104 (1998).

387. . Manceñido, G. Pozzi, L. Zunino, M. Garavaglia, "Interfranja vs rotación de la fuente filamentaria monocromática en eun experimento de Young," Anales de la Asociación Física Argentina 10, 105-106 (1998).

388. L. Angel Toro, M. Tebaldi, R. Henao, A. Tagliaferri, M. Trivi, N. Bolognini, R. Torroba, "Phase stepping technique with photorrefractive crystals in digital speckle pattern interferometry," Optics Communications 149, 235-238 (1998).

389. R. Torroba, A. Tagliaferri, "Precision small angle measurements with a digital moire technique," Optics Communications 149, 213-216 (1998).

390. R. Arizaga, J. Pomarico, R. Torroba, "Digital technique to high precision measurements of focal lengths," Optics Communications 152, 6-10 (1998).

391. R. Henao, J. Pomarico, R. Torroba, "Precision angle measurements by digital speckle pattern interferometry ," Optik 109, 109-112 (1998).

392. M. Tebaldi, L. Angel Toro, M.C. Lasprilla, N. Bolognini, "Image multiplexing by speckle in BSO," Optics Communications 155, 342-350 (1998).

393. M. Tebaldi, L. Angel Toro, N. Bolognini, "Lau fringes formation by using a grating registered in a BSO crystal," Optical Engineering 37, 2971-2978 (1998).

394. D. Zalvidea, E. Sicre, "Phase pupil functions for focal depth enhancement derived from a Wigner distribution function," Applied Optics 37, 3623-3627 (1998).

395. O. Trabocchi, C. Colautti, E. Sicre, "Walsh-Hadamard analysis of the Fresnel diffraction by Cantor fractals," Optik 108, 78-82 (1998).

396. R. Duchowicz, M. Ferrer, A. Acuña, "Kinetic spectroscopy of erythrosin phosphorescence and delayed fluorescence in aqueous solution at room temperature," Photochemistry and photobiology 68, 494-501 (1998).

397. S. Granieri, E. Sicre, W. Furlan, "Performance analysis of optical imaging system based on the fractional Fourier transform," Journal of Modern Optics 45, 1797-1807 (1998).

398. J. Muñoz, R. Di Paolo, J.O. Tocho, F. Cussó, B. Castañeda, R. Pérez-Salas, R. Aceves, M. Barboza-Flores, "Luminescent quantum efficiency of Eu +2 ions in mixed KCl(1-x)Br(x) crystals," Journal of Physics B; Condensed Matter 10, 4113-4118 (1998).

399. D.J. Orzi, G. Bilmes, J.O. Tocho, N. Mingolo, O. Martínez, "Photoacoustic characterization of phase transitions in amorphous metal alloys," Applied Physics B; Lasers and Optics 66, 245-249 (1998).

400. J. Muñoz, J.O. Tocho, F. Cussó, "Experimental determination of the luminescent quantum effieciency of the laser emitting level of Nd ions in lithium niobate," Europhysics Letters 43, 159-164 (1998).

401. J. Muñoz, R. Di Paolo, R. Duchowicz, J.O. Tocho, F. Cussó, "Experimental determination of the luminescent quantum effieciency of the green emission of Er^{3+} ions in lithium niobate," Solid State Communications 107, 487-490 (1998).

402. Pérez, L. Aguirre de Carcer, J.O. Tocho, E. Crino, H. Ranea Sandoval, M. Berni, L. Da Silva, D. Enriques, F. Cussó, F. Jaque, "The extent of the ozone hole over South America during the spring of 1993, 1994 and 1995," Journal of Physics D 31, 812-819 (1998).

403. L. Yebrin, C. Cantera, L. Scaffardi, J.O. Tocho, "Medición por scattering óptico del radio de partículas en polímeros utilizados en la terminación del cuero," Tecnología del Cuero 8, 14-19 (1998).

404. P. Meilán, M. Garavaglia, "Fizeau confocal laser scanning interference microscopy: basis and potentialities," Optics and optoelectronics: theory, devices and applications 2, 1094-1099 (1998).

405. D. Pérez, M. Garavaglia, "Path integral techniques studying intensity distribution of self-image systems into turbulent media," Optics and optoelectronics: theory, devices and applications 2, 1456-1458 (1998).

406. M. Garavaglia, "Quasi-Moire patterns observed when an original transparency is superposed to its scaled-up and -down transparencies," Optics and optoelectronics: theory, devices and applications 2, 1149-1153 (1998).

407. R. Castañeda, F. Medina, M. Garavaglia, L. Zerbino, "Spatial partial coherence in Young's interferograms," Optics and Laser Technology 30, 313-316 (1998).

408. M. Lehman, R. Torroba, M. Garavaglia, "Multiple non-specular shifts in the reflection of super-Gaussian beams from a thin film," Optik 109, 124-132 (1998).

409. R. Sarmiento, M. Gallardo, A. Laquidara, J.G. Reyna Almandos, "Spectral study of ionized xenon using a capillary pulsed discharge," Astrophysics and Space Science 256, 359-363 (1998).

410. J. Muñoz, R. Di Paolo, J.O. Tocho, F. Cussó, B. Castañeda, R. Perez-Salas, R. Aceves, M. Barboza-Flores, "Luminescent quantum efficiency of Eu^{2+} ions in alcali halides determined by simultaneous

multiwavelength photoacoustic and luninescent experiments," Journal of Physics B; Condensed Matter 6, 10625- (1998).

411. J. Muñoz, J.O. Tocho, F. Çussó, "Photoacoustic determination of the luminescent quantum efficiency of Yb^{3+} ions in lithium niobate," Applied Optics 37, 7096-7099 (1998).

412. G.M. Bilmes, N. Bolognini, M. Gallardo, J.O. Tocho, M. Trivi, "Manual de uso de material didáctico de óptica para primer y segundo ciclo de la EGB," Buenos Aires, Ministerio de Educación de la Nación, ? (1998).

413. G.M. Bilmes, N. Bolognini, M. Gallardo, J.O. Tocho, M. Trivi, "Guía para experiencias para realizar con material didáctico de óptica para primer y segundo ciclo de la EGB," Buenos Aires, Ministerio de Educación de la Nación, ? (1998).

414. G.M. Bilmes, N. Bolognini, M. Gallardo, J.O. Tocho, M. Trivi, "Material didáctico de óptica para primer y segundo ciclo de EGB. Guía para docente," Buenos Aires, Ministerio de Educación de la Nación, (1998).

415. M. Tebaldi, L. Angel Toro, N. Bolognini, "Formation of Lau fringes with a grating registered in a BSO crystal," Optical Engineering 37, 2971- (1998).

416. M.C. Lasprilla, M. Tebaldi, N. Bolognini, "Estudio del contraste salida de imágenes binarias registradas como modulación de birrefringencia," Revista Colombiana de Física 30, 355-358 (1998).

417. R. Torroba, Cap, H. Rabal, "Defocus correction using structured illumination," Optik 108, 68-77 (1998).

418. R. Fedrigo, G. Sampallo, A. González Thomas, H. Rabal, "An asymmetrical pupil with focusing properties," Optics Communications ?, 5-11 (1998).

419. M. Manceñido, G. Pozzi, L. Zunino, L. Zerbino, M. Garavaglia, "Experimentos interferenciales de Young empleando una fuente filamentaria monocromática," Anales de la Asociación Física Argentina 10, 111-114 (1998).

420. J. Pombo, M. Lehman, M. Garavaglia, D. Jaggard, "Quasi-self similar Cantor gratings and their diffraction," Microwave and Optical Technology Letters 20, 393-397 (1999).

421. D. Pérez, M. Garavaglia, "Intensity distribution behavior of self-image systems into turbulent media," Journal of the Optical Society of America A 16, 916-918 (1999).

422. M. Lehman, D. Jaggard, M. Garavaglia, "Changes of self-similarity in superlattices through the gaps distribution," Optik 110, 350-352 (1999).

423. L. Zerbino, R. Castañeda, F. Medina, M. Garavaglia, "Coherencia parcial controlada por polarización," Anales de la Asociación Física Argentina 11, 135-137 (1999).

424. E. Alanís, C. Matthews, N. Cap, M. Montero, G. Romero, H. Rabal, "Detección de Tripanosoma Cruzi en sangre mediante speckle dinámico," Anales de la Asociación Física Argentina 11, 135-137 (1999).

425. M. Lehman, M. Garavaglia, "Beam reflection from multilayers with periodic and fractal distributions," Journal of Modern Optics 46, 1579-1593 (1999).

426. M. Manceñido, G. Pozzi, L. Zunino, M. Garavaglia, "Young interference experiments with a laser filamentary light source," Journal of the Optical Society of America A 16, 2767-2771 (1999).

427. N. Russo, J. Pomarico, E. Sicre, D. Patrignani, L. De Pasquale, "Extended range optical velocimetry through spatial correlation of image speckle sub-patterns," Optics Communications 169, 23-28 (1999).

428. S. Granieri, D. Zalvidea, E. Sicre, "Analysis of the asymmetric apodization using the fractional Fourier transform," Journal of Modern Optics 46, 1155-1159 (1999).

429. R. Arizaga, M. Trivi, H. Rabal, "Speckle time evolution characterization by the co-ocurrence matrix analysis," Optics and Laser Technology 31, 163-169 (1999).

430. C. Carletti, R. Torroba, R. Castañeda, "Technique for exploring the spatial coherence in a speckle field," Optik 110, 359-362 (1999).

431. R. Torroba, C. Nunes, A. Tagliaferri, "Object positioning by a digital moiré focusing technique," Optical Engineering 38, 1409-1412 (1999).

432. R. Henao, A. Tagliaferri, R. Torroba, "A contouring approach using single digital shadow Moiré with a phase stepping technique," Optik 110, 199-201 (1999).

433. C. Carletti, R. Henao, R. Torroba, "Measuring velocity of speckle fields with speckle pattern interferometry," Optics Communications 160, 195-200 (1999).

434. Greco, R. Tronconi, C. Del Vecchio, M. Trivi, G. Molesini, "Absolute measurements of planarity with Fritz method: uncertainly evaluation," Applied Optics 38, 2018-2027 (1999).

435. M. Tebaldi, M.C. Lasprilla, N. Bolognini, "Analysis of birrefringence encoded images," Optik 110, 127-136 (1999).

436. M. Tebaldi, L. Angel Toro, N. Bolognini, "Interferometry based on lau effect with a grating registered in a photorefractive crystal," Optics Laser Technology 31, 127-134 (1999).

437. L. Angel Toro, M. Tebaldi, R. Henao, "Phase stepping in lau interferometry," Optics Communications 164, 247-255 (1999).

438. P. Vaveliuk, B. Ruiz, N. Bolognini, "Analysis of the steady-state photorefractive harmonic gratings," Physical Review B 59, 10985-10991 (1999).

439. M. Gallardo, M. Raineri, J.G. Reyna Almandos, H. Sobral, F. Callegari, "Revised and extended analysis in four times ionized xenon, Xe V," Journal of Quantitative Spectroscopy and Radiative Transfer 61, 319-327 (1999).

440. R. Sarmiento, J.G. Reyna Almandos, M. Raineri, M. Gallardo, "Spectroscopic analysis of the configurations 5s5p5d, 5p3 and 5s5p6s of Xe VI," Journal of Physics B; Atomic Molecular and Optical Physics 32, 2853-2858 (1999).

441. H. Sobral, M. Raineri, D. Schinca, M. Gallardo, R. Duchowicz, "Excitation mechanisms and characterization of a multi-ionic xenon laser," IEEE Journal of Quantum Electronics 35, 1308-1313 (1999).

442. H. Sobral, D. Schinca, M. Gallardo, R. Duchowicz, "Time dependent study of a multi-ionic xenon plasma," Journal of Applied Physics 85, 69-73 (1999).

443. J. Muñoz, E. Cantelar, J. Sanz Garcia, R. Duchowicz, D. Serrano, E. Dieguez, G. Lifante, F. Cussó, "Site-selective spectroscopy of Er^{3+} and $Er^{3+}Yb^{3+}$ doped stoichio-metric and congruent lithium niobate," Radiation Effects Defects in Solids 150, 221-225 (1999).

444. S. Abbruzzetti, D. Murgida, R. Erra-Balsells, C. Viappiani, G. Bilmes, "Non toxic, water soluble photocalorimetric reference compunds for UV and visible excitation," Chemical Physics Letters 304, 167-169 (1999).

445. M. Marchi, S. Aldabe Bilmes, G. Bilmes, "Photophysics of rhodamine B interacting with silver spheroids," Journal of Colloid and Interface Science 218, 112-117 (1999).

446. M. Tebaldi, L. Angel Toro, N. Bolognini, "Features on photorefractive registered speckles," Optics and optoelectronics: theory, devices and applications 1, 393-398 (1999).

447. M. Tebaldi, L. Angel Toro, N. Bolognini, "Non holographic register of a grating in a BSO crystal applicattions," Recent research developments in optical engineering 2, 229-240 (1999).

448. M. Cortizo, L. Scaffardi, J.O. Tocho, R. Figini, "Mechanisms of emulsion polymerization of diisopropylfumarate," Applied Machromolecular Chemistry and Physics 271, 1-7 (1999).

449. B. Ruiz, S. Granieri, H. Rabal, "Parity and the self-imaging phenomenon," Optics Communications 168, 157-160 (1999).

450. L. Angel Toro, M. Tebaldi, N. Bolognini, M. Trivi, "Optical operations based on speckle modulation by using a photorrefractive crystal," Optics Communications 168, 55-64 (1999).

451. J.O. Tocho, G. Bilmes, H. Ranea Sandoval, "Photoacoustic method for orientation and optical characterization of nonlinear crystals," Applied Physics B; Lasers and Optics 69, 473-476 (1999).

452. Rosato, M. Rosato, J.G. Reyna Almandos, J. Rípoli, J. Alberino, "Líquenes como indicadores de la calidad del aire en los alrededores del Polo Petroquímico de La Plata," Revista de Seguridad 361, 36- (1999).

453. M. Tebaldi, M.C. Lasprilla, N. Bolognini, "Analysis and applications of birefringence encoded images," Optik 110, 127- (1999).

454. M. Tebaldi, L. Angel Toro, N. Bolognini, "Photorefractive optical processing: some proposals," Optics and optoelectronics. Theory, devices and applications 2, 915-923 (1999).

455. J. Pomarico, E. Sicre, D. Patrignani, L. De Pasquale, "Optical fiber strain Gauge based on speckle correlation," Optics and Laser Technology 31, 219-224 (1999).

456. N. Salamana, D. Patrignani, L. De Pasquale, E. Sicre, "Wavefront sensor using Talbot effect," Optics and Laser Technology 31, 269- (1999).

457. E. Tajahuerce, G. Saavedra, W. Furlan, E. Sicre, P. Andrés, "White light optical implementation of the fractional Fourier transform with adjustable order control," Optics and Laser Technology 31, 269- (1999).

458. P. Torroba, H. Rabal, R. Arizaga, "Correction of defocusing using the co-occurrence matrix and the structure function," Journal of Modern Optics 47, 69-80 (2000).

459. G. Romero, E. Alanís, H. Rabal, "Statistics of the dynamic speckle produced by a rotating diffuser and its application to the assessment of paint drying," Optical Engineering 38, 1652-1658 (2000).

460. E. Alberti, M. Lehman, R. Torroba, M. Garavaglia, "Entropic propagation of Gaussian and super-gaussian-like beams," Optics Communications 175, 1-12 (2000).

461. F. Bredice, M. Raineri, J.G. Reyna Almandos, M. Gallardo, A.G. Trigueiros, "Weighted oscillator strengths for Kr IV spectrum," Journal of Quantitative Spectroscopy and Radiative Transfer 65, 805-19 (2000).

462. D. Mártire, P. Vaveliuk, G. Bilmes, "Photophysical properties of corrphycenes," Spectrochemica Acta A 56, 2043-2048 (2000).

463. F. Luna, F. Bredice, G. Cavalcanti, A.G. Trigueiros, "Atomic transitions for the doubly ionized argon spectrum, Ar iii," Brazilian Journal of Physics 30, 386-391 (2000).

464. P. Vaveliuk, B. Ruiz, R. Duchowicz, N. Bolognini, "Theoretical analysis of the photocurrent dark decay in photorefractive media," Journal of Quantum Electronics 36, 692-697 (2000).

465. M. Raineri, A.G. Trigueiros, M. Gallardo, J.G. Reyna Almandos, "Spectroscopic analysis of the 4p4d configuration of Kr VII," Physica Scripta 62, 474-478 (2000).

466. L. Angel Toro, M. Tebaldi, N. Bolognini, M. Trivi, "Speckle photography with different pupils in a multiple-exposure scheme," Journal of Optical Society of America A 17, 107-119 (2000).

467. E. de Miguel-Sanz, M. Tebaldi, S. Granieri, N. Bolognini, L. Arizmendi, "Photorefractive fixed optical correlator," Applied Physics B; Lasers and Optics 70, 379-383 (2000).

468. M. Tebaldi, L. Angel Toro, M. Trivi, N. Bolognini, "New multiple aperture arrangements for speckle photography," Optics Communications 182, 95-105 (2000).

469. M. Tebaldi, J. Rueda, N. Bolognini, "Talbot interferometer based on a birefringence grating," Optics Communications 185, 65-76 (2000).

470. M. Tebaldi, L. Angel Toro, M. Trivi, N. Bolognini, "Optical processing by fringed speckles registered in a BSO crystal," Optical Engineering 39, 3232-3238 (2000).

471. P. Vaveliuk, B. Ruiz, N. Bolognini, J. Fernández, "Transient behavior of the photorefractive space-charge field," Physical Review B 62, 4511-4518 (2000).

472. G. Bilmes, O. Martinez, P. Seré, D.J. Orzi, A. Pignotti, "On line photoacoustic measurement of residual dirt on steel plates," Review of progress in quantitative nondestructive evaluation 20, 1944- (2000).

473. G. Torchia, J.O. Tocho, F. Jaque, "Site-selective spectroscopy of Cr^{3+} in congruent co-doped $LiNbO_3:Cr^{3+}:ZnO$ crystals," Journal of Physics B; Condensed Matter 12, 8927-8932 (2000).

474. P. Meilán, M. Creus, M. Garavaglia, "Generation of quasi-moiré patterns: fractality and percolation," Visual Mathematics. Art and Science Electronic Journal 2, Ed. Electrónica Nro. 2 (2000).

475. F. Cussó, J. Muñoz, E. Castelar, J.O. Tocho, N. Rodrigo, "Laser optoacoustic of rare-earth doped crystals," Journal of Luminescence 87-89, 620-622 (2000).

476. Garcés Vernier, O. Sotolongo, M. Hernández, L. Scaffardi, J. García Ramos, L. Rivas, "Determination of particle size distribution of particles on aerosols and suspensions by ultraviolet-visible-near infrared absorbance measurements," Physica Status Solidi B 220, 583 (2000).

477. R. Duchowicz, L. Scaffardi, A. Costela, I. García-Moreno, R. Sastre, A. Acuña, "Photothermal characterization and stability analysis of polymeric dye lasers," Applied Optics 39, 4959-4963 (2000).

478. M. Tebaldi, C. Nunes, A. Tagliaferri, R. Torroba, N. Bolognini, "Digital Talbot interferometer," Optik 111, 523-528 (2000).

479. P. Torroba, N. Cap, H. Rabal, "Correction of defocusing using a modified visual model," Optik 110, 341-349 (2000).

480. D. Zalvidea, C. Colautti, E. Sicre, P. Andrés, "Quality parameters analysis of optical imaging systems with enhanced focal depth using the Wigner distribution function," Journal of the Optical Society of America A 17, 867- (2000).

481. R. Henao, R. Torroba, "Surface characterization by a DSPI polarization technique," Optik 111, 468-470 (2000).

482. F. Medina, J. Garcia Sucerquia, R. Henao, M. Trivi, R. Castañeda, "Invariance in speckle patterns," ICTP Report IC/2000/30, 1-10 (2000).

483. F. Medina, J. García Sucerquia, R. Henao, M. Trivi, R. Castañeda, "Entendue invariance in speckle fields," Optik 112, 57-61 (2001).

484. J.G. Reyna Almandos, R. Sarmiento, M. Raineri, F. Bredice, M. Gallardo, "Weighted oscillator strengths and lifetimes for Xe VI spectrum," Journal of Quantitative Spectroscopy and Radiative Transfer 70, 189-194 (2001).

485. G. Torchia, J. Muñoz, F. Cussó, F. Jaque, J.O. Tocho, "The luminescent quantum efficiency of Cr^{3+} ions in co-doped crystals of $LiNbO_3$:ZnO determined by simultaneous multiple-wavelength photoacoustic and luminescence experiments," Journal of Luminescence 92, 317-322 (2001).

486. E. Cantelar, R. Di Paolo, J.O. Tocho, F. Cussó, "Pulsed, broadly tuneable, photoacoustic study of rare-earth doped $LiNbO_3$," Journal of Alloys Compounds 323-324, 351-354 (2001).

487. G. Torchia, O. Martinez Matos, P. Vaveliuk, J.O. Tocho, "Electron-lattice coupling in congruent co-doped $LiNbO_3:Cr^{3+}$:ZnO crystal," Journal of Physics B; Condensed Matter 13, 6577-6583 (2001).

488. M. Ferrer, R. Duchowicz, B. Carrasco, J. De la Torre, A. Acuña, "The conformation of serum albumin in solution: acombined phosphorescence depolarization-hydrodynamic modeling study," Biophysical Journal 80, 2422-2430 (2001).

489. C. Aguirre Vélez, M. Lehman, M. Garavaglia, "Two-dimensional fractal gratings with variable structure and their diffraction," Optik 112, 209-217 (2001).

490. M. Garavaglia, A. Laquidara, "Optoelectronical hidden grids and Moiré patterns: basics and applications in distance measurement," Optical Engineering 40, 2510-2516 (2001).

491. C. Joenathan, R. Torroba, R. Henao, "Influence of surface roughness in dual beam illumination speckle interferometers: Theoretical study," Optik 112, 163-168 (2001).

492. L. Angel Toro, M. Tebaldi, M. Trivi, N. Bolognini, "Properties of speckle patterns generated through multiaperture pupils," Optics Communications 192, 37-47 (2001).

493. L. Angel Toro, M. Tebaldi, M. Trivi, N. Bolognini, "Fringe visibility analysis with different scale apertures in speckle photography," Journal of Modern Optics 48, 1749-1765 (2001).

494. S. Granieri, M. Tebaldi, N. Bolognini, "Parallel factional correlation: an optical implementation," Applied Optics 40, 6439-6444 (2001).

495. M. Tebaldi, M.C. Lasprilla, N. Bolognini, "White light reconstruction of a transparency registered in a BSO crystal," Optik 11, 469-474 (2001).

496. J. Amalvy, C. Lasquibar, R. Arizaga, H. Rabal, M. Trivi, "Aplication of dynamic speckle interferometry to the drying of coatings," Progress in Organic Coating 42, 89-99 (2001).

497. H. Rabal, "Holographic analogues," Optik 112, 153-156 (2001).

498. H. Rabal, "The holodiagram with virtual sources," Optik 112, 487-492 (2001).

499. A.G. Trigueiros, F. Callegari, N. Mansur, G. Cavalcanti, M. Gallardo, J.G. Reyna Almandos, "$3d^2$ configuration in six-times-ionized argon, Ar VII," Journal of the Optical Society of America B 18, 1718-1721 (2001).

500. M. Gallardo, F. Bredice, M. Raineri, A.G. Trigueiros, J.G. Reyna Almandos, "Extended analysis of the six-times ionized xenon, Xe VII," The European Physical Journal D 15, 307-314 (2001).

501. M. Rosato, J.G. Reyna Almandos, G. Ratto, A. Flores, V. Sacchetto, V. Rosato, J. Rípoli, J. Alberino, J.C. Ragaini, "Mesure de SO_2 a La Plata, Argentine," Revue Pollution Atmospherique 169, 85-98 (2001).

502. P. Vaveliuk, B. Ruiz, O. Martínez Matos, G. Torchia, N. Bolognini, "An electro-hole transport model for the analysis of the photorefractive harmonic gratings," IEEE Journal of Quantum Electronics 37, 1040-1049 (2001).

503. F. Luna, F. Bredice, G. Cavalcanti, A.G. Trigueiros, "Weighted oscillator strengths and lifetimes for the dolby ionized argon, Ar III," Journal of Quantum Spectroscopy and Radiative Transfer 69, 171-188 (2001).

504. J. Amalvy, C. Lasquibar, R. Arizaga, H. Rabal, M. Trivi, "Application of dynamic speckle interferometry to the drying of coatings," Progress in Organic Coatings 1091, 1-11 (2001).

505. F. De Zela, G. Baldwin, H. Rabal, "Refraction holodiagrams," Optik, 555-560 (2001).

506. R. Braga, F. Borem, H. Rabal, M. Trivi, R. Arizaga, I. Dal Fabbro, B. Saleh, "Avaliacao da influencia da umidade de sementes de feijao (Phaseolus vulgaris L.)," Engenharia Agrícola 21, 101-106 (2001).

507. O. Martínez, G. Bilmes, D.J. Orzi, P. Seré, R. Musso, A. Pignotti, "On line measurement of residual dirt on steel plates by laser ablation and acoustic detection," Surface Engineering 18, 1- (2002).

508. O. Martinez Matos, G. Torchia, P. Vaveliuk, G. Bilmes, J.O. Tocho, "Surface roughness dependence of noncolinear phase matching," Journal of Optics A; Pure and Applied Optics 4, 130-134 (2002).

509. G. Bilmes, O. Martínez, P. Seré, R. Musso, D.J. Orzi, A. Pignotti, "Laser instrument for determination of the degree of cleanliness in cold-rolled steel plate manufacturing," Latin American Applied Research 32, 263- (2002).

510. F. Callegari, M. Gallardo, M. Raineri, A.G. Trigueiros, Reyna Almandos, "Spectral analysis of the $4d^95d$ and $4d^95f$ configurations in octuple ionization of xenon, Xe IX," Journal of Quantitative Spectroscopy Radiative Transfer 73, 13-22 (2002).

511. N. Russo, R. Duchowicz, J. Mora, J. Cruz, M. Andrés, "High efficiency Q-switched erbium fiber laser using a Bragg grating based modulator," Optics Communications 210, 361-366 (2002).

512. Raineri, F. Bredice, M. Gallardo, A.G. Trigueiros, J.G. Reyna Almandos, "New energy levels of the $4s^24p5s$, $4s^24p4d$ and $4s^24p5p$ configuración of the Kr V spectrum," Journal of Physics B 35, 3411-3419 (2002).

513. Tebaldi, A. Lencina, N. Bolognini, "Analysis and applications of the speckle patterns registered in a photorefractive BTO crystal," Optics Communications 202, 257-270 (2002).

514. R. Torroba, N. Bolognini, M. Tebaldi, A. Tagliaferri, "Moire beating digital technique to collimation testing," Optics Communications 201, 283-288 (2002).

515. L. Angel Toro, M. Tebaldi, M. Trivi, N. Bolognini, "Phase object analysis with a speckle interferometer," Optics Letters 27, 506-508 (2002).

516. R. Torroba, N. Bolognini, M. Tebaldi, A. Tagliaferri, "Positioning method based on digital moire," Optics Communications 209, 1-6 (2002).

517. J. Rueda, M. Tebaldi, S. Granieri, N. Bolognini, "Implementation of a photorefractive correlator based on a fake zoom lens," Optik 113, 309-313 (2002).

518. P. Vaveliuk, A. Lencina, P. de Oliveira, N. Bolognini, "Photorefractive harmonic grating within the shallow trap model," IEEE Journal of Quantum Electronics 38, 1541-1549 (2002).

519. F. Bredice, D.J. Orzi, D. Schinca, H. Sobral, M. Villagrán Muñiz, "Characterization of pulsed laser generated plasma through its perturbation in an electric field," IEEE Transactions on Plasma Science 30, 2139-2143 (2002).

520. R. Arizaga, N. Cap, H. Rabal, M. Trivi, "Display of local activity using dynamical speckle patterns," Optical Engineering 41, 287-294 (2002).

521. H. Rabal, "The holodiagram in a geometrical approach to the calculation of visibility," Optik 113, 260-266 (2002).

522. Fernández Limia, A. Mavilio Nuñez, H. Rabal, M. Trivi, "Wavelet transform analysis of speckle patterns texture," Applied Optics 41, 6745-6750 (2002).

523. D. Patrignani, D. Zalvidea, E. Sicre, "Fraunhofer diffraction analysis from linear and non-linear transformations of the Wigner distribution function," Optik 113, 121- (2002).

524. D. Zalvidea, S. Granieri, E. Sicre, "Space and spectral behaviour of optical systems under broadband illumination by using a Wigner distribution function approach," Optics Communications 204, 99- (2002).

525. R. Arizaga, R. Torroba, "Digital polarization sensitive speckle correlation as optical security validation technique," Optik 113, 333-336 (2002).

526. M. Bento Moreira, R. Braga, F. Borem, H. Rabal, G. Rabelo, I. Dal Fabbro, M. Trivi, R. Arizaga, "Caracterizacao da transmissao da luz laser em semente de feijao (Phaseolus vulgaris L.)," Revista Brasileira de Produtos Agroindustriais 4, 13-19 (2002).

527. M. Vignolo, S. Duhalde, M. Bormioli, G. Quintana, M Cervera, J.O. Tocho, "Structural and electrical properties of lanthanum oxide thin films deposited by laser ablation," Applied Surface Science 197-198, 522-526 (2002).

528. G. Torchia, J.O. Tocho, F. Jaque, "OH - impurities in co-doped $LiNbO_3:Cr^{3+}$:ZnO congruent crystals ," Journal of Physics and Chemistry of Solids 63, 555-559 (2002).

529. G. Torchia, D. Schinca, N. Khaiduko, J.O. Tocho, "The luminescent quantum efficiency of Cr^{3+} ions in Cs 2NaAlF6 single crystals," Optical Materials 20, 301-304 (2002).

530. E. Wolcan, G. Torchia, J.O. Tocho, O. Piro, P. Juliarena, G. Ruiz, M. Féliz, "Photoinduced charge separation in arene-CO2-Re(CO)32,2'-bipyridine complexes metal-to-ligand or ligand-to-ligand charge transfer excited state," Journal of Chemical Society; Dalton Transactions 10, 2194-2202 (2002).

531. R. Duchowicz, N. Russo, E. Sicre, M. Andrés, "Q-switching of an erbium doped fibre laser modulated by a Bragg grating fixed to a piezoelectric," Journal of Optics A: Pure and Applied Optics 5, S216-220 (2003).

532. R. Duchowicz, L. Scaffardi, A. Costela, I. García-Moreno, R. Sastre, A. Acuña, "Photothermal analysis of polymeric dye laser materials excited at different pump rates," Applied Optics 42, 1029-1035 (2003).

533. G. Cavalcanti, A.G. Trigueiros, M. Raineri, J.G. Reyna Almandos, "Configuration 4p4f in six-times ionized krypton, Kr VII," Journal of the Optical Society of America B 20, 1758-1760 (2003).

534. R. Hutton, Y. Zou, J.G. Reyna Almandos, C. Biedermann, R. Radtke, A. Greier, R. Neu, "Ebit spectroscopy of Pm-like tungsten," Nuclear Instruments and Methals in Physics Research B 205, 114-118 (2003).

535. J.G. Reyna Almandos, F. Bredice, J.C. Ragaini, M. Garavaglia, "Métodos ópticos aplicados al estudio y caracterización de lámparas fluorescentes," Revista de Seguridad 379, 28-31 (2003).

536. M. Mesaros, G. Bilmes, J. Rosso, M. González, D. Mártire, "Volume and enthalpy changes of peroxodiphosphate dissociation," Chemical Physics Letters 373, 176-181 (2003).

537. M. Mesaros, S. Bonesi, M. Ponce, R. Erra-Balsells, G. Bilmes, "The photophysics of nitrocarbazoles studied by using spectroscopic, photoacoustic and luminescence techniques ," Photochemical and Photobiological Science 2, 808-816 (2003).

538. M. Tebaldi, L. Angel Toro, M. Trivi, N. Bolognini, "Phase-object detection by use of a double-exposure fringe modulated speckle patterns," Journal of the Optical Society of America A 20, 116-129 (2003).

539. Salazar, M. Tebaldi, N. Bolognini, "Experimental study of volume speckle in four-wave mixing arrangement," Optics Communications 221, 249-256 (2003).

540. Salazar, M. Tebaldi, N. Bolognini, "Analysis of high frequency modulated speckle in a BSO crystal," Optics Communications 223, 1-9 (2003).

541. Lencina, M. Tebaldi, P. Vaveliuk, N. Bolognini, "Modulated speckle simulations based on the random walk model," Optics Letters 28, 1748-1750 (2003).

542. M. Tebaldi, L. Angel Toro, M. Trivi, N. Bolognini, "Photorefractive speckle storage for phase objects analysis," Perspectives in Engineering Optics 1, 97-106 (2003).

543. M. Tebaldi, "Birefringence," Encyclopedia of Optical Engineering 1, 183-200 (2003).

544. M. Asmad, G. Baldwin, R. Arizaga, H. Rabal, M. Trivi, "Calibration of a low cost piezoelectrical mirror for DSPI," Optics and Lasers in Engineering 40, 25-31 (2003).

545. M. Pajuelo, G. Baldwin, R. Arizaga, N. Cap, H. Rabal, M. Trivi, "Bio-speckle assessment of bruising in fruits," Optics and Lasers in Engineering 40, 13-24 (2003).

546. H. Rabal, R. Arizaga, N. Cap, e. Grumel, M. Trivi, "Numerical model for dynamic speckle: an approach using the movement of the scatterers," Jornal of Optics A 5, S381-S385 (2003).

547. H. Rabal, N. Alamo, C. Criado, "Reflecting profiles and generalized holodiagrams," Optik 114, 370-375 (2003).

548. Ruiz, H. Rabal, S. Granieri, "The parity function in optical waves propagation," Optik 114, 207-212 (2003).

549. R. Braga, I. Dal Fabbro, F. Borem, G. Rabelo, R. Arizaga, H. Rabal, M. Trivi, "Assessment of seed's viability by laser speckle techniques," Byosystems Engineering 86, 287-294 (2003).

550. M. Muramatsu, P. Torroba, N. Cap, H. Rabal, "The projection diagram," Applied Optics 42, 4765-4771 (2003).

551. M. Fernández, A. Mavilio, H. Rabal, M. Trivi, "Characterization of viability of seeds by using dynamic speckles and difference histograms," Progress in pattern recognition speech and images analysis. Lecture Notes in Computer Science 2905, 329-333 (2003).

552. Cap, Ruiz, H. Rabal, "Refraction holodiagrams and Snell's law," Optik 114, 89-94 (2003).

553. H. Rabal, N. Cap, K. Gottschalk, M. Simon, "Holodiagrams in birrefringent media," Applied Optics 42, 5825-5830 (2003).

554. F. Videla, D. Schinca, J.O. Tocho, "An alternative method for concentration retrieval in differential optical absorption spectroscopy OAS atmospheric gas pollutant measurements," Applied Optics 42, 3653-3661 (2003).

555. Zalvidea, E. Sicre, "Optical systems under broadband illumination: analysis based on Wigner distribution function approach," Journal of Modern Optics 50, 1937- (2003).

556. Zalvidea, E. Sicre, "Ultrashort light pulse propagation in aberrant optical systems: spatial-temporal analysis," Journal of Optics A 5, 1- (2003).

557. R. Arizaga, R. Torroba, "Validation throuh a binary key code and a polarization sensitive digital technique," Optics Communications 215, 31-36 (2003).

558. R. Torroba, R. Henao, R. Arizaga, "Fully digital encryption technique," Optics Communications 221, 43-47 (2003).

559. G. Torchia, D. Schinca, N. Khaiduko, J.O. Tocho, "Influence of the electron-lattice coupling for Cr^{3+} ions in Nb^{5+} site into congruent co-doped $LiNbO_3:Cr^{3+}:ZnO$ crystal," Solid State Communications 127, 535-539 (2003).

560. L. Zunino, M. Garavaglia, "Fraunhofer diffraction by Cantor fractals with variable lacunarity," Journal of Modern Optics 50, 717-727 (2003).

561. L. Zunino, M. Garavaglia, "Moiré by fractal structures," Journal of Modern Optics 50, 1477-1486 (2003).

562. M. Domenech, E. Cantelar, G. Torchia, G. Lifante, F. Cussó, "Quantum efficiency and laser operation of $LiNbO_3$ Zn-diffused channel waveguides," Journal of Luminescence 102-103, 357-362 (2003).

563. Cortizo, A. Moreno Yeras, J. Lépore, M. Garavaglia, "Application of the structured illumination method to study the topography of the sole of the foot during a walk," Optics an Laser Engineering 40, 117-132 (2003).

564. D. Zalvidea, R. Duchowicz, E. Sicre, "Temporal transformation of periodic incoherent ultrashort light pulses by chirped fiber gratings," Applied Optics 43, 3005-3009 (2004).

565. J. Mora, M. Andrés, R. Duchowicz, "Simple high-resolution wavelength monitor based on a fiber Bragg grating," Applied Optics 43, 744-749 (2004).

566. Arenas, S. Noriega, N. Russo, R. Duchowicz, "Estudio de las propiedades de un sensor de fibra óptica tipo Fabry-Perot," Anales de la Asociación Física Argentina 16, 78-81 (2004).

567. M. Gallardo, M. Raineri, M. Giuliani, C. Lagorio, S. Padilla, J.G. Reyna Almandos, "Láser de Xe neutro y multi-iónico UV-VIS-IR," Anales de la Asociación Física Argentina 16, 45-49 (2004).

568. J. Marañon Di Leo, S. Delnero, J.C. Ragaini, V. Sacchetto, C. Colosqui, J. Colman, U. Boldes, A. Scarabino, M. Rosato, J.G. Reyna Almandos, "Air concentrations of SO_2 and wind turbulence near La Plata Petrochemical Pole (Argentina)," Latin American Applied Research 34, 55-58 (2004).

569. Martínez Matos, G. Torchia, G. Bilmes, J.O. Tocho, "Photoacoustic characterization of transient defects in KDP crystals," Physical Review B; Condensed Matter 69, 224102-1-6 (2004).

570. D.J. Orzi, G. Bilmes, "Identification and measurement of dirt composition of manufactured steel plates by using laser-induced breakdown spectroscopy," Applied Spectroscopy 58, 1475-1480 (2004).

571. M. Tebaldi, N. Bolognini, L. Arizmendi, "Fixing of speckle distribution recorded in $LINBO_3$ crystals," Optics Communications 234, 43-51 (2004).

572. M. Tebaldi, L. Angel Toro, N. Bolognini, M. Trivi, "Speckle interferometric technique to assess soap films," Optics Communications 229, 29-37 (2004).

573. H.O. Di Rocco, J. Pomarico, L. Alvarez, C. Lanuse, L. Mottier, C. Saumell, R. Arizaga, H. Rabal, M. Trivi, "Speckle interferometry applied to pharmacodynamics studies: evaluation of parasite motility," European Biophysics Journal 33, 694-699 (2004).

574. H. Rabal, N. Cap, M. Trivi, "Longitudinal magnification drawing mistake," The Physics Teacher 42, 31-33 (2004).

575. Passoni, H. Rabal, L. Arizmendi, "Characterizing dynamic speckle time series with the Hurst coefficient concept," Fractals 12, 319-329 (2004).

576. Criado, N. Alamo, H. Rabal, "Refracting profiles and generalized holodiagrams," Optics Communications 236, 271-277 (2004).

577. L. Scaffardi, N. Pellegrini, O. de Sanctis, J.O. Tocho, "Sizing gold nanoparticles by optical extinction spectroscopy," Nanotechnology 16, 158-163 (2004).

578. Henao, R. Torroba, "Stokes parameters description for the DSPI polarization behavior," Journal of Holography and Speckle 1, 85-89 (2004).

579. Torchia, O. Martínez Matos, N. Khaidukov, J.O. Tocho, "Phonon coupling of Cr^{3+} ions in Cs2NaAIF6 crystals," Solid State Communications 130, 159-163 (2004).

580. L. Zunino, D. Pérez, M. Garavaglia, O. Rosso, "Characterization of laser propagation through turbulent media by quantifiers based on the wavelent transform," Fractals 12, 223-233 (2004).

581. Pérez, L. Zunino, M. Garavaglia, "Modeling turbulent wave-front phase as a fractional Brownian motion: a new approach," Journal of the Optical Society of America A 21, 1962-1969 (2004).

582. Pérez, L. Zunino, M. Garavaglia, "A fractional Brownian motion model for the turbulent refractive index in lightwave propagation," Optics Communications 242, 57-63 (2004).

583. P. Pérez Millán, A. Diez, M. Andrés, D. Zalvidea, R. Duchowicz, "Q-switched all-fiber laser based on magnetostriction modulation of a Bragg grating," Optics Express 13, (2005).

584. Zalvidea, N. Russo, R. Duchowicz, M. Delgado Pinar, A. Diez, J. Cruz, M. Andrés, "High repetition rate acoustic induced q-switched all fiber laser," Optics Communications 244, 315-319 (2005).

585. M. Gallardo, M. Raineri, M. Giuliani, C. Lagorio, S. Padilla, R. Sarmiento, J.G. Reyna Almandos, "New study on the XeVIII spectrum," Journal of Quantum and Radiative Transfer 95, 365-372 (2005).

586. Borges, F. Bredice, G. Cavalcanti, M. Gallardo, M. Raineri, J.G. Reyna Almandos, A.G. Trigueiros, "Extended analysis of the Ar VII spectrum in the vaccum ultraviolet," European Physical Journal D 36, 23-27 (2005).

587. O. Martínez Matos, G. Torchia, G. Bilmes, J.O. Tocho, H. Ranea Sandoval, "Onthe origin of the acoustic signals generated in KDP by pulsed uv laser excitation," Applied Physics B; Lasers and Optics 80, 535-539 (2005).

588. Sobral, M. Villagrán Muñiz, F. Bredice, "Energy balance in laser ablation of metal targets," Journal of Applied Physics 98, 083305-1-5 (2005).

589. Passoni, A. Dal Pra, H. Rabal, M. Trivi, R. Arizaga, "Dynamic speckle processing using wavelents based entropy," Optics Communications 246, 219-228 (2005).

590. Sendra, H. Rabal, R. Arizaga, M. Trivi, "Biospeckle images decomposition in temporary spectral bands," Optics Letters 30, 1641-1643 (2005).

591. B. Ruiz, N. Cap, H. Rabal, "Local correlation in dynamic speckle," Optics Communications 245, 103-111 (2005).

592. Rabelo, R. Braga, I. Dal Fabbro, M. Trivi, H. Rabal, R. Arizaga, "Laser speckle techniques in quality evaluation of orange fruits," Revista Brasileira de Engenharia Agrícola a Ambiental 9, 570-575 (2005).

593. Braga, G. Rabelo, L. Granato, E. Santos, J. Machado, R. Arizaga, H. Rabal, M. Trivi, "Detection of fungi in beans by the laser biospeckle technique," Biosystems Engineering 91, 465-469 (2005).

594. Federico, G. Kaufmann, G. Galizzi, H. Rabal, M. Trivi, R. Arizaga, "Simulation of dynamic speckle sequences and its application to the analysis of trandient processes," Optics Communications 260, 493-499 (2005).

595. Barrera, R. Henao, R. Torroba, "Optical encryption method using toroidal zone plates," Optics Communications 248, 35-40 (2005).

596. Torroba, "Digital reconstruction of grating distored images throuh virtual optics imaging systems," Optik 116, 71-74 (2005).

597. Cuadrado Laborde, P. Costanzo Caso, R. Duchowicz, E. Sicre, "Pulse propagation analysis based on the temporal Radon-Wigner transform," Optics Communications 266, 32-38 (2006).

598. Andersen, P. Perez Millán, S. Keiding, S. Agger, R. Duchowicz, M. Andrés, "All-fiber actively Q-switched Yb-doped laser," Optics Communications 260, 251-256 (2006).

599. Cuadrado Laborde, P. Costanzo Caso, R. Duchowicz, E. Sicre, "Temporal Talbot effect applied to determine dispersion parameters," Optics Communications 260, 528-534 (2006).

600. M. Raineri, M. Gallardo, J.G. Reyna Almandos, "Spectral analysis of the $4d^9 6s$ configuration in eight times ionized xenon, Xe IX," Journal of Quantitative and Radiative Transfer 102, 391-395 (2006).

601. G. Ratto, F. Videla, J.G. Reyna Almandos, R. Marona, D. Schinca, "Study of meteorological aspects and urban concentration of SO_2 in atmospheric environment of La Plata, Argentina," Environmental Monitoring and Assessment 121, 327-342 (2006).

602. F. Bredice, P. Ixtaina, J.C. Ragaini, J.G. Reyna Almandos, M. Garavaglia, "Estudios de la emisión de lámparas fluorescentes con perforaciones mediante pulsos láser en su recubrimiento," Luminotecnia 82, 66-68 (2006).

603. G. Bilmes, D.J. Orzi, O. Martínez, A. Lencina, "A real time method for surface cleanliness measurement," Applied Physics B; Lasers and Optics 82, 643-648 (2006).

604. M. Mesaros, O. Tarzi, R. Erra-Balsells, G. Bilmes, "The photophysics of some UV-MALDI matrices studied by using spectroscopic, photoacoustic and luminescence techniques," Chemical Physics Letters 426, 334- (2006).

605. Barrera, R. Henao, M. Tebaldi, N. Bolognini, R. Torroba, "Multiplexing encryption-decryption via lateral shifting of a random phase mask," Optics Communications 259, 532-536 (2006).

606. Barrera, R. Henao, M. Tebaldi, N. Bolognini, R. Torroba, "Multiplexing encrypted data by using polarized light," Optics Communications 260, 109-112 (2006).

607. Barrera, R. Henao, M. Tebaldi, N. Bolognini, R. Torroba, "Multiple image encryption using an aperture.modulated optical system," Optics Communications 261, 29-33 (2006).

608. Salazar, H. Lorduy, M. Tebaldi, N. Bolognini, "Analysis of reflection speckle holograms in a BSO crystal," Optics Communications 262, 157-163 (2006).

609. Lencina, P. Vaveliuk, B. Ruiz, M. Tebaldi, N. Bolognini, "Wave propagation and optical properties in slabs with light-induced free-charge-carriers," Physical Review E 74, 056614-056623 (2006).

610. F. Bredice, F. Borges, H. Sobral, M. Villagrán Muñiz, H.O. Di Rocco, G. Cristoforetti, S. Legnaioli, V. Palleschi, L. Pardini, A. Salvetti, E. Tognonni, "Evaluation of self-absorption coefficients of manganese emission lines in laser induced breakdown spectroscopy measurements," Spectrochimica Acta B 61, 1294-1303 (2006).

611. H. Rabal, N. Cap, M. Trivi, R. Arizaga, A. Federico, G. Galizzi, G. Kaufmann, "Speckle activity images based in the spatial variance of the phase," Applied Optics 45, 8733-8738 (2006).

612. Caussat, H. Rabal, M. Muramatsu, "The levitating Buddha: Constructing a realistic cylindrical mirror pseudo image," The Physics Teacher 44, 443-444 (2006).

613. F. Videla, D. Schinca, L. Scaffardi, "Sizing particles by backscattering spectroscopy and Fourier analysis," Optical Engineering 45, 048001-9 (2006).

614. Scaffardi, J.O. Tocho, "Size dependence of refractive index of gold nanoparticles," Nanotechnology 17, 1309-1315 (2006).

615. Barrera, R. Henao, R. Torroba, "Fault tolerance using toroidal zone plate encryption," Optics Communications 256, 489-494 (2006).

616. R. Arizaga, E. Grumel, N. Cap, M. Trivi, J. Amalvy, G. Yepes, Ricaurte, "Following the drying of spray paints using space and time contrast of dynamic speckle," Journal of Coatings Technology Research 3, 295-299 (2006).

617. Zunino, D. Pérez, M. Garavaglia, O. Rosso, "Characterization of laser propagation through turbulent media by quantifiers based on the wavelent transform: dynamic study," Physica A 364, 79-86 (2006).

618. D. Pérez, L. Zunino, M. Garavaglia, O. Rosso, "Wavelet entropy and fractional Brownian motion time series," Physica A 365, 282-288 (2006).

619. G. Torchia, C. Méndez, D. Delgado, J.R. Vázquez de Aldana, I. Arias, L. Roso, "Spatial modulation of linear and quadratic susceptibilities in Lithium Niobate crystals by using femtosecond laser pulses," Ferroelectrics 333, 151-156 (2006).

620. C. Cuadrado Laborde, P. Costanzo Caso, R. Duchowicz, E. Sicre, "Conformación de pulsos aislados energéticos y trenes periódicos de pulsos de muy corta duración," Innovación Tecnológica 28, 82-84 (2006).

621. Rosales, J. Pedroni, J.O. Tocho, "Global spectral UV-radiometer with automatic shadow band ," Photochemistry and Photobiology 82, 844-849 (2006).

Más de 300 publicaciones en Actas de Congresos y Reuniones Científicas / More of 300 publications in Proceedings.

Epílogo

Epílogo

A los 30 años de su creación, el CIOp transita un periodo de transición entre su período fundacional y la etapa de madurez y consolidación definitiva como institución líder en el desarrollo científico y tecnológico de la Óptica en el país y en la región.

Sin duda, la etapa fundacional estuvo regida por la impronta de los investigadores fundadores, la del Dr. Mario Garavaglia, creador del Centro y que fue Director durante 15 años y la del Dr. Mario Gallardo, que dirigió al mismo por otros 10 años.

Esta etapa de transición nos encuentra, como a todo adolescente, ante situaciones conflictivas, cuya evolución sin duda marcará el funcionamiento del Centro en su próxima etapa de madurez. Mencionaré como ejemplo sólo dos de ellas: la necesidad de contar con un marco legal sólido que rija la relación con las instituciones patrocinantes, el CONICET y la CIC y el envejecimiento de la planta de Investigadores, Profesionales de Apoyo y Técnicos.

Con respecto al primer aspecto, podemos decir que en el plano interno hemos avanzado sustancialmente en la definición de las estructuras de funcionamiento. Durante el año 2005 se discutió y se puso en marcha un nuevo Reglamento Interno que espera la aprobación definitiva de CONICET y de CIC. En sus puntos más importantes plantea la conversión del Consejo Asesor en Consejo Directivo, la participación de los becarios, considerados como Investigadores Jóvenes, y la elección del Director por concurso abierto. La aprobación de esta propuesta está supeditada a la firma de un nuevo Convenio entre CONICET y CIC que regule el funcionamiento de centros como el CIOp. El Convenio anterior, si bien vigente, no está siendo aplicado en su totalidad. Por ejemplo, el Comité de Representantes no funciona desde hace mucho tiempo. La firma de un nuevo convenio debe contemplar, entre otros aspectos, el establecimiento de políticas claras de transferencia al sector productivo. El CIOp está cumpliendo las últimas etapas del proceso investigación básica - investigación aplicada - transferencia, y está en condiciones de lograr las primeras transferencias efectivas mediante licenciamiento de patentes o del "know-how" de procesos enteramente desarrollados en el Centro.

El segundo punto al que me quiero referir en esta reseña institucional es el tema del envejecimiento del personal. El problema se puede dividir en dos partes, por un lado el plantel de investigadores, y por otro el grupo de personal de apoyo a la investigación, profesionales, técnicos, artesanos, etc. Hace 30 años el CIOp nació con seis investigadores, dos formados y cuatro recién graduados. Hoy día, con un Investigador Superior y ocho Investigadores Principales, el baricentro del plantel de 19 investigadores se desplaza hacia una edad cercana a los 60 años. De todas maneras, en este sector la situación no parece grave. La pirámide, aunque no bien formada, tiene una base sólida en los jóvenes investigadores que se han ido incorporando al Centro. Este proceso se ha reiniciado recientemente, luego de un periodo de casi 10 años de expulsión provocada por la reducida incorporación a las carreras de investigación o los bajos salarios. En el otro sector, la situación es muchísimo más complicada. El técnico o el artesano que se incorporó a los comienzos de la década de 1980, está a punto de jubilarse o ya lo ha hecho. En muchos casos no tuvimos la oportunidad de incorporar un aprendiz que se capacite y lo reemplace. En otros casos debemos actuar con celeridad para remediar una situación grave, especialmente para los centros como el CIOp donde la actividad experimental es primordial.

Lejos está de mi intención plantear un panorama pesimista al elegir dos situaciones conflictivas para cerrar este libro que se edita con el fin de mostrar nuestra alegría al alcanzar los 30 años de una institución en plena tarea fecunda. El objetivo fue por el contrario contribuir en lograr las mejores condiciones para que la institución se fortalezca y alcance la madurez mencionada al principio.

Jorge Tocho

Epilogue

At 30 years of its creation, CIOp is experiencing a transition period between its foundation and mature era where it has consolidated as a leading institution in the scientific and technological development of Optics both in our country and in the region.
The first period was leaded by its foundational researchers Dr. Mario Garavaglia (creator and Director for 15 years) and Dr. Mario Gallardo (Director for the following 10 years)
The current transition period faces conflict situations whose evolution will set the basis for the future of the Center. Just to mention two examples, there is, on one hand, a need for a strong legal framework within which the relation with our both sponsoring institutions (CONICET and CIC) is set clear, and on the other, the aging of the research, professional and technician staff. With respect to the first issue, we have made a big step when a new set of internal normatives defining the Center´s function structures was set up in 2005, awaiting definitive approval by CONICET and CIC, within the legal framework mentioned before. It establishes a Directive Advisory including young researchers and a conquest-selected Director. Besides, CIOp is due to get the first effective transfers of basic-applied research through patents and "know-how" of processes entirely developed at the Center.
The second issue concerns the lack of incorporation of young personnel to the established staff, in order to reduce the natural aging. In the case of the current 19 researchers, the "age center of gravity" is almost 60 years, although some junior researchers have recently joined CIOp, after more than 10 years of very limited incorporations due to low salaries. The case of Support Professionals and Technicians is even worse since no junior post could be filled and the old ones are almost retiring. This should be remediated immediately considering the important role they play in the experimental activities like those carried out at CIOp.
It is not my intention to show up a pessimistic panorama by choosing these conflictive situations to end this book, which has been done to share our happiness for these 30 years with you all. This epilogue is aimed to contribute to the development of better conditions for the strengthening and consolidating our Center.

Jorge Tocho

Esta publicación se terminó de imprimir
en septiembre de 2007 en

Paideia

47 y 115 (1900) La Plata
paideia@speedy.com.ar





30 años de investigación
en ciencia y tecnología

Dirección Postal: Camino Parque Centenario e/ 505 y 508
Manuel B. Gonnet La Plata
Dirección Postal: Casilla de Correo 124 B1902WAB La Plata Argentina
Teléfonos: + 54 221 484 2957 / 484 0280
Fax: +54 221 471 2771
e-mail: info@ciop.unlp.edu.ar / www.ciop.unlp.edu.ar